Gabi Ben-Dor
Oren Sadot
Ozer Igra *Editors*

30th International Symposium on Shock Waves 1

ISSW30 – Volume 1

Springer

Gabi Ben-Dor • Oren Sadot • Ozer Igra
Editors

30th International Symposium on Shock Waves 1

ISSW30 - Volume 1

Springer

Editors
Gabi Ben-Dor
Department of Mechanical Engineering
Ben Gurion University of the Negev
Beer Sheva, Israel

Oren Sadot
Department of Mechanical Engineering
Ben-Gurion University of the Negev
Beer Sheva, Israel

Ozer Igra
Department of Mechanical Engineering
Ben Gurion University of the Negev
Beer Sheva, Israel

ISBN 978-3-319-46211-0 ISBN 978-3-319-46213-4 (eBook)
DOI 10.1007/978-3-319-46213-4

Library of Congress Control Number: 2017936744

Printed on acid-free paper

This Springer imprint is published by Springer Nature
The registered company is Springer International Publishing AG
The registered company address is: Gewerbestrasse 11, 6330 Cham, Switzerland

Preface

The 30th International Symposium on Shock Waves (ISSW30) was held in Tel Aviv, Israel, during July 19–24, 2015. This was the 30th meeting in a series of symposia that started in Boston in 1957 (then under the name International Symposium on Shock Tubes). These symposia are held biennially in different countries in which active shock wave research is practiced. It is a central event for people active in different fields, such as physics, chemistry, fluid mechanics, gas dynamics, and applied mathematics, who are interested in shock wave-related phenomena. It was last held in Jerusalem, Israel, in 1979. The ISSW30 was held in Tel Aviv Dan Panorama Hotel. When comparing the topics and content of early symposia with the present one, one notices the significant developments that took place in the shock wave research. Hopefully these developments will continue.

A total of 370 abstracts were submitted for review by the deadline for abstracts submission. All submissions were reviewed by at least two members of the International Advisory Committee regarding standard and suitability for inclusion in the program. Out of the 370 submitted abstracts, 358 were accepted for either oral (314) or poster (44) presentations: 88 out of the 314 accepted abstracts for oral presentations and 8 out of the 44 accepted abstracts for poster presentations were submitted by graduate students. Unfortunately, by the time the meeting started 121 accepted papers were withdrawn (almost half of them from Russia, China, and India). The main reasons were lack of travel funds, security fears, and lack of clearance. Hence, the final program included 210 oral presentations and 27 poster presentations: 54 out of the 210 accepted abstracts for oral presentations and 4 out of the 27 accepted abstracts for poster presentations were presented by graduate students who competed on 12 student awards of 250 USD each that were donated by the International Shock Wave Institute (ISWI). The total number of the participants was about 300. In addition, there were 35 accompanying persons from overseas.

In summary, 9 invited presentations and 237 peer-reviewed contributed papers were presented. The Paul Vielle Memorial Lecture was delivered by Prof. Beric Skews on July 20, 2015, and the Irvine Israel Glass Memorial Lecture was delivered by Charles Needham on July 24, 2015. The other plenary lecturers were Prof. Riccardo Bonaza, Prof. Martin Brouillette, Prof. Ron Hanson, Prof. Achim Loske, Prof. Kazuo Maeno, Prof. Marcello Onofri, and Prof. K.P.J. Reddy.

The scientific program was complemented by three social events:

On the eve of the first day of the conference, a Welcome Gathering Cocktail, which included a full dinner, was held.

On the third day of the conference, only morning sessions were held; thereafter two different tours to attractive sites in Israel were offered. Participants and their accompanying persons could choose between a guided tour in Jerusalem and visit to various sites in the Galilee.

- The first option, the Jerusalem tour, included a visit to the Mount of Olives for a panoramic view of the city, a stop at Mount Zion to visit King David's tomb, the room of last supper, and the Dormition Abbey, and thereafter entering the old city and walking through the

Armenian and Jewish quarters to the recently excavated and restored Cardo, the main Roman road, and then proceeding to the Jewish Wailing Wall and continuing to the Christian Quarter. The next sightseeing was a walk along the Via Dolorosa and visiting the Church of the Holy Sepulcher. The last stop of this tour was entering the Tower of David to view the spectacular Sound and Light show there. Ending this long tour was a dinner at a restaurant viewing the Old City walls.

- The second option, the Galilee tour, started with a drive along the coastal plain to Caesarea, capital of Judea under the Roman occupation, seeing there the excavations of the Crusader city and the Roman port, aqueduct, and the amphitheater that has been restored to its former glory as a concert venue. The next stop was the biblical city Megiddo, identified as the site of Armageddon, visiting the archaeological excavations including the well-preserved water supply system, and thereafter driving to Haifa, the largest harbor of Israel, with a breath-taking panoramic view of Haifa Bay and the Western Galilee from the summit of Mount Carmel and a walking tour of the German Colony, and then continuing to Daliat El Carmel, and visiting this pictorial Druze village and finally ending with a dinner at the house of a local Druze family.

The third social activity, for all participants, was the banquet dinner. It was held in Beit Guvrin, an underground "city" where Jews were hiding from the conquering Roman legions 2000 years ago. The dinner was held in a huge cave whose ceiling collapsed.

In addition to the above mentioned three social events, three tours were held to the accompanying persons: to the Galilee; to Masada and Dead Sea; and to Haifa, Acre, and Rosh Hanikra.

The International Advisory Committee (IAC) decided during its meeting that ISSW32 in 2019 will be held in Singapore. The IAC also decided to add to the Paul Vielle and the Irvine Israel Glass Memorial Lectures a third memorial lecture, the Ray Stalker Memorial Lecture.

As decided by the IAC during ISSW29, the 31st International Symposium on Shock Waves (ISSW31) will be chaired by Prof. Akihiro Sasoh, in Nagoya, Japan, in July 2017.

Beer Sheva, Israel

Gabi Ben-Dor
Oren Sadot
Ozer Igra

Contents

Contributors

T. Adachi Saitama Institute of Technology, Saitama, Japan

N.A. Adams Institute of Aerodynamics and Fluid Mechanics, Technische Universität München, Garching, Germany

G.L. Agafonov Semenov Institute of Chemical Physics, Russian Academy of Sciences, Moscow, Russia

M.R. Ajith AMCD, MMG, Vikram Sarabhai Space Centre, Thiruvananthapuram, India

D.A. Aleksandrovsky Novosibirsk State University, Novosibirsk, Russia

V. Alekseev Kurchatov Institute, Moscow, Russia

N. Amen University of Southern California, Los Angeles, CA, USA

Julien Annaloro CNES—DCT/TV/PR, Toulouse Cedex, France

I. Anteby Nuclear Research Center—Negev, Beer-Sheva, Israel

R. Arun Kumar Indian Institute of Technology Madras (IITM), Chennai, Tamil Nadu, India

E. Arunan Department of Inorganic and Physical Chemistry, Indian Institute of Science, Bangalore, India

N. Balakrishnan Indian Institute of Science, Bangalore, India

P.K. Barhai Department of Applied Physics, Birla Institute of Technology, Ranchi, India

A. Beccantini CEA, Saclay, France

N. Bekka Laboratoire de Mécanique et d'Energétique d'Evry LMEE, Université d'Evry Val d'Essonne, Evry Cedex, France

Gabi Ben-Dor Pearlstone Center for Aeronautical Engineering Studies, Department of Mechanical Engineering, Faculty of Engineering Sciences, Ben-Gurion University of the Negev, Beer Sheva, Israel

M.K. Berezkina Ioffe Institute, St. Petersburg, Russia

Barbara Betti Dipartimento di Ingegneria Meccanica e Aerospaziale, University of Rome "La Sapienza", Rome, Italy

L. Biamino Aix-Marseille Université, CNRS-IUSTI UMR 7343, Marseille, France

I.V. Bilera Topchiev Institute of Petrochemical Synthesis, Russian Academy of Sciences, Moscow, Russia

G. Bivol Joint Institute for High Temperatures of RAS, Moscow, Russia

Tatiana Bobarykina Physics Department, Novosibirsk State University, Novosibirsk, Russia

Lab 5, Hypersonic Technologies, Khristianovich Institute of Theoretical and Applied Mechanics SB RAS, Novosibirsk, Russia

A. Boimel Boimel Consulting, Petah-Tiqwa, Israel

R. Bonazza Department of Engineering Physics, University of Wisconsin, Madison, WI, USA

Yevgeny A. Bondar Khristianovich Institute of Theoretical and Applied Mechanics SB RAS, Novosibirsk, Russia

Novosibirsk State University, Novosibirsk, Russia

Aldo Bonfiglioli Scuola di Ingegneria - Università degli Studi della Basilicata, Potenza, Italy

Marina Braun-Unkhoff German Aerospace Center (DLR), Institut für Verbrennung-stechnik, Stuttgart, Germany

Michael Brazhnikov ICP RAS, Moscow, Russia

M. Brouillette Department of Mechanical Engineering, Université de Sherbrooke, Sherbrooke, QC, Canada

P. Bulat ITMO University, St. Petersburg, Russia

Arnaud Bultel Laboratoire CORIA, Normandie Université - CNRS UMR 6614, St Etienne du Rouvray, France

Alexander Burcat Faculty of Aerospace Engineering, Technion—Israel Institute of Technology, Haifa, Israel

M.F. Campbell Mechanical Engineering Department, Stanford University, Stanford, CA, USA

Po-Shiung Chang Temasek Laboratories, National University of Singapore, Singapore, Singapore

P.H. Chang National University of Singapore, Singapore, Singapore

S.M. Chang School of Mechanical and Automotive Engineering, Kunsan National University, Jeonbuk, Korea

Xinyu Chang Institute of Mechanics, Chinese Academy of Sciences, Beijing, People's Republic of China

Arnab Chaudhuri Department of Aerospace Engineering and Engineering Mechanics, San Diego State University, San Diego, CA, USA

Lihong Chen Institute of Mechanics, Chinese Academy of Sciences, Beijing, People's Republic of China

Shuang Chen China Aerodynamics Research & Development Center, Mianyang, China

Zhihua Chen Key Laboratory of Transient Physics, Nanjing University of Science & Technology, Nanjing, China

K.M. Cheng College of Aerospace Engineering, Nanjing University of Aeronautics and Astronautics, Nanjing, China

M.V. Chernyshov Special Materials Corp., St. Petersburg, Russia

Peter the Great Saint Petersburg Polytechnic University, St. Petersburg, Russia

Arun Kumar Chinnappan Department of Aerospace Engineering, Indian Institute of Technology Kanpur, Kanpur, UP, India

Vladimir Chirkashenko Lab 5, Hypersonic Technologies, Khristianovich Institute of Theoretical and Applied Mechanics SB RAS, Novosibirsk, Russia

A. Chpoun Laboratoire de Mécanique et d'Energétique d'Evry LMEE, Université d'Evry Val d'Essonne, Evry Cedex, France

Kiran Chutkey CSIR-National Aerospace Laboratories, Experimental Aerodynamics Division, Bangalore, India

J. Daubech INERIS, Verneuil-en-Halatte, France

D.F. Davidson Mechanical Engineering Department, Stanford University, Stanford, CA, USA

Manoj Kumar K. Devaraj Center of Excellence in Hypersonics, Indian Institute of Science, Bangalore, India

Kunal V. Dhoke Department of Inorganic & Physical Chemistry, Indian Institute of Science, Bangalore, India

Alexander Dolgoborodov JIHT RAS, Moscow, Russia

NRNU MEPhI, Moscow, Russia

H.-S. Dou Faculty of Mechanical Engineering and Automation, Zhejiang Sci-Tech University, Hangzhou, Zhejiang Province, P.R. China

A. Drakon Joint Institute for High Temperatures of Russian Academy of Sciences, Moscow, Russia

Nils C. Dröske Institute of Aerospace Thermodynamics, University of Stuttgart, Stuttgart, Germany

Marie-Claude Druguet Aix-Marseille Univ., CNRS UMR 7343, Laboratoire IUSTI, Marseille, France

E. Dzieminska Sophia University, Tokyo, Japan

V. Eliasson University of Southern California, Los Angeles, CA, USA

University of California, San Diego, La Jolla, CA, USA

V. Emelyanov Baltic State Technical University, St. Petersburg, Russia

A. Eremin Joint Institute for High Temperatures of Russian Academy of Sciences, Moscow, Russia

Alexandr Erofeev Ioffe Institute, St. Petersburg, Russian Federation

J. Falcovitz Institute of Mathematics, The Hebrew University of Jerusalem, Jerusalem, Israel

V.R. Feldgun National Building Research Institute, Technion, Haifa, Israel

M. Foglar Department of Concrete and Masonry Structures, Faculty of Civil Engineering, Czech Technical University in Prague, Prague, Czech Republic

Felix J. Förster Institute of Aerospace Thermodynamics, University of Stuttgart, Stuttgart, Germany

Yang Furong China Aerodynamics Research & Development Center, Mianyang, China

Wenzhi Gao Department of Modern Mechanics, University of Science and Technology of China, Hefei, Anhui, People's Republic of China

School of Mechanical Engineering, Hefei University of Technology, Hefei, Anhui, People's Republic of China

C. Génin Institute of Space Propulsion, German Aerospace Center (DLR), Lampoldshausen, Germany

A. Georges-Picot CORIA – UMR 6614 CNRS – INSA Rouen and Normandie Université, Saint-Étienne-du-Rouvray, France

Meital Geva Department of Mechanical Engineering, Faculty of Engineering Sciences, Pearlstone Center for Aeronautical Engineering Studies, Ben-Gurion University of the Negev, Beer Sheva, Israel

M. Giglmaier Institute of Aerodynamics and Fluid Mechanics, Technische Universität München, Garching, Germany

S. Golovastov Joint Institute for High Temperatures of RAS, Moscow, Russia

V. Golub Joint Institute for High Temperatures of RAS, Moscow, Russia

N.K. Gopinath Centre of Excellence in Hypersonics, Indian Institute of Science, Bangalore, India

A. Govinda Department of Aerospace Engineering, Indian Institute of Science, Bangalore, India

I. Graur Aix Marseille University, IUSTI UMR CRNS 7343, Marseille, France

B.J. Gray Flow Research Unit, University of the Witwatersrand, Johannesburg, South Africa

J. Grune Pro-Science GmbH, Ettlingen, Germany

S. Gruntman Protective Technologies Research and Development Center, Faculty of Engineering Sciences, Ben-Gurion University of the Negev, Beer-Sheva, Israel

Shuaitao Guo Department of Modern Mechanics, University of Science and Technology of China, Hefei, Anhui, People's Republic of China

Li Guojun School of Energy and Power Engineering, Xi'an Jiaotong University, Xi'an, Shanxi, People's Republic of China

E. Gurentsov Joint Institute for High Temperatures of Russian Academy of Sciences, Moscow, Russia

Abdellah Hadjadj CORIA—UMR 6614 CNRS—INSA Rouen and Normandie Université, Saint-É tienne-du-Rouvray, France

R. Hajek Department of Concrete and Masonry Structures, Faculty of Civil Engineering, Czech Technical University in Prague, Prague, Czech Republic

R.E. Hall Flow Research Unit, University of the Witwatersrand, Johannesburg, South Africa

Wenhu Han Key Laboratory of Light-Duty Gas-Turbine, Institute of Engineering Thermophysics, Chinese Academy of Sciences, Beijing, China

R.K. Hanson Mechanical Engineering Department, Stanford University, Stanford, CA, USA

T. Hartmann NUMERICS GmbH, Petershausen, Germany

A.K. Hayashi Aoyama Gakuin University, Kanagawa, Japan

Andrew J. Higgins Department of Mechanical Engineering, McGill University, Montréal, Canada

Koju Hiraki Kyushu Institute of Technology, Kitakyushu, Fukuoka, Japan

M.T. Ho Aix Marseille University, IUSTI UMR CRNS 7343, Marseille, France

S.J. Hooseria Flow Research Unit, University of the Witwatersrand, Johannesburg, Johannesburg, South Africa

L. Houas Aix-Marseille Université, CNRS-IUSTI UMR 7343, Marseille, France

Jiang Hua Hypervelocity Aerodynamics Institute, China Aerodynamics Research and Development Center, Mianyang, People's Republic of China

Huang Jun Hypervelocity Aerodynamics Institute, China Aerodynamics Research and Development Center, Mianyang, People's Republic of China

Dan Igra RAFAEL, Aerodynamics Group, Rafael, Israel

Ozer Igra Professor Emeritus, Department of Mechanical Engineering, Ben Gurion University of the Negev, Beer Sheva, Israel

A. Iwakawa Department of Aerospace Engineering, Nagoya University, Nagoya, Japan

S. Jack Institute of Aerodynamics and Flow Technology, German Aerospace Center (DLR), Braunschweig, Germany

Gopalan Jagadeesh Department of Aerospace Engineering, Indian Institute of Science, Bangalore, India

S. Jallais Air Liquide CRPS, Les Loges en Josas, France

C.M. Jenkins Air Force Research Laboratory, Eglin AFB, FL, USA

H. Jeon University of Southern California, Los Angeles, CA, USA

Man Chul Jeong Department of Mechanical and Aerospace Engineering, Seoul National University, Gwanakgu, Seoul, Republic of Korea

In-Seuck Jeung Department of Mechanical and Aerospace Engineering, Seoul National University, Gwanakgu, Seoul, Republic of Korea

Yinan Jia Institute of Mechanics, CAS, Beijing, People's Republic of China

Z Jiang LHD, Institute of Mechanics, Chinese Academy of Sciences, Beijing, People's Republic of China

Liu Jichun Hypervelocity Aerodynamics Institute, China Aerodynamics Research and Development Center, Mianyang, People's Republic of China

Liu Jie Nanjing University of Science and Technology, Nanjing, China

G. Jourdan Aix-Marseille Université, CNRS-IUSTI UMR 7343, Marseille, France

Y.S. Karinski National Building Research Institute, Technion, Haifa, Israel

S.K. Karthick Department of Aerospace Engineering, Indian Institute of Science, Bangalore, India

S.S. Katsnelson Khristianovich Institute of Theoretical and Applied Mechanics SB RAS, Novosibirsk, Russia

Novosibirsk State University, Novosibirsk, Russia

Abhishek Khatta Department of Aerospace Engineering, Indian Institute of Science, Bangalore, India

Boo-Cheong Khoo Department of Mechanical Engineering, National University of Singapore, Singapore, Singapore

Temasek Laboratories, National University of Singapore, Singapore, Singapore

T. Kikuchi Nihon University, Tokyo, Japan

S.A. Kinelovskii Lavrentyev Institute of Hydrodynamics, Siberian Branch RAS, Novosibirsk, Russia

Novosibirsk State University, Novosibirsk, Russia

Vladimir Kirilenko ICP RAS, Moscow, Russia

Harald Kleine SEIT, University of New South Wales, Canberra, ACT, Australia

S. Kobayashi Saitama Institute of Technology, Saitama, Japan

A.A. Kokhanchik Novosibirsk State University, Novosibirsk, Russia

Khristianovich Institute of Theoretical and Applied Mechanics SB RAS, Novosibirsk, Russia

Y.A. Kolbanovsky Topchiev Institute of Petrochemical Synthesis, Russian Academy of Sciences, Moscow, Russia

Wenjun Kong Key Laboratory of Light-Duty Gas-Turbine, Institute of Engineering Thermophysics, Chinese Academy of Sciences, Beijing, China

L. Kosarev Israel Aerospace Industries, Directorate for Research and Development, Engineering Division, CFD R&D Dept. Corporate Research Center – Computerized Systems Branch, Lod, Israel

I.V. Krassovskaya Ioffe Institute, St. Petersburg, Russia

M. Krüger-Sprengel Institute of Aerodynamics and Fluid Mechanics, Technische Universität München, Garching, Germany

Venkat Rao Kulkarni Department of Aerospace Engineering, Indian Institute of Science, Bangalore, India

Manoj Kumar Centre of Excellence in Hypersonics, Indian Institute of Science, Bangalore, India

Rakesh Kumar Department of Aerospace Engineering, Indian Institute of Technology Kanpur, Kanpur, UP, India

H.K.T. Kumara Center of Applied Research and Nano-Technology, Siddaganga Institute of Technology, Tumkur, India

O. Kunova Saint Petersburg State University, St. Petersburg, Russia

M. Kuznetsov Institute for Nuclear and Energy Technologies, Karlsruhe Institute of Technology, Eggenstein-Leopoldshafen, Germany

Tatiana Lapushkina Ioffe Institute, St. Petersburg, Russian Federation

Sangyoon Lee Department of Mechanical and Aerospace Engineering, Seoul National University, Gwanakgu, Seoul, Republic of Korea

Hyoung Jin Lee PGM R&D Lab., LIG Nex1 Co., Ltd., Seongnamsi, Gyeonggido, Republic of Korea

Jong Kook Lee Agency for Defense Development, Daejeon, Yuseong-Gu, Republic of Korea

Y. Lefler Soreq Nuclear Research Center, Yavne, Israel

L. Leger Institut ICARE/CNRS, Orléans, France

Li Lei Department of Mechanical Engineering, National University of Singapore, Singapore, Singapore

A. Lelyakin Intitute for Energy and Nuclear Energy, Karlsruhe Institute of Technology, Eggenstein-Leopoldshafen, Germany

D. Leriche DGA Techniques navales, Toulon, France

V.A. Levin Institute of Mechanics, M.V. Lomonosov Moscow State University, Moscow, Russia

Institute of Automation and Control Processes, Far Eastern Branch of RAS, Vladivostok, Russia

Jiun-Ming Li Temasek Laboratories, National University of Singapore, Singapore, Singapore

Zhufei Li Department of Modern Mechanics, University of Science and Technology of China, Hefei, Anhui, People's Republic of China

J. Li National University of Singapore, Singapore, Singapore

L. Li National University of Singapore, Singapore, Singapore

Jianling Li School of Power and Energy, Northwestern Polytechnical University, Shaanxi, China

K.S. Lim National University of Singapore, Singapore, Singapore

A. Lipshtat Soreq Nuclear Research Center, Yavne, Israel

Y. Liu LHD, Institute of Mechanics, Chinese Academy of Sciences, Beijing, People's Republic of China

Yan Liu Department of Mechanics and Engineering Science, Center for Combustion and Propulsion, CAPT and SKLTCS, College of Engineering, Peking University, Beijing, China

Y.F. Liu The State Key Laboratory of High Temperature Gasdynamics, Institute of Mechanics, CAS, Beijing, China

Zhang Long China Aerodynamics Research & Development Center, Mianyang, China

J.-C. Loraud Aix-Marseille Université, CNRS-IUSTI UMR 7343, Marseille, France

Achim M. Loske Centro de Física Aplicada y Tecnología Avanzada, Universidad Nacional Autónoma de México, Querétaro, Mexico

Hongbo Lu Chinese Academy of Aerospace Aerodynamics, Beijing, China

Xisheng Luo Advanced Propulsion Laboratory, Department of Modern Mechanics, University of Science and Technology of China, Hefei, China

T. Machida Aoyama Gakuin University, Kanagawa, Japan

K. Maeno National Institute of Technology, Kisarazu College, Professor Emeritus of Chiba University, Kisarazu, Chiba, Japan

K.K. Maevskii Lavrentyev Institute of Hydrodynamics, Siberian Branch RAS, Novosibirsk, Russia

Novosibirsk State University, Novosibirsk, Russia

D. Roy Mahapatra Department of Aerospace Engineering, Indian Institute of Science, Bangalore, India

G. Malaikannan Department of Aerospace Engineering, Indian Institute of Technology Kanpur, Kanpur, UP, India

C. Manisankar CSIR-National Aerospace Laboratories, Experimental Aerodynamics Division, Bangalore, India

I.S. Manuylovich Institute of Mechanics, M.V. Lomonosov Moscow State University, Moscow, Russia

C. Mariani Aix-Marseille Université, CNRS-IUSTI UMR 7343, Marseille, France

V.V. Markov Steklov Mathematical Institute of RAS, Moscow, Russia

Emanuele Martelli Dipartimento di Ingegneria Industriale e dell'Informazione, II University of Naples, Aversa, Italy

S.N. Martyushov The Moscow Aviation Institute, National Research University, Moscow, Russia

H. Saldivar Massimi Department of Mechanical Engineering, The Hong Kong Polytechnic University, Kowloon, Hong Kong SAR

I. Matsukov Kurchatov Institute, Moscow, Russia

T.J. McIntyre Centre for Hypersonics, School of Mathematics and Physics, The University of Queensland, Brisbane, QLD, Australia

Xiaocheng Mi Department of Mechanical Engineering, McGill University, Montréal, Canada

E. Mikheyeva Joint Institute for High Temperatures of Russian Academy of Sciences, Moscow, Russia
Bauman Moscow State Technical University, Moscow, Russia

V.A. Miller Mechanical Engineering Department, Stanford University, Stanford, CA, USA

J. Misawa Toyota Motor Corporation, Toyoda-shi, Aichi, Japan

R.G. Morgan Centre for Hypersonics, School of Mechanical & Mining Engineering, The University of Queensland, Brisbane, QLD, Australia

Ragini Mukherjee Centre of Excellence in Hypersonics, Indian Institute of Science, Bangalore, India

Ch. Mundt Institute of Thermodynamics, University of the Federal Armed Forces Munich, Neubiberg, Germany

T.M. Muruganandam Aerospace Engineering Department, Indian Institute of Technology Madras (IITM), Chennai, India

E. Nagnibeda Saint Petersburg State University, St. Petersburg, Russia

Francesco Nasuti Dipartimento di Ingegneria Meccanica e Aerospaziale, University of Rome "La Sapienza", Rome, Italy

Suraj Natarajan Department of Aerospace Engineering, Laboratory for Hypersonic and Shock Wave Research, Indian Institute of Science, Bangalore, India

Charles Needham Applied Research Associates Inc., Southwest Division, Albuquerque, NM, USA

L. Nel Aeronautic Systems Competency, Defence Peace Safety and Security, Council for Scientific and Industrial Research, Pretoria, South Africa

Flow Research Unit, University of the Witwatersrand, Johannesburg, Johannesburg, South Africa

M. Nguyen University of Southern California, Los Angeles, CA, USA

Van Bo Nguyen Temasek Laboratories, National University of Singapore, Singapore, Singapore

Satoshi Nonaka Japan Aerospace Exploration Agency (JAXA), ISAS, Sagamihara, Kanagawa, Japan

Erna Olchansky Faculty of Aerospace Engineering, Technion—Israel Institute of Technology, Haifa, Israel

Pierre Omaly CNES—DCT/TV/PR, Toulouse Cedex, France

M.G. Omang Institute of Theoretical Astrophysics, University of Oslo, Blindern, Oslo, Norway

Norwegian Defence Estates Agency, Oslo, Norway

S.N. Omkar Department of Aerospace Engineering, Indian Institute of Science, Bangalore, India

Marcello Onofri Dipartimento di Ingegneria Meccanica e Aerospaziale, University of Rome "La Sapienza", Rome, Italy

Renato Paciorri Dipartimento di Ingegneria Meccanica e Aerospaziale, Università di Roma "La Sapienza", Rome, Italy

R.T. Paton Flow Research Unit, University of the Witwatersrand, Johannesburg, South Africa

M. Picard Department of Mechanical Engineering, Université de Sherbrooke, Sherbrooke, QC, Canada

E. Pimonov Khristianovich Institute of Theoretical and Applied Mechanics SB RAS, Novosibirsk, Russia

A. Piquet CORIA – UMR 6614 CNRS – INSA Rouen and Normandie Université, Saint-Étienne-du-Rouvray, France

S. Pistinner Soreq Nuclear Research Center, Yavne, Israel

J.-S. Plante Department of Mechanical Engineering, Université de Sherbrooke, Sherbrooke, QC, Canada

Sergei Poniaev Ioffe Institute, St. Petersburg, Russian Federation

H. Porat Centre for Hypersonics, School of Mechanical & Mining Engineering, The University of Queensland, Brisbane, QLD, Australia

G.A. Pozdnyakov Khristianovich Institute of Theoretical and Applied Mechanics SB RAS, Novosibirsk, Russia

Novosibirsk State University, Novosibirsk, Russia

S. Manoj Prabakar Aerospace Engineering Department, Indian Institute of Technology Madras (IITM), Chennai, India

Federico Alzamori Previtali Mechanical Engineering, McGill University, Montreal, QC, Canada

K.S. Priyamvada Centre of Excellence in Hypersonics, Indian Institute of Science, Bangalore, India

Anupam Purwar Centre of Excellence in Hypersonics, Indian Institute of Science, Bangalore, India

J.F. Quaatz Institute of Aerodynamics and Fluid Mechanics, Technische Universität München, Garching, Germany

G. Rajesh Indian Institute of Technology Madras (IITM), Chennai, Tamil Nadu, India

O. Ram Department of Mechanical Engineering, Protective Technologies Research and Development Center, Faculty of Engineering Sciences, Pearlstone Center for Aeronautical Engineering Studies, Ben-Gurion University of the Negev, Beer Sheva, Israel

D. Rancourt Department of Mechanical Engineering, Université de Sherbrooke, Sherbrooke, QC, Canada

Srisha M.V. Rao Department of Aerospace Engineering, Indian Institute of Science, Bangalore, India

K. Subba Rao Haldipur Hydraulieks, Bangalore, India

Ranjith Ravichandran Laboratory for Hypersonic and Shock Wave Research, Department of Aerospace Engineering, Indian Institute of Science, Bangalore, India

K.P.J. Reddy Department of Aerospace Engineering, Indian Institute of Science, Bangalore, India

B. Yu. Rezunkov Laboratory of Laser-Physical Investigations, Institute of Optoelectronic Instrument Engineering, Sosnovyi Bor, Russia

R.C. Ripley Martec Limited, Halifax, NS, Canada

CNRS – IUSTI UMR 7343, Marseille, France

V. Rodriguez Aix-Marseille Université, CNRS–IUSTI UMR 7343, Marseille, France

Zhao Rongjuan Hypervelocity Aerodynamics Institute, China Aerodynamics Research and Development Center, Mianyang, People's Republic of China

E. Rottenkolber NUMERICS GmbH, Petershausen, Germany

S. Pradeep Roy SandI, Bangalore, India

S.D. Ryan Martec Limited, Halifax, NS, Canada

S. Sadot Department of Mechanical Engineering, Faculty of Engineering Sciences, Pearlstone Center for Aeronautical Engineering Studies, Ben-Gurion University of the Negev, Beer Sheva, Israel

Oren Sadot Mechanical Engineering Department, Faculty of Engineering Sciences, Ben Gurion University of the Negev, Beer Sheva, ISRAEL

A. Sakurai Tokyo Denki University, Tokyo, Japan

A. Sasoh Department of Aerospace Engineering, Nagoya University, Nagoya, Japan

CNRS – IUSTI UMR 7343, Marseille, France

A. Sakurai Tokyo Denki University, Tokyo, Japan

R. Saurel Aix-Marseille Université, CNRS–IUSTI UMR 7343, Marseille, France

F. Seiler Retired from the French-German Research Institute of Saint-Louis (ISL), Saint-Louis, France

Institute of Fluid Mechanics (ISTM), Karlsruhe Institute of Technology (KIT), Karlsruhe, Germany

Noriaki Sekine Fuji Techno Service Co. Ltd., Ohta, Japan

M. Sellam Laboratoire de Mécanique et d'Energétique d'Evry LMEE, Université d'Evry Val d'Essonne, Evry Cedex, France

H. Oertel Sen Retired from the French-German Research Institute of Saint-Louis (ISL), Saint-Louis, France

S. Seror Israel Aerospace Industries, Directorate for Research and Development, Engineering Division, CFD R&D Dept. Corporate Research Center – Computerized Systems Branch, Lod, Israel

N. Sharath Department of Aerospace Engineering, Indian Institute of Science, Bangalore, India

H. Shen Department of Mechanical Engineering, The Hong Kong Polytechnic University, Kowloon, Hong Kong SAR

C. Sheridan University of New South Wales, Canberra, ACT, Australia

Arseny Shevchenko NRNU MEPhI, Moscow, Russia

Liu Shiran Hypervelocity Aerodynamics Institute, China Aerodynamics Research and Development Center, Mianyang, PR China

Georgy Shoev Novosibirsk State University, Novosibirsk, Russia

Khristianovich Institute of Theoretical and Applied Mechanics SB RAS, Novosibirsk, Russia

M.V. Silnikov Special Materials Corp., St. Petersburg, Russia

Peter the Great Saint Petersburg Polytechnic University, St. Petersburg, Russia

Yogendra Singh Center of Excellence in Hypersonics, Indian Institute of Science, Bangalore, India

M. Kiran Singh Inorganic and Physical Chemistry Department, Indian Institute of Science, Bangalore, India

T.G. Sitharam Department of Civil Engineering, Indian Institute of Science, Bangalore, India

B.W. Skews Flow Research Unit, University of the Witwatersrand, Johannesburg, South Africa

V.N. Smirnov Semenov Institute of Chemical Physics, Russian Academy of Sciences, Moscow, Russia

Vineet Soni Normandie Université, CNRS-University & INSA of Rouen (CORIA-UMR 6614), Rouen, France

Chimakurthy Srikanth IITM and Scientist at Defence Research and Development Laboratory, Hyderabad, India

J. Srulijes Retired from the French-German Research Institute of Saint-Louis (ISL), Saint-Louis, France

R. Stark Institute of Space Propulsion, German Aerospace Center (DLR), Lampoldshausen, Germany

M. Starkloff Institute of Thermodynamics, University of the Federal Armed Forces Munich, Neubiberg, Germany

Ulla Steil German Aerospace Center (DLR), Institut für Verbrennungstechnik, Stuttgart, Germany

C. Strand Mechanical Engineering Department, Stanford University, Stanford, CA, USA

Tie Su China Aerodynamics Research & Development Center, Mianyang, China

P. Suriyanarayanan Department of Aerospace Engineering, Indian Institute of Science, Bangalore, India

Kazuyoshi Takayama Emeritus Tohoku University, Sendai, Japan

T. Tamba Department of Aerospace Engineering, Nagoya University, Nagoya, Japan

Teo Chiang Juay Department of Mechanical Engineering, National University of Singapore, Singapore, Singapore

A.M. Tereza Semenov Institute of Chemical Physics, Russian Academy of Sciences, Moscow, Russia

Victor Teselkin ICP RAS, Moscow, Russia

Nimesh Thakor Center of Excellence in Hypersonics, Indian Institute of Science, Bangalore, India

Ruchi Thakur Department of Aerospace Engineering, Indian Institute of Science, Bangalore, India

X.A. Tian College of Aerospace Engineering, Nanjing University of Aeronautics and Astronautics, Nanjing, China

Evgeny Timofeev Mechanical Engineering, McGill University, Montreal, QC, Canada

M. Yu. Timokhin Novosibirsk State University, Novosibirsk, Russia
Moscow State University, Moscow, Russia

R. Tosello DGA Techniques navales, Toulon, France

S. Trélat IRSN, Fontenay-aux-Roses, France

V.A. Troutman Mechanical Engineering Department, Stanford University, Stanford, CA, USA

J.K. Trulsen Institute of Theoretical Astrophysics, University of Oslo,
Blindern, Oslo, Norway

N.M. Tuan Department of Aerospace Engineering, Nagoya University, Nagoya, Japan

A. Tulgestke Mechanical Engineering Department, Stanford University, Stanford, CA, USA

V.N. Uskov Baltic State Technical University, St. Petersburg, Russia

Albin Varghese Department of Aerospace Engineering, Indian Institute of Science, Bangalore, India

C. Venkateswaran AMCD, MMG, Vikram Sarabhai Space Centre, Thiruvananthapuram, India

T. Venketeswaran HWMD, MMG, Vikram Sarabhai Space Centre, Thiruvananthapuram, India

S.B. Verma CSIR-National Aerospace Laboratories, Experimental Aerodynamics Division, Bangalore, India

V. Vignesh Department of Aerospace Engineering, Indian Institute of Science, Bangalore, India

M. Viji CSIR-National Aerospace Laboratories, Experimental Aerodynamics Division, Bangalore, India

P. Vivek Department of Civil Engineering, Indian Institute of Science, Bangalore, India

Jayaram Vishakantaiah Shock Induced Materials Chemistry Lab, Solid State and Structural Chemistry Unit, Indian Institute of Science, Bangalore, India

P.A. Vlasov Semenov Institute of Chemical Physics, Russian Academy of Sciences, Moscow, Russia

National Nuclear Research University "MEPhI", Moscow, Russia

K. Volkov Centre for Fire and Explosion Studies, Kingston University, London, UK

E. Vyazmina Air Liquide CRPS, Les Loges en Josas, France

Q. Wan University of Southern California, Los Angeles, CA, USA

Chun Wang State Key Laboratory of High Temperature Gas Dynamics, Institute of Mechanics, Chinese Academy of Sciences, Beijing, People's Republic of China

Y. Wang LHD, Institute of Mechanics, Chinese Academy of Sciences, Beijing, People's Republic of China

C.P. Wang College of Aerospace Engineering, Nanjing University of Aeronautics and Astronautics, Nanjing, China

S. Wang Mechanical Engineering Department, Stanford University, Stanford, CA, USA

Jianping Wang Department of Mechanics and Engineering Science, Center for Combustion and Propulsion, CAPT and SKLTCS, College of Engineering, Peking University, Beijing, China

Bernhard Weigand Institute of Aerospace Thermodynamics, University of Stuttgart, Stuttgart, Germany

C.Y. Wen Department of Mechanical Engineering, The Hong Kong Polytechnic University, Kowloon, Hong Kong SAR

M.S. Whalley Flow Research Unit, University of the Witwatersrand, Johannesburg, South Africa

K. Willcox Department of Aeronautics and Astronautics, Massachusetts Institute of Technology, Cambridge, MA, USA

Jens von Wolfersdorf Institute of Aerospace Thermodynamics, University of Stuttgart, Stuttgart, Germany

Gaoxiang Xiang State Key Laboratory of High Temperature Gas Dynamics, Institute of Mechanics, Chinese Academy of Sciences, Beijing, People's Republic of China

F.S. Xiao Department of Modern Mechanics, University of Science and Technology of China, Hefei, Anhui, China

Yabin Xiao Institute of Mechanics, Chinese Academy of Sciences, Beijing, People's Republic of China

Xiao Xu Institute of Mechanics, CAS, Beijing, People's Republic of China

A. Yaffe Ben-Gurion University of the Negev, Beer Sheva, Israel

M. Yakovchuck Baltic State Technical University, St Petersburg, Russia

Vladimir Yakovlev Lab 5, Hypersonic Technologies, Khristianovich Institute of Theoretical and Applied Mechanics SB RAS, Novosibirsk, Russia

J. Yanez Institute for Nuclear and Energy Technologies, Karlsruhe Institute of Technology, Eggenstein-Leopoldshafen, Germany

Jianting Yang Department of Modern Mechanics, University of Science and Technology of China, Hefei, China

Jianjun Yang Research & Development Center, China Academy of Launch Vehicle Technology, Beijing, China

Yang Yang Research & Development Center, China Academy of Launch Vehicle Technology, Beijing, China

Jiming Yang Department of Modern Mechanics, University of Science and Technology of China, Hefei, Anhui, People's Republic of China

D.Z. Yankelevsky Faculty of Civil and Environmental Engineering, Technion, Haifa, Israel

Hee Yoon Department of Mechanical and Aerospace Engineering, Seoul National University, Gwanakgu, Seoul, Republic of Korea

A. Yoshinaka Defence Research and Development Canada, Medicine Hat, AB, Canada

J. Young University of New South Wales, Canberra, ACT, Australia

C. Yuan LHD, Institute of Mechanics, Chinese Academy of Sciences, Beijing, People's Republic of China

Lianjie Yue Institute of Mechanics, Chinese Academy of Sciences, Beijing, People's Republic of China

Wu Yungang China Aerodynamics Research & Development Center, Mianyang, China

Zhigang Zhai Advanced Propulsion Laboratory, Department of Modern Mechanics, University of Science and Technology of China, Hefei, China

Enlai Zhang Department of Modern Mechanics, University of Science and Technology of China, Hefei, Anhui, People's Republic of China

Huanhao Zhang Key Laboratory of Transient Physics, Nanjing University of Science & Technology, Nanjing, China

F. Zhang Defence Research and Development Canada, Medicine Hat, AB, Canada

W. Zhang The State Key Laboratory of High Temperature Gasdynamics, Institute of Mechanics, CAS, Beijing, People's Republic of China

Fu Zhang Advanced Propulsion Laboratory, Department of Modern Mechanics, University of Science and Technology of China, Hefei, China

A. Zheltovodov Khristianovich Institute of Theoretical and Applied Mechanics SB RAS, Novosibirsk, Russia

School of Energy and Power Engineering, Xi'an Jiaotong University, Xi'an, Shanxi, People's Republic of China

Hypervelocity Aerodynamics Institute, China Aerodynamics Research and Development Center, Mianyang, People's Republic of China

Lv Zhiguo School of Energy and Power Engineering, Xi'an Jiaotong University, Xi'an, Shanxi, PR China

Hypervelocity Aerodynamics Institute, China Aerodynamics Research and Development Center, Mianyang, PR China

DU Zhong-hua Nanjing University of Science and Technology, Nanjing, China

Y. Zhu Mechanical Engineering Department, Stanford University, Stanford, CA, USA

Yujian Zhu Department of Modern Mechanics, University of Science and Technology of China, Hefei, China

T.A. Zhuravskaya Institute of Mechanics, M.V. Lomonosov Moscow State University, Moscow, Russia

V. Zmijanovic Institut ICARE/CNRS, Orléans, France

Part I

Invited Lectures

Studies of Shock Wave Reflections and Interactions (Paul Vieille Lecture)

B.W. Skews

Introduction

In the past, the Paul Vieille lecture has taken one of two formats: either the exposition on a single topic, such as by Ben-Dor in 2013, or an overview of a range of topics covering work from a single institution or group, such as that by Takayama in 2011. This paper is similar to the latter and will cover a range of experimental studies, some successful, some not, and some started and never completed, done over a number of years in what is now the Flow Research Unit at the University of Witwatersrand. The work covers a number of different aspects covering studies in liquids and deformation of solids using liquid shock waves, but the primary focus has been investigation of the behaviour of gas dynamic shock waves. In a number of cases, it has led to the development of unusual and unique experimental facilities and diagnostic techniques.

Project Topics

The material presented below will be listed by topic and only partially in order of historical development.

Shock Propagation in Bends

The bend studies were initiated resulting from an accidental explosion of two cases of high explosives in an underground gold mining complex, resulting in many fatalities, with an unexplained distribution of injuries, many of the worst remote from the blast. A preliminary study mimicking the tunnel geometry in a small test section attached to a shock tube showed the wave patterns to be exceptionally complex, Fig. 1 left, with multiple regular and Mach reflections, curved shear layers and vortex shedding. In an attempt to understand these, work was extended to shock diffraction around simple bends in a duct, [1] also shown in the figure, and then to needed further simplification to two-dimensional shock diffraction over a corner [2].

The first frame shows the tunnel layout and a schlieren test image. The next two frames are for a 75° bend with a supersonic post-shock flow at two different times. Interesting features are the curl in the slipstream which gets abandoned and the splaying out of the reflected shock in the vortex. The two images for a 90° corner indicate the effect of shock Mach number with the left image having subsonic post-shock flow and supersonic flow in the next image. Flows get complex at larger turning angles as shown in the last image with supersonic post-shock flow.

Interaction with Porous Media

There has been considerable interest in the interaction of shock waves with porous materials regarding their potential for blast amelioration. The early work by Gelfand and Gubin [3] demonstrated that amplification in pressure occurred on the supporting surface and using a heavy gas refraction model with a single transmitted shock explained the basic mechanism.

Subsequent work [4] showed that there were two waves, as shown in Fig. 2; a gas wave passing through the interstitial spaces and a compaction wave as the cells in the foam collapsed. The images on the left show the original specimen with cross-hatched markings and below it, during a test. This shows the compaction wave about a third of the way down the specimen with a slight deformation ahead of it due to the drag of the flow and recovery in front of it due to the constant pressure behind the wave reflected off the surface. The graph demonstrates the significant pressure amplification.

B.W. Skews (✉)
Flow Research Unit, University of the Witwatersrand, PO WITS 2050, Johannesburg, South Africa
e-mail: Beric.Skews@wits.ac.za

G. Ben-Dor et al. (eds.), *30th International Symposium on Shock Waves 1*, DOI 10.1007/978-3-319-46213-4_1

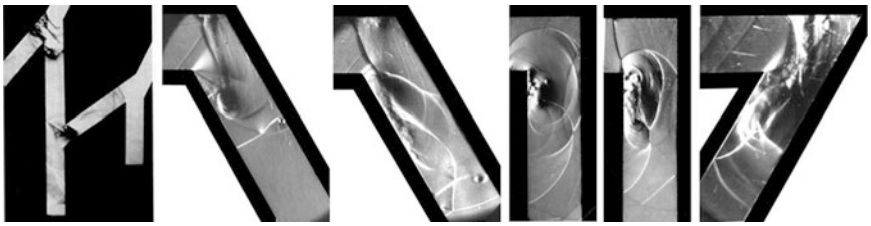

Fig. 1 Shock propagation in a tunnel system and around bends

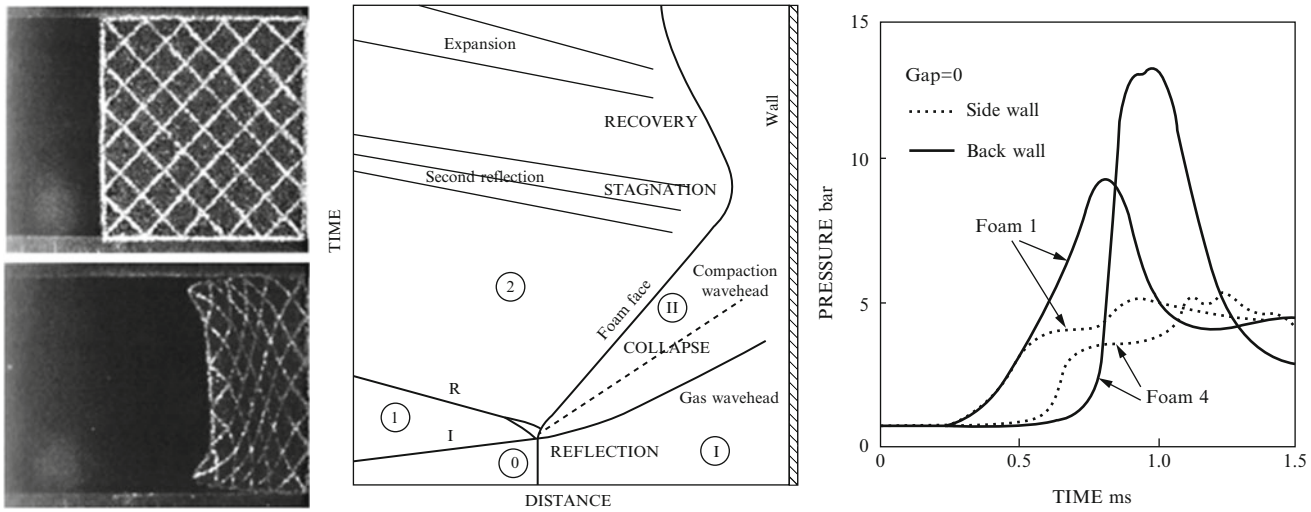

Fig. 2 Shock impact on a porous foam block

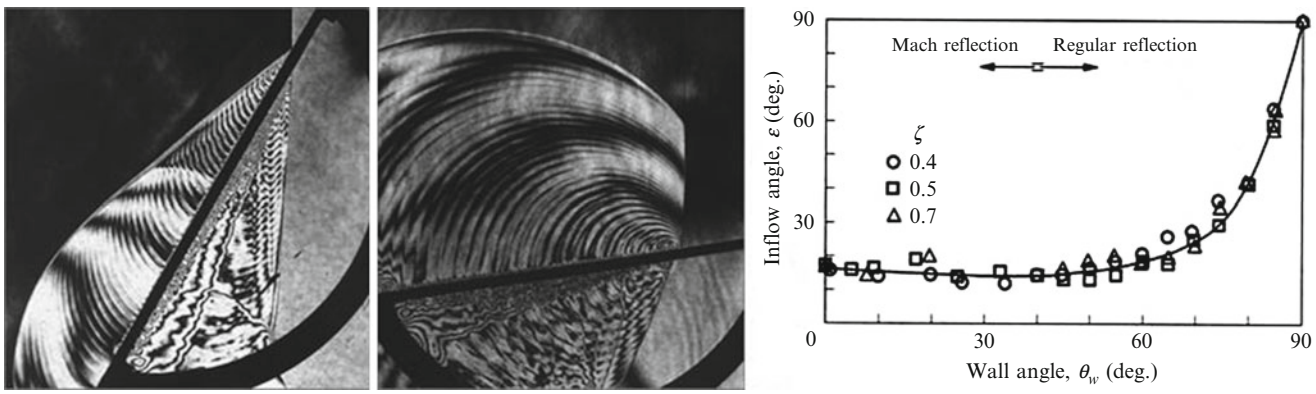

Fig. 3 Interferograms of regular and Mach reflection and a graph of inflow angles

This led to a study of shock interactions with grids using holographic interferometry at the Shock Wave Research Center in Sendai. Figure 3 shows both regular and Mach reflection cases. There is a clear indication of the change between supersonic and subsonic flow behind the reflection point and the small change in transmitted shock strength in the regular reflection case. Perhaps the most surprising is the very small inflow angle into the surface, being well below 25° up to wall angles as high as 70°. The reason for this as well as some other interesting features is indicated in Fig. 4. Due to the flow behind the developing reflected wave, a vortex is shed from the downstream corner of the grid elements, with the reflected wave passing into the gap, reflecting there and resulting in a second reflected wave on both the upper and lower surfaces. In addition a second row of shed vortices is generated with the first row developed from the trailing edge of the gap.

A study was also made of the effect of blast loading on a surface covered by a layer of clothing. Tests were conducted with no surface covering, then with a 10 mm layer of gelatine to simulate flesh and then with a layer of textile positioned 3 mm further forward.

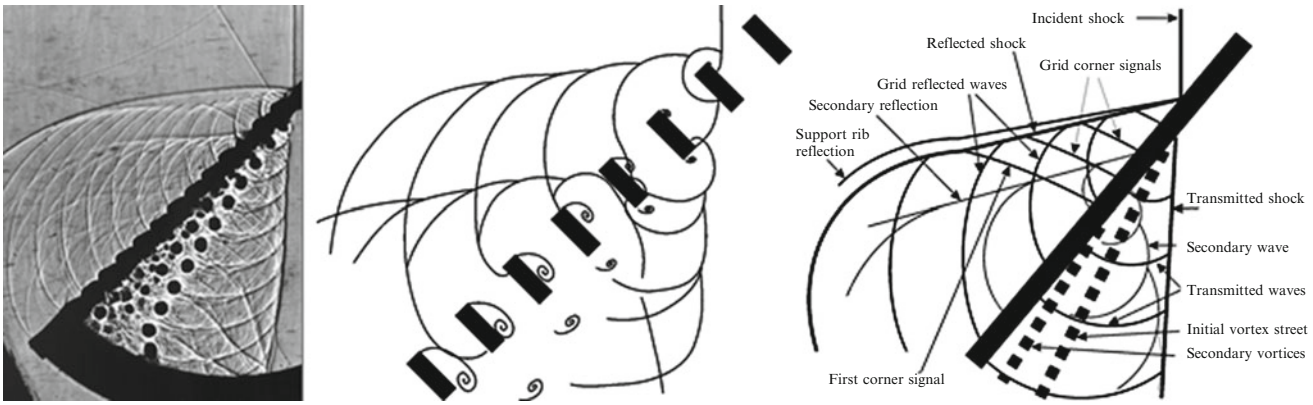

Fig. 4 Schematics showing detail of flow features, based on schlieren imaging

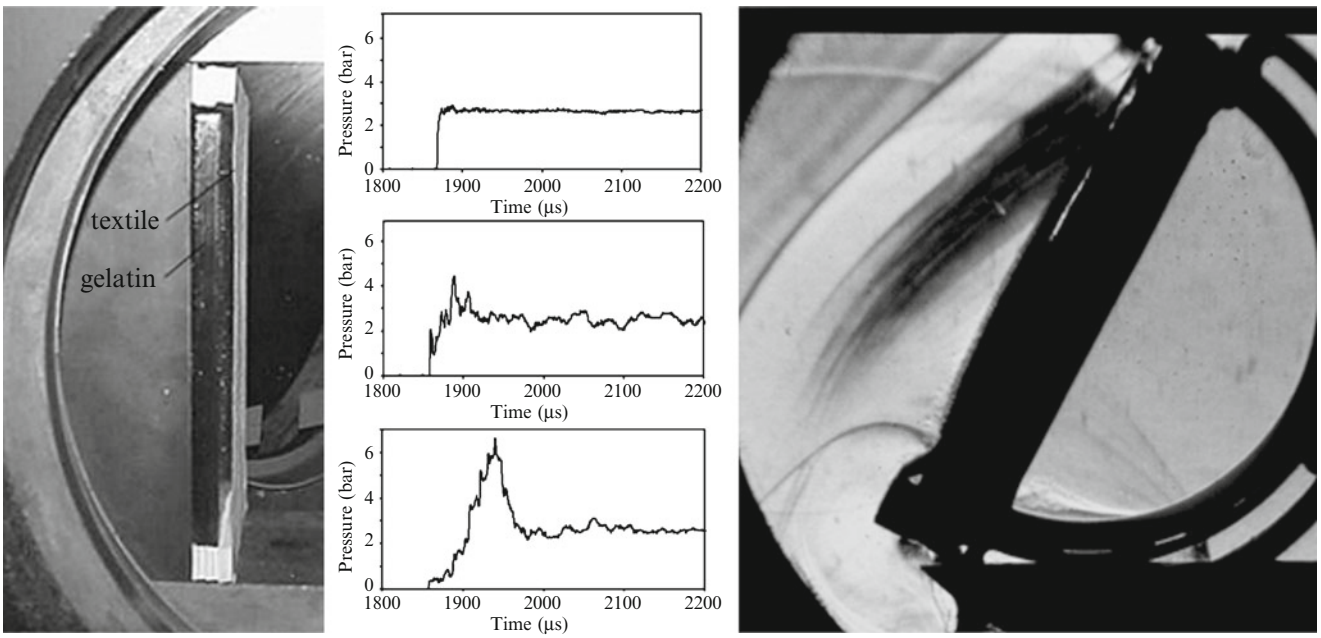

Fig. 5 Wave amplification through a textile covering. Oblique interaction image shows multiple transmitted waves passing back through the textile

The results shown in Fig. 5 clearly indicate the substantial increase in pressure on the underlying surface. Part of the mechanism is that the shock wave transmitted through the textile, coupled with its motion, gets trapped in the air gap and bounces back and forth increasing the pressure in a stepwise pattern. This is confirmed in the schlieren image, for oblique impact, where a series of wavelets emerge back out from the textile.

The von Neumann Paradox I

A paradox arising from von Neumann's theory of shock reflection [5] is that in increasing the reflection wedge angle, regular reflection persists beyond the limit predicted by the theory. Clarity was obtained by Hornung et al. [6] who showed this was due to the boundary layer development behind the reflection point resulting in an apparent larger wedge angle due to the negative displacement thickness.

An alternative approach was devised to remove the boundary layer altogether by reflecting two identical shock waves off each other [7] in the bifurcated shock tube shown in Fig. 6, where a shock is split into two which then arrive simultaneously at a corner as shown in the image. Excellent agreement with the theory was obtained showing a significant difference from wedge tests.

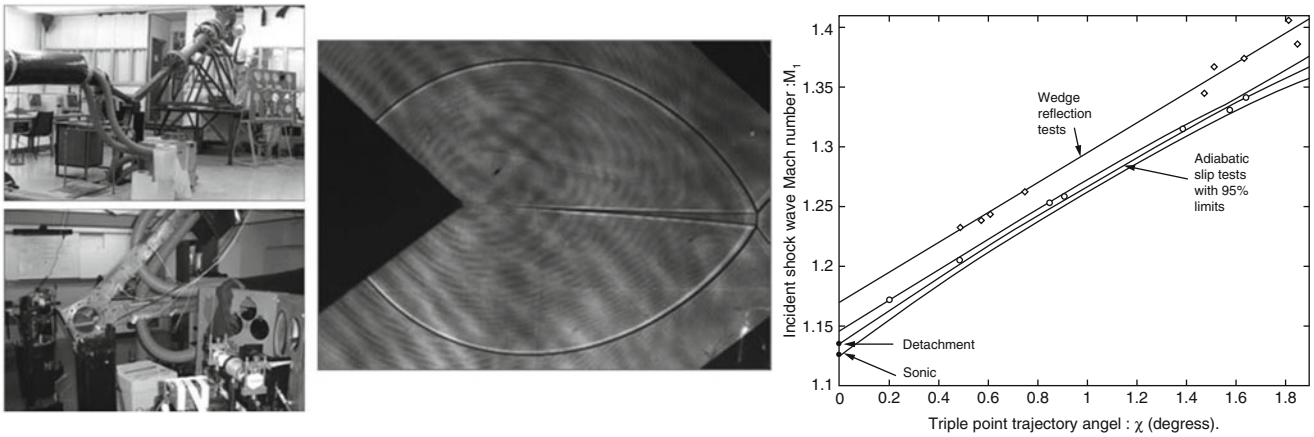

Fig. 6 The bifurcated shock tube experiment showing the reflection of two shock waves off each other, resulting in correlation with theory

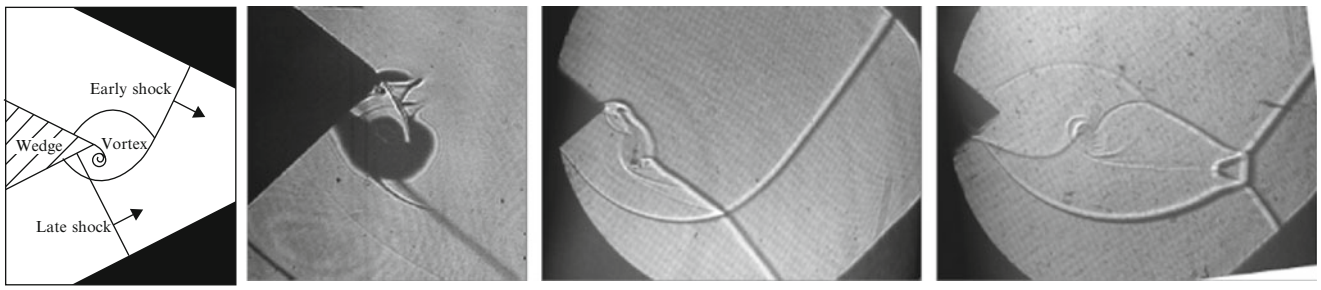

Fig. 7 Shock/vortex interaction in the bifurcated tube. First image at Mach 1.5 and the other two at Mach 2.5

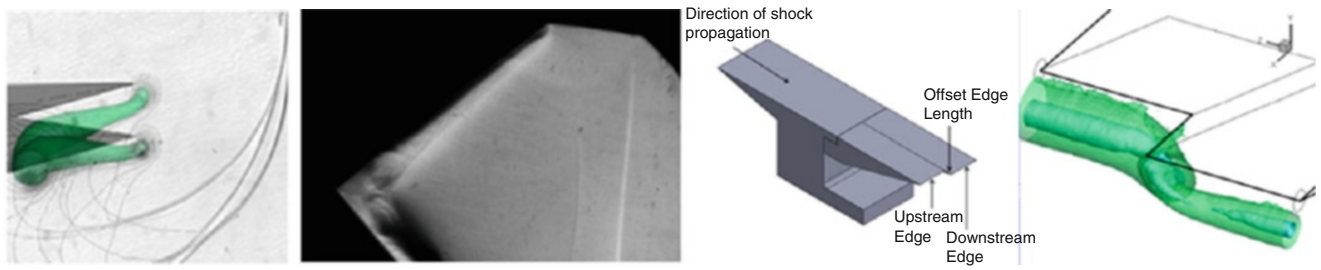

Fig. 8 Three-dimensional vortex shedding from shock diffraction

Shock/Vortex and Vortex Interactions

The above tests required very accurate synchronization in the arrival of the two independent shocks at the corner. When this does not occur, the early arriving shock sheds a vortex at the corner which would then be impacted by the late shock, giving a good facility for examining the interaction as indicated in the sketch in Fig. 7. Most previous work has been done numerically with an isolated vortex rather than a spiral one, and tests have mostly been at low shock Mach numbers [8]. Studies at higher Mach numbers have hardly been explored; some examples are given in the figure, the first at Mach 1.5 showing shocklets above the shear layer and the other two at Mach 2.5 which show behaviour not yet fully explored.

Vortices shed from shock diffraction become more complex if a plane shock wave diffracts over an edge that is not parallel to it. Two examples are given in Fig. 8. The first two frames are for the diffraction over a V-notch, with the left image being an oblique view, obtained from simulation, showing a density isosurface of the vortex [9] and the second image a top view schlieren visualization showing the complex interaction, as yet unexplained, at the apex of the V, where the two vortices interact at a large angle to each other. The two images on the right of the figure are when a shock wave propagates over a discontinuous edge when two two-dimensional vortices from

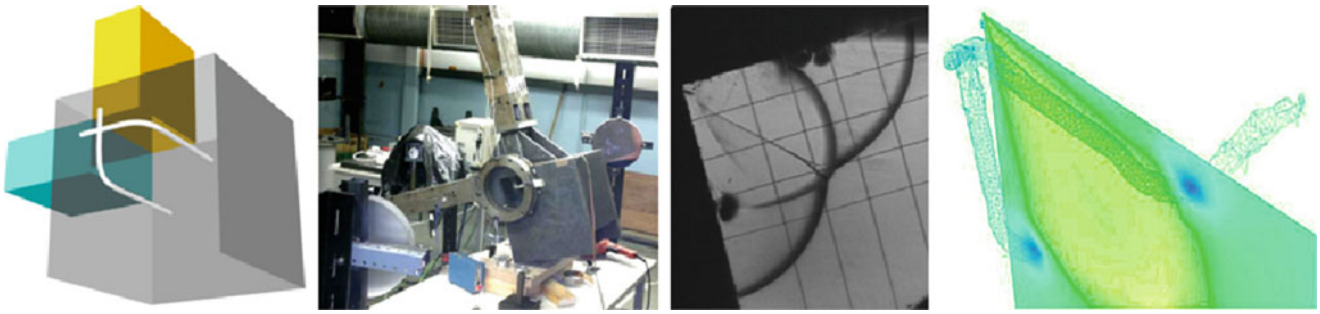

Fig. 9 Shock diffraction from perpendicular shock tubes

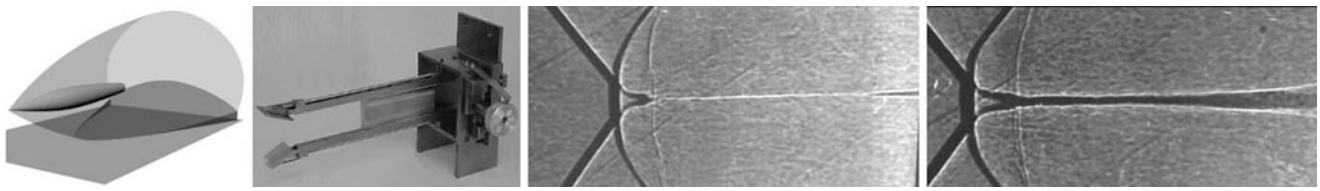

Fig. 10 Oblique views of shock wave reflection between two wedges

well-established shock diffraction meet and merge with each other. Two isosurfaces are plotted. The interaction is complex since the one vortex is ahead and is well established before the second one is generated.

A more complex situation arises when two independent shocks arising from different directions interact with each other. Such an arrangement is shown in Fig. 9 [10]. Here two tubes at 90° to each other with a common exit edge generate two L-shaped vortices. The bifurcated tube was used to generate synchronous shock arrival at the exits. The interaction results in three-dimensional shock surfaces which reflect off each other, initially as regular reflection and then as Mach reflection as the radius grows, with combinations of both reflection types at some stages of the growth. At the intersection of the vortices, they wind up in a complex flow topology as indicated in the last frame of the figure, showing a density isosurface of the vortex, passing through a plane showing pressure contours positioned through the minor axes of the tube exits.

Interactions in Steady Flows

When a supersonic body passes over a ground plane, the bow shock will generally reflect as a regular reflection immediately under the body, but as it propagates sideways will weaken and transition to a Mach reflection as indicated in the surface plot in Fig. 10. A test rig with two small aspect ratio wedges was used to explore the reflection pattern. This is done by yawing the optical axis of the visualization setup so that the intersection of the waves on the symmetry plane is viewed at some 45° to the flow direction as shown in the two schlieren images. The first image shows the Mach reflection on the left which then moves around to become the central regular reflection shown as the central white line which then changes back to the Mach reflection on the other side of the flow. What is interesting is the sudden change in stem height on the left, accentuated by the angle it is viewed at, which is not replicated in numerical simulations and is presumed to be due to the effects of some upstream turbulence.

The effect of rapid pitching motions of a body on reflection transition conditions is of interest. A special facility has been built enabling pitch rates of up to 11,000° per second, with the wedge position and shock pattern recorded with high-speed photography [11]. The wedge, shown in Fig. 11, has an aspect ratio of 4.25 and a chord of 40 mm giving two-dimensional flow in the centre section. Extracts from the movie for transition from Mach to regular reflection at Mach 3.26 are given in the figure with results from this and the reverse transition given in the graph. There are clear differences in the transition criteria for dynamic body motion compared to the well-established steady flow case.

Von Neumann Paradox II: Weak Shocks

The second, more intractable, von Neumann paradox, is the question of why the theory is significantly incorrect for weak waves in its prediction of the three shock Mach reflection patterns. Numerous attempts have been made over the years to resolve the issue. It is interesting to note that way back in 1947, Guderley [12] suggested that a fourth wave, an expansion wave, was positioned immediately behind the reflected wave. Numerical studies, at the turn of the century, indicated

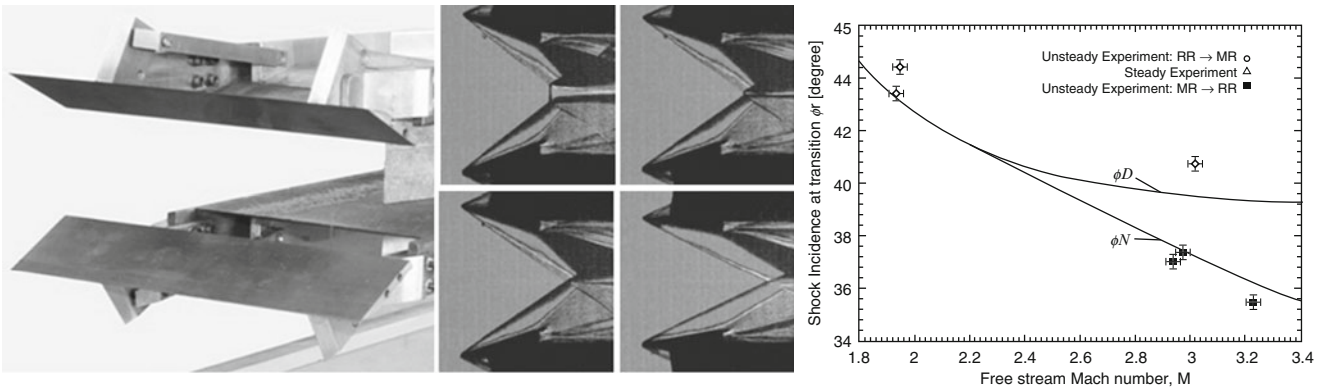

Fig. 11 Rig and results showing transition conditions due to rapid pitching motion

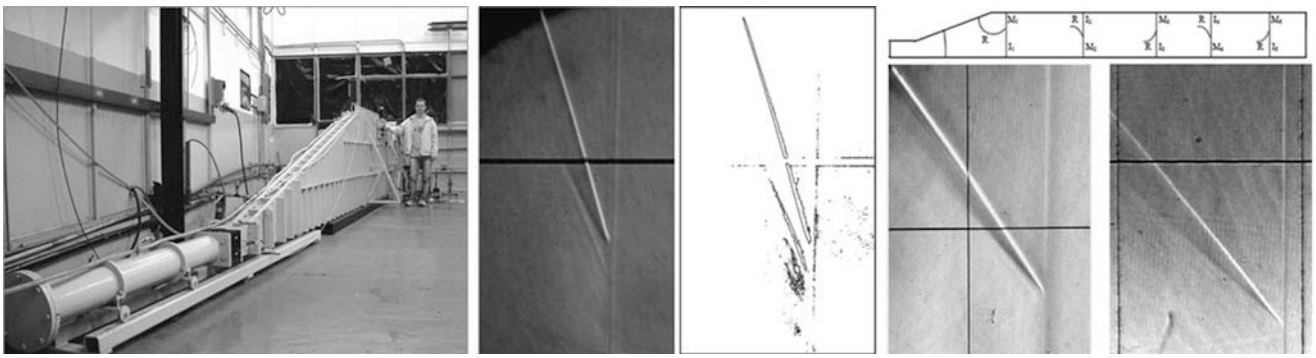

Fig. 12 The large shock tube for weak shock studies and images of Guderley reflection, with edge detection of the first image

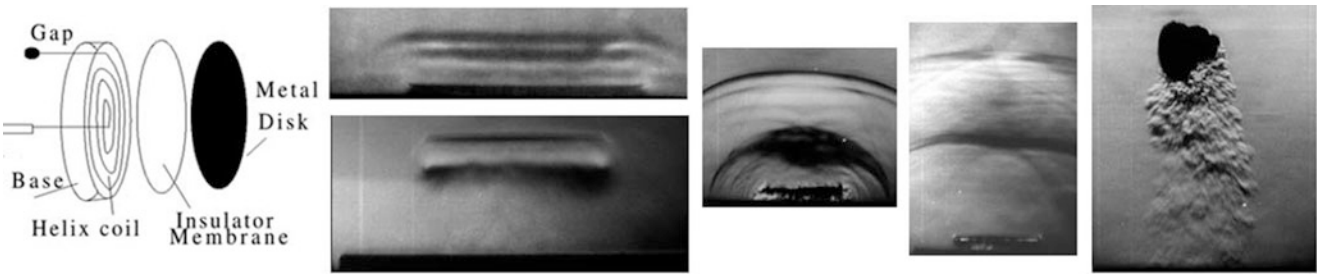

Fig. 13 Repulsion of discs from an electromagnetic source, showing the generation of shock waves

that a fourth wave resulting in a small supersonic patch may indeed exist, but that it would be so small as to be undetectable experimentally and could be terminated by a shock [13]. A unique shock tube with a test section 1.1 m high and producing a cylindrical wave of some 8 m radius reflecting off a wedge was successful in imaging the four-wave system for the first time [14], Fig. 12. More recently another experimental method of generating these patterns was developed [15]. Typical results are given in the figure. Weak shock reflection off curved surfaces has also given indications of non-standard effects [16].

Moving Surfaces

An electromagnetic acoustic source (EMAS) has been developed which can be used to generate very large repulsive forces on a body lying on its surface. It required a driving supply of 8000 V and 6000 amps, and because the circuit was underdamped, it generated multiple shocks as the body was accelerated away from the surface. Figure 13 shows the results for a 1 mm thick aluminium plate and a circular disc of aluminium foil. Shock waves are also developed under the plate at early times due to the radial inrush of gas, and as it

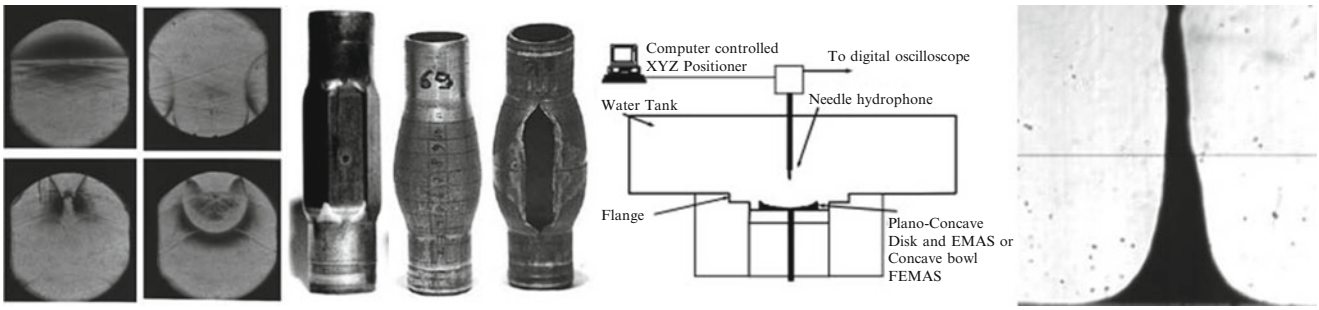

Fig. 14 Shock waves in liquids showing focusing, metal forming and liquid jets

moves away, a strong vortex ring is shed. In contrast the foil distorts into a parachute shape.

Liquids

A number of limited tests have been conducted using liquids as the working medium. For initial studies on liquid shock focusing, Fluorinert was used since it has the highest non-linearity of liquids and a very low sound speed of 655 m/s. A few results are shown in Fig. 14. In addition a liquid shock tube was used to explore the potential of using liquid shocks for metal forming. This has proved to be successful with examples shown in the figure [17]. Moreover it is found that if an undersurface plate is impacted impulsively from the bottom, such as with a shock wave as illustrated in the figure, a discrete jet is ejected from the surface.

Conclusion

A range of studies of both steady and unsteady shock wave flows undertaken in the Flow Research Unit of the University of the Witwatersrand, South Africa, are summarized. They range over a series of investigations with an emphasis on experimentation and clarification of some flows.

References

1. Skews, B.W.: An experimental study of the interaction of shock waves with bends in a duct. In: Symposium on Internal Flows, University of Salford, Paper 29 (1971)
2. Skews, B.W.: The perturbed region behind a diffracting shock wave. J. Fluid Mech. **29**, 705–719 (1967)
3. Gelfand, B.E., Gubin, S.A.: Study of special features of propagation and reflection of pressure waves in a porous medium. Sov. Phys. Appl. Math. Tech. Phys. **6**, 74–77 (1975)
4. Skews, B.W., Atkins, M.D., Seitz, M.W.: The impact of a shock wave on porous compressible materials. J. Fluid Mech. **253**, 245–265 (1993)
5. von Neumann, J.: Oblique reflection of shocks. In: Tech. Rep. 12. Bur. Ord. Explosives Research Report (1943)
6. Hornung, H.G., Oertel, H., Sandeman, R.J.: Transition to Mach reflection of shock waves in steady and pseudosteady flow with and without relaxation. J. Fluid Mech. **90**, 541–560 (1979)
7. Barbosa, F.J., Skews, B.W.: Experimental confirmation of the von Neumann theory of shock wave reflection transition. J. Fluid Mech. **472**, 263–282 (2002)
8. Barbosa, F.J., Skews, B.W.: Shock wave interaction with a spiral vortex. Phys. Fluids **13**, 3049–3060 (2001)
9. Reeves, J.O., Skews, B.W.: Unsteady three-dimensional compressible vortex flows. Shock Waves **22**, 161–172 (2012)
10. Skews, B.W., Bentley, J.J.: Flows from two perpendicular shock tubes with a common exit edge. In: 21st International Shock Interaction Symposium, Riga, Latvia, 21–25 (2014)
11. Naidoo, K., Skews, B.W.: Dynamic transition from Mach to regular reflection of shock waves in a steady flow. J. Fluid Mech. **750**, 385–400 (2014)
12. Guderley, K.: Considerations of the structure of mixed subsonic-supersonic flow patterns. Tech Report F-TR-2168-ND. Wright Field (1947)
13. Tesdall, A.M., Sanders, R., Keyfitz, B.L.: Self-similar solutions for the triple point paradox in gas dynamics. SIAM J. Appl. Math. **68**, 1360–1377 (2008)
14. Skews, B.W., Ashworth, J.T.: The physical nature of weak shock wave reflection. J. Fluid Mech. **542**, 105–114 (2005)
15. Skews, B.W., Li, G., Paton, R.: Experiments on Guderley Mach reflection. Shock Waves **19**, 95–102 (2009)
16. Gruber, S., Skews, B.W.: Weak shock wave reflection from concave surfaces. Exp. Fluids **54**, 1571 (2013)
17. Skews, B.W., Kosing, O.E., Hattingh, R.J.: Use of a liquid shock tube as a device for the study of material deformation under impulsive loading conditions. J. Mech. Eng. Sci. **218**, 39–52 (2004)

Dispelling Misconceptions about Bast Waves (Irvine Israel Glass Lecture)

Charles Needham

Introduction

There are a number of misconceptions about air blast waves interacting with structures that I would like to dispense with. There is a persistent notion that a structure is "blown away" when it is hit by a nuclear blast wave. This image probably comes from the many movies from nuclear tests that show a structure such as a house or an industrial building being torn apart and "flattened" by the air blast. There is no argument that this does not happen; however, the timing of the structure response is what I would like to examine.

Consideration of the timing of the response of structures to air blast loading becomes a dominant factor when predicting the air blast propagation in urban environments. A number of questions have been asked about the absorption of energy and reduction of air blast as the blast wave interacts with structures in the urban environment. How much energy goes in to breaking the structure? How much energy is converted to the kinetic energy of the debris? How much energy is dissipated on the interior of structures? How much debris will be entrained in the blast wave? How far does the debris get thrown? What is the "protection factor" of nearby buildings? How different are the blast waves traveling down streets and the blast waves going over and around buildings?

There have been many high-explosive and shock-tube experiments conducted with urban structures of various scales. A few were done at full scale with houses; others were done at small scale with a few pounds of explosive. Not all of these experiments had a primary purpose of looking at the effects of blast on structures or, more directly, the importance of structures on blast wave propagation. Let me review a few experimental results to demonstrate the fallacy of some of the misconceptions. (I held these views prior to seeing experimental data with corresponding calculational results.)

Some assumptions that I have heard expressed include: (1) At pressures of 2 bars or more, windows will be blown away so rapidly that you can ignore their presence. (2) Once the window is broken, gas will flow through the opening. (3) Debris will be translated to large distances by blast waves.

Let us look at some basic properties of blast waves. Table 1 contains a list of overpressures and their associated dynamic pressures and wind velocities. Remember that the ambient speed of sound is about 750 miles per hour. A blast wave with an overpressure of more than about 36 PSI will have a material velocity at the shock front that is supersonic. For comparison: Sustained winds >155 mph define a Category 5 hurricane, and 3 s gusts >200 mph define an enhanced Fujita scale (EF5) tornado.

The velocities behind a 6 PSI shock are equivalent to the winds in an EF5 tornado, and the winds in a Category 5 hurricane are present at the shock front of a 4 PSI shock. At half a PSI, the dynamic pressure is only 0.006 PSI, but a sudden wind gust of 18 miles per hour will certainly blow the hat off your head.

This is a true story.

I was at a NATO blast effects on animal symposium in Halifax a few years ago when one of the researchers made the statement in his presentation that he had exposed mice to 40 PSI dynamic pressure and they had survived. I found this very hard to believe. At the break I asked him about his experiment which he described as follows: I had the mice walk across a beam in front of a nozzle. When they were in front of the nozzle, I opened the valve to the nozzle and all it did was knock the mice off the beam. The nozzle was connected to a hose which was connected to a tank which was pressurized to 40 PSI. Isn't that 40 PSI dynamic pressure?

From the table below, we see that a blast wave with 40 PSI dynamic pressure has a wind velocity of about 900 miles an hour (Mach 1.3+) material velocity with a corresponding overpressure of 50 PSI.

C. Needham (✉)
Applied Research Associates, Inc., Southwest Division, Albuquerque, NM USA
e-mail: cneedham@ara.com

G. Ben-Dor et al. (eds.), *30th International Symposium on Shock Waves 1*, DOI 10.1007/978-3-319-46213-4_2

Example 1

In 1999 an experiment was conducted at White Sands Missile Range in which a full-sized four-story concrete building, Fig. 1, was subjected to the blast wave from a 300 lb charge detonated on the center line of the building, 50 ft in front of the structure. The front face of the structure had concrete walls with glazed windows. The structure was 80 ft wide and 48 ft deep by four stories tall. The walls on the sides of the building were only wing walls and extended just 6 ft from the front of the structure. Extensive air blast instrumentation was located throughout the building. For this example we need only the gauges on the front wall and on the floor of the fourth story. The fourth floor gauges were located ten feet behind the windows and centered on the windows on either side of the center line (Fig. 2). The windows on either side of the center line were 6 mm thick (∼.25 in.). With the charge located 50 ft in front of the structure, the shock radius was greater than the height or the half width of the building when the front face was struck. The reflected overpressure on the entire front face of the building exceeded 35 PSI, while on the center line, the overpressure exceeded 40 PSI. Without going into all the details, we examined two gauges on the front of the structure and two gauges that were 10 ft inside the building, about 10 ft on either side of the center line, in line with the windows. All expectations were that such a high-pressure blast wave would blow out the windows and hit the interior blast gauges with an incident pressure in excess of 5 PSI, which is just a little less than the unobstructed incident pressure at that range.

Table 1 Some properties of shock waves

Peak overpressure (PSI)	Peak dynamic (PSI)	Maximum wind velocity (mph)
200	330	2078
150	222	1777
100	123	1415
50	41	934
30	17	669
20	8.1	502
10	2.2	294
5	0.6	163
0.5	0.006	18

A comparison of two blast gauges on the front of the building showed that the measured overpressure waveforms were essentially overlays throughout the positive duration of the blast wave, even though one gauge was on the concrete surface and the other was in the middle of a window. This was a good indication that no gas penetrated the window and

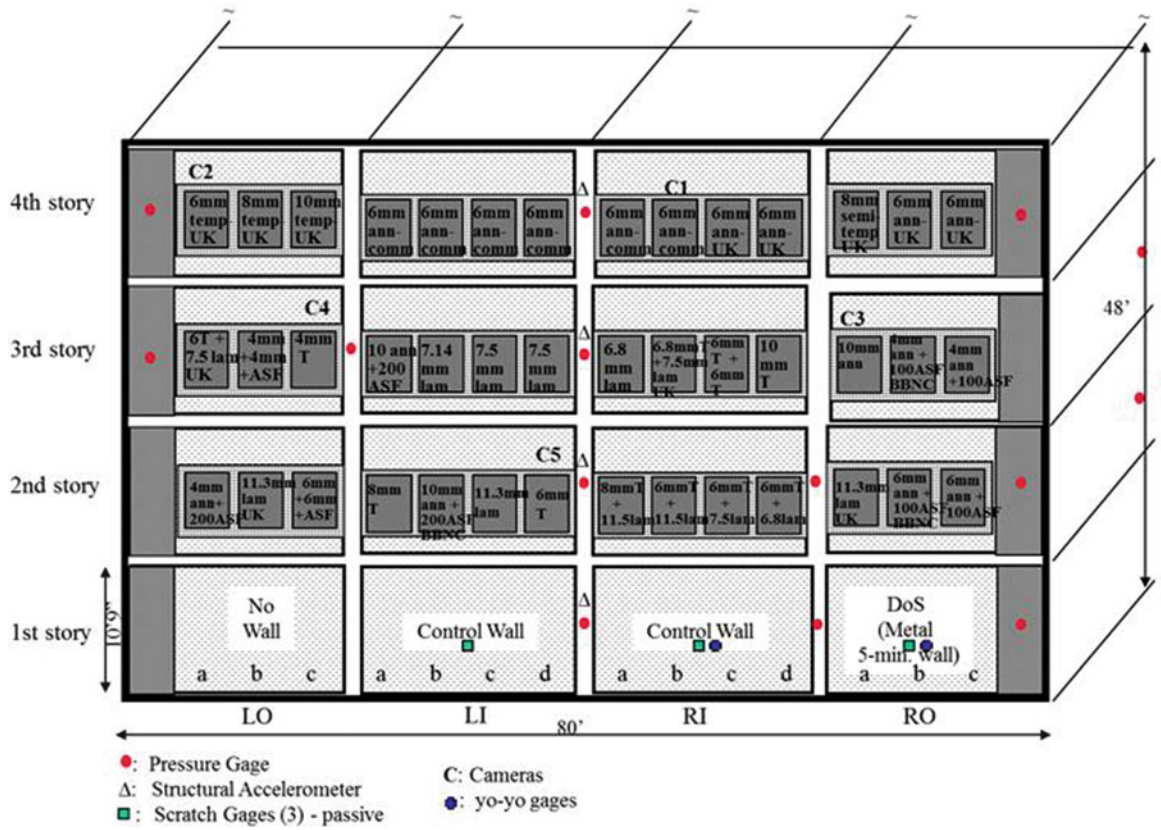

Fig. 1 The four-story full-scale test structure

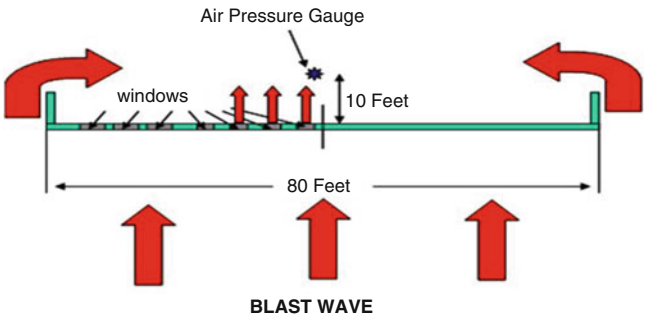

Fig. 2 Plan view of the fourth floor of the building

that the window glass did not move significantly over the entire positive duration of the blast wave.

We then examined the waveforms on the two gauges on the floor, ten feet behind the windows. By looking at the relative arrival of signals at these gauges, we found that the arrival of the first significant signal did not arrive until about 25 ms after the arrival at the window center. The expected arrival, assuming the blast wave came through the window, would be 7 ms later. The 25 ms delay corresponds exactly with the arrival of a blast wave coming around the sidewalls and traveling 30 ft to the gauges on either side of the center line. Further evidence that the shock came from the side was the arrival of a second shock just 20 ms later on both gauges. The 20 ms corresponds to the travel time for a weak shock over the 20 ft separating the gauges. It was not clear whether *any* signal came through the windows.

One additional note from this experiment is the windows were shattered into small pieces and the majority of the glass was found outside in front of the building. This was caused by a combination of the negative phase on the exterior of the building and the arrival of the blast wave from the sides in the interior of the building, pushing the broken glass outward.

An easy way to think of this response is that the density of the glass is more than 1000 times the density of the air in the shock. Because overpressure is a scalar, the air and the glass receive the same impulse, and the air is accelerated 1000 times faster than the glass. The air blast will move 1000 times further than the glass in the same amount of time. The air shock will move at least 20 ft in the time the glass will move 0.25 in.

Another consequence of this timing is that there was very little blast wave wind on the interior. Papers and office furniture would not be blown out the windows as some might envision. The argument against this might be that the positive duration is too short for such a small charge and that, for a nuclear event, the duration would be a large fraction of a second, thus allowing acceleration of interior debris.

Example 2

In 2002, the British conducted a series of scaled experiments using 250 kg of high explosive detonated at a height of burst of ~25 ft near a 1/50th scaled model of downtown San Francisco. The buildings were constructed of concrete and were instrumented for air blast on the back, front, top, and sides. Measurements of air blast and its propagation through the model city were carefully recorded. Calculations using the SHAMRC hydrodynamic code were made and showed excellent agreement with the measured air blast waveforms. Significant criticism was expressed because the structures in the calculation and in the experiment were rigid and non-responding. In the following year, the experiment was repeated except that the structures were constructed of 3 mm-thick mirror glass. The instrumentation was placed in the same locations.

Posttest comparison of the waveforms showed no significant difference of the peak pressures, waveform shapes, or impulses between the concrete structures and the mirror glass structures. This was true throughout the test bed, whether closer to ground zero or after transiting the entire city. In addition there was no measurable difference in arrival time between the two experiments. The mirror glass experiment showed that the debris was concentrated within about four building heights of the original location. Debris was not "blown to long distances" (Fig. 3).

As a side note, the 3 mm glass at 1/50th scale corresponds closely to a 15 cm-thick concrete wall, not too bad an approximation to actual construction thickness.

Again the explanation is that the density of the responding structural material was more than 1000 times the density of the air in the blast wave. The air moves about 1000 times as far as the glass in the same amount of time.

Example 3

The Ernst Mach Institute (EMI) in Freiburg, Germany, did some shock-tube experiments using a small-scale, three-dimensional model of a house. The house was machined from steel and included a pitched roof, a door, and several windows. The house was placed in the test section and loaded with about 1 bar overpressure shock. Some excellent shadowgraphs were made using a multiple spark back-lighting technique to provide a time sequence of the shock reflection, diffraction, and transmission. Someone decided to repeat the experiment with a balsa wood house to see how the responding structure would change the reflected shock wave patterns. A balsa wood house was constructed to the same dimensions as the steel house and carefully placed in

Fig. 3 Blast wave interaction with a scaled glass city and the aftermath

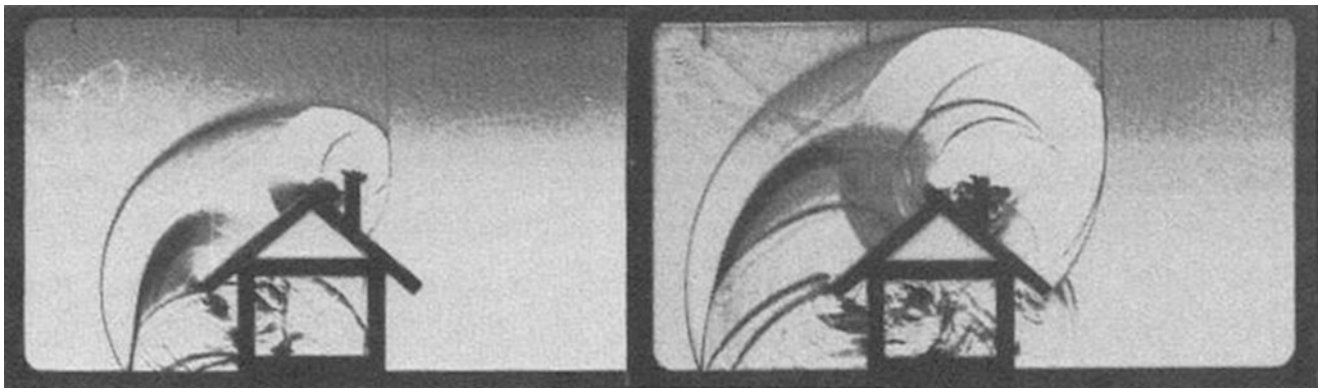

Fig. 4 Shock interaction with a scaled house

the shock tube. The house was exposed to the same shock loading as the steel house, and the same series of shadowgraphs were taken (Fig. 4).

Upon examination of the comparisons from the two experiments, there was no measurable difference between the two shock patterns. In addition, there was no measurable motion of the balsa wood house over the entire duration of the blast passage. The balsa wood house was found in small pieces in the dump tank at the end of the shock tube when the experiment was over.

The factor of ~1000 in density between the balsa wood and the air explains the observed phenomena.

Example 4

Under a contract to Sandia Laboratories, ARA made calculations of building damage and response to nuclear air blast in urban settings. The initial calculations indicated that the debris field from individual structures was translated over a very limited region near the original location of the structure. This was not the anticipated result. It was thought that the debris would be widely spread and translated to large distances. A detailed investigation of the assumptions, drag coefficients, and effects of shape of debris was undertaken. After several months of study and detailed analysis, including examination of photos from nuclear tests and scaled high-explosive tests, it was concluded that the calculated debris distributions were correct.

The general rule of thumb from this study was that debris is translated by the shock wave to distances no more than four times the building height.

Vortices on Sides (Blow Out)

The general consensus of what happens when a blast wave strikes a structure is that the loads are compressive and the structure is collapsed by the external pressure. Let us look at the flow field around a rectangular block (Fig. 5). In the

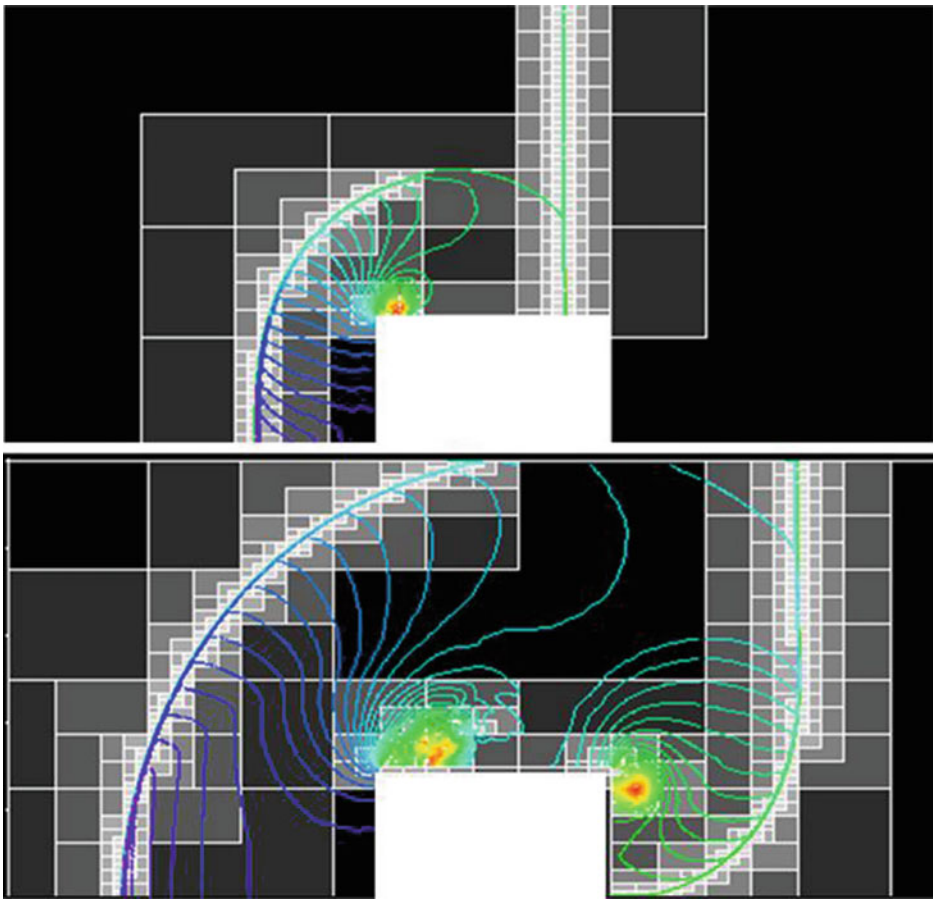

Fig. 5 Shock interaction with a rectangular box

upper figure, the shock wave has reflected from the front of the block and has progressed over the top of the block toward the rear of the structure. A vortex has formed just beyond the leading face of the block. The pressure in the vortex is well below ambient. As the shock progresses over the rear of the structure, a second vortex forms near the top of the rear face and moves down the backside of the structure. The vortex on the roof of the structure has grown and somewhat weakened, but maintains a lower than ambient pressure on the roof of the structure.

The commonly observed resulting damage is that the front wall is blown in, but the top (and sides and back wall) are blown out. This is a direct result of the under pressure on the exterior, caused by the formation of the vortices causing a net outward force because the interior pressure remained at ambient. Thus it appears that the structure "explodes".

Shock Reflection Factors

The behavior of the reflected shock pressure as a function of the incident angle to a surface is well known and has been measured by many experimenters. The peak reflected pressure does not necessarily occur when the incident shock velocity is perpendicular to the reflecting surface. Yet as recently as last year, I heard people saying that they did not "believe" the observed phenomena because either they had never measured it or it must be such a short spike in pressure that it is not important. The accompanying Fig. 6 shows that for incident overpressures below a few hundred PSI, the maximum reflection factor occurs when the impinging shock is oriented about 41° or more from the reflecting plane rather than perpendicular to it.

This phenomenon is associated with the onset of Mach reflection when the reflected shock catches the incident shock. The next two figures are measured (solid) and calculated (dashed) waveforms from replicated detonations of 1080 lb HMX charges at a height of burst of 13.7 ft. Figure 7 is the waveform at a ground range of 12.5 ft. The incident pressure was 2.3 MPa (~330 PSI). The experimental data clearly show a peak reflected pressure very near 14 MPA or a reflection factor of 6. This point is displayed on the reflection factor curve on the right. Note that the reflected peak is not at the shock front; in fact, it is not a shock but is compressive wave caused by the converging flow at ground level just prior to Mach formation.

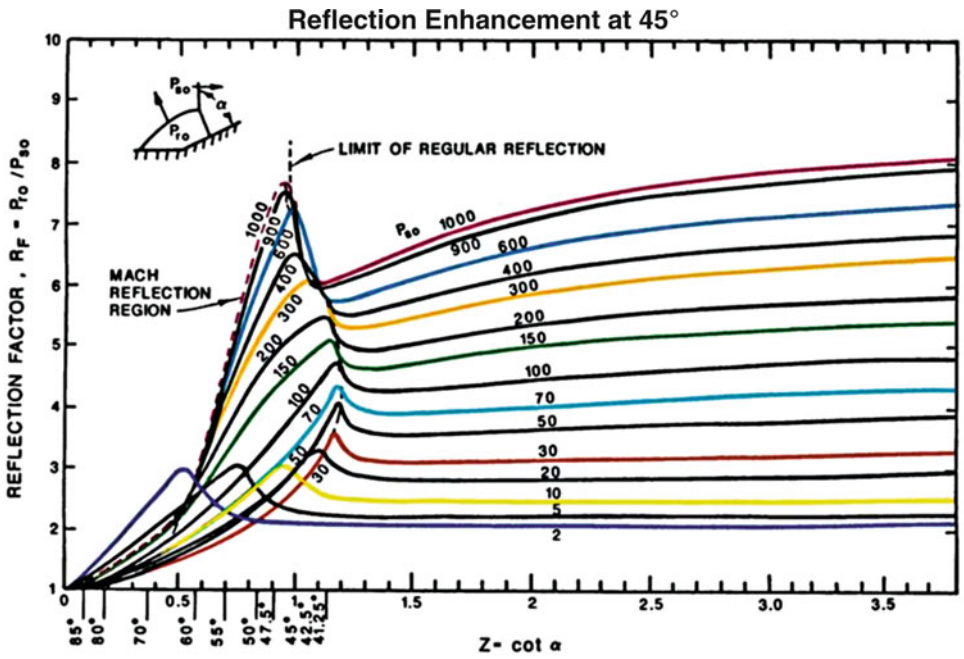

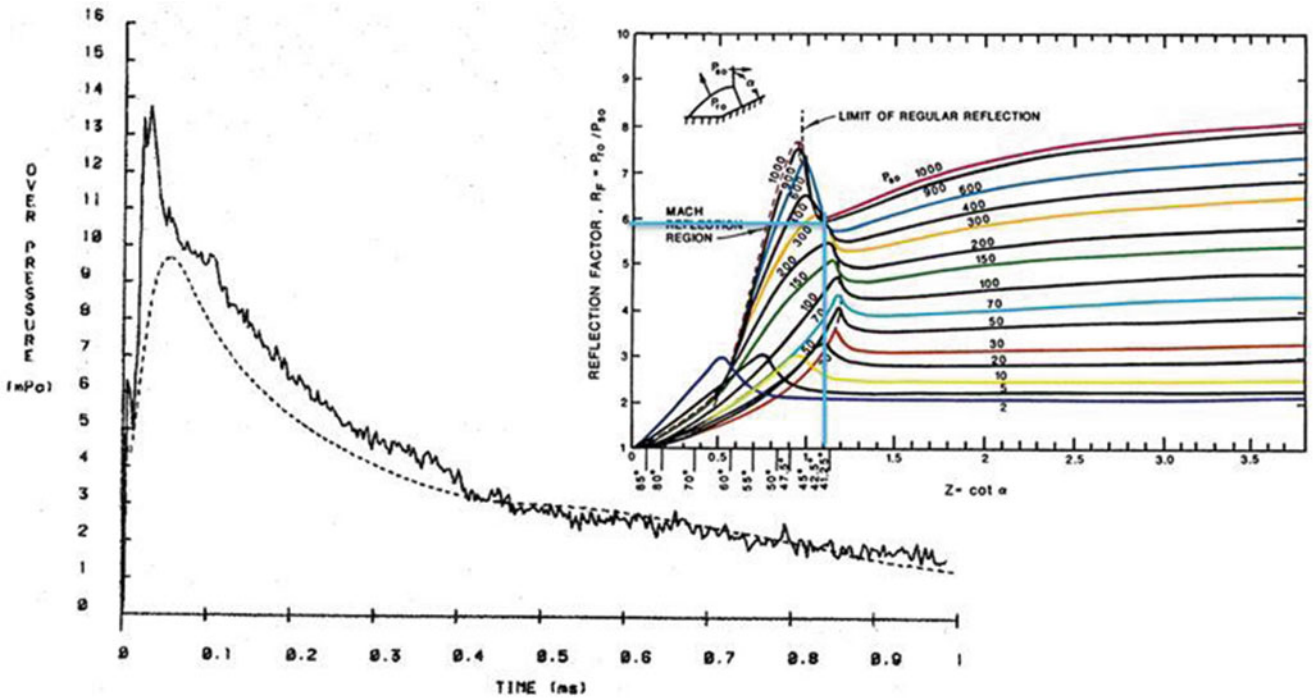

Fig. 6 Reflection factors for selected incident overpressures as a function of incident angle

Fig. 7 High explosive reflected waveform. GR = 12.5, HOB = 13.7, incident OP = 2.3 MPa

At a ground range of 16 ft (Fig. 8), the Mach stem has formed and is growing. Note that the distance between the shock front and the peak pressure has increased significantly. This peak pressure corresponds to the range at which the slip line from the triple point reaches the ground. Again the point on the reflection factor curve is displayed in the plot on the right.

Figure 9 demonstrates the high resolution that is needed to resolve this double-peak phenomenon in numerical calculations. The waveforms were calculated, using the US government code SHAMRC, for a 1 kt detonation at a height of burst of 100 m. The three sets of waveforms were taken at 80, 90, and 100 m from ground zero. With 10 cm zoning, the double peak is not resolved and results in an extended rise

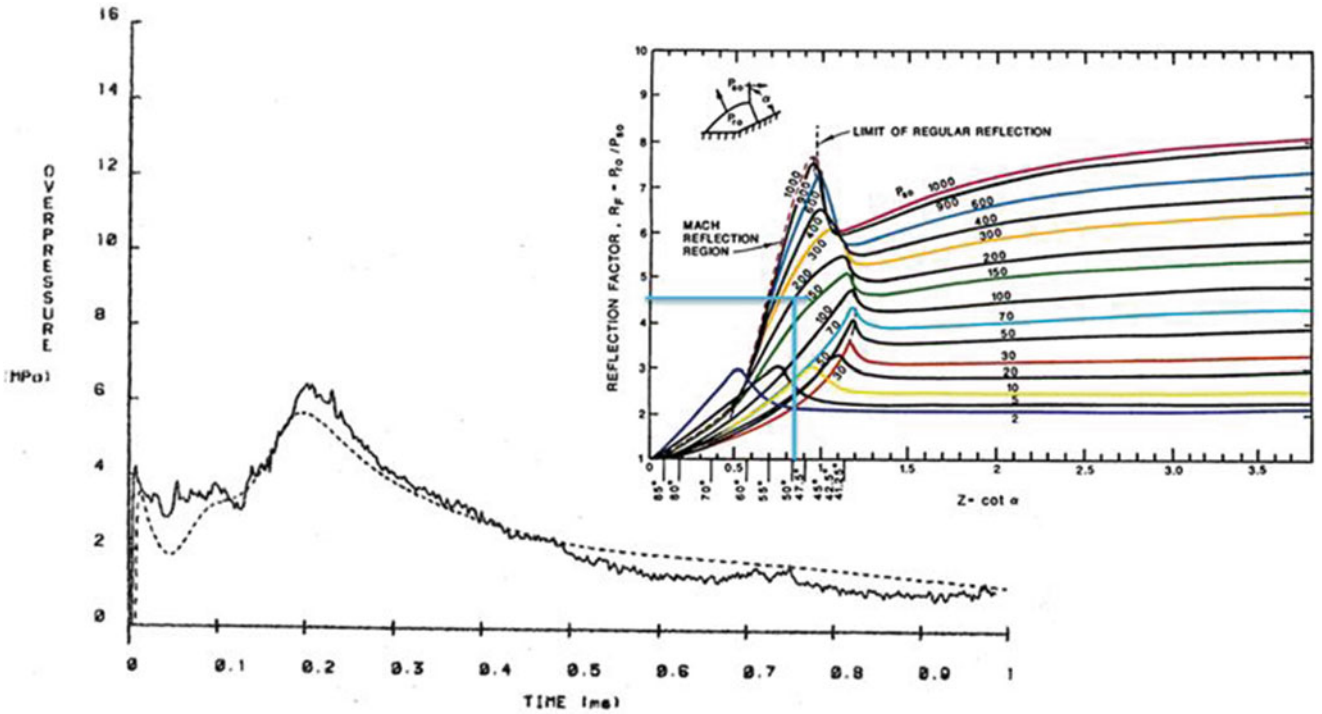

Fig. 8 High explosive reflected waveform. GR = 16, HOB = 13.7, incident OP = 1.5 MPa

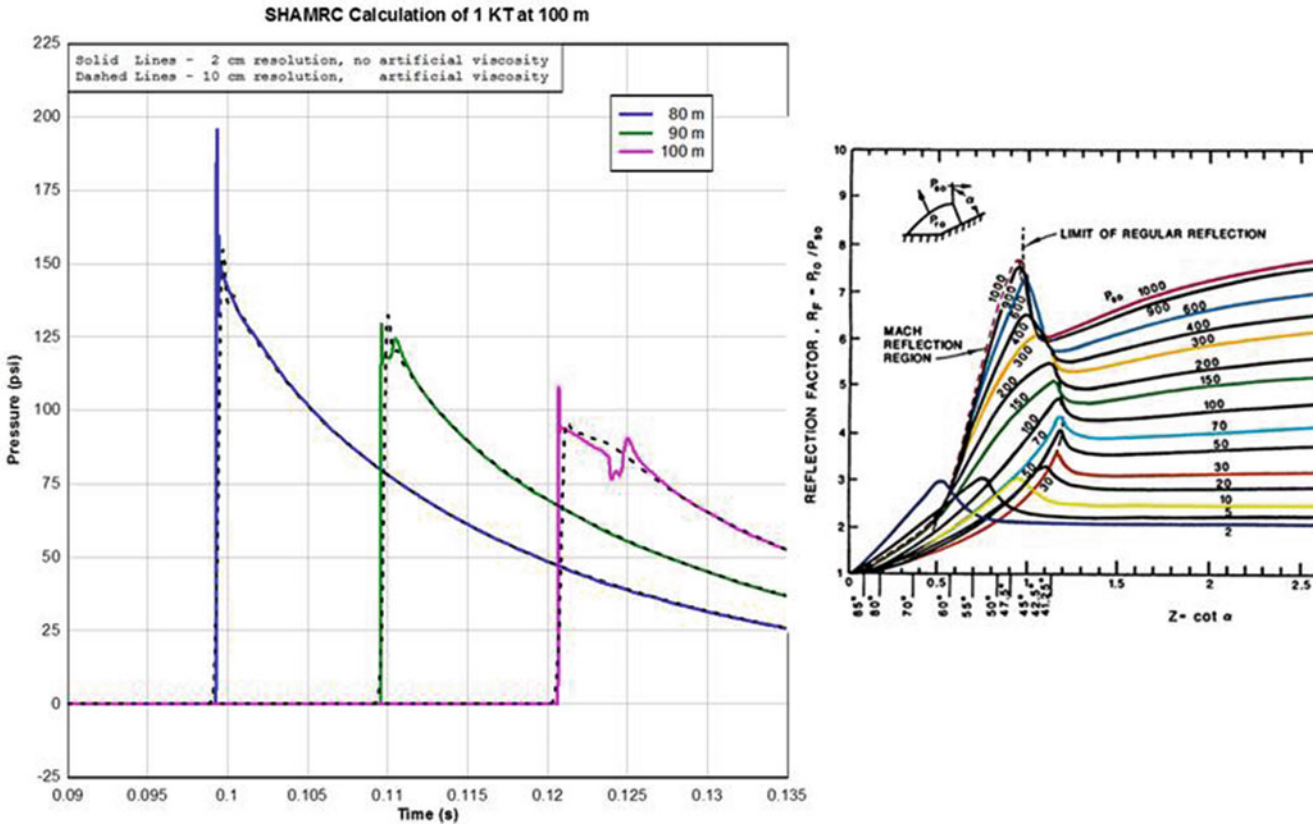

Fig. 9 Nuclear calculation reflection factor resolution example

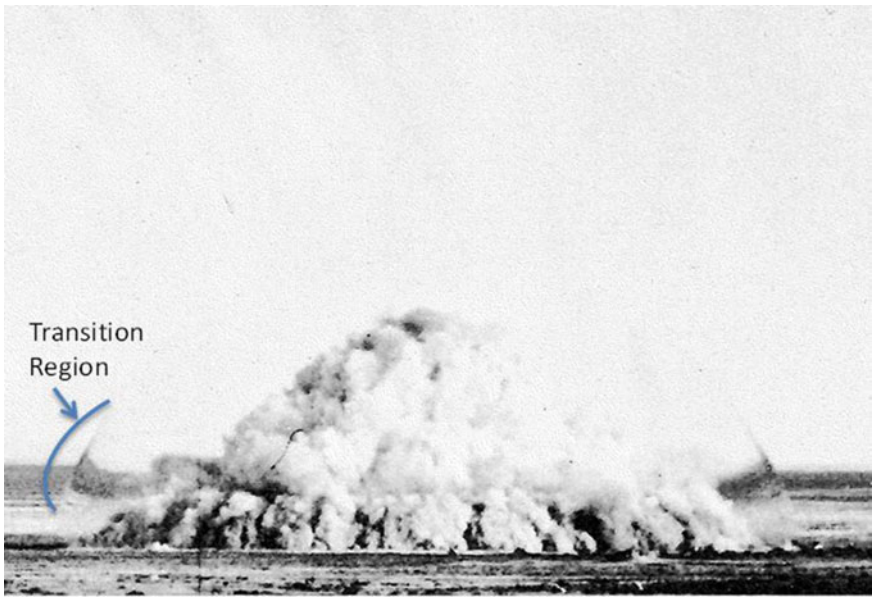

Fig. 10 628 ton event showing shock geometry

time to a peak. With 2 cm resolution (25 times the number of zones in 2-D), the second peak is resolved and can be distinguished from the shock front. Keep in mind that the second peak is not a shock, but a sharp compressive wave resulting from the two-dimensional character of the flow behind the shock reflection. Because the peak pressure is the result of a compressive wave, the Rankine-Hugoniot relations may not apply.

Note that the waveform at 90 m, calculated with 10 cm zoning, is higher than either peak in the resolved 2 cm calculation. Because the 10 cm zoning cannot separate the two signals, they are combined into a single peak with a slightly higher pressure.

A Shock from Cylindrical Source Will Become Spherical at a "Few" L/D

A large-scale experiment included the detonation of 628 tons of AN/FO in the shape of a cylinder with a 4.55 m radius with a hemispherical cap. The cylindrical part of the charge had a height to diameter ratio of 0.75. The charge was detonated at seven equally spaced points on the axis of the cylindrical part of the charge, the highest detonator at the top of the cylinder corresponding to the center of the base of the hemisphere. The assumption was made that at a distance of over 1 km, where the overpressure would be ~1 PSI, the shock would be hemispherical and uniform. The Army wanted to test a helicopter in flight at about this distance and pressure level.

The air blast from the hemispherical part of the charge expands in three dimensions. The air blast from the cylindrical portion expands in only two dimensions, but the shock front must remain continuous. This results in an inflection point in the curvature of the shock front which is induced by the geometrically different flow fields above and below the inflection point. At early times, the difference is dominated by the geometry (spherical vs. cylindrical), Fig. 10. As the shock expands and decays, the pressure gradients parallel to the shock front become small, and energy cannot be moved fast enough to change the shape of the shock front. Thus, even at distances of over 1 km, the shock front is not hemispherical and the pressure at the shock front is not uniform. There are also slip lines that form between the spherically and cylindrically expanding waves. The flow behind the shock in the transition region is complex.

A Shock Will "Clean Up" Within ~4 Diameters of an Obstacle

A widely used rule of thumb for shocks encountering obstacles is that the interrupted shock will heal within about four obstacle diameters. This rule may apply for many applications but is certainly not universally true. Figure 11 is taken from a three-dimensional calculation of a nonideal blast wave interacting with two parallel buildings. The dynamic pressure was higher than for an ideal wave of the same overpressure. The shock front does not "clean up" for over 700 m beyond the buildings. In that distance, the shock pressure has dropped by nearly a factor of 3. We have observed such large shock-healing distances in many experiments. In most cases the shock is prevented from healing because the dynamic pressure exceeds the overpressure, and the overpressure driving forces are insufficient to overcome the momentum of the redirected flow.

Exit Jet Environment

Exit jets from shock tubes cannot be used to generate blast waves simulating those from free field detonations. The shock emanating from the end of a shock tube is nonuniform. The planar shock in the tube suddenly expands in three dimensions. The shock expanding radially has a significantly lower pressure than the portion of the shock near the axis. A strong dynamic pressure jet extends from the end of the tube with little expansion. A strong vortex forms at the edge of the tube.

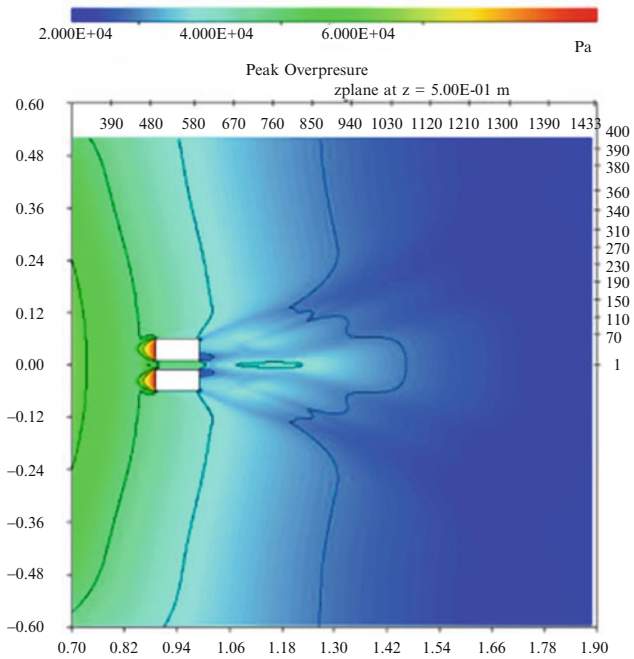

Fig. 11 0.5 bar nonideal blast wave interaction with two parallel structures

Figure 12 is a time sequence showing development of a shock-tube end-jet (efflux gas artificially colored). (A) The muzzle-blast shock front rapidly diffracts, weakens, and separates from the plume. (B) Ring vortex develops and separates from the lip of the tube end and is swept along with the venting column of shock-tube gases. (C) The venting jet of high-speed shock-tube gases has extreme dynamic pressure and long duration having an entirely different time waveform than the static pressure condition.

Because there is a sudden expansion of the shock at the end of the shock tube, rarefaction waves move into the flow from the edge of the tube. This introduces significant nonuniformities to the flow and reduces the useful area in which experiments can be made. To show the variation of the dynamic pressure impulse as a function of position in the exit jet, we include Fig. 13. This figure shows the dynamic pressure impulse in the exit jet in only the inner ½ of the diameter of the tube. The upper figure has the lateral dimension exaggerated by a factor of 5. The lower figure shows the true geometric relation of the dynamic impulse in the core of the jet. The large nonuniformities in the jet make it very difficult to use as a blast simulator.

Shock-Tube Blockage

Similarly, studies of blast-induced drag give the following equation:

$$Q_b = Q_0\left(\exp\left(2.64{*}R^{1.038}\right)\right)$$

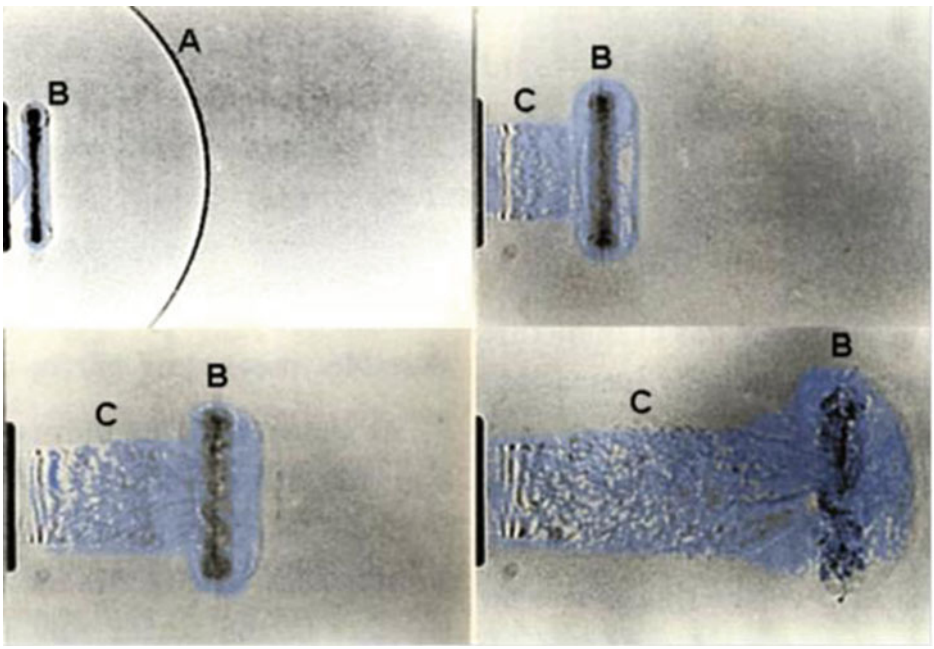

Fig. 12 Time sequence of exit jet formation. Pictures courtesy of Dr. K Kontis, C. Eng., Lecturer in Aerodynamics, University of Manchester

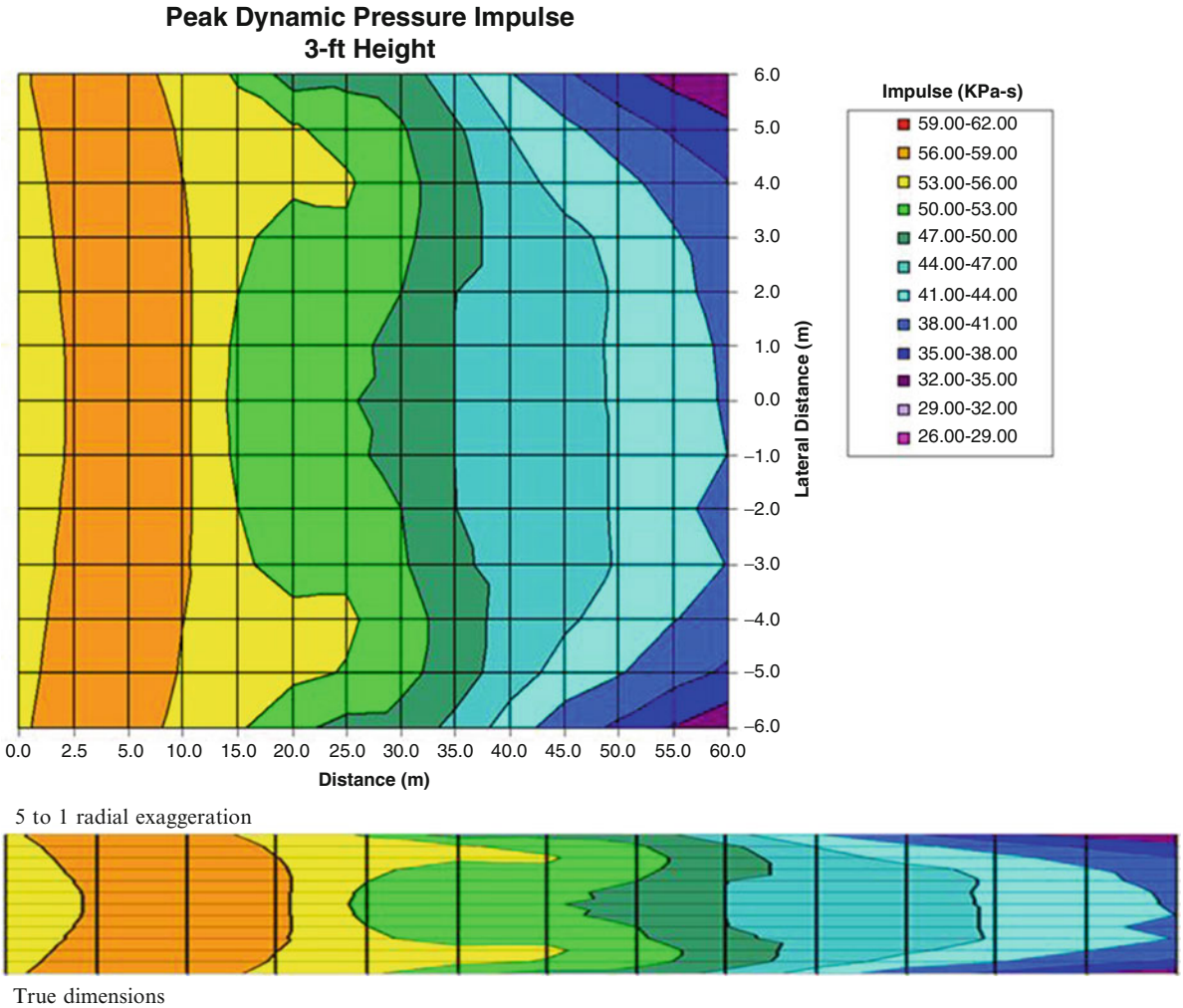

Fig. 13 Dynamic pressure impulse calculated over the center 50 % of the tube diameter at a height of 5 % of the tube diameter; measured from the open end of the tube

where Q_b is the dynamic pressure in the partially blocked tube, Q_0 is the dynamic pressure with no blockage, and R is the blockage ratio (the cross-sectional area of the target divided by the cross-sectional area of the shock-tube test section).

Evaluating this equation at 10 % blockage, the dynamic pressure (and the drag load) is increased by 27 % over the empty tube value. At 20 % blockage, the dynamic pressure is increased by 64 % and at 30 % it is increased by 113 %. This has been known and published for over 30 years, yet experiments continue to be conducted in shock tubes that are much too small for the test subjects.

Upward Force

When we think of air blast effects on buildings, we usually think about crushing and collapse. Buildings are constructed to withstand vertical gravitational loads. Construction techniques provide for large static loads and, to a lesser extent, for dynamic loads. In one test a detonation took place at ground level a few meters in front of a four-story building. The building was constructed of reinforced concrete and a static load was placed on the floors. The load was representative of an occupied office building.

The calculations of the air blast loads indicated that the initial loads on all upper floors were initially upward (Fig. 14). The blast wave came through the windows on the floor below and generated an upward force. The construction was not designed to resist upward motion and the floors were displaced upward. The shock wave then came through the windows on the floor above and drove the floor downward. This downward acceleration generated much higher dynamic loads than the structure was designed for, and the front wall connections failed.

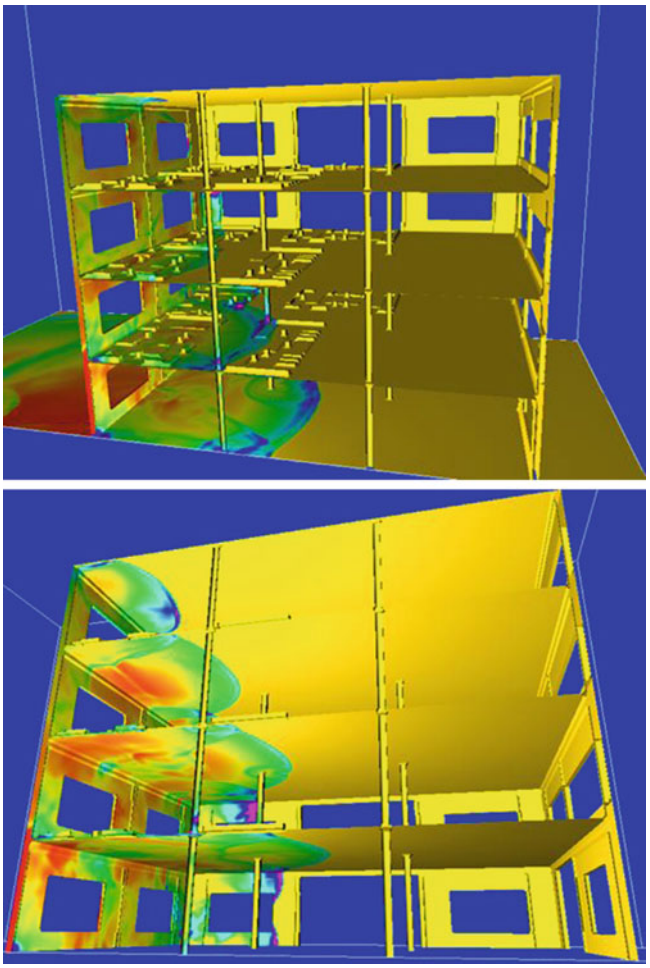

Fig. 14 Internal pressure loads on a four-story office building

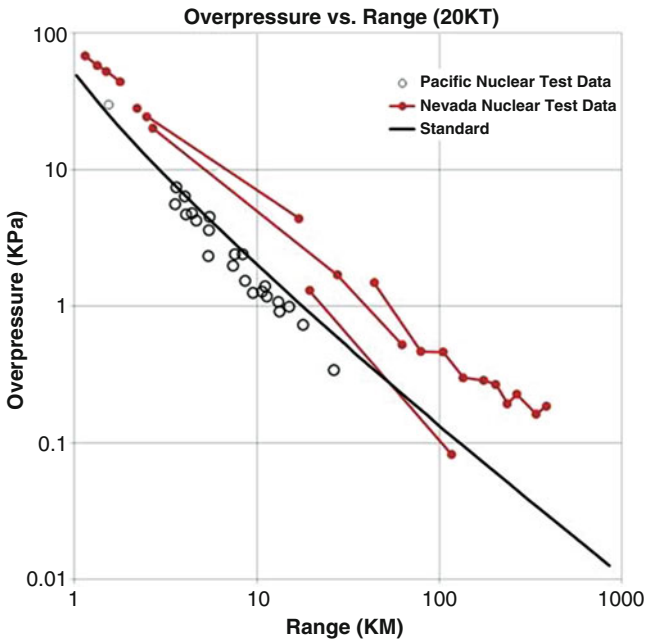

Fig. 15 Overpressure as a function of scaled range for pressures below 1 bar

Pacific vs. NTS

While validating the nuclear blast standard, I encountered arguments that data from some test or series of tests showed that the standard was high or low depending on the specific test cited. Nearly all of the discrepancies were found below an overpressure level of 1 bar or 100 kPa. Further investigation showed that much of the Nevada Test Site data fell above the standard curve. Reluctantly I adjusted the curve upward to agree with the NTS data. I then started comparing the revised curve with the Pacific Proving Ground test data and found that the standard was consistently higher than the PPG data (Fig. 15). After a few years of discussions, we decided that "standard" should represent all of the data. All of the data shows large scatter for overpressures below about 0.1 bar (10 kPa), and because the standard was well above the Pacific data, we decided that the original standard was a better representation of all the data.

The question remained: Why was the PPG data well below the NTS data? While most of the shots in the PPG were in the megaton range, I found that the data from PPG shots with yields below 100 kt agreed well with the NTS data. A few high-resolution calculations were made to investigate this dramatic difference in low overpressure propagation. The calculations revealed that when the radius of the shock front at an overpressure of 0.1 bar is approximately the scale height of the atmosphere (~9 km) or greater, more energy is directed upward, thus reducing the energy and pressure propagating in the horizontal direction.

Perhaps the discussion about the scatter in the data at low overpressures is illustrated by the comparisons shown in Fig. 16. Below a tenth of a bar, the air blast data has a scatter of more than an order of magnitude. Much of the scatter is explained by tracing the path of the shocks through the atmosphere. The effects of the troposphere, ozonosphere, and ionosphere are plotted separately.

Note that at the pressure level associated with threshold window damage, there is about an order of magnitude scatter in the range at which it may be measured. This scatter is caused by differences in the structure of the atmosphere at the time of the shot. Remember that the NTS shots were all conducted with fair weather and relatively calm winds. Departures from "good" weather will cause even greater scatter.

The 1 Kt standard was criticized for "not matching the data." It is difficult to match the data when there is an order of magnitude scatter. This scatter is real and is caused by variations in the real atmosphere.

Jeep Translation

During the NTS nuclear tests, a number of vehicles were exposed to nuclear air blast at different levels to determine the correlation of damage with pressure level. In compiling

the data, it was noted that vehicle displacement correlated well with dynamic pressure impulse. Many more jeeps were tested than any other type of vehicle, and jeep displacement was plotted as a function of dynamic pressure impulse. The correlation was so good that during some later tests, the dynamic impulse was quoted in jeep feet. Figure 17 is a plot of the jeep displacement in feet as a function of dynamic pressure impulse.

Similar curves can be plotted for other types of vehicles, and the damage thresholds for these vehicles are shown at the top of the plot.

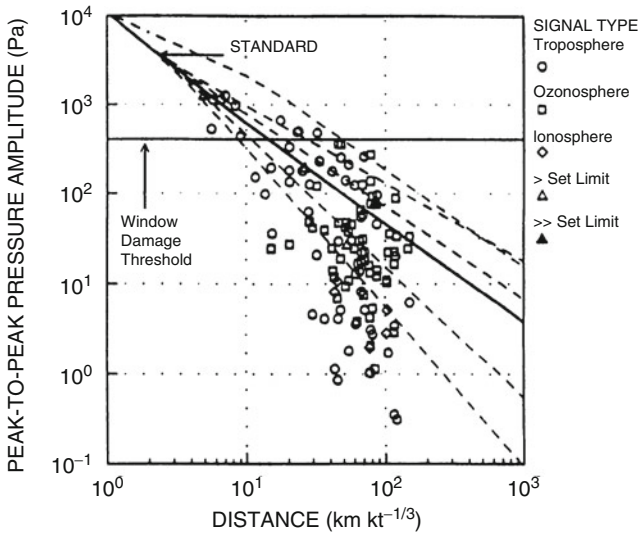

Fig. 16 Peak-to-peak pressure plot from the first six shots of Operation Teapot

Summary

In all the above examples, the shock wave was reflected, and the "responding" material effect on the blast wave was insignificantly different from that of a non-responding material. In all cases the shock wave reflected as if the structure was non-responding. This justifies and simplifies calculations of shock interactions with structures with the assumption that the structures are rigid and non-responding.

The debris velocity of the structures reached a maximum of less than half of the material velocity behind the shock. The debris remains well behind the shock front because the shock velocity is greater than the material velocity at the shock front by the speed of sound. As the velocity of the air behind the shock slows and reverses, the debris falls to the ground or reverses direction and may fall closer to the detonation point than its original location.

With the possible exception of a few buildings that may be in or very near the fireball, urban structures absorb little energy from the blast wave. The debris is almost always at least 1000 times denser than the air in the blast wave. The air responds 1000 times faster than the solid material. The kinetic energy of the debris is therefore much less than 1 % of the air blast energy. The debris from these structures generally falls within about four times the building height.

Many years ago Hal Brode advised me to "not do hydro in your head." The above are several examples of why this is good advice for everyone. Most of the misconceptions about air blast waves and their interactions with structures are caused by a lack of understanding of the differences between overpressure and dynamic pressure. Further we must keep in mind that most solid materials, whether wood or steel, are at least 1000 times more dense than air and will therefore move one thousandth as fast as the air blast that loads them.

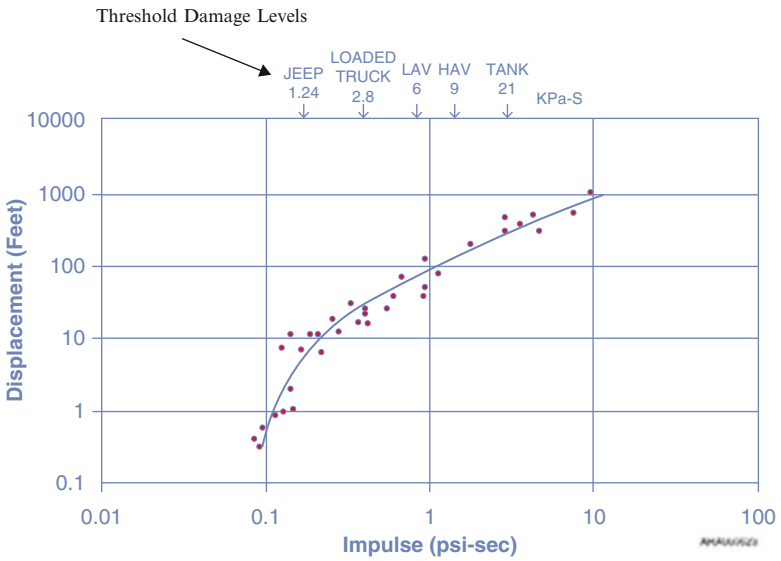

Fig. 17 Jeep displacement as a function of dynamic pressure impulse

A Review of the Richtmyer-Meshkov Instability from an Experimental Perspective

R. Bonazza

Introduction

The events following the impulsive acceleration (e.g. by a shock wave) of the interface between gases of different acoustic impedance can be classified into two main categories: the refraction of the shock (involving a transmitted and a reflected shock and the distortion of their shapes) and the baroclinic generation of vorticity at the interface consequent to the non-zero cross product between the density gradient associated with the interface and the pressure gradient across the shock wave. The resulting flow field leads to the unbounded growth of any perturbations initially present on the interface, a phenomenon called the Richtmyer-Meshkov instability (RMI). Because it originates from baroclinic vorticity, the RMI can be interpreted as the "impulsive analog" of the Rayleigh-Taylor instability (RTI) which develops at an interface subjected to sustained acceleration.

Upon shock acceleration, the perturbation initially grows maintaining its original sinusoidal shape (linear stage: the amplitude remains less than about 10 % of the wavelength); then (non-linear stage) broad 'bubbles' of the light fluid enter the denser one, and narrow 'spikes' of the heavy fluid penetrate the lighter one, with the tips of the spikes eventually developing mushroom-like roll ups. Lastly secondary instabilities develop on the interface, any well-defined shape is lost leading to a 'mixing layer'. Material interfaces occurring in nature or engineered are typically diffuse (finite thickness), with three-dimensional perturbations exhibiting a broad spectrum. In this case, transition from the linear to the non-linear stages proceeds from the high- to the low-wavenumber modes and it involves strong modal interactions, with the interface still transitioning to a mixing layer.

Flows of this type occur in a variety of situations spanning enormous time, length, and energy ranges: from laser-driven experiments in the pursuit of inertial confinement fusion (ICF), to proposed configurations for hypersonic combustion engine inlets, to supernovae explosions. The shock-induced mixing has very negative effects in the case of ICF while it holds great potential to improve the combustion processes in the case of hypersonic engines.

Original Work

It is useful to briefly review the linearized theory for the case of a discontinuous, 2D sinusoidal interface between inviscid fluids of different densities, with amplitude a and wavelength λ, subjected to a constant acceleration field g, as shown in Fig. 1. For the linear case ($a \ll \lambda$), Taylor [1] showed that the amplitude history is described by $d^2a/dt^2 = gkAa$ whose solution is $a = a_0 \exp(\sqrt{gkA}t)$ where a_0 is the initial value, k is the perturbation wavenumber, and $A \equiv (\rho_1 - \rho_2) / (\rho_1 + \rho_2)$ is the Atwood number. Depending on the direction of the density gradient, the eigenvalue is either imaginary (stable, oscillatory solution) or real, leading to the exponential growth of the perturbation (the RTI).

The first study of a 2D, single mode, discontinuous interface accelerated by a planar shock wave is due to Richtmyer [2]. The equations of motion were linearized and the resulting system solved numerically by finite difference methods. After a very short initial transient corresponding to the reverberation of pressure waves between the transmitted and reflected shocks, the growth rate of the perturbation amplitude reached an asymptotic value in good agreement with the "impulsive model" obtained by replacing the acceleration field in the RTI differential equation with $g = V\,\delta(t)$ where V is the velocity jump induced at the interface by the

R. Bonazza (✉)
Department of Engineering Physics, University of Wisconsin, 1500 Engineering Drive, 53706 Madison, WI, USA
e-mail: bonazza@engr.wisc.edu

G. Ben-Dor et al. (eds.), *30th International Symposium on Shock Waves 1*, DOI 10.1007/978-3-319-46213-4_3

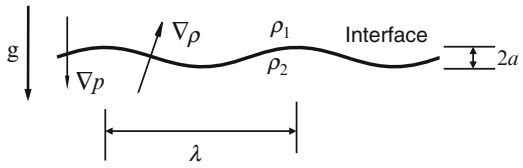

Fig. 1 Rayleigh-Taylor instability

shock wave, and $\delta(t)$ is the Dirac delta function. Integration leads to $a = a_0 VkAt$ and Richtmyer observed that agreement between this result and the numerical integration was best when the values of a_0 and A immediately after shock compression (a_0' and A') were used.

The tool of choice for the gasdynamicist to experimentally study an impulsively accelerated interface is the shock tube. At the time of the first experiments by Meshkov [3], most of the existing shock tubes were horizontal with circular internal cross section requiring: some kind of partition (typically a thin film) to form an interface; and an extension (often referred to as a "cookie cutter") to the shock tube circular structure to add two parallel walls to perform flow visualization. Meshkov used both of these approaches to study single-mode interfaces for a variety of Atwood numbers. He performed high speed schlieren imaging and observed constant growth rates during the linear phase, although at values up to 10 % lower than predicted by the impulsive model with a_0' and A'.

History of Experiments

While the single-mode interface remains an extremely useful testbed for the understanding of the RMI, it presents an important limitation: in the case of multimode initial conditions (more closely representative of actual occurrences of the instability, e.g. in ICF experiments), linear superposition of the growth of the individual modes only applies while all amplitudes are much smaller than the corresponding wavelengths, i.e. during the very early stages of the instability. Mixing of the gases only starts to occur at later times, when most disturbances have grown out of their linear phase and when simple superposition is no longer applicable. Therefore multi-mode initial conditions (nominally flat interfaces with small-amplitude disturbances over a finite range of wavelengths) have also been investigated over the years. For the single-mode interface, the time history of the perturbation amplitude is the main quantity of interest. For the multi-mode interface, the focus is on the thickness of the mixing zone that develops across the interface.

Horizontal Shock Tubes

The use of membranes to prepare the interface in a horizontal shock tube has continued to the present day (examples include [4–9]) to study both: interfaces with a pre-imposed shape, and nominally flat interfaces (small-amplitude, multimode initial conditions). In some cases, a wire mesh is placed just downstream of the membrane to promote membrane rupture upon shock acceleration and, in some cases, to impose a known initial perturbation. A recent improvement on this technique [10] replaces the nitrocellulose with soap film.

Diagnostic techniques include schlieren imaging and planar Mie scattering performed in either single-shot or high-speed mode.

But the presence of a membrane in the flow has no fewer than three adverse implications: (a) before being ruptured by the accelerating shock wave, membranes are liable to leaks across them (especially when one of the two gases is helium) causing an uncertainty in the initial Atwood number; (b) upon shock acceleration, the membrane breaks up into fragments of different sizes whose effect on the ensuing flow is not well known [11]; (c) membrane fragments make any kind of laser-based planar imaging particularly challenging because they scatter back the laser light orders of magnitude more than any flow tracer.

The first to avoid the need for a membrane in a horizontal shock tube was Jacobs [12] who injected a "vertical gas curtain" within the driven gas, giving rise to two diffuse interfaces. With this setup, Jacobs performed the first planar laser induced fluorescence (PLIF) experiments in an RMI environment. The most advanced experiments (e.g., [13]) using the same shock tube setup combined the use of particle image velocimetry (PIV) and PLIF to measure simultaneously 2D velocity and concentration fields.

Vertical Shock Tubes

Sturtevant [14] was the first to propose a vertical shock tube and the use of gravitational stratification to separate the two gases. The tube's driven and test sections had square internal cross sections so as to eliminate the need for a cookie cutter extension to provide parallel walls to perform flow visualization. The first membrane-free initial conditions were set up using a retractable, flat, metal plate to separate a light gas (above the plate) from a heavy gas (below the plate). Retraction of the plate allowed the gases to diffuse into each other and deposited either a near-sinusoidal or a multimode

perturbation on the interface. Diagnostic techniques included single-shot and high-speed schlieren [14, 15] and single-shot X-ray visualization [16].

Jacobs [17] conceived a different strategy to prepare a membrane-free interface in a vertical, square cross section, shock tube. The tube at the University of Arizona is made of fiberglass and polycarbonate and it is light enough that it can be oscillated about a supporting pivot. The test section is 2 m long and entirely transparent, allowing for imaging all along its length. A flat interface is initially formed by flowing a light gas downwards from just below the diaphragm, and a heavy gas upwards from just above the end wall. Where the two gas streams meet, they form a flat stagnation surface with the excess gas exiting the shock tube via slots on two opposite walls. The head-on flows mitigate diffusive effects, keeping the interface thickness below 5 mm. From this stage, initial conditions of three different shapes can be produced: to obtain a 2-D, single-mode sinusoidal interface, the tube is rocked gently about a pivot line perpendicular to two of the shock tube walls, generating a standing wave on the stagnation surface. By vertically oscillating the stagnation surface, using a bellows just above the shock tube end wall, 3-D, single mode perturbations can be imposed on the interface. Faraday waves may be generated at the interface using two out-of-phase loudspeakers, one above and one below the interface. Investigations have been carried out using planar Mie scattering, PLIF, or PIV (e.g., [18, 19]).

The University of Wisconsin shock tube is also vertical, with large (25×25 cm^2) internal cross section, and structural capability to withstand an $M = 5$ shock in atmospheric air. Preparation of the initial conditions starts with the same head-on flow and flat stagnation surface as in the Arizona shock tube. From this stage, a near-single mode perturbation is induced on the interface by oscillating two pistons imbedded in opposite shock tube walls. Broadband, 3-D disturbances can be induced on the flat stagnation surface by superposing onto it a shear layer. In this case, the head-on flows of the two gases exit through slits on a single side of the shock tube while the same two gases are also injected from the opposite side in reverse orientation (the heavy gas above the light one). This produces a statistically steady interface with a spectrum spanning about one and a half decades. Flow diagnostics to date include planar Mie scattering and PLIF (e.g., [20–23]).

State of the Art

Single-Mode Interfaces

Some recent models for the growth of bubbles and spikes in the non-linear regime are based on potential flow theory [24] drag/buoyancy balance [25] or Padé expansions [26]. Others yet are semi-empirical based on experimental evidence [27]. Among the most recent and advanced experiments are those by Morgan et al. [19] who performed planar Mie scattering visualization and PIV velocity and vorticity measurements on a 2D sinusoidal interface between air and SF_6 accelerated by a $M = 1.2$ shock (Fig. 2). These experiments extend to the longest post-shock time reported in the literature to date. The authors also paid careful attention to quantify a secondary effect: as the shock propagates, boundary layers develop along the shock tube walls immediately behind it and affect the motion of the interface causing it to keep accelerating without ever reaching the value predicted by 1-D gasdynamics. This steady acceleration causes the RTI to develop at the interface and to act concurrently with the RMI. The authors also carried out

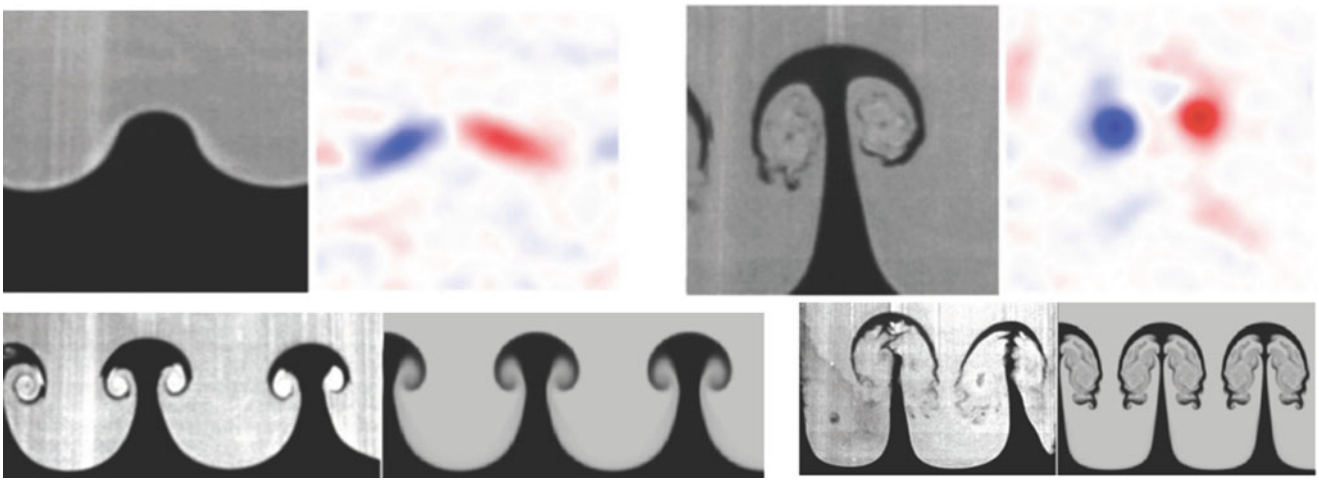

Fig. 2 2-D air/SF_6 interface, $M = 1.2$. *Top*: planar Mie scattering and vorticity field from PIV. *Bottom*: planar Mie scattering and numerical simulations using the *Miranda* code from LLNL. From [19]

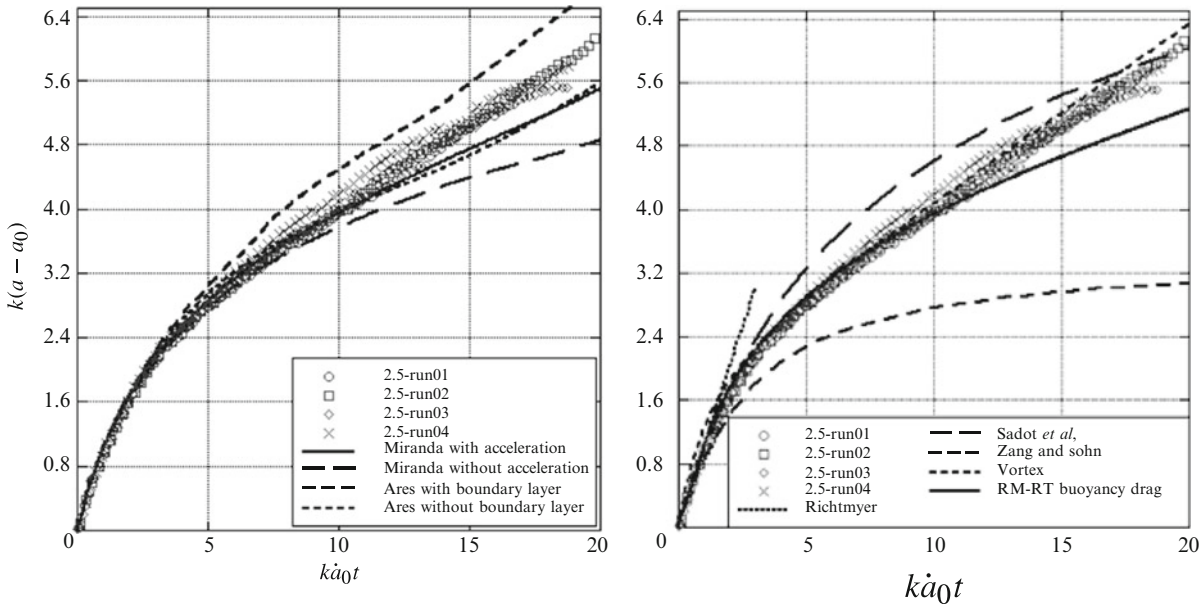

Fig. 3 Dimensionless amplitude *vs*. dimensionless time for the experiments of Fig. 2. *Left*: Comparison of measurements and numerical results. *Right*: Comparison of measurements and models. From [19]

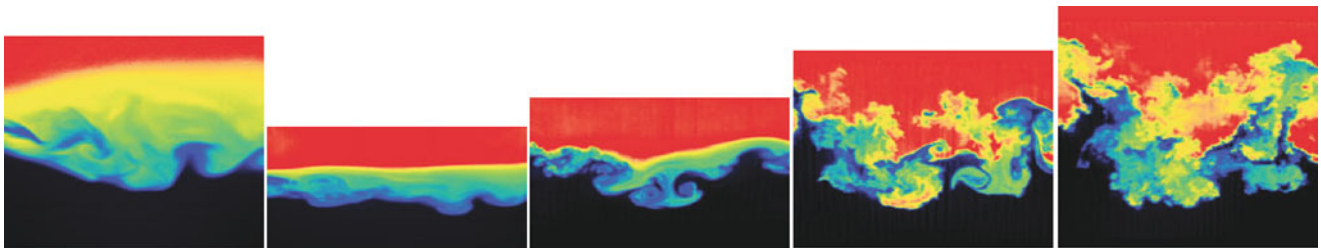

Fig. 4 Sequence of PLIF images for a He/Ar interface, $M = 2$. Times are from initial shock interaction. From [23]

numerical simulations of their experiments using the *Miranda* and *Ares* codes from LLNL. Comparisons between experiments, numerical results, and models are shown in Fig. 3. Time is commonly normalized by the product $k\dot{a}_0$ (requiring detailed knowledge of the initial growth rate or the use of the value from the impulsive model) while the amplitude is shifted by its initial value and normalized by k. The growth rate departs from the linear regime very early but its asymptotic behavior tends to a constant different than unity, unlike the $1/t$ behavior predicted by most models.

Multi-Mode Interfaces

In recent experiments, Weber et al. [22, 23] used PLIF to measure the 2-D He-mole fraction (ξ) at a He/Ar multi-mode interface (examples in Fig. 4; see Sect. 3 for the preparation of the interface) and to extract from it one of its most studied integral properties *viz*. the mixing layer thickness, h. A commonly used definition is $h = h_{5-95}$ i.e., the streamwise distance between spanwise-averaged mole-fraction values $\xi = 0.05$ and $\xi = 0.95$. The results (Fig. 5) are described very well by

$$\frac{h}{h_0'} = b\left(\frac{h_0}{h_0'}t\right)^{\theta} \tag{1}$$

with $b = 1.98$ and $\theta = 0.43$. The values of $h_0'\,\dot{h}_0$ were measured using the first two post-shock PLIF images. The value of θ is comparable to analytical predictions by Mikaelian [28], especially when taking into account the reduction in growth rate consequent to the diffuse nature of the initial conditions (see [15]).

The spatial spectra of the concentration fields were also studied to establish if the flow had reached a fully turbulent regime (examples are in Fig. 6a,b). Tritschler et al. [29] compared radial spectra from their calculations

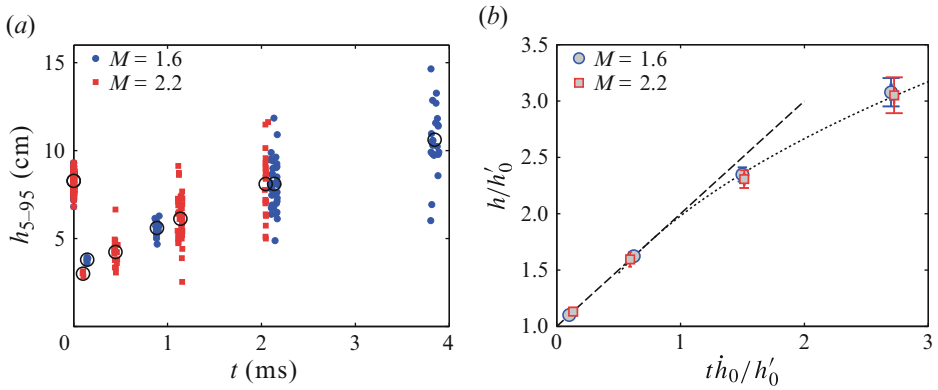

Fig. 5 Mixing layer thickness in dimensional (**a**) and dimensionless (**b**) form. From [23]

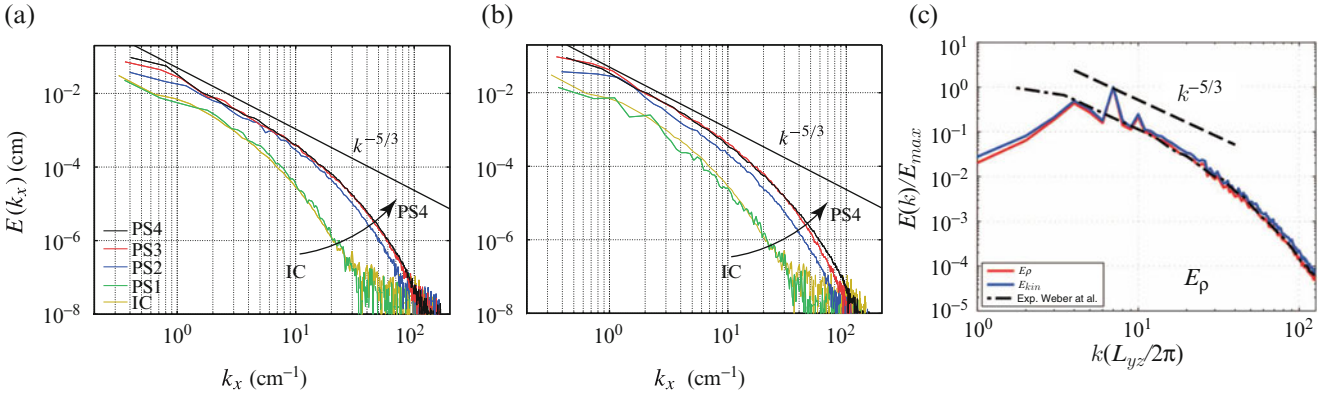

Fig. 6 (**a**) 1-D spectra from measurements of 2-D concentration field for He/Ar, $M = 1.67$. PS1-PS4 indicate post-shock times $t = 0.14$ ms, $t = 0.88$ ms, $t = 2.16$ ms, $t = 3.84$ ms. From [23]. (**b**) Same as (**a**) for $M = 2.2$ with same post-shock times as in Fig. 4. (**c**) Comparison of computed 1-D spectra for air/SF_6, $M = 1.5$ (from [29]) to those from (**a**)

of an O_2-N_2/SF_6 interface accelerated by an $M = 1.5$ shock to Weber et al.'s 1-D spectra with excellent agreement (Fig. 6c). An inertial range ($k^{-5/3}$) seems to exist at the intermediate wavelengths, followed by an exponential scaling.

Another criterion to determine if the flow has reached a fully turbulent regime is for the Reynolds number to exceed a critical value of about 10,000 ∼ 20,000. Several ways have been proposed to estimate the Reynolds number for unsteady flows of this type. One is $Re = h\dot{h}/\nu$ which can be evaluated directly from the measurements of the mixing layer thickness. Another one is $Re \simeq 1/28(\lambda_T/\lambda_B)^4$ where λ_T and λ_B are the Taylor and Batchelor scales. These scales can be determined from the PLIF images using two different approaches (see [23]). The Reynolds numbers for Weber et al.'s experiments are shown in Fig. 7: the results suggest that the flow does indeed reach a fully turbulent stage at the latest post-shock times.

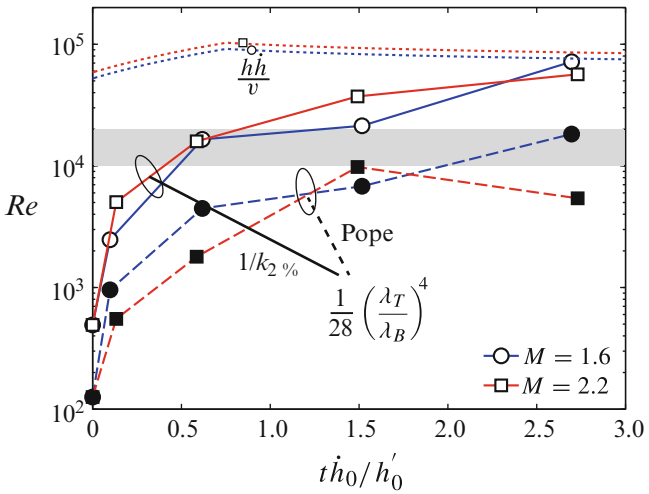

Fig. 7 Estimates of the Reynolds number at different post-shock times (from [23]). The *gray band* indicates the region of transition to full turbulence

Future Directions

The effect of reshock, the dependence of the late time behavior on the initial conditions, compressibility effects, more mixing statistics and their evolution at late times are all currently under investigation at many institutions worldwide indicating that the RMI field will remain vibrantly active for many years to come.

References

1. Taylor, G.I: The instability of liquid surfaces when accelerated in a direction perpendicular to their planes. I. Proc. Roy. Soc. A **201**, 192 (1950)
2. Richtmyer, R.D.: Taylor instability in shock acceleration of compressible fluids. Comm. Pure Appl. Math. **8**, 297 (1960)
3. Meshkov, Y.Y.: Instability of the interface of two gases accelerated by a shock wave. Fluid Dyn. **4**, 101 (1969). [Izv. Akad. Nauk SSSR Mekh. Zhdik. Gaza 5, 151 (1969)]
4. Andronov, V.A., Bakhrakh, S.M., Meshkov, E.E., Mokhov, V.N., Nikiforov, V.V., Pevnitskii, A.V., Tolshmyakov, A.I.: Turbulent mixing at contact surface accelerated by shock waves. Sov. Phys. JETP **44** (2), 424 (1976)
5. Aleshin, A.N., Lazareva, E.V., Zaitsev, S.G., Rozanov, V.B., Gamalli, E.G., Lebo, I.G.: Linear, nonlinear, and transient stages in the development of the Richtmyer-Meshkov instability. Sov. Tech. Phys. Lett. **35** (2), 159 (1990)
6. Vetter, M., Sturtevant, B.: Experiments on the Richtmyer-Meshkov instability of an air/SF_6 interface. Shock Waves **4**, 247 (1995)
7. Nevmerzhitsky, N.V., Sotskov, E.A., Senkovsky, E.D., Razin, A. N., Ustinenko, V.A., Krivonos, O.L., Tochilina, L.V.: The influence of the Mach number of shock waves on turbulent mixing growth at an interface of gases. Phys. Scr. **T142**, 014016 (2010)
8. Vanderboomgaerde, M., Souffland, D., Mariani, C., Biamino, L., Jourdan, G., Houas, L.: An experimental and numerical investigation of the dependency on the initial conditions of the Richtmyer-Meshkov instability. Phys. Fluids **24**, 024109 (2014)
9. Malamud, G., Leinov, E., Sadot, O., Elbaz, Y., Ben-Dor, G., Shvarts, D.: Reshocked Richtmyer-Meshkov instability: Numerical study and modeling of random multi-mode experiments. Phys. Fluids **26**, 084107 (2014)
10. Luo, X., Wang, X., Si, T.: The Richtmyer-Meshkov instability of a three-dimensional air/SF_6 interface with a minimum-surface feature. J. Fluid Mech. **722**, R2 (2013)
11. Erez, L., Sadot, O., Oron, D., Erez, G., Levin, L.A., Shvarts, D., Ben-Dor, G.: Study of the membrane effect on turbulent mixing measurements in shock tubes. Shock Waves **10**, 241–251 (2000)
12. Jacobs, J.W., Jenkins, D.G., Klein, D.L., Benjamin, R.F.: Nonlinear growth of the shock-accelerated instability of a thin fluid layer. J. Fluid Mech. **295**, 2342 (1995)
13. Orlicz, G.C., Balasubramanian, S., Prestridge, K.P.: Incident shock Mach number effects on Richtmyer-Meshkov mixing in a heavy gas layer. Phys. Fluids **25**, 114101 (2013)
14. Brouillette, M., Sturtevant, B.: Experiments on the Richtmyer-Meshkov instability: Small scale perturbations on a plane interface. Phys. Fluids A **5** (4), 916–930 (1993)
15. Brouillette, B., Sturtevant, B.: Experiments on the Richtmyer-Meshkov instability: single scale perturbations on a continuous interface. J. Fluid Mech. **263**, 271–292 (1994)
16. Bonazza, R., Sturtevant, B.: X-ray measurements of growth rates at a gas interface accelerated by shock waves. Phys. Fluids **8** (9), 2496–2512 (1996)
17. Jones, M.A., Jacobs, J.W.: A membraneless experiment for the study of Richtmyer-Meshkov instability of a shock-accelerated gas interface. Phys. Fluids **9** (10), 3078–3085 (1997)
18. Jacobs, J.W., Krivets, V.V., Tsiklashvili, V., Likhachev, O.A.: Experiments on the Richtmyer-Meshkov instability with an imposed, random initial perturbation. Shock Waves **23**, 407–413 (2013)
19. Morgan, R.V., Aure, R., Stockero, J.D., Greenough, J.A., Cabot, W., Likhachev, O.A., Jacobs, J.W.: On the late-time growth of the two-dimensional Richtmyer-Meshkov instability in shock tube experiments. J. Fluid Mech. **712**, 354–383 (2012)
20. Motl, B., Oakley, J., Ranjan, D., Weber, C., Anderson, M., Bonazza, R.: Experimental validation of a Richtmyer-Meshkov scaling law over large density ratio and shock strength ranges. Phys. Fluids **21**, 126102 (2009)
21. Weber, C., Haehn, N., Oakley, J., Anderson, M., Bonazza, R.: Richtmyer-Meshkov instability on a low Atwood number interface after reshock. Shock Waves **22**, 317–325 (2012)
22. Weber, C., Haehn, N., Oakley, J., Rothamer, D., Bonazza, R.: Turbulent mixing measurements in the Richtmyer-Meshkov instability. Phys. Fluids **24**, 074105 (2012)
23. Weber, C, Haehn, N., Oakley, J., Rothamer, D., Bonazza, R.: An experimental investigation of the turbulent mixing transition in the Richtmyer-Meshkov instbility. J. Fluid Mech. **748**, 457–487 (2014)
24. Mikaelian, K.O.: Explicit expressions for the evolution of single-mode Rayleigh-Taylor and Richtmyer-Meshkov instabilities at arbitrary Atwood numbers. Phys. Rev. E **67**, 026319 (2003)
25. Oron, D., Arazi, L., Kartoon, D., Rikanati, A., Alon, U., Shvarts, D.: Dimensionality dependence of the Rayleigh-Taylor and Richtmyer-Meshkov instability late-time scaling laws. Phys. Plasmas **8**, 2108–2115 (2001)
26. Zhang, Q., Sohn, S.I.: Padé approximation to an interfacial fluid mixing problem. Appl. Math. Lett. **10**, 121–127 (1997)
27. Sadot, O., Erez, L., Alon, U., Oron, D., Levin, L.A., Erez, G., Ben-Dor, G., Shvarts, D.: Study of nonlinear evolution of single-mode and two-bubble interaction under Richtmyer-Meshkov instability. Phys. Rev. Lett. **80**, 1654–1657 (1988)
28. Mikaelian, K.O.: Testing an analytic model for Richtmyer-Meshkov turbulent mixing widths. Shock Waves **25**, 35–45 (2015)
29. Tritschler, V.K., Hickel, S., Hu, X.Y., Adams, N.A.: On the Kolmogorov inertial subrange developing from Richtmyer-Meshkov instability. Phys. Fluids **25**, 071701 (2013)

Medical and Biomedical Applications of Shock Waves: The State of the Art and the Near Future

Achim M. Loske

Introduction

Biomedical applications of shock waves are a fascinating subject that is continuously growing. The use of shock waves to break up urinary calculi without surgery, which is known as extracorporeal shock wave lithotripsy (SWL) [1, 2], has led to considerable research in physics, medicine, microbiology, and molecular biology. After the first SWL in 1980, many companies developed clinical devices, and the number of successful treatments increased exponentially. SWL use was expanded to other types of stones, including gallbladder stones, pancreatic calculi, and salivary gland stones. Today, shock waves are also common in orthopedics, traumatology, cardiology, rehabilitation, aesthetic therapy, and veterinary medicine. Many of these treatments, which are referred to as extracorporeal shock wave therapy (ESWT) [2, 3], are attracting increasing attention. The purpose of this article is to give an overview of the biomedical applications of shock waves, including some current research topics.

Shock Wave Use in Medicine and Biomedicine

The nonlinear pressure pulses generated by the devices that are used for clinical applications are commonly called shock waves, regardless of whether they are technically shock waves. They consist of a compression pulse with a full width at half maximum (FWHM) of approximately 0.5–3 μs and a peak positive pressure (p^+) between 10 and 150 MPa. In most biomedical equipment, p^+ is reached within a few nanoseconds and is followed by a pressure trough with an amplitude of up to 25 MPa that lasts between 2 and 20 μs. The frequency ranges between approximately 15 kHz and 20 MHz. For SWL, the pulse energies and energy densities are between 10 and 100 mJ and between 0.2 and 2.0 mJ/mm^2, respectively. Devices that are designed for ESWT produce lower pressures, and their energy densities are between 0.004 and 0.6 mJ/mm^2. So-called "radial shock waves" are also popular for treating diseases of the musculoskeletal system. These pressure pulses have a lower peak pressure and a longer rise time compared with lithotripter shock waves and should be referred to as radial pressure pulses, because they do not fulfill the criteria to be considered shock waves. Electrohydraulic, electromagnetic, and piezoelectric transducers are the most popular devices for producing shock waves [1, 2]. In electrohydraulic shock wave sources, an underwater high-voltage discharge between two electrodes that are located at the focus (*F1*) closest to a paraellipsoidal reflector produces a fast-expanding plasma bubble that generates a spherical shock front. The shock wave is reflected off the reflector and is focused toward the other focus (*F2*).

In electromagnetic transducers, a high voltage is applied to a flat circular copper coil, which is separated from a conductive metallic membrane by a thin insulating layer. The high-voltage discharge induces a strong magnetic field, which results in an abrupt deflection of the membrane. The sudden movement of the membrane produces pressure waves in a wave-propagating fluid, which are focused by an acoustic lens. Other designs use a cylindrical coil inside a parabolic metal reflector. The design works in a fashion that is analogous to the plain coil shock wave source. However, in this case, the pressure pulses are emitted radially to the axis of the cylinder. The cylindrical pressure waves are focused after reflecting off the parabolic reflector. Depending on the energy setting, the resulting pressure pulse may steepen into a shock wave. Self-focusing electromagnetic shock wave sources, with the coil mounted on a concave spherical backing, are also available [2].

A.M. Loske (✉)
Centro de Física Aplicada y Tecnología Avanzada, Universidad Nacional Autónoma de México, Blvd. Juriquilla 3001, Querétaro, Querétaro 76230, Mexico
e-mail: loske@fata.unam.mx

G. Ben-Dor et al. (eds.), *30th International Symposium on Shock Waves 1*, DOI 10.1007/978-3-319-46213-4_4

Piezoelectric transducers produce pressure pulses through a high-voltage discharge across a mosaic pattern of piezoelectric elements mounted on the inner surface of a spherical concave backing. The arrangement is placed inside a fluid-filled container. Each piezo-ceramic element expands and generates a pressure pulse that propagates toward the center, F, of the arrangement. Focusing produces steepening of the resulting wave, and a shock wave is generated in the vicinity of F due to nonlinear effects. Some piezoelectric sources have two layers of piezo-ceramic elements mounted on a bowl-shaped backing [2]. The front layer is excited a short time after the back layer, and the impulses generated by both layers superimpose additively at the surface of the shock wave generator. An advantage of dual-layer sources is their smaller size.

Multichannel electrical discharges in conductive water that are produced by either one or two composite cylindrical ceramic-coated metallic electrodes, which are aligned along the axis of symmetry of a parabolic reflector, have also been used for biomedical applications [4].

Some shock wave generators are used for both SWL and ESWT. A device that is not used in SWL is the radial pressure wave source. Similar to pneumatic jackhammers, compressed air accelerates a projectile inside a small cylindrical hand piece. A pressure pulse is produced when the projectile hits the end of the applicator. Some manufacturers offer equipment with both a shock wave therapy head and a radial pressure wave source.

Shock Wave Interaction with Matter

The interaction of shock waves with matter is a large field of study and includes calculus comminution mechanisms, the response of living tissue and cells to shock waves, and their influence on microorganisms. In many cases, the secondary effects of shock wave passage, such as acoustic cavitation and secondary shock wave emission, are more relevant than the influence of the initial pressure variation. During SWL, stones comminute primarily because of spallation, acoustic cavitation, circumferential squeezing, tensile stress, shear stress, and fatigue [1, 2]. These mechanisms may act together in a synergistic way. However, some of them are more important at the beginning of the treatment, and others are crucial in the final part of the treatment. Because different tissues, such as fat, skin, and muscle, have different acoustical impedances, shock wave scattering and attenuation may occur at their interfaces. Since the high frequencies associated with the shock front are attenuated more than the low-frequency components of the tensile phase, p^+ is attenuated more than the tensile phase. At interfaces with large differences in acoustic impedance such as soft tissue and kidney stones, shock wave reflections cause damage. During SWL, compression and tension form flaws inside the stone. Because the velocity of the shock wave in the medium outside the stone is lower than the elastic velocity inside it, the longitudinal shock wave inside the stone is always ahead of the pressure wave outside it. This produces a squeezing effect on the stone [1, 2]. Fracture may also occur because of spalling, which is the conversion of a positive pressure pulse into tensile stress after reflection at the rear side of the stone. If a stone fragment is too small, spalling will not occur, and other mechanisms such as acoustic cavitation become dominant.

Acoustic cavitation is crucial not only to fracture calculi. It is also responsible for several desired and non-desired effects of shock waves on tissue, cells, and microorganisms [1, 2]. Tiny bubbles form at the focus of most shock wave sources. These microbubbles become compressed as the positive pressure pulse arrives. The forced compression is followed by a fast bubble growth and a violent collapse. Bubbles expand approximately 50–100 μs after shock wave passage and disintegrate 200–700 μs later. In many cases, especially if the bubble is close to a solid boundary, its collapse will be asymmetric, and one side of it will accelerate inward more rapidly than the opposite side, which will result in the development of a high-speed (400 m/s or more) microjet of fluid that burrows through the bubble and hits the boundary. The collision between the inward-moving bubble wall and the jet generates a secondary shock wave, which contributes to further calculi disintegration. Microjets hitting a stone during SWL produce pitting. Cavitation also induces tissue lesions; however, because soft tissue contains fewer cavitation nuclei than do fluids and because the bubbles are constrained, their potential to cause tissue damage is reduced. Bubbles may collapse asymmetrically, even in the absence of a boundary. In this case, the microjets are emitted along the direction of shock wave propagation. This phenomenon is believed to be responsible for shock wave-induced cell transfection.

Bubble collapse and consequent microjet emissions can be enhanced if a second shock wave arrives shortly before the bubbles that were generated by the previous shock wave begin to collapse. These so-called tandem shock waves are defined as two consecutive shock waves and are generated within a time delay of approximately 10 and 900 μs. Tandem shock waves may reduce both the SWL treatment time and the tissue damage [2, 5]. Several authors have proposed different solutions for introducing tandem SWL into clinical practice, such as the design of composite reflectors for electrohydraulic shock wave sources, dual-spark systems, modified piezoelectric and electromagnetic sources, as well as combined electrohydraulic and piezoelectric sources [1, 2]. Tandem shock wave-enhanced cavitation has also been used to increase the bactericidal effect of shock waves [6] and the genetic transformation efficiency of

bacteria [7] and fungi [8]. A different approach for the use of tandem shock waves was proposed by Lukes et al. [4]. If the delay between shock waves is very short (10–15 μs), the bubbles that are produced by the first shock wave have insufficient time to grow before the second wave arrives. The purpose of these "short-delay" tandem waves is to produce a heterogeneous medium at the focal zone that is seeded with cavitation nuclei with which the second shock wave can interact. These pressure profiles have been shown to induce necrosis in tumors and delayed tumor growth in vivo.

Shock wave-induced tissue damage is not fully understood. Several physical and biochemical mechanisms act simultaneously. Whenever the shock wave energy is increased, the risk of tissue trauma also increases. Furthermore, the low-frequency domain produces more tissue damage compared with the high-frequency components. After SWL, the glomerular filtration rate is reduced, which means that renal function is weakened. However, there is no proof that shock waves cause long-term renal trauma. Shear stress can appear in bones, and cavitation may produce free radicals. Hematuria is a consequence of cortical and medullar hemorrhage, glomerular bleeding, and tubular dilation. It normally disappears within a few hours. Shock waves may cause cell membrane permeabilization, cell fragmentation, or alterations in the mitochondria and the nucleus. They can also induce analgesic effects [9] and tissue repair mechanisms [3], trigger mitogenic activities, and stimulate osteogenesis and chondrogenesis [2].

Extracorporeal Shock Wave Lithotripsy

SWL remains the primary treatment for patients with renal, proximal, and midureteral stones [1]. Extracorporeal lithotripters consist of a shock wave source, ultrasound and/or fluoroscopy imaging, a coupling device, and a treatment table. As mentioned above, the shock wave sources either are self-focusing or have a focusing system to concentrate the energy onto the stone. Normally, several hundred to a few thousand shock waves are needed to comminute a stone. In urological applications, stone debris passes through the urinary tract, and the patient is usually free of stones a few days after treatment. However, SWL outcomes depend on several factors, including the physical properties of the stone, the shock wave source, and the shock wave rate and energy.

For many years, a central debate regarding the design of extracorporeal lithotripters (SWL devices) has been with regard to the size of the focal zone. Small focal zones allow treatments with minimal anesthesia, but precise patient positioning is crucial. Shear forces and spallation are the predominant fragmentation mechanisms in lithotripters with a small focal size, whereas circumferential squeezing plays a crucial role in sources with a larger focal zone [1, 2]. There is a consensus that the acoustic energy delivered to the stone correlates with fragmentation efficiency. Qin et al. [10] studied the effect of the focal size on in vitro stone fragmentation by modifying a shock wave generator to produce a pressure field with either a high-pressure narrow-beam size or a low-pressure wide-focal size, with equal acoustic energy. The low-pressure wide-focal mode produced better in vitro stone comminution. Currently, some lithotripters such as the *Piezolith 3000* (Richard Wolf GmbH, Knittlingen, Germany) and the *SLX-F2* (Storz Medical, Tägerwilen, Switzerland) allow adjustments to generate more than one focal size. The recommendation is to treat renal calculi with large focal zone settings and to treat ureteral stones with a small focal zone. The so-called voltage stepping is recommended to protect the kidney from tissue damage and to improve stone fragmentation [1, 2, 11]. Gallbladder SWL is only used in few lithotripsy centers; however, it can be helpful to treat patients with bile duct stones that resist removal after endoscopic sphincterotomy or in patients in whom surgery is contra-indicated [12]. Furthermore, SWL offers good clinical outcomes for patients with large pancreatic duct calculi [13].

Research has focused on generating pressure profiles that reduce tissue damage while improving stone comminution. Some examples include tandem shock waves that enhance cavitation [2, 5] and novel lenses designed to improve the performance of electromagnetic lithotripters [2, 14].

Extracorporeal Shock Wave Therapy

Shock waves were introduced into the treatment of various diseases of the musculoskeletal system because of an incidental observation of osteoblastic response during in vivo studies. Currently, shock waves are used to treat patients suffering from plantar fasciitis, Achilles tendinitis, tennis elbow, slow- or nonhealing bone, avascular necrosis of the femoral head, skin ulcers, Peyronie's disease, erectile dysfunction, myocardial revascularization, and several other painful diseases [2, 3]. ESWT also improves myocardial function in patients with refractory coronary artery disease [15]. Shock waves are believed to initiate signal transduction cascades, i.e., serial responses by activated forms of proteins within the cell, leading a set of processes such as neovascularization, enhanced blood supply, and tissue regeneration. They can alter cell membranes such that the nociceptor neurons cannot build up generator potentials. Furthermore, shock waves may produce free radicals in the proximity of cell membranes, which results in pain-reducing chemicals.

Moreover, as mentioned above, special pressure profiles have been shown to delay tumor growth in vivo [4].

An interesting neural model for pain relief by ESWT suggests that when acute pain develops into chronic pain, the sensory input of afferent signals and the motor response of efferent signals are stored in the nervous system and act in a feedback loop such that the cause of the pain shifts from the organ to another level in the nervous system. In this way, the treatment could erase pain memory instead of modifying the organ itself [16].

Some clinical devices used for ESWT have therapy heads mounted on articulated arms with three-dimensional manual movement, so that the pressure waves can be efficiently coupled into the patient. Depending on the specific case, the shock waves may or may not be focused. Targeting can be aided by ultrasound, fluoroscopy, or feedback from the patient. Some lithotripters can also be used for ESWT. Hundreds to thousands of shock waves are typically applied. The therapy is divided into several sessions, with a few days of rest between sessions. To deliver the energy to a broad area, some devices produce planar or defocused waves. These systems are used to treat superficial lesions, such as cutaneous ulcers where a low penetration depth is desired [17]. Though many articles have reported beneficial effects, additional research is still necessary to identify the optimal treatment parameters and better understand the mechanisms involved in ESWT. Comparing ESWT outcomes is complicated because different pressure wave sources, protocols, and evaluation methods have been used. Subjective scores, evaluations performed at different follow-up times, small sample sizes, a lack of blinding, and short-term follow-ups are common limitations.

Genetic Transfection and Transformation

Cell transfection, i.e., the uptake of DNA to reprogram cellular functions, is a promising therapy to treat oncological diseases, hereditary disorders, and many other ailments. Several physical transfection methods have been developed, but immunological problems, low efficiency, and the inability to reach specific tissues in the patient are challenges that remain. Shock waves may be a solution to these problems because they can be focused deep within the body and can cause an increase in cell membrane permeability [2, 18]. Shear forces and microjets that are generated after the passage of shock waves produce transient pores into cell membranes that can allow large molecules (normally excluded by the membrane) to become trapped inside the cell without causing cell death. This shock wave-induced cell membrane permeability can enhance the cytotoxicity of anticancer drugs. Furthermore, shock wave-mediated transfection of cationic lipid-assembled DNA may enhance the transformation efficiency and reduce the amount of necessary nucleic material [19].

The genetic transformation of filamentous fungi is increasingly used in the pharmaceutical industry to create compounds such as antibiotics, vaccines, anticoagulants, and insulin and to produce various enzymes that are used in the food, textile, paper, and chemical industries. Unfortunately, the standard transformation methods are inefficient, laborious, and difficult to reproduce. Furthermore, many potentially useful species are resistant to transformation by conventional technology. Fortunately, the genetic transformation of fungi using underwater shock waves shows promise [20, 21]. *Aspergillus niger*, the worldwide producer of citric acid; *Trichoderma reesei*, a species that is employed to produce proteins for diverse industries; *Phanerochaete chrysosporium*, a fungus that degrades lignin; and *Fusarium oxysporum*, a pathogen that causes diseases in crops, have all been transformed with a high efficiency using underwater shock waves. The number of transformants obtained per number of cells used was several times greater than that achieved using standard methods [20]. This result was obtained by exposing mixtures of DNA and spores that were placed inside small polyethylene bags to up to 400 shock waves with a peak positive (p^+) and negative pressure (p^-) of approximately 38 and −18 MPa, respectively. In addition to its high efficiency, shock wave-mediated fungi transformation has the advantages that it is easy and fast to use and that no cell wall-digesting enzymes are required to facilitate the transformation. Intact spores can be directly exposed to shock waves and inoculated onto a selective medium.

Jagadeesh and colleagues [22] demonstrated that it is possible to transform bacteria with unfocussed electrohydraulically generated shock waves (p^+~13 MPa). A few years later, the same group achieved the insertion of heterologous DNA into *Escherichia coli* (*E. coli*) and *Agrobacterium* by shock waves (p^+ up to 10 MPa) that were produced with a microexplosive, detonated inside a specially designed small and inexpensive transformation device [23]. The transfer of DNA into bacteria has also been achieved using single pulse and tandem shock waves that were generated by a piezoelectric shock wave source. By enhancing the acoustic cavitation with tandem shock waves at a delay of 750 μs, the transformation efficiency increased more than 50 times compared with the standard $CaCl_2$ transformation method [7]. In the tandem mode, the positive peak pressure of the first and second shock waves was approximately 38 and 31 MPa, respectively. By adjusting the shock wave energy and the delay between tandem pulses, acoustic cavitation can alter the cell membrane without significantly inactivating bacteria and can thus become a genetic tool for mutant construction. The replication of an F-like plasmid obtained from a multidrug-resistant

E. coli strain into a nonpathogenic strain is another recent example of tandem shock wave-mediated transformation [24].

Bactericidal Effects

The bactericidal effects of shock waves have been controversial, probably because they depend on several factors such as the energy source, the dose, the microorganism, the environment, the phase of growth of the microorganisms, and the methodology. The topic is clinically relevant because renal stones can be a consequence of bacterial infections and because bacteremia during SWL may occur. Furthermore, there is hope that extracorporeal shock waves can be used to treat persistent infections. However, one problem is that bacterial destruction can release endotoxins from the outer wall of gram-negative bacteria into the blood stream.

The partial inactivation of several microorganisms such as *E. coli*, *Listeria monocytogenes*, *Salmonella*, and *Staphylococcus aureus* has been achieved after in vitro shock wave exposure [25, 26]. However, other reports have indicated no effects on the viability of *E. coli*, *Staphylococcus aureus*, *Pseudomonas aeruginosa*, and *Streptococcus faecalis* [27]. Studies of shock wave influence on the viability of bacteria that are proliferating inside artificial kidney stones suggest that SWL should not be considered an efficient bacterial inactivation method [28]. Nevertheless, other studies have revealed that, contrary to standard shock waves, tandem pulses might inactivate bacteria. No significant inactivation after exposing *E. coli* and *Listeria monocytogenes* to up to 8000 standard shock waves was observed. However, significant inactivation was achieved after treating the samples with 3400 tandem shock waves, generated with a 900-μs delay [6]. Other groups have reported that pressures of over 200 MPa, that were emitted by a gas gun completely inactivated *Vibrio* sp. in suspension [29].

Conclusions

The use of more versatile systems, such as modified electromagnetic shock wave generators and piezoelectric shock wave systems composed of various individually driven piezoelectric segments, as well as multichannel electrical discharge sources will help improve the existing clinical treatments and develop novel biomedical applications for shock waves. Patients suffering from embolism, hypertonia, and dystonia may benefit from ESWT. New technologies using shock waves for drug release, needleless vaccine delivery, and DNA delivery into bacteria and fungi are being developed. The potential therapeutic use of shock waves in gene therapy and oncology is also promising. Biofilm removal to treat periodontitis, and the inactivation of fungi at the site of infections are other interesting uses of shock waves that are under investigation. Progress in understanding of the detailed phenomena involved in shock wave interactions with living tissue and cells will certainly be followed by an increasing number of biomedical uses and by safer and more efficient clinical shock wave therapies.

Acknowledgments The author acknowledges L. M. López-Marín and F. Fernández for careful revision of the manuscript.

References

1. Rassweiler, J.J., Knoll, T., Köhrmann, K.U., McAteer, J.A., Lingeman, J.E., Cleveland, R.O., Bailey, M.R., Chaussy, C.: Shock wave technology and application: an update. Eur. Urol. **59**, 784–796 (2011)
2. Loske, A.M.: Medical and Biomedical Applications of Shock Waves. Shock Wave and High Pressure Phenomena. Springer International Publishing AG, Cham, Switzerland (2017). ISBN 978-3-319-47568-4
3. Wang, C.J.: Extracorporeal shockwave therapy in musculoskeletal disorders. J. Orthop. Surg. Res. **7**, 11–17 (2012)
4. Lukes, P., Sunka, P., Hoffer, P., Stelmashuk, V., Pouckova, P., Zadinova, M., Zeman, J., Dibdiak, L., Kolarova, H., Tomankova, K., Binder, S., Benes, J.: Focused tandem shock waves in water and their potential application in cancer treatment. Shock Waves **24**, 51–57 (2014)
5. Fernández, F., Fernández, G., Loske, A.M.: Treatment time reduction using tandem shockwaves for lithotripsy: an in vivo study. J. Endourol. **23**, 1247–1253 (2009)
6. Alvarez, U.M., Ramírez, A., Fernández, F., Méndez, A., Loske, A. M.: The influence of single-pulse and tandem shock waves on bacteria. Shock Waves **17**, 441–447 (2008)
7. Loske, A.M., Campos-Guillén, J., Fernández, F., Castaño-Tostado, E.: Enhanced shock wave-assisted transformation of *Escherichia coli*. Ultrasound Med. Biol. **37**, 502–510 (2011)
8. Loske, A.M., Fernández, F., Magaña-Ortíz, D., Coconi-Linares, N., Ortíz-Vázquez, E., Gómez-Lim, M.A.: Tandem shock waves to enhance genetic transformation of *Aspergillus niger*. Ultrasonics **54**, 1656–1662 (2014)
9. Kenmoku, T., Nobuyasu, O., Ohtori, S.: Degeneration and recovery of the neuromuscular junction after application of extracorporeal shock wave therapy. J. Orthop. Res. **30**, 1660–1665 (2012)
10. Qin, J., Simmons, W.N., Sankin, G., Zhong, P.: Effect of lithotripter focal width on stone comminution in shock wave lithotripsy. J. Acoust. Soc. Am. **127**, 2635–2645 (2010)
11. Brown, R.D., De, S., Sarkissian, C., Monga, M.: Best practices in shock wave lithotripsy: a comparison of regional practice patterns. Urology **83**, 1060–1064 (2014)
12. Portincasa, P., Di Ciaula, A., Bonfrate, L., Wang, D.Q.H.: Therapy of gallstone disease: what it was, what it is, what it will be. World J. Gastrointest. Pharmacol. Ther. **3**, 7–20 (2012)
13. Tandan, M., Reddy, D.N., Talukdar, R., Vinod, K., Santosh, D., Lakhtakia, S., Gupta, R., Ramchandani, M.J., Banerjee, R., Rakesh, K., Varadaraj, G., Rao, G.V.: Long-term clinical outcomes of extracorporeal shockwave lithotripsy in painful chronic calcific pancreatitis. Gastrointest. Endosc. **78**, 726–733 (2013)

14. Neisius, A., Smith, N.B., Sankin, G., Kuntz, N.J., Madden, J.F., Fovargue, D.E., Mitran, S., Lipkin, M.E., Simmons, W.N., Preminger, G.M., Zhong, P.: Improving the lens design and performance of a contemporary electromagnetic shock wave lithotripter. Proc. Natl. Acad. Sci. U. S. A. **111**, E1167–E1175 (2014)
15. Wang, Y., Guo, T., Ma, T.K., Cai, H.Y., Tao, S.M., Peng, Y.Z., Yang, P., Chen, M.Q., Gu, Y.: A modified regimen of extracorporeal cardiac shock wave therapy for treatment of coronary artery disease. Cardiovasc. Ultrasound **17**, 10–35 (2012)
16. Wess, O.J.: A neural model for chronic pain and pain relief by extracorporeal shock wave treatment. Urol. Res. **36**, 327–334 (2008)
17. Mittermayr, R., Antonic, V., Hartinger, J., Kaufmann, H., Redl, H., Téot, L., Stojadinovic, A., Schaden, W.: Extracorporeal shock wave therapy (ESWT) for wound healing: technology, mechanisms, and clinical efficacy. Wound Repair Regen. **20**, 456–465 (2012)
18. Delius, M., Hofschneider, P.H., Lauer, U., Messmer, K.: Extracorporeal shock waves for gene therapy? Lancet **345**, 1377 (1995)
19. Millán-Chiu, B., Camacho, G., Varela-Echavarría, A., Tamariz, E., Fernández, F., López-Marín, L.M., Loske, A.M.: Shock waves and DNA-cationic lipid assemblies: a synergistic approach to express exogenous genes in human cells. Ultrasound Med. Biol. **40**, 1599–1608 (2014)
20. Magaña-Ortíz, D., Coconi-Linares, N., Ortiz-Vazquez, E., Fernández, F., Loske, A.M., Gómez-Lim, M.A.: A novel and highly efficient method for genetic transformation of fungi employing shock waves. Fungal Genet. Biol. **56**, 9–16 (2013)
21. Rivera, A.L., Magaña-Ortíz, D., Gómez-Lim, M., Fernández, F., Loske, A.M.: Physical methods for genetic transformation of fungi and yeast. Phys. Life Rev. **11**, 184–203 (2014)
22. Jagadeesh, G., Nataraja, K.N., Udayakumar, M.: Shock waves can enhance bacterial transformation with plasmid DNA. Curr. Sci. India **87**, 734–735 (2004)
23. Divya, P.G., Anish, R.V., Jagadeesh, G., Chakravortty, D.: Bacterial transformation using micro-shock waves. Anal. Biochem. **419**, 292–301 (2011)
24. Soto-Alonso, G., Cruz-Medina, J.A., Caballero-Pérez, J., Arvizu-Hernández, I., Ávalos, L.M., Cruz-Hernández, A., Romero-Gómez, S., Rodríguez, A.L., Pastrana-Martínez, X., Fernández, F., Loske, A.M., Campos-Guillén, J.: Isolation of a conjugative F-like plasmid from a multidrug-resistant *Escherichia coli* strain CM6 using tandem shock wave-mediated transformation. J. Microbiol. Methods **114**, 1–8 (2015)
25. von Eiff, C., Overbeck, J., Haupts, G., Herrmann, M., Winckler, S., Richter, K.D., Peters, G., Spiegel, H.U.: Bactericidal effect of extracorporeal shock waves on *Staphylococcus aureus*. J. Med. Microbiol. **49**, 709–712 (2000)
26. Alvarez, U.M., Loske, A.M., Castaño-Tostado, E., Prieto, F.E.: Inactivation of *Escherichia coli* O157:H7, *Salmonella* typhimurium and *Listeria monocytogenes* by underwater shock waves. Innovative Food Sci. Emerg. Technol. **5**, 459–463 (2004)
27. Kerfoot, W.W., Beshai, A.Z., Carson, C.C.: The effect of isolated high-energy shock wave treatments on subsequent bacterial growth. Urol. Res. **20**, 183–186 (1992)
28. Quintero, M.S., Alvarez, U.M., Wacher, C., Gutiérrez, J., Castaño-Tostado, E., Fernández, F., Loske, A.M.: Interaction of shock waves with infected kidney stones: is there a bactericidal effect? J. Endourol. **22**, 1629–1637 (2008)
29. Abe, A., Mimura, H., Ishida, H., Yoshida, K.: The effect of shock pressures on the inactivation of a marine *Vibrio sp*. Shock Waves **17**, 143–151 (2007)

Making Shock Waves Pay: The Commercial Aspects of Shock Waves

K.P.J. Reddy

Introduction

While the World War I triggered the scientific study on the field of shock waves which was mostly confined to gas dynamics, high-speed aerodynamics, and defense technology, it emerged into a large interdisciplinary field by its own after the onset of World War II [1]. With the progress in the understanding of fundamental theory, methods of producing shock waves in the laboratory, equation-of-state data, high-speed measurement techniques, visualization methods, and computational fluid dynamic techniques, shock waves have become integral part of interdisciplinary research fields. However, the commercial aspects of the shock waves were seldom exploited, and to our knowledge, only major application of shock waves is in the lithotripsy equipment used for kidney stone blasting.

For the past few years, we have been making efforts to exploit the commercial potential of shock waves mainly by developing easy to operate shock tubes and shock tunnels for research and education purpose [2–8]. In addition, we have also explored the application of shock waves for improving the performance of artificial insemination (AI) gun leading to the improved milk production from the dairy animals, processing of tea, enhancement of borewell water output, etc. Details of these efforts with a brief description of few recently launched commercial products are presented in this paper. We conclude the paper with few futuristic applications having appreciable business potential in many fields.

K.P.J. Reddy (✉)
Department of Aerospace Engineering, Indian Institute of Science, Bangalore 560012, India
e-mail: laser@aero.iisc.ernet.in

First Product in the Market

It is well known that the shock waves are produced in the laboratory using a simple device called shock tube. It is also evident from the frequent terrorist attacks and natural calamities such as earthquakes and volcanic eruptions common man is exposed to their effects more often in recent times than before. Hence it is an appropriate time to create awareness on shock waves and their effects. This could be mainly achieved by making the subject of shock waves as part of the curriculum in school and college level courses. While the teaching of basics of shock waves can be simplified for this purpose, it is not easy to use the existing shock tubes to perform laboratory experiments due to the risks involved in handling the high-pressure gases used to drive the shock tubes. In order to address this problem, we have invented a simple hand-operated shock tube which is capable of producing shock Mach numbers of about 2 without using any high-pressure driver gas from the reservoir [2–4]. Named as Reddy tube, this devise is currently being used for teaching basic principles of shock waves in undergraduate education. In addition, this devise has found applications in many diverse fields. We describe the development path of productization of the Reddy tube and Reddy shock tunnel.

The concept of hand-operated shock tube was first conceived using the medical syringe, shown in Fig. 1. The syringe is converted to miniature free piston-driven shock tube in which the syringe with plunger is treated as compression tube with a piston and the needle separated by a thin diaphragm as shock tube. Operation of the tube involves withdrawing of the piston to the extreme end of the compression tube and attaching the shock tube to the end of compression tube after inserting a thin diaphragm. The pressure in the compression tube rises rapidly as the piston is pressed toward the end of the compression tube till the diaphragm rupture. This creates a normal shock wave moving in to the shock tube. The shock wave followed by

G. Ben-Dor et al. (eds.), *30th International Symposium on Shock Waves 1*, DOI 10.1007/978-3-319-46213-4_5

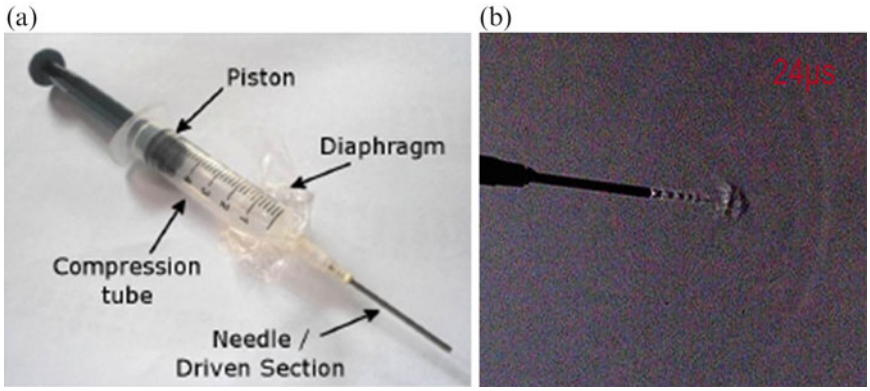

Fig. 1 Medical syringe converted in to piston-driven shock tube (**a**) and the shock wave emerging from the tip of the needle (**b**)

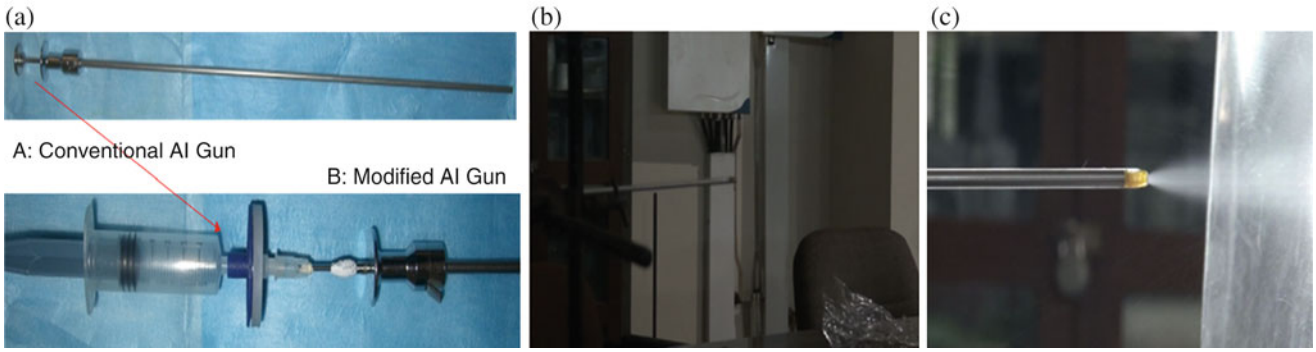

Fig. 2 Artificial insemination gun and Reddy tube-driven AI gun, "SuperBull" (**a**), ejection of semen from the tip of the AI gun (**b**), and SuperBull (**c**)

the compressed test gas emerging out of the open end of the 1.2 mm diameter needle is shown in the Schlieren picture in Fig. 2.

This simple hand-operated shock tube named Reddy tube has many applications. The most important application is in improving the efficiency of the artificial insemination (AI) gun for farm animals [5].

The commercially available artificial insemination (AI) gun is shown in Fig. 2 which consists of 50 cm long steel tube into which a straw tube containing semen is inserted, and the front portion of the straw tube projecting out of the gun is clipped by about 5–7 mm. Plastic sheath is slid onto the gun tightly and locked with a locking system. The plunger is kept in open position before inserting the straw tube, and the semen is discharged into the uterus by manually guiding the gun into the uterus and pushing the plunger forward slowly. The semen delivered at the entrance of the uterus in the form of drops using the AI gun with plunger mechanism, shown in Fig. 2b, many times fails to deliver sufficient number of spermatozoa to reach the fertilization site as the distance it needs to travel is substantial. This failure results in the conception failures in dairy animals which causes substantial loss of milk production leading to economic losses to the farmers. In the SuperBull, we have enhanced the speed of the semen discharge by breaking it into fine spray penetrating deeper into the uterus thus increasing the probability of conception and pregnancy. This is achieved by replacing the plunger rod by a 1 mm diameter and 340 mm long steel tube attached to a Reddy tube at one end while retaining rest of the gun unchanged. The semen delivery is achieved by sending a short pressure pulse behind the shock wave created by the Reddy tube to push the cotton plugs in the straw tube forward which in turn push the semen sample out of the sheath. Since the pressure pulse acts as an impulse of fraction of a second duration, the liquid sample is pushed out as a high-speed jet leading to the breaking up of the sample into fine spray as shown Fig. 2c.

Tabletop Shock Tube

Many scaled-up versions of Reddy tube have been developed for various applications. Mainly a manually operated tabletop shock tube to perform laboratory experiments as shown in Fig. 3 has been developed using the Reddy tube concept [2–4]. This tube essentially consists of a 30 mm diameter shock tube with about 400 mm long driver tube with a hand-driven piston and 500 mm long driven tube as shown in Fig. 3a. The shock tube is instrumented to measure the driver pressure P_4, the driven pressure P_1, the pressure

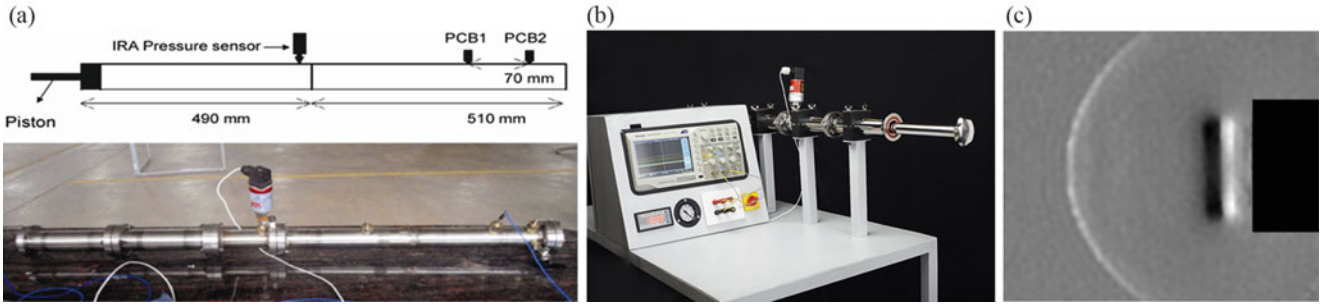

Fig. 3 First version of the Reddy tube as a teaching tool (**a**), fully instrumented commercially available table-mounted Reddy tube for teaching purpose (**b**), and the spherical shock wave and vortex ring emerging out of the open end of Reddy tube (**c**)

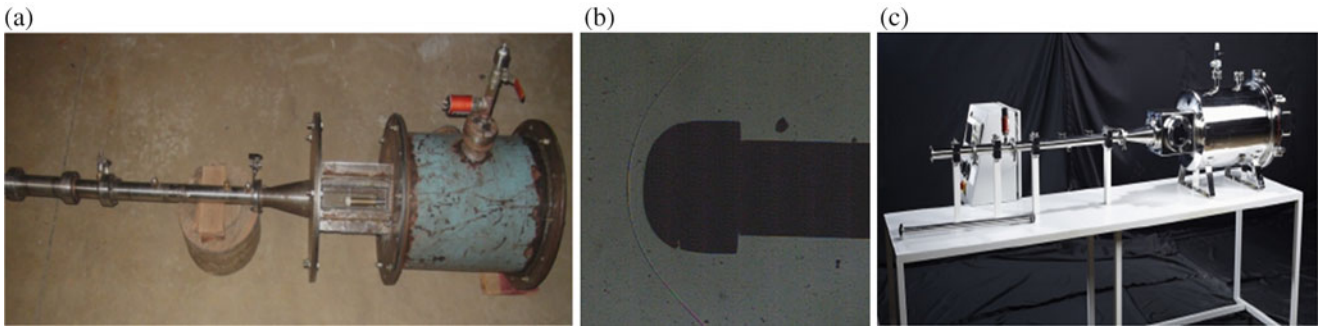

Fig. 4 First version of the Reddy tube-driven tabletop hypersonic shock tunnel (**a**), bow shock wave around the hemisphere in the Mach 6 flow (**b**), and the commercial model of the tabletop hypersonic shock tunnel (**c**)

rise across the shock wave, the speed of the shock wave, and the hand-operated vacuum pump to vary the driven tube pressure. The shock tube is ideally suited for performing undergraduate-level experiments with variable driver gas, driven section pressure, and shock Mach number either as open-ended or reflected mode. The advanced version of the fully instrumented Reddy tube marketed commercially is shown in Fig. 3b. A typical shock wave emerging from the open end of the Reddy tube visualized using recently invented visualization technique and an ordinary camera is shown in Fig. 3c.

Tabletop Hypersonic Shock Tunnel

The tabletop shock tube was further converted into a tabletop hypersonic shock tunnel by adding a conical convergent-divergent Mach 6 nozzle, a test section, and a dump tank [6, 7]. Earlier version of the shock tunnel with hemispherical model mounted in the transparent test section is shown in Fig. 4a. The shock tube attached to this tunnel is the 30 mm diameter internal diameter Reddy tube described before. The shock tunnel performance was evaluated using pitot probes in the test section. The detached bow shock wave in front of hemispherical blunt body in Mach 6 flow visualized using Schlieren technique is shown in Fig. 4b. To our knowledge, this is the first evidence of producing hypersonic flow manually. The final version of the hand-driven tabletop hypersonic shock tunnel marked commercially is shown in Fig. 4c. The tunnel has been successfully used to measure stagnation point heat transfer rate for aerodynamic models, measuring of aerodynamic drag coefficient, and nozzle characterization.

Typical Applications of Tabletop Reddy Tube

Traumatic brain injury (TBI) and blast-induced neurotrauma (BINT) are the most important areas of research in recent times across the globe. TBI investigations are carried out usually by exposing the experimental rats to blast wave produced in the shock tube with overpressures identical to the battle field. However, the rats used in the experiment suffer damages due to exposure of whole body to the blast overpressure which often leads to their death. The overpressure of few atmospheres produced in the Reddy tube, shown in Fig. 1a, in the form of a blast wave is ideally suited for the investigation of TBI by exposing locally on the relevant portion of the experimental animal.

A group of doctors in a famous neurology hospital in Bangalore have utilized the tabletop Reddy tube for the study of pathophysiology in BINT-affected rats. In the

Fig. 5 Reddy tube used for study of blast-induced neurotrauma in rats

laboratory animals, the blast injury was mimicked by exposing the animals to shock waves produced by Reddy tube as shown in Fig. 5 [8]. In this study, 15 rats were subjected to increasing peak pressure blast waves with Friedlander type of waveform. One rat died immediately following exposure to the blast. At the end of 2 weeks, all the live rats were sacrificed and subjected to histopathological examination. The pathology revealed neuronal degeneration and axonopathy in the cortex, cingulum, hippocampus, thalamus, brain stem, and cerebellum with the severity of injury increasing with increasing blast pressure. These findings were consistent with that reported in the literature. This study essentially proved the importance of Reddy tube for such studies extending its utility as a research tool.

Conclusion

We have presented an account of our commercial ventures in order to prove the commercial potential of shock waves. The tabletop hand-operated shock tube has already become part of the undergraduate and graduate programs in India. The estimated business potential of this simple devise in India alone is in excess of few tens of millions of US dollars. Similarly, the hand-operated tabletop hypersonic shock tunnel mainly used for teaching the subject of hypersonics is estimated to fetch a business of at least ten million US dollars. We are in the process of commercializing the SuperBull, and the devise is expected to play an important role in the economic progress of the country in addition to fetching good financial returns. We have ongoing work on the exploitation of shock waves in the agricultural and energy sector.

Acknowledgment The author would like to express sincere gratitude to Prof. P. Balaram, former director of Indian Institute of Science, Bangalore, for granting official permission to start a scientific company (Super-Wave Technology Private Limited) to commercialize our inventions in shock waves.

References

1. Kumar, C.S., Takayama, K., Reddy, K.P.J.: Shock Waves Made Simple. Wiley, New Delhi (2014)
2. Reddy, K.P.J.: Manually operated piston driven mini shock tube. In: Kontis K. (ed.) Proceedings of the 28th International Symposium on Shock Waves, vol. 1, pp. 561–565 (2012)
3. Sharath, N., Reddy, K.P.J.: Manually operated piston-driven shock tube. Curr. Sci. **104**, 172–176 (2013)
4. Surana, K.S., Reddy, K.P.J., Joy, A.D., Reddy, J.N.: Riemann shock tube: 1D normal shocks in air, simulations and experiments. Int. J. Comp. Fluid Dyn., **28**, 6–10, 251–271 (2014)
5. Stone, R.: News focus: science in India—India rising. Science **335**, 904–910 (2012)
6. Reddy, K.P.J., Ramesh, B.R., Murali, R., Saravanan, S.: Reddy Tube Driven Table Top Hypersonic Shock Tunnel. In: 29th International Symposium on Shock Waves, Madison, 14–19 July 2013
7. Chintoo, C.S., Reddy, K.P.J.: Experiments in hand operated hypersonic shock tunnel. Shock Waves 26, 6, 845–849, (2015)
8. Bhat, D.I., Shukla, D., Mahadevan, A., Sharath, N., Reddy, K.P.J.: Validation of a blast induced neurotrauma model using modified Reddy tube in rats: a pilot study. Indian J Neurotrauma **11**, 91–96 (2014)

Time-Developing 3D-CT Measurement of Shock Waves and Supersonic Density Flow Field

K. Maeno

Introduction

In the supersonic and hypersonic flow diagnostics, density field observation has been one of the main targets of experimental fluid-dynamic researchers. From the very beginning of twentieth century, flow visualization methods by optical photographs have been investigated and the pictures by shadowgraph, schlieren method, or interferometry have been widely utilized to the qualitative density flow field clarification. As these methods still give strong power to the researchers of fluid dynamics, new diagnostic technology is dramatically developing together with new optical and digital image instruments and high-power PC. Above all, computed tomography (CT) for 3D reconstruction from the image measurement of the supersonic density flow field including the shock waves is typical and rapid-developing diagnostics with digital image technology. The hardware and software/algorithm for optical CT suitable to the high-speed flows should be investigated in the next decade. In the present paper, the author deals with two CT diagnostic methods, those are density field measurement by CT with traditional Mach-Zehnder interferometry (LICT) for discharging shock wave and vortex, and density gradient field measurement by CT with background-oriented shclieren (BOS) method of colored-grid background (CGBOS) in a supersonic wind tunnel. Furthermore, in each method, the novel time-developing three-dimensional CT measurement (4D-CT) experiments of LICT and CGBOS with high-speed camera are presented. These experiments and CT reconstruction have been successfully done by the author and Prof. M. Ota and our laboratory students in Chiba University.

K. Maeno (✉)
National Institute of Technology, Kisarazu College, Professor Emeritus of Chiba University, 2-11-1 Kiyomidai-Higashi, Kisarazu, Chiba 292-0041, Japan
e-mail: akmaeno@a.kisarazu.ac.jp

CT by Laser Interferometry (LICT) [1, 2]

First, in our laboratory, three-dimensional (3D) and unsteady flow field including shock waves and vortices has been investigated by laser interferometric computed tomography (LICT) measurement by the M-Z interferometry. However, it is still difficult to measure 3D density distribution of the different instants of time in CT reconstruction technique (4D-CT) by single-frame cameras. So, to realize the time-developing 3D-CT measurements, a high-speed camera of framing rate of 700,000 is applied to the LICT measurement. This is because continuous framing images can be obtained by high-speed camera even for our shock-tube-based iterative multi-shots CT operation. The multi-dimensional and quantitative density measurements have been performed on unsteady, compressible, and interacting shock-vortex flow field induced by the discharging shock wave and jets. Quantitative characteristics of the 4D (time scale + 3D) complicated shock-vortex flow are discussed together with the 2D or 3D downgraded and integrated image analysis.

In this LICT method for shock tube experiments, we need multidirectional projection data to reproduce the unsteady flow. We use a diaphragmless shock tube (Maeno-Oguchi tube) to generate the shock waves of high reproducibility. As shown in Fig. 1, optical system consists of a high-speed camera, a Mach-Zehnder interferometer, an argon ion laser as a light source. Shock wave generated by the diaphragmless shock tube passes through a rotating plug set at the end of the tube, and the shock-vortex flow discharges into the test section from two inclined and cylindrical (i.d. 3 mm) holes. The specifications of high-speed camera are indicated in Table 1.

By using these setup instruments, we can obtain, for example, 39 images of finite fringe interferogram from different angles to have the reconstruction of CT density by ART at one instance. The reconstruction procedure is shown in Fig. 2. Then the time-developing huge images constructed by each-time 3D CT sets could be obtained

G. Ben-Dor et al. (eds.), *30th International Symposium on Shock Waves 1*, DOI 10.1007/978-3-319-46213-4_6

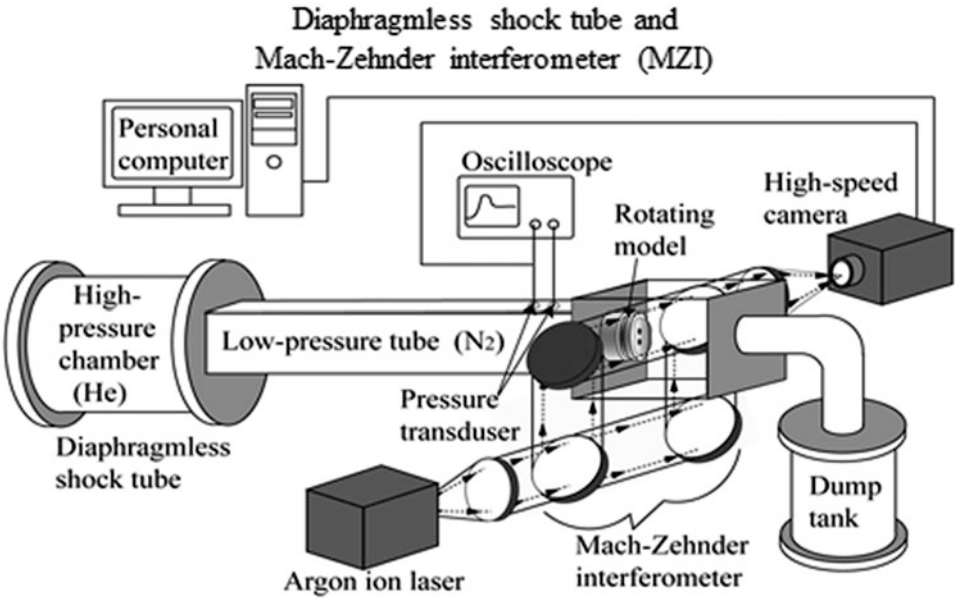

Fig. 1 Experimental setup for time-developing LICT with high-speed camera

Table 1 Specifications of high-speed camera

Image sensor	ISIS-CCD image sensor
Resolution	360 × 410 pixel
Frame rate	700,000 fps (max 1,250,000 fps)
Continuous shooting	120 images
Electronics shutter	200 ns (min 100 ns)

by using high-speed camera with angular rotation of the model. Algebraic reconstruction technique (ART) is much more suitable than FBPs for our optical CT, as we have been suffering by strong artifacts by data lacking by the model existence in experiments. The reduced sizes of each image were used, in reality, to our CT reconstruction, as the power of PC was not sufficient. However, the obtained results are very satisfactory as shown in Figs. 3, 4, and 5, because these obtained data were, of course, quantitative ones and capable to compare directly to the 4D CFD results.

Figure 3 shows the DCST results in the center plane of y–z for developing shock-vortex flow field. Primary (PSW) and transmitted (TSW) interacting shock waves and secondary shock wave (SSW) in the front of discharged and combined vortex are clearly observed. We can cut at any interested planes for time-developing 3D density field. These data are, of course, quantitative ones, so the comparison of the data with CFD results can be realized, as shown in Fig. 4, where the direct comparison of time-developing density CT is realized. In CFD, we used original Euler-system solver and commercial solver (FLUENT) for viscous compressible flows. The grid number was limited to the order of 600million with small WS.

In Fig. 5, the comparison of our results for conventional flow visualization method can be presented. The upper series of photographs are the results by conventional infinite-fringe interferometry, where the integrated density information along a settled optical pass can be observed. Lower two series of graphs are the integrated density data along the same optical pass from 4D reconstructed CT experiments and same data by CFD. As shown in this figure, we can compare directly the CT experimental data with CFD and conventional flow visualization technique by selecting the parameters to the required diagnostics which are already established. Thus, we can discuss the experimental results with direct comparison to CFD and have error estimation on time-developing 3D shock-vortex behavior. It is, of course, a kind of problem to perform these iterative and rotational experiments for the time-depending unsteady shock-vortex phenomena, but if we can have enough number of high-speed cameras and advanced super computers for image processing, the problem can be solved without any serious difficulty.

CT of CGBOS by Supersonic Wind Tunnel [3–6]

Secondly, in this paper a background-oriented schlieren (BOS) experiment is presented by colored-grid (CG) which has been developed by author's group. We call this method as CGBOS (colored-grid BOS), where the merged concept for computer graphics BOS was included, and it is open to an interactive diagnostics for "adaptive" CGBOS for multistage observation by using LCD. By the CGBOS concept, we can move, rotate, or close up to the interested zone of density flow fields based on the in-situ CGBOS-CT measured results to increase and adjust the space-time resolution of the interested zone or closer field of shock-flow interaction to change

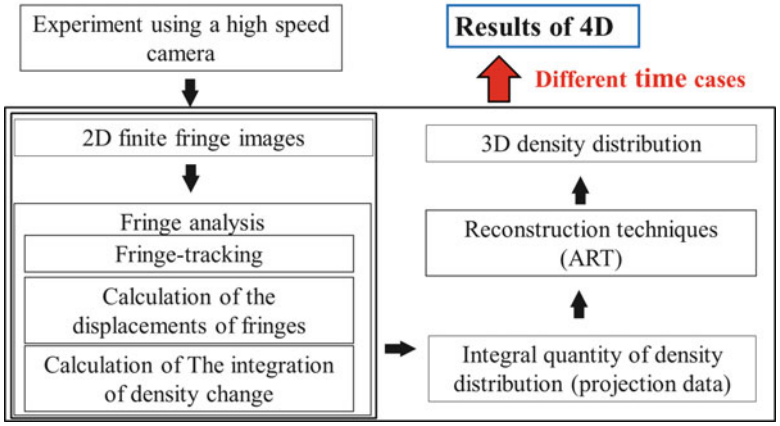

Fig. 2 Schematic flow of 4D-LICT reconstruction process for density field

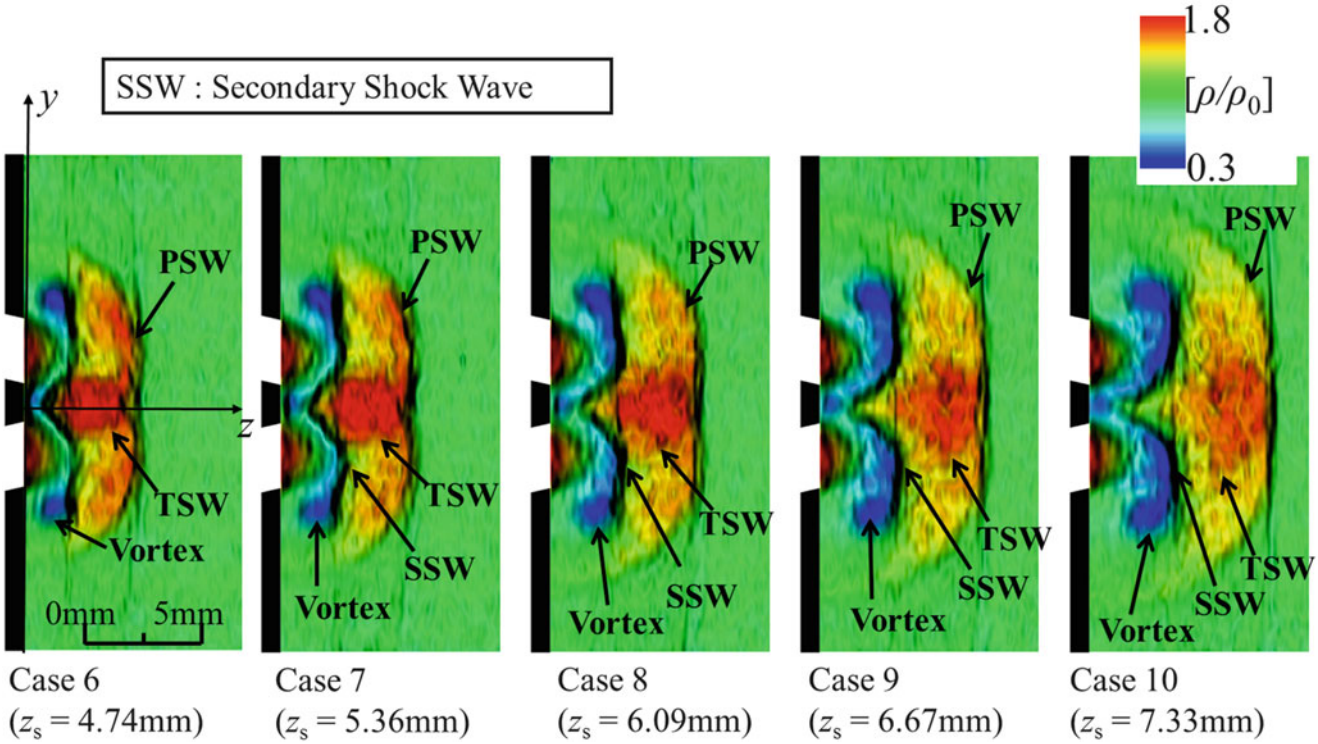

Fig. 3 DCSI (Distribution Combined Schlieren Image) in yz plane

the new adaptive CG background by LCD images. It is on to the next super WS and 8K high-vision LCD. Apart from the future development, as for the present 3D CGBOS, our experiment for an asymmetric model in supersonic wind tunnel is discussed.

In the experiment on 3D CGBOS, we used a square-pyramid asymmetric model. The model has five plane faces with small round nose as indicated in Fig. 6. We can observe the asymmetric flow field with bow shock, separation and interaction of expansion waves, and vortex wakes in the shock cone-like shape in Mach number from 2 to 3 in JAXA-ISAS supersonic wind tunnel flow. Typical CT results for density gradient field in Mach 2 main flow are presented in Fig. 7, where the outer cone-like bow shock wave and the strong separated wake flow from tail edge of the model surfaces are reconstructed, and asymmetric separation vortex shape is clearly observed. Several artifacts are also observed to emit from surfaces of the model. This problem is always facing the CT reconstruction and we have to investigate it.

Based on the above-mentioned experimental results for density gradient field around the asymmetric model, we can proceed time-developing 3D CT experiment by CGBOS. The interaction of the discharging jet [7–9] from a cone-cylinder model with supersonic main flow in JAXA-ISAS wind tunnel has been investigated by colored-grid BOS

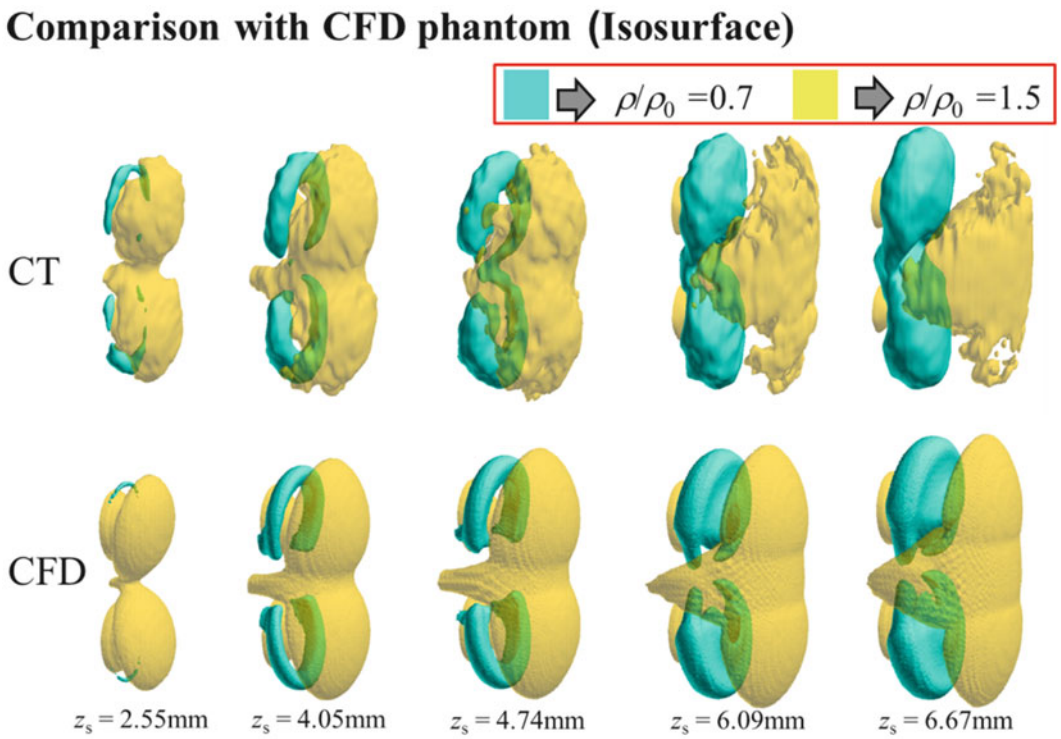

Fig. 4 Direct comparison of time-developing 3D-CT results for isopicnic surfaces

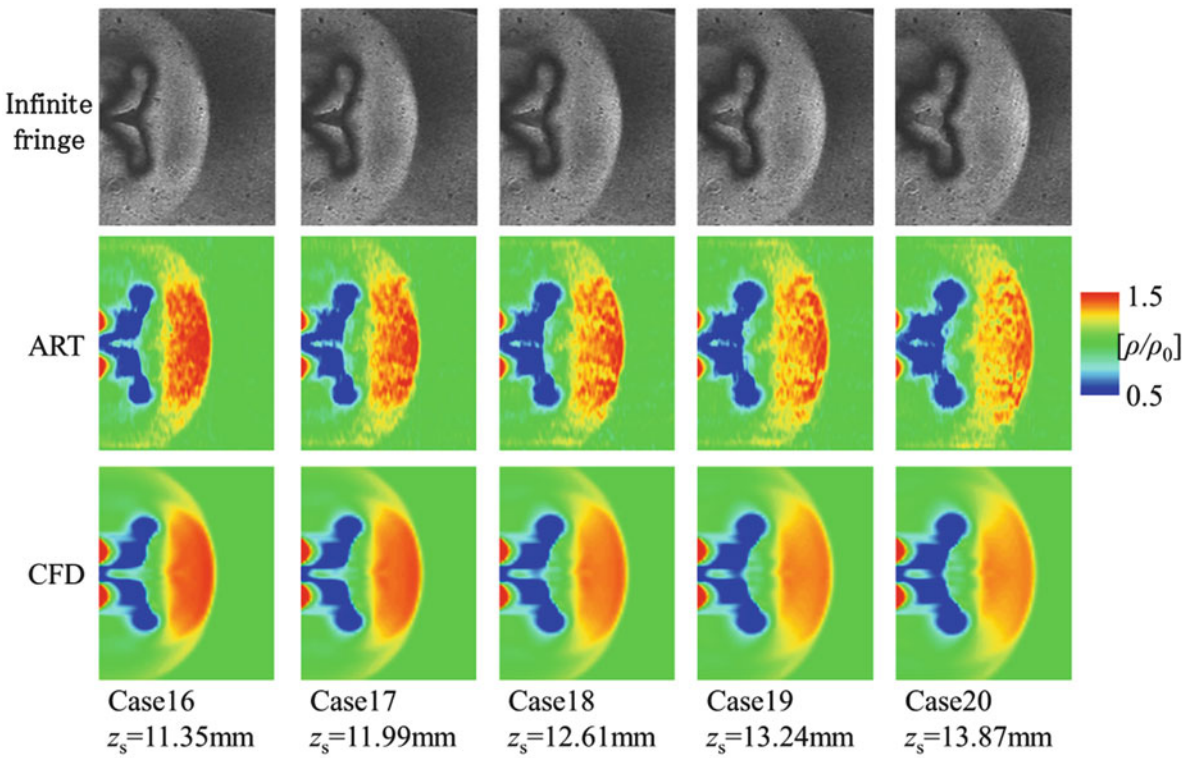

Fig. 5 Direct comparison of measured unsteady emerging shock-vortex flow to CFD

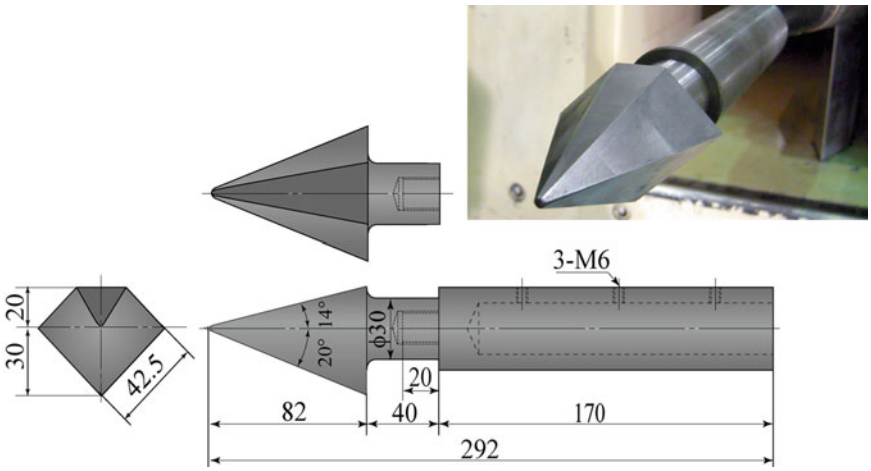

Fig. 6 Square-pyramid asymmetrical model for JAXA-ISAS supersonic wind tunnel

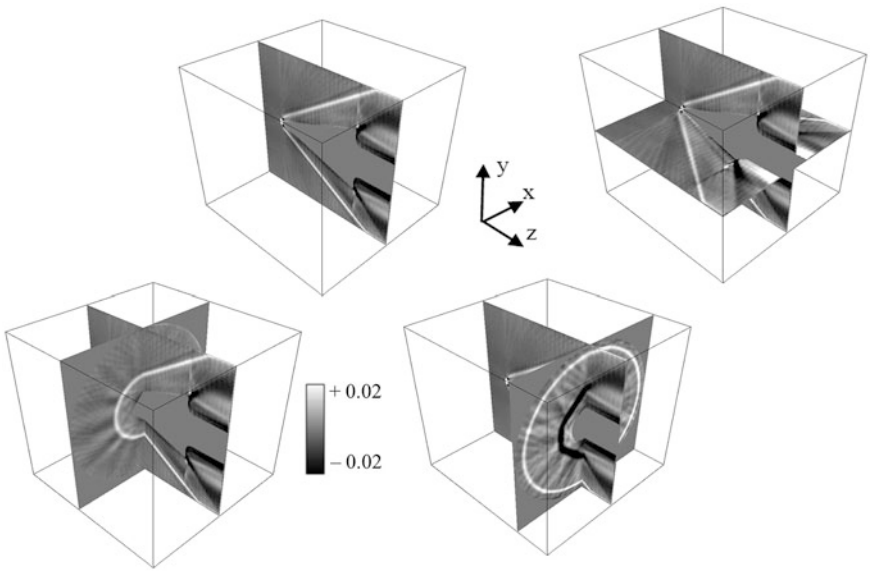

Fig. 7 Quantitative results for density gradient field around the model by CT-CGBOS

method with multidirectional projections. The observed 3D density flow field is discussed. The setup for 4D-CGBOS-CT experiment at JAXA-ISAS supersonic wind tunnel is shown in Fig. 8, where the high-speed camera of 1000fps was used to have the set of BOS images for unsteady interaction of injected jet and $M = 3$ supersonic flow. Telecentric optical system was employed to reduce the off-focusing error in the CGBOS image. This is a trade-off problem between the resolution of the background image and the model boundary in the wind tunnel. For example, an interferometry system is very difficult to introduce in supersonic wind tunnel experiments, as the strong sound and vibration of the wind tunnel system disturb the observed interferometric image. Same problem is facing us in open field BOS experiments.

Among the series of framing data at designated time instance by rotating the jet-emerging model, we can select the suitable time-developing set of 3D-CGBOS-CT images on density gradient by separating the colored grid to the red and green (horizontal and vertical) stripe-shift. By these digital image data, the CT results for the jet-supersonic flow interaction with different time instance can be obtained. Among the results, 3D-CT results-set for an instance can be indicated in Figs. 9 and 10. Figure 9 is the displacement field in the horizontal grids image of fully-developed emerging jet $M = 3$ main flow (quasi-steady conditions). As we took the whole flow image of conical shock wave and expansion wave in the supersonic flow including the jet-flow interaction zone, the space resolution for the observed zone of jet-flow interaction is not high enough. This resolution, nevertheless, is enough to reconstruct CT of the density gradient field and to solve the Poisson equation of the integration to obtain the density field from CT gradient data. We

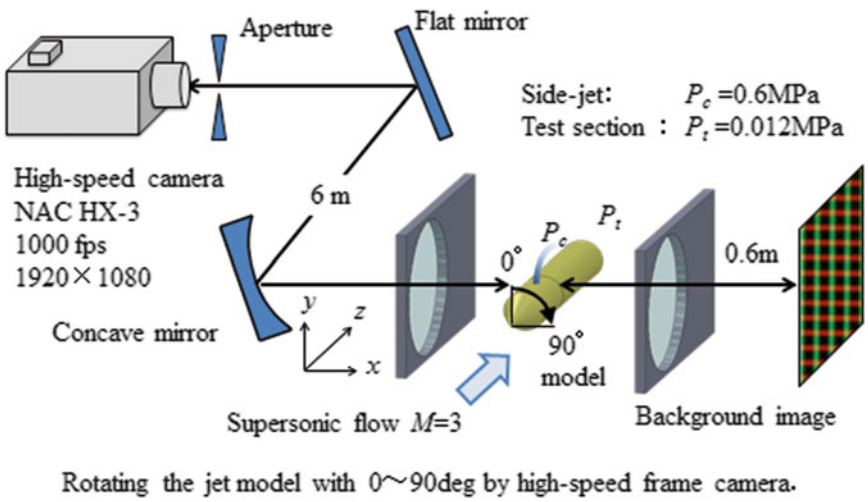

Fig. 8 Experimental setup for CGBOS of jet-interaction with high-speed camera on 4D-CT

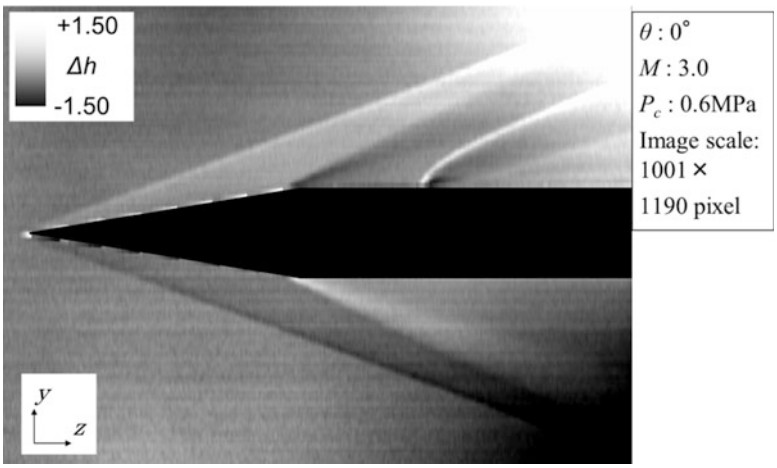

Fig. 9 Displacement BOS image data at quasi-steady time on jet-flow interaction in $M = 3$

are in the progress stage of the improved integration scheme from the density gradient field to the density field to avoid the over-smoothing integration across the density jump of shock waves and the model boundary problem.

This displacement image of Fig. 9 can be grouped together with other images by high-speed camera at same instance to have the BOS-CT reconstruction by ART on density gradient or integrated density field at designated instance. Then the time-developing 3D CGBOS-CT results are obtained by this data processing. The detail of this experiment is to be presented by the other session speech in this ISSW.

Concluding Remarks

In this paper, the author has introduced (1) laser interferometric CT (LICT) in unsteady shock tube flow and (2) -colored-grid BOS CT (CGBOS-CT) for steady and unsteady flow in supersonic wind tunnel, and furthermore, these diagnostic methods are improved to time-developing 3D-CT experiments. The methods are real 4D-CT quantitative visualization experiments. The grid-stripe and fringe analysis of these observed images and CT reconstruction are performed with the strong aid of high-performance PC with the mode of reduced resolution of the images obtained. Still, these experiments were realized by large-scale computer calculation, which is now under rapid development. For example, even in 3D diagnostics, the 39 multidirectional images of 2000 × 3000 pixels have been reduced to 1/25 to utilize the analysis of the 3D density or density gradient reconstruction. Furthermore, to obtain the real unsteady 4D results, we have performed over 80 different time-scale 3D reconstructions. It was really tremendous work. Our experience indicates the new and fruitful development of large-scale computer-aided experimental mechanics (LSCAEM) based on the quantitative and experimental image analysis of multi-dimension.

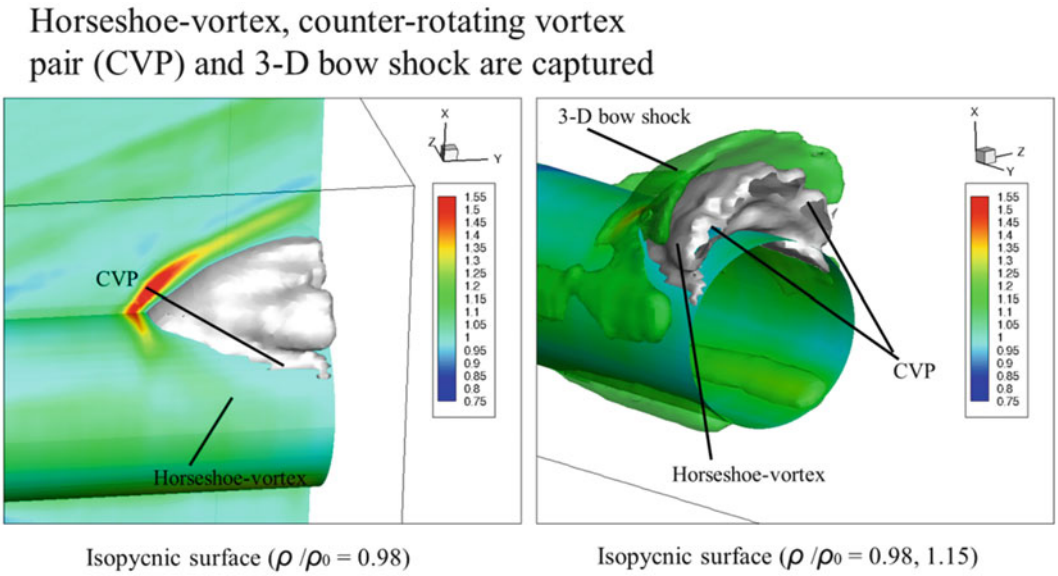

Fig. 10 CT-3D density field of jet-flow interaction after integration of density gradient

References

1. Maeno, K., Kaneta, T., Yoshimura, T., Morioka, T., Honma, H.: Pseudo-schlieren CT measurement of three-dimensional flow phenomena on shock waves and vortices discharged from open ends. Shock Waves **14**, 239–249 (2005)
2. Ota, M., Koga, T., Maeno, K.: Interferometric CT measurement and novel expression method of discharged flow field with unsteady shock waves. Jpn. J. Appl. Phys. **44**(42), L1293–L1294 (2005)
3. Meier, G.E.A.: Computerized background-oriented schlieren. Exp. Fluids **33**, 181–187 (2002)
4. Venkatakrishnan, L., Meier, G.E.A.: Density measurements using the background oriented Schlieren technique. Exp. Fluids **37**, 237–247 (2004)
5. Leopold, F., Simon, J., Gruppi, D., Schäfer, H.J.: Recent improvements of the back-ground oriented schlieren technique (BOS) by using a colored background. In: Proceedings of 12th International Symposium on Flow Visualization, German Aerospace Center (DLR), Göttingen, Germany, ISFV12-3.4, 1–10 (2006)
6. Kindler, K., Goldhahn, E., Leopold, F., Raffel, M.: Recent developments in background oriented schlieren methods for rotor blade tip vortex measurements. Exp. Fluids **43**, 233–240 (2007)
7. Seiler, F., Gnemmi, P., Ende, H., Schwenzer, M., Meuer, R.: Jet interaction at supersonic cross flow conditions. Shock Waves **13**, 13–23 (2003)
8. Ben-Yakar, A., Mungal, M.G., Hanson, R.K.: Time evolution and mixing characteristic of hydrogen and ethylene transverse jets in supersonic crossflows. Phys. Fluids **18**, 026101 (2006)
9. Sthl, B., Emunds, H., Gülhan, A.: Experimental investigation of hot and cold side jet interaction with a supersonic cross-flow. Aerosp. Sci. Technol. **13**, 488–496 (2009)

Chemical Kinetics and Reacting Flows

R.K. Hanson and D.F. Davidson

Introduction

Chemical kinetics plays a crucial role in many high-temperature flows of engineering and scientific interest, particularly including combustion and propulsion systems. Despite significant progress in the fundamental theories associated with chemical kinetics, this field still relies very heavily on experimentation and shock tubes have become a primary source of fundamental and applied chemical kinetic data, and virtually the only source of data at temperatures above about 1500 K. Most shock tube kinetics experiments are conducted behind reflected shock waves, where the reacting gases are effectively stagnated and utilize either in situ optical diagnostics or sampling-based analysis via mass spectrometry or gas chromatography. Of particular value are laser-based measurements of species and temperature using absorption of light in quantum-specific atomic or molecular transitions, which combines both fast time resolution and high species specificity, including ability to monitor critical radical species. Here we present an overview of the state-of-the-art of shock tube methodologies for generating uniform, accurately known reaction conditions, and we discuss the range of laser absorption diagnostics now available for monitoring species time histories.

There are three main areas where recent advances in shock tube methods are providing wider and more accurate test conditions. The first is an effort to achieve significantly longer test times, particularly at lower temperatures where kinetics processes are slower. This can be achieved using a combination of long driver geometries and suitable driver gas tailoring; test times of the order of 100 ms can now be achieved [1]. The second is an effort to compensate for changes in reflected shock conditions due to non-idealities in shock tubes such as boundary layers and shock attenuation. This can be achieved by the use of driver inserts; non-reactive pressure profiles can now be generated with near-zero dP_5/dt [2]. Without this compensation, the changes in test conditions in both temperature and pressure strongly affect the rate of kinetics processes in ways that are difficult to model. The third is an effort to generate constant pressure-reflected shock conditions during reactive, energetic experiments using a constrained-reaction-volume strategy. This driven-section filling strategy has enabled experimenters to provide near-constant-pressure test conditions during exothermic and endothermic processes and greatly facilitates the accurate zero-dimensional modeling of these processes [3].

Laser absorption diagnostics provide quantitative, non-intrusive, high-bandwidth monitoring of many important kinetics species. These measured species concentration time-histories provide a significantly stronger constraint on the development of detailed reaction models than global behavior constraints, such as ignition delay times. In addition, high-sensitivity laser absorption diagnostics can be used in simple kinetics systems (particularly at low concentrations) to isolate and measure the reaction rate constants of individual elementary reactions. Currently available laser systems provide diagnostics for fuel and fuel components (e.g. JP-8 and alkanes), transient radicals (e.g. OH, CH_3, NH_2), stable intermediates (e.g. C_2H_4, CH_4, CO, NO), and combustion products (e.g. H_2O, CO_2). Recent availability of solid-state infrared tunable diode lasers has expanded the set of measurable species to include larger alkenes (propene and iso-butene), alkynes (acetylene), and oxygenated species (methanol, aldehydes). Laser absorption of CO_2 can also be used to monitor temperature, which in the constant pressure systems described above (in constrained reaction volume experiments) can be used to monitor heat release rates [4].

R.K. Hanson (✉) • D.F. Davidson
Mechanical Engineering Department, Stanford University, Stanford, CA, USA
e-mail: rkhanson@stanford.edu

G. Ben-Dor et al. (eds.), *30th International Symposium on Shock Waves 1*, DOI 10.1007/978-3-319-46213-4_7

Advantages of Shock Tubes for Chemical Kinetics Studies

Because of the near-one-dimensionality of the shock tube and the near-planar nature of the shock wave (excluding a very thin boundary layer), it is possible with a precise measurement of the incident shock speed to accurately determine ($<\pm 1$ %) the temperature and pressure behind the reflected shock [5]. And additionally, because of the effective step change in shock conditions and the effective stagnation of the test gas mixture behind the reflected shock wave, the test gas mixture can potentially be treated as a zero-dimensional reactor modeled using either a constant-volume or constant-pressure constraint. Although kinetics studies can be conducted behind incident shock waves, most current work is performed using reflected shock waves.

To investigate low temperature regimes of combustion reactions, longer test times are generally required. This is of particular importance in studies of the negative-temperature-coefficient (NTC) ignition regime seen in diesel and other practical engine fuels. To extend the test time in a shock tube, two requirements are generally needed: a longer driver section to delay the return of the expansion wave from the driver end wall, and a tailored driver gas mixture that matches the "impedance" at the driver gas/driven gas contact surface so that the reflected shock wave passes without disturbance through this contact surface. When optimized, shock tube can have low-temperature test times of 50 ms, thereby enabling overlap with rapid compression machines. See Fig. 1.

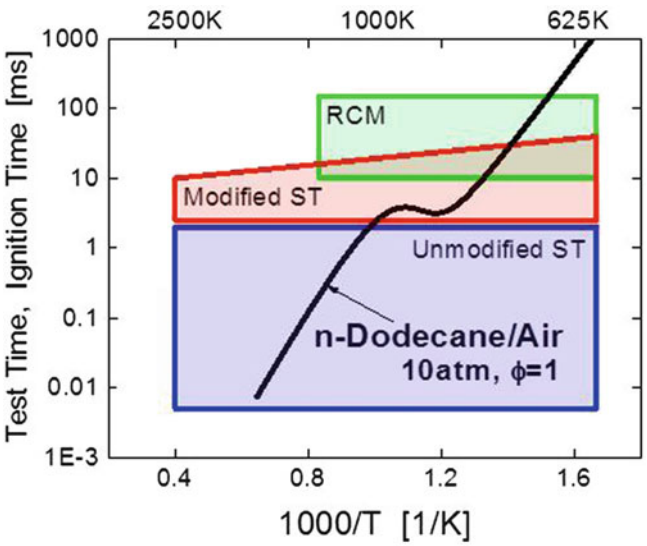

Fig. 1 Typical operation regimes of Stanford shock tubes. Blue area: high-quality test time in conventional configuration; *red* area: with driver modification and tailored driver gases; *green* area: conventional rapid compression machine. Ignition delay times for n-dodecane/air mixtures at 10 atm, $\phi = 1$ are shown in *black*

It should be noted that it is also possible to operate a shock tube with a significantly shorter driver section or attached dump tank [6]. This configuration, because of the shorter test time, enables the experimenter to quench the elevated test gas conditions with a large dT/dt (typically ~1000 K/ms) generated by an arriving expansion wave from the driver end wall. These "single-pulse" shock tubes can be used in conjunction with post-shock gas sampling to measure, e.g. with gas-chromatography, the distribution of stable intermediate components at fixed time after the initial reflected shock heating [7].

While shock tubes have commonly been used to study gas-phase chemistry, the vapor pressure of many practical fuels and their surrogates is so low that they occur only as liquids or butters at room temperature. In practice, the gas-phase kinetics of these fuels has been accessed by heating the entire mixing assembly, gas handling, and shock tube to the point where these fuels are entirely in the gas phase. However, there are complications with this approach; fuels can decompose before they are shock-heated, they can react and oxidize in the mixture preparation tank, or they can fractionate.

A new approach has recently been introduced, known as an aerosol shock tube, which provides an alternative method to study the evaporation and gas-phase kinetics of low-vapor-pressure fuels [8]. In the aerosol shock tube, a spatially-uniform distribution of fuel aerosol droplets and oxidizer/buffer is drawn into the shock tube test section adjacent to the shock tube end wall. When the incident shock wave passes this fuel mixture, it rapidly evaporates the micron-sized droplets and the evaporated fuel quickly diffuses to create a uniform gas-phase mixture of the low-vapor-pressure fuel and oxidizer/buffer. The reflected shock wave further compresses this test gas mixture, as in conventional shock tube operation, enabling the same types of experiments that are performed in conventional shock tubes. The advantage of this method is that the evaporation process and the chemical reaction process of the fuel can be temporally separated and each process can be studied independently.

Types of Experiments

Shock tubes are normally used to acquire kinetics data in three types of experiments: ignition delay time measurements, species time-history measurements, and elementary reaction rate constant measurements.

Ignition delay time experiments provide a global measurement of the behavior of a combustion system [9, 10]. These measurements take advantage of the effectively instantaneous jump in test conditions behind the reflected shock wave to initiate a near-constant volume or

near-constant pressure experiment. The ignition delay time in these experiments is defined as the time from initial heating to the time of rapid radical formation and simultaneous energy release, a time interval that normally can be accurately determined. Two primary concerns face the experimenter for these experiments: accurately determining the fuel loading, and accurately determining the reaction temperature and pressure time-histories. Recent advances in shock tube design, including the use of tailoring and driver inserts to achieve constant temperature and pressures at long test time and the use of laser absorption measurements to measure fuel concentration and test gas temperature, have proven critical to resolving these two primary concerns.

Species time-history experiments provide a temporal record of the concentration of one or more species during the progress of the combustion process. These time-histories provide strong constraints on the reaction pathways and rate constants of detailed reaction mechanisms used to model the chemistry of these processes. As described later in this paper, recently developed multi-wavelength laser absorption diagnostics can now provide constraints on the reactions of fuel, transient and stable intermediates, and product species simultaneously.

Finally, the primary input parameters for detailed reaction mechanisms are the rate constants for individual elementary reactions. These rate constants can be measured accurately in experiments designed such that an individual species time-history shows strong sensitivity to a single reaction rate constant. Shock tube/laser absorption experiments have provided some highly accurate examples of these types of experiments.

Multi-Species Laser Absorption Diagnostics

Laser absorption diagnostics provides a sensitive, quantitative, and non-intrusive method to measure species concentration time-histories in shock tube experiments [11]. Much of the development of these diagnostic methods has been done in our laboratory at Stanford University over the past 35 years. The extension of this method to multi-wavelength, multi-species detection has enabled the development of kinetics databases comprised of species-time-histories for reactants (fuel), transient radical species, (e.g. OH and CH_3) [12, 13], stable intermediates (e.g. C_2H_4 and CH_4) [14, 15], and combustion products (CO, CO_2, and H_2O) [16, 17]. These databases can be used to strongly constrain the hypothetical reaction pathways and rate constants used in detailed sub-mechanisms and full reaction mechanisms proposed for fuel pyrolysis and oxidation. These diagnostics can also be used in pseudo-first order rate measurements of elementary reactions where the kinetics of individual species are dominated by single reactions.

The species concentration can be inferred from laser absorption measurements (I/I_0) using the Beer-Lambert law for a monochromatic (λ) light source, traversing a path L (cm) of uniform species density N_{OH} (mol/cm^3) or mole fraction X_{OH} (e.g. for OH radicals):

$$\begin{aligned}(I/I_0)_\lambda &= \exp(-\sigma_{OH,\lambda} N_{OH} L) \\ &= \exp\left(-k_{OH,\lambda} P_{total} X_{OH} L\right)\end{aligned} \quad (1)$$

where $\sigma_{OH,\lambda}$ is the absorption cross-section (cm^3/mol) and $k_{OH,\lambda}$ is the absorption coefficient (atm^{-1}cm^{-1}), both at the measured wavelength, temperature, and total pressure. Absorption cross-sections or coefficients can be determined either by calculation using known spectroscopic parameters such as transition oscillator strengths, as is done for transient radical species such as OH, or by direct measurement of known species concentrations at known temperatures and pressures, as is done for stable species such as C_2H_4. In general, absorption cross-sections for electronic transitions are relatively large, such as are used for OH and CH_3 detection, and provide ppm or sub-ppm minimum detectivities in shock tube experiments (10 cm pathlength, 1 MHz bandwidth, 1 atm, SNR = 1 for 0.1 % absorption). Ro-vibrational transitions occurring in the infrared are relatively weaker and provide 10–100 ppm minimum detectivities under the same conditions for species such as CO, CO_2, C_2H_4, and H_2O.

The extension to this method to multiple species has provided kinetic modelers with a fuller set of critically important kinetics targets to test and refine detailed reaction mechanisms. Figure 2 shows results from a multi-wavelength

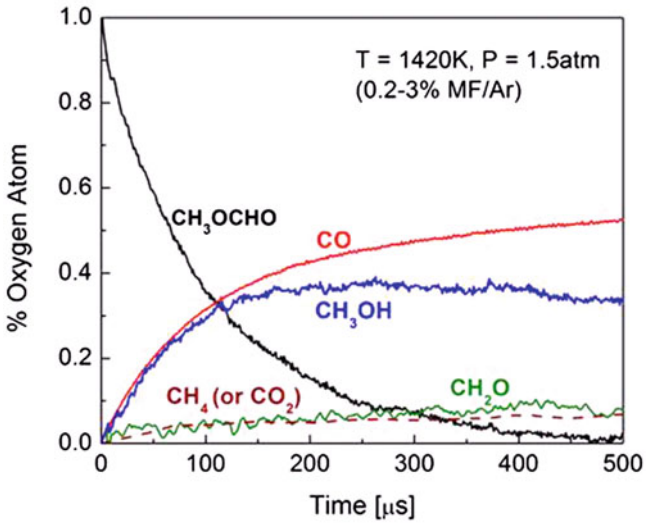

Fig. 2 Oxygen balance during the decomposition of methyl formate at 1420 K and 1.5 atm. In this study, MF (CH_3OCHO), CH_3OH, and CH_2O were measured in 1 % MF/argon mixtures, CH_4 in 3 % MF/argon mixtures, and CO was measured in 0.2 % MF/argon mixtures

study of methyl formate pyrolysis [18]. In this study, five major species were measured using laser absorption: methyl formate (MF, CH_3OCHO) at 9.23 μm, methanol (CH_3OH) at 9.676 μm, carbon monoxide (CO) at 4.56 μm, formaldehyde (CH_2O) at 306.64 nm, and methane (CH_4) at 3.4 μm. Because CH_4 is formed simultaneously with CO_2 and can be assumed to have the same concentration levels as CO_2, the mole fractions of these five species account for over 98 % of the O-atom-bearing species, and enable a near complete oxygen balance for this process to be determined. Using these data, Ren et al. [19] were able to confirm the magnitude of all major O-atom-carrying species and their temporal behavior, provide rate constants for the three major MF decomposition channels that control the decomposition process, and identify reaction pathways and rate constants in the methanol sub-mechanism that, if adjusted, would improve the long-time plateau behavior of formation of the secondary products.

Elementary Reaction Rate Measurements

Shock tube/laser absorption measurements can also provide very accurate determinations of reaction rate constants. Figure 3 presents the results of laser absorption measurements of OH in a simple kinetic system where the reaction $OH + H_2 \rightarrow H_2O + H$ dominates the sensitivity of the OH concentration profile [20]. In these experiments, test gas mixtures of H_2 and tert-butyl hydroperoxide (TBHP) diluted in argon were shock-heated. OH radicals were produced by rapid thermal decomposition of TBHP at high temperatures. The rate constant was inferred by best-fitting the measured OH time-histories with the simulated profiles from a comprehensive reaction mechanism. Significantly reduced uncertainty over earlier studies is evident.

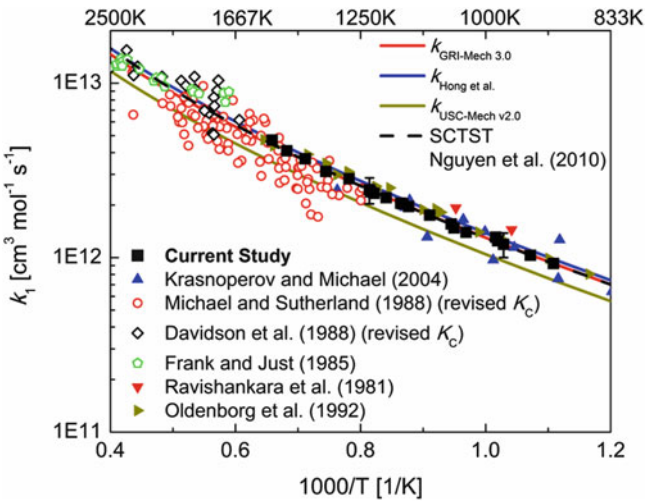

Fig. 3 Laser absorption measurements of the rate constant for the reaction of $OH + H_2 \rightarrow H_2O + H$. Figure adapted from Lam et al. (2013) [20]

Summary and Future Directions

Recent advances in shock tube/laser absorption methodologies are revolutionizing the use of shock tubes for chemical kinetics studies. New operational protocols in shock tube/laser absorption experiments can now provide well-characterized near-constant pressure test conditions, even during energetic reaction events, for test times approaching 50 ms. Laser absorption diagnostics can provide quantitative high-bandwidth measurements of time-histories during these experiments for a wide range of species. With these new methods, new kinetics targets can be studied. We have outlined several of these below.

Longer constant-pressure test times will allow for the validation and refinement of negative-temperature-coefficient (NTC) ignition processes. The existing shock tube NTC ignition delay time database for practical fuels and their surrogate components does not include detailed characterization of the test conditions, and there is a critical need for this characterization for long test time data if these data are to be used as reliable kinetics modeling targets [21]. As well, little, if any, species time-history studies of these fuels have been performed in the NTC regime, and these data are also critically needed to test and refine detailed reactions mechanisms.

The CO_2 laser absorption diagnostic for $T(t)$ provides the capability to test the ability of detailed reaction models to accurately capture heat release rates. Previous modeling studies have relied on the assumption that satisfactory agreement of the model simulations with ignition delay times or flame speeds resulted in accurate model heat release rates, as there were no other simple and accurate bench methods available to test this property of the model. The $T(t)$ time-histories kinetic targets should be considered as important as individual species time history data for mechanism testing and refinement.

Recently advocated, top-down kinetics modeling approaches require accurate measurements of concentration distributions of rapidly forming intermediate species [21]. These distributions can be used as inputs to reduce detailed reaction mechanisms describing slower combustion processes. These concentration measurements are made possible by the ability to measure a wide range of intermediate species. Currently, concentration measurements are possible for a wide range of species such as fuel, CH_3, C_2H_4, CH_4, OH, H_2O, CO, CO_2, and others. For those species that cannot be measured spectroscopically (e.g. homonuclear diatomics molecules such as H_2, or species that are difficult to access

spectrally such as allene), another approach can be used that takes advantage of the new ability to measure T(t) in a constant pressure/constant enthalpy test environment. Accurate measurements of the change in T(t) at constant pressure can be related to changes in the bond energy, i.e. the chemical contribution to the enthalpy change. This quantity can provide, along with atom balances and available measured species concentrations, multiple constraints on the product distribution, thereby allowing the accurate inference of several unmeasured species concentrations.

Finally, the continued development of new laser systems that provide access to wider wavelength coverage will allow for the measurement of an even larger array of species. Recent work in our laboratory has focused on the development of diagnostics to monitor acetylene near 3.0 μm, andiso-butene, and other alkenes and alkynes near 11 μm. This work builds on the past 40 years of laser development and offers to provide a simple direct method to characterize the chemistry of important combustion systems.

Acknowledgments Shock tube kinetics research at Stanford University has been supported by the U.S. Air Force Office of Scientific Research under the Basic Research Initiative Program Grant Number FA9550-12-1-0472 with Dr. Chiping Li as Program Manager, the U.S. Army Research Office under contract/grant number W911NF1310206 with Dr. Ralph Anthenien as Program Manager, the U.S. Department of Energy, Office of Science, Office of Basic Energy Sciences, under Award Number DE-FG02-88ER-13857, with Dr. Wade Sisk as contract monitor, and by the National Science Foundation under Grant No. 0964884.

References

1. Hanson, R.K., Davidson, D.F.: Recent advances in laser absorption and shock tube methods for studies of combustion chemistry. Prog. Energy Comb. Sci. **44**, 103–114 (2014)
2. Hong, Z.K., Pang, G.A., Vasu, S.S., Davidson, D.F., Hanson, R.K.: The use of driver inserts to reduce facility effects behind reflected shock waves. Shock Waves **19**, 113–123 (2009)
3. Hanson, R.K., Pang, G.A., Chakraborty, S., Ren, W., Wang, S., Davidson, D.F.: Constrained reaction volume approach for studying chemical kinetics behind reflected shock waves. Combust. Flame **160**, 1550–1558 (2013)
4. Farooq, A., Jeffries, J.B., Hanson, R.K.: Sensitive detection of temperature behind reflected shock waves using wavelength modulation spectroscopy of CO_2 near 2.7 μm. Appl. Phys. B **96**, 161–173 (2009)
5. Herbon, J.T., Hanson, R.K., Golden, D.M., Bowman, C.T.: A shock tube study of the enthalpy formation of OH. Proc. Combust. Inst. **29**, 1201–1208 (2002)
6. Tsang, W.: Comparative rate measurements with a single-pulse shock tube. J. Chem. Phys. **40**, 1171–1172 (1964)
7. Tranter, R.S., Sivaranmakrishnan, R., Srinivasan, N., Brezinsky, K.: Calibration of reaction temperatures in a very high pressure shock tube using chemical thermometers. Int. J. Chem. Kinet. **33**, 722–731 (2001)
8. Haylett, D.R., Davidson, D.F., Hanson, R.K.: A second-generation aerosol shock tube. Shock Waves **22**, 483–493 (2012)
9. Davidson, D.F., Hanson, R.K.: Interpreting shock tube ignition data. Int. J. Chem. Kinet. **36**, 510–523 (2004)
10. Shen, H.P.S., Steinberg, J., Vanderover, J., Oehlschlaeger, M.A.: A shock tube study of the ignition of n-heptane, n-decane, n-dodecane, and n-tetradecane at elevated pressures. Energy Fuels **23**, 2482–2489 (2009)
11. Hanson, R.K.: Applications of quantitative laser sensors to kinetics, propulsion and practical energy systems. Proc. Combust. Inst. **33**, 1–40 (2011)
12. Rea Jr., E.C., Salimian, S., Hanson, R.K.: Rapid-tuning frequency-doubled ring dye laser for high resolution absorption spectroscopy in shock-heated gases. Appl. Optics **23**, 1691–1694 (1984)
13. Davidson, D.F., Chang, A.Y., DiRosa, M.D., Hanson, R.K.: A cw laser absorption diagnostic for methyl radicals. J. Quant. Spectrosc. Radiat. Transfer **49**, 559–571 (1993)
14. Ren, W., Davidson, D.F., Hanson, R.K.: IR laser absorption diagnostic for C_2H_4 in shock tube kinetics studies. Int. J. Chem. Kinet. **44**, 423–432 (2012)
15. Pyun, S.H., Cho, J., Davidson, D.F., Hanson, R.K.: Interference-free mid-IR laser absorption detection of methane. Meas. Sci. Tech. **22**, 025303 (2011) (9pp)
16. Ren, W., Farooq, A., Davidson, D.F., Hanson, R.K.: CO concentration and temperature sensor for combustion gases using quantum-cascade laser absorption near 4.7 μm. Appl. Phys. B **107**, 849–860 (2012)
17. Li, H., Farooq, A., Jeffries, J.B., Hanson, R.K.: Near-infrared diode laser absorption sensor for rapid measurements of temperature and water vapor in a shock tube. Appl. Phys. B **89**, 407–416 (2007)
18. Ren, W., Lam, K.-Y., Pyun, S.H., Farooq, A., Davidson, D.F., Hanson, R.K.: Shock tube/laser absorption studies of the decomposition of methyl formate. Proc. Combust. Inst. **34**, 453–461 (2012)
19. Ren, W., Dames, E., Hyland, D., Davidson, D.F., Hanson, R.K.: Shock tube study of methanol and methyl formatepyrolysis: CH_3OH and CO time-history measurements. Combust. Flame **160**, 2669–2679 (2013)
20. Lam, K.-Y., Davidson, D.F., Hanson, R.K.: A shock tube study of $H_2 + OH \rightarrow H_2O + H$ using laser absorption. Int. J. Chem. Kinet. **45**, 363–373 (2013)
21. Wang, H.: On potential energy landscape and combustion chemistry modeling. Combust. Flame **160**, 222–223 (2013)

Shock-Induced Combustion and Its Applications to Power and Thrust Generation

M. Brouillette, M. Picard, D. Rancourt, and J.-S. Plante

Introduction

Due to the high pressure and temperature state produced by shock waves, they offer the possibility to greatly speed up combustion processes as compared to diffusive reaction mechanisms. Devices exploiting shock-induced combustion also have the potential for higher compression ratios, and thus better efficiency, and less complexity than systems using mechanical compression systems. These advantages can lead to lighter, more efficient, and more compact propulsion and power systems.

Detonations

A traveling detonation wave is an example of a combustion process coupled to a shock wave, and it is relatively simple to produce in practice, usually in constant section tubes. This phenomenon is used in the pulsed detonation engine (PDE) propulsion concept, which exploits unsteady detonation propagation in the production of cyclic thrust [1].

However, most propulsion and power system applications ideally require a steady release of energy. The unsteady aspects of detonation wave propagation can be smoothed out by having the detonation propagate in a direction perpendicular to that of the main flow, as in rotating detonation wave (RDE) engines [2]. In concept, however, it would be much simpler to just stabilize the detonation at a fixed location in space in a supersonic premixed reactive flow, and many designs have been proposed to achieve this. A fundamental parameter for detonations is obviously the Chapman-Jouguet (CJ) detonation velocity, and to successfully stabilize a normal detonation would require the flow to be supplied at exactly the CJ velocity for the mixture under consideration. A greater range of allowable velocities are possible in theory if the flow velocities exceed the CJ value, in which case an oblique detonation would be produced. Many analytical and numerical studies have demonstrated the feasibility of stabilizing oblique detonations, and this has been experimentally observed over moving projectiles [3, 4]; this, however, has never has been conclusively demonstrated where the wave is actually at rest in the laboratory.

Nevertheless, even if stationary detonations prove to be elusive, many experiments have observed combustion phenomena following stationary shock waves [5]. For these cases, either a stationary normal shock, an oblique shock, or a system of shocks is produced in a supersonic premixed reactive flow, and the shocks are used to compress and ignite the mixture. For these cases, the reactive zone is not coupled as closely to the shocks as in a detonation wave but is coupled nonetheless, therefore retaining many of the advantages of detonation waves.

The Rim-Rotor Rotary Ramjet Engine (R4E)

Toward that end, we are developing a novel engine concept exploiting shock-induced combustion to significantly improve power density and reduce complexity over conventional gas turbines, thus making it an interesting alternative for future transportation and stationary power systems. Simply described, this novel engine comprises a plurality of ramjets arranged tangentially around the periphery of a single rotor, as shown in Fig. 1. In the rotating frame of reference, the premixed reactive mixture is first compressed by an oblique shock diffuser, which also ignites the flow. Combustion takes places behind the shock system in a rotating combustion chamber, and the combustion products are then expanded in a convergent-divergent nozzle to reach supersonic velocities at the exit. The difference in momentum flux between the inlet and outlet produces thrust, as in a

M. Brouillette (✉) • M. Picard • D. Rancourt • J.-S. Plante
Department of Mechanical Engineering, Université de Sherbrooke, Sherbrooke, Québec, Canada J1K 2R1
e-mail: martin.brouillette@usherbrooke.ca

G. Ben-Dor et al. (eds.), *30th International Symposium on Shock Waves 1*, DOI 10.1007/978-3-319-46213-4_8

ramjet, which is converted to torque, and thus mechanical power, by the rotor. The whole thermodynamic cycle is achieved in a single rotating stage, dramatically reducing the number of parts as compared with a conventional gas turbine. Rotating ramjets have been proposed in the past, without actual success, but the present concept introduces two key features that ensure the viability of the concept.

The first key enabling feature of the R4E is the use of a high-strength carbon fiber rim wrapped around the rotor to load the blades in compression under the high centrifugal loads generated at the required supersonic tip speeds. Loading the blades in tension potentially allows for the use of ceramic materials which offer high-temperature operation capabilities, which increase the efficiency of the engine and reduce the cooling requirements. The second enabling feature is a rotating combustion chamber whose geometry correctly exploits the high centrifugal acceleration field created by the rotation to greatly reduce the length of the combustion zone, which allows for a compact rotor.

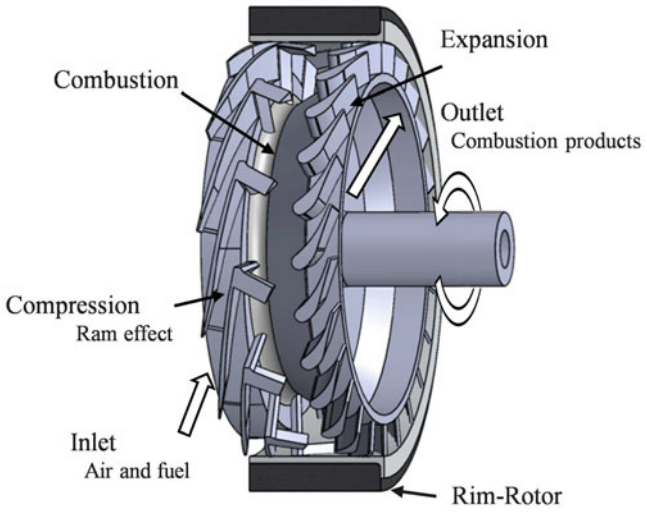

Fig. 1 Schematic of the rim-rotor rotary ramjet engine (R4E)

The performance of an R4E design can be examined using a simple quasi-one-dimensional model inspired from Shapiro's 1D generalized flow theory [6]. The model computes R4E power based on the main flow path properties for the entire discretized ramjet, taking into account the ramjet geometry and its dominant physics, including shockwave compression, high-g field combustion, viscous losses, heat transfer, inlet and outlet periodic conditions, and windage losses. The model is used to predict a given R4E actual and optimum design performance.

The model assumes a steady infinite cascade flow in a rotating reference frame, as shown in Fig. 2. The air-fuel mixture is treated as an ideal gas with varying heat capacities as a function of constituents and temperature. The mixture enters the ramjets and crosses a bow shock generated by a finite blade radius. The flow finally exits the engine through shock waves and expansion fans to match the outlet static pressure. Indicated power, defined as the power generated by the ramjets, can be calculated by the variation of angular momentum using the calculated tangential inlet and outlet velocities. Brake shaft power is obtained by subtracting the windage losses from the indicated power. An estimation of the complete engine weight allows for the evaluation of R4E power density.

The model is used to design a 500 kW version of the R4E. Hydrogen is selected for fuel since its high flame velocity is

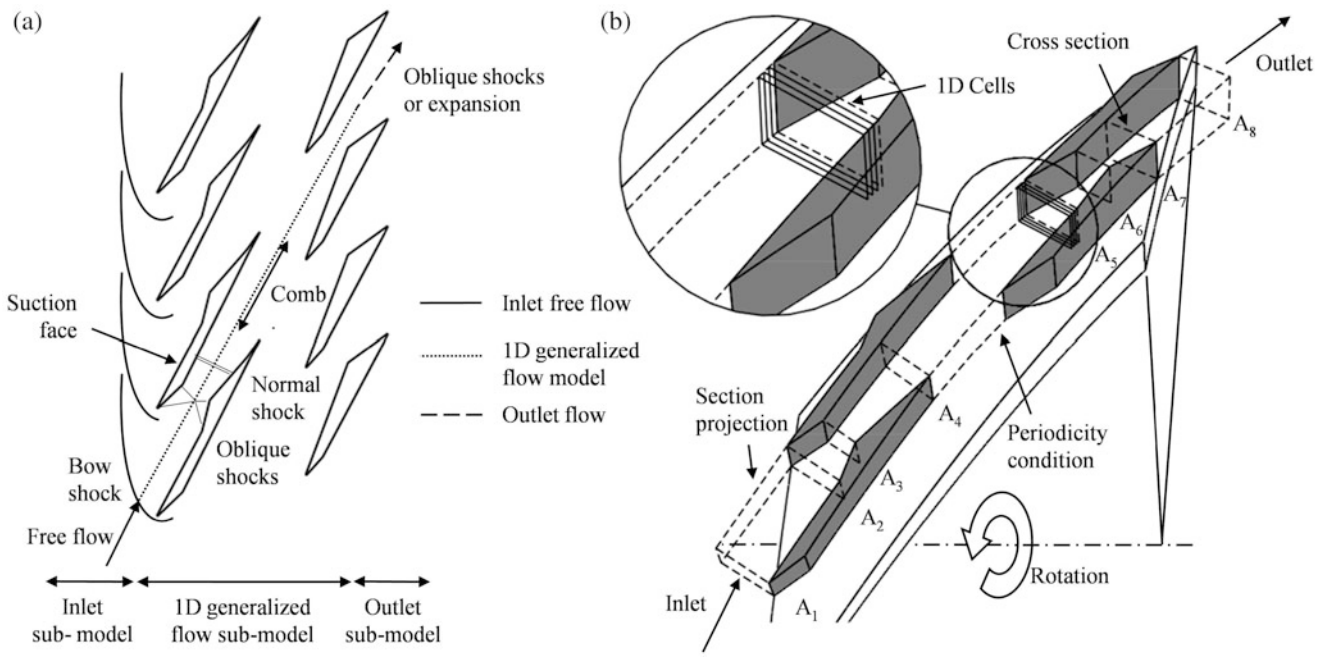

Fig. 2 (**a**) Infinite cascade rotary ramjet engine model sections. (**b**) 3D cross-sectional view

favorable for the combustion experimental validation at small scale. Other fuels can also be used, especially gaseous fuels which can be premixed in the same way as hydrogen. The tangential velocity is limited to 1000 m/s, the maximum velocity achievable by an optimized design using carbon-PEEK rim-rotor and carbon-carbon blades, based on a stress model presented by Rancourt et al. [7]. Windage losses are taken to be 35 % higher than the model to account for surface roughness, and the rim-rotor surrounding gas density is assumed to be reduced by 50 % compared to atmospheric condition, both inferred from experimental observation. The final design for a 500 kW R4E has a 26 cm rim-rotor outside diameter and a disc thickness of 9 cm, and the overall efficiency is predicted to be around 15 %; the power density, with chassis, gearbox, and accessories, is found to be almost 8 kW/kg, which is more than twice that of aircraft gas turbines.

The computed flow properties along a ramjet channel for an inlet Mach number of 2.8 are shown in Fig. 3 as a function

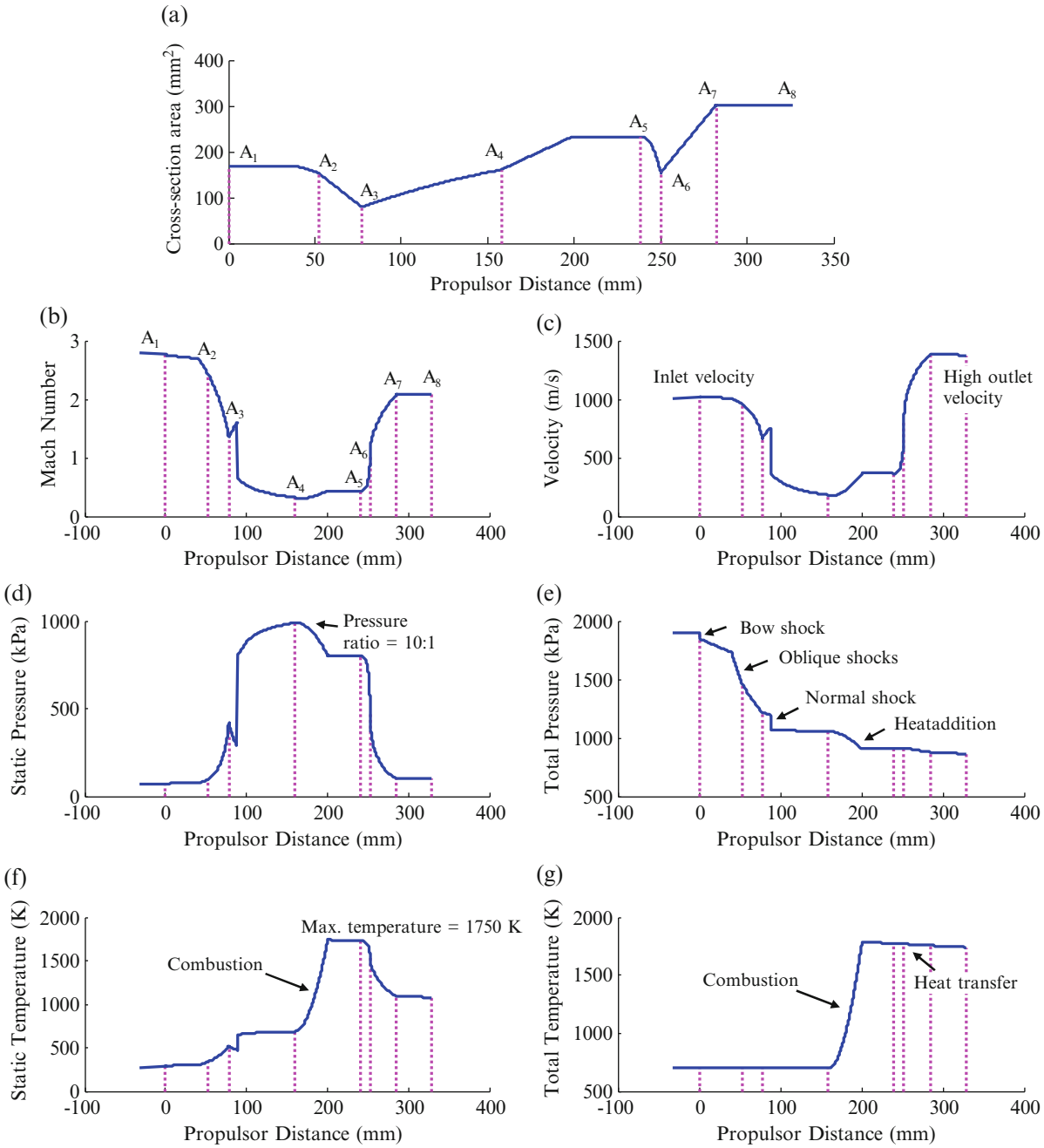

Fig. 3 (**a**) Cross-sectional area and predicted flow properties in the rotating reference frame through the ramjet for an inlet tangential velocity of 1000 m/s: (**b**) Mach number, (**c**) velocity, (**d**) static pressure, (**e**) total pressure, (**f**) static temperature, and (**g**) total temperature. Refer to Fig. 2 for the identification of the various channel sections

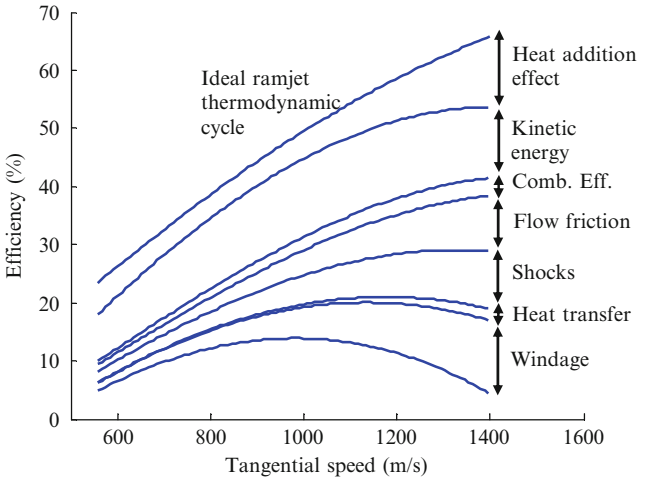

Fig. 4 Effect of loss mechanisms on R4E efficiency for an optimized ramjet geometry with a rotor of 21 cm and a hydrogen equivalence ratio of 0.5

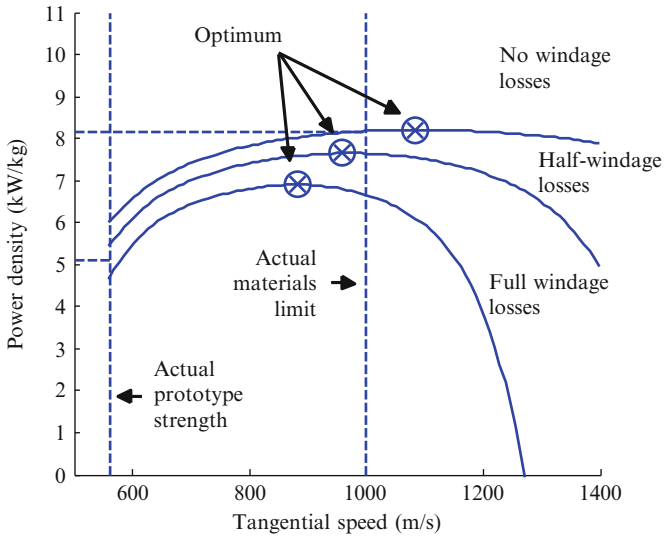

Fig. 5 Effect of windage losses on power density as a function of rim-rotor tangential speed

of position along a flow channel. First, friction on the suction face induces losses (A1 to A2, refer to Fig. 2 for the identification of the various channel sections Ai), followed by oblique shocks which induce important pressure losses and flow deceleration (A2 to A3). After the first throat, the flow slightly accelerates and crosses the normal shock. The flow is then subsonic and decelerates in the divergent section to reach $M = 0.3$ and a pressure ratio of 10:1 (A4). Combustion takes place in those desired conditions, raising the total temperature without exceeding acceptable limits for ceramics in steady-state operation (A4 to A5). The flow accelerates to $M = 1$ at the second throat (A6) and finally expands to match atmospheric pressure (A8). The outlet speed is much higher than the inlet speed, and thrust and shaft power are therefore produced.

Figure 4 shows the R4E efficiency as a function of tangential speed. The top curve represents the ideal thermodynamic Brayton open cycle; loss mechanisms are added one by one to quantify their relative importance. Heat addition effects account for intrinsic pressure losses and changes in gas properties due to combustion. Kinetic energy remaining in the outlet flow is a major source of inefficiency due to the use of a pure reaction turbomachine. Friction in the engine is an important loss component and increases significantly with speed. Losses from bow, oblique, and normal shocks also increase significantly with speed principally due to the oblique shocks strength needed to decrease the Mach number to slightly over 1 at the first throat; heat transfer, however, is found to be of small importance. Finally, at high speeds, windage friction is the most considerable loss mechanism: drag reduction is therefore essential to achieve adequate efficiency.

Windage losses are found to have an important effect on power density, as shown in Fig. 5. Structural strength of available materials limits the complete engine power density to 5.7 kW/kg when drag is reduced by half [7]. R4E power density could be increased to 7.6 kW/kg, by structure optimization using a carbon fiber rim-rotor combined with carbon-carbon blades to increase the maximum tangential speed to 1000 m/s. Furthermore, R4E power density could reach 8.5 kW/kg if windage losses were reduced sufficiently to make them negligible. This represents a valid estimation of the technological limit since further increasing speed would decrease efficiency due to other speed-dependent loss mechanisms, such as flow friction and shock waves.

A proof-of-concept prototype was designed for a maximum operation tangential velocity of 560 m/s (Mach 1.6) with the principal objective of validating combustion efficiency in a high-g field. The aforementioned quasi-1D model was used for the design of the prototype. The quasi-1D model was first validated from engine operation at low tangential Mach number by measuring windage losses, aspirated mass flow, and indicated power with and without combustion. The prototype consisted of CNC machined ramjets in an aluminum hub, assembled in a carbon-PEEK rim-rotor by a strong interference fit to avoid separation at high rotational speed, as shown in Fig. 6. An aluminum rim is placed between the blades and the carbon rim-rotor to prevent direct contact between the combustion products and the resin; hence the flame holder configuration is slightly modified from Fig. 1. A tangential speed 500 m/s is selected to get sufficient ram compression, up to a maximum pressure ratio of 2.6. The overall diameter of the engine is chosen for

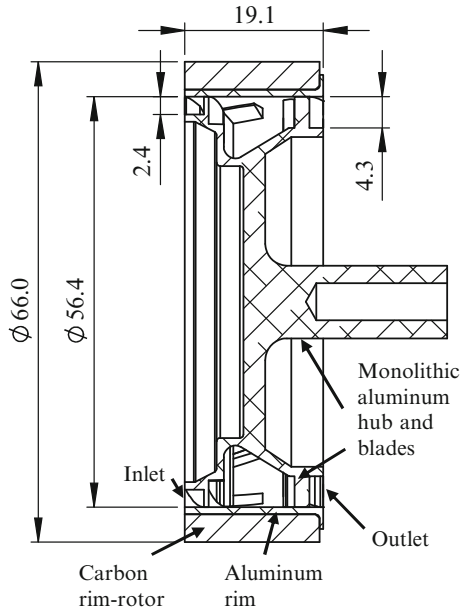

Fig. 6 Cutaway view of the aluminum and carbon-PEEK R4E design (dimensions in mm)

safety reasons in order to minimize the power required to accelerate the prototype before ignition. Hydrogen is selected as fuel for its high laminar flame velocity and small flame diameter. An equivalence ratio of 0.75 is selected so the flame temperature would correspond to the cooled ceramics' maximum temperature in future R4E designs while maximizing flame velocity. A combustion time of 1 s is targeted to reach steady-state combustion while allowing the use of easy-to-manufacture materials. One second is sufficient since it equals 6000 revolutions at maximum speed. Ignition is made in front of the engine, avoiding the need of any rotating ignition system that would add unnecessary load on the rim-rotor thus limiting maximum speed.

After ignition, the prototype accelerated for about 1 s before injection was stopped to minimize damage to the expansion blades. Measured exhaust temperature is stable for about 0.4 s, as shown in Fig. 7 for the test ignited at 288 m/s. Combustion efficiency is calculated with the 1D model equilibrium combustion solver to match the outlet temperature, neglecting heat transfer to aluminum hub. Combustion efficiency is found to be around 70 % even with this pessimistic approximation of negligible heat transfer to the walls. Although optimization is needed to reach state-of-the-art combustion efficiencies of current gas turbines, this shows the feasibility of flame holding and propagating the flame across the combustor up to a g-field of 7×10^5 g.

Positive outlet tangential velocities were measured for the three first tests (tangential speeds of 277, 281 and 326 m/s),

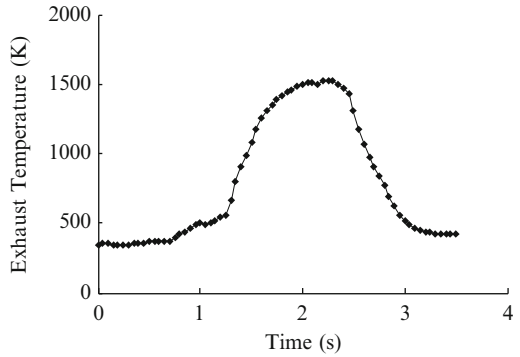

Fig. 7 Exhaust temperature (± 10 K) for the combustion during acceleration from a tangential velocity of 288–326 m/s

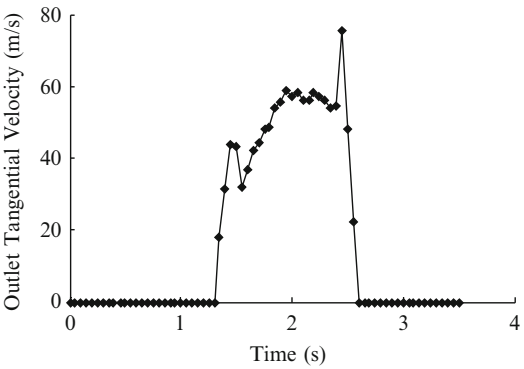

Fig. 8 Outlet tangential velocity (± 15 m/s) for the combustion run from 288 to 326 m/s

demonstrating ramjet thrust. The measured outlet velocity for the case accelerating the prototype from 288 to 326 m/s shows a relatively steady-state outlet velocity of 60 m/s during about 0.4 s, as shown in Fig. 8. Indicated power, or power generated by the blades, can be calculated from an angular momentum balance between inlet and outlet of the R4E in the fixed reference frame: this is to the authors' knowledge the first rotary ramjet engine packaged for power generation generating positive indicated power, an important milestone in rotary ramjet engine development.

Conclusions

Devices exploiting shock-induced combustion have the potential for higher compression ratios, and thus better efficiency, and less complexity than systems using mechanical compression systems. These advantages can lead to lighter, more efficient, and more compact propulsion and power systems. We have demonstrated such a system, the rim-rotor rotary ramjet engine (R4E) both theoretically and experimentally. This opens the door for many exciting applications in propulsion as well as mobile or stationary power.

References

1. Kailasanath, K.: Recent developments in the research on pulse detonation engines. AIAA J. **41**(2), 145–159 (2003)
2. Kailasanath, K.: The rotating-detonation-wave engine concept: a brief status report. In: 49th AIAA Aerospace Sciences Meeting, Orlando, Florida, 4–7 January (2011)
3. Kaneshige, M.J., Shepherd, J.E.: Oblique detonation stabilized on a hypervelocity projectile. In: Twenty-Sixth Symposium (International) on Combustion/The Combustion Institute, pp. 3015–3022 (1996)
4. Verreault, J., Higgins, A.J.: Initiation of detonation by conical projectiles. Proc. Combust. Inst. **33**, 2311–2318 (2011)
5. Morris, C.I., Kamel, M.R., Hanson, R.K.: Shock-induced combustion in high-speed wedge flows. In: Twenty-Seventh Symposium (International) on Combustion/The Combustion Institute, pp. 2157–2164 (1998)
6. Shapiro, A.H.: The Dynamics and Thermodynamics of Compressible Fluid Flow, pp. 186, 219–236. Ronald, New York (1953)
7. Rancourt, D., Picard, M., Denninger, M., Plante, J.-S., Chen, J., Yousefpour, A.: A high power density Rim-Rotor-Rotary Ramjet engine: part 1—structural design and experimental validation. J. Propuls. Power **28**, 1293–1303 (2012)

The Shock Fitting Technique from Gino Moretti Towards the Future

Marcello Onofri, Francesco Nasuti, Renato Paciorri, and Aldo Bonfiglioli

Introduction

Gino Moretti passed away peacefully on 15 March 2015 at the age of 98. He was one of the most active pioneers of the modern Computational Fluid Dynamics (CFD) and his contributions set some of the milestones in the evolution of the simulation of compressible high speed flows, in particular by providing original contributions to the treatment of shock waves and, more in general, of the discontinuities that may occur in a flow-field.

This paper aims at providing a concise memory of his main contributions, based on the development of the "Shock Fitting" technique, and also reports its recent evolutions, which make this approach one of the most powerful and precise tools for the numerical simulation of compressible high speed flows featuring complex shock systems.

Shock-Fitting, Upwinding and Modern Shock-Capturing Schemes

Shock waves occur very frequently in nature and in technological applications. Their presence characterises compressible flows not only in aeronautics and aerospace, but also in other areas of theoretical and applied physics and engineering. In all flows where shock waves occur, these play an important role that affects the overall flow behaviour.

At the dawn of CFD, two alternative approaches were introduced to simulate flows with shocks: shock-fitting and shock-capturing. The shock-fitting approaches showed up capable to provide very accurate solutions and to be very efficient in limiting the computational time required. Unfortunately, it showed also clear limitations in simulating three-dimensional flow-fields and when complex shock interactions occur. As a consequence, nowadays shock-capturing schemes are the most widespread choice for practical fluid-dynamics simulations involving shock waves.

Shock-capturing discretisations lay their foundations in the mathematical theory of weak solutions, which allows to compute all types of flows, including those with shocks, using the same discretisation of the conservation-law-form of the governing equations at all grid cells. This yields obvious consequences in terms of coding simplicity, since a single numerical scheme is used and the same set of operations is repeated within all control volumes of the mesh, no matter how complicated the flow might be.

Coding simplicity comes not for free, however, and shock-capturing solutions of flows featuring strong shock waves are often characterised by the appearance of bizarre anomalies and sometimes by large numerical errors. The deficiencies exhibited by state-of-the-art shock-capturing discretisations appear in some cases such to lead the author of a recent review paper [15] on the numerical methods for high-speed flows to conclude that "these limitations, related to the misrepresentation of discontinuities on a mesh with finite spacing, can only be overcome by some form of shock-fitting".

Shock-fitting consists first in finding and then tracking the discontinuities in the flow-field. These are treated as boundaries between regions where a smooth solution to the governing partial differential equations (PDEs) exists. The flow variables on the two sides of the discontinuities are evaluated analytically by enforcing the Rankine-Hugoniot jump relations, which are simple algebraic equations connecting the states on both sides of the discontinuity and its local speed. Then, this solution is used to compute the

M. Onofri (✉) • F. Nasuti • R. Paciorri
Dipartimento di Ingegneria Meccanica e Aerospaziale, University of Rome "La Sapienza", Via Eudossiana 18, Rome 00184, Italy
e-mail: marcello.onofri@uniroma1.it

A. Bonfiglioli
Scuola di Ingegneria - Università degli Studi della Basilicata, Viale dell'Ateneo Lucano 10, 85100 Potenza, Italy
e-mail: aldo.bonfiglioli@unibas.it

G. Ben-Dor et al. (eds.), *30th International Symposium on Shock Waves 1*, DOI 10.1007/978-3-319-46213-4_9

space-time evolution of the discontinuity, that is, to track its motion.

Shock-fitting methods have enjoyed a remarkable popularity in the early CFD era, thanks to the efforts of Gino Moretti and his collaborators. In order to well understand the reasons behind Moretti's interest in the development of the shock-fitting technique and also to take into due consideration the full extent of Moretti's contribution to the development of CFD, it would be useful to re-read some of his most significant papers [6, 8]. The reader would discover that Moretti's attention was focused not only on the shock-fitting technique, but also on the choice of the most suitable form of the governing PDEs to be discretised when dealing with shock waves and other discontinuities. Indeed, Moretti was convinced [9] that the "codes derived from the conservation equations are clumsier, slower and less efficient than codes based on Riemann's characteristics equations". Since compressible flows are dominated by wave propagation phenomena and the characteristic formulation of the governing PDEs is the one that best reveals the contribution of the various waves that travel within the flow-field, this particular form of the governing equations is the most natural and "clever" choice to build numerical schemes for compressible flows, because of its capability to follow the main physical characteristics of the flow behaviour.

In particular, the choice to respect carefully the physical nature of the phenomenon led Moretti to introduce the upwind differencing for his lambda [4] and FAST [5] schemes.

It is important to underline that these schemes were proposed and successfully used by Moretti in many applications in the 70s, at a time when most of the numerical methods were based on central differencing. Modern shock-capturing methods largely in use today do indeed take into account wave propagation phenomena, but were developed some years later, probably as answer to the pressure of Moretti's criticisms. Therefore, Moretti anticipated the massive use of upwind methods in CFD, while remaining faithful to the use of the characteristic equations. As pointed out by Roe in [17], he "waged a long rearguard action at the Polytechnic Institute of Brooklyn in support of fitting methods and he was involved with ICASE during the years when many of current capturing methods were being forged". Therefore, even though Moretti continued to dislike modern shock-capturing methods, he contributed to the development of these methods by showing the importance of accounting for wave propagation phenomena when developing numerical schemes for compressible flows.

What Roe defines as "a long rearguard action" was actually a coherent path followed without taking shortcuts or avoiding difficulties. The coherence in the use of numerical schemes based on the characteristic equations led Moretti to a continued development of the shock-fitting technique. Since the characteristic equations are not valid across the shocks, shocks cannot be treated with the same numerical scheme used in smooth flow regions. For this reason, the development of a general-purpose shock-fitting technique became the element characterising Moretti's overall scientific production.

Shock-Fitting for Structured Grids

Moretti has been active over a time frame, ranging from the mid-60s to the late 80s, when CFD made almost exclusively use of structured-grid discretisations. He retired by the end of the 80s, whereas unstructured-grid schemes started to be applied to CFD problems at the beginning of the 90s, unveiling new unpredictable opportunities for building more robust and versatile shock-fitting schemes. Within the structured-grid framework, shock-fitting methods took two different approaches: boundary shock-fitting [10] and floating shock-fitting [8].

In the boundary shock-fitting, the shock is made to coincide with one of the boundaries of the computational domain so that the treatment of the algebraic relations that hold across the shock is confined to the boundary points. This greatly simplifies the coding, but unfortunately it does not address flow-fields where other shocks take place. Therefore, it results in the treatment of embedded shocks as a "hard bone to chew" [6], as shown by [3]. According to this approach, the embedded shocks are treated as interior boundaries that separate different blocks of a multi-block grid setting. Two- and three-dimensional shock-fitting calculations featuring embedded shocks and relying on the boundary shock-fitting approach have been carried out [3]. Figure 1 shows a non-trivial application of the boundary shock-fitting method to the computation of the hypersonic flow past a double ellipse in which both the bow and the embedded shocks are fitted. Later on, since these shocks move, the handling of the motion and deformation of the various blocks soon becomes a "topological nightmare" [8] and led Moretti to introduce the floating shock-fitting.

A step forward towards a technique capable of handling more easily complex flow configurations, including shock interactions, was undertaken by Moretti with the development of the floating shock-fitting. In this version of the shock-fitting the discontinuities are allowed to move (float) freely over a fixed background structured grid. A shock front is described by its intersections with grid lines, which gives rise to x and y shock points, as sketched in Fig. 2. The main features of the methodology are the same as those of the boundary fitting technique, except for the need of a special treatment for grid-points neighbouring shocks. This is because approximating derivatives by differences between

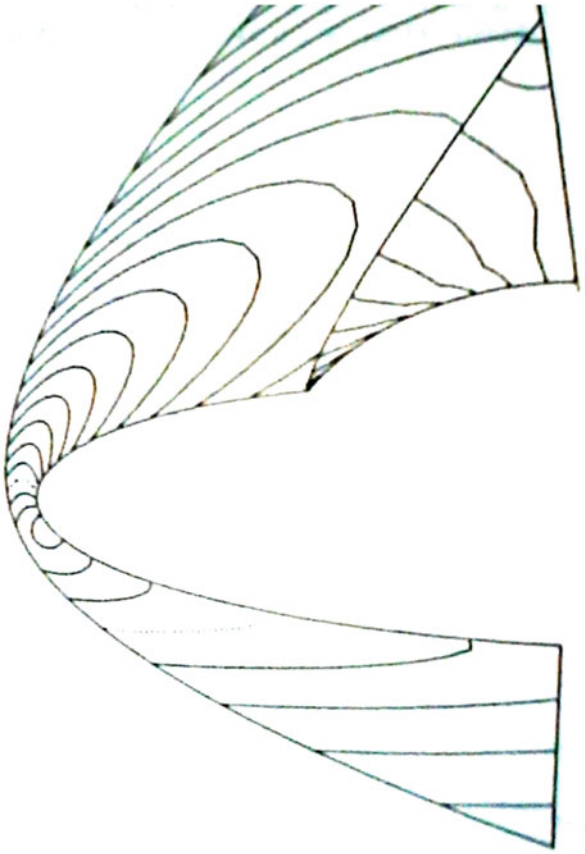

Fig. 1 Hypersonic flow past a double ellipse computed by means of a boundary shock-fitting method

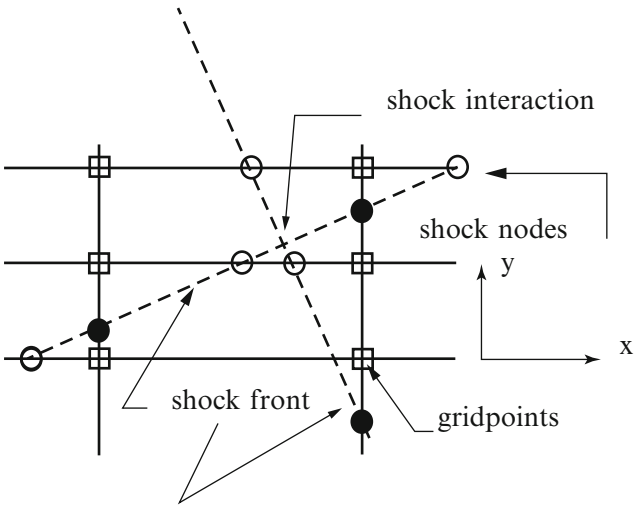

Fig. 2 Two floating shocks on a fixed structured mesh

nodes located on opposite sides of a shock must be avoided and therefore, ad hoc finite difference formulae (see, for instance, [16, 19]) have to be used in this case. Floating shock fitting codes had been successfully used in the past to compute steady and unsteady two-dimensional [7, 11, 12] and three-dimensional [20] flows involving shock reflections and shock interactions. Figures 3 and 4 report two different applications of the floating shock-fitting technique in the simulation of complex flows involving several shocks. More specifically: Fig. 3 shows the change in shock topology detected by the floating technique during the supersonic acceleration of a two-dimensional duct flow, whereas Fig. 4 shows the complex flow, featuring coalescing and interacting shocks, in the afterbody of a plug nozzle. However, these examples of calculation revealed serious limitations of the method. Indeed, the scheme showed up not enough robustness and the nice results were rather due to a heavy, patient and handcraft work of the researchers. Moreover, its three-dimensional extension was just prohibitive. All these considerations led to the abandonment of fitting technique. Only very recently, the floating shock-fitting (denoted as front-tracking) algorithm has been re-proposed by Rawat and Zhong [16] in the framework of high-order, structured-grid schemes.

Shock-Fitting for Unstructured Grids

The continuous advances in computer power and computational science that have taken place over the last two decades have led to the possibility of using unstructured grids more suitably and comfortably. Taking advantage of this opportunity, a new shock-fitting technique for unstructured meshes has been developed in Italy by researchers belonging to the school of Moretti [2, 13, 14].

In this novel unstructured shock-fitting approach the shock front is discretised as a polygonal curve which is treated as an internal boundary. The local shock speed and nodal values on the high-pressure side of the shock are computed by enforcing the Rankine-Hugoniot relations across the discontinuity. The shock is allowed to move over and independently of a background triangular grid which is locally adapted at each time step to ensure that the nodes and the edges that make up the shock are part of a constrained Delaunay triangulation that covers the entire computational domain. This novel shock-fitting technique can be easily coupled with a vertex-centred, shock-capturing solver [1], which is used to discretise the governing PDEs in the smooth regions of the flow-field.

This technique has been successfully applied to different kinds of shock–shock interactions and shock-wall reflections, including the complex type IV shock–shock interaction shown in Fig. 5 and the three-dimensional supersonic flow around a cylinder with a conical flare shown in Fig. 6, in which both the bow shock and the embedded shock are fitted. The results obtained by fitting the shock waves are characterised by a much better solution quality than those

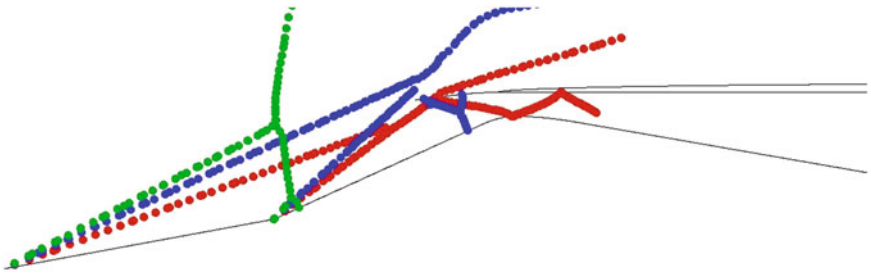

Fig. 3 Topological changes that occur in the supersonic acceleration through a 2D duct inlet

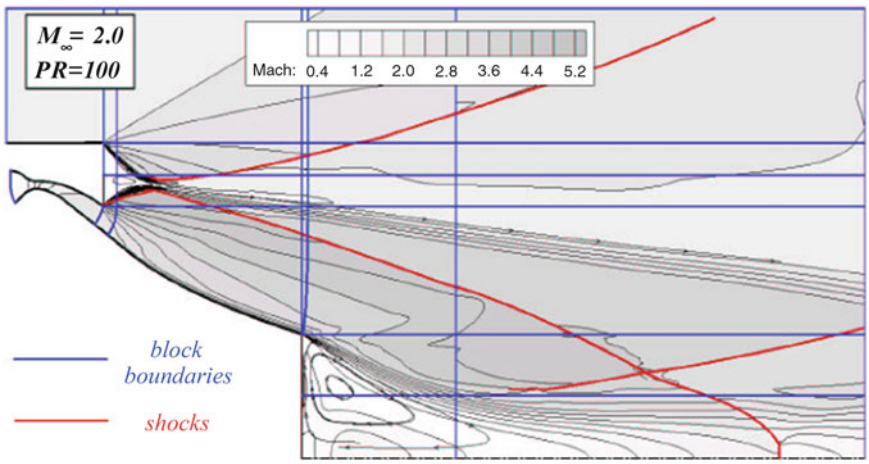

Fig. 4 Complex flow in a plug nozzle

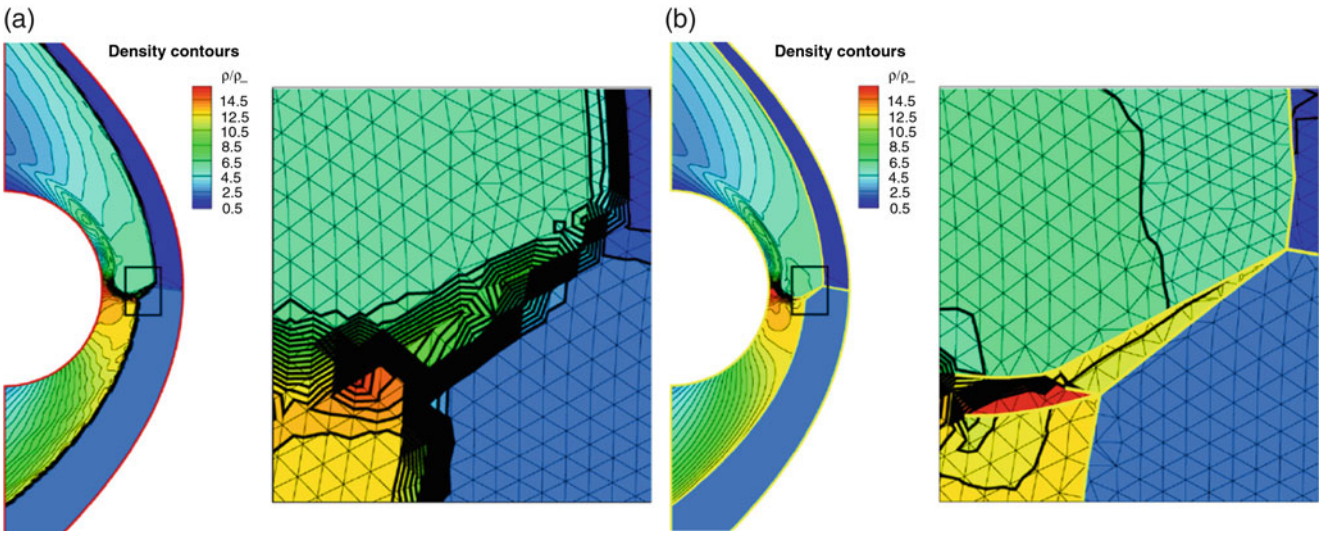

Fig. 5 A type IV shock–shock interaction: comparison between the shock-capturing (*left*) and shock-fitting (*right*) solution

obtained by shock-capturing on meshes of comparable grid resolution, see Fig. 5.

The proposed shock-fitting technique combines the coding simplicity of the "boundary" shock-fitting technique with the capability of treating complex flows of the "floating" shock-fitting technique. At the same time, it does not suffer from the strong topological limitations that plagued the boundary shock-fitting technique when implemented in the structured grid context. Moreover, the integration of the present shock-fitting technique with a pre-existing gas-dynamic solver is algorithmically less complicated than integrating the floating shock-fitting technique within a structured-grid solver.

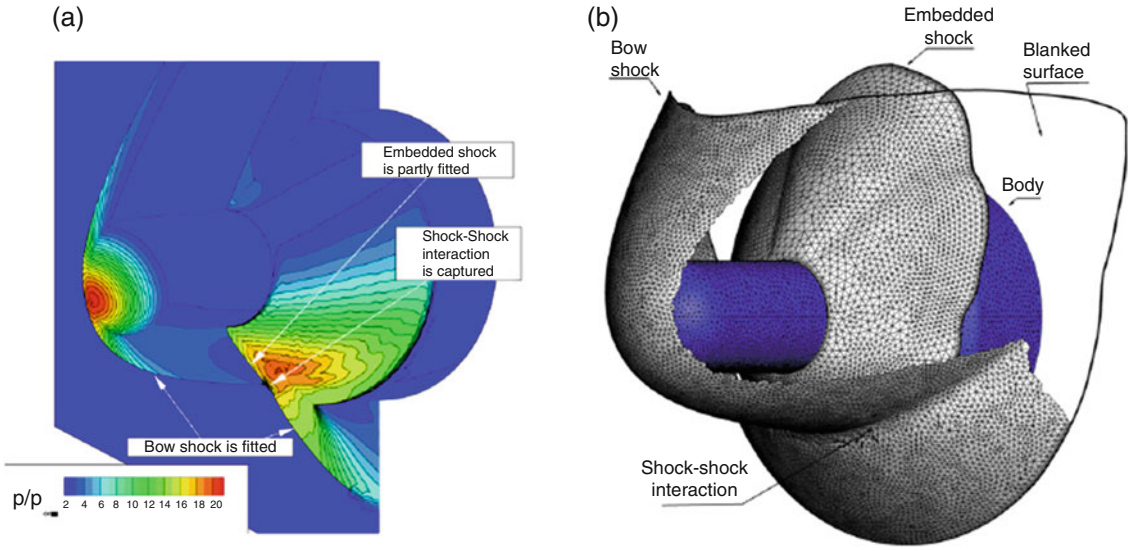

Fig. 6 3D supersonic flow around a cylinder with a conical flare: solution and shock surfaces of the shock-fitting solution. (**a**) Normalised pressure distribution. (**b**) Fitted shock surfaces

Conclusions

At the end of this review of the shock-fitting methods developed by Gino Moretti and of its latest developments in the unstructured-grid framework, two conclusions arise.

Gino Moretti gave a contribution to the development of modern CFD higher than what is commonly believed. The re-discover of his writings can be a very useful experience that is likely to surprise the reader.

The development of shock-capturing schemes seems to be ended in deadlock, whereas the most recent developments in unstructured shock-fitting have removed some of the limitations that plagued the technique when used in the structured-grid context.

These observations suggest that it might be worth to re-assess the unique capabilities of the shock-fitting approach, even if it has been nearly forgotten for years. We can now agree with Roe, who, in his review [17] of Salas' "A Shock-Fitting Primer" book [18], asserts that ".., a reappraisal of fitting methods is timely." since ".. a revival of shock-fitting is one of the few remaining possibilities for revolutionary change [in high-resolution methods]".

References

1. Bonfiglioli, A.: Fluctuation splitting schemes for the compressible and incompressible Euler and Navier-Stokes equations. Int. J. Comput. Fluid Dyn. **14**, 21–39 (2000)
2. Bonfiglioli, A., Grottadaurea, M., Paciorri, R., Sabetta, F.: An unstructured, three-dimensional, shock-fitting solver for hypersonic flows. Comput. Fluids **73**, 162–174 (2013). doi:10.1016/j.compfluid.2012.12.022
3. Marconi, F., Salas, M.: Computation of three dimensional flows about aircraft configurations. Comput. Fluids **1**, 185–195 (1973)
4. Moretti, G.: The λ-scheme. Comput. Fluids **7**, 191–205 (1979)
5. Moretti, G.: Fast Euler solver for steady, one-dimensional flows. Comput. Fluids **13** (1), 61–81 (1985). doi:10.1016/0045-7930(85)90033-7
6. Moretti, G.: Computation of flows with shocks. Ann. Rev. Fluid Mech. **19**, 313–317 (1987)
7. Moretti, G.: A general-purpose technique for two dimensional transonic flows (1987). NASA-CR-194186
8. Moretti, G.: Efficient Euler solver with many applications. AIAA J. **26** (6), 655–660 (1988). doi:10.2514/3.9950.
9. Moretti, G.: Thirty-six years of shock fitting. Comput. Fluids **31** (4–7), 719–723 (2002)
10. Moretti, G., Abbett, M.: A time-dependent computational method for blunt body flows. AIAA J. **4** (12), 2136–2141 (1966)
11. Nasuti, F., Onofri, M.: Analysis of unsteady supersonic viscous flows by a shock-fitting technique. AIAA J. **34**, 1428–1434 (1996)
12. Nasuti, F., Onofri, M.: Viscous and inviscid vortex generation during startup of rocket nozzles. AIAA J. **36**, 809–815 (1998)
13. Paciorri, R., Bonfiglioli, A.: A shock-fitting technique for 2D unstructured grids. Comput. Fluids **38** (3), 715–726 (2009)
14. Paciorri, R., Bonfiglioli, A.: Shock interaction computations on unstructured, two-dimensional grids using a shock-fitting technique. J. Comput. Phys. **230** (8), 3155–3177 (2011)
15. Pirozzoli, S.: Numerical methods for high-speed flows. Ann. Rev. Fluid Mech. **43** (1), 163–194 (2011). doi:10.1146/annurev-fluid-122109-160718
16. Rawat, P.S., Zhong, X.: On high-order shock-fitting and front-tracking schemes for numerical simulation of shock-disturbance interactions. J. Comput. Phys. **229** (19), 6744–6780 (2010). doi:10.1016/j.jcp.2010.05.021

17. Roe, P.L.: Review of the book "A Shock-Fitting Primer" by Manuel D. Salas. SIAM Rev. **53**, 207–210 (2011)
18. Salas, M.: A Shock-Fitting Primer, 1st edn. CRC Applied Mathematics & Nonlinear Science, Chapman & Hall, Boca Raton, FL (2009)
19. Salas, M.D.: Shock-fitting method for complicated two-dimensional supersonic flows. AIAA J. **14**, 583–588 (1976)
20. Yamamoto, Y., Karashima, K.: Floating shock fitting for three-dimensional inviscid supersonic flows. AIAA J. **20** (1), 9–17 (1982). doi:10.2514/3.7897

Part II

Nozzle Flow

New Modified Pekkari Model to Analyse the Aeroelastic Stability Behaviour for a Flexible Overexpanded Rocket Nozzle

N. Bekka, M. Sellam, and A. Chpoun

Introduction

During the transient phases, start-up and shutdown of the rocket engines, or when it operates under no adaptation conditions at low altitude, very complex physical phenomena appear, particularly the aeroelastic effects due to extended boundary layer separation and its interaction with the shock wave in the interior of the divergent of the nozzle. The numerical coupling strategy to study this phenomenon using multi-physics codes is considered to be the most used technique today [1–7]. Knowing that the present study is limited to the analysis of linear stability relative to the small displacements, the choice of the transpiration technique to consider the coupling at the fluid–structure interface is justified by its simple implementation and its low CPU time computation compared to those of the ALE (arbitrary Lagrangian–Eulerian) method, widely discussed in many previous studies.

The fluid dynamic solver used for solving the Euler equations for a 2D inviscid compressible flow case is the NSC2KE code developed at INRIA by Mohammadi [8]. The code uses a combination of the finite volume and finite element methods to simulate perfect or viscous flows around or inside 2D or axisymmetric configurations on unstructured meshes. The structure dynamic solver is based on the implicit Newmark scheme to describe the temporal evolution of the structure displacements. For the coupling technique and for temporal integration, unlike to the code of structure, the NSC2KE fluid code is based on an explicit scheme in which the fluid time step is conditioned by the CFL stability condition. This difficulty leads to a time shift between the two codes, which can be overcome by using the iterative scheme CSS (conventional serial staggered procedure) [9]. To validate the numerical coupling procedure, the main results obtained for a basic 2D configuration of an overexpanded rocket nozzle are compared with those of the aeroelastic stability models developed in previous works for the inviscid flow case [1].

N. Bekka (✉) • M. Sellam • A. Chpoun
Laboratoire de Mécanique et d'Energétique d'Evry LMEE, Université d'Evry Val d'Essonne, 40 rue du Pelvoux, 91020 Evry Cedex, France
e-mail: Nadir.Bekka@ufrst.univ-evry.fr

Numerical Method

As mentioned previously, the simulation of aeroelastic phenomena is done by coupling two numerical codes. The first one is for the fluid dynamics part to resolve the Euler equations using the conservative formulation for a 2D compressible inviscid flow:

$$\frac{\partial U}{\partial t}+\frac{\partial F(U)}{\partial x}+\frac{\partial G(U)}{\partial y}=0 \tag{1}$$

where U, $F(U)$ and $G(U)$ are respectively the vector of the conservative variables and the components of the convective flux:

$$U=\begin{pmatrix}\rho\\ \rho u\\ \rho v\\ \rho E\end{pmatrix} \tag{2}$$

$$F(U)=\begin{pmatrix}\rho u\\ \rho u^2+p\\ \rho uv\\ (\rho E+p)u\end{pmatrix},\quad F(U)=\begin{pmatrix}\rho v\\ \rho uv\\ \rho v^2+p\\ (\rho E+p)v\end{pmatrix} \tag{3}$$

where ρ is the mass density, $\vec{u}=(u,v)$ the velocity, E the total energy and $p=\rho(\gamma-1)\left(E-\frac{u^2+v^2}{2}\right)$ the pressure.

The time integration is achieved by using an explicit Runge–Kutta scheme of order 4, and the time step is determined by the CFL criterion.

G. Ben-Dor et al. (eds.), *30th International Symposium on Shock Waves 1*, DOI 10.1007/978-3-319-46213-4_10

The second code is dedicated to the structure computations using the implicit Newmark scheme to describe the temporal evolution of the structure displacements:

$$\begin{aligned}\{W^{p+1}\} &= \{W^p\} + \Delta t\{\dot{W}^p\} + \frac{\Delta t}{2}\left((1-b)\{\ddot{W}^p\} + b\{\ddot{W}^{p+1}\}\right)\\ \{\dot{W}^{p+1}\} &= \{\dot{W}^p\} + \Delta t\left((1-a)\{\ddot{W}^p\} + a\{\ddot{W}^{p+1}\}\right)\\ \{\ddot{W}^{p+1}\} &= \frac{4}{\Delta t^2}\left(\{W^{p+1}\} - \{W^p\}\right) - \frac{4}{\Delta t}\{\dot{W}^p\} - \{\ddot{W}^p\}\end{aligned} \tag{4}$$

In this scheme, the constants a and b are set equal to 0.5.

$\{W^p\}$, $\{\dot{W}^p\}$ and $\{\ddot{W}^p\}$ are respectively the nodal displacements, velocity and nodal acceleration vectors and the time step p.

The numerical coupling between the two codes is achieved by using the transpiration method. This technique allows to take into account the displacement effect of the structure and to keep simultaneously a fixed domain for the fluid [10]. The main idea of this strategy is shown schematically in Fig. 1. Here, Ω_0^f and Ω_0^s designate respectively the fluid and the structure reference domains, and Γ_0^s designates the fluid–structure interface.

As we can see, the new location of the fluid–structure interface Γ_0^s at the instant t is $\Gamma^s(t)$. The concept of transpiration method requires to keep Γ_0^s as fixed interface (immobile); the calculation of the velocity field and the dynamic loads is obtained by a first-order Taylor development at the interface of reference Γ_0^s. When calculating the structure dynamic, a node which is initially in the position x_0 is displaced by a distance of $\delta x^s(x_0, t)$. By neglecting the higher-order terms and for the inviscid flow case, the transpiration condition for the velocity can be reduced to the flowing simplified form on Γ_0^s [10]:

$$u_E \cdot n_0 = \delta\dot{x}^s \cdot n - u_E \cdot (n - n_0) \tag{5}$$

where n_0 and n are the normal unit vectors to the wall in reference Γ_0^s and in deformed configurations $\Gamma^s(t)$, respectively, and $\delta\dot{x}^s$ is the speed of the flexible interface.

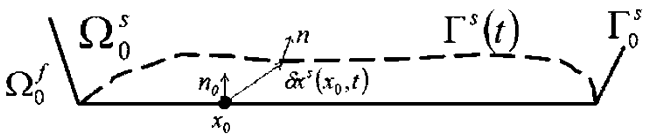

Fig. 1 The illustrated scheme for the law of transpiration [10]

Results

In order to compare the results issued from the numerical coupling to these of the aeroelastic stability models, 2D nozzle geometry has been chosen with fixed nodes at throat and at the exit of the nozzle divergent (Fig. 2). The material properties are summarised in Table 1.

The numerical coupling strategy consists as a first step to identify the initial position of the shock steady state for a rigid structure. Then, in second time, the structure is perturbed following to its first mode, for example. The aeroelastic analysis consists in recording the temporal evolution of the vertical displacements for a given node of the structure and then to compute the frequency values by using the fast Fourier transform (FFT). Figure 3 shows the evolution of the real part of the aeroelastic frequency versus shock wave position. As we can see, except the zone of the static instabilities, the results predicted by the numerical coupling are in general in good agreement with those issued from the model predictions. In the first quarter of divergent and for the region near the exit, the structure is stable as provided by the models. In addition, in the dynamic instability area, corresponding to the coalescence of modes 1 and 2, the coupled computation indicates that the temporal evolution of the normal structure displacement and their Fourier transform adopt the same behaviour in the region of flutter instability as shown in Fig. 4a. This evolution is harmonic having an increasing amplitude,

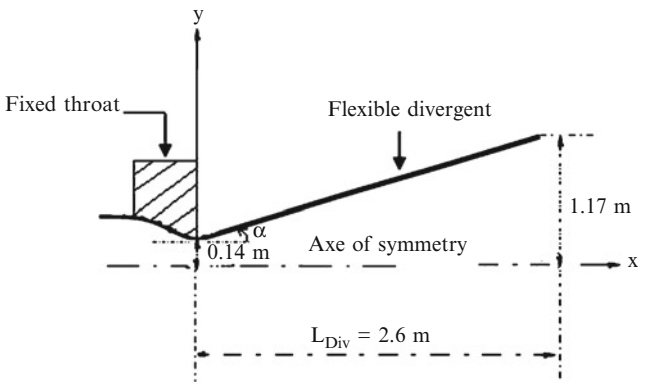

Fig. 2 Nozzle geometry for the studied test case

Table 1 Material properties (2D)

Young modulus (N/m^2)	Thickness h (mm)	Poisson coefficient	Mass density
2.2×10^{11}	10	0.0	2000 kg/m^3

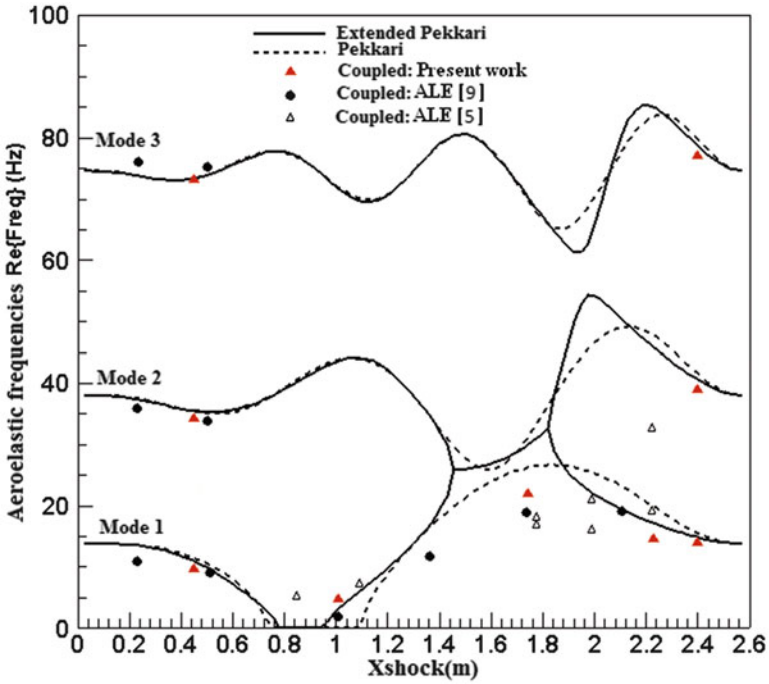

Fig. 3 Evolution of the aeroelastic frequencies versus shock separation position, comparison between the numerical results issued from the coupled computation and the stability models ($\alpha = 22°$)

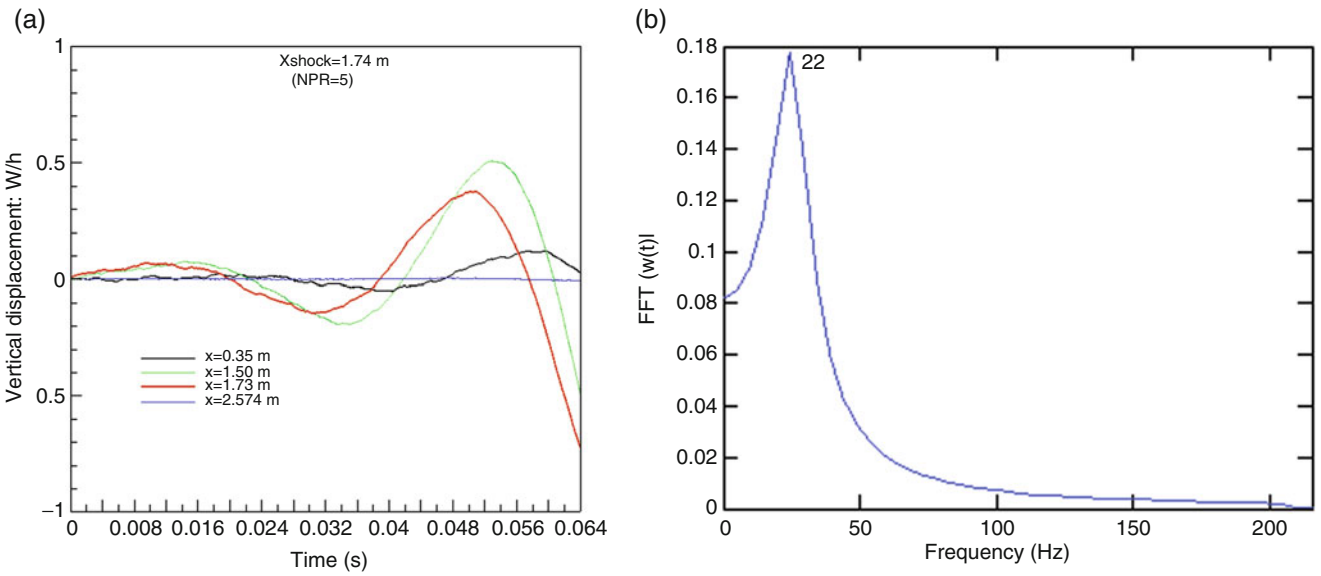

Fig. 4 Evolution of the vertical displacement (**a**) and its Fourier transform (**b**) for NPR = 5

characterising the phenomenon of dynamic instability or flutter. This type of instability may lead to the structure failure and represents a major issue in industrial context.

Conclusions

In this study, the aeroelastic stability analysis for the overexpanded nozzles has been performed using the numerical coupling via the transpiration method. The results show that a linear approach for the small displacements is usually sufficient for the dynamic instabilities prediction. However, the ulterior evolution of the structure behaviour involves necessarily a nonlinear modelling, and the method of transpiration becomes inoperative.

References

1. Bekka, N.: Problématique des ondes de choc dans les tuyères supersoniques et leur interaction avec la structure. Ph.D. thesis, Université d'Evry Val d'Essonne (2014)

2. Blades, E.L., Baker, M., Pray, C.L., Luke, E.A.: Fluid–structure interaction simulations of rocket engine side loads. SIMULIA Customer Conference (2012)
3. Garelli, L., Paz, R.R., Storti, M.A.: Fluid–structure interaction study of the start-up of rocket engine nozzle. J. Comput. Fluids **39**, 1208–1218 (2010)
4. Lefrançois, E.: Numerical validation of a stability model for a flexible over-expanded rocket nozzle. Int. J. Numer. Methods Fluids **49**, 349–369 (2005)
5. Lefrançois, E.: Modèle numérique de couplage fuide-structure pour l'étude des phénomènes aéroélastiques avec applications aux moteurs fusée. Ph.D. thesis, Université de Rouen (1998)
6. Lüdeke, H., Calvo, J.B., Filimon, A.: Fluid structure interaction at the ARIANE-5 Nozzle section by advanced turbulence models. In: European Conference on Computational Fluid Dynamics, ECCOMAS CFD (2006)
7. Mouronval, A.-S.: Etude numérique des phénomènes aéroélastiques en aérodynamique supersonique. Application aux tuyères propulsives. Ph.D. thesis, INSA de Rouen (2004)
8. Mohammadi, B.: Fluid Dynamics Computation with NSC2KE. An User-Guide, Release 1.0, N° RT-0164, INRIA (1994)
9. Piperno, S., Farhat, C.: Energy based design and analysis of staggered solvers for nonlinear transient aeroelastic problems. AIAA Paper 2000-1447 (2000)
10. Fernández-Varela, M.A.: Modèles simplifiés d'Interaction Fluide-Structure. Ph.D. thesis, Université IX Dauphine (2001)

Adaptation of the Transpiration Method to Simulate the Fluid–Structure Interaction Phenomena for a Flexible Overexpanded Rocket Nozzle

N. Bekka, M. Sellam, and A. Chpoun

Introduction

A launcher engine is theoretically designed to operate in optimal mode along the whole trajectory. The engine operates over a large segment of its trajectory in adapted conditions, i.e. with no compression or separation shock inside the nozzle. In fact, during the transient phases, start-up and shutdown of the rocket engines, or when it operates under no adaptation conditions at low altitude, very complex physical phenomena appear, such as the extended boundary layer separation and its interaction with the shock wave in the interior of the divergent of the nozzle. The unsteady and three-dimensional natures of this phenomenon can generate strong side loads which may be further amplified by the aeroelastic effects.

The study of the structure in such circumstances can be done by several ways, particularly, by the aeroelastic stability models [1–3]. The aeroelastic stability models are very advantageous compared to the coupled numerical computations which necessitate large computational resources.

The first model of this kind is that of Pekkari, considered as the first simplified model allowing the study of the aeroelastic stability of a nozzle's divergent part, developed in the early 1990s [4, 5]. This model, based on an extreme simplification of the wall pressure profile in the nozzle, enables the prediction of the static instability (divergence) for the overexpanded flow regime conditions of the nozzle. Later, this model has been reconsidered by Lefrançois [6] and extended to make it able to capture the dynamic instabilities (flutter). In the same context, Mouronval has validated the Pekkari model, and its extended version, for the ONERA flexible nozzle named LEA-TOC [3].

N. Bekka (✉) • M. Sellam • A. Chpoun
Laboratoire de Mécanique et d'Energétique d'Evry LMEE, Université d'Evry Val d'Essonne, 40 rue du Pelvoux, 91020 Evry Cedex, France
e-mail: Nadir.Bekka@ufrst.univ-evry.fr

The originality of our study and the main objective reside in the development of new models of aeroelastic stability. Inspired by the initial Pekkari model dedicated to inviscid fluid flows, the new models are able to implement more complex pressure distributions associated to viscous effects. This requires the introduction of a more realistic wall pressure profile for the shock separation using the free interaction theory of Chapman [7]. To reach this objective, a structural computation code coupled with the aerodynamic excitation effects is developed using different versions of aeroelastic stability models depending on the perfect or a viscous nature of the flow and also on the type of static or dynamic stability analysis.

Aeroelastic Analysis

In order to describe the basic principle of aeroelastic stability model, Fig. 1 shows a sketch of a generic supersonic half nozzle, under different structural responses to the inner supersonic flow excitations, namely, (1) no flow, (2) overexpanded flow at equilibrium state and (3) overexpanded flow at perturbed state. The structural response due to the flow perturbation is sketched in Fig. 1 (4). The derivative of the normal component of the structure displacement (w_n) with respect to the curvilinear coordinate (s) is taken into account by the so-called "piston" theory [8].

Following the analysis of Pekkari model in which we consider a flexible structure with quasi-static behaviour with respect to the flow ($\Delta t_{\text{structure}} >> \Delta t_{\text{flow}}$), the finite element approximation for a flexible structure when neglecting all the damping effects leads to the following system of equations:

$$[M]\{\ddot{W}\} + [K]\{W\} = \{F\} \tag{1}$$

where $[M]$ and $[K]$ are respectively the mass and rigidity matrix, $\{W\}$ and $\{\ddot{W}\}$ are the nodal displacements and nodal

G. Ben-Dor et al. (eds.), *30th International Symposium on Shock Waves 1*, DOI 10.1007/978-3-319-46213-4_11

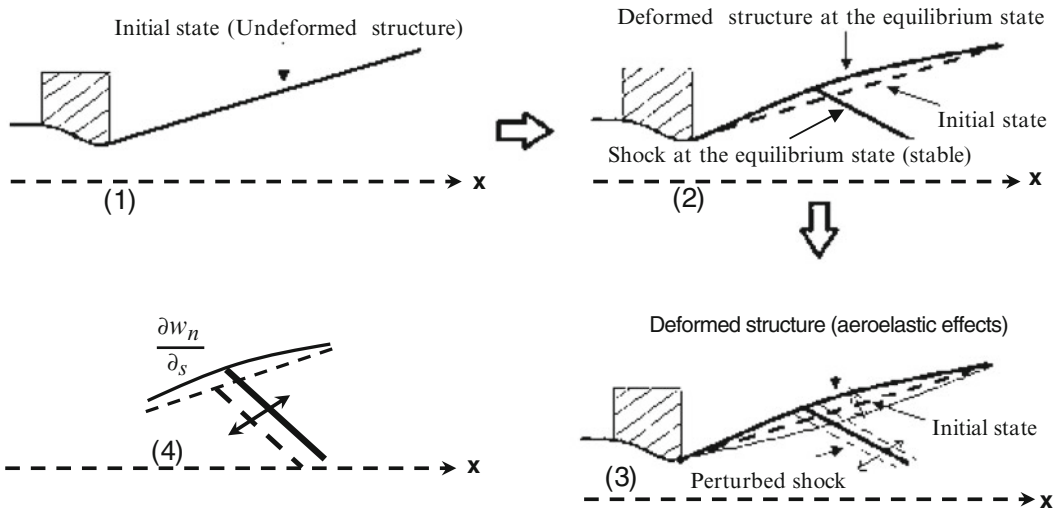

Fig. 1 Different phases of the aeroelastic coupling

acceleration vectors, respectively, and $\{F\}$ is the forcing vector issued from the coupling with aerodynamic loads. Namely, $\{F\}$ represents the instantaneous structure response to the pressure distribution and can be given as a function of the aerodynamic rigidity matrix $[K_{\text{aero}}]$:

$$\{F\} = [K_{\text{aero}}]\{W\}. \tag{2}$$

From physical point of view, the force $\{F\}$ is related to the disturbance of the equilibrium state as shown in Fig. 1, which schematically shows the different phases of the aeroelastic coupling according to the analysis of Pekkari. Consequently, the resultant of the aerodynamic load can be expressed as a wall pressure difference between the equilibrium state $p_{\text{w}}^0(x)$ and the disturbed state $p_{\text{w}}(x, t)$:

$$\vec{f}_{\text{a}}(\vec{w}(t)) = \left(p_{\text{w}}^0(x) - p_{\text{w}}(x,t)\right)\vec{n} \tag{3}$$

where $\vec{n}$ is the unit vector normal to the wall oriented towards the nozzle symmetric axis and $\vec{w}(t)$ represents the displacement from the equilibrium position x_{sep}^0 which have $\vec{w}_0$ as displacement.

The solicitation defined by Eq. (3) allows to study the stability around an equilibrium position according to the Pekkari analysis. In general case and when the viscous effects are considered, the expression of the aerodynamic load $\vec{f}_{\text{a}}(\vec{w})$ can be written as

$$\begin{aligned}\vec{f}_{\text{a}}(\vec{w}) = \Big\{ & p_{\text{sep}}\left(\sigma\left[x - x_{\text{sep}}\right] - \sigma\left[x - x_{\text{sep}}^0\right]\right) \\ & - p_{\text{atm}}\left(\sigma\left[x - x_{\text{p}}\right] - \sigma\left[x - x_{\text{p}}^0\right]\right) \\ & + \left(x_{\text{sep}} - x_{\text{sep}}^0\right)\frac{\mathrm{d}p_k^0(x)}{\mathrm{d}x}\left(\sigma[x] - \sigma[x-L]\right)\Big\}\vec{n}.\end{aligned} \tag{4}$$

where L is the free interaction length and σ is the Heaviside function acting as a filter, defined by $\sigma[X] = \begin{cases} 0, & \text{if } X < 0 \\ 1, & \text{if } X \geq 0 \end{cases}$.

It's clear that the corresponding expression of aerodynamic load for the initial Pekkari model can be deduced from the above generalized form of the modified model by considering a zero value of the free interaction length L:

$$\vec{f}_{\text{a}}(\vec{w}) = \left\{\left(p_{\text{sep}} - p_{\text{atm}}\right)\left(\sigma\left[x - x_{\text{sep}}\right] - \sigma\left[x - x_{\text{sep}}^0\right]\right)\right\}\vec{n}. \tag{5}$$

To study the aeroelastic stability in the proposed model, it is necessary to rewrite the aerodynamic load expression (Eq. 4) in an appropriate form adapted to the principle of virtual works (PVW):

$$\begin{aligned}\langle \delta W\rangle\{F\} = & \int_S \delta\vec{w}\cdot\vec{f}_{\text{a}}(\vec{w})ds = \int_S \vec{w}\cdot \\ & \vec{n}\Big\{p_{\text{sep}}\left(\sigma\left[x - x_{\text{sep}}\right] - \sigma\left[x - x_{\text{sep}}^0\right]\right) \\ & -p_{\text{atm}}\left(\sigma\left[x - x_{\text{p}}\right] - \sigma\left[x - x_{\text{p}}^0\right]\right) \\ & +\left(x_{\text{sep}} - x_{\text{sep}}^0\right)\frac{dp_k^0(x)}{dx}\left(\sigma[x] - \sigma[x-L]\right)\Big\}ds\end{aligned} \tag{6}$$

Unlike the initial Pekkari model where the domain of integration is limited to the interval $[x_{\text{sep}}, x_{\text{sep}}^0]$ (Fig. 2a), in the new modified model, the integration domain extends beyond this range in order to simulate the viscous character of flow along the free interaction length L according to the theory of Chapman (Fig. 2b). Furthermore, the Pekkari model is accurate to first order in space, and the integration at a node and not over an element is widely sufficient. For the modified

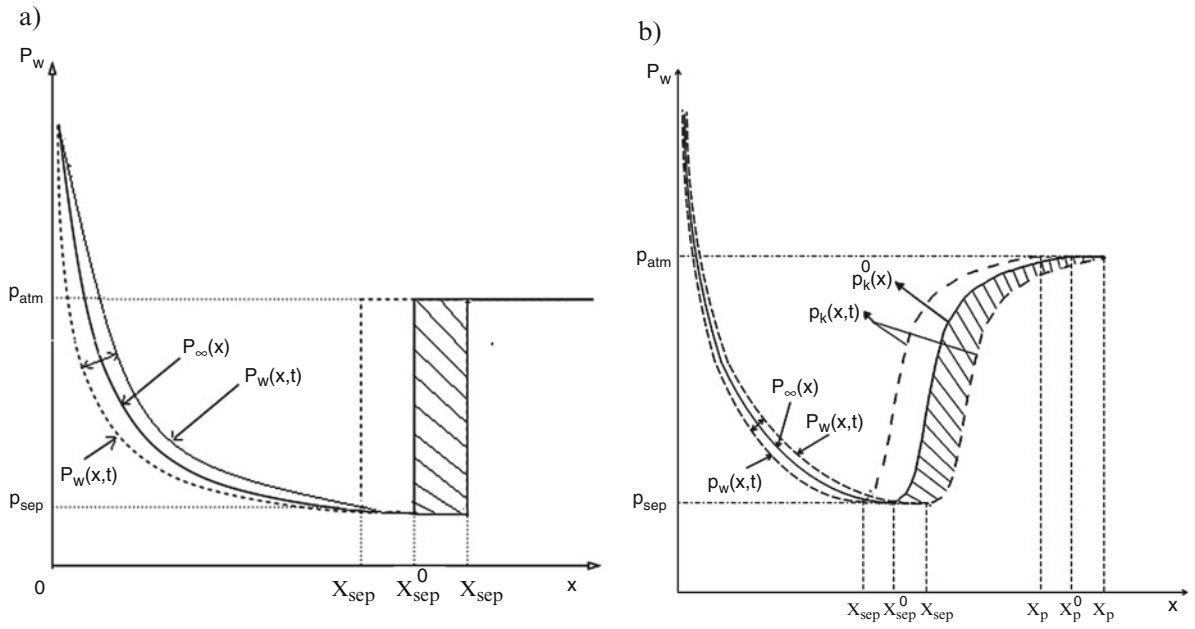

Fig. 2 Schematic presentation of the flow in overexpanded nozzle, (**a**) inviscid flow and (**b**) viscous flow (FSS)

model, it is very appropriate to increase the accuracy by integrating over an element [1]. Consequently, this new approach is more accurate than the initial approach because it takes into account the contribution of all nodes located in the free interaction zone of a length L. For a 2D beam element of a length l and three degrees of freedom per node (u, v, θ), the final expression of the aerodynamic load in the finite element context for the modified Pekkari model can be written as

$$\{F\} = \left[p_{\text{atm}} \begin{Bmatrix} \vdots \\ \eta^x_{j+jp} \\ \eta^y_{j+jp} \\ 0 \\ \vdots \end{Bmatrix} - p_{\text{sep}} \begin{Bmatrix} \vdots \\ \eta^x_j \\ \eta^y_j \\ 0 \\ \vdots \end{Bmatrix} + \frac{1}{2} \sum_{e=j}^{e=j+jp-1} l \frac{dp^0_k(x)}{dx} \begin{Bmatrix} \vdots \\ \vdots \\ \eta^x_e \\ \eta^y_e \\ 0 \\ \eta^x_e \\ \eta^y_e \\ 0 \\ \vdots \\ \vdots \end{Bmatrix} \right] \times \left(\frac{\rho_\infty u^2_\infty}{-\frac{dp_\infty}{dx}\sqrt{M^2_\infty - 1}} \frac{\partial w_n}{\partial s} \right)_j \tag{7}$$

where jp is the number of elementary elements in the free interaction region, and η^x and η^y are the normal unit vector components.

The initial Pekkari model and its modified version developed above are limited to the analysis of static stability only. To generalize the analysis to dynamic instabilities, the extended version of each model is obtained by solving eigenvalue problem defined by Eq. (1) after making the aerodynamic loads as function of aerodynamic rigidity matrix (Eq. 2). Thus, the new homogeneous algebraic system to solve is

$$[M]\{\ddot{W}\} + ([K] - [K_{\text{aero}}])\{W\} = \{0\} \tag{8}$$

This expression shows that the term $\{F\}$ acts directly on the rigidity of the structure $[K_{\text{aero}}]$ whose expression differs from one model to another according to the nature of the flow and the approach used to compute the aerodynamic load $\{F\}$.

Results

In this paper, 2D nozzle geometry has been chosen with fixed nodes at the throat and at the exit of the nozzle's divergent section. For this test case, the computational domain is schematized in Fig. 3 and the material properties are summarized in Table 1.

The main results are presented in a comparative manner using existing models (Pekkari and its extended version) and the modified Pekkari model with its extended version (Fig. 4). Using the modified Pekkari model, we can note that the range of static instability is relatively larger compared to that detected by the basic formulation of the initial Pekkari model. In addition, the coalescence between modes is not limited only to the first two modes, and the dynamic

instabilities area is relatively large compared to that detected by the extended version of the initial Pekkari model. The relatively large areas of the instability whether static or dynamic predicted by the extended version of the modified Pekkari model can be explained by the integration along the interaction length, unlike the Pekkari model where the computation of the aerodynamic load is assumed in a single node.

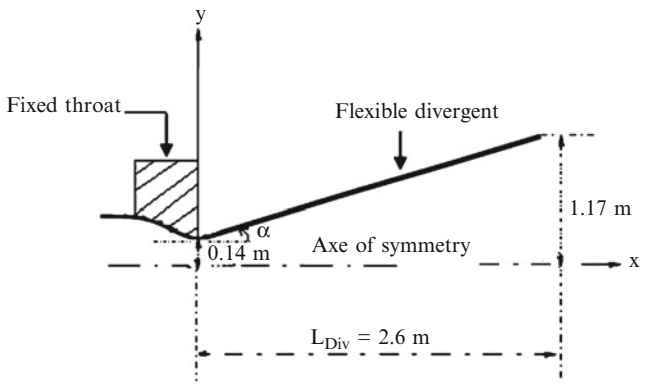

Fig. 3 Nozzle geometry for the studied test case

Table 1 Material properties (2D)

Young modulus (N/m^2)	Thickness h (mm)	Poisson coefficient	Mass density
2.2×10^{11}	10	0.0	2000 kg/m^3

Conclusions

In this paper, the aeroelastic stability analysis for the overexpanded nozzles has been performed using various aeroelastic stability models. The new mathematical formulation of the modified Pekkari model shows that the extension of the original model of Pekkari to simulate the viscous flow effect is made possible by the introduction of a more realistic pressure profile by using the theory of free interaction of Chapman. For the turbulent viscous flows, the prediction of some new instabilities can be observed, and the instability margins, static or dynamic, predicted by the modified Pekkari model (MPM) are relatively large compared to those predicted by the initial Pekkari model for inviscid flow.

References

1. Bekka, N.: *Problématique des ondes de choc dans les tuyères supersoniques et leur interaction avec la structure*. Ph.D. thesis, Université d'Evry Val d'Essonne (2014)
2. Lefrançois, E.: Etude numérique du décollement de jet et du phénomène de charges latérales au sein des moteurs fusée avec prise en compte de l'aéroélasticité, Rapport de post-doctorat. CORIA/CNES (2000)
3. Mouronval, A.-S.: *Etude numérique des phénomènes aéroélastiques en aérodynamique supersonique. Application aux tuyères propulsives*. Ph.D. thesis, INSA de Rouen (2004)
4. Pekkari, L.O.: Aeroelastic analysis of side-loads in supersonic nozzles with separated flow. AIAA Paper 94-3377 (1994)
5. Pekkari, L.O.: Aeroelastic stability of supersonic nozzles with separated flow. AIAA Paper 93-2588 (1993)

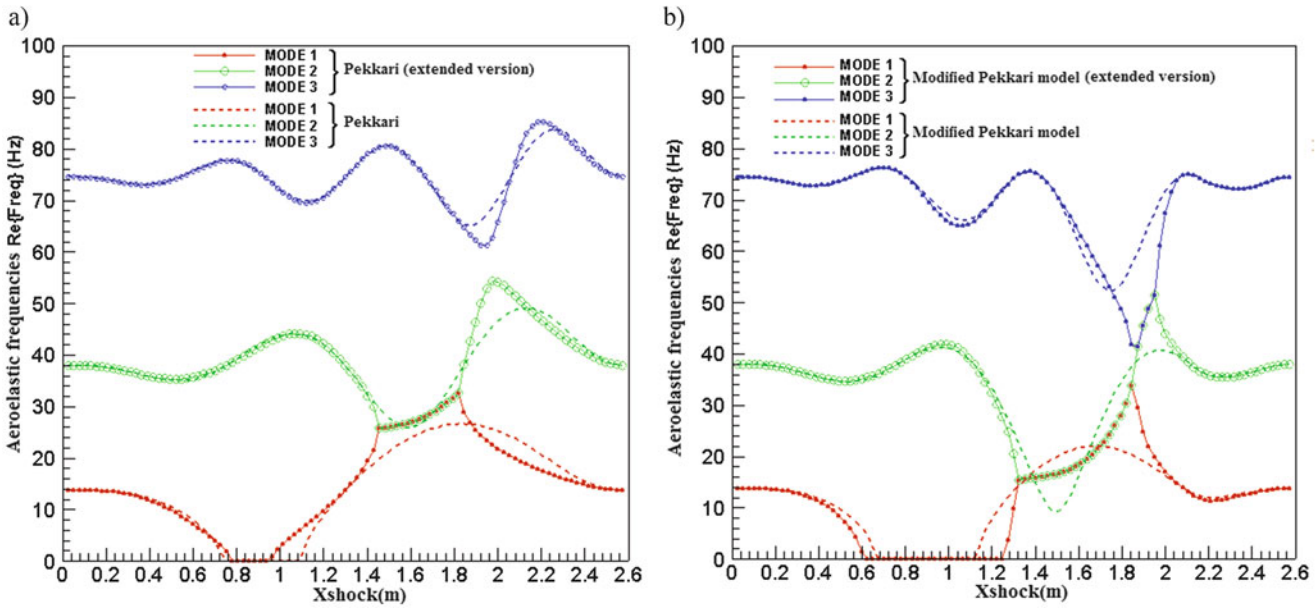

Fig. 4 Evolution of the first three aeroelastic frequencies versus shock separation position obtained by the various stability models: (**a**) Pekkari and its extended version for inviscid flow. (**b**) Modified Pekkari model and its extended version for viscous turbulent flow

6. Lefrançois, E.: Numerical validation of a stability model for a flexible over-expanded rocket nozzle. Int. J. Numer. Methods Fluids **49** (4), 349–369 (2005)
7. Chapman, D.R., Huehn, D.M., Larson, H.K.: Investigation of separated flows in supersonic and subsonic streams with emphasis on the effect of transition. Technical Report NACA TR 1356, NACA (1958)
8. Ashley, H., Zartarian, G.: Piston theory, a new aerodynamic tool for the aeroelastician. J. Aeronaut. Sci. **23**(12), 1109–1118 (1956)

Transverse Jet Injection into a Supersonic Nozzle Flow

V. Emelyanov, K. Volkov, and M. Yakovchuck

Introduction

Thrust vectoring technique can deflect the mean flow of an engine jet from the centerline in order to transfer some force to the aimed axis. The secondary injection thrust vector control is particularly attractive for thrust vectoring in large boosters (especially solid propellant rocket) where large side thrust is generated. Injection of a secondary fluid into the divergent section of the nozzle causes an asymmetrical distortion of the exhaust gas flow. In addition to providing a propulsive force to a flying vehicle or a rocket, a rocket propulsion system can also provide certain control mechanisms to change vehicle's attitude and trajectory via thrust vector control systems. On contrary to mechanically operating thrust vector control systems, such as gimbaled nozzles and jet vanes, which require actuators to deflect mechanical parts, secondary injection does not require any moving parts and regulated by the fluid injection, which reduces axial thrust force losses while changing the direction of the vector.

The supersonic gas jet induces a bow shock in the supersonic stream followed by a deflection of the flow and high pressure on the downstream side of the shock. This influence over a segment of the nozzle alters the pressure distribution on the nozzle surface in an unsymmetrical way about the nozzle axis. It produces the necessary moments to the vehicle. The magnitude of the side force increases as the injection port is moved toward the throat as also when the injecting mass flow rate increases.

Jet injection into a supersonic nozzle flow is a challenging fluid dynamics problem in the field of aerospace engineering which has applications to rocket thrust vector control system, noise control in cavities, and fuel injection in scramjet combustion chambers [1, 2]. The flow field involves shock and viscous interactions that improve mixing while increasing losses. The injected fuel plume forms a barrel shock which acts as a barrier to the incoming supersonic flow. This blockage causes a large encompassing bow shock behind the barrel shock. The bow shock works on separating the boundary layer and forms recirculation zones in front of the jet. The side vortices are spilled and carried axially downstream to enhance mixing. Many experimental [3, 4] and numerical [2, 5, 6] works have been conducted to explore this flow. Air injection through the hole in flat plate is well covered in literature, including assessment of various turbulence models [7].

A numerical analysis of the internal flow in a nozzle with secondary jet injection is performed to improve the current understanding and modeling capabilities of the complex flow characteristics encountered in combustion chambers of SRMs in the presence of transverse jet injection. Mass flow rate of the injected air varies in accordance with periodical dependence in time. Thrust forces corresponding to steady and unsteady problems are compared.

CFD Model

The numerical computations are performed in the domain shown in the Fig. 1. The computational domain is a trapezoid surrounded by adiabatic walls at the top and the bottom, supersonic inlet at the left boundary, inlet at the injection slot, and an outlet at the right boundary. The piston moves up and down and controls mass flow rate through the injection nozzle. A simple periodical dependence of the piston speed on axial coordinate is used in calculations. The length of the domain is $16d_j$ ($5d_j$ before and $10d_j$ behind injection hole), where d_j is the diameter of injection hole. The heights of

V. Emelyanov • M. Yakovchuck
Baltic State Technical University, 190005 St Petersburg, Russia

K. Volkov (✉)
Centre for Fire and Explosion Studies, Kingston University, SW153DW London, UK
e-mail: k.volkov@kingston.ac.uk

G. Ben-Dor et al. (eds.), *30th International Symposium on Shock Waves 1*, DOI 10.1007/978-3-319-46213-4_12

domain at the inlet and outlet sections are $8d_j$ and $10d_j$, respectively. The extension of the computational domain in spanwise direction is $8d_j$.

The block-structured mesh, shown in the Fig. 2a (dimensions are given in millimeters), contains three blocks with nonuniform distribution of mesh nodes within each block. The mesh cells are concentrated around the walls and in the region near the injection slot in order to resolve the boundary layer. The total number of mesh nodes is one million. Nondimensional near-wall coordinate varies from 0.008 to 2.66. Figure 2b, c presents meshes corresponding to the injection nozzle when the piston is located at the top and bottom dead centers, respectively.

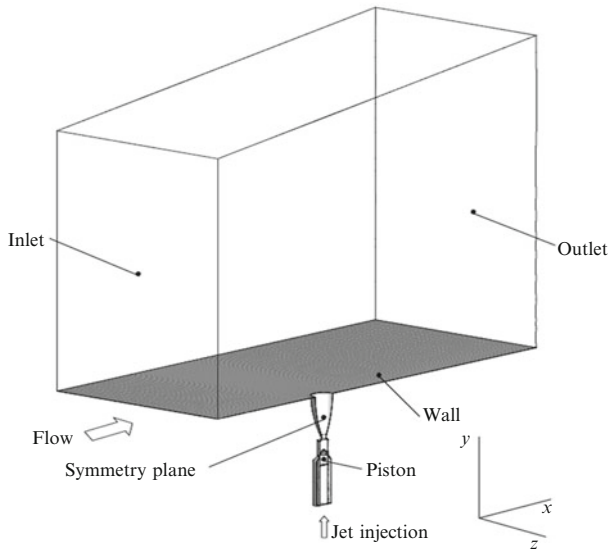

Fig. 1 Computational domain

The Mach number ($M_\infty = 2$), static pressure ($p_\infty = 1.067 \times 10^5$ Pa), static temperature ($T_\infty = 300$ K), and turbulence properties (degree of turbulence and turbulence length scale are fixed at 1 % and 0.1 mm) are specified on the inlet boundary. Total pressure ($p_{0j} = 5.1 \times 10^6$ Pa), total temperature ($T_{0j} = 300$ K), and turbulence properties (degree of turbulence and turbulence length scale are 0.1 % and 0.532 mm) are fixed on the inlet section of the injection nozzle. No-slip and no-penetration boundary conditions for tangential and normal velocities are applied to the nozzle walls. All walls are treated as adiabatic. Slip boundary conditions are used on top boundary and in spanwise direction.

The piston speed changes according to sinusoidal dependence: $u_x = -50 \sin(2000\ t)$ if $t<0.00314$ s and $u_x = 0$ if $t>0.00314$ s. The period of piston motion is 0.00314 s. At time $t = 0$ the piston is located at the top dead center and prevents air injection (mass flow rate of the injected air through the nozzle is zero). When the piston is located at the bottom dead center, the nozzle is fully open, and mass flow rate of the injected air reaches its maximal value.

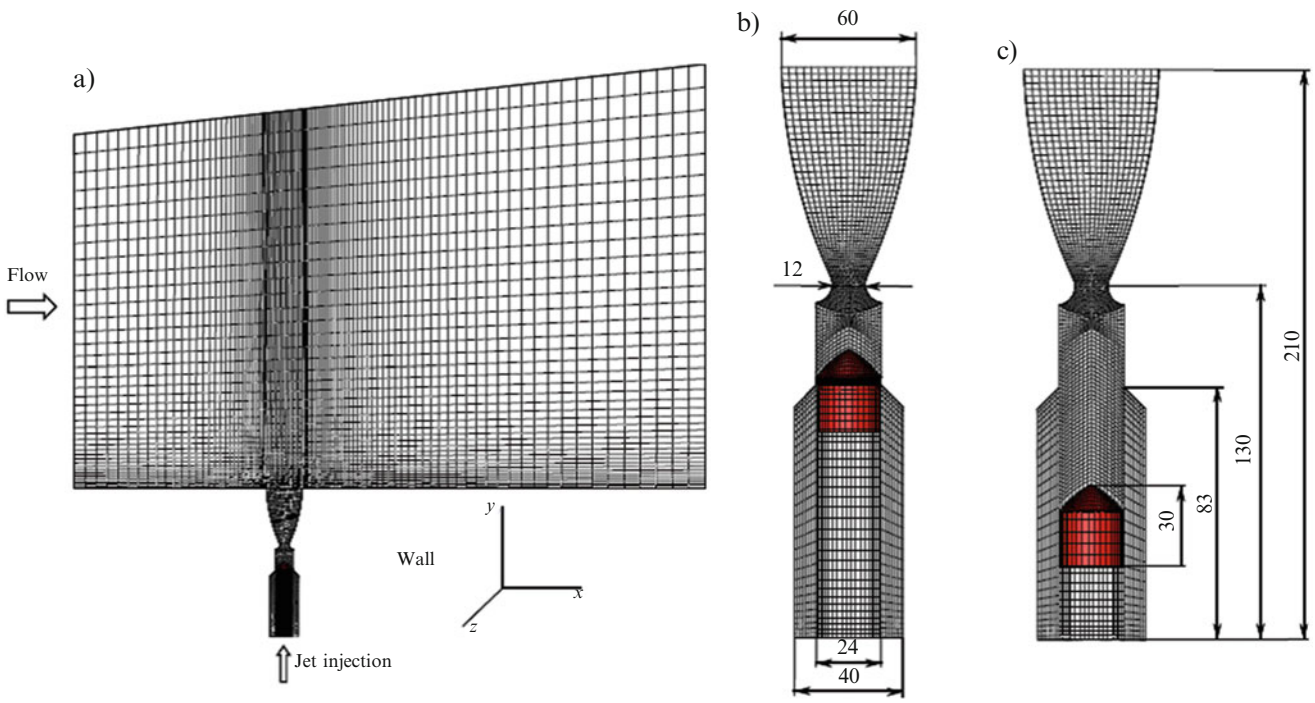

Fig. 2 Mesh in symmetry plane

Computational Procedure

The flow is simulated Reynolds-averaged Navier–Stokes (RANS) equations and shear stress transport (SST) turbulence model. The governing equations are solved with finite volume code on hybrid moving meshes. The unstructured hybrid code developed uses an edge-based data structure to give the flexibility to run on meshes composed of a variety of cell types. The fluxes through the surface of a cell are calculated on the basis of flow variables at nodes at either end of an edge and an area associated with that edge (edge weight). The edge weights are precomputed and take account of the geometry of the cell. The computational procedure involves reconstruction of the solution in each control volume and extrapolation of the unknowns to find the flow variables on the faces of control volume, solution of Riemann problem for each face of the control volume, and evolution of the time step. The nonlinear CFD solver works in an explicit time-marching fashion, based on a three-step Runge–Kutta stepping procedure. Convergence to a steady state is accelerated by the use of geometric multigrid techniques, and by the application of Jacobi preconditioning for high-speed flows, with a separate low Mach number preconditioning method for use with low-speed flows. The sequence of unstructured meshes is created using an edge-collapsing algorithm. Preconditioning improves the rate at which information propagates through the flow domain during the iterations. Parallel computations are implemented using the MPI (CPU cluster) and CUDA technology (GPU).

Results

The study focuses on the averaged and instantaneous flow features including vortex structures downstream of the jet injection, along with the jet penetration, jet mixing, pressure distributions, and turbulent kinetic energy in the downstream flow. It demonstrates that Kelvin–Helmholtz type instabilities in the upper jet shear layer are primarily responsible for mixing of the two fluids. Dynamics of control valve and its influence on flow structure are taken into account. Dependence of forces acting on nozzle walls on parameters of the problem and shock wave structure forming as a result of interaction of injected jet with supersonic nozzle flow are studied.

A typical transverse slot jet interaction flow field is shown in Fig. 3, and a jet-induced bow shock wave 3 is generated due to the injected under-expanded jet 7 which acts as an obstacle in the supersonic flow. Shock wave 2 is induced by the separation of the boundary layer. The boundary layer separation is caused by the subsequent adverse pressure gradient. In the region immediately upstream of the injection slot, a

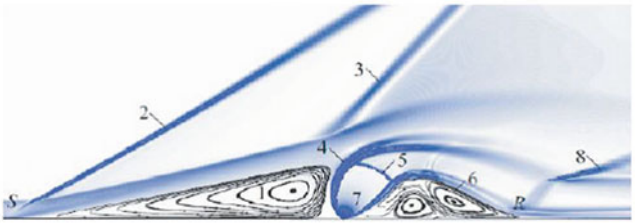

Fig. 3 Transverse injection of under-expended jet in a supersonic flow

recirculation region 1 consisting of counter-rotating primary and secondary upstream vortices is present. Upon exiting the injection slot, expansion of the jet is followed by a rapid decrease in the local pressure. This results in a normal shock wave, and thus a sonic surface and a Mach disk form surrounding the jet plume. The supersonic region is bounded by the barrel shocks 4 and the Mach disk 5. Downstream of the jet, the flow is turned parallel to the wall, producing a recompression shock wave 8 and a corresponding separated, recirculation region 6 in the wake of the injection slot consisting of counter-rotating vortices and trailing counter-rotating vortices.

The results computed with SST turbulence models are in a good agreement with the experimental data [4] in a wide range of pressure ratios. The wall pressure profiles downstream of the injection slot show much better agreement with the experimental data than the upstream pressure profiles. The length of the upstream separation region and the height of the Mach surface both increase with the increase of the jet-to-cross flow momentum flux ratio.

The shape of the pressure contours in this simulation is radically different from the subsonic simulation and covers a much larger area. The contours took a more mushroom like shape with the two-lobe pattern morphing into the stem of the mushroom and the upstream contours resembling the top of the mushroom. The presence of shock and expansion waves alters the shape of the pressure contours, the separation topology, and, ultimately, the surface pressure distributions.

Wall pressure distributions are presented in Fig. 4, showing formation and time evolution of regions of high and low pressure before and behind injection hole. The length of the upstream separation region varies in time, and the peak pressures upstream and downstream of the injection slot are similar and slightly vary in time. The maximum mass flow rate of the injected air corresponds to the time moment located between lines 3 and 4.

The zone adjacent to the wall contains two vortices formed as a result of primary and secondary separations of the flow from the wall upstream of the jet. The vortices rotate in the opposite directions because part of the airflow immediately near the wall passes through shock wave portions,

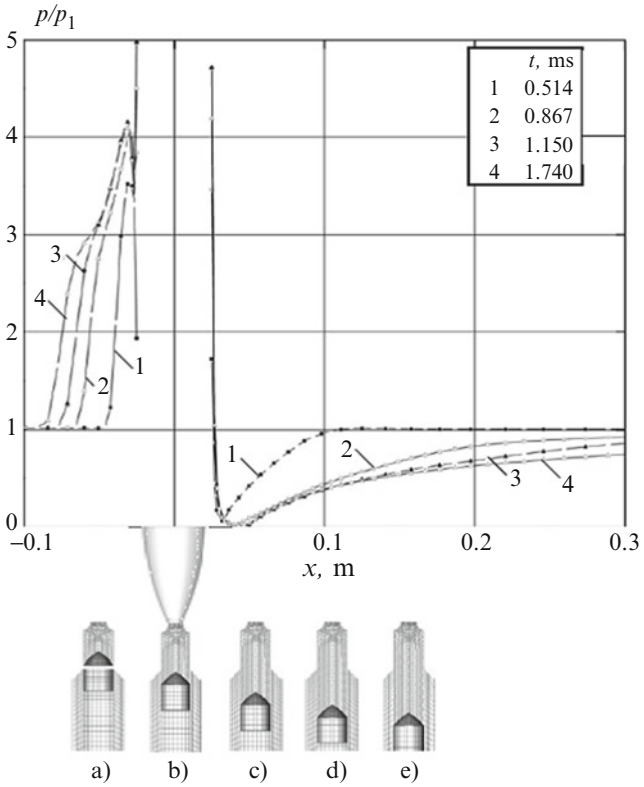

Fig. 4 Wall pressure distributions: 10^{-6} s (**a**), 5.8×10^{-4} s (**b**), 9.2×10^{-4} s (**c**), 1.15×10^{-3} s (**d**), 1.75×10^{-3} s (**e**)

turns downward to the wall, penetrates into the separated flow region, and spreads in the opposite directions. The vortex located closer to the jet moves anticlockwise, and the vortex located at a greater distance moves clockwise.

With secondary injection, complex interaction between the primary and secondary jet streams is accompanied by a high pressure region on the primary nozzle wall near the secondary jet nozzle exit, which is the source of an interaction force that augments the thrust of the control jet. There are other significant factors that strongly affect thrust such as the angle of the secondary injector port and as such the added mass flow. The position of the used injector has a dramatic and significant impact on the generation and alteration of thrust production particularly in the presence of a generated normal shock. If injection occurs too far upstream, flow velocity recovers with expansion, and hence the optimal reduction in flow velocity at the exit plane is not achieved.

The force of interaction is an integral of the product of excess pressure in the separation region and an area element. Time dependence of the thrust force is presented in Fig. 5. The results computed are normalized by the thrust force corresponding to the steady-state problem. The thrust force in unsteady flow is smaller than those in steady-state flow.

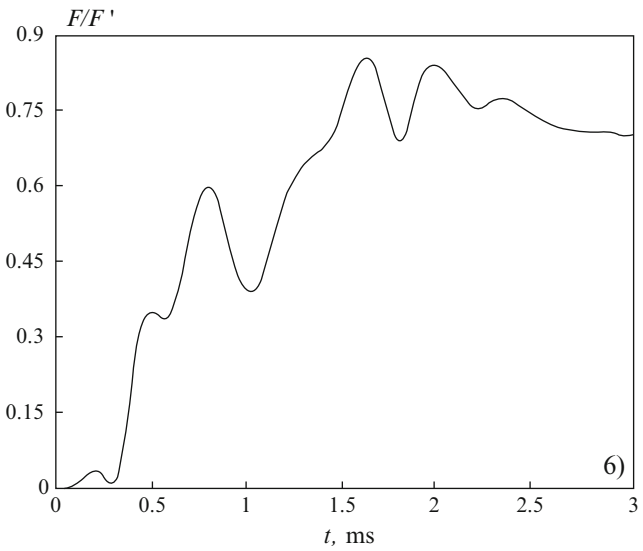

Fig. 5 Time dependence of thrust force

Conclusions

The jet in supersonic cross flow is studied numerically because of its relevance to a wide variety of flows in aerospace applications including fuel injection in scramjet engines and thrust vector control for high-speed rocket vehicles. The problem, involving shocks, turbulent mixing, and large-scale vortical structures, requires special treatment for turbulence to obtain accurate numerical solutions. Different turbulence modeling techniques are reviewed and compared in terms of their performance in predicting results consistent with the experimental data. The sensitivities of the turbulence model predictions to free-stream turbulence and near-wall mesh spacing are discussed. The results related to unsteady transverse injection of turbulent jet are provided and compared with those computed in steady-state formulation of the problem.

References

1. Karagozian, A.R.: Transverse jets and their control. Prog. Energy Combust. Sci. **36**, 531–553 (2010)
2. Hassan, E., Boles, J., Hikaru, A., Davis, D., Shyy, W.: Supersonic jet and cross flow interaction: computational modelling. Prog. Aerosp. Sci. **57**, 1–24 (2013)
3. Schetz, J.A., Billig, F.S.: Penetration of gaseous jets injected into a supersonic stream. J. Spacecr. Rocket. **3**(11), 1658–1665 (1966)
4. Spaid, F.W., Zucoski, E.E.: A study of the interaction of gaseous jets from transverse slots with supersonic external flows. AIAA J. **6**(2), 205–211 (1968)
5. Dickmann, D.A., Lu, F.K.: Shock/boundary layer interaction effects on transverse jets in cross flow over a flat plate. AIAA Paper, 2008–3723 (2008)

6. Huang, W., Liu, W.D., Li, S.B., Xia, Z.X., Liu, J., Wang, Z.G.: Influences of the turbulence model and the slot width on the transverse slot injection flow field in supersonic flows. Acta Astronaut. **73**, 1–9 (2012)

7. Roy, C.J., Blottner, F.G.: Review and assessment of turbulence models for hypersonic flows. Prog. Aerosp. Sci. **42**(7–8), 469–530 (2006)

Flow Visualization in Out-of-Round Rocket Nozzles

C. Génin, S. Jack, and R. Stark

Introduction

Flow fluctuations in or around rocket nozzles can lead to a deformation of their structure. In case of separated nozzle flow, an inward bended nozzle wall shifts the flow separation position downstream, increasing the bending force lever arm. This flow-structure interaction is a self-reinforcing effect, which can potentially lead to heavy structural damages. These disturbances can be produced either by combustion instabilities or ambient pressure fluctuations. Under certain conditions, they may excite the bell nozzle eigenfrequency. As a result, the structure responds and the nozzle ovalizes. For this reason, the investigation of flow-structure interaction in ovalized nozzles under separated flow condition is difficult to realize [1–4].

In order to understand and study these phenomena, a collaborative work between the institutes of Space Propulsion and Aerodynamics and Flow Technology of the German Aerospace Center (DLR) has been started in the framework of in-house project ProTAU. A step-by-step, both numerical and experimental, investigation is carried out on nozzle ovalization. The experimental work is also part of the special research field SFB Transregio 40 collaborative work. The study started with the validation of the numerical method to simulate separated flow in axisymmetric conventional nozzles. Based on three initial non-deformed nozzles, seven different out-of-round geometries have been defined. All of these permanently deformed nozzles were numerically simulated and three geometries were selected out of them for experimental investigation, after the simulation had shown the measurability of the flow behavior within the facility capability. Once the numerical method will be fully validated, it will be implemented to investigate flow-structure interaction in out-of-round nozzles.

C. Génin (✉) • R. Stark
Institute of Space Propulsion, German Aerospace Center (DLR), Lampoldshausen, Germany
e-mail: chloe.genin@dlr.de

S. Jack
Institute of Aerodynamics and Flow Technology, German Aerospace Center (DLR), Braunschweig, Germany

Truncated Ideal Nozzle Exhaust Flow

The present study focuses on the deformation of truncated ideal contour (TIC) nozzles. The homogenous flow without internal shock of a TIC nozzle facilitates the research of contour deformation effects on the flow. For the purpose of this study, three initial non-deformed contours have been chosen. They present design Mach number of 4.8, 5.3, and 5.8 and are designated resp. as TIC-2048, TIC-2053, and TIC-2058. The contours share the same subsonic geometry and a throat radius of 10 mm. Each one of them was truncated to a length allowing full-flowing condition at a nozzle pressure ratio (NPR, total over ambient pressure) of 50, corresponding to the maximal value reached at test bench P6.2. The models were also tested with the same methodology in order to verify the measurement methods and to yield validation data for the accompanying CFD study. Figure 1 illustrates an example of the schlieren pictures taken out of the initial non-deformed TIC-2048. The measurements are not part of the present work, but can be found in previous publications by the authors [5].

Ovalization Principle

The initial contours were deformed into seven out-of-round nozzle contours using various methods. The deformations were chosen to provide a parameter study, with variation of the deformation function and amplitude, the deformation start position, and the initial contour.

G. Ben-Dor et al. (eds.), *30th International Symposium on Shock Waves 1*, DOI 10.1007/978-3-319-46213-4_13

The cross section of the deformed contours features an ellipse. The different deformations are summarized in Table 1. Geometries 1–3 figure the deformations of contour TIC-2048 with variations of the deformation amplitude, resp. 5–15 %. The amplitude is given as a comparison between the initial nozzle end radius and the obtained major axis after deformation. Geometries 2, 4, and 7 feature the same deformation applied to the three initial contours, TIC-2048, TIC-2053, and TIC-2058. Geometries 4–6 are variations of contour TIC-2053, whereas 4 and 5 are deformed with a different starting point and 4 and 6 following different functions.

A preliminary CFD study has been conducted in the framework of the DLR project ProTAU to verify the feasibility of this experimental investigation and to optimize the measurement methodology. Out of this study, three geometries have been chosen for further investigation and have been manufactured for test. The models realized out of geometries 2, 3, and 4 and tested in this study are represented in Fig. 1, left.

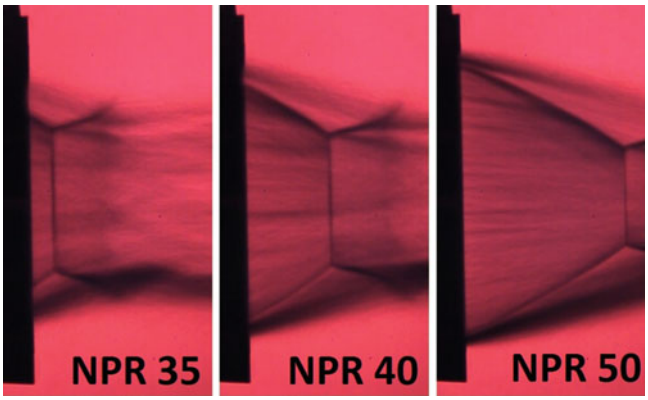

Fig. 1 Shock system out of non-deformed TIC-2048 nozzle for various NPR values

Table 1 Deformation example of a table

	Initial contour	Amplitude	Start point	Function
Geometry 1	TIC-2048	5 %	$\varepsilon = 5$	Polynomial
Geometry 2	TIC-2048	10 %	$\varepsilon = 5$	Polynomial
Geometry 3	TIC-2048	15 %	$\varepsilon = 5$	Polynomial
Geometry 4	TIC-2053	10 %	$\varepsilon = 5$	Polynomial
Geometry 5	TIC-2053	10 %	$\varepsilon = 1$	Polynomial
Geometry 6	TIC-2053	10 %	$\varepsilon = 5$	Linear
Geometry 7	TIC-2058	10 %	$\varepsilon = 5$	Polynomial

Experimental Setup

The test campaign was conducted at P6.2 cold flow facility at DLR Lampoldshausen. The dry nitrogen feeding line provides mass flow up to 4 kg/s with a total pressure up to 5 MPa. The nozzles were mounted on the horizontal rig (see Fig. 2, right) and tests were conducted under ambient conditions. The feeding pressure was progressively varied up and down with a constant gradient of +/−0.2 MPa/s, leading to the displacement of the separation point along the nozzle contour until full-flowing condition. Wall pressure ports placed in line within small axial intervals of 4 mm permit to follow the position of the separation point. The ports were also regularly distributed in circumferential direction. Five rows were positioned between major and minor axis with an angle of 22.5°, each one featuring 19 positions, for a total of 95 wall pressure ports for each nozzle.

The evolution of the shock system outside of the nozzle models was recorded with schlieren optics in Z-configuration. As the shock system was expected not to be axisymmetric, the models were rotated around their own axis. The exhaust flow of each model was recorded in four

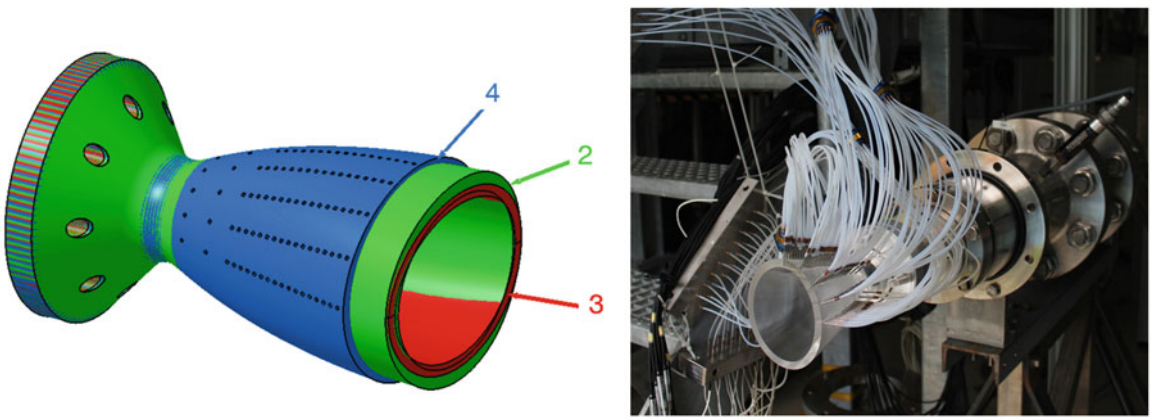

Fig. 2 Sketch of the three nozzle geometries (*left*) and out-of-round nozzle model 4 mounted on the horizontal test position at P6.2 facility, in minor axis view (*right*)

positions, corresponding to four circumferential angles: in the direction of the major axis (0°), a rotation of +45° and −45°, and in the direction of the minor axis (−90°).

Results

Figure 3 gives an example of the shock system out of nozzle model 4 observed with an angle of +45° for the four NPR values 35, 40, 45, and 50. With increasing value of the NPR, the separation point moves downstream the nozzle contour, and the shock system is shifted out of the nozzle. The Mach disk appears in the 45° view in "8" shape, particularly for low NPR values. The classical Mach disk known from axisymmetric nozzle exhaust flow is in a deformed nozzle bended into a saddle shape.

The schlieren pictures were recorded for each nozzle in the four observation angles, while the exact same feeding pressure up and down ramping was conducted. In this manner, for each NPR value, the shock system is available in various angles. The pictures in Fig. 4 represent the exhaust flow out of geometry 3 (15 % deformation) in four views. The shock system was recorded for NPR 40, corresponding to a flow separation position from the wall situated near the nozzle end. The pictures are labeled as follows: picture (a) represents the shock system viewed in the major axis view, (d) in the minor axis view, and pictures (b) and (c) are in the +/−45° directions views. Geometry 3 has been chosen to illustrate the effect of contour ovalization on flow behavior as it presents a deformation amplitude of 15 %, which is the highest deformation value for the tested nozzle models. The general behavior to deformation is comparable, but the shock system variations are more visible with higher ovalization amplitude.

Positions along the shock system were collected for each picture. In Fig. 5, the shock system out of geometry 3 has been reconstituted out of these measurements for three NPR values, 35, 40, and 50. The position of the separation line was interpolated as the intersection of separation shock and wall contour. The deformation of the Mach disk into a Mach saddle is visible in this three-dimensional representation, particularly for NPR 35 (blue shock system) and NPR 50 (red shock system).

Figure 6 is a picture taken during down ramping of a test on geometry 4 model (NPR~42). The cold nitrogen has condensate due to the low temperature and become visible upstream the shock system. It can be seen that the Mach saddle is bended inward. In addition the separation line is visible on the nozzle wall. The models were made out of PMMA (acrylic glass) and are transparent. During down ramping, the separation line moves upstream, leaving the nozzle wall very cold. The back flow is sucked into the nozzle and the air humidity froze directly downstream the separation line, as visible in Fig. 6. The nozzle is observed in

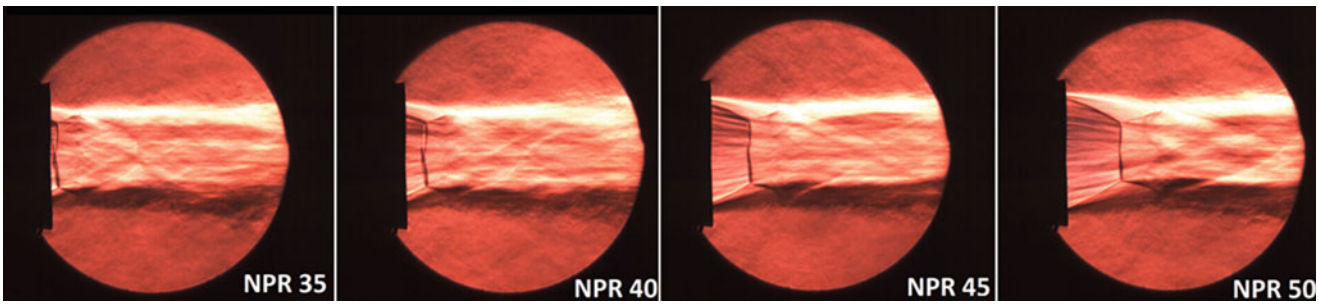

Fig. 3 Shock system out of geometry 4 for various NPR values

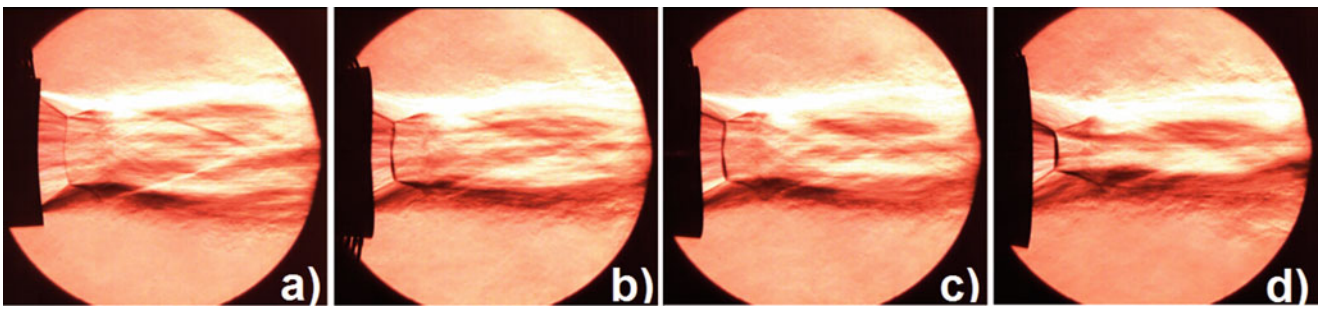

Fig. 4 Schlieren pictures of the exhaust flow out of geometry 3 for NPR 40, (**a**) in major axis view, (**b**) and (**c**) in +/−45° view, and (**d**) in minor axis view

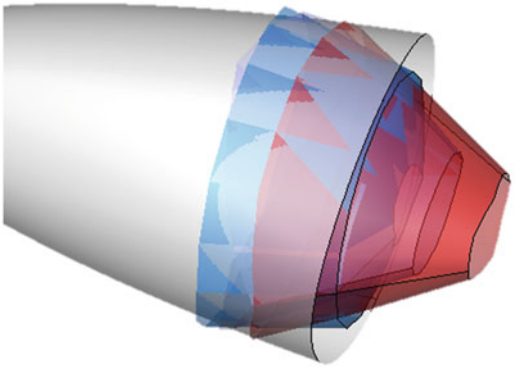

Fig. 5 Reconstitution of the shock system out of geometry for NPR 35, 40, and 50

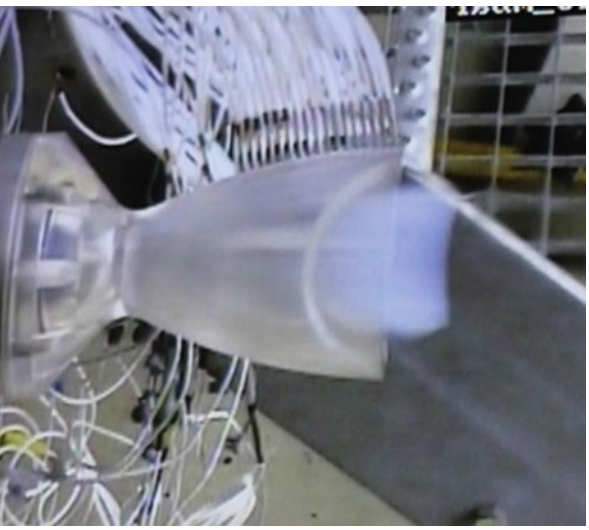

Fig. 6 Picture of geometry 4 model during test at P6.2 bench

the major axis line of sight. The separation point is still at nozzle end on the minor axis (vertical direction), whereas it lies far upstream on the major axis (horizontal direction).

Figure 7 illustrates the evolution of the triple points (filled symbols) and of the intersection point between oblique separation shock and nozzle exit cross section (plain symbols) in geometry 4. At low NPR both symbols are close to one another. The Mach "saddle" is in the vicinity of the nozzle exit cross section. The symbols describe an ellipse, with its major axis in the opposite direction to the ovalized nozzle exit. With increasing NPR values, the separation point moves downstream the wall toward the nozzle end. The intersection of separation shock and nozzle exit is consequently closer to the nozzle wall, as can be seen for NPR 45 and 50 in Fig. 7. The shape of the intersection line evolves from a small ellipse into a large circle. The shape of the Mach saddle follows a similar trend: the elliptic Mach disk at

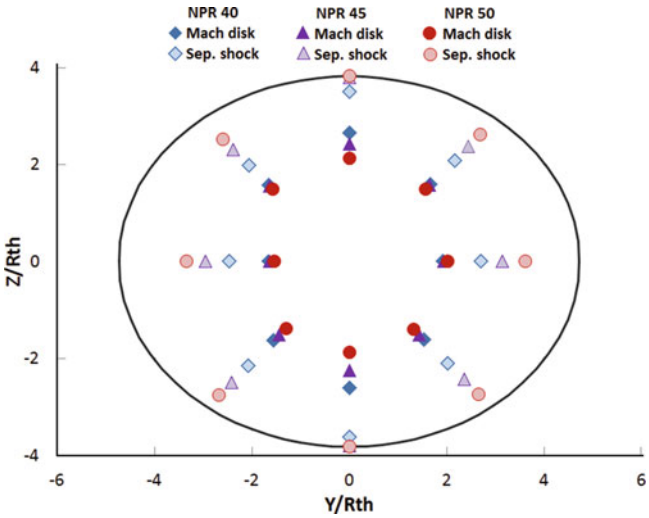

Fig. 7 Position of the triple point and the intersection of separation shock and nozzle exit cross section for various NPR values in geometry 4

NPR 40 changes into a circular shape at NPR 50. As the shock system moves further downstream, the dimensions of the Mach saddle decreases. As the NPR increases, the shock system out of an ovalized nozzle contour behaves more and more like the shock system out of a conventional axisymmetric nozzle contour.

Conclusions

Three stiff ovalized nozzle models have been tested under cold flow conditions. The shock system out of the models was recorded with schlieren optics. The pictures show the evolution of the classical Mach disk into a Mach "saddle." The deformation decreases with increasing nozzle pressure ratio. The observation of the shock system from different angles has permitted to get a sense of its three-dimensional structure. The experimental results obtained in this study will be used as validation data for the numerical investigation of nozzle ovalization. The next step would be to investigate the flow reaction to an applied deformation of the contour.

Acknowledgments This work was co-funded by the special research field SFB-TRR40 of the Deutsche Forschungsgemeinschaft (DFG).

References

1. Tuovila, J., Land, S.: Experimental study of aeroelastic instability of overexpanded rocket nozzle extensions. NASA-TN-D-4471, Langley Research Center (1968)

2. Brown, M., Ruf, J., Reed, D., D'Agostino, M., Keanini, R.: Characterization of side load phenomena using measurement of fluid/structure interaction. In: AIAA 2002–3999, 38th AIAA Joint Propulsion Conference, Indianapolis, IN (2002)
3. Moreaux, N., Girard, S.: Experimental assessment of aeroelastic coupling in a rocket engine nozzle. ONERA TP 2003-80, IFASD, Amsterdam, Netherlands, (2003)
4. Xia, Y., Schwane, R.: Investigation of the aerodynamic influence of a non-axisymmetric flow on side load generation in over-expanded rocket nozzles, DGLR-JT2004-274 (2004)
5. Génin, C., Stark, R., Jack, S.: Flow separation in out-of-round nozzles, a numerical and experimental study. In: Progress in Flight Physics, vol. 7. Springer, Berlin (2015)

Effect of the Adiabatic Index on the Shock Reflection in Overexpanded Nozzle Flow

Emanuele Martelli, Barbara Betti, Francesco Nasuti, and Marcello Onofri

Introduction

The start-up and shutdown phases of liquid rocket engine nozzles are characterized by the overexpansion of the flow, with internal boundary layer separation and shock formation. The overexpansion shocks are characterized by oscillations, which can produce dynamic side loads, reducing the safe life of the engine and possibly leading to the failure of the nozzle structure.

This is the main reason why the shock and flow structures of highly overexpanded nozzles have been studied for several decades [1–5]. Very recently, the works of Gvozdeva et al. [6, 7] have shown a peculiar configuration of shock reflection in a stationary supersonic gas flow and the effect of the adiabatic index γ on the shear layer developing from the slipstream at the triple point. Figure 1 (left) shows a schematic of a Mach reflection: the oblique shock IA with angle ω_1, the reflected shock AR with angle ω_2, the Mach disk AM, and the expansion fan EF. The slipstream develops from the triple point T and divides two regions characterized by the same pressure and different velocities and entropies. The peculiar three-shock configuration is characterized by a negative angle ω_2 of the reflected shock, a Mach number greater than 3, and an adiabatic index γ smaller than 1.4. Gvozdeva et al. [6] computed for the first time this particular configuration by means of a Reynolds-Averaged Navier–Stokes equations solver. As far as slipstreams are concerned, it is well known that they are unstable and that they release a chain of vortices due to the Kelvin–Helmotz instability. In reference [7] it is analytically shown that the mixing parameters of the slipstreams increase when the Mach number increases and the adiabatic index γ decreases. This changes the instability characteristics of the shear layer and consequently could influence the shock stability. In the overexpanded hot supersonic jet exhausting from a rocket nozzle, the Mach number is generally higher than 3 and the adiabatic index less than 1.4. Therefore there could be a negative influence on the instability of the separated flow structure and a consequent effect on the performance and structural integrity compared to the air behavior. In fact, it should be kept in mind that most experimental work is done using air or nitrogen ($\gamma = 1.4$). Therefore the effect of the adiabatic index on the separation shock instability deserves to be investigated.

The principal aim of this work is to evaluate how the decrease in the value of γ affects the mixing parameters, like the mass flux ratio, the convective Mach number, and the vorticity production. The steady-state numerical solutions are carried out by means of an in-house finite volume Reynolds-averaged Navier–Stokes (RANS) equations solver, second-order accurate in space. The convective and diffusive terms are integrated using a third-order accurate Runge–Kutta scheme. This solver has been validated against experimental data [8–11]. The present simulations have been carried out using the hypothesis of laminar flows.

Results

In order to study the shock reflection in an overexpanded 2D planar nozzle exhaust jet, a very simple computational domain is adopted, following the work of Nasuti and Onofri [12]. This domain consists of a rectangular geometry (see Fig. 1, right), which represents the nozzle exit section: on the left side a supersonic flow is imposed (the flow Mach number M_{inflow} is assigned together with the flow direction, the

E. Martelli (✉)
Dipartimento di Ingegneria Industriale e dell'Informazione, II University of Naples, Via Roma 29, Aversa 81131, Italy
e-mail: emanuele.martelli@unina2.it

B. Betti • F. Nasuti • M. Onofri
Dipartimento di Ingegneria Meccanica e Aerospaziale, University of Rome "La Sapienza", Via Eudossiana 18, Rome 00184, Italy

G. Ben-Dor et al. (eds.), *30th International Symposium on Shock Waves 1*, DOI 10.1007/978-3-319-46213-4_14

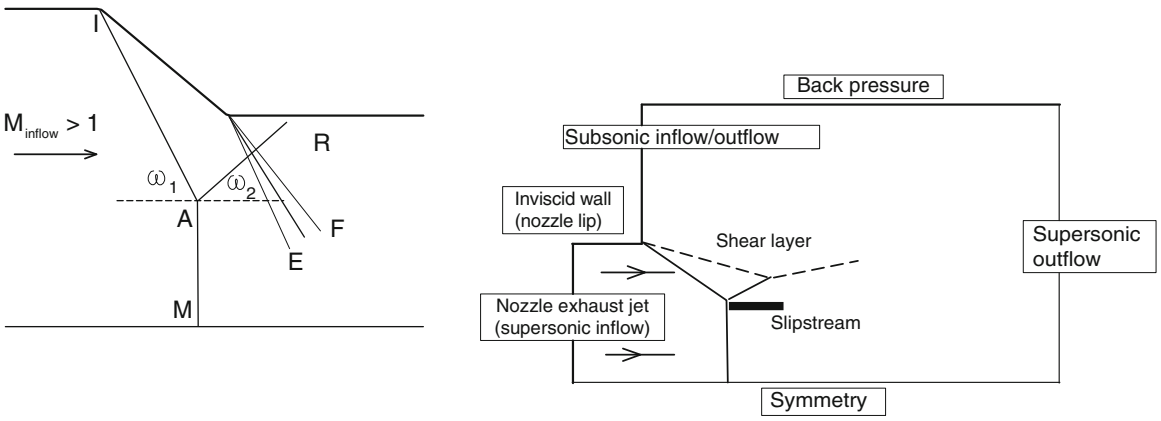

Fig. 1 (*Left*) Schematic of a Mach reflection. (*Right*) Computational domain and boundary conditions for the nozzle exhaust jet in quiescent ambient

Table 1 Flow parameters for the nozzle exhausting jet

γ	1.2	1.3	1.4
M_{inflow}	5.4	5.4	5.4
p_0/p_a	240	90	52
ω_1	43	43	43

total pressure p_0, and temperature T_0), on the upper side an inviscid wall is imposed, and the bottom is a symmetry line. On the right side, this block faces the computational domain which represents the quiescent ambient. In this second block, a subsonic inflow/outflow is prescribed, according to the sign of the vertical velocity, for the left side. In the case of outflow, a static ambient pressure p_a is imposed, while in the case of inflow, total ambient pressure (equal to p_a) and temperature are assigned. On the upper side, a back pressure equal to p_a is imposed. The right side is characterized by a supersonic outflow. Finally the bottom line is a symmetry line. In such a way, it is possible to control the nozzle pressure ratio NPR, defined as the ratio between the total nozzle pressure p_0 and the ambient pressure p_a . The inlet flow parameters are reported in Table 1. For all the selected values of the adiabatic index, the inflow Mach numbers (M_{inflow}) and the incident shock angles (ω_1) are the same, in order to compare the effects on the slipstream parameters. The values of the pressure ratios instead have to change in order to have the same incident shock angle. Figures 2, 3, and 4 show the numerical shadowgraphs of the flow field together with the shock polar of the selected configuration. According to the analytical results of the shock polar, the shock reflections are characterized by a Mach reflection. The interaction between the slipstream (which opens in a shear layer immediately downstream the triple point) and the main shear layer (that downstream the incident shock) is also well visible for all the configurations. This interaction appears to happen closer to the triple point and to be stronger for the lower γ simulated. This is mainly due to the angle of the reflected shock, which is negative with respect to the initial flow direction, and therefore this shock does not redirect the shear layer upward.

Figure 5 (left) shows the maximum value of the vorticity (which can be found immediately after the triple point) versus the adiabatic index. It can be seen that decreasing the γ from 1.4 to 1.2 increases the maximum vorticity by almost 30 %. Figure 5 (right) shows the mass flux ratio behavior, while Fig. 6 (left) shows the convective Mach number versus γ. Both of these parameters control the spreading of the shear layer, and they both increase with the decrease of γ. The shear layer spreading rate increases with the first parameter and decreases [13] with the second [14]. According to Gvozdeva et al. [7], the effect of the mass flux ratio prevails and the spreading rate increases for decreasing γ. Finally Fig. 6 (right) shows the angle ω_{RT} between the slipstream and the reflected shock (according to the definition given in reference [7]). It can be seen that there is a great reduction of this angle with decreasing values of the adiabatic index: from nearly 33° for γ =**1.4** to nearly 8° for Y = **1.2**. In this last case, ω_{RT} is of the same order of the shear layer spreading rate downstream the triple point. Therefore there is a closer interaction between the vorticity generated by the triple point and the reflected shock.

Conclusions

The effect of the adiabatic index on the basic parameters governing the shear layer development after the triple point have been evaluated by means of a numerical solver of the Navier–Stokes equations, considering a **2D** configuration and only laminar flows. The results have shown that the decrease of the adiabatic index can lead to a strong decrease

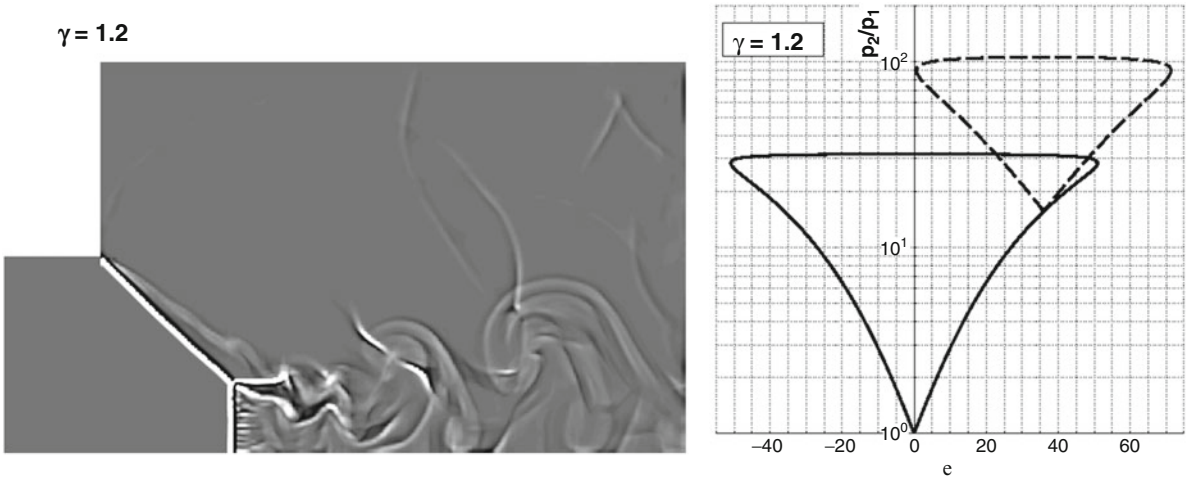

Fig. 2 (*Left*) Numerical shadowgraph of the nozzle exhaust jet, $Y = 1.2$, $M_{\text{inflow}} = 5.4$, $\omega_1 = 43°$. (*Right*) Shock polar

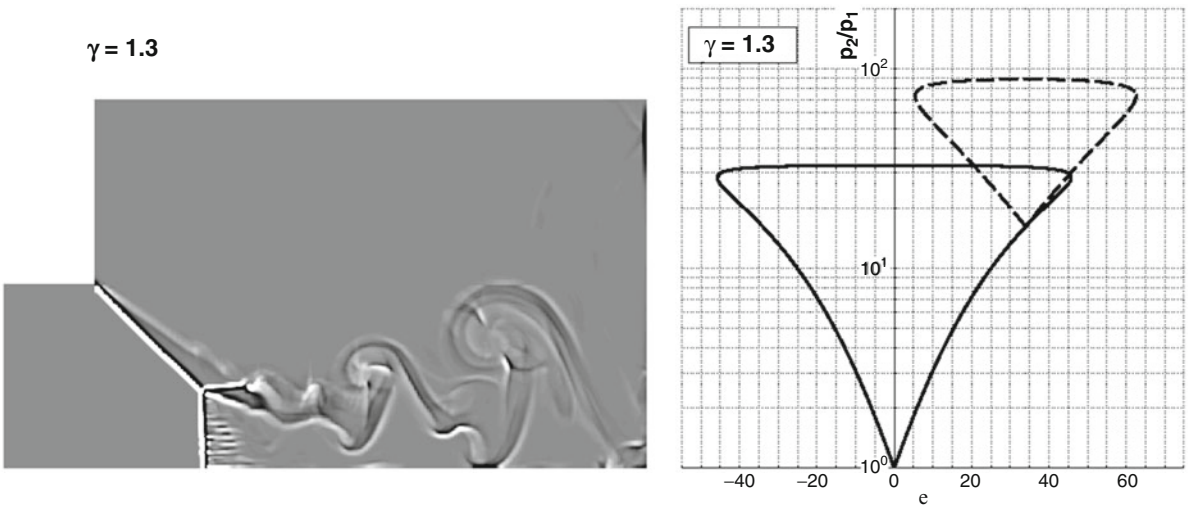

Fig. 3 (*Left*) Numerical shadowgraph of the nozzle exhaust jet, $Y = 1.3$, $M_{\text{inflow}} = 5.4$, $\omega_1 = 43°$. (*Right*) Shock polar

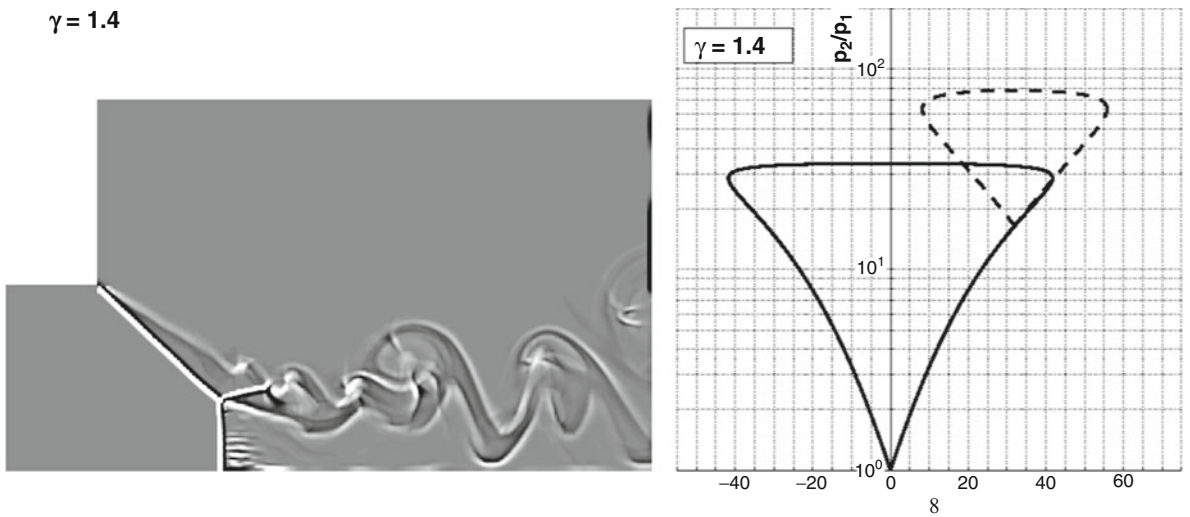

Fig. 4 (*Left*) Numerical shadowgraph of the nozzle exhaust jet, $Y = 1.4$, $M_{\text{inflow}} = 5.4$, $\omega_1 = 43°$. (*Right*) Shock polar

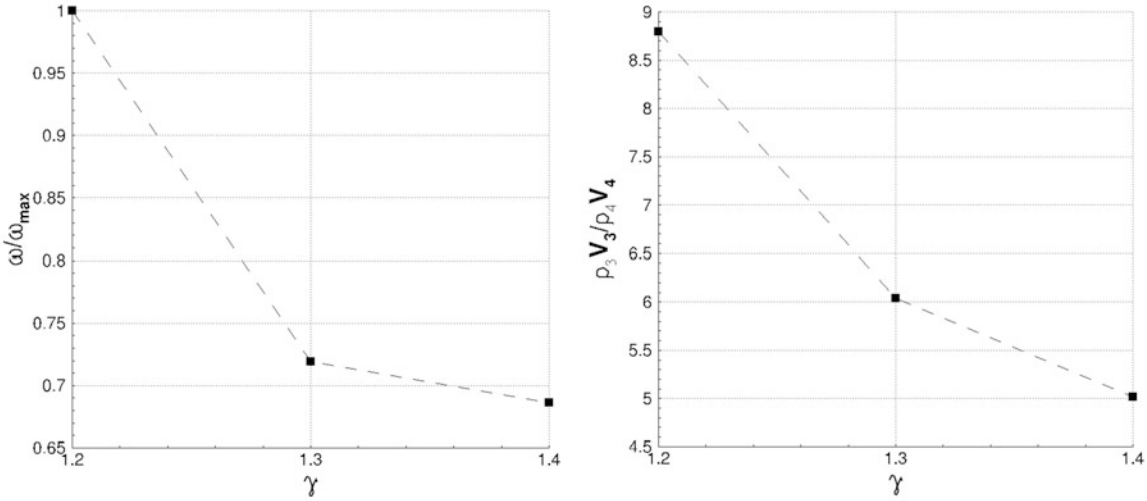

Fig. 5 Effect of the adiabatic index 1 on the z component of the vorticity (*left*) and on the rate of mass fluxes (*right*) at the slipstream

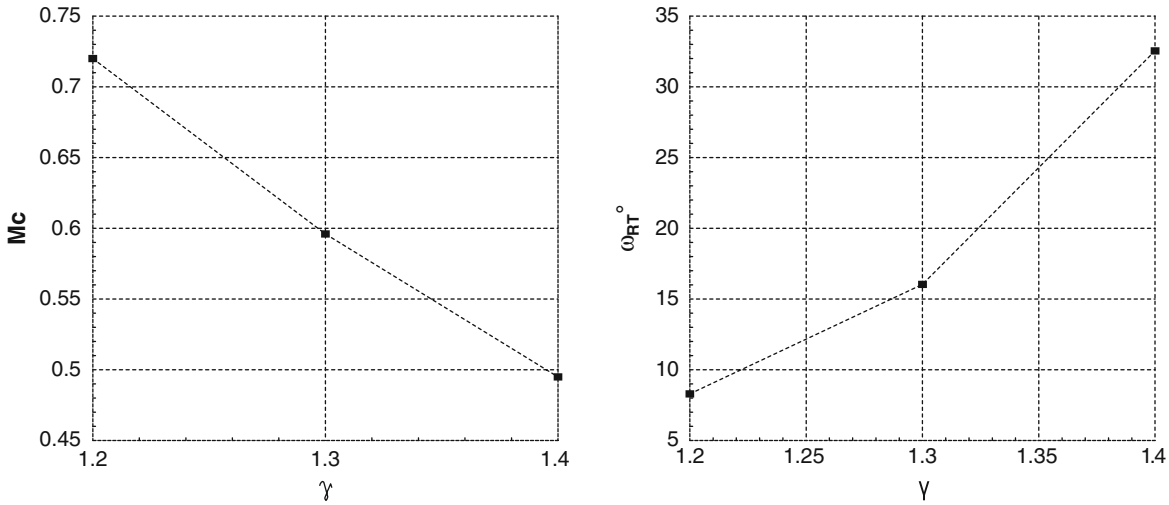

Fig. 6 Effect of the adiabatic index γ on the convective Mach number (*left*) at the slipstream and on the angle ω_{RT} (*right*) between the reflected wave AR and the slipstream

in the value of the angle between the reflected shock wave and the slipstream. As a consequence, there is an important interaction between the vortices released by the slipstream, the reflected shock, and the main shear layer developing from the incident shock. This can enhance the instability of the whole shock configuration and can have an impact on the side loads generation. This is an important issue to be considered when studying the lateral forces generation, since there can be a significant difference between the cold flow behavior (typical of subscale laboratory experiments), characterized by a high Y value and the hot flow behavior, characterized by a low Y value. As a future work, more values of the inflow Mach number and of the nozzle pressure ratio will be considered, together with the effect of turbulence.

References

1. Nave, L., Coffey, G.: Sea level side loads in high-area-ratio rocket engines. In: 9th AIAA/SAE Propulsion Conference. AIAA Paper 73-1284, November 1973
2. Chen, C., Chakravarthy, S., Hung, C.: Numerical investigation of separated nozzle flows. AIAA J. **32**(9), 1836–1843 (1994)
3. Nasuti, F., Onofri, M.: Viscous and inviscid vortex generation during start-up of rocket nozzles. AIAA J. **36**(5), 809–815 (1998)
4. Frey, M., Hagemann, G.: Status of flow separation prediction in rocket nozzles. In: 34th AIAA/ASME/SAE/ASEE Joint Propulsion Conference. AIAA Paper 98-3619, July 1998
5. Kwan, W., Stark, R.: Flow Separation phenomena in subscale rocket nozzles, 38th AIAA/ASME/SAE/ASEE Joint Propulsion Conference & Exhibit, Joint Propulsion Conferences, http://dx.doi.org/10.2514/6.2002-4229 2002

6. Gvozdeva, L., Gavrenkov, S.: A new configuration of irregular reflection of shock waves. In: 5th European Conference for Aeronautics and Space Sciences, Munich, July 2013
7. Gvozdeva, L., Gavrenkov, S., Nesterov, A.: A study of slipstreams in triple shock wave configurations. Shock Waves **25**(3), 283–291 (2015)
8. Betti, B., Martelli, E., Nasuti, F., Onofri, M.: Numerical study of heat transfer in film cooled thrust chambers. In: 48th AIAA/ASME/SAE/ASEE Joint Propulsion Conference & Exhibit, Atlanta, No. 2012-3907, July 2012
9. Pizzarelli, M., Nasuti, F., Paciorri, R., Onofri, M.: Numerical analysis of three-dimensional flow of supercritical fluid in cooling channels. AIAA J. **47**(11), 2534–2543 (2009)
10. Betti, B., Nasuti, F., Martelli, E.: Numerical evaluation of heat transfer enhancement in rocket thrust chambers by wall ribs. Numer. Heat Transf. A Appl. **66**, 488–508 (2014)
11. Betti, B., Pizzarelli, M., Nasuti, F.: Coupled heat transfer analysis in regeneratively cooled thrust chambers. J. Propuls. Power **30**, 360–367 (2014)
12. Nasuti, F., Onofri, M.: Shock structure in separated nozzle flows. Shock Waves **19**(3), 229–237 (2009)
13. Martelli, E., Nasuti, F., Onofri, M.: Numerical analysis of film cooling in advanced rocket nozzles. AIAA J. **47**(11), 2558–2604 (2009)
14. Paciorri, R.: A compressibility correction for turbulence model of Spalart and Allmaras. Private communication, Department of Mechanics and Aeronautics, University of Rome "La Sapienza", Rome, Italy, 2000

Mixing Enhancement in Free Jets from Supersonic ESTS Lobed Nozzles

Albin Varghese, S.K. Karthick, Srisha M.V. Rao, and Gopalan Jagadeesh

Introduction and Motivation

Mixing enhancement of two gaseous streams at high Mach numbers [1] plays an important role in the design of supersonic ejectors and supersonic combustors. In order to obtain mixing enhancements in supersonic jets, many nozzles with exotic shapes have been developed [2].

To achieve enhanced mixing, a nozzle named as the Elliptic Sharp Tipped Shallow (ESTS) lobed nozzle has been developed in the Laboratory for Hypersonic and Shockwave Research (LHSR), Indian Institute of Science (IISc), India [3]. This nozzle has a unique geometry involving elliptical lobes and sharp tips. These lobes are generated using a simple manufacturing process from the throat to the exit. This lobed and sharp-tipped structure introduces streamwise vortices and azimuthal velocity components which must help in enhanced mixing and spreading. The ESTS lobed nozzle has shown mixing enhancement with four lobes. The spreading rate was found to be double of the reference conical nozzle [4]. This paper was motivated by the need to investigate the flow physics involved in the ESTS lobed nozzle.

Visualization experiments have been performed to study the flow field of the nozzles at design and off-design conditions. The mixing region and the primary flow of the jet have been separately visualized. The effect of varying "the number of lobes" and "the design Mach number" of the nozzle on the mixing and spreading characteristics of the jet will be further discussed.

A. Varghese (✉) • S.K. Karthick • S.M.V. Rao • G. Jagadeesh
Department of Aerospace Engineering, Indian Institute of Science, Bangalore, India
e-mail: venalbin@gmail.com

Experimental Setup

A module called variable-frequency drives is used to reduce power consumption and also to control the recurrent load-unload cycle of the air compressor. Air is compressed by a screw compressor. It is rated at 22 HP providing a volume flow rate of 0.0448 m^3/s with a maximum operating pressure of 12.5 bar. After compression the air is passed through an oil filter. The filtered air is dried in a dryer to remove excessive moisture present in it. The compressed filtered and dried air is stored in three receivers with a total 7 m^3 volume. These air receivers have a maximum working pressure of 11 bar. A 2″ pipeline is used to draw the air from the receivers. A simple gate valve is used to feed the air into the pressure regulator. A pressure regulator is used to set an operating pressure of 3–10 bar. A pneumatic rotary actuator is used to start the tunnel using a simple hand-operated switch. A long chamber of 200 mm diameter is used as a stagnation chamber, and at it's end the stagnation pressure of the primary flow is measured. At the end of the stagnation chamber, the nozzles of interest can be mounted by means of the threaded arrangement in the end pipe. This arrangement shown in Fig. 1 was used to operate the free jet facility and conduct visualizations of the free jet flow fields of conical and ESTS lobed nozzles.

Elliptic Sharp Tipped Shallow Lobed Supersonic Nozzle (ESTS Lobed Nozzle)

The ESTS lobed nozzle can be manufactured by the simple process of drilling to obtain the lobed and sharp-tipped structure. The throat was drilled first and then by offsetting and tilting another suitable drill bit, the elliptic lobes were drilled. The conical nozzle was designed with a particular throat diameter for a particular exit Mach number. The ESTS lobed nozzle was designed such that the total exit area remained the same as that of the conical nozzle. Thus according to isentropic area relations, the average exit

G. Ben-Dor et al. (eds.), *30th International Symposium on Shock Waves 1*, DOI 10.1007/978-3-319-46213-4_15

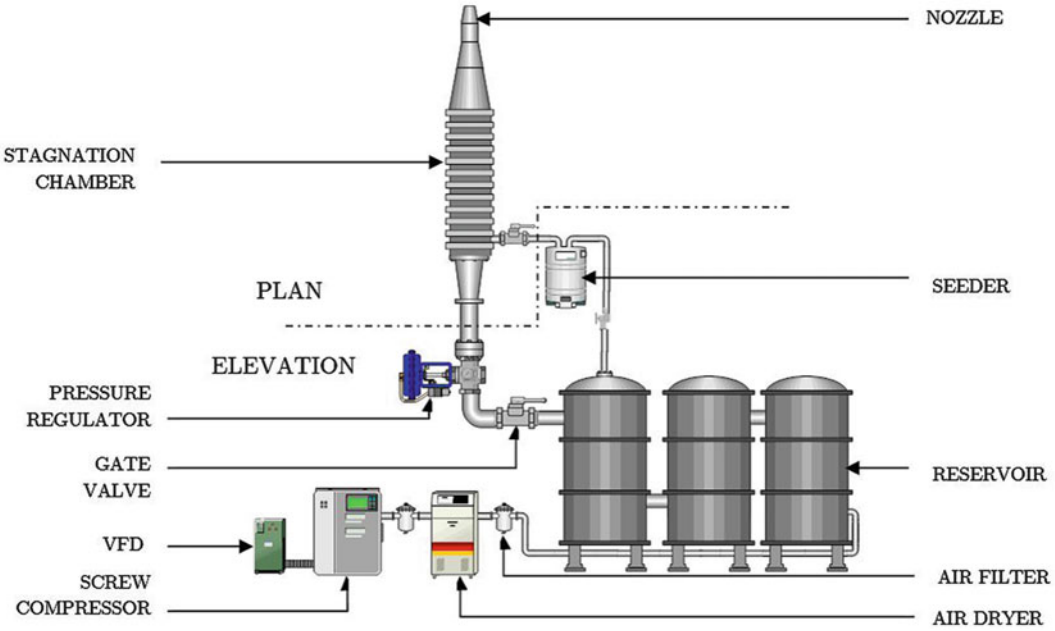

Fig. 1 Schematic of the free jet test facility

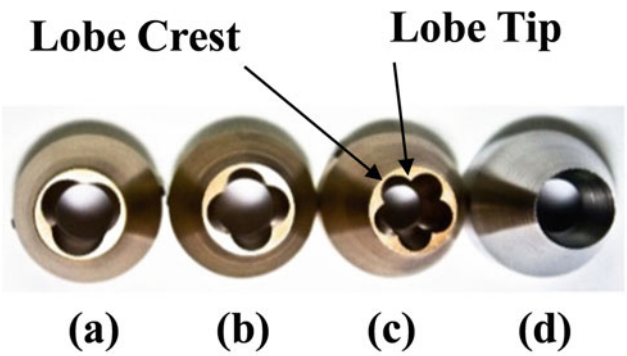

Fig. 2 (**a**) ESTS three-lobed nozzle, (**b**) ESTS four-lobed nozzle, (**c**) ESTS five-lobed nozzle, (**d**) conical nozzle

design Mach number was the same. The manufactured three-lobed, four-lobed, five-lobed, and conical nozzles are shown in Fig. 2. The experiments were conducted on nozzles with different numbers of lobes designed for various Mach numbers at stagnation pressures of 6 bar. Thus the jets of the nozzles for design Mach number 2.3 and 2.5 were overexpanded, while the jets of the nozzles for design Mach number 2 were nearly ideally expanded. The flow fields of these jets were visualized using particle scattering of laser which is explained in the following section.

Planar Laser Mie Scattering (PLMS) Visualization

The flow field from the exit of the nozzle was illuminated using a laser sheet. The scattering of this laser sheet by particles in the flow helps in clear visualization of the flow structures. When the flow is supersonic, shock patterns can be observed using this scattering phenomenon. Also effects like vapor deposition or product formation at the jet and ambient interface can be exploited by particle scattering [5]. Thereby the mixing layer development of the free jet can be studied. The primary flow alone was seeded with particles in these free jet studies, to visualize the jet extents before it mixed with the ambient. The scattering of light by the particles similar to or larger in size than the wavelength of the incident light results in Mie scattering.

For scattering experiments to visualize the primary jet flow, particles were generated using a device called modified Laskin generator. It consists of a chamber in which the material of the particles is stored. Sunflower oil was used to generate particles for this visualization. Sunflower oil was poured into the chamber to submerge the ends of hollow struts hung in the chamber. The ends of these struts have fine holes drilled into their sides. These holes create very small severely under expanded air jets, when appropriately compressed air is passed through them. The air pulverizes the oil to produce particles which were seeded in the flow.

Pressure difference of 2 bar was maintained between the seeder unit and main flow in order to seed the particles into the main flow. The particles thus generated were observed through a Phase Doppler Particle Analyzer (PDPA) to measure their size. The particle sizes were found to be smaller than 1 μm. These particles were used to visualize the internal flow features of the primary flow.

The images of the mixing layers are obtained by scattering of the laser by moisture. The low temperature primary flow coming in contact with the moist ambient air results in the condensation of moisture. This condensed moisture present in the mixing layer scatters incident light.

The particles thus present in the flow field are illuminated by an Nd-YAG laser. The laser was of 532 nm wavelength and had an energy output of 24 mJ. It was pulsed at a frequency of 10 Hz with a pulse width of 7 ns. The circular laser beam passed through a series of optics to produce a laser sheet of approximately 1 mm thickness. This sheet illuminated the flow field which was photographed by a high-speed camera (Phantom Miro 110) of 1 megapixel (1280 × 800). The laser sheet was positioned vertically along the nozzle axis and the camera was placed normal to the sheet, in order to obtain the axial images. Whereas the transverse section images were obtained by placing the laser sheet at the appropriate location on the nozzle axis and transverse to the axis. The camera was placed facing the sheet at about 30° to the nozzle axis.

The experimental procedure followed involved operating the tunnel for a total of about 3 s. The pressure in the stagnation chamber was allowed to stabilize for about a second and then the camera and laser were triggered. The laser sheet lasting 7 ns was scattered by the particles. During this period the camera was operated and it captured the image of the scattered light. The camera lens was attached with a 532 nm band-pass filter to reduce interference from other stray light. This camera provided ten instantaneous images of flow features over the period of operation. The images from the primary flow seeded experiments were averaged to obtain an averaged image of the flow field for each experimental run. The results of these experiments are discussed below.

Results and Discussions

Instantaneous images taken at an axial plane with the conical and ESTS nozzles with three, four, five, and six lobes are shown in Fig. 3a. The three- and four-lobed nozzles are for design Mach number 2.0, while the conical nozzle is for design Mach number 2.3, and five-lobed and six-lobed

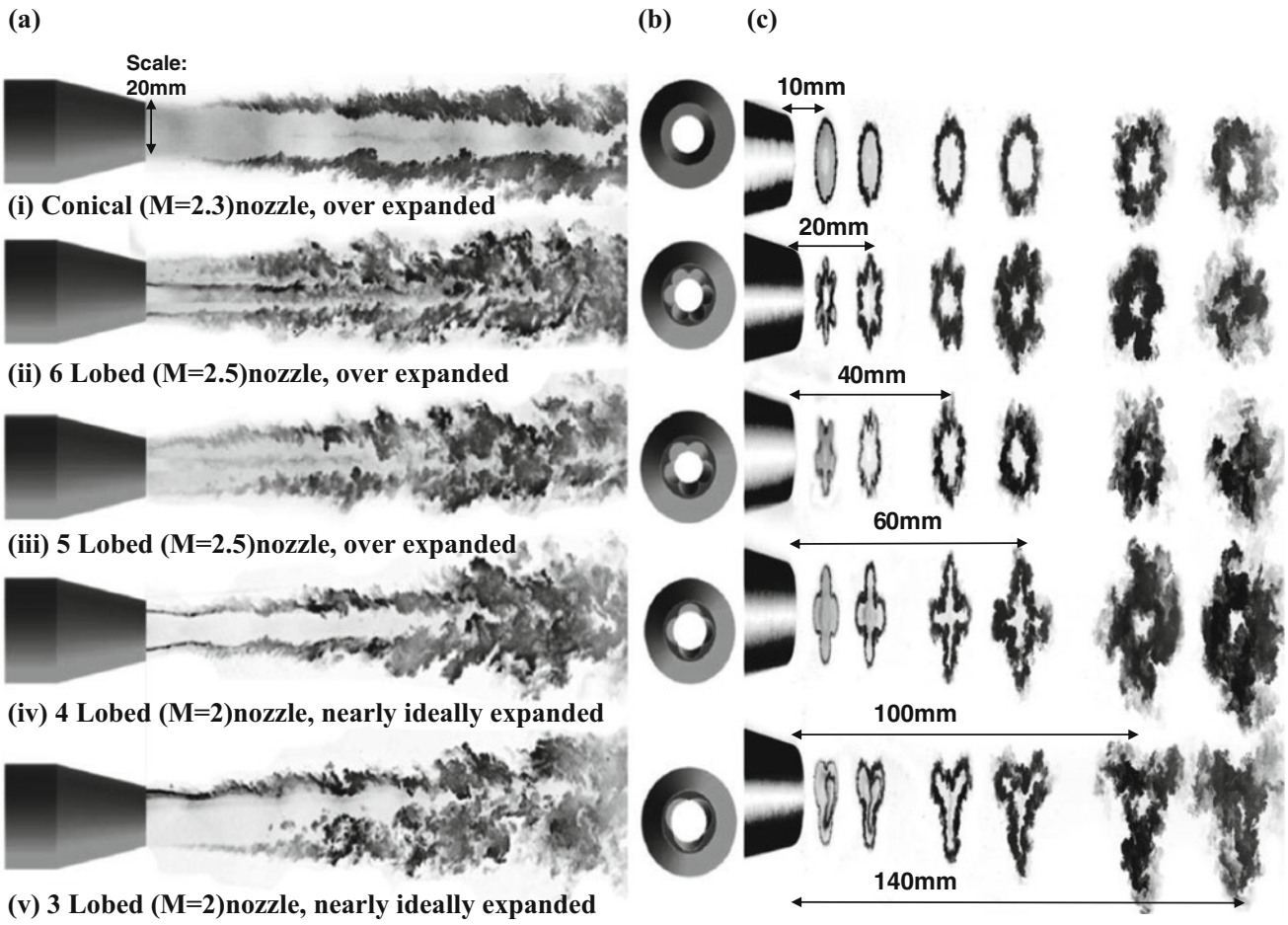

Fig. 3 Instantaneous images at 6 bar stagnation chamber pressure: (**a**) vertical axial slices, (**b**) azimuthal position of nozzle, (**c**) transverse to axis slices at indicated position from nozzle exit

nozzles are for design Mach number 2.5. The stagnation chamber pressure was maintained at 6 bar.

A comparison of the images of the ESTS lobed nozzles with the conical nozzle shows changes in the mixing layers due to the ESTS lobed nozzles. The following qualitative conclusions were derived from the images. The image of the reference conical nozzle shows a distinct potential core and mixing layers all along the length. For the ESTS lobed nozzles, this distinction becomes unclear between five and seven times the nozzle exit diameter, after the nozzle exit. Thus mixing of the primary flow and ambient air is enhanced in the case of all the ESTS lobed nozzles. In the case of odd numbers of lobes, the crest of a lobe is diametrically opposite to the tip of another lobe. Thus in the image of the three-lobed nozzle, the mixing layer from the lobe tip is seen in the upper region and the mixing layer from the lobe crest is seen in the lower region. This image shows that the visual thickness of the mixing layer from the lobe crest has a higher growth rate than the mixing layer from the lobe tip. In the case of even numbers of lobes, a lobe tip is diametrically opposite to another lobe tip. Thus the mixing layers at any longitudinal position appear geometrically similar on both sides, as seen in the image of the four-lobed and six-lobed nozzles. The images of the conical nozzle and five-lobed and six-lobed nozzles also show some additional structures between the two extreme mixing layers that are not seen in the images of the three- and four-lobed nozzles. The free jets from the conical nozzle, five-lobed and six-lobed nozzles are at the stagnation chamber pressure of 6 bar. The flow structures seen in these images could be the result of these jets being overexpanded. The transverse section images of the jets at various locations along the axis are shown in Fig. 3c. These images clearly demonstrate the three-dimensional nature of the flow field of all the ESTS lobed nozzles. The mixing region closely resembles the exit shape of the individual nozzles. The perimeter of the exit plane is minimum for the circular jet and maximum for the six-lobed nozzle. Hence the spreading and mixing of the free jet should show an increasing trend as the number of lobes is increased. However the images show that mixing layer spreads more for the three-lobed nozzle than the six-lobed nozzle. This is evident in the transverse cross-sectional views at 140 mm from nozzle exit. It was also observed that the cores of the jets had diminished earlier for the five-lobed and six-lobed nozzles and at 140 mm are nearly indistinguishable from the mixing region. But the cores of the jets are still present at 140 mm in the three-lobed and four-lobed nozzle jets. This shows that the mixing region spreads faster but the jet core diminishes slower as the number of lobes of the nozzle is decreased. Thus the pinching of the jet effect is stronger as the number of lobes increases whereas the perimeter stretching is prominent for nozzles with fewer lobes.

The averaged images for three lobed, four lobed for design Mach number 2, and four lobed for design Mach number 2.3 are shown in Fig. 4a–e. The averaged images for five- and six-lobed nozzles are shown in Fig. 4f–h. The azimuthal variation of the shock structures in the flow of the ESTS lobed is clearly seen in these images. The shock structures are asymmetric across the axis of the nozzle for the three-lobed and five-lobed nozzles. In the case of four-lobed nozzles, the shock structures are symmetric across the axis of the nozzle. The angle of the oblique shocks is larger for the four-lobed nozzle for design Mach number 2.3 than the angle of the oblique shocks for the four-lobed nozzle for design Mach number 2. Thus the design Mach number determines the strength of shocks in the flow field. At 6 bar the Mach 2 nozzle was nearly ideally expanded and hence weak shock structures should be observed in the flow field. However the shocks present in the flow field of the four lobed for design Mach number 2 are strong. Hence it was concluded that the design Mach number cannot be used to characterize the nozzle. The shock structures for five- and six-lobed nozzles away from the nozzle appear considerably diffused compared to the three-lobed and four-lobed nozzles. This corroborates the observation from the transverse section images that jet core diminishes slower as the number of lobes of the nozzle is decreased.

Conclusions

This study focused on the effect of various parameters on the flow field of the ESTS lobed nozzle. The effect of changing the design Mach number of the nozzles has been studied. The shock structure is dependent on the design Mach number. Increasing the number of lobes reduces the length of the jet core. The spreading rate of the mixing layer is more for nozzles with lower number of lobes. The flow visualizations have enabled the understanding of the flow structures of the free jets from the ESTS lobed nozzles. The three-dimensional flow field of ESTS lobed nozzles with different numbers of lobes has been visualized. Further experiments and analysis are being performed to understand the flow field of the ESTS nozzles.

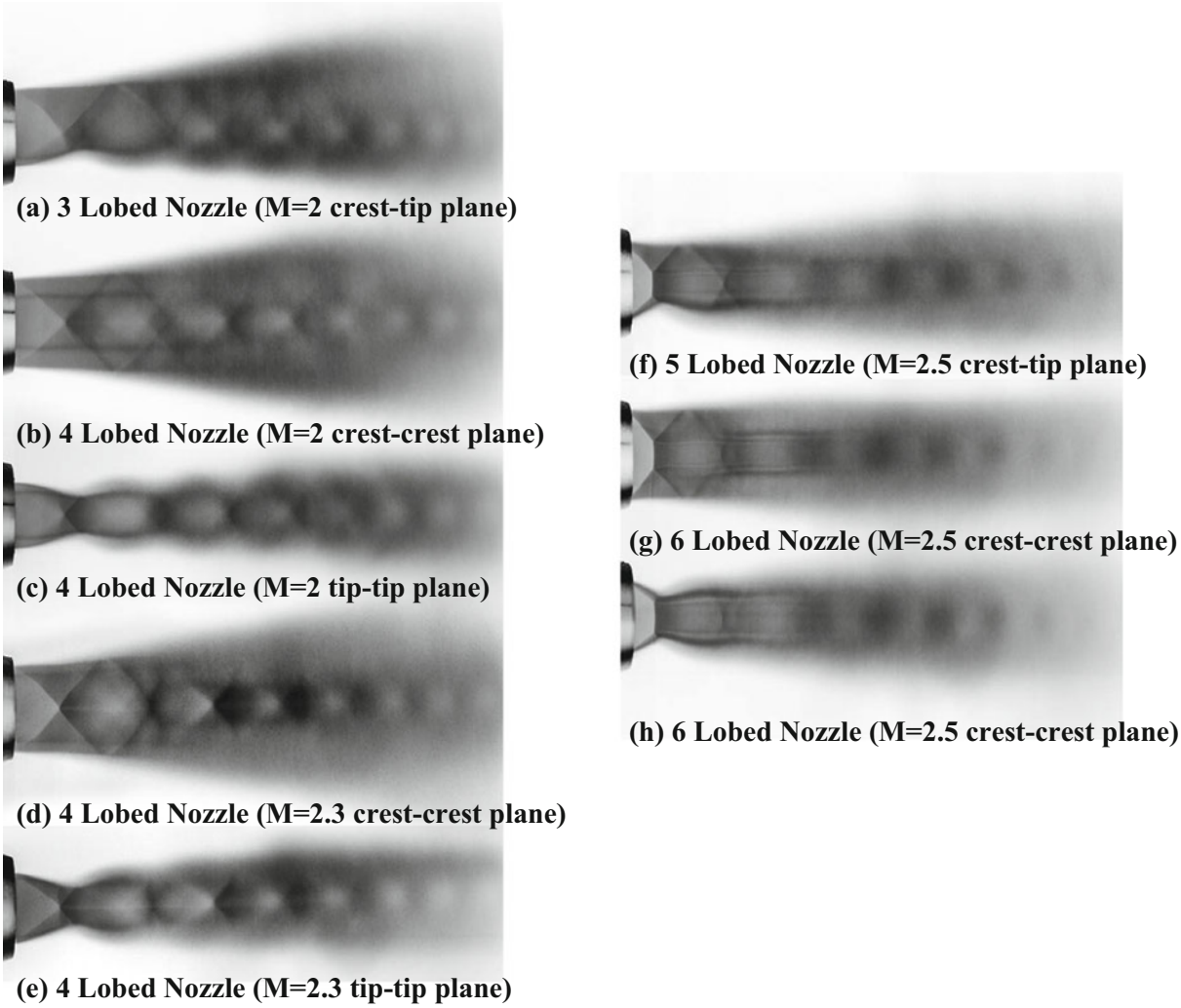

Fig. 4 Averaged image at stagnation chamber pressure 6 bar at vertical axial plane as indicated

References

1. Papamoschou, D., Roshko, A.: The compressible turbulent shear layer: an experimental study. J. Fluid Mech. **197**, 453477 (1988)
2. Gutmark, E., Schadow, K., Yu, K.: Mixing enhancement in supersonic free shear flows. Annu. Rev. Fluid Mech. **27**, 375417 (1995)
3. Rao, S.: Experimental investigations on supersonic ejectors. PhD thesis, Aerospace Engineering, Indian Institute of Science, Bangalore (2013)
4. Rao, S., Jagadeesh, G.: Novel supersonic nozzles for mixing enhancement in supersonic ejectors. Appl. Therm. Eng. **71**(1), 6271 (2014)
5. Clemens, N., Mungal, M.: A planar Mie scattering technique for visualizing supersonic mixing flows. Exp. Fluid **11**(1), 175185 (1991)

Study of Cluster Linear Plug Nozzle Flow Field in Freestream Flow

M. Viji, Kiran Chutkey, and S.B. Verma

Introduction

In the recent years, there has been a lot of interest on the altitude adaptive nozzles [1]. Of all, plug nozzle has been an attractive option because of its altitude adaptive capability [2–4]. The plug nozzle consists of an internal nozzle and a plug surface, over which the jet from the internal nozzle expands externally to the ambient conditions. For practical applications, the cluster plug nozzle seems to be an attractive option because of its thrust vector capability. The cluster plug nozzle is realized by splitting the internal nozzle into modules and allowing the jet from each of these modules to expand over the plug surface. It has been reported previously [5] that the jets from these modules interact with each other resulting in a complex three-dimensional flow field resulting in counter-rotating vortices downstream of the inter-module regions. As a consequence of these three-dimensional flow features, hot spots are observed on the plug surface [5]. The present experiments are a continuation of the previous work [2] of the authors on linear plug nozzle. For this purpose the earlier model was modified to accommodate cluster nozzles. Further, the effect of external flow on the cluster flow field development was also studied.

Geometry Details

Plug nozzle comprises of an internal nozzle, a convergent-divergent one wherein the flow expands to the nozzle wall pressure internally. The jet exiting the internal nozzle is directly in contact to the ambient conditions and expands to this pressure through suitable wave reflections on the plug surface. The model mounted on the tunnel jet pipe is shown in Fig. 1. The internal nozzle used in the present studies is a simple convergent-divergent duct as shown in Fig. 2. The design pressure ratio for the internal nozzle is 14. Regarding the plug surface, the geometry is defined as a ramp surface with a divergence angle of 15°, and the design pressure ratio is 36. The length of the nozzle from the throat of the internal nozzle to the end of plug surface is 100 mm. The width of the nozzle is 72 mm. To ensure two dimensionality of the flow field, rectangular side end plates were mounted on either side of the nozzle. The present geometry was previously tested and the results were published in Ref. [4].

Regarding the cluster nozzles, the cluster modules were realized by modifying the simple plug configuration. Constant thickness plates were placed in the grooves of the internal nozzle to split the internal nozzle into constant width modules. The exit of the internal nozzle is a rectangular one. Two different configurations were studied by varying the inter-module spacing. The number of modules for both the configurations is equal to four. The module width and the inter-module spacing for these configurations were 15.75 and 3 mm and 15 and 4 mm, respectively. The module widths to the inter-module spacing ratio for these two modules are 0.19 and 0.26.

Experimental Details

Experiments were conducted in 0.5 m supersonic base flow tunnel capable of achieving Mach numbers between 0.5 to 3.5 and the corresponding unit Reynolds number is 10–50 million. The tunnel is an axisymmetric one wherein the models can be directly mounted on the tunnel nozzle inner body thereby avoiding the support system interference. More details regarding the facility can be found in Ref. [4].

M.Viji (✉) • K. Chutkey • S.B. Verma
CSIR-National Aerospace Laboratories, Experimental Aerodynamics Division, Bangalore 560017, India
e-mail: vijim@nal.res.in

G. Ben-Dor et al. (eds.), *30th International Symposium on Shock Waves 1*, DOI 10.1007/978-3-319-46213-4_16

Instrumentation and Measurements

To study the effect of clustering, pressure ports were populated on the plug surface along the module centerline (MCL) and splitter plate centerline (SPCL). Seven ports were placed along the MCL and eight ports were placed along SPCL. To check the flow similarity between the modules, extra ports were placed along MCL and SPCL. The jet total pressure (P_{oj}) is measured at the settling chamber which is used to house the plug nozzle. And the ambient pressure (P_a) is measured at 10 mm upstream of the afterbody end. The NPR (P_{oj}/P_a) is defined as the ratio of the jet total pressure to ambient pressure. The steady wall pressures were measured using electronic pressure scanners (ESP).

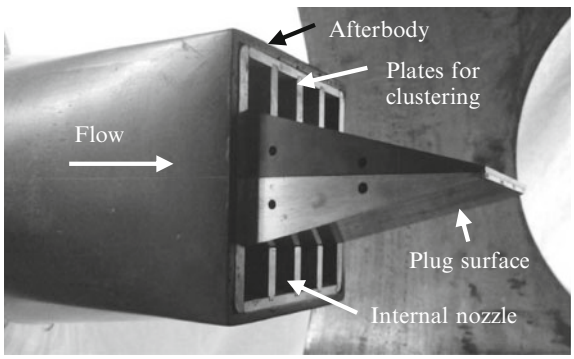

Fig. 1 Cluster nozzle model mounted in base flow tunnel

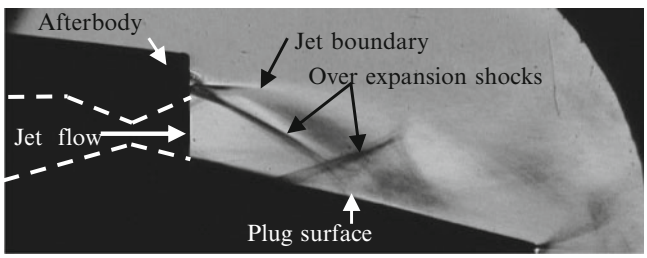

Fig. 2 Schlieren flow visualization for simple plug nozzle, NPR 10

Flow Visualization

To understand the flow field better, conventional schlieren and oil flow visualization methods were used. The schlieren technique has been used only for the simple plug nozzle configuration. The cluster plug flow field is dominated by waves in all three dimensions; hence to understand the flow features, oil flow visualization was carried out. The oil used in the present study was prepared using a mixture of oleic acid, titanium dioxide, and oil.

Results

No Freestream Flow Condition

Simple Plug Nozzle

To start with the results are presented for a simple plug flow case wherein the internal nozzle is not a cluster one. For this case the flow was analyzed for pressure ratios ranging from 3 to 12. All these cases correspond to an overexpanded jet condition for the internal nozzle. Hence the flow on the plug surface is dictated by the overexpansion shock at the exit of the internal nozzle. The flow field of simple plug nozzle for one of the pressure ratios is shown in Fig. 2. The schlieren image shows the overexpansion shocks at the exit of the internal nozzle. The jet from the internal nozzle expands to ambient pressure on the free shear layer side and to the plug surface pressure on the other side. Hence these overexpansion shocks develop in an asymmetric fashion on either side. Further from Fig. 2, it can be seen that the flow adapts to the ambient pressure on the plug surface through multiple wave reflections within the core jet. These wave reflections can be easily inferred from the plug surface pressure distribution shown in Fig. 3. The pressure distribution shown in this figure complies well with results presented in the previous paper [4] on same geometry. From the pressure distribution plot, it can be observed that the pressure rise due to the overexpansion shock occurring on the plug surface decreases with increasing pressure ratio. This is due to the

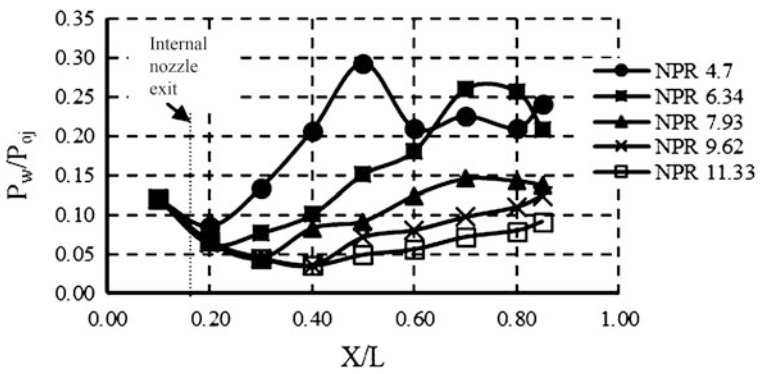

Fig. 3 Wall pressure distribution on the plug surface: no freestream, simple plug nozzle

fact that for increasing pressure ratios, the internal nozzle exit pressure approaches toward ambient pressure. This results in the reduction of the overexpansion shock strength.

Cluster Plug Nozzle Flow

The effect of clustering on the plug surface can be better understood from the oil flow pattern presented in Fig. 4. The surface streamlines downstream of the module exit display convergence of streamlines toward the module centerline. Even the surface streamlines downstream of the splitter plates move toward the module jet. These streamline patterns are completely different from the ones presented by Tsutsumi et al. [5], wherein they have conducted experiments for underexpanded internal nozzle flow. In the present case, the internal nozzle is an overexpanded one and the jets from each of the internal nozzles are expanding to a pressure less than the ambient pressure. As a consequence, the surface streamlines converge toward the module jet. Contrary to the simple plug case, the energy of the module jets is spent to expand flow along streamwise and spanwise directions. As a result, the performance of a cluster nozzle is reduced as compared to the simple plug nozzle. This fact is also reflected in the streamwise pressure distribution shown in Fig. 5. Along SPCL (splitter plate centerline), the pressure values at X/L of 0.2 are higher as compared to the pressure along MCL (module centerline) for pressure ratios less than 10. As the pressure ratio approaches the design pressure ratio of internal nozzle, which is 14, the differences in pressure between the SPCL and MCL decreased. For these cases, the internal nozzle exit pressure approaches the ambient pressure; as a result the differences in pressure between the SPCL and MCL get minimized. The other observation from Fig. 5 is the difference in pressure values between the simple and cluster configurations. In Fig. 6, the pressure distribution for the simple and cluster configuration are compared. The differences between the pressure values exist only in the immediate vicinity of the primary nozzle module exit corresponding to X/L of 0.2 along SPCL. Further down on the plug surface for X/L $>$ 0.3, the differences are minimal and can be attributed to the spanwise wave interactions along the plug surface. Along MCL, the pressure values are about similar to the simple plug nozzle case.

Freestream Flow Condition

Simple Plug Nozzle

In the presence of external flow, the internal nozzle jet expands to a lower ambient pressure localized to the internal nozzle exit afterbody base, which is decided by the external

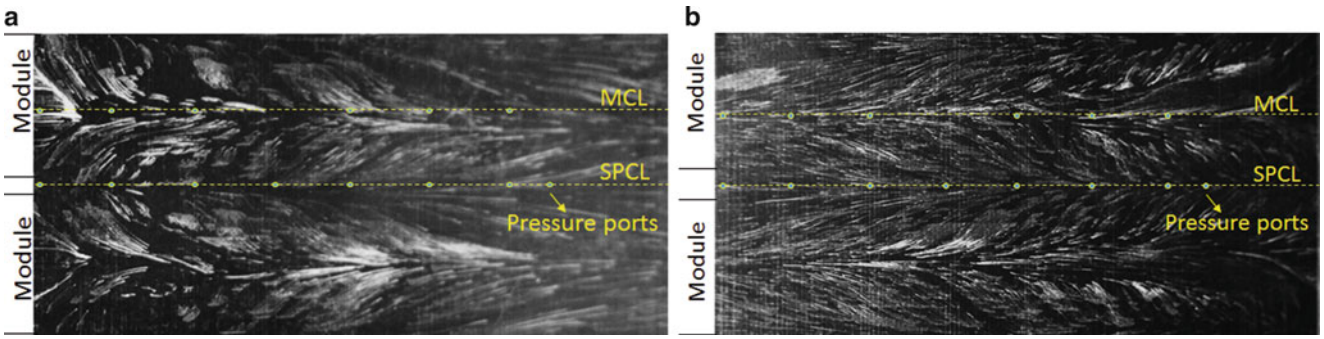

Fig. 4 Oil flow visualization of cluster plug nozzle: no freestream condition

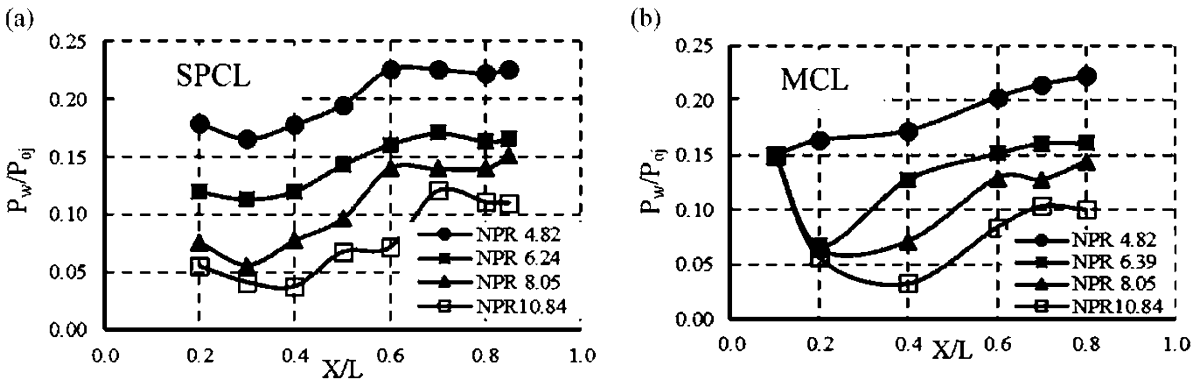

Fig. 5 Pressure along full-length plug nozzle surface: no freestream, 4 mm cluster nozzle

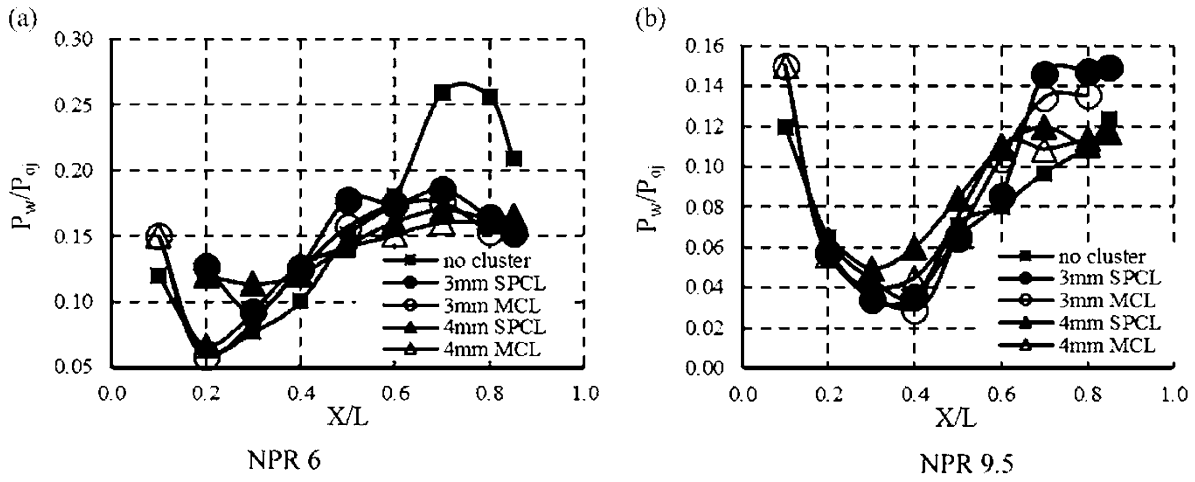

Fig. 6 Comparison of plug surface pressure of cluster and simple plug nozzles

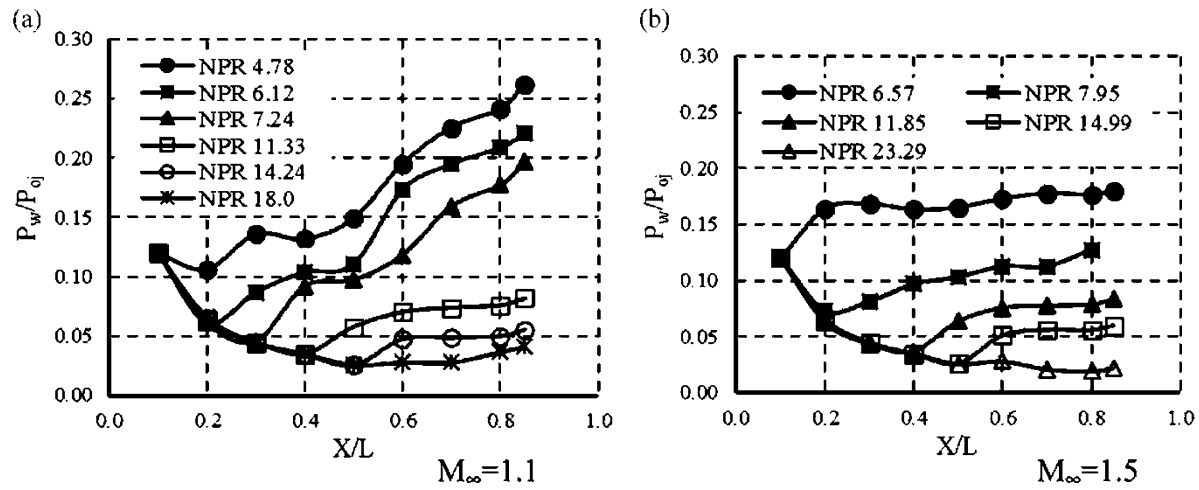

Fig. 7 Wall pressure distribution on the plug surface: simple plug nozzle

Mach number. As a result of this, the internal nozzle jet expands to lower pressure resulting in higher nozzle pressure ratios. In the present studies, for external Mach number of 1.1, the pressure ratios could be varied from 4 to 18, and for external Mach number of 1.5, the pressure ratios could be varied from 6 to 24. The pressure distribution along the plug surface in the presence of external flow is presented in Fig. 7. For pressure ratios less than 11, the pressure distribution looks different as compared to the no external flow case. For example, for NPR of 6.57 and external flow Mach number of 1.5 (see Fig. 7b), the pressure is almost constant all along the plug indicating flow separation which was not observed for similar pressure ratio for no external flow case. The schlieren image presented in Fig. 8a confirms this observation. The present case corresponds to the one wherein the internal nozzle flow does not have sufficient energy to overcome the pressure gradient in the divergent duct of the internal nozzle owing to lower stagnation pressure of the jet. As a result of this, the flow separates within the internal nozzle. Depending on the local flow expansion near the afterbody base to low pressures, the internal nozzle core jet shows a tendency of lift-off from the plug surface. For higher NPR this lift-off behavior of the jet is reduced (Fig. 8b). The other observation from Fig. 7 is the absence of pressure jumps due to wave reflection along streamwise direction which was observed for the no external flow case (see Fig. 3).

Cluster Plug Nozzle Flow

The pressure on the plug surface along SPCL and MCL for 4 mm cluster configuration and external flow Mach number of 1.1 is presented in Fig. 9. As seen before in the no freestream case, hardly any differences are seen along MCL with respect to simple plug case. But along SPCL the differences are

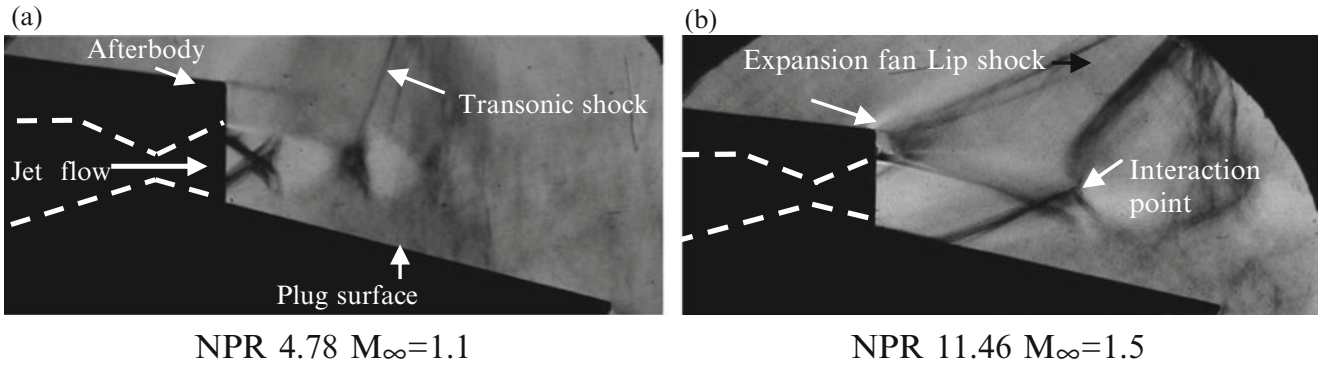

Fig. 8 Schlieren images in the presence of external flow, simple plug nozzle

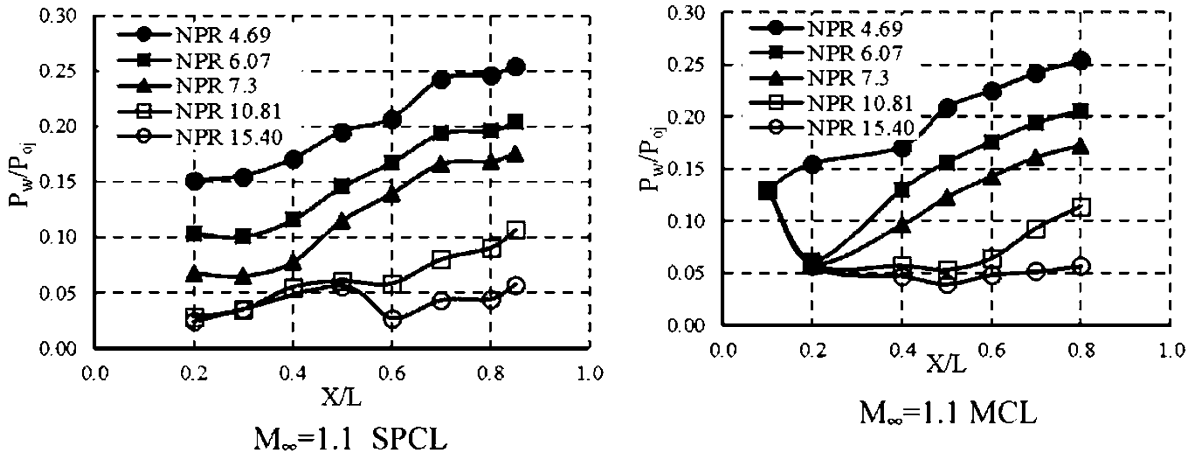

Fig. 9 Wall pressure distribution on the plug surface: 4 mm cluster nozzle

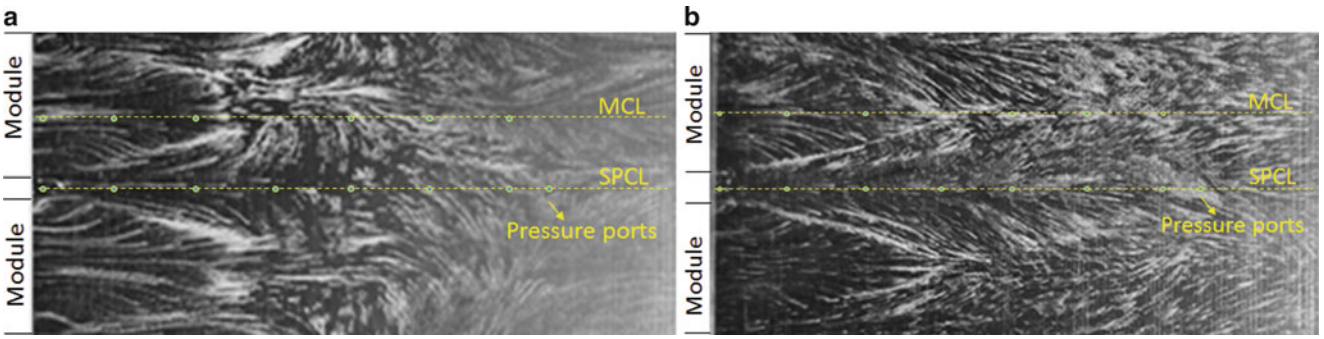

Fig. 10 Oil flow pattern for cluster nozzle in the presence of freestream

observed for X/L of 0.2, corresponding to immediate downstream of module exit, with respect to simple plug case (see Fig. 9a). In the near field of module exit corresponding to X/L of 0.2, the pressure values are higher along SPCL for NPR's less than 11 which corresponds to overexpanded internal module jet. For pressure ratios more than 14, i.e., for underexpanded internal module jet, the pressure along SPCL at X/L of 0.2 is less as compared to simple plug case (see Fig. 9a). Oil flow pattern on the plug surface in the presence of external flow is presented in Fig. 10. These oil flow patterns are similar to the ones presented by Tsutsumi et al. [5] for underexpanded internal jet condition.

Conclusion

Experiments were carried out on a ramp surface plug nozzle to understand the effects of clustering in the absence and presence of freestream. Studies were carried out for both overexpanded and underexpanded internal nozzle jet cases. Clustering the nozzle introduces the spanwise pressure gradient in the immediate vicinity of primary module exit which modifies the two-dimensional nature of the simple plug. Near the end of plug surface, however, the effect of clustering on the pressure distribution is not significant. These complex three-dimensional flow features were clearly captured using oil flow visualization. The presence of freestream separates the flow on the plug surface which reduces the performance of the nozzle.

References

1. Hagemann, G., Immich, H., Nguyen, T.V., Dumnov, G.E.: Advanced rocket nozzles. J. Propuls. Power **14**(5), 620–634 (1998)
2. Tomita, T., Tamura, H., Takahashi, M.: An experimental evaluation of plug nozzle flow field. AIAA paper, 2632, 1996
3. Nasuti, F., Onofri, M.: Theoretical analysis and engineering modeling of flowfields in clustered module plug nozzles. J. Propuls Power **15**(4), 544–551 (1999)
4. Verma, S.B., Viji, M.: Linear-plug flow field and base pressure development in freestream flow. J. Propuls. Power **27**(6), 1247–1258 (2011)
5. Tsutsumi, S., et al.: Clustering effects on performance and heating of a linear Aerospike nozzle. AIAA Paper 122-2007. 2007

Studies in Free Jets from Supersonic ESTS Lobed Nozzles

Albin Varghese, P. Suriyanarayanan, Srisha M.V. Rao, and Gopalan Jagadeesh

Introduction

The flow field associated with supersonic free jets can be understood better by using visualization techniques like schlieren in the laboratory. Supersonic jets are used in the fields of aerospace, refrigeration, and precision manufacturing. The supersonic free jets are normally characterized by a compressible flow field with complex shock structures at off-design conditions. Supersonic free jets from nozzles with exotic shapes like Elliptic Sharp Tipped Shallow (ESTS) lobed nozzle have three-dimensional flow fields that are difficult to completely understand using line-of-sight integrated techniques like schlieren. These nozzles present a challenge to the measurement of flow properties with novel flow diagnostic techniques. Density is one such flow property which is very informative yet difficult to obtain. The three-dimensional density fields can be obtained by the background-oriented schlieren (BOS) [1, 2]. Various nozzle configurations with non-axis symmetric profiles have been studied earlier [3] including the ESTS lobed nozzle [4, 5]. This is an attempt to capture the density flow field of an ESTS lobed nozzle free jet using BOS. In this study, a supersonic ESTS lobed nozzle with four lobes is operated to get a supersonic free jet. The density field of this jet is obtained at several azimuthal positions by turning the nozzle about its axis. The information from all the positions is used to reconstruct the three-dimensional flow field of the nozzle. From this density field, both the basic physics of the complex flow field can be understood as well as CFD modeling of the flow field can be validated.

Experiment Description

Free Jet Setup

As shown in Fig. 1 a module called variable-frequency drives is used to reduce power consumption and also to control the recurrent load-unload cycle of the air compressor. Air is compressed by a screw compressor. It is rated at 22 kW providing a volume flow rate 0.0448 m^3/s with a maximum operating pressure of 12 bar. After compression the air is passed through an oil filter. The filtered air is dried in a dryer to remove excessive moisture present in it. The compressed filtered and dried air is stored in three receivers. Their combined capacity by volume is 7 m^3. 12.5 bar is the maximum working pressure of these air receivers. From the receivers through a simple gate valve, a 2″ pipeline is used to draw the air out. This is larger than the throat of the nozzle and ensured that the nozzle throat is choked when needed. The pressure of this air is regulated by a pressure regulator to set an operating pressure of 3–10 bar. The regulated air is sent through a pneumatic rotary actuator operated by a simple hand switch which starts the tunnel. From the actuator a long chamber of 200 mm diameter is used as a stagnation chamber where the static pressure of the outgoing flow is measured. Beyond the stagnation chamber, a threaded arrangement is provided to mount the nozzles of interest.

The ESTS lobed nozzle is designed such that the area ratio remains the same as that which corresponds to an exit Mach number according to isentropic area relations. Experiments were done on the nozzle with different azimuthal positions at stagnation chamber pressure of 3.5 bar. For CFD simulations and experiments, the nozzle pressure ratio which was 4.8 is the absolute pressure ratio of the stagnation chamber to the ambient.

A. Varghese (✉) • P. Suriyanarayanan • S.M.V. Rao • G. Jagadeesh
Department of Aerospace Engineering, Indian Institute of Science, Bangalore, India
e-mail: venalbin@gmail.com

G. Ben-Dor et al. (eds.), *30th International Symposium on Shock Waves 1*, DOI 10.1007/978-3-319-46213-4_17

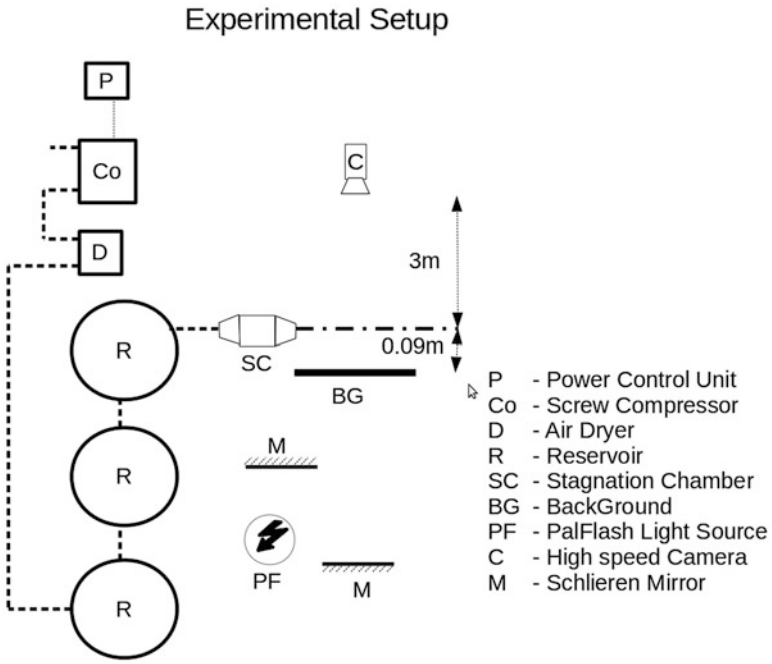

Fig. 1 The experimental setup showing the plan of gas storage and optical devices

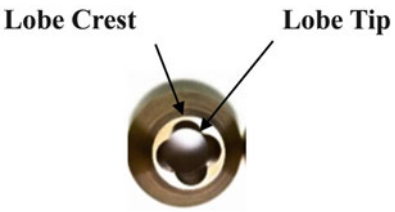

Fig. 2 ESTS four-lobed nozzle

Supersonic ESTS Lobed Nozzle

Figure 2 shows the manufactured ESTS four-lobed nozzle. It has a diverging section profile with elliptic lobes and sharp tips. This nozzle can be manufactured easily by the simple process of drilling.

Background-Oriented Schlieren

The background-oriented schlieren technique is in principle based on the change in refractive index due to the change in density. Using this principle BOS is used to determine the density field using the following steps: (1) a background is imaged through the flow of interest and without the flow. These images are used to calculate the displacements of the background images due to the flow using a PIV-type cross-correlation algorithm. These displacements represent the vectors of density gradient at each point. (2) The gradient of the above displacement which gives the Poisson equation is solved to obtain the line-of-sight integrated density field, and (3) the density field in the actual plane of interest is determined by the use of optical tomography (filtered back projection). The reconstruction function is derived in Venkatakrishnan and Meier [1]. The entire field is reconstructed using inverse tomography [2].

Experiment Setup

In order to obtain images, a dynamic schlieren light source (PAL Flash 501) was used for illumination. It produced a light pulse of 750 ns pulse width. A Phantom v310 camera was used to capture images of the background. A Nikon 400 mm lens was used as the imaging optics. A dot pattern of 2400 dpi resolution was used for the study. The imaged area was 200 × 200 mm. Phantom PCC software was used to acquire and IDT proVISION R software was used to post-process the images to get the density gradient field. The nozzle was kept at a distance of 3 m from the camera and 90 mm from the background to get maximum sensitivity. In order to reduce the noise generated from the density gradients in the ambient, the room was kept well ventilated. The flow was started and an image was acquired by synchronously operating the camera and the light source. The synchronization was done using a pulse from a Stanford DG 535 signal generator which simultaneously triggered the light source and the camera. The camera was operated at a frame rate of 3200 fps and an exposure of 490 μs. The long exposure ensured that the light pulse from the PAL flash was

captured by the first frame of the camera. Each image thus acquired had an effective exposure of less than 1 μs. A total of eight images were acquired at each position to obtain an average image which was used in the tomographic reconstruction. The nozzle was rotated to obtain images at 9° intervals.

Results and Discussions

Schlieren Measurements

Figure 3 shows schlieren images of the four petal nozzle flow taken at two different azimuthal positions. The images show the complex shock structure close to the nozzle exit. It reveals the presence of ten shock diamonds in Fig. 2a and 8 shock diamonds in 2b. Also the shock structures in both images are different. This shows the three-dimensional nature of the flow. But the flow is symmetric across the nozzle axis.

BOS Measurements

Figure 4a, b shows the image of the background without the flow and with the flow. This image was taken with the tip-to-tip plane of the nozzle kept vertical. There is a displacement of the dot pattern in the flow image when compared with the no flow image. The gradients of the line-of-sight integrated density field are shown in Fig. 5. This was obtained by the cross-correlation of the flow image against the no flow image of the background. The vectors point in the direction of lower density. The varying magnitude of the density gradients can be seen with color coding which will resemble bidirectional schlieren (Fig. 6).

CFD Simulations

The CFD simulations have been done on the commercial software ANSYS CFX 13.0. The fluid was set as air as an

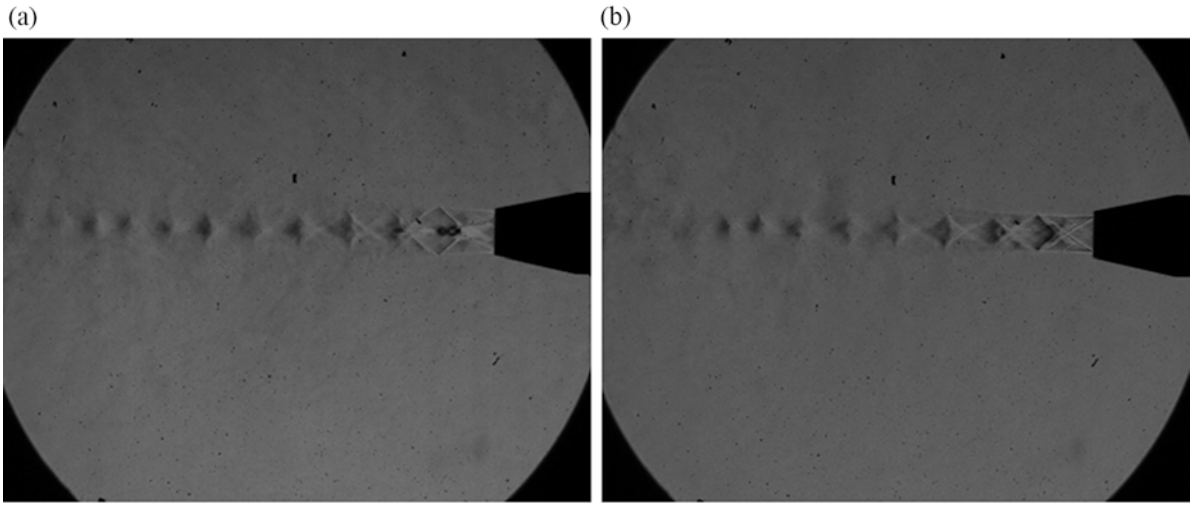

Fig. 3 Schlieren images of four-lobed nozzle with (**a**) tip-to-tip plane vertical and (**b**) crest-to-crest plane vertical

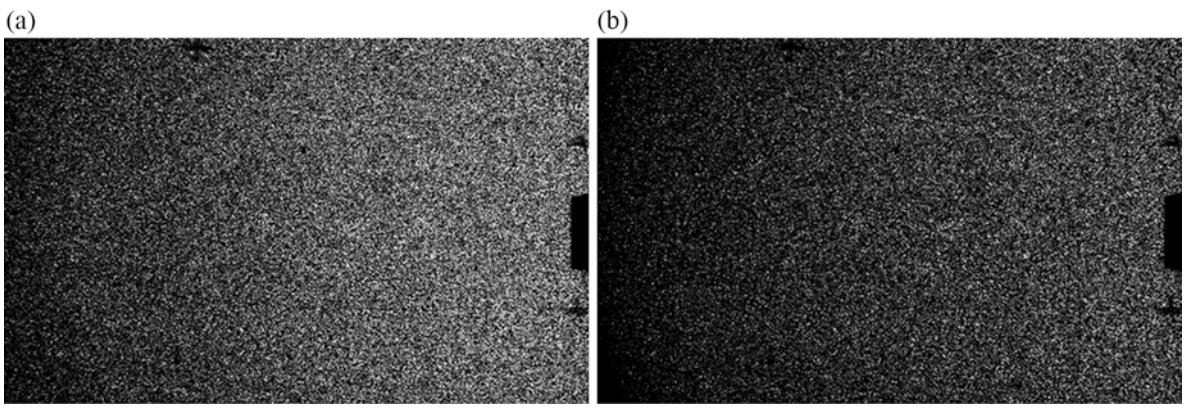

Fig. 4 (**a**) No flow image, (**b**) flow image

ideal gas and calorically perfect. The total temperature was given as 300 K while the total pressure was 4.4 bar. Atmospheric pressure was set as the local pressure of 0.91 bar. K-ε turbulence model with default turbulence intensities was used. Initial values for velocities were set as $u = 30$ m/s, $v = 0$, and $w = 0$. First-order turbulence numerics were applied. A high-resolution advection scheme was used in the solver. The physical time scale set was $1 \times e^{-5}$ s. The convergence criterion was 1000 iterations with target residual of $1 \times e^{-4}$ of the maximum values. The simulation was done using 12 parallel processors on a mesh with 9.43 million nodes. The solution converged and took a wall-clock run time of nearly 39 h.

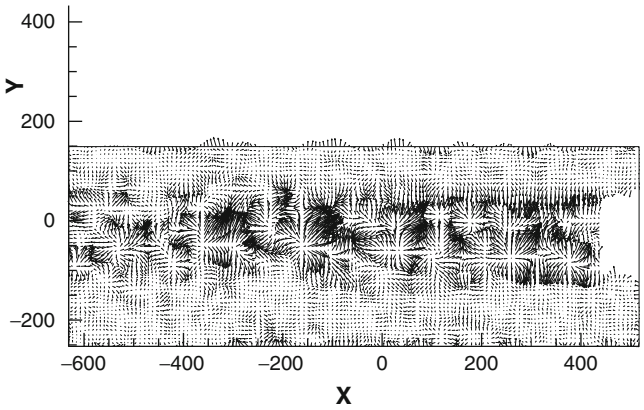

Fig. 5 Vector plot of density gradient

Discussions

Figure 6 shows the comparison of the axial planes of the flow taken along the tip-to-tip plane. The positions of the shock cells are approximately captured by the CFD simulation. The experimental data shows the presence of nine shock cells while only seven are revealed by the CFD simulation. The experimental image shows the low-pressure region seen in dark blue close to the nozzle lip. This is caused by the entrainment of the ambient by the free jet near the thick lip of the nozzle. This effect is not clearly seen in the CFD contours. Figure 7 shows an iso-surface of density corresponding to 1.4 kg/m^3. This surface reveals the shape of the flow at the exit of the nozzle. The lobe shape of the exit cross section is clearly seen in the images. This lobe shape is captured by both the experiments and the CFD simulation. Beyond the lobe-shaped structures, the flow behaves similar to the flow at the exit of an under-expanded nozzle. The CFD simulations did not capture the flow physics very accurately. However it has successfully revealed the general trend of the flow.

Conclusions and Future Work

The flow field of the ESTS four-lobed nozzle has been investigated using BOS. The three-dimensional flow field has been successfully reconstructed from line-of-sight integrated images using optical tomography. CFD simulations of the nozzle have been performed and compared with the experimental data. The CFD results reveal the general features of the flow field. But they do not compare accurately with experimental data. Better simulations with more accurate turbulence models need to

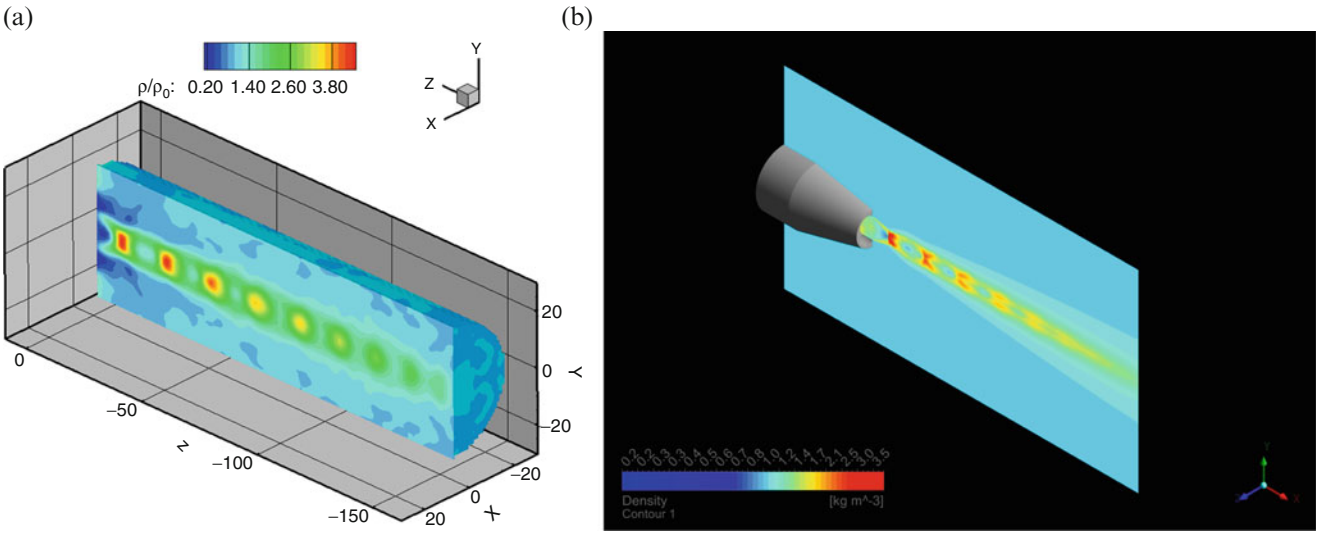

Fig. 6 (**a**) Density field for four-lobed nozzle ($M = 2$) at 4.8 nozzle pressure ratio obtained from BOS normalized with ambient density. (**b**) Density field for four-lobed nozzle ($M = 2$) at 4.8 nozzle pressure ratio obtained from CFD. Tip-to-tip axial plane of the nozzle

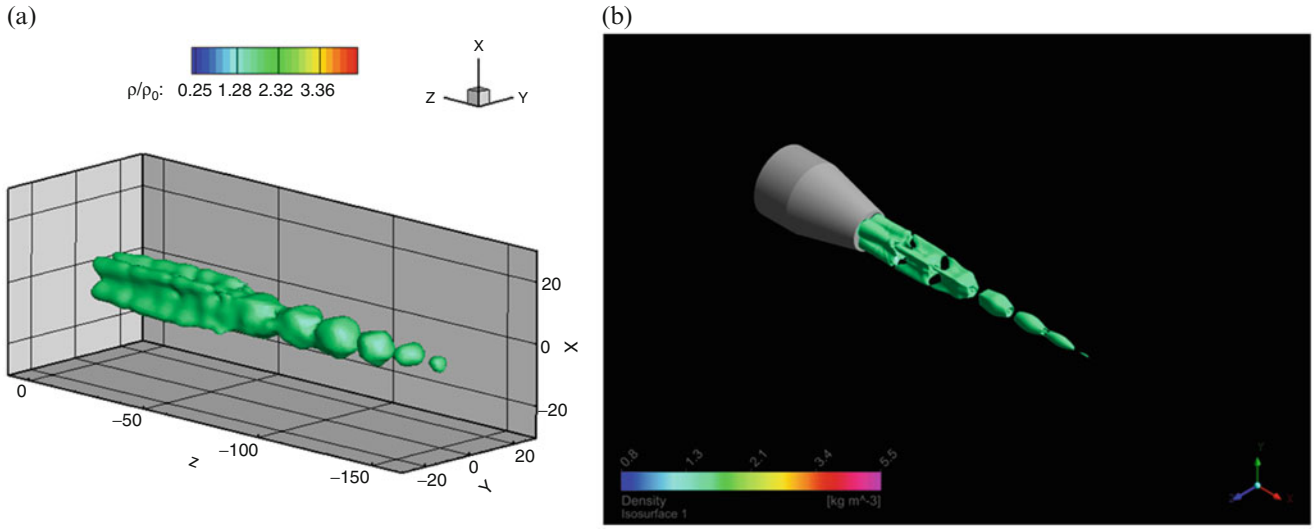

Fig. 7 (**a**) Density iso-surface obtained from BOS for four-lobed nozzle ($M = 2$) at 4.8 nozzle pressure ratio and (**b**) density iso-surface obtained from CFD for four-lobed nozzle ($M = 2$) at 4.8 nozzle pressure ratio

be performed to accurately simulate the flow field. The experiments have been performed at 9° intervals of nozzle rotation. Experiments with smaller angular steps need to be performed to resolve the flow field better.

References

1. Venkatakrishnan, L., Meier, G.E.A.: Density measurements using background oriented Schlieren technique. Exp. Fluids **37**(2), 237–247 (2004)
2. Venkatakrishnan, L., Suriyanarayanan, P.: Density field of supersonic separated flow past an afterbody nozzle using tomographic reconstruction of BOS data. Exp. Fluids **47**(3), 463–473 (2009)
3. Gutmark, E., Schadow, K., Yu, K.: Mixing enhancement in supersonic free shear flows. Annu. Rev. Fluid Mech. **27**, 375–417 (1995)
4. Rao, S.: Experimental investigations on supersonic ejectors. Ph.D. thesis, Aerospace Engineering, Indian Institute of Science, Bangalore (2013)
5. Rao, S., Jagadeesh, G.: Novel supersonic nozzles for mixing enhancement in supersonic ejectors. Appl. Therm. Eng. **71**(1), 62–71 (2014)

Unsteadiness of Supersonic Flows in Over-Expanded Nozzles

A. Piquet, A. Georges-Picot, and A. Hadjadj

Introduction

Optimization of nozzles by increasing their expansion ratio and reducing their size is becoming a real challenge in aerospace application. The main problem in those configurations is the presence of flow separation, which is characterized by flow unsteadiness and strong vortical structures that can interact with various components of the nozzle and lead to asymmetric fluctuating wall-pressure distribution. These complicated flow interactions are the primary cause of nozzle flow instabilities, thermal sollicatations, side loads generation, and material fatigue. Many studies have been conducted on the overexpanded nozzles to better understand the influence of different parameters and operating flow conditions [1–9]. Nevertheless, studies of the origin of shock-induced flow for canonical nozzle are not abundant in the literature. A comprehensive review of nozzle flow separation is given by Hadjadj and Onofri [4]. Papamoschou and Johnson [5], among others, have investigated the stability of the separation phenomenon in experimental planar nozzle. The main parameters that influence the topology of shock structures are the geometry of the nozzle and the NPR. Theoretical studies conducted by Ben-Dor et al. [10] and Chpoun et al. [11] on shock interference phenomena have shown a hysteresis effect in the transition between direct and inverse reflections. Similarly, the transition between a Mach reflection and cap-shock pattern in shock structure is characterized by a hysteresis phenomenon [8]. A detailed study of jet separation phenomena and lateral loads was conducted by Östlund [6]. The authors summarize exhaustively the results of numerical and experimental work obtained on supersonic nozzles. Two phenomena were particularly studied. The first one is related to the transition from Free Shock Separation (FSS) to Restricted Shock Separation (RSS). This transition is at the origin of strong side loads. It occurs mainly in the Thrust Optimized Contour nozzles (TOC or TOP) and is characterized by a hysteresis cycle during the NPR's variation [12]. The second phenomenon is related to the end-effect regime [13, 14]. This occurs when, in a typical RSS flow, the recirculation bubble trapped by the separation-reattachment reached the exit lip. The bubble suddenly opens to the atmosphere and causes a rapid increase in pressure downstream of the separation shock. This cyclic phenomenon causes significant fluctuations of the separation line. The low frequency oscillations phenomenon can be dangerous to the engine integrity especially if they coincide with the natural modes of the mechanical structure. If the origin of these phenomena is still poorly understood in the case of planar shock/boundary layer interaction (impinging shock or supersonic ramp), the literature on the subject gives two main assumptions: (1) low frequency oscillations are the result of disturbances from the upstream [15, 16], (2) the downstream recirculation bubble [17] coupled to the separation shock drive the whole system. This can be assimilated to a mass-spring system with a low-pass filter [18].

Results and Discussion

Large Eddy Simulation (LES) is conducted to study three-dimensional flow unsteadiness in a TOC overexpanded nozzle. High-order WENO scheme based 3D compressible solver equipped with an immersed boundary method (IBM) is used for this purpose. An LES wall-model, which accounts for both Adverse Pressure Gradient (APG) and flow acceleration is developed to overcome the low resolution of the thin boundary layer [19]. The wall model uses appropriate scaling laws for velocity, pressure, and temperature based on a single normalized RANS database. The model takes into account a large number of phenomenon occurring during

A. Piquet (✉) • A. Georges-Picot • A. Hadjadj
CORIA – UMR 6614 CNRS – INSA Rouen and Normandie Université, Avenue de l'Université, 76801 Saint-Étienne-du-Rouvray, France
e-mail: arthur.piquet@coria.fr

G. Ben-Dor et al. (eds.), *30th International Symposium on Shock Waves 1*, DOI 10.1007/978-3-319-46213-4_18

the nozzle flow expansion, such as compressibility and wall curvature, Reynolds number effect, etc. The computational domain is generated from a Cartesian grid with 268 millions points uniformly distributed along the 3 space directions, with $N_x = 1024$, $N_y = 512$, and $N_z = 512$. The nominal nozzle pressure is achieved by gradually increasing the reservoir pressure p_{ch} from ambient to desired chamber conditions. Compared to an impulsive startup, the relatively slow transient process with a gradual pressure ramp-up allows to reach a steady-state solution, while avoiding vortex-pair generation and other flow disturbances due to the sharpness of the startup shock [20, 21]. The outflow boundary conditions are set as far-field atmospheric conditions ($p_a = 1$ bar and $T_a = 300$ K) and the boundary layer is assumed to evolve under adiabatic wall conditions.

Two different nozzle flows have been studied with NPR $= p_{\mathrm{ch}}/p_a = 25$ and 37.9. Since the RSS $\leftrightarrow$ FSS transition occurs at NPR $= 24$, the flow structure of the two studied cases will be characterized by an RSS shock configuration (see Fig. 1). In terms of validation, a good agreement is found between the computed and the experimental mean wall-pressure profiles. This result confirms the ability of the present model to correctly predict the separation location and the associated flow topology (see Fig. 2). The result also shows that the RSS pattern does not exhibit an asymmetrical behavior, neither in the quasi-steady state nor during the transient flow evolution, except at the "*end-effect*" where the separation line reaches the nozzle lip for higher NPR. This result is also in accordance with the findings of Nguyen et al. [7]. The stability of the flow upstream of the shock depends on the type of separation. Due to the high curvature of the TOC design, the internal shock deviates the supersonic jet towards the wall, which results in a lambda shock structure, that is less sensitive to the external pressure fluctuations. Moreover, as the supersonic jet attaches to the wall, the downstream subsonic flow can influence the separation location through the main recirculation bubble. The latter is confined within a supersonic torus supported by the wall and the RSS shock pattern. Thus, the whole structure of the flow is relatively stable due to the high pressure exerted by the recirculation bubble on the supersonic jet. This pressure can influence the separation location. However, as this pressure is mainly exerted uniformly on the Mach disk (the direction of the force is parallel to the streamwise direction), weak oscillations of the separation line is observed with a symmetric behavior.

Figure 3 depicts the iso-contour of the Q criterion (Q being the second invariant of the velocity gradient tensor), used to visualize the three-dimensional flow pattern and to identify the associated coherent structures. Although the separation line is symmetric, the first reattachment line is not. This behavior is attributed to the three-dimensionality of the turbulent eddies in the recirculation zone downstream of the Mach disk.

We focused the study on the large-scale structures characterized by lower frequency ranges which involve high energy, enough to influence the flow. The visualization of the averaged x-velocity fields for the two simulations (Fig. 2, center) highlights the main structures of the flow: a supersonic jet (circular), which relies on the wall of the nozzle, a recirculation bubble bounded by the supersonic jet, a Mach disk and at least two small vortices trapped between the supersonic jet and the wall. The RSS pattern, due to its complex structure, is less sensitive to the external fluctuations than the FSS. The influence of these fluctuations is felt mainly at the exit of the nozzle between the supersonic jet and the shock structure. Indeed, when the supersonic jet is ejected into the atmosphere, it slightly curl up on itself under the effect of the ambient pressure which is greater than the pressure of the recirculation zone. As for the FSS pattern, the closing of the supersonic jet near the wall influences the recirculation zone, which can lead to an instable phenomenon of recirculation bubble. In the case of an RSS pattern, the recirculation bubble is only powered by the main jet and is isolated from the environment by the supersonic jet. This recirculation is composed of one or two large-scale

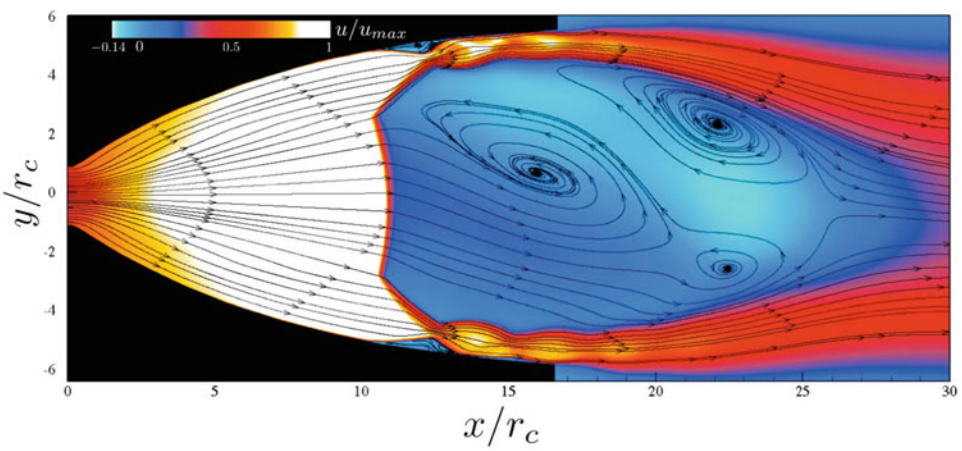

Fig. 1 Mean dimensionless longitudinal velocity with streamline contours for NPR = 37.9

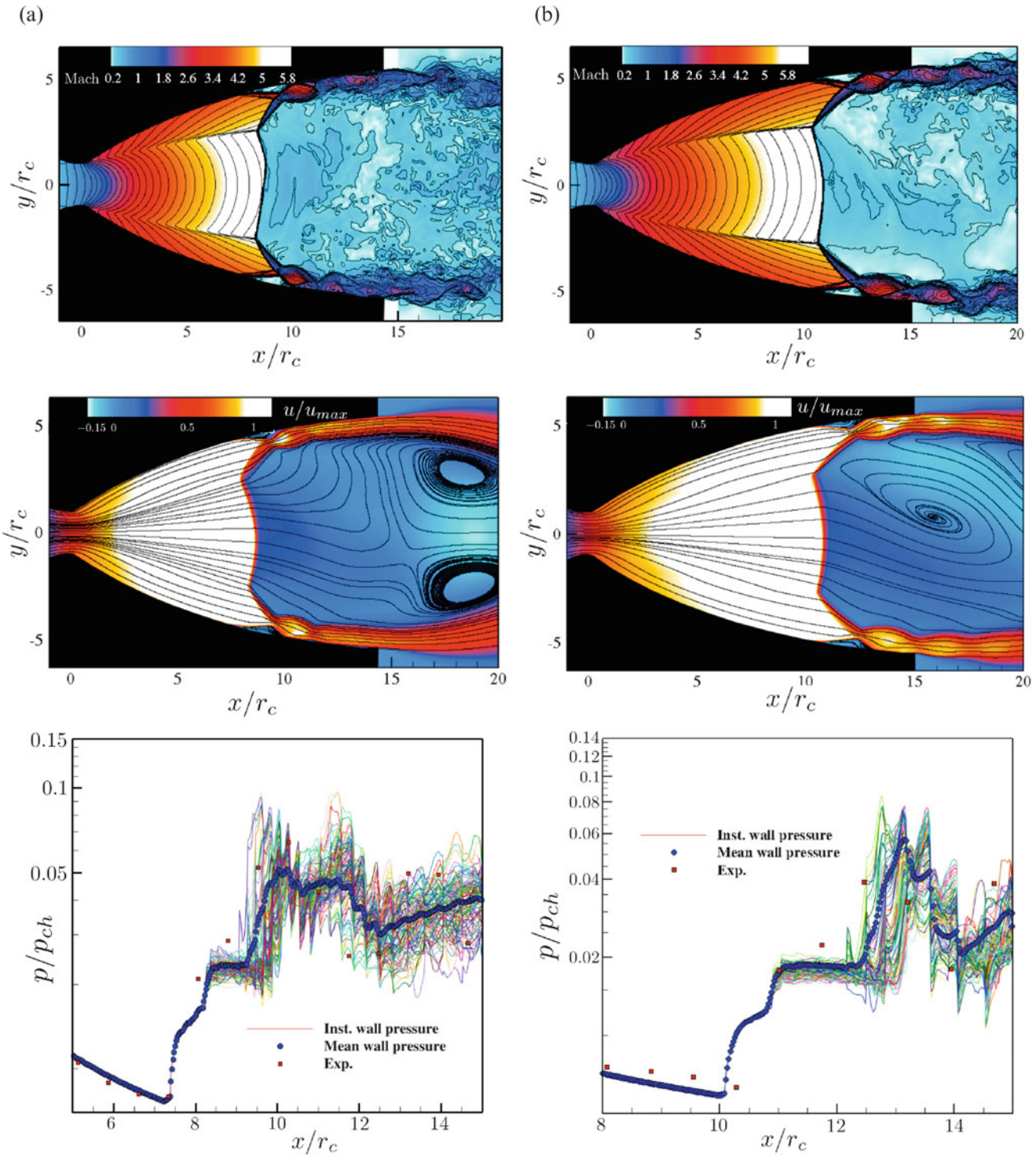

Fig. 2 (*top*) Instantaneous Mach number contour, (*center*) averaged normalized x-velocity contour, (*bottom*) wall-pressure distributions, (**a**) NPR = 25, (**b**) NPR = 37.9

structures (Fig. 2, center). These downstream structures appear to be the main sources of flow asymmetry in the case of an FSS pattern.

The vortex located just behind the Mach disk (Fig. 1) has an asymmetric behavior in relation to the axis of the nozzle, which directly influences the second structure, shaped as a torus. This asymmetric behavior results from the convex shape of the Mach disk which is not fixed in time. Therefore, the structure is mainly positioned eccentrically toward the Triple Point (TP), represented by the interaction of the Mach

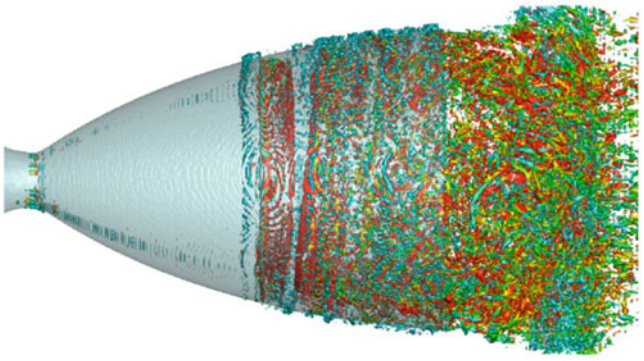

Fig. 3 Instantaneous 3D iso-surface of the second invariant of the velocity gradient tensor $Q = 10^{-3}\, Q_{\max}$ where $Q_{\max} = 10^{11}\ \mathrm{s}^{-2}$ and $Q = \frac{1}{2}\left(\Omega_{ij}\,\Omega_{ij} - S_{ij}\,S_{ij}\right)$ for NPR = 25

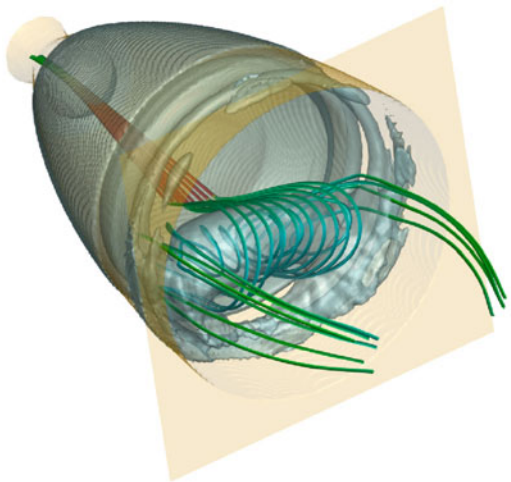

Fig. 4 Main recirculation bubble with streamlines behind the Mach disk, iso-pressure of 82 kPa

disk with the Internal Shock (IS). Unlike the torus (second recirculation bubble), easily identifiable by the two recirculating structures, the shape of this structure is not obvious. 3D representation of an iso-pressure value (Fig. 4) allows us to see that the structure does not look like a circular bubble as one might expect, but rather as a cylindrical structure supported by the supersonic jet. The flow at the downstream of the Mach disk is channeled through the structure, and then evacuated at its edges by the supersonic jet.

Summary

In the present paper, Large Eddy Simulations (LES) are carried out to investigate the three-dimensional flow separation and the complex shock wave/boundary layer interactions associated with shock-induced unsteady flows in a Thrust Optimized Contour (TOC) nozzle. Different nozzle flow regimes are considered by varying the NPR between RSS/FSS pattern. A new near-wall turbulence model is developed, based on self-similarity properties of compressible boundary layers in supersonic nozzles, and using new renormalization laws derived from a tabulated RANS database. This model allows to take into account the dynamics of the flow while significantly reducing the number of computational points and the time step required for LES simulations. The predictions of the model are shown to be in agreement with available experimental data. The study highlights many complex interactions within the flow. In particular, the upstream/downstream interactions (supersonic/subsonic), which strongly influences the separation location and the shock structure, causing the occurrence of energetic peaks associated with low-frequency oscillations and acoustic disturbances. In particular, it is shown that the flapping of the jet associated with the nozzle-lip vortex highly influences the low-frequency jet oscillations. These self-sustaining phenomena are synonymous of lateral forces and are representative of laboratory experiments and real-engine test benches. Despite the fact that the separation line is perfectly axisymmetric, the downstream flow is not. These results have shown that the downstream flow drives significantly the separation location. Our results have significant differences in terms of coherent structures (relatively small scales) compared to the URANS simulations previously reported in the literature [9, 14].

Acknowledgements The first author is supported financially by the DGA (Direction Générale de l'Armement) from the French Ministry of Defense in collaboration with the DSTL, UK. The authors wish to thank the European PRACE project which allocated computer core-hours as part of the 9th PRACE project call. The simulations have been achieved using the TGCC Curie Fat Node cluster of CEA in France.

References

1. Summerfield, M., Foster, C.R., Swan, W.C.: Flow separation in overexpanded supersonic exhaust nozzles. Jet propulsion, **24** (5), 319–321 (1954)
2. Frey, M., Hagemann, G.: Restricted shock separation in rocket nozzles. J. Propuls. Power **16** (3), 478–484 (2000)
3. Chen, C.L., Chakravarthy, S.R., Hung, C.M.: Numerical investigation of separated nozzle flows. AIAA J. **32** (9), 1836–1843 (1994)
4. Hadjadj, A., Onofri, M.: Nozzle flow separation. Shock Waves **19** (3), 163–169 (2009)
5. Johnson, A.D., Papamoschou, D.: Instability of shock-induced nozzle flow separation. Phys. Fluids (1994-present) **22** (1), 016102 (2010)
6. Östlund, J.: Flow processes in rocket engine nozzles with focus on flow separation and side-loads (2002)
7. Nguyen, A.T., Deniau, H., Girard, S., De Roquefort, T.A.: Unsteadiness of flow separation and end-effects regime in a thrust-optimized contour rocket nozzle. Flow Turbul. Combust. **71** (1–4), 161–181 (2003)
8. Frey, M., Hagemann, G.: Status of flow separation prediction in rocket nozzles. AIAA Paper No. 1998-3619 (1998)

9. Hadjadj, A., Perrot, Y., Verma, S.: Numerical study of shock/boundary layer interaction in supersonic overexpanded nozzles. Aerosp. Sci. Technol. **42**, 158–168 (2015)
10. Ben-Dor, G., Ivanov, M., Vasilev, EI., Elperin, T.: Hysteresis processes in the regular reflection ↔ mach reflection transition in steady flows. Prog. Aerosp. Sci. **38** (4), 347–387 (2002)
11. Chpoun, A., Passerel, D., Li, H., Ben-Dor, G.: Reconsideration of oblique shock wave reflections in steady flows. Part 1. Experimental investigation. J. Fluid Mech. **301**, 19–35 (1995)
12. Pilinski, C.: Etude numérique du décollement en tuyères supersoniques. Ph.D. thesis, INSA de Rouen (2002)
13. Afaque, S.: Contribution to the numerical simulation of turbulent shock-induced separated flows: application to supersonic over-expended nozzle flow. Ph.D. thesis, Ecole Nationale Supérieur de Mécanique et d'Aérothechnique (2010)
14. Deck, S.: Delayed detached eddy simulation of the end-effect regime and side-loads in an overexpanded nozzle flow. Shock Waves **19** (3), 239–249 (2009)
15. Dolling, D.S., Or, C.T.: Unsteadiness of the shock wave structure in attached and separated compression ramp flows. Exp. Fluids **3** (1), 24–32 (1985)
16. Beresh, S.J., Clemens, N.T., Dolling, D.S.: Relationship between upstream turbulent boundary-layer velocity fluctuations and separation shock unsteadiness. AIAA J. **40** (12), 2412–2422 (2002)
17. Dupont, P., Haddad, C., Debiève, J.F.: Space and time organization in a shock-induced separated boundary layer. J. Fluid Mech. **559**, 255–277 (2006)
18. Schwane, R., Torngren, L., Wong, H.: Validation of unsteady turbulent flow predictions for over-expanded rocket nozzle. In: Computational Fluid Dynamics 2002, pp. 707–712. Springer, Berlin (2003)
19. Georges-Picot, A.: Développement de modèle physiques et numériques pour la simulation aux grandes échelles des écoulements dans les tuyères supersoniques. Ph.D. thesis, Institut National des Sciences Appliquées de Rouen (2014)
20. Mouronval, A.S., Hadjadj, A., Kudryavtsev, A.N., Vandromme, D.: Numerical investigation of transient nozzle flow. Shock Waves **12** (5), 403–411 (2003)
21. Mouronval, A.S., Hadjadj, A.: Numerical study of the starting process in a supersonic nozzle. J. Propuls. Power **21** (2), 374–378 (2005)

Design of Optimized Two-Dimensional Scramjet Nozzle Contour for Hypersonic Vehicle Using Evolutionary Algorithms

A. Govinda, Manoj Kumar K. Devaraj, Yogendra Singh, Nimesh Thakor, Venkat Rao Kulkarni, S.N. Omkar, and Gopalan Jagadeesh

Introduction

The supersonic combustion ramjet (scramjet) engine proposed by F. S. Billig in 1964 has been perceived as the most hopeful air-breathing propulsion system for the hypersonic flight [1]. The nozzle plays a vital role in accelerating heated air from the combustor to produce thrust in a scramjet engine. The design of nozzle is critical in obtaining necessary thrust margins to perform accelerated flights [2]. Single expansion ramp nozzles are generally used in hypersonic cruise vehicle powered by scramjet engines to produce the necessary thrust and are two-dimensional in nature. Wei Huang et al. [3] has investigated the performance of a single expansion ramp nozzle with the thrust force and the lift force as the objective functions and proposed an efficient way in designing and optimizing the nozzle geometry. Further, they have evaluated the performance of the nozzle by coupling ANN and optimization algorithm. Ogawa et al. [4] evaluated the maximum thrust produced for an axisymmetric nozzle flying at Mach 8. They have adopted surrogate models in the optimization loop in order to obtain the optimum thrust values. The availability of literature for design optimization of two-dimensional contoured scramjet nozzles is scarce. Highly coupled aerothermodynamic phenomena like shock–shock interaction, shock wave shear layer interaction makes the problem nonlinear where conventional optimization techniques will fail. Moreover, there is a necessity for the use of high-fidelity models in designing the nozzle which helps in reducing the uncertainties that appear on the force estimations. Hence, in the present study, a design methodology has been established using an in-house developed Python script for the automation process of computational fluid dynamics (CFD), ANN, and optimization. The nozzle geometry used in this method consists of the inner surface which is represented by a cubic curve. Two-dimensional structured mesh is generated using Ansys ICEM CFD script. An implicit Reynolds-averaged Navier–Stokes (RANS) simulation with Spalart–Allmaras model is carried out using HiFUN [5] scripts. The CFD solutions obtained for a given set of geometric variables are trained and tested to arrive at a meta model using neural network radial basis function (NN-RBF). Sensitivity analysis was carried out to find the effect of design variables on the objective function. The meta model is then used by teaching–learning-based optimization (TLBO) algorithm [6] to obtain an optimized nozzle contour parameters. The optimization is carried out for a hypersonic cruise vehicle nozzle designed to fly at Mach number of 6 and an altitude of 30 km with single expansion ramp nozzle as the baseline geometry. The behavior of optimum and baseline nozzle configurations have been discussed.

A. Govinda (✉) • V.R. Kulkarni
Project Assistant, Department of Aerospace Engineering, Indian Institute of Science, Bangalore, India
e-mail: govinda.a1990@gmail.com

M.K.K. Devaraj • Y. Singh • N. Thakor
Visiting Scientist, Center of Excellence in Hypersonics, Indian Institute of Science, Bangalore, India

S.N. Omkar
Chief Research Scientist, Department of Aerospace Engineering, Indian Institute of Science, Bangalore, India

G. Jagadeesh
Professor, Department of Aerospace Engineering, Indian Institute of Science, Bangalore, India

Methodology

The flowchart of the optimization process is shown in Fig. 1. For a set of design variables, geometry coordinates are generated using Python, which is then fed into ICEM CFD for grid generation and solved using HiFUN. In-house developed Python scripts were used to automate the geometry creation, grid generation, and CFD process. The objective function used in the present work is thrust coefficient, which is calculated based on control volume analysis. The flow

G. Ben-Dor et al. (eds.), *30th International Symposium on Shock Waves 1*, DOI 10.1007/978-3-319-46213-4_19

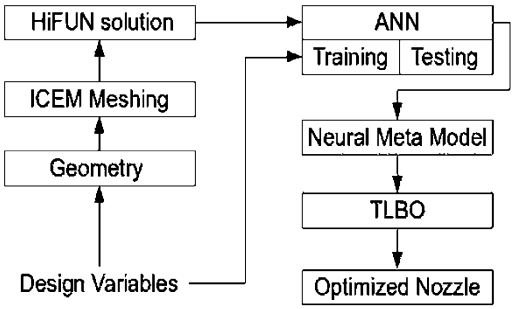

Fig. 1 Flowchart depicting the complete optimization process

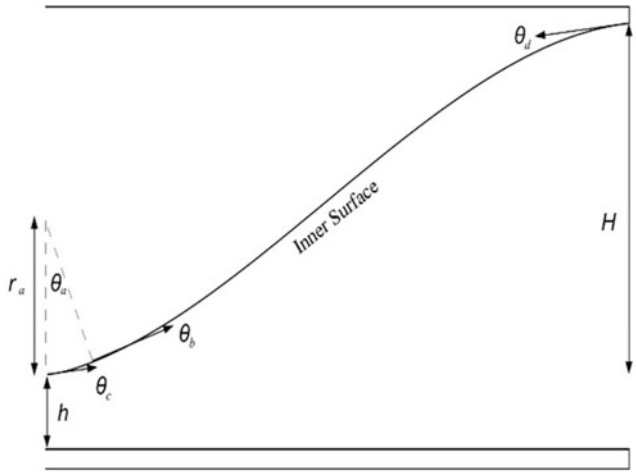

Fig. 2 Schematic of the nozzle geometry

parameters at the nozzle inlet and exit were extracted from the simulations and were integrated over their respective lengths to obtain the average flow parameters. Equation (1) is used for calculating thrust. Thrust coefficient was calculated using free-stream dynamic pressure and nozzle exit area as reference area. The set of design variables and objective function are then fed into ANN to arrive at a meta model, which is used in TLBO to arrive at thrust optimized nozzle contour.

$$T = \dot{m}\,(V_e - V_a) + (P_e - P_a)A_e \qquad (1)$$

where T = thrust, $\dot{m}$ = mass flow rate, V_e = exit velocity, V_a = velocity at the nozzle inlet, P_e = exit pressure, P_a = pressure at the nozzle inlet, and A_e = is the area ratio.

Nozzle Configuration

The nozzle geometry consists of inner surface which is defined by a circular arc and then followed by a cubic spline curve. The parameters considered for the geometry creation are combustor gradient (θ_c), nozzle entrance arc angle (θ_a), nozzle entrance radius (r_a), nozzle length (L), nozzle height (H), nozzle inlet height (h), thickness at the base (t), and inner trailing edge gradients (θ_b,θ_d) (Fig. 2). The combustor gradient (θ_c), nozzle height (H), thickness at the base (t), and nozzle inlet height (h) are fixed at 5°, 0.2, 0.02 m, and 0.0568 m, respectively.

Numerical Methods

Two-dimensional structured grid was generated with 51,070 cells that were created using ICEM CFD scripts with wall spacing of 0.05 mm based on y^+ of 1. Two-dimensional Reynolds-averaged Navier–Stokes simulations were solved using HiFUN shell scripts. The simulations were carried for the nozzle designed to fly at free-stream Mach number of 6 and altitude of 30 km. Dry air, which is treated as an ideal gas approximation, is used as a working fluid. The nozzle inflow conditions are total temperature of 2537 K, total pressure of 447,000 Pa, and jet Mach number of 1.392. These conditions were obtained from a quasi one-dimensional combustor code for hydrocarbon fuel at an equivalence ratio of 0.5. For the CFD results presented, HLLC [7] flux formula has been used for the computation of inviscid fluxes, and a diamond path reconstruction [8]-based procedure has been used for the computation of viscous fluxes. Venkatakrishnan limiter [9] is used to limit the gradients of flow variables for preserving monotonicity. Convergence acceleration is achieved by using symmetric Gauss–Seidel (SGS) implicit relaxation procedure [10]. The effect of turbulence is modeled using the Spalart–Allmaras [11] turbulence model. The simulations were carried out until density residue drops to an order of 10^{-5}, and the maximum CFL was restricted to 5 for all the simulations. The CFD process has been validated using results from available literature (Fig. 3) [12].

Optimization Algorithm

Neural network radial basis function (NN-RBF) is one of the commonly used feed-forward neural networks. It consists of three layers, namely, input layer, hidden layer, and output layer. The activation function in the hidden layer nodes is called radial basis activation function. This function has two parameters, center and spread. The center indicates where the peak of the function is centered at, and the spread indicates the width of the nonlinear curve. Back propagation is used as learning technique for the neural network. A detailed discussion on the learning algorithm is found in [13]. TLBO a population-based algorithm which is inspired

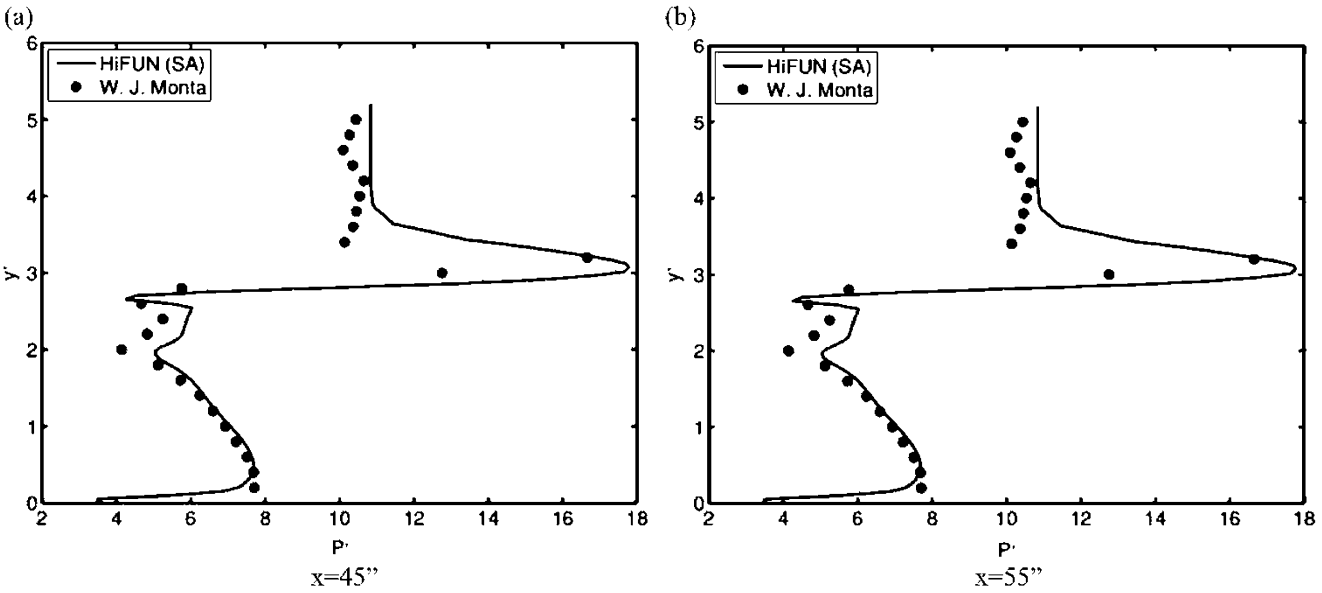

Fig. 3 Pressure comparison between numerical and experimental data along the expansion surface

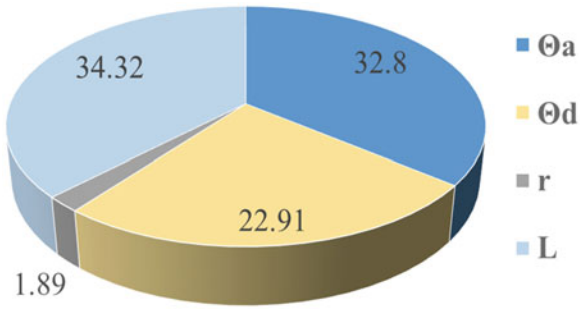

Fig. 4 Sensitivity indices of design variables

by the teaching and learning process in a classroom proposed by Rao is used in the present study. TLBO is specifically used because it is an algorithm-specific parameter-less algorithm, since there are only two common controlling parameters like population size and number of generations.

Results and Discussion

Design optimization was carried out using ANN radial basis function and TLBO using the simulations obtained from HiFUN. The meta model was obtained using 81 individuals, out of which 75 % were used for training and 25 % were used for testing. The variation of the objective function value predicted by the neural model was less than 1 % of the actual CFD simulations. This neural model was used in TLBO to obtain the thrust optimum nozzle contour. In TLBO terminology, population size is represented by number of students in a class and generation by number of classes/courses. In order to perform the optimization, the number of student = 100 in a class and number of iteration/classes = 100. Sensitivity analysis was performed to determine the effect of design variables on the objective function, using Sobol's variance decomposition [14], which generates 1000 random input variable within the limits and calculates the objective function using the meta model. Figure 4 shows the sensitivity indices of the design variables obtained using variance-based global sensitivity analysis (Fig. 4). The length of the nozzle, nozzle entrance arc angle, and inner trailing edge gradient (θ_d) seem to play a major in determining the objective function. Figure 5 represents the comparison of the design variables and objective function for the baseline and optimum geometry. The optimum and baseline nozzle contours are shown in Fig. 6. Comparison of nozzle exit velocity and pressure profile for optimum and baseline configurations is shown in Figs. 7 and 8. It is apparent from the Fig. 7 that the exit velocity from the optimum configuration is higher than that of the baseline, which leads to an increase in the momentum thrust. It is conspicuous from Fig. 8 that both the configurations are underexpanded as the exit pressures are at least an order of magnitude greater than the ambient pressure. The exit pressure of the optimum nozzle configuration is higher compared to the baseline geometry which leads to increase in the pressure thrust. The percentage increase in the thrust coefficient is tabulated in Table 1. For the optimum nozzle configuration, the thrust was found to increase by 16.7 % in comparison with the baseline configuration.

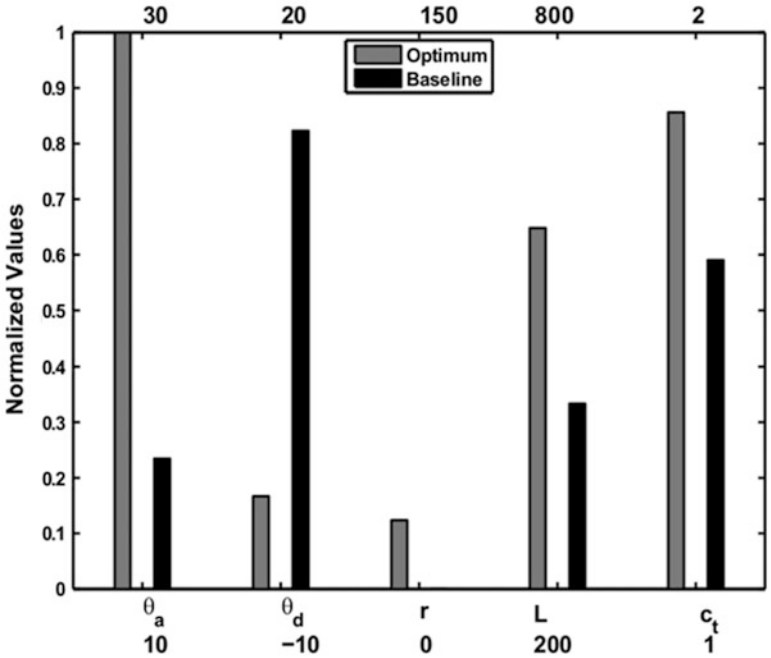

Fig. 5 Normalized design variables and objective function for optimum and baseline geometry

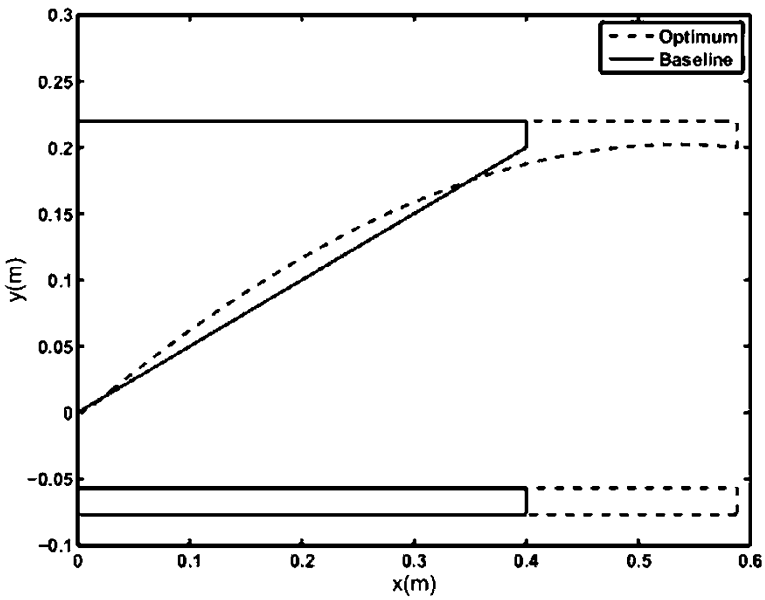

Fig. 6 Optimum and baseline nozzle contour

Conclusion

Design optimization was carried out on a slender two-dimensional nozzle contours for maximum thrust using surrogate-based optimization technique for a hypersonic cruise vehicle nozzle designed to fly at Mach number of 6 and an altitude of 30 km. For the optimum nozzle configuration, the thrust was found to increase by 16.7 % in comparison with the baseline configuration. The methodology established in this paper, using in-house developed scripts, parallel computations, and state-of-the-art

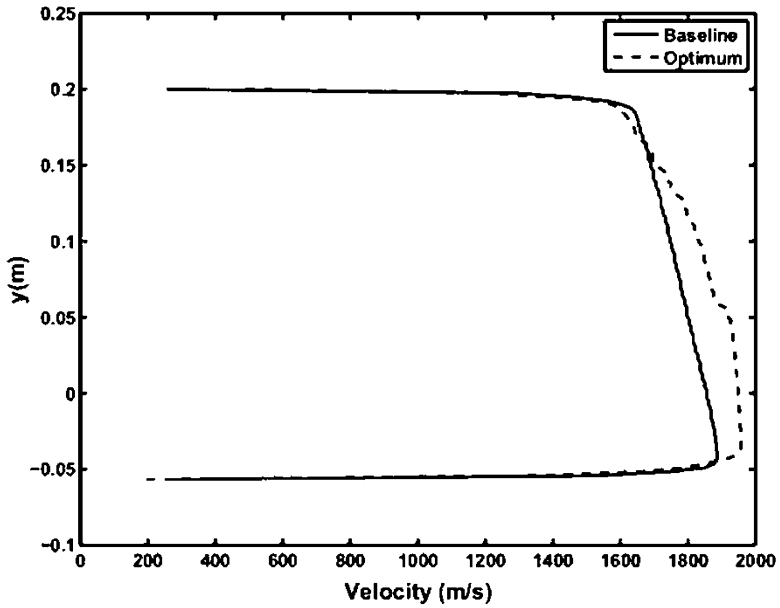

Fig. 7 Comparison of nozzle exit velocity for optimum and baseline configurations

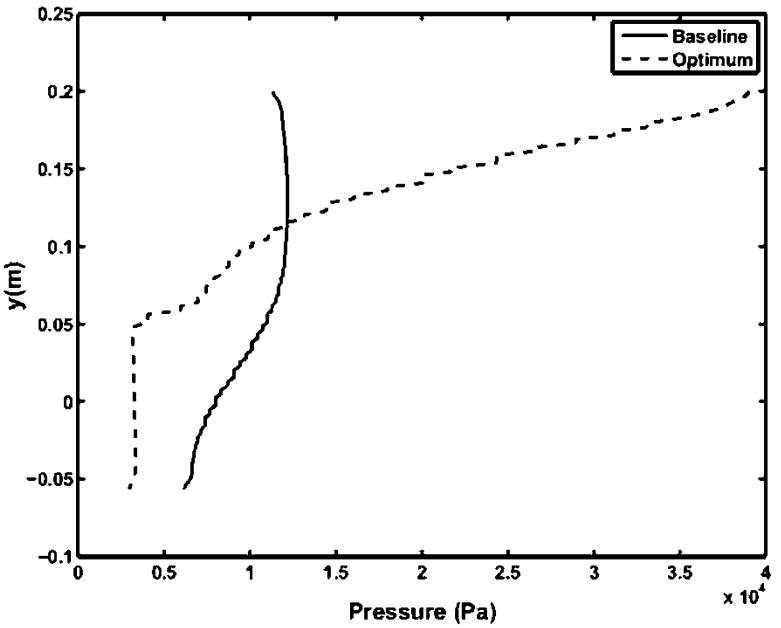

Fig. 8 Comparison of nozzle exit pressure for optimum and baseline configurations

Table 1 Comparison of percentage increase in the thrust coefficient

Thrust coefficient	Baseline	Optimum	% increase
Momentum	1.279	1.491	16.49
Pressure	0.311	0.366	17.58
Total	1.591	1.856	16.70

evolutionary algorithms can be used as an effective design tool to obtain optimized two-dimensional nozzle contours for hypersonic cruise vehicles.

References

1. Billig, F.S.: SCRAM—supersonic combustion ramjet missile. AIAA paper 93-2329 (1993)
2. Edward, T.C.: Scramjet engines: the first forty years. J. Propul. Power **17**, 1138–1148 (2001)
3. Huang, W., et al.: Design exploration for a single expansion ramp nozzle (SERN) using data mining. Acta Astronaut. **83**, 10–17 (2013)
4. Ogawa, H., Boyce, R.R.: Physical insight into nozzle flow behaviour of axisymmetric scramjets for access-to-space via design optimisation. In: Australian Space Science Conference 2010. National Space Society of Australia (2010)
5. www.sandi.co.in/

6. Venkata Rao, R., Patel, V.: An elitist teaching-learning-based optimization algorithm for solving complex constrained optimization problem. Int. J. Ind. Eng. Comput. **3**, 535–560 (2012)
7. Toro, E.F., Spruce, M., Speares, W.: Restoration of the contact surface in the HLL-Riemann solver. Shock Waves **4**, 25–34 (1994)
8. Munikrishna, N.: On viscous flux discretisation procedures for finite volume and meshless solvers. Ph.D. thesis, Department of Aerospace Engineering, Indian Institute of Science, Bangalore (2007)
9. Venkatakrishnan, V.: Convergence to steady state solutions of the Euler equations on unstructured grids with limiters. J. Comput. Phys. **118**, 120–130 (1995)
10. Shende, N.V., Balakrishnan, N.: New migratory memory algorithm for implicit finite volume solvers. AIAA J. **42**(9), 1863–1870 (2004)
11. Spalart, P.R., Allmaras, S.R.: A one-equation turbulence model for aerodynamic flows. AIAA Paper 92-0439 (1992)
12. Monta, W.J.: Pitot survey of exhaust flow field of a 2-D scramjet nozzle at Mach 6 with air or Freon and Argon used for exhaust simulation. NASA TM-4361 (1992)
13. Ranaweera, D.K., Hubele, N.F., Papalexopoulos, A.D.: Application of radial basis function neural network model for short-term load forecasting. In: Generation, Transmission and Distribution, IEE Proceedings, vol. 142. No. 1. IET (1995)
14. Sobol, I.M.: Uniformly distributed sequences with additional uniformity properties. USSR Comput. Math. Mathemat. Phys. **16**(5), 236–242 (1976)

Passive Flow Control in Laval Nozzles Due to Bypass Mass Flow in Narrow Longitudinal Gaps

M. Giglmaier, M. Krüger-Sprengel, J.F. Quaatz, and N.A. Adams

Introduction

The deceleration of supersonic nozzle flow to subsonic flow conditions via a shock involves a shock-wave/boundary-layer interaction (SWBLI). For Mach numbers $M > 1.4$, the SWBLI leads to the formation of a series of oblique shocks and rarefaction waves and forms a so-called pseudo-shock or pseudo-shock system (see Fig. 1). This phenomenon occurs in a broad field of technical applications that range from aerospace to process engineering. Although the topic has already been investigated since the early 50s, several aspects are still of great interest, such as reduction of total pressure loss, mixing mechanism, or flow stabilization. A recommendable review of the topic is given by [1].

Investigation of a Pseudo-Shock System in a Slender Nozzle

In order to visualize a pseudo-shock system by schlieren technique, windows are typically mounted on both sides of the test section. However, to avoid strong stresses within the quartz glass, these windows cannot be flush-mounted to the facility. Thus, small gaps occur between the quartz glass sidewalls and the metal nozzle contour. The effect of these gaps onto the main flow was studied experimentally at the DLR in Cologne (e.g. [2]) and numerically at our institute. A simple sketch of the investigated Laval nozzle is shown in Fig. 2—detailed information about the geometry of the entire test facility can be found in [3].

During our numerical investigations, we observed significant differences concerning the pressure distribution along the nozzle wall and the shock location, if these small gaps with a width of $\delta = O(10^{-4})$ m were considered. Subsequent experiments confirmed the numerical results. We showed that within the gaps, a massive reverse flow establishes itself, which determines the size and the shape of the separation zones occurring at the foot of the oblique primary shock. Hence, the gaps determine the shape of the entire pseudo-shock system [4]. Extensive unsteady flow simulations of the nozzle geometry with gaps revealed that the shear layer between subsonic gap flow and supersonic core flow is subject to a Kelvin-Helmholtz instability resulting in small pressure fluctuations. We showed that these fluctuations can trigger the low frequency shock oscillation [3, 5].

Continuative unsteady Reynolds Averaged Navier-Stokes (URANS) simulations of the full channel geometry confirmed the assumption that the gaps also affect the orientation of the entire shocktrain. In the slender Laval nozzle without gaps, experimental and numerical simulations demonstrated that the pseudo-shock system tends to break its symmetric behavior with increasing pre-shock Mach number. Figure 3a shows the calculated Mach number distribution on the symmetry plane for the gap-free configuration. Below, the 3-D shape of the corresponding pseudo-shock system is shown. The supersonic part of the flow is visualized by the Mach number $M = 1$ iso-surface (yellow), whereas recirculation zones are indicated by the blue iso-surface corresponding to an axial velocity of $u_x = -10$ m/s. Despite unsteady simulations, a steady result is obtained. The shocktrain shows a distinct asymmetry and is bent to the lower channel wall.

In contrast, the flow inside the nozzle with gaps shows a symmetric behavior (see Fig. 3b). Since the gaps are very thin compared to the boundary layer thickness, the flow within the gaps is purely subsonic, and hence, a bypass mass flow is initiated from the high-pressure post-shock region through the gaps into the low-pressure region upstream of the primary shock. Thus, massive corner separations occur and shift the pseudo-shock system from

M. Giglmaier (✉) • M. Krüger-Sprengel • J.F. Quaatz • N.A. Adams
Institute of Aerodynamics and Fluid Mechanics, Technische Universität München, Boltzmannstrasse 15, Garching 85748, Germany
e-mail: marcus.giglmaier@mytum.de

G. Ben-Dor et al. (eds.), *30th International Symposium on Shock Waves 1*, DOI 10.1007/978-3-319-46213-4_20

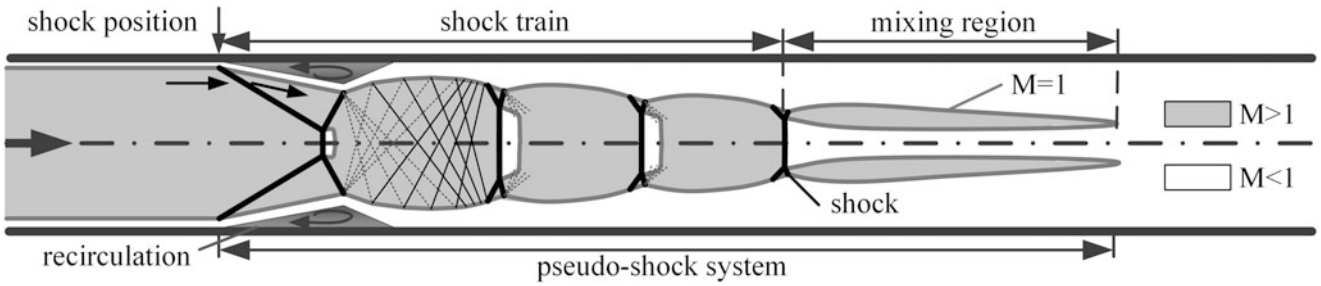

Fig. 1 Schematic sketch of a pseudo-shock system

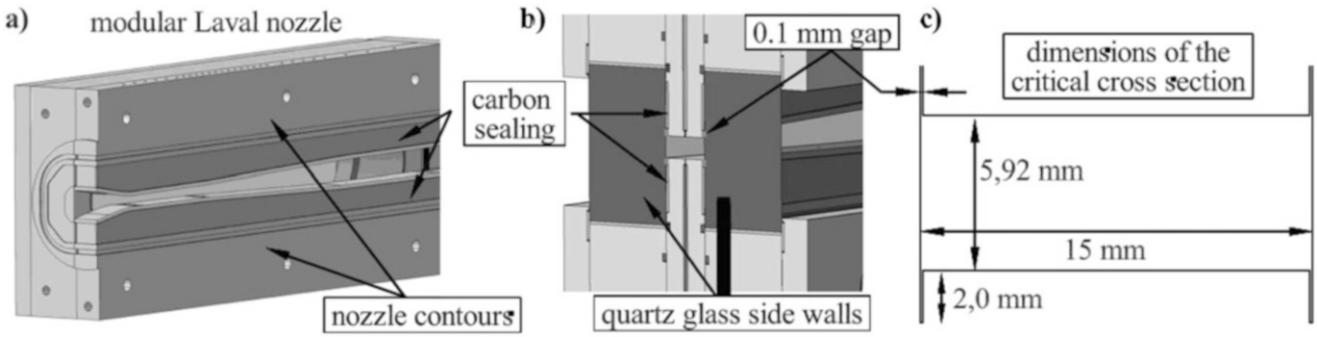

Fig. 2 (**a**) Modular setting of the primary nozzle, (**b**) Cut view through the critical cross section, (**c**) Dimensions of the critical cross section with gaps

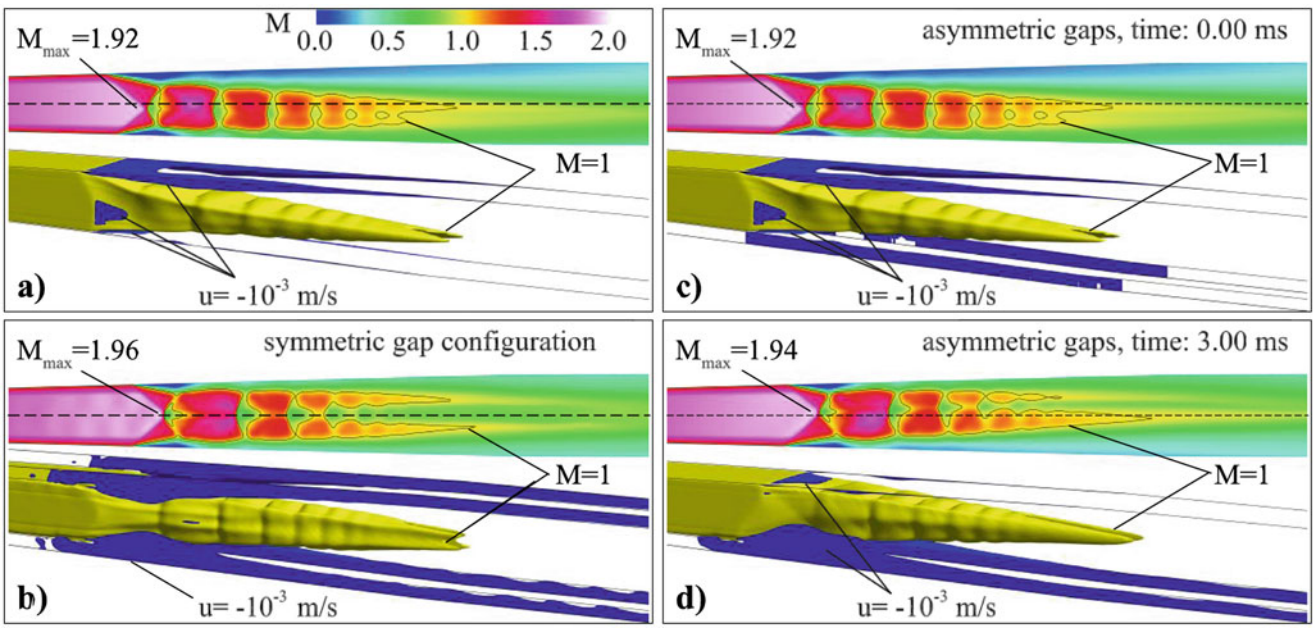

Fig. 3 *Top*: Calculated Mach number distribution of a pseudo-shock system at the symmetry plane within a slender Laval nozzle. *Bottom*: 3-D shape of the corresponding pseudo-shock system with $M = 1$-iso-surface (*yellow*) and recirculation zones (*blue*). (**a**) Configuration without gaps in the channel corners. (**b**) Configuration with gaps in the channel corners. (**c**) Initial condition for a configuration with gaps solely at the lower channel corners. (**d**) Result for a calculated flow time of $\Delta t = 3$ ms

the corners towards the center of the channel. Due to the interaction between gap and core flow, the simulation shows a very unsteady behavior. Nevertheless, the breakage of symmetry is compressed and the shocktrain stays stable at the channel center.

A further simulation with gaps solely on the lower nozzle side demonstrates that the massive recirculation zones (induced by the reverse flow through the gaps) have the ability to deflect the supersonic core flow. The flow field was initialized with the asymmetric result of the gap-free configuration (compare Fig. 3a, c). Upon starting the simulation, the flow inside the gaps downstream of the primary shock is accelerated into upstream direction due to the high pressure gradient. After a calculated flow time of $\Delta t = 3$ ms, two massive flow separations established in the corners of the lower nozzle contour. As assumed, the supersonic core flow is clearly deflected to the upper channel wall.

Numerical Investigation of the Experiments by Reijasse et al. [6]

Above-mentioned findings led to the conclusion that the orientation of pseudo-shock systems can be defined by purposefully placed small gaps along the nozzle contour. This could, for example, be of interest for the intake of Ram and Scramjets. Other conceivable applications are rocket engines: since the propulsive nozzle performance is typically increased by enhancing the expansion ratio, the flow regime of these nozzles at the ground is normally highly overexpanded. Hence, flow separation inside the nozzle occurs. Asymmetric side load in consequence of single-sided flow separation is not only reducing the performance, but can cause complete damage of the engine.

One experimental study on this subject was published by Reijasse et al. [6]. They analyzed the axial shock oscillation as well as the establishment of asymmetric shock configurations in a two-dimensional planar Mach 2 nozzle by LDV, wall pressure measurements, and schlieren visualization. Continuative work containing surface flow and a more detailed analysis of the experimental data was published by Bourgoing and Reijasse [7, 8].

A small sketch of the Onera S8Ch wind tunnel is shown in Fig. 4a. The primary nozzle has a critical cross section of $A_1^* = 120 \times 74.18\,\mathrm{mm}^2$. The shock position can be adjusted by a second Laval nozzle with variable cross section ($A_{2,\max}^* = 120 \times 120\,\mathrm{mm}^2$). The distance between first and second throat is $l = 600$ mm. For an area ratio of $A_2^*/A_1^* = 1.28$, Reijasse et al. [6] observed three different flow configurations: an axis symmetric shocktrain, a shocktrain oriented to the lower channel wall (referred to as *type 1*), and a shocktrain oriented to the upper channel wall (referred to as *type 2*). As [6] states, each of the asymmetrical cases is

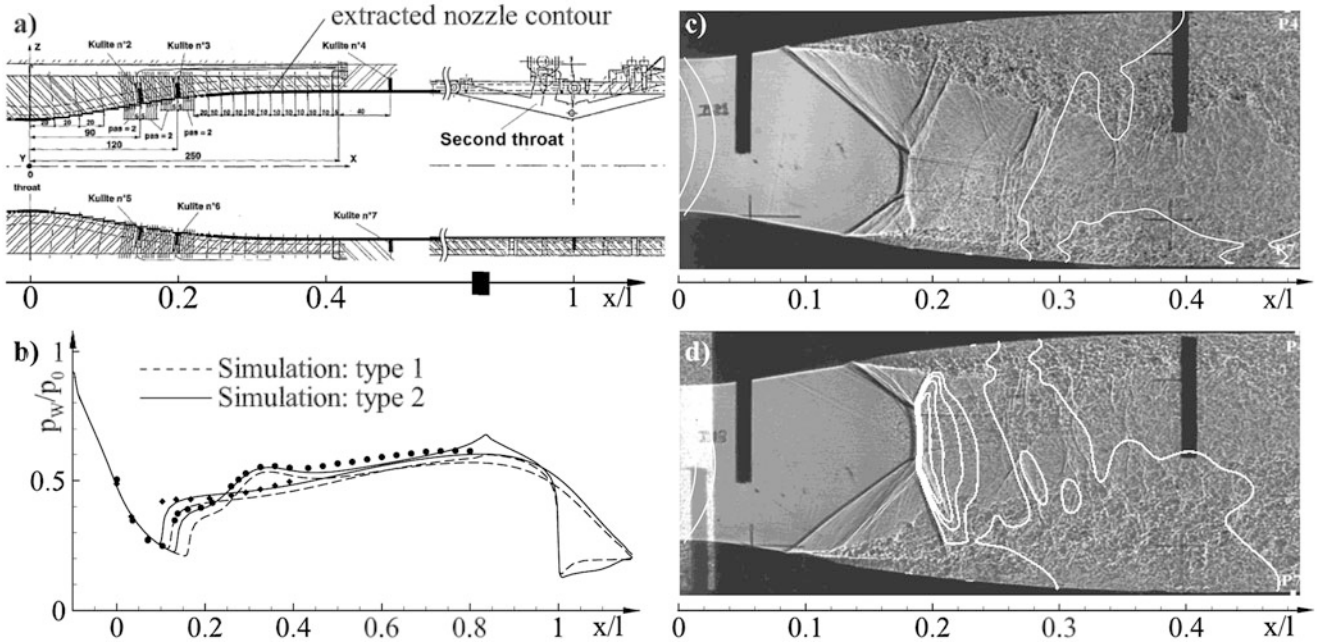

Fig. 4 (**a**) Sketch of the Onera S8Ch wind tunnel by [6], the nozzle curvature was extracted with [9]. (**b**) Experimentally (*dots* [6]) and numerically (*solid and dashed line*) obtained wall pressure distribution along the nozzle symmetry for the type 1 and type 2 asymmetric shocktrain. (**c**) Experimentally obtained schlieren picture of the type 1 asymmetric shocktrain by [6] along with numerically obtained contours of constant pressure ($\Delta p = 5$ kPa). (**d**) According to description of Fig. 4c, but for the type 2 asymmetric shocktrain

stable and they never observed a "bascule" phenomenon, whereas the symmetrical case tends to bascule to one of the asymmetric cases. Since we want to evaluate, if pseudo-shock systems can be stabilized at the axis by passive flow control via small gaps, we will focus on the two asymmetric cases. In order to perform comparable numerical simulations, we had to extract the geometry from the paper. This was realized with [9]. The extracted nozzle contour is also shown in Fig. 4a.

The flow was simulated with the commercial solver Ansys CFX. Boundary conditions were chosen according to the mean conditions reported in [6]. The entire channel including the second critical cross section is resolved by $\approx 5.4 \times 10^6$ finite volumes and all boundary layers are resolved by at least 20 finite volumes in wall-normal direction, so that a dimensionless wall distance of $y^+ \leq 1$ is ensured. An explicit algebraic Reynolds stress turbulence model (BSL EARSM) is applied since the occurrence of secondary flow, such as corner vortices in the square cross section, has to be resolved. Previous investigations clearly demonstrated best results for this turbulence model [3].

A comparison of the calculated and the measured dimensionless wall pressure distribution is depicted in Fig. 4b. In contrast to [6], we observed different shock positions and accordingly different pressure distributions for the *type 1* and *type 2* shock configuration. This is even more obvious by comparing the experimentally obtained schlieren pictures of [6] with the calculated contours of constant pressure (see Fig. 4c, d).

The *type 2* shock configuration (Fig. 4d) shows a remarkable good agreement. Angle and position of the initial oblique shock at the upper nozzle wall, size and position of the following Mach reflection as well as angle and length of the reflected shock match the experiment. The same counts for the shock at the lower nozzle wall with the exception that the primary oblique shock in the experiment is not completely two-dimensional. Hence, the schlieren picture exhibits one further primary shock a little bit upstream.

In contrast, the calculated *type 1* shock configuration (Fig. 4c) is much further downstream compared to the experiment, and thus, a higher pre-shock Mach number is predicted by the simulation. According to the 1-D theory, the ratio of total pressure within a double chocked Laval nozzle system is proportional to the inverse ratio of the critical cross sections. Hence, the overall losses have to be constant in both cases. A higher pre-shock Mach number causes a higher shock loss of total pressure. Thus, losses due to friction for *type 1* must be smaller than for *type 2*.

To the authors' careful interpretation of the flow, other 3-D effects have to be considered too. The flow within the second throat shows a narrower Mach number distribution around $M = 1$. Consequently, the mass flow density $\rho \cdot u_x$ is higher and the virtual critical cross section is bigger than for the *type 2* case. The fact that this difference cannot be detected in the experiment leads to the conclusion that turbulent mixing within the shear layers is under-predicted by the turbulence model. A comparison of the BSL-EARSM turbulence model with a well-resolved large eddy simulation (LES) by Quaatz et al. [10] clearly supports this assumption.

Passive Flow Control with Narrow Longitudinal Gaps

As shown in section "Investigation of a Pseudo-Shock System in a Slender Nozzle," the reverse flow through gaps has the potential to stabilize or even redirect a pseudo-shock system in a slender nozzle. In order to clarify if this mechanism is applicable also to larger nozzles, we apply several gap configurations to the asymmetric nozzle flow investigated in section "Numerical Investigation of the Experiments by Reijasse et al. [6]." The presented results were obtained with a longitudinal gap ranging from $x_1 = 70$ mm to $x_1 = 140$ mm. For reference, the first shock appears at $x_1 \approx 100$ mm. The gap width δ_1 is twice the subsonic part of the boundary layer in order to ensure subsonic flow conditions within the gaps. The presented gap height is $h_1 = 5 \cdot \delta_1$, the distance between the gaps is $\delta_2 = 2 \cdot \delta_1$. For clarity, all dimensions are depicted in Fig. 5.

Since a comparison to the experiment is not possible, the numerical effort is reduced by considering only a section in the center of the channel. The flow field is initialized with

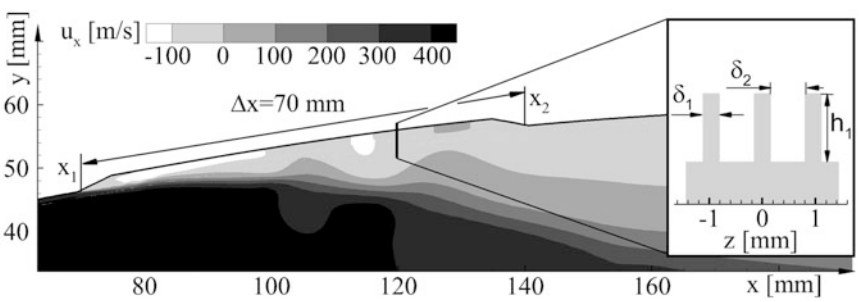

Fig. 5 Position, length, height, and width of the considered gaps: $x_1 = 70$ mm, $x_1 = 140$ mm, $h_1 = 1.6$ mm, $\delta_1 = 0.32$ mm, $\delta_2 = 0.32$ mm. The contour plot shows the axial velocity distribution $u_x = 0$ m/s on the symmetry plane within the gap

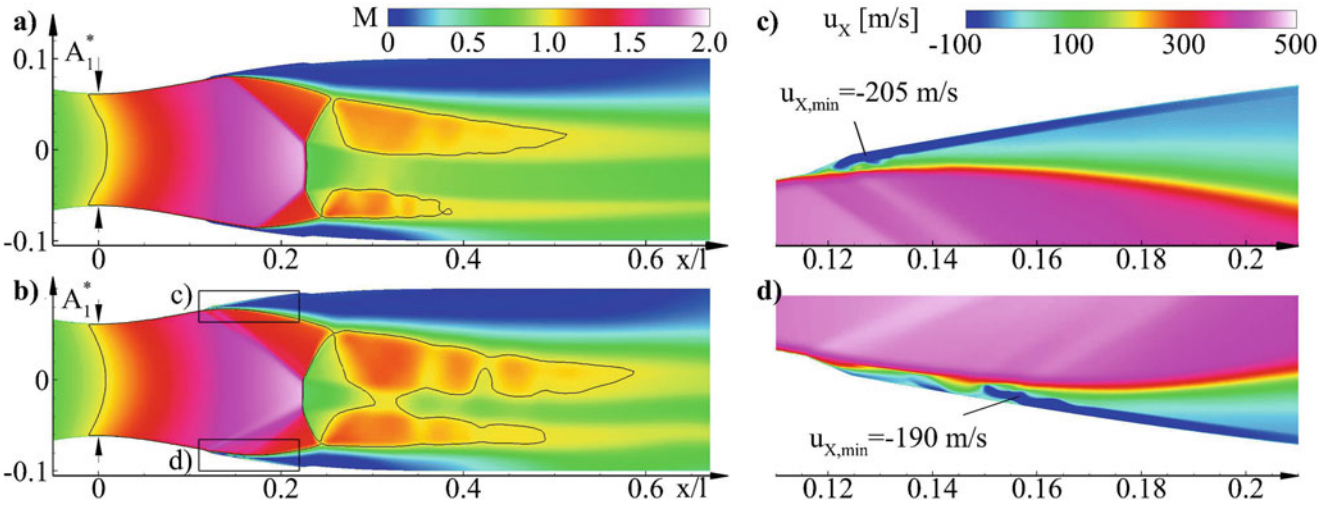

Fig. 6 Temporal evolution of the flow within the nozzle considering gaps. (**a**) Mach number distribution on the center plane for $t = 0$ s. (**b**) Mach number distribution on the center plane for $t = 3.3 \times 10^{-3}$ s. (**c**) Axial velocity within the upper gap (**d**) Axial velocity within the lower gap

the result of a 2-D calculation for a configuration without gaps (see Fig. 6a). Comparable to the previous discussed case, a reverse flow is initiated immediately after beginning the calculation. Within a calculated flow time of $\Delta t = 3.3$ ms, the foot of the first shock at the upper wall moves even further upstream (see Fig. 6b). The bypass mass flow re-enters the main flow and leads to a more continuous deflection of the supersonic core flow, and hence, the involved oblique shock appears smoothed. A similar behavior can be noticed at the lower channel wall, but the effect is clearly reduced. To distinguish the different flow conditions, the distribution of the axial velocity u_x within the upper and lower gap are shown in Fig. 6c, d. The locations of the cutouts are depicted by the black boxes in Fig. 6b.

Concluding Remarks

Although the behavior of the bypass mass flow through the longitudinal gaps and the interaction with the supersonic core flow is comparable to the flow within the slender nozzle, the effect is too weak in this configuration. A higher mass flow through the gaps is required to achieve a more intense impact onto the core flow. Since the gap width cannot be increased without expecting supersonic flow conditions, an increased gap height will be analyzed in the ongoing simulations.

Acknowledgments The authors thank Dr. Thomas Gawehn for the fruitful cooperation. Gruß und Kuss, dein Julius.

References

1. Matsuo, K., Miyazato, Y., Kim, H.-D.: Shock train and pseudo-shock phenomena in internal gas flows. Prog. Aerosp. Sci. **35**(1), 33–100 (1999)
2. Gawehn, T., Gu¨lhan, A., Giglmaier, M., Al-Hasan, N.S., Quaatz, J. F., Adams, N.A.: Analysis of pseudo-shock system structure and asymmetry in Laval nozzles with parallel side walls. In: 19th International Shock Interaction Symposium—ISIS19, Moscow, Russia, 31 August–3 September 2010
3. Giglmaier, M., Quaatz, J., Gawehn, T., Gülhan, A., Adams, N.: Numerical and experimental investigations of pseudo-shock systems in a planar nozzle: impact of bypass mass flow due to narrow gaps. Shock Waves **24**(2), 139–156 (2014)
4. Giglmaier, M., Quaatz, J.F., Gawehn, T., Gülhan, A., Adams, N.A.: Numerical and experimental investigation of the effect of bypass mass flow due to small gaps in a transonic channel flow. In: 28th International Symposium on Shock Waves—ISSW 28, Manchester, UK, 17 July–22 July 2011
5. Giglmaier, M., Quaatz, J.F., Adams, N.A., Gawehn, T., Gühlhan, A.: Impact of bypass mass flow on shock motion in pseudo-shock systems. In: 20th International Shock Interaction Symposium—ISIS20, Stockholm, Sweden, 20 August–24 August 2012
6. Reijasse, P., Corbel, B., Soulevant, D.: Unsteadiness and asymmetry of shock-induced separation in a planar two-dimensional nozzle: a flow description. 1999
7. Bourgoing, A., Reijasse, P.: Experimental investigation of an unsteady and asymmetrical supersonic separated flow. Technical Report, ONERA-TP–01-95, 2001
8. Bourgoing, A., Reijasse, P.: Experimental analysis of unsteady separated flows in a supersonic planar nozzle. Shock Waves **14**, 251–258 (2005)
9. Rohatgi, A.: WebPlotDigitizer. http://arohatgi.info/WebPlotDigitizer. 2015. Version: 3.8
10. Quaatz, J., Giglmaier, M., Hickel, S., Adams, N.: Large-eddy simulation of a pseudo-shock system in a Laval nozzle. Int. J. Heat Fluid Flow **49**(C), 108–115 (2014)

Part III

Hypersonic Flow

Investigation of Chemical Non-equilibrium Hypersonic Flows in Carbon Dioxide–Nitrogen Atmospheres Using a Coupled Euler–Boundary-Layer Method

M. Starkloff and Ch. Mundt

Introduction

Summary

Re-entry flights in carbon dioxide–nitrogen atmospheres such as Mars and Venus became more and more the focal point of interest in the research community lately. During these re-entry flights at hypersonic velocities, a high-enthalpy flow field is generated behind the bow shock. Due to this high-enthalpy flow field, the constituent chemical species inside this field undergo several significant real gas effects, for example, dissociation. With respect to typical re-entry trajectories starting at high altitudes, low density/low pressure regions are passed during re-entry flights, whereby dissociation occurs at a wide range, starting at relatively low gas temperatures affecting aspects like surface chemistry or wall heat fluxes significantly. Therefore it is important to generate accurate thermodynamic, kinetic and transport models with a chemical non-equilibrium approach, where the conservation equations for momentum, total energy and balance equations are solved for each species in the dissociated flow field. Due to the fact that plasma and shock tunnels are subject to several shortcomings, the importance of efficient numerical simulations is still steadily increasing. Furthermore the Navier–Stokes equations, which are still the most comprehensive equations for continuum fluid dynamics, simultaneously are the most computational costly ones. Therefore the usage of an efficient and accurate numerical approach, which is less general, but generates the same order of accuracy in its domain of application, like the coupled Euler–second-order boundary-layer method, is very promising. As long as there are no strong interactions between the viscous and the inviscid flow, the method described here generates analogous flow physics compared to the Navier–Stokes solutions. Also it already proved its good agreements with numerical simulations of the Navier–Stokes solutions for blunt re-entry bodies at high angles of attack and medium to low altitudes [1].

Numerical Approach

A shock-fitting method is applied here using a fourth-order central finite-difference scheme to discretize the bow shock. To handle strong bow shocks in hypersonic flows, effective Rankine–Hugoniot relations are implemented to soften the numerical stiffness and incorporate the effects of the chemical layer at the shock when necessary [2]. Furthermore a third-order upwind finite-difference algorithm based on the integration of quasi-conservative Euler equations for the simulation of the inviscid flow in chemical non-equilibrium is used, including an explicit three-step Runge–Kutta time-stepping scheme with point-implicit chemical source term treatment [2]. Here a split-matrix method is implemented. For the simulation of the viscous flow, second-order boundary-layer equations for a mixture of thermally perfect gases in chemical non-equilibrium derived from non-dimensional Navier–Stokes equations are used [1]. These equations are discretized using a second-order accurate Crank–Nicolson difference scheme, where a constant relative resolution is obtained by normalizing the coordinate normal to the wall with local boundary-layer thickness [1]. The equations containing second derivatives are solved implicitly and simultaneously using the Thomas algorithm [1]. Due to the fact one is dealing with a boundary value problem, the outer edge boundary conditions are obtained by interpolating all variables from the inviscid profiles and are therefore coupled to the Euler method [3]. At the wall several different combinations of boundary conditions are possible, depending on the physical and chemical conditions demanded [3].

M. Starkloff (✉) • Ch. Mundt
Institute of Thermodynamics, University of the Federal Armed Forces Munich, Neubiberg 85577, Germany
e-mail: martin.starkloff@unibw.de

G. Ben-Dor et al. (eds.), *30th International Symposium on Shock Waves 1*, DOI 10.1007/978-3-319-46213-4_21

At first the inviscid Euler flow is solved until convergence is achieved. As mentioned above, the values obtained here are used to interpolate the outer edge boundary conditions for the second-order boundary equations. The initial values for the boundary layer simulation are obtained by solving the stagnation point equations [1]. The resulting system of partial differential equations of the boundary layer is parabolic in space; therefore a space-marching technique is applied, stepping first in circumferential and then downstream direction [3]. The boundary layer solution again provides an equivalent source distribution, which is used as boundary condition for the second-order Euler equations. Here viscous effects of second order, like entropy-layer swallowing, are already considered [3]. After iterating to convergence a second time, the second-order boundary layer is computed until convergence again. In accordance to the theory of small disturbances, the simulation cycle has to be stopped after the second simulation to preserve the parabolic character of the boundary-layer equations [4].

Thermodynamic Properties

The mixture pressure p is obtained using Dalton's law of partial pressures and the perfect gas law for each species [2].

$$p = \sum_s \rho_s \frac{R_u}{M_s} T \tag{1}$$

The total energy is given by $e = \sum_s \rho_s \cdot h_s(T) + \rho/2 \cdot (u^2 + v^2 + w^2) - p$, where h_s is the species enthalpy [2]. The species enthalpy and entropy, for example, can be obtained from curve fits of the form

$$\frac{h_s}{R \cdot T} = -\frac{a_{1_s}}{T^2} + a_{2_s} \cdot \frac{\ln(T)}{T} + a_{3_s} + a_{4_s} \cdot \frac{T}{2} + a_{5_s} \cdot \frac{T^2}{3} + a_{6_s} \cdot \frac{T^3}{4} + a_{7_s} \cdot \frac{T^4}{5} + \frac{a_{8_s}}{T}, \tag{2}$$

$$\frac{s_s}{R} = -\frac{a_{1_s}}{2 \cdot T^2} - \frac{a_{2_s}}{T} + a_{3_s} \cdot \ln(T) + a_{4_s} \cdot T + a_{5_s} \cdot \frac{T^2}{2} + a_{6_s} \cdot \frac{T^3}{3} + a_{7_s} \cdot \frac{T^4}{4} + a_{9_s} \tag{3}$$

Refs. [5, 6].

Because the total enthalpy $h_0 = (e + p)/\rho$ is a constant along stream lines in the steady state, which is also correct across the shock and for non-equilibrium flows, the total energy e can be corrected after each iteration to aid the convergence rate and robustness of the code, reproducing the total enthalpy of the free stream [2]. Thus $e = \rho \cdot h_0^\infty - p$ [2].

Transport Properties

In this approach the species transport properties of the viscous boundary layer are computed using the results of the Chapman–Enskog theory and (m, n) Lennard–Jones potentials as well as the Wilke mixing rule for the transport properties of the mixture [3].

The resulting equations for each species are for the viscosity:

$$\mu_s = 2.6693 \cdot 10^{-6} \cdot \frac{\sqrt{M_s \cdot 1000 \cdot T}}{\sigma_s^2 \cdot \Omega^{*(2,2)}(T^*)}, \tag{4}$$

for the thermal conductivity for nonmolecular species:

$$\kappa_s = 8.334 \cdot 10^{-2} \cdot \frac{\sqrt{T/(M_s \cdot 1000)}}{\sigma_s^2 \cdot \Omega^{*(2,2)}(T^*)}, \tag{5}$$

for molecular species, taking transport of energy by rotatory and vibratory degrees of freedom into account applying the semiempirical Eucken correction:

$$\kappa_s = \frac{\mu_s \cdot c_{ps} + 5/4}{R_u}, \tag{6}$$

and for the binary diffusion coefficient:

$$D_{s,l}^{\text{bin}} = 2.264 \cdot 10^{-3} \cdot \frac{\sqrt{T \cdot 10^{-3} \cdot (1/M_s + 1/M_l)} \cdot M}{\sigma_s^2 \Omega^{*(1,1)}(T^*) \rho} \tag{7}$$

Refs. [1, 3, 7].

Here σ_s is the cross section, $\Omega^{*(1,1)}$ the reduced collision integral related to diffusion and $\Omega^{*(2,2)}$ the one related to viscosity and thermal conductivity, which can be obtained, e.g. by state-of-the-art data and curve fits [8–10]. Polynary diffusion coefficients can be obtained by:

$$D_{s,l} = \frac{n_s}{\frac{n_l}{D_{s,l}^{\text{bin}} \sqrt{D_{s,s}^{\text{bin}} / D_{l,l}^{\text{bin}}}} + \sum_{k \neq l} \frac{n_k}{D_{k,l}^{\text{bin}}}} + \frac{\frac{M - M_s \cdot n_s}{M_l}}{\frac{n_l}{D_{s,l}^{\text{bin}} \sqrt{D_{l,l}^{\text{bin}} / D_{s,s}^{\text{bin}}}} + \sum_{k \neq s} \frac{n_k}{D_{s,k}^{\text{bin}}}} \tag{8}$$

Refs. [1, 3].

Chemistry Model

A finite-rate chemistry model, using the extended Arrhenius approach, is implemented here. The number of species and

reactions is depending on the chosen reaction scheme. The five- and six-species model is using a pure CO_2 as free stream, while the eight- and ten-species model uses the typical Martian atmosphere composition of 97 % CO_2 and 3 % N_2. Ar is neglected as a minor species. The system of n_s species in n_r reactions can be written as:

$$\sum_{s=1}^{n_s}\left[\alpha_{s,r}\frac{\rho_s}{M_s}\right] \Leftrightarrow \sum_{s=1}^{n_s}\left[\beta_{s,r}\frac{\rho_s}{M_s}\right];\quad r=1,\ldots,n_r, \tag{9}$$

and the source terms are of the form:

$$\omega_s = M_s\sum_{r=1}^{n_r}\left[(\beta^{s,r}-\alpha^{s,r})\cdot\left(k_{f,r}(T)\prod_{s=1}^{n_s}\left(\frac{\rho_s}{M_s}\right)^{\alpha^{s,r}} - k_{b,r}(T)\prod_{s=1}^{n_s}\left(\frac{\rho_s}{M_s}\right)^{\beta^{s,r}}\right)\right];$$
$$S=1,\ldots,n_s. \tag{10}$$

While the forward reaction rate $k_{f,r}(T) = C\cdot T_x^n\cdot \exp(-T_d/T_x)$ can be calculated directly [10], the backward reaction rate $k_{b,r}(T)$ can be obtained through detailed balancing $k_{b,r}(T) = k_{f,r}(T)/K_r^{\mathrm{eq}}(T)$ [3]. The equilibrium constant can be calculated through the minimization of Gibbs free energy, where the reference pressure p_0 is set to 1 bar and h_s and s_s can be obtained from curve fits pictured above:

$$K_r^{\mathrm{eq}} = \left(\frac{p_0}{RT}\right)^{(\beta^{s,r}-\alpha^{s,r})}\exp\left(-\sum_s(\beta^{s,r}-\alpha^{s,r})\left[\frac{h_s}{RT}-\frac{s_s}{R}\right]\right). \tag{11}$$

The following figures show, e.g. the mass fractions over the temperature of a pure CO_2 and a 97 % CO_2 and 3 % N_2 atmosphere model at constant pressure (Figs. 1 and 2).

Results

In the following description simulations, using the chemical non-equilibrium pure CO_2 and Martian atmosphere models are compared with chemical equilibrium simulations using state surfaces and a similar numerical approach [12]. Figure 3 shows the hyperbola, which is used as a test configuration. The mesh for the Euler computation consists of 56 × 33 points, while the mesh of the boundary layer consists of 101 points normal to the wall to reach good resolutions of the strong gradients. The flow conditions at an angle of attack of 0° are in case 1:

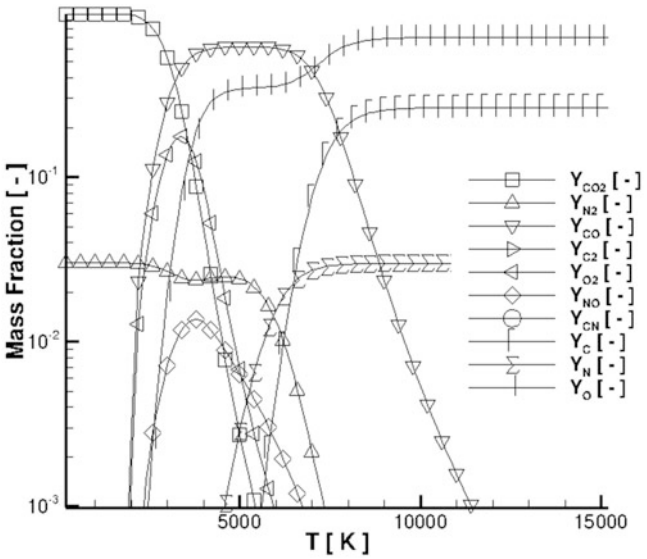

Fig. 2 Ten-species 80-reaction model

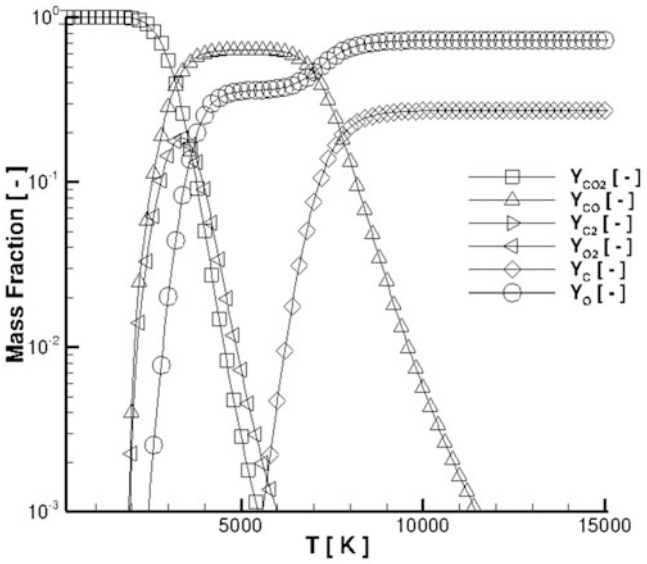

Fig. 1 Six-species 27-reaction model

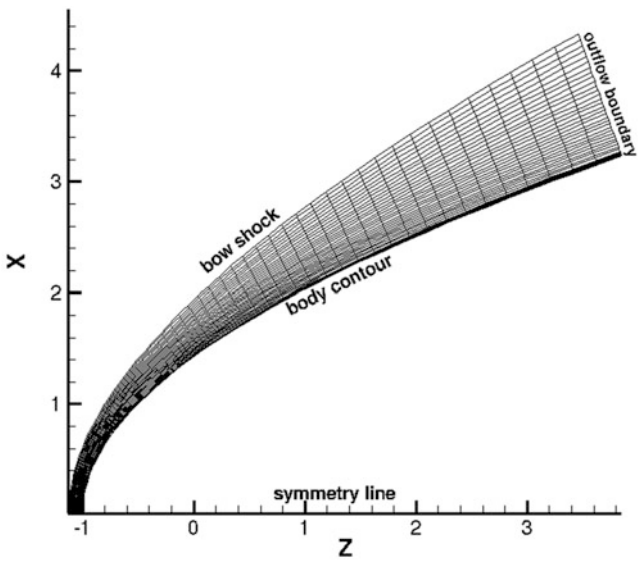

Fig. 3 Hyperbola test configuration

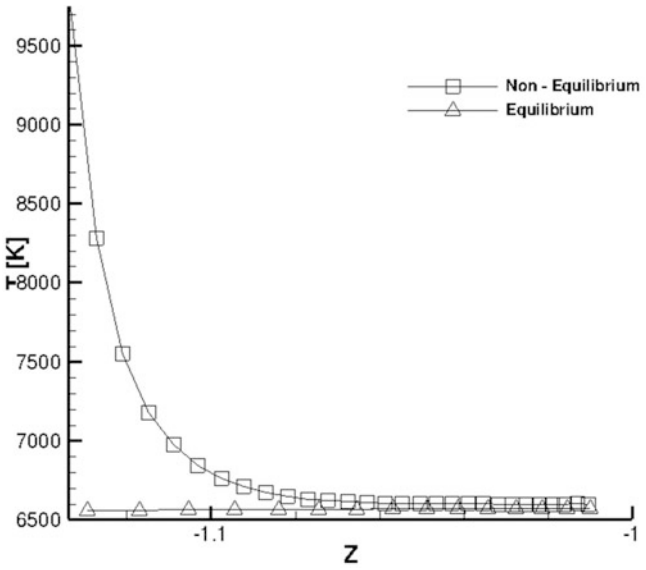

Fig. 4 Case 3 stagnation line temperature

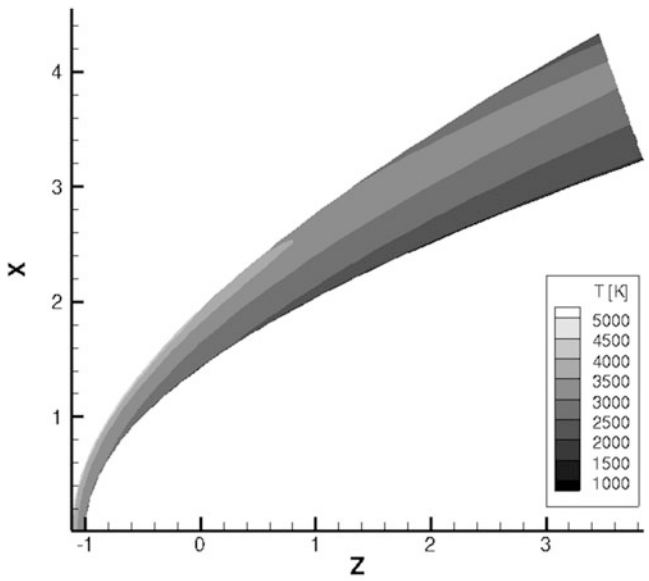

Fig. 5 Case 1 six-species model

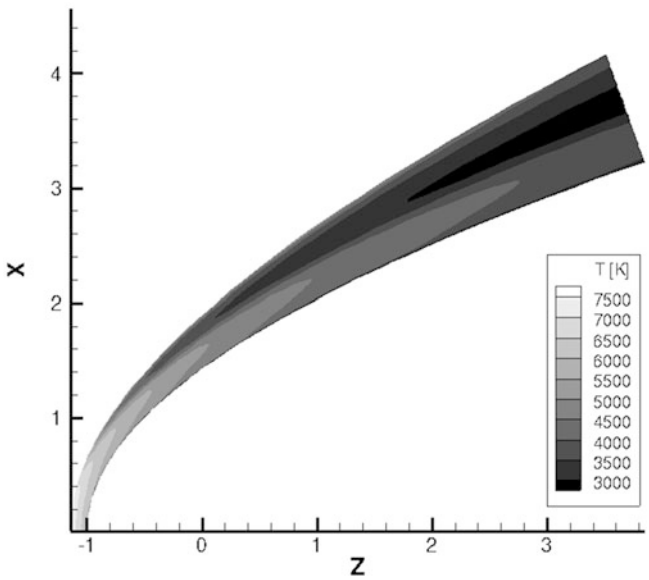

Fig. 6 Case 2 six-species model

$$p_{\text{ref}} = 14.14\,\text{Pa}, \quad \rho_{\text{ref}} = 4.2484 \cdot 10^{-4}\,\text{kg/m}^3,$$
$$T_{\text{ref}} = 174.18\,\text{K}, \quad v_{\text{ref}} = 4645.2\,\text{m/s},$$

and in case 2 analogous to case 1 but $v_{\text{ref}} = 6756.6\,\text{m/s}$ and in case 3:

$$p_{\text{ref}} = 17.66\,\text{Pa}, \quad \rho_{\text{ref}} = 5.3519 \cdot 10^{-4}\,\text{kg/m}^3,$$
$$T_{\text{ref}} = 171.82\,\text{K}, \quad v_{\text{ref}} = 7549.6\,\text{m/s},$$

while an adiabatic and non-catalytic wall condition and radiative equilibrium at the body, with a surface emissivity factor of $\varepsilon = 0.9$, are set.

Figure 4 not only shows the consistency of the chemical non-equilibrium and the equilibrium approach; it also depicts the strong influence of non-equilibrium effects of a ten-species 80-reaction model on the thermodynamic properties of the flow.

Due to the strong dissociation effects in chemical non-equilibrium behind the bow shock, the temperature is decreasing significantly towards an equilibrium condition, while the stagnation line temperature of the equilibrium simulation is increasing slightly due to the deceleration of the flow towards the stagnation point.

Figure 5 and 6 show the temperature distribution of the flow field of the six-species model at different velocities. Here one can not only see a significant higher temperature distribution at higher velocity as well as strong gradients behind the bow shock but also a remarkable smaller shock standoff distance as well as a compression of the flow field.

Figure 7 shows the concentration layer of CN, which is a strong radiator, behind the bow shock in the stagnation line region. Due to the strong influence of species included in the chemical reaction system on the behaviour of the flow and in particular CO, C_2, C and CN on gas radiation effects, a comprehensive and accurate chemical model is of vital importance. The resulting effects of even low concentrated species can be of great significance here [13]. However the influence of NCO can be neglected, due to the fact that NCO only occurs immediately behind the shock, where CO_2 is present and therefore will not alter the rate of equilibration [11].

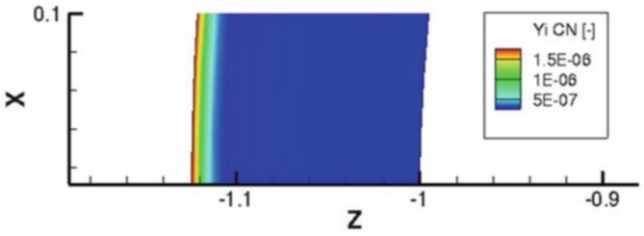

Fig. 7 Case 1 ten-species model CN layer

Conclusions

An efficient and accurate approach for the simulation of re-entry phenomena using the second-order boundary layer–Euler method has been demonstrated. Formulations describing thermodynamic properties, transport quantities and chemical kinetics are discussed and have been applied to equilibrium and non-equilibrium flow simulations around a hyperbola test configuration, which already proved their applicability for earth re-entry simulations.

In near future works, thermal non-equilibrium models will be implemented as well as an enhanced chemical reaction scheme including ionization as recommended by Noeding [14].

Furthermore gas radiation models will be implemented and investigated in the medium term.

References

1. Mundt, Ch.: Calculation of hypersonic, viscous, non-equilibrium flows around reentry bodies using a coupled boundary layer/Euler method. In: AIAA-92-2856, AIAA 27th Thermophysics Conference (1992)
2. Pfitzner, M.: A 3-D non-equilibrium shock-fitting algorithm using effective Rankine-Hugoniot relations. In: AIAA 91-1467, AIAA 22nd Fluid Dynamics, Plasma Dynamics & Laser Conference (1991)
3. Mundt, Ch.: Rechnerische Simulation reibungsbehafteter Strömungen im chemischen Nichtgleichgewicht. PhD Thesis (1992)
4. van Dyke, M.: Perturbation Methods in Fluid Mechanics. The Parabolic Press, Stanford (1975)
5. Gordon, S., McBride, B.J.: Computer Program for Calculation of Complex Chemical Equilibrium Compositions and Applications. RP-1311, NASA Ref. Pub., Cleveland (1994, 1996)
6. Gordon, S., McBride, B.J.: Thermodynamic Data to 20000 K for Monoatomic Gases. NASA/TP-1999-208523, Cleveland (1999)
7. Hirschfelder, J.O., Curtiss, C.F., Bird, R.B.: Molecular Theory of Gases and Liquids. Wiley, New York (1966)
8. Wright, M.J., Hwang, H.H., Schwenke, D.W.: Recommended collision integrals for transport property computations. Part 2: Mars and Venus entries. AIAA J. **45**(1), 281–288 (2007)
9. Kovalev, R.V., Vlasov, V.I., Zalogin, G.N.: Modelling of transport properties of CO_2+N_2 gas mixture. SACOMAR, SPA.2010.3.2-04, D 6.2 (2012)
10. Laricchiuta, A., Bruno, D., Catalfamo, C., Pirani, F., Colonna, G., Diomede, P., Pagano, D., Gorse, C., Longo, S., Celiberto, R., Giordano, D., Capitelli, M.: Transport properties of high-temperature mars-atmosphere components. In: AIAA 2007-4043, 39th AIAA Thermophysics Conference (2007)
11. Park, Ch., Howe, T., Jaffe, R.L.: Review of chemical-kinetic problems of future NASA missions, II: Mars entries. J. Thermophys. Heat Trans. **8**(1), 9–23 (1994)
12. Starkloff, M., Mundt, Ch.: Accurate interpolation of state surfaces for thermodynamic properties of equilibrium carbon dioxide—nitrogen atmospheres and their implementation in a coupled Euler—boundary layer method. In: AA-1-2011-37, 3rd International ARA—Days (2011)
13. Brandis, A.M., Morgan, R.G., McIntyre, T.J.: Analysis of nonequilibrium CN radiation encountered during titan atmospheric entry. J. Thermophys. Heat Trans. **25**(4), 493–499 (2011)
14. Noeding, P.: Review of physico-chemical CO_2 modelling and recommendation for improvement. SACOMAR, SPA.2010.3.2-04, D 6.1 (2011)

Radiative Heat flux Measurements for Titan Atmospheric Entry Condition in a Superorbital Expansion Tunnel

H. Porat, R.G. Morgan, and T.J. McIntyre

Introduction

Prediction of the radiative portion of the heatflux expected by a spacecraft entering an atmosphere still poses a challenge even to the state-of-the-art numerical models. On ground testing facilities, these atmospheric entry flows can be simulated using a superorbital expansion tunnel. In such experiments the test gas used in the facility is a representative atmospheric mixture of the celestial body of interest. Entry into the atmosphere of Titan, a moon of Saturn, was studied using the X2 superorbital expansion tunnel. For Titan atmospheric entry conditions, the radiative heat transfer is expected to be significant even at what is considered to be a relatively low shock speed of 6.5 km/s. In the Titan Explorer mission study, peak radiative heat transfer was estimated to be 4.5 times greater than the convective heating heat rate for an aerocapture manoeuvre [1]. This is a result of the carbon content in Titan's atmosphere, leading to the formation of CN, a strong radiator. To further our understanding of superorbital flows, the experiments presented hereafter use newly developed radiation gauges to measure the radiative heatflux and emission spectroscopy to provide quantitative information about the radiating species in the shock layer for a Titan atmospheric entry condition.

Experimental Conditions

Experiments were conducted using a 22 MJ/kg Titan 6.5 km/s atmospheric entry condition [2]. It simulates peak radiative heating for Titan entry at the stagnation point, using a test flow with an equivalent flight velocity of 6.8 km/s, Mach 11. The test time for this condition was found to be 150 μs using a pressure survey study. While the short test time can be challenging at times, fast response instrumentation and recording equipment are sufficient to gather the data during the experiment. The test gas used was a mixture of 95 % nitrogen to 5 % methane (by volume).

Experimental Arrangement

Two models were used in the experimental campaign: a cylindrical and a hemispherical model. The 75 mm cylindrical model, with 25 mm diameter, was instrumented with two radiation gauges along the stagnation streamline. The cylindrical model was placed in the X2 expansion tunnel, and radiative heatflux measurements were made in parallel with emission spectroscopy. The optical arrangement for the emission spectroscopy can be seen in Fig. 1. It was designed to image the region between the shock and the body over the wavelength range of 320–440 nm. The wavelength range was chosen to view the CN violet bands (spectral lines around 358, 384 and 418 nm) that are the main source of radiation for Titan atmospheric entry.

For comparative radiative heatflux measurements, a hemispherical model with 75 mm diameter was used, instrumented with a single radiation gauge at the stagnation point. The purpose of using the two models was to confirm the hypothesis that the same amount of radiation will be measured if the appropriate scaling is applied to keep the same shock standoff. The hemispherical model was scaled from the cylindrical model, using empirical correlations of the shock standoff. Ambrosio and Wortman [3] showed that for a hemisphere and a cylinder, the shock standoff can be related to the Mach number using the following equations:

H. Porat (✉) • R.G. Morgan
Centre for Hypersonics, School of Mechanical & Mining Engineering, The University of Queensland, Brisbane, QLD 4072, Australia
e-mail: h.porat@uq.edu.au

T.J. McIntyre
Centre for Hypersonics, School of Mathematics and Physics, The University of Queensland, Brisbane, QLD 4072, Australia

G. Ben-Dor et al. (eds.), *30th International Symposium on Shock Waves 1*, DOI 10.1007/978-3-319-46213-4_22

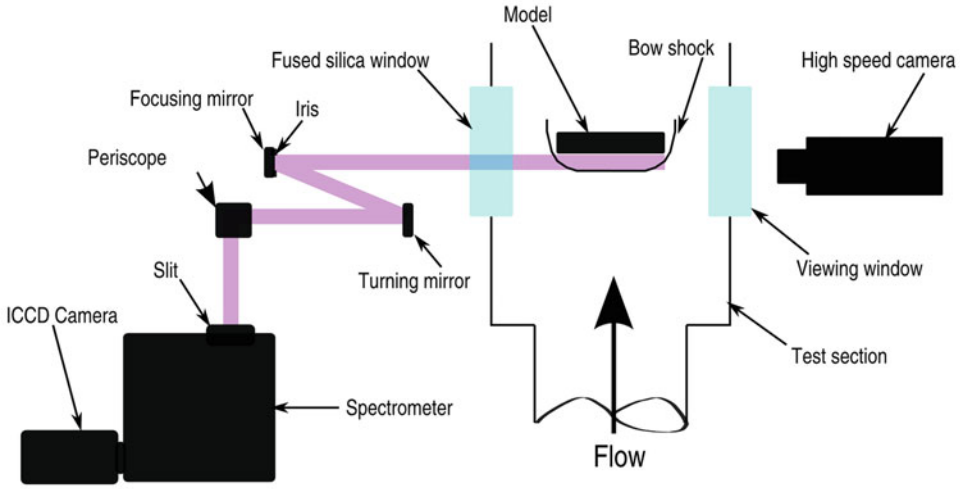

Fig. 1 Optical arrangement for emission spectroscopy (first published in [4])

$$\text{Hemisphere,} \quad \Delta/R = 0.143\exp\left(3.24/M^2\right)$$

$$\text{Cylinder,} \quad \Delta/R = 0.386\exp\left(4.67/M^2\right)$$

where Δ, R and M are the shock standoff distance, the model radius and the Mach number, respectively.

These shock standoff correlations were used to acquire a scaling factor between the cylindrical and hemispherical models. Note that prediction of the shock standoff itself using these correlations will overpredict the shock standoff distance, as these correlations were developed based on experiments with relatively low temperature and are effectively valid for ideal gas. The calculations made for the scaling factor indicated that scaling the hemispherical radius by ~3 will result in the similar shock standoff as the cylindrical model. Hence the 25 mm diameter cylinder was scaled to a 75 mm diameter hemisphere to test the hypothesis that matching the shock standoff will result in a comparative level of radiative heat transfer.

Radiation Gauges

A new radiation gauge was developed using a multiwalled carbon nanotube (CNT) thin-film sensing element. The thin-film heat gauge radiation gauge construction, whereby the thin-film heat gauge is mounted behind a viewing window to isolate the measurement of the radiative heat transfer, was first demonstrated successfully in expansion tunnels by Capra and Morgan [5]. The new gauge, CNT-Rad, was coated on a Macor substrate with the CNT sensing element at the Indian Institute of Science in Bangalore using a one-step pyrolysis process originally developed by Mahanandia and Nanda [6]. The development of the CNT-Rad gauge followed a successful use of the carbon cluster sensing element by Srinath and Reddy [7] in a shock tube experimental environment. The CNT-Rad gauge was wired using silver tabs that were applied along the sides as shown in Fig. 2. After calibration the gauge was placed in a brass housing and set behind a viewing window. As indicated before, this configuration has been proven to allow measurements of the radiative heat transfer alone, independently of the convective heat transfer [5]. The thin films were annealed at 160 °C for 12 h for the stability of the gauge [8] and then calibrated in accordance with standard procedures [9]. This calibration was used to measure the temperature coefficient value per gauge, averaging at 0.00193 C^{-1}. A new technique was developed to quantify the transmissivity of the new CNT sensing element. The technique used a spectrometer scan of a calibration source through a quartz slide that was covered with the CNT sensing element during the pyrolysis process, comparing it to a scan through a blank quartz slide. The analysis of the results was used to determine the transmissivity of the coating across the near-UV wavelength range. It was found to be 0.99 and 0.96 for the final and penultimate CNT pyrolysis batches, respectively. This value was then used with the transmission through the gauge fused silica window, and the gauge configuration solid angle, to convert the *measured radiative heatflux* into a calibrated *surface radiative heatflux*.

Results

In Fig. 3 the *measured radiative heatflux* for the hemispherical model and cylindrical model is shown. A steady heatflux was observed throughout the test time, as indicated on the plot. The test time start was identified to start at 70 μs, and this was verified with the high-speed camera footage for the experiments. The shock standoff distance was measured

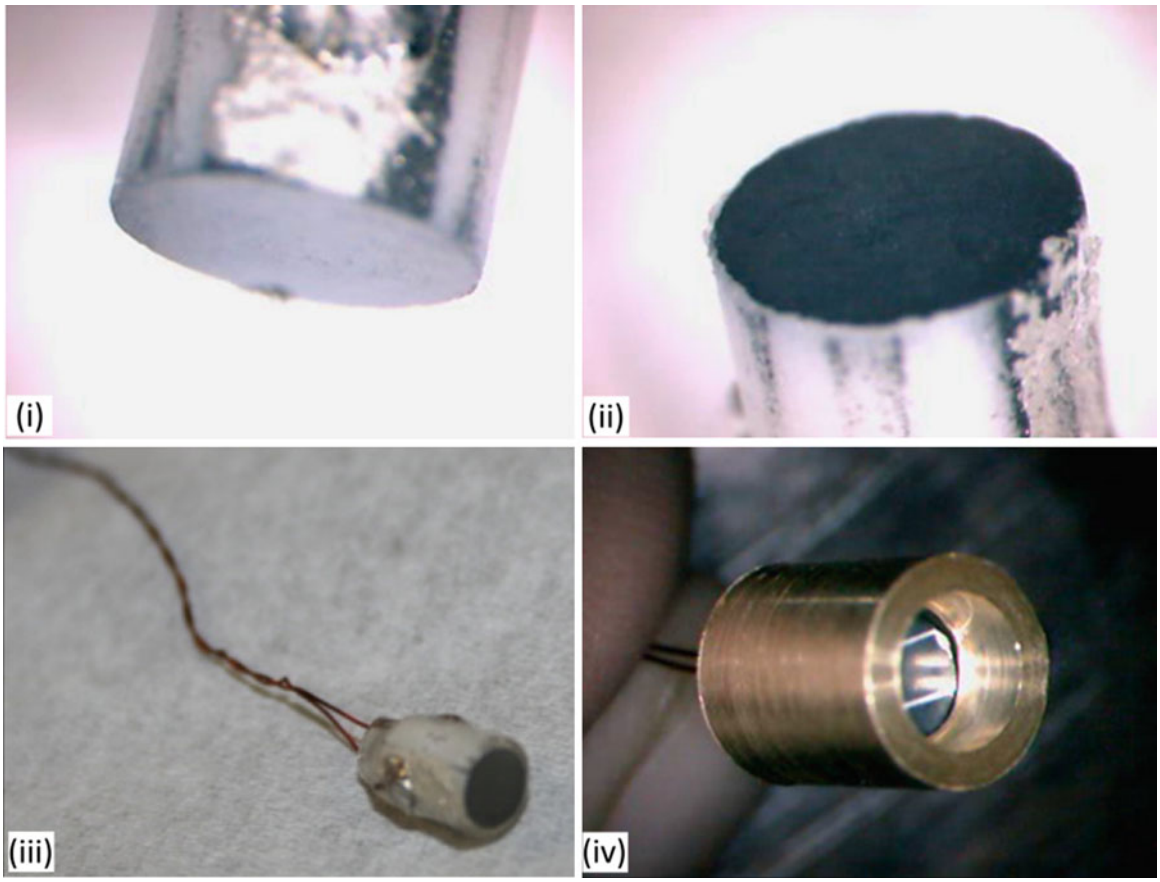

Fig. 2 CNT-Rad radiation gauges. (*i*) The polished face of the Macor with the CNT coating, (*ii*) the surface of the gauge and the silver connection tabs, (*iii*) insulated wires soldered to the silver tabs and (*iv*) the assembled gauge in the brass housing behind a window (first published in Porat et al. [10])

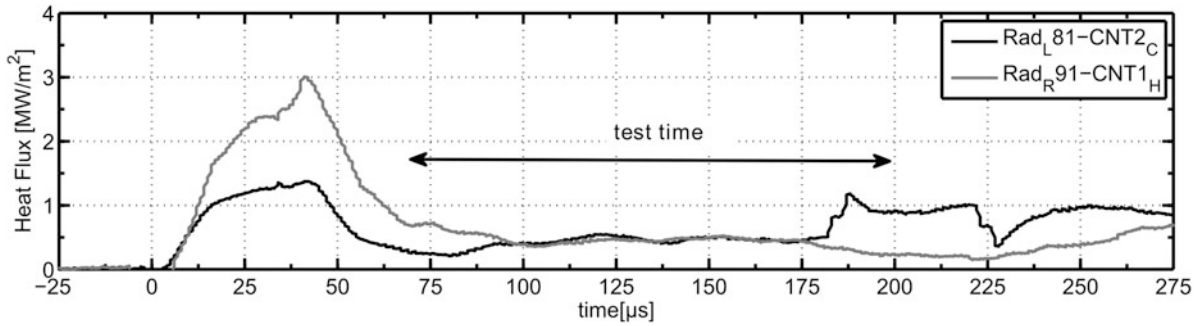

Fig. 3 *Measured radiative heatflux* for Titan 6.5 km/s condition, using a cylindrical model (C) and a hemispherical model (H), as it was recorded by the CNT-Rad radiation gauges (tests x2s2281,x2s2291)

using a scaling technique from the high-speed camera footage taken during the tests, shown in Fig. 4 for the cylindrical model and in Fig. 5 for the hemispherical model. It was found to be (1.9 ± 0.5) mm and (2.0 ± 0.4) mm for the cylindrical and hemispherical models, respectively. Referring back to Fig. 3, it is evident that an agreement between the radiative heatflux measurements from the cylindrical and hemispherical models was observed. The calibrated *surface radiative heatflux* averaged over 50 μs of test time was found to be (1.37 ± 0.25) MW/m^2 and (1.23 ± 0.17) MW/m^2 for the cylindrical and hemispherical models, respectively.

Emission spectroscopy measurements were then conducted for the Titan 6.5 km/s condition using the cylindrical model, in order to identify the radiating species in the shock layer and quantify their relative contribution towards the radiation. Results from the near-UV optical system,

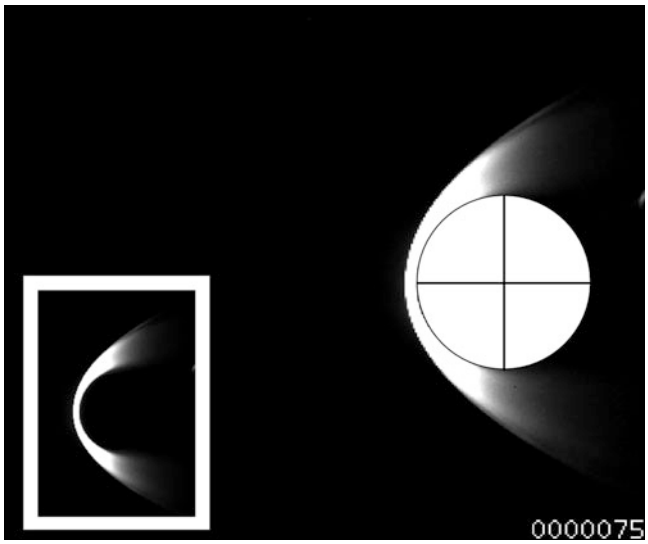

Fig. 4 Shock standoff fit for Titan 6.5 km/s condition cylindrical model using a high-speed camera frame, test x2s1804

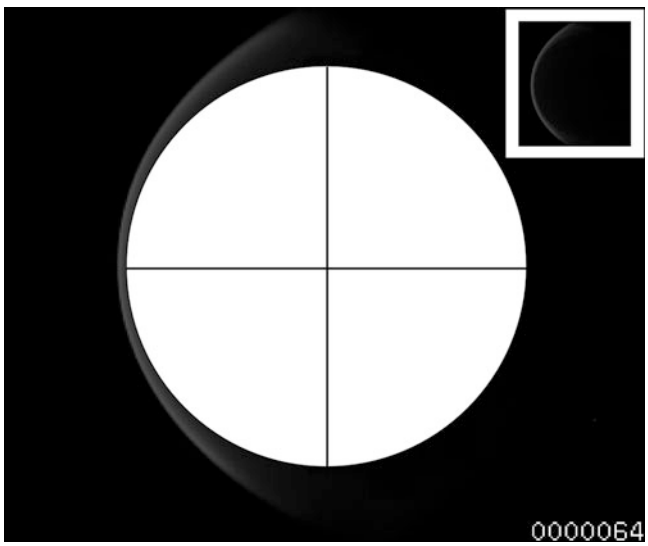

Fig. 5 Shock standoff fit for Titan 6.5 km/s condition hemispherical model using a high-speed camera frame, test x2s2289

using a 600 lines/mm grating and centred at 380 nm wavelength, are plotted in Fig. 6. Calibration of the results follows the procedure established by Eichmann and detailed in Eichmann et al. [11]. Referring to the spectrum image, the flow orientation is from the bottom to the top of the image, where the *y*-axis was calibrated to indicate the distance upstream of the model face, placed at zero. The data was then sliced along the marked dotted lines, and the intensity in the post-shock location was integrated and averaged in the horizontal and vertical directions. The horizontal slice produces the species distribution across the wavelength range in the post-shock location. The vertical slice is plotted across the CN (B-X) violet rovibronic transition $\Delta v = 0$

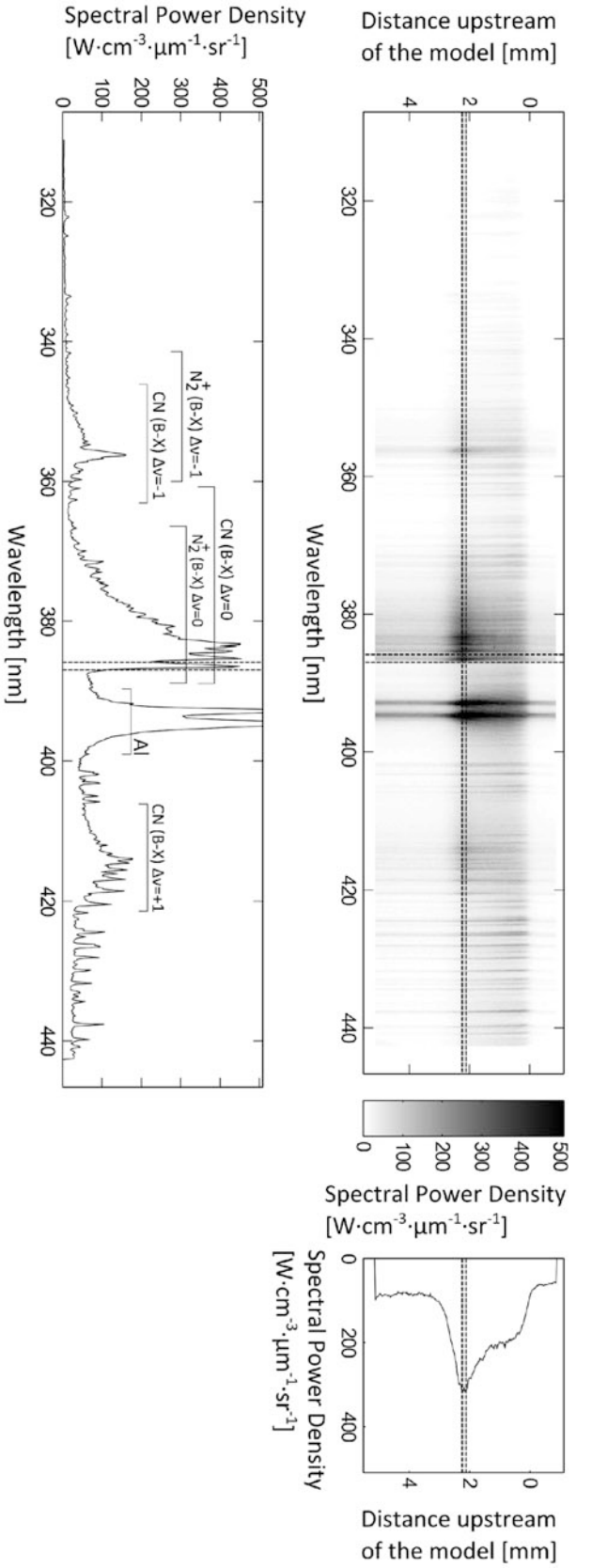

Fig. 6 Spectrum from experiment x2s2271 for the Titan 6.5 km/s condition. A slice through the data is plotted for the CN violet band, integrated and averaged across five pixels at the post-shock location

band across the vibronic level $v' = 0$, showing the intensity across the shock layer, with the model located at zero. The profile shows the level of CN rises rapidly behind the shock, but relaxes towards the body location.

As expected the flow was indeed dominated by the CN (B-X) $\Delta v = -1,0,+1$ bands, indicated on the integrated spectrum. A weak N_2^+ peak at 390.61 nm was also identified, and the location of the N_2^+(B-X) bands is also indicated on the plot although they are overlapping with the CN (B-X) $\Delta v = -1,0$ bands and will have a limited contribution due to the very low levels detected. The last two species identified belong to atomic lines of aluminium that originated from the secondary diagram and various low level iron lines that are contaminants from the facility operation.

Conclusions

The radiative heatflux for a Titan 6.5 km/s entry condition was successfully measured by newly developed CNT-Rad radiation gauges. Radiative heatflux measurements were made using cylindrical and hemispherical models, confirming that scaling the shock standoff has successfully resulted in comparable radiative heatflux measurements. The spectral distribution and radiative intensity was also measured for the cylindrical model along the stagnation streamline. The results show that CN violet bands are dominating the spectra and can be analysed to allow a temperature analysis to further characterise the flow.

References

1. Levine, J.S., Wright, H.S.: Titan explorer: the next step in the exploration of a mysterious world. Technical Report No. 20050212185, NASA, Hampton (2005)
2. Porat, H., Morgan, R.G. McIntyre, T.J.: Study of radiative heat transfer in titan atmospheric entry. In: 18th Australasian Fluid Mechanics Conference, Launceston, Australia (2012)
3. Ambrosio, A., Wortman, A.: Stagnation-point shock-detachment distance for flow around spheres and cylinders in air. J. Aerospace Sci. **29**(7), 875–875 (1962)
4. Porat, H., Morgan, R.G., McIntyre, T.J.: Study of radiative heat transfer in titan atmospheric entry. In: 28th International Congress of the Aeronautical Sciences, Brisbane, Australia (2012)
5. Capra, B., Morgan, R.G.: Radiative and total heat transfer measurements to a titan explorer model. J. Spacecr. Rocket. **49** (1), 12–23 (2012)
6. Mahanandia, P., Nanda, K.K.: A one-step technique to prepare aligned arrays of carbon nanotubes. Nanotechnology **19**(5), 155602 (2008)
7. Srinath, S., Reddy, K.P.J.: Large carbon cluster thin film gauges for measuring aerodynamic heat transfer rates in hypersonic shock tunnels. Meas. Sci. Technol. **26**, 025901 (2015)
8. Schultz, D.L., Jones, T.V.: Heat transfer measurements in short duration hypersonic facilities. Technical Report, AGARD-AG-165, Paris (1973)
9. Dann, A.: The Manufacturing of Thin Film Heat Gauges, 2nd edn. Technical Report, The University of Queensland, Brisbane (2010)
10. Porat, H., Allsop, B., Morgan, R.G., Srinath, S., Reddy, K.P.J., McIntyre, T.J.: Amplifier design for new CNT radiation gauges in expansion tunnels. In: 19th Australasian Fluid Mechanics Conference, Melbourne, Australia (2014)
11. Eichmann, T.N., Rubinsztein-Dunlop, H., McIntyre, T.J.: Radiation measurements of flow over a cylinder at mars aerocapture conditions. AIAA J. Thermophys. Heat Trans. (2013, submitted)

Study of Hypersonic Dissociating Flows over Spheres Using the Space-Time CE/SE Method

H. Saldivar Massimi, H. Shen, and C.Y. Wen

Introduction

Over the last years, a renewed interest in manned missions to Mars has brought back attention to the field of hypersonic aerothermodynamics. Several space agencies as well as private companies are currently designing hypersonic vehicles (ZEHST by EADS and Dragon by Space Exploration Technologies Corporation) that, hopefully, will become the next generation of space vehicles.

When the space vehicle enters the atmosphere at an orbital speed, a detached bow shock forms in front of its blunt nose, and the temperature behind the shock, especially in the stagnation region, can reach high levels, due to the conversion of kinetic flow energy into thermal energy by strong shock compression. The important gas molecule dissociation and other real gas effects of hypersonic flows will occur. Consequently, the air can no longer be treated as a perfect gas, and the dissociative non-equilibrium phenomenon complicates the flow physics [1].

Although the nose of a space vehicle is not completely a sphere, many previous theoretical, experimental and numerical researches concentrated on the hypersonic flows over spheres for model simplification. Many flow physics and flow features can be extracted from such spherical nose flows, and some significant analytical solutions can be derived. Due to the extreme flow conditions, experimental approaches to study the hypervelocity flows are difficult in general, not to mention expensive. Therefore, to thoroughly understand the hypersonic dissociative non-equilibrium flows is essential to develop a reliable, efficient and accurate numerical method.

Because in the field of computational fluid dynamics (CFD) a conflict between stability and numerical accuracy is one that affects most of the established methods, Chang and To [2] developed the space-time conservation element and solution element (CE/SE), using the unique approach of enforcing flux conservation in both space and time with extensive physics considerations. Since its inception in 1991, it has been used to obtain highly accurate numerical solutions for 1D, 2D and 3D flow problems involving shocks, contact discontinuities, vortices, etc. [2–5].

In the present work, the inviscid CE/SE code based on hybrid meshes consisting of triangular and quadrilateral elements [6] is extended to solve hypersonic chemical-reacting non-equilibrium flows. Both chemical dissociation and vibrational energy relaxation are taken into account. The code uses a two-temperature chemical-kinetic model developed by Park [7], where one temperature T is used to characterize the translational energy of the atoms and molecules and the rotational energy of the molecules and another temperature T_v to characterize the vibrational energy of the molecules, translational energy of the electrons and electronic excitation of atoms and molecules. For nitrogen flows, only two species (N_2 and N) and two chemical reactions are used; for CO_2 and airflows, five species ((CO_2, O_2, CO, C and O) and (N_2, O_2, NO, N and O), respectively) and 17 reactions are considered. The chemical reaction parameters used can be found in Refs. [8, 9].

The source terms involving chemical reactions or energy exchange rates may cause the stiffness problem, i.e. the rates may be orders of magnitude higher than the flow velocity. To overcome this problem, the reacting and energy exchange source term is solved by an implicit trapezoidal method of integration, which is expressed as

$$\left(\mathbf{I} - \Delta t\left[\frac{\partial \mathbf{R}}{\partial \mathbf{U}}\right]^n\right)\left(\mathbf{U}^{n+1} - \mathbf{U}^n\right) = \Delta t \mathbf{R}^n,$$

where $\frac{\partial \mathbf{R}}{\partial \mathbf{U}}$ is the Jacobi matrix of the stiff reacting source term **R. I** and **U** are unit matrix and conservative quantity vector, respectively.

Due to the inherent nature of the CE/SE method, the physical quantities and their derivative are solved simultaneously. Therefore the process to calculate the viscous flux is straightforward.

H.S. Massimi • H. Shen • C.Y. Wen (✉)
Department of Mechanical Engineering, The Hong Kong Polytechnic University, Kowloon, Hong Kong SAR
e-mail: cywen@polyu.edu.hk

G. Ben-Dor et al. (eds.), *30th International Symposium on Shock Waves 1*, DOI 10.1007/978-3-319-46213-4_23

Cases of nitrogen, air and carbon dioxide are provided to demonstrate the accuracy and reliability of the method regarding non-equilibrium flows. A driven cavity and the reflection of a normal shock wave from the end wall of a shock tube have been simulated as a benchmark to demonstrate the capability of the CE/SE solver for viscous flows.

Results

Dissociating Flows over Spheres

When the hypersonic flow encounters a sphere, a bow shock will detach from the surface of the sphere. Special attention is placed on the reliability of the code to predict the shape of the bow shock and the distance between the shock and body on the stagnation line, namely, the shock stand-off distance, Δ, two important flow characteristics. We apply the CE/SE code to simulate the experimental cases performed by Wen and Hornung's [10] and study of these two flow features.

The flow is assumed to be axisymmetric, such that the computational domain is reduced to only one-half of the complete flow field. Grid-independence tests were carefully performed. This was achieved by running a series of simulations increasing the mesh size by a factor of 1.5 until the difference in the stagnation streamline properties between mesh models was smaller than 2 %.

The freestream conditions of the selected cases and the comparison of experimental, theoretical and numerical dimensionless shock-off distances $\left(\overline{\Delta} \equiv \frac{\Delta}{R}\right)$ are listed in Table 1.

From it, we can see that the present numerical results agree very well with Wen and Hornung's experimental and theoretical results. To further compare the numerical results with Wen and Hornung's experimental results, we compare the bow shock shapes by overlapping the numerical density contours in the experimental finite fringe differential interferograms in Fig. 1. It is shown that the shapes of the numerical bow shocks fit the experimental results very well.

Figure 2 shows the distributions of species for the airflow case. From it, we can see that the mass fraction of O atoms is much higher than that of N atoms. It is because the characteristic dissociating temperature of O_2 (59,500 K) is much lower than that of N_2 (113,200 K). Under the same temperature, the dissociating level of O_2 is much higher than that of N_2. On the upper side of the sphere, there is almost no presence of N due to the flow expansion; the consequent significant temperature decrease during the flow expansion yields the full recombination of the atomic nitrogen. On the other hand, O is still considerable with a mass fraction higher than 0.15.

Driven Cavity

A driven cavity was simulated as a benchmark to demonstrate the capability of the CE/SE solver for viscous flows. The results were compared with the works done by Ghia et al. [11]. Figure 3a shows the comparison of the u-velocity profile along vertical centerline for $Re = 400$. The Reynolds number is based on the height of the cavity and the moving speed of the top wall (Mach 0.15). It can be seen from

Table 1 Freestream conditions and comparison of dimensionless shock-off distances

Case	Gas	R (m)	ρ_∞ (kg/m^3)	u_∞ (m/s)	T_∞ (K)	Dimensionless shock-off distances		
						Experiment (Wen and Hornung)	Theory (Wen and Hornung)	Simulation
1	N_2	0.038	0.0195	5140	2200	0.100	0.095	0.100
2	Air	0.025	0.0278	3930	1370	0.105	0.093	0.095
3	CO_2	0.051	0.0326	3490	2010	0.088	0.086	0.087

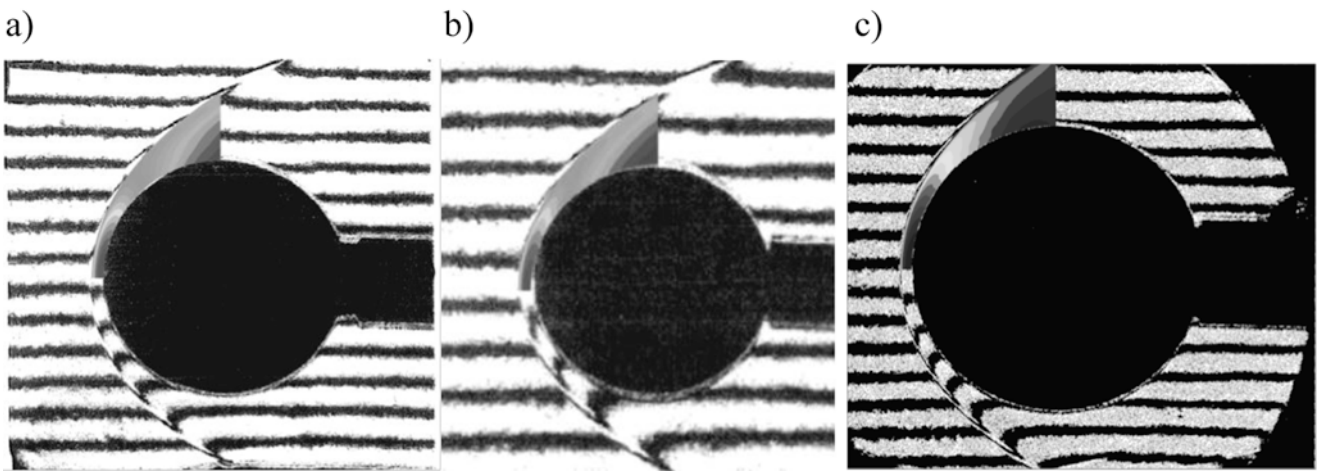

Fig. 1 Comparison of numerical and experimental bow shock shape for (**a**) N_2, (**b**) air and (**c**) CO_2 flows around spheres

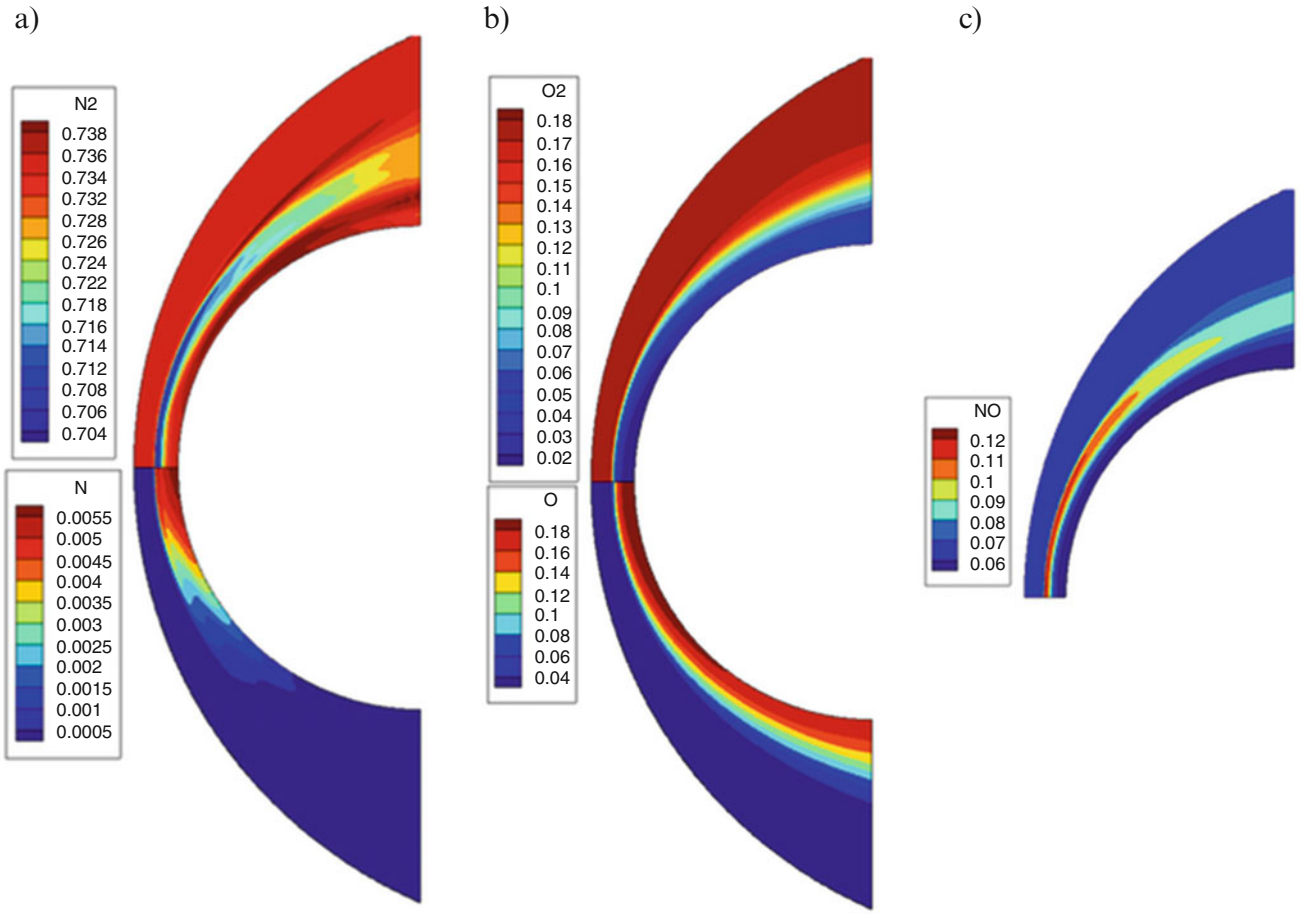

Fig. 2 Mass fraction of N_2, N, O_2, O and NO molecules for airflows

Fig. 3b that the method has captured the primary vortex and the two secondary vortices.

Shock Bifurcation

To validate the code capabilities regarding high-speed viscous and compressive flows, the reflection of a normal shock wave from the end wall of a shock tube has been simulated. In this test case, the shock bifurcation is simulated based on experiments performed by Matsuo et al. [12]. To save computational resources, only the last 0.15 m of the channel adjacent to the end wall and half a domain of 0.02 m with an incident Mach number of 2.6 were simulated. The results provided by the CE/SE code were then compared against the experimental results of Matsuo et al. and the numerical results of Weber et al. [13].

Figure 4 shows the triple-point trajectories from the CE/SE simulations (adiabatic wall), the reference calculations from Weber et al. (adiabatic and isothermal wall) and the experimental values obtained from Matsuo et al. It can be seen that the CE/SE results follow a trend that predicts the triple-point trajectory similarly to the results of the reference calculations and the experimental results. However, the calculations predict an equilibrium height 20 % higher that the experimental one, being similar with the isothermal simulations of Weber et al. whom suggested that these discrepancies can have several implications.

The first one being a growth of the interacted zone caused by the lower density found in an adiabatic wall boundary layer. The second reason is the lack of a turbulence model in the simulation; therefore, the viscous layer contains less energy and this creates a larger displacement.

Conclusions

A CE/SE code based on hybrid meshes is applied to study the hypersonic carbon dioxide, nitrogen and airflows over spheres. The code is proved capable of simulating hypersonic flows accurately by comparing the numerical shock stand-off distances and bow shock shapes with Wen and Hornung's experimental results and theoretical model. Moreover, the code shows good accuracy in predicting viscous flows as shown by comparing the results of a driven cavity with the works done by Ghia et al. and shock bifurcation compared against the experimental results of Matsuo et al. and the numerical results of Weber et al. Future work will focus on solving viscous hypersonic dissociating flows.

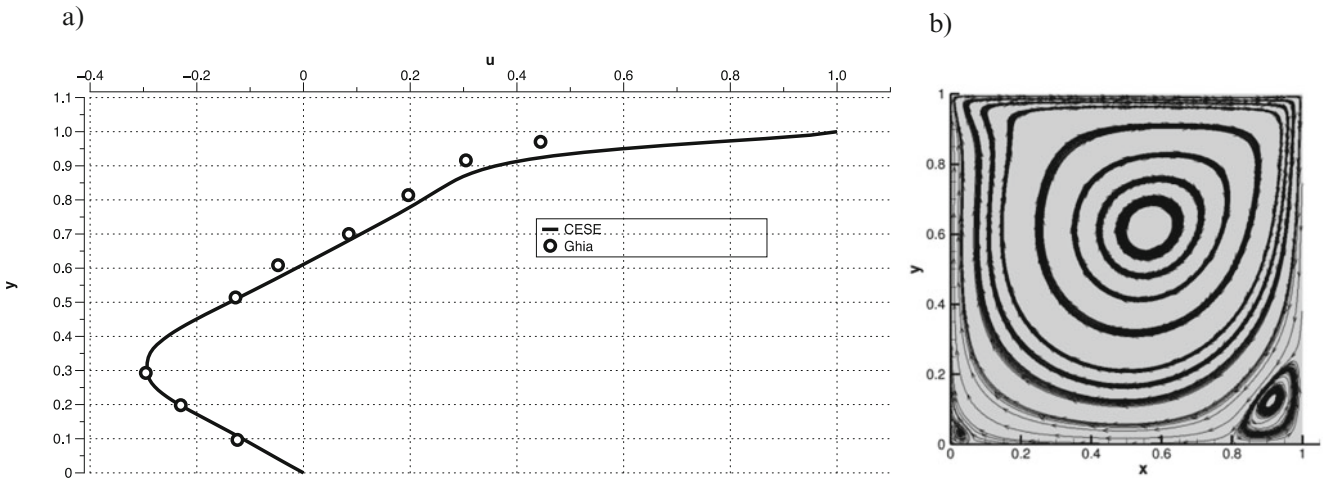

Fig. 3 Comparison of the *u*-velocity profile along vertical centerline and streamline contour for a driven cavity benchmark

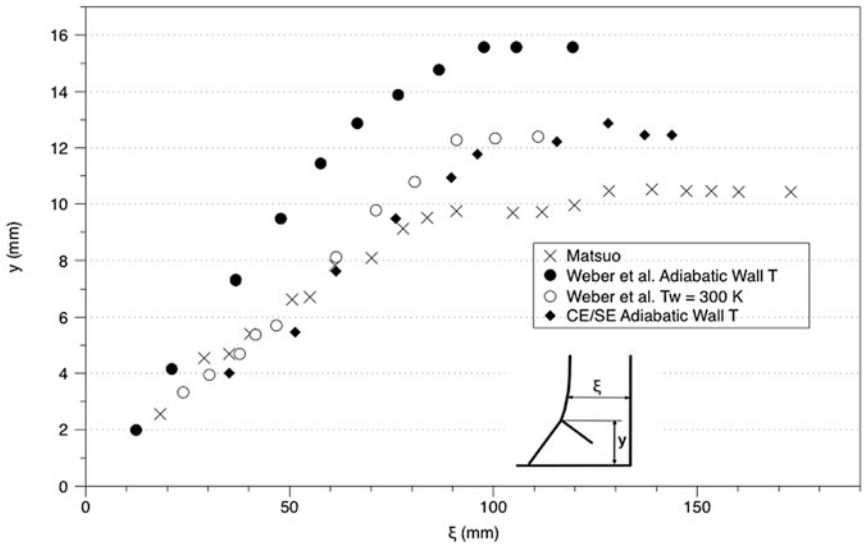

Fig. 4 Comparison of the variation of the height of the bifurcated foot with distance from the end wall

References

1. Anderson, J.D.: Modern Compressible Flow with Historical Perspective. McGraw-Hill, Boston (2003)
2. Chang, S.C., To, W.M.: A New Numerical Framework for Solving Conservation Laws—The Method of Space-Time Conservation Element and Solution Element. NASA TM 104495, Cleveland (1991)
3. Chang, S.C., Wang, X.Y., Chow, C.Y.: The Space-Time Conservation Element and Solution Element Method—A New High-Resolution and Genuinely Multidimensional Paradigm for Solving Conservation Laws. I. The Two-Dimensional Time Marching Schemes. NASA TM 208843, Cleveland (1998)
4. Chang, S.C., Wang, X.Y., Chow, C.Y.: New Developments in the Method of Space-Time Conservation Element and Solution Element—Applications to Two-Dimensional Time-Marching Problems, NASA TM 106758, Cleveland (1994)
5. Wang, X.Y. Chang, S.C.: A 3D structured/unstructured Euler solver based on the space-time conservation element and solution element method. In: A Collection of Technical Papers, 14th AIAA CFD Conference, Norfolk, AIAA Paper 99-3278, 28 June–1 July 1999
6. Shen, H., Wen, C.Y., Liu, K.X., Zhang, D.L.: Robust high-order space–time conservative schemes for solving conservation laws on hybrid meshes. J. Comput. Phys. **281**, 375–402 (2015)
7. Park, C.: Assessment of two-temperature kinetic model for ionizing air. J. Thermophys. Heat Trans **3**, 233–244 (1989)
8. Park, C.: Review of chemical-kinetic problems of future NASA missions. I-Earth entries. J. Thermophys. Heat Trans. **7**(3), 385–398 (1993)
9. Park, C.: Review of chemical-kinetic problems of future NASA missions. II-Mars entries. J. Thermophys. Heat Trans. **7**(3), 385–398 (1994)
10. Wen, C.Y., Hornung, H.G.: Non-equilibrium dissociating flow over spheres. J. Fluid Mech. **299**(1), 389–405 (1995)
11. Ghia, U., Ghia, K.N., Shin, C.T.: High-re solutions for incompressible flow using the Navier–Stokes equations and a multigrid method. J. Comput. Phys. **48**, 387–411 (1982)
12. Matsuo, K., Kawagoe, S., Kage, K.: The interaction of a reflected shock wave with boundary layer in a shock tube. Bull. JSME **17**, 1039 (1974)
13. Weber, Y.S., Oran, E.S., Boris, J.P., Anderson, J.D.: The numerical simulation of shock bifurcation near the end wall of a shock tube. Phys. Fluids **7**(10), 2475 (1995)

The Direct Measurement of Skin Friction in Shock Tunnel

Lv Zhiguo, Li Guojun, Zhao Rongjuan, Jiang Hua, Liu Jichun, Huang Jun, and Liu Shiran

Introduction

In hypersonic flight, drag is composed of two main components besides abduction drag: wave drag, which is caused by shock waves, and skin friction drag, which is caused by friction. Wave drag is correlated to the Mach number, and skin friction drag is related to the flow state of the surface in the flight. The flow state corresponds to the Reynolds number, the rough degree of the surface, and the flight vehicle's angle of attack. In hypervelocity, the skin friction is proportional to the product of the gas density multiplied by the square of the flight velocity. Related research results [1] show that the skin friction drag accounts for almost 50 % of the total drag in hypersonic vehicles with scramjet. In high lift-to-drag ratio vehicles, such as wave riders, the ratio is the same. Research on the skin friction balance measurement in shock tunnels is useful to vehicle layout research, drag reduction, and structure optimization, as well as the design of the engine shape, inlet, and insulate section of vehicles.

The skin friction test has long been used, and after several decades several mature test methods have been developed, including the optical skin friction gauge measurement [2, 3], the oil film interference skin friction measurement [4, 5], the liquid crystal skin friction measurement [6], the stress-strain film skin friction measurement [7, 8], the MEMS-based skin friction measurement [9, 10], the strain gauge skin friction balance measurement [11–13], the piezoelectric skin friction balance measurement [14–16], and the flight tests in the USA [17, 18].

Queensland University began to develop the skin friction gauge in 1992. The skin friction gauge is composed of a measuring element, an acceleration element, and two charge amplifiers, all mounted within a brass housing [14, 19, 20]. The skin friction gauges had typical response times of 5 μs and a lowest natural frequency of 40 kHz. Many skin friction tests that were carried out with scramjet combustors in the T4 shock tunnel and X3 expansion tunnel used this skin friction gauge.

The skin friction balance with a strain gauge as the sensitive element was developed by researchers at the Virginia Polytechnic Institute and State University. The skin friction balance with a cantilever beam constructed out of engineering plastics LEXAN, ULTEM, and Vitrex PES met all of the above criteria. The skin friction measurement with a combustor model was conducted in the NASA Ames 16-in. high-enthalpy shock tunnel and CALSPAN 96-in. shock tunnel [11, 12, 21].

Another piezoelectric skin friction balance was developed by CUBRC in the LENS shock tunnel; this gauge has been refined and further developed for several decades. The transducer consists of a diaphragm that is supported flush with the model surface by two piezoelectric ceramic beams, which develop a charge when bent by a surface shear on the diaphragm. A third beam is used to provide acceleration compensation; the beams are connected electrically to eliminate thermal, normal, and transverse pressure effects. This type of skin friction gauge is widely used in LENS series shock tunnels for broad skin friction tests, and the total test precision is within 8 % [15, 22–25].

In this paper, research on the skin friction measurement technique in the CARDC shock tunnel is introduced. The balance design, calibration, shock tunnel test, and result discussion are also presented in this paper.

L. Zhiguo (✉)
School of Energy and Power Engineering, Xi'an Jiaotong University, Xi'an, Shanxi 710049, PR China

Hypervelocity Aerodynamics Institute, China Aerodynamics Research and Development Center, Mianyang, PR China
e-mail: lzgde2003@cardc.cn

L. Guojun
School of Energy and Power Engineering, Xi'an Jiaotong University, Xi'an, Shanxi 710049, PR China

Z. Rongjuan • J. Hua • L. Jichun • H. Jun • L. Shiran
Hypervelocity Aerodynamics Institute, China Aerodynamics Research and Development Center, Mianyang, PR China

G. Ben-Dor et al. (eds.), *30th International Symposium on Shock Waves 1*, DOI 10.1007/978-3-319-46213-4_24

Skin Friction Balance

Skin Friction Balance Design

Through a synthetic comparison, the structure with a cantilever beam is adopted in the design of the skin friction balance. A high natural response of the skin friction balance is needed to satisfy the requirement of the shock tunnel for its short test time. In this design, the sensing elements use the piezoelectric ceramic, which maintains high sensitivity. Thus, the skin friction balance can maintain high stiffness, which could improve the natural response. The additional advantages of adopting this structure for the skin friction balance are as follows. First, the sensing head shape of the skin friction balance (circle, square, or triangle) can be easily changed, and the surface can also be changed to fit well with many kinds of measuring surfaces, which can enhance the testability of the skin friction balance. Second, with a thermal insulation sensing head, the skin friction balance testability can be improved for high-temperature flows, which can be used as a useful tool for skin friction measurement in flow fields such as the scramjet inlet and the combustion chamber. Third, the response frequency of the skin friction balance can be improved by using the light sensing head, which would be used in a high-frequency test, such as the skin friction measurement where the flow field changes fast.

In this research, the structure of the skin friction balance is shown in Fig. 1. The skin friction balance is composed of the main body, the protecting shroud, the floating head, and four bolts. The main includes the joint, the cantilever beam, and the base. The floating head is used to sense the skin friction of the flow, and the piezoelectric ceramics are stuck to the cantilever beam, which is attached to the floating head. The protecting shroud is used to protect the piezoelectric ceramic from the flow during the test time. In the function of the skin friction, the location of the floating head changes, the cantilever beam bends, and the piezoelectric ceramic senses the stress of the cantilever beam and produces the charge signal.

Finite Element Analysis

We used the ANSYS software to analyze the performance of the balance with static force and mode analysis. To model and plot grid mesh easily, a simple configuration is applied in the analysis.

The material of the skin friction balance is 30CrMnSiA, the modeling parameter is Solid Tet10node 92, the density is 7.9×10^3 kg/m^3, the elastic modulus is 1.98×10^{11} Pa, and the Poisson ratio is 0.3. The computing grid mesh is a non-structure tetrahedron.

Mode analysis is used to obtain the dynamic characteristics of the skin friction balance, including natural frequency and vibrancy. The running time of the shock tunnel is only 2–18 ms, so the frequency of balance must be sufficiently high. Mode analysis is used to analyze whether the response of the skin friction balance can meet the need. We calculate the natural frequency of the skin friction balance with different cantilever beam thicknesses,

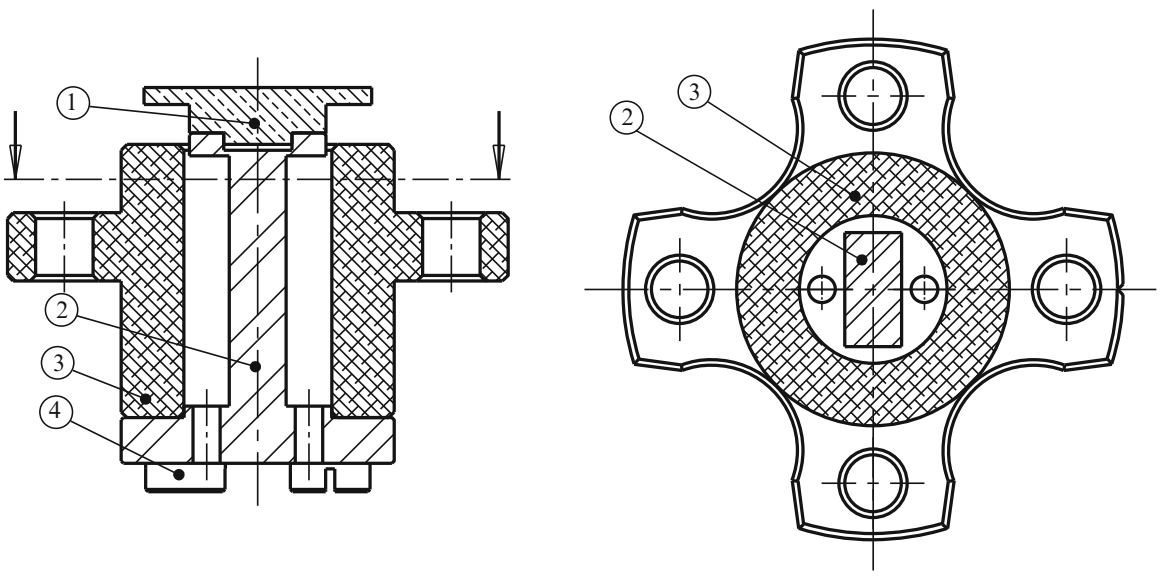

① floating head, ② skin balance main body, ③ protecting shroud, ④ bolt

Fig. 1 The skin friction balance

and the results are shown in Table 1. It can be concluded from Table 1 that the natural frequency increases with the thickness of the cantilever beam. The first-order vibration frequency for the 4-mm thickness with the value of 2662 Hz was drawn from the shock tunnel test, which is close to the simulation result.

Table 1 The former third-order natural frequencies of the skin friction balance

Cantilever beam thickness	3 mm	4 mm	5 mm
First order (Hz)	1761	2699	3277
Second order (Hz)	4690	6296	6114
Third order (Hz)	5222	8124	7925

The purpose of the static force analysis is to determine the distortion and stress of the sensitive unit under different loads. Figure 2 shows the stress contour under a 500-Pa shear stress in the *Z* direction, which is the direction of the skin friction measurement. Under the shear stress, one side is the compressive stress, whereas the other side is the tensile stress. The stress decreases from the root to the top of the cantilever beam. Figure 3 shows the stress contour of the cantilever beam under a 5000-Pa compressive stress in the *Z* direction. From Fig. 3, we can see that the compressive stress is the same on both sides of the cantilever beam. Thus, the shear stress response of the skin friction parallel to the surface can be obtained by fixing the piezoelectric ceramic stuck on the cantilever beam.

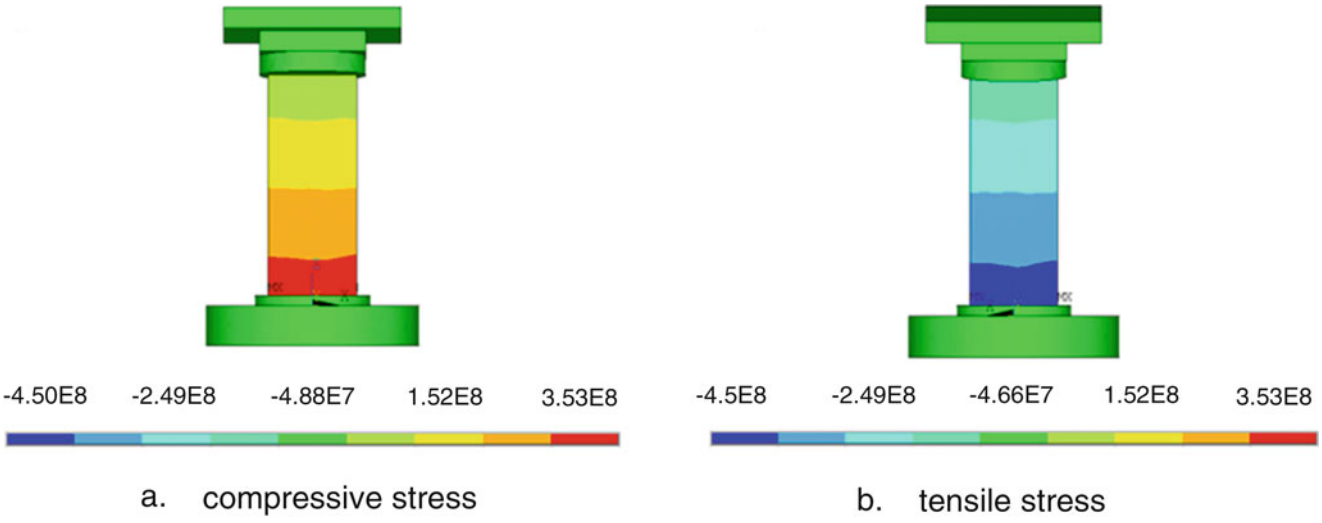

Fig. 2 The stress contour of skin friction under the shear stress in the *Z* direction

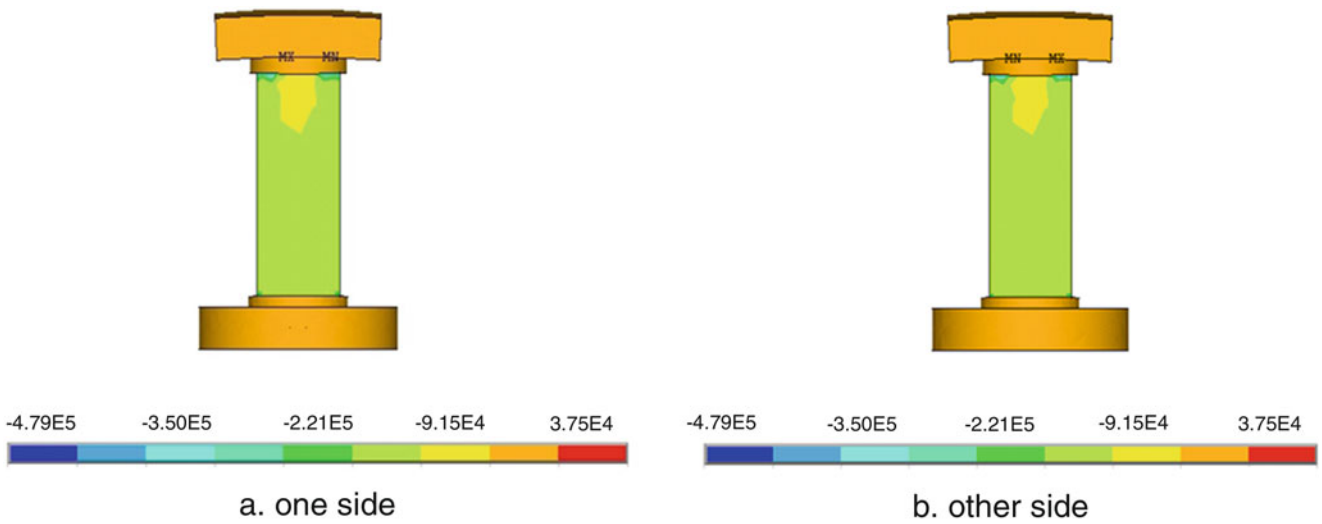

Fig. 3 The stress contour of skin friction under the compressive stress

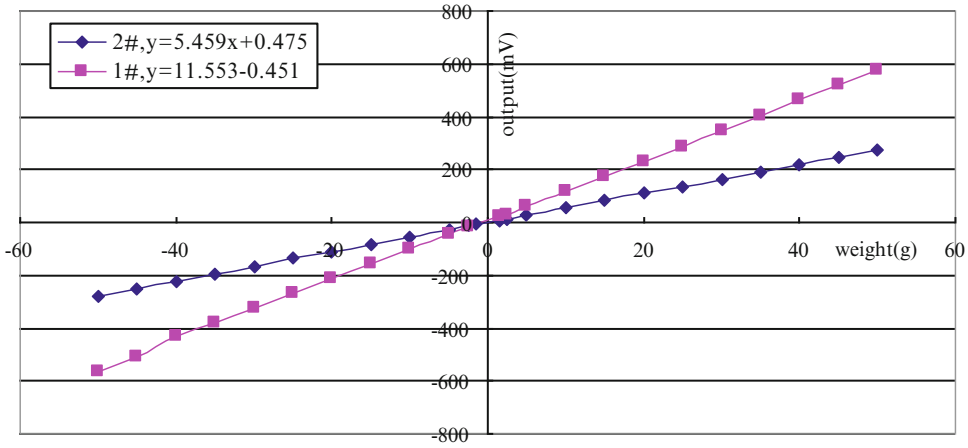

Fig. 4 The calibration result of the skin friction balance

Skin Friction Balance Calibration

During calibration, the skin friction balance is fixed in a horizontal position, and then the calibration load is hung vertically by a thin thread, which is fixed to the calibration head. The calibration load ranges from −50 to 50 g, and the minimal load is 0.13 g. The error caused by the pulley and horizontal thread in the conventional calibration can be minimized by this calibration method. The sensitivities of two typical skin friction balances are 11.55 mV/g and 5.46 mV/g, and the precision errors are 0.36 % and 0.29 %, respectively. From the calibration results shown in Fig. 4, it can be seen that, within the calibration range, the linearity of the balance output is preferable, and the correlation coefficient of the balance output and the shear force is higher than 99.99 %.

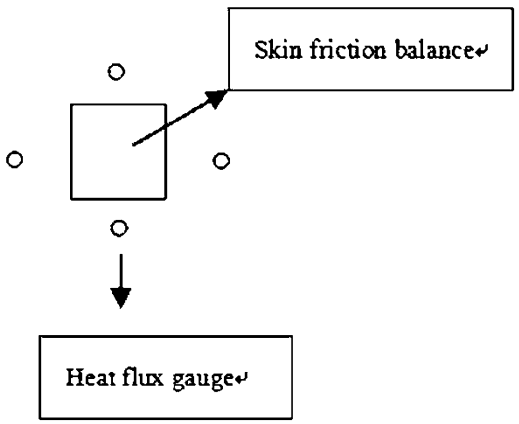

Fig. 5 Schematic diagram of the model surface

Facility and Flow Field

The model used in this research is a flat-plate model with a sharp leading edge. The total length of the model is 486 mm, the width is 300 mm, and the leading edge angle is 20°. To obtain the desired skin friction distribution in the model surface, the surface of the model is designed with several blocks, and different test locations are obtained by using different blocks. In this test, two skin friction test points are chosen, which are 160 and 274 mm from the leading edge. The test is conducted separately because of the restriction of the room for the skin friction balance mounting. Four thin-film flux gauges are located around the skin friction sensing head to test the heat flux around the skin friction test location. The mounting sketch of the skin friction balance and the heat flux gauge in the model surface are shown in Fig. 5. To minimize the mass of the model, all the models are made of aluminum alloy.

The skin friction test was performed in a 0.6 m shock tunnel in CARDC. The inner diameter of the shock tube is 80 mm. The driver section and the driven section are 7.5 m and 12.5 m long, respectively. The exit diameter of the contour nozzle is 0.6 m, and the cross-sectional diameter of the test section is 1 m. The test gas is nitrogen or air, and the driver gas is hydrogen or a mixture of hydrogen and nitrogen. The different Mach numbers are obtained by replacing the throat of the nozzle, and different Reynolds numbers are obtained by adjusting the pressure of the driver and driven section gas to satisfy different simulation conditions. The Mach number of the shock tunnel varies from 6 to 12, the attack angle ranges from −30° to 30°, and the testing time ranges from 2 to 13 ms.

The skin friction test was conducted in the flow field with a Mach number of 5.78 and a unit Reynolds number of 3.09×10^7/m. The attack angle of the model is 0°.

Shock Tunnel Test

When the experiment is conducted, the model is tail mounted in the shock tunnel. The measuring head of the skin friction balance is mounted flush with the surface of the model. In the test, the material of the measuring head is the

same as in the flat-plate model, so the influence of the material on the skin friction test result is minimized. The flat-plate model mounted in the shock tunnel is shown in Fig. 6. The heat flux and skin friction are tested at the same time.

The typical curve of skin friction measurement is shown in Fig. 7. During the test time, the signal of the skin friction balance output is acceptable, that is to say, the dynamic performance and the static performance such as sensitivity of the skin friction are high and can satisfy the measurement of the skin friction of the hypersonic vehicles in shock tunnel.

The centerline skin friction distributions tested are shown in Fig. 8, along with the CFD estimates using turbulent boundary layer theory. The tested results are higher than the theory results. The difference between tested results and the theory results may be that the model in the test has a rough surface, whereas the theory results were calculated for a smooth surface.

The heat flux in the model surface changing with the distance from the model edge is shown in Fig. 9. The trend of the test result is the same as that of the theoretical result, but the values are slightly larger.

The uncertainty of measurement is an important parameter correlated to the test result, which was used to estimate the decentralization of the measured value. In this research, the uncertainty of the skin friction test result is calculated by the precision limit and bias limit and is shown to be the same as in AGARD-AR-304 [26].

In this research, the uncertainty range of the skin friction for the flat-plate model is 6.8–14.4 %, which could be accepted in the actual experimental condition and technique level. The uncertainty of the skin friction testing will be fixed to approximately 10 % in future research.

Conclusion

In this paper, the skin friction of the flat-plate model is tested with a piezoelectric skin friction balance, and the uncertainty of the result is less than 15 %.

In future research, the structure and manufacture process of the piezoelectric skin friction balance will be modified and optimized. The disturbance of the shock tunnel flow field environment, especially the pressure influence on the skin friction measurement, will be considered and studied. At the same time, the correlation between the skin friction and the heat flux measurement will be further researched.

Fig. 6 The flat-plate model installed in the shock tunnel

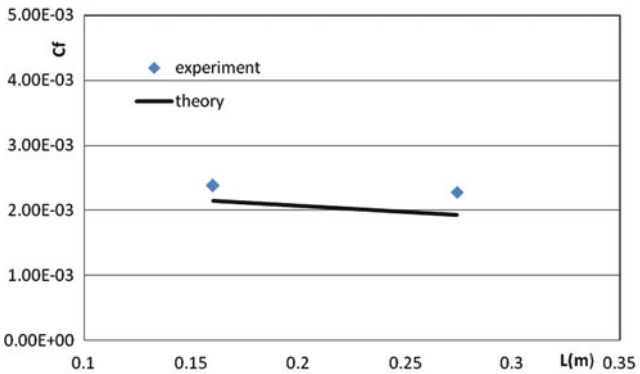

Fig. 8 Skin friction distribution along the model centerline

Fig. 7 Typical skin friction history of the flat-plate model

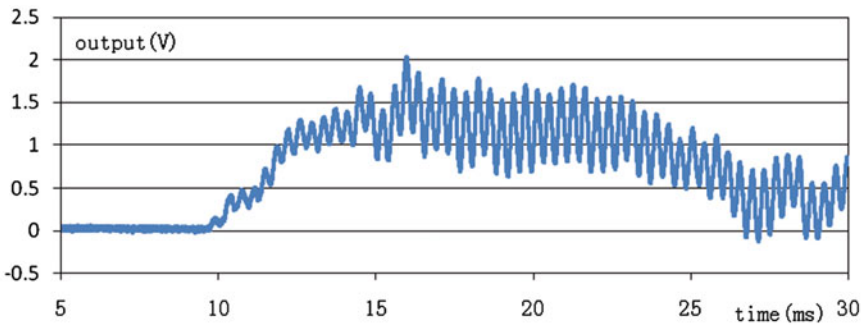

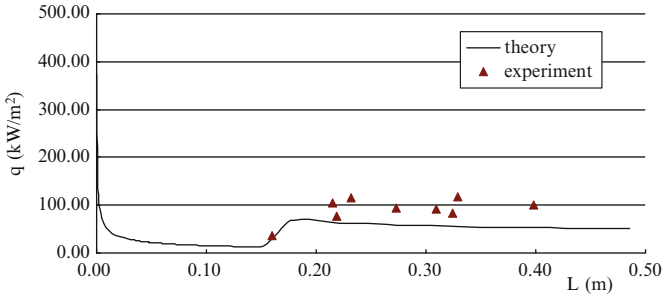

Fig. 9 Heat flux distribution along the model centerline

The purpose of skin friction measurement research is to provide high-quality experimental data for the development of hypersonic vehicles in shock tunnels.

References

1. Silvester, T.B., Morgan, R.G.: Skin friction measurements and flow establishment within a Long Duct at superorbital speeds. AIAA J. **46**(2), 527–536 (2008)
2. Vasudevan, B.: Measurement of Skin Friction at Hypersonic Speeds Using Fiber-Optic Sensors. AIAA 2005-3323
3. Pulliam, W., Schetz, J.: Development of Fiber Optic Aerodynamic Sensors for High Reynolds Number Supersonic Flows. AIAA 2001-2045
4. Liu, T., Montefort, J., Woodiga, S., Merati, P., Shen, L.: Global luminescent oil-film skin-friction meter. AIAA J. **46**(2), 476–485 (2008)
5. David, M.D., Aaron, D.: Skin-friction measurements using oil-film interferometry in NASA'S 11-foot Transonic Wind Tunnel. AIAA J. **46**(10), 2401–2407 (2008)
6. Kheireddine, A.S., Chaturvedi, S.K., Parmar, D.S.: Novel Technique for Skin Friction Measurement in Wind Tunnel Environment Utilizing Polymer Dispersed Liquid Crystals. AIAA 97-2218
7. Davie, E.H., Thomas, C.F., Jerome, P.F.: Naval Maneuvering Research and the Need for Shear Stress Measurements. AIAA 2004-2605
8. Jim, C., Sergey, F., Alan, F., Larry, G.: Skin Friction Measurements Using Elastic Films. AIAA 2010-42
9. Schober, M., Obermeier, E., Pirskawetz, S., Fernoholz, H.H.: A MEMS skin friction sensor for time resolved measurements in separated flows. Exp. Fluids **36**, 593–599 (2004)
10. Jessica, M., John, C., Jeremy, S., Vijay, C., Louis, N.G., Mark, S.: Experimental Verification of a MEMS Based Skin Friction Sensor for Quantitative Wall Shear Stress Measurement. AIAA 2011-3995
11. Rodney, D.W., Bowersox, J.A., Schetz, K.C., Steve, D.: Technique for direct measurement of skin friction in high enthalpy impulsive scramjet flowfields. AIAA J. **33**(7), 1286–1291 (1995)
12. Alexander, K.S., Rolling, A.J., Schetz, J.A.: A Novel Skin Friction Sensor for Hypersonic Flow. AIAA 2006-3837
13. August, J.R., Schetz, J.A.: Direct Skin Friction Measurements with Shock-Impingement Compensation in Complex Turbulent Flows. AIAA 2006-3838
14. Kelly, G.M., Simmons, J.M., Paull, A.: Skin-friction gauge for use in hypervelocity impulse facilities. AIAA J. **30**(3), 844–845 (1992)
15. Michael, S.H., Erik, P.M., Timothy, P.W.: A Review of Experimental Studies of Surface Roughness and Blowing on the Heat Transfer and Skin Friction to Nosetips and Slender Cones in High Mach Numbers Flows. AIAA 2008-3097
16. Seun, K.K.: Development of Piezoelectric Skin Friction Force Vector Transducer for a Hypersonic Wind Tunnel. NASA-CR-127447
17. Theodore, B.S., Joseph, A.S., Trong, T.B.: Development of direct-measuring skin friction gauges for hypersonic flight tests. AIAA J. **41**(8), 1429–1437 (2003)
18. Trong, T.B., Brett, J.P., Keith, L.K.: In Flight Capability for Evaluation Skin-Friction Gages and Other Near-Wall Flow Sensors. AIAA 2003-741
19. Todd, B.S., Richard, G.M., Peter, A.J.: Skin Friction Measurements in a Duct in the X3 Superorbital Expansion Tube. AIAA 2004-3551
20. Goyne, C.P., Stalker, R.J., Paull, A.: Shock-tunnel skin friction measurement in a supersonic combustor. J. Propul. Power **15**(5), 699–705 (1999)
21. Bowersox, R., Schetz, J.: Skin Friction Gauges for High Enthalpy Impulsive Flows. AIAA 93-5079
22. Michael, S.H., Erik, P.M., Matthew M.: Heat Transfer Measurements to Examine Surface Roughness and Blowing Effects in Hypersonic Flows. AIAA 2011-760
23. Calspan-UP Research Center: Large Energy National Shock Tunnel, Description and Capabilities. AD-A338839 (1990)
24. Michael, S.H.: An Experimental Investigation of Turbulent Boundary Layers at High Mach Number and Reynolds Numbers. NASA CR-112147 (1972)
25. Frank, K.L., Dan, E.M.: Advanced Hypersonic Test Facilities. AIAA, pp. 83 (2002)
26. American Institute of Aeronautics and Astronautics: Assessment of Experimental Uncertainty with Application to Wind Tunnel Testing. Standard AIAAS-071A-1999 (1999)

Effects of Attack Angle on Starting Performance of a Hypersonic Inlet

Shuaitao Guo, Wenzhi Gao, Enlai Zhang, Zhufei Li, and Jiming Yang

Introduction

The inlet starting characteristic is one of the key factors governing the performance and operation of a hypersonic air-breathing propulsion system. For efficient and safe operation, the engine requires the inlet to work in a starting mode [1]. There are many factors that cause a hypersonic inlet to unstart, such as large internal contraction ratio, high back pressure, low Mach number, serious shock wave/boundary interactions, angle of attack, etc. [2–3]. During a real flight, when the vehicle suffers from a sudden change in the environment or undergoes a maneuver, the inlet will inevitably experience the variation of incoming flow, in which the angle of attack may play an important role in the inlet starting behaviors.

Many investigations have been conducted on hypersonic inlet flow to study the influence of angle of attack on starting performance, including numerical simulations and experiments. Stephen [4] conducted wind tunnel experiments of HIFiRE 6. The combined schlieren and pressure data indicated that the model would only start at Mach 4.3 with angle of attack of $-5.4°$ to $5.7°$. Zha [5] calculated the unstart transient of an axisymmetric inlet at Mach 2 and attack angle of $2°$ by using a 3D time accurate Navier-Stokes solver. The results showed that when an angle of attack is imposed, the flow on the leeward side has a stronger compression. Recently, Liu [6] conducted wind tunnel experiments on a sidewall compression scramjet inlet at Mach number 3.85 and suggested that in the dynamic process, the inlet goes through an unstart-restart process and the value of unstarting angle of attack will increase and the restarting value will decrease with a rising of the frequency in the oscillation.

Many details of unstart characteristics of the hypersonic inlet related to angle of attack remain unknown. On the other hand, shock tunnel recently exhibits attractive potential on the investigations of the inlet performance, although the experiments related to angle of attack are insufficient, especially the self-starting experiments. Therefore, additional numerical simulations and shock tunnel experiments are valuable. In the present work, we focus on the effects of attack angles on the inlet starting behaviors under a given incoming flow Mach number. Both starting and self-starting characteristics are the main interests of this study.

Experimental Facility and Test Model

The experiments were conducted in the shock tunnel JB300 of the University of Science and Technology of China (USTC). The shock tunnel was operated in an equilibrium interface mode. The test time was about 40 ms. The freestream flow conditions for the wind tunnel were Mach number $M_\infty = 5.9$, total pressure $p_0 = 1.27$ MPa, total temperature $T_0 = 810$ K, static pressure $P_\infty = 831$ Pa, static temperature $T_\infty = 102$ K, and unit Reynolds number $Re_\infty = 5.1 \times 10^6$/m.

The inlet model for this study was a generic 2D mixed compression system, as shown in Fig. 1. It consists of two compression ramps, a horizontal cowl and a constant area isolator. Two sidewalls with sharp leading edge to avoid bow shock were adopted to ensure the flow to be close to two dimensional. The first ramp has an angle of $9°$ and

S. Guo • E. Zhang • Z. Li (✉) • J. Yang
Department of Modern Mechanics, University of Science and Technology of China, 96 Jinzhai Road, Hefei, Anhui 230026, People's Republic of China
e-mail: gst@mail.ustc.edu.cn; lizhufei@mail.ustc.edu.cn

W. Gao
Department of Modern Mechanics, University of Science and Technology of China, 96 Jinzhai Road, Hefei, Anhui 230026, People's Republic of China

School of Mechanical Engineering, Hefei University of Technology, 193 Tunxi Road, Hefei, Anhui 230009, People's Republic of China

G. Ben-Dor et al. (eds.), *30th International Symposium on Shock Waves 1*, DOI 10.1007/978-3-319-46213-4_25

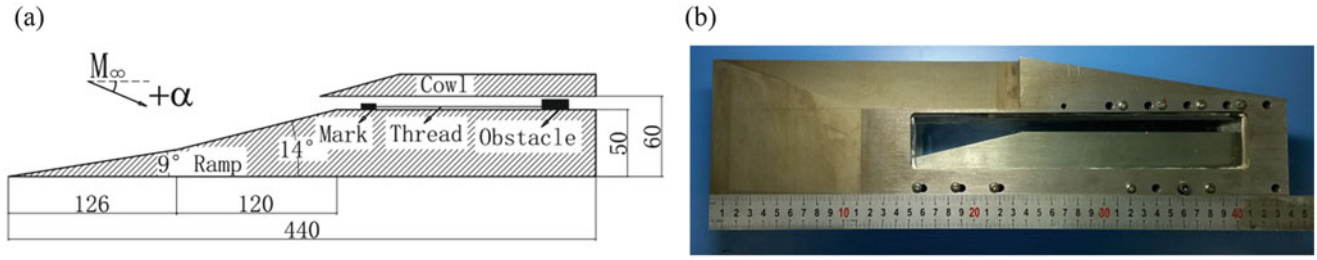

Fig. 1 Test inlet model

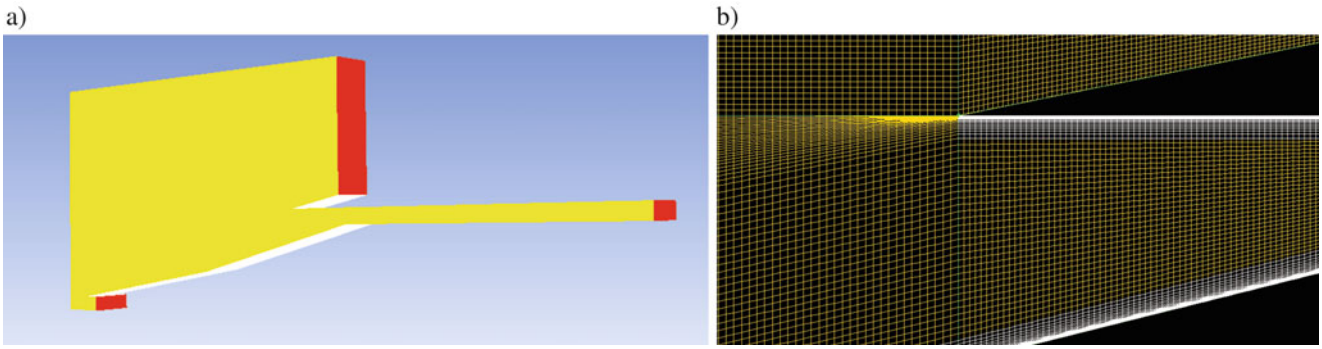

Fig. 2 Computational grids and domains

length of 126 mm. The second ramp provides additional 5° compression with a length of 120 mm. The height of the isolator is 10 mm and the internal contraction ration is 1.77. Figure 1a shows the schematic dimension of the model. In order to visualize the flow field of the inlet model, the JB300 shock tunnel is equipped with a high-speed schlieren system. The high-speed camera is operated at a framing rate of 10 kHz and exposure time of 4 μs.

Numerical Simulation Method

The CFD simulations were performed using Fluent solver. The Roe flux difference split scheme and a second-order upwind scheme were used to solve governing equations. The case was analyzed with standard S-A turbulence model. The computational domains and grids are shown in Fig. 2. The computational domains are set to be three-dimensional to take into account the viscous effects of sidewalls. To capture detailed flow features in boundary layer, the structured mesh is refined at the near-wall region, and the smallest mesh height is 4 μm.

Results

Numerical Results

In order to find the critical value of unstarting attack angle, the angle of attack is increased step by step based on a started flow field of small attack angle. Similar method is used for finding the critical value of self-starting attack angle, although based on an unstarted flow field of large attack angle. The numerical results show that the critical value of unstarting attack angle is in the range of 12°–14°, above which the inlet flow will be unstarted no matter what initial flow field is used for the calculation. On the other hand, the self-starting attack angle is in the range of 0°–1°, below which a started inlet flow will be established independent of the initial conditions. The numerical schlieren images are shown in Fig. 3 with $\alpha = 0°$, $\alpha = 7°$, $\alpha = 12°$, and $\alpha = 14°$. As can be seen, for started flow field, the internal flow field consists of a series of shock waves reflecting between the ceiling and floor of the duct. The cowl shock impinges near the shoulder of the inlet and causes flow separation of small

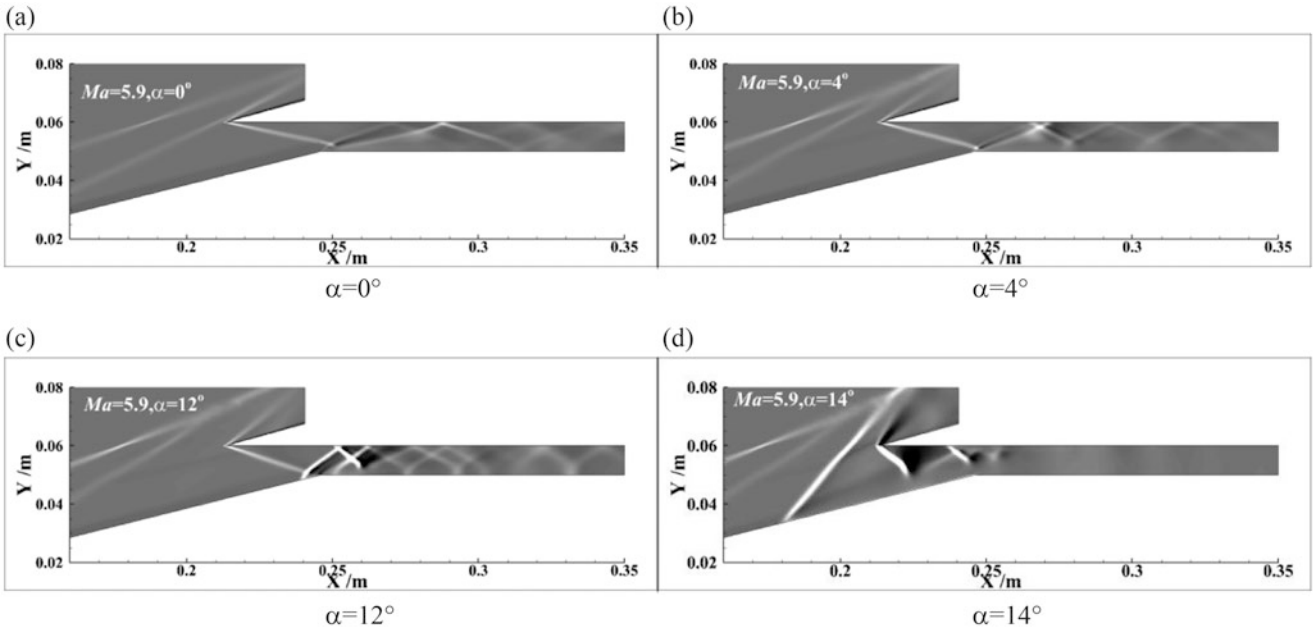

Fig. 3 Flow-field characteristics with increasing α (for the unstarting attack angle estimation)

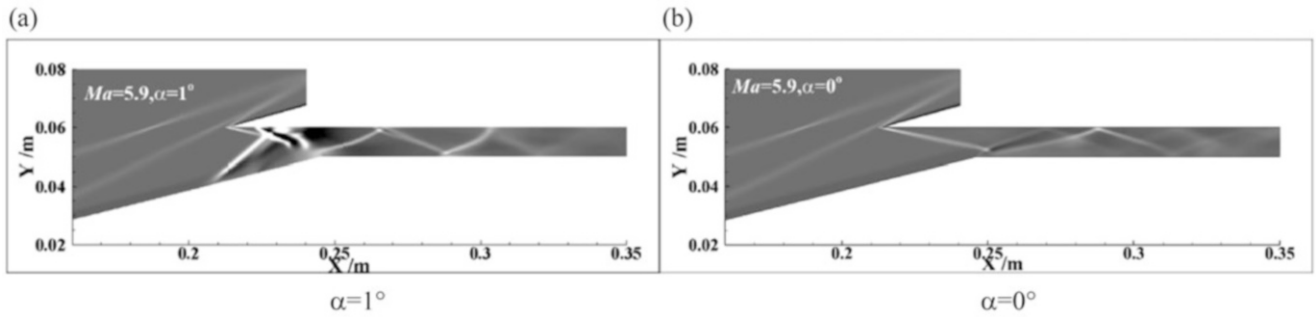

Fig. 4 Flow-field characteristics with different α (in the restarting process)

scale. The induced separation shock and reflected shock impinge on the ceiling of the duct. In the rising process of α, the strength of external ramp shock wave and the scale of flow separation near the shoulder are increasing gradually. For $\alpha = 12°$, the flow field of the inlet is still in started state, but the flow separation region is larger than the case of 4° angle of attack. When α increases from 12° to 14°, the mass captured by the inlet chokes in the throat. The separation shock is pushed to the second ramp and the separation region is spilled out, and consequently the inlet suffers from an unstarting process. Therefore the critical value of unstarting attack angle can be estimated to be in the range of 12°–14°.

During the decreasing process of α, the numerical schlieren images are shown in Fig. 4 with $\alpha = 1°$ and $\alpha = 0°$, respectively. For $\alpha = 1°$, the separation bubble is still located in the second ramp, and the inlet is in unstarted mode. However, when α decreased to 0°, the separation bubble and additional separation shock are swallowed by the incoming flow and disappeared. The internal flow field is therefore recovered to starting mode and the shock structure is clear. Thus, the critical values of self-starting attack angles can be reasonably determined to be in the range of 0°–1°. As shown in Fig. 5, the curves of exit Mach number and total pressure recovery in the increasing process of α are different from that in the decreasing process of α. This phenomenon is called hysteresis effect and the curves form a hysteresis loop.

It can be imagined that, when a positive angle of attack is imposed, the flow has a stronger compression than that at zero angle of attack. For an increased angle of attack, the effective incoming flow Mach number decreases before the entrance of a 2D inlet, therefore the unstarting/self-starting

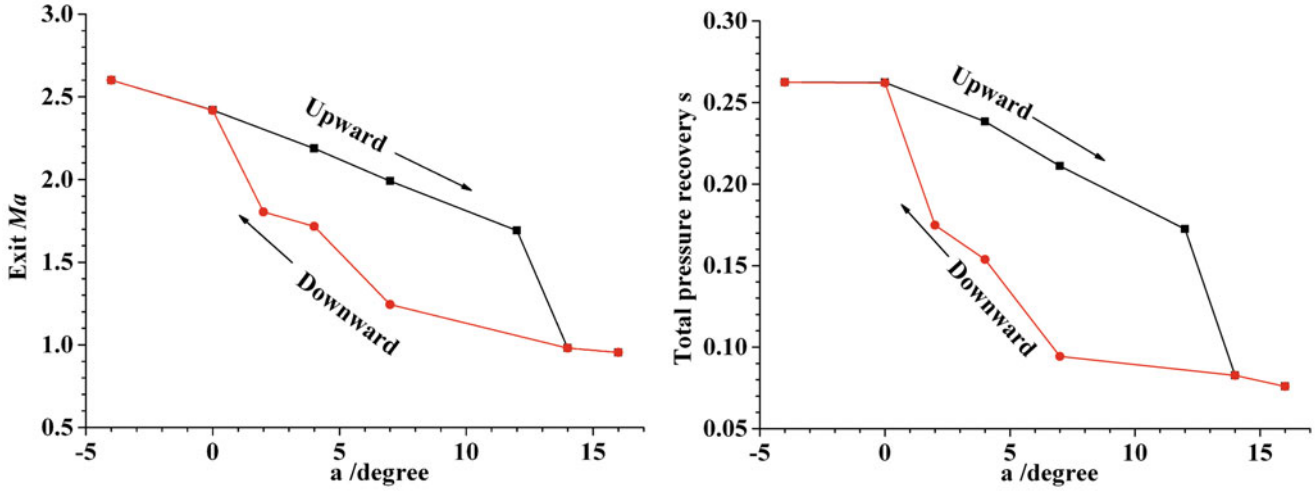

Fig. 5 Comparison of performance parameters as a function of α

Table 1 The effective incoming entrance flow Mach number

Flow M_∞	Attack angle α(°)	Effective entrance M_1	Status
3.7	0	2.86	Unstarting
5.8	0	4.20	Self-starting
5.9	0	4.25	Self-starting
5.9	1	4.14	Double solution
5.9	4	3.81	Double solution
5.9	12	2.96	Double solution
5.9	14	2.76	Unstarting

capability declines accordingly. For zero angle of attack, the calculated critical values of self-starting and unstarting Mach number are 5.8 and 3.7, respectively, for this inlet model. As mentioned before, the numerical results show that the critical values of starting and self-starting attack angles are in the range of 12°–14° and 0°–1°, respectively. Thus the corresponding effective incoming flow Mach numbers before the entrance of this 2D inlet are compared as shown in Table 1. When flow M_∞ is 3.7, the effective incoming entrance Mach number is 2.86, which is between 2.96 and 2.76, corresponding to the attack angle of 12° and 14°, respectively. On the other hand, when flow M_∞ is 5.8, the effective incoming entrance Mach number is 4.20, which falls between 4.25 and 4.14, corresponding to the attack angle of 0° and 1°, respectively. Therefore it can be reasonably concluded that the effective incoming flow Mach numbers before the entrance of this 2D inlet are consistent either by changing the incoming flow Mach number or by changing the angle of attack. This indicates that we can change flow Mach numbers indirectly by changing attack angle in the shock tunnel experiments, although this conclusion may not fit for other case and need further investigation.

Experimental Results

The shock tunnel experiments were conducted with $\alpha = 4°$, 0°, and −4°, including both starting and self-starting experiments. Since the shock tunnel has a strong help-to-start effect during the establishment of the operation as long as the initial pressure of the vacuum tank is sufficiently low, an examination of the inlet starting capability can be performed directly. On the other hand, a light moveable obstacle that serves as a temporal flow plug is placed in the downstream of the isolator to check the self-starting capability of the inlet [7].

The schlieren images of starting process at $\alpha = 4°$ are shown as Fig. 6. At $t = 0$ ms, the hypersonic flow is near to come. And when $t = 1$ ms, the separation shock impinges on the ceiling of the duct and interacts with the cowl shock. But the separation shock disappears quickly at $t = 2$ ms when the tunnel flow is established, and the cowl shock impinges near the shoulder of the inlet. The shock structure is clear and the separation bubble is small. This starting state continues during the rest period of the operational time, thus the inlet is started at $\alpha = 4°$. Compared with the numerical simulation in Fig. 3b, the shock structures are similar. The schlieren images of self-starting process at $\alpha = 4°$ are shown in Fig. 7. As the obstacle located at the rear part of the inlet channel, beyond the visualization region, a little mark attached to the obstacle by a cotton thread is set near the shoulder to ensure that the obstacle is blown out. In Fig. 7, $t = 0$ ms, the flow is near to come and the thread is slack. At $t = 1.0$ ms, the flow field in the inlet shows a sign of supersonic flow, although followed by an obstacle-choked process, which induces separation shock to move upstream. At about $t = 5.5$ ms, the obstacle is already blown out, but the expelled separation shock still stands

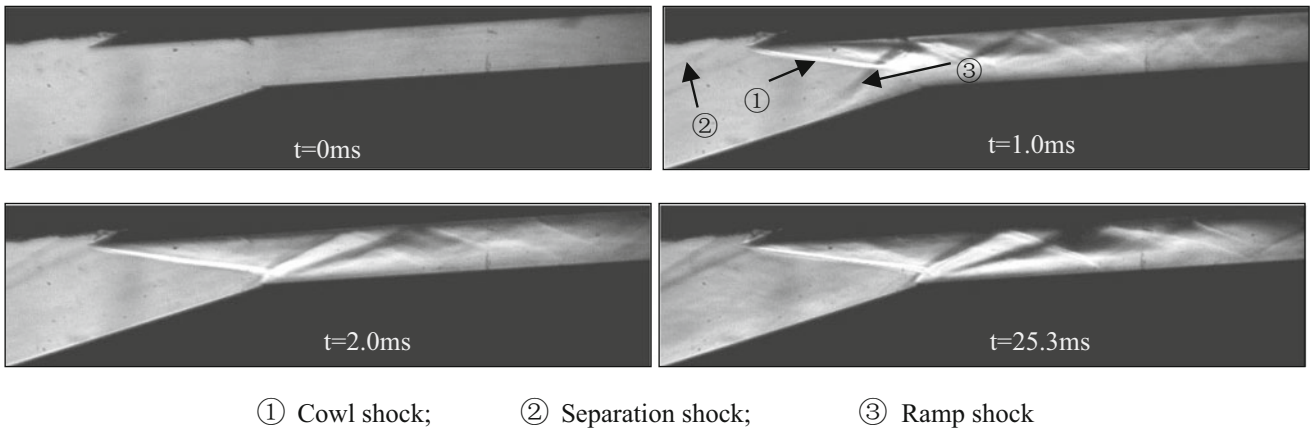

Fig. 6 Schlieren images of starting process at $\alpha = 4°$

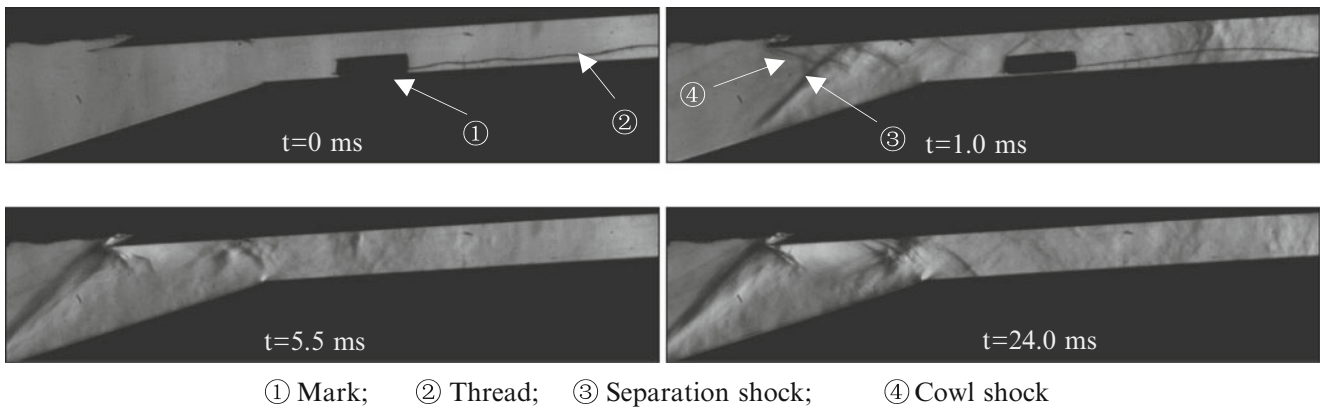

Fig. 7 Schlieren images of self-starting process at $\alpha = 4°$

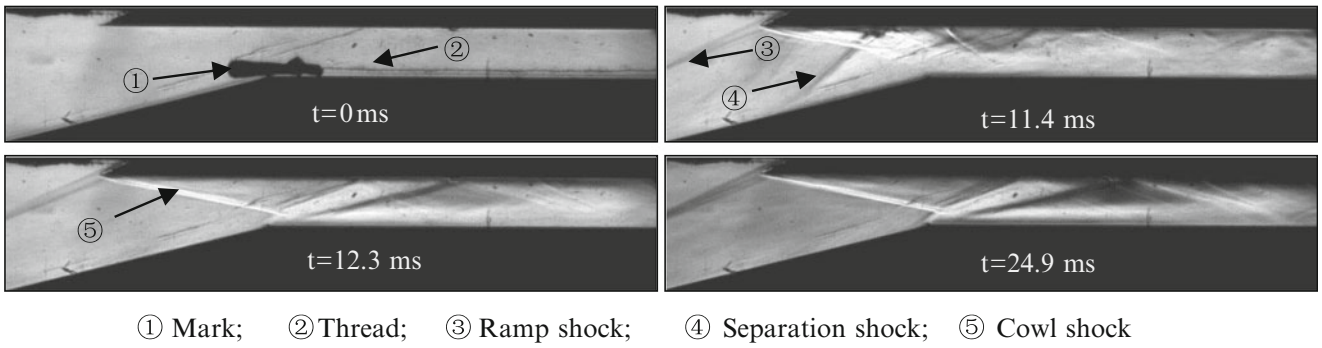

Fig. 8 Schlieren images of self-starting process at $\alpha = 0°$

at the second ramp. The inlet is in unstarting mode and this state retains till test flow breaks up. So the inlet at $\alpha = 4°$ cannot self-start.

The schlieren images of self-starting process at $\alpha = 0°$ are shown in Fig. 8. For $t = 0$ ms, the flow is near to enter the inlet and the mark is located near the shoulder of the inlet statically. Then the flow comes, the channel is firstly choked because of the obstacle. The obstacle is moving downstream and the induced separation shock is moving upstream. First, the obstacle is blown out but the separation shock still exists. The inlet is in unstarting mode temporarily, as shown at $t = 11.4$ ms. Then the separation shock begins to move back and the flow in the inlet will be reestablished. At $t = 12.3$ ms, the separation

shock disappears and the inlet is in a starting mode. This state retains till the end of test time. Therefore the self-starting ability of the inlet at $\alpha = 0^\circ$ is confirmed.

Conclusions

Both numerical simulations and shock tunnel experiments were conducted. The simulation results agree with experimental observations. Some conclusions can be summarized as follows:

1. The self-starting behaviors are different for various angles of attack, and a pitching down motion exhibits a favorable trend to the self-starting performance, whereas a pitching up is the opposite.
2. The variation of inlet performance parameters with increasing or decreasing process of α go through different route, or there exists a hysteresis effect.
3. The effective flow Mach numbers before the entrance of this 2D inlet are reasonably consistent either by changing flow Mach numbers or by changing attack angles.

Acknowledgments This work was supported by the National Natural Science Foundation of China (Grant No. 11402263).

References

1. Van Wie, D.M., Kwok, F.T., et al.: Starting Characteristics of Supersonic Inlets. AIAA Paper 1996-2914 (1996)
2. Li, Z., Huang, B., Yang, J.: A Novel Test of Starting Characteristics of Hypersonic Inlets in Shock Tunnel. AIAA Paper 2011-2308 (2011)
3. Liu, K., Zhang, K.: Numerical Investigation of 2-D Hypersonic Inlet Starting Characteristic Caused by Dynamic Angle-of-Attack. AIAA 2010-7034 (2010)
4. Stephen, E.J., Hoenish, S.R., et al.: HIFiRE 6 Unstart Conditions at Off-Design Mach Numbers. AIAA 2015-0109 (2015)
5. Zha, G-C., Knight, D.D., et al.: Numerical Investigations of HSCT Inlet Unstart Transient at Angle of Attack. AIAA 98-3583 (1998)
6. Liu, K., Zhang, K.: Experiment of Dynamic Angle-of-Attack on a Side Wall Compression Scramjet Inlet at Mach 3.85. AIAA Paper 2011-2348 (2011)
7. Li, Z., Huang, B., Yang, J.: Starting characteristics of hypersonic inlets in shock tunnel. In: 28th International Symposium on Shock Waves, Manchester (2011)

Optimization of Hypersonic Power Law Derived Waverider Using TLBO

Yogendra Singh, Manoj Kumar K. Devaraj, S.N. Omkar, and Gopalan Jagadeesh

Introduction

Hypersonic cruise system is a potential candidate for easing the space flight and for developing high-speed systems for defense application. In hypersonic flow regime, high lifting bodies are of special interest to scientific community. Waverider is an option to create such high lifting bodies. Waverider is a lifting body tailored to create high lift to drag ratio in high-speed flow. The tailoring is done in such a manner that the shock formed is attached to the leading edge of the configuration leading to no pressure leakage across the top and bottom surface. Waverider concept was first introduced by Nonweiler [1] in 1959 as a new concept of higher-speed winged atmospheric reentry vehicles promising high lift coefficient. Shapes derived by him were based on two-dimensional analytical solution for an oblique shock over a wedge. Waveriders from conical flow field were later on derived by Jones [2] based on inviscid flow assumption. Since then the design methodology has evolved many fold resulting in viscous optimized and osculating cone configurations. In 2000 Starkey et al. [3] developed a power law derived aerodynamic model to study the lift and drag characteristics of the waverider. Having an analytical model at an early stage is beneficial for the design; this model reduces the complexities associated with the flow. Aerodynamic coefficients can be estimated using such models, and designing higher lifting bodies becomes less computationally demanding.

Y. Singh (✉) • M.K.K. Devaraj
Center of Excellence in Hypersonics, Indian Institute of Science, Bangalore, India
e-mail: ygsingh101@gmail.com

S.N. Omkar
Chief Research Scientist, Department of Aerospace Engineering, Indian Institute of Science, Bangalore, India

G. Jagadeesh
Department of Aerospace Engineering, Indian Institute of Science, Bangalore, India

Classical optimization techniques are useful in estimating unconstrained maxima (or minima) for continuous and differentiable functions. Functions which are discontinuous and/or not differentiable can be optimized using evolutionary or swarm intelligence algorithms. Teacher-learner-based optimization (TLBO) [4] is one such evolutionary algorithm and is used in this study to get optimized waverider geometry parameters. TLBO is population-based evolutionary algorithm which simulates the teacher-learning environment of a class. Unlike other evolutionary and swarm intelligence algorithms, TLBO requires only common controlling parameters like population size and number of generations, making it an algorithm-specific parameter-less algorithm.

This paper presents the results and generic trends obtained using Starkey's model. Single-objective design optimization study is performed to maximize the overall aerodynamic efficiency (L/D) and to maximize aerodynamic efficiency volume along with minimum heat flux. Optimum geometry parameters for various Mach numbers from 5 to 8 in steps of 0.5 are presented here. Also the aerodynamic model is examined using variance-based sensitivity analysis to determine the level of dependency of design variables on the objective functions.

Methodology

Waverider Configuration

Waverider configuration designed in present study is based on 2-D wedge flow field. Variables pertaining to waverider design are given in Fig. 1, where n is power law exponent; θ is the ramp angle of the 2-D wedge required for flow field generation; β is the shock wave angle; l, w, and h are length, width, and height, respectively; and subscripts "u" and "l" denote the upper and lower surface of the waverider. Aspect ratio λ for waverider is defined as l/w. Waverider design process includes following steps:

G. Ben-Dor et al. (eds.), *30th International Symposium on Shock Waves 1*, DOI 10.1007/978-3-319-46213-4_26

(a) Consider a wedge in a hypersonic flow field, assume trailing edge contour (in present case it is taken to be a power law), (b) this contour (power law) is backtracked in a direction parallel to the freestream velocity till the shock plane, this forms the upper surface of the waverider, (c) now the intersection contour with the shock plane is traced in flow direction parallel to the wedge till the start of the initial power law contour, and this completes the lower surface of the configuration. An example of waverider configuration is shown in Fig. 2. A vast design space is created by varying n, θ, and λ for a given design Mach number (M).

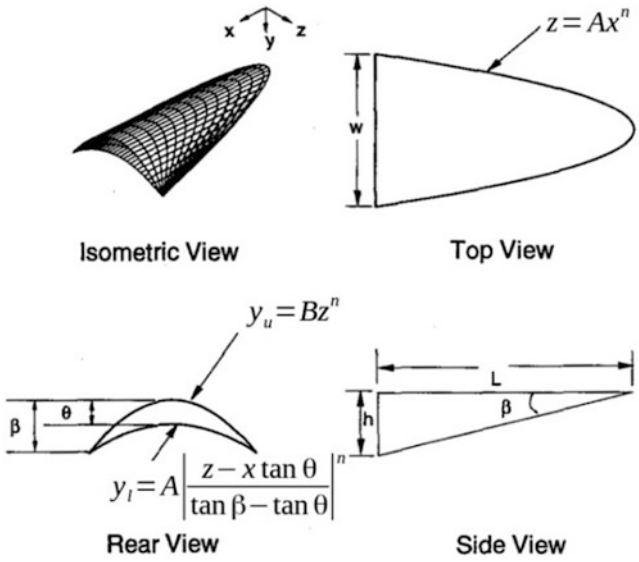

Fig. 1 Parametric wedge derived waverider definition [2]

Analytical Model

Model proposed by Starkey [3] is used to calculate lift and drag over power law based wedge derived waverider configurations over a range of angles of attack from −2 to 6 over Mach number range from 5 to 8. While shock expansion theory is used to calculate lift and wave drag, Eckert's reference temperature is used to calculate viscous drag. The model used in present study is validated by comparing lift to drag ratios obtained using in-house CFD solver HiFUN. Figure 3 shows the variation of aerodynamic efficiency with angle of attack for a Mach 7 waverider for analytical and numerical simulations. Numerical solution obtained using HiFUN is also validated with experimental data [5] from available literature to gain confidence over the analytical model. Table 1 shows the comparison of lift and drag coefficients obtained using HiFUN and experiments.

Optimization

Optimization function: The objective functions used in present analysis are as follows: (a) Maximize aerodynamic efficiency which can be mathematically written as L/D. (b) Maximize lift to drag ratio and volume for minimum surface area, this objective function can be written as $L/D \times \left(V^{(2/3)}/S\right)$. Design optimization is performed for specific Mach number. The input variables considered in this study are (a) $0.2 \leq n \leq 1$, (b) $5 \leq \theta \leq 15$, and (c) $0.7 \leq \lambda \leq 1.2$.

Optimization algorithm: Teacher-learner-based optimization (TLBO) algorithm developed by Rao [4] is employed

Fig. 2 Waverider configuration designed at $M = 6$; $n = 0.3$; $\theta = 8.2°$; $\lambda = 1$

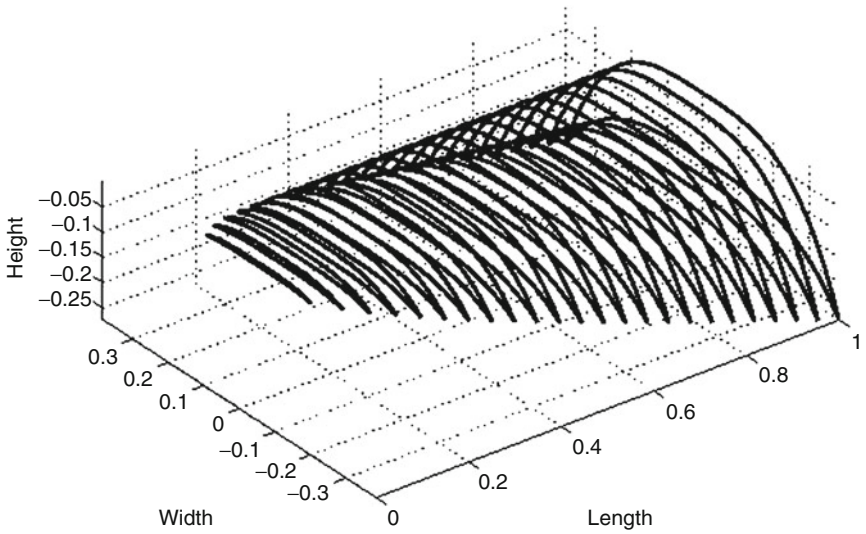

to perform the optimization. TLBO is specifically used because it is an algorithm-specific parameter-less algorithm, since there are only two common controlling parameters like population size and number of generations. In TLBO terminology, population size is represented by the number of students in a class and generation by a number of classes/courses. In order to perform the optimization, the number of student = 100 in a class and number of iteration/classes = 100.

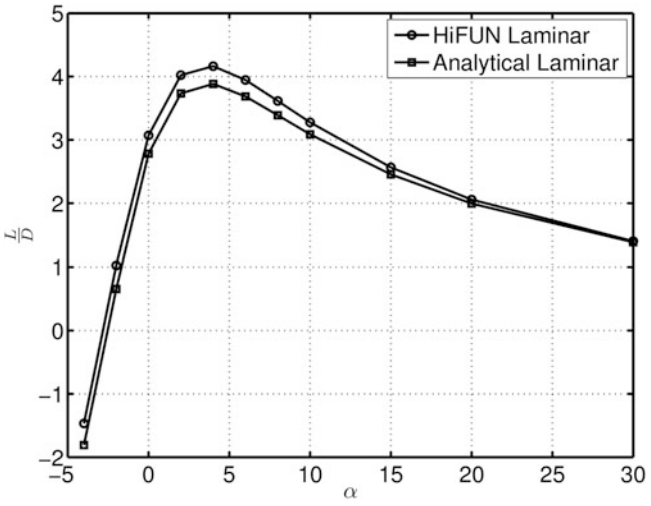

Fig. 3 Comparison of L/D with alpha for waverider geometry with the design parameters $M = 7$; $n = 0.3$; $\theta = 5°$; $\lambda = 1$[6]

Table 1 Comparison of force coefficients

Tool	C_L	C_D
Experiment [5]	0.039	0.0091
HiFUN	0.0369	0.010

Results and Discussions

Sensitivity Analysis

Sensitivity analysis is carried out to determine the effect of design variables on the objective functions, using Sobol's variance decomposition [7], which generates 1000 random input variable within the limits and calculates the objective function using the analytical model. Figure 4a–d shows the sensitivity indices of the design variables obtained using variance-based global sensitivity analysis. It is conspicuous from Fig. 5 that n, α, and θ play a major role when L/D is considered as objective function and n plays a major role when $L/D \times V^{(2/3)}/S$ is considered as objective function. Since lower values of n give maximum wetted area, the lower limit of n, i.e., 0.2, is the optimum solution for all the cases considered in this study.

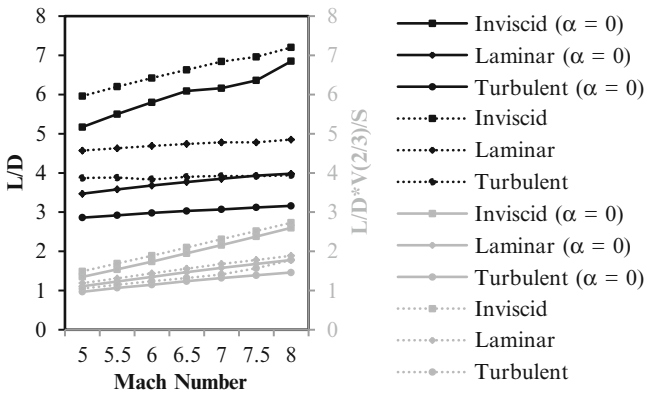

Fig. 5 Variation of objective functions with freestream Mach number

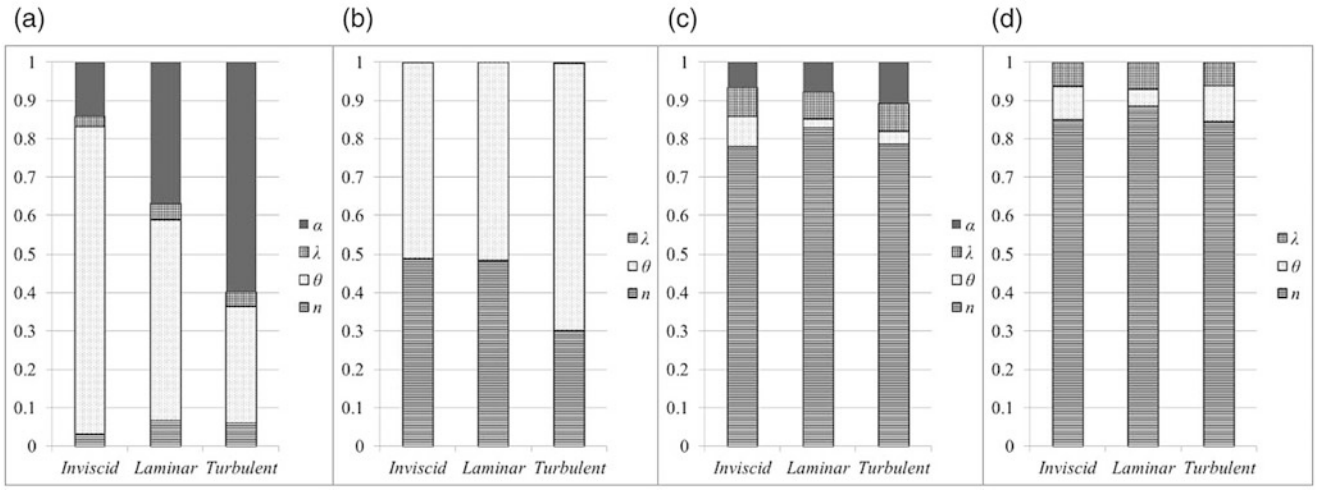

Fig. 4 Sensitivity indices for design variables: (**a**) L/D with α variation, (**b**) L/D with $\alpha = 0$, (**c**) $L/D \times V^{(2/3)}/S$ with α variation, and (**d**) $L/D \times V^{(2/3)}/S$ with $\alpha = 0$

Optimization

It can be inferred from Tables 2, 3, 4, and 5 and Fig. 5 that the objective function magnitude increases with increase in Mach number, irrespective of flow being viscous or nonviscous, but the value of objective function is lesser for viscous cases compared to inviscid case due to the effect of skin friction as expected. The magnitude of the objective function is more when angle of attack is considered as a variable compared to zero angle of attack cases irrespective of the objective functions. The effect of design variables on the objective functions for each case is discussed below.

1. *Maximize lift to drag ratio with design angle of attack equal to zero:* The optimum lift to drag ratio and the input variables, considering design angle of attack to be zero, is shown in Table 2. It can be seen that the value of θ is least from the design space irrespective of Mach number in inviscid case, θ increases with Mach number in laminar case, and the trend of θ variation is not monotonous with Mach number in turbulent case. The optimum value of θ for the viscous cases is higher when compared to the inviscid case.
2. *Maximize lift to drag ratio with angle of attack variation:* The optimum value of the lift to drag ratio and the input variables with angle of attack variation is shown in Table 3. Irrespective of the inviscid, laminar, or turbulent case, the following observations can be made: (a) θ is constant and its value is least from the design space considered and (b) angle of attack decreases with increase in Mach number.

Table 2 Optimum results for the first objective function (design angle of attack = zero)

	Objective function = maximize L/D											
	Inviscid				Laminar				Turbulent			
Design Mach number	n	θ	λ	L/D	n	θ	λ	L/D	n	θ	λ	L/D
5	0.2	5.00	0.7	5.17	0.2	6.43	0.7	3.47	0.2	8.19	0.7	2.86
5.5	0.2	5.00	0.7	5.50	0.2	6.51	0.7	3.58	0.2	8.21	0.7	2.92
6	0.2	5.00	0.7	5.80	0.2	6.60	0.7	3.68	0.2	8.22	0.7	2.98
6.5	0.2	5.00	0.7	6.09	0.2	6.64	0.7	3.77	0.2	8.21	0.7	3.03
7	0.2	5.00	0.7	6.16	0.2	6.65	0.7	3.85	0.2	8.15	0.7	3.07
7.5	0.2	5.00	0.7	6.36	0.2	6.67	0.7	3.93	0.2	8.15	0.7	3.12
8	0.2	5.00	0.7	6.85	0.2	6.70	0.7	3.98	0.2	8.01	0.7	3.16

Table 3 Optimum results for the first objective function with alpha as a variable

	Objective function = maximize L/D														
	Inviscid					Laminar					Turbulent				
Design Mach number	N	θ	λ	α	L/D	n	θ	λ	α	L/D	n	θ	λ	α	L/D
5	0.2	5.00	0.7	1.82	5.96	0.2	5.00	0.7	3.11	4.57	0.2	5.00	0.7	3.94	3.87
5.5	0.2	5.00	0.7	1.56	6.20	0.2	5.00	0.7	3.02	4.63	0.2	5.00	0.7	3.79	3.88
6	0.2	5.00	0.7	1.48	6.42	0.2	5.00	0.7	2.92	4.69	0.2	5.00	0.7	3.69	3.84
6.5	0.2	5.00	0.7	1.29	6.63	0.2	5.00	0.7	2.81	4.74	0.2	5.00	0.7	3.53	3.90
7	0.2	5.00	0.7	1.13	6.84	0.2	5.00	0.7	2.76	4.78	0.2	5.00	0.7	3.47	3.92
7.5	0.2	5.00	0.7	1.02	6.96	0.2	5.00	0.7	2.75	4.78	0.2	5.00	0.7	3.47	3.92
8	0.2	5.00	0.7	0.89	7.20	0.2	5.00	0.7	2.61	4.85	0.2	5.00	0.7	3.20	3.94

Table 4 Optimum results for second objective function (design angle of attack = zero)

	Objective function = maximize $L/D \times V^{(2/3)}/S$											
	Inviscid				Laminar				Turbulent			
Design Mach number	n	θ	λ	L/D	n	θ	λ	L/D	n	θ	λ	L/D
5	0.2	7.39	1.2	1.35	0.2	10.34	1.2	1.11	0.2	11.62	1.2	0.97
5.5	0.2	6.85	1.2	1.54	0.2	9.99	1.2	1.23	0.2	11.27	1.2	1.07
6	0.2	6.40	1.2	1.74	0.2	9.68	1.2	1.35	0.2	10.92	1.2	1.15
6.5	0.2	5.95	1.2	1.95	0.2	9.40	1.2	1.47	0.2	10.60	1.2	1.24
7	0.2	5.59	1.2	2.16	0.2	9.14	1.2	1.58	0.2	10.31	1.2	1.32
7.5	0.2	5.26	1.2	2.38	0.2	8.91	1.2	1.68	0.2	10.10	1.2	1.39
8	0.2	5.00	1.2	2.60	0.2	8.70	1.2	1.78	0.2	9.77	1.2	1.46

Table 5 Optimum results for the second objective function with alpha as a variable

Design Mach number	Objective function = maximize $L/D \times V^{(2/3)}/S$														
	Inviscid					Laminar					Turbulent				
	n	θ	λ	α	L/D	n	θ	λ	α	L/D	n	θ	λ	α	L/D
5	0.2	5.00	1.2	1.91	1.49	0.2	7.80	1.2	2.52	1.19	0.2	8.34	1.2	2.79	1.05
5.5	0.2	5.00	1.2	1.64	1.69	0.2	8.00	1.2	1.81	1.31	0.2	8.39	1.2	2.68	1.15
6	0.2	5.00	1.2	1.37	1.89	0.2	7.69	1.2	2.06	1.44	0.2	7.79	1.2	2.71	1.24
6.5	0.2	5.00	1.2	1.12	2.10	0.2	7.25	1.2	2.29	1.56	0.2	8.84	1.2	2.57	1.32
7	0.2	5.00	1.2	1.13	2.31	0.2	6.97	1.2	2.11	1.68	0.2	7.95	1.2	2.57	1.41
7.5	0.2	5.00	1.2	1.00	2.52	0.2	6.87	1.2	2.07	1.78	0.2	6.85	1.2	1.99	1.57
8	0.2	5.00	1.2	0.93	2.73	0.2	6.73	1.2	2.00	1.89	0.2	7.45	1.2	2.47	1.78

3. *Maximize lift to drag ratio and volume and minimize heat flux with design angle of attack equal to zero:* Results for this case are shown in Table 4. As volume is considered in the present case, the values of n and λ are 0.2 and 1.2 where the volume is maximum. It can be inferred that θ decreases with increase in Mach number for all the cases.
4. *Maximize lift to drag ratio and volume and minimize heat flux with angle of attack variation:* Results specific to this case are shown in Table 5. Observations of this analysis are (a) θ is constant and its value is least from the design space for inviscid case irrespective of the Mach number. Variation of theta and alpha are non-monotonous for all the other cases.

Conclusion

An attempt has been made to use TLBO as an optimization tool for designing high lift to drag waverider configurations. Two objective functions are considered, namely, L/D and $L/D \times V^{(2/3)}/S$. Inviscid solution has been validated using CFD codes as well as experiments. The effect of design variables is thoroughly discussed. Optimization methodology is established, and accuracy of the results can be increased further by using experimental data or validated CFD codes.

References

1. Nonweiler, T.R.F.: Aerodynamic problems of manned space vehicles. J. R. Aeronaut. Soc. **63**, 521–528 (1959)
2. Jones, J.G.: A method for designing lifting configurations for high supersonic speed using the flow fields of non-lifting bodies. Royal Aircraft Establishment, Report-2674, March (1963)
3. Starkey, R.P., Lewis, M.J.: Analytical off-design lift-to-drag ratio analysis for hypersonic waveriders. AIAA J. Spacecr. Rocket. **37**(5), 684–691 (2000)
4. Venkata Rao, R., Patel, V.: An elitist teaching-learning-based optimization algorithm for solving complex constrained optimization problem. Int. J. Ind. Eng. Comput. **3**, 535–560 (2012)
5. Hemanth, K., Jagadeesh, G., Saravanan, S., Nagashetty, K., Reddy, K.P.J.: Shock tunnel testing of a Mach 6 hypersonic waverider. In: Proceedings of 26th International Symposium on Shock Waves, Gottingen, Germany (2007)
6. Pradeep Roy, S. et al.: High angle of attack characteristics of power law derived hypersonic waveriders—computational study. In: Proceedings of the 16th Annual CFD Symposium, Bangalore, India (2014)
7. Saltelli, A., Ratto, M., Andres, T., Campolongo, F., Cariboni, J., Gatelli, D., Saisana, M., Tarantola, S.: Global Sensitivity Analysis: The Primer. Wiley, Hoboken (2008)

Experimental Analysis of Shock Standoff Distance in Hypersonic Flows over Spherical Bodies

Ruchi Thakur and Gopalan Jagadeesh

Introduction

Shock standoff distance is one of the basic parameters associated with the detached shock over blunt bodies in hypersonic flows. Considerable amount of work has been done in this area ranging from theoretical to experimental. Despite that, there is no universally followed correlation or method to determine the shock standoff distance. The first major breakthrough was provided by Van Dyke [1] in 1958 when he proposed a numerical method to predict the shock standoff distance over a spherical body in high-speed flows. In 1964, Lobb [2] experimentally proved Van Dyke's theory and gave a mathematical expression for the same. Another theory was proposed by Hornung [3] in 1995 giving two correlations to determine shock standoff distance in non-equilibrium flows considering two cases of a constant and a linearly varying density behind the shock. He proposed that the shock standoff distance does not depend on the density behind the shock alone but also on a reaction rate parameter which was defined using dissociation rate behind the shock and the freestream kinetic energy. Experimental data was given to support the theory. Olivier [4] in 2000 used the conservation equations to introduce a new theoretical model to determine shock standoff distance in frozen and equilibrium flows. He also showed the dependence of shock standoff distance on the density ratio between the shock and the body. In addition, he showed that the tangential velocity gradient also affects the shock standoff distance. He further extended his theory to nonequilibrium flows in 2007. In 2013, Zander et al. [5] gave experimental data for high enthalpy flows with velocities of 8.7 and 9.7 km/s. All these studies indicate that the major experimental data lies beyond 2 km/s velocity range. The present paper focuses on the velocities lying between 1 and 2 km/s. The results thus obtained are compared with the theories given by Lobb and Olivier and are found to match within the uncertainty. The results are also compared with those from a commercial in-house computational package HiFun, and a good match was seen.

R. Thakur (✉) • G. Jagadeesh
Department of Aerospace Engineering, Indian Institute of Science, Bangalore 560012, India
e-mail: ruchi.rivera@gmail.com

Experiments

The experiments were conducted in a hypersonic shock tunnel (HST2) of Laboratory for Hypersonic and Shock Wave Research, Indian Institute of Science. HST2 is a conventional shock tunnel with a 2 m long driver, 5.12 m long driven, and 50 mm inner diameter. It can work in a Mach number range of 6–12, a Reynolds number range of 0.3–6 million/m, and a maximum stagnation flow enthalpy of 3 MJ/kg. The effective test time in this tunnel is 700–800 μs. The experiments conducted for this work had nominal freestream Mach numbers of 6 and 8. Air was used as the test gases in this study. The freestream flow conditions for these cases are given in Table 1. The experiments were conducted on three hemispherical models of radii 25, 40, and 50 mm. Each model comprised a hemisphere and a cylindrical after body of 20 mm length. These models were fabricated from Duralumin. Figure 1 shows the 25 mm model mounted in the tunnel.

Image Analysis

The gross features of the flow were analyzed using the schlieren flow visualization technique. Figure 2 shows a sample image used for analysis. The position of the shock was found using a canny edge detection scheme in

G. Ben-Dor et al. (eds.), *30th International Symposium on Shock Waves 1*, DOI 10.1007/978-3-319-46213-4_27

Table 1 Freestream conditions

Test gas	M_∞	U_∞ (m/s)	P_∞ (kPa)	T_∞ (K)	ρ_∞ (kg/m^3)	Re_∞ (million/m)	h_0 (MJ/kg)
Air	5.4	1589.3	0.829	213.8	0.0264	2.99	1.48
Air	5.6	1417.2	0.914	157.3	0.0430	5.67	1.16
Air	8.3	1512.3	0.166	82.8	0.0069	1.86	1.22

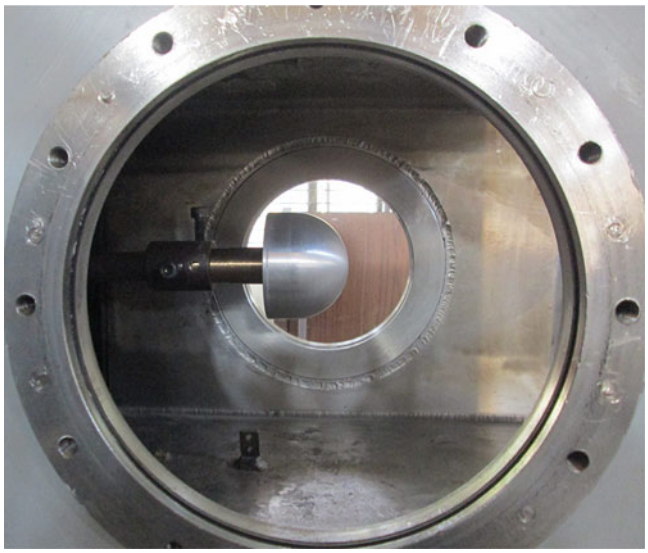

Fig. 1 25 mm model mounted in HST2

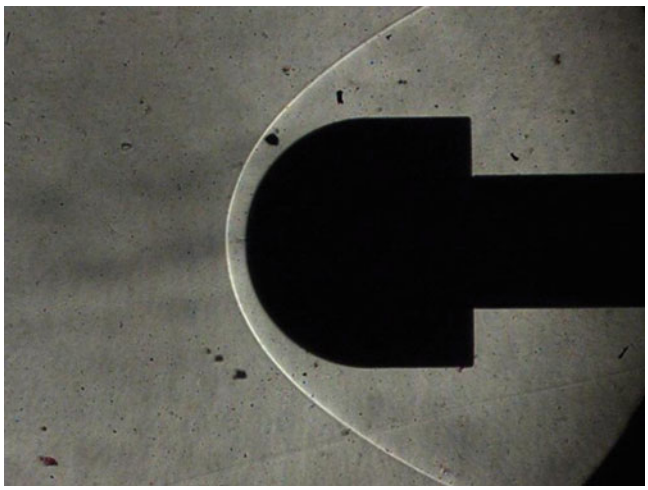

Fig. 2 Schlieren image obtained for a Mach 6 run obtained in HST2 over 25 mm model

MATLAB. Owing to the short test times, the resolution of the images was low. Thus, the shock standoff distance measured for bigger models was more certain with regard to the theory as compared to the smaller model. For a single run, it was observed that the shock standoff distance increases during buildup, stays more or less constant during the test time, and increases further during flow termination. There was a fluctuation in shock position of about 1–2 pixels during the test time which shows that there was slight fluctuation in the flow. Figure 3 shows the flow buildup, the test time, and the flow termination for a Mach 6 run.

Computational Analysis

HiFUN (High Resolution Flow Solver on Unstructured meshes) is an in-house solver developed at the Indian Institute of Science employing unstructured data-based algorithms. The code is cell-centered finite volume solver which uses the Green-Gauss theorem based on linear reconstruction procedure. The simulations were carried out for second-order flux reconstruction scheme with the initialization from the converged solutions of the first-order scheme for accuracy and reduction of computational effort. An unstructured 2D mesh of size 200,000 was used for the simulations. Figure 4a, b show the pressure contours obtained for a Mach 8 test condition on a 50 mm model for first-order Euler and second-order laminar simulations. The shock position was obtained by observing the point while going through freestream where the jump in pressure was 30 % as given by Zander et al. [5].

Results

The experiments in HST2 were carried out at three different conditions giving three different freestream densities 0.02, 0.04, and 0.006 kg/m^3. Figure 5a–c shows the data obtained through experiments in HST2 for the three densities. Also shown are the theoretical predictions given by Lobb and Olivier. Lobb predicted the shock standoff distance to be

$$\frac{\Delta}{d} = 0.41\,\frac{\rho_1}{\rho_2}$$

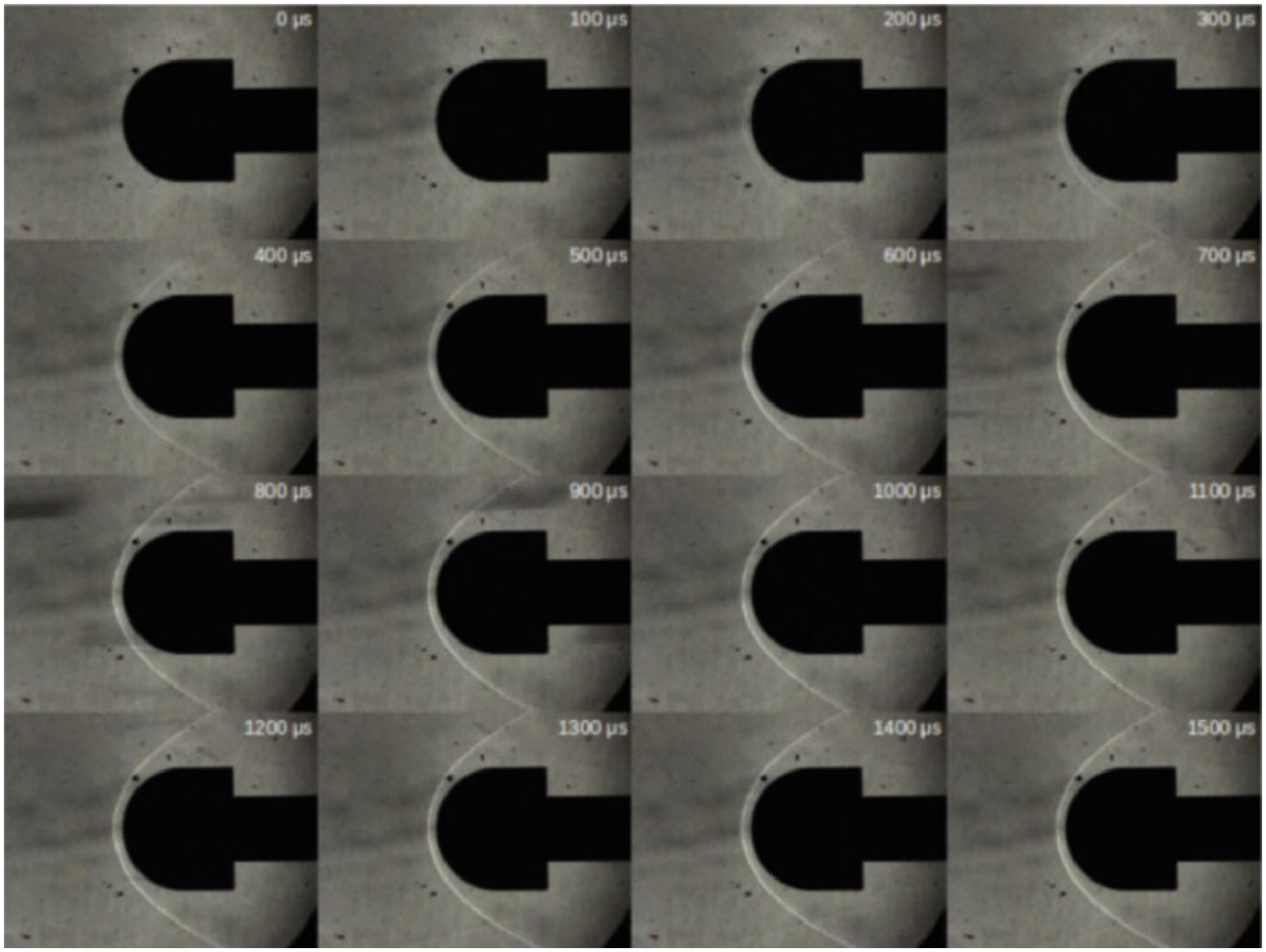

Fig. 3 Schlieren images showing the flow building, test time, and flow termination for Mach 6 run

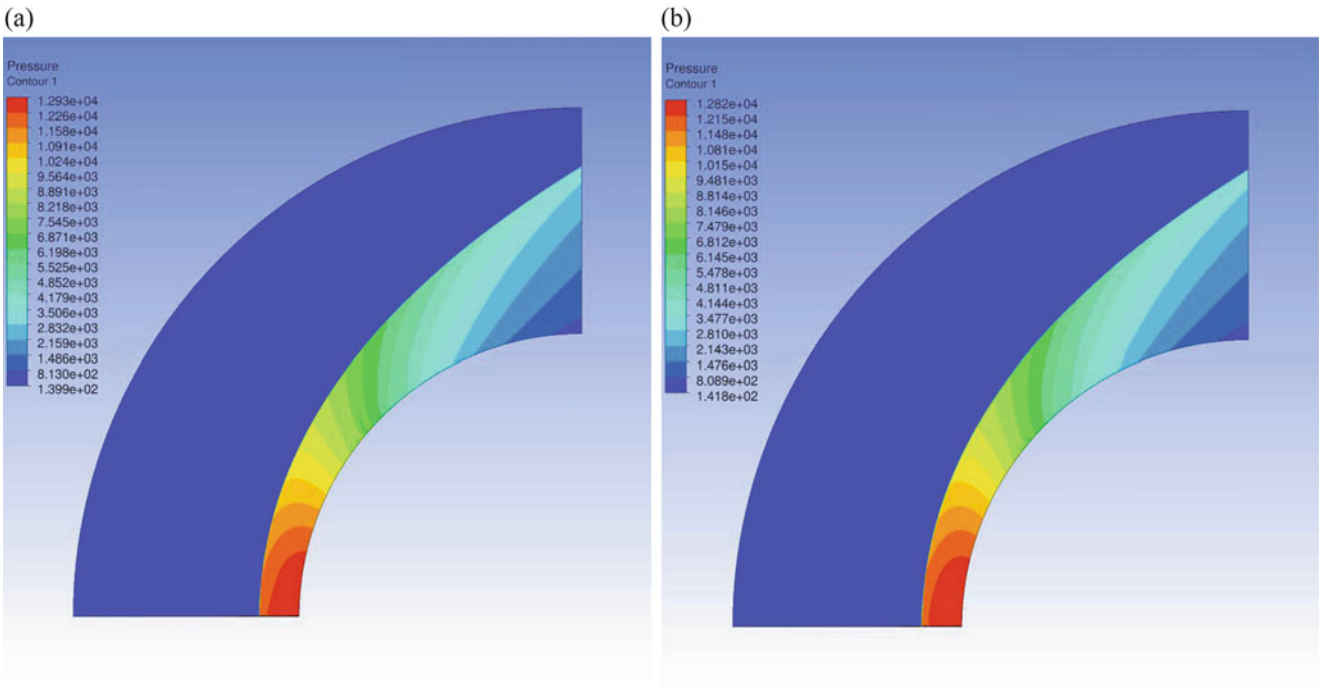

Fig. 4 (**a**) Pressure contours for first-order Euler computations for Mach 8 run. (**b**) Pressure contours for second-order laminar computations for Mach 8 run

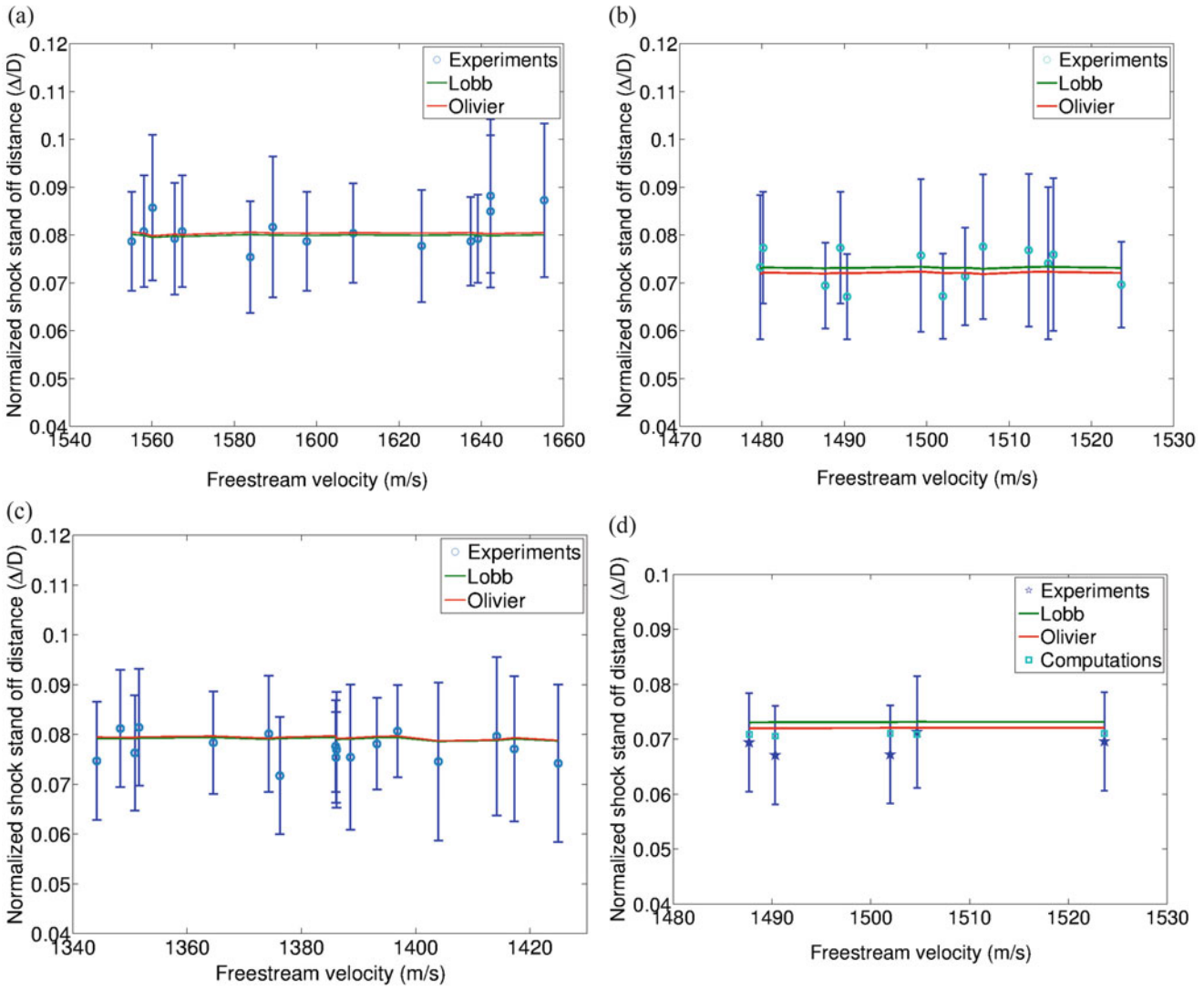

Fig. 5 (**a**) Normalized shock standoff distance for Mach 6 runs with 0.02 kg/m^3 freestream density. (**b**) Normalized shock standoff distance for Mach 8 runs with 0.006 kg/m^3 freestream density. (**c**) Normalized shock standoff distance for Mach 6 runs with 0.04 kg/m^3 freestream density. (**d**) Comparison of the experimental, computational, and theoretical normalized shock standoff distance for Mach 8 runs

where

Δ—shock standoff distance
d—diameter of the sphere

ρ_1/ρ_2—density ratio across the shock

Olivier gave the correlation

$$\frac{\Delta}{2d}\frac{\rho_s}{\rho_\infty} = \left\{\frac{\rho_s}{\rho_\infty}\sqrt{\frac{1}{4}\left[1+\left(\frac{\partial u}{\partial \phi}\right)_b\right]^2 - \frac{1}{3}\frac{\rho_s}{\rho_b}\frac{\rho_\infty}{\rho_s}\left[1+2\left(\frac{\partial u}{\partial \phi}\right)_b\right]} - \frac{1}{2}\left[1+\left(\frac{\partial u}{\partial \phi}\right)_b\right]\frac{\rho_\infty}{\rho_s}+\frac{\rho_s}{\rho_b}\right\} \times \left(\frac{4}{3}+\frac{2}{3}\left(\frac{\partial u}{\partial \phi}\right)_b - 2\frac{\rho_s}{\rho_b}\frac{\rho_\infty}{\rho_s}\right)^{-1}$$

where

Δ—shock standoff distance
d—diameter of the sphere

ρ_s/ρ_∞—density ratio across the shock
ρ_b—density at the body
$(\partial u/\partial \phi)_b$—tangential velocity gradient at the body

The data is found to match well with the theory within the uncertainty of measurement. The measured experimental data for the 40 and 50 mm radii models was found to match with the theoretical models within 2–3 % barring a few odd cases, while for the 25 mm radius model, it matched within 5 % owing to the low resolution of the images. Figure 5d shows the comparison of computational results with that of experimental and theoretical results which match well. Computational results for both first-order Euler and second-order laminar were generated and were found to differ by up to 2 %. The data shown here is for second-order laminar flow. This data matches with the experimental data within 5 %.

Conclusions

Shock standoff distance is one of the basic parameters which is used to validate CFD codes. Also, knowing the position of the shock helps in finding the aerodynamic heating which in turn aids in designing the body. The experimental and the computational data is found to match well with the theoretical models given by Lobb and Olivier. The current work also provides data for the moderate velocity range of 1–2 km/s where data is not available in the open literature. The work can be further extended for different body shapes and different test gases.

References

1. Van Dyke, M.D.: The supersonic blunt-body problem-review and extension. J. Aerospace Sci. **25**(8), 485–496 (1958)
2. Lobb, K.R.: Experimental measurement of shock detachment distance on spheres fired in air at hypervelocities. In: Nelson, W.C. (ed.) The High Temperature Aspects of Hypersonic Flow, pp. 519–527. Pergamon Press, New York (1962)
3. Wen, C.Y., Hornung, H.G.: Non-equilibrium dissociating flow over spheres. J. Fluid Mech. **299**, 389–405 (1995)
4. Olivier, H.: A theoretical model for the shock stand-off distance in frozen and equilibrium flows. J. Fluid Mech. **413**, 345–353 (2000)
5. Zander, F., Gollan, R.J., Jacobs, P.A., Morgan, R.G.: Hypervelocity shock standoff on spheres in air. Shock Waves **24**, 171–178 (2014)

Oscillatory Behaviors of a Hypersonic Inlet with Trips

Wenzhi Gao, Shuaitao Guo, Zhufei Li, and Jiming Yang

Introduction

A hypersonic inlet should be operated in a started mode for the efficient operation of an air-breathing propulsion system [1]. Various factors, either in design or in usage, may cause the hypersonic inlet to unstart, such as a large internal contraction ratio, low operating Mach number, delay of boundary layer transition, and high back pressure in the combustor, etc. When unstarted, a typical type of oscillatory flow (known as buzz) is often observed [2–5]. Violent shock oscillation, prominent pressure fluctuation, and substantial supersonic airflow spillage can occur in the oscillation flow [2, 3, 5], which are not only harmful to the engine performance but also highly detrimental to structural safety and flight control. Therefore the prevention of the oscillatory flow is important to hypersonic flights, and such a tough task is a complicated engineering problem that is intensively related to complex fluid mechanism [6–8]. As an important method to enhance boundary layer transition and help-to-start capabilities, trips are widely applied to hypersonic inlets design and practical flights [9–11]. The tripping mechanism requires the formation of streamwise vorticity on a scale within the boundary layer; hence the vortexes in trip wakes would act as that of micro vortex generators [12] to some extent. In Valdivia's experiments [8], vortex generators were fixed on the side walls of a two-dimensional inlet/isolator model to reduce the movement scales of isolator shocks. However how such trips affect inlet oscillatory flow was overlooked. To the best of the authors' knowledge, effects of trips have hardly been considered in the previous researches of hypersonic inlet oscillation. Consequently the present work is to experimentally investigate the effects of trips on the oscillatory behaviors of a hypersonic inlet, in which an axisymmetric inlet model was chosen to avoid the sidewall complexity.

W. Gao
Department of Modern Mechanics, University of Science and Technology of China, 96 Jinzhai Road, Hefei, Anhui 230026, People's Republic of China

School of Mechanical Engineering, Hefei University of Technology, 193 Tunxi Road, Hefei, Anhui 230009, People's Republic of China

S. Guo • Z. Li • J. Yang (✉)
Department of Modern Mechanics, University of Science and Technology of China, 96 Jinzhai Road, Hefei, Anhui 230026, People's Republic of China
e-mail: jmyang@ustc.edu.cn

Experimental Setup

Experimental investigations were conducted in the shock tunnel at University of Science and Technology of China (hereafter shorten as the shock tunnel?) [5]. For the present study, the shock tunnel was operated in an equilibrium interface mode, and the Mach number, total temperature, and total pressure of the freestream was 5.9, 920 K, and 1.5 MPa (Table 1), respectively. Under the above condition, the test time was longer than 20 ms with a nozzle exit of 300 mm in diameter. To ensure the repeatability of experimental results, each case was fired twice in the shock tunnel.

The test model is an axisymmetric hypersonic inlet designed at a shock-on-lip Mach number of 6.5. As shown in Fig. 1, the inlet capture radius is 64 mm and the nose of the inlet is blunted with a radius of 0.8 mm. The external compression surfaces are consisted of an initial conical surface inclined 10 ° and followed by curved surfaces with total turning angle of 9.7°. The flow turning angle at the inlet entrance is 9°, while the internal contract section smoothly transits to a horizontal isolator. The total contract ratio and the internal contract ratio of the inlet are 6.41 and 1.58, respectively. The model was aligned with the freestream flow direction. A circular block was fixed (Fig. 1a) at the model exit to generate buzz flows with a throttle ratio (TR) of 66 %, which is defined as:

G. Ben-Dor et al. (eds.), *30th International Symposium on Shock Waves 1*, DOI 10.1007/978-3-319-46213-4_28

$$\mathrm{TR} = (1 - A_{t,b}/A_e) \times 100\ \%,$$

where $A_{t,b}$ is the throat area of flow passage at the block and A_e is the exit area of the inlet model without block.

The 1-mm-thick Teflon trips were carved in a shape of diamond with a side length of 3 mm and an internal angle of 60°. As shown in Fig. 2, 12 trips were circumferentially adhered to the forebody surface at 180 mm upstream of the inlet entrance, which is the end of the demountable nose part. Experiments were also conducted without trips to evaluate the effects of trips on the oscillatory flow.

To capture the transient characteristics of the oscillatory flows, schlieren imaging equipped with a high-speed camera and pressure measurement were adopted and synchronized with a digital delay generator. The frame rate of the schlieren imaging is 15,000 Hz, and the acquisition rate of pressure measurement is 1 MHz. As shown in Fig. 1a, only part of the inlet external flow field were visualized due to the limited size of schlieren mirrors. To obtain the streamwise pressure distributions along the inlet path, 13 pressure transducers with an accuracy of ±0.3 % and a response frequency up to 50 kHz were mounted on the centerbody surfaces (labeled CH3 to CH15 as shown in Fig. 1a).

Results and Discussions

TR = 0 %, Started Flow

The effects of trips were primarily evaluated under started flows. The schlieren photos in Fig. 3 demonstrate well-started flows as TR equals to 0 %, although the windows of the shock tunnel provided a limited view of the external flow field. For the untripped case as shown in Fig. 3a, the external shock system is consisted of leading edge shocks, followed by a series of compression shocks/waves generated from the curved surfaces. Figure 3b shows the schlieren photo of the tripped case, which demonstrates a very similar flow pattern despite the trip-induced shocks. Furthermore, surface pressure distributions of the tripped case agree well with that of the untripped case (see Fig. 4), although the CH11 signal of the tripped case is blanked due to the transducer damage. Consequently negligible interferences of trip wakes were exerted on the started flow.

Table 1 Test conditions

Property	Value
Ma	5.9
Total temperature, K	920
Total pressure, MPa	1.5
Experimental time	>20 ms
Diameter of nozzle exit, mm	300

TR = 66 %, Oscillatory Flow

Oscillatory flow appears as TR of the exit block rises to 66 %. Figure 5 shows the schlieren photos in a typical oscillatory cycle of the untripped case. The throttling of the exit blockage accumulates high-pressure gas in the inlet duct, which generates shock trains and upstream spread of boundary layer separations. As shown in Fig. 5a–c, the separations spread upstream to the external surfaces, subsequently unstart the inlet, and result in an upstream movement of external shocks and a severe flow spillage. As the high-pressure gas of the inlet duct is exhausted by the flow

Fig. 2 Drawing and photograph of trips

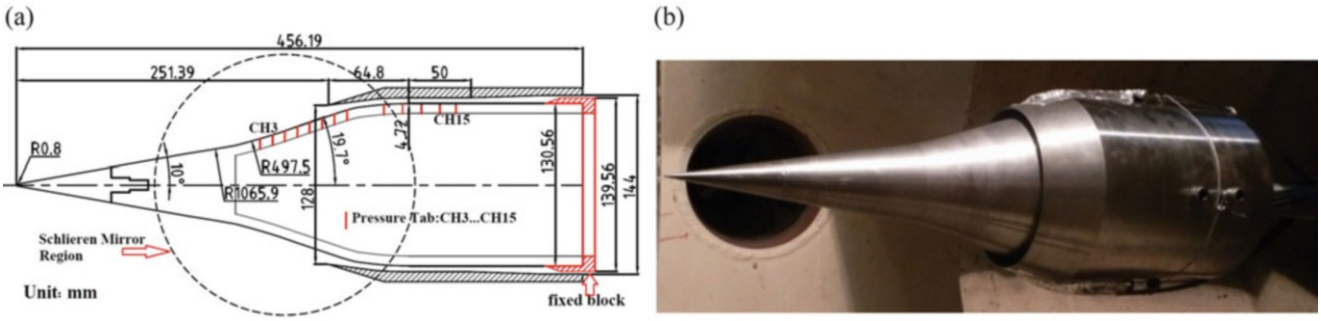

Fig. 1 Drawing and photograph of the inlet model: (**a**) dimensional drawing; (**b**) photograph of the inlet model

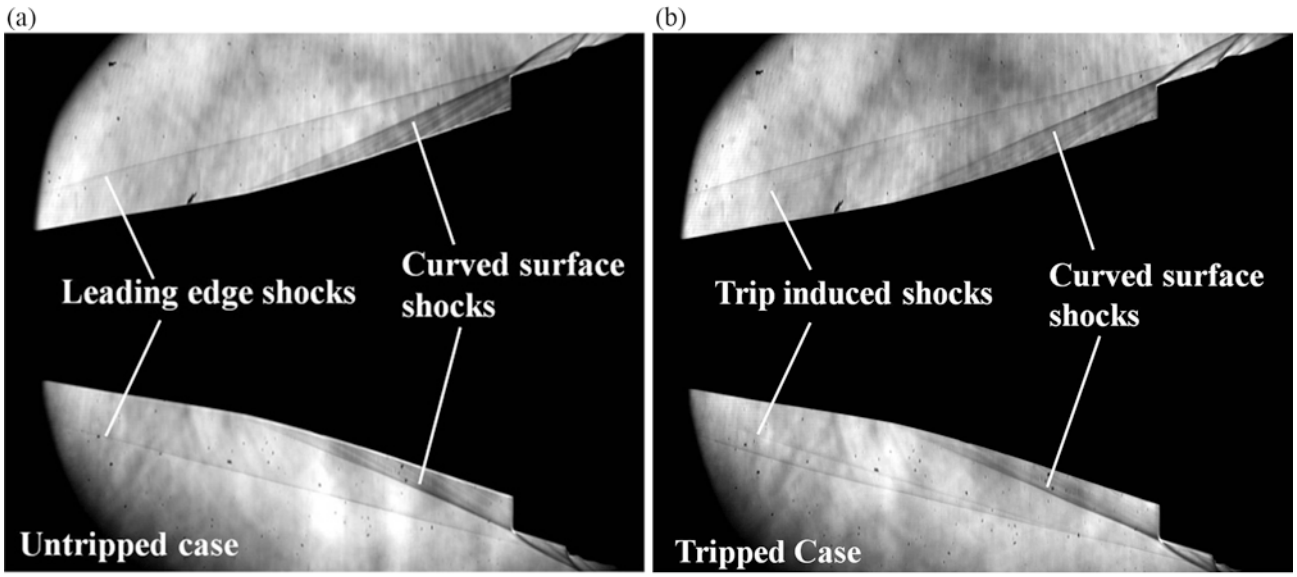

Fig. 3 Schlieren photos of the shock tunnel as TR = 0 %: (**a**) untripped case; (**b**) tripped case

Fig. 4 Pressure distribution of centerbody surface as TR = 0 %

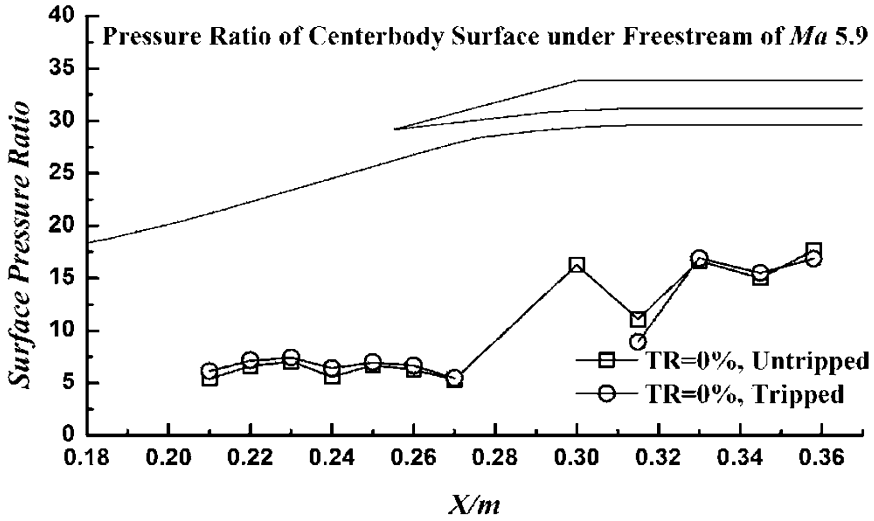

spillage, the external shocks move downstream, and the inlet undergoes a short phase of restart as shown in Fig. 5d, e. It needs to be mentioned that the farmost position of the oscillatory separation exceeds the observation range of the schlieren system (Fig. 5c), although from the information of the neighboring images (Fig. 5b, d), it can be estimated that the leading shock the separation can reach is around the inlet nose. The oscillatory process also fits for the tripped case, but the farmost position of the external separations is near the end of the initial conical surface, which can be fully captured with the limited view size (Fig. 6c). The flow patterns of the oscillation are also varied by the trips, as the separation shocks of the tripped case reach closer to the near-wall region of the external surfaces (see Fig. 6b, d). Furthermore, obvious asymmetry of external separations can be found intermittently for the tripped case as shown in Fig. 6b, d. It is well demonstrated that the trips can suppress the oscillatory flow as prominently decreasing the movement scale of external separations. With the effects of the trips, oscillation frequency was increased from 250 to 319 Hz.

In addition, the pressure-time histories at some typical survey points are exhibited in Fig. 7. One can notice that the periodic fluctuations of the surface pressures and the averaged magnitudes in the tripped case are higher than that of the untripped cases. Especially for the pressure signals of CH5, which is located about 16 mm upstream of inlet entrance, the tripped case reflects obviously larger fluctuation amplitude than that of the untripped case. The pressure

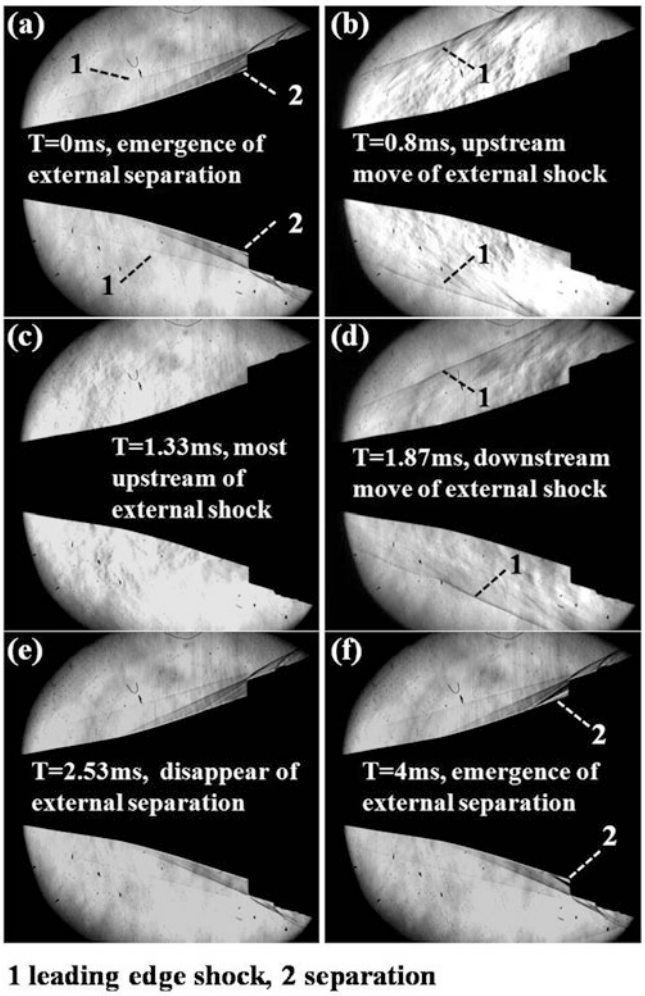

Fig. 5 Schlieren photos during a typical cycle of the untripped case

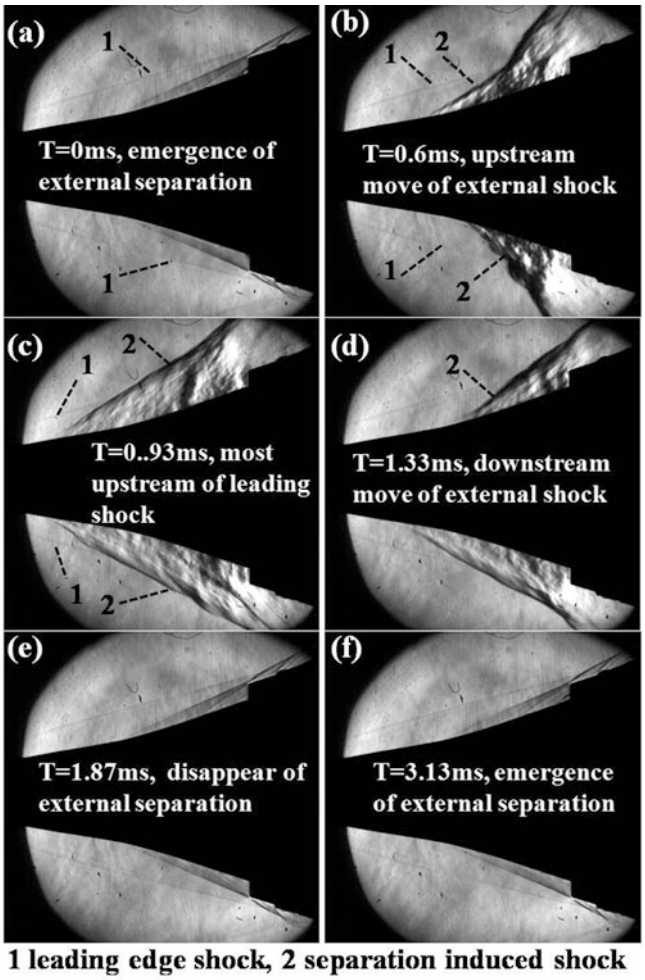

Fig. 6 Schlieren photos during a typical cycle of the tripped case

discrepancies are probably owing to the stronger separation shock of tripped case, as can be observed from the steeper shapes of the separation shocks shown in Fig. 6. With the additional compression of separation-induced shocks, averaged pressure magnitude of the tripped case is higher than that of the untripped case. And in Fig. 6b–d, the separation shock sweeps CH5 periodically and thereby enlarges its fluctuation amplitude. With the help of fast Fourier transform (FFT), it was found that the most prominent peaks of FFT results are 239.8 and 320.1 Hz for the untripped and tripped cases, respectively, which agree well with the results obtained from the schlieren photos.

To evaluate the backpressure characteristics caused by exit throttling, the time-averaged surface pressures of buzz flows were calculated, and the results were overlapped with pressure distributions of started flow (TR = 0 %) as shown in Fig. 8. Due to the exit throttling, the surface pressures increase monotonically from forebody to the inlet exit. For pressure distributions of external surfaces as X varies from 0.2 to 0.25 m, one can notice the coincidence between the started flows and the oscillatory flows in the untripped cases, while the tripped cases of oscillatory flows show higher pressure magnitudes than that of the started flows. The pressure increase of tripped case on external surfaces is mainly caused by the stronger separation shocks as analyzed in the above paragraph. For inlet duct section, surface pressures of the tripped case are higher than that of the untripped case, with an enhancement of about 20 times of freestream static pressure. Therefore, it can be concluded that the trips will increase the averaged pressure magnitude of centerbody surfaces during oscillation, indicating better resistance to back pressure.

Conclusions

The effects of trips on oscillatory flow were experimentally investigated in an axisymmetric hypersonic inlet. According to above results, trips prominently decrease the

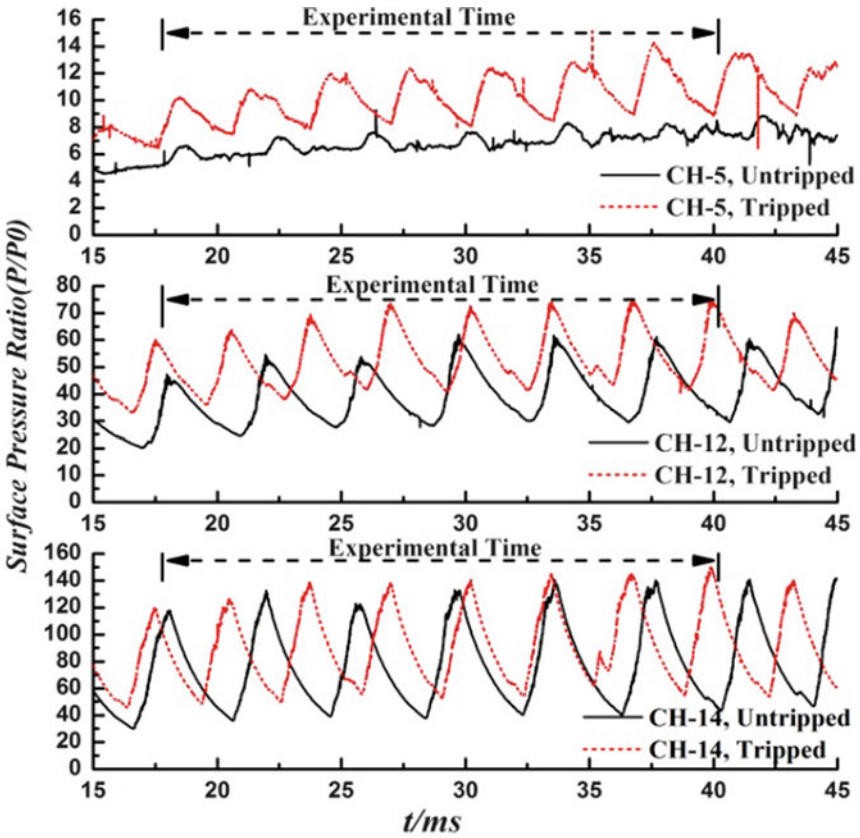

Fig. 7 Pressure-time histories of typical survey points

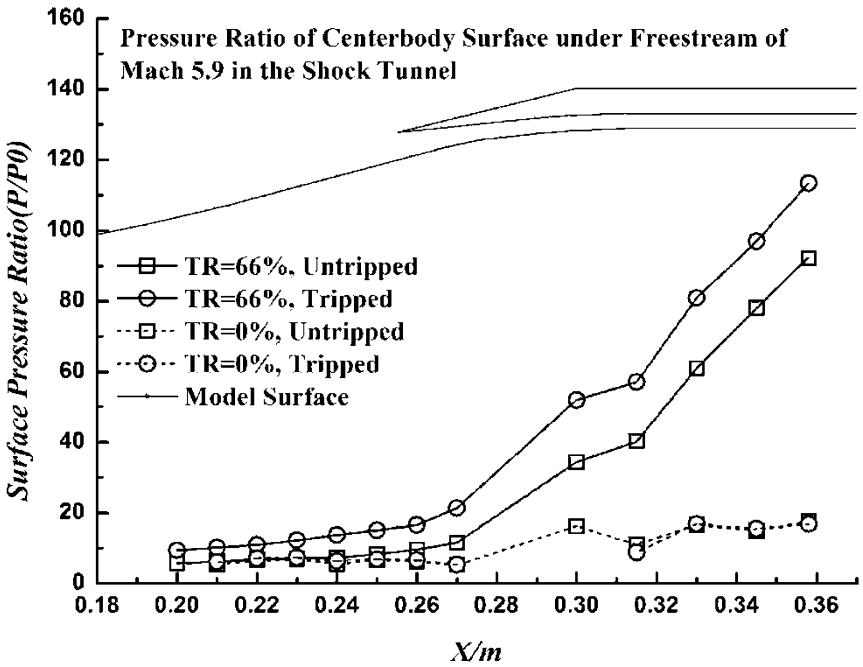

Fig. 8 Distributions of time-averaged surface pressure along centerbody

scale of external separations during oscillation. The farmost positions of the oscillatory flow are suppressed from the nose for the untripped cases to near the end of initial cone for the tripped cases. Trips also transform the flow patterns of external separations as the flow asymmetry emerges and separation-induced shocks get stronger. With the additional compression of separation shocks, averaged magnitude of centerbody pressures of the tripped cases are higher than that of the untripped cases. It is concluded that trips prominently suppress the scales of oscillation flows, as well as increasing resistance of inlet to back pressure from combustor.

The prominent suppression of external separations shows potential of trips in the prevention of inlet oscillation. Furthermore, this method is convenient and robust as trips are widely used in the design of hypersonic inlets.

More works should be carried out before applications of trips to the prevention of inlet oscillation. Effects of trips on oscillatory flows need to be investigated more comprehensively, such as the generalities among various inlet configurations, regulations under different levels of back pressure, influences of locations, and sizes of trips. The quantitative transition locations should be measured in following researches. On these bases, the potential of trips on the oscillation prevention would be adequately evaluated to instruct the engineering applications.

Acknowledgment This work was supported by the National Natural Science Foundation of China (Grant No. 11402263 and 11132010) and the Fundamental Research Funds for the Central Universities (JZ2015HGBZ0471).

References

1. Curran, E.T., Murthy, S.N.B.: Scramjet Propulsion, Progress in Astronautics and Aeronautics, vol. 189, pp. 477–483. AIAA, Reston (2001)
2. Tan, H.J., Guo, R.W.: Experimental study of the unstable-unstarted condition of a hypersonic inlet at Mach 6. J. Propuls. Power **23**(4), 783–788 (2007)
3. Tan, H.J., Sun, S., Yin, Z.L.: Oscillatory flows of rectangular hypersonic inlet unstart caused by downstream mass-flow choking. J. Propuls. Power **25**(1), 138–147 (2009)
4. Wagner, J.L., Valdivia, A., Clemens, N.T., Dolling, D.S.: Experimental investigation of unstart in an inlet/isolator model in Mach 5 flow. AIAA J. **47**(6), 1528–1542 (2009)
5. Li, Z.F., Gao, W.Z., Jiang, H.L., Yang, J.M.: Unsteady behaviors of a hypersonic inlet caused by throttling in shock tunnel. AIAA J. **51** (10), 2485–2492 (2013)
6. Tan, H.J., Li, L.G., Wen, Y.F., Zhang, Q.F.: Experimental investigation of the unstart process of a generic hypersonic inlet. AIAA J. **49**(2), 279–288 (2011)
7. Srikant, S., Wagner, J.L., Valdivia, A., Akella, M.R., Clemens, N.: Unstart detection in a simplified-geometry hypersonic inlet-isolator flow. J. Propuls. Power **26**(5), 1059–1071 (2010)
8. Valdivia, A., Yuceil, K.B., Wagner, J.L., et al.: Control of supersonic inlet-isolator unstart using active and passive vortex generators. AIAA J. **52**(6), 1207–1218 (2014)
9. Berry, S., Daryabeigi, K., Wurster, K.: Boundary-layer transition on X-43A. J. Spacecr. Rorket. **47**(6), 922–934 (2010)
10. Holden, M.S., Wadhams, T.P., Candler, G.V.: Experimental studies and numerical predictions for hypervelocity vehicle design and code validation. AIAA paper 2003-6905
11. Borg, M.P., Schneider, S.P., Juliano, T.J.: Effect of freestream noise on roughness-induced transition for the X-51A forebody. AIAA paper 2008-592
12. Lu, F.K., Li, Q., Liu, C.Q.: Microvortex generators in high-speed flow. Prog. Aerosp. Sci. **53**, 30–45 (2012)

Aerodynamic Force and Moment Measurement Under Duplicated Hypersonic Flight Conditions in the JF12 Shock Tunnel

Z. Jiang, Y. Wang, Y. Liu, and C. Yuan

Introduction

Traditional hypersonic wind tunnels usually produce test flows with low total temperatures and at low sound speeds, and therefore, the thermochemical reaction, one of the key mechanisms in hypersonic flows, could be ignored in its experiments. As a result, the real gas effect on the aerodynamic force and moment measurement becomes a very difficult problem to solve in the hypersonic ground tests, and once it was identified as an unknown "unknown" [1]. During the high Mach number and high-altitude segment of the first entry flight of the Space Shuttle orbiter, the vehicle exhibited a nose-up pitching moment increment relative to preflight prediction. Woods et al. [2] noted that preflight predictions based on the aerodynamics in the aerodynamic design data book indicated that a 7.5° deflection of the body flap would be required to trim the Space Shuttle orbiter for the center of gravity and vehicle configuration. In reality, the body flap had to deflect too much large values ($\delta \approx 16°$) to maintain trim at the proper angle of attack ($\alpha = 40°$). The deflection of 16° was close to the possible deflection limitation, and the more deflection would lead to a serious flight test accident. The comparison of equilibrium-air computations with perfect gas mode indicates that at least the main part of the so-called hypersonic anomaly was due to real gas effects at very high Mach numbers [3].

In order to improve the accuracy of ground experimental data, various advanced hypersonic test facilities were developed [4]. One of the main concerns was related to the aerodynamic forces and moments during hypersonic vehicle reentry. Unfortunately, there is no single ground-based facility capable of duplicating the hypersonic flight environment, and so far different facilities are used to address various aspects of the design problems associated with hypersonic flight [1, 5]. Considering the thermochemistry in hypersonic flows, high-enthalpy shock tunnels are capable of generating high-temperature flows, but its effective test duration is too short to do the force and moment measurement. Moreover, for hypersonic experiments, there is no any reliable scaling criterion available as that in low-speed wind tunnel tests, which makes the aerodynamic force and moment measurement for hypersonic vehicles become even more difficult.

Under the support of National Major Project of Scientific Instrumentation R&D, a long-test-duration hypervelocity detonation-driven shock tunnel was developed based on the backward-running detonation driver and named the JF12 hypervelocity shock tunnel under the serial number in LHD laboratory. Its performance tests demonstrated that the super-large facility in hypersonic research area is capable of reproducing the pure airflows with Mach numbers from 5 to 9 at an altitude of 25–50 km [6]. By large, it means large nozzle diameter and large facility length. A large nozzle enables the shock tunnel accommodate large test models, and the long facility makes it possible to produce an effective test duration of more than 100 ms. Taking advantage of the JF12 hypervelocity shock tunnel, the research project on aerodynamic force measurements was carried out with a homemade six-component stress balance. The test condition is for Mach 7 at about 35 km altitude with the total temperature of 2200 K. The test model is a sharp cone with 10° half-angle and measured 1500 mm in length and 57 kg in weight. Some of the experimental data collected at a series of the attack angles demonstrated two important issues. One issue is that voltage signals of the pitching moment indicate that low frequency oscillations are observable at three periodical cycles within the 100 ms test duration. This means that high accuracy of experimental data could be reached with this stress balance. Another issue is that the experimental data of the JF12 hypervelocity shock tunnel is in good agreement with blowdown hypersonic wind tunnels when the attack angle is small; however, the significant difference

Z. Jiang (✉) • Y. Wang • Y. Liu • C. Yuan
LHD, Institute of Mechanics, Chinese Academy of Sciences, No. 15 Beisihuanxi Road, Beijing 100190, People's Republic of China
e-mail: zljiang@imech.ac.cn

G. Ben-Dor et al. (eds.), *30th International Symposium on Shock Waves 1*, DOI 10.1007/978-3-319-46213-4_29

is observed from the test cases of high attack angles for the same Mach number. It is believed that the conic shock of the test model becomes strong enough to excite gas molecular vibrations at high attack angles, and it is one kind of the real gas effects that were demonstrated from the flight test of the Space Shuttle orbiter. This paper will give a brief summary on this experimental research.

Experimental Setup

The JF12 hypervelocity shock tunnel is used for this research work, and the facility is capable of reproducing the pure airflow with Mach numbers from 5 to 9 at an altitude of 25–50 km with 100 ms test duration. This is a unique tool for investigating into physical issues in high-temperature gas dynamics. Figure 1 shows schematically the entire system of the JF12 hypervelocity shock tunnel.

Looking at Fig. 1 from its right to the left, the first part is the vacuum system for damping wave reflection during the nozzle starting process, and its vacuum tank with a volume of 600 m^3 is 40 m in length. The second part is the test section that is 15 m in length and 3.5 m in diameter. The contoured nozzle is 15 m in length and 2.5 m in diameter, and another nozzle is smaller, having an exit of 1.5 m in diameter for Mach numbers of 5–7. Next to the nozzle, there is the driven section being 89 m in length and 720 mm in diameter. The detonation driver is 99 m in length and 400 mm in diameter. The driver operates in the backward-running detonation mode, that is, the detonation is ignited at its right end and propagates to left. The detonation driver and the driven section are connected with the transient part by which the tube diameter is gradually reduced from 720 to 400 mm. Between the detonation driver and the transient part, there is the diaphragm rig that is used to produce the proper incident shock wave in the shock tunnel after the direct detonation initiation. The damping section is located at the far left end of the facility and is 19 m in length and 400 mm in diameter.

The experimental work for aerodynamic force and moment measurements was carried out with a six-component stress balance that was specially designed for JF12 hypervelocity shock tunnel to insure that the low-frequency vibration of the balance output signs has enough full periods within the 100 ms test duration. Such the requirement is an important issue to obtain reliable experimental data, and this homemade stress balance is named SWPD-S01 under laboratory serial number. The test model for the experiment is selected to be a sharp cone with 10° angle because of its wide acceptance for hypersonic wind tunnel calibrations. The model is measured 1500 mm in length and 57 kg in weight and may be the largest model for shock tunnel tests. By and large, the force signal of the stress balance would be much larger than nozzle flow perturbations, and the data reliability would be improved significantly. The test condition is for Mach 7 at about 35 km altitude with the total temperature of 2200 K.

Results and Discussions

A series of the experiments were carried out with various changes of the attack angle at Mach 7. The reason for such the experimental design is to examine the effect induced with different post-shock temperatures at different attack angles. It is believed that the temperature at a small angle is below the critical temperature at which air molecular vibrations are excited, but it will be raised higher than the critical temperature when the attack angle is high enough to induce strong cone shock wave at the windward side of the test model. It is one kind of the real gas effects that the Space Shuttle orbiter experienced.

The experimental data collected from the SWPD-S01 stress balance at a 5° attack angle are presented in Fig. 2. Voltage signals indicate that the lowest frequency oscillations observable from the pitching moment present at least three full periodical cycles within the 100 ms test duration. It means that the high accuracy of the pitching moment could be reached with this stress balance by applying simple data processing techniques. As to the axial force and normal force, their low frequency oscillations have more than enough periodical cycles to achieve high accurate data. The periodicity of the force measurement data from the JF12 hypervelocity shock tunnel indicates that its accuracy could

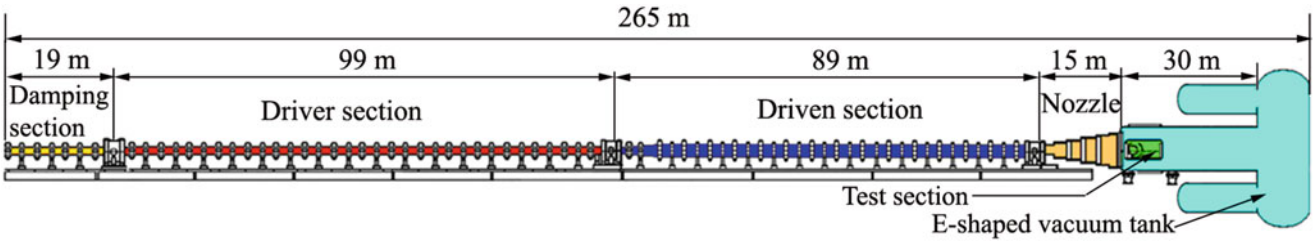

Fig. 1 Schematic of the long-test-duration hypervelocity detonation-driven shock tunnel

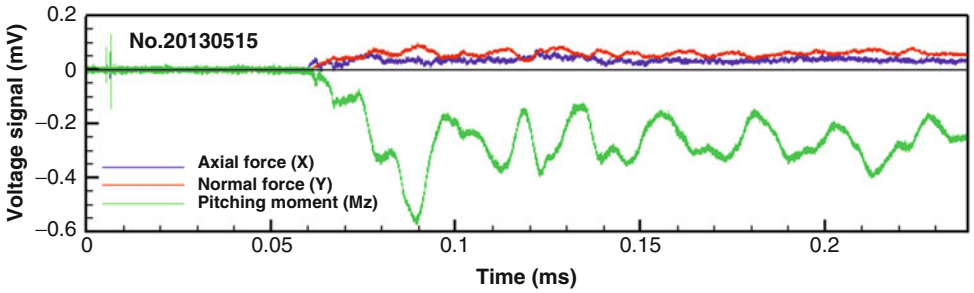

Fig. 2 Balance signals from aerodynamic force and moment tests for Mach number 7

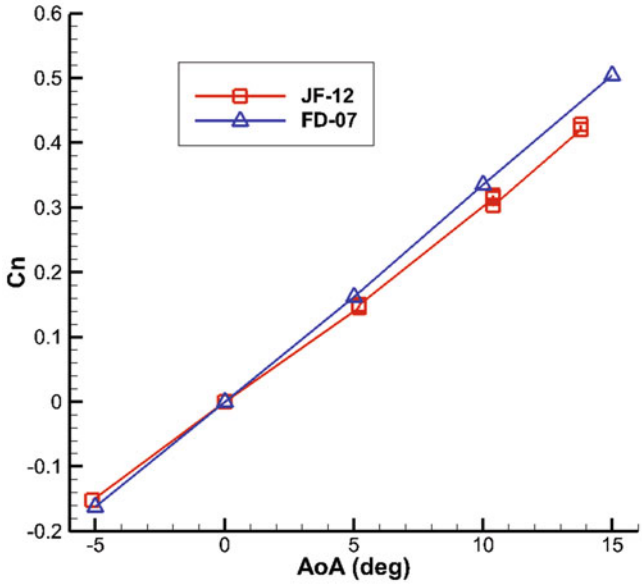

Fig. 3 Experimental data of the normal force coefficient for Mach number 7

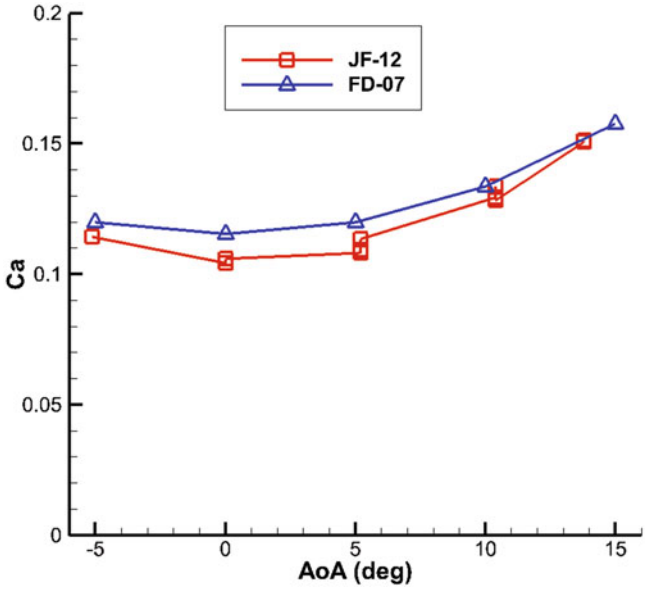

Fig. 4 Experimental data of the axial force coefficient for Mach number 7

be as high as that from blowdown hypersonic wind tunnels. However, the data accuracy will be ruined if the wind tunnel test time is shorter than 30 ms for this test or the low frequency of the natural vibration of the force measurement system is lower. Superposition of the balance signals from the forced and inertia vibrations of the force measurement system could make picking up of the force and moment become very difficult.

A series of the aerodynamic force measurements for Mach 7 were carried out at different attack angles, and the experimental data of the normal force coefficient are plotted in Fig. 3 with the corresponding results from a conventional hypersonic wind tunnel [7]. By examining the discrepancy between the data from two wind tunnel tests, it could be concluded that the normal force coefficient of the JF12 hypervelocity shock tunnel is smaller than that from DF-07 hypersonic wind tunnels. The discrepancy is increased as the attack angle is set to be larger and larger and reaches to about 10 % at the 15° attack angle. The axial force coefficient is plotted in Fig. 4, and the curve from the JF12 hypervelocity shock tunnel is located below the one from the DF-07 hypersonic wind tunnel. By considering differences in wind tunnel test conditions, several main physical issues are discussed below for future investigation.

The big difference in wind tunnel test conditions is the total temperature. It is 2200 K for the JF12 hypervelocity shock tunnel and about 800 K for the DF-07 hypersonic wind tunnel. This temperature can induce two main physical issues that will affect more or less the aerodynamic forces acted on the sharp cone model. The first issue is the high-temperature boundary development. The boundary layer will get thicker when the temperature is higher. The thicker boundary will reduce the drag force and this effect is demonstrated in Fig. 4. The other is the pressure variation distributed along the cone model surface, and it will cause differences on both the normal and axial forces. There are two important things that are related with the pressure variations. One of the two is the temperature-induced pressure change in boundary layers, but it could be very small according to the boundary layer theory that says the pressure gradient normal

to the solid surface could be assumed to be zero. Furthermore, there is no stagnation area for the sharp cone model, and the stagnation pressure change related to chemical reactions can be ignored. Another is the post-shock pressure change. The post-shock temperature at the windward side is different from the leeward side if the attack angle is not zero. For the JF12 hypervelocity shock tunnel tests, the post-shock temperature at the windward side can vary from 350 to 700 K when the attack angle varies from 5 to 15°. Meantime, the post-shock temperature variations at the leeward side are below 400 K. It is well known that gas molecular vibrations are excited significantly when the static temperature is raised to above 500 K, and this will result in the pressure-specific heat change and the energy transfer from mechanical to internal energy. For the JF12 hypervelocity shock tunnel tests, the gas molecular vibrations exist at the windward side and do not at the leeward side. This physical phenomenon will lead to the pressure unbalance behind the conic shock wave around the cone model and result in the normal force coefficient difference as shown in Fig. 4. The difference appears to be larger and larger as the attack angle increases because the conic shock wave is getting stronger and stronger.

Another difference in wind tunnel test conditions is the test model scale. The test model used in the JF12 hypervelocity shock tunnel is five times bigger than the one in the DF-07 hypersonic wind tunnel. This will lead to Reynolds number difference and affect the drag force in some way. It is believed that the contribution from Reynolds number difference is included in Fig. 3. It is puzzled a lot that predictions of numerical simulations agree well with the experimental data from DF-07 hypersonic wind tunnel but are underestimated in the JF12 experimental data. It is interesting to recall Park's comments on aerothermodynamics [8]. Still there are many more unsolved problems than solved problems. The first of these unsolved problems is not as much an unsolved problem but cavalier attitude of the scientists. It concerns the definition of reaction rates. Many researchers think that the rate of reaction is a sum of all state-to-state transitions from an initial state to a final state. It is not. A reaction rate is a sum of only those components of the state-to-state transition rates proportional to the initial state density under a quasi-steady-state condition.

Conclusions

Experiments of a sharp cone model were carried out under duplicated hypersonic flight conditions in the JF12 hypervelocity shock tunnel, and the force measurement data collected at a series of the attack angles are presented in this paper. Some remarks are summarized as follows:

1. The experimental data at duplicated hypersonic flight conditions show obvious discrepancy from these of the cold hypersonic wind tunnels. The main physical issue is considered to be due to gas molecular vibrations, one of the key phenomena belong to the so-called real gas effects.
2. The cold wind tunnel tests can be numerically simulated by CFD techniques with acceptable accuracy, but modeling thermochemistry in hypervelocity flows is still a challenge. The thermochemical reactions should be taken place for a correct temperature in a proper rate at a proper location.
3. The gas molecular vibrations, oxygen dissociations, nitrogen dissociations, and ionizations are dominated, respectively, at different temperature regions. It is necessary to classify their effect and modeling them separately to understand the real gas effect in hypervelocity flows.

Acknowledgments The authors would like to acknowledge all the staff members in the research group of shock and detonation physics in LHD for their invaluable work. This research work is carried out with the support of the National Natural Science Foundation of China under the project number of 11532014.

References

1. Bertin, J.J., Cummings, R.M.: Critical hypersonic aerothermodynamic phenomena. Annu. Rev. Fluid Mech. **38**, 129–157 (2006)
2. Woods, W.C., Arrington, J.P., Hamilton, H.H.: A review of preflight estimates of real-gas effects on space shuttle aerodynamic characteristics. In: Shuttle Performance: Lessons Learned. NASA Conference Publication, 2283(1983)
3. Maus, J.R., Griffith, B.J., Szema, K.Y., Best, J.T.: Hypersonic Mach number and real gas effects on space shuttle orbiter aerodynamic. J. Spacecr. Rocket. **21**, 136–141 (1984)
4. Lu, F.K., Marren, D.E.: Advanced hypersonic test facilities. In: Progress in Astronautics, vol. 198, AIAA, Washington (2002)
5. Bertin, J.J., Cummings, R.M.: Fifty years of hypersonics: where we've been, where we're going. Prog. Aerosp. Sci. **39**, 511–536 (2003)
6. Jiang, Z., Yu, H.: Experiments and development of long-test-duration hypervelocity detonation-driven shock tunnel (LHDst), AIAA paper 2014-1012 (invited), (2014)
7. Chen, H.: Investigation on the link-up between the aerodynamic force data measured in supersonic and hypersonic wind tunnel. ACTA Aerodynamica Sinica 18(3), 345–349
8. Park, C.: Hypersonic aerothermodynamics: past, present and future. Int. J. Aeronaut. Space Sci. **14**(1), 1–10 (2013)

Part IV

Supersonic and Hypersonic Flows with Shocks

A Method of Detecting Self-Starting Ability of Hypersonic Inlets: A Numerical Investigation

Zhufei Li and Jiming Yang

Introduction

The inlet starting characteristic is an important factor that governs the performance of a hypersonic air-breathing propulsion system [1]. However, it is still a challenge to accurately predict the inlet starting ability. The self-starting ability of an inlet could be confirmed in wind tunnels with sufficiently long running times. Restart of an inlet after a mechanically throttling induced unstart is proof of its self-starting ability at the test conditions [2]. The authors have proposed a method to detect an inlet self-starting ability in a shock tunnel by presetting a blockage with a suitable weight in the inlet [3]. The blockage nearly closes the flow path to unstart the inlet at the initial running phase, and then it also can be blown out of the flow path to detect the ability of the inlet to restart in the test flow durations of the shock tunnel. However, the entire flow features of such a testing process are not well understood due to the limited view scope in the experiments and the unsteady nature of the flow. To thoroughly study the details and improve the method of detecting the ability of an inlet to self-start, computational fluid dynamics is used in the present paper.

Method and Model

A two-dimensional compressible flow solver, for unsteady Reynolds-averaged Navier–Stokes equations, is used to conduct the simulations. The flow equations are discretized by the finite volume method in which the spatial fluxes are obtained by a second-order Roe's scheme [4]. The turbulent flow is modeled by employing the k-ω SST turbulence model [5]. A dual-time stepping method with a physical time step size of 0.25 μs is employed in the present computations. To validate the numerical methods involved in the present paper, an experiment on the starting process of a two-dimensional nozzle conducted by Saito [6] is tested. As can be seen in Fig. 1, the holographic images obtained by present simulation agree reasonably well with the experimental results.

In the present study, two inlet models with internal concentration ratios (ICR) of 1.4 and 1.6 are tested. As shown in Fig. 2a, the cowl of the inlet can be moved forward by 9 mm to increase the internal compression. A blockage with a size of 8×8 mm is placed near the exit of the hypersonic inlet/isolator model. The motion of the blockage is simplified as a rigid body with one degree of freedom, and then two-dimensional numerical simulations are performed by applying dynamic mesh technique of layering. The computational domain is divided into two parts with interfaces, as illustrated in Fig. 2b, in which the larger one is a stationary zone and the smaller one with the blockage is a dynamic mesh zone. To resolve the boundary layer, the grid is refined in the near-wall region with the typical value of y^+ approximately unit. The grid system contains approximately 225,000 cells.

The free-stream conditions are Mach number $Ma = 5.9$, total pressure $P_0 = 1.27$ MPa, and total temperature $T_0 = 810$ K. The temperature of the wall is specified as 283 K. The unsteady simulation is initiated by a started flow of the inlet in the absence of a blockage. The mass of the blockage is varied to study whether and how the blockage duration affects the self-starting ability testing result.

Results and Discussions

Three types of flow in the testing process of the inlet with an ICR = 1.4 are obtained by varying the mass of the blockage, as listed in Table 1. The aerodynamics of

Z. Li • J. Yang (✉)
Department of Modern Mechanics, University of Science and Technology of China, 96 Jinzhai Road, Hefei, Anhui 230026, People's Republic of China
e-mail: jmyang@ustc.edu.cn

G. Ben-Dor et al. (eds.), *30th International Symposium on Shock Waves 1*, DOI 10.1007/978-3-319-46213-4_30

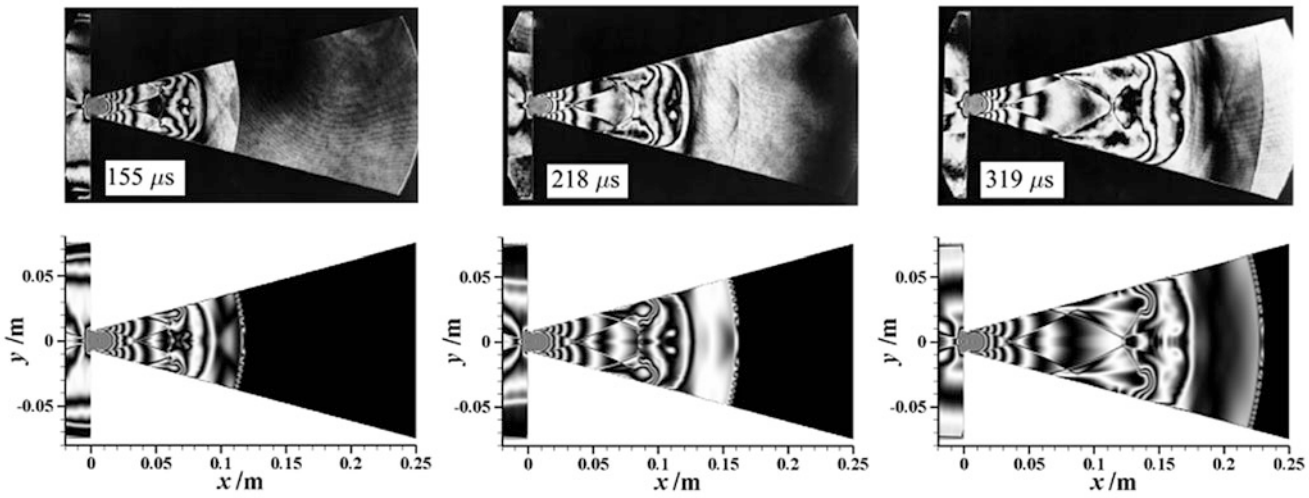

Fig. 1 Holographic images of a two-dimensional nozzle starting process

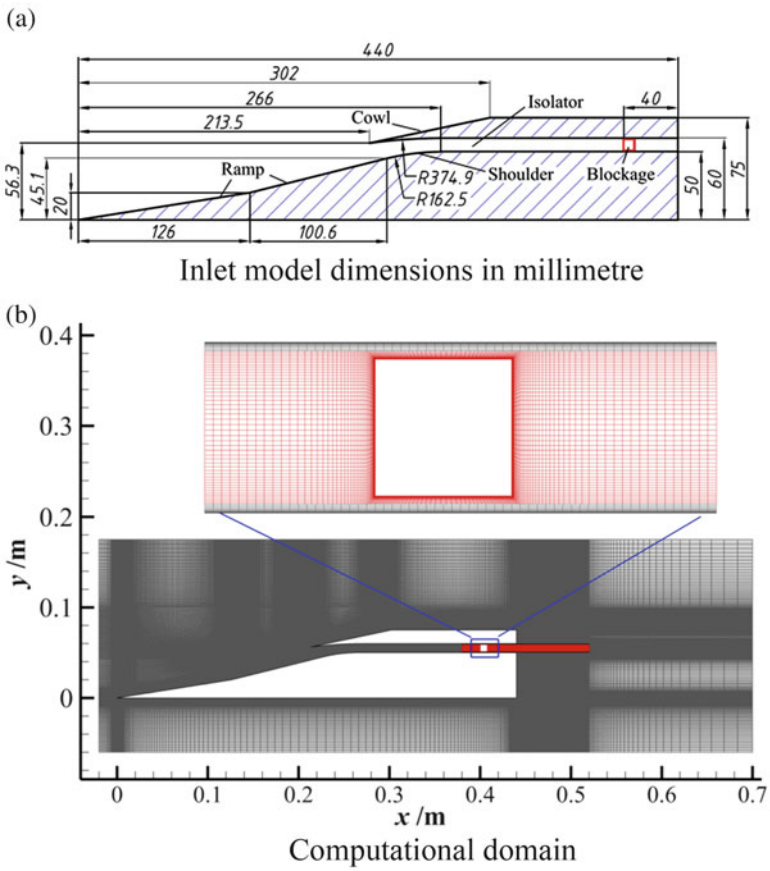

Fig. 2 Schematic of the inlet model and computational domain. (**a**) Inlet model dimensions in millimeter; (**b**) computational domain

the blockage and the involved unsteady flow features in the inlet are discussed to understand the physical mechanism of the testing process. The velocity of the blockage decreases with the increasing mass as shown in Fig. 3.

Case A: Light Blockage

Figure 4a shows the Mach contour of the flow in the isolator induced by a very light blockage (case A). Although shock trains are formed in the isolator, the inlet maintains starting

in the testing process. To reveal the unsteady flow features, the *x*-*t* diagram of the bottom wall pressure is employed, as shown in Fig. 4b. The trajectories of the leading and trailing edges of the blockage are denoted by A and B, respectively. The blockage prevents the flow, and therefore, the pressure in the isolator rises abruptly. The high-pressure flow accelerates the blockage in return. At the initial stage ($t < 0.2$ ms), the velocity of the blockage is small and the flow is dominated by the throttling effects. As a result, the shock train moves upstream quickly as illustrated by C in Fig. 4b. However, the propagation of the shock train slows down because of a significant increase in the volume of the duct, which is a result of the backward movement of the blockage. At 0.33 ms, the blockage moves out of the isolator with a velocity of approximately 220 m/s (in the laboratory frame of reference). Although the pressure in the isolator gradually reduces because of the open of the duct, the separation on the bottom wall still can extend to the throat of the

Table 1 Setup of cases

Case no.	Blockage mass (m_b/kg)	Blockage description	Blockage duration (t_b/ms)
A	0.0018	Light	0.331
B	0.0448	Medium	1.886
C	0.3650	Heavy	7.491

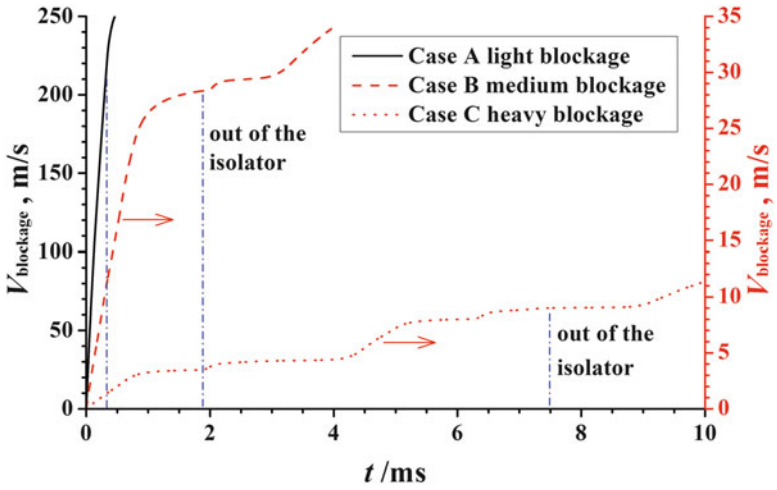

Fig. 3 Velocity of the blockage

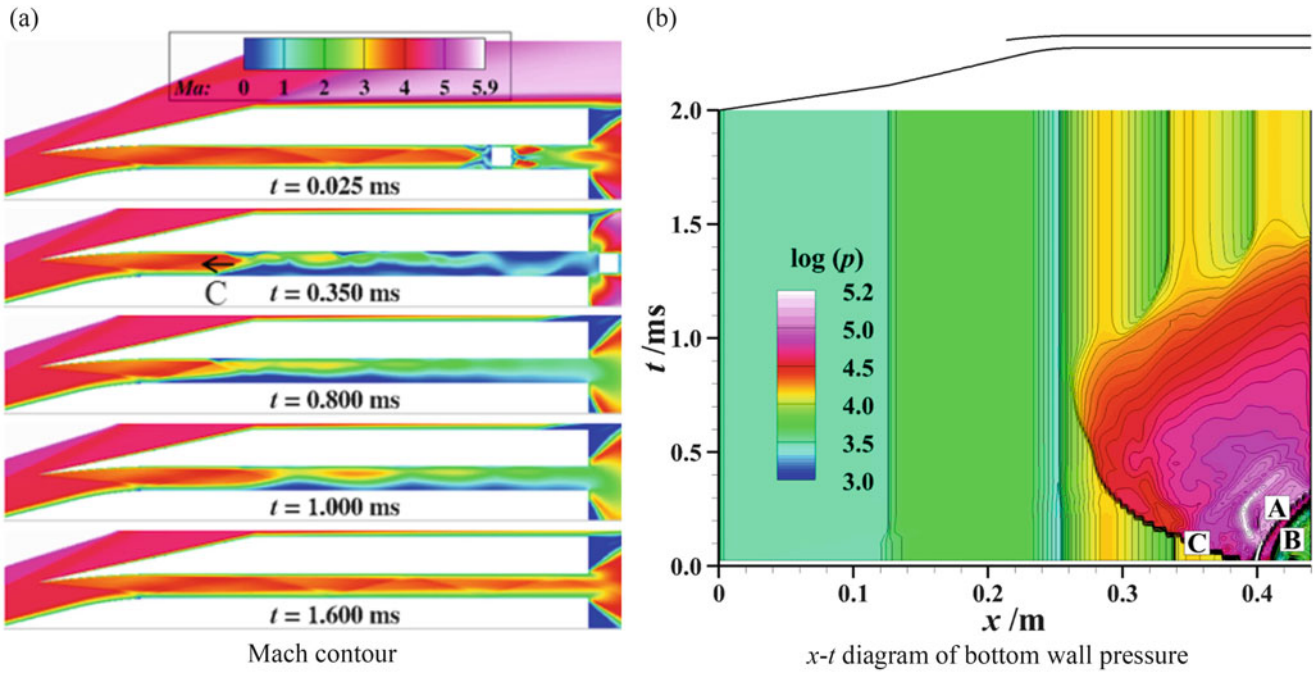

Fig. 4 Mach contour and *x*-*t* diagram of case A (light blockage). (**a**) Mach contour; (**b**) *x*-*t* diagram of bottom wall pressure

inlet at 0.8 ms. The separation smoothly shrinks and the shock train retreats when the pressure in the isolator fall further. When the accumulated flow is discharged at 1.6 ms, the flow recovers from the disturbance of the blockage.

Case B: Medium Blockage

The throttling effects are enhanced when the mass of the blockage increases to be medium (case B). The shock train induced by the blockage extends toward the throat and moves faster than that in case A. At $t = 0.55$ ms, flow spills over the cowl, and thus, the inlet is imposed to unstart, as shown in Fig. 5a. The unstart shock continues to propagate upstream with a speed of approximately 350 m/s, even after the spillage has begun, as illustrated by C in Fig. 5d. Meanwhile, the decreasing entering flow rate causes the pressure in the isolator to gradually reduce, and downstream-propagating rarefaction waves are observed and denoted by D in Fig. 5d. In Fig. 5a, after the unstart shock is expelled from the inlet, an upstream-facing expansion zone is

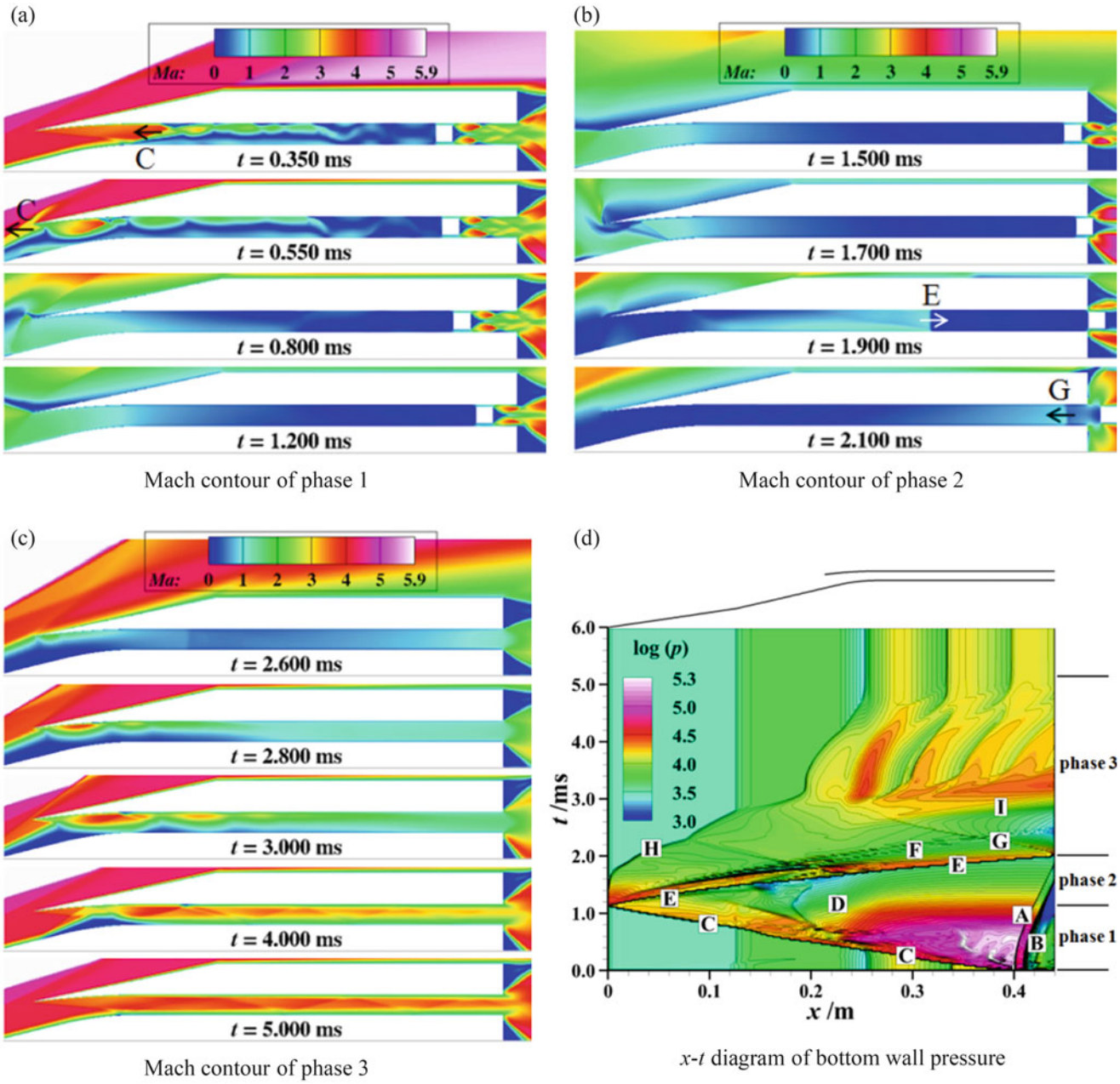

Fig. 5 Mach contour and *x-t* diagram of case B (medium blockage). (**a**) Mach contour of phase 1; (**b**) Mach contour of phase 2; (**c**) Mach contour of phase 3; (**d**) *x-t* diagram of bottom wall pressure

noticeable near the shoulder at $t = 0.8$ ms. According to the stream lines, the flow in the duct is mainly reversed, and therefore, the internal concentration part of the inlet becomes a "divergent nozzle." Moreover, weak shocks and shear layers come about to balance the incoming flow. The entire flow in the isolator is likely subsonic and the velocity of the blockage increases slowly (see Fig. 3). However, such a reversed flow can only remain for a short duration. On the other hand, the former upstream-propagating unstart shock (C) appears to be reflected at the tip of the inlet and generates a downstream-propagating shock (E) at $t = 1.1$ ms with a speed of approximately 500 m/s, as presented in Fig. 5d. When the pressure decreases, the shock (E) enters the inlet, becoming noticeable in the image of $t = 1.7$ ms (see Fig. 5b), and quickly propagates downstream. The former reversed expansion features consequently disappear.

Although the blockage is blown out of the isolator at $t = 1.9$ ms, the shock (E) reflects at the blockage and generates an upstream-propagating weak shock (G) at $t = 2$ ms. Meanwhile, the pressure in the rear section of the duct gradually decreases, and rarefaction waves appear to accelerate the flow because of the recoveries of the duct exit exhaust capability. As the shock (G) moves forward, it meets the rarefaction waves (F) following the shock (E). When the pressure in the isolator decreases further, the separation shock (H) begins to retreat from upstream. The entering flow rate gradually increases, and downstream-propagating compression waves (I) are observed in the isolator (see Fig. 5d). The flow on the first ramp has rebuilt, and the separation shock stands on the second ramp in the image of $t = 2.8$ ms. At $t = 3$ ms (see Fig. 5c), the separation shock impinges on the cowl lip. As the adverse pressure gradient gradually decreases, the separation flow at the inlet entry becomes smaller, and the separation shock enters the inlet at $t = 4$ ms. The inlet restarts when the large separation vanishes in the image of $t = 5$ ms. The distribution of the bottom wall pressure is stable from then on.

According to the x-t diagram of the bottom wall pressure (see Fig. 5d), the testing process is divided into three phases based on the reflection of shocks (C) and (E), which may be helpful for a better description and understanding of the unsteady flow. Phase 1 is complete when the separation shock (C) moves to the furthest upstream position, which is the moment of the reflection. The shock (E) moves toward the exit of the duct and reflects at the blockage in phase 2. Phase 3 begins when the reflection shock (G) appears. In case B, phase 3 is complete when the inlet restarts.

Case C: Heavy Blockage

When a heavy blockage is adopted (case C), the blockage duration is long. Shock wave oscillations are presented, and the velocity of the blockage increases in a stepwise manner with the varying of the entering mass flow of the inlet (see Fig. 3). The inlet also restarts when the heavy blockage is blown out. According to the x-t diagram in Fig. 6b, the testing process is divided into two oscillation cycles based

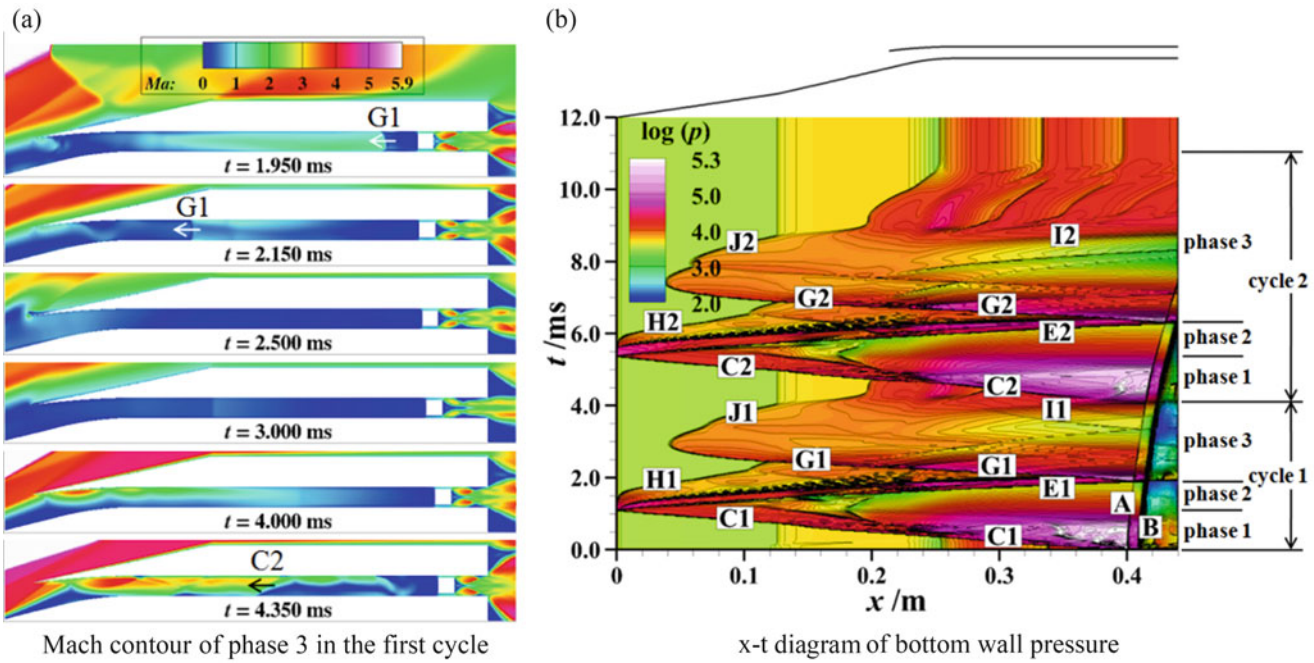

Fig. 6 Mach contour and x-t diagram of case C (heavy blockage). (**a**) Mach contour of phase 3 in the first cycle; (**b**) x-t diagram of bottom wall pressure

on the formation of high-pressure region upstream of the blockage. Each oscillation cycle contains three phases, as defined in case B. The flow variations of the first oscillation cycle are similar to that of case B except phase 3. As shown in Fig. 6, at the beginning of phase 3, the blockage remains in the duct and reflects a strong shock (G1). The upstream-propagating shock (G1) moves forward and meets the shock (H1) retreating from upstream at approximately $t = 2.5$ ms, which prevents the flow to rebuild on the second ramp. As the shock (G1) expels out of the inlet, the entering flow rate decreases. When the pressure reduces, the separation shock (J1) on the first ramp begins to retreat at $t = 3$ ms. Meanwhile, the entering flow rate gradually increases. At approximately $t = 4$ ms, the separation shock stands on the second ramp and continues to move toward the inlet entry. However, the blockage remains in the duct. As a result, the rate of flow accumulation in the duct increases and a new high-pressure region is formed upstream of the blockage. Phase 1 of the second oscillation cycle begins when the separation shock (C2) moves upstream. The lessening of the inlet entry separation is stopped by the high back pressure soon after. As shown in the Fig. 6b, the x-t diaphragm of the second oscillation cycle is very similar to that in case B. The flow features of the second oscillation in case C can refer to that in case B. The inlet restarts at the end of the phase 3 in the second oscillation cycle.

It can be inferred that the blockage duration does not affect the inlet self-starting ability and the inlet can restart when the blockage is blown out. The blockage duration of approximately 0.6 ms is needed to unstart the inlet. However, very heavy blockage is not suitable for self-starting ability test in shock tunnels because of its insufficient flow durations.

Moreover, according to Fig. 3, the motion of the blockage can be pre-estimated as a uniform motion following a uniformly accelerating motion. The blockage is accelerated when the flow accumulates in the duct and then it moves uniformly when the inlet unstart. The total pressure behind an assumed normal shock that stands downstream of the throat is adopted to calculate the average acceleration of the blockage. The estimation of the acceleration agrees reasonably well with the simulations, which is helpful in the selection of a blockage in shock tunnels.

The self-starting Mach number of the inlet model with an ICR of 1.4 is Ma 4.9, which is simulated by successively increasing the free-stream Mach number in the absence of a blockage. As expected, the inlet is unstarting at Ma 4.8 and restarting at Ma 4.9 after a blockage-induced unstart, which are consistent with the results obtained by successively increasing Mach number. Furthermore, a medium blockage is also employed to test the self-starting ability of the inlet model with a larger ICR of 1.6 at Ma 5.9. However, it cannot be restarted after the blockage has been blown out. This variation trend is expected to be similar to that in our prior experiments [3]. Therefore, the reliability of the detecting method of self-start ability with the blockage is confirmed.

Conclusions

The presetting blockage method is helpful for us to detect the self-starting ability of an inlet in shock tunnels. The mass of the blockage plays an important role in the detecting process, which determines the blockage duration. Although the blockage duration does not affect the ability of an inlet to restart, a suitable blockage which can be pre-estimated by an accelerating motion model is recommend in consideration of the limited testing times of shock tunnels.

Acknowledgments This work was supported by the National Natural Science Foundation of China (Grant No. 11402263), China Postdoctoral Science Foundation (Grant No. 2014 M551818), and the Fundamental Research Funds for the Central Universities (WK 2090050030).

References

1. Van Wie, D.M., Kwok, F.T., et al.: Starting characteristics of supersonic inlets. AIAA Paper 1996–2914 (1996)
2. Smart, M.K.: Experimental testing of a hypersonic inlet with rectangular-to-elliptical shape transition. J. Propul. Power **17**(2), 276–283 (2001)
3. Li, Z., Huang, B., Yang, J., et al.: Starting characteristics of hypersonic inlets in shock tunnel. In: Kontis, K. (ed.) 28th International Symposium on Shock Waves, vol. 2, pp. 1015–1020. Springer Berlin Heidelberg, Manchester, UK (2012)
4. Roe, P.L.: Approximate Riemann solvers, parameter vectors, and difference schemes. J. Comput. Phys. **43**(2), 357–372 (1981)
5. Menter, F.R.: Two-equation eddy-viscosity turbulence model for engineering applications. AIAA J. **32**(8), 1598–1605 (1994)
6. Saito, T., Takayama, K.: Numerical simulations of nozzle starting process. Shock Waves **9**(2), 73–79 (1999)

Experimental Investigation on the Self-Starting Characteristics of Hypersonic Inlets

Xiao Xu, Lianjie Yue, Yinan Jia, and Xinyu Chang

A method of diaphragm rupture controlled by igniter to simulate inlet unstart/restart process is used to investigate the self-starting characteristics in shock tunnel. Based on Van Wie's inlet models, various experiments have been conducted to investigate the effects of cowl shock wave strength on the inlet self-starting performance. Results show that the cowl shock wave strength dominates the inlet self-starting capability, and the inlet self-starting internal contraction ratio (ICR) decreases rapidly with a relatively strong cowl shock wave in a certain range. Based on the results, noncoalesced shock design was taken to reduce the cowl shock strength, and the ICR of inlets increased significantly.

Introduction

The mixed compression inlet is a crucial component of hypersonic air-breathing engines, which should decelerate and compress the airflow with minimum losses [1]. For efficient engine operation, hypersonic inlets must operate in a start mode. However, many factors can trigger the inlet unstart, such as low cowl Mach number and high back pressure from the combustor [2]. The unstarted inlets will capture, much less mass flow with lower efficiency, resulting in vehicle flight failure. Hence, efficient methods must be taken to assure the inlet can restart. For hypersonic inlets with fixed geometry, the self-starting capability is the prerequisite for the vehicle efficient operation in wide flight Mach number [3]. However, the inlet unstart/restart process, involving complex shock patterns and strong interactions with boundary layers, is one of the most challenging problems of hypersonic gas dynamics. Numerous studies have been conducted to investigate the inlet self-starting characteristics, ranging from key factors affecting inlet self-starting and prediction of inlet self-starting contraction limit [4–8] to the inlet unstart/restart unsteady behaviors and three-dimensional effects [9–15].

Lots of research was carried out to study key influencing factors of inlet self-starting capability. Kantrowitz proposed a theoretical model for supersonic inlet restart with assumption of a normal shock wave in front of the internal contraction and quasi-steady one-dimensional isentropic internal flow with sonic condition at the inlet throat [4, 5]. The internal contraction limit was then derived to be a function of the inflow Mach number. Three regimes were further divided by two curves. The inlet can always start spontaneously above the Kantrowitz line and never start below the isentropic line, while a dual solution area exists between two lines, where some method will have to be devised to start the inlet. The Kantrowitz theory provides a basic criterion for inlet design, but unfortunately, the restart flow pattern for hypersonic inlet is much different from the assumption of swallowing a normal shock, and there is a strong shock associated with a large-scale boundary layer separation [6]. Many experiments have verified that the inlet can restart at internal contraction ratio beyond Kantrowitz limit and this theory is not applicable to hypersonic inlet [6–8]. Up to now, no accurate theory has been developed to estimate the characteristics of hypersonic inlet self-starting. Sun Bo presented a fitted equation to predict inlet self-starting capability based on preceding experimental data [6]. Veillard proposed the strong-shock design based on the Kantrowitz theory, and he gave the limitations of contraction for the inlets starting with overboard spillage [7]. Molder introduced the starting capability factor S [8] to divide the dual solution area, which simulated inlet self-starting contraction limits in various conditions with different S. All the studies above which prescribe the inlet self-starting capability have quite different results, for the inlet self-starting capability varies with different inlet designs and wind tunnel

X. Xu • L. Yue (✉) • Y. Jia • X. Chang
Institute of Mechanics, CAS, No. 15 Beisihuanxi Road, Beijing 100190, China
e-mail: yuelj@imech.ac.cn

G. Ben-Dor et al. (eds.), *30th International Symposium on Shock Waves 1*, DOI 10.1007/978-3-319-46213-4_31

operating conditions. Some inlets in these experiments also take the variable geometry or bleeding methods to improve the inlet self-starting ability.

Other studies centered on the inlet unstart/restart flow patterns [9–15]. Goldberg studied various parameters that affected the inlet self-starting capability and took the Schlieren images of flow patterns [9]. He found that the inlets started with separation from the optical images which could cause much shock losses with full mass flow capture; thus, he introduced the total pressure recovery $P_{0,re}$ as the key parameter dominating whether an inlet can restart. Results showed that $P_{0,re}$ was mainly related with the cowl height H and boundary layer thickness δ. When H/δ was smaller than 2, the $P_{0,re}$ became sensible, even small perturbation caused inlet unstart. On the other hand, the $P_{0,re}$ didn't change obviously when H/δ was larger than 2. Van Wie investigated the starting characteristics of a small-scale rectangular inlet at Mach 3 condition [10]. He classified the inlet unstart profile into two broad categories as either "hard" or "soft" according to a series of experimental results. The hard unstart/restart, resulted by the choke at the throat, was consistent with the Kantrowitz theory; while the soft unstart/restart occurred as large-scale separation bubble existed in the inlet, in this case, the Kantrowitz theory became invalid. Li et al. investigated the unsteady behaviors during the inlet unstart caused by throttling [11]. In this paper, they studied the oscillation characteristics of the upstream-propagating shocks and then explained how some relative factors effected on oscillation frequency. More self-starting flow profiles were investigated in three-dimensional inlets [12–15], indicating that three dimensions and unsteady flow effects play an important role in inlet self-starting.

All these researches have revealed some characteristics of inlet self-starting, but no universal results can prescribe the inlet self-starting capability due to different inlet geometry and coupled factors effect. So single-factor experiment on simple inlet model to investigate self-starting capability is necessary. Based on a series of inlet self-starting experiments, this paper is concerned primarily with the effect of cowl shock strength on the inlet performance, and the limits of inlet self-starting internal contraction ratio (ICR) are obtained. With the help of simultaneous high-speed Schlieren image and surface pressure measurements, the inlet unstart/restart behaviors are observed. Results are discussed to determine the key factors of the inlet self-starting capability and give directions to inlet design.

Experimental Setup

Wind Tunnel

The experiments were conducted in the GJF shock tunnel of the Institute of Mechanics, Chinese Academy of Science. The shock tunnel is equipped with an 11.2-m-long driver section and a 22-m-long driven section filled with compressed air, downstream which is the axisymmetric nozzle and vacuum experimental tank, as shown in Fig. 1. For these experiments, the nozzle Mach number M_∞ was 4.0. The total pressure P_0 and total temperature T_0 of the air were 13.8 MPa and 415 K, and the unit Reynolds number $Re_{\infty,\,m}$ was 1.62×10^8/m. Figure 2 shows the curve of the total pressure variation during the shock tunnel operation, and the valid experimental duration is nearly 40 ms. The Mach spatial distribution of the flow field is shown in Fig. 3. The two curves show the horizontal Mach distribution at the position of 0 and 400 mm away from the exit of the nozzle, respectively. The outflow of the nozzle center is uniform to ensure the reliability of the experiments, for any perturbation can cause the inlet start or unstart.

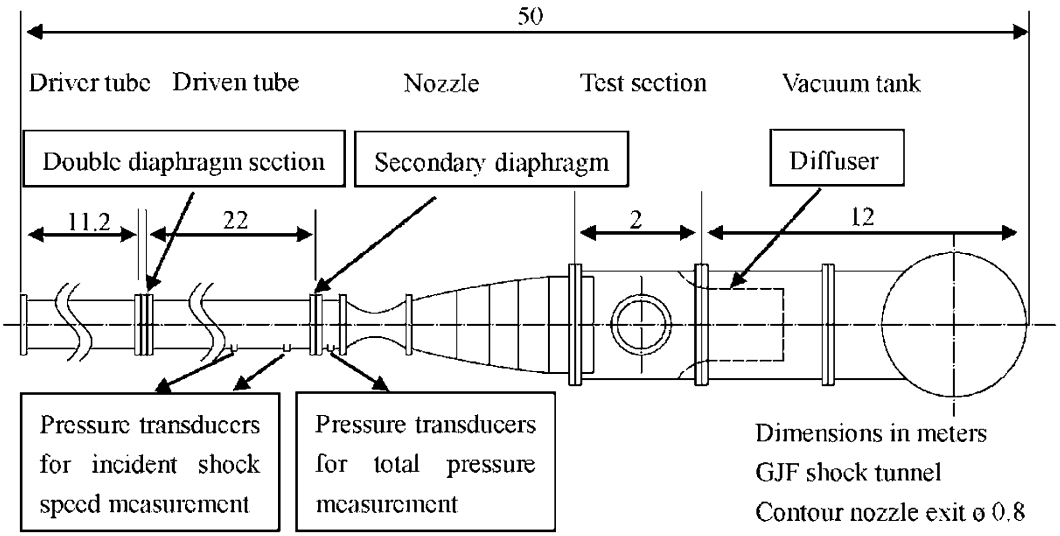

Fig. 1 Sketch of the shock tunnel

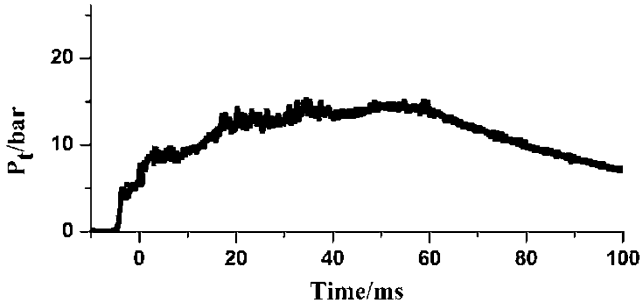

Fig. 2 Total pressure variation of the inflow

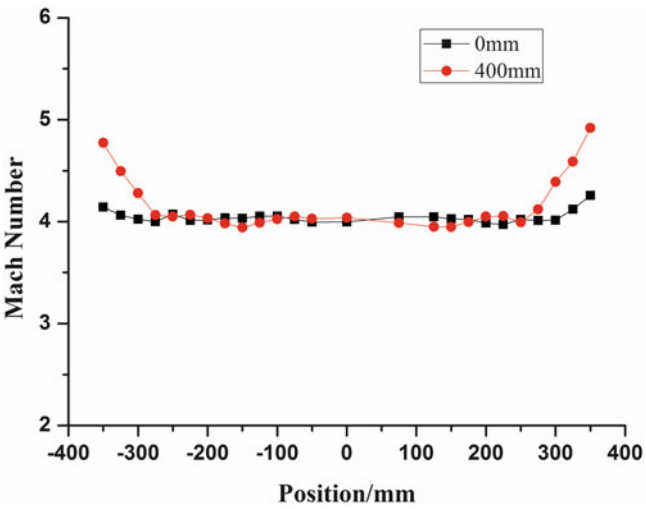

Fig. 3 Mach number spatial distribution at the nozzle exit

Experimental Method

A novel test method is proposed for surveying the hypersonic inlet self-starting capability within the short running time of the shock tunnel [16]. A set of equipment are designed to accomplish the inlet self-starting experiments, as shown in Fig. 4.

A terylene diaphragm is placed at the inlet exit with a coherent electric resistance wire on its leeward insulated from the shock tunnel and inlet model. During the initial experimental stage, the inlet would be choked into big buzz due to the obstruction of the diaphragm. Concurrently, the total pressure of the shock tunnel starts the delay-time signal generator, which in turn outputs a pulse voltage signal after a few milliseconds to trigger the high-voltage igniter. The diaphragm is then ruptured by the heating effect of the electric resistance wire. Note that the delay time is preset so that the diaphragm rupture will occur after the unstart flow of the inlet reaches a quasi-steady state.

As with that in conventional wind tunnels, the restarting flow process of the inlet can be therefore investigated to check its self-starting capability after the choke disappears. The validation of this method to study the capability of the inlet starting has been testified in [16].

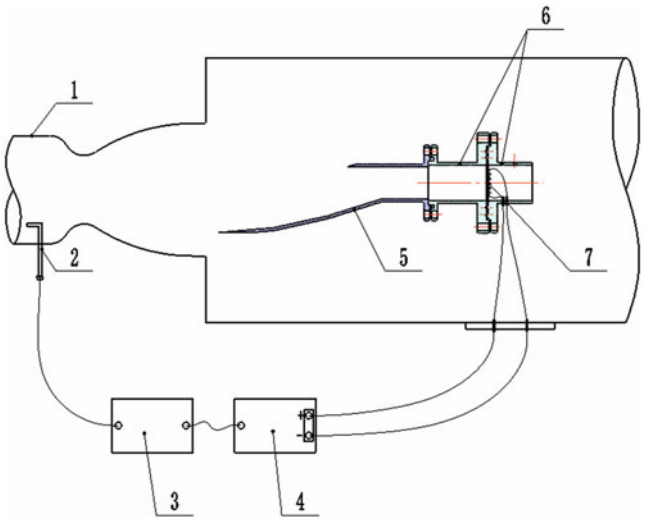

Fig. 4 Devices for inlet self-starting experiments. 1 Shock tunnel nozzle, 2 Pressure probe, 3 Delay time signal generator, 4 Electrical igniter, 5 Hypersonic inlet, 6 Device for diaphragm installation, 7 Terylene diaphragm

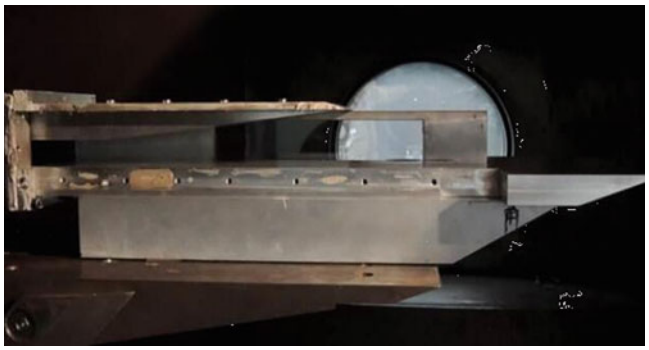

Fig. 5 Inlet model

Inlet Models

The experiments conducted by Van Wie investigated the self-starting capability by rotating the cowl lip, but it changed the cowl shock strength as well as the internal contraction ratio. So fixed cowl was used in our experiments, as shown in Fig. 5. Three parameters were investigated during the experiments, α, H, and L. α was the wedge angle of the cowl; the cowl shock strength varied with α under the same inflow condition. Five angles were used in the experiments, which were 7 deg, 8 deg, 9 deg, 11 deg, and 15 deg, respectively. L determined the boundary layer thickness at the cowl lip, the longer L was, the thicker the boundary layer at the cowl was. H measured the ratio that the cowl boundary layer thickness to cowl lip height, which may effect on the inlet self-starting capability. In these experiments, L varied as 200, 300, and 400 mm and H varied

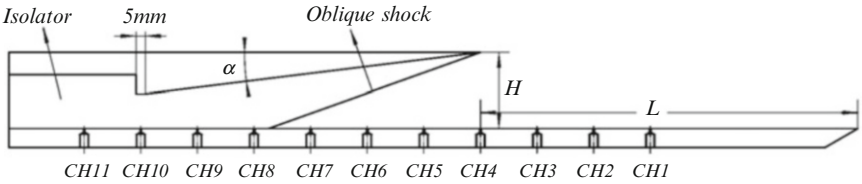

Fig. 6 Sketch of the inlet model

as 20, 30, and 40 mm. A gap between the compressing section and isolator was designed to fix the geometric throat location, and the throat length was 5 mm, as shown in Fig. 6.

Measurements

Two optical windows in the sidewalls allow optical access to the isolator part of the inlet model, as illustrated in Fig. 5. These windows were equipped with silica glasses for flow visualization. During the experiments, Schlieren images were taken to observe the unstart/restart flow field. The frame frequency was set 5000/s, and the camera would record 500 images which covered the valid test time of the wind tunnel.

The inlet model was equipped with 11 static pressure ports along the centerline of the bottom wall with an interval distance of 20 mm. The 128-channel data acquisition system, consisting of voltage signal amplifiers and the National Instruments DAQ PXI-6150 cards, was used for pressure measurement. The results of the static pressure measurements were displayed as pressure ratios with regard to the free stream static pressure. For each channel, the maximum sampling frequency was 1.25 M/s with resolution of 12 bits. Dynamic pressure transducers were used to monitor the unsteady flow pattern with an error of 0.1 % of the full scale and a natural response frequency of 30 kHz. In these experiments, the transducers were installed directly on the model wall lest the internal cavum, and the conduit degrades the actual frequency response. During the test, the pressure data were recorded at a rate of 31.25 kHz per channel.

Results and Discussion

Inlet Restart Behaviors and Critical Phenomenon

The inlet self-starting process, choke firstly occurs at the cowl of the inlet, as the diaphragm ruptures, the choke will go downstream with a decrease of downstream pressure. Whether the separation goes through the throat determines the inlet start or unstart. Figure 7 shows the typical inlet start and unstart processes, respectively, when the inlet starts, as we can see from Fig. 7a, strong choke oscillates periodically since the diaphragm blocks the air flow. When the

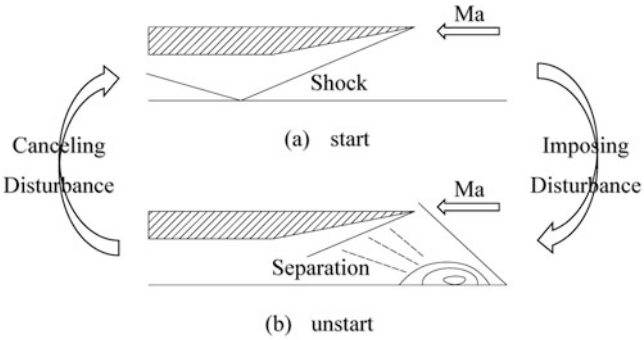

Fig. 7 Typical inlet start and unstart mode

diaphragm ruptures, the choke will go downstream the throat with small contraction ratio, and oblique waves exist stably in the internal section of the inlet. On the other hand, when the inlet unstarts, as shown in Fig. 7b, the separation will not go through the throat with large contraction ratio, at which case the overflow occurs and inducing shock oscillates beyond the cowl.

The critical phenomenon has been observed clearly in the experiments. The critical condition, that is, the inlets can start with separation existing in the internal section, indicates the inlet will capture all the mass flow while the total pressure recovery will stand quite low due to the shock loss by separation. This phenomenon was firstly observed by Goldberg, who gave his results in the [9]; he considered that the inlets started with separation in these cases, and then the $P_{0,re}$ was induced as the key parameter to measure the inlet self-starting capability.

Some critical results have been obtained during the experiments, and typical Schlieren images are shown in Fig. 8. Different from the flow pattern of inlet start or unstart, separation bubble exists in the internal section and oscillates slightly after the diaphragm ruptures during the experimental period. As the separation bubble induces the shock which rapidly increases the shock loss, the recovery of the total pressure decreases, and the inlet cannot obtain enough efficient air to work in the combustion. Figure 9 shows the pressure variation of the cowl (CH4) during the inlet unstart/restart process. Before the diaphragm ruptures, air cannot get through the inlet; thus, intense oscillation occurs at the cowl before 30 ms. As the diaphragm ruptures, the pressure downstream decreases rapidly and the choke is swallowed into the cowl. Whether the choke gets through the throat determines the inlet start or unstart. From Fig. 9,

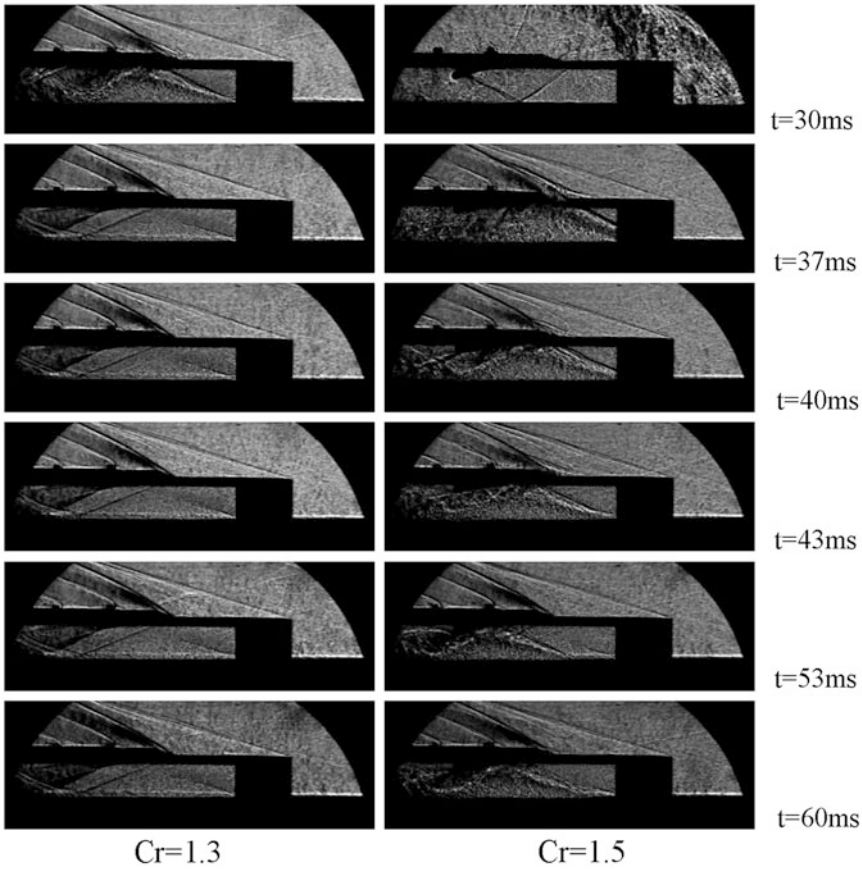

Fig. 8 Critical condition of inlet self-starting

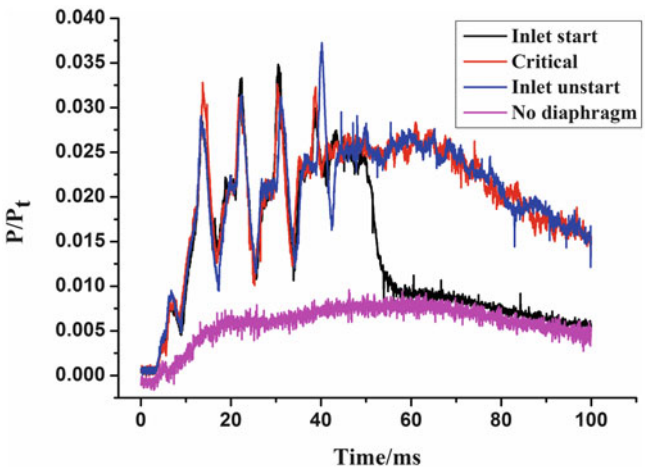

Fig. 9 Pressure variations of different inlet self-starting behaviors

after the diaphragm ruptures and the expansion waves propagate upstream, the pressure at the cowl decreases rapidly and keeps the same with the inlet start condition, which means that the inlet can restart. While in the critical or unstart process, the pressure at the cowl still keeps high but oscillates with small amplitude. The reason for that is the separation bubbles located at the cowl, and they oscillate and achieve a dynamic equilibrium under the interaction of inflow and the back pressure.

As the inlet operates in the critical condition, the recovery of total pressure decreases rapidly; the combustion cannot obtain enough energetic air, which can seriously reduce the efficiency of the scramjets, so the inlets are considered unstart under the critical conditions in this paper.

Effects of Cowl Shock Strength on Inlet Self-Starting

A set of cowl plates with different angles and ICR are designed to investigate the shock strength effects on inlet performance. The cowl shock strength changes with different cowl angles under the same inflow condition, and the ICR is determined by the compression wall length with a fixed sidewall. Here we take the case that the $L = 200$ mm and $H = 40$ mm, and the results are shown in Fig. 10.

From Fig. 10, the inlet self-starting ICR decreases as the cowl angle increases. The cowl shock wave, interacts with the boundary layer, determines the size of the separation bubbles. As the shock strength increases, the size of separation bubbles expands and may cause the choke at the throat, so relatively large throat area which means relatively small

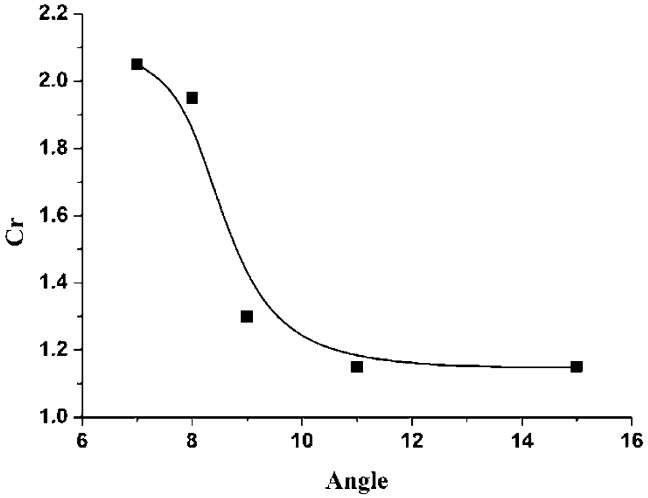

Fig. 10 ICR variation with cowl angle

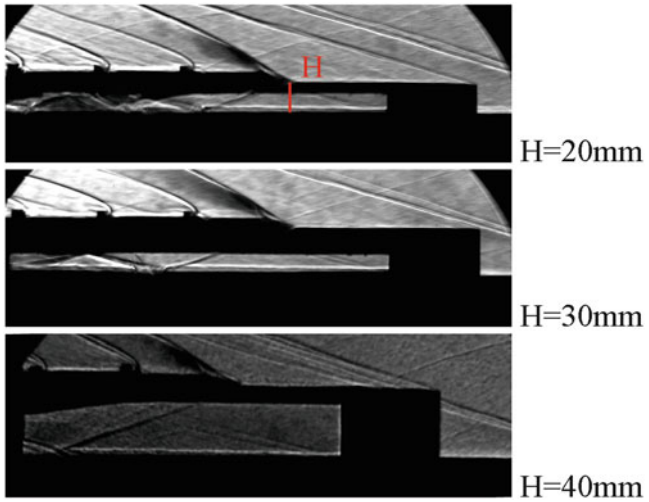

Fig. 12 ICR variation with different H

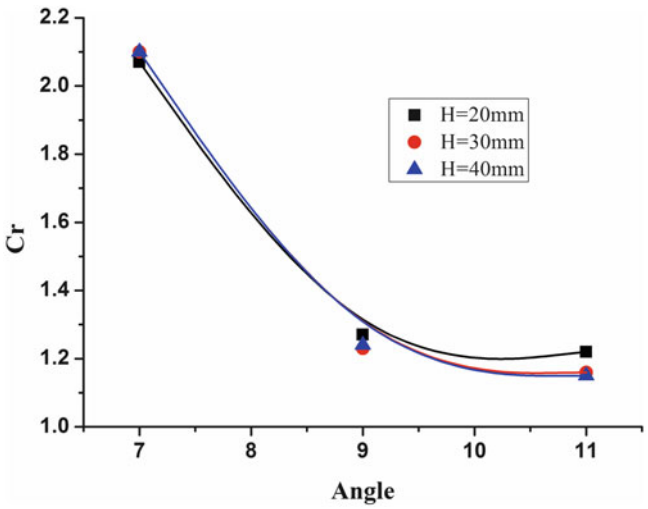

Fig. 11 ICR variation with different H

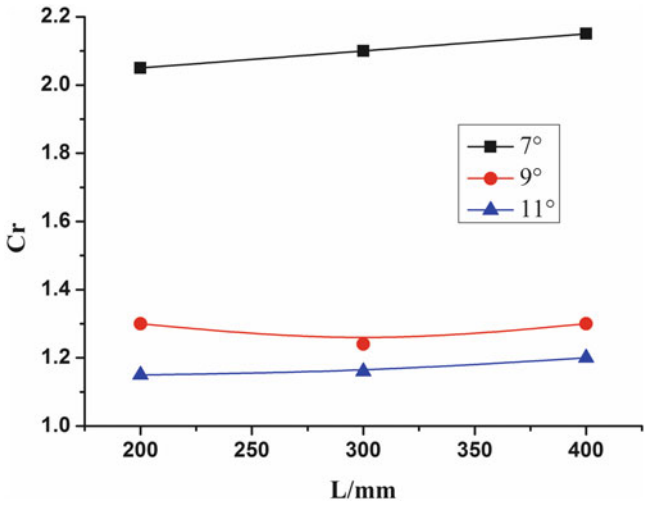

Fig. 13 ICR variation with different L

ICR is needed to assure that the separation bubbles can get through.

Then the shock wave strength is studied under the cases with different H, and $L = 300$ mm in these cases. The results are shown in Fig. 11; it turns out that H does not affect the inlet self-starting ICR in these conditions. Figure 12 shows the Schlieren images of the starting cases of the inlets. From the images we can see that the boundary layer thickness δ at the cowl lip is quite small, and then H/δ is very large even when $H = 20$ mm, so the cowl height H does not affect the inlet self-starting ICR as the H/δ is very large.

Figure 13 shows the inlet self-starting ICR with different L; when the angle is fixed, the results hardly change with different L. Because L determines the boundary layer thickness δ at the cowl lip, when L varies from 200 to 400 mm, the boundary layer thickness δ changes little, so the ICR of inlet self-starting keeps the same in all these cases with different L.

Noncoalesced Shock Wave Design

Based on the results above, noncoalesced shock wave design to reduce the cowl shock wave strength is proposed to improve the inlet self-starting capabilities. The cowl turning angle $\alpha = 11°$ is then designed in two cases which are 7° + 4° and 5.5° + 5.5°. Figure 14 shows the two designs and the shock waves when the inlets start.

According to the shock theory, when the air turns the same angle as 11°, distracting the turning angle can reduce the shock strength significantly. So the shock waves are the weakest with the 5.5° + 5.5° design, and the shock waves of 7° + 4° design are stronger than those of 5.5° + 5.5°, while the shock is strongest when the air turns 11° without distraction.

Figure 15 shows the experimental results of the three designs in shock tunnel. It turns out that the noncoalesced shock design can significantly improve the inlet self-starting

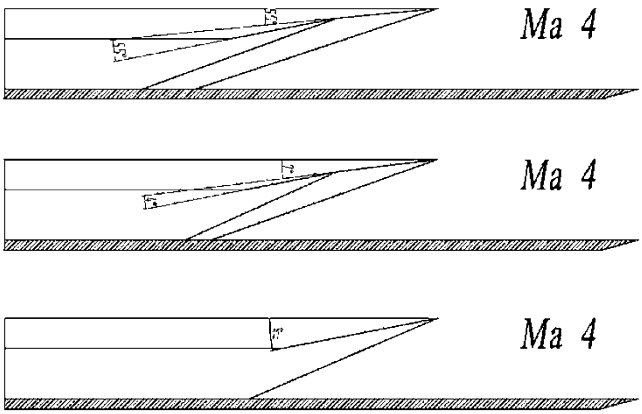

Fig. 14 Noncoalesced shock design and shock wave location

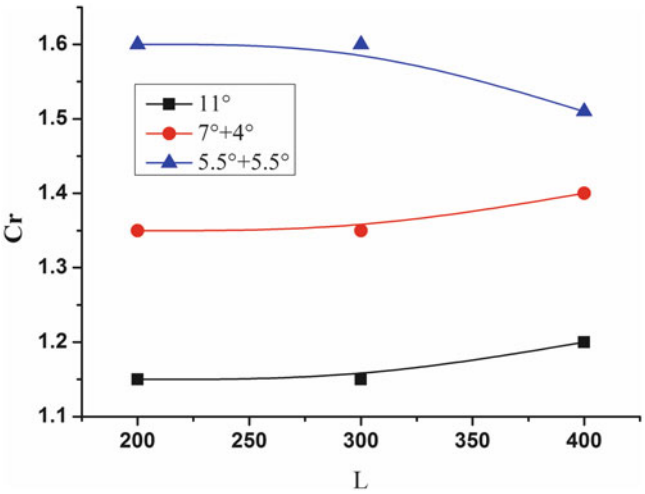

Fig. 15 ICR variation with different noncoalesced shock design

ICR. Take $L = 200$ mm as an example, compared with the single 11° compression, the inlet self-starting ICR increases 18 % with the 7° + 4° design and 39 % with the 5.5° + 5.5° design, respectively. So the distraction shock wave design certainly benefits to the inlet self-starting capabilities, and this method can apply to the industry design.

Conclusion

An experimental study is conducted to investigate self-starting characteristics of hypersonic inlets in the shock tunnel. Based on the method of diaphragm rupture controlled by igniter, the key factors affecting inlet self-starting capability-cowl shock strength are investigated. The inlet unstart/restart flow field is obtained by Schlieren images, and the critical phenomenon is identified. By taking the parameter ICR to measure the capability of the inlet self-starting, various experiments are conducted to study the effects of cowl shock strength on the inlet performance.

The cowl strength is the key factor that determines the inlet self-starting capability. Strong cowl shock causes large separation in the internal section of the inlets, resulting in decrease of the inlet self-starting ICR. Studies show that a sensitive range (8–11°) exists where the inlet self-starting ICR decreases rapidly. Based on the result, noncoalesced shock wave design is proposed, and the experiments have verified that this method can significantly improve the inlet self-starting capability.

The research provides some insight into the flow characteristics during the inlet unstart/restart process and also gives the design directions of inlets from the point of the self-starting capability.

References

1. Heiser, W.H., Pratt, D.T.: Hypersonic Airbreathing Propulsion, 1st edn. AIAA Education Series, Washington, DC (1994)
2. Evgeny, V.T., Tahir, R.B.: On recent developments related to flow starting in hypersonic air intakes. AIAA Paper 2008-2512
3. Michael, K.S.: How much compression should a scramjet inlet do? AIAA J. **50**(3), 610–619 (2012)
4. Kantrowitz, A., Donaldson, C.: Preliminary investigation of supersonic diffusers. NACA ACR-L5D20, May 1945
5. Kantrowitz, A.: The formation and stability of normal shock waves in channel flows. NACA TN 1225, March 1947
6. Bo Sun, K.-Y.Z.: Empirical equation for self-starting limit of supersonic inlets. J. Propul. Power **26**(4), 874–875 (2010)
7. Veillard, X., Tahir, R.B., Timofeev, E.V., Molder, S.: Limiting contractions for starting simple ramp-type Scramjet intakes with overboard spillage. J. Propul. Power **24**(5), 1042–1049 (2008)
8. Molder, S., Timofeev, E.V., Tahir, R.B.: Flow Starting in high compression hypersonic air inlets by mass spillage. AIAA Paper 2004-4130
9. Tbeodore, J.G., Jerry, N.H.: Starting phenomena for hypersonic inlet with thick turbulent boundary layers at Mach 6. NASA TN D-6280, August 1971
10. Van Wie, D.M., Ault, D.A.: Internal flowfield characteristics of a two-dimensional scramjet inlet at Mach 10. AIAA Paper 1965-088
11. Zhufei, L., Wenzhi, G., Hongliang, J., Jiming, Y.: Unsteady behaviors of a hypersonic inlet caused by throttling in shock tunnel. AIAA J. **51**(10), 2485–2492 (2013)
12. Oliver, M.H., Ali, G.: Experimental investigation on the influence of sidewall compression on the flowfield of a scramjet inlet at Mach 7. AIAA Paper 2011-2150
13. Oliver, M.H., Ali, G.: Analysis of a three-dimensional, high pressure ratio scramjet inlet with variable internal contraction. AIAA Paper 2012-5975
14. Ogawa, H., Grainger, A.L., Boyce, R.B.: Inlet starting of high-contraction axisymmetric scramjets. J. Propul. Power, 2010 **26**(6), 1247–1258
15. Grainger, A.L., Boyce, R.R., Tirtey, S.C., Ogawa, H.: The unsteady flow physics of hypersonic inlet starting processes. AIAA Paper 2012–5937
16. Liu, H., Yue, L., Xiao, Y., Peng, H., Zhang, X.: Experimental method for hypersonic inlet self-starting in shock tunnel. AJCPP 2012-173

An Investigation of Type IV Shock Interaction Over a Blunt Body with Forward-Facing Cavity

F.S. Xiao, Zhufei Li, Yujian Zhu, and Jiming Yang

Introduction

Shock wave interaction occurs in many external and internal flow fields around hypersonic vehicles. The type IV shock interaction is one of the six types of shock interactions categorized by Edney [1] and is characterized by a supersonic jet embedded with the surrounding subsonic flow. It receives the most attention because it creates the most complex flow pattern and severe heating problem. Substantial experimental [2–4] and computational [5–8] research efforts have been made to study such type of shock interaction. Unsteady oscillations with typical frequencies of 3–10 kHz were first observed by Holden et al. [3]. With the same conditions as that of the experiments [3] however, Gaitonde and Shang [5] performed a numerical study with a modified Steger–Warming scheme and revealed that the dominant frequency was about 32 kHz. Zhong [7], Chu, and Lu [8] solved the Navier–Stokes equations using high-order schemes to analyze the characteristics of the unsteady type IV shock interaction. Unfortunately, the frequencies of their calculations were still far from that of the experiment. In addition, there has been an interesting speculation that introducing an opposing jet [9] or a forward-facing cavity [10] at the nose region of a blunt body may reduce the drag and aerothermal loads. However, it needs to be pointed out that the introduction of a cavity or an opposing jet in the stagnation-point region will inevitably bring some new flow features especially when shock interaction occurs.

Many studies have been made to reveal the flow phenomena of the unsteady type IV shock interaction, although the mechanism of the unsteadiness remains unclear. There are still problems which require further investigation to get a better understanding of the feedback mechanism and the frequency of the oscillation. In the present work, the effects of a forward-facing cavity on the unsteady behaviors of hypersonic type IV shock interaction of a blunt body are numerically investigated. The objective is to study the unsteadiness of the interaction and clarify how flow field structure is affected by the presence of the cavity.

Numerical Methods and Validation

Numerical simulations were conducted by solving two-dimensional Navier–Stokes equations using the finite volume method with an adaptive mesh technique as shown in Fig. 1. This code [11] has second-order accuracy in both temporal and spatial scales. A hypersonic flow past a circular cylinder with a freestream Mach number 8.03, temperature 110.56 K, and a Reynolds number based on the diameter of the cylinder 5.15E05 was considered to validate the numerical method. The selected parameters are the same as those performed in the experiments in Ref. [3]. Figure 2 shows the distributions of the mean pressure and heating which are normalized by the stagnation pressure p_0 and heating q_0 of the undisturbed cylinder, respectively. The results agree well with the experimental data.

Results and Discussion

A forward-facing cavity is introduced in the stagnation-point region as shown in Fig. 3. The cylinder has a diameter of 30 mm and the depth and width of the cavity are 7 mm. The freestream conditions are set to be Ma = 6.0, p_∞ = 800 Pa, and T_∞ = 115 K, the same as the exit parameters of the shock tunnel in the USTC (Fig. 4).

F.S. Xiao (✉) • Z. Li • Y. Zhu • J. Yang
Department of Modern Mechanics, University of Science and Technology of China, 96 Jinzhai Road, Hefei, Anhui 230026, People's Republic of China
e-mail: xfshou@mail.ustc.edu.cn

G. Ben-Dor et al. (eds.), *30th International Symposium on Shock Waves 1*, DOI 10.1007/978-3-319-46213-4_32

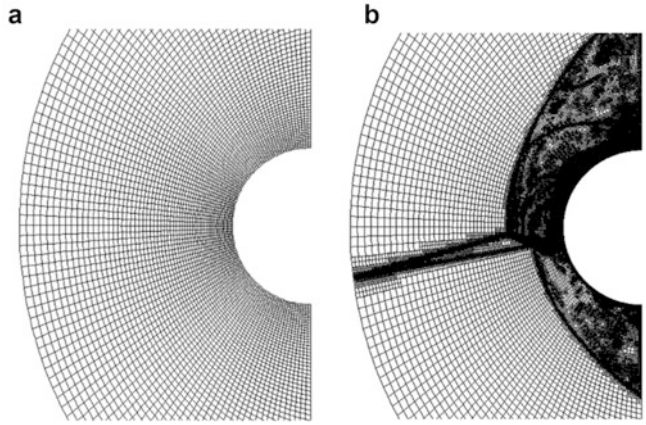

Fig. 1 Computational meshes: (L) initial coarse grid; (R) a transient solution-adaptive grid

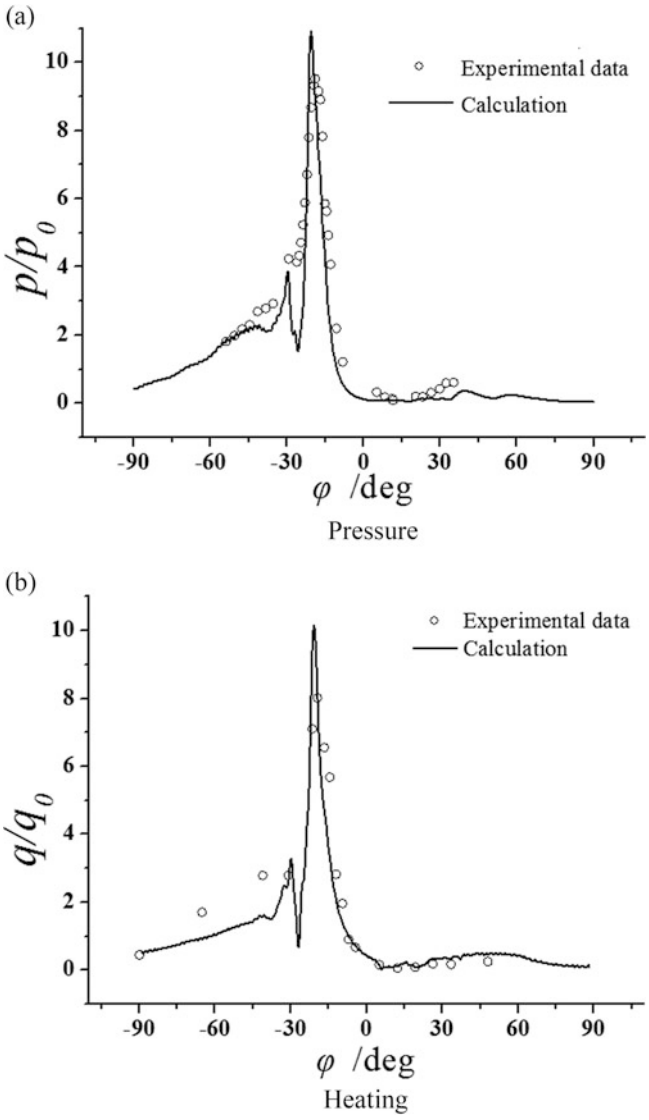

Fig. 2 Distribution of the mean pressure and heating on the surface. (**a**) Pressure (**b**) Heating

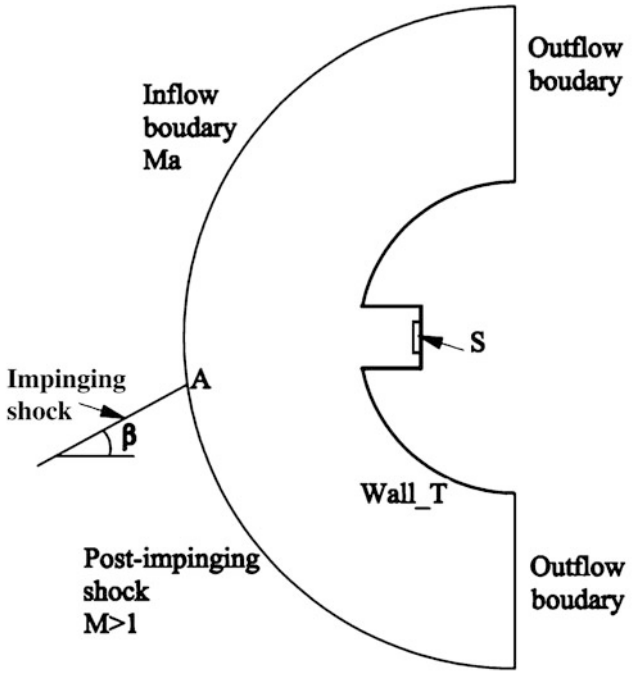

Fig. 3 Boundary conditions

With reference to Fig. 3, the boundary conditions are as follows. The impinging shock wave is introduced by the Rankine–Hugoniot relation. The shock angle β is determined by the freestream Mach number and the wedge angle (15°). Point A stands for the impinging shock location. No-slip and isothermal boundary is used on the solid surface with the temperature 300 K. Nonreflecting boundary is employed in the inlet and outlet boundaries.

Both steady and unsteady results of type IV shock interaction were obtained in the numerical simulations. Two different oscillation modes were observed, which were named in this paper as high-frequency forward–backward mode and low-frequency up–down mode, respectively, according to the oscillation frequency and the motion of the supersonic jet. Details are shown and discussed in the following parts.

Steady Type IV Shock Interaction

Two kinds of steady type IV shock interaction were observed. The first one is shown in Fig. 5a, in which the supersonic jet is deflected upward sufficiently to graze the upper surface of the cylinder rather than impinge on the surface, and this situation is known as type IVa shock interaction [4]. The second kind is shown in Fig. 5b, where the jet steps over the cavity and impinges on the lower surface.

High-Frequency Forward–Backward Oscillation Mode

Moving down the shock intersection point on the basis of type IVa shock interaction (Fig. 5a), the forward–backward mode occurs. The bow shocks and supersonic jet move forward and backward in front of the cavity of the cylinder periodically.

Figure 6 shows the flow feathers with instantaneous temperature contours and the fluid streamlines. The temperature contours are very suitable to characterize the flow field structures such as shocks, supersonic jet, and shear layers. Compared with the steady type IVa shock interaction, when the forward–backward mode occurs, the supersonic jet gets closer to the upper wall, and a weak interference between the jet and cavity shows up. As shown in Fig. 6a, a small part of fluids in the jet enters the cavity, causing a rise of the pressure in the cavity. The disturbances created by the pressure rise travel upstream through the subsonic region outside of the supersonic jet, until they encounter with the bow shocks and cause oscillations of the bow shocks and the jet. The bow shocks are forced to move upstream with small amplitude, and the jet moves upstream away from the cavity, turning upward in a similar way as type IVa configuration as can be seen in Fig. 6b. This provides an opportunity for the high-pressure fluids stacked in the cavity to flow away rapidly, after which the pressure in the cavity drops, making the supersonic jet and the bow shocks moving downstream back to their positions again. Once the jet moves back to the position near the cavity, part of the fluids in the jet will enter the cavity again and the next oscillation cycle will begin. The process described above demonstrates that the bow shocks, transmitted shock, and jet move forward and backward against the upper edge of the cavity. In this oscillation mode, only a small part of the jet flows into the cavity, having weak effect on the cavity pressure oscillation amplitude. The characteristics of this mode are small amplitude of movement of the bow shocks and jet, as well as small amplitude of pressure oscillation with high frequency.

A pressure history at the bottom of the cavity is plotted in Fig. 7, which is normalized by the stagnation pressure of the cylinder for undisturbed flow. The periodic fluctuation of pressure shows that the flow is oscillatory as observed by the temperature contours. A fast Fourier transform (FFT) of the pressure signals was also performed. The FFT analysis reveals a dominant frequency of 8.44 kHz in the computations.

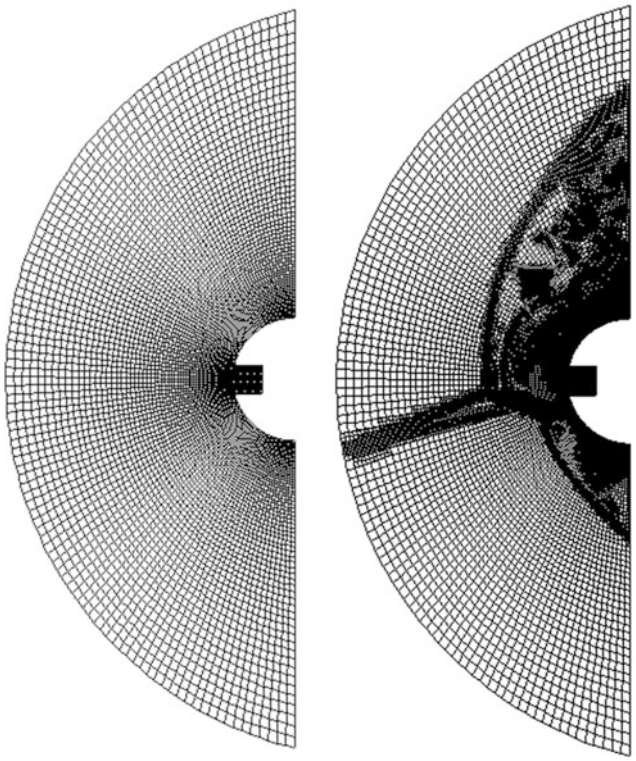

Fig. 4 Computational meshes

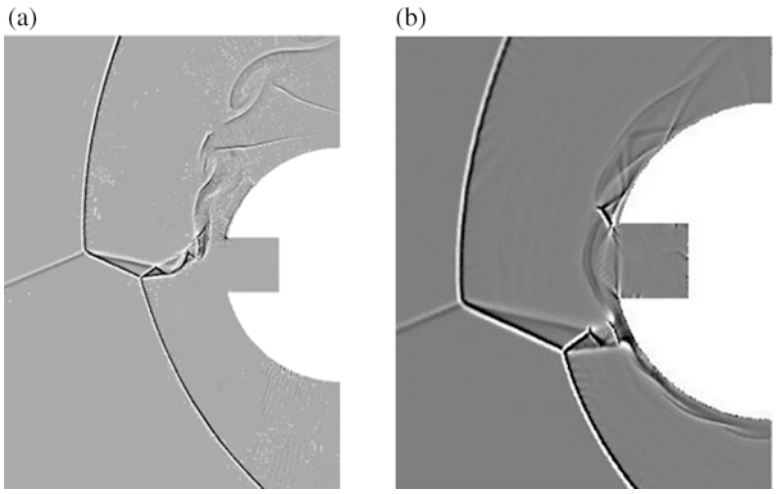

Fig. 5 Flow patterns of steady type IV shock interaction

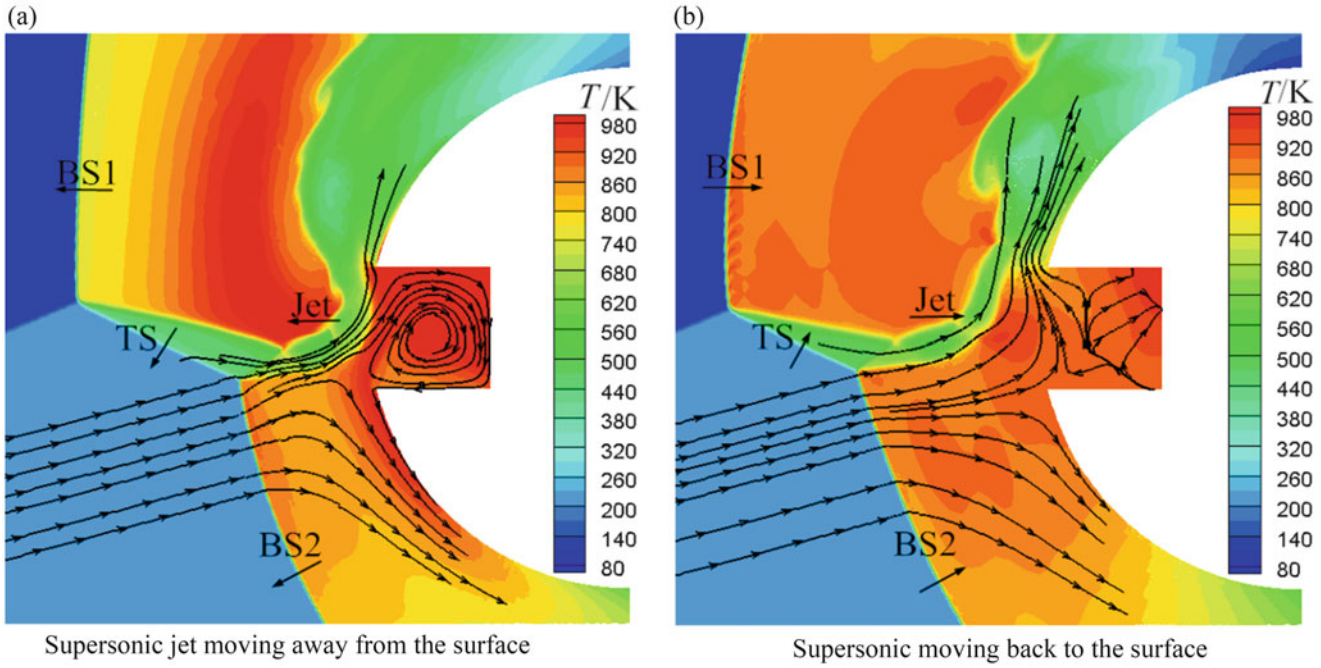

Fig. 6 The temperature contours and streamlines: forward–backward oscillation mode. (**a**) Supersonic jet moving away from the surface; (**b**) Supersonic jet moving back to the surface

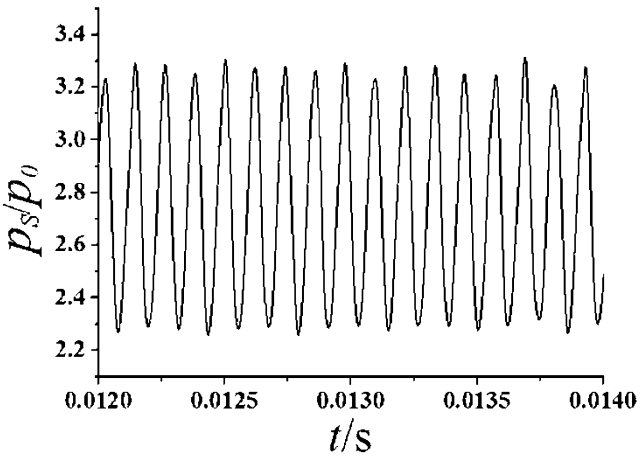

Fig. 7 Pressure histories in the cavity: forward–backward oscillation mode

Low-Frequency Up–Down Oscillation Mode

Once the major part of the supersonic jet enters into the cavity, another different oscillation mode appears. In this oscillation mode, the shock intersection point and the supersonic jet move up and down, in the meantime the bow shocks move forward and backward in front of the cavity.

Compared with the former oscillation mode, the whole jet impinges into the cavity in this mode as shown in Fig. 8a. The pressure in the cavity rises rapidly, and a strong interference between the jet and the cavity is resulted in. Meanwhile, the strong disturbances caused by the rapidly rising pressure in the cavity propagate upstream through the subsonic region and cause the unsteadiness of the upstream bow shocks. A violent positive feedback behavior appears within a period of the oscillating cycle. The bow shocks are forced to move further upstream by the strong disturbances, which in turn leads to the increase of the width of the supersonic jet and results in an even more severe interference between the jet and the cavity. Such a strong coupled process lives on until the downward-moving jet completely steps over the cavity and impinges on the lower surface as shown in Fig. 8b. The pressure in the cavity reduces after the jet impinges on the lower surface, which leads the bow shocks and the jet to move back to the original positions. When the upward-moving jet impinges in the cavity again, it triggers the next oscillation cycle. It is worth noting that the bow shocks move forward and backward with an even larger amplitude in this mode than that in the former mode. Owing to its large-amplitude oscillation, the frequency is consequently lower. The characteristics of this mode are large amplitude of movement of the bow shocks and the jet and large amplitude of pressure oscillation with low frequency.

Figure 9 shows the time history for the pressure at the base of the cavity. The FFT analyses figured out that the dominant frequency in the computations is 3.28 kHz.

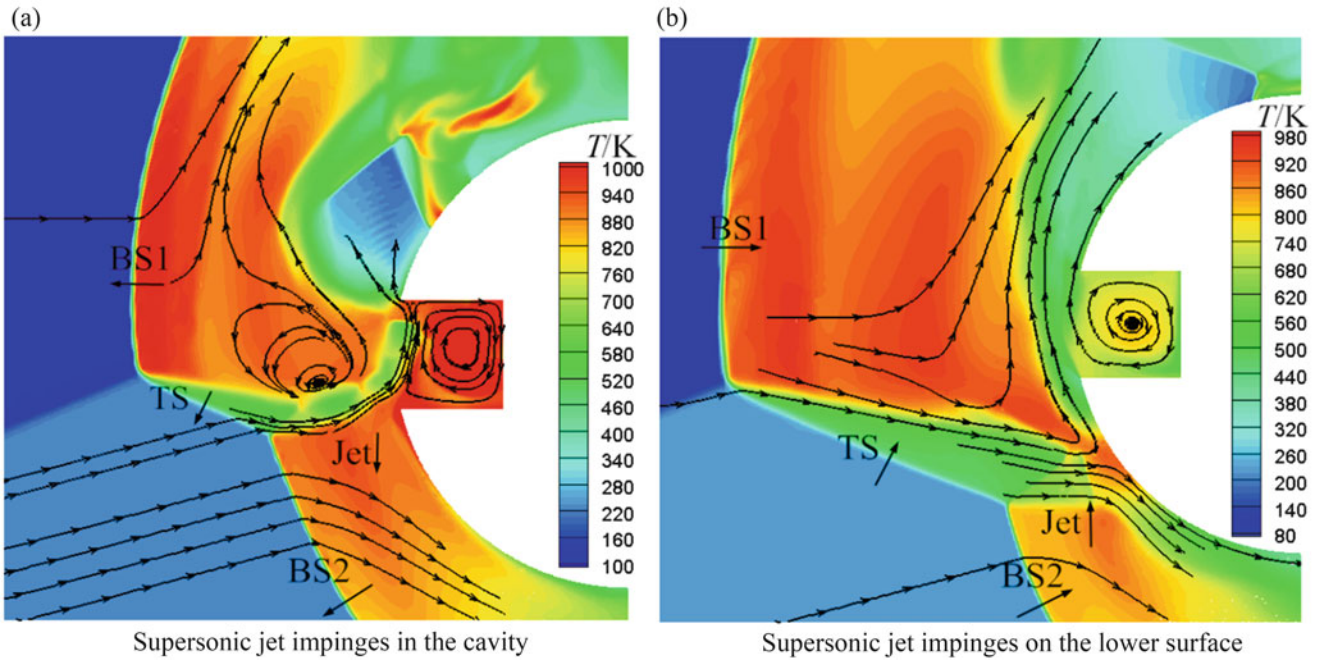

Fig. 8 The temperature contours and streamlines: up–down oscillation mode. (**a**) Supersonic jet impinges in the cavity; (**b**) Supersonic jet impinges on the lower surface

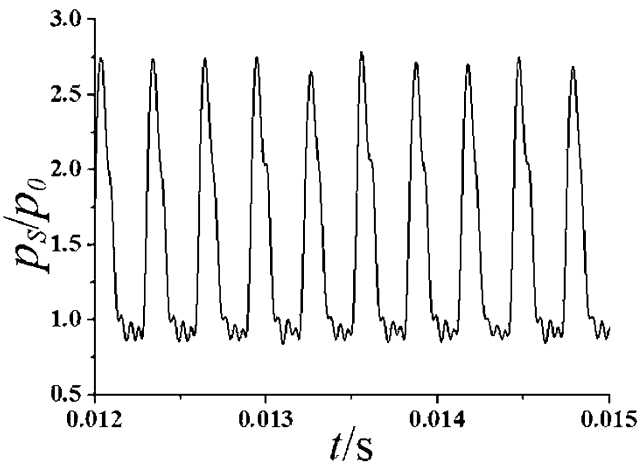

Fig. 9 Pressure histories in the cavity: up–down oscillation mode

From the results and discussion mentioned above, it can be concluded that the characteristics of the type IV shock interaction within the present interests are different from that of the well known [5–8]. For the conventional unsteady type IV shock interactions [5–8], the mechanisms behind the oscillation are related to vortices shedding, shear-layer instability, etc. For present case however, the interference between the supersonic jet and the cavity plays a key role in the oscillation phenomena, and the oscillation is much more intense and easier to be observed.

Conclusions

The hypersonic type IV shock interaction of a blunt body with a forward-facing cavity was investigated numerically. The results show that the flow behaves to be either steady or unsteady depending on the supersonic jet impingement location. Under the conditions within the current work, two different oscillation modes, namely, high-frequency forward–backward oscillation and low-frequency up–down oscillation modes, were observed. The interference between the supersonic jet and the forward-facing cavity plays a key role for the oscillating flows.

References

1. Edney, B.: Anomalous Heat Transfer and Pressure Distributions on Blunt Bodies at Hypersonic Speeds in the Presence of an Impinging Shock. Aeronautical Research Institute of Sweden, FFA Report No. 115, 1968
2. Wieting, A.R., Holden, M.S.: Experimental shock-wave interference heating on a cylinder at Mach 6 and 8. AIAA J. **27**(11), 1557–1565 (1989)
3. Holden, M.S., Wieting, A.R., Moselle, J.R., et al.: Studies of Aerothermal Loads Generated in Regions of Shock/Shock Interaction in Hypersonic Flow. AIAA 1988-0477.
4. Boldyrev, S.M., Borovoy, V.Y., Chinilov, A.Y., et al.: A thorough experimental investigation of shock/shock interferences in high mach number flows. Aerosp. Sci. Technol. **5**(3), 167–178 (2001)

5. Gaitonde, D., Shang, J.S.: On the structure of an unsteady type IV interaction at Mach 8. Comput. Fluids **24**(4), 469–485 (1995)
6. Lind, C.A., Lewis, M.J.: Computational analysis of the unsteady type IV shock interaction of blunt body flows. J. Propul. Power **12** (1), 127–133 (1996)
7. Zhong, X.: Application of essentially nonoscillatory schemes to unsteady hypersonic shock-shock interference heating problems. AIAA J. **32**(8), 1606–1616 (1994)
8. Chu, Y.B., Lu, X.Y.: Characteristics of unsteady type IV shock/shock interaction. Shock Waves **22**(3), 225–235 (2012)
9. Prabhu, R.K., Wieting, A.R., Thareja, R.R.: Computational studies of a fluid spike as a leading edge protection device for shock-shock interference heating. AIAA 1991-1734
10. Engblom, W.A., Yuceil, B., Goldstein, D.B., et al.: Experimental and numerical study of hypersonic forward-facing cavity flow. J. Spacecr. Rockets **33**(3), 353–359 (1996)
11. Sun, M., Takayama, K.: Conservative smoothing on an adaptive quadrilateral grid. J. Comput. Phys. **150**(1), 143–180 (1999)

Particularities of the Shock Wave Propagation Through the Region of Gas Discharge Plasma

Tatiana Lapushkina, Alexandr Erofeev, and Sergei Poniaev

Introduction

The problem of action on strong gasdynamic breakdowns including different origin shock waves with the purpose of control or considerable weakening of them is important not only for applied science but interesting for fundamental investigations. For solving this task for supersonic flows with Mach number more than 4, the plasma action method is actual from the point of view of operation speed. Plasma method supposes to use the gas discharges and plasma jets of different nature and intensities. In the row of papers for the purpose of supersonic flow and boundary layers control high energy plasma sheets [1], low current dielectric-barrier discharge (DBD) [2] and plasma jets [3] are used. In this paper the propagation of strong shock waves through the region of electrical and magnetic field applying is investigated.

In the previous papers, the gas discharge action on the bow shock wave at supersonic flow around the body by means of arranging it in the flow before the body [4] or near the body's surface in the region between bow shock wave and body [5] was investigated. The strong influence of nonequilibrium degree T_e/T_h incoming to the body plasma flow and surface discharge on the position and form of the bow shock wave up to destruction of it was founded (Fig. 1).

The main goal of this work partly is to investigate the propagation process of strong shock wave through the region of gas discharge with different intensities from low current up to powerful current in the absence and in the presence of cross magnetic field. The investigation is carried out in direct channel with square cross section (Fig. 2) which connects with cylindrical shock tube where shock wave formation with Mach number $M = 8$ is carried out. The uniform discharge is arranged by means of special LC chains, connected with pin electrodes built in top and bottom working chamber walls. The zone with pin electrodes has dimension 8 × 2 cm and includes 34 pin electrodes in the top wall and the same in the bottom. Each pin electrodes has load resistance $R = 3$ Ohm. Gas discharge current is closed by ionized gas that passes through electrical field which is applied to electrodes in advance. It is possible to vary the gas discharge intensity by means of changing the applied voltage value and the width of it by changing the number of connected electrodes. Additionally it is possible to switch on the magnetic field $\boldsymbol{B}$ in orthogonal to flow velocity $\boldsymbol{u}$ and discharge current $\boldsymbol{I}$ direction.

Energy input to the flow $\mathbf{J}\cdot\mathbf{E}$ and heating of heavy particles in a gas brake a flow in the region near shock wave and after that promote the shock wave weakening [6]. The ponderomotive force $\mathbf{J} \times \mathbf{B}$ appears when external magnetic field is switched on additionally to the discharge in orthogonal to the discharge current direction. At determining current direction, this force acts on the flow in the direction, which is opposite to a propagation velocity of the shock wave that decreases the wave intensity. The selection of a ratio between plasma, heating, and magnetohydrodynamic actions at common influence of them on a shock wave allows decreasing efficiently destruction action of it on the environment up to full weakening of the shock wave.

For compare of degree of action on shock wave, the comparison of propagation velocity of shock wave before action region and after it was chosen as the main criteria. For this purpose, the special piezo sensors were built in channel wall, two sensors before action zone and two after it. The distance between sensors is 6 cm. Additionally, a change of shock wave form and intensity of it by means of Schlieren method and measurement of dynamic pressure by front piezo sensor is obtained. The piezo sensors positions are shown in Fig. 2.

T. Lapushkina (✉) • A. Erofeev • S. Poniaev
Ioffe Institute, 26 Polytekhnicheskaya, St. Petersburg 194021, Russian Federation
e-mail: tanyusha@mail.ioffe.ru

G. Ben-Dor et al. (eds.), *30th International Symposium on Shock Waves 1*, DOI 10.1007/978-3-319-46213-4_33

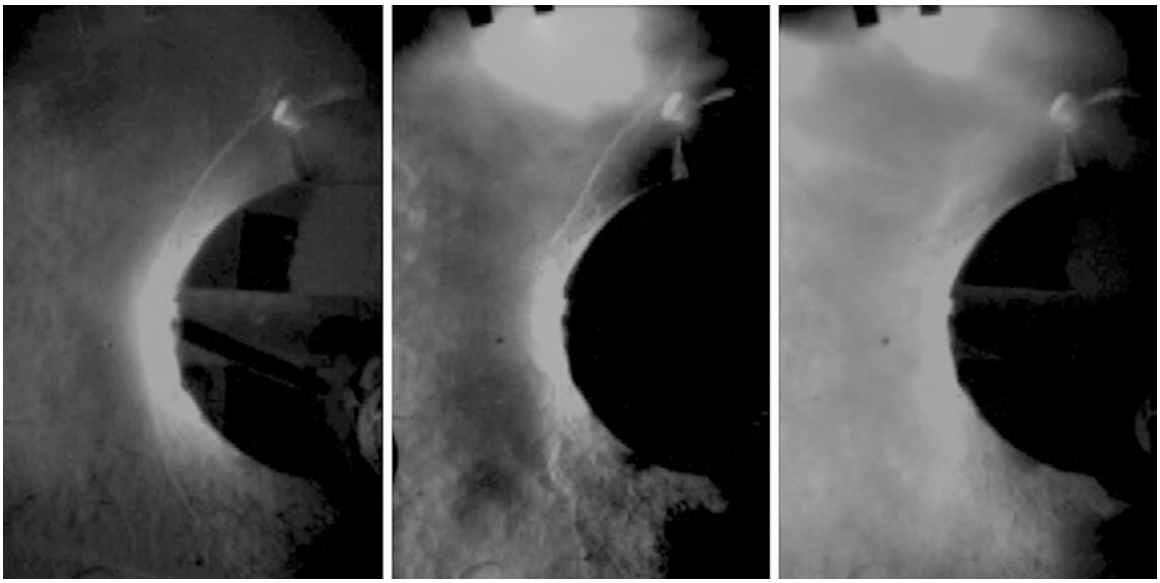

Fig. 1 The bow shock wave at a flow around the body by nonequilibrium plasma: (**a**) $T_e/T_h = 2.9$ regular bow shock wave; (**b**) $T_e/T_h = 5.1$ unstable bow shock wave; (**c**) $T_e/T_h = 5.3$ destruct bow shock wave

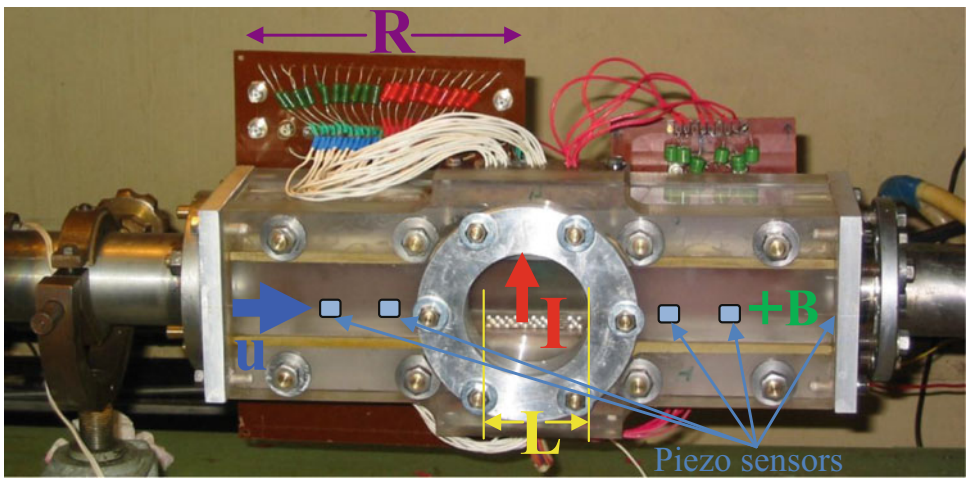

Fig. 2 Photo of the direct channel with gas discharge zone

Results

In the work, the strong shock wave $M = 8$ in zenon is formed in cylindrical channel of the shock tube with a diameter of 5 cm cross section which connects with direct working channel of square cross section. The round cross section of shock tube is inscribed into square section of working channel where the process of interaction of the shock wave with the region of electrical and magnetic fields applying takes place. Incomplete connection of both channels with each other is followed by the formation in working channel of complete shock wave configuration which is shown in Fig. 3. The primary shock wave includes a few shocks and becomes three dimensional from two dimensional with formation of Mach stems. It is followed by zone of changing density that appeared due to interaction of team of surge waves which formed in square channel corners. Figure 3 demonstrates Schlieren pictures of the flow in working channel in the moment when shock wave passes through the middle of control zone. For evidence two pictures are shown with different adjustment of Schlieren system which is dissimilar from visualized knife position. In the top picture, the knife covers left half of entry-lighting slit image; the bottom picture corresponds to covering of right half of slit image. As a result, the gradients of gas density

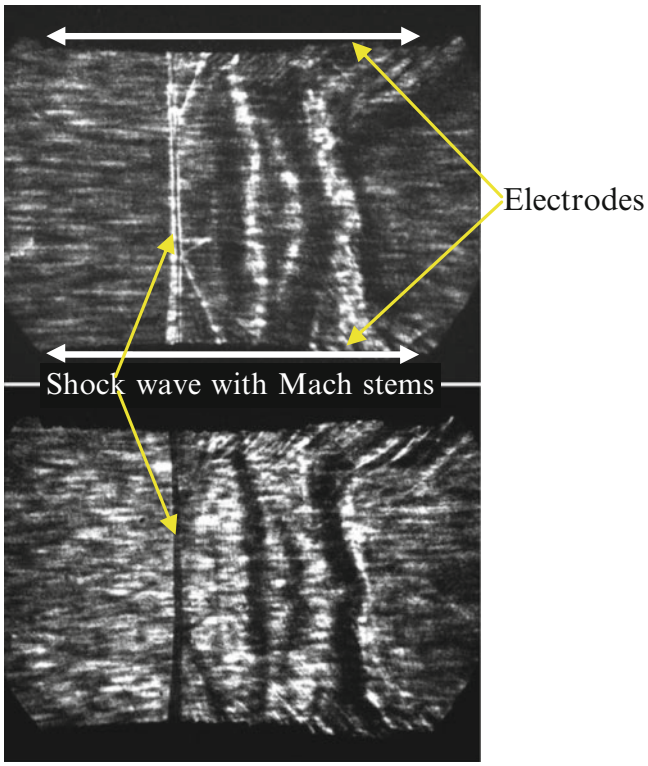

Fig. 3 Schlieren pictures of shock wave configuration in the middle of control zone

increasing or decreasing are described on the pictures by opposite colors. One can see that shock wave structure is complete and includes both regions of violent density increasing (white regions in the top picture and black in the bottom one) and decreasing of it (duck line between two increasing gradients in shock wave).

Shock wave configuration changes in the process of passing of it through observation zone that demonstrates Fig. 4 where Schlieren pictures of flow in different moments of time in the absence of external fields are shown. One can see in this process oblique shocks (Mach stems) appear and grow. They reflect from the shock wave (this process is well shown on the fourth and seventh pictures) that is followed by reflected shock formation. On the ninth and tenth pictures, one can see the reflection of oblique shock from each other. The structure which is formed behind the shock wave is weekly changed in the process of flow through control zone. The time of shock wave passing through control zone is 60 mks.

Action zone in the channel with pin electrodes is shown in Fig. 3 by horizontal arrows (in Fig. 2 width of this zone L is shown). If to apply external voltage to the pin electrodes when the shock wave and ionized behind it gas passes between the electrodes, current short circuiting occurred. The current pulse duration was on the order of 500 mks. Depending on the applied voltage, the current increased from 400 to 1600 A. Oscilloscope traces of the flowing currents are shown in Fig. 5. Figure 5a demonstrates the full discharge current through all pin electrodes. It is interesting that discharge current starts in the moment when shock wave passes at the end of the action zone, although we expected discharge current short circuiting in the moment when shock wave as ionized media enters the region of first pin electrodes at the beginning of the action zone. The voltage applied to the interelectrode spacing V_{pl} is shown in the same figure. Discharge current through the first pair of pin electrodes I_{R1} in the beginning of action zone and the last pair I_{R2} in the end of it in comparison with full current I_{all} for applying voltage $V_{pl} = 140$ V is shown in Fig. 5b. One can see that delay between I_{R1} and I_{R2} is about 60 mks that corresponds to the time of shock wave passing through all action zones in spite of current starting later than shock wave passing.

In the experiment, Schlieren pictures of flow without discharge and with discharge were obtained (Fig. 6). Figure 6a shows four frames of the Schlieren pictures of shock wave passage through the region studied without discharge. The shock wave and a complicated configuration of gasdynamic inhomogeneities after it are well seen.

Figure 6b–e shows Schlieren pictures of the shock wave passage through discharge at different discharge currents. In this figure, the time frame of exposure is 200 ns, and the period between frames is 15 microseconds. The maximum discharge current $I_{\max}$ during shock wave propagation is shown above frames. It can be seen that in the case with maximum current $I_{\max} = 500$ A, the gas discharge channel with an enhance luminosity appears at the Schlieren pictures in the region behind the shock wave. This constricted discharge channel is the beginning of diffuse gas discharge in the whole action zone. As current increases, the intensity of the luminosity of the initial gas discharge channel becomes higher. This initial channel moves after the shock wave with the velocity somewhat lower than the velocity of shock wave propagation. Shock wave velocity is 1.3 mm/mks and initial gas discharge channel velocity is 1.0 mm/mks. During passage in the action zone, the distance between the shock wave and gas discharge channel increases. After the shock wave leaves the discharge region, the initial channel disappears; though the gas discharge current continues to flow between the electrodes and its magnitude remains unchanged during 500 mks (Fig. 5), the discharge remains diffuse as in the region after the initial gas discharge channel. This discharge channel is very thin, and note that a turbulence region is observed at the axis of the working chamber in the region of

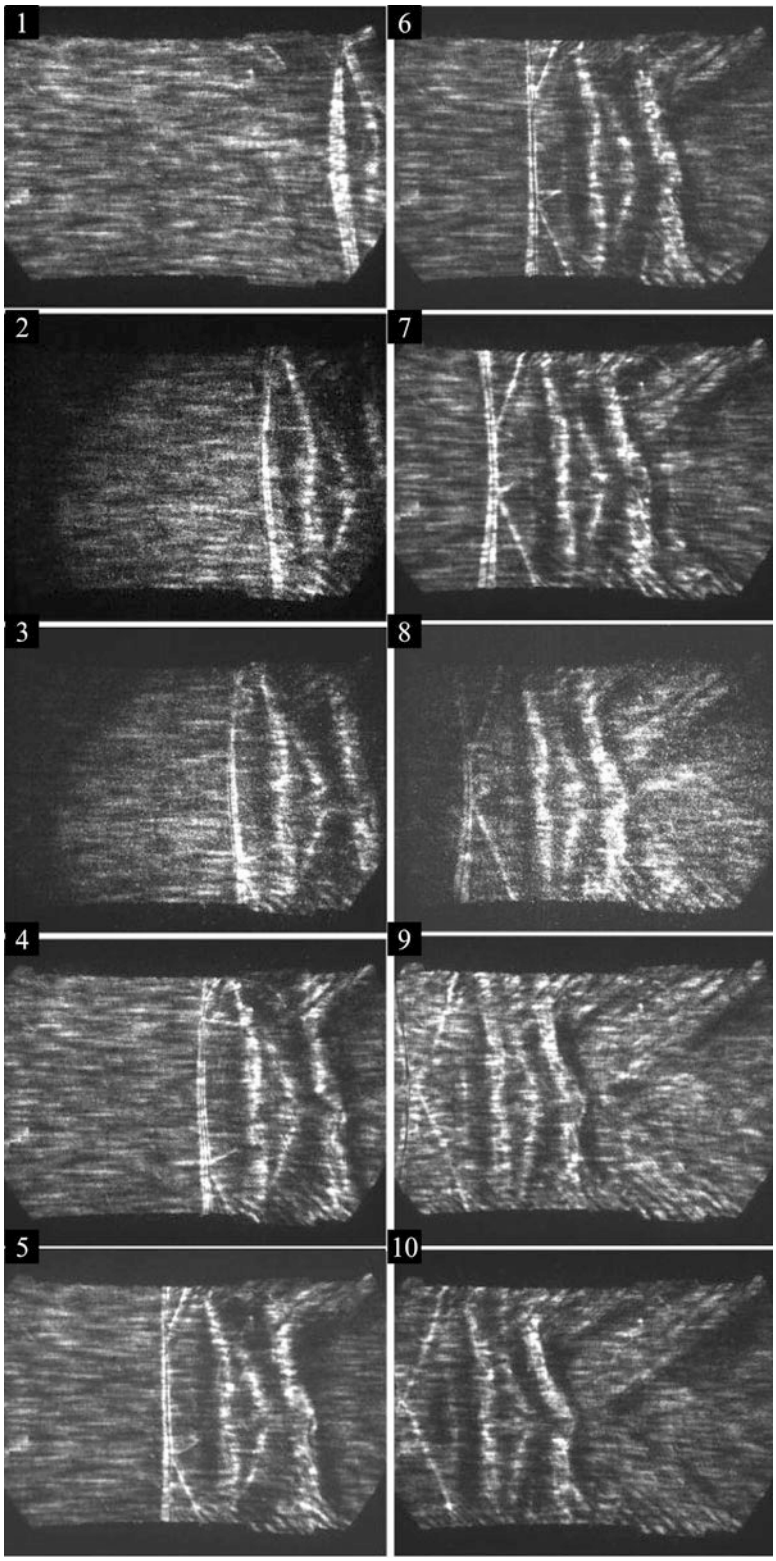

Fig. 4 Schlieren pictures of shock wave propagation through the control zone

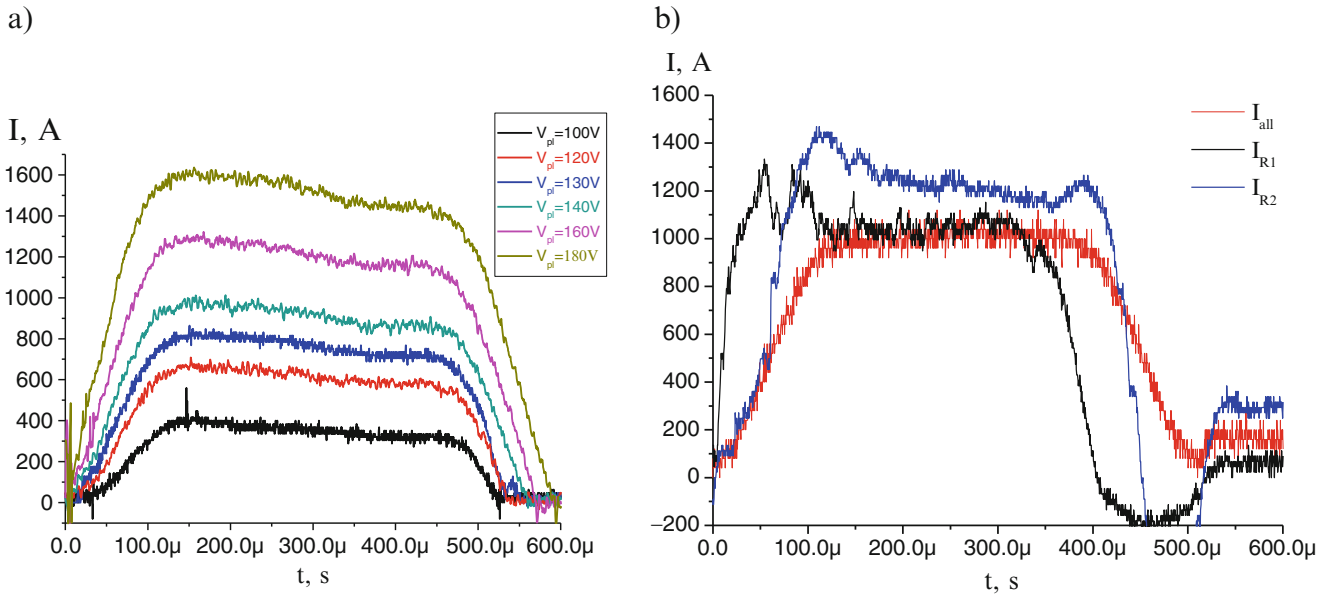

Fig. 5 Oscilloscope traces of gas discharge currents used in experiments

the gas discharge channel. As the current grows, the turbulence of this region increases, which is seen in Fig. 6c–e obtained for different currents.

Conclusions

The investigations have led to the following conclusions:

At experiment arrangement when the gas discharge is switch on by ionized media propagation, the current connection takes place not through shock wave but through thin initial gas discharge channel which appears behind the shock wave and follows it. Discharge current starts in the moment when the shock wave leaves the action zone.

Schlieren pictures and the sensors of static pressure show that the shock wave velocity does not change as it passes through the discharge region and is independent of the flowing current. The initial gas discharge channel velocity is less than shock wave velocity and remains the same with increasing discharge current in spite of increasing of luminosity intensity in it.

The sensor of dynamic pressure indicates that the dynamic pressure does not change as the current grows.

The external magnetic field switching on does not change the intensity and velocity of shock wave but influents on velocity of initial discharge.

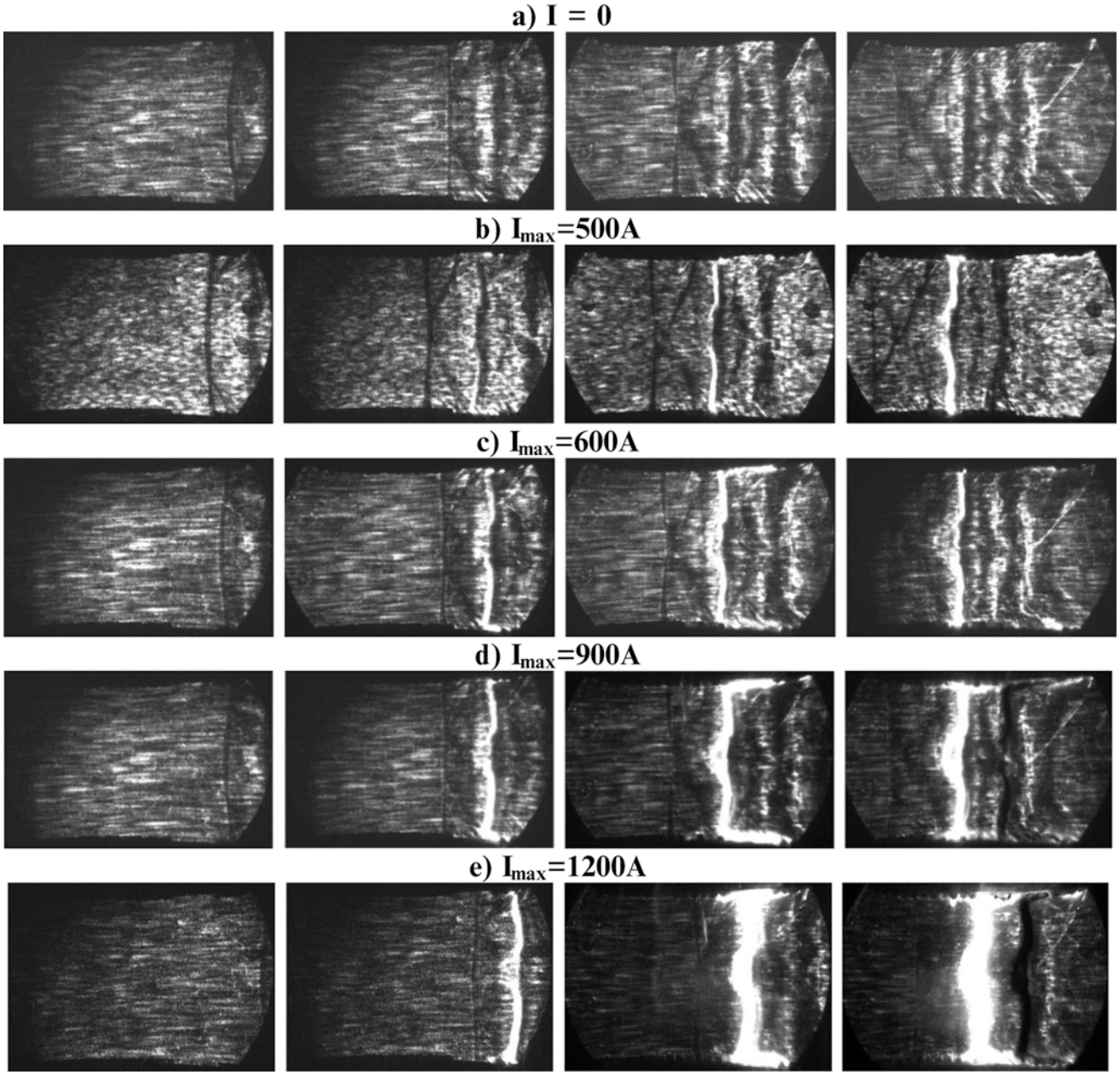

Fig. 6 Schlieren pictures of shock wave passage through the action region at different gas discharge currents. (**a**) $I = 0$; (**b**) $I_{max} = 500$ A; (**c**) $I_{max} = 600$ A; (**d**) $I_{max} = 900$ A; (**e**) $I_{max} = 1200$ A

Acknowledgment This work is supported by grant RFBR #15-01-04635a.

References

1. Jin, J., Znamenskaya, I.A., Sysoev, N.N.: Two regimes of pulsed volume discharge action upon a shock wave. Tech. Phys. Lett. **39**(5), 418–420 (2013)
2. Starikovskiy, A., Post, M., Tkach, N., Miles, R.: Dielectric barrier discharge control and thrust enhancement by diode surface. AIAA Paper-2014-0144, (2014)
3. Narayanaswamy, V., Clemens, N.T., Raja, L.L.: Investigation of a pulsed-plasma jet for shock/boundary layer control. AIAA 2010-1089, (2010)
4. Lapushkina, T., Erofeev, A., Poniaev, S., Bobashev, S.: Investigation of nonequilibrium gas discharge plasma supersonic flow around body. AIAA-2008-1383, (2008)
5. Lapushkina, T.A., Erofeev, A.V., Ponyaev, S.A.: Supersonic flow about a body exposed to electric and magnetic fields. Tech. Phys. **56** (5), 616–622 (2011)
6. Abramovich, N.: Applied Gas Dynamics. Nauka, Moscow (1969) (in Russian)

Numerical Research of Supersonic Mixing in Conditions of Localized Pulse-Periodic Energy Supply Upstream of Tandem Shock and Expansion Waves

E. Pimonov and A. Zheltovodov

Introduction

As is generally known, supersonic mixing enhancing imposes a great challenge for development of high-performance scramjet engines. For a long time, the possibility of using different conventional active and passive methods for enhancing the supersonic mixing by generation of instability and coherent vortex structures in the mixing layers was actively studied in application to scramjet [1]. One of passive methods, the introduction of oblique shock waves into the flowfield, attracts attention of researchers up to day. Because such shock waves are inherent flow structures in the combustor of scramjet, their utilization to promote supersonic mixing is considered as preferable and expected to be economic and effective approach [2]. At the same time, a localized pulse-periodic energy supply in supersonic flows upstream of shock waves, which in practice could be realized by means of optical, electric, or microwave discharges, can be considered as a more promising approach for the supersonic mixing control [3]. The arising Richtmyer–Meshkov (R–M) instability at such conditions can favor generation of intensive vortex structures in the shear layers during interaction of localized regions of energy supply with oblique shocks.

Therefore, a possibility of using a localized pulse-periodic energy supply for the supersonic mixing control in conditions of planar parallel jets interaction with a tandem oblique shock wave (OSW) and expansion waves (EW), generated by compression/expansion ramp (CER) and expansion/compression (ECR) ramp configurations, is considered in this paper on a basis of parametric numerical computations.

E. Pimonov (✉) • A. Zheltovodov
Khristianovich Institute of Theoretical and Applied Mechanics SB RAS, Institutskaya St. 4/1, Novosibirsk 630090, Russia
e-mail: pimonovevgeny@gmail.com

Methodology

The computations were performed within the framework of 2-D unsteady Euler equations for an ideal perfect gas. The equations were solved using the Godunov-type finite volume scheme of the third order of accuracy in space. Time integration was carried out using the explicit third-order TVD Runge–Kutta method. The used numerical algorithm and boundary conditions are described in details in the work [3]. The applicability of such approach for solving similar problems with the localized energy sources in quiescent air and in supersonic flows with the normal shock waves was validated before [4, 5].

Results

Considered calculations were performed for planar isobaric co-flowing supersonic ($M_j = 1.05$) and subsonic ($M_j = 0.7$) jets of a light gas ($\rho_j/\rho_\infty = 0.5$) propagating through tandem OSW/EW or EW/OSW systems generated, respectively, by 20-deg. CER or ECR configurations in incident flow with Mach number $M_\infty = 2.0$. The incident flow stagnation pressure and temperature values were, respectively, $p_0 = 0.25$ MPa and $T_0 = 288$ K. The jet's initial thickness was set equal to $h_j = 1$ cm, and its axis was located at ordinate $y_{j0} = 10.5$ cm above a surface, as shown in Fig. 1, where the calculated instantaneous density gradient flowfields are demonstrated for the flow around CER configuration at the time moments t indicated in the figures. We used pulse-periodic energy source with an elliptic section (horizontal and vertical semiaxes, respectively, $\Delta x_0 = 0.5$ cm and $\Delta y_0 = 0.25$ cm) at different locations of its center (x_0, y_0) relatively to the jet axis, varying frequency $f = 2$–20 kHz and the energy supplied by a pulse $E = 0.003$–0.3 J with the pulse duration $\tau = 10$ ns. The calculation domain is taken as $L_x = 76$ cm and $L_y = 35$ cm,

G. Ben-Dor et al. (eds.), *30th International Symposium on Shock Waves 1*, DOI 10.1007/978-3-319-46213-4_34

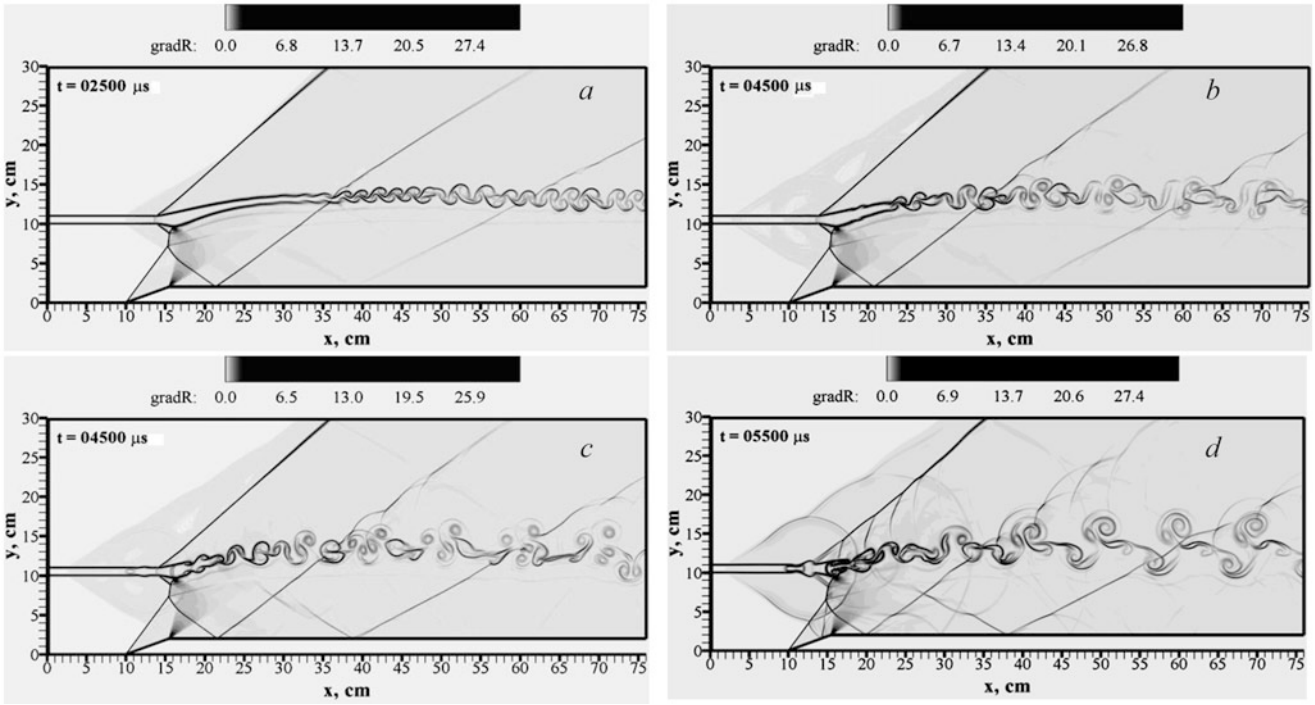

Fig. 1 Influence of supplied energy rate E for energy source with $f = 5$ kHz located at the axis ($x_0 = 3$ cm, $y_0 = 10.5$ cm) of the supersonic jet on its development in the vicinity of CER: (**a**) initial flowfield without energy supply ($E = 0$); (**b**) with energy source $E = 0.003$ J; (**c**) $E = 0.03$ J; (**d**) $E = 0.3$ J

and the grid resolution is set as $N_x \times N_y = 2400 \times 600$ after performing a grid-independence variation.

In accordance with Fig. 1, substantial intensification of the mixing of co-flowing supersonic jet ($M_j = 1.05$) with ambient air flow can be stimulated by a localized pulse-periodic energy sources with $f = 5$ kHz, located on the jet axis upstream of initial OSW. The density discontinuities, initiated by such energy source, generate the large-scale coherent vortex structures downstream of the shock wave due to development of Richtmyer–Meshkov (R–M) instability (Fig. 1b–d). As seen, arising the vortexes significantly enhances the jet mixing as compared with initial situation without energy supply (Fig. 1a). Increase of the source energy rate from $E = 0.003$ J up to $E = 0.3$ J promotes significant growth of the vortexes scales as well as the vorticity level and additional mixing enhancing, as a result.

Influence of the energy source frequency and location relatively to the supersonic jet axis is illustrated by Figs. 2 and 3. In accordance with Fig. 2b–d, increase of the energy source frequency causes formation of the jet breakdown (or "separation") zone with arising separated oblique shock wave in its apex. Such zone can be used as a flame holder to stabilize the supersonic combustion. However, with increasing the source frequency, the rising breakdown zone stimulates appearing the detached shock wave from the compression ramp vertex that points to the oncoming regime of chocking the supersonic flow area between the jet and the surface (Fig. 2c, d).

The remarkable fact is that, in the case of the energy source arrangement below the jet (Fig. 3a–c) or above it (Fig. 3d–f), shock waves that are close to spherical and propagate from the source generate initial disturbances in the jet, which are sufficient to form the same large-scale vortex structures behind the shock that enhance the mixing process.

Influence of deposited energy E and frequency f of the energy source located on the subsonic ($M_c = 0.7$) jet axis is illustrated by Figs. 4 and 5. The grid resolution was set as $N_x \times N_y = 2400 \times 600$ in the calculation domain with $L_x = 105$ cm and $L_y = 30$ cm.

In a case without energy supply, the high-pressure region that propagates upstream through the subsonic jet abruptly increases (Fig. 4a) compared to the case of the supersonic jet (see Fig. 1a). The detachment of the shock from the vertex of the compression angle points to the oncoming regime of blockage of the supersonic flow below the jet. The pulsating source of energy, placed at the axis of the considered jet ($x_0 = 11$ cm, $y_0 = 10.5$ cm), contributes to the suppression of the extending upstream subsonic region and initiates large-scale vortex structures behind the front of the disturbed

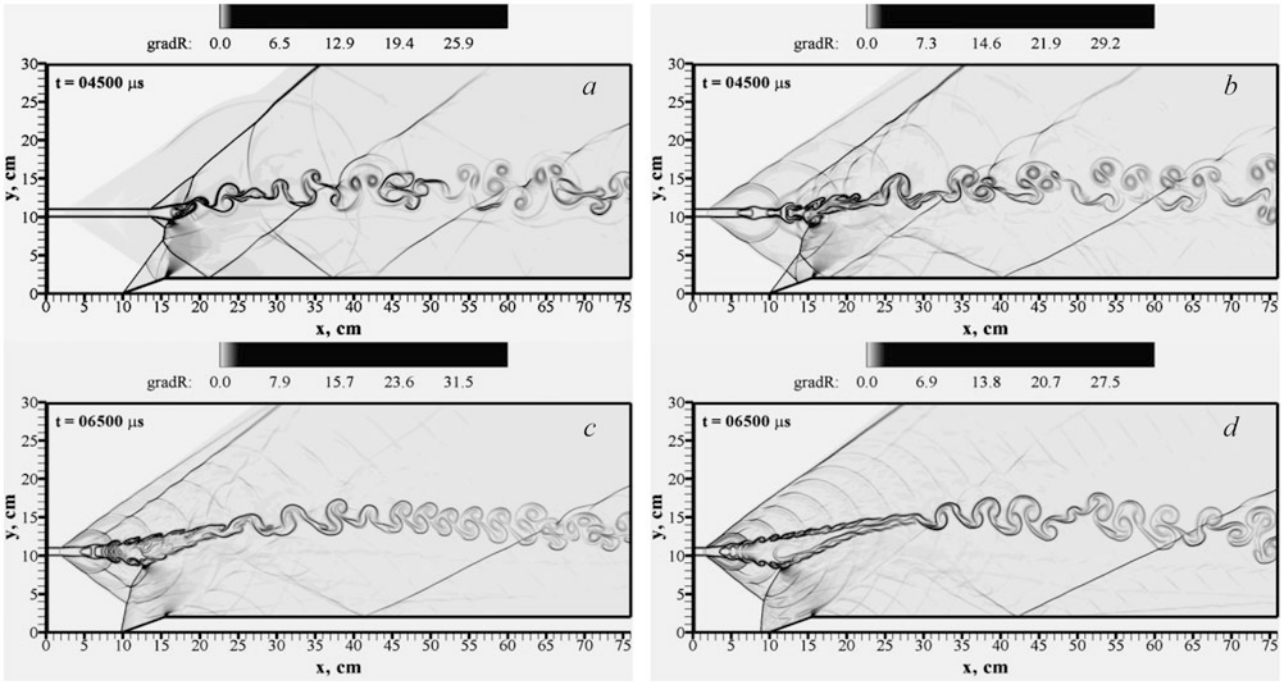

Fig. 2 Influence of energy supply frequency f for energy source with $E = 0.3$ J located at the axis ($x_0 = 3$ cm, $y_0 = 10.5$ cm) of the supersonic jet on its development in the vicinity of CER: (**a**) $f = 2$ kHz, (**b**) $f = 10$ kHz, (**c**) $f = 15$ kHz, (**d**) $f = 20$ kHz

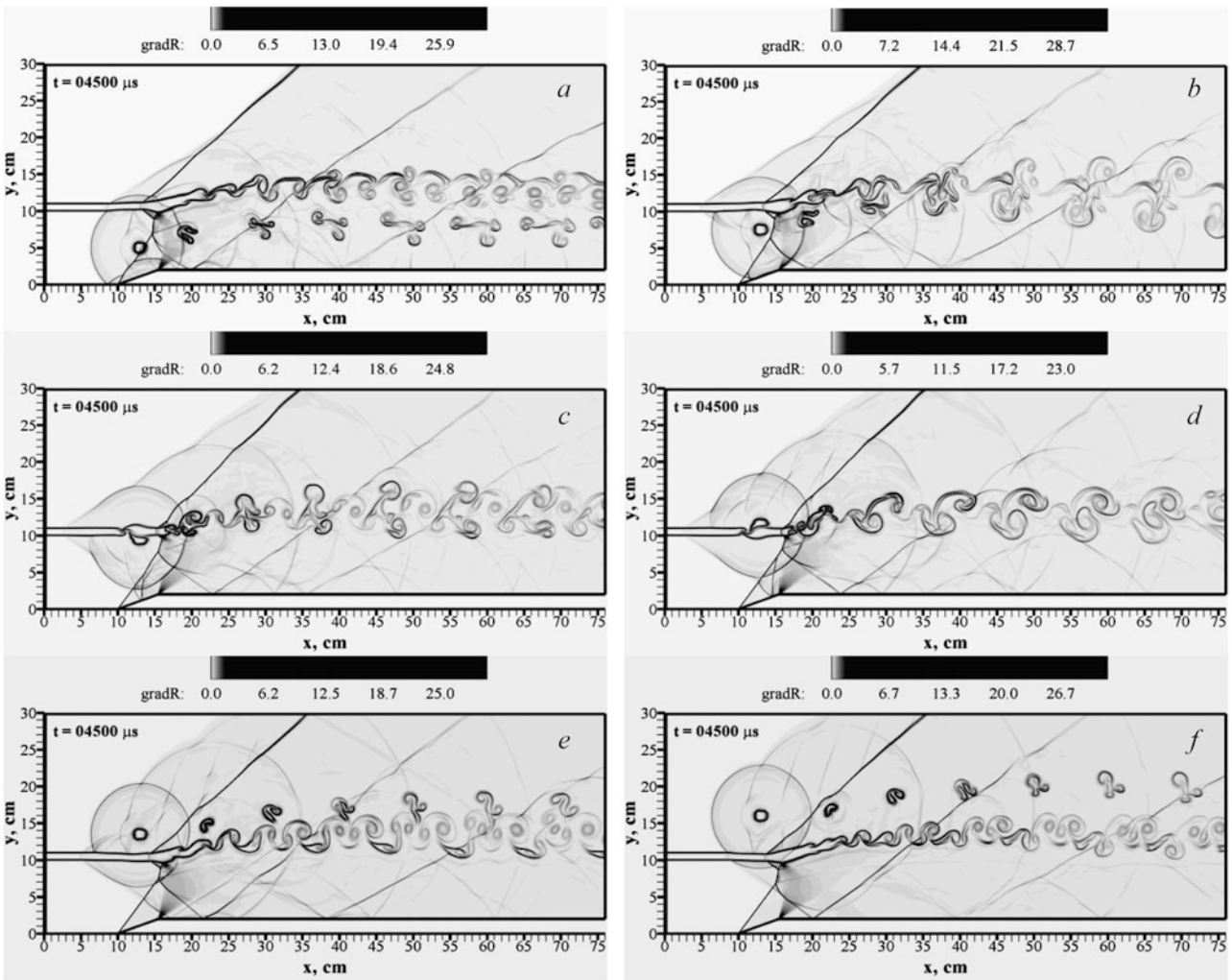

Fig. 3 Influence of energy source vertical location y_0 on development of the supersonic jet in the vicinity of CER at $E = 0.3$ J, $f = 5$ kHz, $x_0 = 3$ cm: (**a**) $y_0 = 5$ cm, (**b**) $y_0 = 7.5$ cm, (**c**) $y_0 = 9.5$ cm, (**d**) $y_0 = 11.5$ cm, (**e**) $y_0 = 13.5$ cm, (**f**) $y_0 = 16$ cm

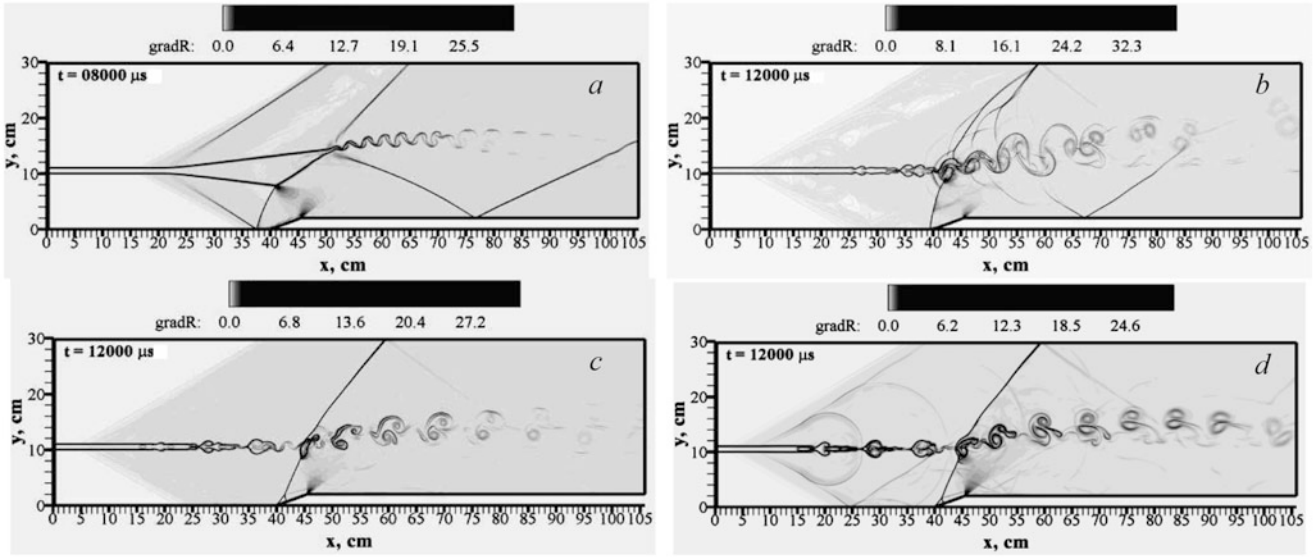

Fig. 4 Influence of deposited energy rate E of energy source with $f = 5$ kHz located at the axis ($x_0 = 11$ cm, $y_0 = 10.5$ cm) of the subsonic jet on its development in the vicinity of CER: (**a**) initial flowfield without energy source ($E = 0$), (**b**) with energy source $E = 0.003$ J, (**c**) $E = 0.03$ J, (**d**) $E = 0.3$ J

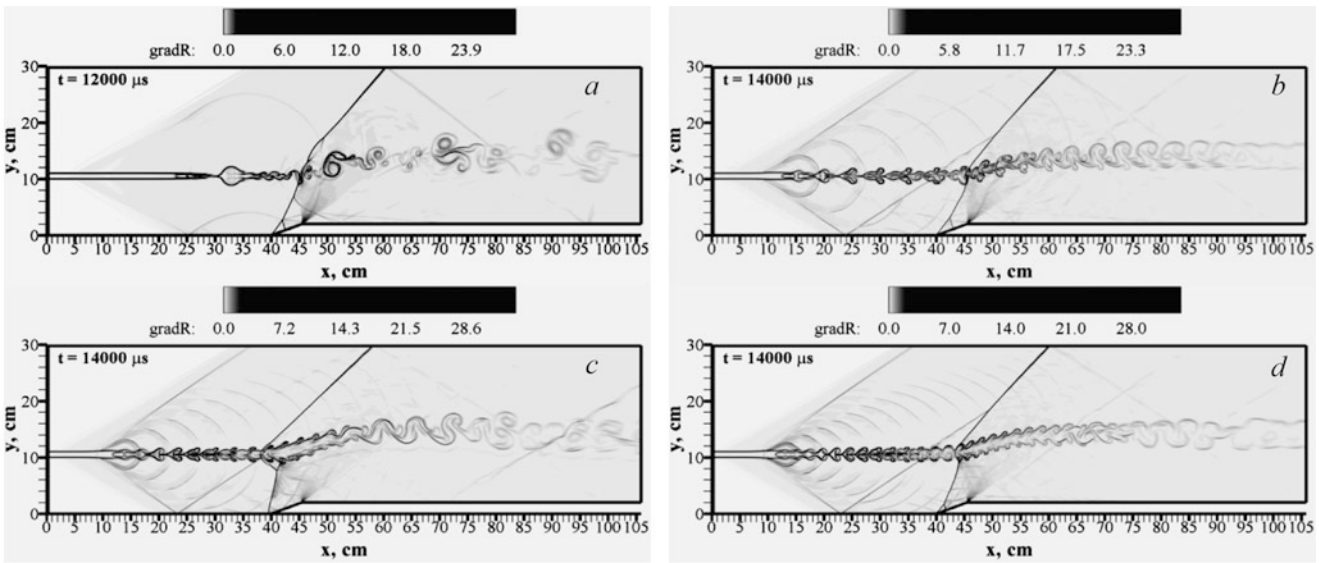

Fig. 5 Influence of energy source frequency f for energy source $E = 0.3$ J located at the axis ($x_0 = 11$ cm, $y_0 = 10.5$ cm) of the subsonic jet on its development in the vicinity of CER: (**a**) $f = 2$ kHz, (**b**) $f = 10$ kHz, (**c**) $f = 15$ kHz, (**d**) $f = 20$ kHz

shock that propagates from the compression ramp at different energy levels $E = 0.003$–0.3 J (Fig. 4b–d) and energy source frequencies $f = 2$–20 kHz (Fig. 5).

Similar effects of suppression of a high-pressure large-scale region upstream of the shock wave as well as the large-scale vortexes generation downstream it remain under conditions for an energy supply at different locations outside of such subsonic jet (Fig. 6).

To analyze preliminary influence of expansion waves (EW) on supersonic mixing downstream of subsequent oblique shock wave (OSW), additional computations were performed for the supersonic jet ($M_j = 1.05$) propagating around 20-deg. ECR configuration (or backward-facing step) (Fig. 7). As seen from Fig. 7b–d, the energy deposition also can lead to some mixing enhancement, as compared with initial situation without energy supply (Fig. 7a). The

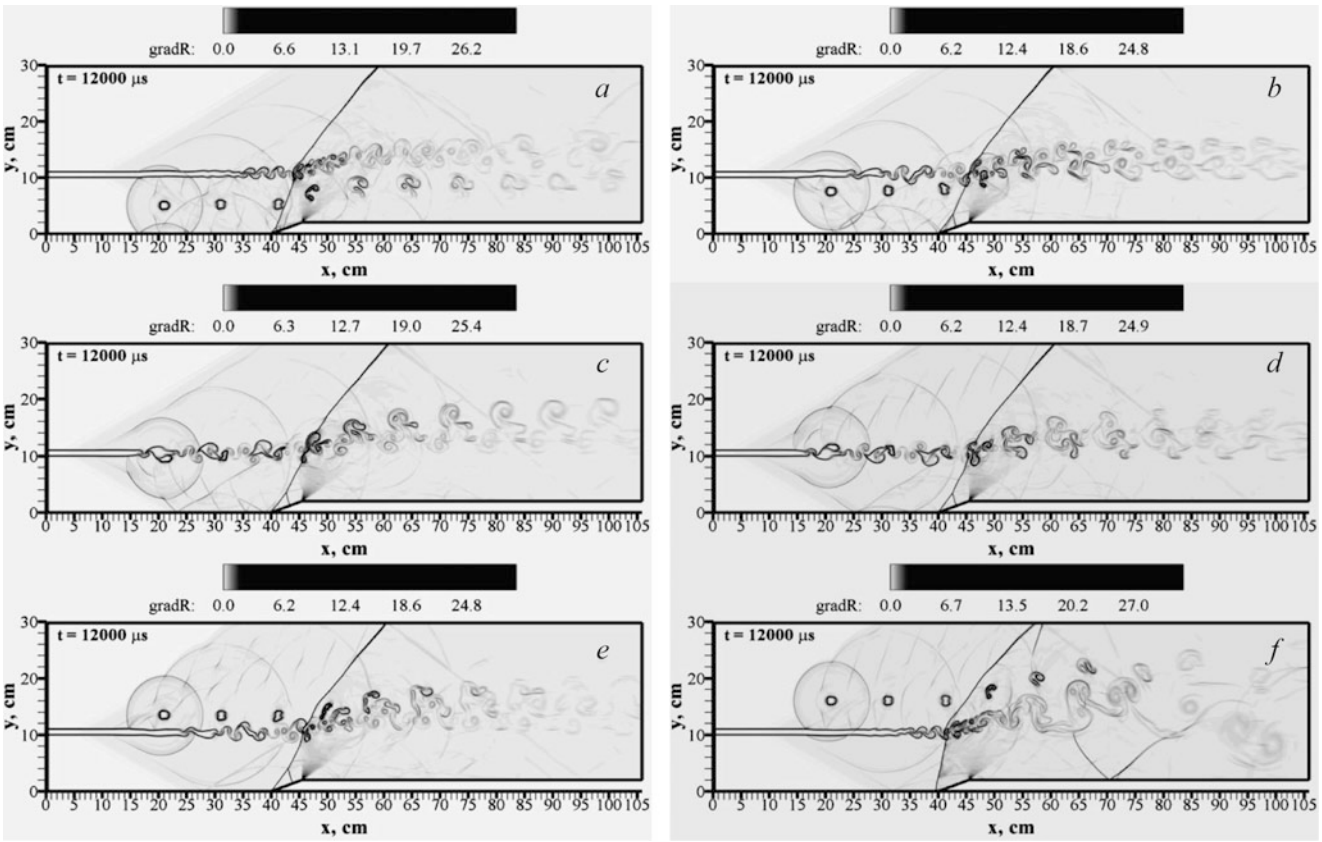

Fig. 6 Influence of energy source vertical location y_0 on development of the subsonic jet in the vicinity of CER at $E = 0.3$ J, $f = 5$ kHz, $x_0 = 11$ cm: (**a**) $y_0 = 5$ cm, (**b**) $y_0 = 7.5$ cm, (**c**) $y_0 = 9.5$ cm, (**d**) $y_0 = 11.5$ cm, (**e**) $y_0 = 13.5$ cm, (**f**) $y_0 = 16$ cm

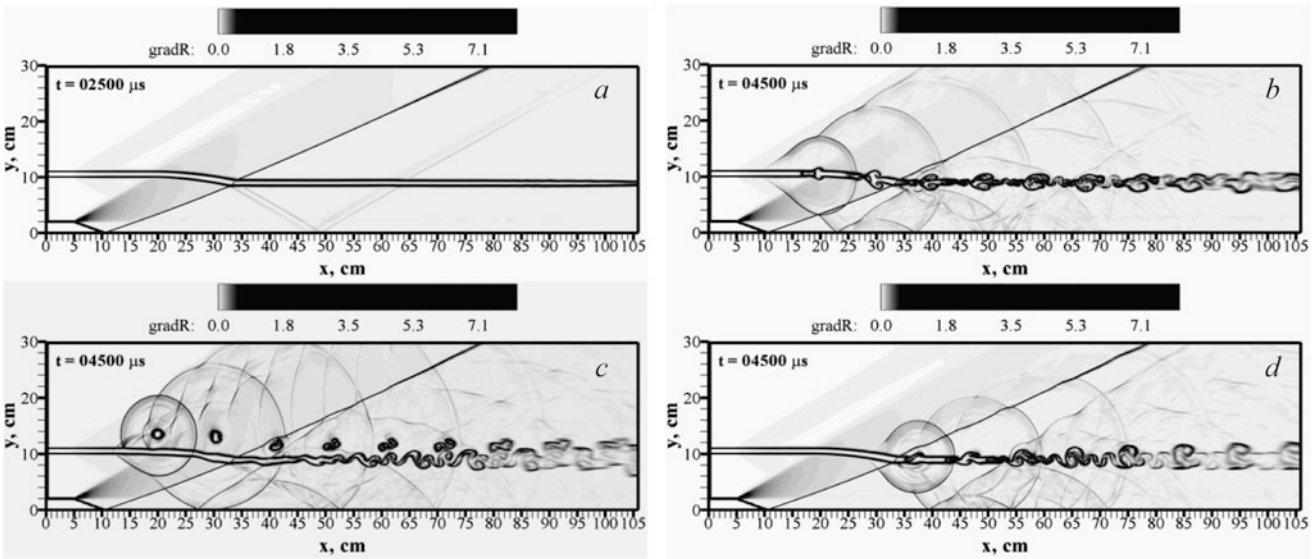

Fig. 7 Influence of energy source ($E = 0.3$ J, $f = 5$ kHz) location on development of the supersonic jet in the vicinity of ECR: (**a**) initial flowfield without energy supply ($E = 0$), (**b**) with energy source at $x_0 = 10$ cm, $y_0 = 10.5$ cm, (**c**) $x_0 = 10$ cm, $y_0 = 13.5$ cm, (**d**) $x_0 = 27$ cm, $y_0 = 10.5$ cm

appearing downstream distinct vortexes may be considered as a sign of such positive trend. However, due to preliminary influence of EW, the observed positive effect is not such pronounced as in conditions of flow around CER configuration, where OSW is located before EW (see, e.g., Figs. 1, 2, and 3).

Performed calculations for subsonic ($M_j = 0.7$) co-flowing jet in the vicinity of ECR configuration (not shown) demonstrated qualitatively similar peculiarities as for the supersonic jet conditions.

Conclusions

Performed parametric numerical investigations within the framework of 2-D unsteady Euler equations for an ideal perfect gas demonstrate the perspectives of significant intensification for the process of supersonic and subsonic jets mixing with an ambient cocurrent supersonic flow by using a localized pulse-periodic energy supply under conditions of their interaction with oblique shock waves. It was shown that the positive effect could be reached when the energy was supplied in front of the shock waves both inside the jets and in the external flow. Preliminary expansions of waves promote the weakening of the observed effect for mixing enhancing by pulse-periodic energy supply. Further experimental and computational investigations are important for quantitative predicting of the supersonic mixing enhancing level as well as the influence of three-dimensional and viscous effects under the considered conditions to define the mixing parameters and schemes of energy supply most suitable for practical purposes.

References

1. Seiner, J.M., Dash, S.M., Kenzakowski, D.C.: Historical survey on enhanced mixing in scramjet engines. J. Propul. Power **17**(6), 1273–1286 (2001)
2. Zhang, Y., Wang, B., Zhang, H., Xue, S.: Mixing enhancement of compressible planar mixing layer impinged by oblique shock waves. J. Propul. Power **31**(1), 156–169 (2015)
3. Zheltovodov, A.A., Pimonov, E.A.: Intensification of mixing of parallel compressible flows using a localized pulse-periodic energy supply. Tech. Phys. Lett. **13**(11), 1016–1018 (2013)
4. Zheltovodov, A.A., Pimonov, E.A.: Numerical simulation of an energy deposition zone in quiescent air and in a supersonic flow under the conditions of interaction with a normal shock. Tech. Phys. **58**(2), 170–184 (2013)
5. Schülein, E., Zheltovodov, A.A., Pimonov, E.A., Loginov, M.S.: Experimental and numerical modeling of the bow shock interaction with pulse-heated air bubbles. Int. J. Aerosp. Innov. **2**(3), 165–187 (2010)

Effect of Differential Sweep on a Three-Dimensional Sidewall-Type Intake at Mach 3.5

C. Manisankar and S.B. Verma

Introduction

For developing future hypersonic space transportation, air-breathing propulsion using scramjet engine is one of the key technologies. The inlet particularly is of great importance for the efficient operation of such propulsion system. The efficient design of intake greatly depends on the amount of mass flow captured (MFC) and the level of pressure recovery achieved. Most of the earlier research [1, 2] was focused on a two-dimensional air intake which utilizes vehicle nose-generated shock wave for pre-compression. Although such intakes provide better aerodynamic characters at higher operational Mach number regime, they induce severe performance penalties at low flight Mach numbers. It is primarily found to be caused due to the lack in mass handling capacity at off-design conditions of such two-dimensional-type intakes leading to unwanted phenomenon like buzzing and unstart of intake. Such disadvantages made researchers [3–5] to look into three-dimensional intakes as in Fig. 1 which provide stable operation in the entire Mach number regimes with the compromise in efficiency in terms of MFC and pressure recovery.

The three-dimensional intakes achieve pre-compression through an external shock train created by a wedge of minimum flow turning angle. Earlier studies [3–6] show a wedge angle of 6° was an optimal angle as it generates weaker shock wave-boundary layer interaction on the wedge surface. Another highlight in such three-dimensional intakes was the absence of bounding surface at the bottom of the protruding wedge which aids in relieving the adverse pressure behind the separation region, thereby effectively suppressing the bubble size. This creates an additional dimension for the supersonic flow field, hence gets its name three-dimensional intakes. All these phenomena help in avoiding unstart of intake with compromise in aerodynamic performance at all Mach number regimes. There were few attempts in the past [3, 4] to improve the aerodynamic performance of the three-dimensional intakes by having leading edge sweep as in Fig. 2. There are shortfalls in using such sweep as BS showed [3] an increase in MFC at the cost of reduction in pressure recovery wherein for FS pressure recovery increased at the cost of reduction in the MFC.

The focus of the present paper was to understand the effect of having a differential leading edge sweep and its impact on the aerodynamic performance in terms of improvement in both MFC and pressure recovery. The importance of having such study was to utilize the advantages of three-dimensional intakes in terms of stable operation at all flight operational speeds without any compromise in the aerodynamic performance of the vehicle (Figs. 3 and 4).

Experimental Setup and Procedure

Wind Tunnel Facility and Model Details

Tests were conducted in 0.457 m × 0.3 m blowdown tri-sonic wind tunnel at National Aerospace Laboratories (NAL). The sidewall intake model was mounted on a mounting block and aligned along the tunnel centerline in order to avoid effects of noise levels from turbulent boundary layer present on wind tunnel wall. The test Mach number was 3.5 ± 0.02, while the stagnation pressure and temperature were 95 psia ± 1 % and 298 K ± 0.4 %, respectively. This gives a unit Reynolds number of 38.0×10^6 m^{-1}. The wall temperature was approximately adiabatic. The model is 685 mm (l) × 48 mm (w) × 24 mm (h), with 130 mm contraction region which has converging section of 6° on both the sidewalls with a contraction ratio of 2.29 followed

C. Manisankar (✉) • S.B. Verma
CSIR-National Aerospace Laboratories, Experimental Aerodynamics Division, Bangalore 560017, India
e-mail: manisankar@nal.res.in

G. Ben-Dor et al. (eds.), *30th International Symposium on Shock Waves 1*, DOI 10.1007/978-3-319-46213-4_35

by 120 mm isolator, 100 mm diffuser, and 335 long mass flow measuring unit as shown in Fig. 1. The mass flow capture (MFC) ratio of intake was determined using the method suggested by Smart and Trexlar [1]. In order to study the effect of differential leading edge sweep, two sweep angles (30° and 45°) were varied as shown in Table 1.

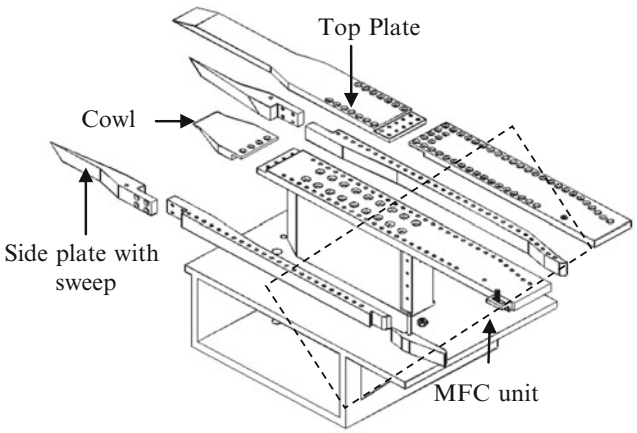

Fig. 1 Schematic of model assembly

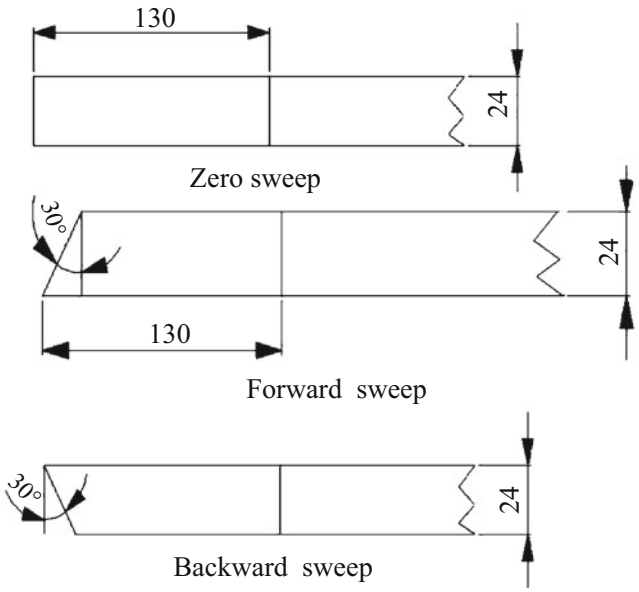

Fig. 2 Sketch of different sweep angles

Data Acquisition System and Analysis

For measurement of wall surface static pressures, 6 ESP scanners of 16 ports each and of ranges ±15 psid and, for total pressure measurement using the rake, ±100 psid were used. Static pressure of the test section and total pressure of the flow in the settling chamber were measured using ±10 psid transducer and 0–150 psia transducer, respectively. The pressure data was acquired through the data acquisition system (LABVIEW) of the tunnel and processed in the format required using the in-house developed software.

Results and Discussion

Streamwise Mean Pressure Distribution

Figures 5 and 6 show the streamwise pressure distribution for no-sweep case, along the sidewall and the top wall for the minimum cowl length configuration. Initially there was a slight drop in the pressure (up to 3.4×/h) along the sidewall which may be due to the pressure-relieving effect occurring at the bottom as shown in Fig. 4. The BS shows more drop in pressure relative to baseline (zero sweep) and FS, which ascertain the spillage effect at the bottom. By having the leading edge sweep, the shock is swept at the same angle as that of leading edge resulting in modification of junction of two crossing shocks as in Fig. 3 which in turn shift the impingement point location on the sidewalls. The pressure distribution further shows for differential sweep combinations the rise in pressure occurs at 4.4×/h which is downstream relative to baseline 3.9×/h confirms the swept nature of the shockwave. There was also a reduction in peak pressure (shock strength) by 3.35 % for BS relative to baseline, whereas for FS, it increases by 17.5 %. The above

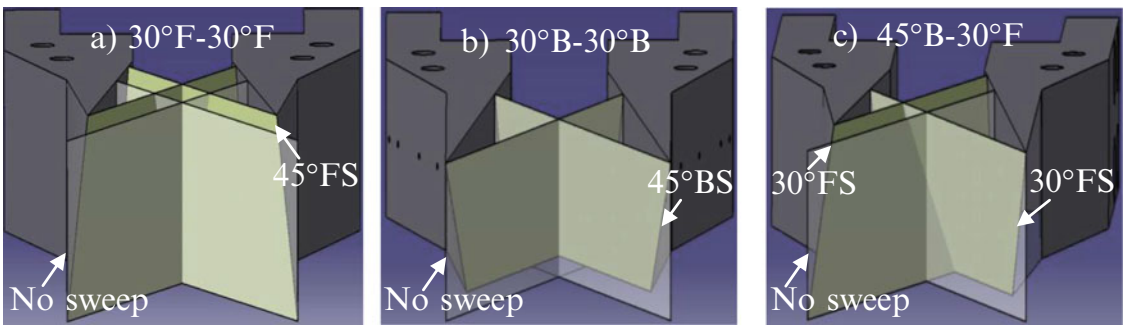

Fig. 3 Schematic of the shock pattern for differential sweep combinations

changes may be caused by spillage shock as in Fig. 4 which was formed in order to have mass balance as FS tries to capture more mass than the intake can handle. The top wall also shows the similar trend as in Fig. 6 where at 2.68×/h, there is sudden increase of pressure followed by constant pressure region up to 5.44×/h which indicates the shock was strong enough to form a separation bubble.

Table 1 Differential sweep combinations

Sweep number	Sweep combination
0	0°-0°
1	30°B-30°B
2	45°B-45°B
3	30°F-30°F
4	45°F-45°F
5	45°F-30°F
6	30°F-30°B
7	45°F-30°B
8	45°F-45°B
9	45°B-30°B
10	45°B-30°F

Where "B" refers to backward sweep (BS), "F" refers to forward sweep (FS)

Effect of Cowl Extension

Figure 7 shows a comparison of pressure distribution for two different cowl lengths (1.86 h, 0.42 h) for the baseline configuration. The pressure distribution significantly varies between the maximum cowl length and minimum cowl configuration; this may be because of the reduction in area of spillage on the bottom resulting into increase of back pressure which in turn raises the shock strength and angle. The MFC for different sweep combination was shown in Fig. 7 which shows for all the configuration minimum cowl helps to capture more mass which was contradictory to what was expected. This may be due to the rate at which mass spillage occurring ahead of cowl lip was more than the rate at which mass spillage was stopped by the extension of the cowl lip.

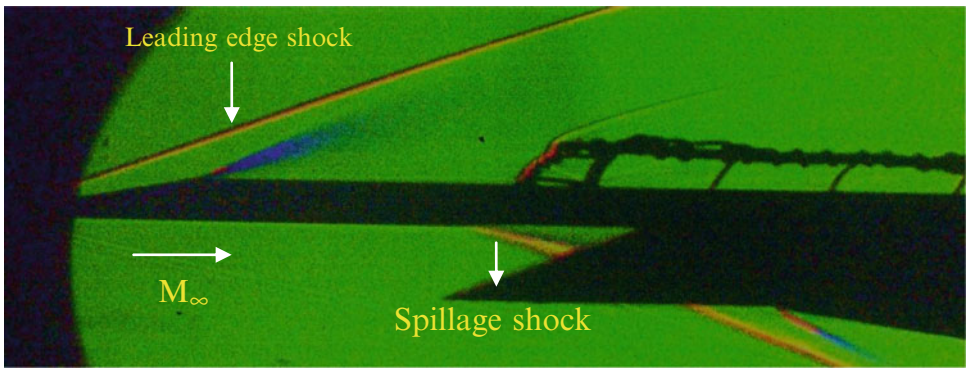

Fig. 4 Schlieren visualization for 30° forward sweep with maximum cowl length

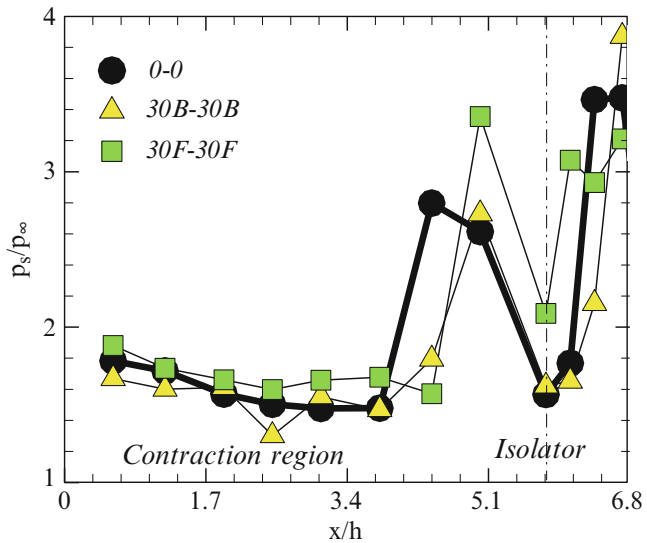

Fig. 5 Sidewall pressure distribution

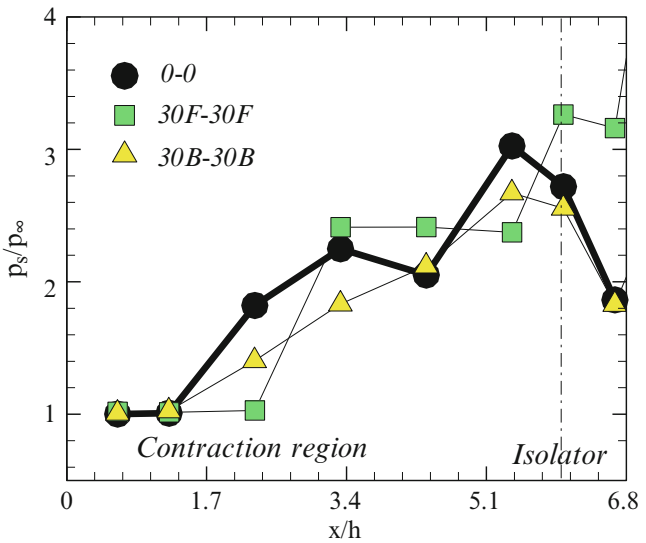

Fig. 6 Top wall pressure distribution

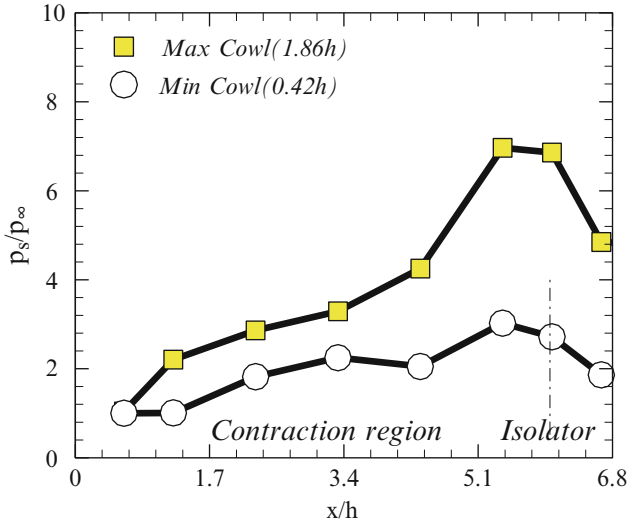

Fig. 7 Comparison of different cowl

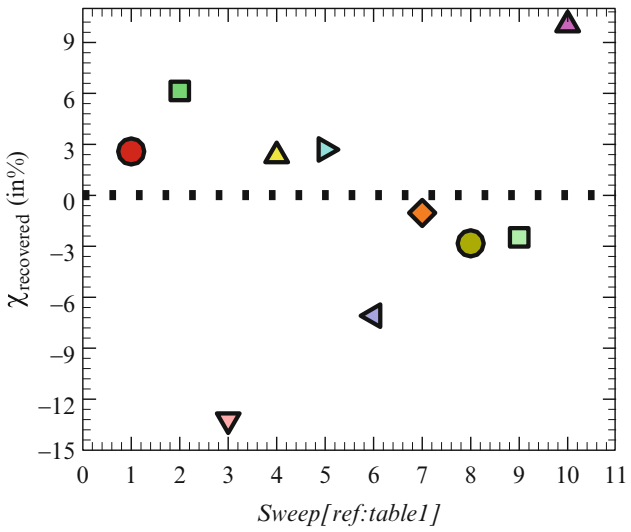

Fig. 9 Total pressure recovery ratio

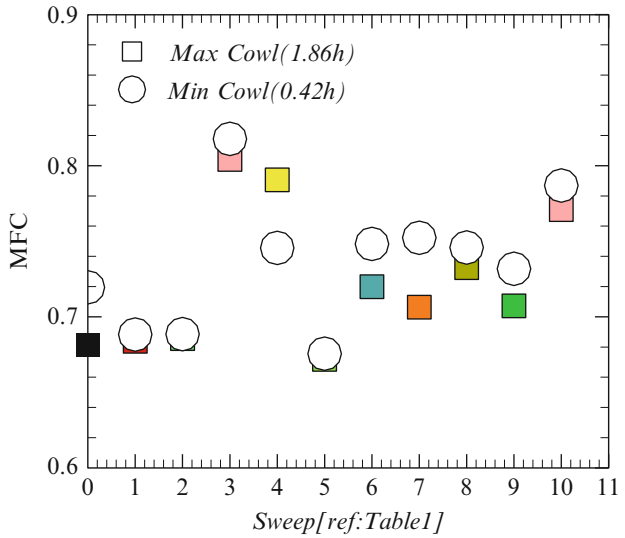

Fig. 8 MFC variation for sweep

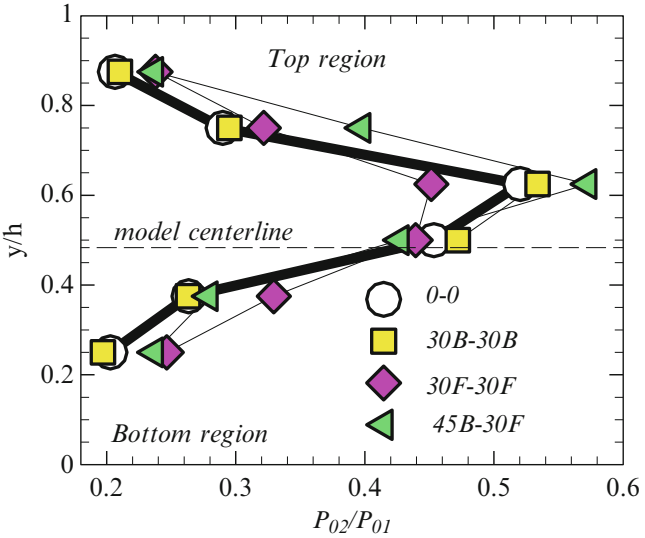

Fig. 10 Total pressure profile

Effect of Differential Sweep

It was known that by sweeping the leading edge backward, we can achieve larger operational Mach number regimes with a compromise to MFC. Figure 8 shows by sweeping the leading edge forward, the MFC was improved (for 30° and 45°, MFC increased by 14 % and 3 %) more than the no-sweep case, but there was a significant loss in total pressure recovery ratio as shown in Fig. 10. To identify optimal leading edge sweep configuration which provides better MFC and pressure recovery, different leading edge configurations were tested as shown in Fig. 8. Among the entire configuration tested, 45°B-30°F provides better MFC (8.3 % relative to no-sweep case) (Fig. 9).

Total Pressure Recovery for Maximum Cowl Length

Figure 9 shows the variation in total pressure recovery ratio (X) which was given by the ratio change in total pressure (difference in sweep to the no-sweep) to that of the no-sweep total pressure near the isolator exit. It can be seen that same sweep combination in backward direction for 30° gives better total pressure recovery ratio (2.58 %) than 30° forward case (−2.47 %). As the leading edge sweep angle was varied to 45° in both directions (backward and forward), there was a positive increase in pressure recovery ratio (6.2 % for backward and 2.34 % for forward sweep). The skew in shock plane brought by having differential sweep

combination has major effect in pressure recovery ratio as it reduces the total pressure recovery ratio to almost −13.2 % for 30F-30B case but peaks to 10 % in 45F-30B. The pressure recovery profile (P_{02}/P_{01}) as in Fig. 10 was obtained through a rake placed at the exit of isolator. There was an asymmetry in the profile which may be due to the presence of cowl lip shock which causes the bottom region to have more total pressure loss than the top. Among all, the profile 45°B-30°F shows better pressure recovery.

Conclusions

An experimental study was conducted to understand the effect of differential leading edge sweep on a three-dimensional sidewall-type intake configuration in a Mach 3.5 flow. Mass flow captured by the intake and total pressure recovery was obtained for all the sweep combinations. It was observed that there was an optimum differential sweep combination for which the pressure recovery was maximum.

Experimental flow visualization shows that beyond the mass handling capacity of the intake additional mass was spilled through the leading edge sweep generated swept shock wave thereby having a stable operational Mach number regime. By extending the cowl lip beyond certain distance, the MFC and the pressure recovery significantly get affected. Of all the combinations tested, 45°B-30°F gave optimal MFC and pressure recovery. Further investigations are required to find the optimum cowl lip extension for the differential sweep combination.

References

1. Trexlar, C.A.: Inlet performance of integrated Langley scramjet module. AIAAPaper No. 75–121, Sept-Oct 1975
2. Smart, M., Trexlar, C.A.: Mach 4 performance of fixed geometry hypersonic inlet with rectangular to elliptic shape transition. 41st Aerospace Science Meeting and Exhibit AIAA 2003-12
3. Holland, S.D.: Mach 10 Computational study of three dimensional scramjet flow field. NASA TM 4602, 1995
4. Kumar, A., Trexlar, C.A.: Numerical study of the effect of the reverse sweep on scramjet inlet performance. J. Propul. Power **8**(3), pp. 714–719 (1992)
5. Watanabe, Y., Murakami, A., Fujiwara, H.: Effect of sidewall configuration on the aerodynamic performance of the supersonic air-intake. AIAA 2002-3777
6. Ahmed, S., Merchant, L., Mathur, N.B.: Experimental Studies to improve the performance of sidewall compression inlet at Mach 3. In: Paper Presented at 17th International Symposium on Air breathing Engines, Munich, Germany, ISABE Paper 2005-1172

Experimental Study of Dynamic Characteristics of Oblique Shock Trains in Mach 5 Flow

C.P. Wang, X.A. Tian, and K.M. Cheng

Introduction

The oblique shock train (OST) flow diffusion phenomenon, which involves an interaction between the duct's peripheral boundary layer and central oblique-shock-wave field, usually appears in constant or nearly constant cross-sectional-area supersonic/hypersonic duct flows. The study of such a complex flow structure in a confined duct under a finite adverse pressure gradient has important implications for the design and operation of a variety of devices including hypersonic vehicle inlet/isolator [1, 2], supersonic wind tunnel diffusers [3], supersonic ejectors, and so on. To develop the design methods and control strategies of the flow devices, it is necessary to fully understand the mechanism of the OST. Different flow conditions will lead to different kinds of shock train structure: normal shock train occurs for lower incoming Mach numbers of about 1.2–2, whereas oblique shock train occurs for higher incoming Mach numbers. The aerodynamic performance of the fluid devices is well related to the features of the OST, which include the structure of the OST, the pressure recovery in the OST flow region, the dynamic characteristics of the flow separation region nearby the OST, and so on. In addition to complex flow structure, the OST inside the duct has an important feature of unsteady characteristics; even if the boundary conditions such as the pressures upstream and downstream of the OST region are held constant, the OST is still in "self-oscillation" state [4]. This self-excited oscillation may cause the structural fatigue, unstart of inlet/isolator, and instability of combustion. Therefore, the study of dynamic characteristics of the OST is important for aircraft structural design and aerodynamic performance evaluation.

C.P. Wang (✉) • X.A. Tian • K.M. Cheng
College of Aerospace Engineering, Nanjing University of Aeronautics and Astronautics, 29 Yudao Street, Nanjing 210016, China
e-mail: wangcp@nuaa.edu.cn

Although a large number of previous studies have been done on the dynamic characteristics of the OST in duct [5–13], but there are still many issues unresolved, and the rational understanding of OST phenomenon is not enough. Especially, the knowledge about the dynamic propagation process is the key issue for the development of hypersonic aircraft design and propulsion systems.

The current paper describes the results of an experimental study of the OST in a simple duct model that was mounted in a Mach 5 wind tunnel. Optical visualization of the flow in the duct was performed, and distributions of static pressure in typical longitudinal sections were obtained. Patterns of the OST in the duct were identified. The forward propagation process of the OST has been analyzed based on the above data. The purpose of this study is to deepen the understanding of the dynamic characteristics of the OST in the duct and provide a fundamental research for the engineering applications.

Experimental Facility

The current experiments were conducted in the hypersonic wind tunnel (NHW) of Nanjing University of Aeronautics and Astronautics. The ϕ0.5 m NHW is a conventional intermittent hypersonic blowdown facility and operates in a blowdown to vacuum mode with a Mach range of 4–8, which is composed of high-pressure air supply, heater, nozzle, test section, diffuser and vacuum ball, etc. (Figs. 1 and 2).

Figure 3 shows the schematic of the model configuration and layout details of the pressure measurement. The model consisted of a convergent portion with the length of 110.0 mm and an approximate constant-area duct with the length of 295.1 mm; the inlet entrance height is 54.6 mm, the throat height at the entrance of the duct is 27.5 mm, and the duct exit height is 35.3 mm; the compression angle of the convergent portion is 7.0°; the entire duct is in the micro-expansion state and the expansion angle is 1.5°; the constant

G. Ben-Dor et al. (eds.), *30th International Symposium on Shock Waves 1*, DOI 10.1007/978-3-319-46213-4_36

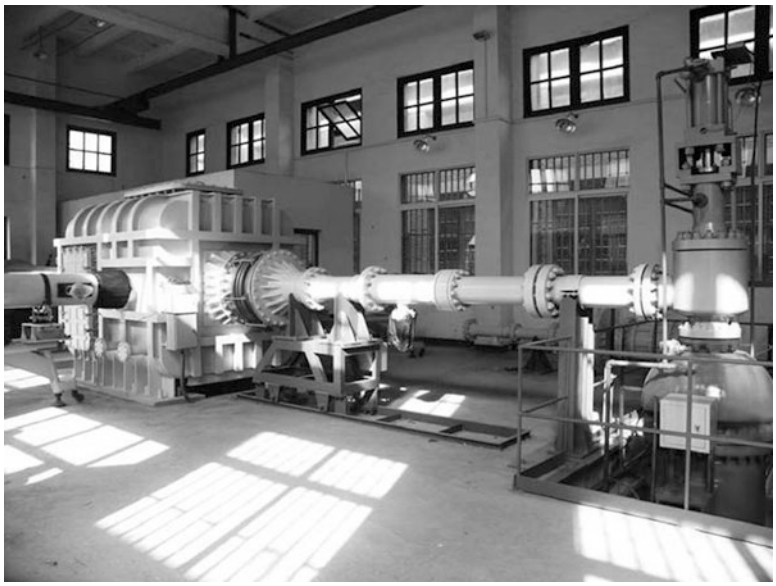

Fig. 1 Hypersonic wind tunnel of Nanjing University of Aeronautics and Astronautics

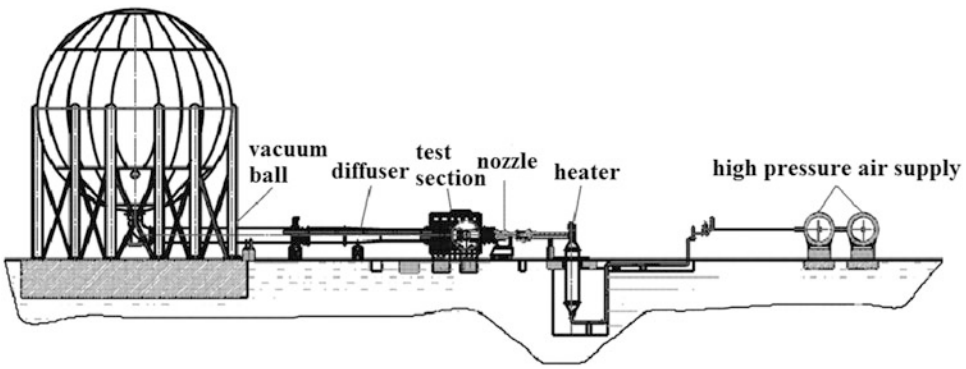

Fig. 2 Schematic of NHW

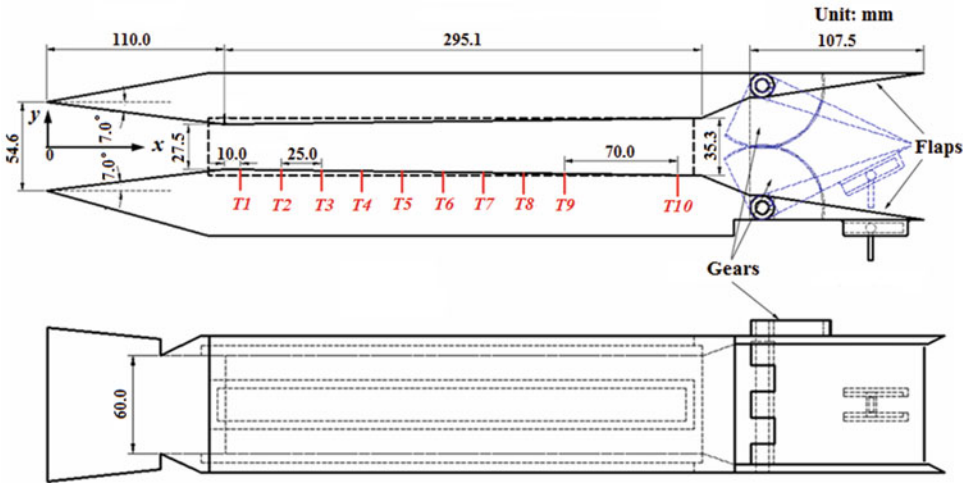

Fig. 3 Schematics of the experimental model

width of the model portion is 60.0 mm. In order to observe the flow structure, two optical glasses, which are 300 × 35.4 mm, are mounted on the two sides of the model (the dash line range in Fig. 3). The coordinate origin of the model is set at the entrance of the duct. Two ramps installed in the tail of the duct model can open and close to simulate the backpressure varying. In the experimental initial state, both the ramps are closed to 9.7°, wherein the ramp closed angle is set as the angle of inner surface between the horizontal planes. A row of seven fast-response pressure

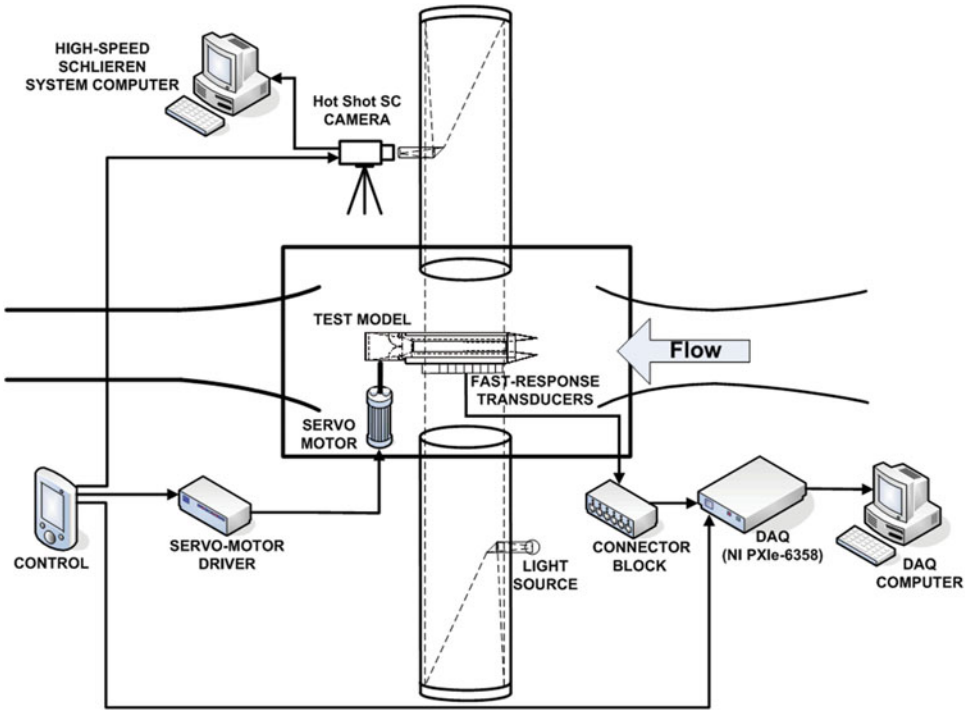

Fig. 4 Schematic of the model in the NHW with Schlieren imaging and instantaneous pressure measurement setup

Table 1 Parameters for the experimental condition

P_0 (kPa)	T_0 (K)	Ma	Closed angle of ramp (°)	Rising speed of rod (mm/s)
637	505	4.93	17.6	2.0

transducers are flush mounted along the flow centerline of the inlet/isolator model. The transducers had an effective frequency response of 10 kHz and all the transducers have the ranges of 0–160 kPa. The transducer locations are labeled T1–T10 on the schematic of Fig. 3. A dynamic signal acquisition card (National Instruments PXIe-6358) was used to be the core of data acquisition (DAQ) system. The high-speed Schlieren acquisition system uses the NAC's HotShot SC systems. The sampling rate of the Schlieren system can reach as high as 5000 frames per second. A schematic of the measurement system setup is shown in Fig. 4.

In the experiment, the controller of servo motor is selected as the master control hub. At the beginning of the experiment, the controller of servo motor first drives the dynamic pressure signal acquisition system and high-speed Schlieren system to work; then after 1.5 s, the servo motor starts to run as the program that is preset in the controller. The moment when the dynamic pressure signal acquisition system and high-speed Schlieren system begin to work is set as the origin time ($t = 0$ s). The wind-tunnel flow conditions for the current test are summarized in Table 1. The rod that connects the flaps in Fig.3 rise at a constant speed of 2.0mm/s during this experiment.

Results

The supersonic flow field without OST is shown in Fig. 5. Because the tail ramps are in the initial state, the backpressure is very small, so there is no OST in the flow field of the duct. The first picture of Fig. 5 is the schlieren image for the reflected shock structures for undisturbed flow. Owing to the size of the schlieren mirrors and the effect of the bracket of the mirrors, the upstream flow field of the test model cannot be visualized fully. Further downstream, the separation region (arrow 1) due to the incident shock wave and boundary layer interaction can be seen and the induced shocks of the separation (arrows A and B) also can be observed. Because of the boundary layer reattachment, induced shocks (arrows C and D) are formed after the separation regions, and then they interact with the boundary layer to generate the separation region (arrow S2) again. Expansion waves are formed when the flow passes through the top of the separation region, and the induced shock waves reflect on the wall and produce the reflected shock waves (arrows E and F).

In order to understand the flow characteristics better, a numerical simulation has been done to describe the flow field at this moment. Figure 5 also shows the Mach number contours for the supersonic flow field. As can be seen by comparing with each other, the result gotten by numerical simulation is coincident with the experimental Schlieren and the wave structures gotten by theoretical analysis. The mean pressure and rms pressure distributions are shown in Fig. 6.

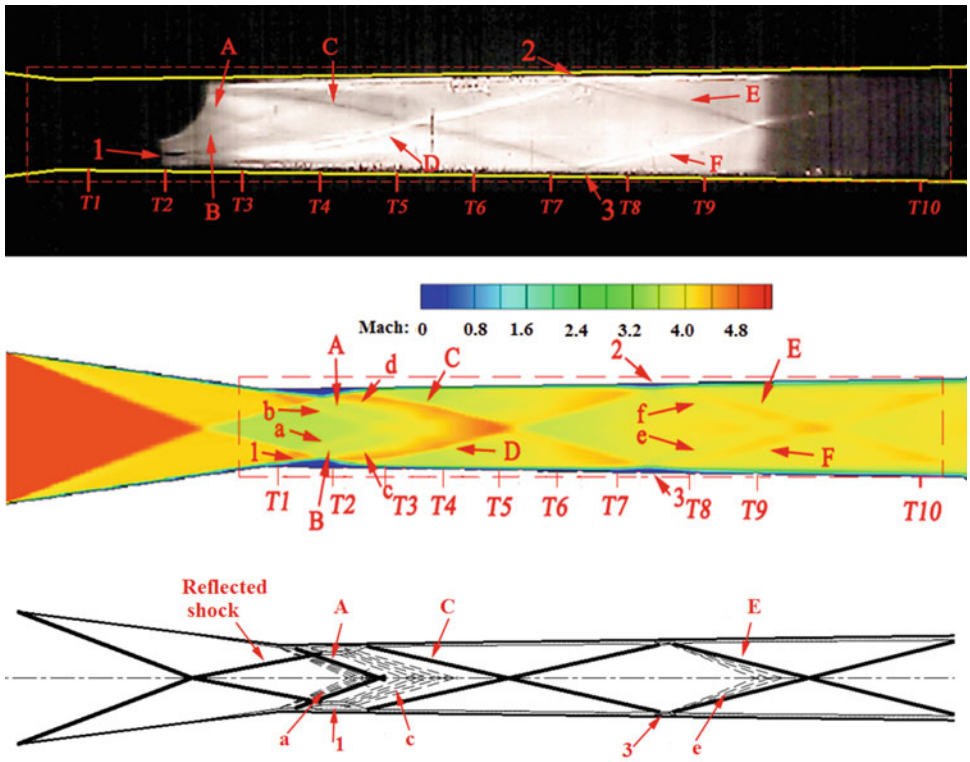

Fig. 5 Flow pattern of supersonic flow field without OST

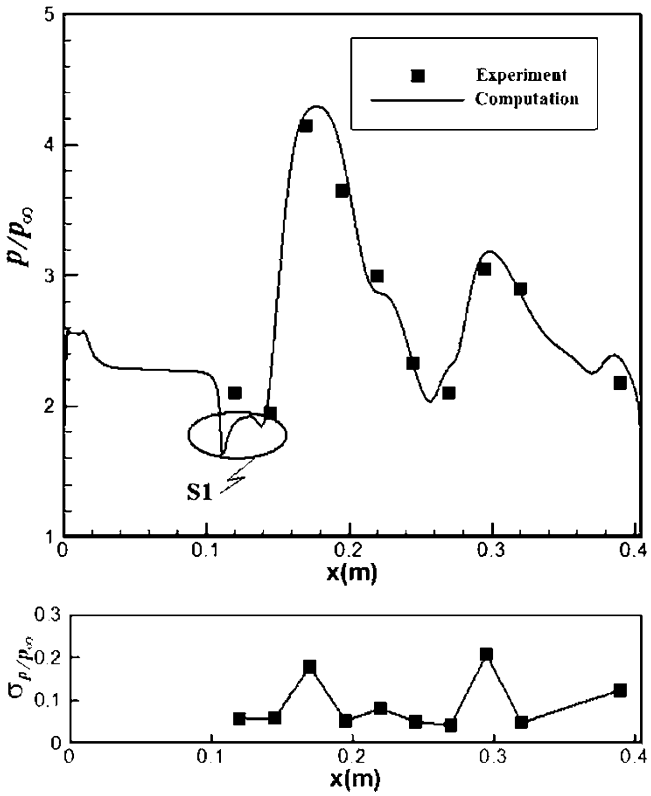

Fig. 6 Mean pressure distribution and standard deviation distribution

Figure 7 shows the pressure time histories of all transducers for the whole propagation progress. The pressures at T7–T9 have the rapidly rising characteristics due to the rapidly forward propagation of OST. At $t = 5.75-5.85$ s, a sharp increase in the pressure rise behavior is also simultaneously observed at T1–T4. At $t = 4.2-5.6$ s, a gradual rise in pressure is sensed by T5 and T6.This indicates that the OST moved forword steadily. It should be noted that the same phenomena are found in several repeated cases. It is also observed that the leading edge of OST sweeps rapidly the locations T7 and T8 in the high-speed Schlieren images (Fig. 8).

Conclusions

The dynamic characteristics of the OST in a simple duct model are investigated experimentally in a Mach 5 wind tunnel. The OST forward propagation process is not a stable motion process. It contains two kinds of motion modes: rapidly forward and steadily forward. Both modes are relative to some factors, such as the flow structure, the wall pressure distribution, and the length to the exit of model.

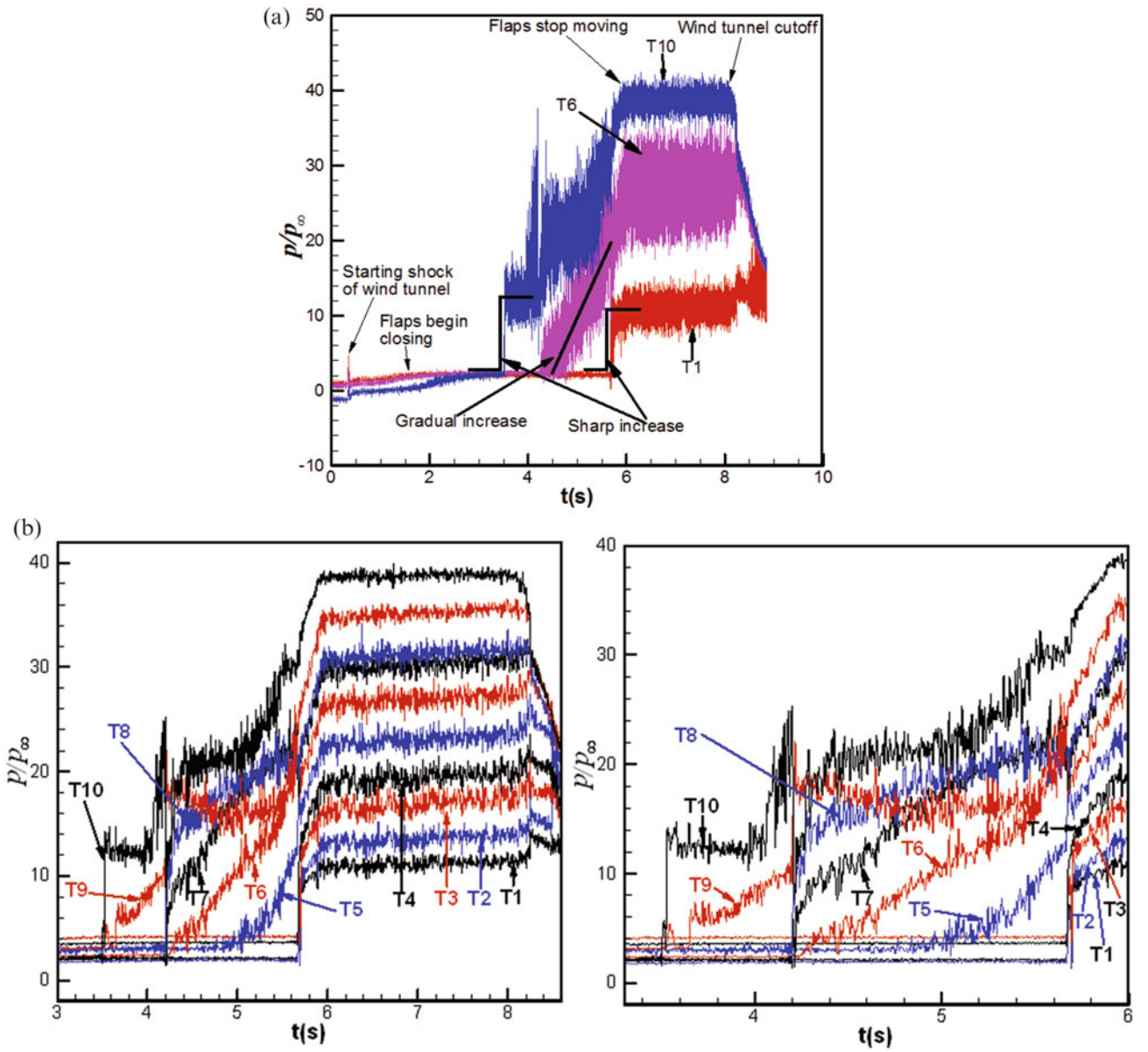

Fig. 7 Pressure time histories of all transducers for the whole propagation progress

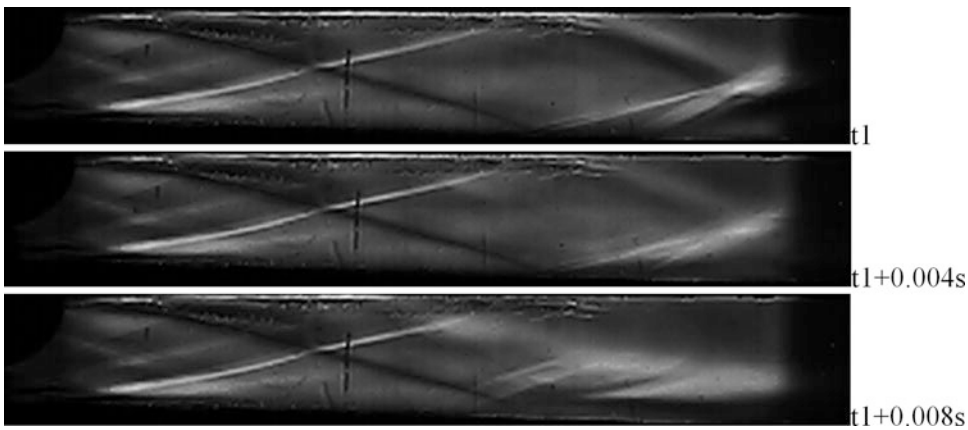

Fig. 8 The leading edge of OST sweeps rapidly the locations T7 and T8

Acknowledgments This work was funded by the National Natural Science Foundation of P. R. China (No. 10702029、51476076).

References

1. Le, D.B., Goyne, C.P., Krauss, R.H., McDaniel, J.C.: Experimental study of a dual-mode scramjet isolator. AIAA 2005-0023 (2005)
2. Nedungadi, A., Van Wie, D.M.: Understanding isolator performance operating in the separation-shock mode. AIAA 2004-3832 (2004)
3. Li-hong, C., Xin-Yu, Z., Hong-Bin, G.: Investigation for effect of supersonic diffusers on the start of the hypersonic propulsion test facility. J. Propul. Technol. **25**(2), 430–434 (2004)
4. Meier, G.E.A., Szumowski, A.P., Selerowicz, W.C.: Self-excited oscillations in internal transonic flows. Prog. Aerosp. Sci. **27**, 145–200 (1990)
5. Ikui, T., Matsuo, K.: Oscillation phenomena of pseudo-shock waves. Bull. JSME **17**(112), 1278–1185 (1974)
6. Rodi, P.E., Emami, S., Trexler, C.A.: Unsteady pressure behavior in a Ramjet/Scramjet inlet. J. Prop. Power **12**(3), 486–493 (1996)
7. Wagner, J.L., Yuceil, K.B., Valdivia, A., et al.: Experimental investigation of unstart in an inlet/isolator model in Mach 5 flow. AIAA J. **47**(6), 1528–1542 (2009)
8. Wagner, J.L., Yuceil, K.B., Clemens, N.T.: Velocimetry measurements of unstart in an inlet-isolator model in Mach 5 flow. AIAA J. **48**(9), 1875–1888 (2010)
9. Gawehn, T., Gülhan, A., Al-Hasan, N.S., Schnerr, G.H.: Experimental and numerical analysis of the structure of pseudo-shock systems in laval nozzles with parallel side walls. Shock Waves **20**, 297–306 (2010)
10. Waltrup, P.J., Billig, F.S.: Structure of shock waves in cylindrical ducts. AIAA J. **11**(10), 1404–1408 (1973)
11. Sugiyama, H., Tsujiguchi, Y., Honma, T.: Structure and oscillation phenomena of pseudo-shock waves in a straight square duct at Mach 2 and 4. AIAA 2008-2646 (2008)
12. Piponniau, S., Dussauge, J.P., Debieve, J.F., Dupont, P.: A simple model for low-frequency unsteadiness in shock-induced separation. J. Fluid Mech. **629**, 87–108 (2009)
13. Babinsky, H., Harvey, J.K.: Shock Wave-Boundary-Layer Interactions. Cambridge University Press (2011)

Aero-Optical Measurement in Shock Wave of Hypersonic Flow Field

Sangyoon Lee, Man Chul Jeong, In-Seuck Jeung, Hyoung Jin Lee, and Jong Kook Lee

Introduction

Hypersonic flow field around a flight vehicle has density fluctuating elements such as shock wave and boundary layer. Since refractive index of light is related to density of medium, light propagation path changes while passing through the flow field. Influence of flow field property on optical characteristics is called aero-optics. As in Fig. 1, aero-optics distorts the image obtained by an optical instrument on the flight vehicle and degrades light intensity, displaces the position of an object, blurs the image, etc. To avoid these effects, various studies were conducted to relate optical characteristics with flow characteristics and to measure aero-optical aberration [1–3].

The optical instrument for aberration measurement is essential for aero-optics experiment, and recently a device called Shack-Hartmann sensor is developed. Wind tunnel experiment conducted at Arnold Engineering Development Center (AEDC) validated the performance of Shack-Hartmann sensor. In this research three devices were used to measure optical aberration. Imaging camera system (ICS) and X-Y detector were used to measure far-field pattern directly, and Point Spread Function (PSF) calculated from Shack-Hartmann sensor used to measure near-field pattern. Far-field pattern from ICS and PSF from Shack-Hartmann sensor were compared and both showed similar result [3].

S. Lee • M.C. Jeong • I.-S. Jeung (✉)
Department of Mechanical and Aerospace Engineering, Seoul National University, 1 Gwanakro, Gwanakgu, Seoul, Republic of Korea
e-mail: enjis@snu.ac.kr

H.J. Lee
PGM R&D Lab., LIG Nex1 Co., Ltd., Pangyoro, Bundanggu, Seongnamsi, Gyeonggido, Republic of Korea

J.K. Lee
Agency for Defense Development, Daejeon, Yuseong-Gu, Republic of Korea

Generally wind tunnel is used to demonstrate flow field on the ground. For hypersonic flight condition, enthalpy should be much higher than atmospheric temperature since nozzle expansion ratio is huge. Usually shock tunnel is used to increase enthalpy since the operation cost is relatively cheap and operating is simple than other high-enthalpy facility.

In this research aero-optical characteristics at shock wave in hypersonic flow field is studied. A wedge model is installed inside a hypersonic shock tunnel to demonstrate flow field on the ground. Optical aberration induced on light propagating through flow field is measured using Shack-Hartmann sensor.

Experiment Setup

Facility

AST-1 shock tunnel in the Aerospace Propulsion and Combustion Laboratory (APCL) at Seoul National University (SNU) is used to demonstrate hypersonic flow field on the ground [4]. Figure 2 is the image of AST-1 shock tunnel. Nitrogen is used for driver gas and air is used for driven gas. PET film is used as the diaphragm for both ends of the driven tube to split the gases. Thickness of PET film is varied to conduct experiment on different free-stream conditions. Two types of nozzle are used to produce Mach 7 flow. One is conical nozzle and another is contoured nozzle. A conical nozzle has constant wall inclination and a contoured nozzle has a different wall inclination designed by method of characteristics (MOC) [5]. The exit diameter of a conical nozzle is 150 mm and of a contoured nozzle is 189 mm. Flow property at each nozzle exit is validated using pitot rake and wedge model. Pitot rake measured stagnation pressure on nozzle radial direction, and wedge model validated the Mach at the nozzle exit. From pitot rake measurement, effective nozzle diameter is also conducted. Conical nozzle

G. Ben-Dor et al. (eds.), *30th International Symposium on Shock Waves 1*, DOI 10.1007/978-3-319-46213-4_37

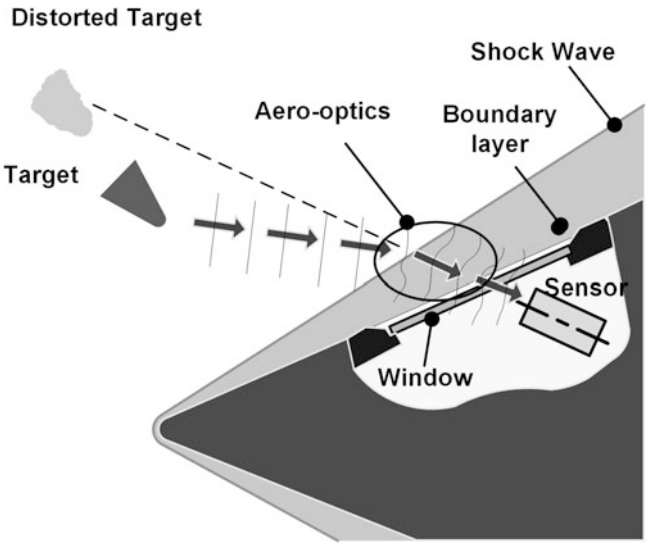

Fig. 1 Aero-optics induced by flow field near-flight vehicle

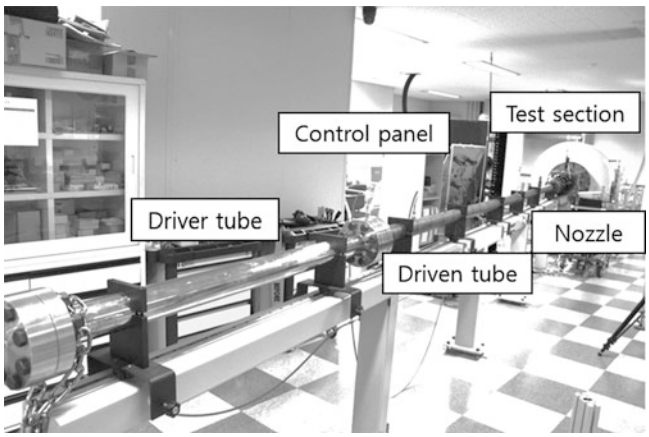

Fig. 2 AST-1 shock tunnel at SNU

has Mach 6.8 flow at the exit and effective diameter is 120 mm. Contoured nozzle has Mach 7 flow at the exit and effective diameter is 144 mm. Size of a test section is 300 × 300 × 600 mm. The test section has a window on each side for flow visualization and one window on top for aero-optical measurement.

Experiment Model

Aero-optics experiment model is installed in AST-1 as in Fig. 3. The left image in Fig. 3 is a schematic diagram of aero-optics experiment model, and the right image in Fig. 3 is an image of aero-optics model installed in shock tunnel test section. Aero-optics model consists of four parts: laser, optical components, sensor, and model. A laser beam becomes a plane wave through a collimation lens, propagates through flow field around wedge model, is guided with mirror, reduces to beam size appropriate for optical sensor aperture, and finally is captured by optical sensor, and optical aberration information is acquired.

A wedge model with 10° angle is used to introduce oblique shock wave to hypersonic flow field. Thickness of the model is 66 mm and height is 50 mm. A window is installed on the surface of the wedge for laser beam path. Diameter of the model window is 45 mm and material is Pyrex. To analyze flow property, stagnation pressure and surface pressure are measured. Stagnation pressure is measured using pitot tube near the wedge front. Measurement result is used to verify Mach number of free-stream flow and pressure loss throughout the nozzle. Position of pitot tube is considered not to affect the flow field on the wedge model. For surface pressure measurement, a pressure hole is placed near the optical window.

Shack-Hartmann Sensor

Shack-Hartmann sensor is one of the optical sensors that measure wave front slope and intensity of incident beam. Figure 4 is schematic of the wave front measurement using Shack-Hartmann sensor. Shack-Hartmann sensor consists of a lenslet array and a Charge Coupled Device (CCD). Incident distorted wave is divided to each lens of the lenslet and focuses to a point. Since CCD is placed at the focal length of the lenslet array, the image of each focused point is captured with CCD. From captured image, position and intensity of the point are analyzed. Comparing the image with reference image, which is usually the image of plane wave captured before each measurement, position difference and intensity difference are obtained. The position difference of focused point is wave front slope at corresponding lens of the lenslet array. From wave front slope matrix at each point, wave front is reconstructed using various methods. Depending on the reconstruction method, the obtained wave front is different. In this thesis, wave front reconstruction is conducted with a modal method using Zernike polynomial. Since Shack-Hartmann sensor measures difference from reference data, only optical aberration is obtained from results. In other words, the effect of aberration induced by optical system itself is neglected during measurement.

Shack-Hartmann sensor from Lumetrics (model: CLAS-XP) is used for the experiment. Data acquisition and analysis software is also provided from Lumetrics. The frame speed of Shack-Hartmann sensor is 30 hz and shutter speed in the experiment is 0.025 ms. Since the interval between each frame is 33 ms, only one frame is captured during shock tunnel test time. 635 nm diode laser is used as a light source for Shack-Hartmann sensor.

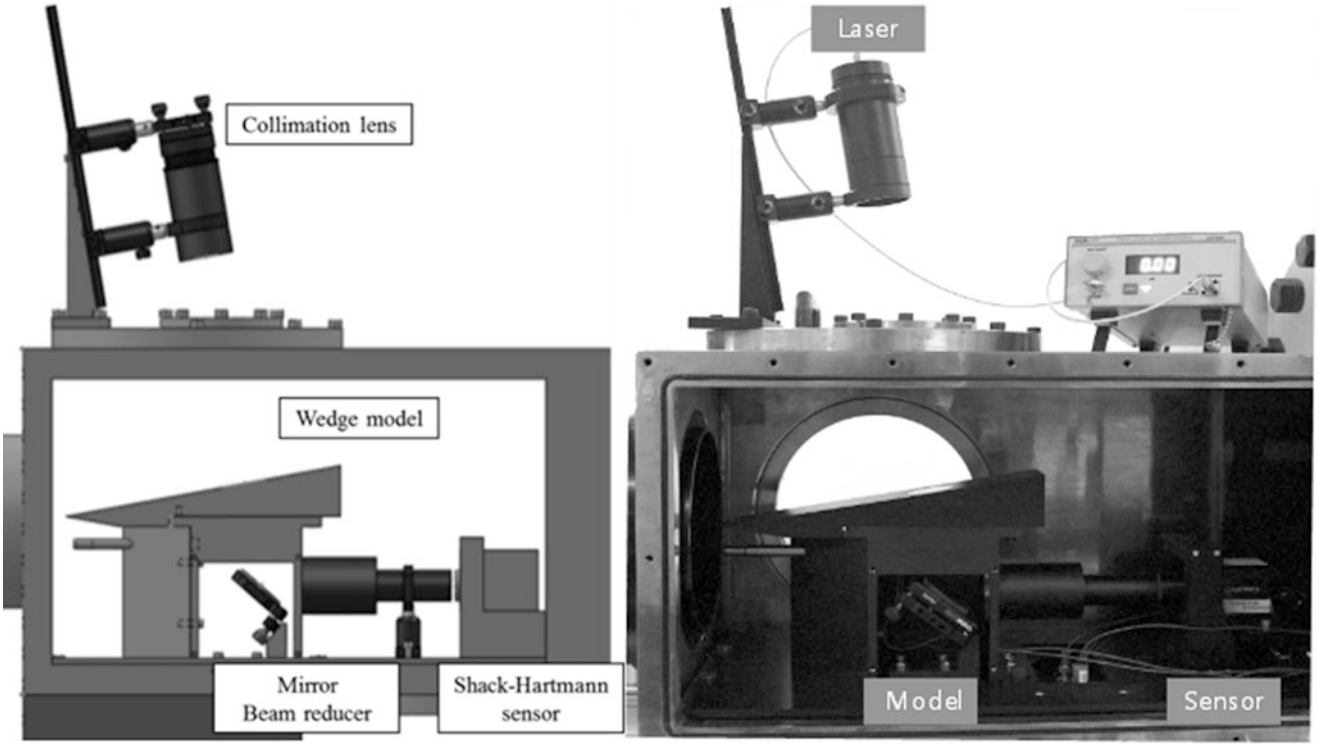

Fig. 3 Aero-optics experiment model installed in AST-1

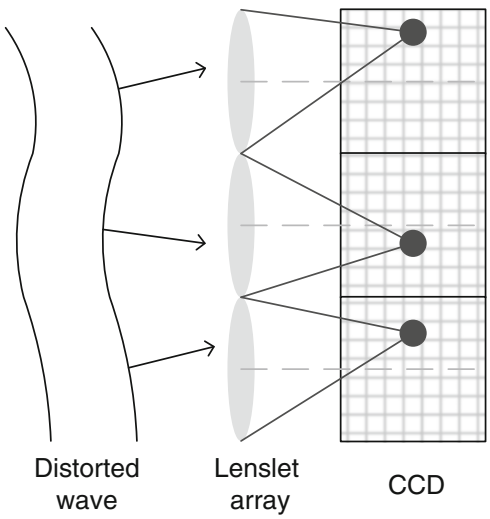

Fig. 4 Principle of wave front measurement with Shack-Hartmann sensor

Results

Aero-optics experiment in hypersonic flow is conducted for three altitudes: 29.1, 32.3, and 38.6 km. For each altitude, pressure and temperature are as in Table 1. Since temperature is not controllable in current shock tunnel system, pressure is controlled to match each static pressure. For 29.1 km, p1, which is pressure of driven tube, is 0.76 Mpa and p4 is 8.3–8.5 Mpa (pressure ratio 11); for 32.3 km p1, p4 is same with 29.1 km altitude but conical nozzle is used so pressure loss is introduced. For 38.6 km, two kinds of pressure ratio are used. One condition is that p1 is 0.26 Mpa and p4 is 27.5–28.5 Mpa (pressure ratio 11). The other condition is that p1 is 0.09 Mpa and p4 is 6.9 Mpa (pressure ratio 76.7) which is the case for 1.5 higher temperature. But since there is not much difference between low temperature and high temperature, the temperature effect is neglected and condition two is considered as same altitude condition. For each experiment, wave front information is acquired, and PSF is calculated. From PSF Bore Sight Error (BSE), Strehl ratio is obtained. From wave front information, certain tilt induced by shock wave is observed. Figure 3.17 is typical wave front information acquired, and Table 3.4 is all of the aero-optics experiment data acquired with Shack-Hartmann sensor.

Table 1 General pressure and temperature of atmosphere at each altitude

Condition (km) Altitude	Pressure (kpa)	Temperature (K)
29.1	1.353	228.56
32.3	0.851	238.28
38.6	0.360	256.76

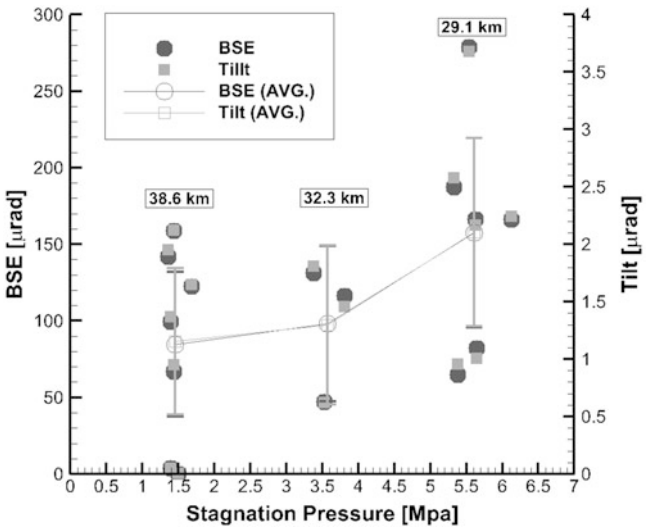

Fig. 5 BSE and tilt depending on stagnation pressure

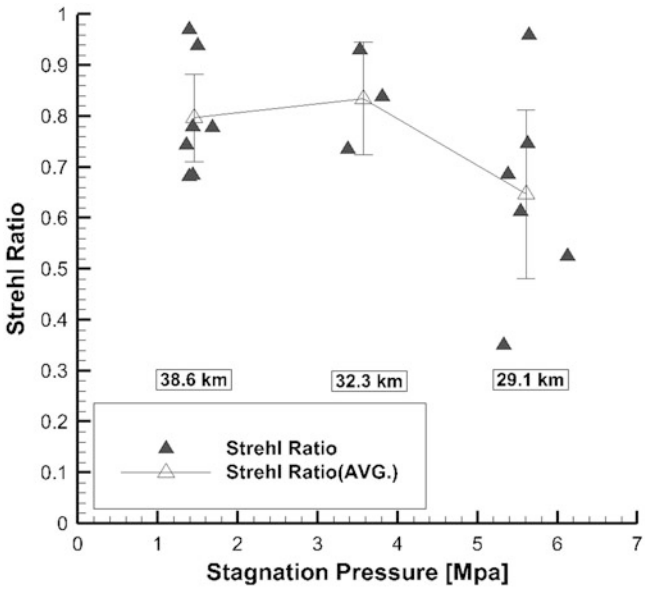

Fig. 6 Strehl ratio depending on stagnation pressure

All of the BSE, tilt, and Strehl ratio are plotted as in Fig. 5 and Strehl ratio is plotted as in Fig. 6. The error bar at each graph represents 95 % confidence interval on the mean. Standard deviation is acquired for each set of altitude population mean estimated. The average value and maximum value for each altitude are presented as Table 2.

There seems no relation between maximum value and altitude. For the average value, BSE and tilt increase when altitude is decreased, and Strehl ratio is increased while altitude is increased. Since air is sparser at lower altitude, effect of aero-optics seems to be less. In hypersonic flow field, shock wave induces BSE of 80–150 μrad and it means that when the target is 10 km far away, 0.8–1.5 m position error will occur. Overall light system performance, which is Strehl ratio, will also decrease for 0.8.

Table 2 Average and maximum value of aero-optical characteristics

Condition (km) / Altitude	BSE (μrad)		Tilt (μrad)		Strehl ratio
	Average	Maximum	Average	Maximum	
29.1	157.487	278.660	2.104	3.677	0.647
32.3	98.139	130.927	1.296	1.810	0.835
38.6	84.638	158.764	1.157	2.124	0.797

Conclusions

Experiment is conducted to study hypersonic flow field characteristics. Shock tunnel is used to demonstrate hypersonic flow field on the ground. Conical nozzle and contoured nozzle is used to generate Mach 7 flow. Wedge model with pitot tube is used to measure Mach and pressure loss. Pitot rake is used to measure flow distribution by radial direction. Conical nozzle has Mach 6.8 flow at the exit and effective diameter is 120 mm. Contoured nozzle has Mach 7 flow at the exit and effective diameter is 144 mm.

Aero-optics experiment model is designed and installed inside shock tunnel test section to study shock wave effect on aero-optical characteristics. 10° wedge model is used to generate shock wave. 635 nm diode laser, which is the object of Shack-Hartmann sensor, is directed perpendicular to wedge model surface. Aero-optics experiment is held for conical and contoured nozzle. In hypersonic flow field, shock wave induces BSE of 80–150 μrad, and it means that when the target is 10 km far away, 0.8–1.5 m position error will occur. Overall light system performance, which is Strehl ratio, will also decrease for 0.8.

References

1. Jumper, E.J., Fitzgerald, E.J.: Recent advances in aero-optics. Prog. Aerosp. Sci. **37**(3), 299–339 (2001)
2. Holden, M.S.: Calibration and Validation Studies in the LENS Facility. Defense Technical Information Center (1994)
3. Yanta, W.J., Spring III, W.C., Lafferty, J.F., Collier, A.S., Bell, R.L., Neal, D., Hamrick, D., Copland, J., Pezzaniti, L., Banish, M., Shaw, R.: Near- and far-field measurements of aero-optical effects due to propagation through hypersonic flows. 31st Plasmadynamics and Lasers Conference, (2000)
4. Lee, H.J., Lee, B.J., Kim, S.H., Jeung, I.-S.: Design/construction and performance test of hypersonic shock tunnel: part II: construction and performance test of hypersonic shock tunnel. J. Kor. Soc. Aeronaut. Space Sci. **36**(4), 328–336 (2008)
5. Kim, S.Y., Kim, S.D., Jeung, I.-S., Lee, J.K., Choi, J.Y.: Boundary layer correction of hypersonic wind-tunnel nozzle designed by the methods of characteristics. J. Kor. Soc. Aeronaut. Space Sci. **42**(12), 1028–1036 (2014)

Super-/Hypersonic Aero-Optical Effects Induced by External Jet Cooling

Sangyoon Lee, Hee Yoon, In-Seuck Jeung, Hyoung Jin Lee, and Jong Kook Lee

Introduction

Usually, the forepart of an optical-guided missile generally composes of the body with a cone or hood shape and the optical window to seek a target. Additionally, a cooling system is necessary to reduce the surface temperature of the optical window when a missile system is flying in hypersonic flow fields, because the aero-optical window of a missile can undergo severe aerodynamic heating problems causing high heat and cracks to optical windows which eventually lead to failure of optical windows [1–3].

External jet film cooling and internal convection cooling can be adopted for optical window cooling. This study focused on the external jet cooling with planar optical side on a missile system, which functioned using a cooling airflow injected from the front of the window and sprayed on the outside of the window. This method is simple and easy to implement; however, injected cooling gas and the external flow can be interacted and form a complex turbulence flow fields with shock-boundary interactions. These complex interactions will cause image transmission interference to the optical imaging detection system, which results in target image offset, jittering, and fuzziness. This effect is known as the aero-optical effects [4]. Therefore, it is necessary to apply a proper cooling system and to understand the aero-optical effects for operating the hypersonic missile (Fig. 1).

In this study, the aero-optical effects induced by external jet cooling are investigated in supersonic and hypersonic flow fields. To observe the effects, the aero-optical test model with a simple wedge and an injection system was designed and installed in the supersonic wind tunnel and the hypersonic shock tunnel which are constructed in the Aerospace Propulsion and Combustion Laboratory (APCL) of Seoul National University (SNU) of Korea. The operating Mach number of supersonic wind tunnel and hypersonic shock tunnel of APCL are 2.5 and 7.0, respectively. Basically, shadowgraph images were obtained using high-speed camera to measure flow field characteristics. To observe the aero-optical characteristics, Shack-Hartmann sensor was used to measure wave front of a laser passing through the flow field. Phase and intensity measured through Shack-Hartmann sensor were transferred to PSF, and aero-optical parameter such as Strehl ratio, bore sight error (BSE), and contained energy diameter (CED) were calculated.

Experiment Setup

Facility

Wind tunnel at Seoul National University was used to demonstrate flow field. Figure 2 represents the overall image of supersonic wind tunnel and Fig. 3 the image of the test section. Half of the contoured nozzle is used to generate Mach 2.5 flow inside the test section. Both sides of the window are used for flow visualization, and a laser window is installed on top of the test section for aero-optics experiment. To avoid vibration of the wind tunnel affecting the optical measurement, optical components including Shack-Hartmann sensor are installed on an isolated table. Test section size is 36.7 mm × 30 mm, and test time of the wind tunnel is longer than 10 s which is sufficient to obtain several images of the Shack-Hartmann sensor.

S. Lee • H. Yoon • I.-S. Jeung (✉)
Department of Mechanical and Aerospace Engineering, Seoul National University, 1 Gwanakro, Gwanakgu, Seoul, Republic of Korea
e-mail: enjis@snu.ac.kr

H.J. Lee
PGM R&D Lab., LIG Nex1 Co., Ltd., Pangyoro, Bundanggu, Seongnamsi, Gyeonggido, Republic of Korea

J.K. Lee
Agency for Defense Development, Daejeon, Yuseong-Gu, Republic of Korea

G. Ben-Dor et al. (eds.), *30th International Symposium on Shock Waves 1*, DOI 10.1007/978-3-319-46213-4_38

Experiment Model

Aero-optics experiment model is a simple 2-D wedge with an angle of 10°. Figure 4 is the schematic of the wedge model with external film cooling. For external film cooling system, the window is installed inside the cavity of the wedge model. Three 1 mm diameter holes, which are parallel to the window, are drilled for cooling jet injection. These three holes are connected to a single chamber below the model. Nitrogen is used as a cooling jet. Flow visualization of the nitrogen from the holes is obtained for validation.

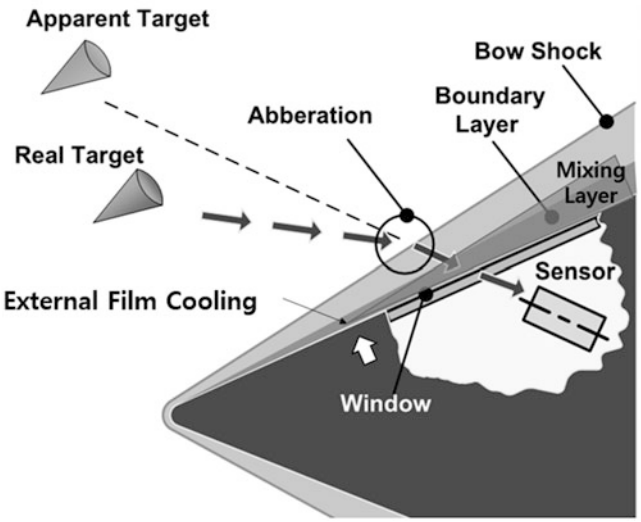

Fig. 1 Optical aberration induced by flow field around flight vehicle

Optical Measurement

Shack-Hartmann sensor acquires near-field wave front data. However, to obtain optical parameters, such as BSE, Strehl ratio, and CED, far-field data should be obtained. Therefore far-field pattern which is called point spread function (PSF) is calculated as Fig. 5, and optical parameter is obtained. BSE is defined as displacement of peak intensity of the PSF, Strehl ratio is defined as ratio of peak intensity, and CED is defined as a diameter of integrated intensity within a specific ratio of total intensity. Before the wind tunnel is operated, reference data for each experiment is captured in no-flow condition. Then when flow is developed inside the test section, 635 nm diode laser is propagated through the flow field, and Shack-Hartmann sensor measures the aberration in 30 Hz rate. Simultaneously with the wave front data, shadowgraph visualization image is obtained using high-speed camera. Experiment is held for three cases:

1. No flow with injection
2. Flow without injection
3. Flow with injection

Results

Wave front measurement of case 1 showed little change in optical property. BSE is 0.339 μrad and Strehl ratio is 0.8. For cases 2 and 3, stagnation pressure of the wind tunnel

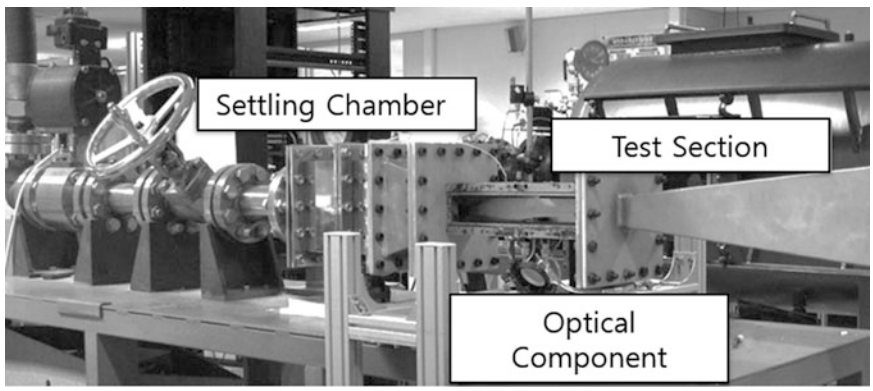

Fig. 2 Image of supersonic wind tunnel used for experiment

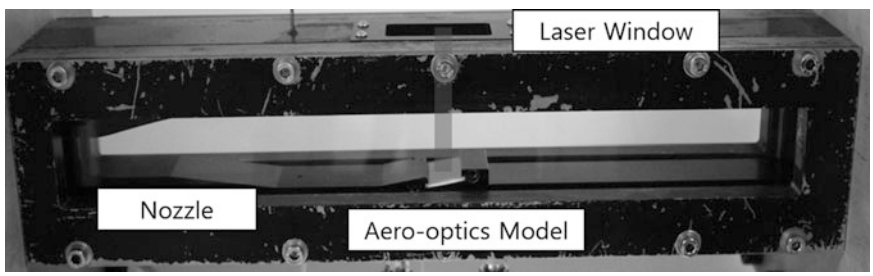

Fig. 3 Test section of supersonic wind tunnel

settling chamber is 0.8 Mpa, and stagnation pressure of the cooling jet is 1.5 Mpa. Figure 6 is shadowgraph image per 2 ms of case 2, and Fig. 7 is shadowgraph image per 2 ms of case 3. Unfortunately, flow field inside the test section is unstable and various shock structure appeared. Especially, shock structure oscillates inside the test section, disturbing the whole flow field seriously. On the other hand, complex shock structure seems to appear at case 3, but shock oscillation disappeared.

Wave front measurement result is similar with shadowgraph images. Wave front measurement of both case 2 and case 3 is highly unsteady and varied for time. For the analysis, each was averaged and PSF, BSE, and Strehl ratio result is presented in Fig. 8. As in the figure, case 3 has bigger bore sight error and lower Strehl ratio and larger CED diameter. These results conclude to worse optical performance of case 2. This result agrees with the more unstable flow field of case 3.

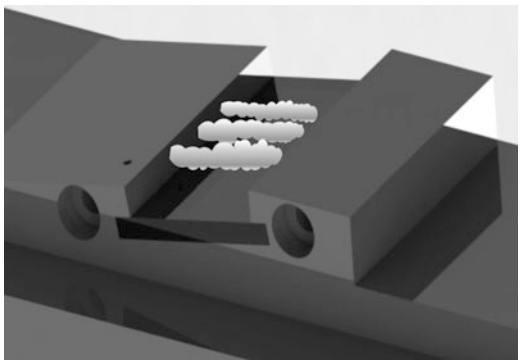

Fig. 4 Schematic of external film cooling on the model

Conclusions

The effect of external film cooling on optical aberration is studied by wind tunnel experiment. Shadowgraph image is obtained and Shack-Hartmann sensor measured the wave front propagating through the test section. From the result, injection itself does not affect the optical performance seriously. However, when merged with the supersonic flow field, various shock structures appear and aero-optical degradation increases. Especially, when flow field is more unstable, aero-optical aberration increased.

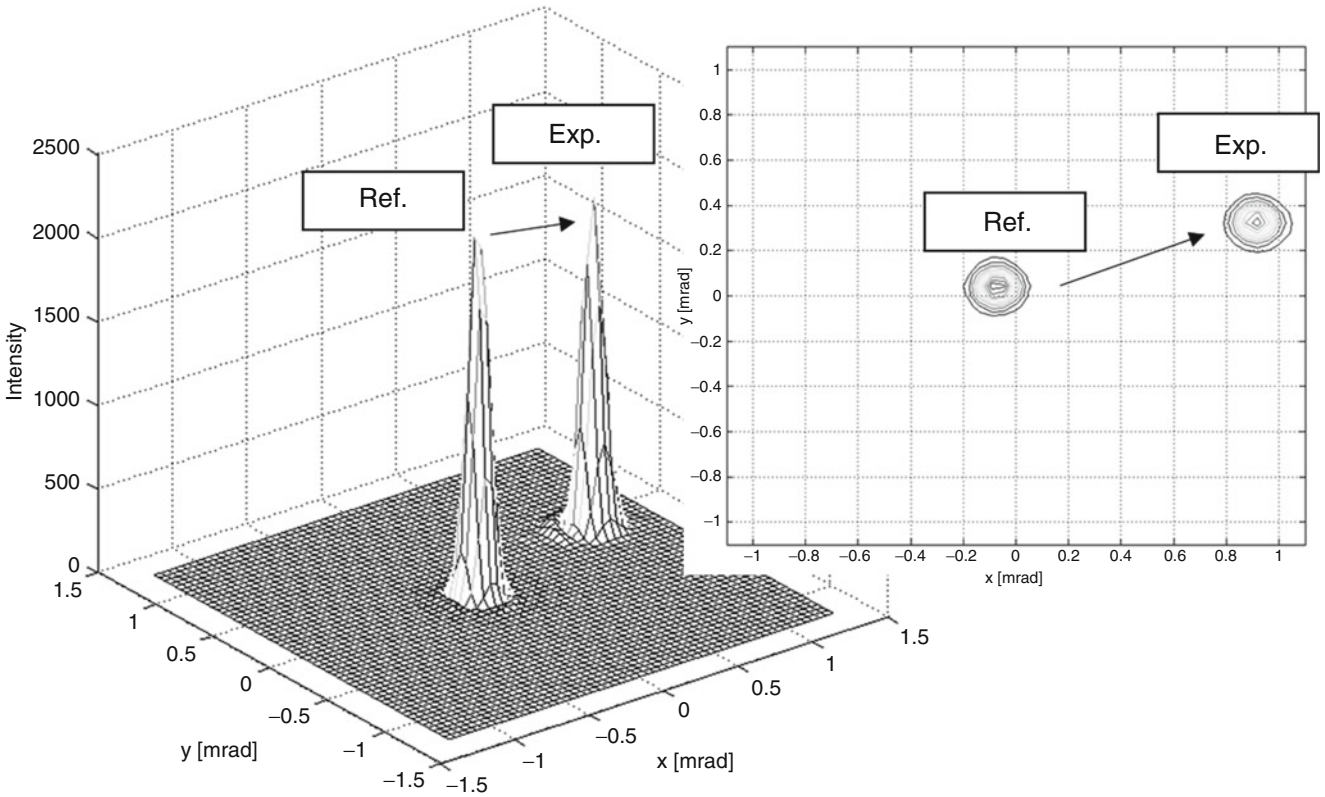

Fig. 5 Point spread function calculated from phase and intensity of wave front

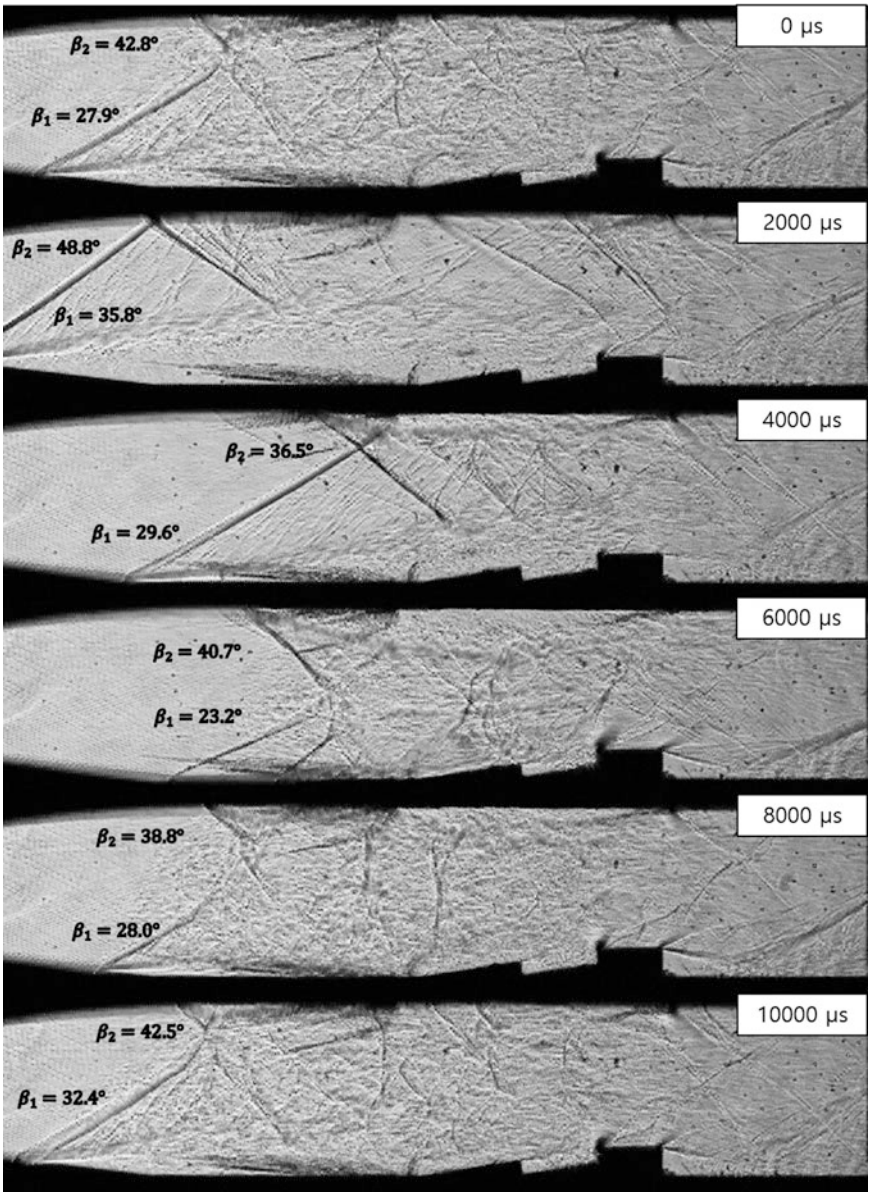

Fig. 6 Shadowgraph image of flow without injection case (case 2)

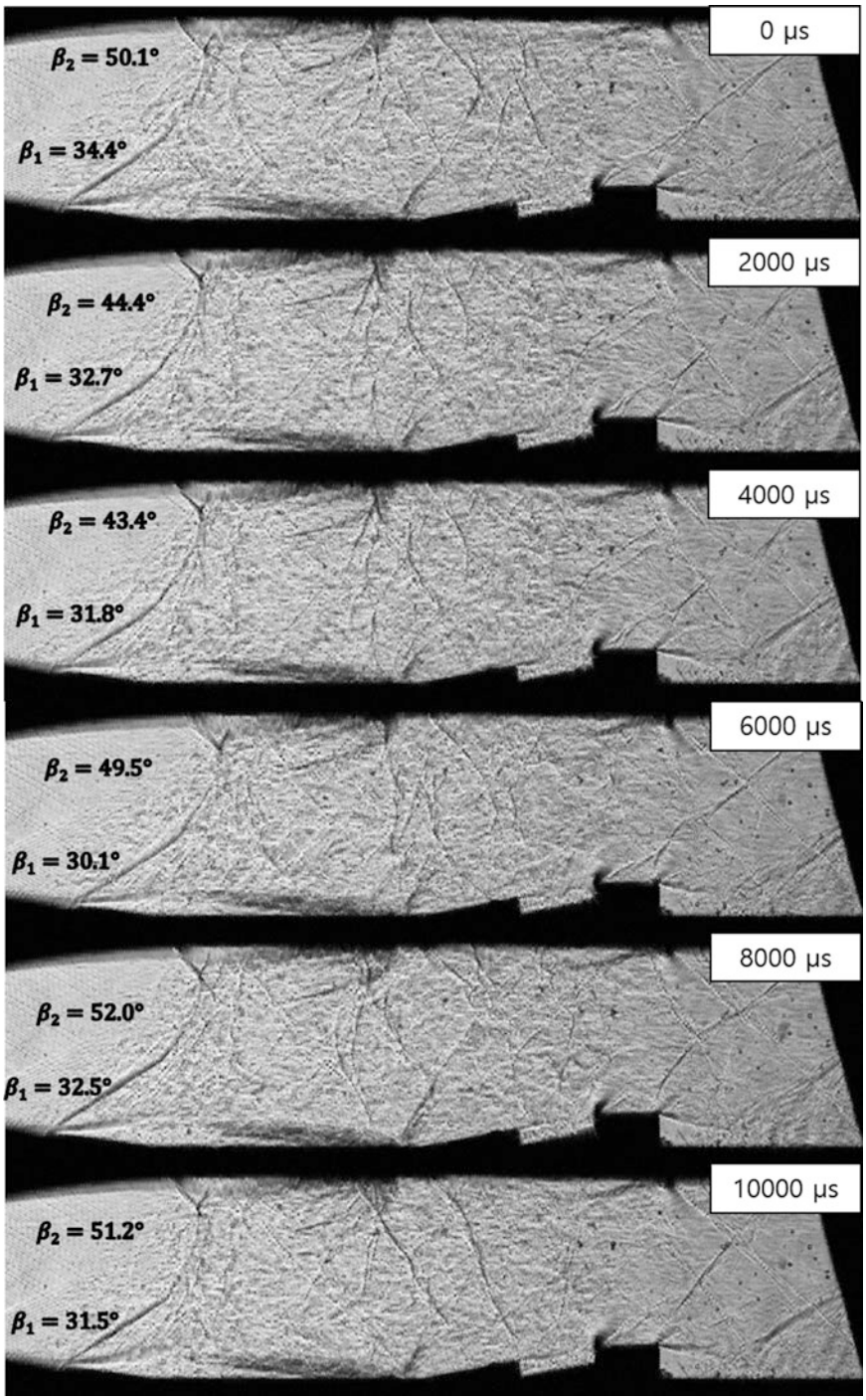

Fig. 7 Shadowgraph image of flow with injection case (case 3)

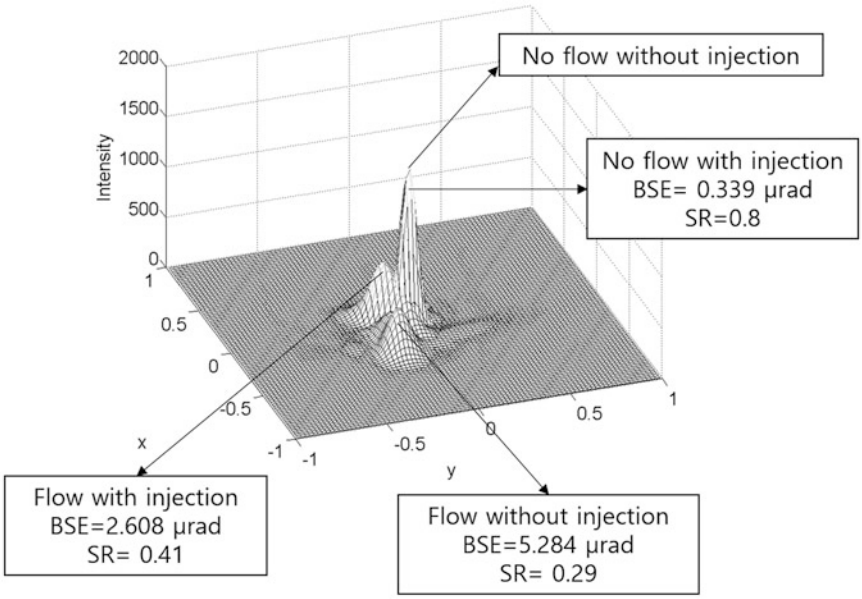

Fig. 8 Averaged PSF, BSE, and Strehl ratio for each case

References

1. Yang, X.Y., Liu, C.H., Gu, Y.Q.: Design of hypersonic vehicle infrared cooling dome. Infr. Laser Eng. **33**(6), 576–579 (2004)
2. Li, C.C., Lin, Y.C., Hsieh, M.C.: 3-D Simulation of external cooling of aero-optical side window. FDIT 214–218 (2011)
3. Kelly, H.N., Blosser, M.L.: Active cooling from the sixties to NASP. Presented at Current Technology for Thermal Protection Systems Workshop (1992)
4. Jumper, E.J., Fitzgerald, E.J.: Recent advances in aero-optics. Prog. Aerosp. Sci. **37**(3), 299–339 (2001)

Thermal Analysis of Scramjet Combustor Panel with Active Cooling Using Cellular Materials

Ragini Mukherjee, N.K. Gopinath, V. Vignesh, Anupam Purwar, and D. Roy Mahapatra

Introduction

The past few decades have seen phenomenal research in the area of scramjet-powered hypersonic air-breathing flight vehicles owing to its tremendous potential in civil and defence applicability. However, such long-duration vehicles experience very high temperatures as a result of air stagnation, shock waves and skin friction along the surfaces due to viscous dissipation. Notably, extreme heat flux is experienced by the scramjet combustor wall due to exothermic reaction involving heat addition to produce thrust. Additionally multiple shocks and shock train further result in local hotspots with increased temperature and pressure in the combustor. Withstanding severe thermal loads in scramjet combustion chambers is a great challenge, and as a result, cooling of combustor becomes critical where passive dissipation of heat is not sufficient. Published studies indicate that regenerative cooling with fuel used as coolant is regarded as one of the key approaches [1]. In regenerative cooling, an endothermic hydrocarbon fuel which undergoes heat-absorbing chemical reactions supported by the energy extracted from heated air/surfaces, is passed through the cooling channel to cool the engine wall before it is used for combustion. A major concern for such fuels is the formation of coke, which is considered undesirable as it reduces heat transfer by acting as an insulator on surfaces and can clog small passages in fuel systems and injectors [2]. As the fuel temperature increases while absorbing combustor wall heat, it must be ensured that coking temperature limit is not reached. Furthermore, recent emergence of multifunctional cellular materials has made it possible to tailor the vehicle structure in such a way that it can be used for cooling as well as a load-bearing member for the airframe with reduced mass. Periodic cellular metals like honeycomb, prismatic cores and lattice trusses are highly porous structures with 20 % or less of their interior volume occupied by metals [3]. Corrugated or prismatic core structures are widely used to dissipate heat because they provide opportunity to conduct the heat from the hot face sheet into the web structure for convective cooling [4, 5]. As coolant flows through the web structure, heat transfer occurs at the metal–coolant interface, thereby transporting heat away from the web and reducing temperature of the metal core. This results in a temperature gradient through the thickness of the web. Survivability of the structure under the specified aero-thermal environment often leads to the utilization of combination of multiple high-temperature materials modelled into a cellular structure with ceramic coatings. Such multilayered composite materials can be modelled as a single, equivalent material with an effective conductivity that reflects the more complex behaviour of the underlying structure [6]. An effective property is the property that a homogenous material must have if it is to behave in the same way as a composite.

The design of a scramjet requires input from a comprehensive thermal analysis involving the coupled heat transfer problem of hot gas, chamber wall and coolant [7]. In this perspective, a one-dimensional analytical heat transfer model has been developed to study regenerative cooling in a representative scramjet combustor panel in order to predict the cooling performance of the endothermic hydrocarbon fuel. The Eckert reference technique has been adopted to predict the heat flux of the combustor, and empirical relations are used for determining heat transfer coefficient of the coolant [1]. Through-thickness temperature profile and interface temperatures of the combustor wall have been estimated. Parametric studies have been carried out to determine the effect of flight Mach number, coolant mass flow rate and cooling channel dimensions on the cooling

R. Mukherjee (✉) • N.K. Gopinath • A. Purwar
Centre of Excellence in Hypersonics, Indian Institute of Science, Bangalore 560012, India
e-mail: raginirulez@gmail.com

V. Vignesh • D.R. Mahapatra
Department of Aerospace Engineering, Indian Institute of Science, Bangalore 560012, India

G. Ben-Dor et al. (eds.), *30th International Symposium on Shock Waves 1*, DOI 10.1007/978-3-319-46213-4_39

performance of combustor panel. Predictions of initial heat transfer characteristics, wall temperatures and the impact of various parameters are a prerequisite for designing an advanced thermal protection system like regenerative cooling for air-breathing hypersonic flight vehicles.

Methodology of Analysis

The development of the flow in an active cooling circuit of a scramjet combustor is a complex fluid dynamical problem [8]. Supercritical hydrocarbon endothermic fuel flowing through rectangular channels is heated from the hot combustor side and thus exposed to strong thermo-physical property variations. The one-dimensional analytical model estimates initial heat transfer characteristics of active regenerative cooling and through-thickness temperature distribution by considering the attributes of combustion hot gases, wall heat conduction, coolant heat convection.

Geometry and Modelling Assumptions

The combustor panel comprises of a multilayered cellular structure with endothermic fuel flowing through the core as coolant. The present work considers a single rectangular cooling channel of the combustor panel having constant area as shown in Fig. 1. Coolant flow and heat flux are assumed to be uniform across the width and height of the cooled scramjet engine. The approach for analysis assumes a steady-state one-dimensional energy balance across the active cooling jacket. To further simplify the analysis, it is assumed that wall conduction in axial direction is negligible, channel walls are smooth and flow is fully developed. All the thermo-physical properties of coolant are considered at bulk mean temperature and regarded as constant. Nonlinearity introduced by radiation heat flux has been neglected for simplification of analysis. The study has been performed at the combustor cross section experiencing peak hot-gas temperature. Despite the conjugate nature of hot-gas temperature and the heat flux generated, the influence of both on the combustor wall must be studied together and optimized as design constraint.

Effective Thermal Conductivity

As a preliminary estimation, the multilayer cellular panel may be approximated as a single, homogeneous equivalent material with an effective conductivity that reflects the complex behaviour of the underlying structure. If the structure is anisotropic, then the effective conductivity may depend on direction, reflecting some underlying characteristic of the composite structure that allows heat to flow more easily in certain directions. The process of determining the effective conductivity involves (theoretically) imposing a temperature gradient in one direction and evaluating the resulting heat transfer rate. This effective property in y direction is dominated by the thicker and low conductivity material layer, which is a typical behaviour of a series of resistance network, where the larger resistance is most important. It is therefore observed that endothermic fuel has a dominant effect:

$$k_{\text{eff}_x} = \frac{k_1 h_1}{h_1 + h_2} + \frac{k_2 h_2}{h_1 + h_2} \tag{1}$$

$$k_{\text{eff}_y} = \frac{1}{\dfrac{h_1}{(h_1 + h_2)k_1} + \dfrac{h_2}{(h_1 + h_2)k_2}} \tag{2}$$

where k represents thermal conductivity, h represents thickness and subscripts 1 and 2 represent first and second layer as seen in Fig. 1. Similar combination of subsequent layers

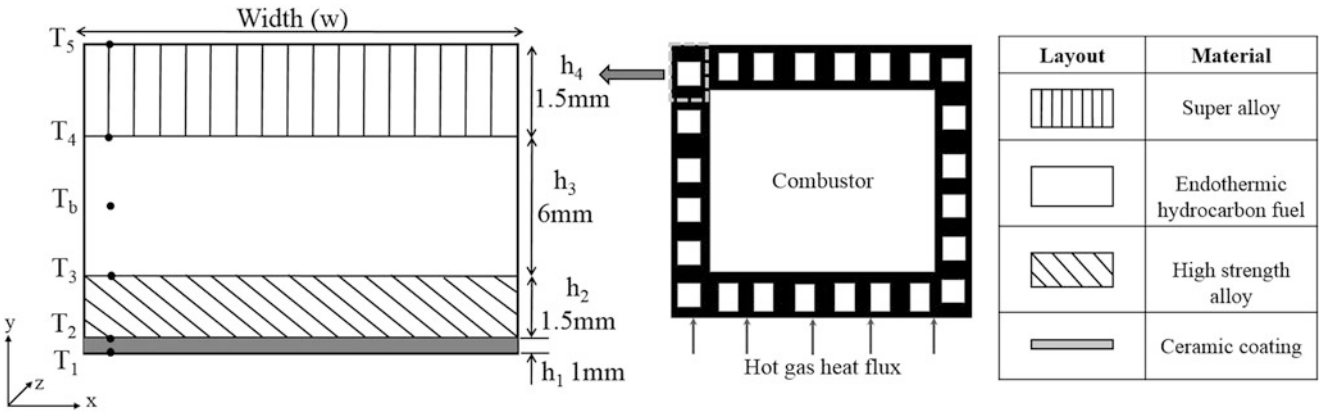

Fig. 1 Schematic of single cooling channel

leads to k_{eff}, effective thermal conductivity of the equivalent material. While this is applicable for solid–solid system, the presence of internal flow of coolant requires the estimation of local conductivity of coolant based on the heat flux carried by convection, in order to estimate total effective conductivity using Eq. (2). For a steady-state system, the coolant heat flux is the difference between heat flux entering and leaving the coolant layer. This may be considered as a local approximation to account the presence of fluid medium in between solid media and estimate the total effective conductivity.

1-D Heat Transfer Model

Typical heat transfer in scramjet combustor with active regenerative cooling includes heat convection and radiation transfer from hot combustion gas to combustor wall, conduction of heat through wall and the heat convection from cooling-side wall to coolant which is maintained at supercritical condition [9]. A separate one-dimensional steady-state combustor model provides the distribution of gas flow parameters, such as pressure, velocity and temperature. The combustor cross section encountering maximum gas temperature is considered for the heat transfer model.

Heat Convection from Hot Gas to Combustor Wall

Reference enthalpy technique is a semiempirical treatment employed to calculate the heat flux in the hypersonic boundary and to obtain the heat flux from hot gas to combustor inner wall [10]. As a function of Mach number, wall temperature and the incoming flow temperature, the Eckert reference enthalpy method is accurate enough in treating both laminar and turbulent flows. The heat flux from hot gas to combustor wall can be determined using the following equation [11]:

$$q_w{}^* = St^* \rho_g^* V_g{}^* (h_{aw} - h_w) \tag{3}$$

where * signifies that the gas properties used for these parameters gained under reference temperature obtained through the reference enthalpy, ρ is the density, V_g is the hot-gas velocity, and h_{aw} and h_w are adiabatic wall and wall enthalpy, respectively. The Stanton number (St) associated with the Eckert reference method under the typical condition of zero-pressure gradient, constant wall temperature and flow over flat plate can be obtained using the following equations:

$$\text{Laminar flow:}\quad St^* = \frac{0.332}{\text{Pr}_g^{*2/3}\text{Re}_{gx}^{*1/2}} \tag{4}$$

$$\text{Turbulent flow:}\quad St^* = \frac{0.0287}{\text{Pr}_g^{*2/5}\text{Re}_{gx}^{*1/5}} \tag{5}$$

where Pr_g is the Prandtl number of hot gas and Re_{gx} is the local gas Reynolds number.

Heat Conduction Through Combustor Wall

The inner wall of combustor separates the combustor from the regenerative cooling system. Heat transfer through the wall material occurs by conduction:

$$q_w = k\frac{(T_1 - T_2)}{h} \tag{6}$$

Heat Convection from Combustor Wall to Coolant

Heat transfer between coolant side wall and coolant occurs by convection:

$$q_w = h_c(T_w - T_b) \tag{7}$$

T_w is wall temperature, T_b is coolant bulk temperature, and h_c is heat transfer coefficient of coolant. Gnielinski's correlation is used to estimate the turbulent Nusselt number where the friction factor f can be determined from the Petukhov equation [12]. This relation is applicable for $0.5 \leq \text{Pr} \leq 2000$ and $3\times10^3 \leq \text{Re} \leq 5\times10^6$:

$$Nu = \frac{(f/8)(\text{Re} - 1000)\text{Pr}}{1 + 12.7(f/8)^{0.5}\left(\text{Pr}^{2/3} - 1\right)} \tag{8}$$

The internal flow of coolant necessitates the evaluation of temperature variation across the layers, in order to assess the impact of coolant on heat transfer and wall temperature. Furthermore, the Eckert reference enthalpy technique gives the heat flux for the hot-gas-side wall if the hot-gas-side wall temperature is known [12]. Since hot-gas wall temperature is an unknown in the present study and is to be found, this requires the simultaneous solving of energy balance equation instead of a sequential approach. Accordingly, to capture the distribution of temperature along the thickness at discrete interfaces of the cellular material, steady-state energy balance has been solved simultaneously across each of the layers of the panel. Five equations are solved to obtain

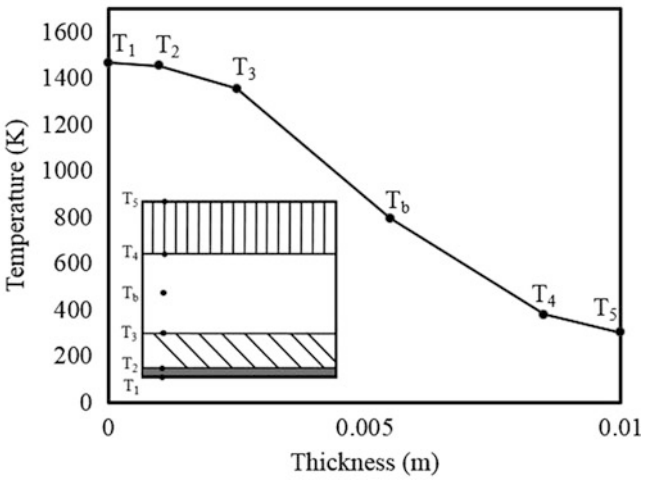

Fig. 2 Temperature profile in multilayered cellular cross section of combustor panel

the multilayer interface temperatures and through-thickness temperature profile:

$$\begin{bmatrix} T_1 \\ T_2 \\ T_3 \\ T_b \\ T_4 \end{bmatrix} = \begin{bmatrix} 0 & B_{12} & 0 & 0 & 0 \\ 0 & 0 & B_{23} & 0 & 0 \\ 0 & 0 & 0 & B_{34} & 0 \\ 0 & 0 & 0 & 0 & B_{45} \\ 0 & 0 & 0 & 0 & B_{55} \end{bmatrix} \begin{bmatrix} T_1 \\ T_2 \\ T_3 \\ T_b \\ T_4 \end{bmatrix} + \begin{bmatrix} A_1 \\ A_2 \\ A_3 \\ A_4 \\ A_5 \end{bmatrix} \quad (9)$$

where matrix elements of [A] and [B] are derived from energy balance as described above.

Results

Multilayer Cellular Structure Interface Temperature Distribution

The temperature distribution along the thickness at discrete interfaces is shown in Fig. 2. In the present channel of 10 mm width and 6 mm height, a mass flow rate of 0.0195 kg/s corresponds to fluid velocity of 0.8817 m/s. The Reynolds number is based on hydraulic diameter and a convective heat transfer coefficient of 1777.6 W/m^{2}K is considered between the fluid and wall. As expected, peak temperature is observed at hot-gas-side wall, which is reduced by high thermal conductivity ceramic coating and high strength alloy by conduction heat transfer. Furthermore reduction is detected due to endothermic hydrocarbon fuel which dominates heat transfer mechanism by convection, thereby resulting in highest temperature drop between temperatures T_3 and T_4. Top wall is considered isothermal at 300 K.

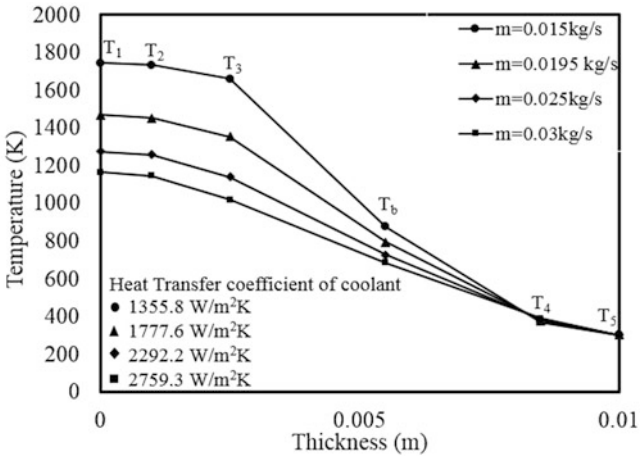

Fig. 3 Temperature distribution for varying coolant mass flow rates

Parametric variation analysis is a useful basis for system performance analysis, to obtain an optimal design considering the effect of each parameter and to identify the dominant parameters. Three critical parameters, viz. coolant mass flow rate, channel dimensions and the flight Mach number have been varied to assess their impact on cooling performance.

Effect of Coolant Mass Flow Rate

Mass flow rate of coolant is an operation parameter of the cooling system, which may be varied to achieve an optimized condition [13]. For a constant channel flow area, an increase in mass flow rate increases coolant flow velocity, thereby enhancing convection heat transfer coefficient. Since this escalates the rate of heat transferred from the coolant side wall, the wall temperature decreases which is reflected in the through-thickness temperature distribution of Fig. 3.

Effect of Channel Dimensions

Coolant channel dimension is a design parameter of the cooling system which has impact on velocity of fuel along the channel [14]. Since coolant convection is found to be the dominant mode of heat transfer in the study, coolant channel height (h_3) and width (w) have been varied, keeping other layer heights constant to assess its impact on wall temperature reduction. The flight Mach number is 7, and the mass flow rate is kept constant at 0.0195 kg/s for all three cases. As seen in Fig. 4, there is a marked reduction in the wall temperature as channel dimensions reduce. A smaller flow area results in a higher flow velocity leading to increased heat transfer coefficient. Therefore, more heat will be

transferred to the cooling side, resulting in a more pronounced reduction in wall temperature.

Figure 5 compares the effects of mass flow rate and channel dimension on convection coefficient. Since the mass flow rate is relatively high for smaller channel dimension variation, this leads to tremendous increase in heat transfer coefficient. Moreover, reduction in coolant channel dimension has larger effect than mere increase in mass flow rate. Additionally, change in channel width will change the total number of cooling channels across the panel, thus mass flow rate of fuel will be redistributed in each cooling channel. Therefore based on design requirements and constraints, the channel dimensions, the number of cooling channels and mass flow rate must be optimized together to obtain optimal heat transfer enhancement for the scramjet combustor panel.

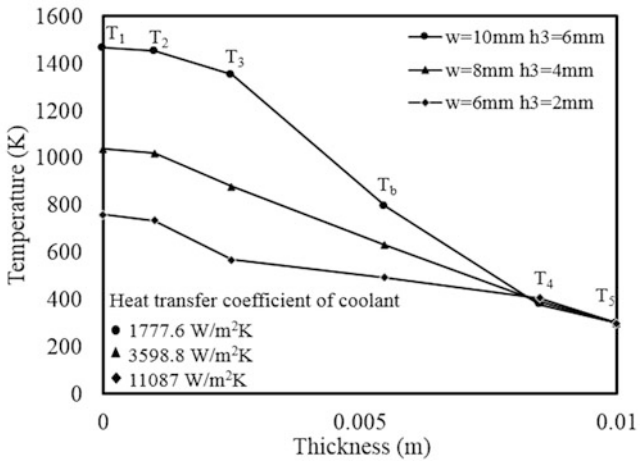

Fig. 4 Temperature profile for different coolant channel dimensions

Effect of the Flight Mach Number

The total gas temperature in combustor increases as the flight Mach number increases due to an increase in incoming flow enthalpy, which induces an increase in hot-gas heat flux. This results in an increase in wall temperature. The flight Mach number has been varied for the present study for cooling channel width 10 mm, height 6 mm and mass flow rate of 0.0195 kg/s. The increasing wall temperature corresponding to increasing Mach number is reflected in Fig. 6. Despite the conservative nature of results, it is observed that for Mach 8, temperature of high strength alloy exceeds its maximum operating temperature (~1900 K) and endothermic fuel approaches coking limit. This implies that the flight Mach number for a scramjet-powered hypersonic air-breathing vehicle must be optimized based on thrust requirements keeping material constraints and cooling effectiveness under consideration.

Conclusions

A one-dimensional analytical heat transfer model has been developed to study basic regenerative cooling in a representative scramjet combustor panel in order to predict the cooling performance of the endothermic hydrocarbon fuel in terms of wall temperature reduction, considering the attributes of combustion hot gases, wall heat conduction and coolant heat convection. It is found that endothermic hydrocarbon fuel as coolant dominates heat transfer mechanism by convection. It is seen that reducing channel dimensions has a more pronounced effect on heat transfer coefficient than merely increasing mass flow rate.

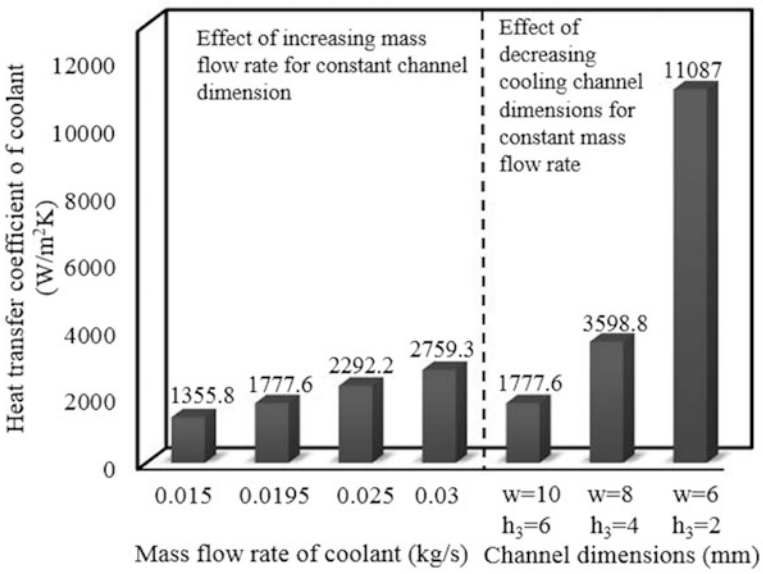

Fig. 5 Comparison of impact of mass flow rate and channel dimension on heat transfer coefficient

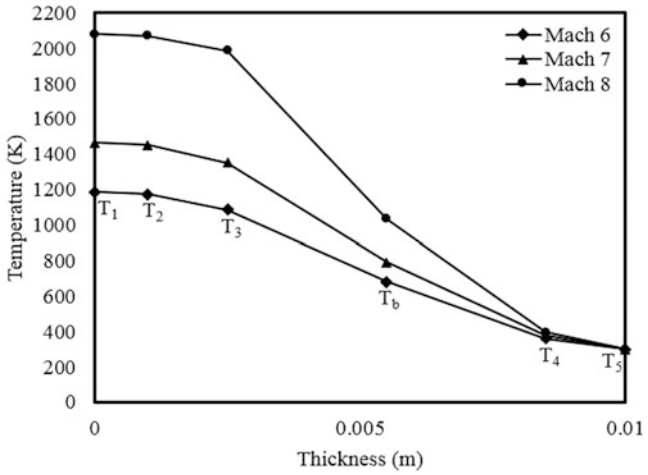

Fig. 6 Effect of the flight Mach number on temperature profile

Hence individual cooling channel dimensions and mass flow rate must be optimized together to obtain optimal heat transfer enhancement, keeping design requirements, manufacturing and other constraints under consideration. Increase in the flight Mach number increases wall temperatures, thereby requiring designers to carefully decide the vehicle Mach number based on thrust requirements along with material and cooling constraints. This work has opened up multiple avenues to improve the study by going into greater depth, increasing more complexities such as inclusion of radiation heat transfer, modelling thermal cracking of fuel as it gets heated and its impact on heat transfer and capturing the finer details of the active cooling mechanism for such a thermal protection system. Further studies will attempt to numerically validate the analytical results including conjugate heat transfer analysis, which will capture the coolant behaviour during cooling.

References

1. Bao, W., Duan, Y., Zhou, W., Yu, D.: Hydrogen-fuelled scramjet cooling system investigation using combustor and regenerative cooling coupled model. Proc. Inst. Mech. Eng. Part G J. Aerosp. Eng. **0**(0) 1–1 (2013)
2. Linne, D.L., Meyer, M.L., Edwards, T., Eitman, D.A.: Evaluation of Heat Transfer and Thermal Stability of Supercritical JP-7 Fuel. NASA Technical Memorandum 107485. AIAA-97-3041 (1997)
3. Wadley, H.N.G., Fleck, N.A., Evans, A.G.: Fabrication and structural performance of periodic cellular metal sandwich structures. Compos. Sci. Technol. **63**, 2331–2343 (2003)
4. Lu, T.J.: Heat transfer efficiency of metal honeycombs. Int. J. Heat Mass Transfer **42**, 2031–2040 (1999)
5. Brautsch, A., Griffin, T., Schlegel, A.: Heat transfer characterization of support structures for catalytic combustion. Int. J. Heat Mass Transfer **45**, 3223–3231 (2002)
6. Nellis, G., Klein, S.: Heat Transfer. Cambridge University Press, New York (2009)
7. Bao, W., Qin, J., Zhou, W.X., Yu, D.R.: Effect of cooling channel geometry on re-cooled cycle performance for hydrogen fueled scramjet. Int. J. Hydrogen Energy **35**, 7002e11 (2010)
8. Qin, J., Bao, W., Zhou, W.X., Yu, D.R.: Flow and heat transfer characteristics in fuel cooling channels of a recooling cycle. Int. J. Hydrogen Energy **35**, 10589–10598 (2010)
9. Schuff, R., Maier, M., et al.: Integrated modeling and analysis for a LOX/methane expander cycle engine: Focusing on regenerative cooling jacket design. In: 42nd AIAA/ASME/SAE/ASEE Joint Propulsion Conference & Exhibit, AIAA 2006–4534 (2006)
10. Richard, M.T., John, L.F. Jr., Tony, L.: A thermal management system model for the NASA GTX RBCC Concept. NASA/CR-2002-211587 (2002)
11. Heiser, W.H., Pratt, D.T., Dayley, D.H., Mehta, U.B.: Hypersonic Airbreathing Propulsion. AIAA Education Series, AIAA, Washington DC (1993)
12. Simeonides, G.: Generalized reference enthalpy formulations and simulation of viscous effects in hypersonic flow. Shock Waves **8**(3), 161–172 (1998)
13. Yunus, C.: Heat Transfer-A Practical Approach. McGraw Hill, New York (2003)
14. Jiang, Q., Silong, Z., Wen, B., Weixing, Z., Daren, Y.: Thermal management method of fuel in advanced aeroengines. J. Energy **49**, 459–468 (2013)

A Methodology for Coupled Thermal-Structural Analysis and Structural Design of Scramjet Combustor

Anupam Purwar, D. Roy Mahapatra, Nimesh Thakor, K.S. Priyamvada, and Ragini Mukherjee

Introduction

Scramjets are the most promising propulsion systems for hypersonic air breathing cruise vehicles. Hypersonic flow decelerate around a hypersonic vehicle through shock formation exposing the scramjets to intense thermal-structural loads. Also, there are stringent limits on maximum allowed deformation and weight of scramjet structure to meet the aero-propulsive requirements. This work describes structural design methodology for a generic single-strut scramjet combustor flying at Mach 7 at 30 km altitude. Multiple shocks across the mixed compression air intake reduce the Mach number to 2.2 and expose the scramjet to very high heat flux and intense pressure. The high heat flux (~1.5MW/m^2) experienced by scramjet structure heats scramjet walls up to temperatures up to 2000 K, which requires selection of suitable high-temperature materials and thermal barrier coatings to protect metallic airframe. Also, thermal stress-induced deformation becomes very significant in these high-temperature flows causing coupled thermal-structural interaction [1]. Hence, a coupled thermal-structural analysis is very crucial to designing a scramjet combustor. Coupled thermal-structural analysis of flying vehicles under high-speed flow with shock-induced loading has been studied in details by Thornton and Dechaumphai [1], Culler and Namara [2], Ho and Paull [3] and Ho et al. [4]. Life prediction of hypersonic structures has been attempted by Sobotka et al. [5]. Another important aspect is the use of thermal barrier coatings on the combustion chamber walls to reduce heat transfer and to keep the wall temperature within the operational limits of available materials. Relevant studies on thermal barrier coatings have been reported by many researchers [6–8]. A stiffened structure is required to limit the deformation because thermally induced deformation has significant effect on aerodynamic heating [1]. In this work, a semi-monocoque structure consisting of inner and outer skin and stiffeners has been selected for the scramjet to minimize weight and enhance strength. Important design parameters for a structurally reliant design have been identified namely selection of material, skin thickness and parameters related to thermal barrier coating and stiffener spacing. Multiple thermal-structural analysis iterations have been carried out to estimate the most suitable value of these design parameters in order to contain stress and deformation within safe limits.

A. Purwar (✉) • N. Thakor • K.S. Priyamvada • R. Mukherjee
Centre of Excellence in Hypersonics, Indian Institute of Science, Bangalore, India
e-mail: anupam@mrc.iisc.ernet.in

D.R. Mahapatra
Department of Aerospace Engineering, Indian Institute of Science, Bangalore, India

Design and Analysis Methodology

The structural design is an iterative process, and the methodology adopted in this work has been shown in Figs. 1 and 2. The first step in this process is the estimation of the pressure and the heat flux inside the scramjet combustor. Both of these have been simulated by computational fluid dynamics (CFD) analysis performed in ANSYS FLUENT with supersonic inlet boundary condition and reactive flow with liquid fuel injection. The heat flux distribution and pressure load are then mapped to structural domain of combustor. In the second step, the transient thermal analysis with radiation boundary conditions has been performed. The temperature distribution obtained from the transient thermal analysis and the pressure distribution has been applied to the scramjet to perform a coupled 3D static thermal-structural analysis. The coupled thermal-structural analysis involves iteration with design loop. The design loop consists of CAD modeller (PTC Creo), meshing software (HyperMesh) and finite element method (FEM) solver (ANSYS) which seamlessly performs analysis by

G. Ben-Dor et al. (eds.), *30th International Symposium on Shock Waves 1*, DOI 10.1007/978-3-319-46213-4_40

parametric variation of design variables. High-fidelity structured hexahedral mesh is generated in HyperMesh as shown in Fig. 3, and 20-node solid elements SOLID 226 [9], with thermal as well as structural degree of freedom, for coupled thermal-structural analysis. Figure 1 shows schematic of thermal-structural analysis, and Fig. 2 shows the structural design loop.

The pressure and heat flux values for the scramjet have been calculated from CFD analysis which predicts maximum pressure of 1.6 bar and maximum heat flux of 1.5 MW/m^2. These values closely match the heat flux and pressure values predicted by experimental work [10, 11]. In hypersonic regime, the thermal loads are very high which is also evident from the CFD analysis; hence, thermal stress-induced buckling needs to be managed by properly stiffening the semi-monocoque structure. In present work, a stiffened structure with two metal skins has been proposed as shown in Fig. 4. Besides this, thermal barrier coating has been used for internal lining of the scramjet combustor to bring down the temperature faced by the inner skin. Based on literature survey [12, 13], titanium-zirconium-molybdenum (TZM) alloy for inner skin, René 41 alloy for stiffeners and Titanium 6242 alloy for the outer skin have been selected.

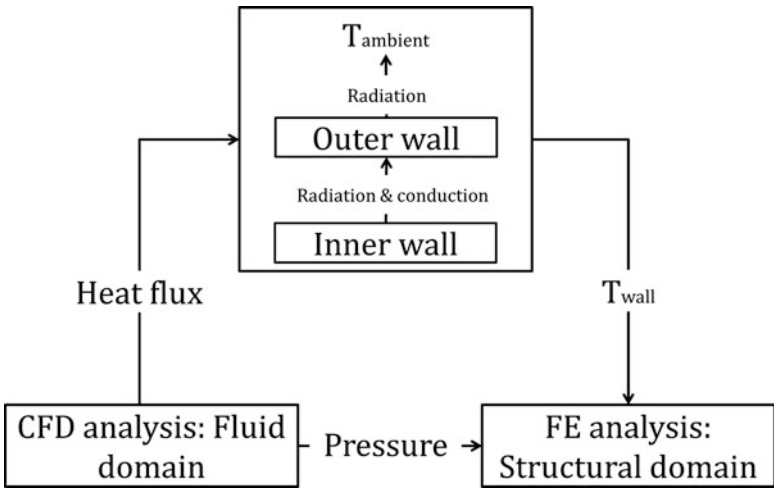

Fig. 1 Thermal-structural analysis scheme

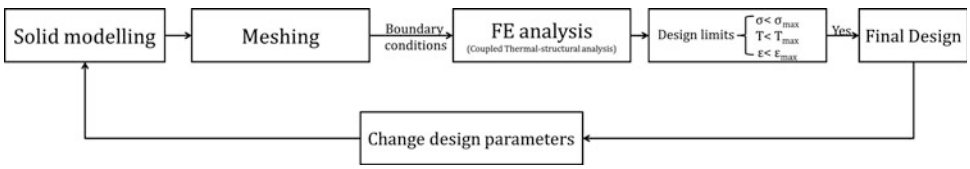

Fig. 2 Structural design loop

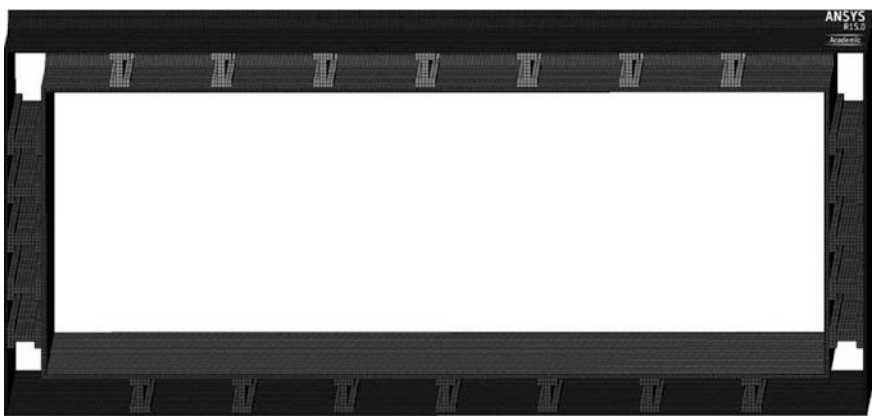

Fig. 3 Zoomed view of structured mesh used for thermal-structural analysis

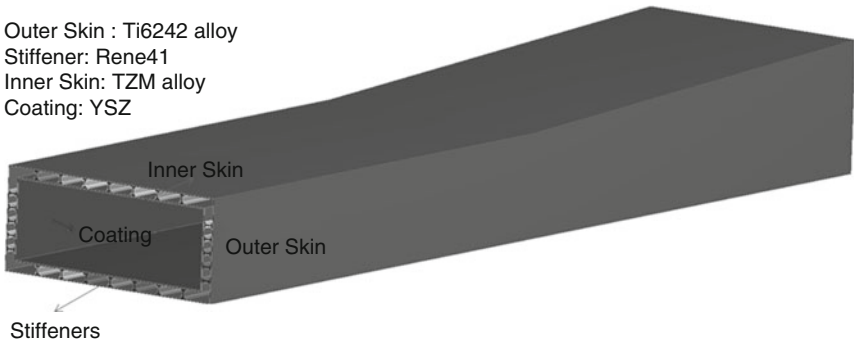

Fig. 4 Isometric view of stiffened monocoque structure showing inner skin with thermal barrier coating, outer skin and stiffener arrangements

Thermal-Structural Analysis

Coupled thermal-structural analysis has been performed using ANSYS based FEM solver and following Eqs. (1) - (4) have been solved to calculate deformation and stress. The thermal and structural domains have been sequentially coupled. The temperature obtained from transient heat transfer analysis has been mapped to the mesh of solid domain. Multiple design iterations aided by thermal-structural analysis have been carried out to optimize the following design parameters: thickness of inner and outer skin, cross section of I stiffeners, spacing of stiffeners to minimize the deformation and stress and structural weight.

$$\begin{bmatrix} \mathrm{M} & 0 \\ 0 & 0 \end{bmatrix} \begin{Bmatrix} \ddot{u} \\ \ddot{T} \end{Bmatrix} + \begin{bmatrix} \mathrm{C} & 0 \\ 0 & \mathrm{C^t} \end{bmatrix} \begin{Bmatrix} \dot{u} \\ \dot{T} \end{Bmatrix} + \begin{bmatrix} \mathrm{K} & 0 \\ 0 & \mathrm{K^t} \end{bmatrix} \begin{Bmatrix} u \\ T \end{Bmatrix} = \begin{Bmatrix} f \\ q \end{Bmatrix} + \begin{Bmatrix} f^{\mathrm{th}} \\ \end{Bmatrix} \tag{1}$$

$$\begin{aligned} \{\sigma\} &= [E]\{\varepsilon\} \\ \{\varepsilon\} &= [\partial][U] \\ [U] &= [N]\{d_e\} \\ d_e &= \begin{Bmatrix} d_{e1} \\ d_{e2} \\ \vdots \\ \vdots \\ d_{e20} \end{Bmatrix} \\ N &= [N_1 N_2 \cdots \cdots N_{20}] \end{aligned} \tag{2}$$

$$\begin{aligned} \sigma_{1,2} &= \frac{(\sigma_x + \sigma_y)}{2} \pm \sqrt{\frac{(\sigma_x - \sigma_y)^2 + \tau^2_{xy}}{2}} \\ \sigma_{2,3} &= \frac{(\sigma_z + \sigma_y)}{2} \pm \sqrt{\frac{(\sigma_z - \sigma_y)^2 + \tau^2_{zy}}{2}} \end{aligned} \tag{3}$$

$$\sigma_{\text{Von-Mises}} = \sqrt{\frac{(\sigma_1 - \sigma_2)^2 + (\sigma_1 - \sigma_3)^2 + (\sigma_1 - \sigma_3)^2}{2}} \tag{4}$$

In the above equations, [M] = element mass matrix, [C] = element structural damping matrix, [K] = element stiffness matrix, $\{f\}$ = sum of element nodal force & pressure, $\{f^{\mathrm{th}}\}$ = thermal strain force vector, $[\mathrm{C^t}]$ = element specific heat matrix, $[\mathrm{K^t}]$ = element diffusion conductivity matrix, $\{T\}$ = temperature vector, $\{q\}$ = sum of element heat generation load and element convection surface heat flow and $[U]$ = displacement vector or structural deformation, $[d_e]$ = displacement matrix, $\{d_{ei}\}$ = displacement at node i (i = 1–20, for 20-node SOLID 186 element), $[N]$ = shape function matrix, $\{N_i\}$ = Shape functions (i = 1–20) and $[E]$ is Elastic constant matrix. Following the above scheme of equations, the components of strain $\{\varepsilon\}$ and stress $\{\sigma\}$ are calculated using Eq. (2). Additionally, the principal stresses $\{\sigma_{1,2,3}\}$ and Von-Mises stress are calculated using Eqs. (3) and (4) respectively.

Boundary Conditions

The heat flux and pressure values are mapped from CFD analysis to structural domain; radiation boundary conditions have been applied with emissivity 0.85 on outer skin and emissivity 0.65 on inner skin. The displacement boundary conditions on the top wall of scramjet combustor have been modelled in accordance with integration of scramjet with airframe by applying displacement constraints along the top surface of scramjet mating with airframe.

Results: Effect of Thermal Barrier Coating

The thermal barrier coating is crucial to reducing temperature faced by the metallic skin. The transient thermal analysis shows a reduction in maximum temperature from 1800 to 1484 K with the use of 0.5 mm thick Yttria-stabilized zirconia (YSZ) coating as shown in Fig. 5. This brings the tem-

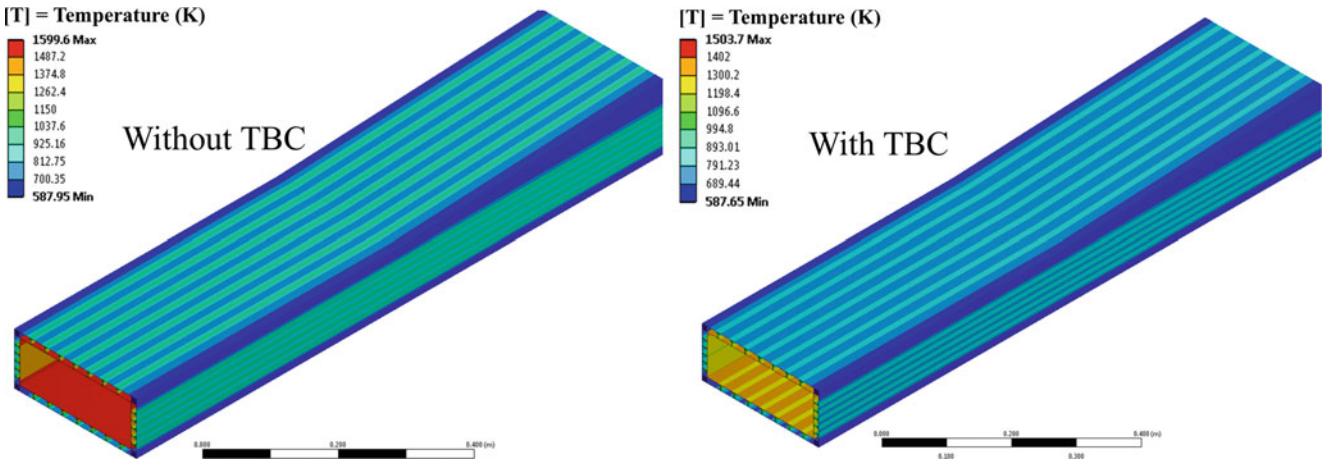

Fig. 5 Transient thermal analysis: Temperature (Kelvin) contour without TBC (left) and with TBC (right)

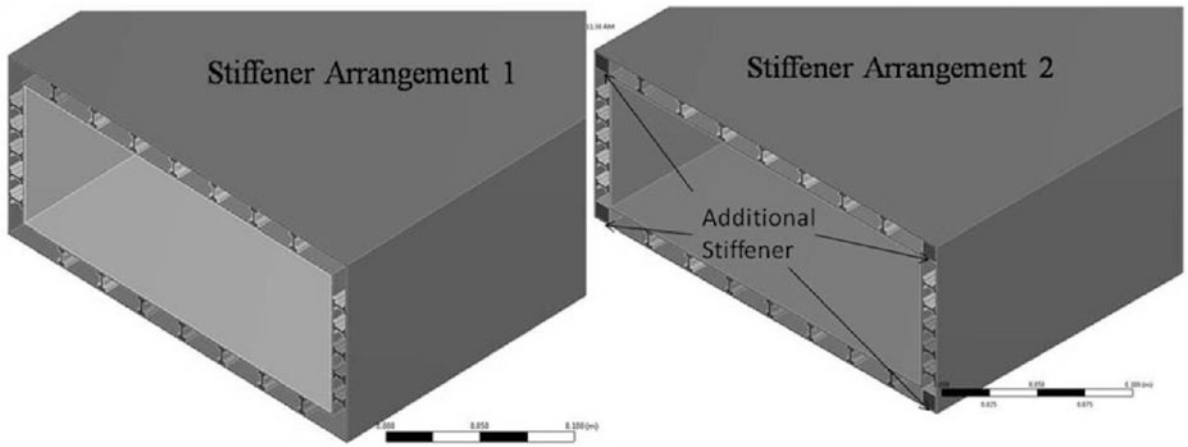

Fig. 6 Stiffener arrangement: view of scramjet from air intake side

perature of inner skin within its maximum operational temperature limit of 1673 K.

Results: Effect of Stiffener Spacing

The stiffeners provide structural rigidity and help in reducing deformation. I cross section stiffeners have been selected owing to their higher moment of inertia and easy manufacturability compared to other cross sections. These stiffeners have been placed longitudinally to arrest deformation owing to higher loads in longitudinal direction. Coupled thermal-structural analysis has been carried out for various stiffener arrangements. Stiffener arrangements are shown in Fig. 6 and the corresponding deformation in Fig. 7. To minimize structural deformation, additional stiffener at corners that have been added as shown in Fig. 6. It can be observed from Fig. 7 shows deformation is further reduced by additional stiffening at the corners. The stiffening has been provided in such a way that there is minimum deformation towards the air intake side to maintain the shock on lip condition for the airframe-integrated scramjet engine. The structural analysis shows deformation of less than 1 mm in scramjet air intake as shown by deformation contours in Fig. 7. For the stiffener arrangement 2, it has been found that skin thickness of 1 mm for inner, outer skin with thermal barrier coating thickness of 500 μm and stiffener spacing of 3 mm is most optimum to contain stress and deformation within the safe limits.

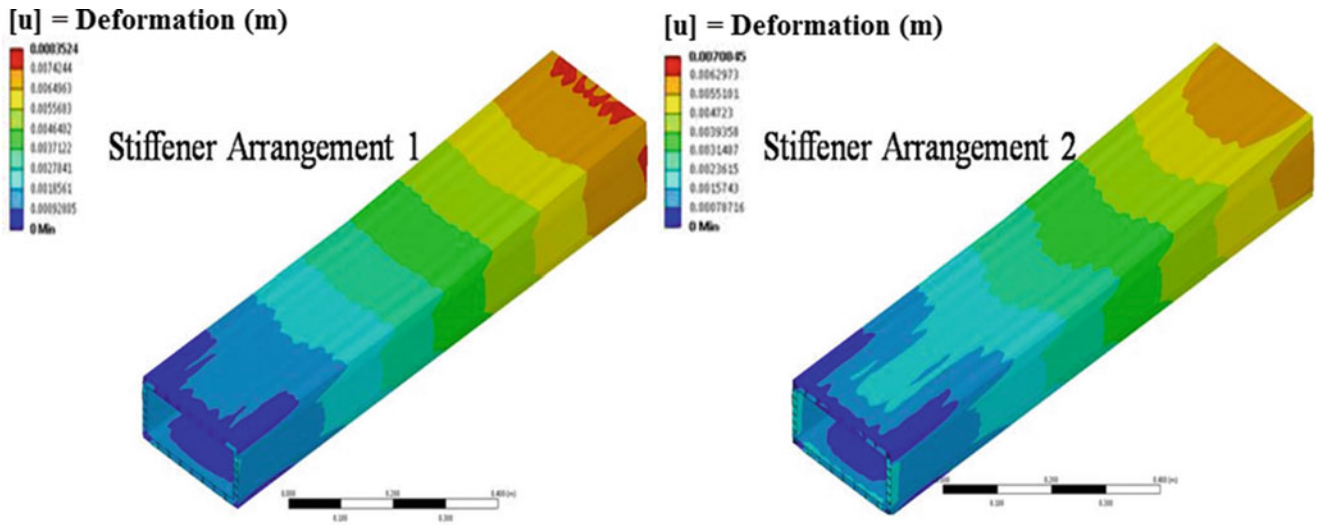

Fig. 7 Coupled thermal-structural analysis: deformation contour (deformation in metres)

Conclusions

The structural design loop for scramjet combustor has been established, and multiple iterations of coupled structural analysis have been performed to study the effect of thermal barrier coating and stiffeners on temperature and deformation experienced by scramjet walls. The results of the thermal-structural analysis clearly show reduction in metal skin temperature by using thermal barrier coating which is in confirmation with works by Clarke [14] and Cao [15]. This work also demonstrates the effectiveness of stiffener in reducing total deformation of scramjet; this is also in agreement with work by Killackey [16], Zuchowski [17] and Antonin et al. [18]. Thus, the agreement of results of the performed thermal-structural analysis with literature establishes the capability of coupled thermal-structural analysis methodology outlined in this work. Other important aspects like selection of suitable material and thermal barrier coating for scramjet application have also been discussed. The same structural design methodology loop can also be extended for the thermal-structural design of the entire hypersonic vehicle.

References

1. Thornton, E.A., Dechaumphai, P.: Coupled flow, thermal, and structural analysis of aerodynamically heated panels. J. Aircraft **25**(11), 1052–1059 (1988)
2. Culler, A.J., McNamara, J.J.: Fluid-thermal-structural modeling and analysis of hypersonic structures under combined loading. In: 52nd AIAA Structures, Structural Dynamics and Materials Conference, 2011
3. Ho, S.-Y., Paull, A.: Coupled thermal, structural and vibrational analysis of a hypersonic engine for flight test. Aerosp. Sci. Technol. **10**(5), 420–426 (2006)
4. Ho, S.-Y., Kotousov, A., Nguyen, P., Harding, S., Codrington J., Tsukamoto, H.: FGM (Functionally Graded Material) Thermal Barrier Coatings for Hypersonic Structures – Design and Thermal Structural Analysis, Source: http://www.dtic.mil/dtic/tr/fulltext/u2/a474097.pdf, Accessed Oct 2014
5. Sobotka, J.C., Oral, A., Culler, A.J.: Towards a coupled loads-response-life prediction framework for hypersonic structures in combined extreme environments. In: 54th AIAA/ASME/ASCE/AHS/ASC Structures, Structural Dynamics, and Materials Conference, 2013
6. Zhao, H.: Low Conductivity Thermal Barrier Coatings. University of Virginia, Source: http://www.virginia.edu/ms/research/wadley/Thesis/HZhaoPhD.pdf, Accessed Oct 2014
7. Cao, X., Vassen, R.: Development of New Thermal Barrier Coating Materials for Gas Turbines, Source: http://juser.fz-juelich.de/record/44814/files/Juel_4127_Cao.pdf, Accessed Dec 2014
8. Di Girolamo, G., Blasi, C., Pagnotta, L., Schioppa, M.: Phase evolution and thermophysical properties of plasma sprayed thick zirconia coatings after annealing. Ceram. Int. **36**(8), 2273–2280 (2010). Doi:10.1016/j.ceramint.2010.07.035. http://www.sciencedirect.com/science/article/pii/S0272884210002877. ISSN 0272–8842
9. ANSYS Documentation, Release 15.0
10. Tohru, M., Kouch, T.: Flame structures and combustion efficiency computed for a Mach 6 scramjet engine. Combust. Flame **142**(3), 187–196 (2005)
11. Kenne, P.J., Donbar, J.M.: Heat flux measurements in a scramjet combustor using direct write technology. In: 17th AIAA International Space Planes and Hypersonic Systems and Technologies Conference 2011
12. Tjong, W.C.: High temperature materials for hypersonic flight vehicle. http://seit.unsw.adfa.edu.au/ojs/index.php/Hypersonics/article/viewFile/21/12. Accessed Jan 2015
13. Pollock, T.: Nickel-based superalloys for advanced turbine engines: chemistry, microstructure, and properties. J. Propul. Power (2006)

14. Clarke, L.: Materials design for next generation thermal barrier coatings, Source: http://topaz.ethz.ch/function/web-het-secured/pdfs/Clarke-03.pdf. Accessed Nov 2014
15. Cao, X., Vassen, R.: Ceramic materials for thermal barrier coatings. J. Eur. Ceram. Soc. (2004)
16. Killackey, K.: Thermal Structural design of an airframe integrated scramjet. NASACR159039,Source:ntrs.nasa.gov/archive/nasa/casi.ntrs.nasa.gov/19800016839.pdf, Page99-135. Accessed Feb 2015
17. Zuchowski, B.: Air vehicle integration and technology research, AFRL-RQ-WP-TR-2012-0280, pp. 100–154, Source:www.dtic.mil/dtic/tr/fulltext/u2/a564268.pdf. Accessed Mar 2015
18. Pistek, A., Pesak, M.: Optimization of stiffened panel with the help of mathematical programming experimental verification. In: 26th International Congress of the Aeronautical Sciences (ICAS), Brno, Czech Republic (2008)

Thermomechanical Deformation Behavior of a Hypersonic Waverider Using Finite Element Method

N.K. Gopinath, V. Vignesh, Yogendra Singh, Manoj Kumar K. Devaraj, and D. Roy Mahapatra

Introduction

Waverider is an aerodynamically derived hypersonic lifting body configuration that effectively rides on the shock waves generated by itself which provides additional compression lift leading to higher lift-to-drag (L/D) ratio. This distinct feature of waverider makes it an attractive candidate for the hypersonic air-breathing cruise mission as compared to conventional vehicle configuration. This was successfully proven in flight by "X-51A Waverider" hypersonic research vehicle [1]. Typically waverider forms the forebody of vehicle airframe which compresses the incoming hypersonic flow through a series of shocks and ingests into the scramjet combustor for adding energy and expands in nozzle to generate positive thrust in order to propel the vehicle. As hypersonic air-breathing cruise vehicle travels within atmosphere, it gleans oxygen from the surrounding rather than carrying it on-board, which enhances the payload mass fraction [2] but at the same time results in extreme thermomechanical loads due to shock waves, air stagnation at leading edges, skin friction along the body surfaces, high dynamic pressures, etc. Such elevated loads exposed to the structure for longer duration may thermally deform the forebody, which can degrade the performance of scramjet engine due to flow distortion at combustor inlet, shift in on-design shock-on-lip condition, etc. Thus, waverider forms critical part of hypersonic cruise system and needs to be analyzed in detail. Costa et al. [3] performed finite element-based structural analysis of hypersonic waverider in unpowered mode at Mach 7 considering aerodynamic pressure loads and acceleration load. Maximum deformation of 1.76×10^{-3} m and maximum strain of 0.48×10^{-3} without any thermal load were reported. Squire and Marschall [4] presented thermomechanical response of wing leading edge made of ultra-high temperature ceramic using finite element method. Based on sequentially coupled analysis approach, the results showed that strain contours closely followed the temperature contour and location of maximum stress was not occurring at the expected stagnation point but at interior regions. Ho and Paull [5] carried out coupled aero-thermo-structural analysis of HyShot scramjet engine at Mach 10 and concluded that the effect of combined thermal and pressure loading resulted in forebody bending by 1×10^{-3} m and predicted von Misesstresses 1–25 % higher than thermal loading. Ko and Gong [6] did thermo-structural analysis on wing structure of the Hyper-X vehicle under Mach 7 condition and presented the structural temperature-time history as well as predicted shear failure of wing and spar welded sites. Falkiewicz et al. [7] analyzed the deformation of control surface at an angle of attack 6° in Mach 8 flow considering thermomechanical loads and observed deformation up to 0.062 m and maximum relative change in lift force to be 1.5 % and that of drag force to be 5.6 %. It can be observed from the literature study that thermomechanical loading critically affects the deformation and stress in hypersonic bodies and needs to be studied in detail. In the present research, finite element (FE) method is used to numerically investigate the effect of combined thermomechanical loading on the deformation behavior of hypersonic waverider. The novelty of this research lies in the development of computational fluid dynamics (CFD) solution coupled with FE methodology to assess the response of hypersonic waverider to heat flux and pressure load.

N.K. Gopinath (✉) • Y. Singh • M.K.K. Devaraj
Centre of Excellence in Hypersonics, Indian Institute of Science, Bangalore 560012, India
e-mail: gopinathnk@aero.iisc.ernet.in

V. Vignesh • D. Roy Mahapatra
Department of Aerospace Engineering, Indian Institute of Science, Bangalore 560012, India

G. Ben-Dor et al. (eds.), *30th International Symposium on Shock Waves 1*, DOI 10.1007/978-3-319-46213-4_41

Hypersonic Waverider Configuration

A power law based wedge-derived sharp-leading-edged waverider is chosen for the study. The waverider consists of two major surfaces, viz., windward surface and leeward surface. The leeward surface of the waverider is designed parallel to the free stream flow, while the design of windward surface follows the streamline generated based on the selected obstructing body, wedge in this case. The power law shape is defined by Wang et al. [8]:

$$y = az^n \tag{1}$$

where n is the power law exponent and a is the constant dependent on n. The waverider geometry and the corresponding design parameters are presented in Fig. 1 and Table 1, respectively.

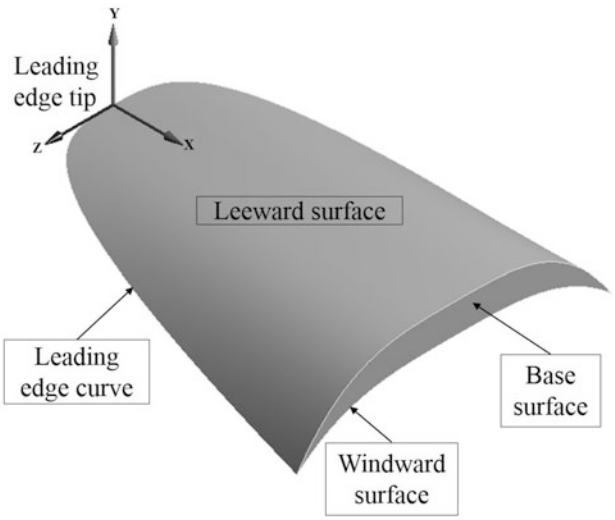

Fig. 1 Hypersonic waverider geometric details

Table 1 Design parameters of waverider

Parameter	Value
Mach number (M)	7
Angle of attack (α)	0°
Power law exponent (n)	0.3
Wedge angle (θ)	5°
Aspect ratio (λ)	1.2
Length (L)—along x axis	0.2 m
Width (W)—along z axis	0.185 m
Height (H)—along y axis	0.042 m
Leading edge radius (R)	Nil

Finite Element Methodology

The coordinates of the waverider obtained from the abovementioned design process is modeled using computer-aided design (CAD) package. The structure of waverider is modeled with FE mesh having ten node-coupled-field solid elements with translational displacement and temperature degrees of freedom. On the meshed structure, thermal load in terms of convective cold wall heat flux obtained from CFD simulation along with initial temperature condition and radiation boundary condition (to ambient atmosphere) is applied. The semi-coupled thermomechanical analysis is carried by applying the load on FE model using FE software package. The nodal temperature at different time instants and pressure load obtained from CFD simulation are mapped on the structure for solving deformation. The general form of the global equation solved for a sequentially coupled thermomechanical analysis is given as [9]

$$\begin{bmatrix} \mathbf{M} & \mathbf{0} \\ \mathbf{0} & \mathbf{0} \end{bmatrix} \begin{Bmatrix} \ddot{\mathbf{u}} \\ \ddot{\mathbf{T}} \end{Bmatrix} + \begin{bmatrix} \mathbf{C} & \mathbf{0} \\ \mathbf{0} & \mathbf{C^t} \end{bmatrix} \begin{Bmatrix} \dot{\mathbf{u}} \\ \dot{\mathbf{T}} \end{Bmatrix} + \begin{bmatrix} \mathbf{K} & \mathbf{0} \\ \mathbf{0} & \mathbf{K^t} \end{bmatrix} \begin{Bmatrix} \mathbf{u} \\ \mathbf{T} \end{Bmatrix} = \begin{Bmatrix} \mathbf{f} + \mathbf{f^{th}} \\ \mathbf{q} + \mathbf{q^{th}} \end{Bmatrix} \tag{2}$$

where [M], [C], and [K] are the mass, damping, and stiffness matrices; [C^t] and [K^t] are the specific heat and diffusion conductivity matrices; {u} and {T} are the displacement and temperature vectors (superscript · and · ·represents first and second time derivative); {f} is the sum of the nodal force and pressure vectors; {f^{th}} is the thermal strain force vector; {q} is the sum of the heat generation load and convection surface heat flow vectors; and {q^{th}} is the applied nodal heat flow rate vector. The parameters used for CFD and FE analysis for the present study are listed in Table 2.

Results and Discussions

During the initial FE analysis, mesh size of 44,341 is used. This was increased in the succeeding analyses to 70,426 and 113,399 in order to assess the sensitivity of the solution (in this case, temperature) to the mesh. Figure 2 shows the centerline temperature distribution on the leeward surface of the hypersonic waverider at the end of 300 s as predicted by varying mesh sizes. As it can be observed, there is very minimal change (<0.2 %) in temperature between mesh sizes of 70,426 and 113,399. Hence, mesh size of 70,426 is selected for this study.

Table 2 Details of parameters used in CFD & FE analysis

CFD	
Mach number	7
Angle of attack	0°
Dynamic pressure	0.3 bar
Reynolds number	0.55 million
Wall condition	Isothermal (300 K)
Solver type	Density based
Analysis type	Steady
Turbulence model	Spalart-Allmaras
Flux scheme	Harten-Lax-van Leer-Contact
Height of the first mesh cell from wall	17 μ-m
FEM	
Material	Niobium C103
Initial temperature	300 K
Analysis type	Transient thermal and static structural
Solver type	Iterative
Analysis time	300 s
Time steps	1 ms to 1 s
Thermomechanical coupling	Volumetric temperature transfer

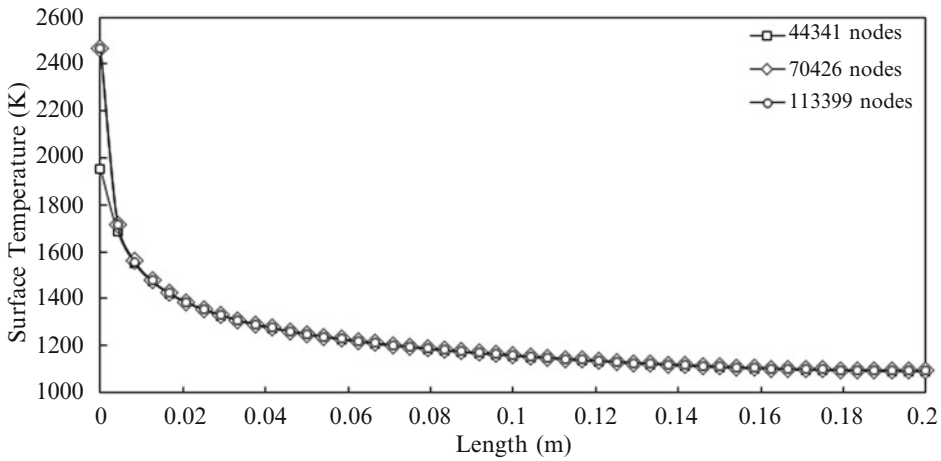

Fig. 2 Mesh convergence study for hypersonic waverider model

The temperature distribution from transient thermal analysis is presented in Fig. 3 along with time history of temperature at nodes located in leading edge tip, i.e., $x = 0$, and in base of the leeward surface along the centerline, i.e., $x = 0.2$ m. As expected, the temperature at $x = 0$ is higher than at $x = 0.2$ m due to air stagnation at leading edge resulting in extreme heat flux of the order of 2.5 MW/m^2. High heat flux at the leading edge makes it to attain thermal equilibrium quickly, whereas the node at $x = 0.2$ m has not reached steady state during the entire simulation time of 300 s.

The deformation pattern obtained from static structural analysis at different time instants is presented in Fig. 4 along with leading edge displacement vs. time curve. As the shock wave is attached along the leading edge curve of waverider, thermal and pressure load becomes asymmetric with respect to the midplane of waverider. As a result, the deformation behavior shows bending of waverider with maximum displacement occurring near the leading edge tip. But the maximum displacement decreases after 33 s, as the thermal gradient between windward and leeward surface causing bending reduces.

The deformation of waverider along the centerline of the leeward surface is presented in Figs. 5 and 6. Increase in deformation with time can be observed in Fig. 5, whereas

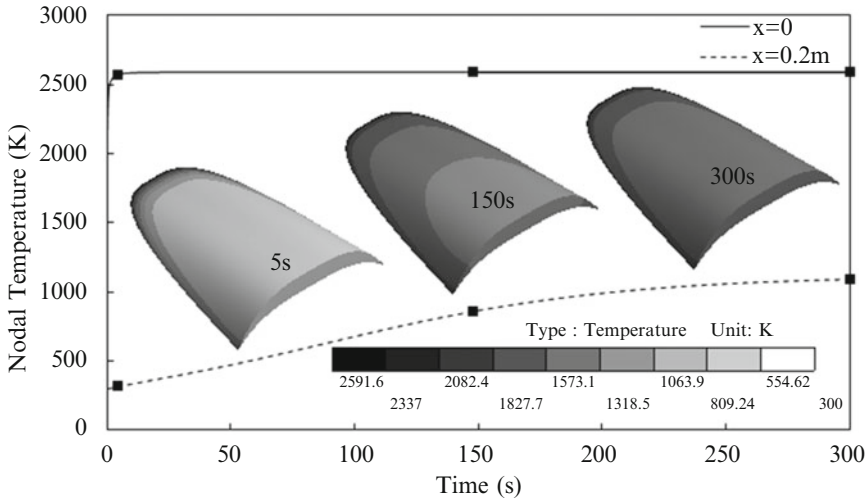

Fig. 3 Temperature distribution of the hypersonic waverider subjected to thermal load

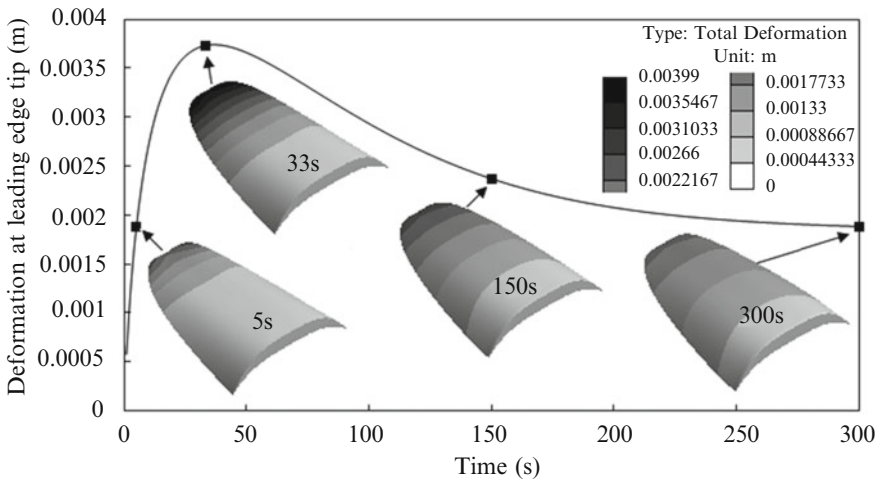

Fig. 4 Deformation of the hypersonic waverider subjected to thermomechanical load

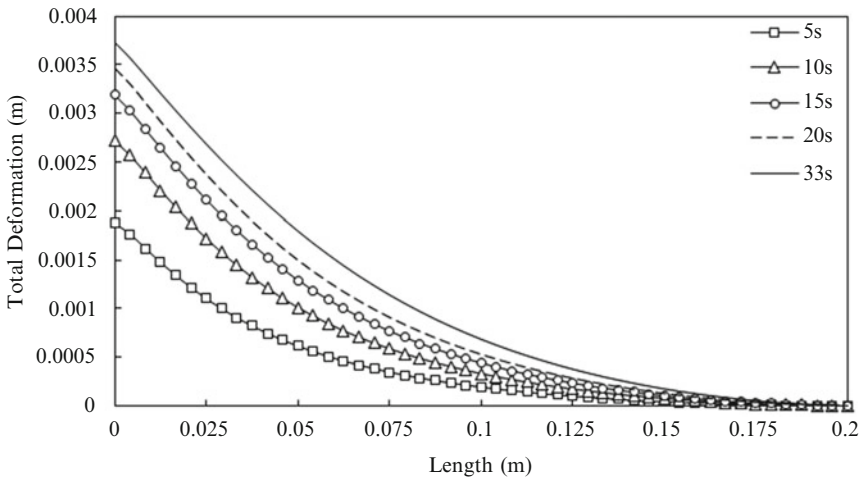

Fig. 5 Deformation trend along the centerline of the waverider leeward surface at various time instants before peak deformation

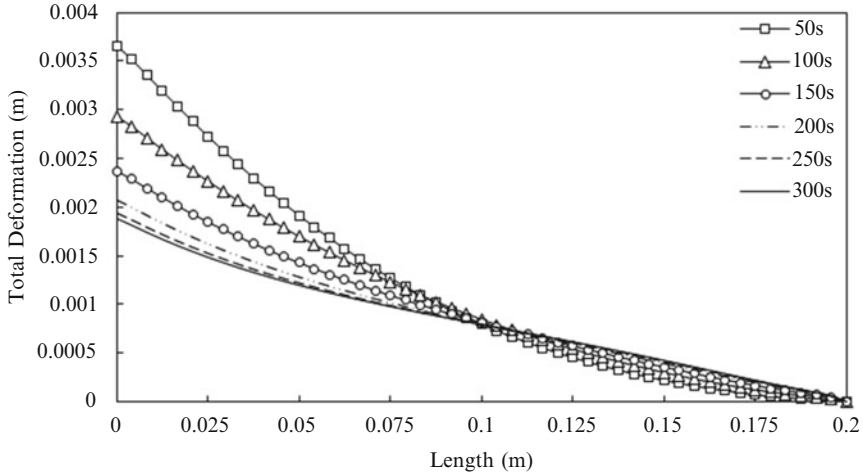

Fig. 6 Deformation trend along the centerline of the waverider leeward surface at various time instants after peak deformation

Fig. 6 depicts decrease in deformation with time, which is found to be in compliance with the results shown in Fig. 4. As compared to the trend before 33 s, an alteration in the deformation behavior can be observed at $x = 0.1$ m. This could be accounted for the fixed boundary condition along the base surface, variation of the thermal gradient between windward and leeward surface, and their combined effect.

Conclusions

Based on this methodology, semi-coupled thermomechanical analysis can be performed on complex three-dimensional bodies with loads estimated through CFD. The obtained temperature distribution and deformation pattern of the Mach 7 hypersonic waverider are in accordance with the underlying physics. Maximum temperature of 2591.6 K and maximum deformation of 3.99×10^{-3} m are found to be occurring at the leading edge location. The present approach can be extended for parametric analysis-based design to understand the relationship between critical deformation/stress and the aero-thermal loading. Important inferences can be drawn in terms of material choices by addressing thermal management issues including control of thermal gradient by designing optimal placement of stiffeners and cooling segments.

References

1. Factsheets: X-51A Waverider, U.S. Air Force (Website link: http://www.af.mil/AboutUs/FactSheets/Display/tabid/224/Article/104467/x-51a-wave rider.aspx), 2013 (accessed 20.04.2015)
2. Heiser, W.H., Pratt, D.T.: Hypersonic Airbreathing Propulsion, pp. 14–17. AIAA Education Series, Washington, DC (1994)
3. Costa, F.J., Toro, P.G.P., Camillo, G.P., Pivetta, A.F.S.: Brazilian 14-X Hypersonic Unpowered Waverider Scramjet Aerospace Vehicle Structural Analysis at Mach Number 7. International Congress of Mechanical Engineering, SP Brazil (2013)
4. Squire, T.H., Marschall, J.: Material property requirements for analysis and design of UHTC components in hypersonic applications. J. Eur. Ceram. Soc. **30**(11), 2239–2251 (2010)
5. Ho, S.Y., Paull, A.: Coupled thermal, structural and vibrational analysis of a hypersonic engine for flight test. Aerosp. Sci. Technol. **10**, 420–426 (2006)
6. Ko, W.L., Gong, L.: Thermostructural analysis of unconventional wing structures of a hyper-X hypersonic flight research vehicle for the Mach 7 mission. NASA TP-2001-210398 (2001)
7. Falkiewicz, N.J., Cesnik, C.E.S., Bolender, M.A., Doman, D.B.: Thermo elastic formulation of a hypersonic vehicle control surface for control-oriented simulation. In: AIAA Guidance, Navigation, and Control Conference, 1–18 (2009)
8. Wang, F.M., Han, H.Q., Lei, M.F., Zhang, J.: Aerodynamic and aerothermal performance of power-law shaped leading edge of hypersonic waveriders. Proc. Eng. **67**, 207–217 (2013)
9. Godoy, P.H., Silva, E.C.N.: Aspects of fabrication and characterization of electro-thermal micro actuators. ABCM Symposium series in Mechatronics, **2**, 517–524 (2006)

Effect of Mach Number on Shock Oscillations in Supersonic Diffusers

S. Manoj Prabakar, Chimakurthy Srikanth, and T.M. Muruganandam

Introduction

Unsteady characteristics of shock wave oscillations are one of the most prevalent phenomena occurring in a supersonic diffuser. In such oscillations, significant boundary layer separation leads to a highly unsteady flow field resulting in inlet instability, aircraft buffeting, and aero-structure fatigue. From an engineering point of view, this phenomenon can have a significant impact on performance of supersonic diffusers operating near critical mass flow because of the complex interaction between the boundary layer and many shock waves. This includes a shock-wave/turbulent boundary-layer interaction (SBLI) followed by a subsonic region with an adverse pressure gradient and rapidly thickening boundary layer.

To understand the behavior of unsteadiness and its effects, extensive study was carried out over a decade focusing on the fluctuating nature of wall-pressure signal in the interaction region by various researchers [1–9]; supersonic SBLIs, unsteady flows, and driving mechanisms are discussed in various review papers [10, 11]. Dussauge et al. [12] investigated the effect of possible sources of unsteadiness from upstream and downstream flow conditions. More recently low-frequency shock oscillations in various flows were studied by Grilli et al. [13] and Clemens et al. [14]. Even though many studies have been performed so far to clarify the mechanism of shock oscillation, the effect of Mach number on these oscillations across a convergent-divergent (C-D) supersonic diffuser is not understood. This work focuses on the effect of Mach number on unsteady behavior of shock wave across the throat of a supersonic diffuser.

Experiments have been conducted to study the characteristics of shock oscillations in a C-D diffuser for Mach numbers between 1.6 and 3.2 and at various stagnation pressures. Objective of this investigation was to obtain structure of shock waves, amplitude of shock oscillations across the throat, shock displacement velocity, and frequency of oscillation at various Mach numbers. Experiments were conducted to indentify major mechanism which contributes to the unsteadiness of shock oscillations. Overall objective of this work is to understand the flow behavior in supersonic diffuser at the start of a supersonic wind tunnel.

Experimental Setup

The experiments were conducted in an open freejet supersonic blowdown wind tunnel at IIT Madras. Schematic of test facility along with the instrumentation is shown in Fig. 1a. Supersonic flow of air was generated by a contoured C-D nozzle in two-dimensional test section of width 40 mm and height 32 mm. Nozzle and diffuser were fabricated in a single block made of mild steel (MS). Geometrical details of the block assembly are given in Fig. 1b. The block was held in proper position by two supporting MS plates (top and bottom), and side walls were made of polycarbonate sheet for better optical access and possible viewing area. Specific design Mach numbers were 1.6, 2.0, 2.2, 2.4, and 3.2, and the Reynolds numbers based on hydraulic diameter will be in the range of 8×10^5–2×10^6. All the blocks for various Mach numbers had the same nozzle exit height and same diffuser geometry. Throat size was decided based on diffuser contraction ratio given by Lukasiewicz [15].

The high-speed schlieren images (with vertical knife edge) were captured using IDT N4-S3 high-speed CMOS camera, at sampling rates (2000–4000 fps). Piezo-resistive transducers (GE DRUCK PMP-4110) were used to measure

S.M. Prabakar • T.M. Muruganandam
Aerospace Engineering Department, Indian Institute of Technology Madras (IITM), Chennai, India

C. Srikanth (✉)
IITM and Scientist at Defence Research and Development Laboratory, Hyderabad, India
e-mail: srikanth.drdo@gmail.com

G. Ben-Dor et al. (eds.), *30th International Symposium on Shock Waves 1*, DOI 10.1007/978-3-319-46213-4_42

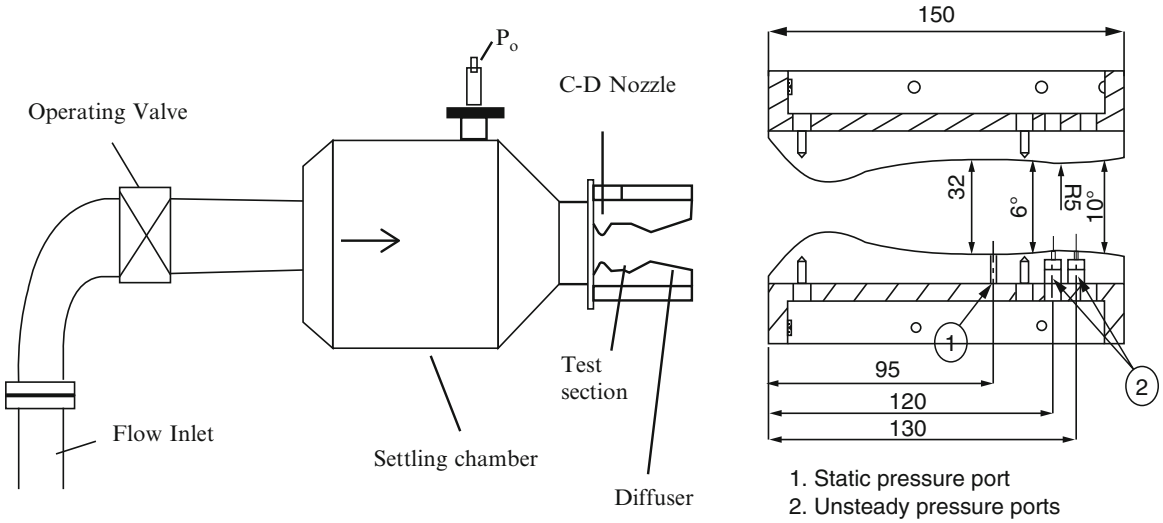

Fig. 1 (**a**) Schematic of test facility. (**b**) Geometrical details of the block assembly

stagnation pressure (P_0) in the settling chamber and static pressure at the exit of the nozzle (p_e), while piezo-electric transducers (PCB 113B28) were mounted on the convergent and divergent section of diffuser for transient pressure measurements [16, 17].

The desired configuration of nozzle blocks is assembled to support plates. Then the side walls are assembled. There are two types of experiments carried out: one with constant P_0 and the other with increasing and decreasing P_0. Several values of constant P_0 cases were taken for each Mach number, such that the shock is located at different points in the diffuser. The variation in flow Mach number is achieved by changing the nozzle blocks. Schlieren method is an easy way to detect the presence of shock oscillations, and it also yields some understanding of the phenomenon. The position of the terminal shock was controlled by varying the chamber pressure.

Results and Discussion

The Mach number upstream of the diffuser was estimated by both pressure and image processing, and they were in good agreement with each other and theoretical value. Figure 2a shows selected images from high-speed schlieren imaging for three different Mach number cases, showing various locations of shock for constant stagnation pressure conditions. While experiments were done for five different Mach numbers, due to space constraints, only three Mach numbers are represented here. It can be seen that the first shock after the inlet is moving across the diffuser throat. This study focuses only on the oscillation of this first shock across the diffuser throat. It can also be seen that there are secondary shocks and boundary layer separations. These features are similar but with different strengths for each Mach number case. The dark black region behind the normal shock in the diffuser is caused by water condensation behind the shock, which blocks the schlieren light path. This phenomenon is also observed by Sudani et al. [18]. Results show that the normal shock oscillates with λ-structure on both sides of the throat, up to Mach 2.2. With further increase in Mach number, transition from Mach to regular reflection takes place across the throat, and the Mach stem decreases and becomes X-structure downstream of the throat. At $M = 3.2$, shock oscillation is not observed across the throat, and X-structure is observed on both sides of the throat.

Figure 2b shows the shock location derived from these high-speed images, through image processing. It can be seen that the shock jumps across the diffuser throat several times. While it appears to be moving at random times and not have any periodicity, there appears to be some weak periodicity which is intermittent, as will be shown later from Fourier analysis. It was observed that the oscillatory behavior was sensitive to stagnation pressure. In fact, by careful adjustment of operating stagnation pressure, it is possible to cause shock oscillations across the diffuser throat. The range of shock travel across the throat depends on Mach number upstream of diffuser. The amplitude of oscillations (Δx) is defined as the maximum distance the shock traverses across the throat within a few cycles.

The variation of Δx with P_0/P_{0c} is shown in Fig. 3. P_{0c} is the minimum pressure required to position the normal shock at the throat of the diffuser, based on one-dimensional frictionless calculations. The plot shows that for each Mach

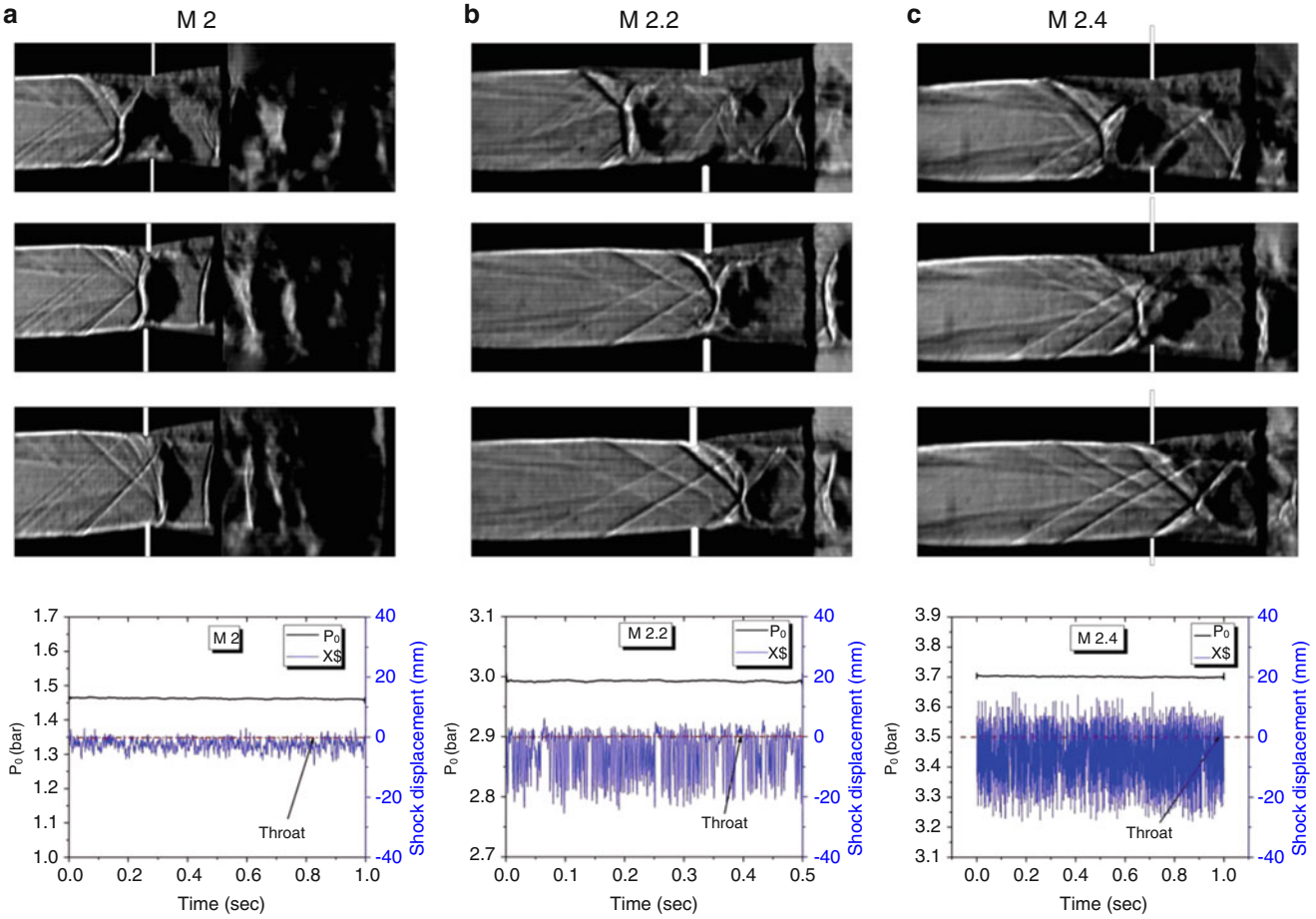

Fig. 2 (**a**) High-speed schlieren images of shock oscillation across the diffuser throat. Flow is from left to right. *Vertical white lines* represent the throat location. (**b**) Time variation of shock location for three different Mach numbers from image processing

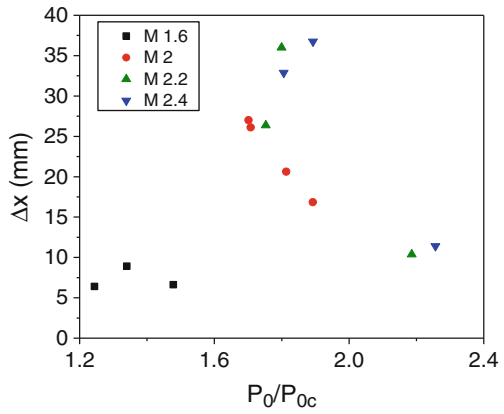

Fig. 3 Effect of Mach number on amplitude of oscillations (Δx) for various P_0/P_{0c}

number, the Δx increases up to certain P_0/P_{0c} and then decreases gradually. Beyond certain value of P_0/P_{0c}, Δx decreases such that the shock oscillates only in divergent section. This trend is observed for all Mach numbers (1.6–2.4). For $M = 2$, there was no data with condition where Δx increases since that data was not taken. It is also evident that with increase in Mach number, the peak Δx also increases.

Frequency of oscillation of shock in convergent region and divergent region of diffuser for different Mach numbers is shown in Fig. 4a. It can be seen that both upstream and downstream pressure transducers pick the same exact frequency of oscillations, even though the quality of peak is not very good. This bad quality of oscillation is due to intermittency observed in the oscillatory behavior. It was also observed from the FFT of shock location from image processing (Fig. 4b) that same peak frequency is observed. It can also be seen that the frequency is not a function of Mach number. However, the amplitude of peak oscillation appears to be increasing with Mach number, similar to the observations from Figs. 2 and 3.

The shock location data derived from the schlieren imaging can also give the velocity of shock movement in the upstream and downstream directions. Table 1 shows the most common shock velocity data for various Mach

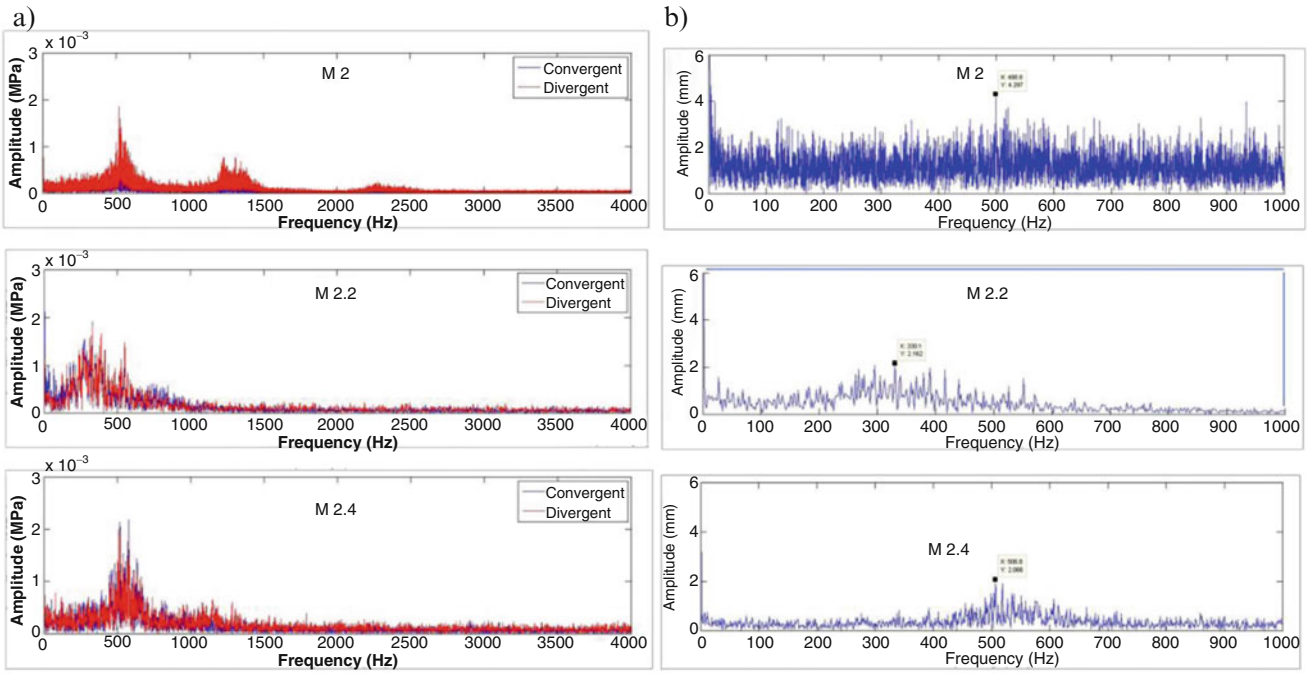

Fig. 4 FFT of (**a**) pressure data in convergent and divergent regions and (**b**) shock location data from high-speed schlieren imaging

Table 1 Shock velocity data for various Mach numbers

Mach number	Upstream shock velocity (m/s)	Downstream shock velocity (m/s)
2.0	20.8	14.7
2.2	17.2	28.3
2.4	31.1	32.3

numbers. This data was obtained by simple differentiation of the temporal shock location data.

This data shows that upstream velocity is typically slower than the downstream movement velocity of the shocks, for all Mach numbers (except for Mach 2). This can be easily explained by the fact that the shock has to go against the flow in the upstream direction. It is also observed that the velocity values in general are higher for higher Mach number cases.

Figure 5 shows a plot of instantaneous shock location versus the stagnation pressure at that instant, during a run where the P_0 was increased and then decreased continuously. It can be seen that at low P_0 values, the shock has only minor jitter in space, and then at some critical value of P_0, the shock starts to jump across the diffuser throat. When the pressure is increased to much higher values, the oscillations are again small in amplitude, and the shock stays in the divergent region alone. On the return phase, the same behavior is observed but at different stagnation pressure values. Thus, there appears to be a hysteresis in this oscillatory behavior.

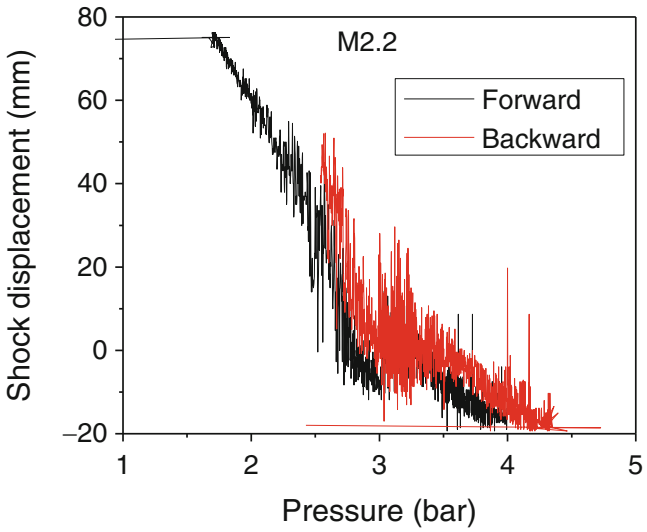

Fig. 5 Temporal variation of shock location derived from images plotted with instantaneous stagnation pressure values

Conclusion

An extensive experimental study in supersonic diffuser at Mach numbers $1.6 \leq M_\infty \leq 3.2$ was performed to investigate phenomenon of shock oscillation across the diffuser throat at various stagnation pressures. Time-varying pressure data at different wall locations on diffuser as well as

high-speed schlieren images were recorded during shock oscillations. It was observed that the shock oscillates very little in the upstream and downstream regions of the diffuser, and when the shock is near the diffuser throat, it oscillates with large displacements across the throat of the diffuser. The shock had λ-structure on both sides of the throat, up to Mach 2.2, and with increase in Mach number, transition from Mach to regular reflection takes place across the throat, and the Mach stem decreases and becomes X-structure downstream of the throat. At $M = 3.2$, shock oscillation is not observed across the throat, and X-structure is observed on both sides of the throat. The range movement of shock across the throat depends on the stagnation pressure, and it increases and decreases with increase in stagnation pressure. It was also observed that the shock oscillation across the throat is intermittently periodic. Fourier analysis shows that the frequency of oscillations is not a function of Mach number, but the amplitude of oscillations increases with Mach number. From the schlieren images, the rate of movement of shock across the throat was calculated. It was found that the shock moves faster in the downstream direction compared to the upstream direction for a given Mach number case. However, the shock velocities were found to increase on both directions with increase in Mach number. Finally, when the stagnation pressure was increased and decreased in a single run, it was observed that the range of pressures where the oscillations occur is not the same in both directions. Work is under process to understand the basic flow of physics.

References

1. Ikui, T., Matsuo, K., Nagai, M.: The mechanism of pseudo-shock waves. Bull. JSME **17**(108), 731–739 (1974)
2. Ikui, T., Matsuo, K., Nagai, M., Honjo, M.: Oscillation phenomena of pseudo-shock waves. Bull. JSME **17**(112), 1278–1285 (1974)
3. Chen, C.P., Sajben, M., Kroutil, J.C.: Shock-wave oscillations in a transonic diffuser flow. AIAA J. **17**(10), 1076–1083 (1979)
4. Bogar, T.J., Sajben, M., Kroutil, J.C.: Characteristics frequencies of transonic diffuser flow oscillations. AIAA J. **21**(9), 1232–1240 (1983)
5. Bogar, T.J.: Structure of self-excited oscillations in transonic diffuser flows. AIAA J. **24**(1), 54–61 (1986)
6. Dolling, D.S., Or, C.T.: Unsteadiness of the shock wave structure in attached and separated compression ramp flows. Exp. Fluids **3**, 24–32 (1985)
7. Matsuo, K., Kim, H.D.: Normal shock wave oscillations in supersonic diffusers. Shock Waves **3**, 25–33 (1993)
8. Matsuo, K., Mochizuki, H., Miyazato, Y., Gohya, M.: Oscillatory characteristics of a pseudo-shock wave in a rectangular straight duct. JSME Int. J. Ser. B **36**(2), 222 (1993)
9. Papamoschou, D., Zill, A., Johnson, A.: Supersonic flow separation in planar nozzles. Shock Waves **19**, 171 (2009)
10. Meier, G.E.A., Szumowski, A.P., Selerowicz, W.C.: Self-excited oscillations in internal transonic flows. Prog. Aerosp. Sci. **27**, 145–200 (1990)
11. Kazuyasu, M., Yoshiaki, M., Heuy-Dong, K.: Shock train and pseudo-shock phenomena in internal gas flows. Prog. Aerosp. Sci. **35**, 33–100 (1999)
12. Dussauge, J.P., Dupont, P., Debieve, J.F.: Unsteadiness in shock wave boundary layer interaction with separation. Aerosp. Sci. Technol. **10**, 85 (2006)
13. Grilli, M., Schmid, P.J., Hickel, S., Adams, N.A.: Analysis of unsteady behavior in shockwave turbulent boundary layer interaction. J. Fluid Mech. **700**, 16–28 (2012)
14. Clemens, N.T., Narayanaswamy, V.: Low-frequency unsteadiness of shock wave/turbulent boundary layer interactions. Annu. Rev. Fluid Mech. **46**, 469–492 (2014)
15. Lukasiewicz, J.: Diffusers for supersonic wind tunnels. J. Aeronaut. Sci. **20**(9), 617–626 (1953)
16. Abhishek, P., Muruganandam, T.M.: Shock movement in a supersonic tunnel with increment in pressure. In: Proceedings of 5th International Conference on Theoretical Applied Computational and Experimental Mechanics (ICTACEM), IIT-Kharagpur, India, 27–29 Dec 2010
17. Jintu, K.J., Muruganandam, T.M.: Dynamics of shock oscillation across second throat of a supersonic diffuser under geometry variation. In: Proceedings of the International Conference on Mechanics, Fluid Mechanics, Heat and Mass Transfer, 2014
18. Sudani, N., Sato, M., Karasawa, T., Noda, J., Tate, A., Watanabe, M.: Irregular effects on the transition from regular to Mach reflection of shock waves in wind tunnel flows. J. Fluid Mech. **459**, 167–185 (2002)

Turbulence Compressibility Effects for Supersonic and Hypersonic Separated Flows

S. Seror and L. Kosarev

By definition, a compressible flow is one in which significant density changes occur, even when pressure changes are small. Generally speaking, compressibility has a relatively small effect on turbulent eddies in wall-bounded flows. This appears to be true for Mach numbers up to about 5 (and perhaps as high as 8), provided the flow doesn't experience large-pressure changes over a short distance such as we might have across a shock wave. At subsonic speeds, compressibility effects on eddies are usually unimportant for turbulent boundary layers provided that $\frac{T_{\text{wall}}}{T_{\text{edge}}} < 6$. Based on these observations, Morkovin [1] hypothesized that the effect of density fluctuations on the turbulence is small provided that they remain small relative to the mean density, that is, $\frac{\rho'}{\overline{\rho}} \ll 1$.

This is a major simplification for the turbulence modeler because it means that, in practice, he needs only to account for the nonuniform mean density in computing compressible, shock-free, non-hypersonic turbulent flows. There are limitations to the applicability of Morkovin's hypothesis even at non-hypersonic Mach numbers. For example, because $\frac{\rho'}{\overline{\rho}}$ is typically not small, it applies neither to flows with significant heat transfer nor to flows with combustion. Also, because density fluctuations generally are much larger in free shear flows, models based on Morkovin's hypothesis fail to predict the measured reduction in spreading rate with increasing freestream Mach number for the compressible mixing layer [2].

S. Seror (✉) • L. Kosarev
Israel Aerospace Industries, Directorate for Research and Development, Engineering Division, CFD R&D Dept. Corporate Research Center – Computerized Systems Branch, Ben Gurion International Airport, Lod 70100, Israel
e-mail: sseror@iai.co.il

Engineering prediction of turbulent flows relies mostly on Reynolds-averaged Navier–Stokes (RANS) simulations that compute the time-averaged flow field. Turbulence closure is obtained using RANS turbulence models which were originally developed for incompressible flows. Several important breakthroughs on compressible turbulence research have been noticed in the works of Smits at Princeton University [3] jointly with the team of Prof. Dussauge at the French CNRS [4] concerning compressible turbulence structure and energetic scales from experiments in supersonic flows like supersonic shear layers and wall-bounded flows. They proposed new model for the dissipation equation in supersonic turbulent mixing layers with high density gradients [5, 6].

Fluid compressibility can remarkably modify the behavior of turbulent flow with respect to the incompressible case. The presence of strong pressure-induced density changes adds to the turbulence phenomenology new specific processes and mechanisms, such as new pathways for energy exchanges, a strong coupling between momentum and energy exchanges, etc., significantly altering the flow behavior.

We note here the main drawbacks of standard models that do not take into account the compressibility:

- They cannot reproduce the equilibrium in the logarithmic layer in the presence of large density gradients and thus result with significant errors on the skin friction coefficient prediction.
- They predict too high skin friction and heat transfer coefficients at separation and reattachment points.
- They predict a too short influence length: the pressure starts to increase too much downstream compared to its measured position.
- They fail to give the size of the separated regions inside the mixing layer and as a consequence to predict the afterbody drag.
- They predict a too high pressure inside the recirculation bubble.

G. Ben-Dor et al. (eds.), *30th International Symposium on Shock Waves 1*, DOI 10.1007/978-3-319-46213-4_43

- They predict an excessive flow deceleration inside the boundary layer after the reattachment.
- They predict a too large mixing layer thickness growth rate.

Many research groups are working on methods of including these compressibility effects in conventional turbulence models to predict more realistically the flow field for compressible conditions. The simplest way is to rewrite the incompressible SA equation [7] with the help of mass-weighted average $\overline{\rho}\widetilde{\nu}$ [8–11], where variations of density were introduced in the viscous diffusion flux via the use of continuity equation. But as it has been shown in [12], this method cannot reproduce the equilibrium in the logarithmic layer when density gradients appear and tend to underestimate the skin friction and the wall heat flux as the Mach number increases.

Seror et al. [10], Catris and Aupoix [13], Paciorri and Sabetta [14, 15], Spalart [16], and Secundov et al. [17, 18] have shown various compressibility modifications for the classical incompressible Spalart–Allmaras turbulence models to predict the effects of compressibility on shear layers, boundary layers, shock-induced separation, shock–boundary layer separation, and other aspects of a flow field.

A separate issue is the interaction of the boundary layer with the shock waves. This problem is common in hypersonic flight, for example, on control surfaces, wing–body junctions, and air-breathing inlets. The shock/turbulent boundary layer interaction can lead to high pressure and high heat flux, as well as regions of separated flow. These play an important role in the design and operation of high-speed aerospace vehicles and propulsion systems, and so it is imperative to predict it accurately. Commonly studied flow configurations include compression corners, cylinder flares, and shock waves impinging on flat-plate boundary layers, single or double fins on plates.

In a shock/turbulent boundary layer interaction, the shock wave oscillates about its mean position in response to the unsteady turbulent fluctuations passing through it; thus, the flow field generated by this interaction is inherently unsteady as demonstrated by experimental works of the team of Dussauge et al. [20–22] on unsteadiness and time properties of turbulence compressible in shock/turbulent boundary layer interactions with separation. The scale of turbulent motion is a function of the boundary layer flow properties, like the Reynolds number, which in turn is expected to influence the scale of shock motion. Turbulence models used in RANS codes usually treat the shock wave as steady, and they do not account for the unsteady motion of the shock. This has been pointed out as one of the major limitations of existing turbulence models [23, 24].

Some recent works to account for shock unsteadiness have been done in the team of Prof. Graham Candler along the works of Sinha et al. [19, 25, 26] who applied the shock-unsteadiness modification used in one- and two-equation turbulence models like the Spalart–Allmaras and $k-\varepsilon$, $k-\omega$ models. The implementation is such that the correction is applied only in regions of strong compression, leaving the original model unchanged otherwise. In supersonic compression corner flows [25], the shock-unsteadiness model reduces the amplification of turbulent kinetic energy at the separation shock. A lower turbulence level enhances flow separation, such that the separation location moves upstream to match experimental measurement. In case of oblique shock impinging on a turbulent boundary layer, the shock-unsteadiness model shows similar improvement. The size of the separation bubble and the wall-pressure distribution match experimental data better than the standard model. The location of the separation shock, its interaction with the incident shock wave, and the resulting pattern of shocks and expansion waves match the experimental schlieren closely [26].

The aim of this work [41] is the verification, validation, and further implementation of relevant compressible corrections to the Navier–Stokes IAI in-house code NES [32–40] within the "baseline" Spalart–Allmaras turbulence model [8–10, 35, 37] in order to:

- Improve the prediction of shocked lambda flow when there is a shock/turbulent boundary layer interaction like in transonic flow at the root wing–fuselage, or in hypersonic flow for cone–flare configurations, or shocked inlet in transonic flows
- Better predict the flow distortion DC(60) and pressure recovery for internal ducted flows at high transonic and supersonic speeds
- Correct over prediction of the eddy viscosity near-curved shocks, one of the causes of carbuncle phenomena which deteriorates heat flux prediction at the stagnation point
- Improve the skin friction and heat transfer coefficient prediction for strongly separated flows at hypersonic speeds

Two different types of flow have been investigated to assess the differences between the compressibility correction models [13–18] that have been implemented within NES. The first type of flow addresses the base pressure enhancement for supersonic after-body computations [27–31] (see Figs. 1 and 2). Then the second type of flow deals with shock/turbulent boundary layer interaction at the junction of a cone–flare configuration for 2D and 3D configurations (see Figs. 3 and 4) using the latest hypersonic

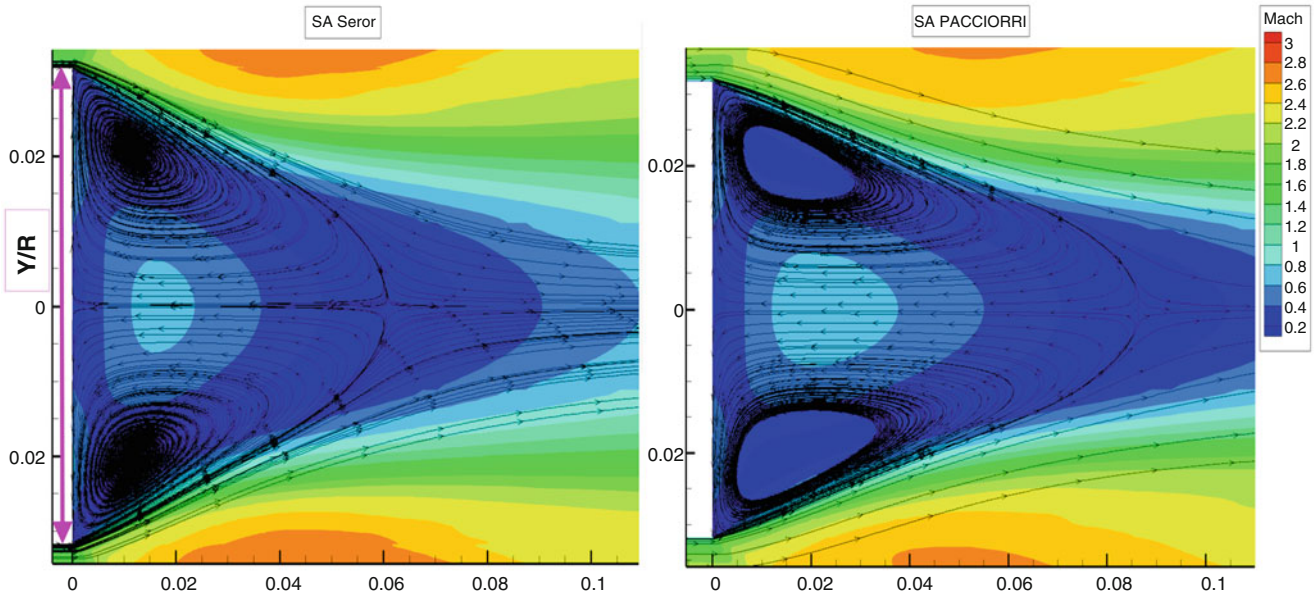

Fig. 1 Comparison of streamlines solutions of axisymmetric backward-facing flow at $M_\infty = 2.46$. "Baseline" SA turbulence model [8–10, 35, 37] (*left*) vs. compressible corrected [14, 15] SA computations (*right*)

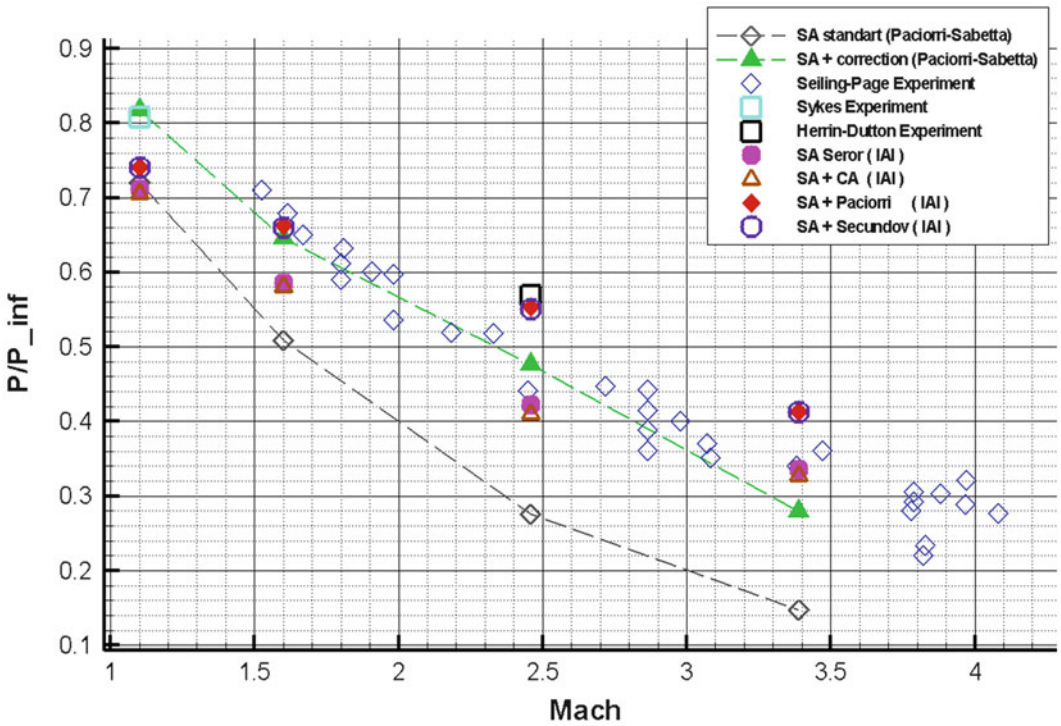

Fig. 2 Comparison of averaged base pressure $^{P}/_{P_\infty}$ versus the Mach number M_∞.

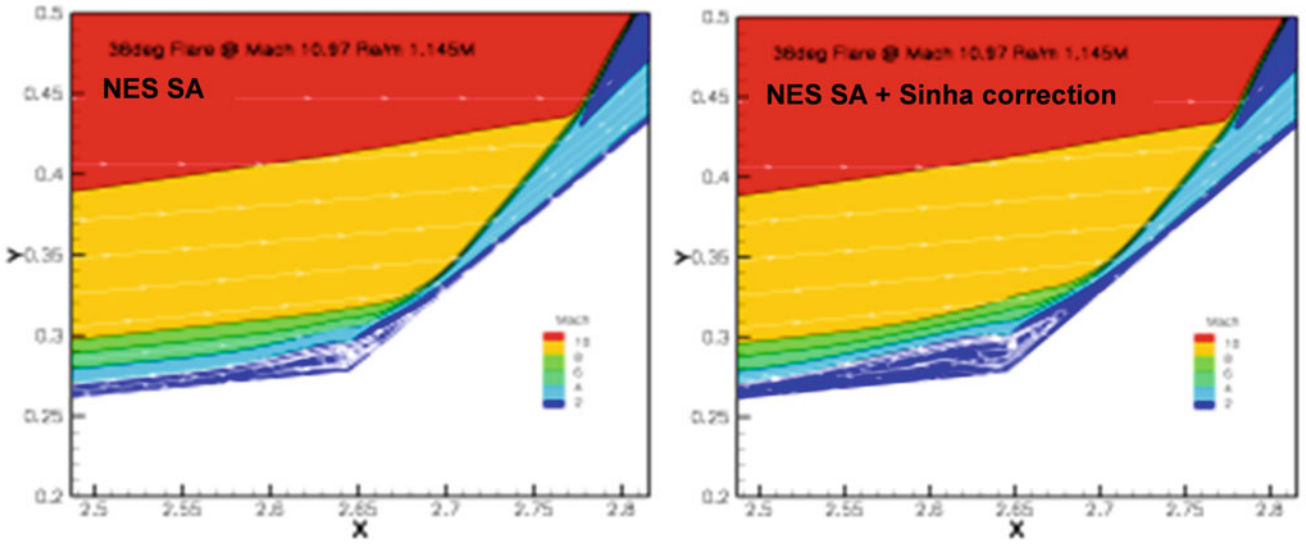

Fig. 3 Mach number & streamlines at corner. CFD NES 3D computation of 36° flared cone at $M_\infty = 10.97$, $\mathrm{Re}/m = 1.145\mathrm{M}$, $AoA = 0°$. "Baseline" SA turbulence model (left) vs. compressible corrected [21, 22] SA model (right).

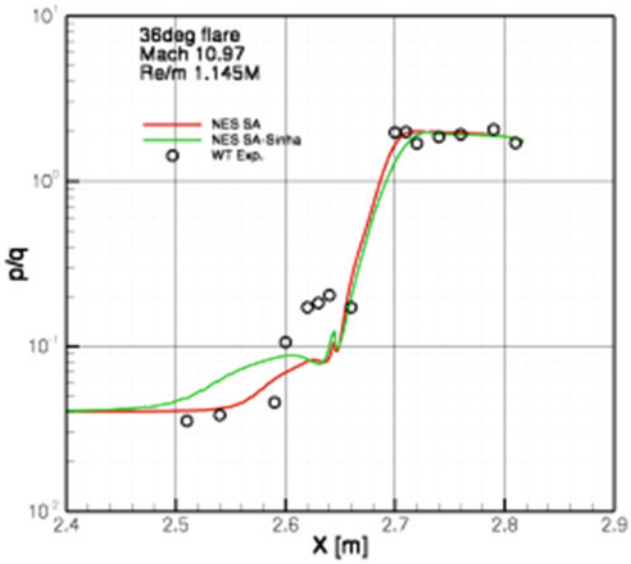

Fig. 4 Normalized pressure distributions on the model. Comparison of WT experiment[23] vs. CFD NES turbulence.

multigrid version of NES developed by Seror [39, 40] that permits to speed up the convergence to steady state by a factor of 5 compared to the grid sequencing solver.

References

1. Morkovin, M.V.: Effects of compressibility on turbulent flow. In: Favre, A. (ed.) The Mechanics of Turbulence, p. 367. Gordon and Breach (1962)
2. Wilcox, D.C.: Turbulence Modeling for CFD. DCW Industries, Inc. (1994)
3. Smits, A.J.: Hypersonic turbulent boundary layers and the need for basic experiments. In: Princeton University Seminar at French CNRS Day Conference on Turbulence and Mixing in Compressible Flow, 7–12 July 2008
4. Dussauge, J.P.: Compressible turbulence and energetic scales: what is known from experiments in supersonic flows? Flow Turbul. Combust. **66**, 373–391 (2001)
5. Guézengar, D., Guillard, H., Dussauge, J.P.: Modelling the dissipation equation in supersonic turbulent mixing layers with high density gradients. AIAA J. **38**(9), 1650–1753 (2000)

6. Debiève, J.F., Dupont, P., Laurent, H., Menaa, M., Dussauge, J.P.: Compressibility and structure of turbulence in supersonic shear flows. Eur. J. Mech. Fluids **19**(5), 597–614 (2000)
7. Spalart, P.R., Allmaras, S.R.: A one-equation turbulence model for aerodynamic flows. In: 30th Aerospace Sciences Meeting and Exhibit, Reno, NV, AIAA paper 92-0439 (January 1992)
8. Séror, S., Rubin, T., Peigin, S., Epstein, B.: Implementation and validation of the Spalart-Allmaras turbulence model in parallel environment. AIAA J. Aircraft **42**(1), 179–188 (2005)
9. Séror, S.: Implementation of a robust laminar/turbulent transition formulation of the Spalart-Allmaras model in NES. In: Proceedings of the 45th Israel Annual Conference on Aerospace Sciences, Tel-Aviv (February 2005)
10. Burtschell, Y., Séror, S., Parisse, J.D., Zeitoun, D.: Numerical Simulation of air/H_2 combustion processes in a scramjet turbulent flow. Progress Comput. Fluid Dyn. **8**(6), 320–330 (2008)
11. Catris, S.: Etude de contraintes et qualification de modèles à viscosité turbulente. PhD thesis, SupAéro (1999)
12. Wilcox, D.C.: Progress in hypersonic turbulence modeling. In: AIAA paper 91-1785, 22nd Fluid Dynamic, Plasmadynamics and Lasers Conference, June 24–26 (1991)
13. Catris, S., Aupoix, B.: Density corrections for turbulence models. Aerosp. Sci. Technol. **4**, 1–11 (2000)
14. Paciorri, R., Nasuti, F., Sabetta, F.: Evaluation of turbulence modelling in supersonic afterbody computations. In: 31st AIAA Fluid Dynamics Conference and Exhibit, AIAA 2001-3039 (June 2001)
15. Paciorri, R., Sabetta, F.: Compressibility correction for the spalart-allmaras model in free-shear flows. J. Spacecr. Rocket. **40**(3), 326–331 (2003)
16. Spalart, P.R.: Trends in turbulence treatments. AIAA paper 2000-2306 (June 2000)
17. Shur, M., Strelets, M., Zaikov, L., Gulyaev, A., Kozlov,V., Secundov, A.: Comparative numerical testing of one- and two-equation turbulence models for flows with separation and reattachment. AIAA 95-0863 (1995)
18. Гуляев, А.Н., Козлов, В.Е., Секундов, А.Н.: К созданию универсальной однопараметрической модели для турбулентной вязкости. Изв. АН СССР, МЖГ, No.4, с. 69–81., in Russian, (1993)
19. Kedia, K.S., Sinha, K.: Effect of Compressibility Corrections to Turbulence Models Applied to a Hypersonic Re-Entry Configuration, NCFMFP2006-1221. In: Proceedings of 33rd National and 3rd International Conference on Fluid Mechanics and Fluid Power, **28** (1), 46–60, India (December 2006)
20. Dupont, P., Debiève, J. F., Ardissone, J.P., Haddad, C.: Sometime properties in shock boundary layer interaction. In: Proceeding: West-East High Speed Flows, pp 392–400, CIMNE first edition (January 2003)
21. Debiève, J.F., Ardissone, J.P., Dussauge, J.P.: Shock motion and state of turbulence in a perturbed supersonic flow over a sphere. J. Turbul. **4**, 026 (2003)
22. Dussauge, J.P., Dupont, P., Debiève, J.F.: Unsteadiness in shock wave boundary layer interactions with separation. Aerosp. Sci. Technol. (2006)
23. Knight, D.D., Degrez, G.: Shock wave turbulent boundary layer interactions in high mach number flows: a critical survey of current numerical prediction capabilities. AGARD Advisory Rept. 319, **2**, 1.1–1.35 (1998)
24. Thivet, F., Knight, D., Zheltovodov, A., Maksimov, A.: Insights in turbulence modeling for crossing shock wave boundary layer interactions. AIAA J. 39(6), 985–995 (2001)
25. Sinha, K., Mahesh, K., Candler, G.V.: Modeling the effect of shock-unsteadiness in shock/turbulent boundary-layer interactions. AIAA J. **43**(3), 586–594 (2005)
26. Pasha, A., Sinha, K.: Simulation of hypersonic shock/turbulent boundary-layer interactions using shock-unsteadiness model. J. Propul. Power **28**(1), 46–60 (January-February 2012)
27. Holden, M.S.: Studies of the mean and unsteady structure of turbulent boundary-layer separation in hypersonic flow. AIAA Paper 1991-1778 (June 1991)
28. Sieling, W.R., Page, R.H.: A Re-Examination of Sting Interference Effect. AIAA 5th Aerodynamic Testing Conference, AIAA Paper 70-585 (May 1970)
29. Sykes, D.M.: Cylindrical and boat-tailed afterbodies in transonic flow with gas ejection. AIAA J. **8**(3), 588–590 (1970)
30. Herrin, J.L., Dutton, J.C.: Supersonic base flow experiments in the near wake of a cylindrical afterbody. AIAA J. **32**(1), 77–83 (January 1994)
31. Settles, G.S., Dodson, L.J.: Supersonic and hypersonic shock/boundary layer interaction database. AIAA J. **32**(7), 1377–1383 (1994)
32. Séror, S., Rubin, T., Epstein, B.: Construction of a multiblock 3D full navier-stokes code for practical aerodynamic computations. In: Proceedings of the 41st Israel Annual Conference on Aerospace Sciences, Tel-Aviv, 231–241 (February 2001)
33. Epstein, B., Rubin, T., Séror, S.: An accurate ENO driven Navier-Stokes solver for complex aerodynamic configurations. AIAA J. **41** (4), 582–594 (2003)
34. Séror, S., Rubin, T., Epstein, B., Arad., E.: Recent enhancement of the 3D Navier-Stokes code NES. In: Proceedings of the 42th Israel Annual Conference on Aerospace Sciences, Tel-Aviv (February 2002)
35. Séror, S., Rubin, T., Peigin, S., Epstein, B.: Development of an accurate multiblock multiface parallel 3d eno driven multigrid cycling Navier-Stokes code NES with the Spalart-Allmaras model for complex aerodynamic configurations. In: Proceedings of the West East High Speed Flow Fields Conference, Marseilles (April 2002)
36. Peigin, S., Epstein, B., Rubin, T., Séror, S.: Parallel large scale high accuracy Navier-Stokes computations on distributed memory clusters. J. Supercomput. **27**, 49–68 (2004)
37. Séror, S.: Parallelization of the Spalart-Allmaras model in NES - Final Status. IAI Internal document (April 2002)
38. Séror, S., Rubin, T.: Drag Prediction of Engine Airframe Interference Effects with NES. In: Proceedings of the 44th Israel Annual Conference on Aerospace Sciences, Tel-Aviv, February 2004 also presented at the 2nd Drag Prediction Workshop, Orlando, Florida, USA (June 2003)
39. Séror, S.: Development of a 3D multigrid solver for accelerating the convergence to steady state of hypersonic viscous flows. IAI internal R&D report 4475/1000/3977 (June 2011)
40. Séror, S.: Two Major Steps Towards a Multigrid Hypersonic Real Gas Version of the Industrial Code NES for Accurate Heat-Transfer Predictions of High Speed Vehicles. In: Proceedings of the 54th Israel Annual Conference on Aerospace Sciences, Tel-Aviv (February 2014)
41. Kosarev, L., Séror, S., Wexler, J.: Compressibility Effects for Turbulence Models at Supersonic and Hypersonic Flow Regimes. Consistency and Implementation of Mathematical Models versus Flow Physics of Strongly Separated Flows. In: Proceedings of the 54th Israel Annual Conference on Aerospace Sciences, Tel-Aviv (February 2014)

Imaging of the Conical Kelvin-Helmholtz Instability

R.T. Paton and B.W. Skews

Introduction

The dynamics of the contact surfaces in compressible flows, specifically shear layers originating in irregular reflections, is an ongoing study with applications in fluid mixing and transition to turbulence. One such instability currently being studied is the Kelvin-Helmholtz instability (KHI).

Originally described by Lord Kelvin [1] and von Helmholtz [2] in the nineteenth century, the majority of the early work was focused on incompressible flows. It took until the later part of the twentieth century for the first detailed experimental studies of Kelvin-Helmholtz instabilities, such as that of incompressible shear layers by Brown and Roshko [3]. Naturally this led to a study of compressible shear layers, where the velocities on either side of the shear layer can be much higher. Papamoschou [4] compared these compressible shear layer results to the incompressible values and compared them using the parameter M^c similar to that derived by Bogdanoff [5] (M^+) to characterise the degree of compressibility of the shear layer. M^c represents the convection Mach number of the vortices within the shear layer.

Around the same time Dimotakis [6] had theoretically examined the entrainment of the fluid by the shear layer as it grows in time given that this mechanism acts to mix the fluids either side of the previously stable shear layer. The approach taken by Rikanati et al. [7] compared experimentally measured shear layer thickness to the theoretical thickness of KHI and suggested that this is a mechanism for shear layer thickening in the compressible flow behind a Mach reflection of a shock wave. However, in this study the structure of the KHI was not visually resolved.

An experimental study which directly resolved the structure of the KHI of the compressible shear layer behind a Mach reflection was undertaken by Rubidge and Skews [8]. Although the measured spread of the shear layer was half of that estimated by Rikanati et al., it demonstrated that the mechanism proposed was not only a plausible but a likely explanation for early thickening of the compressible shear layer trailing a Mach reflection.

Although much has been determined about the behaviour of two-dimensional instabilities, no experimental evidence has previously been found for three-dimensional forms of this instability.

The behaviour of a conical shock wave reflecting off of itself was first studied numerically by Hornung [9] and three reflection regimes defined by the number of Mach reflection lines formed were identified. It was thought that this could not be studied experimentally as the boundary conditions were considered impractical to produce repeatably. Through a shaped focusing of a plane shock wave, an experimental facility was developed which allows for the study of these flow systems. Based on this apparatus experimental studies were undertaken and a fourth reflection pattern was identified [10].

As in all cases of Mach reflection, there is a shear layer which forms in the flow field behind the triple point where the incident shock wave, reflected shock wave, and Mach stem meet, due to the difference in fluid velocity downstream of the reflected shock wave and Mach stem, respectively. In the case of the conical shock wave reflection, this shear layer will itself be conical in form. During some of these experiments of self-reflection of conical shock waves striations of the conical shear layer formed behind the Mach reflection triple line were noted suggesting the existence of a conical KHI.

R.T. Paton (✉) • B.W. Skews
Flow Research Unit, University of the Witwatersrand, PO WITS 2050, Johannesburg, South Africa
e-mail: Randall.Paton@wits.ac.za

G. Ben-Dor et al. (eds.), *30th International Symposium on Shock Waves 1*, DOI 10.1007/978-3-319-46213-4_44

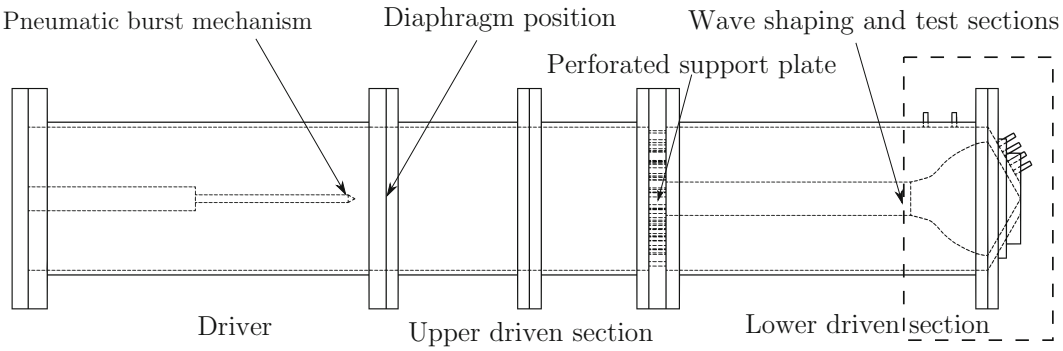

Fig. 1 General arrangement of conical shock tube (*top to the left*)

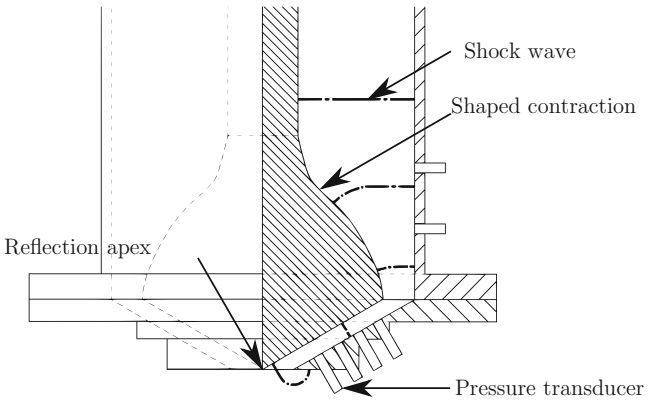

Fig. 2 Detailed view of wave shaping and test sections of conical shock tube showing general change of wave shape

Experimental Setup

Experiments were conducted in the conical shock tube at the Flow Research Unit. This facility turns a plane shock wave produced in a conventional air driven shock tube expanding into ambient conditions into a conical shock wave through focusing around a shaped insert as shown in Fig. 1. The manner in which the plane shock wave is changed into a converging conical wave is shown in Fig. 2.

For this study, diaphragm pressure ratios of approximately 3.6, 5.9, and 8.5 were tested resulting in plane incident shock wave strengths of M1.2, 1.28, and 1.36, respectively. These plane wave speeds resulted in estimated apex Mach numbers of the conical shock waves of M1.4, 1.6, and 1.85, respectively. The flow field was visualised using a conventional z-type schlieren system illuminated by a Canon HX-II flash lamp and images were captured using a Photron SA5-775K operating at a frame rate of 75 kfps and exposure of 1 μs with a frame size of 320 × 264 px.

Results and Discussion

Description of Basic Flow Field

The description of the basic flow field will be based on the images for the Mach 1.2 flow in the left of Fig. 3. In the first figure the shear layer can be seen extending between the triple points (one marked as TP in the figure) of the Mach reflection and the vortex ring toward the centre of the frame. What is referred to as the triple point in this text is logically a triple point ring for an axisymmetric flow but the term triple point is retained for ease of comparison with two-dimensional flow field terminology. While there are other vortex rings shed from the outer diffraction lip at later times for most of the Mach numbers, the vortex ring of interest here is the first one caused by the axial jet formed when the shock wave first reflects at the reflection apex.

It should be noted that the shape seen here of the line connecting the tangent edges of the shear layer defines a concave cone where the outer edges of the cone are at the same level as the protruding portion closer to the centreline. The angle between the incident, reflected, and Mach stem waves is already quite shallow at this time. While some striations are visible in the shear layer near the centreline, the tangent edge of the shear layer still appears smooth.

In the second image, there is noticeable striation of the tangent of the edge of the shear layer suggesting a KHI. The shear layer is still a concave cone but the entire cone now appears to extend away from the plane of the base defined by the outer edge and the curvature is noticeably lower than at earlier times.

In the third image the outer edge region of the shear layer is becoming indiscernible and the inner section seems to be approximately a plane cone. There is noticeable striation of the tangent edges of the shear layer and the striations running through the centre of the image seem to link dark points in

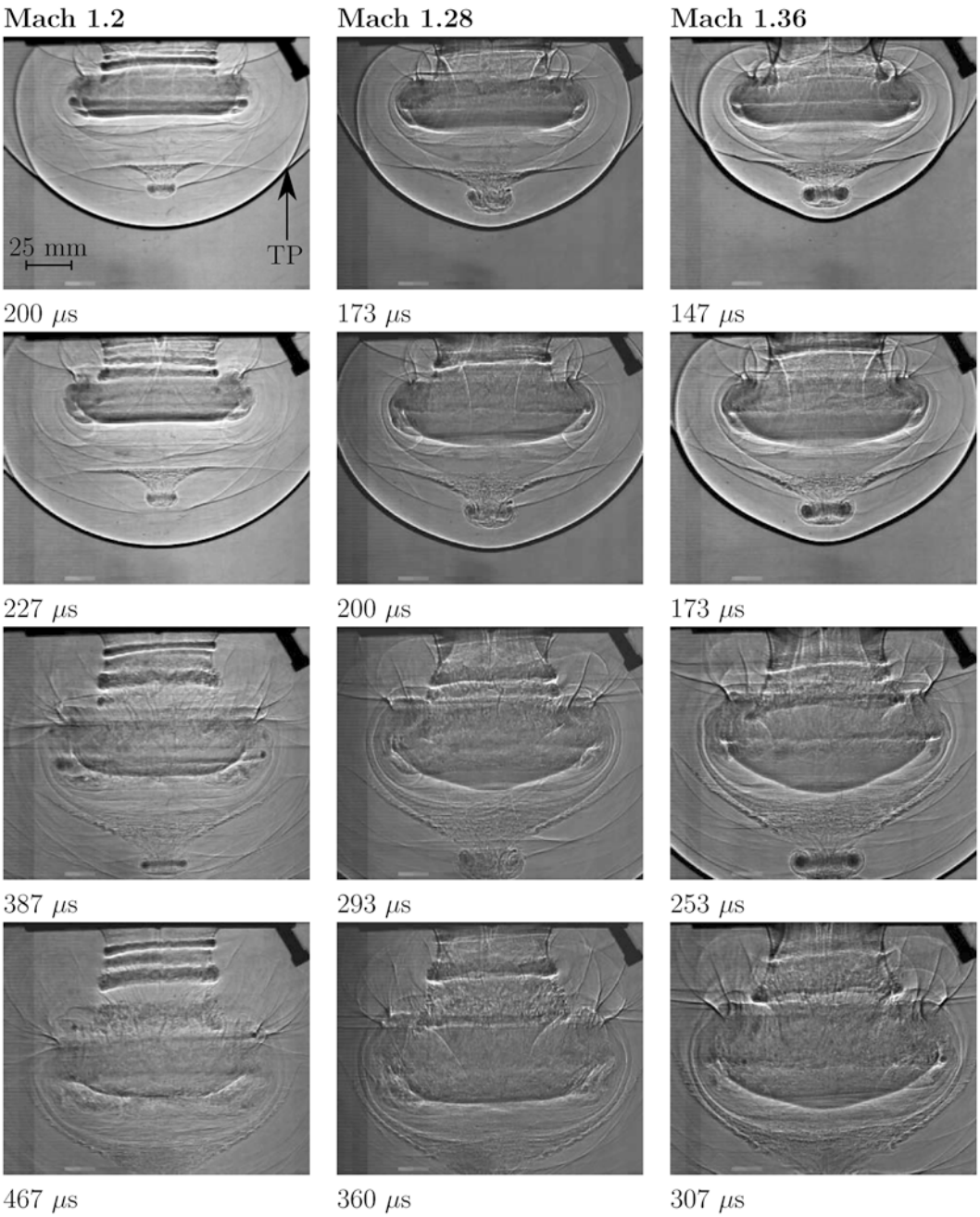

Fig. 3 Schlieren images of the flow field for Mach 1.2 (*left*), 1.28 (*centre*), and 1.36 (*right*) when: the shear layer is first clearly visible (*top*); the tip of the shear layer reaches the edge of the frame (*top-middle*); the central vortex reaches the edge of the frame (*bottom-middle*); and the shear layer conforms to the central plume (*bottom*). Times given are the approximate time since the first arrival of the incident shock wave at the reflection apex

each of the tangent edges, suggesting that a Kelvin-Helmholtz instability has indeed formed as a series of vortex loops.

In the final image the shear layer is now a convex cone conforming to the shape of the central plume resulting from the flow toward the reflection apex.While the portions closest to the centreline of the shear no longer show much evidence of KHI, likely as a result of the vortex ring below it out of frame, the middle portion still shows indications of the instability though the striations linking dark nodes in the tangent edges are difficult to discern through the distortions of the central plume.

Comparison of Flow Field for Different Incident Wave Strengths

There are two notable differences in the behaviour as the Mach number increases: the Kelvin-Helmholtz instability is visible at earlier times and the shear layer cone is less concave initially. The first aspect is evident in the first images of the flows for the Mach 1.28 and 1.36 flows, respectively, where the amplitude of the perturbation of the shear layer by the KHI is noticeably larger for the higher Mach number suggesting that the instability has been present longer.

The change in curvature of the shear layer surface can be attributed to the higher convection speed of the axial flow for the higher initial Mach number since the central portion of the shear layer is entrained in the axial vortex ring. It can also be seen in the early images that the shock wave for the higher Mach numbers has greater curvature than for the lower Mach numbers and so the vertical distance travelled by the Mach line is less and hence a steeper shear layer cone geometrically. There is also a noticeable discontinuity in the slope of the shear layer in the first frame of the Mach 1.36 data though the cause of this is not immediately apparent.

Comparison to Two-Dimensional Flow Field

The most significant difference between the conical and two-dimensional Kelvin-Helmholtz instabilities is that the scale of the instability seems larger for comparable Mach numbers. However, the portion of the shear layer affected by the instability seems to be limited to the flatter portions of the conical surface (i.e. with minimal radial curvature) while the entire two-dimensional shear layer shows signs of instability (Fig. 4).

The conical KHI also shows signs of discontinuities in the slope of the shear layer but the origin of this is uncertain. This feature causing this discontinuity also appears to cause a change in the stability of the shear layer since the KHI is evident in the region between the axis and the discontinuity while the shear layer between the triple point and discontinuity seems unperturbed. This behaviour is also evident at lower Mach numbers even without the discontinuity in shear layer radial slope and so this may be unrelated.

Another possible cause of the greater stability of the portions of the shear layer farther from the axis may be due to the change in the shear along the shear layer. As the shock waves expand from the reflection apex the strength decreases so that the velocity immediately behind the shock wave farther from the axis is much lower. As part of this the slope between the incident wave and Mach disk decreases and so the difference in velocity between the two sides of the shear layer must decrease. Eventually the Mach disc, incident wave, and reflected wave will merge into a single continuous wave and the shear layer will terminate.

These two factors combined mean that the absolute shear across the shear layer decreases quite quickly as the waves expand. This also explains the greater portion of the shear layer length affected by the KHI for higher Mach numbers. Given the small range of Mach numbers tested in this experiment it is clear that the behaviour of the conical KHI is very sensitive to the Mach number of the incident wave.

Conclusion

The existence of the conical Kelvin-Helmholtz instability has been demonstrated experimentally. The local radial curvature of the shear layer seems to stabilise the shear layer in that the KHI does not seem to appear on highly curved conical shear layers. The KHI also appears to occur only in regions fairly close to the axis of the shear layer since the local shear for portions farther from the axis is lower and hence these parts of the shear layer remain laminar. While the amplitude of the KHI seems to grow with time, the length of the portion of the shear layer affected by the KHI grows initially and then seems to decrease again as the shear layer grows.

Much of the description of this phenomenon remains speculative. Further data processing of the experimental

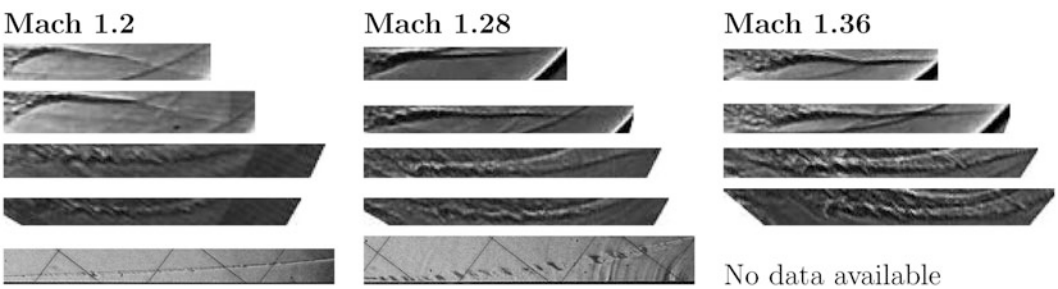

Fig. 4 Detailed view of the development of the Kelvin-Helmholtz instability along the tangent edge of the shear layer (axis to the left) as well as a comparison of the developed instability for the nearest Mach number for the plane wedge case in Rubidge [8]

data should be undertaken and a second experiment using a visualisation technique such as focusing schlieren should be conducted to consider only a tightly defined plane of through the flow field. Understanding of the flow field gathered by these means should be complemented by suitable computational fluid dynamics models though these are beyond the current capability of the group.

Acknowledgements This work was performed utilising funding from South African National Research Foundation grants 75249 and 80816.

References

1. Thomson, W.: Hydrokinetic solutions and observations. Lond. Edinb. Dubl. Phil. Mag. **42–281** , 362–377 (1871)
2. Helmholtz, H.L.F.: Monthly reports of the royal Prussian academy of philosophy in Berlin **23** , 215-228 (1868)
3. Brown, G.L., Roshko, A.: On density effects and large structure in turbulent mixing layers. J. Fluid Mech. **64** , 775–816 (1974)
4. Papamoschou, D., Roshko, A.: The compressible turbulent shear layer: an experimental study. J. Fluid Mech. **197** , 453–477 (1988)
5. Bogdanoff, D.W.: Compressibility effects in turbulent shear layers. AIAA **21–6** , 926–927 (1983)
6. Dimotakis, P.E.: Two-dimensional shear-layer entrainment. AIAA **24–11** , 1791–1796 (1986)
7. Rikanati, A., Sadot, O., Ben-Dor, G., Schvarts, D., Kuribayashi, T., Takayama, K.: Shock-wave Mach-reflection slip-stream instability: a secondary small-scale turbulent mixing phenomenon. Phys. Rev. Lett. **96–17** , 1–4 (2006)
8. Rubidge, S.R., Skews, B.W.: Shear-layer instability in the Mach reflection of shock waves. Shock Waves **24–5** , 479–488 (2014)
9. Hornung, H.G.: Oblique shock reflection from an axis of symmetry. J. Fluid Mech. **409** , 1–12 (2000)
10. Paton, R.T., Skews, B.W., Rubidge, S.R., Snow, J.: Imploding conical shock waves. Shock Waves **23–4** , 317–324 (2012)

Shock Standoff Distance over Spheres in Unsteady Flows

T. Kikuchi, Kazuyoshi Takayama, Dan Igra, and J. Falcovitz

Introduction

A bow shock appears in front of a blunt body placed in a steady supersonic flow. When the flow speed is approaching to sonic one, its standoff distance would tend to be elongated. This is one of the fundamental topics of high-speed gasdynamics, and hence many researches have been reported, for example, in 1 and 2. Van Dyke [3] reviewed works before 1958, and Liepmann and Roshko [4] summarized previous experimental results in their book.

Related to the atmospheric reentry problem, the shock standoff distance over spheres typically represents the degree of the real gas effect in air in intermediate hypersonic flow ranges. This can be studied by using a ballistic range. Hence we visualized, by using double-exposure holographic interferometry, bow shocks over spheres at 3–4 km/s launched in a ballistic range [5]. We then reproduced the free flight of 40 mm diameter spheres at transonic speed ranges and visualized flows over the spheres shock quantitatively with double-exposure holographic interferometry [6, 7]. We confirmed that the shock standoff distance was elongated in approaching the Mach number of the spheres toward unity. However, the bow shock appeared at finite standoff distance even in high subsonic free flight Mach number. We then observed, by using direct shadowgraph with sequential high-speed video recording, the free flight of 10 mm diameter spheres. This paper summarizes the shock standoff distance of spheres at transonic free flights.

T. Kikuchi
Nihon University, Tokyo, Japan

K. Takayama
Emeritus Tohoku University, Sendai, Japan

D. Igra (✉)
RAFAEL, Aerodynamics Group, P.O.B. 2250 Haifa 31021, Israel
e-mail: danigra@gmail.com

J. Falcovitz
Institute of Mathematics, The Hebrew University of Jerusalem, Jerusalem, Israel

Experiments

Figure 1 illustrates the main structure of the present ballistic range as already described by Kikuchi et al. [6]. The experiments were performed in atmospheric air at room temperature. The sphere speed was measured at 1205 mm in front of the observation windows but does attenuate not more than 1 % from that estimated at the observation section. In order to assure the effect of the projectile attenuation on the shock standoff distance, we performed series of direct shadowgraph observation and record the images with a high-speed video camera (Shimadzu Ltd.) at framing rate of 500,000 frames/s. The sphere speed and the shock standoff distance were collected directly from the images.

Results and Discussion

In Fig. 2, see one of the interferograms of a 40 mm sphere: the free flight Mach number, Ms of 0.998, and the Reynolds number Re in terms of the diameter of 0.92e6. The bow shock appeared at a finite distance δ even in subsonic flows, whereas in steady flows, it never occurs over subsonic blunt bodies!

In Fig. 3, we summarize dimensionless shock standoff distances δ/d in the ordinate and Ms in the abscissa. The present interferometric data are shown in red circles. The black circles [5] were collected by ballistic range experiments, and data in yellow circles [2], white circles [3], and blue circles [4] were collected by wind tunnel experiments. It is noticed that δ/d tends to diverge when Ms approaches to unity. However, in free flight experiments, as seen in Fig. 2, δ/d remains finite even in high subsonic

G. Ben-Dor et al. (eds.), *30th International Symposium on Shock Waves 1*, DOI 10.1007/978-3-319-46213-4_45

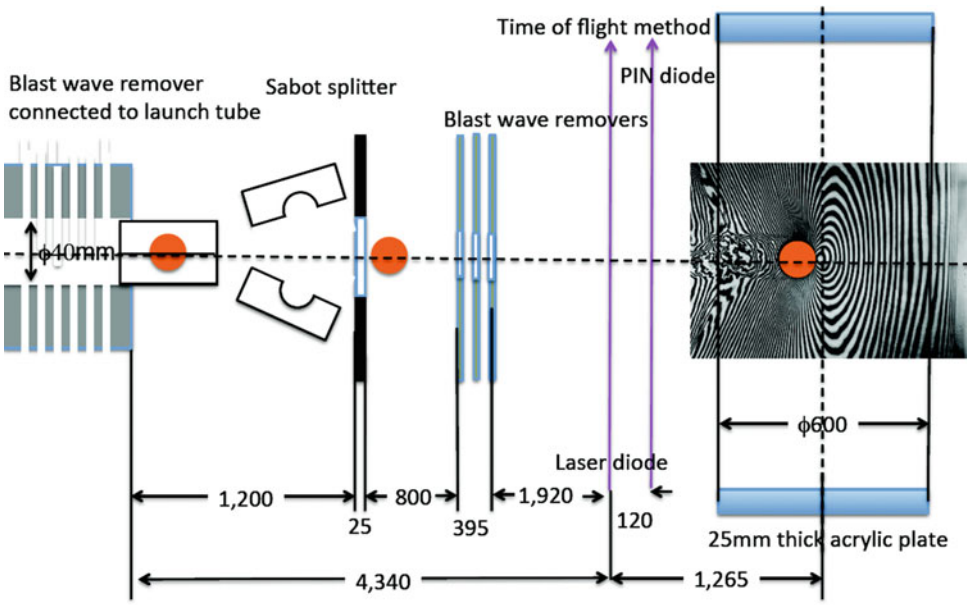

Fig. 1 Schematic illustration of the test section

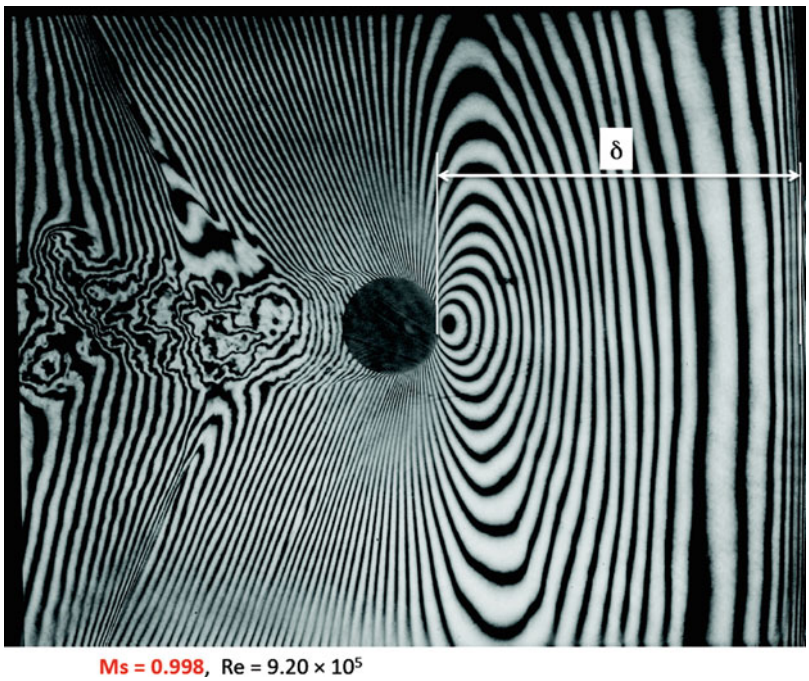

Fig. 2 The presence of a bow shock in front of a subsonic sphere, Ms = 0.998 and Re = 0.92e6 in terms of sphere diameter

free flight, where d is the sphere diameter. The region filled within orange color designates the area under study.

Figure 4 shows selective images of the high-speed video recording of a 10 mm diameter high subsonic sphere. Its initial Mach number was Ms = 0.949, while it resulted in Ms = 0.939 after moving 500 mm. Even ahead of the subsonic sphere, a bow shock was built up. It was not necessarily complete straight shock but slightly curved.

In Fig. 5, see the time variation of the position of the sphere in red circle and the bow shock in green circles. The variation of the corresponding δ/d in blue circles with time was shown in the ordinate at the left-hand side. In propagating for 500 mm, δ/d varied from about 11 to 16 with the decrease of shock wave Mach number.

Figure 6 summarizes the results of the present experiments. The ordinate designates δ/d and the abscissa

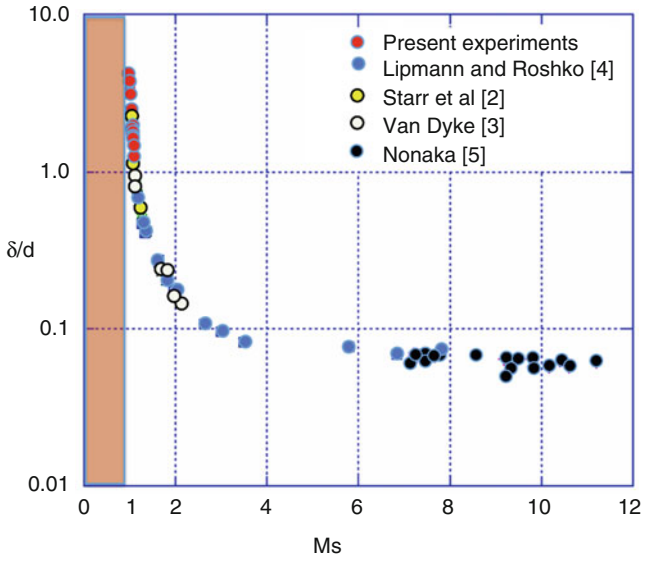

Fig. 3 Present interferometric results and their comparison with previous results

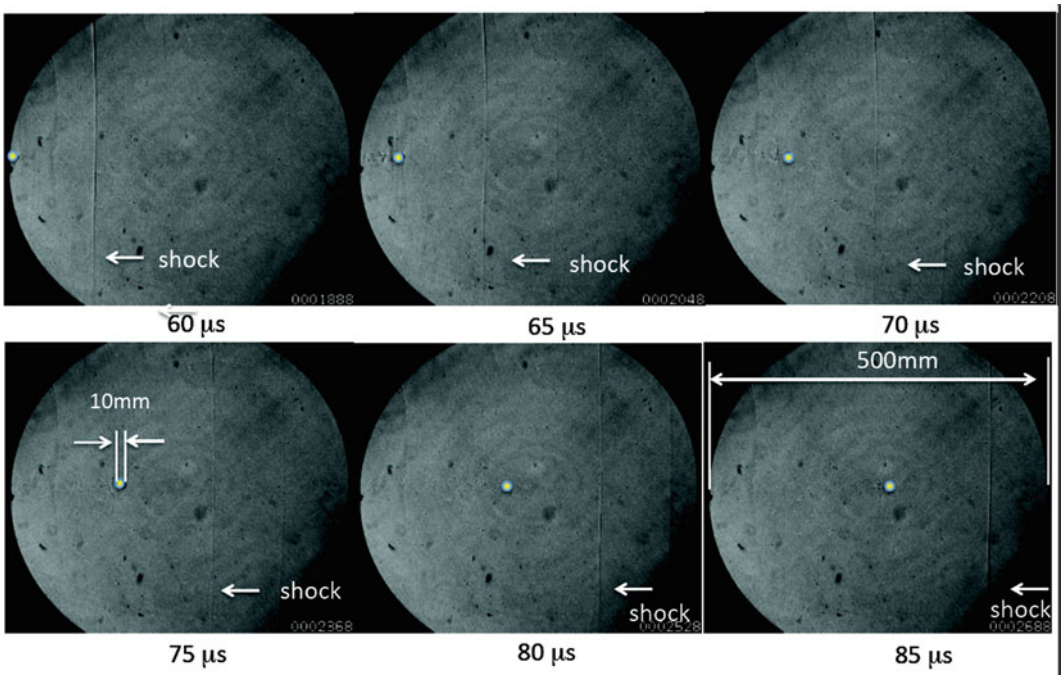

Fig. 4 High-speed images at 60, 65, 70, 75, 80, and 85 μs from the entry

Ms of free flight spheres. Blue circles show the results collected from high-speed images, and red circles show the results collected from interferograms.

We conclude that, unlike the steady flow theory, bow shocks exist and are detached even the head of the subsonic blunt body sphere in unsteady flows. The fact we conclude never contradicts memoirs of an experienced artillery office [8]. He could estimate whether or not enemy shells arrived at him or somewhere else. At that time the overpressures driven by the shells were not those of simple sound waves but of weak shock waves. In out terminology, the shock standoff distance would have been well over 1000. In steady flow experiments, we know that technically not wind tunnel could create flows exactly at Ms = 1.0.

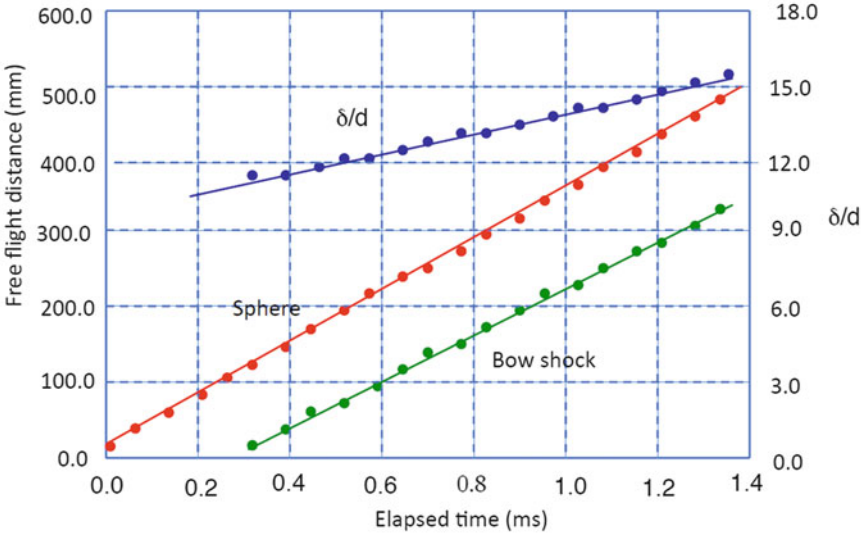

Fig. 5 Positions of spheres and shock waves with time and resulting δ/d

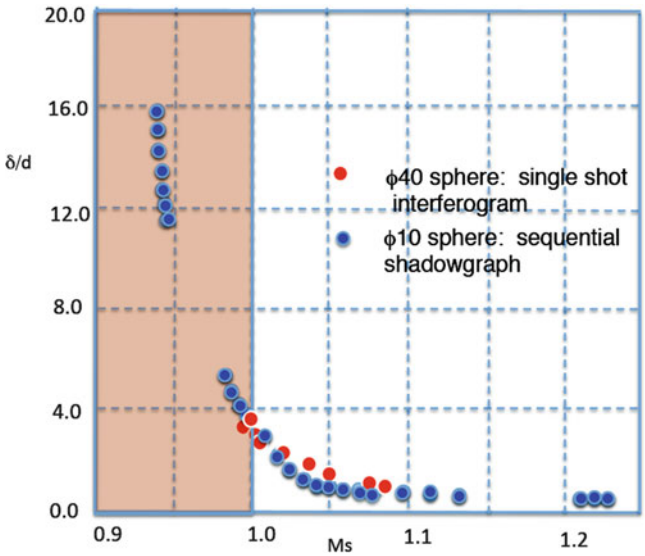

Fig. 6 Summary of variation of δ/d with Ms collected in the present ballistic range tests

Conclusions

Bow shocks are driven in front of subsonic blunt body in unsteady flows. Gasdynamicists must be careful to distinguish unsteady flows from the steady flow theories.

References

1. Herberle, J.W., Wood, G.F., Gooderum, P.B.: Data on shape and locations of detached shock waves on cones and spheres. NACA TN 2000 (1950)
2. Starr, R.F., Railey, A.B., Varner, M.O.: Shock stand-off distance at near sonic speeds. AIAA J. **14**, 537–539 (1976)
3. van Dyke, M.D.: The supersonic blunt-body problem – review and extension. J. Aeronaut. Sci. 485–496 (1958)
4. Liepmann, H.W., Roshko, A.: Elements of Gasdynamics. Wiley, New York (1957)
5. Nonaka, S., Mizuno, H., Takayama, K.: Shock standoff distances over spheres in a ballistic range. J. Thermophys. Heat Transfer **14**, 275–279 (2000)
6. Kikuchi, T., Numata, D., Takayama, K., Sun, M.: Shock standoff distance over spheres flying at transonic speed range in air. Proceeding of the ISSW26, 516–520 (2008)
7. Falcovitz, J., Kikuchi, T., Takayama, K.: Shock over spheres in unsteady near-sonic free flight. Proceeding of the ISSW26, 1461–1466 (2008)
8. Ben-Dor, G.: Private communication (1977)

Part V

Supersonic Jets

The Formation of Mach Waves from Supersonic Jets with Outer Co-flowing

H. Oertel sen., F. Seiler, and J. Srulijes

Introduction

Optical studies of regular Mach waves inside and outside of supersonic jets, published by Oertel [1] in 1978, have shown that their angles, shock distances, and shock compressions depend quite simply on the jet data. At that time, it had long been known that a bypass reduces the noise of jet engines [2], i.e., that a subsonic jet cowling changes the angle of the Mach waves outside of the jet and, at well-defined jets' conditions, can completely prevent the occurrence of the periodic Mach waves in the flow's environment. Especially Oertel [3] and Oertel and Patz [4] conducted extensive experiments with supersonic free jets surrounded by a subsonic envelope. These experiments showed that by reasonably adapted secondary jet conditions, the primary Mach waves can be largely suppressed. Figure 1 shows shock tube visualizations [4] of a supersonic air jet at Mach number $M_i = 2$, a single jet in Fig. 1a, and with surrounding air moving at Mach number $M_a = 0.79$ in Fig. 1b. The Mach waves are almost suppressed in Fig. 1b, as predicted by the theory presented in this paper.

Noise reduction is important for supersonic aircraft exhausting jet engines and other noisy supersonic jet devices, e.g., burners, cutting torches, and oxygen injection systems in the steel industry. For many decades studies of noise suppression with surroundings of coaxial jets were carried out to investigate this effect, e.g., with supersonic jets [5]. It was found that a variety of gas cowlings can dampen the noise, showing that a surrounding secondary jet can diminish the primary supersonic jet noise exerted by the Mach waves to the outer space. Nevertheless, suppression of supersonic jet noise is still a challenge and continues to animate scientists to study this phenomenon in detail, among others, Papamoschou [6, 7], Papamoschou and Debiasi [8], and Rossman et al. [9]. Especially Papamoschou highly contributed to explain experimentally and theoretically the fundaments of the effect of a gas shell on the suppression of the Mach waves.

Mach Wave Dynamics

With regard to the theory of Oertel sen. et al. [10] for describing the Mach wave dynamics of a simple supersonic jet, extended relations were derived for the case with infinite outer co-flow. This theory is based on the well-known Kelvin-Helmholtz instabilities (KHI) which appear when sound waves and other disturbances cause the nozzle boundary layer to become unstable when it leaves the nozzle exit to form the jet's mixing layer. Described by Oertel sen. et al. [10], if Mach waves exist, the KHI break into two vortices which move stably downstream in two separate vortex trains with generally different vortex spacing. The vortex velocities are w' and w'' with $w' > w''$, and the mean velocity is w. Figure 2 shows schematically a section of the mixing layer with the two vortex trains. The two vortex trains are drawn with the same thickness, which is only the case of identical sound speeds a_i inside the jet and a_a outside.

The vortices in the inner zone move with velocity w' and in the outer one with w''. The vortices propagating with w' within the inner zone produce the w'-Mach waves outside. Those vortices moving with w'' in the outer zone produce the w''-Mach waves inside. The w'-vortices move faster than the w''-vortices and, as they pass each other during downstream motion, form periodical vortex pairs. So-called weak w-Mach waves can be produced if the overtaking movement fails, and a single w-vortex forms by vortex pairing.

H. Oertel sen. • J. Srulijes
Retired from the French-German Research Institute of Saint-Louis (ISL), Saint-Louis, France

F. Seiler (✉)
Retired from the French-German Research Institute of Saint-Louis (ISL), Saint-Louis, France

Institute of Fluid Mechanics (ISTM), Karlsruhe Institute of Technology (KIT), Karlsruhe, Germany
e-mail: friedrich.seiler@kit.edu

G. Ben-Dor et al. (eds.), *30th International Symposium on Shock Waves 1*, DOI 10.1007/978-3-319-46213-4_46

The vortex shock formation is sketched in Fig. 3 left in the form of idealized round- or tubelike-shaped vortices. Based upon gasdynamic considerations on the stability of vortices inside the mixing layer, Oertel sen. et al. [10–13] developed engineering formulas for calculating the velocities w, w', and w'' of the vortices, depending on the jet Mach number M_i and the speeds of sound: a_a, respectively, a_i. The correlations are obtained by observing the flow past the vortices as they move downstream while acting inward as well as outward, similar to a protrusion constricting the flow cross section, as schematically shown in Fig. 3 right-hand side. For stability reasons, the gas pressures for the w''-vortex must be the same to the outside periphery as well as to the w-plane. The same applies to the w'-vortex, where the pressure equality applies to both, the w-plane and the inner jet periphery. Only in this case, the vortices can remain stable for long during their downstream motion inside the mixing layer.

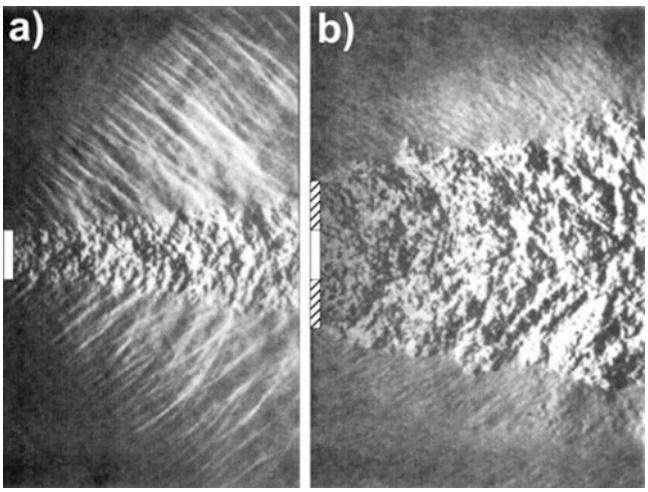

Fig. 1 (**a**) Supersonic air jet, (**b**) cowling with damped out Mach waves

To obtain a pressure equality relation, we first consider the relative Mach numbers at the bulges. For the w'-vortices and for the w''-vortices, they are as taken from Fig. 3 right. For the characterization of the relative Mach numbers in expressions (1a, 1b, 1c, 1d), the speeds of sound in the two vortex trains are assumed to be practically constant, a_i in the w'-train and a_a in the w''-train. This is justified because, as described in Oertel sen. et al. [10], the vortices entrain fresh gas from outside as well as from inside the jet into the mixing layer. The degrees of freedom f_i and f_a are considered also to be constant:

$$w' - \text{vortex(toinsideofthejet)}: \quad \frac{u_i - w'}{a_i} \tag{1a}$$

$$w' - \text{vortex}(w - \text{plane}): \quad \frac{w' - w}{a_a} \tag{1b}$$

$$w'' - \text{vortex(tooutsideofthejet)}: \quad \frac{w'' - u_a}{a_a} \tag{1c}$$

$$w'' - \text{vortex}(w - \text{plane}): \quad \frac{w - w''}{a_i} \tag{1d}$$

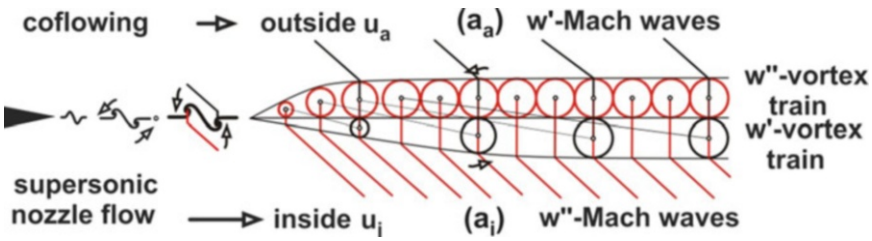

Fig. 2 Two vortex trains inside the mixing layer. Example with $w'/w'' = 3$

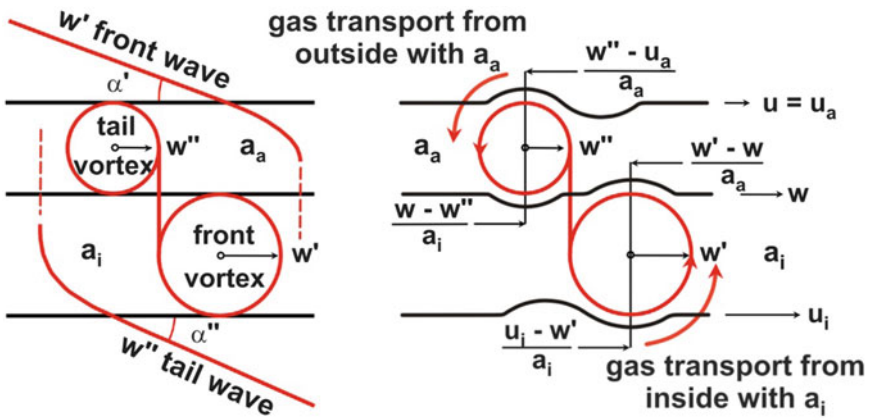

Fig. 3 Two vortex trains inside the mixing layer

Following the idea (see Oertel sen. et al. [13]) that large-scale structures, represented here by vortices, form a local stagnation point flow in the reference system displaced with the vortices, and that the pressures at the bulges of a vortex can be related to the same stagnation pressure p_0, using the general Eq. (2):

$$\frac{p_0}{p} = \left(1 + \frac{M^2}{f}\right)^{\frac{2+f}{2}} \tag{2}$$

Equation (2) is applied to form a pressure matching condition, linking the relative flow Mach numbers to each other with respect to (a) the w'- and (b) the w''-vortices, i.e., matching relations (1a) with (1b) and (1c) with (1d). The relative Mach numbers for stability reasons must always be subsonic which is explained further in the text. The expression in Eq. (2) can be developed in a power series as function of the Mach number in question, and it is justified to take only the first-power term of the power series applied. It results:

$$\sqrt{\frac{2+f_i}{2f_i}}\frac{u_i - w'}{a_i} = \sqrt{\frac{2+f_a}{2f_a}}\frac{w' - w}{a_a} \tag{3a}$$

$$\sqrt{\frac{2+f_a}{2f_a}}\frac{w'' - u_a}{a_a} = \sqrt{\frac{2+f_i}{2f_i}}\frac{w - w''}{a_i} \tag{3b}$$

Assuming no gas slippage between the two vortex trains at the w-plane closes the system of equations for the calculation of w, w', and w'':

$$w' - w = w - w'' \tag{4}$$

The solutions of the system of Eqs. (3a, 3b) and (4) yield:

$$\frac{w}{a_a} = \frac{M_i + kM_a}{k + a_a/a_i} \tag{5a}$$

$$\frac{w'}{a_a} = \frac{M_i + k(w/a_a)}{k + a_a/a_i} \tag{5b}$$

$$\frac{w''}{a_a} = \frac{M_i - k(w/a_a) + 2\,k\,M_a}{k + a_a/a_i} \tag{5c}$$

$$\frac{u_i - w''}{a_i} = \frac{k\,[M_i + (a_a/a_i)(w/a_a)] - 2\,k(a_a/a_i)\,M_a}{k + a_a/a_i} \tag{5d}$$

$$k = \sqrt{\frac{f_i(2+f_a)}{f_a(2+f_i)}}$$

The factor k describes the influence of the degrees of freedom of the gases in the jet, f_i, and outside, f_a, on the w, w', and w''. In the case of weak shocks, what Mach waves are, the well-known Mach number relations (6a, 6b, 6c) can be taken as a good approximation for determining the angles α, α', and α'' of the Mach waves:

$$\sin\alpha = \frac{a_a}{w - u_a} = \frac{a_i}{u_i - w} \tag{6a}$$

$$\sin\alpha' = \frac{a_a}{w' - u_a} \tag{6b}$$

$$\sin\alpha'' = \frac{a_i}{u_i - w''} \tag{6c}$$

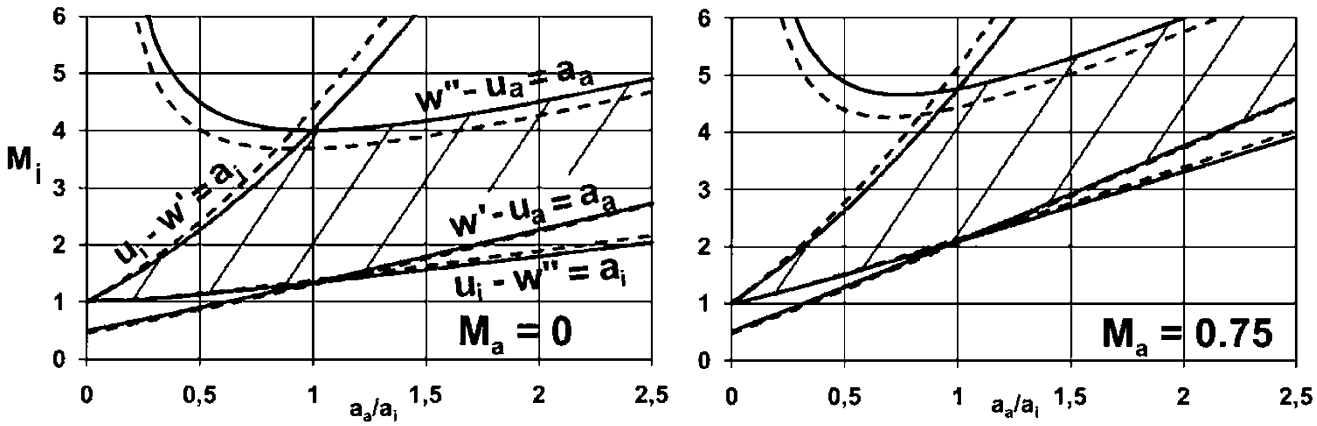

Fig. 4 Wave stability field for $M_a = 0$ and $M_a = 0.75$

Comparison of Theory with Experiments

The data for the visualized jets shown in Figs. 1, 5, 6, and 7 are listed in Table 1, together with the corresponding Mach wave angles calculated with Eqs. 6a, 6b, and 6c. The helium jets presented in Fig. 7 are included with kind permission of Papamoschou [7]. The other images are given by Oertel and Patz [4]. Figures 1a, 5a, and 7a show regular Mach waves of single supersonic jets. The other ones have a co-flowing surrounding. For comparison the Mach angles α'_{exp} taken from the jet visualizations are also listed. The comparison of the α'_{exp} with the calculated angle α' (see in Table 1) shows that both do match quite well within the angle variations of the Mach waves seen on the jet visualizations.

Domain of Existence

Limitations arise from the considerations [10–13] that w'-Mach waves can only emerge in the case if $(w' - u_a) > a_a$ and w''-Mach waves if $(u_i - w'') > a_i$, i.e., the w'- and w''-vortices need to move supersonically relative to the speeds of sound outside a_a as well as inside a_i. Eqs. (5a), (5b), and (5c) give the inequalities for the w'- and w''-waves depending on M_i:

$$w' - u_a > a_a : M_i > \frac{(k + a_a/a_i)^2}{2k + a_a/a_i} + \frac{a_a}{a_i} M_a \qquad (7a)$$

$$u_i - w'' > a_i : M_i > \frac{1}{k} \frac{(k + a_a/a_i)^2}{k + 2(a_a/a_i)} + \frac{a_a}{a_i} M_a \qquad (7b)$$

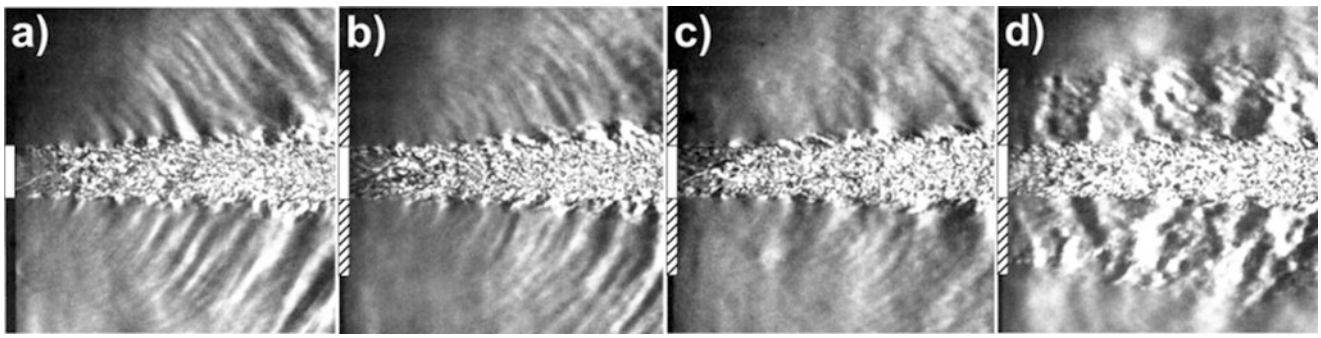

Fig. 5 (**a**, **b**) Supersonic air jet [4] with Mach waves; (**c**, **d**) damped out Mach waves

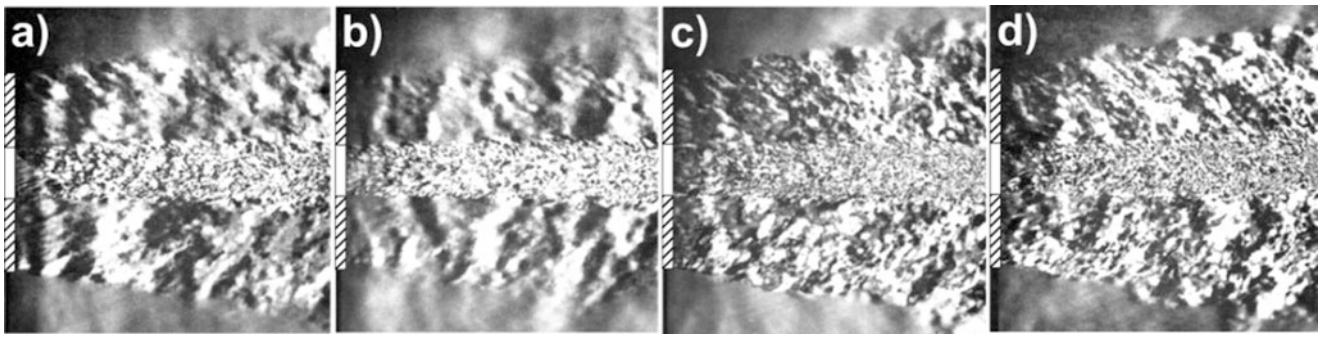

Fig. 6 Damped out Mach waves [4] with a nitrogen/x% helium mixture (**a**) $x = 20$, (**b**) $x = 40$, (**c**) $x = 60$, (**d**) $x = 80$

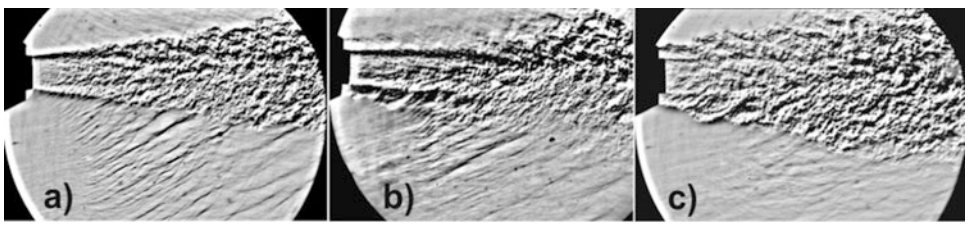

Fig. 7 Helium jet [7] in air at $M_i = 1.5$, (a) $M_a = 0$, (b) $M_a = 1.15$, (c) $M_a = 0.75$

Table 1 Jet data

	M_i	M_a	a_a/a_i	f_i	f_a	k	Equation (7a)	α (°)	α' (°)	α'' (°)	α'_{exp} (°)
Figure 1a	2	no	1	5	5	1.0	0.67	90	41.8	41.8	35–45
Figure 1b	2	0.79	1.28	5	5	1.0	2.6	No	No	No	No
Figure 5a	2	No	1.43	5	5	1.0	1.72	No	59.5	50.0	54–60
Figure 5b	2	0.12	1.46	5	5	1.0	1.92	No	73.6	57.5	65–75
Figure 5c	2	0.23	1.44	5	5	1.0	2.06	No	No	No	No
Figure 5d	2	0.59	1.40	5	5	1.0	2.52	No	No	No	No
Figure 6a	2	0.27	1.56	5	4.6	1.01	2.27	No	No	No	No
Figure 6b	2	0.24	1.77	5	4.2	1.03	2.47	No	No	No	No
Figure 6c	2	0.20	2.09	5	3.8	1.04	2.77	No	No	No	No
Figure 6d	2	0.16	2.79	5	3.4	1.13	3.49	No	No	No	No
Figure 7a	1.5	No	0.56	3	5	0.92	0.95	79.8	37.5	51.2	36–40
Figure 7b	1.5	1.15	0.57	3	5	0.92	1.58	No	No	No	No
Figure 7c	1.5	0.75	0.82	3	5	0.92	1.75	No	No	No	No

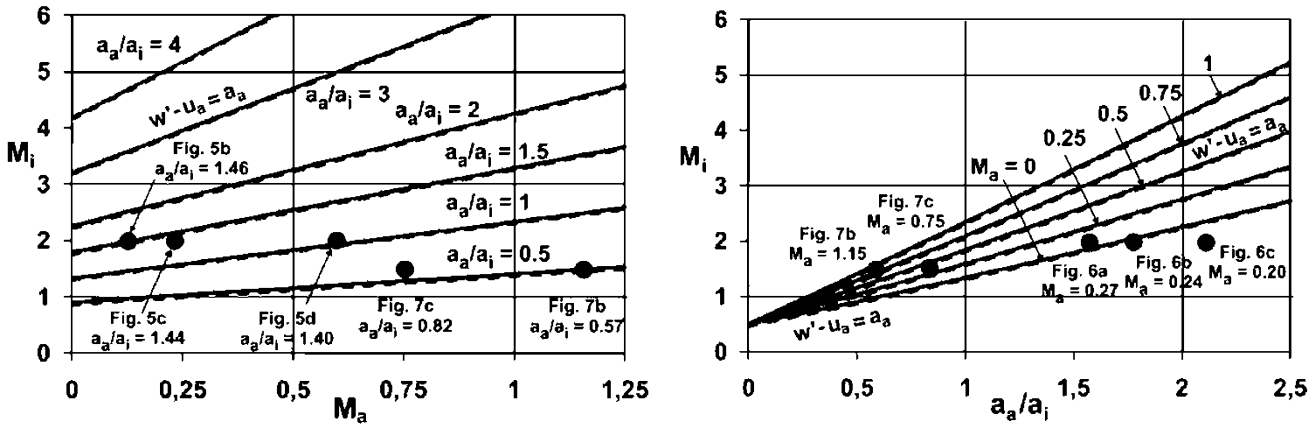

Fig. 8 Wave stability field, lines according to Eq. (7a)

Two other limitations restrict the existence of Mach waves. Each vortex represents a "hump" protruding from the cross section. It can only persist if the static flow pressure is smaller outside than inside of the vortex, i.e., the lower pressure "sucks" at the vortex periphery. This happens at relative subsonic Mach numbers with $(w''-u_a) < a_a$ and $(u_i - w') < a_i$. This pressure effect tends to increase the amplitude of the vortex chains, i.e., the mixing layer behaves stable [10]. At supersonic relative Mach numbers with $(w''-u_a) > a_a$ and $(u_i - w') > a_i$, shock waves occur. As each of the vortices forms a bulge, the flow is forced to evade this obstacle, and in a supersonic flow, this leads to localized pressure increase, and the regularity of the w'- and w''-vortices, as a postulate [11], can only exist at relative subsonic Mach numbers:

$$u_i - w' < a_i : M_i < \frac{1}{k^2}\left(k + \frac{a_a}{a_i}\right)^2 + \frac{a_a}{a_i} M_a \qquad (8a)$$

$$w'' - u_a < a_a : M_i < \frac{a_i}{a_a}\left(k + \frac{a_a}{a_i}\right)^2 + \frac{a_a}{a_i} M_a \qquad (8b)$$

The four limits (7a, 7b) and (8a, 8b) are shown in Fig. 4 forming the coarse dashed regions with stable Mach waves: Figure 4 (left) without and (right) with co-flow. Two cases are shown: $k = 1$ (solid lines with $f_a = f_a$) and $k = 0.92$ (dashed lines with $f_i = 3$ and $f_a = 5$). Below the limiting lines with $w'-u_a = a_a$ and $u_i - w'' = a_i$ in supersonic free jets, absolutely no Mach waves can occur. This is a very strict and strong condition, called the "unstable subsonic region." The transition to the region above the boundary lines $w''-u_a = a_a$ and $u_i - w' = a_i$, which is called the "unstable supersonic region," is smooth. Whether and how in this area the Mach waves are suppressed needs to be examined more in detail. Figure 4 makes clear that with outer flow, the limiting lines shift to larger Mach numbers M_i, by the term $(a_a/a_i) \times M_a$, i.e., responsible for Mach wave suppression: Eqs. (7a, 7b) and (8a, 8b).

The free jet in Fig. 5b with co-flowing produces Mach waves at $M_a = 0.12$. Increasing M_a to 0.23 and 0.59,

(Fig. 5c, d), causes the Mach waves to disappear. This is also the case for the supersonic jets with co-flowing shown in Fig. 6a–d at increased a_a/a_i. A look at Figs. 5c, d, and 6a–d suggests that the theoretically predicted Mach wave suppression (Table 1) is practically fulfilled. An example from literature is shown in Fig. 7a without co-flowing and in Fig. 7b, c with it. The ratio a_a/a_i and M_a are given in Table 1. For Fig. 7b, c, no w'-Mach waves can exist because of the value of Eq. (7a) $> M_i$, (see Table 1). In Fig. 7b, it can be seen that the estimation derived from the formula (7a) is nearly met, in Fig. 7c in any case.

In the diagrams of Fig. 8, the limiting lines given by Eq. (7a) are drawn versus a_a/a_i (right) and M_a (left). Plotted by dots are the presented conditions of the jets with outer cowling flow. A closer look at the individual dots shows that they are located below the corresponding limiting line, i.e., no Mach waves occur. Herewith the "unstable subsonic region" stability estimations are valid and show good agreement with the experiments.

Conclusions

The considerations proposed by Oertel et al. [10–13] for a supersonic jet have been extended, giving analytical formulas to describe the dynamics of Mach waves emitted by supersonic jet with moving outer co-flow. The analytical derivations for the Mach wave dynamics based on the assumption that vortices in the mixing layer run into two zones at different speeds, called w' and w'', are given. These vortices are the sources for the outer w'-Mach waves and inner w''-Mach waves. Different degrees of freedom for the jet and the environment are taken into account. The theory provides information on the Mach angles α' (surrounding) and α'' (jet), the speeds of the Mach waves w' and w'', and the jet stability conditions. Comparing these predictions with experiments showed a good applicability of the developed theory.

References

1. Oertel, H.: Kinematik der Machwellen in der Umgebung von Überschallstrahlen (Kinematic of Mach waves surrounding supersonic jets). ISL Report R 112/78, (1978)
2. Rowe, W.T., Johnson, E.S., McKinnon, R.A.: Technology status of jet noise suppression concepts for advanced supersonic transports. J. Aircraft **16**, 2, (1979)
3. Oertel, H.: Les ondes de Mach à l'intérieur et à l'extérieur du jet supersonique avec ou sans envelope subsonique. ISL report, CO 205/81, (1981)
4. Oertel, H., Patz, G.: Wirkung von Unterschallmänteln auf die Machwellen in der Umgebung von Überschallstrahlen (Effects of subsonic cowling on the Mach waves around supersonic jets). ISL Report RT 505/81, (1981)
5. Dosanjh, D.S., Blutiani, P.K., Ahuja, K.K., Bassionni, M.R.: Supersonic jet noise suppression by cold/heated jet flows. In: AIAA 3th Aeroacoustics Conference, Palo Alto, (1976)
6. Papamoschou, D.: Linear model of Mach wave suppression in a dual-stream jet. AIAA-2000–2062, (2000)
7. Papamoschou, D.: Mach wave elimination in supersonic jets. AIAA-97-0147, (1997)
8. Papamoschou, D., Debiasi, M.: Noise measurements in supersonic jets treated with the Mach wave elimination method. AIAA J. **37** (2), (1999)
9. Rossmann, T., Mungal, M.G., Hanson, R.K.: Character of Mach wave radiation and convection velocity estimation in supersonic shear layers. AIAA 2002-257, (2002)
10. Oertel sen., H., Seiler, F., Srulijes, J.: Visualization of Mach waves produced by a supersonic jet and theoretical explanations. J. Visual. **16**(4), (2013)
11. Oertel sen., H., Seiler, F., Srulijes, J.: New explanation of noise production by supersonic jets with gas dredging. In: Notes on Numerical Fluid Mechanics and Multidisciplinary Design, vol. 112. Springer, Berlin, (2010)
12. Oertel sen., H., Seiler, F., Srulijes, J., Hruschka, R.: Mach waves of supersonic jets produced by shock/vortex interaction. In: Proceedings of the 21th International Shock Interaction Symposium, Riga, Latvia, (2014)
13. Oertel sen., H., Seiler, F., Srulijes, J.: The limits of Mach wave emission from supersonic jets. Proceedings of the 30th International Symposium on Shock Waves, Israel, (2015)

The Limits of Mach Wave Emission from Supersonic Jets

H. Oertel sen., F. Seiler, and J. Srulijes

Introduction

Supersonic jets emit Mach waves which appear inside as well as outside the jet and are quite regular, long, almost straight, and nearly parallel, as can be seen by visualizing density differences with light intensity variations in Fig. 1 (left, right). Based on experimental studies by Oertel [1, 2] to measure the Mach waves' angles, the movement of the Mach waves resulted in three different speeds, denoted by w, w', and w''. Many publications indicate "large-scale structures" as well as "vortices" as a trigger mechanism for generating the Mach waves, but a theoretical description for the three speeds w, w', and w'' has not been given conclusively yet. Oertel sen. et al. [3] assumed that inside of the mixing layer, vortices are formed, and this postulate allowed to derive gasdynamic engineering formulas to determine the speeds w, w', and w''. In [3], the formulas for the same gases inside and outside the jet are specified, showing that the three speeds only depend on the jet Mach number M_i and the sound speed ratio from the outside and the inside jet gases, a_a/a_i. These considerations also allow to determine the jet conditions at which Mach waves can exist stably. Extended formulas are presented in this paper for different gas species with various degrees of freedom f_i inside the jet and f_a outside.

There are numerous publications about the behavior of Mach waves in supersonic jets and many attempts to explain the reasons for their existence. Noteworthy publications are, among others, Tam [4–6], Tam and Hu [7], Papamoschou [8, 9], Papamoschou and Bunyajitradulya [10], Colonius et al. [11], Lele et al. [12], Freund et al. [13], Rossmann et al. [14], and Mendez et al. [15]. They describe the Mach wave dynamics in great detail, but an unambiguous explanation for the behavior of the Mach waves still remains open. Especially Tam and Hu [7] have assumed the Mach waves to originate from turbulence as well as from coherent/large-scale structures of different nature. Based on this thought, they developed an analytical model, called "vortex sheet model," to theoretically describe Oertel's w, w', and w'' speeds. Their derivatives, however, need to be more precisely validated using experimental results, e.g., those of Oertel [1, 2]. Most articles assume that the large-scale structures are represented by vortices moving downstream inside of the mixing layer.

The Dynamics of the Vortices

The instability development just downstream of the exit of a supersonic jet is sketched in Fig. 2 represented by the growth of a deformation, well known as Kelvin-Helmholtz instability. This instability can be considered as a shear-layer deformation which usually develops into two vortices rolling up around each other. By vortex pairing they form a single vortex which moves downstream inside the mixing layer. The topology described here is mostly present in the absence of Mach waves, i.e., normally in subsonic jet mixing zones.

If the Kelvin-Helmholtz instability moves supersonically, Mach waves are produced, as shown schematically in Fig. 2, and consequently the rolling-up process is interrupted by these shock waves. Instead of a single vortex, two vortices form by shock/vortex interaction, moving downstream in two zones inside the mixing layer as schematically outlined in Fig. 3. The vortex topology is described in detail by Oertel sen. et al. [3, 16–18].

The vortices in the inner zone move with velocity w' and in the outer one with w''. The vortices propagating with w' in

H. Oertel sen. • J. Srulijes
Retired from the French-German Research Institute of Saint-Louis (ISL), Saint-Louis, France

F. Seiler (✉)
Retired from the French-German Research Institute of Saint-Louis (ISL), Saint-Louis, France

Institute of Fluid Mechanics (ISTM), Karlsruhe Institute of Technology (KIT), Karlsruhe, Germany
e-mail: friedrich.seiler@kit.edu

G. Ben-Dor et al. (eds.), *30th International Symposium on Shock Waves 1*, DOI 10.1007/978-3-319-46213-4_47

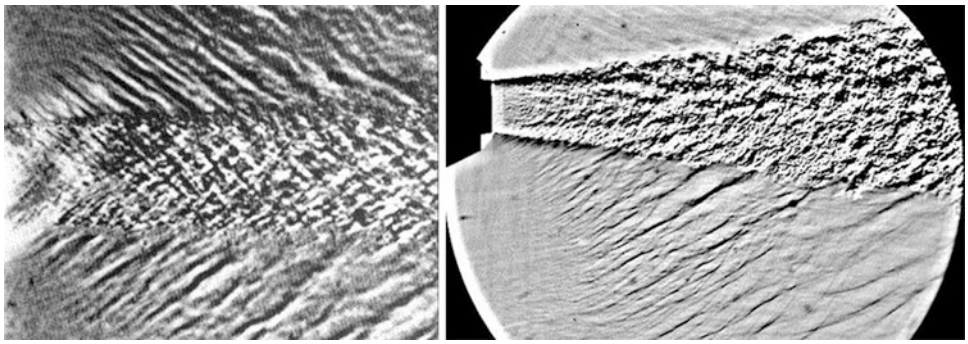

Fig. 1 Air jet in air [1] (*left*), jet Mach number $M_i = 2.2$; helium jet in air [8] (*right*), $M_i = 1.5$

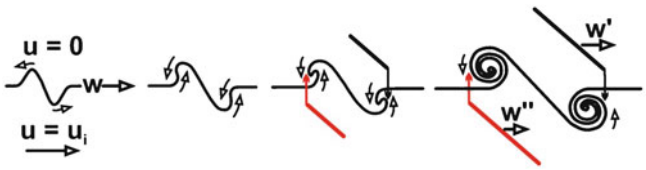

Fig. 2 Interruption of vortex pairing by Mach waves in supersonic jet mixing layer

the inner zone produce the w'-Mach waves outside. Those vortices moving with w'' in the outer zone produce the w''-Mach waves inside. The w'-vortices move faster than the w''-vortices forming periodically vortex pairs as they pass each other during downstream motion. Weak w-Mach waves can be produced if the overtaking process fails, and a single w-vortex is formed by vortex pairing.

The vortex shock formation is sketched in Fig. 4 left in the form of idealized round-shaped or tubelike vortices. Based upon gasdynamic considerations on the stability of vortices inside the mixing layer, Oertel sen. et al. [3, 16–18] developed engineering formulas for calculating the velocities w, w', and w'' of the vortices, depending on the jet Mach number M_i and the speeds of sound, a_a, respectively, a_i. The correlations for these formulas were obtained by observing the flow past the vortices as they move downstream acting inward as well as outward, similar to a protrusion constricting the flow cross section, as schematically shown in Fig. 4 right. For stability reasons, the gas pressures for the w''-vortex must be the same to the outside periphery as well as to the w-plane in between the two zones. The same applies to the w'-vortex, where the pressure equality applies to both, the w-plane and the inner jet periphery. Otherwise, the vortices become deformed and cannot remain stable for long during their downstream motion inside the mixing layer.

The relative Mach numbers at the vortex bulges can be deduced from Fig. 4 right, (a) for the w'-vortices and (b) for the w''-vortices. For the characterization of the relative Mach numbers in the expressions (1a, 1b) and (1c, 1d), the speeds of sound in the two vortex trains are assumed to be practically constant, a_i (w'-train) and a_a (w''-train). This is so because the vortices entrain fresh gas from outside as well as from inside the jet into the mixing layer, as described in Oertel sen. et al. [3]. The degrees of freedom f_i and f_a are constant as well:

$$w' - \text{vortex(to inside of the jet)}: \quad \frac{u_i - w'}{a_i} \tag{1a}$$

$$w' - \text{vortex}(w - \text{plane}): \quad \frac{w' - w}{a_a} \tag{1b}$$

$$w'' - \text{vortex(to outside of the jet)}: \quad \frac{w''}{a_a} \tag{1c}$$

$$w'' - \text{vortex}(w - \text{plane}): \quad \frac{w - w''}{a_i} \tag{1d}$$

Rossman [19] assumes that large-scale structures are represented by vortices forming a local stagnation point flow in a reference system moving with the vortices. Following this assumption and using Eq. (2), the one-dimensional compressible energy equation with the isentropic pressure-temperature relation, the pressures at the bulges of a vortex as described above can be related to the same stagnation pressure p_0:

$$\frac{p_0}{p} = \left(1 + \frac{M^2}{f}\right)^{\frac{2+f}{2}} \tag{2}$$

Equation (2) is applied to form a pressure matching condition, linking the relative flow Mach numbers (1a, 1b) and (1c, 1d) to each other with respect to (a) the w'-vortices and (b) the w''-vortices:

$$\left(1 + \frac{1}{f_i}\left(\frac{u_i - w'}{a_i}\right)^2\right)^{\frac{2+f_i}{2}} = \left(1 + \frac{1}{f_a}\left(\frac{w' - w}{a_a}\right)^2\right)^{\frac{2+f_a}{2}} \tag{3a}$$

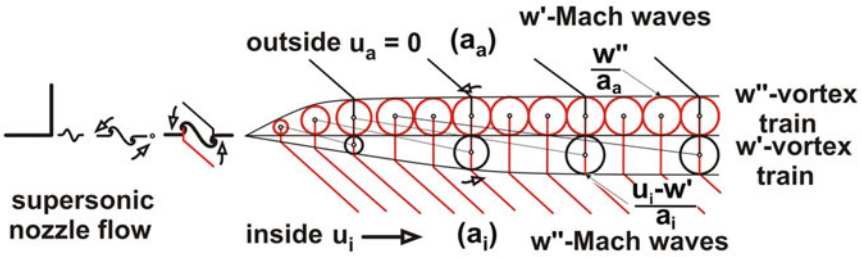

Fig. 3 Vortex train model. Example with $w'/w'' = 3$ at $a_a = a_i$, $M_i = 2$

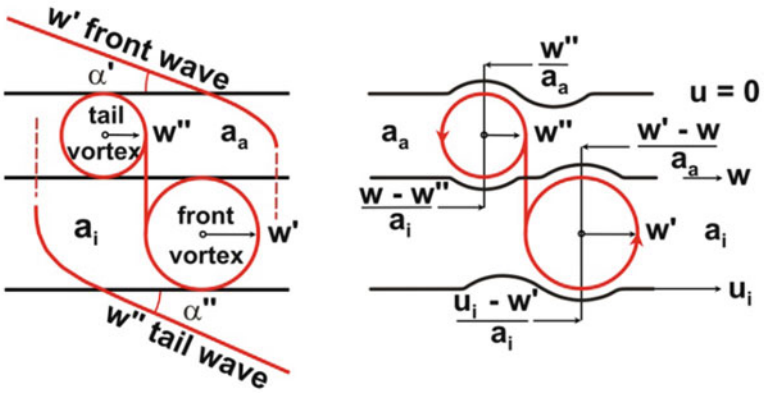

Fig. 4 Idealized front and tail Mach wave (*left*), relative Mach numbers (*right*)

$$\left(1+\frac{1}{f_a}\left(\frac{w''}{a_a}\right)^2\right)^{\frac{2+f_a}{2}} = \left(1+\frac{1}{f_i}\left(\frac{w-w''}{a_i}\right)^2\right)^{\frac{2+f_i}{2}} \tag{3b}$$

The expressions in Eqs. (3a, 3b) can be developed in power series as functions of the corresponding Mach numbers. For a stable formation of Mach waves, the relative Mach numbers for stability reasons are always subsonic (see section "Limits"). Then, the power series converges very fast so that, without large error, only the first-power term can be considered:

$$\sqrt{\frac{2+f_i}{2f_i}}\frac{u_i - w'}{a_i} = \sqrt{\frac{2+f_a}{2f_a}}\frac{w' - w}{a_a} \tag{4a}$$

$$\sqrt{\frac{2+f_a}{2f_a}}\frac{w''}{a_a} = \sqrt{\frac{2+f_i}{2f_i}}\frac{w - w''}{a_i} \tag{4b}$$

Assuming no gas slippage between the two vortex trains at the w-plane closes the system of equations for the calculation of w, w', and w'':

$$w' - w = w - w'' \tag{5}$$

The solutions of the system of Eqs. (4a, 4b) and (5) yield:

$$\frac{w}{a_a} = \frac{M_i}{k + a_a/a_i} \tag{6a}$$

$$\frac{w'}{a_a} = \frac{M_i + k(w/a_a)}{k + a_a/a_i} \tag{6b}$$

$$\frac{w''}{a_a} = \frac{M_i - k(w/a_a)}{k + a_a/a_i} \tag{6c}$$

$$k = \sqrt{\frac{f_i(2+f_a)}{f_a(2+f_i)}}$$

The factor k describes the influence of the degrees of freedom on the w, w', and w''. The relations for oblique shocks allow calculation of the Mach waves' angles. In the case of weak shocks (or Mach waves), the well-known Mach number relations (7a, 7b, 7c) can be taken as a good approximation for determining their angles α, α', and α''. Angle dependencies vs. M_i; see Fig. 5 left with $k = 1$ (solid lines with $f_i = f_a$) and 0.92 (dashed lines with $f_i = 3$, $f_a = 5$). It turns out that the influence of different degrees of freedom is small:

$$\sin\alpha = \frac{a_a}{w} = \frac{a_i}{u_i - w} \tag{7a}$$

$$\sin\alpha' = \frac{a_a}{w'} \tag{7b}$$

$$\sin\alpha'' = \frac{a_i}{u_i - w''} \tag{7c}$$

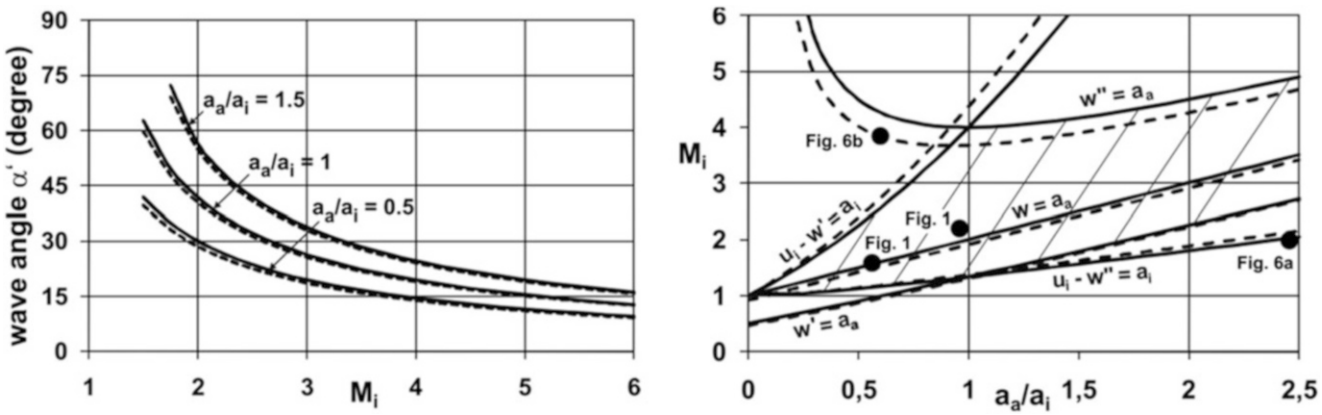

Fig. 5 *Left*: Mach wave angles vs. M_i, *right*: Mach wave stability field

Table 1 Jet data

	M_i	a_a/a_i	f_i	f_a	k	α (°)	α' (°)	α'' (°)	α'_{exp} (°)
Figure 1 [1]	2.2	0.95	5	5	1.0	63.4	36.2	37	33–39
Figure 1 [8]	1.5	0.56	3	5	0.92	79.8	37.4	51.1	36–40
Figure 6a [20]	1.98	2.44	5	5	1.0	No	No	No	No
Figure 6b [20]	3.95	0.66	5	5	1.0	24.9	15.2	12.1	15–25

For calculating the Mach wave angle α'', relation (6c) can be transformed into:

$$\frac{u_i - w''}{a_i} = \frac{k\,[M_i + (a_a/a_i)\,(w/a_a)]}{k + a_a/a_i} \tag{7d}$$

Experimental Comparison

Figure 1 shows the Mach waves of supersonic jets in air (left image with an air jet and right one with a helium jet), included with kind permission of Papamoschou [8]. The jet data and the Mach angles α, α', and α'', calculated with Eqs. 7a, 7b, and 7c, and α'_{exp} taken from the jet visualizations are listed in Table 1.

Limits

It is known that there are supersonic jets that do not emit Mach waves, which suggests that there must be a limited range where Mach waves can exist. The limitations arise from the considerations [16–18] that w'-Mach waves can only emerge if $w' > a_a$ and w''-Mach waves if $(u_i - w'') > a_i$, i.e., the w'- and w''-vortices need to move supersonically relative to the speeds of sound outside a_a as well as inside a_i. From Eqs. (6a, 6b, 6c), the given inequalities are obtained for the w'- and w''-waves depending on M_i:

$$w' > a_a \text{ at } M_i > \frac{(k + a_a/a_i)^2}{2k + a_a/a_i} \tag{8a}$$

$$u_i - w'' > a_i \text{ at } M_i > \frac{1}{k}\,\frac{(k + a_a/a_i)^2}{k + 2(a_a/a_i)} \tag{8b}$$

Two other limitations restrict the existence of Mach waves. Each vortex represents a "hump" protruding from the cross section. It can only persist if the static flow pressure is smaller outside than inside the vortex, which means that the lower pressure "sucks" at the vortex periphery. This happens at relative subsonic Mach numbers with $w'' < a_a$ and $(u_i - w') < a_i$. This pressure effect tends to increase the amplitude of the vortex chains, i.e., the mixing layer behaves stable, as described, e.g., by Tam and Hu [7]. At supersonic relative Mach numbers with $w'' > a_a$ and $(u_i - w') > a_i$, shock waves occur. As each of the vortices forms a bulge, the flow is forced to evade this obstacle, and in a supersonic flow, this leads to a localized pressure increase. The suction is replaced by "compression" and the w'- and the w''-vortices may disappear. The regularity as a postulate of the current theory only exists at relative subsonic Mach numbers:

$$u_i - w' < a_i \text{ at } M_i < \frac{1}{k^2}(k + a_a/a_i)^2 \tag{9a}$$

$$w'' < a_a \text{ at } M_i < \frac{a_i}{a_a}\,(k + a_a/a_i)^2 \tag{9b}$$

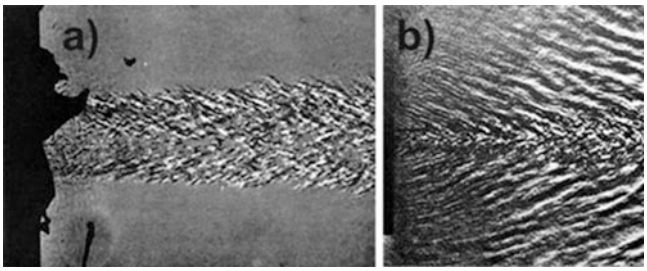

Fig. 6 (**a**) No Mach waves at $M_i = 1.98$, (**b**) w-Mach waves at $M_i = 3.95$

The four limits (8a, 8b) and (9a, 9b) are shown in Fig. 5 right forming the coarse dashed region in which stable Mach waves are present. Two cases are shown: $k = 1$ (solid lines with $f_a = f_a$) and $k = 0.92$ (dashed lines with $f_i = 3$ and $f_a = 5$). Below the limiting lines with $w' = a_a$ and $u_i - w'' = a_i$, absolutely no Mach waves can occur in supersonic free jets. Hence, we call this region the "unstable subsonic region." This is a very strict and strong condition. The free jet in Fig. 6a shows no Mach waves, and this observation is confirmed by the data dot in the stability diagram in Fig. 5 right placed below the lower borderlines. Plotted by dots are also the conditions of the jets in Fig. 1, which are placed well within the permissible range. The transition to the region above the boundary lines $w'' = a_a$ and $u_i - w' = a_i$, which is called the "unstable supersonic region," is smooth. Whether and how in this area the Mach waves are suppressed, needs to be examined more closely in the future.

In the "unstable supersonic region," w-Mach waves may exist provided the condition (10) is fulfilled. The black solid/dashed w-limit lines (10) with $w = a_a$ are integrated in Fig. 5 right. This may happen if the w'- and/or the w''-vortex chains cannot form stably above the lines $w'' = a_a$ and $u_i - w' = a_i$, as it is the case for the jet in Fig. 6b. However, the w-vortices will also not last long, because they move supersonically and are destroyed by the outside pressing flow force too. Candidates for this presumption are discussed in Oertel sen. et al. [20], one of them is that in Fig. 6b with Mach angles in between 15 and 25° and is dotted in Fig. 5 right. A look at the data in Table 1 confirms that there are α- and α'-angles coincidently visible:

$$w > a_a \text{ at } M_i > (k + a_a/a_i) \tag{10}$$

Conclusions

The theory proposed by Oertel et al. [3, 20] to describe the Mach wave dynamics of supersonic jets is based on the fact that vortices in the mixing layer run into two zones at different speeds, called w' and w''. These vortices are the sources for both the outer and inner Mach waves. The theory was developed for equal degrees of freedom for the jet and the environment [3]. In a further step, the theoretical derivatives have now been formulated for gases having different degrees of freedom as, for example, a helium jet blowing into nitrogen. The theory provides information on the Mach angles α' (surrounding) and α'' (jet) and the speeds of the Mach waves w' and w'' and gives information on the jet conditions where Mach waves can exist. Testing the evidence of this stability prediction with experiments showed a good reproducibility [20].

References

1. Oertel, H.: Kinematik der Machwellen in der Umgebung von Überschallstrahlen (Kinematic of Mach waves surrounding supersonic jets). ISL Report R 112/78, (1978)
2. Oertel, H.: Mach wave radiation of hot supersonic jets investigated by means of a shock tube and new optical techniques. In: Proceedings of the 12th International Symposium on Shock-Tubes and Waves, Israel, (1980)
3. Oertel sen., H., Seiler, F., Srulijes, J.: Visualization of Mach waves produced by a supersonic jet and theoretical explanations. J. Visual. **16**(4), (2013)
4. Tam, C.K.W.: The radiation of sound by the instability waves of a compressible plane turbulent shear layer. J. Fluid Mech. **98**, Part 2, (1980)
5. Tam, C.K.W.: Supersonic jet noise. Ann. Rev. Fluid Mech. **27**, (1995)
6. Tam, C.K.W.: Mach wave radiation from high-speed jets. AIAA J. **47**(10), (2009)
7. Tam, C.K.W., Hu, F.Q.: On the three families of instability waves of high-speed jets. J. Fluid Mech. **201**, (1989)
8. Papamoschou, D.: Mach wave elimination in supersonic jets. AIAA-97-0147, (1997)
9. Papamoschou, D.: Structure of the compr. turbulent shear layer. AIAA J. **29**(5), (1991)
10. Papamoschou, D., Bunyajitradulya, A.: Evolution of large eddies in compressible shear layers. Phys. Fluids **9**(3), (1997)
11. Colonius, T., Lele, S.K., Moin, P.: Sound generation in a mixing layer. J. Fluid Mech. **330**, (1997)
12. Lele, S.K., Mendez, S., Ryu, J., Nichols, J., Shoeybi, M., Moin, P.: Sources of high-speed jet noise: analysis of LES data and modeling. Proc. Eng. **6C**, (2010)
13. Freund, J.B., Lele, S.K., Moin, P.: Numerical simulation of a Mach 1.92 turbulent jet and its sound field. AIAA J. **38**(11), (2000)
14. Rossmann, T., Mungal, M.G., Hanson, R.K.: Character of Mach wave radiation and convection velocity estimation in supersonic shear layers. AIAA 2002-2571, (2002)
15. Mendez, S., Shoeybi, M., Sharme, A., Ham, F.E., Lele, S.K., Moin, P.: Large-eddy simulation of perfectly expanded supers. jets using an unstructured solver. AIAA J. **50**(5), (2012)
16. Oertel sen., H., Seiler, F., Srulijes, J.: New explanation of noise production by supersonic jets with gas dredging. In: Notes on Numerical Fluid Mechanics and Multidisciplinary Design, vol. 112. Springer, Berlin, (2010)

17. Oertel sen., H., Seiler, F., Srulijes, J.: Vortex induced Mach waves in supersonic jets. In: Proceedings of the 28th International Symposium on Shock Waves, UK, (2011)
18. Oertel sen., H., Seiler, F., Srulijes, J., Hruschka, R.: Vortical structures as Mach wave sources in the mixing layer of supersonic jets. In: Proceedings of the 29th International Symposium on Shock Waves, Madison, WI, USA (2013)
19. Rossmann, T.: An experimental investigation of high compressibility mixing layers. Technical Report TSD-138, Stanford University, Stanford, California 94305-3032, (2001)
20. Oertel sen., H., Seiler, F., Srulijes, J., Hruschka, R.: Mach waves of supersonic jets produced by shock/vortex interaction. In: Proceedings 21th International Shock Interaction Symposium, Latvia (2014)

Overexpanded Jet Flow Theoretical Analysis in the Vicinity of the Nozzle Lip

M.V. Silnikov, M.V. Chernyshov, and V.N. Uskov

Introduction

Differential characteristics of the supersonic flow field in the vicinity of the nozzle edge often relate to such physical effects as Taylor-Görtler instability, regular/Mach reflection mutual transition at small Mach numbers, and self-oscillation phenomena in submerged and impact jets.

This article presents a fragment of a complex study on supersonic jet flows in a vicinity of a nozzle edge. Differential conditions of dynamic coexistence [1] are applied to gasdynamic variables and their spatial derivatives at both sides of oblique shock waves emanating from an edge of two-dimensional (plane or axis-symmetric) overexpanded jet flowing into submerged media. Isobaricity condition at the inviscid gas jet boundary allows us to investigate a change of the shock geometry and of the jet flow boundary, finding special and extreme cases of the emanation. A crucial characteristic which allows defining all main flow unevenness functions in the edge vicinity is the geometrical curvature of the oblique shock emanating from the nozzle lip. This study presents analysis of variations of the differential characteristics in a two-dimensional jet of a nonviscous perfect gas in relation to the outflow conditions.

M.V. Silnikov • M.V. Chernyshov (✉)
Special Materials Corp., 28A Bolshoy Sampsonievsky Ave., 194044 Saint Petersburg, Russia

Peter the Great Saint Petersburg Polytechnic University, 29 Polytechnicheskaya Str., 195251 Saint Petersburg, Russia
e-mail: mvcher@mail.ru

V.N. Uskov
Baltic State Technical University, 1 1st Krasnoarmeyskaya Str., 190005 Saint Petersburg, Russia

Governing Relations

The shock AT (Fig. 1) emanating from the edge A of the supersonic nozzle with θ opening angle has the strength (intensity) $J = 1/n$ where $n = p_a/p_n$ n is jet incalculability determined by comparison between static pressure p_a of the emanating jet in the nozzle edge vicinity and the surrounding pressure p_n.

The intensity J (relation between pressures behind and ahead of a shock wave [2]) is limited in the range $1 < J < J_m$ where

$$J_m = (1+\varepsilon)M^2 - \varepsilon$$

is the strength of a direct shock wave in the flow with the Mach number M ahead of it; M is flow Mach number in the vicinity of point A upstream of the shock, $\varepsilon = (\gamma-1)/(\gamma+1)$; and γ is the ratio of gas specific heats (it is assumed in the further calculations that $\gamma = 1.4$).

Flow deflection angle β at the shock relates to its intensity and the Mach number ahead of it:

$$\mathrm{tg}|\beta| = \sqrt{\frac{J_m - J}{J+\varepsilon}}\,\frac{(1-\varepsilon)(J-1)}{J_m + \varepsilon - (1-\varepsilon)(J-1)}. \qquad (1)$$

Shock slope angle σ to the flow velocity vector ahead of the shock and the flow Mach number M_2 downstream the shock wave are related to M and J as follows:

$$J = (1+\varepsilon)\mathrm{M}^2 \sin^2\sigma - \varepsilon, \qquad (2)$$

$$\mathrm{M}_2 = \sqrt{\frac{(J+\varepsilon)\mathrm{M}^2 - (1-\varepsilon)\left(J^2-1\right)}{J(1+\varepsilon J)}}. \qquad (3)$$

In a general case, spatial derivatives of various jet parameters undergo a break at the shock wave surface, as well as flow parameters themselves. The variations of the spatial derivatives on the shock sides are described by

G. Ben-Dor et al. (eds.), *30th International Symposium on Shock Waves 1*, DOI 10.1007/978-3-319-46213-4_48

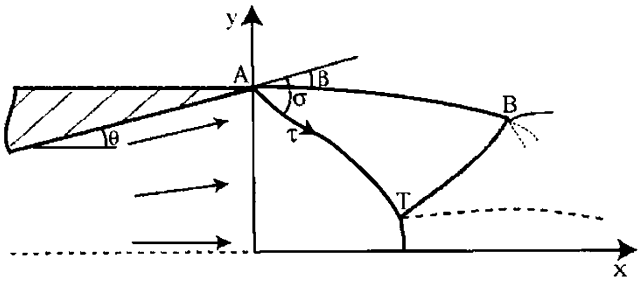

Fig. 1 Scheme of the overexpanded jet flow into ambient gas media

differential conditions of dynamic coexistence [1] in the following form:

$$N_{i2} = C_i \sum_{j=1}^{5} A_{ij} N_j, \quad i = 1 \ldots 3 \tag{4}$$

where N_{i2} are flow unevenness functions behind the shock wave, N_j are unevenness functions ahead of the shock, and C_i and A_{ij} are the factors which depend on M, J, and θ. The functions $N_1 = \partial \ln p/\partial s$, $N_2 = \partial\theta/\partial s$, and $N_3 = \partial \ln p_0/\partial n$ characterize, correspondingly, flow non-isobaricity, streamline curvature, and the gradient of the total pressure in isoenergetic flow; $N_4 = \delta/y$ is symmetry-type factor ($\delta = 0$ in plane flow and $\delta = 1$ in axis-symmetric one); $N_5 \equiv K_\sigma$ is shock geometrical curvature. Conditions (4) determine, in particular, the flow unevenness functions in the compressed layer directly behind the shock wave of the known curvature, if the flow field ahead of it is known.

The writing (4) of the differential conditions on the stationary shocks in steady nonuniform flow is certainly not unique. One of the most modern forms of differential flow field parameters mutual dependence on shock sides was deduced in [3] and applied later [4] for gas entropy variation and flow vorticity analysis. The results reached below and elaborated in [5–7] for plane overexpanded jet and oblique shock interactions in nonuniform flow are independent of form of writing of correctly deduced differential relations on stationary shock.

Condition of flow isobaricity ($N_{12} = 0$) along the jet boundary AB (Fig. 1) determines a sought shock wave curvature:

$$K_\sigma = -\sum_{j=1}^{4} A_{1j} N_j / A_{15}, \tag{5}$$

and other differential flow field parameters immediately behind the shock.

In particular, jet boundary curvature ($N_{22} \equiv K_\tau$) in point A depends on it as follows:

$$K_\tau = C_2 \sum_{j=1}^{4} \left(A_{2j} A_{15} - A_{1j} A_{25}\right) N_j / A_{15}. \tag{6}$$

The quantity K_τ determines some features of the Taylor-Görtler longitudinal instability [8–11].

Relation (5), two-dimensional perfect gas flow equations applied in front of the shock wave and behind it in natural coordinates (s, n):

$$\frac{M^2 - 1}{\gamma M^2} N_1 + \frac{\partial \theta}{\partial n} + N_4 \sin\theta = 0, \gamma M^2 N_2 = -\frac{\partial \ln p}{\partial n}, \frac{\partial p_0}{\partial s} = 0$$

and relations (1, 2, and 3) between the shock wave shape, its intensity, and the Mach number on the shock wave sides determine, after some transformations, e.g., local changes in the intensity and the Mach number behind the shock wave in τ direction along the shock wave:

$$\frac{dJ}{d\tau} = -2(J + \varepsilon)(B_1 N_1 + B_2 N_2 + B_3 N_3 + \chi ac N_4 \sin\theta + q K_\sigma) \tag{7}$$

$$\frac{dM_2}{d\tau} = -\left[1 + \varepsilon\left(M_2^2 - 1\right)\right] \cdot \left(\frac{M_2 N_{22}}{1 - \varepsilon} + \frac{N_{32}}{(1 + \varepsilon) M_2}\right) \cdot \sin(\sigma - \beta).$$

Here the direction index χ =–1 relates to the incident shock wave at Fig. 1, $c = \sqrt{(J + \varepsilon)/(J_m + \varepsilon)}$, $q = \sqrt{(J_m - J)/(J + \varepsilon)}$, and factors B_i have the following form:

$$B_1 = \chi ac \cdot \frac{1 - (1 - 2\varepsilon)\left(M^2 - 1\right)}{(1 + \varepsilon) M^2},$$

$$B_2 = c \cdot \left(\frac{1 + \varepsilon\left(M^2 - 1\right)}{1 - \varepsilon} - q^2\right),$$

$$B_3 = c \cdot \frac{1 + \varepsilon\left(M^2 - 1\right)}{J_m + \varepsilon}.$$

Total pressure preservation coefficient at the shock is

$$I = p_{02}/p_0 = (J E^\gamma)^{(1-\varepsilon)/2\varepsilon}.$$

Here p_0 and p_{02} are flow stagnation pressures before the shock wave and behind it, $E = \rho_0/\rho_{02} = (1 + \varepsilon J)/(J + \varepsilon)$ is the inverse ratio of gas densities at shock wave sides, and ΔS is entropy variation:

$$\Delta S = c_v \ln(J E^\gamma)$$

(c_v is gas specific heat at constant volume.) All these parameters are in uniform dependence on shock intensity. Thus, the flow vorticity rate N_{32}, according to (4), and the

direction of an isoenergetic jet velocity vortex vector, according to Crocco formula, are determined by derivative $dJ/d\tau$ of the shock wave strength in the direction of its incidence. The strength derivative, in its turn, depends on the shock wave geometrical curvature defined by (7).

Condition $A_{15} = 0$, at which the shock curvature and jet parameters related to it become unlimited, is fulfilled at shock strength equal to

$$J_p = \frac{3J_m - 2 - 3\varepsilon + \sqrt{9J_m^2 + 2\varepsilon(17 + 8\varepsilon)J_m + 16 + 16\varepsilon + 9\varepsilon^2}}{2(3 + \varepsilon)}. \tag{8}$$

This strength corresponds to so-called constant pressure point. The inequality $1 < J_p(M) < J_m(M)$ is fulfilled at any Mach number and the ratio of specific heats exceeding a unit. The flow velocity behind the oblique shock of J_p intensity is subsonic.

Thus, the geometrical curvature of a shock wave emanating from the nozzle edge is the governing parameter for determining all differential characteristics of the compressed layer behind the shock wave.

Variation of the Shock Geometrical Curvature in Plane Jet and Axis-Symmetric One

As an example of a jet flow parameter ahead of a shock wave, we consider, here and below, an isentropic flow from a cylindrical or spherical source with the following basic unevenness functions:

$$N_1 = -\frac{(1 + \delta)\gamma M^2 \sin\theta}{y\left(M^2 - 1\right)}, \quad N_2 = N_3 = 0, \quad N_4 = \delta/y.$$

To determine the curvature K_σ of the incident shock wave, it is necessary to give emanation conditions (5), i.e., the values of M, θ, jet incalculability $n_a = 1/J$, the ratio γ of the specific heats, and the type of symmetry. The jet incalculability and the shock wave strength, its inverse value, can be easily changed in practice. Two other parameters require change in the gas type and the nozzle design.

Therefore, $rK_\sigma(J)$ dependence of the shock wave curvature on its intensity caused by the jet incalculability is considering below at various outflow Mach numbers and nozzle semi-angles. Here r is nozzle exit section radius or half-width.

In plane jet flow, the shock wave curve depends monotonously on the opening semi-angle (pro rata sin θ). Therefore, in further plane flow examples, a nondimensional value $K_\sigma^- = rK_\sigma/\sin\theta$ is considered as in 5.

At small Mach numbers of the plane flow, K_σ^- value is positive (shock wave AT in Fig. 1 is curved downward in the edge vicinity). This value is increasing as the shock wave intensity function in the region (1; J_p), and at $J \to J_p$ it tends to infinity (Fig. 2a). At $J > J_p$ shock curvature is negative. At all special values of intensity (which correspond, e.g., to sonic flow velocity downstream of the shock, maximum flow deflection angle at given Mach number, or Crocco point) that are not equal to J_p, the shock wave curve is finite.

In particular, at $J \to 1$ (degeneracy of the shock into weak discontinuity) and at $J \to J_m$ (normal shock), it is expressed by general relations for plane and axis-symmetric flows:

$$\lim_{J\to 1} K_\sigma^- = \frac{(1 - 2\varepsilon)M^2 - 2(1 - \varepsilon) - \delta\mu(\mathrm{M})}{(1 - \varepsilon)M\left(M^2 - 1\right)},$$

$$\lim_{J\to J_m} K_\sigma^- = \frac{M^2 + \delta\mu(\mathrm{M})}{(1 - \varepsilon)\left(M^2 - 1\right)}, \quad \mu(M) = 1 + \varepsilon\left(M^2 - 1\right).$$

Increase of the plane flow Mach number up to $M_a = \sqrt{(2 - \varepsilon)/(1 - \varepsilon)}$ =1.483 value leads at first to the minimum curvature (Fig. 2b) in $J = 1$ point. The shock wave curvature value in the minimum point falls to zero at Mach number $M_b = 1.571$ and intensity $J_b = 1.242$, and after that it becomes negative (Fig. 2c). At voluntary gas specific heats ratio, the values M_b and J_b are the greatest real roots of the equations:

$$(3 - 4\varepsilon)^2\mathrm{M}_b^8 - 8\left(3 - 6\varepsilon + 4\varepsilon^2\right)\mathrm{M}_b^6 + 8\left(1 - 3\varepsilon + 4\varepsilon^2\right)\mathrm{M}_b^4 + 32\varepsilon(1 - \varepsilon)\mathrm{M}_b^2 + 16(1 - \varepsilon)^2 = 0,$$

$$\sum_{k=0}^{4} a_k J_b^k = 0, \quad a_4 = (1 - \varepsilon)(3 - 4\varepsilon)(3 + 5\varepsilon),$$

$$a_3 = -4(1 - \varepsilon)\left(6 + \varepsilon - 3\varepsilon^2 + 16\varepsilon^3\right)$$

$$a_2 = -2\left(7 + 36\varepsilon - 45\varepsilon^2 - 94\varepsilon^3 + 32\varepsilon^4 - 32\varepsilon^5\right),$$

$$a_1 = 4\left(4 + 11\varepsilon + 6\varepsilon^2 + 39\varepsilon^3 + 52\varepsilon^4 - 16\varepsilon^5\right)$$

$$a_0 = 13 + 62\varepsilon + 85\varepsilon^2 - 16\varepsilon^4 + 48\varepsilon^5.$$

At Mach number $M_c = \sqrt{2(1 - \varepsilon)/(1 - 2\varepsilon)} = 1.581$, the curvature of the shock degenerating into a weak discontinuity (i.e., in correctly expanded jet) becomes negative for the first time (Fig. 2d). Another value of the strength of the shock wave with the zero curvature at the same Mach number is equal to $J = M_c^2 - 1 = 1/(1 - 2\varepsilon) = 1.5$. At $M > M_c$, the strength of the zero-curvature oblique shock grows fast, and the flow behind it becomes subsonic at $M = 1.787$ and $J = 2.699$. At large Mach numbers, the zero curvature point

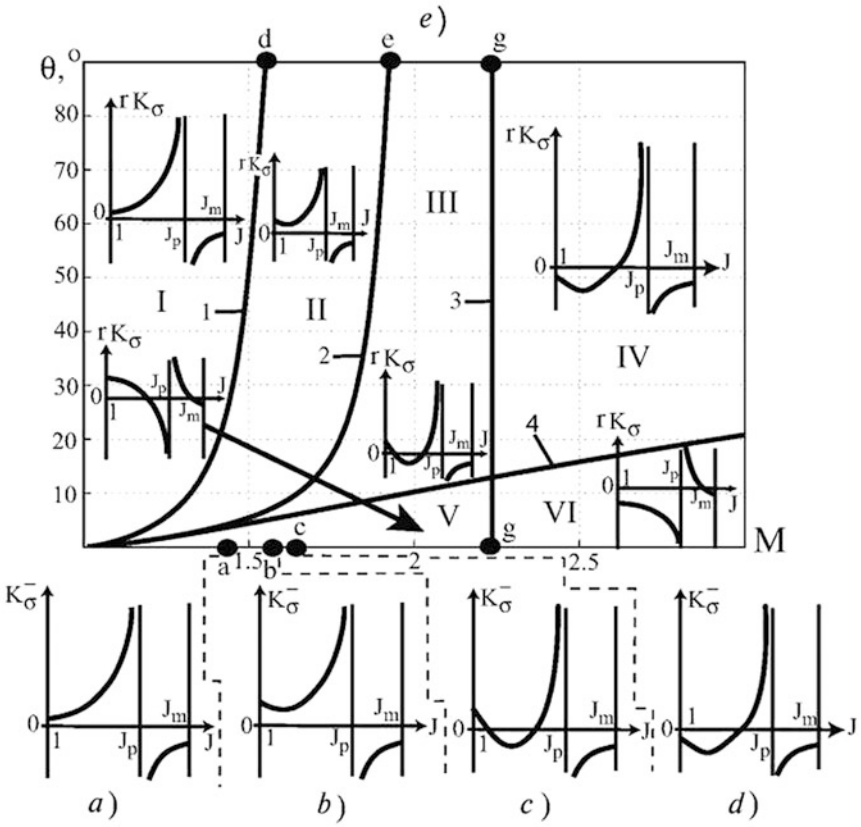

Fig. 2 Variation of the geometrical curvature of the shock emanating from the nozzle edge in relation to the emanation conditions

corresponds to a strong shock wave with subsonic flow behind it, and on the contrary, the intensity $J_{\min}$ of the shock with minimal curvature corresponds to the supersonic flow in the compressed layer.

Unlike the plane flow case, change in the curvature K_σ (or dimensionless curvature rK_σ) of shock wave AT depends on the angle θ value non-monotonously, which makes the two-parametrical study on the (M, θ) plane which is presented in Fig. 2e necessary. Curves 1–4 determined analytically are the boundaries of the regions I–VI with different dependence of the shock geometrical curvature on jet incalculability. In particular, curve 1, on which (similar to the plane jet at $M = M_a$) the minimum of the dependence $rK_\sigma(J)$ in point $J = 1$ occurs, is described by the following expression:

$$\cot\theta = -\frac{3(1-\varepsilon)M^4 - 2(3-\varepsilon)M^2 - (1-\varepsilon)}{(1-\varepsilon)\left(M^2-1\right)^{3/2}}.$$

This curve finishes at $\theta = 90^0$ and the Mach number

$$M_d = \frac{3-\varepsilon+2\sqrt{3-3\varepsilon+\varepsilon^2}}{3(1-\varepsilon)} = 1.551.$$

A problem of the practical implementation of "source flow" at a large nozzle angles is not considered here. Curve 2 corresponding to the moderate strength and negative curve of the shock wave ends at the Mach number $M_e = 1.925$ which is defined as the root of the equation:

$$\sum_{k=0}^{4} b_k \mathrm{M}_e^{2k} = 0, \quad b_6 = -24\varepsilon(2-3\varepsilon)^2,$$

$$b_5 = -80 + 672\varepsilon - 1036\varepsilon^2 + 384\varepsilon^3 + 252\varepsilon^4,$$

$$b_4 = 296 - 930\varepsilon + 412\varepsilon^2 + 886\varepsilon^3 - 1096\varepsilon^4 + 48\varepsilon^5,$$

$$b_3 = -(1-\varepsilon)\times(101 + 609\varepsilon - 1365\varepsilon^2 + 1775\varepsilon^3 - 192\varepsilon^4),$$

$$b_2 = -3(107 - 208\varepsilon + 423\varepsilon^2 - 96\varepsilon^3)(1-\varepsilon)^2,$$

$$b_1 = (61 - 337\varepsilon + 192\varepsilon^2)(1-\varepsilon)^3,$$

$$b_0 = (1+48\varepsilon)(1-\varepsilon)^4.$$

Vertical line 3 relates to the curvature direction change of the shock degenerating into the weak discontinuity. It corresponds to Mach number $M_g = 3(1-\varepsilon)/(1-3\varepsilon) = 2.236$ (in the plane case, the similar phenomenon takes place at $M = M_c$).

The direction change of the shock wave curvature infinite break in the diagram $rK_\sigma(J)$ at $J = J_p(M, \gamma)$ takes place at curve 4 which is defined by the equation:

$$\cot\theta = -\frac{\sqrt{J_p+\varepsilon}\left[(3+\varepsilon)(9\varepsilon-1)J_p^3 + (28+34\varepsilon+82\varepsilon^2+16\varepsilon^3)J_p^2 + cJ_p + d\right]}{(1-\varepsilon)\left((3+\varepsilon)J_p+2+4\varepsilon\right)\left(J_p-1\right)^{3/2}\sqrt{\left(1+\varepsilon J_p\right)\left(3J_p+1+4\varepsilon\right)}},$$
$$c = 33+94\varepsilon+49\varepsilon^2+48\varepsilon^3,$$
$$d = 2(1+2\varepsilon)(3+13\varepsilon).$$

It has the following horizontal asymptote at $M \to \infty$: $\theta = \arctan\frac{(1-\varepsilon)\sqrt{3\varepsilon}}{9\varepsilon-1} = 49.684^0$.

The character of the shock wave curvature behavior in I–IV zones is similar to the plane flow case at the Mach numbers corresponding to Fig. 2a–d. However, the I–IV zones analogous to plane flow correspond only to rather large values of the nozzle opening semi-angle in axis-symmetric jet. At small angles of θ (zones V and VI), the axis-symmetric flow factor is the prevailing one. The character of the shock wave curvature variation at small angles of θ does not have analogy in the plane jet flow case. At the emanation of the uniform axis-symmetric jet from a specially shaped nozzle ($\theta = 0$), the only difference from the adjacent regions (V and VI) is in zero values of the shock wave curvature at $J \to 1$ and $J = J_m$.

Conclusions

The calculations and analytical investigation performed have revealed definite peculiarities of nozzle tip flows. Shock wave formed at nozzle edge could have different curvature (positive or negative) depending on the flow conditions and type of symmetry (plane or axis-symmetric supersonic jet). The geometrical curvature dependence on the supersonic jet parameters is not uniform and not monotonous. The oblique shock that is convex to the axis or plane of flow symmetry occurs usually in the region of small Mach numbers, which might be relevant to inter-transition of regular/irregular reflection and excitation of auto-oscillation modes of the jet. The shock wave curvature behavior in axis-symmetric and plane jet greatly depends on a type of jet symmetry.

References

1. Adrianov, A.L., Starykh, A.L., Uskov, V.N.: Interference of Stationary Gasdynamic Discontinuities. Nauka, Novosibirsk (1995)
2. Smirnov, N.N., Nikitin, V.F., Alyari, S.S.: Investigation of self-sustaining waves in metastable systems. J. Propul. Power **25**, 593–608 (2009)
3. Emanuel, G., Hekiri, H.: Vorticity and its rate of change just downstream of a curved shock. Shock Waves **17**, 85–94 (2007)
4. Emanuel, G., Hekiri, H.: Vorticity jump across a shock in nonuniform flow. Shock Waves **21**, 71–72 (2011)
5. Uskov, V.N., Chernyshov, M.V.: Differential characteristics of flow filed in plane overexpanded jet in vicinity of nozzle lip. J. Appl. Mech. Tech. Phys. **47**, 366–376 (2006)
6. Omel'chenko, A.V., Uskov, V.N., Chernyshev, M.V.: An approximate analytical model of flow in the first barrel of an overexpanded jet. Tech. Phys. Lett. **29**, 243–245 (2003)
7. Silnikov, M.V., Chernyshov, M.V., Uskov, V.N.: Analytical solutions for Prandtl-Meyer wave – oblique shock overtaking interaction. Acta Astronaut. **99**, 175–183 (2014)
8. Glaznev, V.N., Zapryagaev, V.I., Uskov, V.N., Terekhova, N.M., Erofeev, V.K., Grigoryev, V.V., Kozhemiakin, A.O., Kotenok, V. A., Omel'chenko, A.V.: Jets and Unsteady Flows in Gas Dynamics. Siberian Branch of RAS, Novosibirsk (2000)
9. Terekhova, N.M.: Longitudinal vortices in supersonic jets. Dokl. RAN. **347**, 759–762 (1996)
10. Zapryagaev, V.I., Solotchin, A.V., Kiselev, N.P.: Structure of supersonic jet with varied geometry of nozzle entrance. J. Appl. Mech. Tech. Phys. **43**, 538–543 (2002)
11. Zapryagaev, V.I., Kiselev, N.P., Pavlov, A.A.: Effect of streamline curvature on intensity of streamwise vortices in the mixing layer of supersonic jets. J. Appl. Mech. Tech. Phys. **45**, 335–343 (2004)

Design and Validation of an Uncooled Pitot Probe for Hot, Supersonic Flow Investigations

Felix J. Förster, Nils C. Dröske, Jens von Wolfersdorf, and Bernhard Weigand

Introduction

Supersonic free jets are investigated in much detail for various reasons. Investigations may be motivated to gain further insight in the underlying flow phenomena [1, 2]. A technical application might be, for instance, the exhaust nozzle of aircraft [3] or rocket engines [4], or the free jet is used as defined test case for the validation of numerical setups [5, 6].

The accurate determination of flow parameters is hence essential. Intrusive pitot probes represent a simple and widely used way to measure flow velocities [7, 8].

At the Institute of Aerospace Thermodynamics (ITLR), supersonic air and mixing free jets are used as reference case for a laser-based, nonintrusive technique called laser-induced thermal acoustics (LITA), which allows simultaneous point measurements of the local Mach number and the speed of sound. So far, a comparison between this technique and conventional probes has only been carried out for free jets with an inlet total temperature up to 550 K [9], since the commercial probes available at the institute are limited to these moderate temperatures.

In order to obtain reference data for a hot free jet, a pitot probe needs to be built that can withstand the high total temperatures generated in the ITLR supersonic test facility (up to 1300K). At such temperatures, steel probes require a cooling system [4, 10], which increases the complexity of the measurement system, or more heat-resistant materials need to be used as reported by Springer et al. [11]. There, a hybrid design with a temperature-resistant silicon carbide probe tip and a water-cooled base is used.

In this paper we suggest an uncooled, low-cost pitot probe made from a high-performance ferritic iron-chromium-aluminium alloy (FeCrAl alloy) distributed by the Sandvik Group under the trade name Kanthal A1™. Designed for electrical heating elements in industrial furnaces, Kanthal A1™ is certified for the use at temperatures up to 1673K and has good mechanical properties even for elevated temperatures [12].

The presented approach combines a low-cost design due to the use of stock size raw material with an easy manufacturing process because of the good processability of a metal material. In addition, the need for a cooling system is removed.

The paper describes the design of the Kanthal probe, the obstacles during the manufacturing process, a validation with the already available reference probe in a free jet with moderate inlet total temperature and an application case for a hot free jet with an inlet total temperature up to 1100 K.

Design and Manufacturing

Kanthal A1™ is already available at the institute as it is used for the electrical heater system of the facility. Therefore, the institute holds a small stock for repair and maintenance. For simplicity, the design is tailored to the available rods, which restricts the probe head dimensions to 10 mm in width and height. Generally, Kanthal is offered in a variety of shapes, including strips, rods or pipes. It is also potentially available as sample material making such probes a real low-cost alternative. A second design constraint is for the probe tip to be congruent with the reference probe to minimise any deviations due to the probe's shape.

Figure 1 shows a technical drawing of the probe head. The tip is turned down to an outer diameter of 5mm with a 26.6° cone at its end. The pressure is sampled via a hole 0.5 mm in diameter. The head is welded onto a 3 mm strip as holder and connected to a pipe, which allows the pressure transducer to be located further away from the hot fluid.

F.J. Förster (✉) • N.C. Dröske • J. von Wolfersdorf • B. Weigand
Institute of Aerospace Thermodynamics, University of Stuttgart, Pfaffenwaldring 31, 70569 Stuttgart, Germany
e-mail: Felix.Foerster@itlr.uni-stuttgart.de

G. Ben-Dor et al. (eds.), *30th International Symposium on Shock Waves 1*, DOI 10.1007/978-3-319-46213-4_49

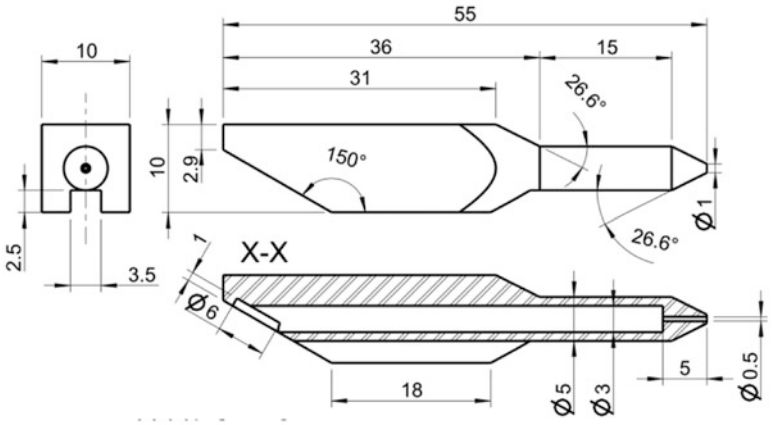

Fig. 1 Probe head (dimensions in mm)

Fig. 2 Kanthal A1™ rod

The manufacturing process consists only of standard machining techniques, namely, milling, turning and drilling. The material shows a brittle behaviour due to its almost crystalline structure, as one can see in Fig. 2. All machines are set to slow feed motion to reduce the lateral forces, as otherwise even thick rods with diameters up to 20 mm would shear off.

After machining, the probe is put in a high-temperature oven to oxidise the surface of the probe, as only this oxide layer ensures the high-temperature resistance of Kanthal. However, a second feature of this layer is found, which makes the oxidation a compulsory step for any pressure probe made from Kanthal. As after machining, the probe is not sealed, meaning that air is allowed to migrate through the material, probably due to the crystalline structure. Melting the top surface with a welder to change the structure shows no effect on the permeability, but the oxide layer results in a reduced leakage. The probe is completely airtight after eight cycles in an oven, resulting in a total oxidation time of 40 h at 1200 K. After this exposure time, a mass gain through oxidation of 0.14 mg/cm^2 is reported [13], which corresponds to an oxide layer approximately 1 µm in thickness.

Experimental Setup

Figure 3 illustrates the supersonic combustion facility at ITLR. A screw compressor continuously compresses air taken from the ambience. The compressed air is dried in a dehumidifier and heated in a three-staged electric heating system, summing up to a total power consumption of 1 MW for the test facility. Four pressure tanks with a total volume of 8m^3 store air at 100 bar as a backup to allow an emergency shutdown of the heating system at all times.

The test envelope is defined by the maximum total temperature of $T_t = 1300\text{K}$ and a maximum mass flow of $\dot{m} = 1.45\ \text{kg/s}$ at a maximum total pressure of $p_t = 10$ bar. The key features of this facility are its continuous operation and the electric heating system, which allow very long test times with clean, hot air.

The nozzle used in this study is shown in Fig. 4. This convergent-divergent nozzle is made of stainless steel and has an exit diameter of $D_{\text{exit}} = 32.2\text{mm}$. Its contour design is based on the method of characteristics as introduced by Prandtl and Busemann [14] and corrected by the absolute displacement thickness. The nozzle generates a free jet with an exit Mach number of approximately $M \approx 1.5$ at its design pressure ratio of $p_\infty/p_t = 0.2724$. To prevent deforming due to thermal loads at elevated temperatures, the nozzle is water-cooled. The inlet conditions are defined by the total pressure and total temperature and measured in the nozzle plenum.

Two supersonic air free jets are investigated for an inlet total temperature of $T_t = 550\text{K}$ and $T_t = 1100\text{K}$, respectively. The flow parameters for the experiments are summarised in Table 1.

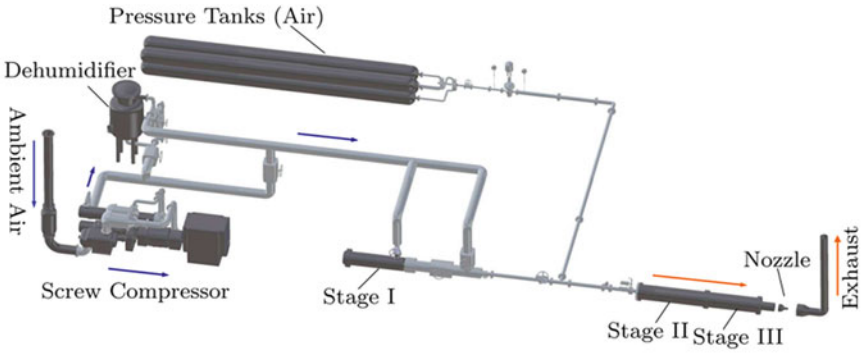

Fig. 3 Supersonic test facility at ITLR

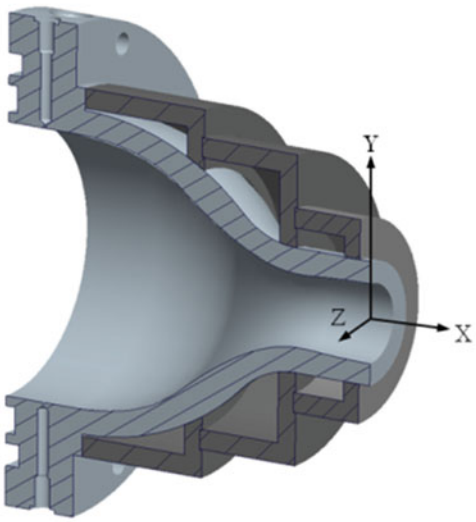

Fig. 4 Supersonic nozzle

Results

Data Processing

The air is assumed as ideal gas with constant ratio of specific capacities $\gamma = c_p/c_v$. As the pressure at the nozzle is matched to the ambient pressure, the static pressure inside the jet is set to be constant and equal to the ambient pressure ($p_{\text{static}} = p_\infty$).

For these assumptions, the total pressure can be converted into the flow Mach number using the isentropic flow equation for the subsonic flow regime:

$$\frac{p_t}{p_\infty} = \left(1 + \frac{\gamma - 1}{2} M^2\right)^{\frac{\gamma}{\gamma-1}} \tag{1}$$

and the Rayleigh-Pitot equation for the supersonic flow regime

$$\frac{p_t}{p_\infty} = \left(\frac{\gamma + 1}{2} M^2\right)^{\frac{\gamma}{\gamma-1}} \left(\frac{2\gamma}{\gamma + 1} M^2 - \frac{\gamma - 1}{\gamma + 1}\right)^{\frac{1}{1-\gamma}}. \tag{2}$$

An uncertainty in Mach number arises due to errors made in the measurements of the total pressure at the probe tip and the ambient pressure. Both quantities are treated as independent and normally distributed parameters. Their propagation is estimated via a first-order Taylor expansion of Eqs. (1) and (2) and the full-scale errors of the devices used. The full-scale errors are $\Delta p_t = 0.04$ bar and $\Delta p_\infty = 0.01$ bar for the total pressure transducer and the ambient pressure gauge, respectively, which leads to a maximum uncertainty for the Mach number within ± 1.5 % for the supersonic flow regime.

Validation

Since the reference probe is limited to moderate temperatures, the validation is conducted for the heated jet ($T_t = 550$ K). The probes are mounted on a three-axis translation table to conduct the measurements with both probes. The same total pressure transducer was used to minimise deviations between the readings other than due to the probes themselves. For Eqs. (1) and (2), γ is said to be constant and set to 1.4 as the temperature rise inside the jet is relatively small for the heated free jet.

The measurements are taken at three planes downstream of the nozzle exit at $X/D_{\text{exit}} = 1$, 3 and 5. For each plane, measurements are taken in radial direction Y starting at the symmetry line. The positions are normalised by the exit radius R of the nozzle.

Figure 5 shows the Mach number distribution for the reference (○) and the Kanthal (◇) probes together with the measurement uncertainty (∇) and the deviation (Δ) between the readings of both probes.

The plots show a core flow with approximately homogeneous flow conditions and a mixing layer towards the ambient. The core flow diminishes for axial positions further downstream due to the increasing mixing process between the core flow and the ambient air.

The deviation between both probes is approximately $\Delta M \approx 0.014$ for the core flow and hence within 1 % relative to the exit Mach number. Deviations larger than the measurement uncertainty are only found for the shear layer region in the $X/D_{\text{exit}} = 1$ and 3 planes. This can be explained by the high turbulence in the starting shear layer, where the time-average measurements of both probes are prone to error. The observed deviation is hence due to the flow structure rather than disclosing a difference of the probes. This idea is further supported as the deviations decline for planes further downstream until both probes match very well for the entire jet in the last plane, where the shear layer is fully developed.

Overall, the new Kanthal probe achieves a similar performance to the commercial reference probe. After this validation, the Kanthal probe can now be used for the investigation of high-temperature jets.

Table 1 Flow parameters for the supersonic air free jets

	T_t (K)	T_∞ (K)	p_t (bar)	p_∞ (bar)
Heated jet	550	290	3.55	0.970
Hot jet	1100	292	3.54	0.965

Application

To demonstrate the probe performance in a high-temperature flow field, a hot jet was investigated ($T_t = 1100\text{K}$). For the measurements, the probe was exposed repeatedly to the hot flow for up to 30 s. The high temperature causes a rapid heat-up of the probe and visible thermal load on the same as illustrated in Fig. 6. Although the total pressure reading remained approximately constant over the heat-up process, the measurements were taken over several seconds to ensure a sufficient averaging over time. Between the measurements in the core flow region, the probe was traversed outside the jet to allow a cool down before the next measurement. The probe showed no visual damage from this procedure, and the readings were reproducible within the uncertainty range for the entire test campaign.

The resulting Mach number distributions are presented in Fig. 7 and show the typical flow regimes identified before for the heated free jet. It should be noted that for the post-processing, γ was set to 1.385 to account for the high flow temperature. The value used represents the average of the value for the core flow, where the total temperature can be

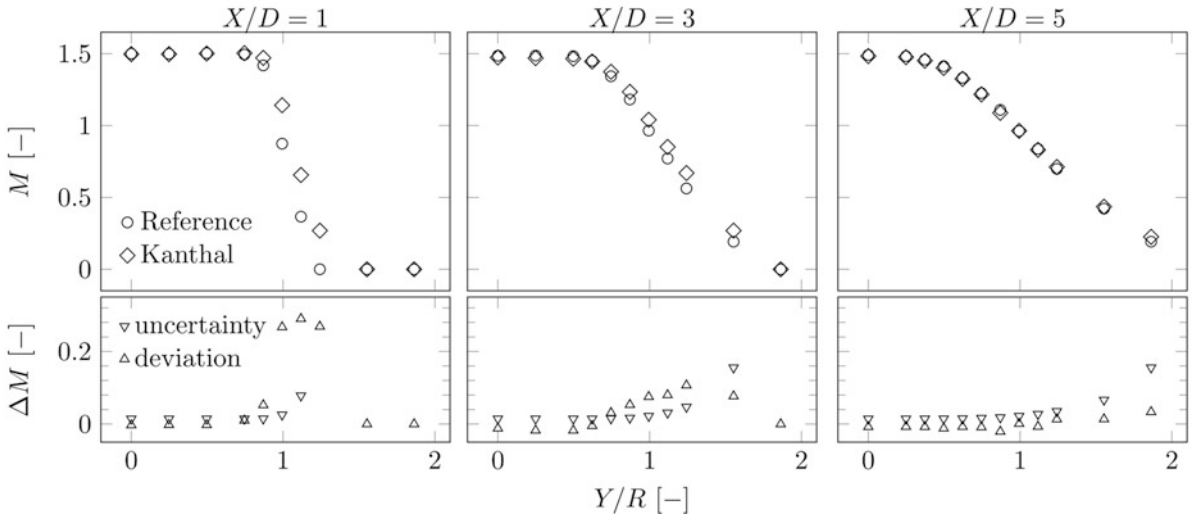

Fig. 5 Mach number distributions for the heated jet

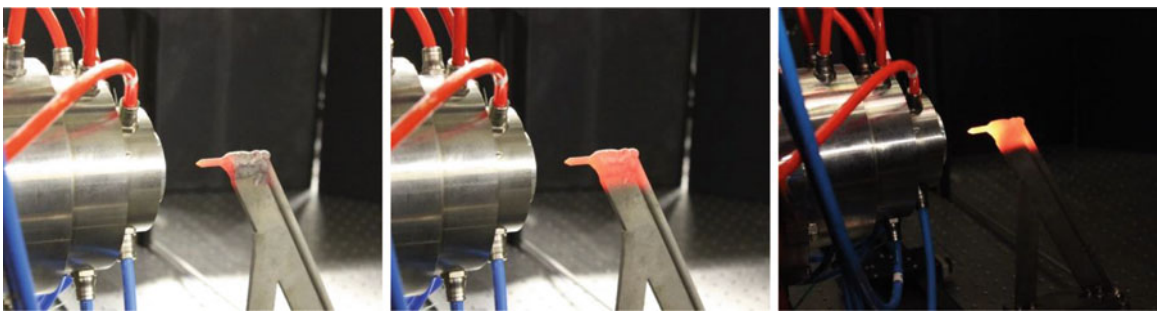

Fig. 6 Heat-up of the probe inside the jet

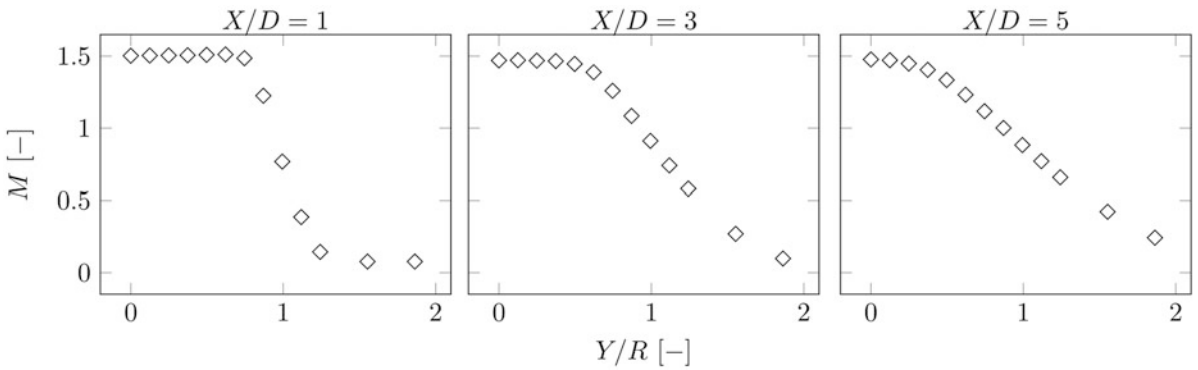

Fig. 7 Mach number distributions for the hot jet

assumed to be the same as the inlet total temperature ($\gamma = 1.37$) and the value for the ambient air ($\gamma = 1.4$). This is an additional source of error, as, in contrary to the heated jet, the temperature gradient in radial direction is not negligible. Accounting for changes in γ would require the temperature distribution to be obtained, for instance, via a total temperature probe. However, for the intended demonstration of the Kanthal probe in a high-temperature flow field, the proposed assumption may be made.

The obtained plots shall therefore been seen as proof of concept for the Kanthal probe rather than quantitative data. Consequently, the plots are presented without the uncertainty bars. More accurate measurements of the Mach number will require the separate determination of the local total temperature in order to derive the local static temperature. As the Kanthal probe was successfully used in the high-temperature jet, a total temperature probe using the same design concept is planned for the future to address this issue.

Conclusion

A cost-efficient pitot probe was made from the high-performance FeCrAl alloy Kanthal A1™ using standard machining techniques. The probe was validated in a heated, supersonic free jet ($T_t = 550\text{K}$) against a commercial reference steel probe. Deviations are found to be within the measurement uncertainty of $\pm 1.5\%$ except for regions of high turbulence, primarily at the developing shear layer close to the nozzle exit. Subsequently, the probe was successfully used to investigate a hot, supersonic free jet ($T_t = 1100\text{K}$) along several planes downstream of the nozzle exit. The probe was traversed repeatedly into the core flow regime and showed no visual effect due to the high thermal loads, although long sampling times were required for the time-averaged measurements made. Without the need for a cooling system, this probe is an easy-to-use, low-cost alternative to commercially available total pressure probes. As the concept proved to be very promising, a total temperature probe will be designed analogously to determine static temperature profiles as well. Furthermore, the probe will be used as a reference technique for the verification of more sophisticated, laser-based measurement techniques like LITA.

Acknowledgement This work was performed within the Research Training Group "Aero Thermodynamic Design of a Scramjet Propulsion System for Future Space Transport Vehicles" (GRK1095/2). The authors would like to thank the German Research Foundation (Deutsche Forschungsgemeinschaft). Thanks are also due to Dennis Nehring from the mechanical workshop at ITLR for his excellent work conducting the CNC machining and welding.

References

1. Edgington-Mitchell, D., Honnery, D., Soria, J.: The underexpanded jet mach disk and its associated shear layer. Phys. Fluid **26**, 1–18 (2014)
2. Katanoda, H., et al.: Pitot pressures of correctly-expanded and underexpanded free jets from axisymmetric supersonic nozzles. Shock Waves **10**, 95–101 (2000)
3. Veltin, J., McLaughlin, D.: Flow field and acoustic measurements of rectangular supersonic jets. In: 47th AIAA Aerospace Sciences Meeting, AIAA-2009-19, (2009)
4. Legge, H., Dettleff, G.: Pitot pressure and heat-transfer measurements in hydrazine thruster plumes. J. Spacecr. **23**, 357–362 (1986)
5. Cutler, A., et al.: Supersonic coaxial jet experiment for CFD code validation. In: 30th AIAA Fluid Dynamics Conference, AIAA-99-3588, (1999)
6. Miller, S., et al.: Validation of computational fluid dynamics for supersonic shock containing jets. In: 14th AIAA/CEAS Aeroacoustics Conference, AIAA-2008-2988, (2008)
7. Bryer, D., Pankhurst, R.: Pressure-Probe Methods for Determining Wind Speed and Flow Direction. National Physical Laboratory, Teddington (1971)
8. Porro, A.: Pressure probe designs for dynamic pressure measurements in a supersonic flow field. In: 19th International Congress on ICIASF, 417-426, (2001)
9. Förster, F., Weigand, B.: Characterization of a heterodyne LITA setup for simultaneous flow velocity and speed of sound measurements. In: 19th AIAA International Space Planes and Hypersonic Systems and Technologies Conference, AIAA-2014-2506, (2014)

10. MacKinnon, H., et al.: Advances in aerodynamic probes for high-enthalpy applications. In: 24th AIAA Aerodynamic Measurement Technology and Ground Testing Conference, AIAA-2004-2594, (2004)
11. Springer, R.R., et al.: Conventional/laser diagnostics to assess flow quality in a combustion-heated facility. In: 35th AIAA/ASME/SAW/ASEE Joint Propulsion Conference and Exhibit, AIAA-99-2170, (1999)
12. Sandvik Group.: Kanthal Appliance Heating Alloy Handbook, accessed via kanthal.com
13. Cueff, R.: Oxidation behavior of Kanthal A1 and Kanthal AF at 1173 K: effect of Yttrium alloying addition. Appl. Surf. Sci. **207**, 246–254 (2003)
14. Anderson, J.: Modern Compressible Flow with Historical Perspective. McGraw-Hill (2007)

Large Eddy Simulation of a Supersonic Underexpanded Square Jet

Huanhao Zhang and Zhihua Chen

Acknowledgment This work was supported by the National Natural Science Foundation of China under Grant No. 11502117.

H. Zhang (✉) • Z. Chen
Key Laboratory of Transient Physics, Nanjing University of Science and Technology, Nanjing, China
e-mail: zhanghuanhao9@163.com

G. Ben-Dor et al. (eds.), *30th International Symposium on Shock Waves 1*, DOI 10.1007/978-3-319-46213-4_50

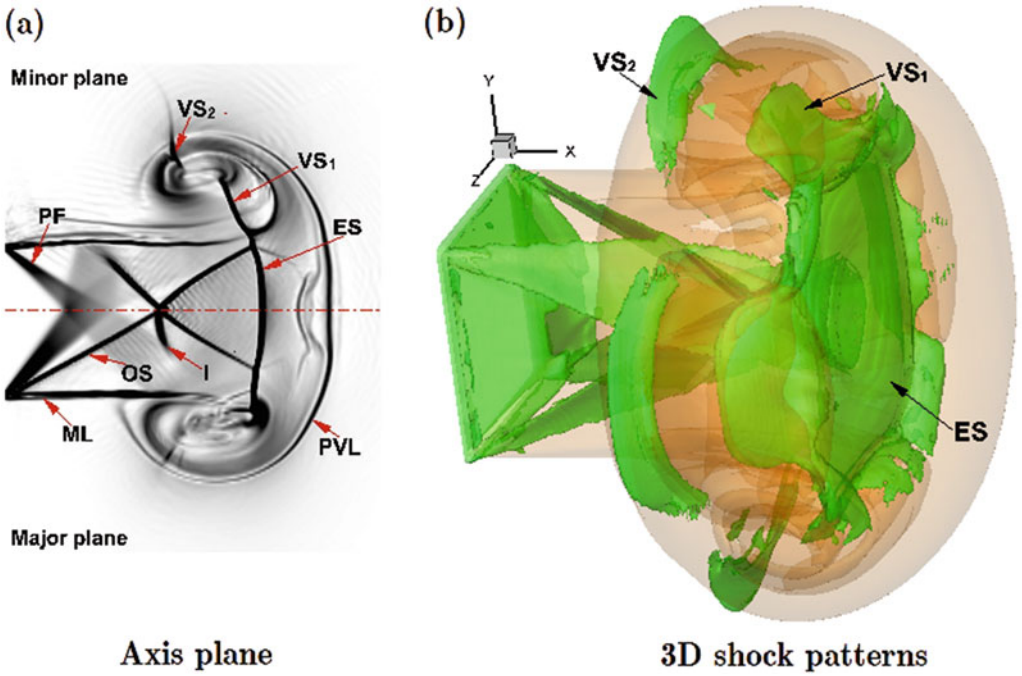

Fig. 1 The typical initial flow structures of square jet at $t = 0.11$ ms. (*ES* embedded shock, *ML* mixing layer, *PVL* primary vortex loop, *PF* Prandtl-Meyer expansion fan, *OS* oblique shock patterns, *VS1*,*VS2* vortex-induced shock pair.)

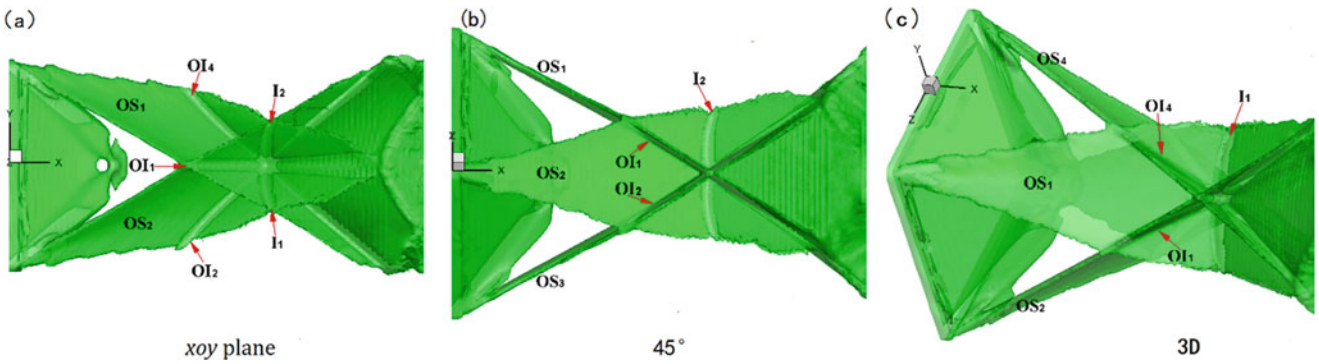

Fig. 2 The typical three-dimensional shock wave structures of the upstream of vortex loop

Part VI

Chemical Kinetics and Chemical Reacting Flows

Species Time-History Measurements During Jet Fuel Pyrolysis

D.F. Davidson, A. Tulgestke, Y. Zhu, S. Wang, and R.K. Hanson

Introduction

The aerospace industry and various national combustion laboratories are attempting to develop reliable computer models for jet fuels and jet engines. University laboratories support this effort by the development of accurate chemical kinetics models of jet fuels. This modeling is divided into two parts: the development and refinement of detailed reaction mechanisms and the development of an experimental kinetic target database for model testing and validation. Here we are concerned with the role of shock tube/laser absorption measurements in providing accurate kinetic targets for this kinetic database.

Large detailed reaction mechanisms are able to capture much of what we know about oxidation kinetics of surrogates for large hydrocarbon fuels. Mechanisms such as the NUI/Galway Malewicki et al. [1] model and surrogate [2] provide the modeler and the experimentalist with a guide to the likely intermediate species and their kinetic progress that occur during jet fuel pyrolysis or oxidation. The primary disadvantages of these large mechanisms are their size and their limited, generic relationship with real fuel composition. The Malewicki et al. model, for example, has 2072 species and 8310 reactions. The Dooley #2 surrogate uses only four components to capture jet fuel chemical kinetics.

Simulations using the Malewicki et al. model show that at early times in pyrolysis, there is rapid conversion of the fuel components to five major decomposition products, C_2H_4, C_3H_6, H_2, CH_4 and i-C_4H_8, as well as a remaining fuel fraction that includes a significant aromatic fraction. Figure 1 shows the time histories of the six species with the largest concentrations during pyrolysis at 1200 K. A soup of minor species (not shown) exists in the mixture at significantly lower concentrations. However, these minor species are low enough in concentration that the remaining initial fuel components and the five major product species account for 90+% of the initial fuel carbon.

A smaller reaction mechanism approach, based on the observation that a limited stable fuel decomposition product distribution exists, could overcome the disadvantages of larger mechanisms. Wang of Stanford has proposed such a HyChem model [3] that combines a smaller pyrolysis sub-mechanism constrained by measurements of real fuel pyrolysis products and a well-established C6 oxidation mechanism [4]. A primary advantage of this model is its size; preliminary versions of this model have 112 species (1/20th of the Malewicki et al. model, for example) and 812 reactions (1/10th of the Malewicki et al. model). And because of the experimentally constrained pyrolysis product distribution, this model also provides a direct chemical relationship to a real fuel. Its main disadvantage is that it does not provide a full picture of the intermediate species that occur during fuel pyrolysis. However, because of the actual temporal separation of the pyrolysis and oxidation processes that occurs (due to the rapid decomposition of the fuel before significant oxidation progress and heat release) during high-temperature fuel combustion, this limited picture of pyrolysis is not a serious disadvantage.

Evaluation of the fuel decomposition product distribution can be measured in flow reactor studies at long times (i.e., 5+ ms). However, complications in flow reactor studies because of the initial fuel mixing time, and in some cases vitiated flow conditions, preclude drawing conclusions from the flow reactor measurements at shorter times. Species concentration measurements relevant to actual jet engine resident times require time-history data over significantly shorter test times. It is here, in the first 500 μs to 1 ms of high-temperature engine environment, where the relevant engine chemistry matters, and it is here where measurements, behind reflected shock waves, of species

D.F. Davidson (✉) • A. Tulgestke • Y. Zhu • S. Wang • R.K. Hanson
Mechanical Engineering Department, Stanford University, Stanford, CA 94305, USA
e-mail: dfd@stanford.edu

G. Ben-Dor et al. (eds.), *30th International Symposium on Shock Waves 1*, DOI 10.1007/978-3-319-46213-4_51

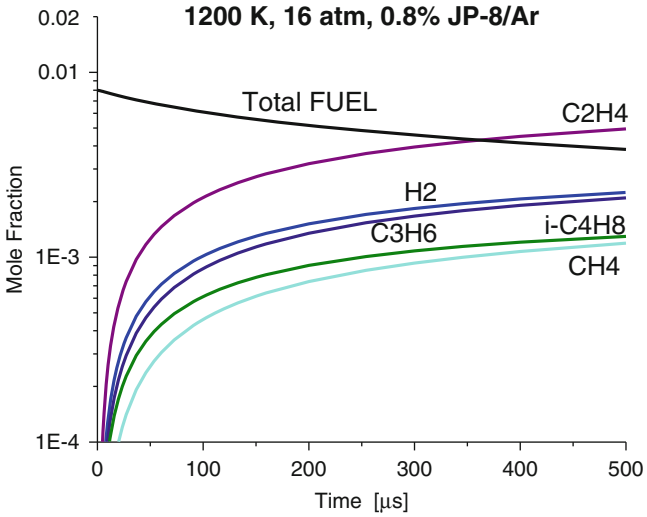

Fig. 1 Simulation of JP-8 pyrolysis using the Malewicki et al. [1] mechanism with the Dooley #2 surrogate. Initial reflected shock conditions: 1200 K, 16 atm, 0.8 % JP-8/argon. The six major species are shown

concentration time histories using laser absorption methods can provide the necessary data.

In the current study, the stagnated flow behind reflected shock waves provides the near-constant high-temperature, high-pressure, test gas conditions for jet fuel pyrolysis experiments. Measurements were made in the Stanford University 5 cm ID, high-pressure, helium-driven, heated (90 °C) shock tube [5]. Mixtures were made using fully evaporated jet fuel in research-grade argon (Praxair™). Multiple incident shock arrival time measurements were used to extrapolate the incident shock speed to the end wall, and the frozen-chemistry shock equations were used to determine the initial reflected shock conditions. Uncertainties in the reflected shock temperatures and pressures are typically ±1 %.

Laser Absorption Measurements

As the above discussion implies, an accurate description of jet fuel pyrolysis in a jet engine can be based on time-history measurements of six species: fuel, CH_4, C_2H_4, C_3H_6, i-C_4H_8, and aromatics. Narrow-linewidth laser absorption takes advantage of the Beer-Lambert law to relate the measured absorbance to the unknown species concentrations:

$$\alpha_\lambda = \ln(I_0/I)_\lambda = \sum (\sigma_i N_i)\, L \qquad (1)$$

where α_λ is the measured absorbance at wavelength λ, $(I/I_0)_\lambda$ is the measured fractional laser transmission through the test gas over the path length L (the inner diameter of the shock tube), σ_i is the absorption cross section at wavelength λ for the i-th species, and N_i is the number density of the i-th species.

When one $\sigma_i N_i$ product dominates the absorbance at a particular wavelength and other species have broad, nearly constant, and featureless absorbance at this wavelength, we can use a two-wavelength differential method, i.e., online minus offline, to determine the concentration of the dominant absorber. This is the case for ethylene, C_2H_4, and methane, CH_4. When several species have significant $\sigma_i N_i$ products at a particular wavelength, we can take advantage of differences in these absorbances at different wavelengths and use a matrix approach to determine the concentration of each of the absorbers. This method would be used to determine fuel, propene, isobutene, and aromatic concentrations.

The current study uses the following wavelengths and laser types for the species indicated:

3.175 μm	ICL	Methane online
3.177 μm	ICL	Methane offline
3.280 μm	ICL	Aromatics
3.391 μm	HeNe	Fuel
10.532 μm	CO_2	Ethylene online
10.675 μm	CO_2	Ethylene offline
10.958 μm	QCL	Propene
11.345 μm	QCL	Isobutene

For each wavelength, absorption cross-sectional data is needed for each species where the $\sigma_i N_i$ product is significant. Wide variation in the absorption cross sections at each wavelength and for each species occurs; the particular species wavelengths were chosen to maximize the signal for that particular species relative to other absorbers. Current work in our laboratory is involved with accurately measuring the absorption cross sections for each species as a function of wavelength, temperature, and pressure (where relevant).

Species mole-fraction time histories are determined from the absorbances (converted from the measured transmissions), the temperature and pressure time histories, and the measured array of absorption cross sections. In the current experiments, pressure is measured using a sidewall-mounted Kistler™ PZT; temperature is determined from an initial chemical kinetics model of the fuel pyrolysis with the pressure profile as a constraint.

Results and Discussion

Here we present the results of the species time-history measurements for methane and ethylene (using the two-wavelength method) during jet fuel pyrolysis. Absorption cross sections at the ethylene wavelengths are derived from Ren et al. [6]; absorption cross sections at the methane wavelengths are derived from Sur et al. [7]. Knowledge that

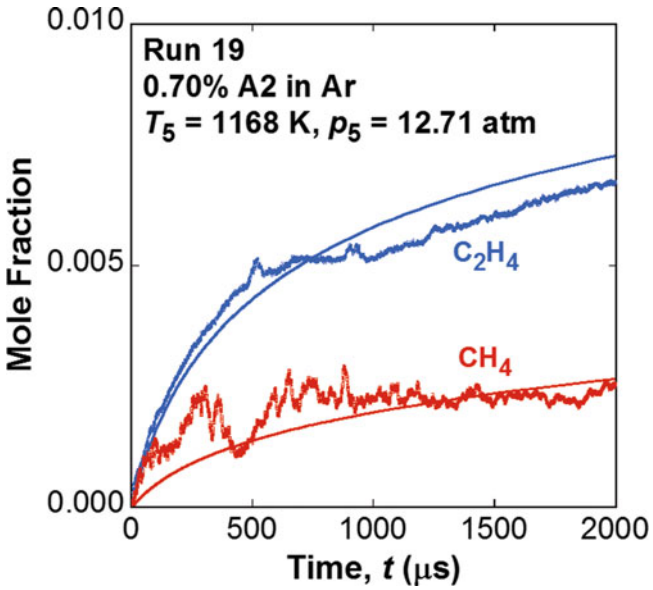

Fig. 2 Laser absorption measurements of C_2H_4, and CH_4 during Jet A pyrolysis. Initial reflected shock conditions: 1168 K, 12.71 atm, 0.7 % Jet A/argon. Solid lines are HyChem simulations

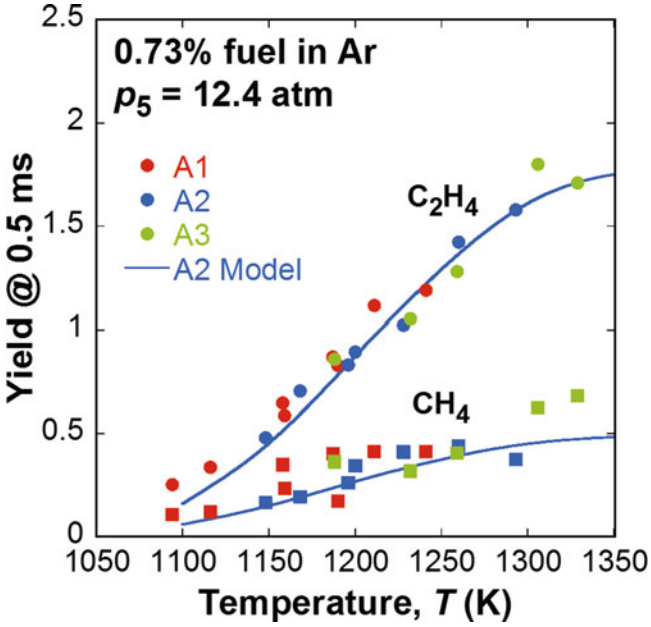

Fig. 3 Ethylene and methane product yields during jet fuel pyrolysis; yields at 500 μs. Average reflected shock pressure and fuel loading: 12.4 atm and 0.73 % fuel in argon

the interfering species absorption is not strongly wavelength dependent enables the simple two-wavelength subtraction process to be used. Uncertainty in the species concentrations is typically ±10 % of signal. Fuel concentrations were simultaneously measured using in situ 3.39 μm laser absorption to ensure accurate fuel loading.

Three kerosenic jet fuels were studied. These fuels were identified by the Federal Aviation Administration (FAA) [8] as Category A fuels: A-1 is a low-aromatic JP-8 fuel POSF 10264 with $C_{10.8}H_{21.8}$; A-2 is an average Jet A fuel POSF 10325 with $C_{11.4}H_{22.1}$; and A-3 is a high flash point, low-H-content JP-5 fuel POSF 10289 with $C_{11.9}H_{22.6}$.

Figure 2 shows representative time-history data for one reflected shock wave experiment: pyrolysis of A-1 fuel in argon at 1168 K, 12.71 atm. Excellent signal-to-noise ratios are achieved for fuel and C_2H_4, and good SNR for methane is achieved, considering its weaker $\sigma_i N_i$ product. At the temperature and pressure of this experiment over 2 ms, approximately 13 % of the fuel carbon has converted to ethylene and approximately 2 % to methane.

A large series of these types of measurements were acquired for a range of temperatures for the three Category A fuels. A summary of the product yields is shown in Fig. 3. Here product yield is defined as molecules of product per equivalent molecule of fuel.

Several observations can be made about these measurements. The first is that there is significant fuel conversion during pyrolysis/decomposition to ethylene. At the highest temperature tested, approximately 32 % of the fuel carbon is converted to C_2H_4. However, at 1350 K, only 5 % of the fuel carbon is converted to methane. At the highest temperatures, the ethylene yields reach a maximum; subsequent decomposition of ethylene (to C_2H_2 and CH_4) is expected at these high temperatures. Thus as ethylene decomposes, higher methane yields at higher temperatures are also expected.

Perhaps more surprisingly, given that the three Category A fuel compositions are very different, is that the product yields for all three fuels are very similar. In general all three fuels exhibit very similar decomposition product distributions for C_2H_4 and CH_4 over the entire temperature range studied.

Figure 4 presents pyrolysis product yields as a function of time at 1228 K. For ethylene, at the higher temperatures, most of the fuel decomposition to ethylene occurs in the first 500 μs. However for methane, there is slow continued formation at higher temperatures. This occurs as other products begin to slowly decompose to methane, owing to its greater thermochemical stability.

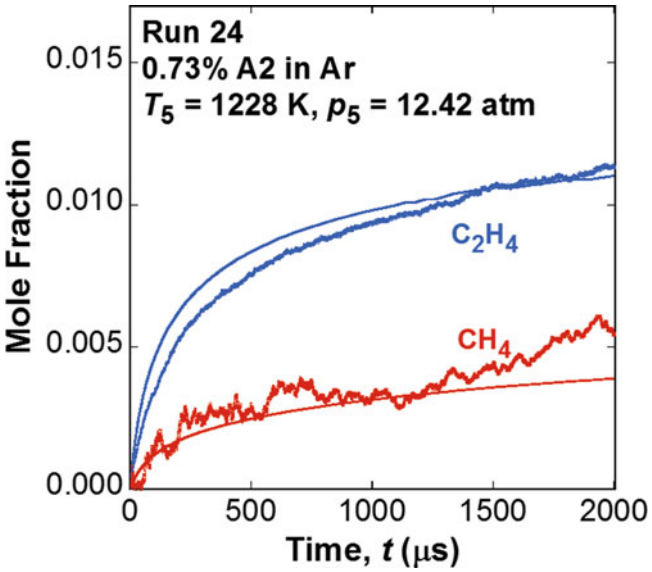

Fig. 4 Representative example of time dependence of ethylene and methane product yields during jet fuel pyrolysis. Lines represent HyChem model simulations. Reflected shock conditions:1228 K, 12.42 atm and 0.73 % fuel in argon

Conclusion

A database of jet fuel pyrolysis product species time histories was acquired for three FAA Category A fuels. These laser absorption data are characterized by very accurate and uniform test conditions, fuel loading, and species concentrations. Measured ethylene and methane product yields were found to be similar for all three Category A fuels over temperatures from 1100 to 1350 K.

These C_2H_4 and CH_4 data provide kinetic targets for jet fuel models that use product yields to constrain reduced pyrolysis sub-mechanisms. Current work is directed toward making measurements of these fuels with additional wavelengths to place constraints on the propene, isobutene, and total aromatic product distribution using the matrix approach.

Acknowledgments This work was supported by the Air Force Office of Scientific Research through AFOSR Grant No. FA9550-11-1-0217 under the AFRL Integrated Product Team with Dr. Chiping Li as contract monitor. A portion of the analysis of this data was funded by the US Federal Aviation Administration (FAA) Office of Environment and Energy as a part of ASCENT Project 35 under FAA Award Number 13-C-AJFE-SU-008. Any opinions, findings, and conclusions or recommendations expressed in this material are those of the authors and do not necessarily reflect the views of the FAA or other ASCENT sponsors.

References

1. Malewicki, T., Gudiyella, S., Brezinsky, K.: Experimental and modeling study on the oxidation of Jet A and the n-dodecane/iso-octane/n-propylbenzene/ 1,3,5-trimethylbenzene surrogate fuel. Combust. Flame **160**, 17–30 (2013)
2. Dooley, S., Won, S.H., Heyne, J., et al.: The experimental evaluation of a methodology for surrogate fuel formulation to emulate gas phase combustion kinetic phenomena. Combust. Flame **159**, 1444–1466 (2012)
3. Wang, H.: Hybrid, experimentally constrained pyrolysis – detailed oxidation (Hybrid ECP-DO) model. AFOSR Contractors Meeting June 3, 2014
4. Wang, H., You, X., Joshi, A.V., et al.: USC Mech Version II. High-Temperature Combustion Reaction Model of H_2/CO/C_1-C_4 Compounds. http://ignis.usc.edu/USC_Mech_II.htm, May 2007
5. Zhu, Y., Li, S., Davidson, D.F., Hanson, R.K.: Ignition delay times of conventional and alternative fuels behind reflected shock waves. Proc. Combust. Inst. **35**, 241–248 (2015)
6. Ren, W., Davidson, D.F., Hanson, R.K.: IR laser absorption diagnostic for C_2H_4 in shock tube kinetics studies. Int. J. Chem. Kinet. **44**, 423–432 (2012)
7. Sur, R., Wang, S., Sun, K., et al.: High-sensitivity interference-free diagnostic for measurement of methane in shock tubes. J. Quant. Spectrosc. Radiat. Transfer **156**, 80–87 (2015)
8. Edwards, J.T.: CIV USAF AFMC AFRL/RQTF, Private communication, January 2015

Rapid Chemiluminescent Imaging Behind Reflected Shock Waves

D.F. Davidson, A. Tulgestke, C. Strand, M.F. Campbell, V.A. Troutman, V.A. Miller, and R.K. Hanson

Introduction

Current shock tube combustion experiments generally assume that the test environment behind a reflected shock wave is quiescent and that ignition processes progress uniformly over the entire test volume. However, various past investigations, including those based on schlieren data and sidewall imaging [1, 2], have observed nonuniform ignition in certain test regimes. Here, we use both conventional diagnostics (pressure, emission, and laser absorption) and a high-speed chemiluminescent imaging system to investigate the ignition behavior of n-heptane/oxygen/argon in shock tubes at long test times (greater than 2 ms), in an attempt to map the boundary of uniform and nonuniform ignition behavior in one of our shock tubes.

Ignition delay times from separate low-pressure n-heptane/O_2/argon experiments conducted in our laboratory are shown in Fig. 1. Note the relatively good agreement between the model of Mehl et al. [3] and experiment at the highest (above 1100 K) and lowest (700 K) temperatures for the second-stage (primary) ignition delay time. However, modeling and experiment vary significantly and the data exhibits larger scatter, over the intermediate temperature regime from 700 to 1100 K for second-stage ignition. Note that this temperature window includes the negative-temperature-coefficient (NTC) regime, and the observed second-stage ignition delay times at temperatures above about 850 K have similar values to those seen in the first-stage ignition below 800 K. Also, we note that the Mehl et al. model has been very successful in modeling NTC ignition behavior at higher pressures (12–55 atm). Thus it is worth considering whether the differences between the model and experiment in Fig. 1 are due to deficiencies in the reaction mechanism describing the oxidation of n-heptane at this low pressure or because the assumptions about uniform zero-dimensional chemistry in the test volume are not justified.

Because of these significant and consistent differences between model and experiment, n-heptane oxidation experiments at low pressures appear to represent an opportunity to investigate combustion behavior where nonuniform ignition processes are very likely. Measurements of ignition delay time combined with high-speed imaging of the test gas volume should provide evidence of combustion nonuniformity if and when it exists and permit a mapping of the boundary of uniform and nonuniform ignition behavior in this particular shock tube facility. Furthermore, these diagnostics should enable study of strategies for ameliorating these nonideal effects and expanding the boundary of uniform behavior.

High-Speed Imaging Measurements

A schematic of the experimental setup including the imaging arrangement through the end wall of the shock tube is shown in Fig. 2. Images of OH* were acquired with a Phantom v710 CMOS camera that provides grayscale images using a 12 kHz acquisition rate, with a typical resolution of 200 μm per pixel. This light from the shock tube was intensified using a LaVision UV Intensifier High Speed IRO. OH* emission and sidewall pressure were used to determine ignition delay time in the conventional manner. In situ fuel concentration time-history measurement was used to accurately determine initial fuel loading and time histories.

D.F. Davidson (✉) • A. Tulgestke • C. Strand • M.F. Campbell
V.A. Troutman • V.A. Miller • R.K. Hanson
Mechanical Engineering Department, Stanford University, Stanford, CA 94305, USA
e-mail: dfd@stanford.edu

G. Ben-Dor et al. (eds.), *30th International Symposium on Shock Waves 1*, DOI 10.1007/978-3-319-46213-4_52

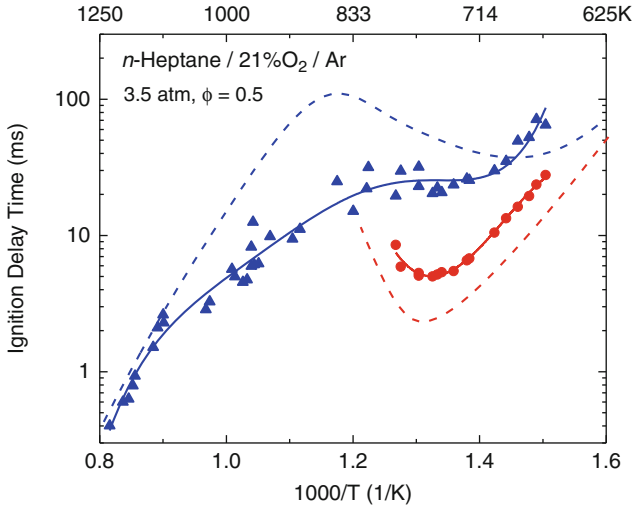

Fig. 1 Low-pressure ignition delay time measurements in n-heptane/O_2/Ar mixtures. *Blue symbols* and *lines*, second-stage ignition; *red symbols* and *lines*, first-stage ignition. *Solid lines*: best fit to data. *Dashed lines*: constant-pressure modeling using the Mehl et al. (2011) mechanism [3]. Ignition delay times in this study were based on times of complete fuel removal or OH* emission

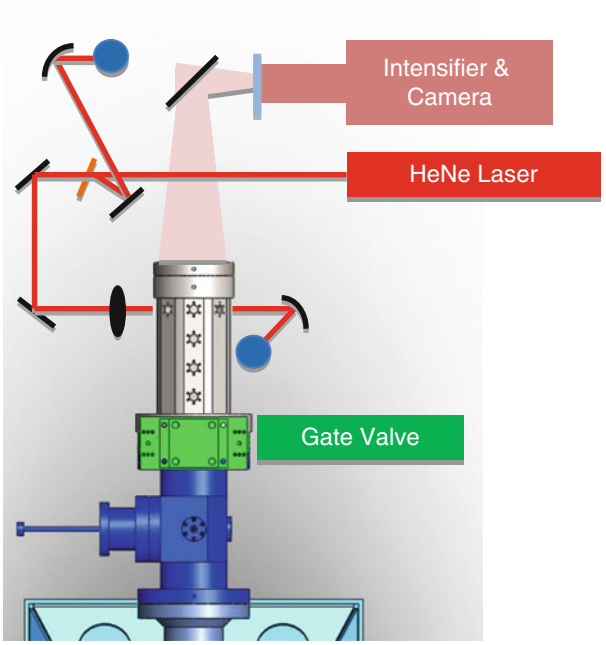

Fig. 2 Experimental setup for rapid imaging through the shock tube end wall. The CRV gate valve is 35 cm from the shock tube end wall

Constrained Reaction Volume Shock Tube

Measurements were performed in the Stanford University with 10 cm ID long-test-time shock tube. The acquisition of the long-test-time data was made possible by extending the shock tube driver and using tailored driver gas mixtures, and uniform pressure and temperature conditions were achieved by using driver inserts [4]. This arrangement allowed the reliable achievement of 50+ ms of test time.

The shock tube was operated using the constrained reaction volume (CRV) strategy [5]. This strategy provided a short test volume adjacent to the end wall followed by a long nonreactive buffer gas section extending back to the diaphragm. The two zones of the shock tube-driven section could be filled separately by closing the gate valve near the end wall. The arrangement reduced the chance of remote ignition and allowed near-constant pressure operation (until the very rapid energy release at ignition).

Results and Discussion

Figures 3 and 4 exhibit images of two different CRV reflected shock experiments. The frames have been artificially colored to assist the viewer in observing details of the image, and times of each image are indicated. In addition, the figures include the corresponding time-dependent graphs of sidewall pressure (P) acquired using a Kistler™ PZT, OH emission (OH*) using a Si photodiode and UG-5 Schott glass filter, relative fuel concentration (HeNe) using 3.39 μm IR laser absorption, and beam steering across the tube diameter (Schlieren) using 0.628 μm visible laser extinction. All diagnostics were located 2 cm from the shock tube end wall. The horizontal red line in the images is the beam path for the HeNe and Schlieren lasers; the blue lines outline the observation volume for OH emission.

The higher-temperature example (1166 K), Fig. 3, experiences sharp detonation-like ignition, as indicated by the rapid increase of the pressure and OH* emission graphs, at 1.28 ms. Previous to that there is evidence of burning, limited to the regions around the circumference, but no sign of emission in the core flow. Until the ignition event at 1.28 ms, the pressure is effectively constant, and the burning around the circumference does not appear to affect the measured core ignition delay time. At 1.28 ms, there appears to be effectively uniform homogenous ignition throughout the test volume. Hence this time can be taken as a correct value for the ignition delay time at the reflected shock conditions.

As indicated in the HeNe trace, fuel is consumed slowly over the entire ignition time, until 1.28 ms when there is a rapid final removal of fuel. The laser beams traversing the shock tube diameter experience very little steering/beam schlieren from density variations until the ignition event.

The lower-temperature (986 K) case, Fig. 4, by contrast, does not experience a rapid ignition event. The pressure remains near constant, as expected for CRV-fill experiments. The OH emission rises over a long time interval of 3 ms (5–8 ms) even though the stoichiometry is the same as that of

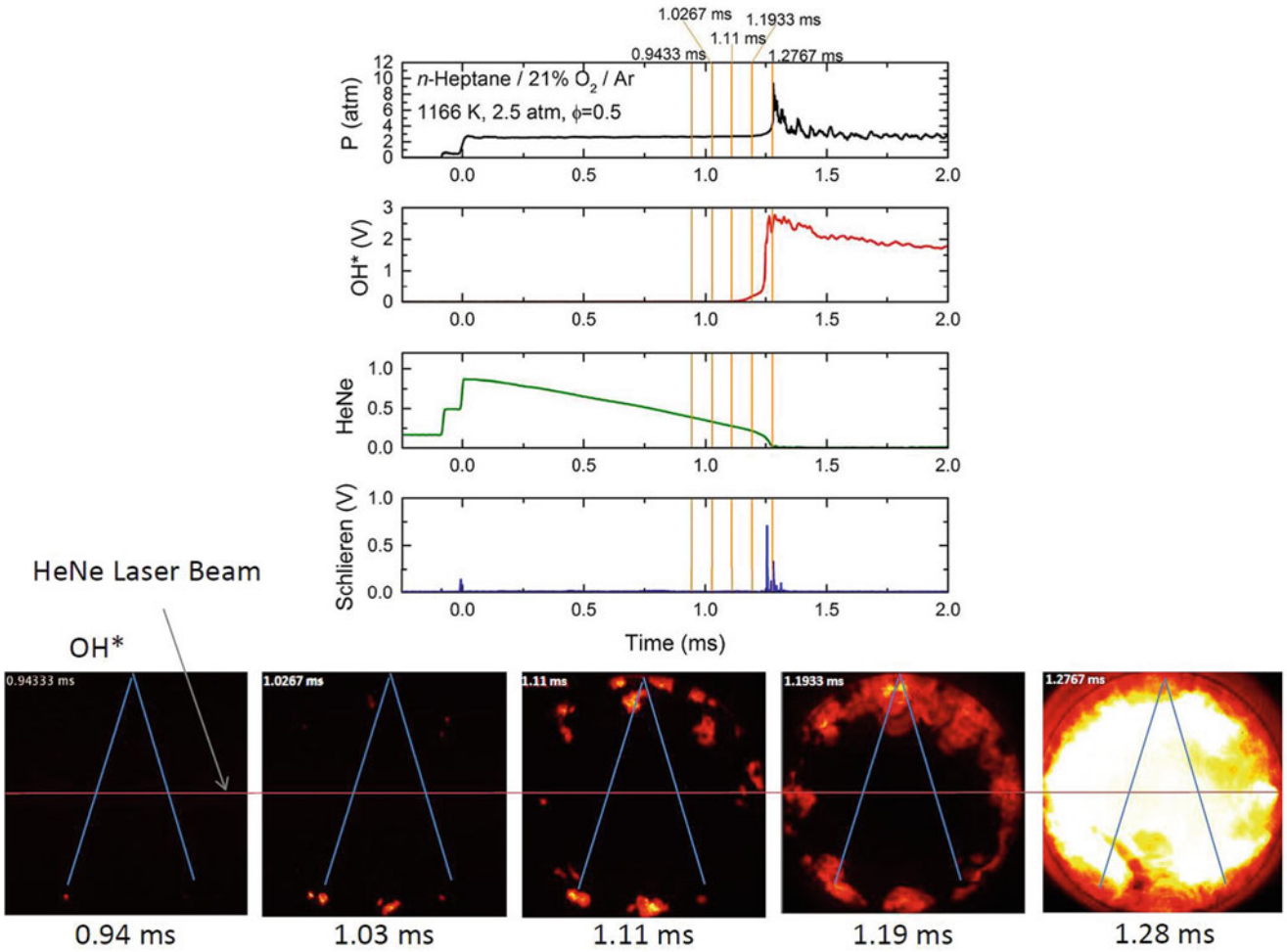

Fig. 3 1166 K ignition delay experiment. Initial reflected shock conditions: 2.5 atm n-heptane/21 % O_2/argon, $\phi = 0.5$

the Fig. 3 experiment. Here, the ignition event is dominated by early burning in regions growing from the circumference, as revealed by the chemiluminescence images. An ignition delay time using the conventional definition of extrapolating the fastest rise of the OH* emission signal to the baseline would give a value of approximately 6 ms, but clearly this does not accurately reflect the ignition delay for homogeneous ignition. An ignition delay time cannot properly be derived from the sidewall pressure signal.

Some of the fuel appears to be abruptly consumed at 5.96 ms; this is consistent with the growing combustion region crossing the HeNe laser beam. The Schlieren signal also exhibits large variations with time consistent with non-uniform burning.

A comparison of both these two examples reveals early evidence of ignition near the circumference. By cleaning the shock tube between shock wave experiments, only a limited number of hot spots are caused from dust or diaphragm particles. The relatively uniform distribution of the ignition hot spots around the circumference in both experiments suggests that this ignition process is related to the boundary layer rather than to particle hot spots.

In the higher-temperature example, the core ignition rapidly dominates the test volume before the boundary layer flame can expand significantly into the core. In the lower-temperature example, the core ignition shows no evidence of occurring before the flame from the boundary layer covers the greater portion of the test gas volume.

In both examples, at the lower temperatures expected in the boundary layer, first-stage ignition can occur at relatively short times, as evident in Fig. 1. The NTC ignition chemistry is very pressure sensitive, approaching a pressure scaling for ignition of $P^{-1.6}$ in the case of n-heptane [6], and very temperature sensitive. Thus, early ignition in the boundary layer for fuels, such as n-heptane with strong NTC character, is difficult to avoid. However, efforts to mitigate this behavior, e.g., using lower fuel concentrations and different stoichiometries, have shown favorable results.

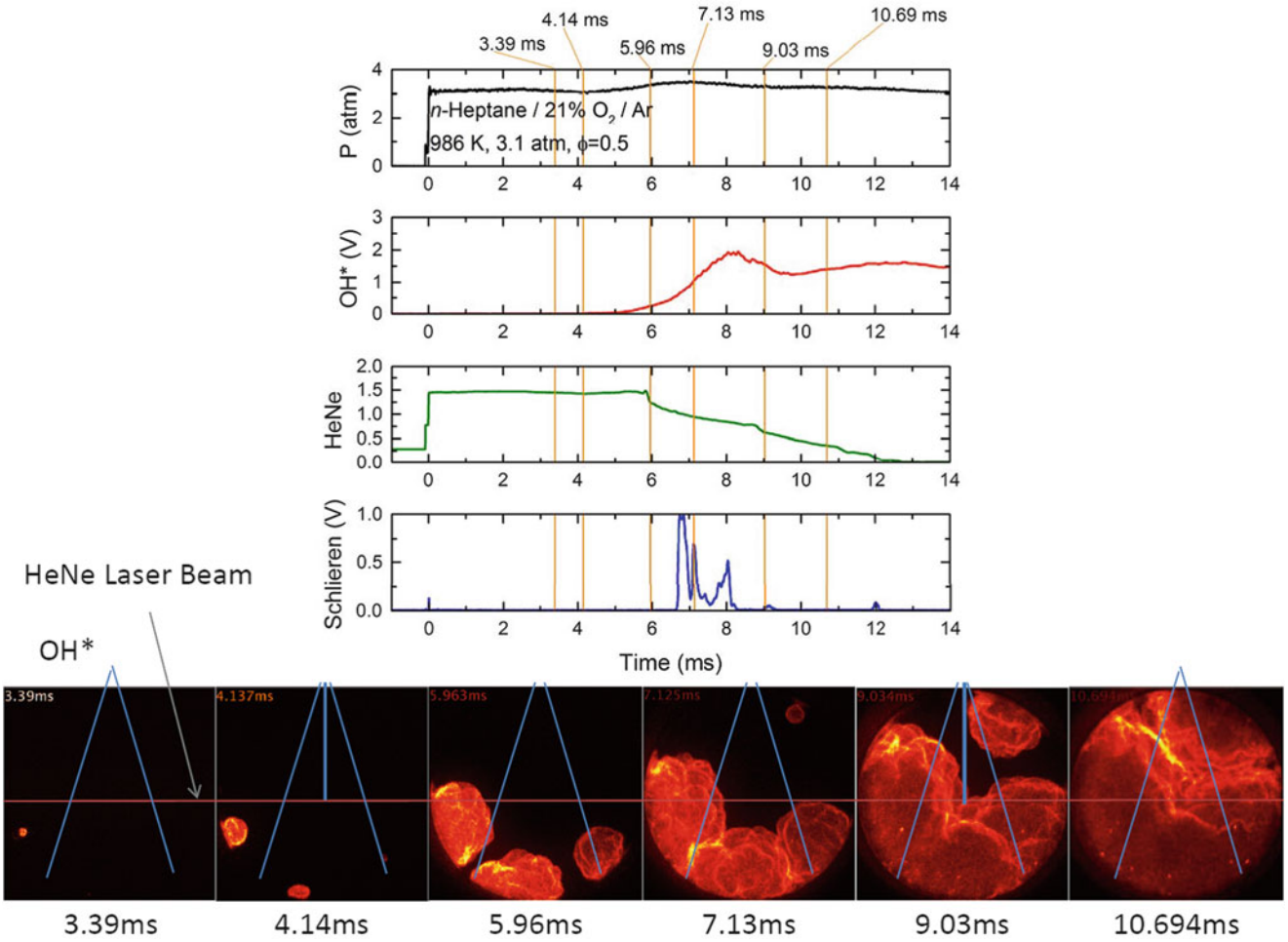

Fig. 4 986 K ignition delay experiment. Initial reflected shock conditions: 3.1 atm n-heptane/21 % O_2/argon, $\phi = 0.5$

Conclusion

It is critically important to identify the combustion regimes that occur in long-test-time ignition delay time experiments. Current detailed reaction mechanism modeling assumes in many cases that these processes are zero dimensional, and as is evident in this study, this is not accurate under some test conditions. A facility-dependent test-condition map is thus needed to identify the regimes where more detailed gasdynamic/combustion modeling is needed for quantitative combustion kinetics experiments. Work on the development of this operational map is in progress for the current shock tube facility.

Acknowledgments This material is based upon work supported by, or in part by, the US Army Research Laboratory and the US Army Research Office under contract/grant number W911NF1310206.

References

1. Heufer, K.A., Olivier, H., Medvedev, S.P., Khomik, S.V.: Optical investigation of shock induced ignition of different biofuels. In: 23rd International Colloquium on the Dynamics of Explosions and Reactive Systems (ICDERS) at Irvine, California, USA, 2011
2. Lee, C., Vranckx, S., Heufer, K.A., Khomik, S., Uygun, Y., Olivier, H., Fernandes, R.X.: On the chemical kinetics of ethanol oxidation: shock tube, rapid compression machine and detailed modeling study. Zeitschrift für Physikalische Chemie **226**, 1–28 (2012)
3. Mehl, M., Pitz, W.J., Westbrook, C.K., Curran, H.J.: Kinetic modeling of gasoline Surrogate components and mixtures under engine conditions. Proc. Combust. Inst. **33**, 193–200 (2011)
4. Hanson, R.K., Davidson, D.F.: Recent advances in laser absorption and shock tube methods for studies of combustion chemistry. Prog. Energy Combust. Sci. **44**, 103–114 (2014)
5. Hanson, R.K., Pang, G.A., Chakraborty, S., Ren, W., Wang, S., Davidson, D.F.: Constrained reaction volume approach for studying chemical kinetics behind reflected shock waves. Combust. Flame **160**, 1550–1558 (2013)
6. Gauthier, B.M., Davidson, D.F., Hanson, R.K.: Shock tube determination of ignition delay times in full-blend and surrogate fuel mixtures. Combust Flame **139**, 300–311 (2004)

Shock Tube Experimental and Theoretical Study on the Thermal Decomposition of 2-Phenylethanol

M. Kiran Singh, K.P.J. Reddy, and E. Arunan

Introduction

2-Phenylethyl alcohol (commonly known as phenethyl alcohol) is the main component of rose oils obtained from rose blossoms. It is a colourless liquid with a mild and warm rose-honey-like odour because of which it is widely used as perfume chemicals [1]. Biochemically, it is also known to cause the limited breakdown of cellular membrane which in turn causes a greatly increased uptake of acriflavine (a drug normally excluded from the cells) and an increased rate of efflux [2] (leakiness) of cellular potassium (which is accumulated against a 100-fold concentration gradient).

Our laboratory has been interested in HX/H_2O elimination reactions from haloethanes and haloethanols [3–5] and naturally we were interested in the phenyl substitution effect. The present study aims at understanding in detail, the thermal decomposition of β-phenyl substituted ethanol (viz 2-phenylethanol) at high temperature. Interestingly, the amount of studies so far reported in the literature on the pyrolysis of 2-phenylethanol is quite less [6–9]. Both the previous experimental studies [6, 7] used static reactors and performed the pyrolysis studies in the temperature range of 720–766 K revealing the formation of styrene, toluene, ethylbenzene as the main products. However, to our knowledge, there has been no report so far in the literature on the high temperature pyrolysis of this molecule using shock tube as the reactor. This has been one of the motivating factors in taking up this study to see whether any interesting observations could be made in the high temperature regime. Not surprisingly, the high temperature experiments show the formation of other additional products which were not observed in previous studies. Our study finds the formation of benzene in large abundance at high temperature in addition to styrene, toluene, and ethylbenzene. Moreover Phenylacetylene and benzaldehyde are also observed as products during the analyses.

Experimental Methods

The high temperature thermal decomposition of 2-phenylethanol in argon bath has been carried out in the single pulse shock tube facility available in our laboratory [10]. Owing to the low volatility of the sample (2-phenylethanol), the sample-chamber containing the sample and argon mixture has been maintained at 80 °C during the experiments in order to get sufficient sample in the vapour phase for reaction to take place. Before the sample has been loaded in the test section, the liquid sample has been purified using a freeze-pump-thaw procedure to remove dissolved volatiles and air. All shock properties have been estimated from the measured incident shock velocity using normal shock relations. The reaction mixtures have been exposed to reflected shock temperature and pressure range of 1011–1446 K and 7–13 atm, respectively, with the dwell times of the experiments ranging from 1.330 to 1.430 ms. The quantitative analyses of the pre-shocked and post-shocked mixtures have been achieved using the gas-chromatography with flame Ionization detector (GC-FID) and gas-chromatography mass spectrometry (GCMS) diagnostics.

Results and Discussion

The analyses of the post-shock mixtures reveal the formation of products such as styrene, toluene, and benzene in abundance along with the formations of ethylbenzene,

M.K. Singh (✉) • E. Arunan
Inorganic and Physical Chemistry Department, Indian Institute of Science, Bangalore 560012, India
e-mail: mkiransingh@ipc.iisc.ernet.in

K.P.J. Reddy
Department of Aerospace Engineering, Indian Institute of Science, Bangalore 560012, India

G. Ben-Dor et al. (eds.), *30th International Symposium on Shock Waves 1*, DOI 10.1007/978-3-319-46213-4_53

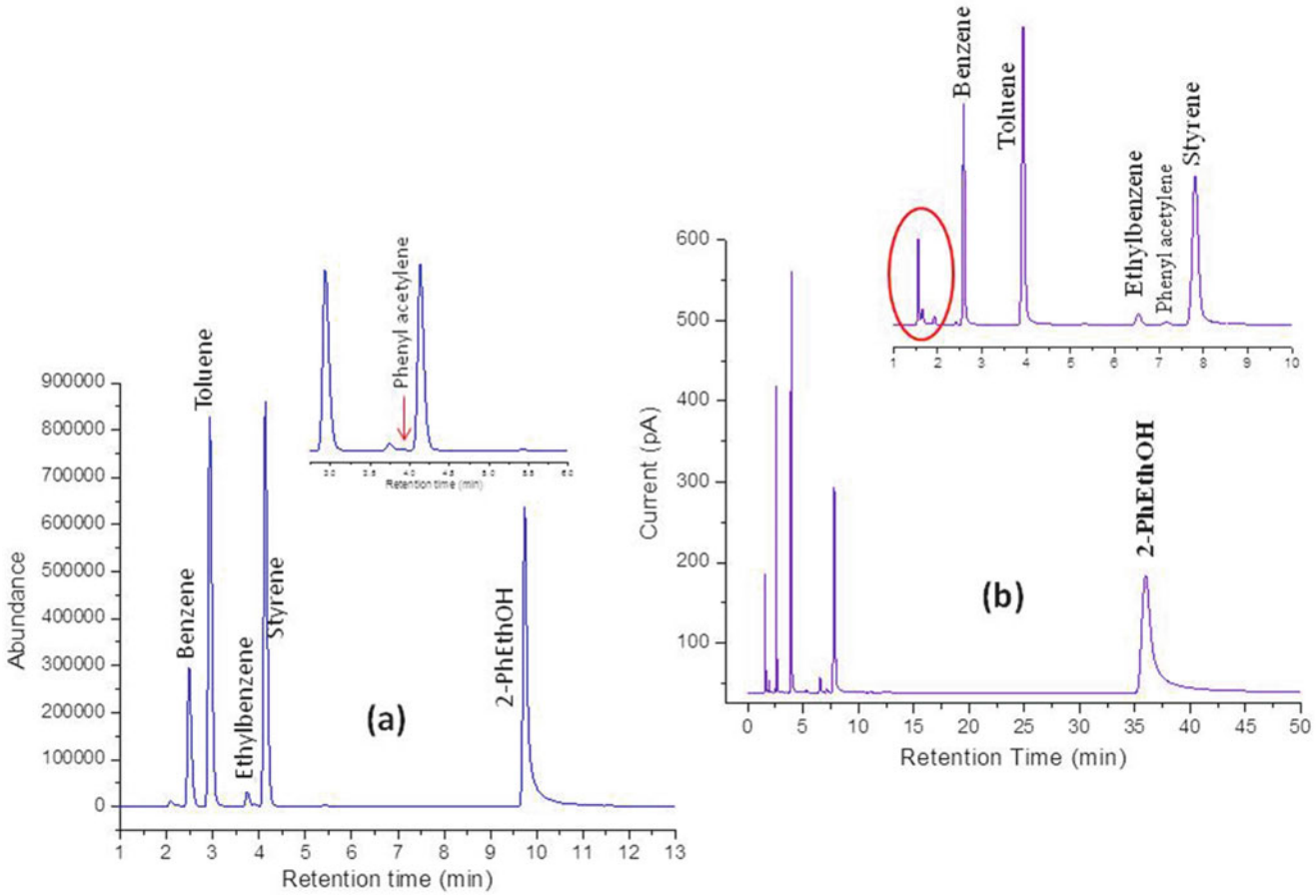

Fig. 1 Total ion chromatogram of a post-shock mixture of *2-Phenylethanol* in Argon heated to 1229 K as obtained from : (**a**) GC-MS analysis (**b**) GC-FID

phenylacetylene in little amount. Benzaldehyde (in negligible amount) could also be observed during the analysis. Styrene, toluene, and ethylbenzene formations were observed in the lowest range of the temperature covered in this study, whereas benzene and phenylacetylene formations were found to be occurring at higher temperature (≈1200 K). The formation of the products can be seen in the total-ion-chromatograph from GCMS and a typical chromatograph from GC-FID shown in Fig. 1. However identification of a very few low masses species in the post-shock mixture is yet to be completed. The unidentified species are highlighted with red circle as can be seen in the chromatograph from GC-FID (Fig. 1b)

The formations of products such as Styrene, ethylbenzene, and toluene in the low temperature had been well explained by chuchani et al. [8], which is shown in Fig. 2. Gaussian09 packages [11] are being used for the computational analysis of the system. Theoretical calculations are still in progress to identify the transition states for each reaction pathway and estimate the activation energies for each pathway. We have also employed Quantum Theory of Atoms in Molecules (QTAIM) [12–14] to give a description

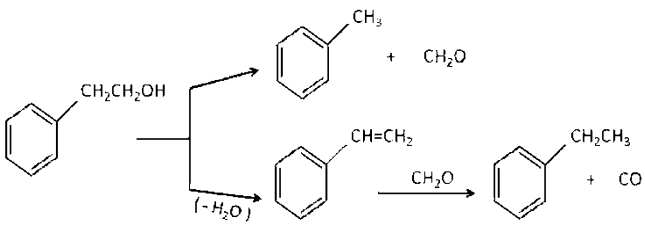

Fig. 2 Diagram showing the formation of styrene, ethylbenzene and toluene during the low temperature thermal decomposition of 2-phenylethanol

of the bond breaking/forming processes involved during the reaction pathways. QTAIM makes use of the quantum mechanics in providing a rigorous and exact definition of bonding within an atomic ensemble in terms of the topological properties of its charge density. Thus, a molecular mechanism of a given chemical reaction can be studied from the redistribution of the electron density along the reaction path connecting the stationary points. The transition state for H_2O elimination has been optimized which predicted activation energy barrier of around 60 kcal/mol

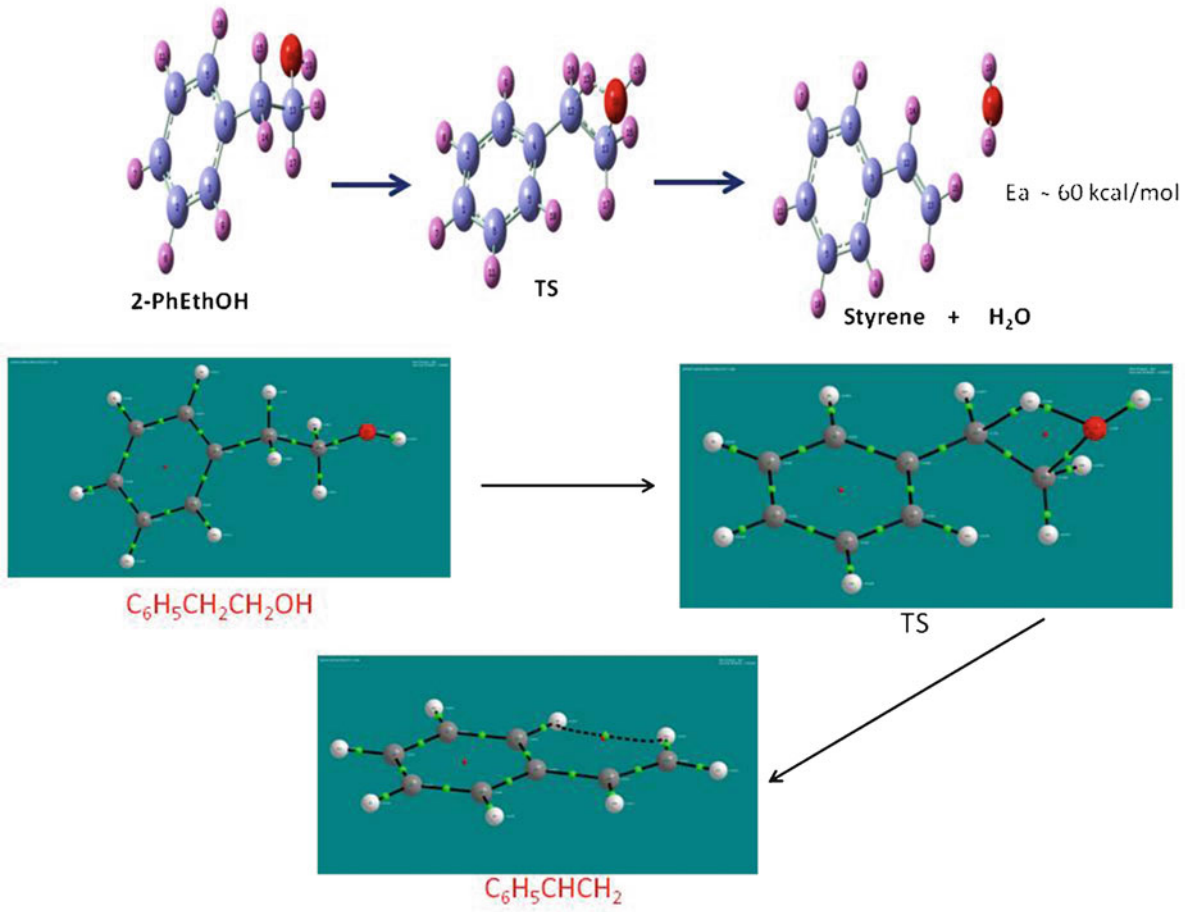

Fig. 3 The transition state for H_2O elimination from 2-phenylethanol shown as molecular graph

Table 1 QTAIM atomic charges (Q) for atoms in the H_2O elimination reaction of $C_6H_5CH_2CH_2OH$ for the structures optimized at B3LYP/6311++G(d,p)

Atom	Q (ground state)	Q (TS)	Q (final)
C_{12}	+0.0577	−0.1701	−0.0121
C_{13}	+0.4956	+0.1366	−0.0453
O_{18} (eliminating)	−1.0615	−1.0158	−1.0972
H_{15} (eliminating)	+0.0095	+0.4390	+0.5486
H_{19} (bonded to O_{18})	+0.5424	+0.5299	+0.5486
H_{14} (bonded to C_{12})	+0.0095	+0.0071	+0.0111
H_{16} (bonded to C_{13})	−0.0071	+0.0530	+0.0141
H_{17} (bonded to C_{13})	−0.0071	+0.0744	+0.0235
C_4 (bonded to C12)	−0.0088	+0.0043	+0.0026

for styrene formation. This is an indication that the β-phenylsubstitution on CH_3CH_2OH brings about reduction in activation energy for H_2O elimination in going from ethanol (Ea ≈ 67 kcal/mol) to 2-phenylethanol. The H_2O elimination transition state geometry is shown as a molecular graph in Fig. 3.

The QTAIM atomic charges for HOH elimination from 2-Phenylethanol is given in Table 1. Here, it can be seen that the transition state geometry for HOH elimination shows the presence of four bond paths (C─C, C─H, C─O, O─H) and a ring critical point which is an indication that neither the C─O nor the C─H has broken in the highest energy point in the reaction. The pattern in atomic charges is remarkably similar to that seen for HOH elimination from CH_3CH_2OH as reported by Heard et al. [13].

Conclusions

The quantification of the various species in the reaction mixture is still in progress. Simultaneously, theoretical calculations based on transition state theory (TST) and Quantum theory of Atoms in Molecules (QTAIM) have also been taken up to give an in-depth explanations of the various reaction pathways involved in the experiments. Finally, a detailed kinetic mechanism using Chemkin will also be developed for the pyrolysis of the sample at high temperature. The results will be presented in the final presentation.

Acknowledgements We are grateful for the financial support from IISc-ISRO Space Technology Cell, ARDB and DRDO, Government of India.

References

1. Arctander, S.: Perfume and Flavour Chemicals. Allured Publishing Corporation, Montclair (1969)
2. Silver, S., Wendt, L.: Mechanism of action of phenethyl alcohol: Breakdown of the cellular permeability barrier. J. Bacteriol. **93**(2), 560–566 (1967)
3. Rajakumar, B., Reddy, K.P.J., Arunan, E.: Unimolecular HCl elimination from 1,2-dichloroethane: A single pulse shock tube and ab initio study. J. Phys. Chem. A **106**(36), 8366–8373 (2002)
4. Chakravarty, H.K., Pathak, A., Reddy, K.P.J., Arunan, E.: Thermal Decomposition of 2-chloroethanol: Single-pulse shock Tube and ab Initio Studies. In: Proceedings of the 27th InternationalSymposium on Shock waves, St.-Petersburg, Russia, p. 32 (2009)
5. Rajakumar, B., Arunan, E.: Ab initio, DFT and transiton state theory calculations on 1,2-HF, HCl and ClF elimination reactions from CH2F−CH2Cl. Phys. Chem. Chem. Phys. **5**, 3897–3904 (2003)
6. Taylor, R.J.: The Mechanism of thermal eliminations. Part 25. Arrhenius data for pyrolysis of lsochroman-3-one, benzyl methyl ether, 2-hydroxyethylbenzene, phenyl acetate, and 3,4-dihydro-ZH-pyran. J. Chem. Soc., Perkin Trans. 2, 183 (1988). doi:10.1039/P29880000183
7. Chuchani, G., Rotinov, A., Dominguez, R.M.: The kinetics and mechanisms of gas phase elimination of primary, secondary, and tertiary 2-hydroxyalkylbenzenes. Int. J. Chem. Kinet. **31**, 401–407 (1999)
8. Mora, J.R., Lezema, J., Albornoz, J.M., Hernandez, A., Cordova, T., Chuchani, G.: Theoretical calculations of the kinetics and mechanisms of the gas phase elimination of primary, secondary, and tertiary 2-hydroxyalkylbenzenes. J. Phys. Org. Chem. **22**, 1198–1207 (2009)
9. Sakai, Y., Ando, H., Oguchi, T., Murakami, Y.: Thermal decomposition of 2-phenylethanol: A computational study on mechanism. Chem. Phys. Lett. **556**, 29–34 (2013)
10. Rajakumar, B., Reddy, K.P.J., Arunan, E.: Thermal decomposition of 2-fluoroethanol : Single pulse shock tube and ab initio study. J. Phys. Chem. A **107**, 9782–9793 (2003)
11. Frisch, M.J., et al.: Gaussian 09 Revision A.1. Gaussian Inc., Wallingford CT (2009)
12. Bader, R.F.W.: Atoms in Molecules: A Quantum Theory. Clerendon Press, New York (1990)
13. Parworth, C.L., Tucker, M.K., Holmes, B.E., Heard, G.L.: QTAIM analysis of the HF, HCl, HBr, and HOH elimination reactions of halohydrocarbons and halohydroalcohols. J. Phys. Chem. A **115** (45), 13133–13138 (2011)
14. Andres, J., Berski, S., Contreras-Garcia, J., Gonjalez-Navarrete, P.: Following the molecular mechanism for the NH3 + LiH → LiNH2 + H2 chemical reaction: A study based on the joint use of the Quantum Theory of Atoms in Molecules (QTAIM) and Noncovalent Interaction (NCI) index. J. Phys. Chem. A **118**, 1663–1672 (2014)

Soot Formation During Pyrolysis and Oxidation of Aliphatic and Aromatic Hydrocarbons in Shock Waves: Experiments and Detailed Kinetic Modeling

G.L. Agafonov, I.V. Bilera, Y.A. Kolbanovsky, V.N. Smirnov, A.M. Tereza, and P.A. Vlasov

Introduction

Our experimental and modeling study of soot formation during the pyrolysis of a number of aromatic (benzene, toluene, and ethylbenzene [1]) and saturated aliphatic hydrocarbons (methane, propane [2–4]) showed good agreement between the results of experiments and detailed kinetic modeling. However, certain difficulties were encountered in the kinetic simulation of soot formation in the pyrolysis of acetylene, a hydrocarbon with a triple bond. These difficulties have been overcome by introducing additional reaction channels of soot nucleation from hydrogenated polyyne-like fragments, in particular, diacetylene dimers. The experiments performed in [5] confirmed the possibility of the formation of high concentrations of diacetylene dimers in the reaction mixture.

The aim of this work was to perform experimental and kinetic modeling studies of soot formation in the pyrolysis and oxidation of various mixtures of aliphatic and aromatic hydrocarbons in argon behind reflected shock waves and to demonstrate the predictive capabilities of the modified kinetic model of soot formation.

G.L. Agafonov • V.N. Smirnov • A.M. Tereza
Semenov Institute of Chemical Physics, Russian Academy of Sciences, Kosygin Str. 4, 119991 Moscow, Russia

I.V. Bilera • Y.A. Kolbanovsky
Topchiev Institute of Petrochemical Synthesis, Russian Academy of Sciences, Leninskii Prospekt 29, 119991 Moscow, Russia

P.A. Vlasov (✉)
Semenov Institute of Chemical Physics, Russian Academy of Sciences, Kosygin Str. 4, 119991 Moscow, Russia

National Nuclear Research University "MEPhI", Kashirskoye Shosse 31, 115409 Moscow, Russia
e-mail: iz@chph.ras.ru

Results

The soot yield and temperature of soot particles were determined using a two-beam technique that enables to simultaneously measure the optical absorption and emission of soot particles. Details of the shock-tube setup were described elsewhere [3]. Figure 1 shows typical time histories of the absorption (1) and emission (2) signals after the arrival of the reflected shock wave front at the observation section, as well as the time evolution of the soot yield (3) and the soot particle temperature (4) obtained from signals (1) and (2) for the pyrolysis of a 5 % mixture of acetylene in argon under various conditions behind the reflected shock wave.

Experimentally measured dependences of the soot yield on the initial temperature of the test mixture behind the reflected shock wave for three different acetylene–argon mixtures are displayed in Fig. 2. These curves have a characteristic bell-like shape. As can be seen, the soot yield strongly depends on the initial concentration of acetylene in the test mixture. Figure 3 shows the deviation of the temperature of soot particles formed during the pyrolysis of acetylene–argon mixtures for a reaction time of 1 ms from the calculated initial temperature behind the reflected shock wave.

Taking into account that acetylene plays a key role in soot formation, that the pyrolysis and oxidation of virtually all hydrocarbons under fuel-rich conditions lead to the formation of high concentrations of acetylene, and that the role of acetylene as a building material in the surface growth of soot particles has been recognized for a long time, being beyond doubt, we performed the kinetic model validation for acetylene and diacetylene. The kinetic model was tested by a direct comparison of the experimentally measured [6, 7] and calculated product yields during diacetylene and acetylene pyrolysis and oxidation. The results are presented in Figs. 4 and 5. Three different $C_2H_2/H_2/Ar$ mixtures were investigated (Fig. 5): (a) 4.0 % C_2H_2 + 96 % Ar, (b) 2.5 % C_2H_2 + 97.5 % Ar, and

G. Ben-Dor et al. (eds.), *30th International Symposium on Shock Waves 1*, DOI 10.1007/978-3-319-46213-4_54

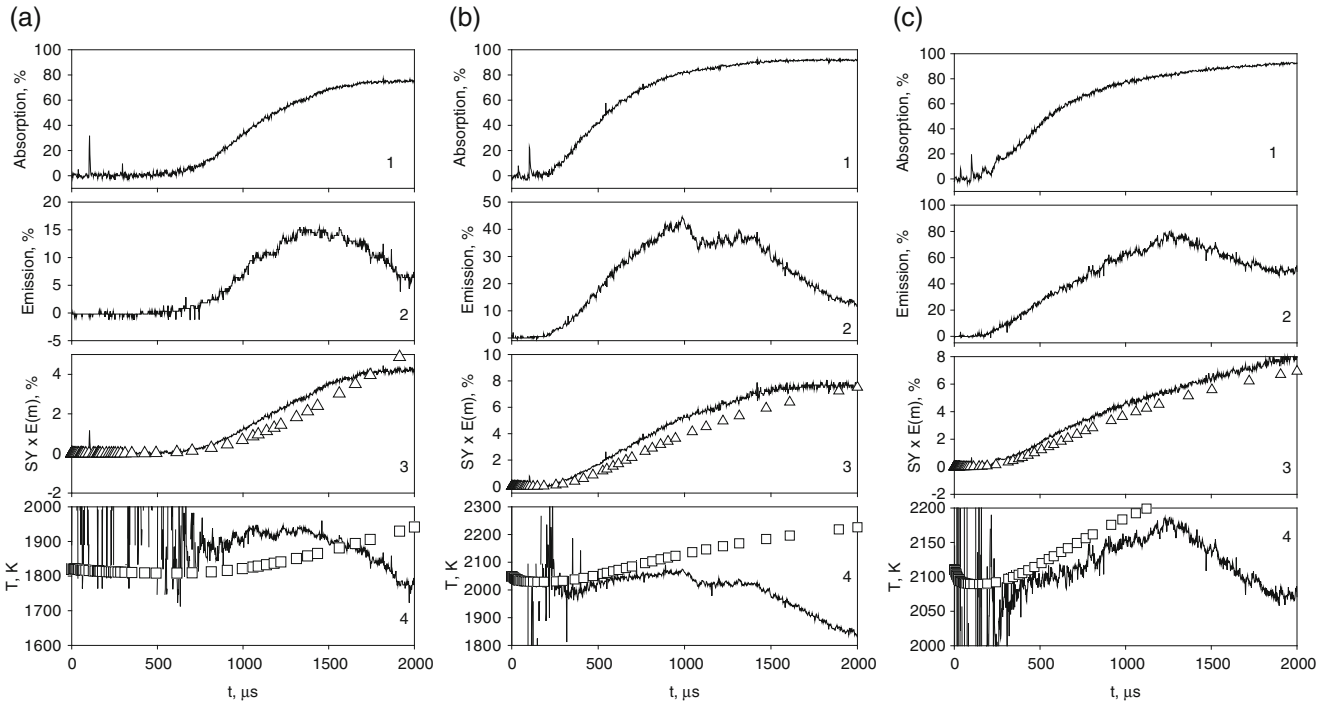

Fig. 1 Typical time histories of the absorption (1) and emission (2) signals after the arrival of the reflected shock wave front at the observation section and of the soot yield (3) and soot particles temperature (4) obtained from signals (1) and (2) for a 4.8 % mixture of acetylene in argon at various conditions behind the reflected shock wave: (**a**) $T_{50} = 1821$ K, $[M]_{50} = 2.36 \times 10^{-5}$ mol/cm^3, $P_{50} = 3.53$ bar; (**b**) $T_{50} = 2049$ K, $[M]_{50} = 1.93 \times 10^{-5}$ mol/cm^3, $P_{50} = 3.25$ bar; (**c**) $T_{50} = 2111$ K, $[M]_{50} = 2.32 \times 10^{-5}$ mol/cm^3, $P_{50} = 4.02$ bar. The probe light wavelength was $\lambda = 632.8$ nm. The points (*triangles* and *squares*) represent the calculated values of the soot yield and soot particles temperature, whereas the lines in panels 3 and 4 are the results of processing the experimental absorption (*curve 1*) and emission (*curve 2*) signals, respectively

(c) 2.5 % C_2H_2 + 7.5 % H_2 + 90.0 % Ar. The results for diacetylene are shown in Fig. 4: (a)–(d) the pyrolysis of three different C_4H_2/H_2/Ar mixtures (1.0 % C_4H_2 + 99.0 % Ar, 1.0%C_4H_2 + 1.0 % H_2 + 98.0 % Ar, 1.0 % C_4H_2 + 4.0 % H_2 + 95.0 % Ar) and (e)–(h) the oxidation of a 0.4 % C_4H_2 + 0.9 %O_2 + 98.7 %Ar mixture. As can be seen from Figs. 4 and 5, the calculated and experimentally measured values are in close agreement.

The kinetic model of soot nucleation used in our previous works, which was based on reactions of recombination of polyaromatic fragments, was supplemented by reactions of nucleation through the combination of C_8H_4 aliphatic dimers. This modification was motivated by the experimental results from [5, 8, 9], where these species were reliably detected.

It was concluded in [5] that the C_8H_4 excited isomer is a common intermediate for the formation of polyynes and oligomers, that higher polyynes cannot be formed in the direct reactions $C_4H_2 + C_2H_2 = C_6H_2 + H_2$ and $C_4H_2 + C_4H_2 = C_8H_2 + H_2$, and that the C_8H_4 linear isomers dissociate to C_8H_2, whereas branched C_8H_4 isomers react further to produce heavier oligomers or decompose to form C_6H_2 molecules. The addition of C_4H_2 to the C_8H_4 branched isomer is accompanied by cyclization into a species containing an aromatic ring, with the resulting product being capable of further polymerization. In this case, the larger the oligomers formed, the less likely is the formation of relatively stable condensed aromatic compounds with side chains.

In [9], the polyynic structures (polyynes and substituted derivatives thereof) were observed in fuel-rich low-pressure allene, propyne, and cyclopentene flames by using photoionization time-of-flight mass spectrometry with tunable vacuum-ultraviolet synchrotron radiation; in particular, a number of C_7H_4 and C_8H_4 isomers were detected.

In contrast to $C_{2n}H_2$ polyyne molecules, the possible reaction pathways that lead to the formation of the C_7H_4 and C_8H_4 isomers remain mostly unexplored. Probably, such reactions proceed through the formation of similar but smaller intermediates.

Our kinetic simulations were performed using the mechanism of soot formation developed in [4]. This mechanism of the formation of soot particles includes a submechanism of gas-phase reaction for describing the pyrolysis and oxidation of the starting hydrocarbons, in particular acetylene, and the formation and growth of polyaromatic hydrocarbon molecules through various channels, up to coronene.

The core of the gas-phase reaction mechanism is the reaction sequence of PAH formation in laminar premixed

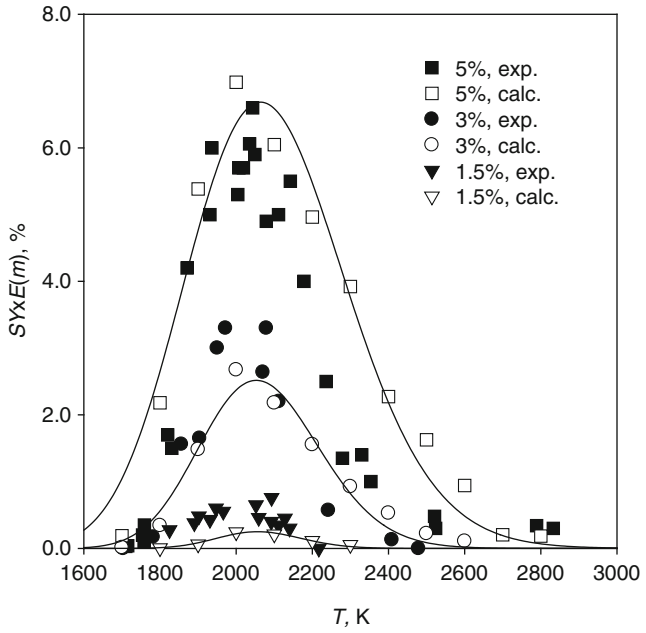

Fig. 2 Experimentally measured and calculated temperature dependences of the soot yield in the pyrolysis of three different acetylene–argon mixtures behind reflected shock wave: (*filled square*) 5 %, (*filled circle*) 3 %, and (*filled inverted triangle*) 1.5 % C_2H_2 in argon (P_{50} = 3.0–4.5 bar, $E(m)$ = 0.37, τ_{reac} = 1 ms). The closed symbols represent the results of experimental measurements; open symbols represent the results of detailed kinetic calculations, and lines represent the results of approximation of experimental values by a nonlinear regression (the left figure)

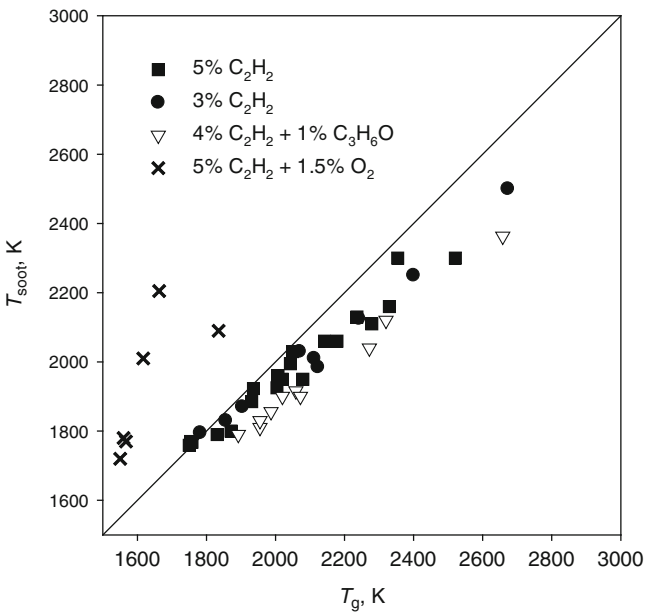

Fig. 3 Dependence of the temperature of soot particles formed in the pyrolysis of acetylene–argon mixtures for a time of τ_{reac} = 1 ms after shock heating of the mixture on the calculated initial temperature behind the reflected shock wave. The compositions of the mixtures are given in the figure panels, where C_3H_6O is acetone (the right figure)

acetylene and ethylene flames (HACA). At the same time, the mechanism was extended to include a number of additional channels of PAH formation and growth (up to coronene) and a comprehensive set of reactions involving C_3, C_5, and C_7 hydrocarbons. More specifically, the mechanism included (1) the alternating H-abstraction/C_2H_2-addition route, resulting in the successive growth of PAHs, (2) the combination reactions of phenyl with C_6H_6, (3) the cyclopentadienyl recombination, and (4) the ring-closure reactions of aliphatic hydrocarbons.

The principles of constructing this kinetic mechanism were outlined in [4]. The modified gas-phase reaction mechanism consisted of 3531 direct and inverse reactions involving 300 different components, with the rate constants of several important reactions being pressure dependent.

The processes of formation, growth, oxidation, and coagulation of soot particle nuclei and actually soot particles were simulated using the discrete Galerkin method [10].

According to our model, soot precursors are formed by radical–molecule reactions of different PAHs, starting from phenylacetylene, acenaphthylene, and ethynylnapthalene up to coronene, by radical–radical reactions (from cyclopentaphenanthrene up to coronene radicals), and by combination reactions of unsaturated polyyne-like aliphatic hydrocarbons C_8H_4. The reactions of formation of soot precursors are assumed irreversible. These reactions result in the formation of polyaromatic molecules containing 16–48 carbon atoms and reactive aliphatic oligomers, containing initially 16 carbon atoms. All these compounds grow further, being stabilized by the formation of new chemical bonds. Soot precursors are activated in reactions with H and OH radicals and deactivated in reactions with H, H_2, and H_2O. Soot precursors grow via reactions with C_2H_2, C_4H_2, and C_6H_2 (the concentrations of which are rather high in the pyrolysis and oxidation of aliphatic and aromatic hydrocarbons), reactions with polyaromatic molecules and radicals, and the process of coagulation. Soot precursors are oxidized by O and OH radicals. They are transformed into soot particles through internal conversion reactions, in which the number of active sites in the reacting system is preserved. Soot particles grow in the reactions with C_2H_2, C_4H_2, C_6H_2, and PAH molecules and radicals and are oxidized by O and OH radicals. All soot particles were postulated to participate in coagulation.

Since the temperature behind the reflected shock wave varies with time in a complicated way (rapid fall to a quasi-steady-state value, growth, and a new decrease upon the arrival of the rarefaction wave), the ultimate soot yield is determined by the entire temperature profile, not only by the quasi-steady-state temperature. Thus, all kinetic calculations were performed for nonisothermal conditions and a constant density, and the calculated kinetic data are in good agreement with the corresponding experimental data. For this

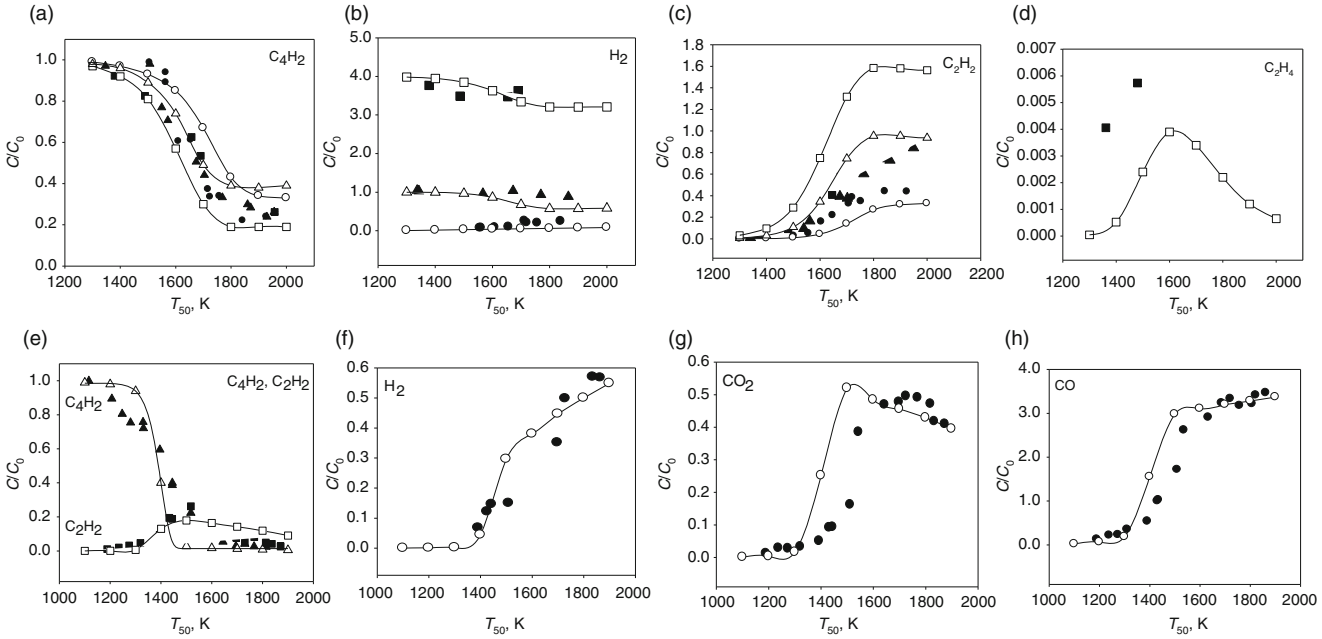

Fig. 4 Direct comparison of the experimentally measured (*closed symbols*) [6] and calculated (*open symbols*) product yields during (the *top row*) pyrolysis of three different C_4H_2/H_2 mixtures in Ar ((*filled circle*) 1.0%C_4H_2 + 99.0%Ar, (*filled inverted triangle*) 1.0% C_4H_2 + 1.0%H_2 + 98.0%Ar, and (*filled square*) 1.0%C_4H_2 + 4.0% H_2 + 95.0%Ar) and (the *bottom row*) oxidation of a 0.4% C_4H_2 + 0.9%O_2 + 98.7%Ar mixture. The reaction time τ_{react} was varied with the initial temperature T_{50} behind the reflected shock wave by exactly the same way as presented in [6]; C/C_0 means the ratio of the corresponding product concentration and the initial C_4H_2 concentration in a particular experiment or calculation

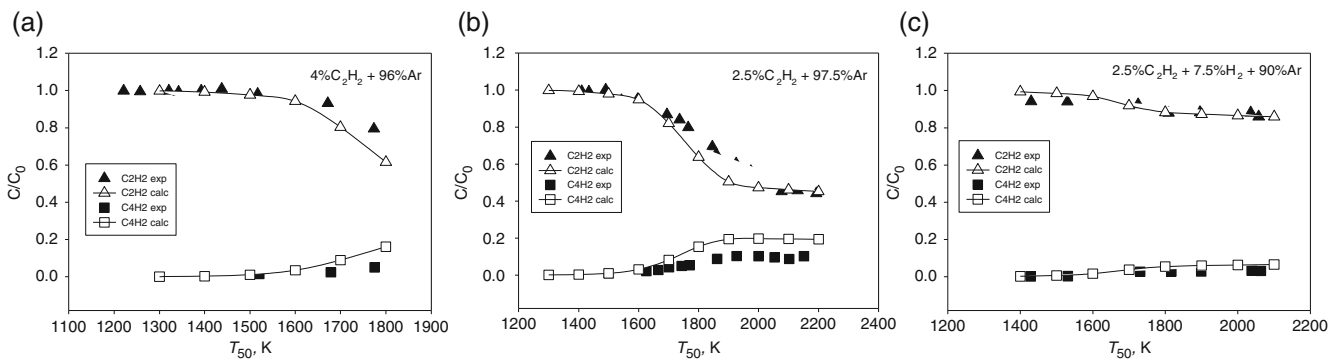

Fig. 5 Comparison of the experimentally measured [7] (*closed symbols*) and calculated (*open symbols*) product yields for the pyrolysis of various C_2H_2/H_2/Ar mixtures: (**a**) 4.0%C_2H_2 + 96%Ar, (**b**) 2.5% C_2H_2 + 97.5%Ar, (**c**) 2.5%C_2H_2 + 7.5%H_2 + 90.0%Ar. The reaction time τ_{react} was varied with the initial temperature T_{50} behind the reflected shock wave in the exactly same way as described in [7]; C/C_0 is the ratio of the corresponding product concentration and the initial C_2H_2 concentration in a particular experiment or calculation

reason, we did not adjust our experimental data points to some "effective temperature" behind the reflected shock wave and used the initial temperature T_{50} both in the representation of experimental data and in the calculations.

Introduction into the soot formation kinetic model of the soot nuclei produced from unsaturated aliphatic hydrocarbons, along with those arising from polyaromatic compounds, makes it possible to significantly improve the kinetic description of the experimental time histories of soot formation (Fig. 1) and temperature and concentration dependences of the soot yield (Fig. 2) not only for acetylene pyrolysis but for pyrolysis and oxidation of all aliphatic and aromatic hydrocarbons being investigated. The proposed kinetic model of soot formation correctly predicts the location of the maximum in the temperature dependences of the soot yield for all hydrocarbons studied, including C_2H_2/Ar mixtures. Within the scatter in experimental values of the soot yield, the model predictions of this quantity obtained

using a fixed value of $E(m) = 0.37$ for all hydrocarbons investigated are in good agreement with our experiments.

Since there is a considerable discrepancies between the reported values of $E(m)$, we plotted the quantity $SY \times E(m)$ as a function of the time and the initial shocked-gas temperature T_{50}. Studying the formation of soot during the pyrolysis of toluene behind reflected shock waves [1], we estimated $E(m)$ as 0.37, a value in close agreement with most recent data [11, 12]: according to [11], $E(m) = 0.373$, whereas in [12], $E(m) = 0.259$. The quantity $E(m) = 0.37$ has the advantage of being determined under conditions similar to those used in the present experiments.

Prior to the appearance of soot particles, the signal-to-noise ratio is too low to reliably determine the soot particle temperature. After the arrival of the rarefaction wave to the observation section (~1100–1500 μs), the emission signal begins to decrease markedly, indicative of a decrease in the mixture temperature in this cross section. The formal procedures and details of soot yield determination and measuring the soot particle temperature are presented in [1].

Conclusions

The experiments on the pyrolysis and oxidation under fuel-rich conditions of C_2H_2/Ar, C_2H_6/Ar, C_2H_4/Ar, C_2H_4/O_2/Ar, CH_4/Ar, CH_4/O_2/Ar, C_3H_8/Ar, C_3H_6/Ar, toluene/Ar, and benzene/Ar mixtures behind reflected shock waves were performed. The soot yield and the soot particle temperature were determined using the double-beam absorption-emission technique. Our experiments demonstrated that the soot formation in the pyrolysis of all aliphatic and aromatic hydrocarbons tested except for acetylene is accompanied by a pronounced temperature decrease due to the predominance of endothermic decomposition stages. In the case of acetylene pyrolysis, the temperature remains nearly constant, as it does in the oxidation of rich hydrocarbon/oxygen mixtures due to exothermic oxidation reactions. By contrast, a sharp and pronounced temperature increase is observed in the oxidation of rich acetylene/oxygen mixtures. Our previous kinetic model of soot formation during the shock-tube pyrolysis and oxidation of aliphatic and aromatic hydrocarbons is augmented by introducing an additional subset of reactions of soot nucleation, involving both polyaromatic and unsaturated aliphatic hydrocarbons. The proposed kinetic model was successfully tested by describing the published data on the products yield in the pyrolysis and oxidation of acetylene and diacetylene in shock-tube experiments. It closely reproduces our experimental data on the time histories of the soot yield and soot particle temperature, as well as the temperature and concentration dependences of the soot yield at fixed reaction times, for the pyrolysis and oxidation of C_2H_2/Ar, C_2H_6/Ar, C_2H_4/Ar, C_2H_4/O_2/Ar, CH_4/Ar, CH_4/O_2/Ar, C_3H_8/Ar, C_3H_6/Ar, toluene/Ar, and benzene/Ar mixtures under fuel-rich conditions in reflected shock waves ($T_{50} = 1400$–2850 K, $P_{50} = 2.5$–5.5 bar).

References

1. Agafonov, G.L., Smirnov, V.N., Vlasov, P.A.: Soot formation in the pyrolysis of benzene, methylbenzene, and ethylbenzene in shock waves. Kinet. Catal. **52**(3), 358–370 (2011)
2. Agafonov, G.L., Borisov, A.A., Smirnov, V.N., Troshin, K.Y., Vlasov, P.A., Warnatz, J.: Soot formation during pyrolysis of methane and rich methane/oxygen mixtures behind reflected shock waves. Combust. Sci. Technol. **180**(10), 1876–1899 (2008)
3. Agafonov, G.L., Smirnov, V.N., Vlasov, P.A.: Shock tube and modeling study of soot formation during pyrolysis of propane, propane/toluene and rich propane/oxygen mixtures. Combust. Sci. Technol. **182**(11), 1645–1671 (2010)
4. Agafonov, G.L., Smirnov, V.N., Vlasov, P.A.: Shock tube and modeling study of soot formation during the pyrolysis and oxidation of a number of aliphatic and aromatic hydrocarbons. Proc. Combust. Inst. **33**, 625–632 (2011)
5. Homann, K.H., Pidoll, U.: The low-pressure pyrolysis of butadiyne (C_4H_2). Ber. Bunsenges. Phys. Chem. **90**, 847–854 (1986)
6. Hidaka, Y., Henmi, Y., Ohonishi, T., Okuno, T., Koike, T.: Shock-tube and modeling study of diacetylene pyrolysis and oxidation. Combust. Flame. **130**, 62–82 (2002)
7. Hidaka, Y., Hattori, K., Okuno, T., Inami, K., Abe, T., Koike, T.: Shock-tube and modeling study of acetylene pyrolysis and oxidation. Combust. Flame. **107**, 401–417 (1996)
8. Homann, K.H.: Formation of large molecules, particulates and ions in premixed hydrocarbon flames; progress and unresolved questions. Proc. Combust. Inst. **20**, 857–870 (1984)
9. Hansen, N., Klippenstein, S.J., Westmoreland, P.R., Kasper, T., Kohse-Höinghaus, K., Wang, J., Cool, T.A.: A combined ab initio and photoionization mass spectrometric study of polyynes in fuel-rich flames. Phys. Chem. Chem. Phys. **10**, 366–374 (2008)
10. Deuflhard, P., Wulkow, M.: Computational treatment of polyreaction kinetics by orthogonal polynomials of a discrete variable. Impact Comput. Sci. Eng. **1**, 269–301 (1989)
11. Williams, T.C., Shaddix, C.R., Jensen, K.A., Suo-Anttila, J.M.: Measurement of the dimensionless extinction coefficient of soot within laminar diffusion flames. Int. J. Heat Mass Transfer. **50**, 1616–1630 (2007)
12. Smyth, K.C., Shaddix, C.R.: The elusive history of m = 1.57 – 0.56i for the refractive index of soot. Combust. Flame. **107**, 314–320 (1996)

3-Carene Oxidation Mechanism

N. Sharath, K.P.J. Reddy, P.K. Barhai, and E. Arunan

Introduction

3-Carene, the 2D structure of which is shown in Fig. 1 and is a monoterpene with molecular formula $C_{10}H_{16}$, can be extracted from the plant sources [1–3]. The application of 3-carene as a biofuel was suggested by Kulkarni et al. [4], who found that a combination of 75 % ethylidene norbornene and 25 % 3-carene can act as an effective fuel. Our recent studies also found lower ignition delay times for 3-carene compared to JP-10 [5]. It is known that oxidation mechanism of a fuel is particularly important to understand combustion in high-speed vehicles. Thus, it is important to obtain the oxidation mechanism of fuels that can be used in high-speed vehicles. As far as we know, the oxidation mechanism of 3-carene does not exist in the literature and needs to be derived. The present paper discusses the results obtained from the simulation of preliminary oxidation mechanism of 3-carene.

It is well known that oxidation of fuel will be preceded by its decomposition. Thus we carried pyrolysis experiments of 3-carene to derive a detailed thermal decomposition [6]. The reactions in the thermal decomposition mechanism have been used as the initial steps in the oxidation mechanism. The oxidation mechanism was then derived to fit the obtained ignition delay values from our previous work.

N. Sharath (✉) • K.P.J. Reddy
Department of Aerospace Engineering, Indian Institute of Science, Bangalore 560012, India
e-mail: sharathnu2008@gmail.com

P.K. Barhai
Department of Applied Physics, Birla Institute of Technology, Ranchi 835215, Mesra, India

E. Arunan
Department of Inorganic and Physical Chemistry, Indian Institute of Science, Bangalore 560012, India

Computational Method

The constant volume method available in CHEMKIN [7] has been used to simulate the mechanism. The ignition delay in the present simulation is defined as the time taken by CH mole fraction to reach its peak value for equivalence ratios 0.5 and 1. In the case of equivalence ratio 2, the computed ignition delay time was defined as the time taken for the temperature in the reactor to rise by 400 K. The thermochemistry for the intermediates was obtained using the VIBE thermodata fit available in the CHEMKIN.

The reaction scheme used in the present work can be written as:

1. 3-carene→Products
2. 3-carene + H→products + H_2
3. Radicals formed in the unimolecular dissociation of 3-carene (only below C_9 radicals are considered to reduce the computational time) + O_2
4. Oxidation mechanism of products formed in the dissociation of 3-carene

Here, steps 1 and 2 correspond to thermal decomposition mechanism of 3-carene. The 3D molecular structures of intermediates formed in the process of oxidation and unimolecular decomposition of 3-carene are given in Fig. 2.

Results

Initial simulation was done using the following procedure. The thermal decomposition mechanism used in the oxidation process involves only step 1 (unimolecular decomposition) to explain the observed product concentrations. An ignition delay variation with temperature shown in Fig. 3 was obtained using the above mechanism. Here, the rate parameters in the mechanism were fitted to obtain the product concentration observed in the experiments. For the above

G. Ben-Dor et al. (eds.), *30th International Symposium on Shock Waves 1*, DOI 10.1007/978-3-319-46213-4_55

condition, the obtained pressure profile and CH mole fraction profile in the simulation of oxidation mechanism are given in Fig. 4. However, given the fact that the rate parameters used in the above process could be wrong, the following modifications were done to the decomposition mechanism.

The rate parameters were obtained from theory and used as an initial guess in the thermal decomposition mechanism, and step 2 given in the computational method was included to account for the bimolecular reactions. With this reactions included in the oxidation mechanism, a pressure profile and mole fraction profile of CH shown in Fig. 5 were obtained. The variation ignition delay with temperature for the refined oxidation mechanism is given in Fig. 6. It is clear that ignition delay values fairly match with the experimental value as it happened in the case shown in Fig. 3.

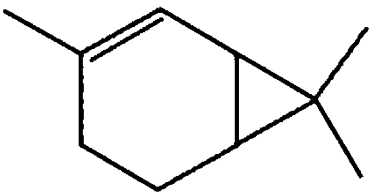

Fig. 1 A 2D structure of 3-carene

Conclusion

The oxidation mechanism with decomposition mechanism that includes only unimolecular decomposition of 3-carene to explain the observed product concentration reasonably fitted the obtained ignition delay values. Since rate parameters used in the reactions are different from the one used in the mechanism, a refined oxidation mechanism with decomposition mechanism that includes unimolecular and bimolecular reactions of 3-carene has been derived. The ignition delay values from the refined mechanism also fairly match with the experimentally obtained ignition delay values. However, the current oxidation mechanism needs

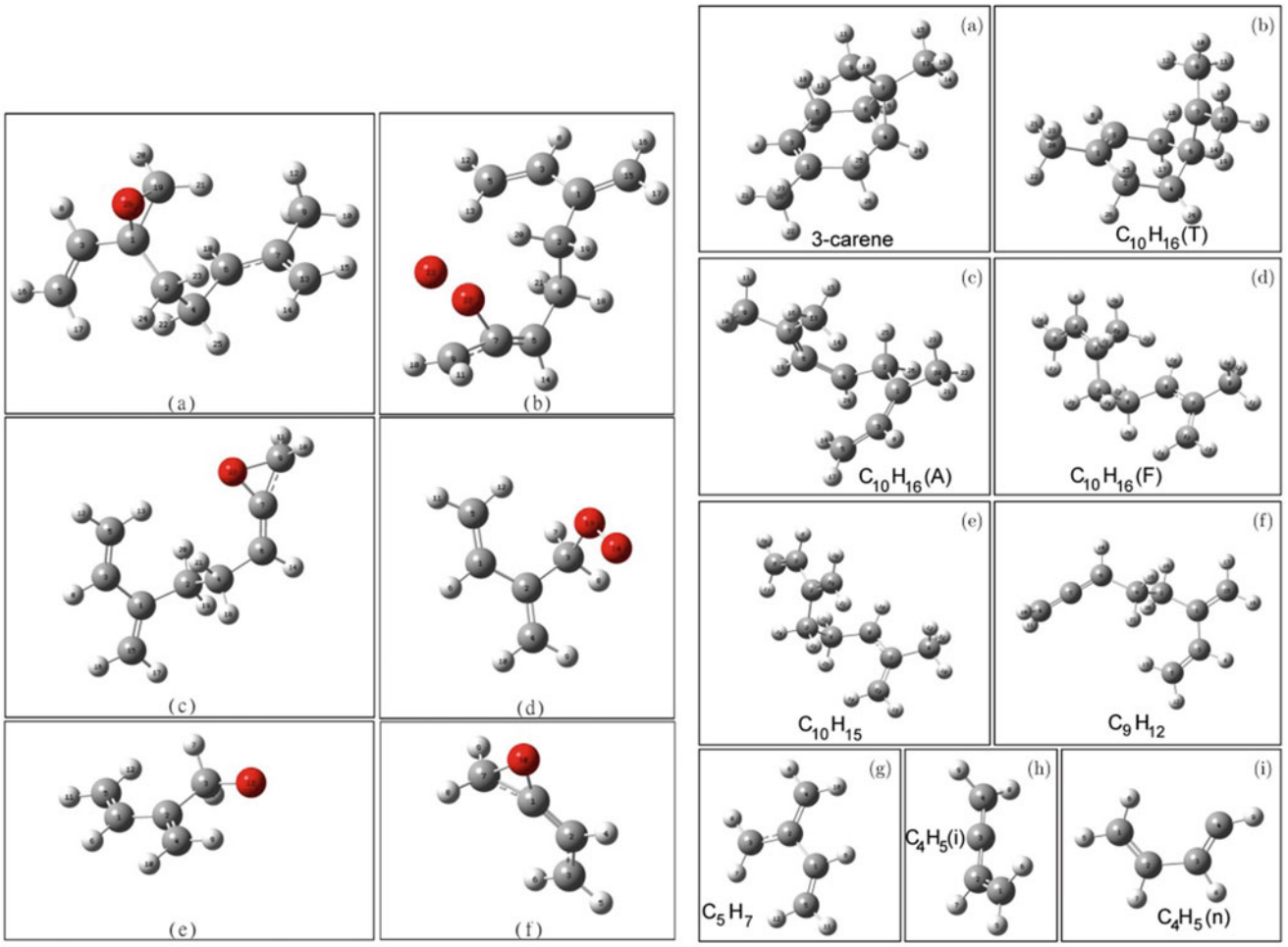

Fig. 2 Structure of intermediates considered in the oxidation mechanism (*left*) and in the decomposition mechanism (*right*)

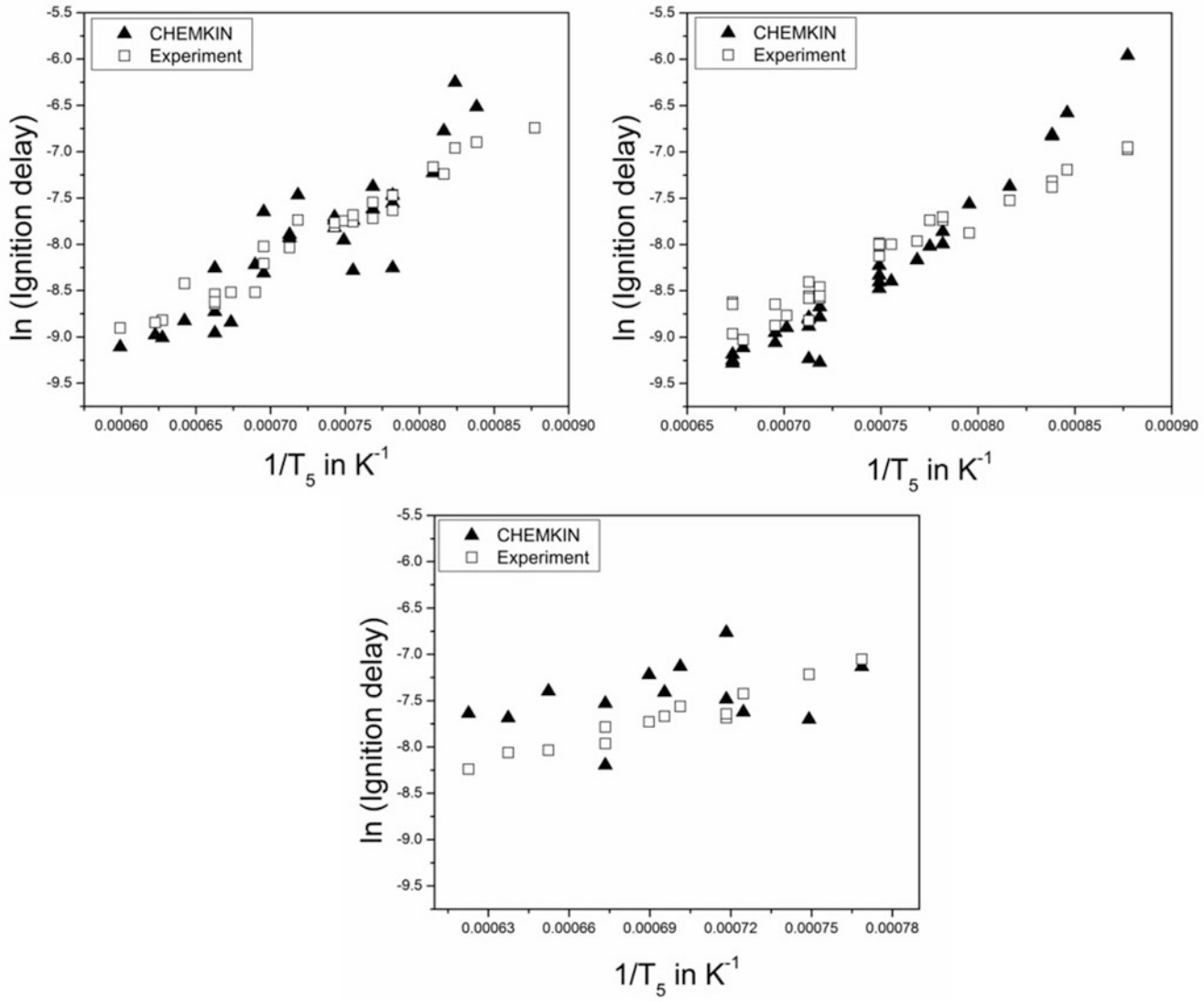

Fig. 3 Comparison between experimental and computed ignition delay values for equivalence ratios 1, 0.5, and 2, in cyclic order

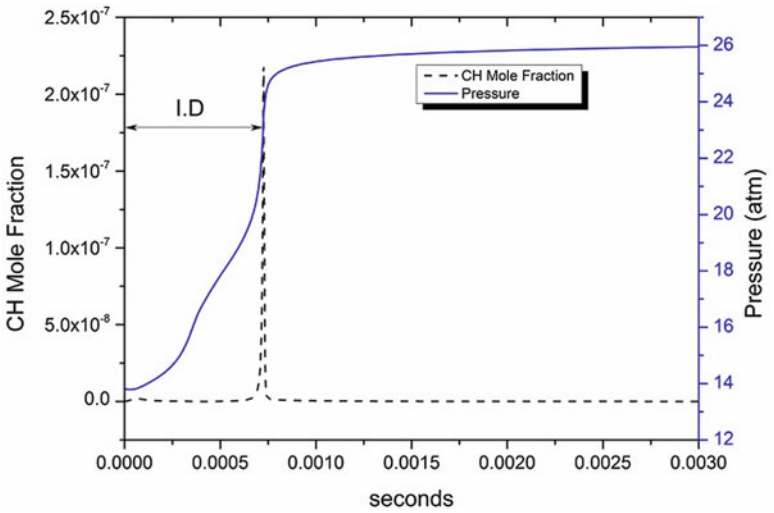

Fig. 4 The pressure and CH mole fraction profiles obtained in the simulation at 1236 K for stoichiometric 3-carene/O_2/argon mixture

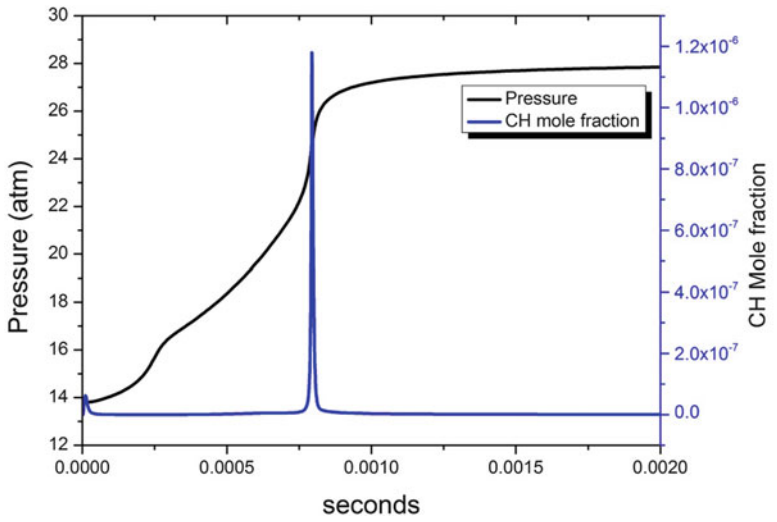

Fig. 5 The pressure and CH mole fraction profiles obtained in the present simulation at 1236 K for stoichiometric 3-carene/O_2/argon mixture

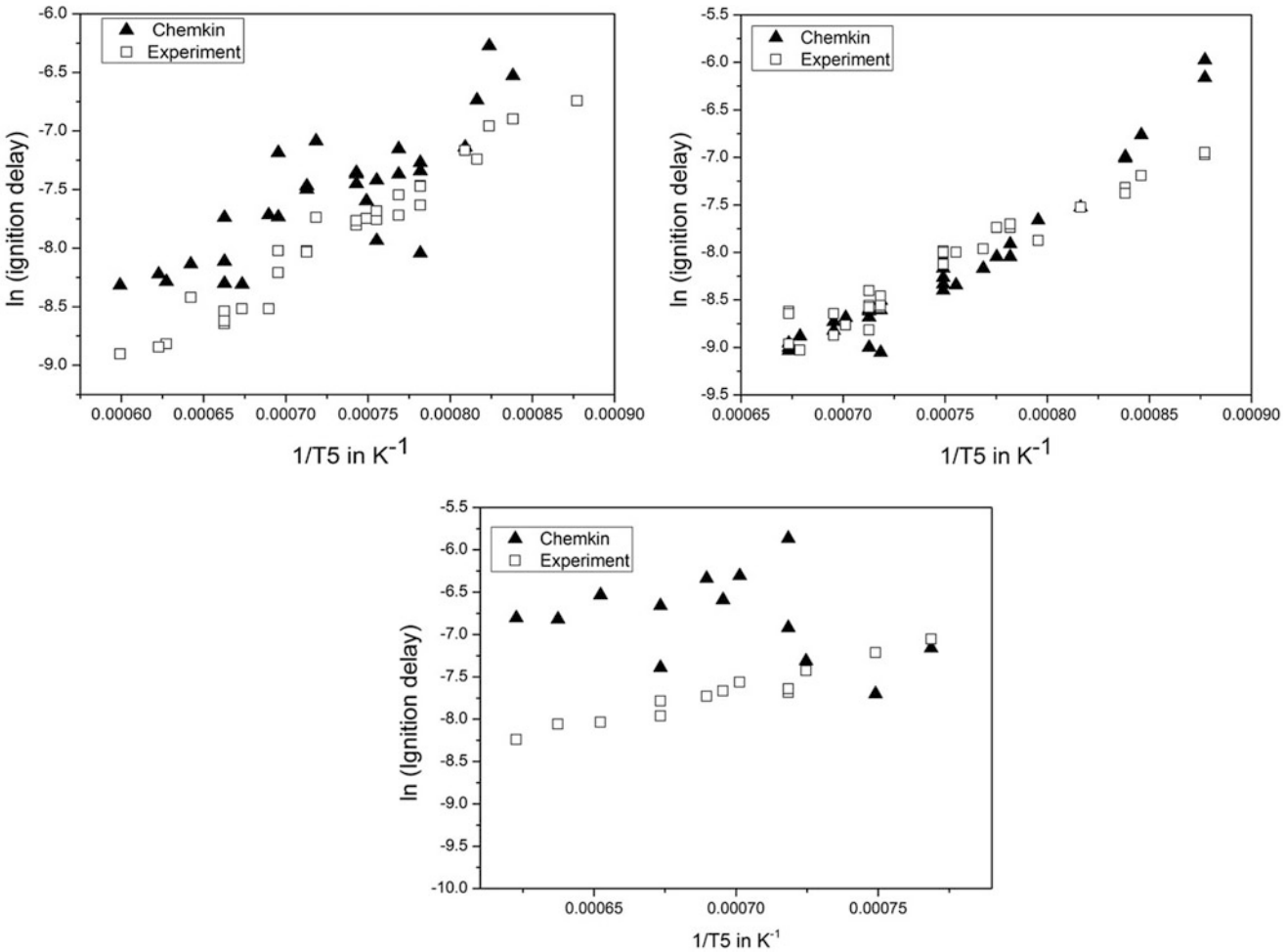

Fig. 6 Comparison between experimental and computed ignition delay values for equivalence ratios 1, 0.5, and 2, in cyclic order

to be added with reactions to include for the oxidation of $C_{10}H_{15}$ intermediates formed in the abstraction reaction of hydrogen in 3-carene by an H atom.

References

1. Simonsen, J.L.: LXI.—The constituents of Indian turpentine from *Pinuslongifolia*, Roxb. Part I. J. Chem. Soc. Trans. **119**, 1644–1654 (1921)
2. Simonsen, J.L.: CCLXXVII.—The constitution of the terpene present in the essential oil from *AndropogonJwarancusa*, Jones. J. Chem. Soc. Trans. **121**, 2292–2299 (1922)
3. Simonsen, J.L., Rau, M.G.: LXVII.—The constituents of Indian turpentine from *Pinuslongifolia*, roxb. Part II. J. Chem. Soc. Trans. **123**, 549–560 (1923)
4. Kulkarni, S.G., Bagalkote, V.S., Patil, S.S., PramodhKumar, U., Anil Kumar, V.: Theoretical evaluation and experimental validation of performance parameters of new hypergolic liquid fuel blends with red fuming nitric acid as oxidizer. Propellants Explos. Pyrotech. **34**, 520–525 (2009)
5. Sharath, N, Reddy, K.P.J., Arunan, E.: Oxidation of 3-carene at high temperature. In: 28th International Symposium on Shock Waves, Edited by Konstantinos Kontis
6. Sharath, N, Reddy, K.P.J., Arunan, E.: Thermal decomposition study of 3-carene, ISSW-29, Madison, USA, Jul 14–19, 2013
7. CHEMKIN-PRO 15101, Reaction Design: San Diego 2010

Shock Tube Ignition Delay Studies of Dicyclopentadiene

Kunal V. Dhoke, K.P.J. Reddy, and E. Arunan

Introduction

Over the past decades, dicyclopentadiene (DCPD) has been researched for many uses in combustion for various purpose such as fuel, binder, etc. The formation of five-membered rings in the combustion is of great interest due to the high reactivity and toxicity of compounds that lead these moieties [1]. The cyclopentadienyl radical is one of the most abundant radical present in high-temperature gaseous environment such as flame. It is considered as a starting point of reaction pathways leading to the formation of polycyclic aromatic hydrocarbons (PAHs) due to its multiple reaction sites and its ability of self-recombination [2]. Qualitatively, there is a large agreement that the chemistry of cyclopentadienyl radical plays a significant role in the formation of naphthalene and phenanthrene [3]. The kinetics of the reaction between two cyclopentadienyl radical has been the subject of several investigations since it was proposed by Melius et al. [4] that it can be one of the major production pathways for naphthalene [2].

DCPD (tricyclo[5.2.1.0]deca-3,8-diene) is a hydrocarbon heterodimer of cyclopentadiene that can be obtained by dehydrogenation of JP-10. The following figure shows the optimized structure of DCPD on MP2/6-311G level of theory.

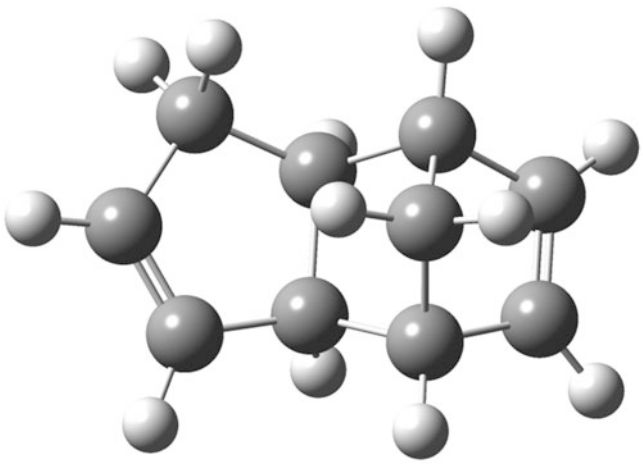

DCPD has been researched for several years for use as a potential binder in composite solid propellant formulation. The binder of a composite solid propellant is very important in defining the mechanical, combustion, and ballistic characteristics of a propellant [5]. In all composite solid propellant which are currently in use, polymers perform the important role of binder for the oxidizer, metallic fuel, and other additives. The binder performs the dual role of imparting dimensional stability to the composite and good mechanical properties to the propellant. Hydroxy-terminated polybutadiene (HTPB) is the most popular binder used in composite solid propellants which is normally cured by reaction with diisocyanates such as tolylene diisocyanate (TDI) or isophorone diisocyanate (IPDI) to form polyurethane networks. However, this reaction is highly susceptible to spurious reaction with moisture, leading to deterioration in the properties of the propellant. In addition, the high reactivity of the isocyanate group limits the pot life of the propellant. However, the inherent incompatibility of isocyanates with energetic oxidizers such as ammonium dinitramide (ADN) and hydrazinium nitroformate (HNF) also requires new cure methodologies to be evolved for processing high-energy propellants using HTPB as binder [6]. DCPD is capable of forming a highly cross-linked

K.V. Dhoke • E. Arunan (✉)
Department of Inorganic and Physical Chemistry, Indian Institute of Science, Bangalore, India
e-mail: arunan@ipc.iisc.ernet.in

K.P.J. Reddy
Department of Aerospace Engineering, Indian Institute of Science, Bangalore 560012, India

G. Ben-Dor et al. (eds.), *30th International Symposium on Shock Waves 1*, DOI 10.1007/978-3-319-46213-4_56

polymeric structural network through ring-opening metathesis polymerization [8]. Relevant thermodynamic properties of the HTPB and DCPD fuels are summarized in Table 1.

This study involved the detailed investigation of ignition delay studies of DCPD in order to address the above problem.

Experiment

Ignition delay (τ) studies of DCPD were carried out in a single-pulse shock tube [9]. Figure 1 shows the schematic diagram of the chemical shock tube-3 (CST3) [10] facility used in the ignition delay studies of DCPD. The details of CST-3 established in Laboratory for Hypersonic and Shock Wave Research are as follows. The lengths of driver and driven sections of the shock tube which have an inner diameter of 54 mm are 2 and 5 m, respectively. The diaphragms were made from an aluminum sheet of thickness 1 mm. It was grooved to different depths to vary the shock strength and hence obtain different temperatures. For all the experiments, argon and helium were used as driven and driver gas, respectively. Measurements were made in the reflected shock region for different equivalence ratios (φ) of DCPD/O_2/Ar reactant mixture summarized in Table 2.

The incident shock velocity was measured using two piezoelectric pressure transducers (Model No. 113A24) spaced over the last 0.561 m of the driven section. A Tektronix TDS-2014B oscilloscope was used to record the pressure profile history. The pressure profile from the final pressure transducer located at a distance of 1.5 cm from the end wall was also used to measure the ignition delay values. A vacuum monochromator (Acton VM 502) coupled to the shock tube using an optical port situated near the end wall of the driven section has been used to record CH* emission signal following ignition of any fuel. The monochromator has an inbuilt photo-multiplier tube (DA-780-VUV). The monochromator covers a wide range of wavelength from 30 nm to 600 nm, and PMT has a wavelength range of 200–600 nm. In the present study, the monochromator was fixed at 431.5 nm to record CH* emission signal.

Ignition delay (τ) times were measured using chemiluminescence from electronically excited CH radical (CH*) and pressure profile. Figure 2 depicts one of the obtained signals used in ignition delay time measurements from pressure as well as CH* emission signals. The ignition delay (τ) time is defined as the time interval between the arrival of reflected shock at the pressure transducer and pressure rise due to the ignition of fuel. The ignition of the fuel was also validated using CH* emission signal. In case of CH* emission, the

Table 1 HTPB and DCPD properties [7]

Sr. no	Fuel	Density g/cc	Decomposition temperature (K)	ΔH_f (kcal/mol)
1	HTPB	0.92	887	−5.16
2	DCPD	0.98	932	−50.66

Table 2 DCPD/O_2/Ar mixture studied

Sr. no	φ	Mol % DCPD	Mol % O_2	Mol % Ar
1	0.5	0.30	8.66	91.03
2	1.0	0.41	5.41	94.16
3	1.5	0.50	4.34	95.16

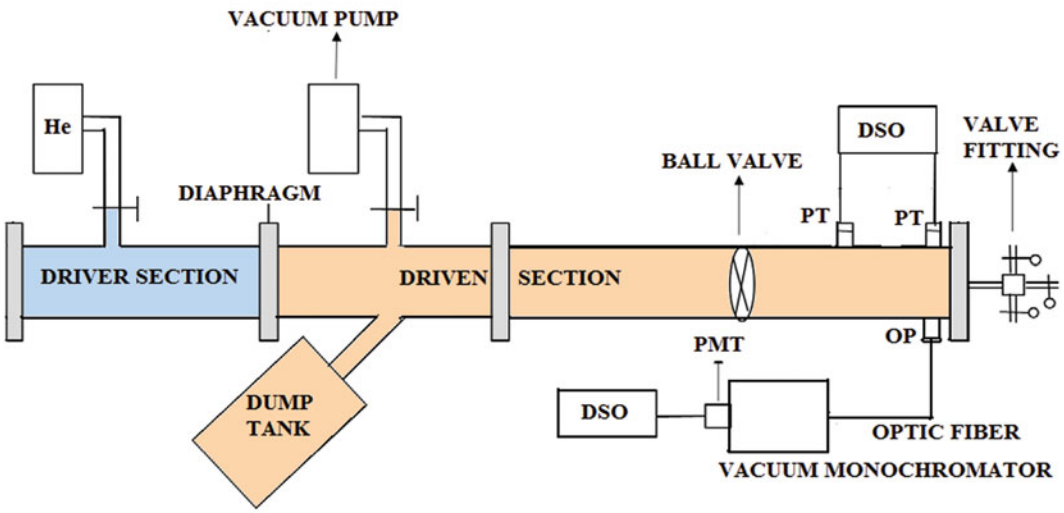

Fig. 1 Schematic diagram of the chemical shock tube (CST3) facility equipped with emission spectroscopy used for combustion experiments on DCPD. *DSO* digital storage oscilloscope (Tektronix, TDS 210); *PMT* photo-multiplier tube; *OP* optical port; *PT* pressure transducer (PCB model 113A24)

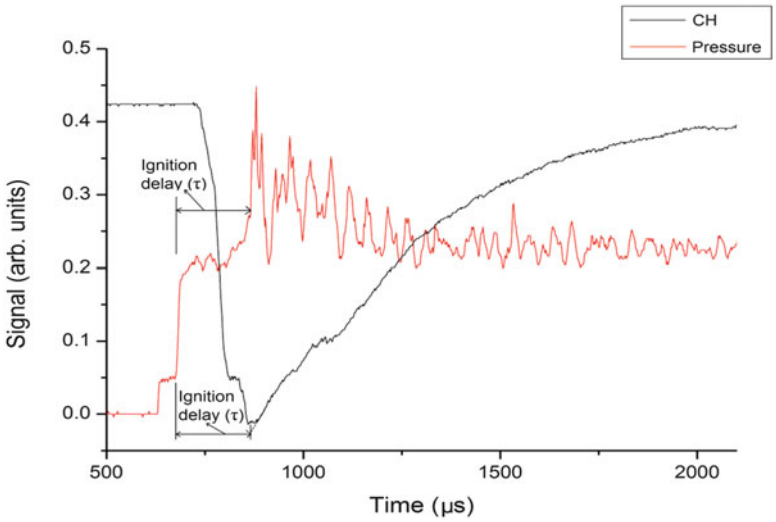

Fig. 2 Example ignition delay time measurement for a 0.416/5.4166/94.1647 mol% DCPD/O_2/Ar mixture ($\varphi = 1.0$) at reflected shock condition of 1607 K and 14.08 atm. The ignition delay time (τ) measured by pressure signal and CH* emission was 180 μs

Table 3 Activation energy for three equivalence ratios

Equivalence ratio	E_a (kcal/mol)
0.5	31.30 ± 2.34
1	30.79 ± 1.18
1.5	29.84 ± 1.84

ignition delay has been defined as the time taken to reach the peak of CH* emission after the arrival of reflected shock at the pressure transducer.

Result

The ignition experiments were carried out for temperatures ranging from 1200 to 1800 K and pressure ranges from 12 to 19 atm for three equivalence ratios 0.5, 1, and 1.5. A plot showing variation of measured ignition delay times as a function of temperature is given in Fig. 3. The data show Arrhenius exponential dependence on inverse temperature, typical of high-temperature ignition. The activation energy for all equivalence ratios is summarized in Table 3.

It has been observed that ignition delay increases with increasing equivalence ratio and it decreases with increasing fuel concentration.

Theoretical investigations of oxidation kinetics of DCPD are being carried out. It is necessary to have the knowledge of pyrolysis of a fuel to understand its oxidation process. Atoms in molecules (AIM) is a tool based on electron density [11] topology used to understand bond making and breaking process during the course of reaction. Figure 4 shows AIM analysis of DCPD.

Conclusions

Ignition delay studies of DCPD/O2/Ar mixture have been carried out using shock tube for three equivalence ratios 0.5, 1.0, and 1.5. A plot showing variation of measured ignition delay times as a function of temperature has been reported. AIM analysis of DCPD was reported.

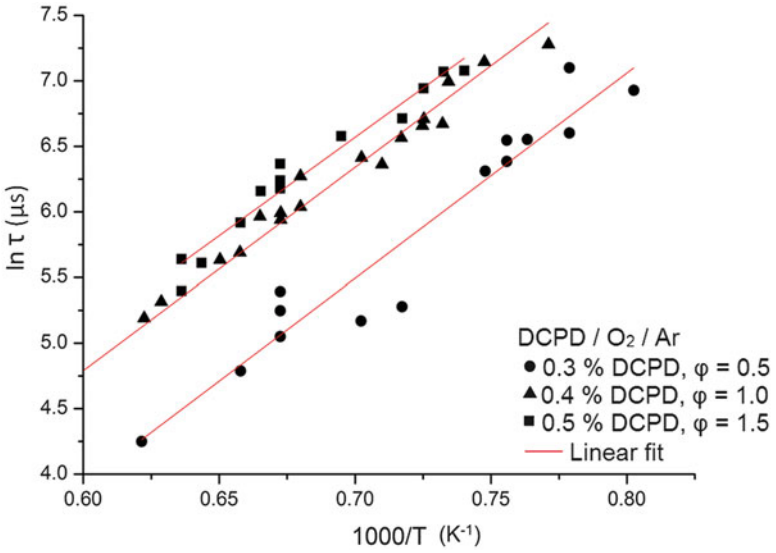

Fig. 3 Arrhenius plot of experimental results for ignition delay of DCPD

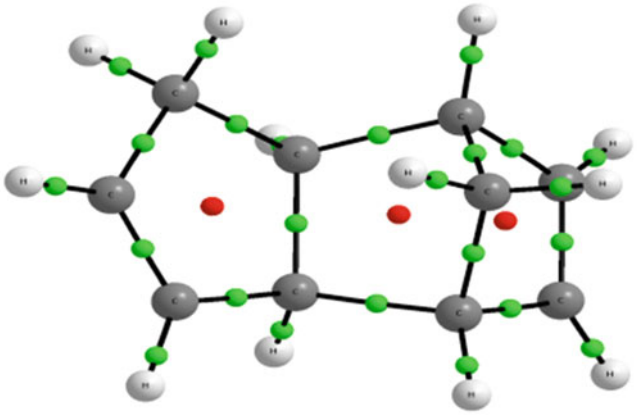

Fig. 4 AIM analysis of Dicyclopentadiene. *Green solid* corresponds to bond critical point (bcp), whereas *red solid* corresponds to ring critical point (rcp)

References

1. Do, H.K., James, A., Mulholland, Dong, W., Violi, A.: Pyrolytic hydrocarbon growth from cyclopentadiene. J. Phys. Chem. A **114**, 12411–12416 (2010)
2. Violi, A., Sarofim, A.F., Truong, T.N.: Quantum mechanical study of molecular weight growth process by combination of aromatic molecules. Combust. Flame **126**, 1506–1515 (2001)
3. Fascella, S., Cavallotti, C., Rota, R., Carra, S.: The peculiar kinetics of the reaction between acetylene and the cyclopentadienyl radical. J. Phys. Chem. A **109**, 7546–7557 (2005)
4. Melius, C.F., Colvin, M.E., Marinov, N.M., Pitz, W.J., Senkan, S. M.: Reaction mechanisms in aromatic hydrocarbon formation involving the C_5H_5 cyclopentadienyl moiety. Proc. Combust. Inst. **26**, 685–692 (1996)
5. O'Neil, P.T.: Developments in processing and ballistics of dicyclopentadiene-based composite solid propellants. Purdue University, ProQuest, UMI Dissertations Publishing, 1529722 (2012)
6. Reshmi, S., Arunan, E., Raghunadhan Nair, C.P.: Azide and alkyne terminated polybutadiene binders: synthesis,cross-linking, and propellant studies. Ind. Eng. Chem. Res. **53**, 16612–16620 (2014)
7. Shark, S.C., Zaseck, C.R., Graham Jr., J.T., Pourpoint, T.L., Son, S. F., Heister, S.D.: Visualization and performance of hybrid rocket solid fuels in an optical cylindrical combustor. In: 49th AIAA/ASME/SAE/ASEE Joint Propulsion Conference 3966 (2013)
8. Sirjean, B., Fournet, R., Glaude, P.A., Battin-Leclerc, F., Wang, W., Oehlschlaeger, M.A.: Shock tube and chemical kinetic modeling study of the oxidation of 2,5-dimethylfuran. J. Phys. Chem. A **117**, 1371–1392 (2013)
9. Nagaboopathy, M., Vijayanand, C., Hegde, G., Reddy, K.P.J., Arunan, E.: Single-pulse chemical shock tube for ignition delay measurements. Curr. Sci. **95**, 1 (2008)
10. Rajakumar, B., Reddy, K.P.J., Arunan, E.: Unimolecular HCl elimination from 1,2-dichloroethane: a single pulse shock tube and ab initio study. J. Phys. Chem. A **106**(36), 8366–8373 (2002)
11. Caroline, L.P., Mary, K.T., Holmes, B.E., Heard, G.L.: QTAIM analysis of the HF, HCl, HBr, and HOH elimination reactions of halohydrocarbons and halohydroalcohols. J. Phys. Chem. A **115** (45), 13133–13138 (2011)

Model Order Reduction for Reacting Flows: Laminar Gaussian Flame Applications

Van Bo Nguyen, H.-S. Dou, K. Willcox, and Boo-Cheong Khoo

Introduction

Numerical simulation of reacting flows is important for improving combustion processes, but is a computationally challenging task. The accurate modelling of combustion processes using detailed reaction mechanisms leads to stiff systems of differential equations with multi-scale dynamics. Therefore, fine spatial grids and small time steps are usually needed. In addition, a detailed chemistry model involves many chemical species and many reactions, which means that these models can quickly become large. To address these challenges, we develop a projection-based model reduction technique for reacting flows that reduces computational cost while maintaining accuracy.

Over the past years, several methods have been developed to reduce the computational cost of evaluating the chemical source term. These methods include, among others, the quasi-steady-state approximation, partial equilibrium approximation [1], principal component analysis [2], intrinsic low-dimensional manifold (ILDM) [3–5], and computational singular perturbation (CSP) [6, 7]. The CSP method decomposes the equations governing the chemistry into fast and slow modes. The species and reactions corresponding to fast modes are eliminated from the system in the following integration step. Thus, the system of equations becomes smaller and, since the small (fast) timescales have been removed, non-stiff. However, the algorithm is usually initialized using the eigen-modes of the Jacobian of the chemical source term. Similarly, the ILDM, a method based on a dynamical systems approach, separates automatically the slow and fast timescales. The ILDM is usually applied in conjunction with a tabulating procedure that allows its use in CFD simulation codes. Although timescale separation methods have been applied successfully in numerical simulations of reacting flows, their computational cost is usually still high when the number of chemical species and/or reactions is high.

In this paper, we focus instead on projection-based model reduction, in which the reduced models are obtained by performing Galerkin projection of the large-scale system of equations onto the space spanned by a small set of basis vectors. Different methods exist to construct the required basis vectors. Such methods include, for example, Krylov subspace methods [8, 9], balanced truncation [10, 11], and proper orthogonal decomposition (POD) [12, 13]. The method is able to obtain in many cases orders-of-magnitude reduction in the order of the system, since the dynamics of interest can often be represented by a small number of POD modes. The POD modes are constructed as the span of a set of state solutions (snapshots). Such snapshots are computed by solving the large-scale system for selected values of parameters and selected inputs. However, in the case of nonlinear systems, the POD–Galerkin method leads to inefficient reduced models since the projected nonlinear term requires computations that scale with the dimension of the original large-scale problem. Methods to approximate the projected nonlinear term in a POD reduced model include the missing point estimation technique [12, 14]. Another approach is the empirical interpolation method (EIM) [15, 16]. The coefficients of this expansion are determined by interpolation. We use here the discrete empirical interpolation method (DEIM), a discrete variant of the EIM [17]. We show that a POD–DEIM reduced model can accurately represent chemical kinetics while providing significant speedups in computation times.

V.B. Nguyen (✉) • B.-C. Khoo
Temasek Laboratories, National University of Singapore, T-Lab Building 5A, Engineering Drive 1, #09-02, Singapore 11741, Singapore
e-mail: tslngvb@nus.edu.sg

H.-S. Dou
Faculty of Mechanical Engineering and Automation, Zhejiang Sci-Tech University, Hangzhou, Zhejiang Province 310018, P.R. China

K. Willcox
Department of Aeronautics and Astronautics, Massachusetts Institute of Technology, Cambridge, MA 02139, USA

G. Ben-Dor et al. (eds.), *30th International Symposium on Shock Waves 1*, DOI 10.1007/978-3-319-46213-4_57

Section "Reacting Flow Model" of this paper introduces the reacting flow model and numerical solution approach. Section "Model Reduction Methodology" presents the POD–DEIM model reduction approach. Section "Reduced Model For Gaussian Premixed Flame" presents an application of the model reduction method to a premixed Gaussian flame model, and Section "Conclusions" concludes the paper.

Reacting Flow Model

The combustion process is modelled by a detailed chemical kinetics model of $H_2/O_2/Ar$ with N_s species and N_r elementary reactions. All gas species are considered thermally perfect, and we assume the equation of state (EOS) of perfect gases is applicable. We assume that there is no body force acting on the chemical species and that there is no external heat source. Therefore, the governing equations for this problem can be expressed in Cartesian coordinates:

$$\frac{\partial Q}{\partial t}+\frac{\partial F}{\partial x}+\frac{\partial G}{\partial y}=\frac{1}{\mathrm{Re}}\left(\frac{\partial H}{\partial x}+\frac{\partial T}{\partial y}\right)+S \tag{1}$$

In this expression, Q is the conservative variable, F and G are convection terms, H and T are diffusion terms, and S is the source term.

The mass production rate, $\dot{\omega}$, of species k in the reaction I can be computed by

$$\begin{aligned}\dot{\omega} = W_k\sum_{i=1}^{Nr}\left(v''_{ki}-v'_{ki}\right)\left(\alpha_{ki}[X_k]\right)\\ \left\{K_{f,i}\prod_{k=1}^{Ns}[X_k]^{v'_{ki}}-K_{b,i}\prod_{k=1}^{Ns}[X_k]^{v''_{ki}}\right\}\end{aligned} \tag{2}$$

Here v'_{ki} and v''_{ki} are the chemical stoichiometric coefficients of the reactant and the product for species k in reaction i, respectively. $K_{f,i}$ and $K_{b,i}$ are the forward and backward coefficients of the reaction computed through the Arrhenius law for the state value of pressure, temperature, and mole fraction, W_k is the molecular weight of species k, and $[X_k]$ is the molar concentration of species k in reaction i. This molar concentration of species k is defined by $[X_k]=\rho Y_k/W_k$, and α_{ki} are the third-body coefficient factors of species k in reaction i.

We use an operator-splitting scheme to separate the governing Eq. (1) into a fluid dynamics part and chemical kinetics part. This splitting allows us to use a specific numerical scheme developed for the fluid dynamic part in conjunction with a numerical method especially developed to deal with stiff systems of ODEs for the chemical kinetics part. For fluid dynamics part, we use the fifth-order weighted essentially non-oscillatory (WENO) scheme [18–20] for the inviscid flux terms and the fourth-order central difference scheme [21] for the viscous flux terms. The third-order Runge–Kutta method is used to evolve the solution in time. The chemical kinetics part is solved using CHEMEQ, a solver of stiff nonlinear ODEs, developed by Young et al. [22]. For the boundaries, we use Navier–Stokes characteristic boundary conditions [23].

Model Reduction Methodology

Projection-based methods derive a reduced-order model by projecting the governing equations onto a subspace spanned by a set of basis vectors [24]. In this section, we describe the projection-based model reduction idea, the POD technique, and the DEIM employed in the approximation of the nonlinear source term.

Projection Framework

Consider the nonlinear system of ODEs resulting from spatial discretization of the chemical dynamic source term:

$$dY/dt=g(Y,T,p) \tag{3}$$

with the initial conditions $Y(t=0)=Y^0$. Here, $Y=\left[Y_1^1,\ldots,Y_1^N,\ldots,Y_{Ns}^N,\ldots,Y_{Ns}^N\right]\in R^M$ is the vector of mass fraction of species discretized over the computational domain, which has N grid points, T is temperature, and p is pressure of the gas mixture. The vector $g(Y,T,p)=\left[g_1^1(Y,T,p),\ldots,g_1^N(Y,T,p),\ldots,g_{Ns}^N(Y,T,p),\ldots,g_{Ns}^N(Y,T,p)\right]\in R^M$ contains the reaction rates of species over the computational domain. The total number of unknown of Eq. (3) is $M=N_sN$.

Assume that the state vector Y can be represented as a linear combination of K basis vector, $Y=VY_r$, where $Y_r\in R^K$ is the reduced state vector with $K\ll M$ and the basis $V\in R^{M\times K}$. With this assumption, the reduced-order model is obtained by performing Galerkin projection of Eq. (3) onto subspace spanned by column basis vectors:

$$dY_r/dt=V^Tg(VY_r(t),T,p) \tag{4}$$

With the initial condition, $Y_r^0=V^TY^0$. Although the reduced-order model obtained after applying the projection technique is low in dimension, as can be observed in Eq. (4), the evaluation of the nonlinear reaction source term at each time step still depends on the dimension M. This makes the solution of the obtained reduced-order model as expensive as the solution of the original system. An effective way to

overcome this difficulty is to approximate the nonlinear function by projection and interpolation. This is the idea behind the DEIM [17], which is a discrete version of the EIM proposed by Barrault et al. [15].

Proper Orthogonal Decomposition

The POD technique, also known as the Karhunen–Loeve decomposition [25], is a method for constructing basis vectors with global support that capture the dominant characteristics of a dynamical system. In the method of snapshots, such basis vectors (POD modes) are computed from an ensemble of solutions (snapshots) obtained by solving the large-scale system for selected values of parameters and inputs. The POD modes are computed as follows.

Given a set of Q snapshots $\{Y_j\}_{j=1}^{Q}$, where $Y_j \in R^M$, the POD compute the set of $K \leq Q$ basis vectors $\{v_i\}_{i=1}^{K}$, where $v_i \in R^M$ is the ith basis vector, which is obtained by solving the minimization problem

$$\underset{\{v\}_{i=1}^{K}}{Min} \sum_{j=1}^{Q} \left\| Y_j - \sum_{i=1}^{K} \left(Y_j^T v_i \right) v_i \right\|_2^2, \text{ s.t. } v_i^T v_j = \delta_{ij}, \quad 1 \leq i,j \leq K \tag{5}$$

The solution of (5) can be obtained by finding the singular vectors of the snapshots matrix Y, in particular, supposing that the singular value decomposition of Y is $Y = V\Sigma W^T$, where $V = [v_1, \ldots v_Q] \in R^{M \times Q}$ and $W = [w_1, \ldots w_Q] \in R^{M \times Q}$ are orthogonal, and singular values are $\Sigma = \text{diag}(\sigma_1, \ldots, \sigma_Q) \in R^{Q \times Q}$ with $\sigma_1 \geq \sigma_2 \geq \ldots \geq \sigma_Q \geq 0$. Then the POD basis $\{v\}_{i=1}^{K} \subset V \in R^{M \times Q}$. The error in approximating the snapshots using K POD modes is given by

$$\sum_{j=1}^{Q} \left\| Y_j - \sum_{i=1}^{K} \left(Y_j^T v_i \right) v_i \right\|_2^2 = \sum_{i=K+1}^{Q} \sigma_i^2 \tag{6}$$

Discrete Empirical Interpolation Method

The DEIM provides an efficient approach to build reduced-order models whose computational cost is independent of the dimension of the original large-scale system. To construct the POD–DEIM reduced-order model, two sets of basis vectors are used: the POD modes V obtained from the solution snapshots and the DEIM modes U obtained from snapshots of the nonlinear source term. Computation of U proceeds as described above for V, but replacing state snapshots $Y_j \equiv Y(t_j, T, p)$ with snapshots of the nonlinear terms $g_j \equiv g(t_j, T, p)$. The nonlinear source term is approximated by a linear combination of L basis vectors $U \in R^{M \times L}$ with the corresponding expansion coefficient $c \in R^L$ as $g(Y, T, p, t) \approx Uc(t)$. In this study, we use the DEIM algorithm proposed in [17] since it provides an efficient methodology to compute the desired interpolation indices for determining the coefficients $c(t)$.

From the DEIM basis vectors U, the DEIM finds a set of interpolation indices that allow the determination of the coefficients $c(t)$ in (14). This involves the evaluation of the nonlinear source term at only a subset of points $L << M$, hence, eliminating the dependence on M of the reduced-order model. The POD–DEIM reduced-order model then becomes

$$\frac{dY_r(t)}{dt} = V^T U \left(P^T U \right)^{-1} g\left(P^T V Y_r(t), T, p \right) \tag{7}$$

where P is index matrix, which determines the interpolation points that were determined from the indices the maximum errors of the approximations. The temperature and pressure are evaluated at the interpolation points. In Eq. (7), $V^T U \left(P^T U \right)^{-1} \in R^{K \times L}$ and $P^T V \in R^L$ can be precomputed in an offline stage. Therefore, the online computation of the reduced-order model requires solution of K nonlinear equations with L values of $g(., T, p)$ at the interpolation points.

Reduced Model for Gaussian Premixed Flame

Problem Setup

In this application, the evolution of the Gaussian flame is modelled by the system of coupled nonlinear PDEs introduced in the previous section. The gas mixture is composed of 9 chemical species (O_2, H_2, O, H, OH, HO_2, H_2O_2, H_2O, Ar) participating in 19 reversible elementary reactions corresponding to the chemical kinetics model employed in Wilson and MacCormack [26]. The transport properties of the mixture and the species are computed using classical kinetic theory and the mixture-average approach and employing the GRI-Mech 3.1 database [27]. The POD–DEIM model reduction technique is applied to the nonlinear source term (3), since, as in typical reacting flow applications, the solution of this term drives the computational cost of the numerical simulation.

For all simulations, a two-dimensional square domain of 1.0 mm × 1.0 mm is discretized using a uniform mesh grid with 101 grid points in each direction. The dimension of the full model unknowns Y is $M = 91,809$. Initial conditions specify a pressure of 101,325.0 Pa and velocity components

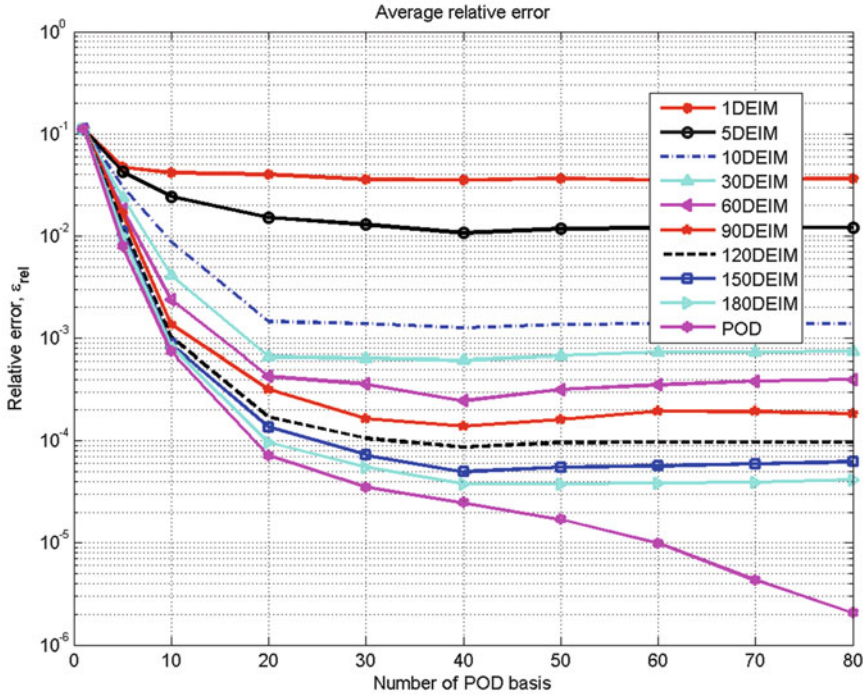

Fig. 1 Average relative errors (2-norm) for varying number of POD and DEIM

of 0 m/s. A premixed mixture of $H_2/O_2/Ar$ with mole fractions 0.333:0.167:0.5 is imposed at each grid point of the computational domain. To start the reaction (the flame), we use a two-dimensional Gaussian distribution located at the centre of the domain:

$$T(x,y) = T_0 e^{-\left(\frac{(x-x_0)^2}{2a^2}+\frac{(y-y_0)^2}{2a^2}\right)} \tag{8}$$

In this expression, T_0 is the temperature amplitude, a is the width of the temperature distribution, and (x_0, y_0) are the coordinates of the centre point. Outlet subsonic flow characteristic boundary conditions are applied to the four boundaries of the computational domain.

Fixed Parameters and Inputs

In this subsection, we test the capabilities of the reduced-order model in terms of the approximation errors and computational time savings. To this end, several models of different sizes (values of K and L) are constructed for fixed simulation parameters and inputs. All the models are built using 400 snapshots of state solution Y and 400 corresponding snapshots of nonlinear term $g(Y, T, p)$. For each model, the snapshots are collected from simulations of the full-order model lasting 400 flow time steps. To assess the performance of the reduced-order models, a simulation of 400 flow time steps is carried out for each reduced model, and the average relative error at the final time step and the average simulation time of one chemistry time step are calculated.

Figure 1 shows the average relative error of the solutions obtained using the reduced models of different sizes. The results indicate that both the number of POD modes and the number of interpolation points drive the average relative error when the number of POD modes is smaller than 40. For reduced-order models with state dimensions greater than 40, the average relative error is driven by the number of interpolation points, indicating that the approximation of the nonlinear term is the most significant source of error.

Figure 2 shows comparisons of the average computational time for one chemistry time step between the full model, classical POD reduced-order models, and POD–DEIM reduced-order models, again for different choices of K and L. Figure 2 shows that the computational time is driven by both K and L. It also shows that POD–DEIM models are on average two orders of magnitude faster than POD models. However, if we consider models of similar size (e.g. a POD model of size $K = 40$ and a POD–DEIM model of size $K = 40$, $L = 60$), the POD model is more accurate. We also note that despite the good speedup factors obtained by the POD–DEIM models in the solution of the nonlinear source term, the speedup factor for the coupled flow-chemistry simulation is of the order of a factor of 10.

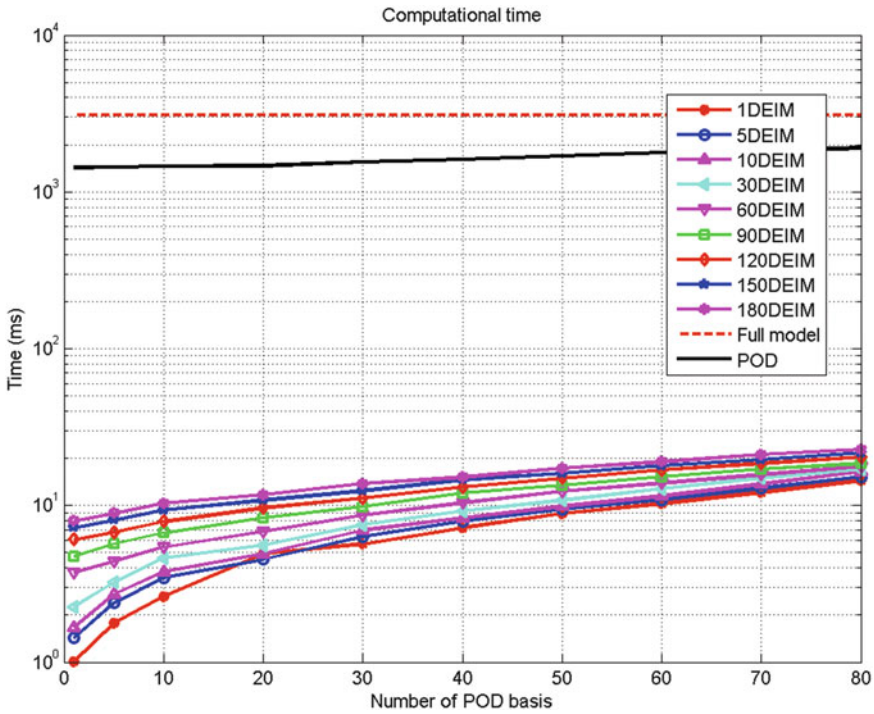

Fig. 2 Comparison of average computational time

Table 1 Average relative error and online computational time for different POD modes

POD			POD–DEIM			
K	Average relative error	Online time			Average relative error	Online time
1	1.33×10^{-1}	4.61×10^{-1}	1	40	2.36×10^{-1}	2.32×10^{-3}
5	3.27×10^{-2}	4.65×10^{-1}	5	40	6.11×10^{-2}	2.55×10^{-3}
10	5.01×10^{-3}	4.71×10^{-1}	10	40	2.47×10^{-2}	2.71×10^{-3}
20	1.16×10^{-3}	4.73×10^{-1}	20	40	1.39×10^{-3}	2.97×10^{-3}
40	3.18×10^{-4}	5.02×10^{-1}	40	40	8.65×10^{-4}	3.35×10^{-3}
60	1.11×10^{-4}	5.31×10^{-1}	60	40	5.95×10^{-4}	3.87×10^{-3}
80	4.59×10^{-5}	6.46×10^{-1}	80	40	4.78×10^{-4}	4.23×10^{-3}
100	8.74×10^{-6}	5.74×10^{-1}	100	40	4.28×10^{-4}	4.71×10^{-3}

Computational times are normalized by the time of the full model chemistry time step

Varying Prandtl Number: $Pr \in [0.5, 1.0]$

In the combustion process, the Prandtl number, Pr, plays an important role in the heat convection and diffusion. In this section, we test the ability of a POD–DEIM reduced-order model to estimate solutions of the full model for values of Pr in the range [0.5, 1.0]. The reduced-order model is constructed using 400 snapshots, which are taken from two simulations of the full system at $Pr = 0.5$ and $Pr = 1.0$. Two hundred snapshots, one at every flow time step, are taken for each value of Pr. To demonstrate the prediction capability of our reduced-order model, we select a value of $Pr = 0.8$ and simulate the full model, POD reduced-order models of varying dimension, and POD–DEIM reduced-order models of varying dimension K and fixed $L = 40$.

Table 1 summarizes the results obtained in terms of average relative error and relative computational simulation time, with respect to the full model, of one chemistry time step. It can be seen from the table that the POD models are, in general, more accurate but they are again about two orders of magnitude slower than the models constructed using POD–DEIM. In addition, the table shows that for a satisfactory level of accuracy, say, the average relative error of about 5.0×10^{-4}, the computation of the nonlinear source term using the POD–DEIM model is more than 200 times faster than the full model calculation.

Effect of the parameter Variability on Total Heat Release

The POD–DEIM reduced-order model is now used to analyse the impact on outputs of interest of variability in the parameters describing the initial Gaussian temperature profile given by Eq. (8). To this end, a POD–DEIM model is constructed using 4000 snapshots. The snapshots are computed from 16 simulations corresponding to the combination of four different values of the temperature amplitude T_0 with four different values of the width a of the Gaussian temperature profile (see Fig. 3a). For each of the simulations, 250 snapshots are taken corresponding to 250 flow time steps. The range of amplitude of temperature is chosen so that the chemical reactions occur slowly at the minimum value of the amplitude and quickly at its maximum value. A particular case of the initial condition is shown in Fig. 3b.

Monte Carlo simulations (MCSs) are then performed to analyse the impact of variability in temperature amplitude on the total heat release over the computational domain. In which, the width is kept constant at $a = 0.2$. The amplitude T_0 is modelled as a Gaussian random variable with a mean of 1550 K and standard deviation of 26 K. 500 samples are drawn randomly from this normal distribution. In this case, the samples are evaluated using the full model and a POD–DEIM reduced model of order $K = 60, L = 60$.

Figure 4 shows the comparison between the full and reduced model histograms for the average total heat release, for the case with varying T_0. Table 2 summarizes estimated statistics and computation times. The results show that the

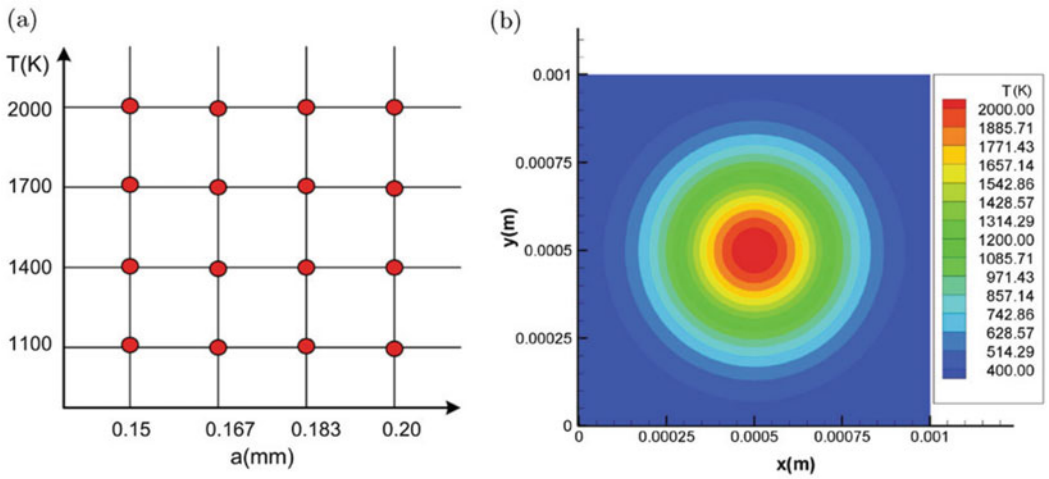

Fig. 3 Input parameters: (**a**) 16 sample points. (**b**) Gaussian distribution of temperature for a typical case ($T_0 = 2000$ K and $a = 0.2$ mm)

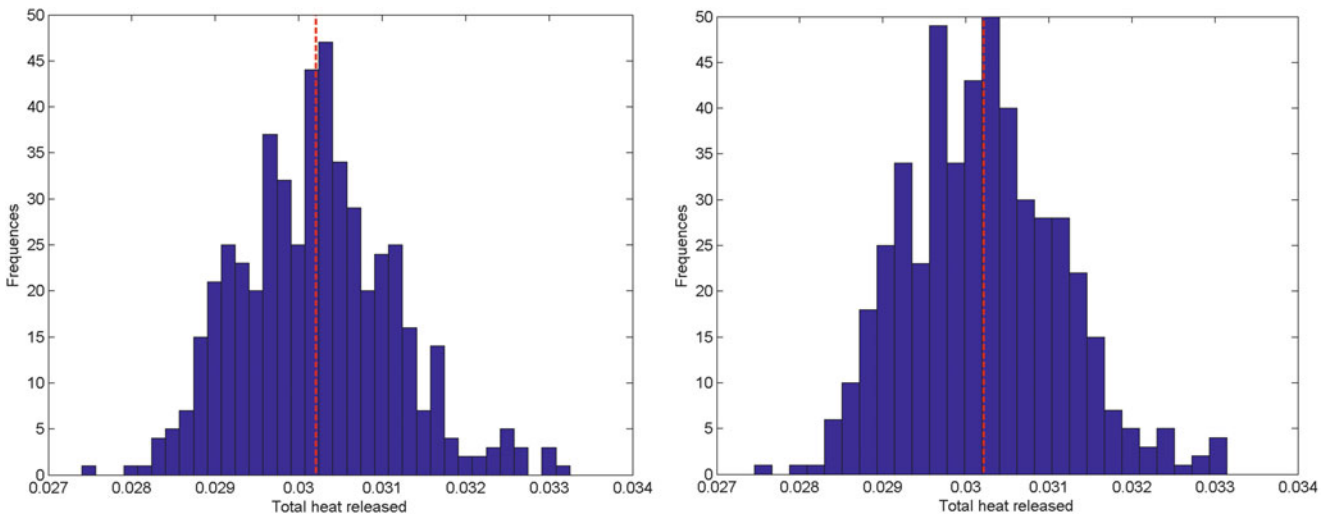

Fig. 4 Comparison of histograms of total heat released between the full model and reduced-order model. MCS results are shown for 500 randomly sampled values of the peak temperature of the initial condition. The *dashed line* shows the sample mean. (*Left*) full model. (*Right*) reduced model

Table 2 Comparison between the full model and reduced-order model

Name	Full model	Reduced model
Model size	91,809	60
Offline cost	–	16.65 h
Online cost	464.87 h	45.83 h
Mean of total heat release	3.02×10^{-2}	3.02×10^{-2}
Variance of total heat release	8.51×10^{-7}	8.85×10^{-7}
Mean of species HO_2	2.10×10^{-6}	2.10×10^{-6}
Variance of species HO_2	3.34×10^{-14}	3.53×10^{-14}

MCS results are shown for the average value of species HO_2 and total heat released for 500 randomly sampled values of the peak temperature of the initial conditions

reduced model is able to estimate the mean and the variance of the total heat release and of the average concentration of HO_2 with small errors. In fact, the mean estimates of the reduced-order model agree with those of the full model to within two decimal places.

Conclusions

This paper shows how projection-based reduced modelling using the POD method combined with the DEIM is an effective strategy for reducing the cost of chemical kinetics evaluations in reacting flow simulations. The methodology was demonstrated here using a premixed H_2/O_2/Ar mixture problem but is applicable to general reaction models. Here we focused on the application of the POD–DEIM approach to the chemical kinetics model only; however, the POD method can also be applied to obtain a reduced model of the fluid dynamics model to gain additional reduction in overall simulation time of the coupled system. The reduced-order models can be parameterized and then used for design space studies as well as quantification of the effects of parameter uncertainties on output quantities of interest.

References

1. Peters, N., Williams, F.A.: The asymptotic structure of stoichiometric methane-air flames. Combust Flame **68**(2), 185–207 (1987)
2. Brown, N.J., Li, G., Koszykowski, M.L.: Mechanism reduction via principal component analysis. Int. J. Chem. Kinet. **29**(6), 393–414 (1997)
3. Maas, U., Pope, S.B.: Implementation of simplified chemical kinetics based on intrinsic low-dimensional manifolds. Int. Symp. Combust. **24**(1), 103–112 (1992)
4. Maas, U., Pope, S.B.: Simplifying chemical kinetics: intrinsic low dimensional manifolds in composition space. Combust. Flame **88**, 239–264 (1192)
5. Maas, U., Pope, S.B.: Laminar flame calculations using simplified chemical kinetics based on intrinsic low-dimensional manifolds. Int. Symp. Combust. **25**(1), 1349–1356 (1194)
6. Lam, S.H.: Using CSP to understand complex chemical kinetics. Combust. Sci. Technol. **89**, 375–404 (1993)
7. Lam, S.H., Goussis, D.A.: The CSP method for simplifying kinetics. Int. J. Chem. Kinet. **26**(4), 461–486 (1994)
8. Gallivan, K., Grimme, E., Van Dooren, P.: Model reduction of large-scale systems: rational Krylov versus balancing techniques. In: Haydar, B., Christoph, Z. (eds.) Error Control and Adaptivity in Scientific Computing. Kluwer Academic pp. 177–190. Springer, Dordrecht (1999)
9. Feldmann, P., Freund, R.W.: Efficient linear circuit analysis by pade approximation Via the Lanczos process. IEEE Trans. Comput. Aided Des. Integr. Circuits Syst. **14**(5), 639–649 (1995)
10. Gugercin, S., Antoulas, A.: A survey of model reduction by balanced truncation and some new results. Int. J. Control **77**(8), 748–766 (2004)
11. Sorensen, D., Antoulas, A.: The sylvester equation and approximate balanced reduction. Linear Algebra Appl. **351–352**, 671–700 (2002)
12. Everson, R., Sirovich, L.: The Karhunen-Loeve procedure for Gappy data. J. Opt. Soc. Am. **12**(8), 1657–1664 (1995)
13. Holmes, P., Lumley, J.L., Berkooz, G.: Turbulence, Coherent Structures, Dynamical Systems and Symmetry. Cambridge University Press, London, UK (1998)
14. Astrid, P., Weiland, S., Willcox, K., Back, T.: Missing point estimation in models described by proper orthogonal decomposition. IEEE Trans. Autom. Control **10**, 2237–2251 (2008)
15. Barrault, M., Maday, Y., Nguyen, N.C., Patera, A.: An 'Empirical Interpolation' method: application to efficient reduced-basis discretization of partial differential equations. Comptes Rendus Mathematique **339**(9), 667–672 (2004)
16. Grepl, M.A., Maday, Y., Nguyen, N.C., Patera, A.: Efficient reduced-basis treatment of non-affine and nonlinear partial differential equations. ESAIM Math. Model. Numer. Anal. **41**(3), 575–605 (2007)
17. Chaturantabut, S., Sorensen, D.: Nonlinear model reduction via discrete empirical interpolation. SIAM J. Sci. Comput. **32**, 2737–2764 (2010)
18. Jiang, G.-S., Shu, C.-W.: Efficient implementation of weighted ENO schemes. J. Comput. Phys. **126**(1), 202–228 (1996)
19. Shu, C.-W., Osher, S.: Efficient implementation of essentially non-oscillatory shock-capturing schemes. J. Comput. Phys. **77**(2), 439–471 (1988)
20. Shu, C.-W., Osher, S.: Efficient implementation of essentially non-oscillatory shock-capturing schemes II. J. Comput. Phys. **83** (1), 32–78 (1989)
21. Shen, Y., Zha, G., Chen, X.: High order conservative differencing for viscous terms and the application to vortex induced vibration flows. J. Comput. Phys. **228**(22), 8283–8300 (2009)
22. Young, T.R., Boris, J.P.: A numerical technique for solving stiff ordinary differential equations associated with the chemical kinetics of reactive-flow problems. J. Phys. Chem. **81**(25), 2424–2427 (1977)
23. Poinsot, T., Veynante, D.: Theoretical and Numerical Combustion, 2nd edn. R.T. Edwards (2005)
24. Antoulas, A., Sorensen, D., Gugercin, S.: A Survey of Model Reduction Methods for Large-Scale Systems. American Mathematical Society, Providence, RI (2001)
25. Loeve, M.: Probability Theory I–II. Springer, New York (1977)
26. Wilson, G.J., MacCormack, R.W.: Modeling supersonic combustion using a fully implicit numerical method. AIAA J. **30**(4), 1008–1015 (1990)
27. Smith, G.P., Golden, D.M., Frenklach, M., Moriarty, N.W., Eiteneer, B., Goldenberg, M., Thomas Bowman, C., Hanson, R. K., Soon ho Song, Gardiner Jr., W.C., Lissianski, V.V., Qin, Z.: GRI-Mech 3.1. http://www.me.berkeley.edu/grimech

Numerical Simulation of the Flow with Chemical Reactions Around a Wedge

Georgy Shoev and Yevgeny A. Bondar

Introduction

The flow behind shock waves generated by various bodies at hypersonic velocities substantially differs from the perfect gas flow. Phenomena inherent in such flows are excitation of vibrational degrees of freedom of polyatomic molecules and dissociation. These effects of thermochemical nonequilibrium lead to significant changes in the flow structure.

There is a severe fundamental problem in numerical simulations of high-velocity flows with thermochemical nonequilibrium based on the Navier–Stokes equations: correct description of vibrational relaxation and dissociation of polyatomic molecules. It is well known that the popular classical Landau–Teller model [1] sometimes fails to predict correctly the process of vibrational relaxation, which is especially important under thermochemical nonequilibrium conditions. It is also well known that the classical one-temperature Arrhenius formula is inapplicable for the description of dissociation if the translational and vibrational temperatures differ from each other. On the other hand, the intuitive Park model [2], which takes into account thermal nonequilibrium and is widely used in commercial software packages, does not always provide a correct prediction of the molecule dissociation rate.

The goal of the present study is a comparative analysis of various models of vibrational relaxation and dissociation, including numerical simulations based on the Navier–Stokes equations.

G. Shoev (✉) • Y.A. Bondar
Khristianovich Institute of Theoretical and Applied Mechanics SB RAS, 4/1 Institutskaya Str., 630090 Novosibirsk, Russia

Novosibirsk State University, 2 Pirogova St., 630090 Novosibirsk, Russia
e-mail: shoev@itam.nsc.ru

Governing Equations and Numerical Methods

Let us consider a system of the Navier–Stokes equations for a binary mixture consisting of a diatomic and a monatomic component:

$$\frac{\partial \rho}{\partial t} + \nabla \cdot (\rho \vec{v}) = 0 \tag{1}$$

$$\frac{\partial \rho Y_0}{\partial t} + \nabla \cdot (\rho Y_0 \vec{v}) = -\nabla \cdot \vec{J}_0 + R_0 \tag{2}$$

$$\frac{\partial}{\partial t}(\rho \vec{v}) + \nabla \cdot (\rho \vec{v}\vec{v}) = -\nabla p + \nabla \cdot (\bar{\bar{\tau}}) \tag{3}$$

$$\begin{aligned} \frac{\partial}{\partial t}(\rho E) + \nabla \cdot (\vec{v}(\rho E + p)) \;=\; & \nabla \cdot \left(k \nabla T + (\bar{\bar{\tau}} \cdot \vec{v}) - \sum_i h_i \vec{J}_i \right) \\ & - \sum_i h_i R_i - e_{v,1} \cdot R_1 - \dot{e}_{v,1} \end{aligned} \tag{4}$$

$$\begin{aligned} & \frac{\partial}{\partial t}\left(\rho Y_1 e_{v,1}\right) + \nabla \cdot \left(Y_1 \rho \vec{v} e_{v,1} - Y_1 \mu_1 \nabla e_{v,1} \right) \\ & \quad = e_{v,1} \cdot R_1 + \dot{e}_{v,1} \,. \end{aligned} \tag{5}$$

The system is closed by the equation of state

$$p = \rho T R \sum_i \frac{Y_i}{M_{w,i}} \tag{6}$$

It is assumed that the translational and rotational modes are in equilibrium; therefore, only two temperatures are taken into account: translational temperature T and vibrational temperature T_v. The equation of conservation of translational energy (4) contains an additional source term $-\dot{e}_{v,1}$ corresponding to exchange between translational and vibrational energies. The equation of relaxation of vibrational

G. Ben-Dor et al. (eds.), *30th International Symposium on Shock Waves 1*, DOI 10.1007/978-3-319-46213-4_58

energy (5) also contains this source term, but it has the opposite sign. Actually, the energy exchange between the translational and vibrational modes occurs via these source terms.

The vibrational energy $e_{v,1}$ of the diatomic component in the gas mixture is written as a function of vibrational temperature in the harmonic oscillator approximation as

$$e_{v,1} = \frac{\theta_v R/M_{w,1}}{\exp(\theta_v/T_v) - 1}, \tag{7}$$

where θ_v is the characteristic vibrational temperature of the diatomic component of the mixture.

Vibrational relaxation is described in this paper with the use of two forms of the source term $\dot{e_{v,1}}$, which follow from the Landau–Teller model [1] and from the model [3] obtained from the kinetic Boltzmann equation by the Chapman–Enskog method (the latter can be considered as a more precise model). The corresponding expressions for these two models are presented as

$$\dot{e_{v,1}} = \rho Y_1 \frac{e_{v,1}(T) - e_{v,1}(T_v)}{\tau_1} \tag{8}$$

$$\begin{aligned} e_{v,1}{}^{\bullet} &= \frac{T}{T_v}(T - T_v)\rho Y_1 c_{\text{vibr},1} \sum_i \frac{n_i}{n\,\tau_{i,1}}, \\ \text{where } c_{\text{vibr},1} &= \frac{\partial e_{v,1}}{\partial T_v} = \frac{R}{M_{w,1}} \frac{\theta_v^2}{T_v^2} \frac{\exp\left(\theta_v/T_v\right)}{\left(\exp\left(\theta_v/T_v\right) - 1\right)^2} \end{aligned} \tag{9}$$

where n is the number density of the entire mixture and n_i is the number density of individual components of the gas mixture. The relaxation time τ_1 is calculated by the Millikan–White semiempirical formula [4]:

$$\tau_1 = \frac{1}{\sum_i x_i/\tau_{i,1}}, \tag{10}$$

where x_i is the molar fraction of the i-th species

The relaxation time $\tau_{i,1}$ used in Eq. (9) is calculated by the formula

$$\begin{aligned} &\tau_{i,1} = \frac{1}{p} \exp\left(AT^{-1/3} + B\right), \quad \text{where} \quad A = 1.16 \cdot 10^{-3} (m_R)^{1/2} \theta_v^{4/3} \\ &B = -\left(1.74 \cdot 10^{-5} (m_R)^{3/4} \theta_v^{4/3} + 18.42\right), \\ &m_R = \frac{M_{w,i} M_{w,1}}{M_{w,i} + M_{w,1}} \end{aligned} \tag{11}$$

In the general form, the system of chemical reactions proceeding in the multicomponent gas mixture can be written as

$$\sum_{i=1}^{N} \upsilon'_{i,\gamma} M_i \overset{k_{f,\gamma}}{\rightarrow} \sum_{i=1}^{N} \upsilon''_{i,\gamma} M_i \tag{12}$$

where $\upsilon'_{i,\gamma}$ and $\upsilon''_{i,\gamma}$ are the stoichiometric coefficients of the reactions, M_i are the symbols of the main reacting substances (reagents) and reaction products, and γ is the reaction number.

The molar rate of formation (disappearance) of the i-th component of the mixture in a unit volume within a unit time in the dissociation reaction γ can be written as

$$\hat{R}_{i,\gamma} = \left(\upsilon''_{i,\gamma} - \upsilon'_{i,\gamma}\right)\left(k_{f,\gamma} \prod_{i=1}^{N} [C_i]^{\eta'_{i,\gamma}}\right) \tag{13}$$

where $k_{f,\gamma}$ is the rate constant of chemical reactions and C_i is the molar fraction of the i-th component of the mixture. In this work, we use three forms of the chemical reaction rate constant: those proposed by Arrhenius, Park [2], and Kuznetsov [5]:

$$k_0(T) = AT^B e^{-\frac{E_d}{kT}} \tag{14}$$

$$k(T, T_v) = A\left(\sqrt{TT_v}\right)^B e^{-\frac{E_d}{k\sqrt{TT_v}}} \tag{15}$$

$$\begin{aligned} k(T, T_v) = &\frac{1 - \exp\left(-\theta_v/T_v\right)}{1 - \exp\left(-\theta_v/T\right)} \\ &\cdot \exp\left(0.7 \cdot E_d \left(\frac{1}{T} - \frac{1}{T_v}\right)\right) \cdot k_0(T) \end{aligned} \tag{16}$$

(E_d is the activation energy.)

For calculating R_i included into the source terms in Eqs. (2), (4), and (5), we use the expression

$$R_i = M_{w,i} \sum_{\gamma=1}^{N_R} \hat{R}_{i,\gamma} \tag{17}$$

In this work, system (1), (2), (3), (4), and (5) is solved numerically by the commercial Ansys Fluent solver. The equations of conservation of mass (1), (2), momentum (3), and translational–rotational energy (4) are solved by the main solver, and the equation of relaxation of vibrational energy (5) of polyatomic components of the gas mixture is added by using the option of the user-defined scalar transport equation. The vibrational energy relaxation equation is solved with respect to $e_{v,1}$, and then Eq. (7) is solved for determining the vibrational temperature. The source terms $-\dot{e_{v,1}}$ in Eq. (4) and $e_{v,1} \cdot R_1$ and $\dot{e_{v,1}}$ in Eq. (5) are calculated with the use of user-defined functions (UDF). All computations take into account the chemical reaction rate, which is also calculated with the use of UDF.

All computations are performed in a steady implicit formulation by a density-based solver specially developed for supersonic and hypersonic flows, by a second-order upwind scheme.

Results

We consider a steady supersonic ($M_\infty = 7.7$) flow around a wedge. The flow consists of a binary mixture of nitrogen (N_2–N) with mass fractions of the diatomic and monatomic components equal to $Y_{N2} = 0.8925$ and $Y_N = 0.1075$. This problem is considered in a two-dimensional formulation. The free stream is assumed to be thermally equilibrium at the temperature $T_\infty = T_{v\infty} = 1100$ K and pressure $p_\infty = 940.3$ Pa. The length of the inclined part of the wedge is $w = 5.1$ cm. Under the conditions used in this problem, the Reynolds and Knudsen numbers calculated on the basis of the free-stream parameters and wedge length w (Fig. 1a) are $\mathrm{Re_w} = 14485$ and $\mathrm{Kn_w} = 6.52 \times 10^{-4}$. The free-stream parameters correspond to the conditions used in the experiments [6] and calculations [7]. The above-described conditions are imposed on the left (inflow) boundary. All variables are extrapolated out of the computational domain on the right (outflow) boundary. This problem is solved in a symmetric formulation; therefore, the condition of symmetry is imposed on the lower boundary. The wedge is subjected to no-slip conditions, and the wall is assumed to be isothermal at the temperature $T_w = 300$ K.

Two types of computations are performed: with and without allowance for dissociation reactions. The following reactions are taken into account in computations with the dissociating nitrogen mixture: (1) $N_2 + N- > N + N + N$; (2) $N_2 + N_2- > N + N + N_2$. For each case, three computations are performed with different dependences of the coefficients $k_{f,\gamma}$ in the chemical reaction rate: Arrhenius (14), Park (15), and Kuznetsov (16) formulas. The factor A, the power-law exponent of temperature B, and the activation energy E_d are taken the same as in [7]: for the first reaction, $A = 4.154 \times 10^{22}$ $\mathrm{cm^3 mol^{-1} s^{-1}}$, $E_d = 1.561 \times 10^{-18}$ J, and $B = -1.5$; for the second reaction, $A = 4.797 \times 10^{17}$ $\mathrm{cm^3\ mol^{-1} s^{-1}}$, $E_d = 1.561 \times 10^{-18}$ J, and $B = -0.5$. The Landau–Teller model (8) is used in all cases for the description of vibrational relaxation, except for specially mentioned cases.

The results of numerical simulations with the use of different models of dissociation are illustrated in Fig. 1b–d, which show the translational temperature fields. The computations with the use of the Park and Kuznetsov formulas, which take into account the vibrational temperature in dissociation rate, predict a higher temperature than the computation with the classical one-temperature Arrhenius dependence.

The results calculated with allowance for dissociation are compared with the computations performed in [7] with the use of the CFD-FASTRAN software package. The dissociation rates are calculated by the one-temperature Arrhenius formula (14). In this case, the data obtained by different software packages are in good agreement (Fig. 2).

The shock wave standoff distance from the wedge as a function of the wedge angle is compared with the numerical data [7] in Fig. 3a. The numerical results are again in good agreement. The bow shock wave standoff distances calculated with the use of different dissociation models are

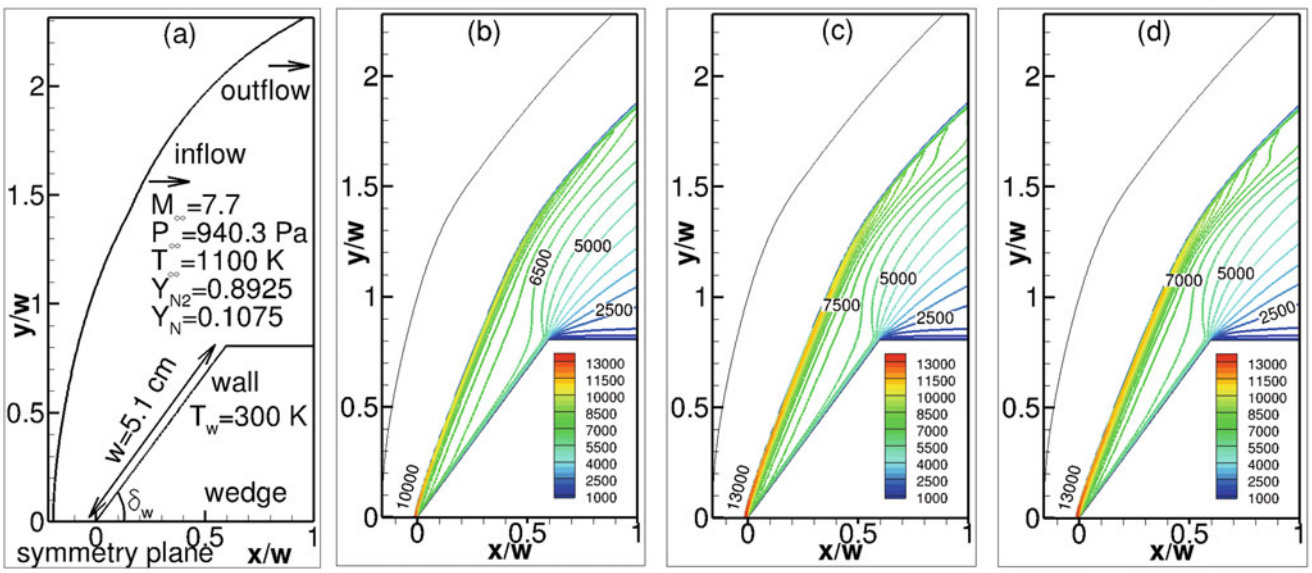

Fig. 1 Computational domain (**a**). Flowfields of translational temperature around the wedge ($\delta_w = 53.5°$) with allowance for dissociation according to the Arrhenius (**b**), Park (**c**), and Kuznetsov (**d**) dependences

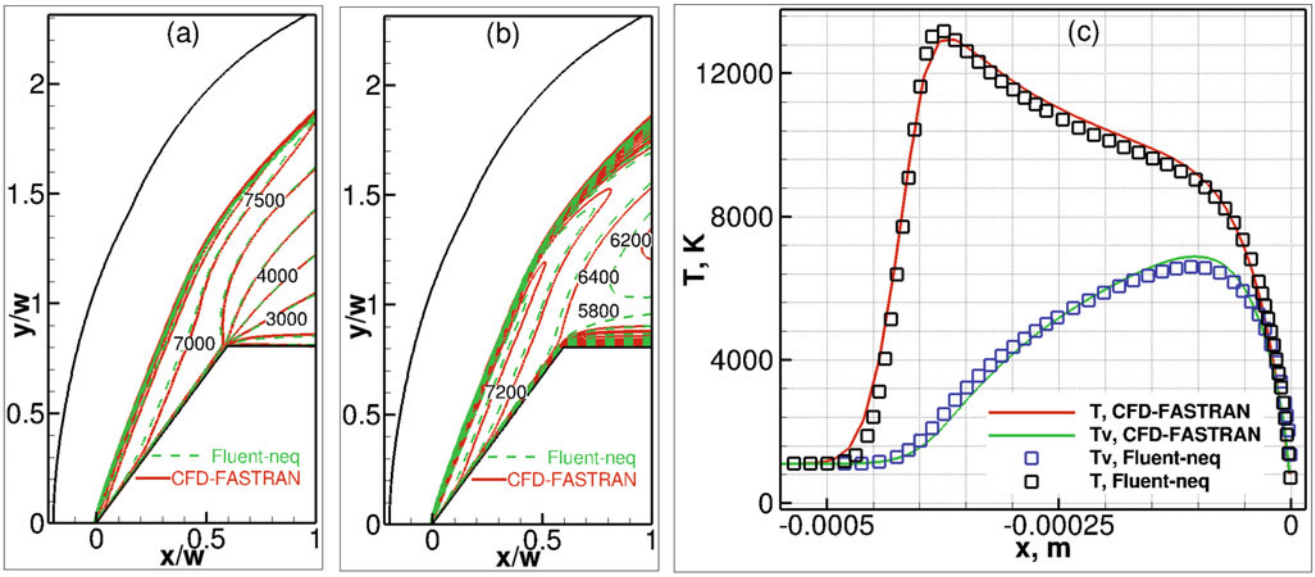

Fig. 2 Numerical simulations of the flow around the wedge ($\delta_w = 53.5°$) with allowance for dissociation: (**a**) translational temperature; (**b**) vibrational temperature; (**c**) distributions of temperatures on the plane of symmetry (*stagnation line*)

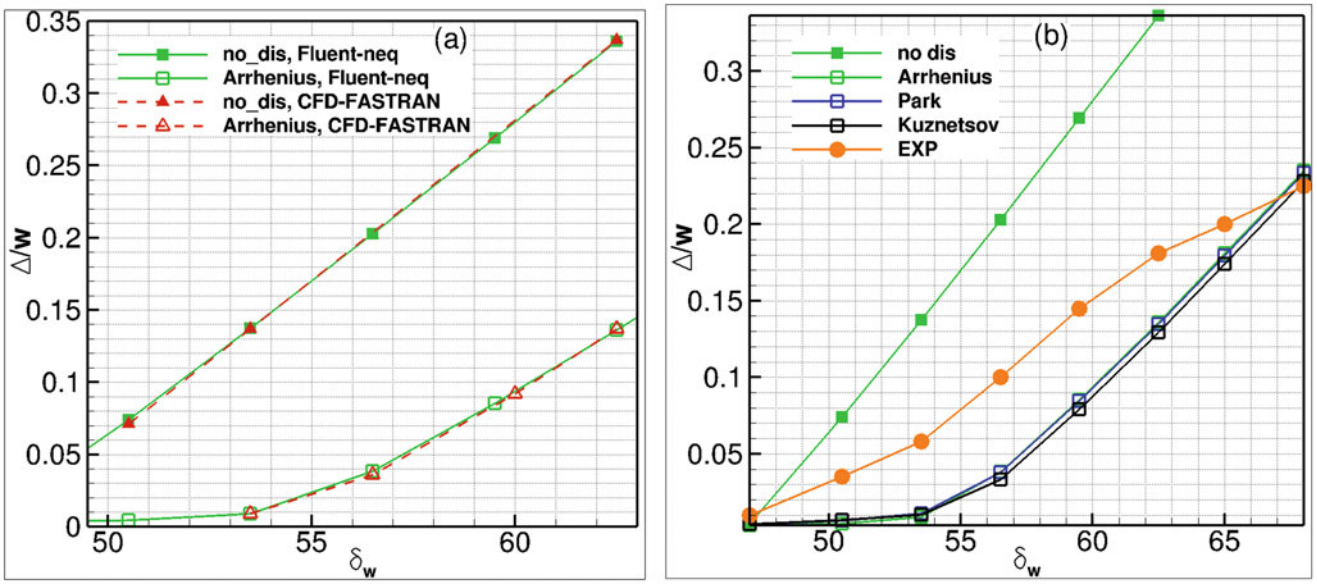

Fig. 3 Shock wave standoff distance from the wedge versus the wedge angle: (**a**) comparison with the numerical data [7]; (**b**) comparison with the experimental data [6]

compared with the experimental measurements [6] in Fig. 3b. The computations with the dissociation rate being ignored predict a much greater shock wave standoff distance than the experimental values. At the same time, the shock wave standoff distances predicted in computations with all three dependences of the dissociation rate are smaller than the experimentally measured value.

The numerical solution of the considered system of Eqs. (1), (2), (3), (4), (5), and (6) largely depends on the source term corresponding to energy exchange between the translational and vibrational modes. This influence is primarily manifested in the temperature distributions, which, in turn, affects the chemical reaction rates (14), (15), and (16), and a change in the chemical reaction rate leads to changes in the composition of the mixture and the bow shock wave standoff distance. As a result, significant reconstruction of the flow pattern can be expected owing to changes in the mechanism of vibrational-dissociation coupling. The influence of the vibrational relaxation model on the temperature distribution is analyzed in Fig. 4. If dissociation is ignored

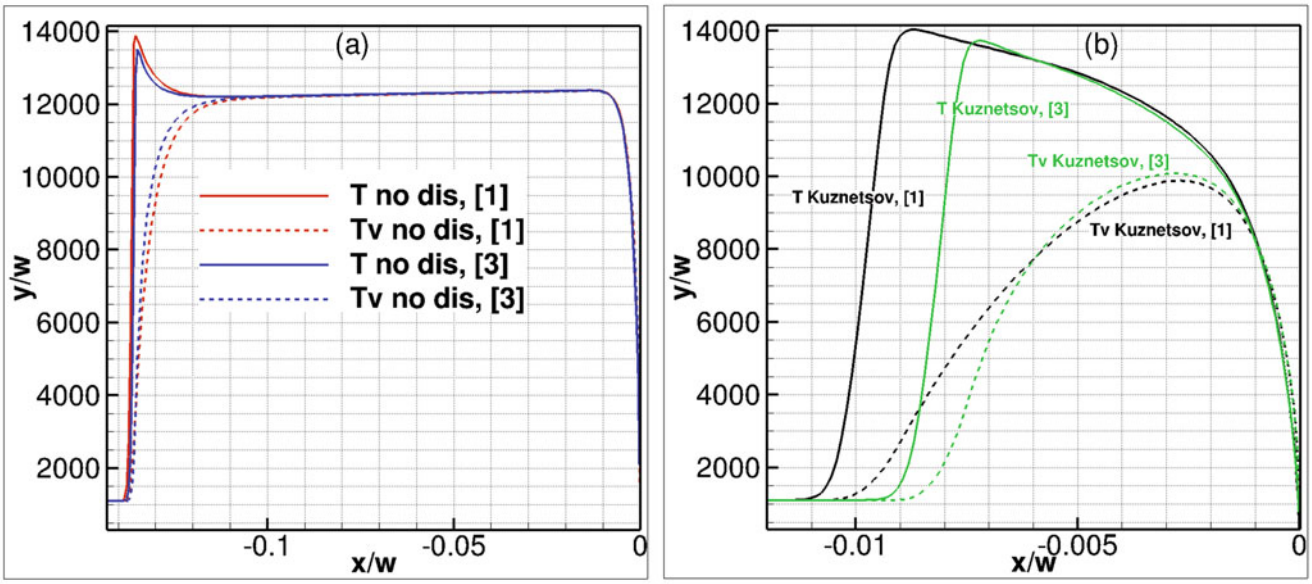

Fig. 4 Comparison of the temperature distributions with different models of vibrational relaxation on the plane of symmetry (*stagnation line*) ahead of the wedge ($\delta_w = 53.5°$)

(Fig. 4a), the model developed in [3] predicts a smaller zone of vibrational relaxation than the classical Landau–Teller model, the peak of the translational temperature becomes lower, and the vibrational temperature in the relaxation region increases. The shock wave standoff distance is almost the same. In the case when a dissociation is taken into account, for example, in accordance with the Kuznetsov dependence (Fig. 4b), a minor decrease in the bow shock wave standoff distance is observed.

Conclusions

A code based on user-defined functions is developed for taking into account thermochemical nonequilibrium effects in Ansys Fluent. The resultant numerical tool (Fluent-neq) is verified through comparisons with the numerical solution obtained by using the CFD-FASTRAN software package for a two-dimensional problem of a supersonic flow of a binary mixture of nitrogen (N_2-N) around a wedge with allowance for dissociation in accordance with the one-temperature Arrhenius model.

If the vibrational temperature in the molecule dissociation rate is taken into account, the translational and vibrational temperature distributions in the relaxation zone behind the shock wave become significantly different. Comparisons of the numerical data for the bow shock wave standoff distance in the nitrogen flow around the wedge (in the two-dimensional formulation) with experimental measurements reveal their qualitative agreement.

This work was supported by the Russian Government under grant “Measures to Attract Leading Scientists to Russian Educational Institutions” (contract No. 14. Z50.31.0019) and Russian Foundation for Basic Research (RFBR) grant No. 15-58-52044.

References

1. Landau, L.D., Teller, E.: In: Landau, L.D., Collected Papers, Nauka, Moscow, **1**, 181 (1969) (in Russian)
2. Park, C.: Nonequilibrium Hypersonic Aerothermodynamics. Wiley, New York (1990)
3. Kustova, E.V., Oblapenko, G.P.: Reaction and internal energy relaxation rates in viscous thermochemically non-equilibrium gas flows. Phys. Fluids **27**, 016102 (2015). doi:10.1063/1.4906317
4. Millikan, R.C., White, D.R.: J. Chem. Phys. **39**(12), 3209–3213 (1963)
5. Kuznetsov, N.M.: Kinetics of Molecular Reactions. Nauka, Moscow (1982) (in Russian)
6. Hornung, H.G., Smith, G.H.: The influence of relaxation on shock detachment. J. Fluid Mech. **93**(Pt. 2), 225–239 (1979)
7. Bondar, Y., Markelov, G., Gimelshein, S., Ivanov, M.: Numerical modeling of near-continuum flow over a wedge with real gas effects. J. Thermophys. Heat Transfer **20**(4), 699–709 (2006)

Computations of a Shock Layer Flow Field with Global and Detailed Chemistry Models

Marie-Claude Druguet, Arnaud Bultel, Julien Annaloro, and Pierre Omaly

Introduction

The present work is a first step in computing a reactive gas flow behind a shock wave with detailed collision-radiative models. If simulating high-temperature, high-enthalpy, non-equilibrium gas flows in shock layers has been widely done so far with global models for the chemical kinetics and the vibrational non-equilibrium, it is quite new to compute such flow fields with detailed chemistry models. This is now possible as the computation and memory resources of the computers allow to run CFD codes with detailed models. State-specific vibrational models are efficient to model both the chemical reactions and the vibrational non-equilibrium at once, without making strong assumptions (like Boltzmann distribution) as it is the case with multi-temperature models for vibrational non-equilibrium modeling.

The continuous, non-equilibrium, hypersonic gas flow past a space probe is modeled with axi-symmetric, compressible, time-dependent conservation equations that include the conservation equations of mass of each reacting chemical species, of momentum (Navier-Stokes equations), of total energy, and of non-equilibrium vibrational energies. The code used to solve those equations is the Parallel Implicit NonEquilibrium Navier-Stokes (PINENS) code, developed by Druguet [1]. This code is based on a finite volume formulation on structured grids, where the convective fluxes at the interfaces between cells are evaluated with the approximate Riemann solver of Roe. The time resolution is implicit and done by the data parallel line relaxation (DPLR) method [2].

The present study is done on the flow past an axi-symmetric blunt body for the following point of a Mars Sampler Return Orbiter (MSRO) trajectory : $\rho = 2.933 \quad 10^{-4}$ kg/m^3, $V = 5223$ m/s, T = 140 K. This corresponds to a test case (TC3) proposed by the ESA working group on radiation of high-temperature gases in atmospheric entry [3]. Under the conditions of an atmosphere composed of 100 % CO_2 and of the considered chemical kinetics models [4], the molecules CO_2 dissociate through the shock wave leading to a gas mixture composed of 5 species : CO_2, CO, O_2, C, O. The molecular species are supposed to be in a vibrational non-equilibrium state. The thermodynamical state of the gas mixture is then described by several temperatures, the equilibrium temperature T, and one vibrational temperature for each vibrating molecule.

Before modeling the non-equilibrium and reactive gas flowing in the shock layer surrounding a probe with detailed models, global models are tested and compared. First, two global chemical kinetics rate models (the usual Park model for Mars entries [4] and a more recently developed model from CORIA) are compared and their effect on the flow field in the front shock layer past an axi-symmetric probe is assessed. Thermal non-equilibrium is modeled with a multi-temperature vibrational relaxation model, where vibration–translation [4] and vibration–vibration exchanges [5] are taken into account and their respective influence on the flow field solution assessed. Finally, preliminary computations with a detailed chemical kinetics model [6] are done in a one-dimension configuration, using the Rankine-Hugoniot equations.

M.-C. Druguet (✉)
Aix-Marseille Univ., CNRS UMR 7343, Laboratoire IUSTI,
5 rue Enrico Fermi, 13013 Marseille, France
e-mail: Marie-Claude.Druguet@univ-amu.fr

A. Bultel
Laboratoire CORIA, Normandie Université - CNRS UMR 6614,
St Etienne du Rouvray, 76800, France

J. Annaloro • P. Omaly
CNES - DCT/TV/PR, BPI 1717, 18 Avenue Edouard Belin,
Toulouse Cedex 9, 31401 Toulouse, France

G. Ben-Dor et al. (eds.), *30th International Symposium on Shock Waves 1*, DOI 10.1007/978-3-319-46213-4_59

Comparison of Global Chemical Kinetics Rates for CO_2 Gas Mixture

Two chemical kinetics models for gas mixtures resulting from CO_2 dissociation through a shock wave are compared. The first model (Table 1)—referred to as kin302—is the Park model slightly corrected by Bultel for the backward rates, in order to restore the equilibrium constant in reaction rates 11 to 18. The second model (Table 2) is a new model proposed by Annaloro and Bultel at CORIA (referred to as kin303) [6].

A comparison of the flow variables (temperature, pressure, density) obtained successively with the 2 kinetics models is shown in Fig. 1. The observed differences on the shock stand-off distance may be explained by looking at the chemical source terms resulting from the various chemical rates, for example the source term for the CO_2 density (Fig. 2). The chemical source term corresponding to the dissociation of CO_2 is smaller (in absolute value) in CORIA model than in Park model. Because less dissociation of CO_2 occurs, less thermal energy is taken away from the high-temperature gas in the shock layer. This makes the shock stand further from the probe surface.

Multi-Temperature Model for Vibrational Relaxation

When modeling vibrational relaxation, the following vibrational energy conservation equation is added to the set of equations already gathering the Navier-Stokes, mass, and total energy conservation equations :

$$\frac{\partial E_{V_v}}{\partial t} + div\left(E_{V_v}\vec{V}\right) = \omega_{C_v}\frac{E_{V_v}}{\rho_v} + \omega_{V_v}^{VT} + \omega_{V_v}^{VV}, \quad v = vibrating\ \ species \tag{1}$$

The first term in the right-hand side of Eq. (1), $\omega_{C_v}E_{V_v}/\rho_v$, comes from a variable change in writing the vibrational energy conservation equation. The second and third terms are the vibrational source terms for the Vibration–Translation (VT) and the Vibration–Vibration (VV) exchanges.

The vibrational energy conservation equation source term corresponding to the VT exchanges is written as [4]:

$$\omega_{V_v}^{VT} = \frac{E_{V_v}(T) - E_{V_v}(T_{V_v})}{\tau_v^{VT}}, \tag{2}$$

where τ_v^{VT} is the characteristic time of relaxation for VT exchanges (see [4] or [3]).

Table 1 TC3 booklet Park chemical kinetics model corrected by Bultel (referred to as kin302 in the figures), for 5 species: CO_2, O_2, CO, C, O

Reaction no.	A_f	b_f	E_f (K)	A_b	b_b	E_b (K)	A_{eq}	b_{eq}	E_{eq}
01–03	6.900E+15	− 1.5	63275	1.140E+05	− 0.75	535	6.053E+10	− 0.75	62740
04–05	1.380E+16	− 1.5	63275	2.280E+05	− 0.75	535	6.053E+10	− 0.75	62740
06–08	2.000E+15	− 1.5	59500	2.000E+06	− 1	0	1.000E+09	− 0.5	59500
09–10	1.000E+16	− 1.5	59500	1.000E+07	− 1	0	1.000E+09	− 0.5	59500
11–13	2.300E+14	− 1	129000	5.134E+06	− 1	0	4.480E+07	0	129000
14–15	3.400E+14	− 1	129000	7.590E+06	− 1	0	4.480E+07	0	129000
16	2.100E+07	0	27800	3.469E+06	0.25	24560	6.054E+01	− 0.25	3240
17	2.330E+03	0.5	65710	3.148E+06	− 0.25	− 550	7.402E-04	0.75	66260
18	3.900E+07	− 0.18	69200	8.705E+08	− 0.68	− 300	4.480E-02	0.5	69500

Table 2 Annaloro and Bultel chemical kinetics model [6] (referred to as kin303 in the figures) for 5 species: CO_2, O_2, CO, C, O

Reaction no.	A_f	b_f	E_f (K)	A_b	b_b	E_b (K)	A_{eq}	b_{eq}	E_{eq}
01–03	5.400E+14	− 1.407	64010	8.922E+03	− 0.657	1270	6.053E+10	− 0.75	62740
04–05	1.080E+15	− 1.407	64010	1.784E+04	− 0.657	1270	6.053E+10	− 0.75	62740
06–08	3.460E+10	− 0.474	58700	3.460E+01	0.026	− 800	1.000E+09	− 0.5	59500
09–10	1.730E+11	− 0.474	58700	1.730E+02	0.026	− 800	1.000E+09	− 0.5	59500
11–13	2.300E+14	− 1	129000	5.134E+06	− 1	0	4.480E+07	0	129000
14–15	3.400E+14	− 1	129000	7.590E+06	− 1	0	4.480E+07	0	129000
16	2.185E+08	− 0.25	27315	3.610E+06	0	24075	6.054E+01	− 0.25	3240
17	2.300E+03	0.5	65710	3.107E+06	− 0.25	− 550	7.402E-04	0.75	66260
18	3.900E+07	− 0.18	69200	8.705E+08	− 0.68	− 300	4.480E-02	0.5	69500

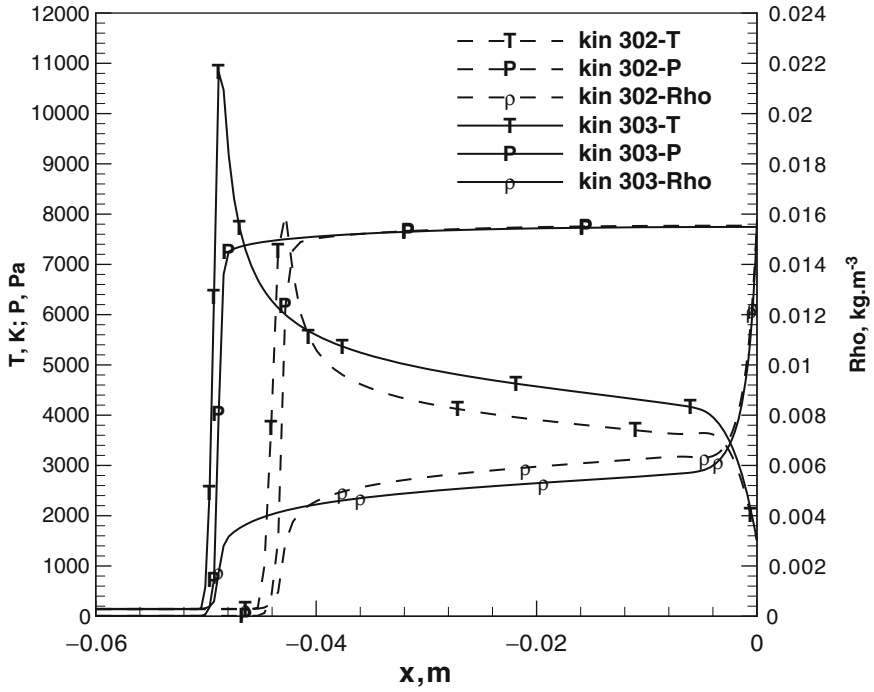

Fig. 1 Temperature, pressure, density profiles along the stagnation line. Comparison between the two chemical rates models

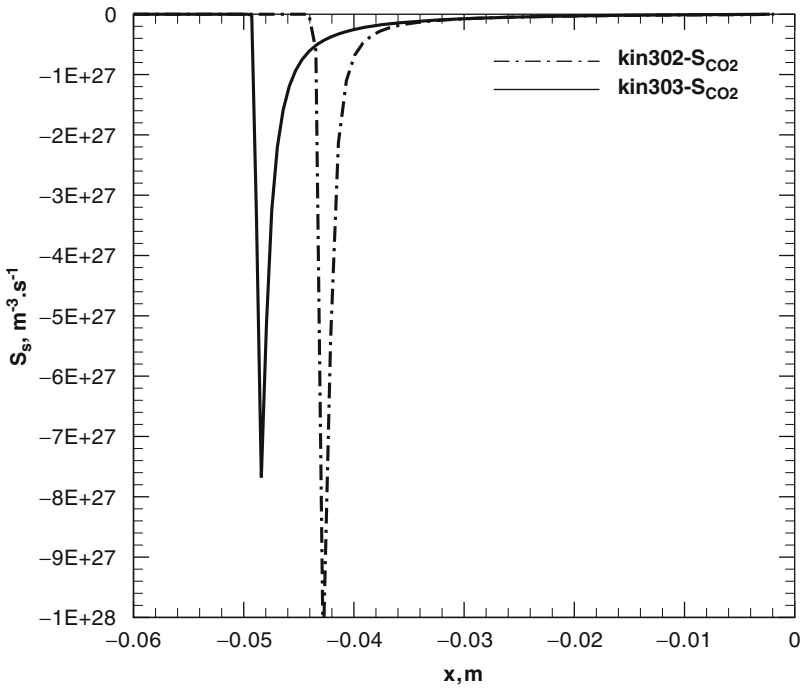

Fig. 2 Chemical source term for CO_2 densities along the stagnation line. Comparison between the two chemical rates models

According to Stupochenko et al. [5], the source term for the vibrational energy conservation equation due to the VV exchanges between two molecular species, v and w, may be expressed as:

$$\omega_{V_{vw}}^{VV} = \frac{1}{p\,\tau_{vw}^{VV}}\frac{T}{\theta_{V_w}}\left\{E_{V_w}(E_{V_v}+\rho_v R_v \theta_{V_v})\exp\frac{\theta_{V_w}-\theta_{V_v}}{T} - E_{V_v}(E_{V_w}+\rho_w R_w \theta_{V_w})\right\}, \tag{3}$$

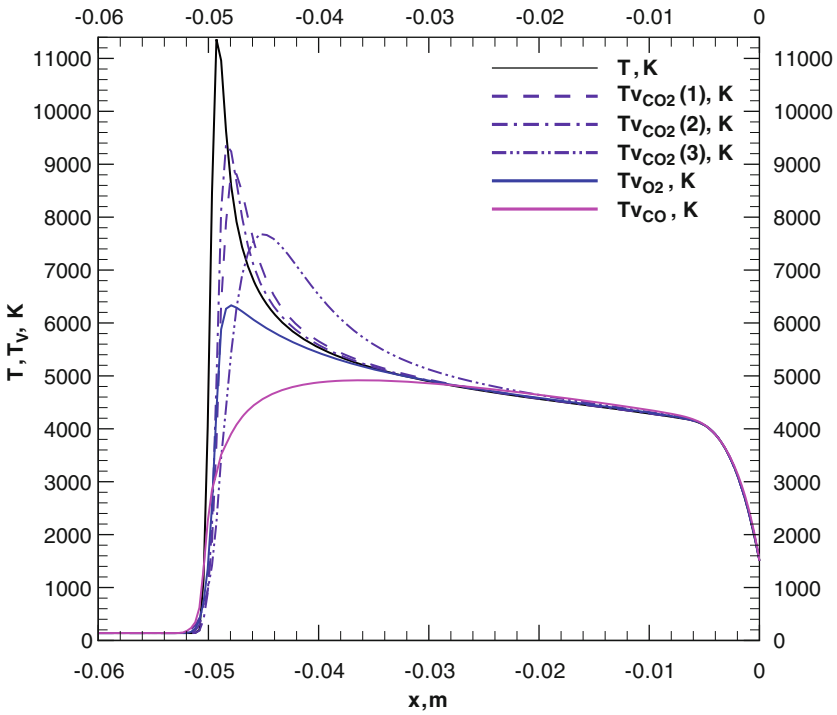

Fig. 3 Translational and vibrational temperatures along the stagnation line, obtained with a multi-temperature vibration relaxation model

where $p\,\tau_{vw}^{VV}$ is the characteristic time of vibrational relaxation through VV exchanges. The source term $\omega_{V_{vw}}^{VV}$ corresponds to the vibrational energy gained by the molecule v when exchanging vibrational energy with the molecule w during collisions taking place in a mixture composed of two chemical species only. When the vibration–vibration exchanges take place in a gas mixture composed of more than two species, a more general expression for the VV energy source term must be used: $\omega_{V_v}^{VV} = \sum_{w=1}^{n_v} X_w \omega_{V_{vw}}^{VV}$, where X_w is the mole fraction of molecule w in the gas mixture.

Using the Park expressions for τ^{VT}, the evolution of the vibrational and translational-rotational temperatures along the stagnation line is presented in Fig. 3. The vibrational temperature of the second mode of vibration of CO_2 is close to the translational temperature, meaning that the second mode is easily excited and reaches equilibrium fast. This is due to the fact that $p\tau_{CO_2(2),s}^{VT}$ is lower than other $p\,\tau_{v,s}^{VT}$. On the other hand, the third mode of vibration of CO_2 is excited with some delay. Indeed, its characteristic relaxation time of vibration is the largest one among the three modes of vibration of CO_2. It is a mode that is known to be not easily excited. The relaxation time of O_2 is globally larger than that of $CO_2(3)$, which makes the vibrational relaxation of O_2 slower. As for the vibrational temperature of CO, it is the further one from the translation temperature behind the shock, which means that the molecule CO is in a strong vibrational non-equilibrium state. This is due to the characteristic relaxation time of this molecule that is larger than the other characteristic relaxation times [5].

Chemical and Vibrational Non-equilibrium Modeling with Detailed Models

The reactions between chemical species on their vibrational excited states and the spatial evolution of these pseudo-species (chemical species on various vibrational states) behind a normal shock wave resolved with a one-dimension Rankine-Hugoniot solver were simulated by CORIA, by means of one of the detailed collisional-radiative models recently developed, CoRaM-N_2 [6]. This numerical experiment is done for the typical Fire II flight experiment (near the peak heating undergone by the thermal protection) which corresponds to the following upstream conditions : $M_0 = 32$, $p_0 = 54$ Pa, and $T_{A_0} = 274$ K. Results obtained at CORIA with one-dimension Rankine-Hugoniot simulations are the space evolution of N_2 and N concentrations behind the shock wave, for the 69 vibrational states of N_2 and the fundamental electronic state of N (see Figs. 5 and 6). This model will be implemented in the CFD code PINENS developed at IUSTI, in which the shock resolution is done with a shock capturing method. The expected results to be presented at the symposium are the evolution of the chemical species on their vibrational excited states in a two-dimension shock layer flow resolved by the PINENS code. Comparisons between results obtained with detailed models and results obtained with global models will also be

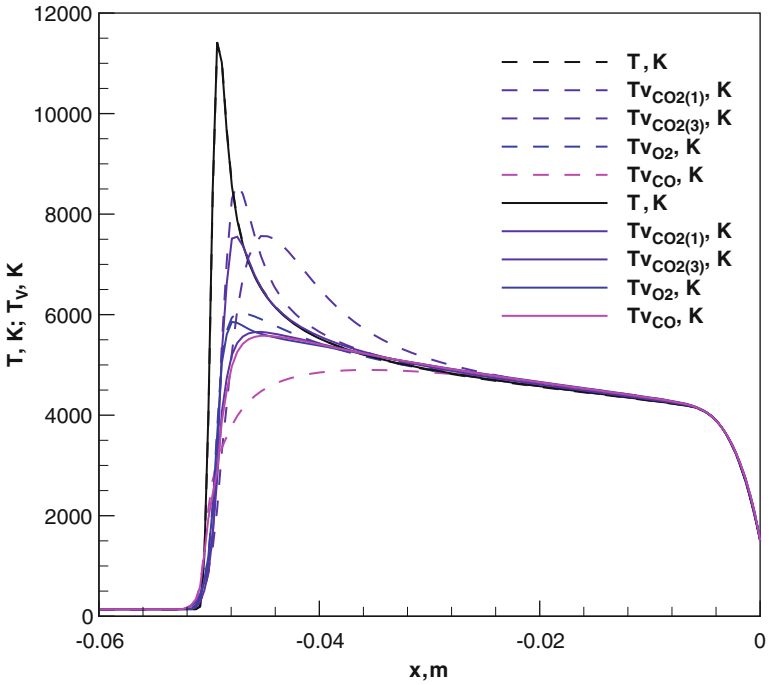

Fig. 4 Translational and vibrational temperatures along the stagnation line, obtained with a multi-temperature vibration relaxation model. Effect of the VV exchanges on the vibration relaxation in the shock layer

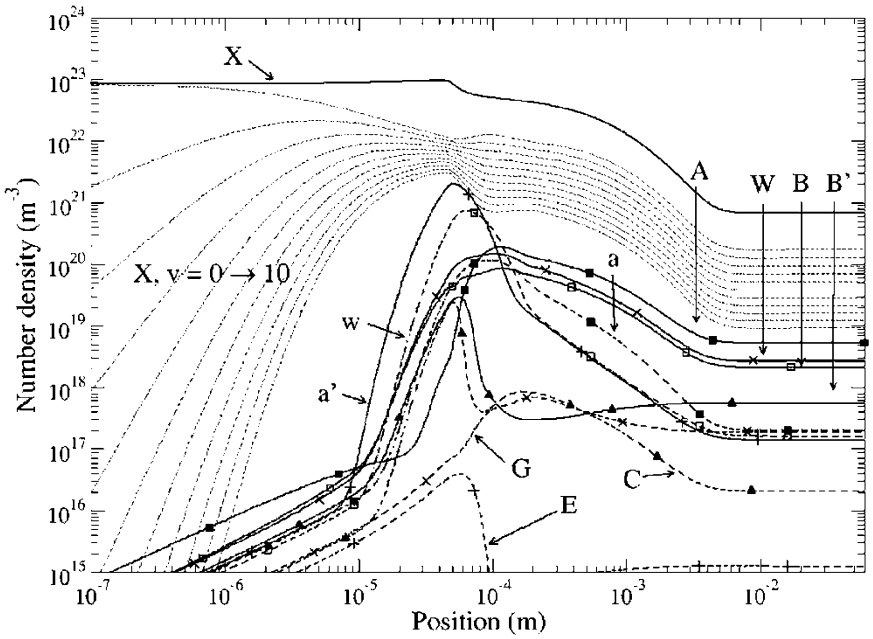

Fig. 5 Post-shock spatial evolution of the first 11 vibrational states of $N_2(X)$, the electronic ground state, and the excited states of N_2

presented, to show how the global models perform compared to the detailed models in the prediction of the chemical species and vibrational states evolution past a shock wave.

Summary and Concluding Remarks

The non-equilibrium and reactive flow field in the shock layer past an axi-symmetric blunt body entering a Mars-type atmosphere was modeled and simulated with the CFD code PINENS. Two global chemical kinetics rate models were compared. The results showed that the shock standoff distance predicted by the two models differ greatly, meaning that the chemical reactions influence the flow field a lot. A multi-temperature model for CO_2, O_2, CO vibrationally relaxing in a gas mixture composed of the same molecules plus atoms C and O was implemented in PINENS code. The results showed that the vibration of the molecules in the shock layer relaxes towards a non-equilibrium state. Results obtained with the Park characteristic times for vibrational

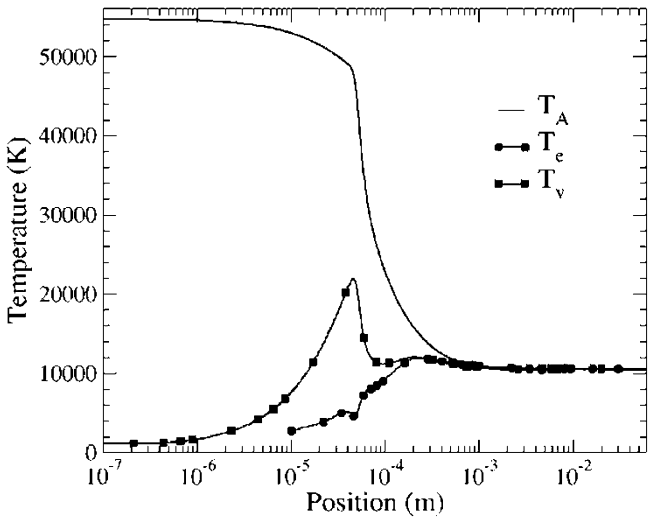

Fig. 6 Post-shock spatial evolution of the heavy-particle temperature T_A, the electron temperature T_e, and the vibrational temperature T_V of the electronic ground state of N_2

relaxation showed that the symmetric stretching mode and particularly the bending mode of CO_2 are close to equilibrium with the translational mode, even when the VV exchanges are not taken into account. The anti-symmetric mode relaxes much slower than the other two modes. This study also showed that VV exchanges are important in the shock layer flow, for that particular atmosphere entry condition. When the VV exchanges are taken into account, the vibrational temperatures converge towards the same value much faster, making the equilibrium of vibration with translation much faster.

In parallel to the computations done with PINENS code and global models, calculations with a one-dimensional Rankine-Hugoniot code and detailed collisional-radiative models were conducted behind a normal shock wave. The results showed that the Boltzmann distribution is not observed in the flow area behind the shock wave.

Perspectives to this work are to implement vibrationally specific models into the CFD code PINENS, in order to predict more precisely the non-equilibrium behavior of the gas mixture behind a shock wave. The comparison of state-specific vibrational results with multi-temperature results will show how the global models perform compared to the detailed models.

Acknowledgements This work was granted access to the High-Performance Computing resources of the "Institut du Développement et des Ressources Informatiques et Scientifiques" (IDRIS) under the allocation i20142b9076 made by GENCI (Grand Equipement National du Calcul Scientifique).

References

1. Druguet, M.-C., Candler, G.V., Nompelis, I.: Effects of numerics on Navier-Stokes computations of hypersonic double-cone flows. AIAA J. **43** (3), 616–623 (2005)
2. Wright, M.J., Bose, D., Candler, G.V.: Data-parallel line relaxation method for the Navier-Stokes equations. AIAA J. **36** (9), 1603–1609 (1998)
3. Omaly, P.: Proceedings of the International Workshop on Radiation of High-Temperature Gases in Atmospheric Entry, ESA SP-583 (2004), ESA SP-629 (2006), ESA SP-667 (2008), ESA SP-689 (2010)
4. Park, C., Howe, J., Jaffe, R., Candler, G.V.: Review of chemical-kinetics problems of future NASA missions, 2: Mars entries. J. Thermophys. Heat Transfer **8** (1), 9–23 (1994)
5. Stupochenko, Y.V., Losev, S.A., Osipov, A.I.: Relaxation in Shock Waves. Springer, New York (1967)
6. Annaloro, J., Bultel, A., Omaly, P.: Collisional-radiative modeling behind shock waves in nitrogen. J. Thermophys. Heat Transfer (2014). DOI: 10.2514/1.T4263

On a Relaxation Zone Structure for Shock Waves Forming in Non-equilibrium Air Flows

O. Kunova and E. Nagnibeda

Introduction

Modeling of non-equilibrium physical-chemical kinetics in high-temperature air flows is important in the Earth-entry problems, for evaluation of the flow parameters in high enthalpy facilities, investigations of combustion and detonation processes and other applications. This problem is considered by many authors with the use of detailed state-to-state description for relaxation processes or simplified multi-temperature kinetic models (see Refs. in [1, 2]). In the present paper we study reacting flows of the mixture $N_2(i)$/$O_2(i)$/NO/N/O behind shock waves taking into account non-equilibrium molecular distributions over vibrational states i. According to experimental data [3, 4], equilibration of translational and rotational energies in high temperature shock heated air flows proceeds much faster than vibrational and chemical relaxation. Therefore in this study the equilibrium distributions over translational and rotational energies are supposed to establish within a thin shock front and then exist along the relaxation zone whereas vibrational and chemical kinetics is considered out of equilibrium.

Following the state-to-state model proposed in [2] the equations for vibrational level populations of molecules and densities of atoms are coupled to the equations of momentum and total energy conservation and solved numerically. Test cases for free stream Mach numbers $M = 10$, flight altitudes $H = 48$ km with different vibrational distributions of molecules before a shock front are studied.

Along with the traditional case of the thermally equilibrium undisturbed flow before a shock, we examine the conditions of initially excited free stream molecules. Such a situation appears in a shock tube test section after freezing of a flow in a nozzle [5], in the flows near bodies of a complicated form or in result of another kinds of vibrational energy pumping before a shock wave. Peculiarities of vibrational relaxation behind shock waves originated in a one-component pre-excited gas are discussed in [6, 7] whereas for the reacting air mixture this effect is studied numerically in [2]. In the present paper we continue the study started in [2] and focus the attention on peculiar features of the relaxation zone structure behind shock waves occurring in non-equilibrium air flows.

Basic Equations

We consider the scheme of non-equilibrium processes in the air mixture including TV (VT) vibrational energy transitions, VV and VV' vibrational energy exchanges between molecules of the same or different species, dissociation and recombination

$$N_2(i) + M = N + N + M, \tag{1}$$

$$O_2(i) + M = O + O + M, \tag{2}$$

$$NO + M = N + O + M, \tag{3}$$

$$(M = N_2,\ O_2,\ NO,\ N,\ O),$$

as well as Zeldovich exchange reactions of NO formation

$$N_2(i) + O = NO + N, \tag{4}$$

O. Kunova (✉) • E. Nagnibeda
Saint Petersburg State University, 28, Universitetski pr., Saint Petersburg 198504, Russia
e-mail: kunova.olga@gmail.com; e_nagnibeda@mail.ru

G. Ben-Dor et al. (eds.), *30th International Symposium on Shock Waves 1*, DOI 10.1007/978-3-319-46213-4_60

$$O_2(i) + N = NO + O. \quad (5)$$

In the frame of the detailed state-to-state kinetic model [1, 2], the 1-D steady-state air flow behind a plane shock wave is described by the equations for vibrational level populations $n_{N_2 i}(x)$, $n_{O_2 i}(x)$, number densities of atoms $n_N(x)$, $n_O(x)$ and NO molecules $n_{NO}(x)$, the gas temperature $T(x)$ and velocity v(x) (x is the distance from the shock):

$$\frac{d(vn_{ci})}{dx} = R_{ci}^{vibr} + R_{ci}^{2\leftrightarrow 2} + R_{ci}^{2\leftrightarrow 3}, \quad i = 0, 1, \ldots l_c, \quad c = N_2, O_2, \quad (6)$$

$$\frac{d(vn_c)}{dx} = R_c^{2\leftrightarrow 2} + R_c^{2\leftrightarrow 3}, \quad c = NO, N, O, \quad (7)$$

$$\rho_0 v_0^2 + p_0 = \rho v^2 + p, \quad (8)$$

$$h_0 + \frac{v_0^2}{2} = h + \frac{v^2}{2}. \quad (9)$$

Here $p = nk_BT$ is the pressure, k_B is the Boltzmann constant, ρ is the mass density, subscript "0" indicates the values of parameters in a free stream, h is the mixture enthalpy per unit mass:

$$h = \sum_c h_c \frac{\rho_c}{\rho}, \quad \rho_c = m_c n_c,$$

$$h_c = \frac{5}{2}\overline{R}_c T + \frac{\varepsilon_c}{m_c} \quad \text{for} \quad c = N, O, \quad (10)$$

$$h_c = \frac{7}{2}\overline{R}_c T + \frac{1}{\rho_c}\sum \varepsilon_i^c n_{ci} + \frac{\varepsilon_c}{m_c} \quad \text{for} \quad c = N_2, O_2, NO,$$

where $\overline{R}_c$ is the specific gas constant of species c, m_c is a particle mass, ε_i^c is the vibrational energy of a molecule c species at the i-th vibrational level, ε_c is the formation energy of a particle c species.

The source terms in Eqs. (6) and (7) describe vibrational energy transitions and chemical reactions and contain state-specific rate coefficients of these processes. In the present paper rate coefficients involved in R_{ci}^{vibr}, $R_{ci}^{2\leftrightarrow 3}$, $R_{ci}^{2\leftrightarrow 2}$ are computed with the use of the generalized Schwartz, Slawsky, Herzfeld formulas [3, 8] for vibrational energy transitions, the modified Treanor-Marrone dissociation model [1, 9] and expressions proposed in [10] for exchange reactions. Rate coefficients of forward and backward processes are connected by the detailed balance principle [7]. Vibrational energies of N_2 and O_2 molecules ε_i^c are simulated by the anharmonic oscillator model with the numbers of excited vibrational states $l_{N_2} = 46$ and $l_{O_2} = 35$. In this paper, following the Zeldovich scheme of reactions we do not consider vibrationally excited NO molecules keeping in mind a small part of NO molecules in the air mixture.

The equations (6)–(9) are solved numerically for the following conditions in a free stream: $T_0 = 271$ K, $p_0 = 100$ Pa, $M_0 = 10$, $n_{N_2} = 0.79n$, $n_{O_2} = 0.21n$ ($n = p_0/k_BT_0$), $n_{NO} = n_N = n_O = 0$. The values of the gas temperature and velocity just in the beginning of the relaxation zone (for $x = 0$) are connected with the free stream parameters by the gas dynamic consistency equations at the shock front. In the considered state-to-state approach vibrational energy transitions and chemical reactions are supposed to be frozen within a shock front.

Level populations in the undisturbed flow are described by the Boltzmann distributions:

$$n_{ci}^B = \frac{n_c}{Z_c^{vibr}(T_v^c)} \exp\left(-\frac{\varepsilon_i^c}{k_B T_v^c}\right), \quad (11)$$

where $Z_c^{vibr}(T_v^c)$ is the vibrational partition function, T_v^c is the vibrational temperature. We consider three cases: (1) thermal equilibrium free stream $T_v^c = T_0$; (2) weakly non-equilibrium free stream $T_v^{N_2} = 2400$ K, $T_v^{O_2} = 1150$ K (this case is closed to air parameters in a nozzle exit obtained in [11]); (3)–(4) strongly non-equilibrium free stream $T_v^{N_2} = 8000$ K, $T_v^{O_2} = 4000$ K and $T_v^{N_2} = 4000$ K, $T_v^{O_2} = 8000$ K.

Results and Discussion

Now we report the comparison of gas flow parameters and vibrational distributions obtained solving Eqs. (6)–(9) for four cases of initial conditions listed above.

The evolution of the gas temperature and N_2 molar fractions along the relaxation zone for considered cases is shown in Fig. 1a,b for $M_0 = 10$. In the first and second cases the gas temperature decreases with x monotonically in result of the translational energy loss through vibrational activation and chemical reactions. During this process, T values in the relaxation zone occur higher in the second case than in the first case because free stream molecules are already vibrationally excited at $x = 0$ and their vibrational energy makes a contribution to the total mixture energy.

The gas temperature behavior in the third and fourth cases differs dramatically from previous cases because the vibrational temperature of N_2 (third case) and O_2 molecules (fourth case) occurs higher than the gas temperature T_1 immediately behind a shock (at $x = 0$). In the third case

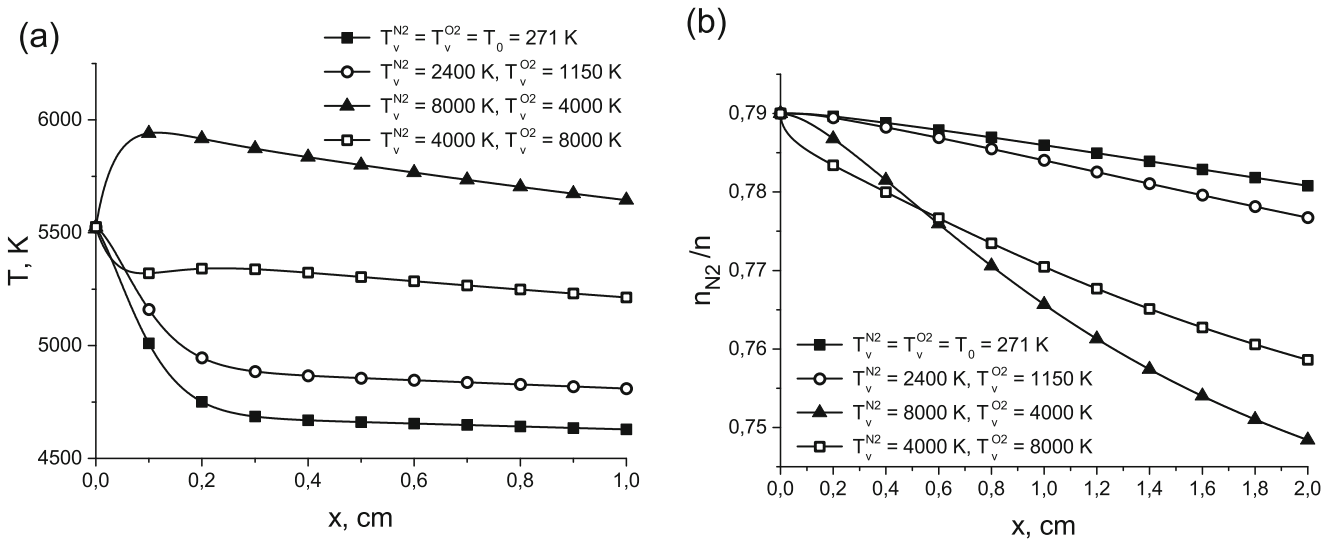

Fig. 1 The temperature T and molar fractions n_{N_2}/n as functions of x

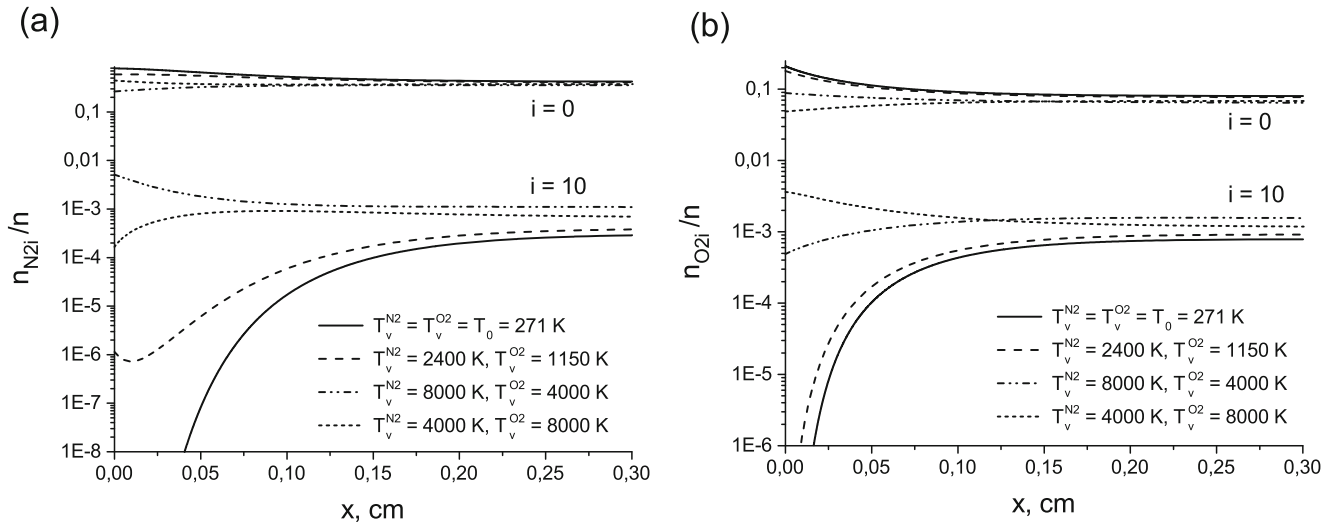

Fig. 2 The level populations of molecules N_2 (**a**) and O_2 (**b**) as functions of x

the gas temperature changes non-monotonically: it increases close to the shock front in result of the nitrogen vibrational energy transfer to the translation energy and then T decreases due to chemical reactions. In the fourth case highly pre-excited O_2 molecules occur very active in chemical reactions which start just from the beginning of the relaxation zone and call the gas temperature diminishing. Then the temperature changes slightly in result of competition of vibrational energy transitions and reactions. The influence of initial vibrational excitation of N_2 molecules on the gas temperature variation occurs more noticeable than for O_2 molecules because nitrogen molecules constitute the major portion in the mixture composition.

The molar fraction of N_2 molecules decreases more noticeably in the third and fourth cases (Fig. 1b) in result of more active N_2 dissociation and exchange reaction called by the high initial vibrational energy of N_2 molecules.

Figure 2a,b depicts level populations of N_2 and O_2 molecules for $i = 0$ and $i = 10$ in dependence of x for four cases. The peculiar regime of deactivation of highly excited ith level molecules and activation of the zeroth level molecules is found in the third case for N_2 and in the fourth case for O_2 molecules whereas in all other cases populations rise with x due to activation of molecules close to the shock front. It can be noticed that initial vibrational excitation leads to more populated all levels for $i > 0$.

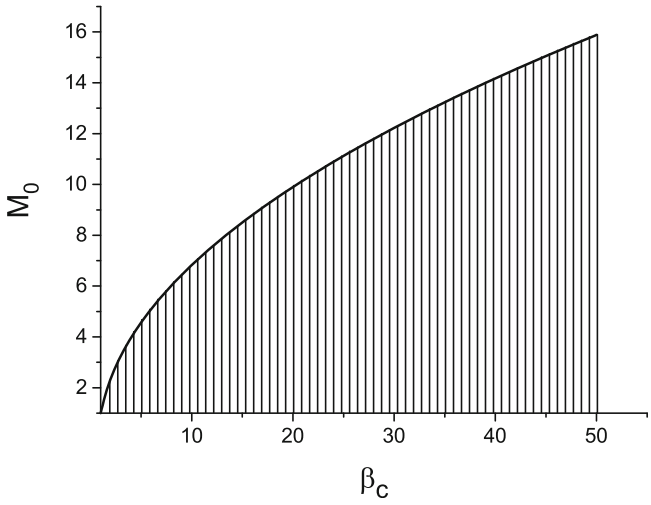

Fig. 3 The values of the Mach number as a function of the parameter β_c (for $\beta_c > T_1/T_0$)

The effects found in the third and fourth cases become weaker for lower T_v^c values and higher M_0 numbers. Calculations show that a peculiar regime of vibrational-chemical relaxation of molecules behind a shock front occurs if $\beta_c > T_1/T_0$ (where $\beta_c = T_v^c/T_0$, $c = N_2, O_2$). By contrast, for $\beta_c < T_1/T_0$ the traditional regime of vibrational excitation behind a shock due to translation energy transfer to the vibrational energy is observed. Using the expression $T_1/T_0 = f(M_0, \gamma)$ following from the Rankine-Hugoniot equation (γ is the ratio of equilibrium heat capacities for translation-rotation degrees of freedom) it is easy to show that $\beta_c > T_1/T_0$ if M_0 satisfies the condition:

$$M_0^4 - \frac{2(\gamma-1)^2 + (\beta_c - 1)(\gamma+1)^2}{2\gamma(\gamma-1)} M_0^2 - \frac{1}{\gamma} < 0, \qquad (12)$$

The condition (12) is illustrated in Fig. 3: if M_0 occurs lower than that given by the curve in Fig. 3 for the fixed β_c value, the condition $\beta_c > T_1/T_0$ holds and a peculiar regime of relaxation processes behind a shock arises. For example, this condition asserts for $\beta_c = 20$ if $M_0 < 9.9$, for $\beta_c = 30$ if $M_0 < 12.2$.

Concluding Remarks

A dramatic influence of non-equilibrium vibrational excitation of N_2 and O_2 molecules before shock waves occurring in high velocity air flows on gas dynamic parameters and vibrational distributions behind a shock is found. This effect is particularly pronounced for moderate free stream Mach numbers and a strong vibrational energy pumping before a shock front. The condition connecting Mach numbers in the undisturbed flow with parameters characterizing vibrational excitation of free stream molecules and providing a peculiar regime of relaxation processes behind a shock front is given.

Acknowledgements This study is supported by Saint-Petersburg State University, project 6.50.2522.2013, and Russian Foundation for Basic Research, grant 15-01-02373.

References

1. Nagnibeda, E., Kustova, E.: Nonequilibrium Reacting Gas Flows. Kinetic Theory of Transport and Relaxation Processes. Springer, Berlin (2009)
2. Kunova, O., Nagnibeda, E.: State-to-state description of reacting air flows behind shock waves. Chem. Phys. **441**, 66–76 (2014)
3. Chernyi, G., Losev, S., Macheret, S., Potapkin, B.: Physical and Chemical Processes in Gas Dynamics, vols. 12. American Institute of Aeronautics and Astronautics, USA (2004)
4. Ibraguimova, L., Shatalov, O.: In: Brun, R. (ed.) High Temperature Phenomena in Shock Waves, pp. 99–147. Springer, Berlin (2012)
5. Park, C.: J. Thermophys. Heat Transfer **20** (4), 689–698 (2006)
6. Osipov, A.I., Uvarov, A.V.: Physics-Uspekhi **35** (11), 903–923 (1992) (in Russian)
7. Capitelli, M., Ferreira, C., Gordiets, B., Osipov, A.: Plasma Kinetics in Atmospheric Gases. Springer Series on Atomic, Optical and Plasma Physics, vol. 31. Springer, Berlin (2000)
8. Schwartz, R., Slawsky, Z., Herzfeld, K.: Calculation of vibrational relaxation times in gases. J. Chem. Phys. **20**, 1591–1599 (1952)
9. Marrone, P., Treanor, C.: Chemical relaxation with preferential dissociation from excited vibrational levels. Phys. Fluids **6**, 1215–1221 (1963)
10. Warnatz, J., Riedel, U., Schmidt, R.: Advanced in Hypersonic Flows, Modeling Hypersonic Flows, vol. 2. Birkhäuser, Boston (1992)
11. Colonna, G., Tuttafesta, M., Capitelli, M., Giordano, D.: J. Thermophys. Heat Transfer **13** (3), 372–375 (1999)

Investigation of Non-catalytic Reaction of Shock-Heated Nitrogen Gas with Powder SiO_2

Jayaram Vishakantaiah, Ranjith Ravichandran, H.K.T. Kumara, K. Subba Rao, and K.P.J. Reddy

Introduction

Reentry vehicles protected with high-temperature materials enter the atmosphere at very high Mach numbers giving rise to a bow shock in front of the vehicle. Due to the very high temperatures produced by the shock wave in the gas, a strong thermochemical nonequilibrium scenario prevails inside the shock layer. The dissociated and ionized gas species in this region react among themselves and/or with the atomic species ablated from the thermal protection system (TPS). Because of these exothermic reactions, heat loads increase and directly affect the vehicle surface [1]. Recombination of atomic species on the vehicle surface contributes to an additional heat flux on the vehicle surface that can be up to 30 % of the total heat flux [2]. Based on the degree of recombination, such reactions are classified as (finite) catalytic and non-catalytic surface reactions. The nature of the reaction determines the amount of heat flux radiated to the vehicle surface, which is very critical in designing the TPS of the reentry vehicles. Amorphous SiO_2 is used in both the ablative and reusable TPS, and silica-based tiles are used for the shuttle's primary insulation system [3]. Silica tiles made out of SiO_2 fibers show low catalycity when they interact with the dissociated air. TPS materials having low catalytic property will prevent recombination of dissociated gas atoms on the surface [4, 5]. During reentry the TPS materials might ablate and become fine powders which eventually interact with the dissociated and ionized gas species. Hence it is important to study the reaction mechanisms involved in the interaction of these materials with gas species. The present work discusses the non-catalytic reaction on SiO_2 powders in presence of shock-heated nitrogen gas using shock tubes. Different characterization techniques are used to characterize the samples before and after shock treatment. Although nitridation is done by many other chemical methods such as thermal nitridation, plasma nitridation [6], diffusion–reaction [7], etc., a novel method of nitridation by shock waves is discussed in this paper.

Experimental Procedure

To study the non-catalytic reactions in presence of N_2 test gas in a shock tube, commercially available SiO_2 powder is used. Shock waves are generated in Material Shock Tube 1 (MST1) facility established at the Shock Induced Materials Chemistry Laboratory, SSCU, Indian Institute of Science, Bangalore, operating at a stagnation enthalpy of 2–4 MJ/kg. MST1 comprises of two sections: the driver section and the driven section. The OD and ID of the shock tube are 115 mm and 80 mm, respectively. The length of the driver section is 2 m and that of the driven section is 5 m. Powder sample mounting facility and an extension of 0.6 m long shock tube with an end flange is attached to the driven section. The driver section is separated from the driven section by the aluminum diaphragm of 3 mm thickness. The driven section is purged with ultrahigh pure (UHP) argon gas and pumping up to a vacuum level of 0.05 mbar. After the purging is completed, the driven section is filled with mixture of UHP argon (99.9993 %) and UHP nitrogen (99.999 %) gas at equal pressure. Argon gas is filled into the driven section up to 0.05 bar and nitrogen up to 0.05 bar so that the mixture

J. Vishakantaiah (✉)
Shock Induced Materials Chemistry Laboratory, Solid State and Structural Chemistry Unit, Indian Institute of Science, Bangalore, India
e-mail: jayaram@sscu.iisc.ernet.in

R. Ravichandran
Laboratory for Hypersonic and Shock Wave Research, Department of Aerospace Engineering, Indian Institute of Science, Bangalore, India

H.K.T. Kumara
Center of Applied Research and Nano-Technology, Siddaganga Institute of Technology, Tumakuru, India

K.S. Rao
Haldipur Hydraulieks, Bangalore, India

K.P.J. Reddy
Department of Aerospace Engineering, Indian Institute of Science, Bangalore 560012, India

G. Ben-Dor et al. (eds.), *30th International Symposium on Shock Waves 1*, DOI 10.1007/978-3-319-46213-4_61

of both the gases amounts to about 0.1 bar (P_1). The shock speed and reflected shock pressure are measured by dynamic pressure sensors (PCB Piezotronics Model No. 113B22), and pressure signals from the sensors are acquired and recorded by Tektronix digital oscilloscope (Model no. TBS2014B). The pressure sensors used are capable of measuring 5000 psi for full-scale voltage of 5 V output with a sensitivity of 1.0 mV/psi and a resolution of 20 mpsi. Helium gas is used as the driver gas to burst the aluminum diaphragm to produce shock waves. SiO_2 powder of 0.1 g interacts with the shock wave along the 0.6 m tube, and finally the reacted powder gets deposited on the end flange. This powder is collected and subjected to shock wave once again.

The shock Mach number M_S can be calculated from the data acquired by the oscilloscope. The pressure–time graph gives the time taken (Δt) for the shock wave to sweep the distance between two given sensor locations (Δx). From this information, the shock speed (V_S) and shock Mach number M_S are calculated as follows:

$$V_S = \frac{\Delta x}{\Delta t}; \quad M_S = \frac{V_S}{a} = \frac{V_S}{\sqrt{\gamma R T_1}}$$

where a is the local speed of sound, T_1 is the temperature of driven gas, R is the gas constant. and γ is the specific heat ratio. All the abovementioned properties are for the driven gas mixture (Ar + N_2). The temperature (T_5) across the reflected shock wave is calculated using the following 1D normal shock relation [8]:

$$\frac{T_5}{T_1} = \frac{\{2(\gamma-1)M_S{}^2 + (3-\gamma)\}\{(3\gamma-1)M_S{}^2 - 2(\gamma-1)\}}{(\gamma+1)^2 M_S{}^2}$$

In the present experiment, the obtained shock Mach number is 4.5 (calculated) which produces a T_5 value of ~4000 K (calculated using the above relation) for a short duration of 1–2 ms. Experimentally recorded reflected shock pressure (P_5) is about 30 bar. SiO_2 powders after shock interaction is analyzed using characterization techniques to understand the crystal structure, surface morphology, reaction mechanisms, and chemical composition.

Characterization

The characterization techniques used for analyzing samples before and after shock treatment are powder X-ray diffraction (XRD), scanning electron microscopy (SEM), and X-ray photoelectron spectroscopy (XPS). Powder XRD study is done to understand the changes in crystal structure and chemical composition that SiO_2 has undergone during shock interaction. PANalytical Empyrean model X-ray diffractometer with an X-ray source of Cu Kα ($\lambda = 1.5418$ Å) is used for this study. SEM micrographs are recorded to study the changes in surface morphology of SiO_2 (FEI Quanta SIRION). XPS study is carried out using Al Kα (1486.6 eV) radiation with an accuracy of ±0.1 eV in binding energy (AXIS Ultra DLD, Kratos Analytical). The position of C(1s) peak at 284.6 eV is taken as reference for calibrating the shift in the binding energy (BE) of the insulating sample.

Results and Discussion

The SiO_2 samples have been analyzed before and after shock exposure, and their XRD pattern is shown in Fig. 1. The XRD of SiO_2 powder shows peaks corresponding to the mixture of both cristobalite (JCPDS number 075-0923) and α-quartz (JCPDS number 078-1253) crystal structures as shown in Fig. 1a. After treatment with the shock wave in presence of argon and nitrogen gas mixture, SiO_2 forms silicon oxynitride (Si_2N_2O) and silicon nitride (Si_3N_4). After one shock treatment, the presence of Si_2N_2O (JCPDS number 072-1307) and Si_3N_4 (JCPDS number 076-1407) can be seen from the peaks assigned in Fig. 1b, and it is more pronounced after two shock treatments as shown in Fig. 1c. The main peak corresponding to cristobalite diminishes with shock treatment with a slight shift to the left due to the formation of nitride and oxynitride compounds.

SEM is used to study the microstructure of SiO_2 samples before and after shock treatments. The SEM micrographs at

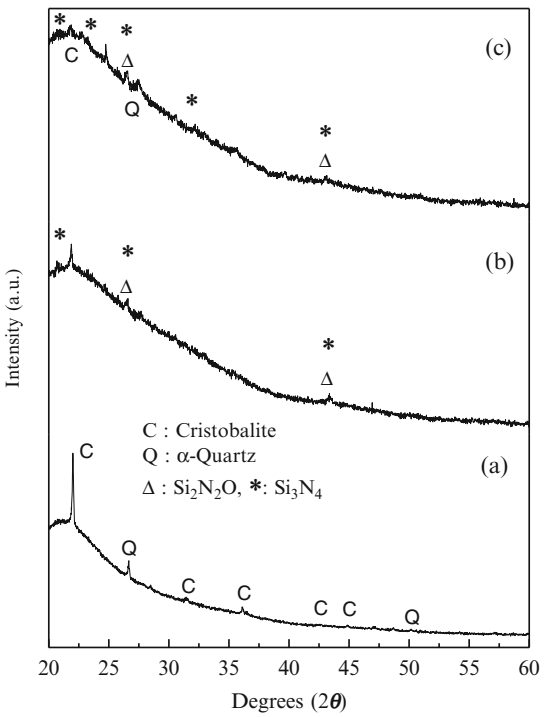

Fig. 1 XRD pattern of SiO_2: (**a**) before shock, (**b**) after one shock treatment, and (**c**) after two shock treatments in the presence of Ar + N_2 mixture

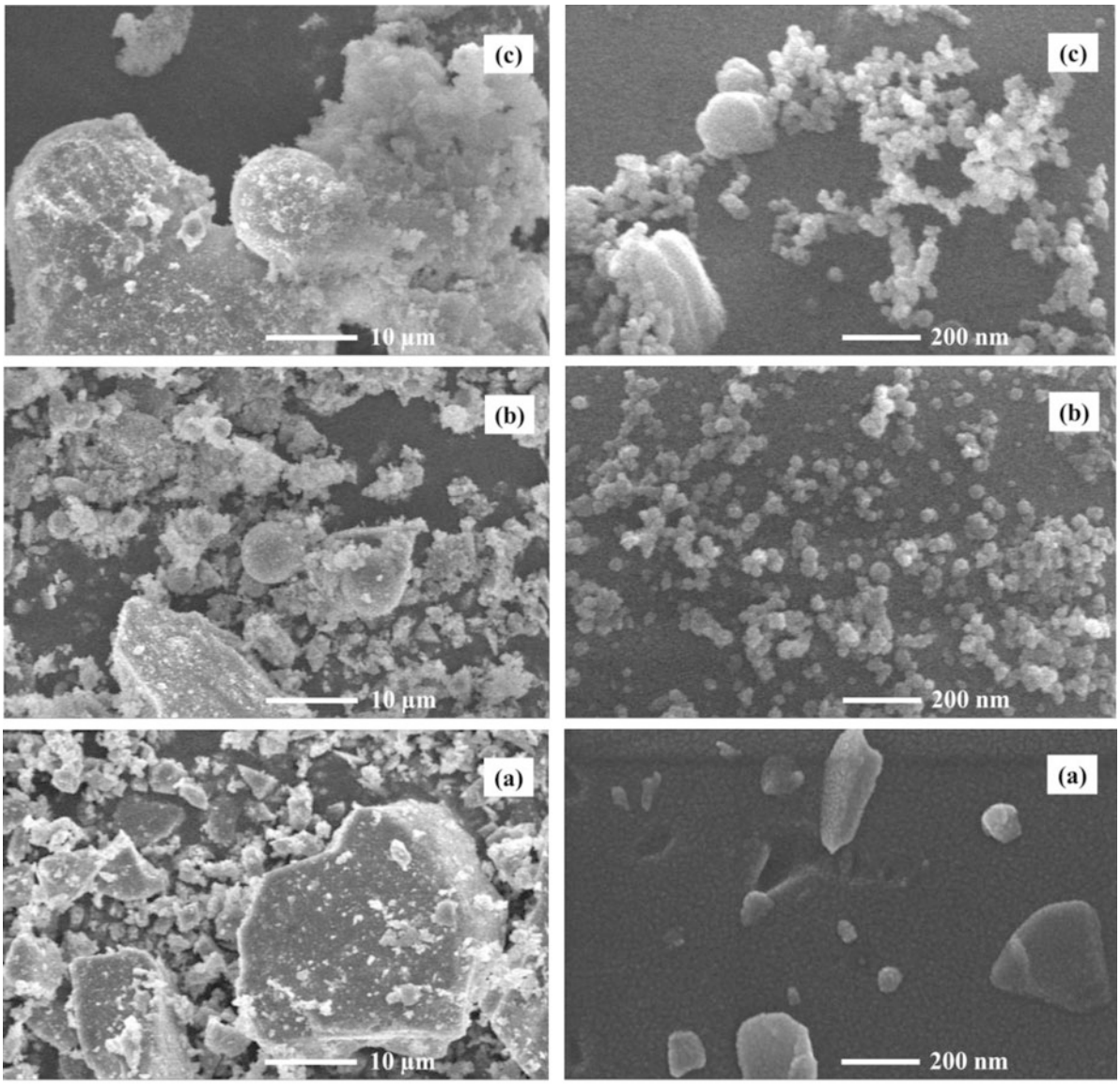

Fig. 2 SEM micrographs of SiO_2—left (5000×) and right (200,000×): (**a**) before shock, (**b**) after one shock treatment, and (**c**) after two shock treatments in the presence of Ar + N_2 mixture

different magnifications like 5000× (left) and 200,000× (right) are shown in Fig. 2. The micrographs of SiO_2 sample show particles of different shape and size as it can be seen from Fig. 2a [left], and an [right] SiO_2 after shock treatment undergoes changes in surface morphology forming spherical particles due to the reaction with shock-heated N_2 gas. Both left and right side of Fig. 2b and c show the SEM micrographs of SiO_2 after one and two shock treatments, respectively. Spherical particles can be seen from those figures along with some traces of the unreacted SiO_2 particles.

XPS study is a surface analysis technique, and it is significant in understanding the chemical composition and the mechanism of the reactions due to N_2 shock interaction with SiO_2 powders. XPS spectra of Si(2p) and O(1s) of SiO_2 samples before and after shock treatment is analyzed and shown in Fig. 3. XPS spectra of the shock treated samples show well-pronounced changes indicating the formation of new compounds, silicon nitride (Si_3N_4), and silicon oxynitride (Si_2N_2O), due to shock treatment. After two shock treatments, Si(2p) peak occurs at 103.4 eV due to SiO_2, while the peaks at 101.3 and 102.1 eV are attributed to Si_3N_4 and Si_2N_2O, respectively, as shown in Fig. 3c [left]. O(1s) peak due to SiO_2 occurs at 532.2 eV, whereas peaks at 533.0 and 534.3 eV are due to Si_3N_4 and Si_2N_2O, respectively, as shown in Fig. 3c [right]. The peaks at 105.1 eV for Si(2p) and 534.3 eV for O(1s) are attributed to Si-OH due to the effect of adsorbed water molecules in the SiO_2 samples.

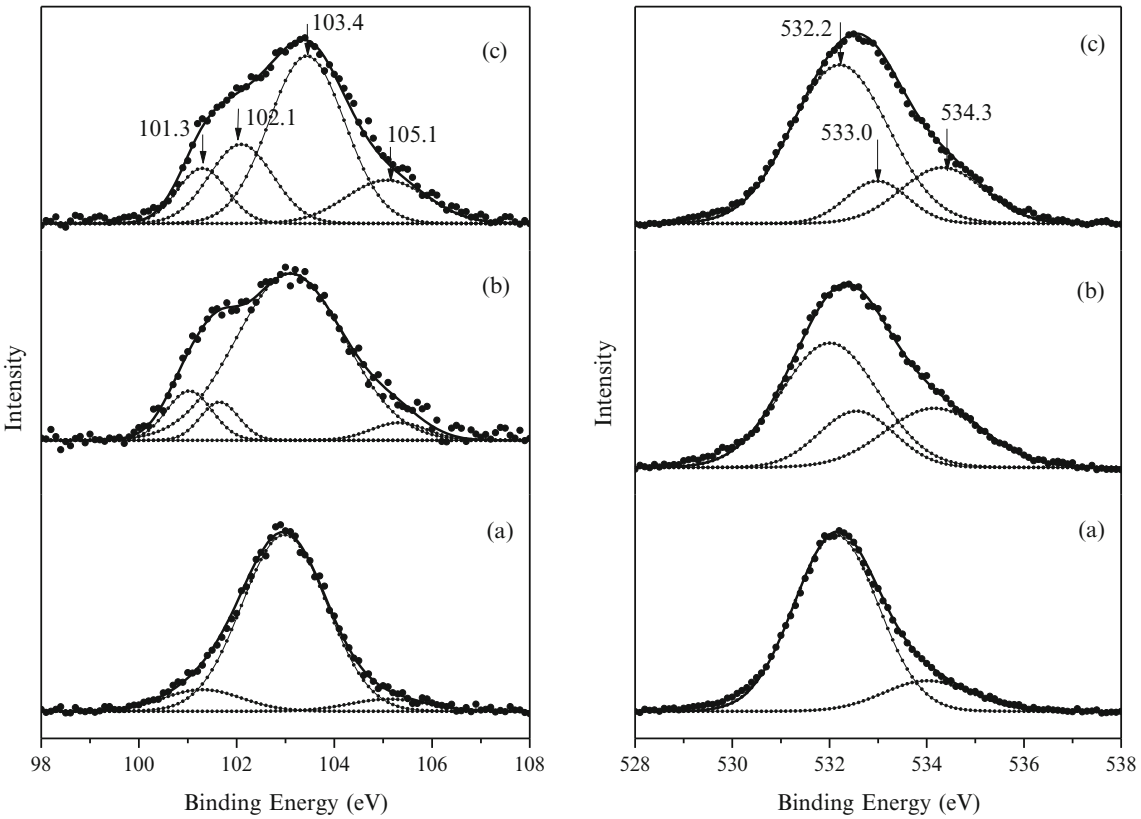

Fig. 3 XPS spectra of Si(2p) [*left*] and O(1s) [*right*] in SiO_2: (**a**) before shock, (**b**) after one shock treatment, and (**c**) after two shock treatments in presence of Ar + N_2 mixture

In case of one shock treatment, XPS spectra of Si(2p) show peaks corresponding to SiO_2, Si_3N_4, and Si_2N_2O as shown in Fig. 3b [left]. XPS spectra of O(1s) also confirm the presence of SiO_2, Si_3N_4, and Si_2N_2O by the appearance of the corresponding O(1s) peaks as shown in Fig. 3b [right].

The peak positions have been attributed to the new compounds formed by comparison with the reported literature [9]. XPS spectra of SiO_2 powder before shock show Si (2p) peak and O(1s) peak corresponding to SiO_2 as shown in Fig. 3a [left] and a [right]. Si(2p) peak at 101.3 eV might be due to nitride impurity in the SiO_2 powder before shock.

The SiO_2 powder, while interacting with N_2 shock, forms Si_3N_4 and Si_2N_2O as a result of the non-catalytic heterogeneous reactions where SiO_2 acts as the third body. Two possible non-catalytic reactions which form the nitride and oxynitride are shown below, though other reactions also would form nitride and oxynitride.

$$3SiO_2(s) + 2N_2(g) \rightarrow Si_3N_4(s) + 3O_2$$

$$Si + SiO(g) + N_2(g) \rightarrow Si_2N_2O(s)$$

Conclusions

SiO_2 powder is exposed to shock waves in presence of N_2 test gas using Material Shock Tube 1 (MST1) facility. Due to shock interaction, SiO_2 powder undergoes changes in crystal structure and chemical composition by forming new compounds like silicon nitride (Si_3N_4) and silicon oxynitride (Si_2N_2O). Changes in surface morphology due to shock interaction are observed from SEM micrographs. XRD analysis show new diffraction lines corresponding to the new compounds. The formation of nitride and oxynitride is also confirmed from the deconvoluted XPS spectra of Si(2p) and O(1s). The reactions which have taken place are heterogeneous non-catalytic reactions in which SiO_2 acts as a third body resulting in the formation of silicon oxynitride and silicon nitride.

Acknowledgment Financial supports for this project from ISRO-IISc STC, JATP, DRDO, and DST, Government of India, are gratefully acknowledged.

References

1. Oguri, K., Sekigawa, T., Kochiyama, J., Miho, K.: Catalycity measurement of oxidation-resistant CVD-SiC coating on C/C composite for space vehicle. Mater. Trans. **42**, 856–861 (2001)
2. Barabto, M., Reggiani, S., Bruno, C., Muylaert, J.: Model for heterogeneous catalysis on metal surfaces with applications to hypersonic flows. J. Thermophys. Heat Transfer **14**, 412–420 (2000)
3. Cozmuta, I.: Molecular mechanisms of gas surface interactions in hypersonic flow. In: 39th AIAA Thermophysics Conf., Miami, FL, 2007
4. Ueda, S., Weiland, M., Itoh, K., Hannemann, K.: Comparative experiment on the surface catalysity in two high enthalpy shock tunnels. In: 24th AIAA Aerodynamic Measurement Technology and Ground Testing Conference, Portland, Oregon, 28th June–1st July, 2004
5. Reddy, K.P.J., Hedge, M.S., Jayaram, V.: Material processing and surface reaction studies in free piston driven shock tube. In: 26th International Symposium on Shock Waves, Gottingen, Germany (Plenary talk), 35–42, 15–20 July 2007
6. Itakura, A.N., Shimoda, M., Kitajima, M.: Surface stress relaxation in SiO_2 films by plasma nitridation and nitrogen distribution in the film. Appl. Surf. Sci. **216**, 41–45 (2003)
7. Orellana, W., da Silva, A.J.R., Fazzio, A.: Diffusion–reaction mechanisms of nitriding species in SiO_2. Phys. Rev. B **70**, 125206 (2004)
8. Gaydon, A.G., Hurle, I.R.: The Shock Tube in High-Temperature Chemical Physics, pp. 23–28. Reinhold Publishing Corporation, New York (1963)
9. Castanho, S.M., Moreno, R., Fierro, J.L.G.: Influence of process conditions on the surface oxidation of silicon nitride green compacts. J. Mater. Sci. **32**, 157–162 (1997)

Part VII

Detonation, Combustion and Ignition

On the Deflagration-to-Detonation Transition in Narrow Tube with Varying Prechamber-Initiator

S. Golovastov, G. Bivol, and V. Golub

Introduction

Prechamber method of detonation initiation is most relevant for the dissemination of research of combustion in a narrow channel, i.e., in such channel, the diameter of which is less than or comparable with the detonation cell width gas mixture. The transition slow burning to detonation in these channels is virtually impossible to carry out due to the heat sink wall and the significant effect of the boundary layer.

The impact of the prechamber on the combustion of detonable gas inside the connected channel (below: "channel") is similar to "finger flame" acceleration. The mechanism of finger flame acceleration in channels at the early stage of burning was studied for slow and fast propane–air flames [1, 2].

Prechambers of greater diameter are usually used as a method of steady detonation initiation for studies of the detonation propagation in the connected "narrow" channel. Propagation detonation limits in narrow channels have been studied [3] focusing on velocity deficits and variations in detonation cell widths. A channel was formed by a pair of metal plates which were inserted into a detonation tube. Some investigations of DDT in narrow tubes or gaps were undertaken [4, 5]. Detonation was initiated in a large diameter tube before propagating into the narrow tube. Near-limiting propagation of detonation waves under reduced pressures in capillary tubes with inner diameters of around 1 mm using acetylene–oxygen mixtures was studied [5].

Larger diameter chambers, as well as specially designed chambers, are used for additional acceleration of the flame front [6]. A chamber was used to discharge the combustion product jet that interacted with the flame front [7]. Transmission of single-cell and spinning detonation waves in $C_2H_4/O_2/N_2$ mixtures through a sudden two-dimensional (2-D) expansion was experimentally studied [8].

Prechamber initiation is relevant in the investigation of the dynamics of the flame front and detonation in the narrow channels. The critical conditions for the onset of detonation and the conditions for the propagation of the detonation wave were determined [9]. A parametric study was undertaken of several different combustible mixtures and tubes of different sizes [10]. A number of attempts have been made to determine detonability limits for various mixtures [9].

The key element is the presence of the boundary layer that develops along the walls ahead of the flame [11]. Exploring the limits of detonation in narrow channels for diluted mixtures and blends, consisting only of the oxidizer and fuel, the authors [12] concluded that the decrease in the velocity of the detonation wave and, as a consequence, its attenuation is mainly caused by friction and energy losses in the wall tube. It was shown [13] that the wall dissipative effects decrease the speed of the detonation wave compared to the Chapman–Jouguet (DCJ) detonation velocity.

One of several prospective applications of microscale detonation is in-space propulsion devices. The topic is of considerable importance not only due to industrial safety concerns but also the potential application to microscale propulsion and power devices [14].

It was stated in the detail [15] that a prolongation in time of the source of ignition has to be taken into account for evaluation of the energy of the direct initiation of detonation. Particular attention should be paid to the work [16], where the transition of a laminar flame from the prechamber into the narrow channel was studied. The cooling of the combustion products in the prechamber is able to slow down the flame front in the channel.

As a result of the acceleration of the flame front, compression waves and then multiple reflected waves can occur inside the prechamber. Therefore, at the output of the prechamber, virtually any distribution of velocity-expanded

S. Golovastov • G. Bivol • V. Golub (✉)
Joint Institute for High Temperatures of RAS, Izhorskaya str., 13, 2, Moscow, Russia
e-mail: golub@ihed.ras.ru

G. Ben-Dor et al. (eds.), *30th International Symposium on Shock Waves 1*, DOI 10.1007/978-3-319-46213-4_62

combustion products, pressure or temperature can be generated. Thus, in using such extended sources for detonation initiation as the prechamber of finite volume, it is necessary to strongly define the boundary conditions at the entrance to the channel.

In this paper, we are interested in the pressure profile at the entrance to the channel. The aim of this study was also to determine the pre-detonation distance in the channels of propane–butane–oxygen and acetylene–oxygen mixtures. The aim was to define a minimum energy of direct initiation of detonation by the prechamber method.

Experimental Setup

The experimental setup is shown in Fig. 1. It consisted of (1) a prechamber, connected to an open channel with a round cross section, (2) a pumping system, (3) a detonable mixture filling system, (4) ignition system with a spark gap, and (5) a measuring system. The prechamber and the channel were made of brass. The inner diameter of the channel was 3 mm and wall thickness was 7–8 mm. The channel length was 500 mm, i.e., equal to 166 tube diameters. The diameter of the prechamber was 10, 16, or 20 mm. The minimum wall thickness of the prechamber was 8 mm and the maximum 15 mm. The prechamber length varied in the range 7–37 mm.

An open channel was used to prevent the formation of reflected compression waves.

A detonable mixture was prepared by partial pressure of the components in a 3 liter vessel. The maximum pressure of the mixture in the vessel was 4×10^5 Pa. The mixture was maintained for at least 1 h. The propane–butane mixture used preferably comprised 17 %(mol) propylene, 52 % (mol) propane, and 47 %(mol) butane.

A spark gap was used to ignite the mixture in the prechamber. The aircraft spark gap was used with a planar surface. The energy released did not exceed 0.1 J. The energy released in the spark gap was 2–3 orders less than the energy released during the combustion of the gas mixture in the prechamber.

To measure the velocity of the flame front, photodiodes were used, installed along the axis of the channel. The measuring system consisted of 12 FD-256 photodiodes with temporal resolution of less than 1 μs. Conclusions about detonation formation were drawn if the velocity of the flame was close to the velocity of the stationary detonation, CJ detonation.

To determine the boundary conditions at the entrance to the narrow channel just after the prechamber, a PCB 113A piezoelectric pressure transducer was used. The transducer was established at a distance of 30 mm from the beginning of the channel. Since the pressure transducer was not located directly at the entrance to the narrow channel, but at a distance of 30 mm, we determined the pressure profiles listed below as "conditional boundary conditions."

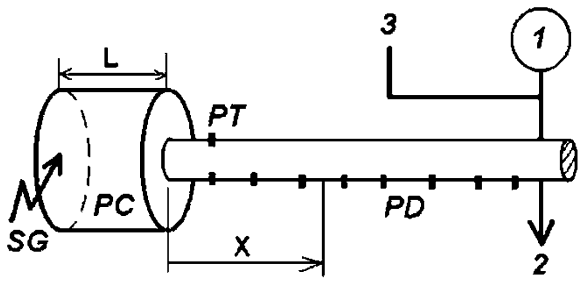

Fig. 1 Schema of the experimental setup. *PC* prechamber, *SG* spark gap, *PT* pressure transducer, *PD* photodiodes, *X* distance along the channel, *L* length of the prechamber, *1* manometer, *2* pumping system, *3* mixture filling system

Summary of the Data and Discussion

Figure 2 shows oscillograms of pressure and evolution of the flame front velocity at ER = 0.9 for prechambers of the following diameter/length: 10/7, 20/8, and 10/20 mm.

Based on the experimental data, it was shown that the dynamics of the flame front and shock waves in the channel can occur in different ways depending on the geometry of the prechamber: the push-effect of the prechamber due to spreading of the combustion products, the combined effect of the combustion products and the compression wave, or direct detonation formation.

Based on the obtained results, we have attempted to define two limiting effects of the prechamber detonation initiation in the channel: the push-effect in the prechamber due to the spreading of the products of combustion with consequent DDT and direct detonation formation.

Changing the ratio between the components of the combustible mixture, it may be possible to vary the maximal dimensions of the prechamber at which the push-effect occurs. As an example, we described a series of experiments that demonstrate the influence of the ER on the dynamics of the flame front and shock waves for configurations of the prechamber, diameter/length 10/20 mm. We used three values of ER of the propane–butane–oxygen mixture: 0.9, 0.65, and 0.4. For these dimensions (diameter/length of the prechamber 10/20 mm), there are principal different evolutions of the flame front (Fig. 3). At ER = 0.9 the direct initiation of detonation in the channel was registered. The pre-detonation distance did not exceed 10 tube diameters (30 mm). By reducing the ER to 0.65, the intensity of the shock wave formed in the prechamber was insufficient to initiate detonation in the beginning of the channel.

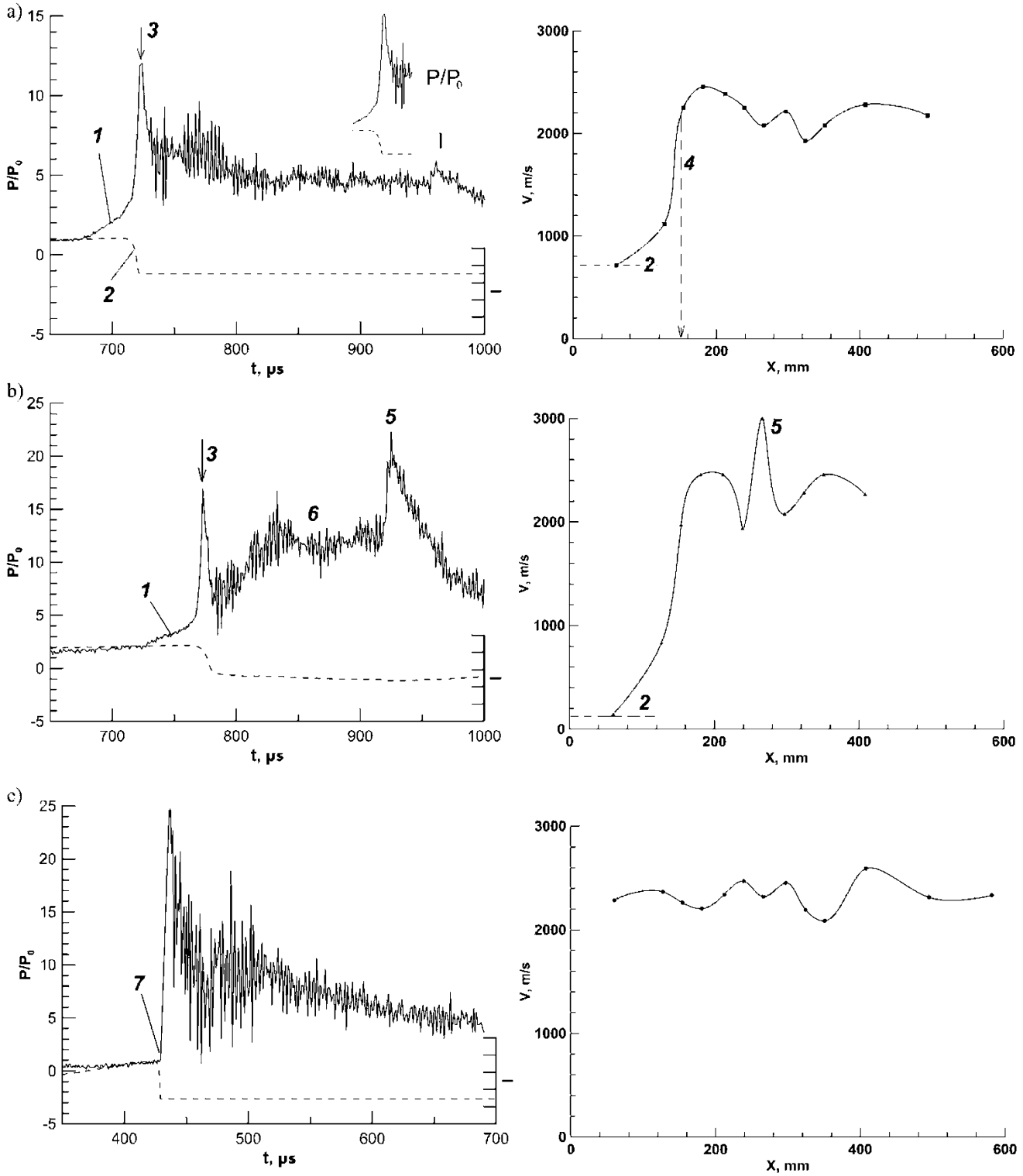

Fig. 2 Readings of pressure transducer (*P*/*P0*, up) and photodiode (*I*, r. u., down) at the position of 10 tube diameters from the beginning of the channel and evolution of the velocity of the flame front along the axis of the channel. Prechamber diameter/length: (**a**) 10/7 mm, (**b**) 20/8 mm, and (**c**) 10/20 mm. *0* increase in pressure due to compression waves, *2* flame front and flame front velocity, *3* pressure peak due to flame front, *4* pre-detonation distance, *5* pressure/velocity peak due to superposition of waves, *6* steady in pressure due to combustion products, *7* detonation wave

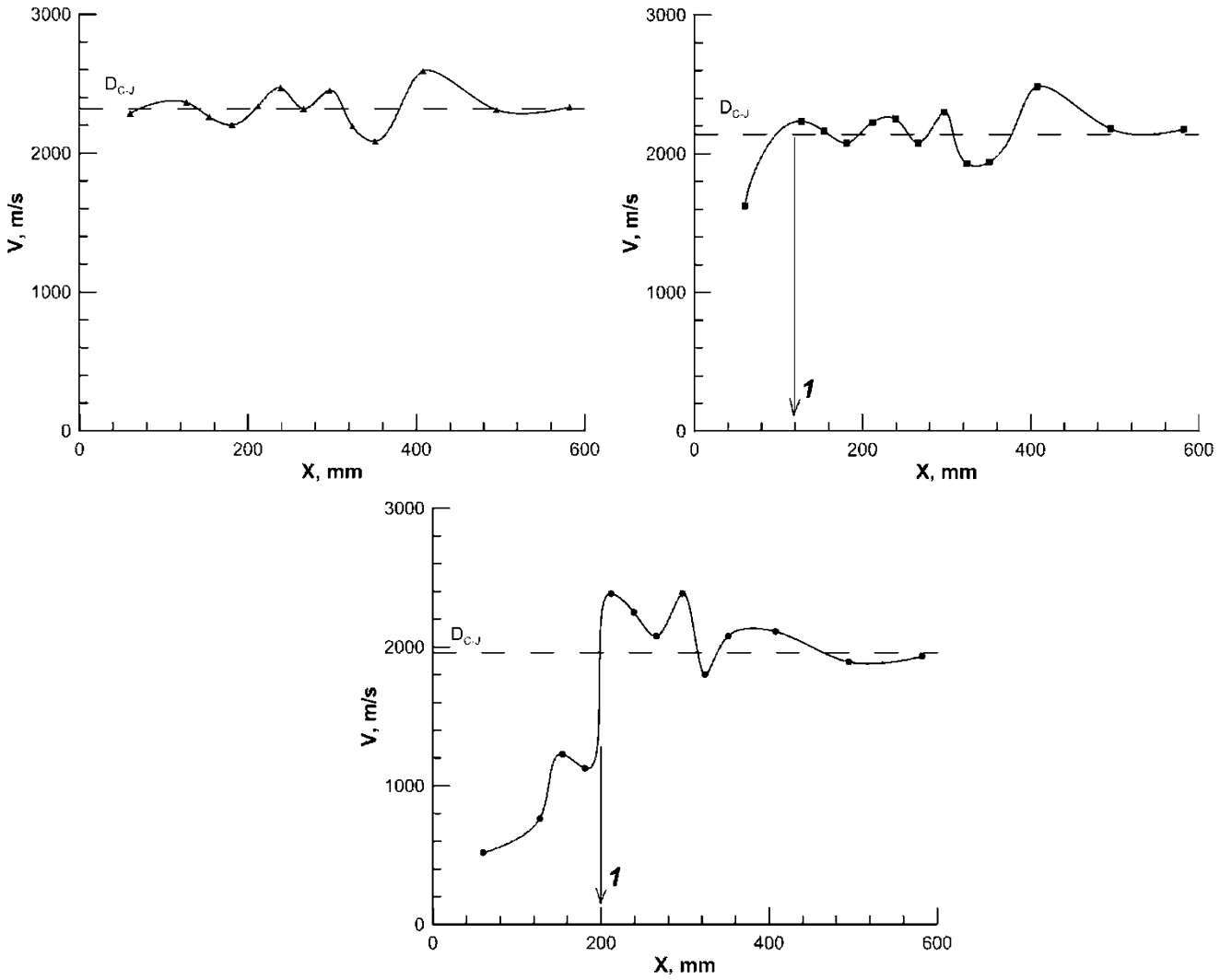

Fig. 3 Evolution of the velocity of the flame front along the axis of the channel with prechamber diameter 10 mm, length 20 mm. (**a**) ER = 0.9; (**b**) ER = 0.65; (**c**) ER = 0.4. *1* pre-detonation distance

Detonation was registered only at a distance of 40 tube diameters (120 mm) from the channel entrance. By further reducing the ER to 0.4, the gradual increase in the velocity of the flame front to the formation of the stationary detonation was observed. Pre-detonation distance was equal to 67 tube diameters (200 mm). The combustion of the mixture in the prechamber could have occurred due to the push-effect.

The detonation is formed in the channel at some distance from the entrance to the channel.

For the same value of ER, the distances in the acetylene–oxygen mixture are 30–40 % less than in the propane–butane–oxygen mixtures. This is explained by the smaller cell size of the detonation cells in the acetylene–oxygen mixture. For example, in a stoichiometric acetylene–oxygen mixture, the size is 0.1 mm, while in the stoichiometric propane–butane–oxygen mixture, it is 1 mm, approximately. The values of ER are limited by the maximal values of 0.5 for acetylene mixtures and of 0.9 for propane–butane mixtures. For excess values of ER, the impact of the prechamber will be considered as having no push-effect but a combination of combustion products and compression waves.

At direct detonation initiation, the formed detonation wave enters the channel. However, the first measuring pair pressure transducer–photodiode was installed at a distance of ten tube diameters from the entrance to the channel. Therefore, we would not detect the detonation wave directly at the channel inlet. So, the considered detonation initiation was termed “conditionally direct” (below—“direct”).

Figure 4 shows the experimental data for the possibility of direct detonation initiation depending on the energy value of combustion in the prechamber and the ER for the

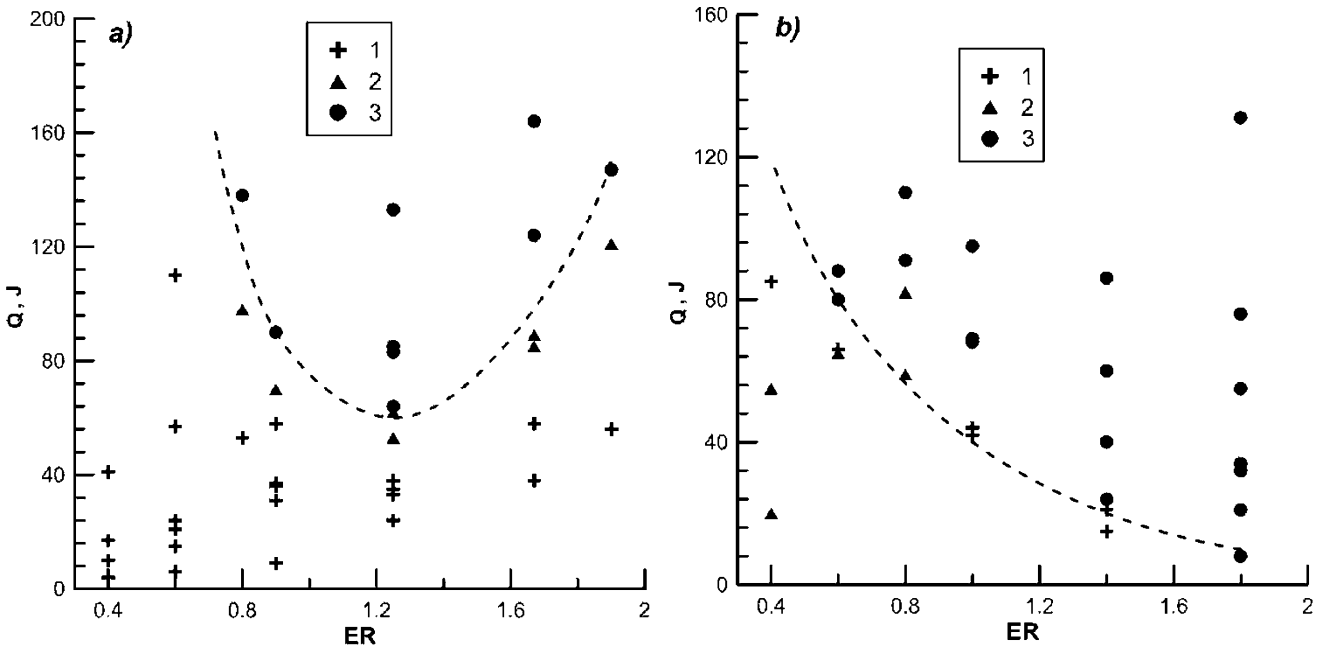

Fig. 4 Map of direct detonation formation in dependence on energy, released in the prechamber and ER of mixture. (**a**) Propane–butane–oxygen, (**b**) acetylene–oxygen. *1* no direct formation, *2* formation of detonation between 10 and 40 tube diameters, *3* direct formation

propane–butane and acetylene–oxygen mixtures. The curve separating the conditions for the direct initiation of detonation of propane–butane mixture has the form of a parabola with index ~3. At ER more than 1 for acetylene–oxygen mixture, the process of self-decomposition occurs. Then, we have not obtained the minimum. Energy, released in the prechamber, was calculated using the heat of combustion proportionally the volume of the prechamber. The energy was determined by the amount of fuel (ER $<$ 1) or oxygen (ER $>$ 1) in the prechamber.

Figure 4 shows the points marked by triangles. These points correspond to experiments in which the first measuring pair pressure transducer–photodiode does not register a detonation wave. However, the detonation formation is recorded at the second measuring base, 30 tube diameters.

Data for the oxyacetylene mixture is limited by an ER equal to 1.8. Further increases in the ER lead to a decrease in the prechamber volume. A further decrease is inexpedient because the dimensions of the prechamber become comparable with the diameter of the channel. The concept of the prechamber in this case can lose meaning.

These energy values for prechamber detonation initiation are substantially higher than the energy for planar or spherical direct detonation initiation: 10–2–0.5 J for acetylene [17] and 0.6 J (ER = 1) for propane–butane mixture [18]. This is due to the fact that the energy release does not occur in a narrow combustion front plane, whose width is comparable to the induction length, but in a finite volume of the prechamber.

Conclusions

1. It was found that the dynamics of the flame front and the shock waves in the channel can occur in different ways depending on the geometry of the prechamber: deflagration to detonation transition or direct detonation formation. For each specific configuration of the prechamber, the equivalence ratio of a gas mixture can be determined, at which the dynamics of the flame front and the shock waves in the channel can occur due to one of the above scenarios.

2. The experimental map of the possibility of direct detonation initiation depending on the energy released in the prechamber and ER for propane–butane and acetylene–oxygen mixtures was obtained.

Acknowledgments The work was supported by RFBR-13-08-01227-a and by Presidium of RAS, program "Combustion and Explosion."

References

1. Clanet, C., Searby, G.: On the "tulip flame" phenomenon. Comb. Flame. **105**, 225–238 (1996)
2. Valiev, D.M., Akkerman, V., Kuznetsov, M., Eriksson, L.E., Law, C.K., Bychkov, V.: Influence of gas compression on flame acceleration in the early stage of burning in tubes. Comb. Flame. **160**, 97–111 (2013)

3. Ishii, K., Monwar, M.: Detonation propagation with velocity deficits in narrow channels. Proc. Comb. Inst. **33**, 2359–2366 (2011)
4. Ishii, K., Itoh, K., Tsuboi, T.: A study on velocity deficits of detonation waves in narrow gaps. Proc. Comb. Inst. **29**, 2789–2794 (2002)
5. Manzhalei, V.I.: Low-velocity detonation limits of gaseous mixtures. Comb. Expl. Shock. Waves **35**, 296–302 (1999)
6. Smirnov, N.N., Nikitin, V.F.: Effect of channel geometry and mixture temperature on detonation-to-deflagration transition in gases. Comb. Expl. Shock Waves **40**, 186–199 (2004)
7. Frolov, S.M., Aksenov, V.S., Basevich, V.Y.: Detonation initiation by shock wave interaction with the prechamber jet ignition zone. Doklady Phys. Chem. **410**, 255–259 (2006)
8. Wu, M.H., Kuo, W.C.: Transmission of near-limit detonation wave through a planar sudden expansion in a narrow channel. Comb. Flame **159**, 3414–3422 (2012)
9. Dupre, G., Peraldi, O., Joannon, J., et al.: Limit criterion detonation in circular tubes. Prog. Astronaut. Aeronaut. **133**, 156–169 (1991)
10. Gao, Y., Ng, H.D., Lee, J.H.S.: Minimum tube diameters for steady propagation of gaseous detonations. Shock Waves **24**, 447–454 (2014)
11. Ott, J.D., Oran, E.S., Anderson Jr., J.D.: A mechanism for flame acceleration in narrow tubes. AIAA J. **41**, 1391–1396 (2003)
12. Camargo A, Ng HD, Chao J, Lee JHS. *Propagation of gaseous detonations in small tubes*. Proc. 22nd ICDERS, Minsk, Belarus. (2009)
13. Chinnayya, A., Hadjadj, A., Ngomo, D.: Computational study of detonation wave propagation in narrow channels. Phys. Fluids **25**, 036101 (2013)
14. Gamezo, V.N., Oran, E.S.: Flame acceleration in narrow tubes: Applications for micropropulsion in low-gravity environments. AIAA J. **44**, 329–336 (2003)
15. Levin, V.A., Markov, V.V., Osinkin, S.F.: Simulation of detonation initiation in a combustible mixture of gases by an electric-discharge. Khimicheskaya fizika **3**, 611–614 (1984)
16. Iida, N., Kawaguchi, O., Sato, G.T.: Premixed flame propagating into a narrow channel at a high speed, part 1: flame behaviors in the channel. Comb Flame **60**, 245–255 (1985)
17. Knystautas, R., Lee, J.H.: On the effective energy for direct initiation of gaseous detonations. Comb. Flame. **27**, 221–228 (1976)
18. Vasil'ev A. Dynamic parameters of detonation. In: Zhang F (ed.) Shock Wave Science and Technology Reference Library, vol. 6: detonation dynamics. Shock Waves Science and Technology Library, Springer, Berlin, Heidelberg (2012)

Experimental Research on Deflagration-to-Detonation Transition (DDT) in an S-Shaped Tube

Li Lei, Teo Chiang Juay, Li Jiun-Ming, Po-Shiung Chang, and Boo-Cheong Khoo

Introduction

With its higher efficiency compared to a traditional engine, a pulse detonation engine (PDE) has been of interest to researchers for the past few decades as a potential solution for future engine system. However, because of the large length needed for the initiation of a detonation wave, the PDE has not been commercialized yet. In order to achieve a more compact PDE structure, detonation propagation inside a bent tube is proposed. This would not only reduce the PDE size because of the tube bending, but it would also accelerate the deflagration-to-detonation transition (DDT) process. It has been proved by Frolov [1] that by using a 180° bent tube, DDT can happen if the deflagration speed is only faster than 800 m/s.

It is agreed that the DDT in a 180° bent tube is primarily caused by the compression near the outer wall, while at the same time the inner area is greatly weakened by the diffraction. In order to obtain uniform wave strength, DDT using an S-shaped tube is proposed here since the being weakened part can be compressed again. It is still a question if the critical velocity for an S-shaped tube can be further decreased or not. What really happens inside the tube to accelerate the flame and onset the detonation is still unknown. To answer these questions, this research is to provide experimental data on the DDT using an S-shaped tube.

L. Lei (✉) • T.C. Juay
Department of Mechanical Engineering, National University of Singapore, Block EA, #07-08, 9 Engineering Drive 1, Singapore, Singapore
e-mail: lilei@u.nus.edu

L. Jiun-Ming • P.-S. Chang
Temasek Laboratories, National University of Singapore, #09-02, 5A Engineering Drive 1, Singapore, Singapore

B.-C. Khoo
Department of Mechanical Engineering, National University of Singapore, Block EA, #07-08, 9 Engineering Drive 1, Singapore, Singapore

Temasek Laboratories, National University of Singapore, #09-02, 5A Engineering Drive 1, Singapore, Singapore

Results

The valveless PDE system was described in details in the previous literature [2]. As shown in Fig. 1, three different ignition locations are used to change the wave speed before entering the S-shaped tube. Pressure transducers and ion probes are installed before and after the S-shaped tube to monitor the inlet and outlet wave speed.

Experiment results are shown in Fig. 2. Every equivalent ratio at each ignition location has 20–40 detonation shots. From the results, we can see that, despite different misfire rates, if the incoming shock wave speed is lower than 1500 m/s, then DDT successful rate is almost higher than 90 % with equivalent ratio from 1.0–1.4. Since detonation is a very stochastic phenomenon, shock waves within a large velocity range are generated. Further sort it down with different incoming wave speed as shown in Fig. 3, it can be found that the minimum shock speed that can successfully initiate detonation through this S-shaped tube is around 500 m/s.

In order to see how a reactive shock wave propagates inside this tube and how DDT is initiated, an optical accessible channel with the same S-shaped geometry as shown in Fig. 4 was designed and implemented for direct observation. A Z-type schlieren system was used for wave observation. In order to keep track of the dynamic changes of the waves, a high-speed camera which can boost up to 2 M frame/s (Photron SA-Z) was used. Sensors were installed before and after this channel to monitor wave velocity. Besides, the velocity can also be calculated alternatively by measuring the wave location difference at two consecutive imaging frames. The tube cross section is designed to be 20 mm (width) × 50.8 mm (height).

G. Ben-Dor et al. (eds.), *30th International Symposium on Shock Waves 1*, DOI 10.1007/978-3-319-46213-4_63

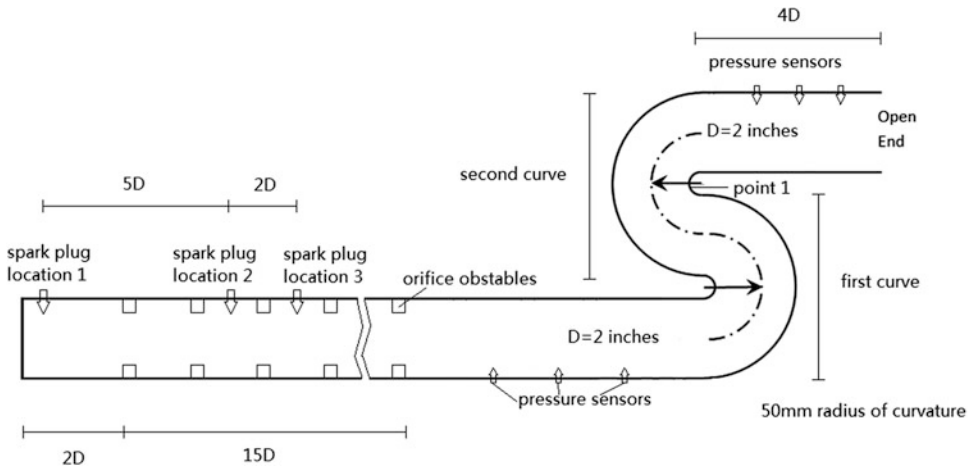

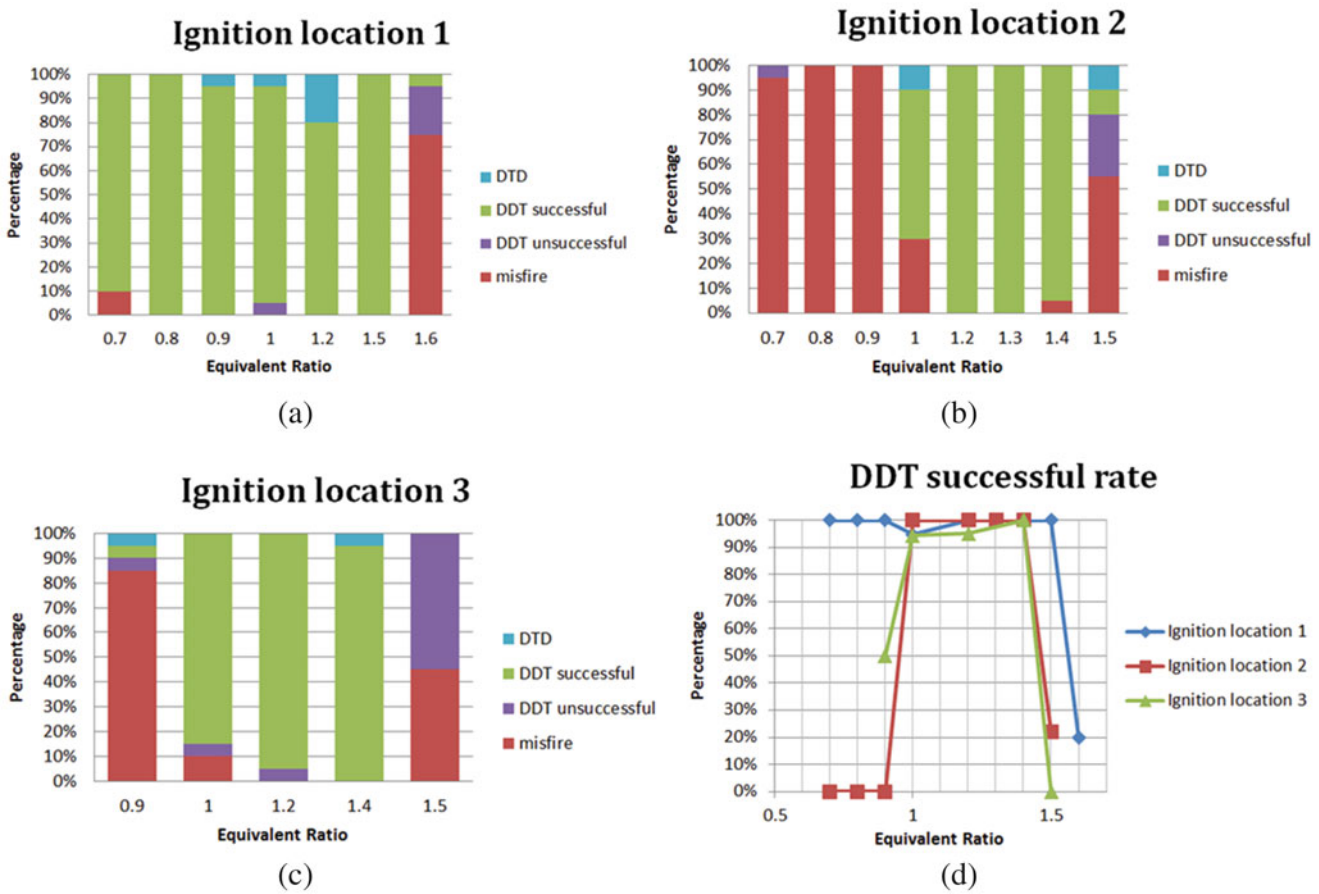

Fig. 2 (**a**–**c**) are the experiment results at ignition locations from (**a**) to (**c**). (**d**) DDT successful rate = (DDT successful)/(DDT successful + DDT unsuccessful). DDT means inlet wave is detonation, and outlet wave is also detonation

Waves with velocities range from 600 m/s to detonation C-J velocity were successfully generated by changing the spark plug location and fuel equivalent ratio. In order to synchronize the trigger signal with the data acquisition system, a digital delay is used here to send a trigger to the high-speed camera after receiving a pressure peak signal from the first pressure sensor.

Schlieren measurement was firstly implemented to measure the bottom curve area. As shown in Fig. 5, four different deflagration and detonation reflection patterns were identified.

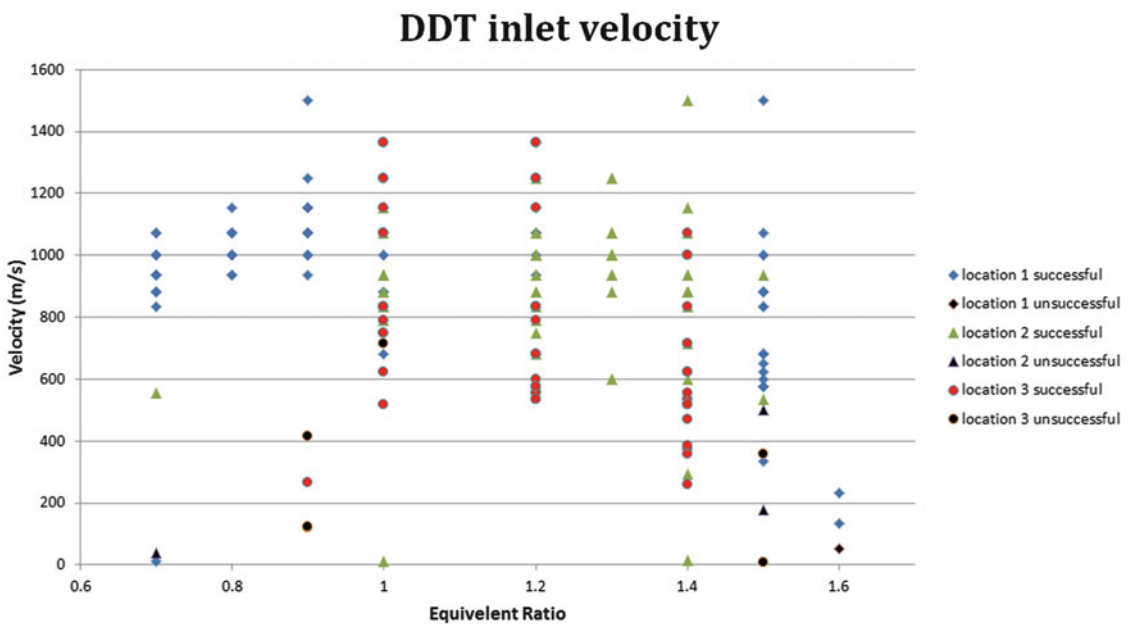

Fig. 3 Inlet shock wave velocity for successful and unsuccessful DDT

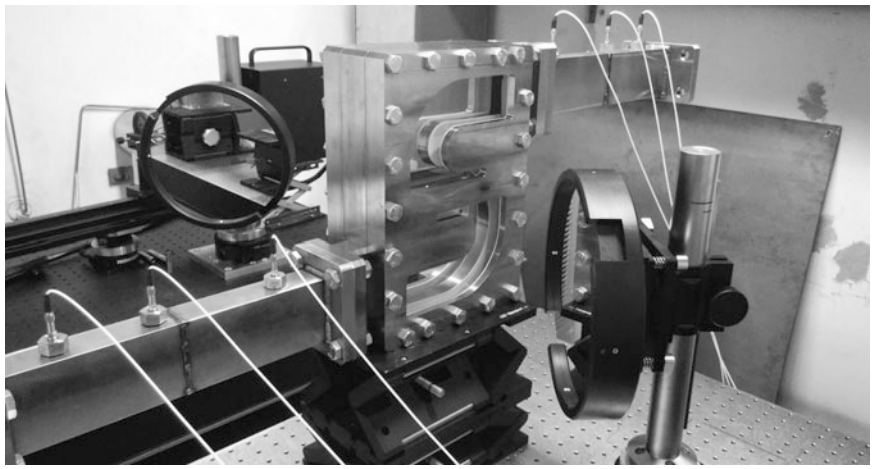

Fig. 4 Detonation tube and schlieren setup

The first three cases are leading shock reflection with a relatively low propagation speed, and the last one is detonation reflection case with C-J velocity. From case 1, we can see a normal shock (with the speed of 696 m/s) reflection configuration with a small Mach stem, incident wave, reflection wave, and shear layer. The weak compression waves are closely located after this leading shock. The strong compression waves also exist at the outlet area of the bottom horizontal tube. Case 2 and 3 show two other deflagration cases with shock moving speed of 883 and 878 m/s, respectively. In both cases, a small Mach stem is generated, but the reflection wave and the shear layer are closer to each other and to the curved wall compared to case 1. A big compression effect below the reflection wave and the shear layer turbulence make the gas to be highly flammable, and a localized explosion or explosion within the explosion [3] in this turbulent flame zone was observed to be responsible for the onset of detonation as shown in case 3. After analyzing similar onset of the localized explosion, it is discovered that all the onset locations always coincide with one strong compression wave behind the leading shock. Thus it is assumed that a strong compression wave can further compress the reactive gas and act as a trigger to the onset of explosion. The localized explosion may also attribute to the generation of turbulent flame area behind the detonation Mach stem near the wall. After the explosion onset, the small core can instantaneously expand outward and catch up with the leading reactive Mach stem because this spherical detonation is highly overdriven. Subsequent images in the same experiment firing shot of case 3 indicate that this explosion makes the sole contribution to the successful DDT process,

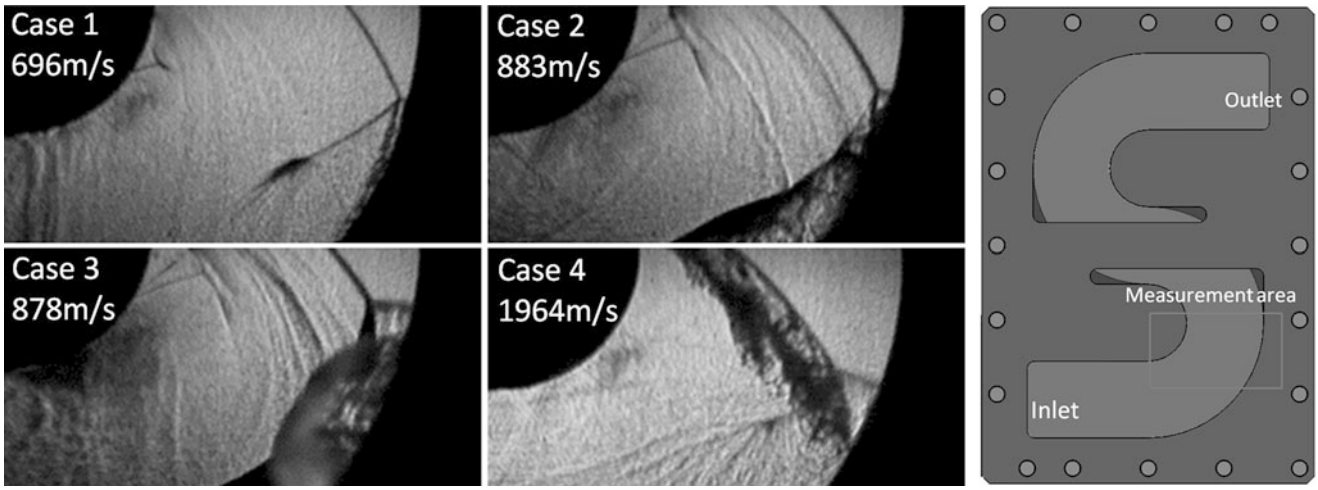

Fig. 5 Different deflagration and detonation reflection patterns inside the S-shaped tube

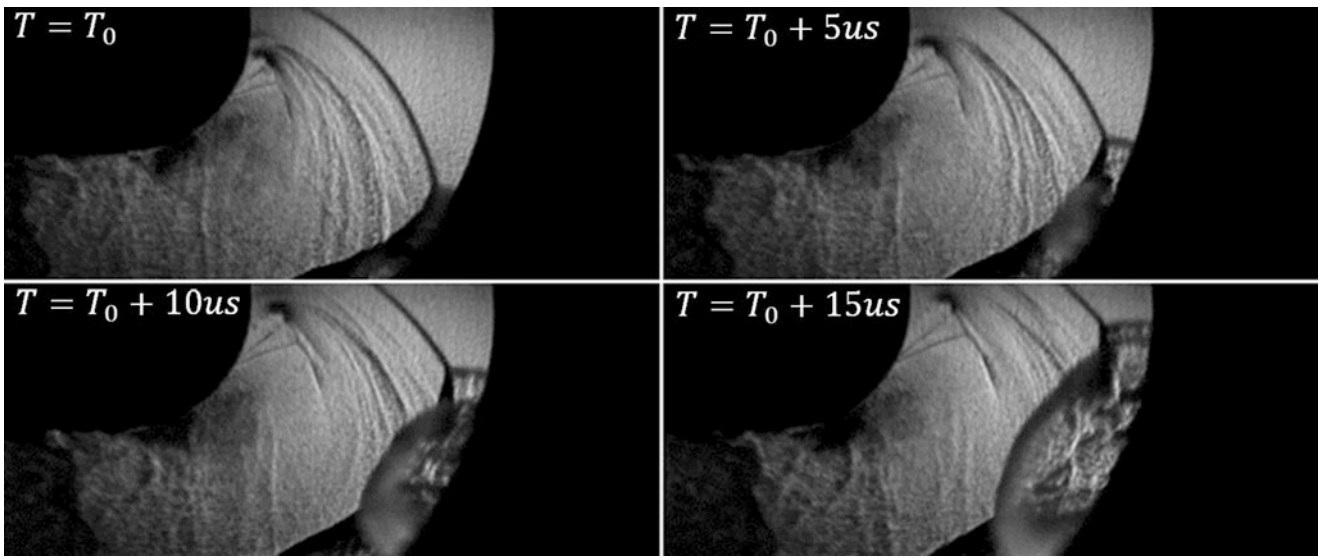

Fig. 6 High-speed imaging of the localized explosion at bottom curve (200,000frame/s)

while the original deflagration flame front would rapidly die out because of the lack of unburnt mixture which is completely consumed by the explosion before flame runs by. Figure 5 case 4 shows a reflection case with an incoming detonation wave. Even though the flame and the shock wave are slightly decoupled after diffraction, this diffraction can change the incident wave propagation direction, thus making the generated detonation Mach stem to become larger gradually after Mach reflection (MR). In this way, detonation can be re-initiated.

All the four cases described above experience successful DDT processes. Waves with relatively higher speed and stronger shock strength can make the detonation transition at the first curve as shown above. Others may have to go through the second curve of the S-shaped tube for detonation initiation (Fig. 6).

While shock strength is not strong enough to initiate detonation in the first curve, the same explosion can also be observed at the junction of the S tube outlet and the connected straight tube in the second curve. As shown in Fig. 7, after going through the whole S-shaped tube, the leading shock and the corresponding transverse wave are reflected back and forth between the channel walls, leaving pressure and temperature increase along the path. The following flame area thus accelerates and becomes a flame front with a clear boundary as shown in Fig. 7 at $T = T_0 + 75us$. As measured from these high-speed images which were captured under 80,000 frame/s, the deflagration wave after

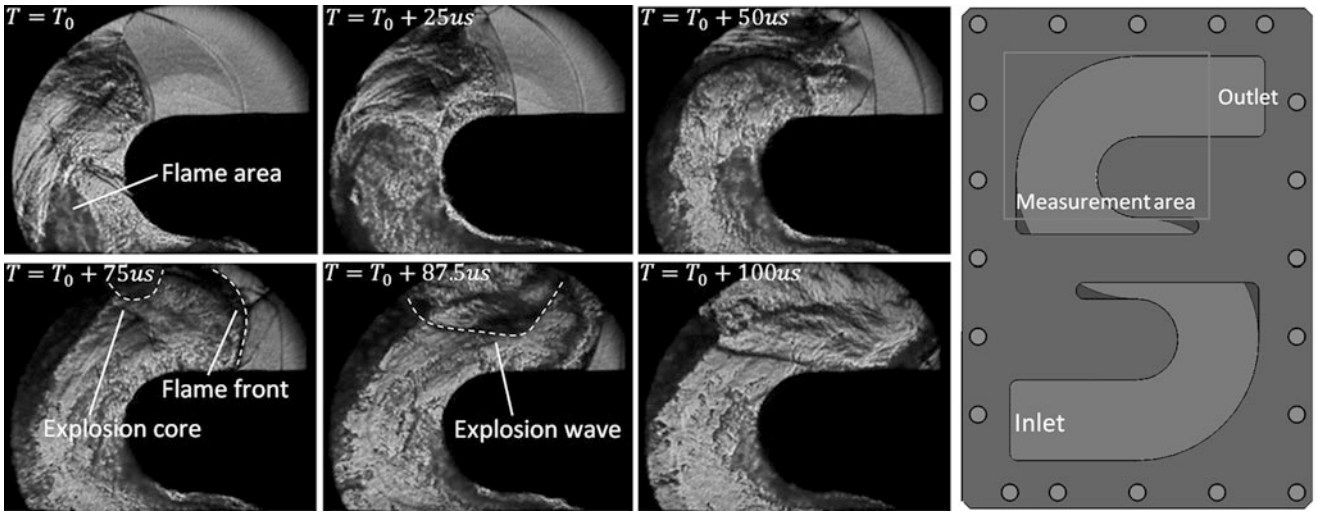

Fig. 7 High-speed imaging of the localized explosion at top curve (80,000frame/s)

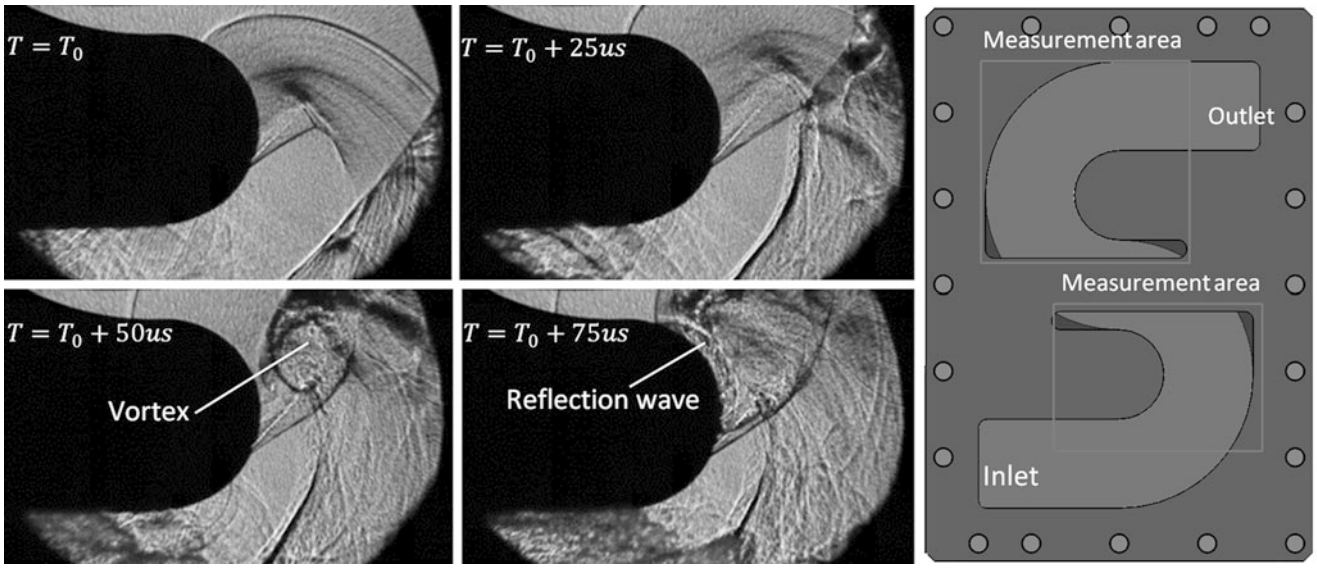

Fig. 8 Interaction of shear layer and transverse wave at bottom curve (80,000frame/s)

this S-shaped tube is around 797 m/s, which is roughly half of the detonation C-J velocity, or previously defined as the maximum C-J deflagration velocity. This velocity is one of the prerequisites for explosion to be initiated. The explosion can then provide subsequent multiple transverse waves between the top and bottom walls and thus offer stable driving force for the leading detonation to be self-sustainable. This detonation onset mechanism observed in the S-shaped tube is identical to what Lee has proposed as the SWACER mechanism [3].

Aside from the previously mentioned mechanisms, other factors were also observed to play a significant role in assisting detonation to occur. One of them is the interaction between shear layer and transverse wave. From the high-speed imaging, it is proved to be responsible for turbulence generation and thus prompt deflagration to accelerate and explosion to onset. As shown in Figs. 8 and 9, this interaction can be found in both two sections of the S-shaped tube. While a transverse wave goes through the shear layer, because of the different flow directions and velocities, the shear layer is found to be able to break the transverse wave into two parts. The bottom wave would go back into the previous tube, and the top one would wrinkle to a curved shape which reflects the shape of the vortex near the shear layer. This process could not only help compress and mix the mixture better, but it could also lead the wave to have a head-on reflection on the inner curved wall. This reflection subsequently would form another Mach stem and interact with the

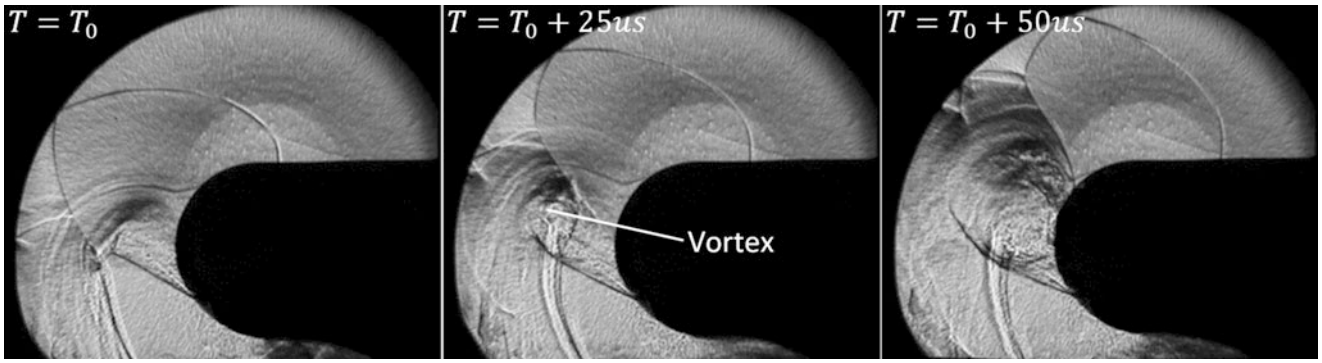

Fig. 9 Interaction of shear layer and transverse wave at top curve (80,000frame/s)

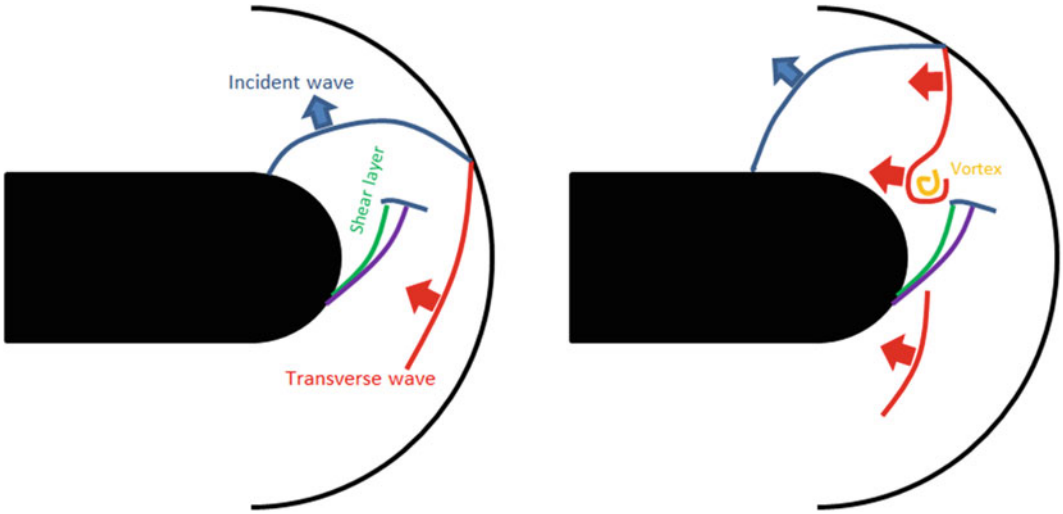

Fig. 10 The configuration of shear layer and transverse wave interaction

other one on the outer curve. The multiple reflection waves at the leading shock are responsible for its further acceleration. Figure 10 describes how this interaction evolves, and the left image of the wave diffraction configuration is found to be similar with what Skew has previously described [4].

Conclusions

The S-shaped tube is found to be an effective device for deflagration-to-detonation transition. It is measured that deflagration wave with the velocity as low as 500 m/s can successfully be transited to detonation in this geometry. High-speed schlieren photography was used for direct experimental observation of the dynamic changes of the waves. Different reflection phenomena were identified with waves propagating at various speeds. Localized explosions were captured at different locations near the wall, which served as the trigger for deflagration-to-detonation transition. A strong compression wave which follows behind the leading shock could be responsible for the localized explosion to happen. It is calculated that the wave velocity instantaneously before explosion is around half the C-J velocity, which corresponds to what Lee summarized. Except for the abovementioned phenomenon, the interaction between the shear layer and the transverse wave is also found to be useful for detonation initiation. It can generate a curved transverse wave, advance a better mixing, and increase instability at the front shock, thus making detonation onset to be easier.

References

1. Frolov, S.M., Aksenov, V.S., Shamshin, I.O.: Propagation of shock and detonation waves in channels with U-shaped bends of limiting curvature. Russ. J. Phys. Chem. B **2**(5), 759–774 (2008)
2. Li, J., Teo, C.J., Lim, K.S., Wen, C., Khoo, B.C.: Deflagration to detonation transition by hybrid obstacles in pulse detonation engines, AIAA paper 2013-3657, (2013)
3. Lee, J.H.S.: The detonation phenomenon. Cambridge University Press, New York (2008)
4. Skews, B.W.: Shock diffraction on rounded corners, Conference on hydraulics and fluid mechanics, 20–22, (1968)

DDT Triggered by SWBLI: Numerical and Experimental Research

E. Dzieminska, A.K. Hayashi, T. Machida, and J. Misawa

Introduction

Deflagration-to-detonation transition (DDT) is one of the most important subjects of detonation study. When we will be able to control and fully predict it, the detonation can be safely used in everyday devices. Our interest is the autoignition phenomenon as well as using hydrogen as a fuel.

We were able to show by numerical approach that autoignition, which triggers DDT, in the vicinity of a wall is due to shock wave–boundary layer interaction (SWBLI). The numerical research is confirmed not only with the well-known experiments done by Oppenheim's group [1] but also with the new results.

DDT Background

Many DDT studies were performed from the 1940s to 1960s. Zel'dovich [2, 3] made a theory of detonation early in the 1940s, which is now well known as ZND model of detonation. Over the years, Sokolik [4], Shchelkin and Troshin [5], and many other scientists studied the transition process theoretically and experimentally. In the early 1960s, Laderman and Oppenheim [6] designed a new tube with smooth walls and carried out flame acceleration experiments leading to DDT. Just a new year later, Urtiew and Oppenheim [1] measured DDT process in oxyhydrogen mixture using a laser schlieren photographic method to visualize clearly four modes of DDT process. Since then, many researchers implemented non-smooth walls in their experimental work. Recently Kuznetsov et al. [7] performed detailed DDT study experimentally to see its further detail. Meanwhile numerical analysis on detonation was started in the 1970s by Taki and Fujiwara [8], and then Oran and Boris [9] group started numerical studies on detonation using their FCT scheme. Recently detailed DDT mechanism is extensively investigated numerically by Liberman et al. [10], Fukuda et al. [11], and Dzieminska and Hayashi [12]. They show that the important factors for DDT are flame acceleration, shock wave formation in front of flame, and transition to detonation.

DDT Triggered by SWBLI Mechanism

In Fig. 1 the schematic scenario of the mechanism of SWBLI triggering DDT is shown [12]. At the first stage (A), there is a propagating flame and precursor shock moving in front of the flame with some distance. A boundary layer is illustrated only on the bottom wall in order to simplify the drawing. The flame starts producing weak shock waves (B) which are slightly raising temperature of the boundary layer (C), which is initially heated up by the precursor shock wave. At the point when temperature is high enough and reactions are sensitive, autoignition happens in the vicinity of the wall (D). If the autoignition does not go to detonation, a new flame can develop. The new flame transits quickly to a fast flame and propagates much faster than the main flame and the precursor shock (E) causing DDT (F) and detonation (G).

The mechanism's formulation was carried out though numerical simulation using 2-D and later on 3-D compressible Navier–Stokes equations for highly viscous and diffusive flow field in its early stage of deflagration. The chemical model was the Stanford model with nine chemical species (H_2, H, O_2, O, OH, HO_2, H_2O_2, H_2O, and N_2) and

E. Dzieminska (✉)
Sophia University, 7-1 Kioi-cho, Chiyoda-ku, Tokyo 102-8554, Japan
e-mail: edyta.d@sophia.ac.jp

A.K. Hayashi • T. Machida
Aoyama Gakuin University, 5-10-1 Fuchinobe, Chuo-ku, Sagamihara-shi, Kanagawa 252-5258, Japan

J. Misawa
Toyota Motor Corporation, 1 Toyota-cho, Toyoda-shi, Aichi 471-8571, Japan

G. Ben-Dor et al. (eds.), *30th International Symposium on Shock Waves 1*, DOI 10.1007/978-3-319-46213-4_64

20 elementary reactions including a dependency of pressure with Troe's formulation. The unsteady term is calculated with a Strang-type time splitting method, the convection term using a Harten–Yee non-MUSCL modified-flux TVD scheme, and the production term with a point implicit method.

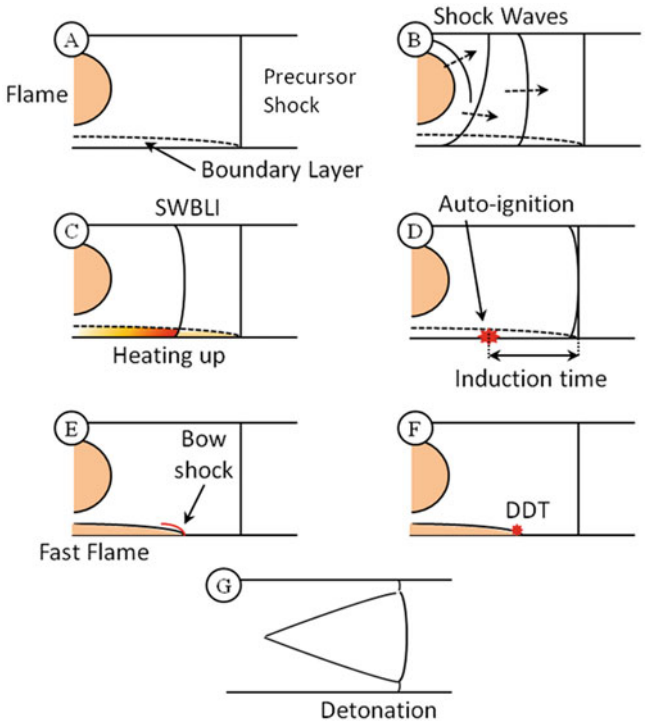

Fig. 1 SWBLI causing autoignition and DDT scenario [12]

Results

In the numerical analysis, autoignition and DDT were observed in the vicinity of the wall. The comparison between *x–t* diagrams obtained experimentally and numerically, respectively, is presented in Fig. 2. Onset of deflagration-to-detonation transition can be clearly seen in both cases and it has the same features. The experiment as well as 3-D calculations used stoichiometric mixture of hydrogen and oxygen. In both cases, autoignition in the vicinity of the wall (or even we can say in the boundary layer) leading to DDT and detonation was clearly observed. Weak shock waves produced by the propagating flame heated up the boundary layer causing the mixture to ignite. High changes in pressure behind those shock waves do not make such a big difference as, paradoxically, small changes in temperature. Maybe the most important parameter is induction time. The mixture becomes sensitive after the first precursor shock and further changes in temperature create perfect conditions for autoignition. Induction time combined with the heating up maintains that special conditions and finally we can observe DDT and detonation.

In Fig. 3 pressure record taken during the experiment is shown. There were six pressure sensors mounted on the tube so that we can keep accurate track of what happens in the tube. In this case, induction time is comparable to that from numerical simulation. It is hard to compare the exact numbers as the experiment took much larger space and, therefore, longer time than the numerical calculation. In both cases, the induction time seems to be significantly small; nevertheless, it pays a big part of the autoignition and DDT process.

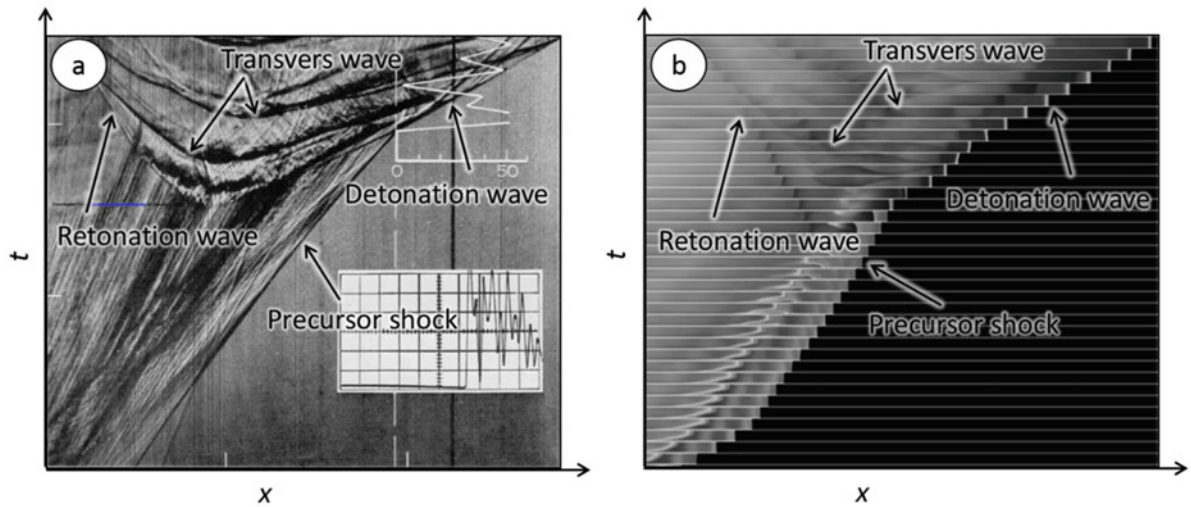

Fig. 2 Comparison between *x–t* diagram obtained with (**a**) experiments [1] and (**b**) 3-D numerical simulation

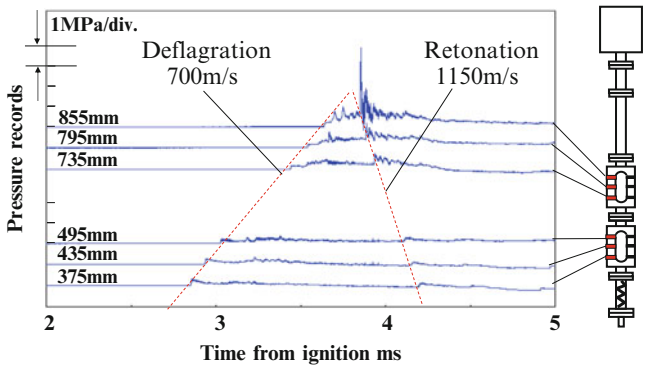

Fig. 3 Pressure records of six sensors: (**a**) 375 mm, (**b**) 435 mm, (**c**) 495 mm, (**d**) 735 mm, (**e**) 795 mm, (**f**) 855 mm, from the tube end (at the ignitor position)

Conclusions

The new mechanism for an autoignition in the vicinity of a wall was discussed and based on both numerical and experimental researches. The cause for DDT in the vicinity of the wall (or in the boundary layer) is shock wave–boundary layer interaction in reactive mixtures.

DDT is one of the most important subjects of detonation study. When we will be able to control and fully predict it, the detonation can be safely used in everyday mechanisms.

References

1. Urtiew, P.A., Oppenheim, A.K.: Experimental observation of the transition to detonation in an explosive gas. Proc. Roy. Soc. Lond. A **295**, 13–28 (1966)
2. Zel'dovich, Ya.B. Theory of combustion and detonation of gases. Moscow-Leningrad, Izd-vo AN SSSR, (1944)
3. Zel'dovich, Ya.B. Theory of detonation. Moscow, Gostekhizdat, (1955)
4. Sokolik, A.S.: Self-ignition, flame, and detonation in gases. Izdatel'stvo Akademii Nauk SSSR, Moskva (1960)
5. Shchelkin, K.I. Troshin, Ya.K. Gasdynamics of combustion. Izdatel'stvo Akademii Nauk SSSR, Moscow, (1963)
6. Laderman, A.J., Oppenheim, A.K.: Initial flame acceleration in an explosive gas. Proc. Roy. Soc. Lond. A. **268**, 153–180 (1962)
7. Kuznetsov, M.S., Alekseev, V., Matsukov, I., Dorofeev, S.: DDT in smooth tube filled with a hydrogen-oxygen mixture. Shock Waves **14**, 205–215 (2005)
8. Taki, S., Fujiwara, T.: Numerical analysis of two-dimensional nonsteady detonations. AIAA J. **16**, 73–77 (1978)
9. Oran, E.S., Young, T.R., Boris, J.P., Picone, J.M. Edwards, D.H: Study of detonation structure: the formation of unreacted gas pockets. 19th Sympo. (Int.) Combust., 573–582, (1982)
10. Liberman, M.A., Ivanov, M.F., Kiverin, A.D., Kuznetsov, M.S., Chukalovsky, A.A., Rakhimova, T.V.: Deflagration-to-detonation transition in highly reactive combustible mixtures. Acta Astronaut. **67**, 688–701 (2010)
11. Fukuda, M., Dziemińska, E., Hayashi, A.K., Yamada, E., Tsuboi, N.: Effect of wall conditions on DDT in hydrogen-oxygen mixtures. Shock Waves **23**, 191–200 (2013)
12. Dziemińska, E., Hayashi, A.K.: Auto-ignition and DDT driven by shock wave – boundary layer interaction in oxyhydrogen mixture. Int. J. Hydrogen Energ. **38**, 4185–4193 (2013)

Flame Acceleration and DDT in a Torus Geometry

M. Kuznetsov, J. Yanez, and J. Grune

Introduction

The ignition, flame propagation with a flow ahead of the flame, and shock waves generation with turbulent boundary layer behind the shock are the sequence of principal events leading to the deflagration onset in smooth channels. A specific effect of geometry connected with boundary layer phenomena, turbulent flow generation, and shock–flame interaction might also be of the great interest for the deflagration-to-detonation transition (DDT) phenomena.

An experimental and numerical study of detonation propagation in an annular structure was recently investigated with respect to rotating detonation engines (RDE) [1, 2]. A stability of gaseous detonation propagating in a coaxial cylinder was numerically and experimentally studied for hydrogen/oxygen/nitrogen mixtures. Due to a curvature of the annular tube, the size of cellular pattern along the concave wall is smaller than that along the convex wall. This implies that the detonation wave near the concave wall is convergent and therefore is stronger than that near the divergent convex wall [3]. A possibility of hydrogen combustion and then detonation in annular geometry was numerically analyzed for safety purposes of hydrogen–air mixtures in vacuum vessel of ITER fusion reactor [4]. The process of flame propagation in coaxial annular geometry leads to additional stretching and acceleration of the flame.

A similar problem was experimentally investigated for methane–air mixtures in an open duct with 90° bend [5]. Again, the stretching of the flame and 1.5 times flame velocity increase observed experimentally and numerically modeled. Premixed flame propagation in a closed duct with a 90° bend was experimentally and numerically studied in papers [6, 7]. It was shown that the flame area at the bend part increased 3–4 times. It results in eight times faster propagation of the outer part of the concaved flame. It was also shown that a 90° bend in a long tube had the ability to enhance flame speeds and overpressures and shorten the run-up distance to DDT to a varying degree for a number of gasses [8]. Experimental and numerical results showed that flame at the bend part could behave as a thrust resource for the unburned mixture to generate or induce very complex flow fields which could facilitate unburned material that subsequently affects the flame behavior [9]. This interaction between the flame and the flame-induced flows results in higher dynamic pressure acting forward on the corner portions of the flame front. The presence of a streamwise-oriented vortex pair near the inner surface of the bend and the high-pressure region near the outer surface significantly affects the flame dynamics.

Most of the studies focus on the flame propagation in linear geometry or straight channel combined with a bent part. It was found to have a strong promoting effect of bending of the channel for flame acceleration and then DDT. The main advantage of the annular channel is that the flame should propagate along two surfaces with different curvatures. It additionally can stretch the flame with an increase of the flame surface and in turn the flame propagation velocity. It should also produce a funnel of unburned material along outer surface with larger radius of curvature producing strong turbulent flow within the shear layer. It may lead to additional flame acceleration and DDT. Therefore, the problem of flame acceleration and DDT in an annular geometry is of great interest for many practical applications.

M. Kuznetsov (✉) • J. Yanez
Institute for Nuclear and Energy Technologies, Karlsruhe Institute of Technology, Hermann-von-Helmholtz Platz 1, Eggenstein-Leopoldshafen 76344, Germany
e-mail: kuznetsov@kit.edu

J. Grune
Pro-Science GmbH, Parkstrasse 9, 76275 Ettlingen, Germany

G. Ben-Dor et al. (eds.), *30th International Symposium on Shock Waves 1*, DOI 10.1007/978-3-319-46213-4_65

Experimental Details

The experiments on propagating hydrogen–oxygen flames were carried out in an annular channel of 1 cm thick and 28 cm of outer diameter. The facility, schematically illustrated in Fig. 1, is a closed duct with a ring-shaped channel of 1 cm thick and varied widths of 1, 3, and 5 cm. It comprises 0.084, 0.236, and 0.36 l of the test mixture, respectively. The outer channel diameter of 28 cm was kept constant and limited by the light beam diameter of 30 cm. To be able to vary the channel width, the inner metal disk of 18 cm, 22 cm, and 26 cm in diameter was installed coaxially to outer annular surface. Two glass windows as side walls of 35×35 cm^2 provided an optical access to the test channel. In order to visualize the transparent hydrogen flames and shock waves, a high-speed CCD camera combined with a Z-shape optical schlieren system was used. The Photron Fastcam SA1.1 performance was changed from 25,000 to 300,000 fps. Since the spatial resolution at highest frame rates is limited, a magnified zoomed view of upper part of test channel was applied where the detonation onset appears. The maximum light beam diameter was limited by the size of two parabolic mirrors (∅300 mm).

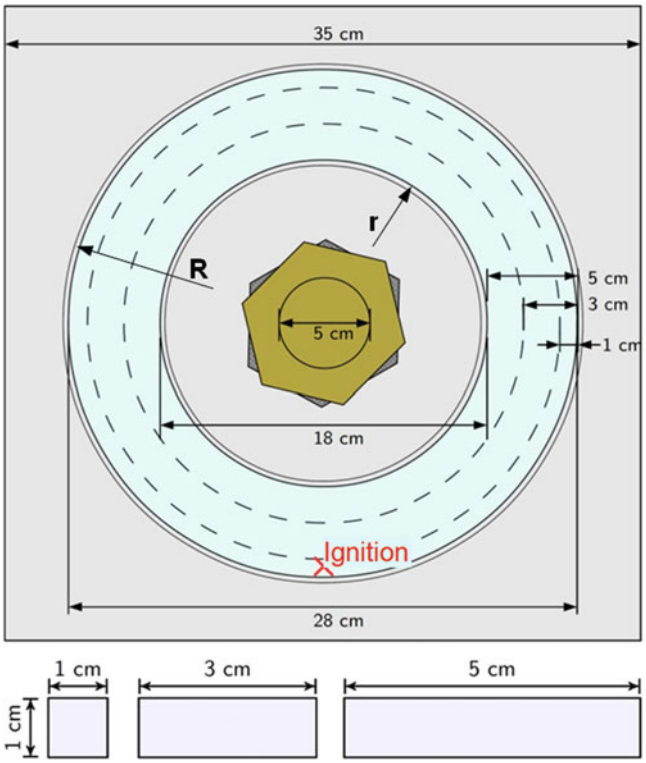

Fig. 1 Experimental facility. Channel cross section (*bottom*)

The test channel was filled with a premixed hydrogen–oxygen mixture of different concentration via a bottom inlet port. Hydrogen concentration was changed in the range 15–85% H_2. The initial pressure and temperature of test mixtures were $p_0 = 1$ bar and $T_0 = 293$ K, respectively. Combustion properties of tested mixtures were calculated using STANJAN and Cantera codes [10, 11] (Table 1). The exposure time of a test mixture in the channel was set about 30 s before ignition to eliminate the effect of initial turbulent motion. The mixture was ignited by a single spark gap located bottom of the channel in 5 mm from the outer surface (in 13.5 cm from the center). The distance between the two electrode tips was set to about 3 mm. The spark energy was less than 10 mJ. The spark energy might be changed for less sensitive mixtures by means of multiple spark repetition with a frequency of 20 kHz.

Experimental Results and Discussions

An experimental study of hydrogen combustion in annular geometry is presented in order to demonstrate an effect of specific annular geometry on flame acceleration and detonation onset. The effects of solid surface curvature depending on width of the channel was investigated for highly reactive hydrogen–oxygen mixtures in the range 15–85 % vol. H_2 with respect to the flame stretching and flame acceleration leading to DDT. Figure 2 shows summary of experimental results as a dependence of maximum combustion velocity

Table 1 Combustion properties of hydrogen–oxygen mixtures

$[H_2]$	Speed of sound			Adiabatic combustion		Detonation Chapman–Jouguet		
	Reactants	Products	Expansion ratio	Temperature	Pressure	Pressure	Velocity	Laminar flame velocity
mol. fr.	c_r, m/s	c_p, m/s	σ	T_b, K	P_b, bar	P_{CJ}, bar	D_{CJ}, m/s	u_{f0}, m/s
0.15	352	715	4.505	1427	5.46	10.47	1416	0.23
0.3	385	926	6.918	2362	8.01	15.60	1859	2.93
0.4	413	1028	7.677	2705	8.79	17.16	2084	5.23
0.5	448	1139	8.112	2912	9.29	18.18	2325	7.32
0.6	494	1274	8.394	3041	9.65	18.89	2612	8.98
0.667	523	1384	8.498	3076	9.79	19.18	2843	9.69
0.7	557	1447	8.504	3069	9.80	19.21	2972	9.85
0.8	654	1669	8.054	2827	9.34	18.29	3410	8.68
0.85	725	1799	7.300	2490	8.59	16.77	3638	6.60

against hydrogen concentration. Two thresholds as dashed lines corresponding to speed of sound in reactants and theoretical Chapman–Jouguet velocity indicate the capability of test mixtures to accelerate to sonic flame and detonation. The highly reactive mixtures with hydrogen concentration 60 ± 20 % were found to be able to accelerate to sonic velocity or even to detonate. The mixtures beyond the range 60 ± 20 % of hydrogen are not capable to accelerate to speed of sound.

The advantage of the annular geometry is that since the flame preferentially propagates along the solid surface due to an effect of boundary layer, it may have an additional stretching with significant flame area increase because of different curvature of coaxial outer and inner annular solid surfaces. The flame initially develops as a sphere and then as a "finger" flame (Fig. 3). Thanks to the different inner and outer channel curvature, the additional flame stretching leads to flame instability and dramatic increase of flame surface, three to four times according to the data [6, 7], which in turn results in rapid flame acceleration compared to a linear geometry. In general, the flame area increases as higher as greater the difference of radii of curvature r and R for internal and outer annular surfaces of the torus structure (Fig. 1).

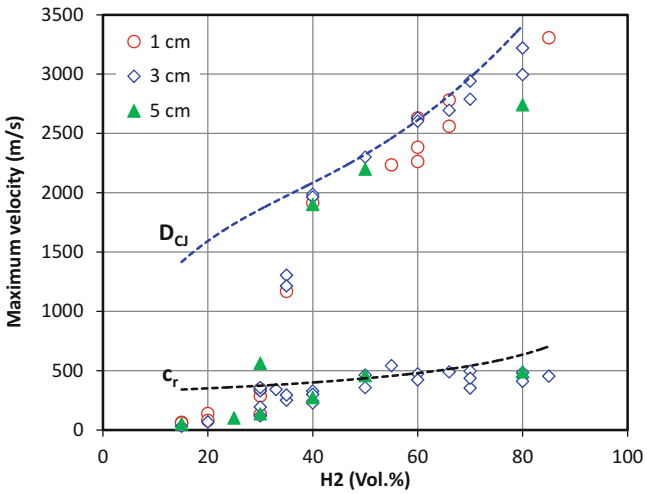

Fig. 2 Maximum velocity vs. hydrogen concentration for different widths of the channel

According to the papers [8, 9], an additional factor promoting the flame acceleration and DDT is the co-flow of nonreacting material in a deep funnel between the flame surface and external wall producing a turbulent boundary layer within the pre-compressed and preheated zone where the flame can efficiently accelerate to sonic speed and then detonate. Figure 3 shows the positions of the flame front for lean and rich hydrogen–oxygen mixtures in three different channels of 1, 3, and 5 cm width starting from the bottom ignition position. The flame surfaces were captured at five different moments and put together to compare the evolution of the flame surface. A semispherical flame shape in the beginning transforms to a wedge shape with a leading point at the internal surface. At the middle stage, the flame surface increases several times with formation of very deep funnel of 15–20 cm at the outer annular wall of the channel. One can see an existence of a small-scale cell due to thermodiffusion instability for mixtures with Lewis number Le $<$ 1 (Fig. 3c) and larger-scale cell modes of Landau–Darrieus instability for the mixture with Le $>$ 1 (Fig. 3 a, b).

As for wrinkled flames, the visible flame velocity u_f is proportional to the actual flame area A_f

$$u_f = \frac{A_f}{A_0} u_{f0} \tag{1}$$

where A_0 is the channel cross section and u_{f0} is the fundamental flame velocity for planar flame. So that the flame may accelerate very efficiently even to sonic velocity due to the stretching along the internal surface of smaller radius with formation of fast propagating "knife" structure (Fig. 4).

A flow ahead the flame generates a turbulent boundary layer in vicinity of solid surface. Due to the increasing pressure and temperature of unreacted material, the flame may rapidly be accelerated within the boundary layer with formation of a "knife" structure of the flame propagating

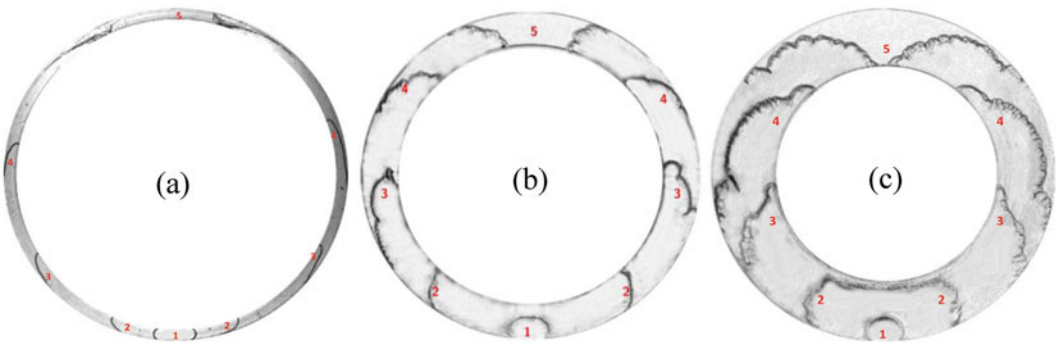

Fig. 3 Flame dynamics in torus geometry: (**a**) 1-cm channel, 50 % vol. H_2; (**b**) 3-cm channel, 80 % vol. H_2; (**c**) 5-cm channel, 50 %vol. H_2 mixture

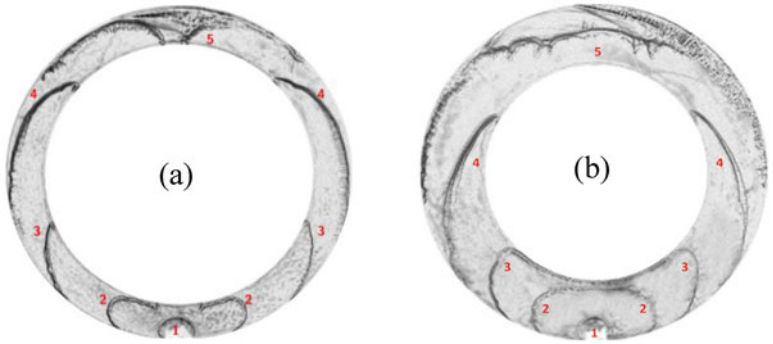

Fig. 4 "Frozen" flame positions for flame acceleration and DDT experiments in a torus geometry: (**a**) 3-cm channel, 70 % vol. H_2; (**b**) 5-cm channel, 50 %vol. H_2 mixture

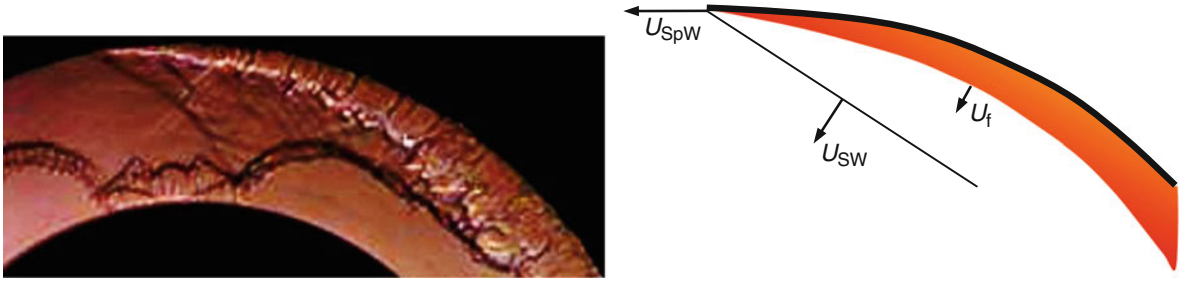

Fig. 5 Abrupt flame acceleration as a "knife" structure: (**a**) 5-cm channel, 40 %vol. H_2 mixture; (**b**) a scheme of spontaneous reaction wave propagation U_{SpW}

with a velocity of the order of 2000 m/s, approaching to CJ detonation velocity (Fig. 3). Our first hypothesis was that the flame propagates as a quasi-stationary "spontaneous wave" in Zeldovich terminology governing by the gradient of induction time due to the elevated temperature within a viscous boundary layer [12]. In a linear geometry, the boundary layer thickness δ at a distance x behind a precursor shock wave might be evaluated as follows [13]:

$$\delta = 0.22x^{0.8}\left(\frac{\nu}{U_s}\right)^{0.2} \tag{2}$$

where ν is the kinematic viscosity and U_s is the shock wave velocity. In our case, it gives the values from 1.2 to 4.5 mm for distances 10 and 50 cm from precursor shock wave. Final flame acceleration and DDT in a torus geometry appeared approaching to complete combustion of the mixture when the state of unburned material is close to adiabatic combustion pressure. For instance, for stoichiometric mixture, the preignition conditions Pi = 9.7 bar and Ti = 562 K are still too low to ignite the mixture within a proper time because the induction time is order of 200 s. Hydraulic resistance of the flow may lead to an additional temperature increase proportional to the Mach number M of the flow:

$$\Delta T \propto T_0\left(1 + \tfrac{1}{2}(\gamma - 1)\cdot M^2\right) \tag{3}$$

where γ is the adiabatic coefficient and T_0 is the initial temperature. Still, even for precursor shock wave with a strength of $M = 1.5$, induction time $\tau_i = 4.2$ s is still too long to provide spontaneous wave velocity leading to detonation. Even for $M = 2$, the induction time $\tau_i = 4.3$ ms does not provide the proper value for spontaneous wave velocity within a boundary layer thickness $\Delta x = 4.5$ mm:

$$D_{sp} = \left|\frac{d\tau_i}{dx}\right|^{-1} \approx \left|\frac{\tau_i(T_{sh})}{\Delta x}\right|^{-1} \approx 1 \text{ m/s} \tag{4}$$

This means it should be another mechanism of the flame acceleration leading to DDT. The alternative mechanism leading to abrupt flame acceleration as a "knife" structure could be a Mach reflection of precursor shock wave produced by the stretched flame front within a funnel structure. Figure 5 shows a magnified view and a scheme of a stationary Mach reflection according to papers [14, 15], propagating with Chapman–Jouguet velocity along the channel. Due to the Mach reflection, the mixture is ignited and a complex of reaction zone and an oblique shock wave propagates with characteristic velocity $U_{SpW} = 1900$ m/s ($M = 4.6$); a tangential shock velocity $U_{SW} = 630$ m/s ($M = 1.52$) and a flame velocity $U_f = 200$–230 m/s were measured for 40 % H_2/60 % O_2 mixture. Independent of the leading point velocity almost equal to $D_{CJ} = 2084$ m/s, the detonation onset did not occur because it was a local ignition of the mixture due to Mach reflection of relatively weak precursor shock wave ($M = 1.5$) which is not able to support a stationary detonation structure.

Similar behavior of accelerating flame as a "knife" structure occurred for mixtures in the range of 50–80 % H2 with a

difference that finally detonation onset occurred in channels of 1 and 3 cm width. All experimental data on characteristic maximum flame velocity for different hydrogen–oxygen mixtures are summarized in Fig. 2.

Conclusions

Very specific effects of torus geometry connected with boundary layer phenomena and Mach reflection are analyzed in current work. The effect of channel width from 1 to 5 cm on flame acceleration and an efficiency of DDT are also investigated. It was also demonstrated that detonation preconditioning history, starting from the ignition, plays an important role on the success of the detonation transition. Two mechanisms of very specific flame acceleration as a "knife" structure were proposed. For instance, a recently developed concept of flame acceleration within a boundary leading to detonation transition was compared against a mechanism of abrupt flame acceleration due to Mach reflection of advanced shock waves in annular structure. The main idea of this work was to accumulate still unresolved key aspects of the DDT mechanism to be analyzed experimentally and theoretically for the nearest future.

References

1. Kindracki, J., Wolanski, P., Gut, Z.: Experimental research on the rotating detonation in gaseous fuels-oxygen mixtures. J. Shock Waves **21**(2), 75–84 (2011)
2. Hishida, M., Fujiwara, T., Wolanski, P.: Fundamentals of rotating detonations. J. Shock Waves **19**(1), 1–10 (2009)
3. Pan, Z., Fan, B., Zhang, X., Gui, M., Dong, G.: Wavelet pattern and self-sustained mechanism of gaseous detonation rotating in a coaxial cylinder. Comb. Flame **158**(11), 2220–2228 (2011)
4. Redlinger, R., et al.: 3D-analysis of an ITER accident scenario. Fusion Eng. Des. **75–79**, 1233–1236 (2005)
5. Sato, K., Sakai, Y., Chiga, M.: Flame propagation along 90° bend in an open duct. Symp. Combust. **26**(1), 931–937 (1996)
6. Xiao, H., He, X., Wang, Q., Sun, J.: Experimental and numerical study of premixed flame propagation in a closed duct with a 90° curved section. Int. J. Heat Mass Transf. **66**, 818–822 (2013)
7. Xiao, H., He, X., Duan, Q., Luo, X., Sun, J.: An investigation of premixed flame propagation in a closed combustion duct with a 90° bend. Appl. Energy **134**, 248–256 (2014)
8. Blanchard, R., Arndt, D., Grätz, R., Poli, M., Scheider, S.: Explosions in closed pipes containing baffles and 90 degree bends. J. Loss Prev. Proc. Ind. **23**(2), 253–259 (2010)
9. Zhou, B., Sobiesiak, A., Quan, P.: *Flame behavior and flame-induced flow in a closed rectangular duct with a 90° bend*. Int. J. Therm. Sci. **45**(5), 457–474 (2006)
10. Reynolds W.C.: The element potential method for chemical equilibrium analysis: implementation in the interactive program STANJAN Version 3. Dept. of Mechanical Engineering, Stanford University, Palo Alto, California, January 1986 (1986)
11. Goodwin, D.G.: Cantera User's Guide. California Institute of Technology, Pasadena, CA (2001)
12. Zeldovich, Y.B., Librovich, V.B., Makhviladze, G.M., Sivashinsky, G.I.: On the development of detonation in a non-uniformly preheated gas. Astronautica Acta **15**, 313–321 (1970)
13. Fay, J.A.: Two-dimensional gaseous detonations: velocity deficit. Phys. Fluids **2**, 283–289 (1959)
14. Ben-Dor, G.: Steady, pseudo-steady and unsteady shock wave reflections. Prog. Aerospace Sci. **25**(4), 329–412 (1988)
15. Hornung, H.: Regular and Mach reflection of shock waves. Annu. Rev. Fluid Mech. **18**, 33–58 (1986)

Unconfined Hybrid Detonation in Gas–Particle Flow

F. Zhang, A. Yoshinaka, and R.C. Ripley

Introduction

Fine aluminum (Al) particles suspended in air are insensitive to detonation, with a detonation cell size of larger than 0.5 m [1]. Rapid Al combustion, however, is able to support so-called hybrid detonation when mixed with a reactive gas mixture. Veyssiere reported the first laboratory observation of a detonation wave comprising "double shocks" when Al particles were suspended in a lean reactive gas mixture in a tube [2]. In the same time period, Afanasieva et al. theoretically postulated the existence of double-shock detonations from two successive energy releases [3]. Recent experiments in an 80 mm diameter by 10 m long tube provided additional evidence supporting the existence of a number of self-sustained propagation of hybrid detonation modes for Al particles suspended in a detonable gas mixture [1]. The double-shock detonation modes were explained as weak detonation solutions of reactive gases followed by particle reaction with different time delays and energy release rates. In the present paper, studies of hybrid detonation were extended to unconfined free field conditions in order to investigate its self-sustained propagation without the influence of tube confinement.

Experimental Results

Theoretically, a cloud size optimized for detonation performance is determined by its proximity to a stoichiometric fuel–air ratio. In practice, this will be limited by fuel physical properties and a mixing process in air. In the present research, a cylindrical charge was used, consisting of a small C4 burster explosive packed in a central PVC tube surrounded by an annulus of aluminum particles saturated with a C–H–N–O liquid fuel. The Al liquid fuel mass ranged from 170 to 1000 kg, contained in a thin-walled polyethylene cylindrical case with a length-to-diameter ratio of 2:1. The C–H–N–O liquid fuel was characterized by a mean detonation cell size of 33 mm in its stoichiometric vapor–air mixture as determined from laboratory detonation tube experiments. Figure 1 displays the dispersal process of a 170 kg Al particle-liquid fuel into a suspension in air above a 15.24 × 15.24 m^2 concrete pad. The pad has 1 m interval parallel grooves to permit installation of ground-level pressure transducers.

Detonation of the C4 burster explosive disperses the Al liquid fuel spray in air to a radius of up to 11–12 m and a height of 3.5–4 m. The suspension touching the ground as shown in the last photograph represents the moment at which the mixture is nearly stoichiometric. Coherent particle jets are emerging from the cylindrical hybrid fuel cloud later in time. When compared to the pure liquid or dry powder alone, the dispersal radius of the hybrid mixture was considerably larger due to the effect of added liquid mass on the solid particle jets and their interactions. An increase in Al particle size further increased the dispersal radius in later times due to particle inertia. The mechanisms responsible for the particle jetting instabilities in explosive dispersal remain a challenging topic [4, 5].

Detonation of the Al-liquid spray-air cloud was then initiated by a secondary C4 charge near the center of the cloud. The hybrid detonation wave phenomena were recorded using high-speed video cameras, pyrometry sensors for the particle temperature, and Endevco piezoresistive pressure transducers radially located on the ground from the secondary charge, toward the front edge of the concrete pad. Detonation cell sizes were registered using Al smoked foil installed on the ground 6 m from the secondary charge and, in certain cases, vertically along the flow streamline.

F. Zhang (✉) • A. Yoshinaka
Defence Research and Development Canada, PO Box 4000 Station Main, Medicine Hat, AB, CanadaT1A 8K6
e-mail: fan.zhang@drdc-rddc.gc.ca

R.C. Ripley
Martec Ltd., 1888 Brunswick St. Suite 400, Halifax, NS, CanadaB3J 3J8

G. Ben-Dor et al. (eds.), *30th International Symposium on Shock Waves 1*, DOI 10.1007/978-3-319-46213-4_66

Fig. 1 Time sequence of a 170 kg Al particle-liquid fuel cylindrical dispersal into air above a 15.24 × 15.24 m^2 concrete pad (#U08178A)

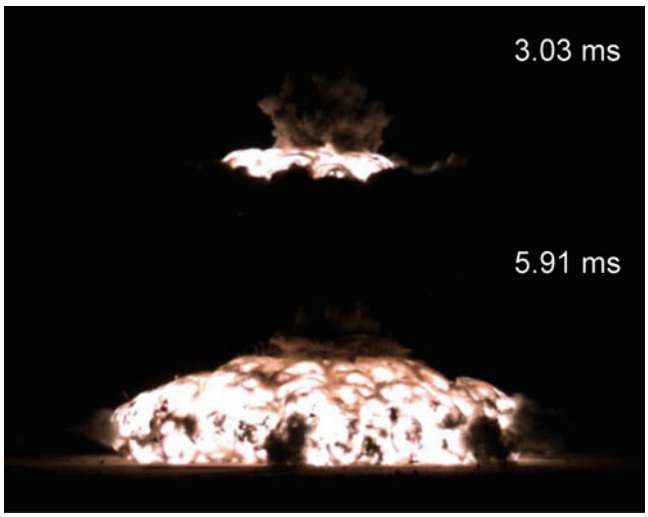

Fig. 2 Macro-cell structure in the detonation front (#U08178A)

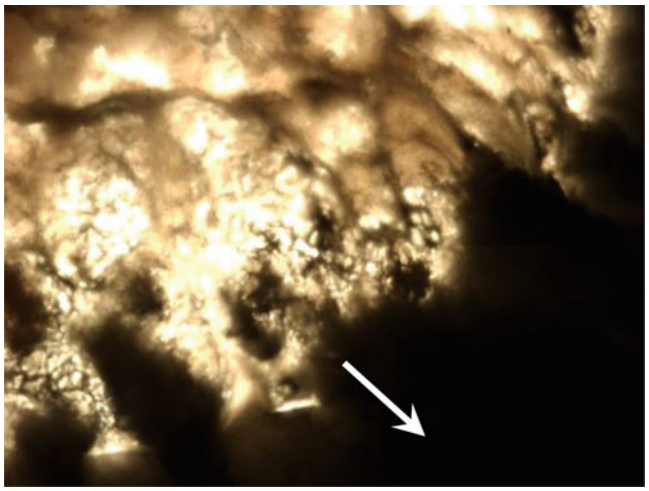

Fig. 3 Fine cellular structure in a quarter of circular detonation front (#U09266A)

Detonation with Small Al Particles

Figure 2 shows high-speed photographs (6600 frames/s) of the flame surface as the hybrid detonation front propagating cylindrically outward. It displays a macro-cell structure about 0.6–0.7 m in each scale, indicating the interactions of macroscopic transverse waves generated by the heat release likely from the local particle concentrations depicted by the jets in Fig. 1. Embedded in this macroscopic nonuniform structure, the detonation intrinsically exhibits a fine cellular structure in the cylindrical wave front. The photograph in Fig. 3 provides a close overhead view of the fine cellular structure for a quarter of the cylindrical detonation front ($R \approx 5$ m) propagating into the dark reactant cloud. The detonation is initiated in the cylindrical center at the top left corner of the photograph. This detonation cell size is about 25 mm in average as recorded on the ground and side smoke foils shown in Fig. 4.

Detonation pressure histories along the hybrid cloud radius are given in Fig. 5a, with an average propagation velocity of 1700 m/s and a maximum deviation of ±300 m/s. The jet-induced local concentration nonuniformity thus manifests itself by the fluctuation in detonation pressure and velocity. The pressure records suggest a single shock structure of hybrid detonation front for the small Al particles. This is consistent with the smaller hybrid detonation cell size of 25 mm, with respect to the 33 mm cell size of the ideal vapor–air mixture of the baseline liquid fuel. These facts suggest that the Al particles react considerably within the liquid vapor reaction zone and therefore enhance the vapor detonation.

Detonation with Large Al Particles

When the Al particle size was sufficiently increased, the particles behaved inertly within the liquid vapor reaction zone, and particle heat release took place behind this zone. Consequently, the detonation cell size was increased to 40–50 mm, as given in the ground smoke foil record. Figure 5b provides the detonation pressure histories along the hybrid cloud radius, indicating that a double-shock structure develops over large radii due to the two heat releases, namely, from the liquid vapor detonation and, with a time delay, the particle combustion behind the vapor detonation

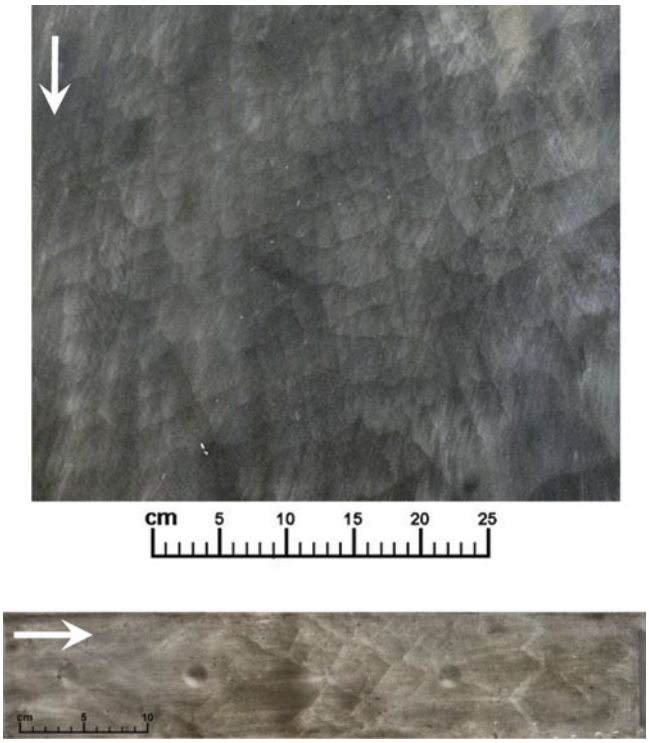

Fig. 4 Ground (upper) and side (lower) smoke foil records of detonation cellular structure for small Al particle liquid fuel (#U09238A)

zone. Owing to temperature differences between the combustion from the liquid vapor and that from the Al particles, it is possible to distinguish this wave structure from distant pyrometric temperature measurements, as shown in Fig. 6. The temperature at the first front (at the beginning of the temperature curve) is 2300–2400 K and reaches 2700–2800 K at the second peak with a time delay of about 1 ms. This is consistent with the time delay between the two shocks in the pressure histories displayed in Fig. 5b.

It was experimentally found that the spray vapor–air detonation alone is insufficient to initiate combustion of large Al particles rapidly enough to form a secondary shock. A 4 kg secondary C4 charge was used for rapid initiation of these particles in the vapor–air detonation flow as shown in Fig. 5b. For a C4 initiation charge mass of 1 kg or less, a distinguishable secondary shock was not observed.

Discussion

Critical Initiation Charge Mass for Double-Shock Hybrid Detonation

In order to verify the necessity of a large charge mass for initiating an unconfined double-shock hybrid detonation, one-dimensional, spherical, unsteady numerical simulations using a two-phase fluid dynamics model were conducted for

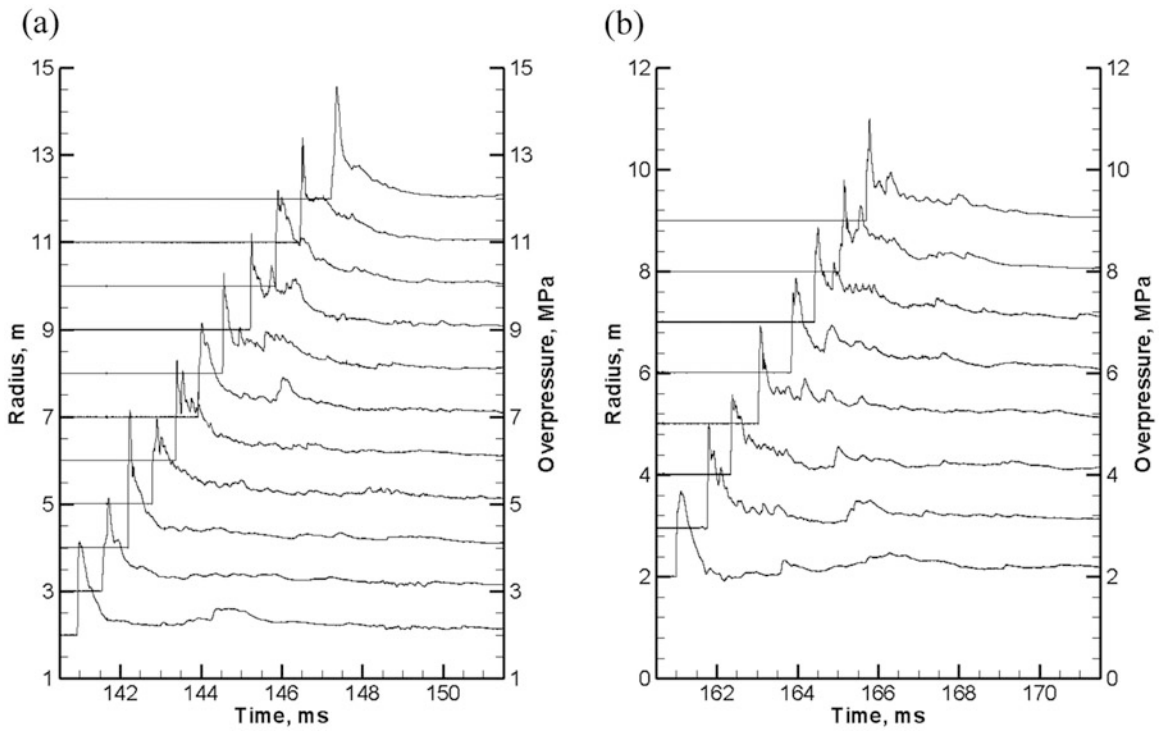

Fig. 5 Detonation pressures along the radius on the ground for: (**a**) small Al particle liquid fuel (#U08178A), and (**b**) large Al particle liquid fuel (#U09229A)

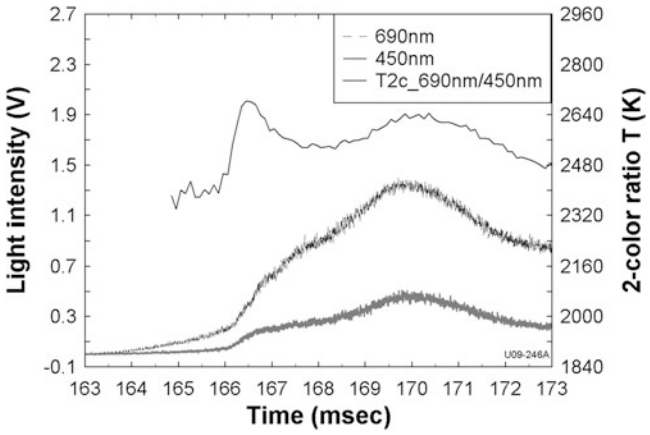

Fig. 6 Temperature from pyrometry remotely facing hybrid detonation front of large Al liquid fuel–air mixture

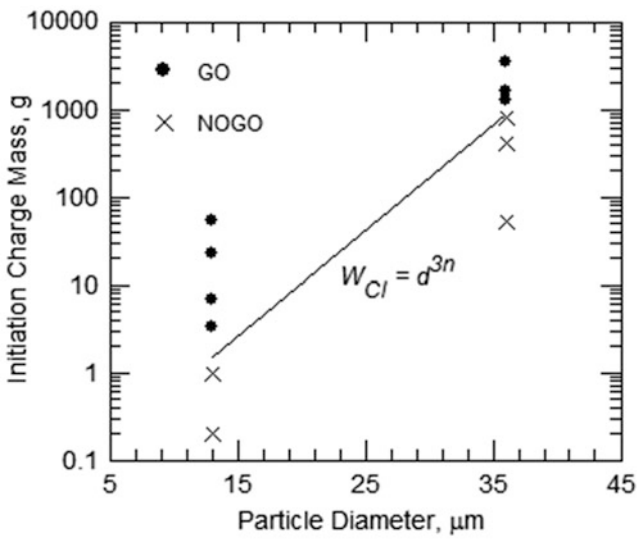

Fig. 7 Dependence of initiation charge mass for second shock formation on Al particle diameter

a premixed ideal hybrid system of Al particles and C_2H_2–air mixture [6], the latter with an equivalence ratio of $\phi = 0.8$. In all the calculations, the mesh had a cell size of 50 μm. The spherical cloud was initiated at the center by explosion of a spherical C4 explosive burster charge. It is clear that the experimental hybrid detonation of Al liquid fuel dispersed in air is a nonuniform, transient, three-dimensional flow problem. The 1D simulation is only used to display the concept.

For small Al particles whose energy release rate was sufficiently high, the long-time asymptotic numerical solution yielded a steady hybrid detonation wave with a single shock structure, in which the particle reaction produced a compression wave within the gas reaction zone to increase detonation velocity and pressure. As the energy release rate of Al particles decreased by increasing particle size to 13 μm, a weak detonation solution with a double-shock structure was developed using an initiation charge mass of $W_I = 1$ g. The second shock arose downstream at the location of a minimum in the pressure profile at which a so-called generalized CJ locus appeared. When further decreasing the energy release rate by using 36 μm Al particles, the second shock was developed only when increasing the initiation charge to $W_I = 1230$ g; the wave structure developed over a long distance asymptotically toward a double-shock weak detonation solution, where the second shock arose behind the generalized CJ locus with an interval of 0.81 m from the first shock near a propagation distance of 19 m. The second shock was not initiated with $W_I = 800$ g; instead, only a compression wave was developed far behind the detonation front.

The phenomena obtained from the spherical numerical simulations were in agreement with that analyzed in the planar geometry [1]. In the spherical case, the source terms associated with the area expanding rate, $1/r^2$, describe the gas-phase mass momentum and energy losses. This further augments the necessary conditions for a weak detonation solution in addition to the losses due to momentum and energy transfer to the particles within the gas detonation zone. As shown in the above simulations, the gaseous fuel–air detonation alone cannot initiate combustion of the large Al particles quickly enough to form the secondary shock until a 1230 g C4 explosive charge is used for initiation. Figure 7 summarizes the numerical results to determine a critical charge mass for initiating the second shock in the spherical detonation front of the mixture of lean C_2H_2–air and Al particles. The critical C4 charge mass, W_{CI}, required to initiate the secondary shock appears to scale with particle diameter through [6]

$$W_{CI} \sim d_p^{3n} \tag{1}$$

where n approaches 2 for larger Al particles. Since the detonation critical initiation charge mass and detonation cell size, λ, have been experimentally correlated with $W_I \sim \lambda^3$ and $\lambda \sim d_p^n$ in reference 1, the relationship [1] seems reasonable.

Particle Jetting Instabilities

Particle jetting in explosive dispersal may originate near the boundaries between the central explosive burster, shock-dispersed media, and outer edge of the charge, where the various interfaces may entail a thin casing material that fragments and influences the jetting instabilities. The fact that particle jets also form in the absence of an outer casing, both in experiments and landmine or shallow underwater explosions, indicates that an interior instability might be the critical condition.

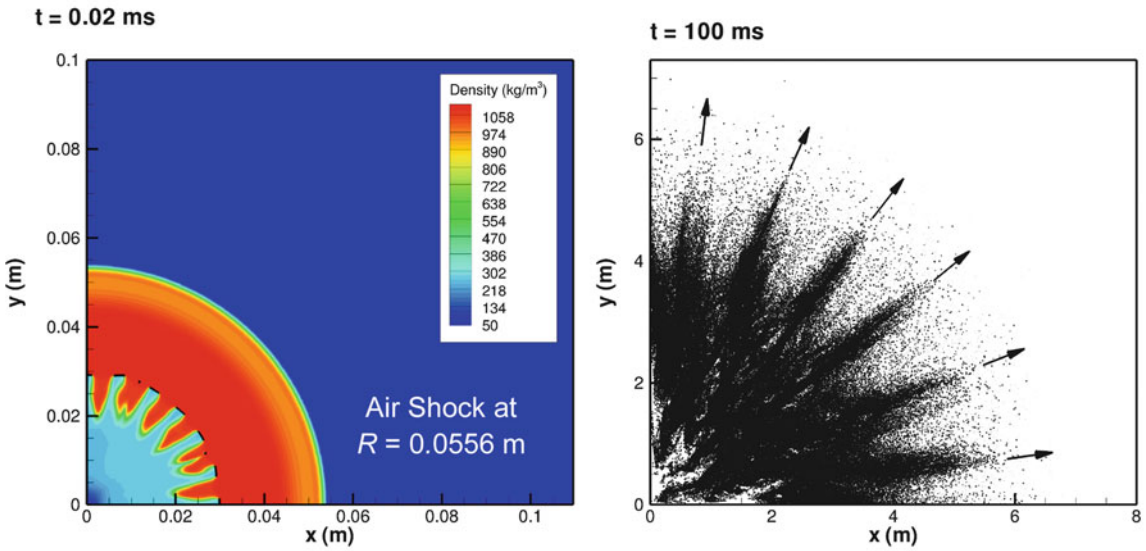

Fig. 8 Cylindrical water (0.1 m in diameter) dispersal, breakup, and jet formation using a 0.02 m diameter TNT explosive burster with its thin steel casing pre-fragmented

Sufficient details can be provided through large-scale experiments in distinguishing various jetting instability phenomena and their associated origins. Figure 1 has shown a dual jetting structure from dispersal of the hybrid mixture, where the outer boundary introduces minor surface instabilities leading to micro-jets, the edge of which is overtaken by macroscopic jet structures later in time. Similar phenomena were also observed in bulk compressible liquid dispersal by a central cylindrical explosive burster [5]. Figure 8 provides a 2D multiphase modeling example of bulk liquid dispersal, indicating that the macro-jet structure is triggered by the instabilities associated with inner burster casing fragmentation. In this case, the number of macro-jets is dictated by the main fragment number of the inner casing. In a hybrid particulate mixture, however, the interior perturbation length scale can also be generated by shock-compacted or shock-consolidated agglomerates of solid particles, originating from a hydrodynamic multiphase Richtmyer–Meshkov instability as the detonation shock enters the dispersing media. The particle flow adds the additional complexity of dissipation mechanisms including nonelastic collision, compaction, and agglomeration to affect the length scale of macro-jetting instability and its growth. The mechanism for the formation of this macro-jet structure requires further investigation in both theory and numerical modeling.

Conclusion

Hybrid detonation in an unconfined Al-liquid fuel spray suspended in air was demonstrated in experiments over a range of fuel masses from 170 to 1000 kg. For small Al-particles, the particle energy release started within the liquid vapor detonation zone and thus reduced the detonation cell size and enhanced the detonation pressure. In the case of large Al particles, the particle energy release was behind the liquid vapor detonation zone to form a second shock following the detonation shock front (a double-shock structure). The phenomena were in agreement with that observed in the previous confined tube studies.

A large initiation charge mass or energy, which can be significantly higher than that of the baseline gas-phase detonation, is required to initiate the hybrid detonation, particularly for the rapid combustion of large particles to form a double-shock structure. One-dimensional spherical numerical multiphase simulations indicated that a double-shock weak detonation solution can be realized only when the initiation charge mass is above a large critical mass at which the rate of Al energy release can support the formation and subsequent propagation of the second shock. This critical charge mass seems to be proportional to a power of the Al particle diameter. The mechanism for the formation of particle macro-jet structures from explosive dispersal of a particulate mixture remains challenging for future studies.

References

1. Zhang, F.: Detonation of gas-particle flow. In: Zhang, F. (ed.) Heterogeneous detonation, pp. 87–168. Springer, Berlin, Heidelberg (2009)
2. Veyssiere, B.: Double-front detonations in gas-solid particles mixtures. Prog. Astronaut. Aeronaut. **94**, 264–276 (1984)
3. Afanasieva, L.A., Levin, V.A., Tunik, Y.V.: Multifront combustion of two-phase media. Prog. Astronaut. Aeronaut. **87**, 394–413 (1983)

4. Zhang, F., Ripley, R.C., Yoshinaka, A., Findlay, C.R., Anderson, J., von Rosen, B.: Large-scale spray detonation and related particle jetting instability phenomenon. Shock Waves **25**, 239–254 (2015)
5. Xu, T., Lien, F.-S., Ji, H., Zhang, F.: Formation of particle jetting in a cylindrical shock tube. Shock Waves **24**, 537–553 (2013)
6. Zhang, F., Yoshinaka, A., Ripley, R.: Hybrid detonation waves in metalized explosive mixtures. Proceedings of the14th International Detonation Symposium, Office of Naval Research, Arlington, VA, pp. 714–723 (2011)

Numerical Simulation of Combustion Process for Two-Phase Fuel Flows Related to Pulse Detonation Engines

Van Bo Nguyen, Li Jiun-Ming, Teo Chiang Juay, and Boo-Cheong Khoo

Introduction

During the detonation combustion process, the liquid fuel is injected to the combustion chamber and mixed with airflows. Liquid droplet then evaporates to the ambient due to the high pressure and temperature inside the combustion chamber. The droplet might or might not evaporate completely before starting detonation process. If all liquid droplets are completely evaporated, the detonation process is so-called gaseous detonation process. When liquid droplets are not completely evaporated, the remaining liquid droplets will affect to detonation combustion process. The physical and chemical phenomena in the detonation combustion will be much more complicated due to the effect of droplet size on detonation parameters, poor or too rich fuel-air mixing, complex reaction zone structure, etc. [1]. It is even more difficult to determine the interaction between the two-phase fuel and three-dimensional structure of detonation waves. However, the high energy density of liquid fuel compared to gaseous fuel is an attractive argument in pulse detonation engines development. It therefore can reduce the mass, drag, and structure of storage tank. This is greatly important in aerospace applications. Hence, it is necessary to study and understand physical and chemical insights in the detonation process to improve the performance of pulse detonation engines.

The effects of liquid fuel droplets in the detonation chamber are really complicated. Different detonation velocities were observed in the experiment, which were caused by different droplet sizes [2–4]. Dabora et al. [2] found that detonation propagation velocity in liquid fuel mixtures was in general lower than CJ velocity when the droplet size was accounted. The smallest velocity deficit observed was 2–10 % for droplet size of dp0 = 290 μm and 940 μm, while the largest velocity deficit is about 30–35 % for droplet size of 2600 μm. For a very small droplet size (2 μm), Bowen et al. [4] found self-sustained detonations in decane fogs at near CJ velocity. Bull et al. [5] observed that the velocity deficit increases for larger droplet size, while high vapor pressure fuels detonated relatively easily. They also concluded that a certain quantity of fuel prior to ignition might be required for self-sustained detonation for low vapor pressure. In the study of Brophy and his co-workers [6], the mixture was characterized with respect to droplet size, temperature, and pre-evaporation. They found the near CJ detonation velocity of all fuels for droplet size of dp0 = 11 μm. In addition, Knappe and Edwards [7] performed experiments to study the detonation spray in a long tube. In their study, the effects of the droplet size on detonation velocity were observed to be relatively minor in oxygen mixture. For theoretical and numerical study, William [8] reported a 1D theoretical model of spray detonation. He concluded that the size of burning region was order of a meter as the droplet spray is about 60 μm. Borisov et al. [9] considered the effects of droplet stripping and deformation in liquid-fueled detonations. They found that stripping, shattering, and deformation can be negligible when dp0 < 20 μm. However, those effects resulted in detonation propagating at near CJ values, and a significant velocity deficit was predicted at 50 % when droplet diameter is greater than 2000 μm. Chang and Kailasanath [10] showed that the attenuation shockwaves caused by dispersed phase are increased when droplets break up and evaporation effects are included. Cheatham and Kailasanath [11] showed that detonation structure is varied with initial droplet size and the amount of initial fuel vapor. They also found that smaller droplet size, higher level of heating, and pre-evaporation are shown

V.B. Nguyen (✉) • L. Jiun-Ming • B.-C. Khoo
Temasek Laboratories, National University of Singapore, Singapore 117411, Singapore
e-mail: tslngvb@nus.edu.sg

T.C. Juay
Department of Mechanical Engineering, National University of Singapore, Block EA, #07-08, 9 Engineering Drive 1, Singapore 119260, Singapore

G. Ben-Dor et al. (eds.), *30th International Symposium on Shock Waves 1*, DOI 10.1007/978-3-319-46213-4_67

to enhance quickly transition to sustained self-propagation of detonation. It can be seen that the explanations are ranging from many different aspects from frictional, heat transfer loss to incomplete reaction or reaction beyond the CJ plane. However, the effects of droplet size still on detonation parameters still remain place for investigation.

In this paper, we perform numerical simulations for two-phase fuel flows in detonation combustion to study the detonation propagation process in the pre-evaporated fuel to understand the physical and chemical insights. In which the droplet fuel might be completely evaporated or might not, will be study through the simulations. This paper is presented as follows: Sect. 2 describes the mathematical and chemistry model, Sect. 3 is numerical method and validations, Sect. 4 shows preliminary results and discussions, and Sect. 5 is conclusion of this paper.

Mathematical and Chemistry Model

In this paper, the multiphase flows of liquid fuel droplets and gas mixture are modeled for detonation process and numerically simulated by Lagrangian–Eulerian approaches. In which, the liquid fuel droplet equations are expressed in Lagrangian frame of references, while the gas-phase equations are described in Eulerian frame of references. The interaction between liquid droplets and gas phase is represented through the two-way coupling interactions. The following is the mathematical model for the gas phase, as tracking for liquid droplets, and chemical kinetic model for Jet-A fuel:

Gas-phase equations can be expressed as

$$\frac{\partial \rho}{\partial t} + \nabla .\rho \mathrm{v} = \mathrm{S}_{\rho} \tag{1}$$

$$\frac{\partial \rho_i}{\partial t} + \nabla .\rho_i \mathrm{v} = \mathrm{S}_i \tag{2}$$

$$\frac{\partial \rho \mathrm{v}}{\partial t} + \nabla .\rho \mathrm{vv} \ + \nabla p = S_D + S_v \tag{3}$$

$$\frac{\partial E}{\partial t} + \nabla .E\mathrm{v} \ + \nabla .p\mathrm{v} = S_{Ev} + qS_{\Omega} \tag{4}$$

In this expressions, ρ is the density of the mixture and v is velocity of the mixture. $\rho_i = \rho Y_i$ is density of the specie ith in the gas mixture. $E = e + 1/2|V|^2$ is total energy of the gas system, in which the internal energy $e = p/(\gamma - 1)$. p is the pressure and $\gamma = c_p/c_v$ is the ratio of specific heat. The source terms that appear at the right-hand side are defined as the following form: $S_{\rho} = \dot{M}$ represents for the additional mass added to the gas phase due to evaporation of the liquid droplet. $S_D = -MdV/dt$ represents for the drag on the gas phase caused by droplet liquid, $S_v = \dot{M}V$ is momentum transfer to the gas phase due to the droplet, and $S_E = -MV.dV/dt - \dot{M}\,c_{pg}\left(T_g - T_s\right)/B$ is energy source term that accounts for the work done by the droplets on the gas phase and the heat flux. $S_{Ev} = \dot{M}\,h_{v,f} + 1/2\dot{M}\,|V|^2$ accounts for enthalpy and kinetic energy addition to the gas phase due to the newly vapor phase. M and $\dot{M}$ denote the local droplet mass per unit volume and local droplet mass vaporization rate per unit volume, respectively.

Assume that the volume fraction of the liquid fuel droplet is sufficiently small. Therefore, the particle–particle interaction can be neglected. Equations governing the ith droplet feature (velocity ($V_{\mathrm{i}}(t)$), position ($X_{\mathrm{i}}(t)$), temperature ($T_{\mathrm{si}}(t)$), and diameter ($d_{\mathrm{pi}}(t)$)) are expressed by

$$\frac{\mathrm{d}V_i}{\mathrm{d}t} = \frac{3}{4}\frac{\rho_g}{\rho_l}\frac{C_{Di}}{d_{pi}}|v - V_i|(v - V_i) \tag{5}$$

$$\frac{\mathrm{d}X_i}{\mathrm{d}t} = V_i(t) \tag{6}$$

$$m_i c_l \frac{\mathrm{d}T_{si}}{\mathrm{d}t} = \frac{\dot{m}_i c_{\mathrm{pg}}}{B_i}\left(T_{\mathrm{g}} - T_{\mathrm{si}}\right) - \dot{m}_i L \tag{7}$$

$$\frac{\mathrm{d}d_{pi}^2}{\mathrm{d}t} = -\frac{8\lambda}{\rho_l c_{\mathrm{pg}}}\ln(1 - B_i)F_{\mathrm{conv}} \tag{8}$$

where ρ_{g}, T_{g}, and c_{pg} are density, temperature, and specific heat of local gas phase surrounded the droplet ith, respectively. ρ_l is density of the liquid fuel droplet. C_{Di} is the drag coefficient. B_i is evaporation rate (or transfer number). $\mathrm{F}_{\mathrm{conv}}$ is the correction of convective flow effect.

For the chemistry model, the reduced model with ten steps of Jet-A fuel oxidation is employed. The reaction steps are shown in Table 1. The Arrhenius rate coefficient can be expressed in the form: $k = A(T/T_0)^n \exp(-E/RT)$. In which, A is pre-exponential factor, T is current temperature (in K), T_0 is reference temperature (in K), E is activation energy (cal/mole), and R is universal gas constant. This model was developed and validated by Ajmani et al. [12]. This reduced mechanism consists of (1) fragmentation of the hydrocarbon, (2) oxidation of the hydrocarbon fragment, (3) combustion of hydrogen, and (4) oxidation of carbon monoxide.

Numerical Methods and Validations

We assume that the chemical reactions only happen at the gas phase. Therefore, we can use an operator-splitting scheme to separate the governing equations (1)–(4) into a fluid dynamics part and chemical kinetics part. This splitting

Table 1 Reduced kinetics mechanism for Jet-A surrogate fuel

No	Reaction	A	n	E
1	$C_{11}H_{21} + O_2 = > 11CH + 10\,H + O_2$	1.00E + 12	0.00	3.10E + 04
2	$CH + O_2 = > CO + OH$	2.00E + 15	0.00	3.00E + 03
3	$CH + O = > CO + H$	3.00E + 12	1.00	0.00E + 00
4	$H_2 + O_2 \leftrightarrow H_2O + O$	3.98E + 11	1.00	4.80E + 04
5	$H_2 + O \leftrightarrow H + OH$	3.00E + 14	0.00	6.00E + 03
6	$H + O_2 \leftrightarrow O + OH$	4.00E + 14	0.00	1.80E + 04
7	$H_2O + O_2 \leftrightarrow 2O + H_2O$	3.17E + 12	2.00	1.12E + 05
8	$CO + OH \leftrightarrow CO_2 + H$	5.51E + 07	1.27	-7.58E + 02
9	$CO + H2O \leftrightarrow CO_2 + H_2$	5.50E + 04	1.28	-1.00E + 03
10	$CO + H_2 + O_2 \leftrightarrow CO_2 + H_2O$	1.60E + 14	1.60	1.80E + 04
11	$N + NO \leftrightarrow N_2 + O$	3.00E + 12	0.30	0.00E + 00
12	$N + O_2 \leftrightarrow NO + O$	6.40E + 09	1.00	3.17E + 03
13	$N + OH \leftrightarrow NO + H$	6.30E + 11	0.50	0.00E + 00
14	$N + N + M \leftrightarrow N_2 + M$	2.80E + 17	-0.75	0.00E + 00
15	$H + N_2O \leftrightarrow N_2 + OH$	3.50E + 14	0.00	7.55E + 02
16	$N_2 + O_2 + O \leftrightarrow N_2O + O_2$	1.00E + 15	0.00	3.02E + 02
17	$N_2O + O \leftrightarrow 2NO$	1.50E + 15	0.00	3.90E + 04
18	$N_2O + M \leftrightarrow N_2 + O + M$	1.16E + 15	0.00	3.32E + 04

allows us to use a specific numerical scheme developed for the fluid dynamic part in conjunction with a numerical method especially developed to deal with stiff systems of ODEs for the chemical kinetics part. For fluid dynamics part, we use the fifth-order weighted essentially non-oscillatory (WENO) scheme [13] for the inviscid flux terms and the fourth-order central difference scheme [14] for the viscous flux terms. The third-order Runge–Kutta method is used to evolve the solution in time. The chemical kinetics part is solved using CHEMEQ, a solver of stiff nonlinear ODEs, developed by Young et al. [15]. For the boundaries we use Navier–Stokes characteristic boundary conditions [16].

For the liquid-fueled droplet, the droplet trajectory is dominantly driven by the drag, which is acting on that droplet, and the evaporation rate is calculated through the transfer number with assumption based on spherical droplet. The drag coefficient is calculated using two different models, which are Schiller and Naumann model [17] and Igra and Takayama model [18]. The Schiller and Naumann model is used as the Reynolds number is smaller than 200, while the Igra and Takayama model is used as the Reynolds number is greater than or equal to 200. The evaporation transfer number, Bi, is calculated as $B_i = (Y_{Fsi} - Y_F)/(1 - Y_{Fsi})$. In this expression, the Y_F is local gaseous fuel mass fraction, and Y_{Fsi} is fuel mass fraction at the droplet surface, calculated using the Clausius–Clapeyron relation. The Ranz and Marshall [19] correlation was used to account for the heat transfer between the fueled droplet and surrounding gaseous phase. The empirical corrections for the effects had been counted for the increased rates of heating and evaporation.

Table 2 Comparison between numerical results and experimental results for equivalent ratio of 0.5

Ignition temperature T(K)	Ignition pressure (P(atm))	Delay time (second)	
		Current model	Experiment
970	19.6	1921	1961
1032	21.0	903	917
1081	19.9	522	530
1081	22.2	455	463
1187	22.1	114	117

For model and numerical validations, the ignition delay time for different conditions (temperature and pressure) are recorded and compared with experimental data [20] as shown in Table 2 to validate for the chemistry model. It can be observed that the numerical results are in good agreement with experimental data.

Moreover, the propagation detonation velocity and maximum temperature are also compared with experimental and other numerical results to validate for the numerical method and approaches. Our obtained propagation detonation velocity (CJ velocity) in pure gas phase is about 1804 m/s; it is fairly close to 1770 m/s in experimental result of [21] and 1830 m/s in numerical results of NASA CEA software online [22]. The maximum temperature obtained is in good agreement with numerical result obtained from CHEMKIN code, which is about 3000 K.

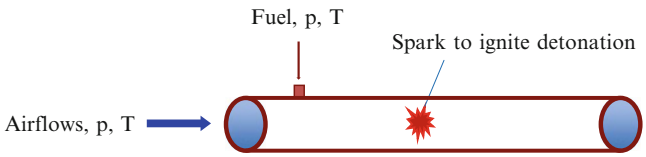

Fig. 1 Schematic of numerical setup for two-phase pulse detonation simulations

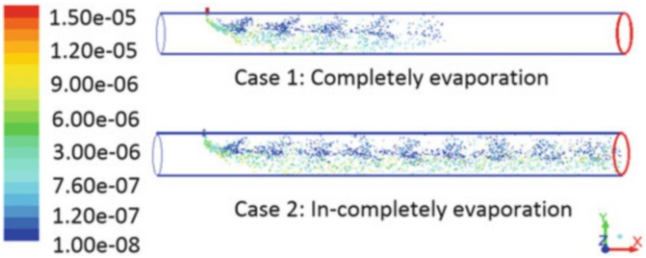

Fig. 2 Liquid fuel droplet evaporation tracking inside detonation chamber

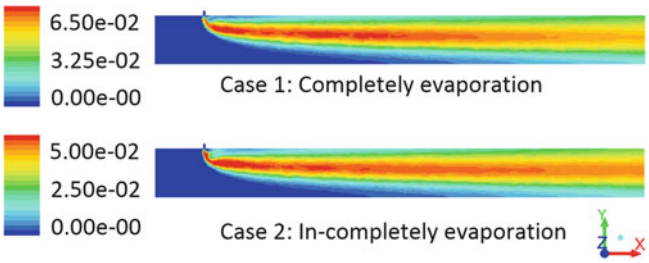

Fig. 3 Mass fraction contour of the fuel vapor raised from evaporation process

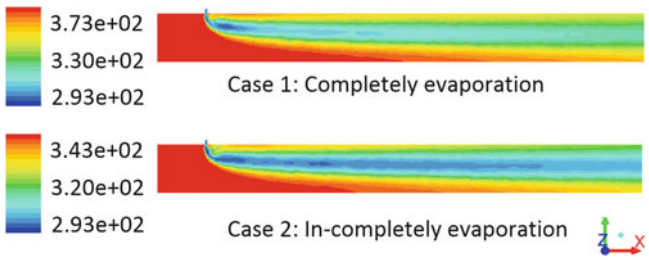

Fig. 4 Temperature contour of the mixture after evaporation process

Preliminary Results

In this study, the liquid fuel is pre-evaporated inside the detonation chamber to ensure that the detonation can sustain during the propagation process. In the following, we will consider both cases of completing and in-completing evaporation of droplet fuel. To get completely evaporated, we preheat the incoming airflow until 373 K at the inlet of detonation chamber before mixing with droplet fuel. For in-completing evaporation, we only heat the airflow up to 343 K before mixing with droplet fuel. For both cases, the mass flow rate of air is controlled at 0.1 kg/s, while the mass flow rate of fuel is set at 0.0067 kg/s. Therefore, we get the equivalent ratio of about 1.0. The initial diameter of the droplets is the same and set at 15 μm. Figure 1 shows the numerical setup of our detonation simulations.

Figure 2 shows the completing evaporation (upper) and in-completing evaporation (lower) of the droplet fuel inside the detonation chamber for different inlet airflows temperature of 70 and 100 °C, respectively. It can be seen that the liquid fuel droplet completely evaporated and transferred to vapor phase at a distance from the injections in the completing evaporation case, while the liquid droplet does not completely evaporate after that distance in the in-completing evaporation case. In another words, there is no droplet fuel found in the domain after the distance d in the completing evaporation case, while there exist a certain amount of droplet fuel in the in-completing evaporation case. It can be explained that the liquid droplets are mixed and received the heat from hot air flow inside the detonation chamber. The droplets then gain their internal energy and start evaporating. The higher temperature of air will transfer more heat to droplets; it therefore causes a higher evaporation rate. Hence, with the higher temperature (100 °C) of incoming airflows, the liquid fuel droplets evaporate faster and completely at a short distance after rejecting from nozzle.

Figure 3 shows the mass fraction contour of the fuel vapor phase inside the detonation chamber after evaporating from liquid fuel droplets. The upper figure represents for completing evaporation case, while lower represents for in-completing case. It can be seen that the fuel vapor patterns are mostly similar for these both case. However, the value of mass fraction of completing evaporation case is higher because more liquid fuel is changed to vapor phase. Hence, for higher temperature of incoming airflows, the fuel is richer in the mixture of vapor phase.

Figure 4 shows the temperature contour of the mixture inside the detonation chamber for completing evaporation case (upper) and in-completing evaporation case (lower). During movement inside the hot airflows of the liquid fuel droplets, the heat energy is transferred from hot airflows to the cool droplets. The increasing of internal energy of the droplet then is carried in evaporating the liquid fuel to the vapor phase. Therefore, the temperature of vapor phase decreases, while the temperature of droplets increases. It is possible that the effects will be important feature of spray detonation.

Moreover, we have observed that the change of droplet size is consistent with the change of the liquid phase to the vapor phase of the droplet. It can be seen that the size of the

droplet strongly depends on evaporation rate, fuel properties, ambient temperature, ambient pressure, as well as fraction of fuel vapor phase in the fuel/air mixture. However, in this study, the evaporation of the droplet followed the D^2-law. In other words, the square droplet diameter is linear in time. This is consistent with public experimental as well as numerical data. It implies that the current approaches as well as implemented program for evaporation were benchmarked.

In order to study the physical and chemical insights of detonation waves propagating in the two-phase flows, we have considered both one- and two-dimensional cases. Detonation in both completed evaporation and in-completed evaporation cases is numerically simulated and compared between one and two dimensions to study the effect of fuel droplet in detonation process. The following are the details.

Figure 5 shows the comparison of total pressure and temperature between completing evaporation and in-completing evaporation process in one-dimensional detonation. It significantly shows that the induction zone of completing evaporation is much shorter than the in-completing case. It means that the mixture is heated up very fast in the completing evaporation case, while it is slower in the in-completing case. It also implies that the chemical reactions occur rapidly in the induction region of the completing evaporation case; it results a strong coupling between reaction zone and detonation front. For the in-completing evaporation case, the fuel may be only partially consumed by the time CJ plane established, it results a slower in detonation velocity. Hence, energy release due to the combustion of the large droplet might be unable to couple completely with detonation front. It is therefore important that the basis detonation characteristic is observed. It would be expected that the effects of the droplet size are significant in contributing to the high velocity of the flow behind detonation waves. Moreover, in the in-completing evaporation case, we also observed that the liquid droplet still evaporate after the shock front past through. Therefore chemical reactions also still occur, and more energy is released in this region to support for detonation waves and shock front. That is the reason why we see both pressure and temperature of in-completing case is still high and just gradually decreases, while they decrease rapidly in the completing case.

Moreover, we also observed that increasing or decreasing the induction zone (time) does not affect much to the detonation velocity; it only affects to the detonation onset process. During an induction period, there is no energy conversion. In addition, increasing the mass faction of fuel in the vapor phase will increase the detonability of the mixture, and the CJ detonation velocity is achieved. The fraction of fuel in the vapor increases, the detonation velocity steadily approaches to CJ state, and the mass of the fuel contributing the detonation increases; therefore, the detonation velocity also increases in respond.

Figure 6 (upper) shows the comparison of the pressure contour and (lower) shows the temperature contour of the detonation front between completing and in-completing evaporation case. It is clear that the detonation head is more regular in the completing case than in the in-completing case. There are more detonation heads in the completing case. This is because of the instability of the detonation waves in the in-completing case. We also see that the detonation waves move slower in the in-completing case compared to the completing case. It is significantly seen that the induction zone is larger in the in-completing case because the mixture needs longer time to evaporate the remaining droplets and heat up the mixture after the shock front.

Figure 7 shows the comparison of the detonation cell structure detonation process inside detonation

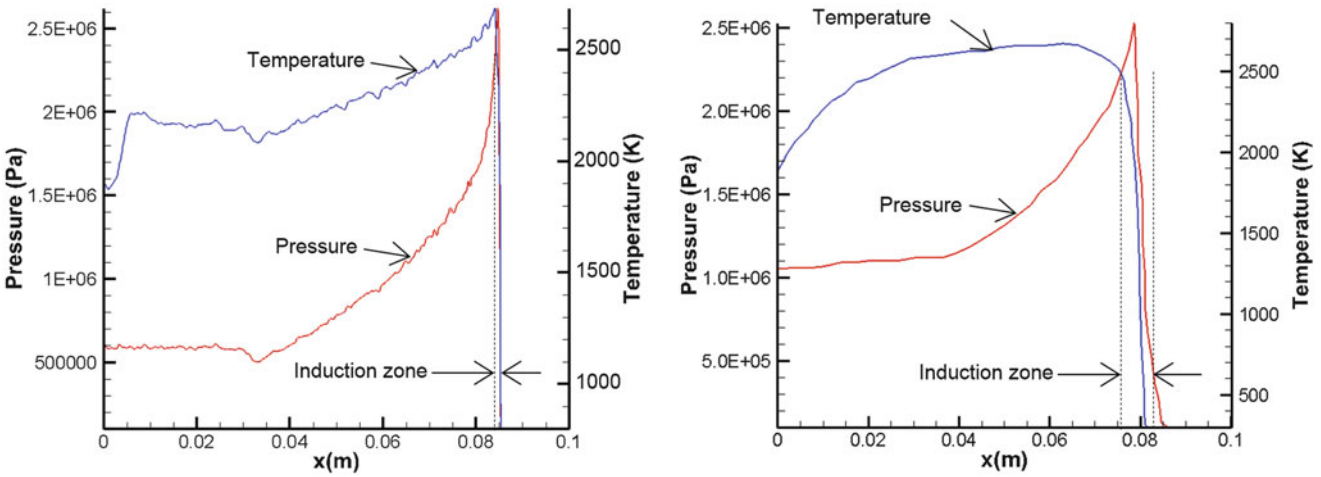

Fig. 5 Comparison of 1D detonation waves between completed evaporation case (left) and in-completed evaporation case (right)

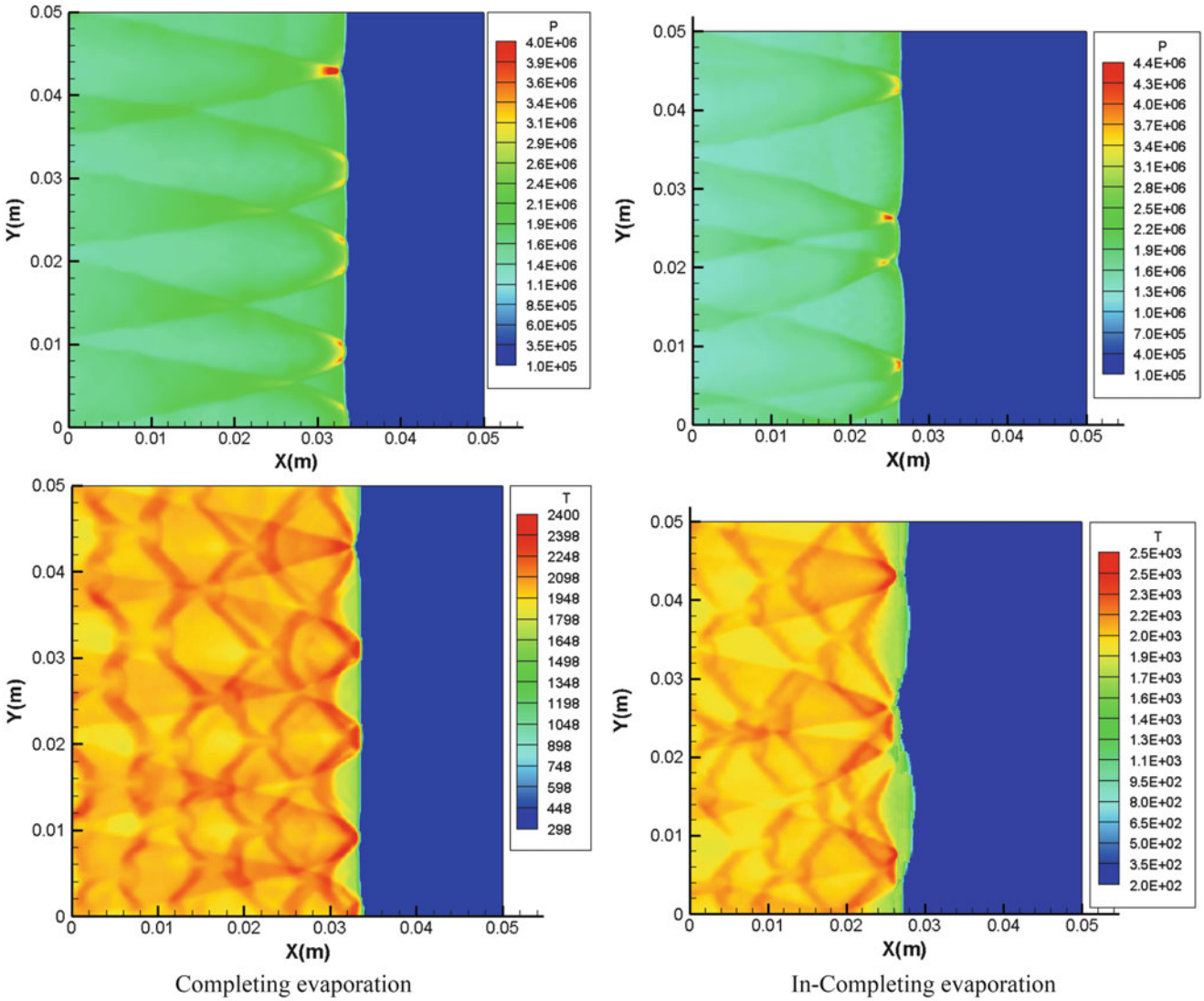

Fig. 6 Comparison of pressure contour and temperature contour at the detonation front of the completing evaporation and in-completing evaporation case

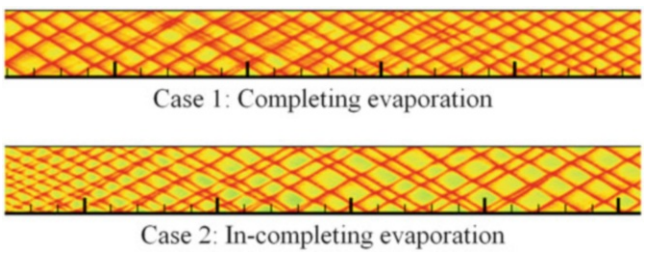

Fig. 7 Comparison of detonation cell structure between completing and in-completing evaporation process

chamber between completing and in-completing evaporation process. It can be seen that detonation cell in in-completing evaporation process is significantly bigger than the completing one. However, the detonation cell in completing evaporation process is more regular than the in-completing one.

Conclusions

In this study, the numerical model has been developed and implemented to simulate for the two-phase fuel flow of pulse detonation engines, in which the Lagrangian–Eulerian approaches are employed. The gas phase is treated as continuous phase and mathematically modeled using Eulerian approach, while the fuel droplets are treated as the discrete phase and modeled using Lagrangian approach. The reduced chemical kinetics of Jet-A fuel is used as the chemical kinetic model. The implemented program is benchmarked via available numerical and experimental results. Both numerical results of one and two dimension are used to study the effects of droplet fuel on detonation characteristics, as well as used to understand the physical and chemical insight of the detonation process in two-phase fuel flows.

References

1. Kailasanath, K.: Recent developments in the research on pulse detonation engines. AIAA J. **41**, 145–159 (2003)
2. Dabora, E.K., Ragland, K.W., Nicholls, J.A.: Droplet size effects in spray detonation. Proc. Combust. Inst. **12**, 19–26 (1969)
3. Ragland, K.W., Dabora, E.K., Nicholls, J.A.: Observed structure of spray detonations. Phys. Fluids **11**, 2377–2389 (1968)
4. Bowen, J.R., Ragland, K.W., Steffs, F.J., Loflin, T.G.: Heterogeneous detonation supported fuel fogs or films. Proc. Combust. Inst. **13**, 1131–1139 (1971)
5. Bull, D.C., McLeod, M.A., Mizner, G.A.: Detonation of unconfined fuel aerosols. Prog. Astronaut. Aeronaut. **75**, 48–60 (1981)
6. Brophy, C.M., Netzer, D.W., Sinlibali, J., Johnson, R.: High speed deflagration to detonation: fundamentals and control. ELEX-KM, Moscow (2001)
7. Knappe, B.M., Adwards, CF.: Results of decane/propane split-fuelled spray detonation. Paper presented at the 16th ONR propulsion meeting, Los Angeles CA, 9–11 June, (2003).
8. William, F.A.: Structure of detonations in diluted spray. Phys. Fluids **4**, 1434–1443 (1961)
9. Borisov, A.A., Gelfand, B.E., Gubin, S.A., Kagarko, S.M., Podgrebenkov, A.L.: The reaction zone of two-phase detonations. Astronautics Acta **15**, 411–417 (1970)
10. Chang, E.J., Kailasanath, K.: Shock waves interactions with particles and fuel droplets. Shock Waves **12**, 333–341 (2003)
11. Cheatham, A., Kailasanath, K.: Numerical modelling of liquid-fuelled detonations in tubes. Combust. Theory Modell. **9**, 23–48 (2005)
12. Ajmani, K., Kundu, K., Penko, P. F.: A study on detonation of JET-A using reduced mechanism. 48th AIAA Aerospace Science Meeting Including the New Horizons Forum and Aerospace Exposition, Orlando, FL, 4–7 January, (2010)
13. Jiang, G.-S., Shu, C.-W.: Efficient implementation of weighted ENO schemes. J. Comput. Phys. **126**(1), 202–228 (1996)
14. Shen, Y., Zha, G., Chen, X.: High order conservative differencing for viscous terms and the application to vortex induced vibration flows. J. Comput. Phys. **228**(22), 8283–8300 (2009)
15. Young, T.R., Boris, J.P.: A numerical technique for solving stiff ordinary differential equations associated with the chemical kinetics of reactive-flow problems. J. Phys. Chem. **81**(25), 2424–2427 (1977)
16. Poinsot, T., Veynante, D.: In Edwards, R.T. (Ed.) Theoretical and numerical combustion. 2nd edn. (2005)
17. Schiller, L., Naumann, A.Z.: A drag coefficient correlation. VDI Zeitung **77**, 318–332 (1935)
18. Igra, O., Takayama, K.: Shock tube study of the drag coefficient of a sphere in non-stationary flows. Proc. R. Soc. Lond. A. **442**, 231–247 (1993)
19. Ranz, W.E., Marshall, W.R.: Evaporation from drops. Chem. Eng. Prog. **48**, 141–146 (1952)
20. Vasu, S.S., Davidson, D.D., Hanson, R.K.: Jet fuel ignition delay times: shock tube experiments over wide conditions and surrogate model predictions. Combust. Flames **152**, 125–143 (2008)
21. Akbar, R., Thibault, P.A., Harris, P.G., Lussier, L.S., Zhang, F., Murray, S.B., Gerrard, K.: Detonation properties of unsensitized and sensitized JP10 and Jet-A fuels in air for pulse detonation engines. 36th AIAA/ASME/SAE/ASEE Joint Propulsion Conference & Exhibit, 16–19 July 2000, Huntsville, AL. (2000)
22. https://cearun.grc.nasa.gov

Simulation of Laser-Induced Detonation in Particulate Systems with Applications to Pulse Detonation Engines

P. Bulat and K. Volkov

Introduction

A pulse detonation engine is an unsteady propulsive device in which the combustion chamber is periodically filled with a reactive gas mixture, a detonation is initiated, the detonation wave propagates through the chamber, and the combustion products are exhausted. The high pressures and resultant momentum flux out of the chamber generate thrust. The use of laser pulse allows to create desired temporal and spatial distributions of ignition centers and to perform a homogeneous ignition within the sub-microsecond interval. In the propagation of a detonation wave in a curvilinear channel (e.g., in a toroidal channel), reflection of detonation wave from the channel walls can be regular or Mach with the formation of triple points. A rapid combustion, as shown by previous experience, takes place behind the Mach stem.

The reactive metal particles are used to enhance blast performance. Although the total energy released by the metal combustion is significant and comparable to the total energy released by the explosive itself, the timescale of this energy release (timescale of particle reaction), for typical particle sizes, is too long to contribute directly to the detonation front itself. The metal particles react with gas or detonation products behind the blast wave. It has been shown that the metal particle reaction significantly increases the strength of the blast and the total impulse delivered to nearby objects or structures [1].

The injection of metal particles with low evaporation temperature and low ionization potential (e.g., aluminum) leads to drop of detonation minimum pulse energy (MPE) due to optical breakdown on individual particles. Vapor aureole around metal particle is a source of free electrons, and optical breakdown in the gas–particle mixture comes for lower energy of laser pulse than in pure gas. Many experimental, theoretical, and numerical studies have been performed for the past years [2–4]. Processes that control transport and combustion of particles remain unresolved and introduce significant uncertainties into modeling and simulation. They include qualitative and quantitative description of processes around individual particle, knowledge in particle microphysics and optical properties of particles, sub-models of heating and evaporation, transport of aggregates of complex morphology, threshold values of optical breakdown, and dependence of MPE on the contributing factors (laser pulse, composition of gas mixture, shape of particles).

Physical and mathematical models of optical breakdown on individual metal particle and numerical methodology for computer modeling are developed. Laser-induced detonation in gas–particle mixtures is studied, and advantages of the new methodology are demonstrated. The in-house computer code has been developed, and contribution of parameters of laser pulse and composition of the mixture is reported. Comparison of some numerical results with experimental data is made.

Breakdown Mechanism

A chain of processes leading to explosion and optical breakdown of individual metal particle is developed (Fig. 1). These processes depend on optical properties of particle, its shape, and ratio of particle size to radius of laser spot.

The particle is heated up to high temperature; melting and evaporation start (Fig. 1a). Evaporation of a particle leads to the formation of a vapor aureole around the particle. Free electrons are generated in the vapor aureole as a result of thermal emission from particle surface (if $T < T_b$) and isothermal ionization in vapor aureole (if $T > T_b$).

P. Bulat
ITMO University, 197101 St. Petersburg, Russia

K. Volkov (✉)
Centre for Fire and Explosion Studies, Kingston University, SW153DW London, UK
e-mail: k.volkov@kingston.ac.uk

G. Ben-Dor et al. (eds.), *30th International Symposium on Shock Waves 1*, DOI 10.1007/978-3-319-46213-4_68

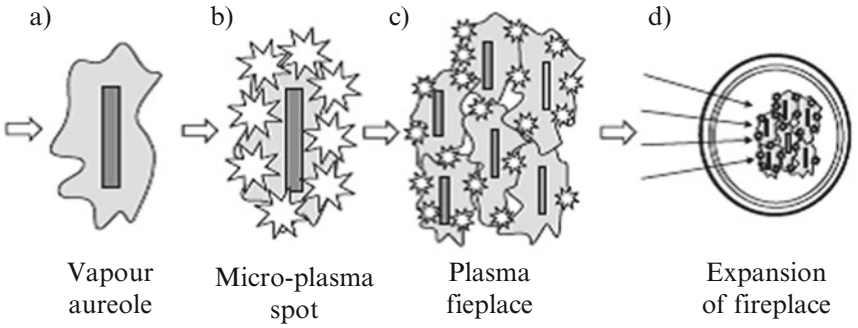

Fig. 1 Optical breakdown on metal particle

This leads to collisions of electrons with ions and atoms and electron–electron collisions. Ionization of vapor aureole due to reverse drag effect leads to development of electron avalanche and formation of micro-plasma spots around the particle (Fig. 1b). The cascade ionization process is significant at high pressure and longer laser pulse because under these conditions, electron–atom or electron–ion collisions have sufficient time to occur during the laser pulse [5]. Micro-plasma spots are expanded due to thermal diffusion of electrons and ionization of molecules and atoms of surrounding gas. Micro-plasma spots are merged, and plasma fireplace is formed around the ensemble of particles (Fig. 1c). The plasma fireplace absorbs laser radiation and contributes to development and propagation of self-sustaining shock wave in the gas–particle mixture (Fig. 1d).

Mathematical Model

The mathematical formulation of the problem is divided into low-level and high-level models. Low-level models correspond to the processes in the volume occupied by an individual particle. The high-level models correspond to the processes in the volume occupied by multiphase mixture.

Low-level models describe melting, heating, evaporation, and formation of vapor aureole, appearance of free electrons due to thermal ionization on front of shock wave, and development of electron avalanche due to reverse drag effect. The particles are considered to have a uniform temperature distribution, and heterogeneous surface reactions are neglected. When the temperature of the particle reaches the melting point, the particle temperature is kept constant until an amount of heat equal to the latent heat of fusion is transferred to the particle. The equations describing electron avalanche in the vapor aureole include the equation of heating of vapor aureole due to electron–atom collisions, the equation of warming-up of electrons, the ionization kinetic equation of vapor as a result of electron impact, and the equation of particle mass. The plasma in vapor aureole is considered as an ideal gas. The Euler equations are used for the simulation of gas dynamical processes in vapor aureole. A simple model of one-step chemical reaction is used in order to reproduce explosion of individual particle. Threshold value of optical breakdown on an individual particle is computed as a result of the solution of low-level models.

The fluid and the solid particles are treated as two separated continua with mass, momentum, and energy conservation equations for each phase, continuity equations for species, and conservation equations for solid particle numbers. The interactions between the two continua are described using the source terms for the rate of mass, momentum, and energy transfer. The data obtained from solution of low-level problems are used to calculate source terms in the governing equations describing high-level problem. It is assumed that particles are uniformly distributed in the domain. Some volume of the mixture depending on particle volume fraction is associated with each particle (individual reactor of a particle). The model of unsteady well-stirred reactor is used to calculate physical quantities in this volume. The fuel–oxidizer mixture is considered as one species (reactant) and all the products are treated as single species (products).

Computational Procedure

Equations describing heating and evaporation of particle and development of electron avalanche are solved numerically to obtain the threshold irradiance required to produce breakdown for a given pulse duration, using a Runge–Kutta fourth-order technique with adaptive time step. Optical breakdown is assumed to occur when the free electron density obtained during the laser pulse exceeds the given critical value (10^{19}–10^{20} cm^{-3}).

Nonlinear CFD solver works in an explicit time-marching fashion, based on a three-step Runge–Kutta stepping procedure and piecewise parabolic method. The governing equations are solved with Chakravarthy–Osher scheme for inviscid fluxes. Convergence to a steady state is accelerated by the use of multigrid techniques and by the application of block-Jacobi preconditioning for high-speed flows, with a separate low-Mach number preconditioning method for use

with low-speed flows. The numerical simulations are performed in a rectangular computational domain using a uniform Cartesian mesh with about ten cells to resolve the structure of the reaction zone. The length of the reaction zone is the smallest characteristic length of the problem (it is shorter that length of dynamic and thermal relaxation times of particles). Proper resolution of the reaction zone ensures that all other characteristic lengths have been properly resolved.

Results

The intensity of laser pulse is represented as a product of the maximal intensity, the function describing the time distribution of the intensity, the function taking into account the spatial distribution of the intensity, and the function describing absorption of radiation in the medium. The time distribution of the intensity is represented by a continuous piecewise linear function. In a plane normal to the direction of laser pulse, the spatial distribution of the intensity is described by the normal distribution.

The theoretical peak intensity of laser pulse at any radial point is calculated for given power and degree of focus. The laser does not reach its peak operating power at the moment when it is turned on. It requires a short time to ramp up to its peak output. For a laser pulse which lasts 8 μs, the laser output reaches its peak intensity in about one fourth of a pulse duration and will have dropped to roughly three fourth of its peak value when the laser is shut off. The laser model includes a ramp time parameter during which time the laser's output increases linearly to a maximum (Fig. 2).

The source of laser radiation is provided by a pulsed chemical HF laser with the following characteristics: time of laser pulse is 2.6 μs, wave length is 4.2 μm, radius of laser spot is 5 mm, and integral temporal characteristic is 1.5 μs. Particle location relative to the centerline of the laser beam, total energy, time, and shape of laser pulse vary in the calculations. In all simulations, a Gaussian intensity profile in time is assumed.

Figure 3 shows heating of metal particle up to the boiling temperature. The particle temperature depends on total energy of laser pulse and distance from particle to centerline of laser beam. The first plateau at 923 K corresponds to the melting of the particle. The second plateau at 2792 K corresponds to the boiling point. Larger particles take a longer time to heat up to the melting point and the boiling point.

The results computed show that the energy required to heat particle up to evaporation temperature depends of particle size and particle material [6]. The particle reaches the temperature of phase transition for short time (about 1 μs). Development of electron avalanche takes about 0.1 % from the time of breakdown formation.

Laser pulse with intensity of 10^{11} W/cm^2 leads to gas breakdown. In a laser-induced plasma, inverse bremsstrahlung absorption leads to an increase in electron energy. Electrons are able to ionize the surrounding gas and form an exponentially growing electron cascade. Development of an electron avalanche in the form of its dependence on the degree of ionization of the vapor aureole with time is shown in Fig. 4. The particle is located on the centerline of the laser beam. The electron avalanche is developed in 0.68 μs from the laser pulse started, and ionization takes place within a

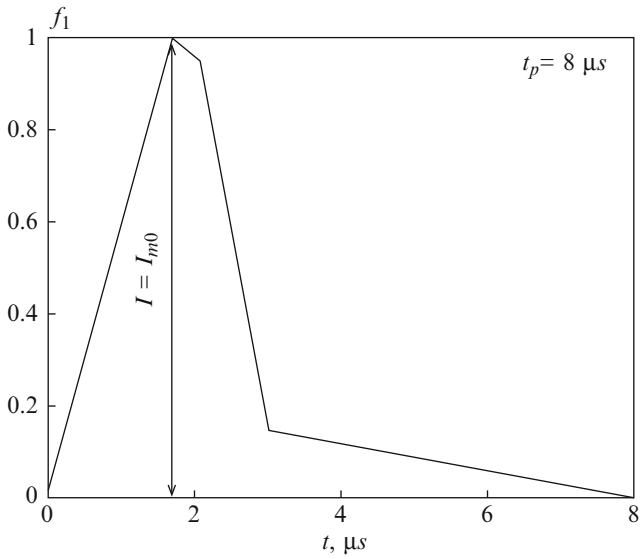

Fig. 2 Intensity of laser pulse as a function of time

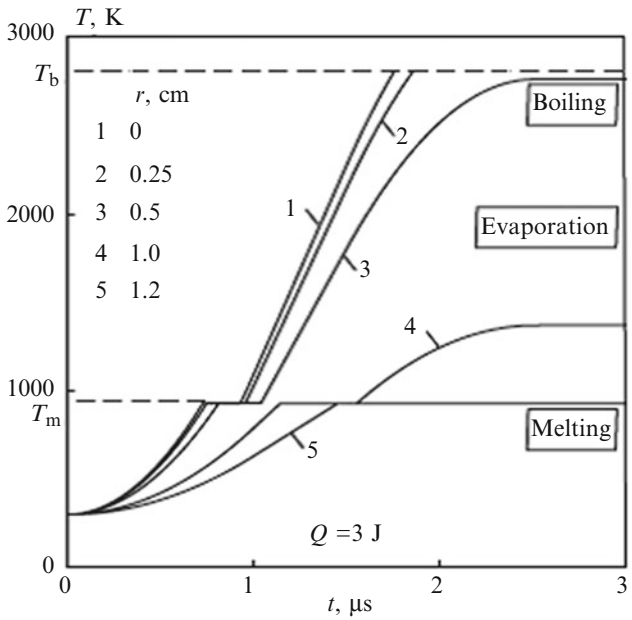

Fig. 3 Temperature of metal particle

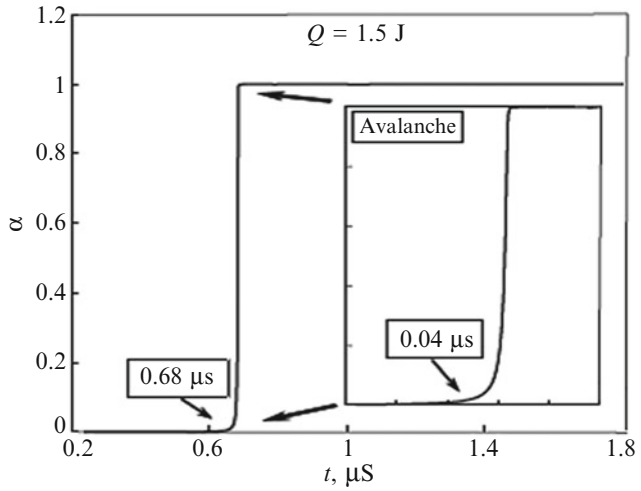

Fig. 4 Development of electron avalanche

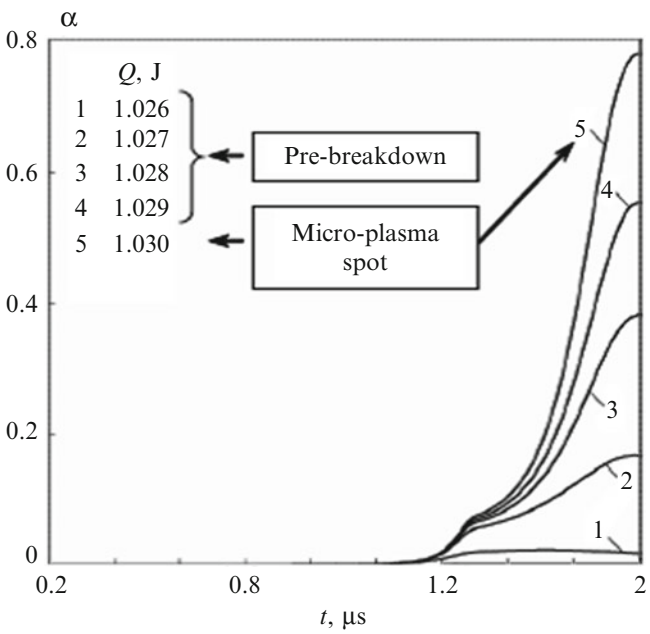

Fig. 5 Degree of ionization of vapor aureole

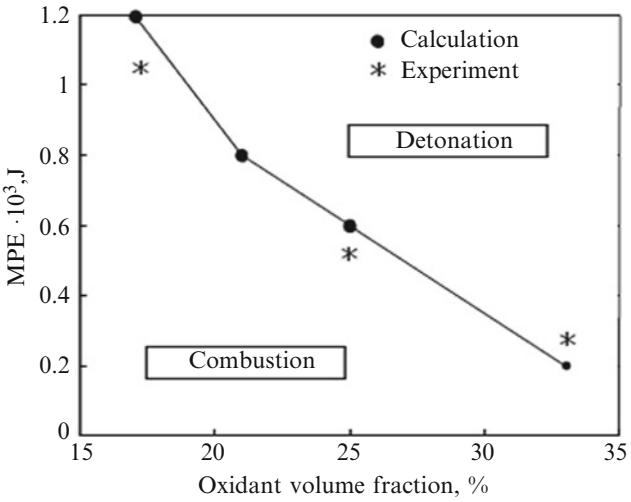

Fig. 6 MPE as a function of oxidizer volume fraction

short time interval (about 0.04 μs). The electron density starts to grow after a period of 0.5 μs with an electron density not exceeding 10 cm^{-3}. Beyond this time, line suffers a sudden increase reaching a value of 10^{20} cm^{-3} at a time of 0.68 μs. At that intensity, the rate of cascade ionization is so high that the breakdown proceeds almost instantaneously to the critical electron density (10^{20} cm^{-3}).

The degree of ionization as function of time and total energy of the laser pulse is shown in Fig. 5. Micro-plasma spots around the particle are formed at an energy of 1.03 J. Pre-breakdown conditions are sensitive to a small change of energy of the laser pulse. The threshold of plasma formation is defined as a proportion of the laser energy used up to the beginning of breakdown.

Interaction of laser pulse with individual metal particle is related to one of the following stages.

1. Pre-threshold energy of laser pulse ($Q < 1$ J). Energy of laser pulse is not enough to ionize vapor aureole around particle. Evaporation of particle exists but degree of ionization is small, and vapor aureole is transparent for laser radiation.
2. Near-threshold energy of laser pulse ($Q = 1$–2 J). Degree of ionization changes from some percents to 100 %.
3. Post-threshold energy of laser pulse ($Q > 2$ J). The process proceeds at completely ionized vapor aureole around particle. Ionization has an avalanche character within short time interval.

Threshold intensity of LIB on metal particle corresponds to that observed in experimental study [6] (qualitative comparison is complicated by various temporal profiles of laser pulse).

The computational results are presented in Fig. 6 in comparison with the experimental data [7] for flake aluminum particles in the hydrogen–oxygen–nitrogen mixture. Volume fraction of hydrogen is 15 %. Volume fraction of oxygen changes from 15 to 35 %. Mass fraction of particles is 1 g/m^3. At $Q = 150$ J, combustion of hydrogen takes place in small region adjacent to shock wave front. At $Q = 200$ J, the temperature and pressure in shock wave front increase, and volume fraction of hydrogen decreases on 20–30 % for time of laser pulse. Further energy supply to mixture leads to considerable increase in temperature and pressure in the mixture and development of unsteady gas dynamics processes in vapor aureole. At $Q = 300$ J, about 60 % of hydrogen is used, and at $Q = 300$ J, about 95 % of hydrogen burns beyond the shock wave front. The energy of laser pulse 350–400 J is the MPE of detonation.

Conclusions

Sub-models of optical breakdown on metal particle include heating of particle to boiling temperature, evaporation and formation of vapor aureole around the particle, ionization of vapor aureole around particle and droplet and development of electron avalanche, appearance of micro-plasma spots and their expansion, and propagation of shock wave in the volume occupied by the particle. The threshold intensity of optical breakdown on individual metal particle and its dependence on contributing factors (location of particle, total energy and time of laser pulse, radius of laser spot) are studied. Laser-induced detonation in the mixture of hydrogen with flake aluminum particles is simulated based on Eulerian approach, and MPE of detonation is calculated.

Acknowledgments The work was supported by the Ministry of Education and Science of the Russian Federation (agreement 14.575.21.0057).

References

1. Frost, D.L., Zhang, F.: Non-ideal blast waves from heterogeneous explosives. Mater. Sci. Forum **465–466**, 421–426 (2004)
2. Armstrong, R.L., Zardecki, A.: Propagation of high energy laser beams through metallic aerosols. Appl. Opt. **29**(12), 1786–1792 (1990)
3. Papalexandris, M.V.: Numerical simulation of detonations in mixtures of gases and solid particles. J. Fluid Mech. **507**, 95–142 (2004)
4. Emelyanov, V.N., Volkov, K.N.: Numerical simulation of laser-induced detonation in mixture of hydrogen with suspended metal particles. Int. J. Hydrog. Energy **39**(11), 6222–6232 (2014)
5. Kopecek, H., Maier, H., Reider, G., Winter, F., Winther, E.: Laser ignition of methane-air mixtures at high pressures. Exp. Thermal Fluid Sci. **27**(4), 499–503 (2003)
6. Negin, A.E., Osipov, V.P., Pakhomov, A.V.: Optical breakdown in aerosols under the influence of pulsed CO_2 laser radiation. Quant. Electron. **16**(11), 1458–1463 (1986)
7. Aleksandrov, B.S., Klimuk, E.A., Kutumov, K.A., Lacour, B.M., Puech, V., Troshchinenko, G.A.: A repetitively pulsed HF laser with a large discharge gap operating on the F_2–H_2 mixture. Quant. Electron. **35**(9), 805–808 (2005)

Criterion for Detonation Transition in Liquid-Fuel Pulse Detonation Engines

J. Li, Teo Chiang Juay, L. Li, P.H. Chang, and Boo-Cheong Khoo

Introduction

In the present study, experiments on liquid-fuel air-breathing pulse detonation engines (PDEs) are conducted using a low-vapor-pressure fuel: Jet A-1. Past studies have mostly focused on demonstrating the use of high-vapor-pressure fuels (e.g., heptane) or low-vapor-pressure fuels (e.g., JP8 and Jet A-1) with a predetermined air temperature (e.g., 398 K) or with some pretreatments on the liquid fuels (e.g., preheating of fuel). Based on previous notable studies [1–3], critical conditions for success or failure of liquid-fuel PDEs are mainly related to fuel types, inlet air temperatures, and spray droplet sizes. Essentially, these conditions determine the amount of pre-vaporized fuel prior to ignition. The present paper attempts to establish a criterion for detonation transition of two-phase Jet A-1/air mixtures.

In a liquid-fuel PDE, the long tube required to achieve detonation via deflagration-to-detonation transition process makes it advantageous for the allowable filling time t_f to induce more vaporization of the incoming spray droplets, so as to promote sufficient fuel to exist in the vapor phase for detonation transition. Assuming a situation where sufficient pre-vaporized fuel is present, the data for droplet equilibration lifetime t_e can provide a threshold for the allowable filling time t_f of a PDE. For the case of $t_f \ll t_e$, it is impossible to achieve detonation within the PDE tube. When these two time scales are comparable, there would be a critical ratio of these two characteristic times identifying the success or failure of detonation transition.

J. Li (✉) • L. Li • P.H. Chang • B.-C. Khoo
National University of Singapore, Singapore 117576, Republic of Singapore
e-mail: tslljm@nus.edu.sg

T.C. Juay
Department of Mechanical Engineering, National University of Singapore, Block EA, #07-08, 9 Engineering Drive 1, Singapore 117576, Singapore

Note that the calculation of t_e is based on monodispersed droplet diameters (see next paragraph). In reality, the spray has polydispersed droplet diameters ranging from 2.25 to 300 μm from droplet distribution measurements. In the present study, to simplify this problem, the statistical Sauter mean diameter (SMD) representing the mean diameter of spray droplet distribution is applied to establish the criterion of t_f/t_e for detonation transition of two-phase mixtures, based on experimental results.

Droplet Equilibration Lifetime

Applying the known vapor-phase fraction of a two-phase mixture in equilibrium at a specific temperature, which is computed using SUPERTRAPP, we can estimate t_e during which the droplet undergoes vaporization following the d-squared (D^2) law. However, this process ceases when the vaporized fuel amount is identical to that at the phase equilibrium state. Equation (1) can be used to compute t_e:

$$t_e = \frac{d_0^2}{\beta}\left(1 - (1 - X_v)^{\frac{2}{3}}\right) \quad (1)$$

where X_v = fraction of vaporized fuel at phase equilibrium state.

d_0 = initial droplet diameter.

β = evaporation coefficient.

Figure 1 shows the computed values of t_e for different mixture compositions (ϕ = 0.9–4.5) with varying d_0 SMD size. For lower mixture temperatures, t_e is shorter than the complete lifetime until a higher temperature is reached where the liquid fuel has fully vaporized. For the case of a more fuel-rich mixture, t_e can be further decreased. However, a shorter equilibration time principally indicates a two-phase mixture attaining phase equilibrium within shorter time duration. It does not mean that sufficient vaporized fuel will be generated for detonation transition. For example, at T_{air} = 57 °C, for

G. Ben-Dor et al. (eds.), *30th International Symposium on Shock Waves 1*, DOI 10.1007/978-3-319-46213-4_69

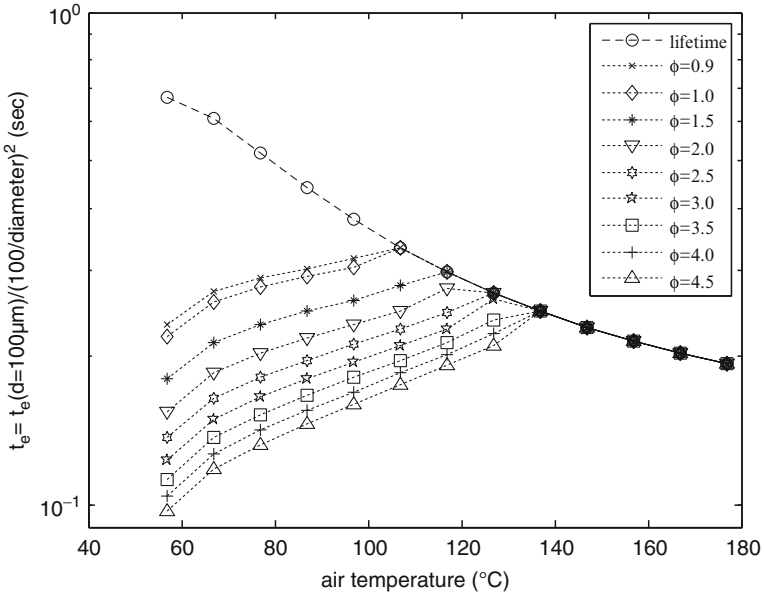

Fig. 1 Equilibration lifetime of varying d_0, in basis of $d_0 = 100$ μm

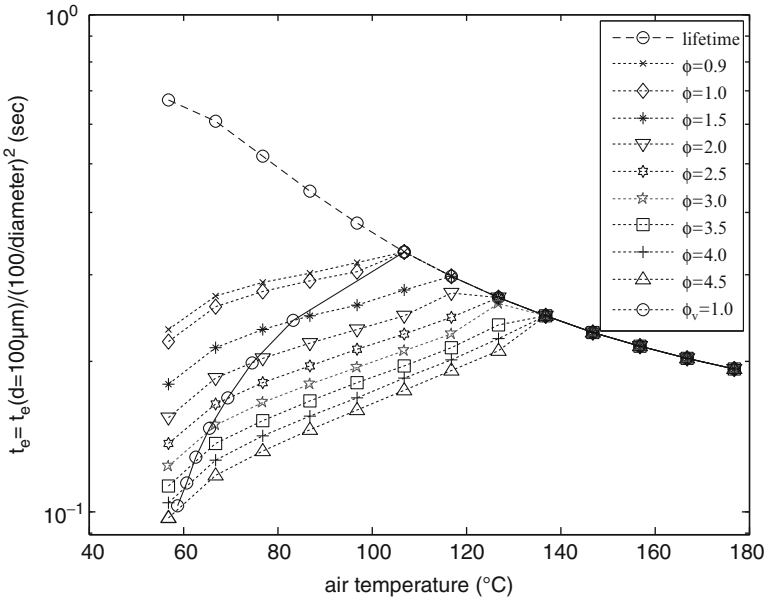

Fig. 2 Equilibration lifetime for attaining a vapor-phase equivalence ratio $\phi_v = 1$ (*open circle*)

$d_0 = 100$ μm and $\phi = 1$, t_e is 0.22 s, but its vapor-phase equivalence ratio (ϕ_v) is 0.414, which would be too lean for the onset of detonation. Figure 2 shows the required t_e for the vapor-phase composition of a two-phase mixture to achieve stoichiometric conditions, marked by (○). The t_e to attain $\phi_v = 1.0$ decreases as an increasingly fuel-rich mixture is employed. This implies that it is possible to achieve detonation transition even for relatively low mixture temperatures.

Criterion for Detonation Transition

Figure 3 presents experimental results of the critical conditions for three controlled inlet air temperatures. The makers in "x" correspond to unsuccessful detonation transition caused by the lower injection pressure or the lower inlet air temperature than their critical values. The critical ratio t_f/t_e for detonation transition is 32, 17.1, and 14.1 corresponding to mixture temperatures of 158.1, 196.1, and 208.7 °C, respectively. This indicates that the critical t_f/t_e ratio depends on the mixture temperature. With a lower mixture temperature, in order to attain successful detonation transition, a longer filling time relative to the droplet equilibration lifetime is required. Figure 4 presents the results for the cases using heated Jet A-1 (100 °C). At the mixture temperature of 144.4 °C, the critical t_f/t_e is 32.1, which is consistent with the case for unheated Jet A-1 with the identical droplet SMD size. Actually, the use of heated Jet A-1 causes a decrease in the droplet lifetime by 22.4 % and in the SMD diameter by 25 %. This consistency between the cases

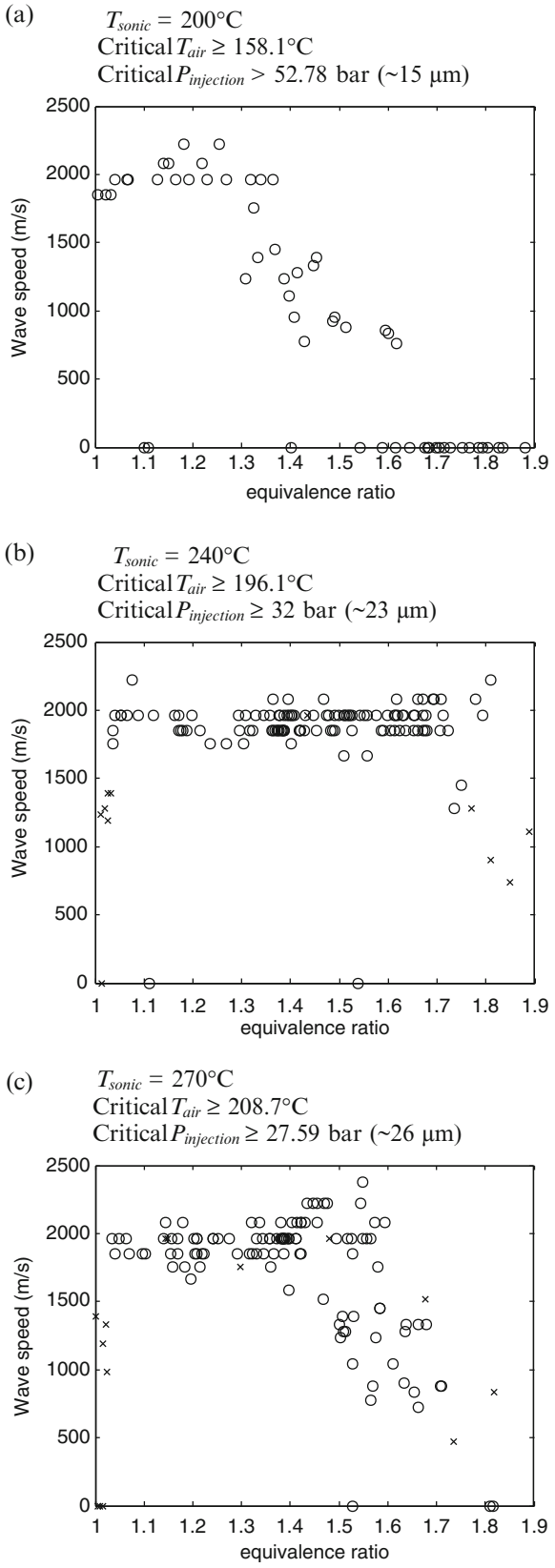

Fig. 3 Unheated Jet A-1

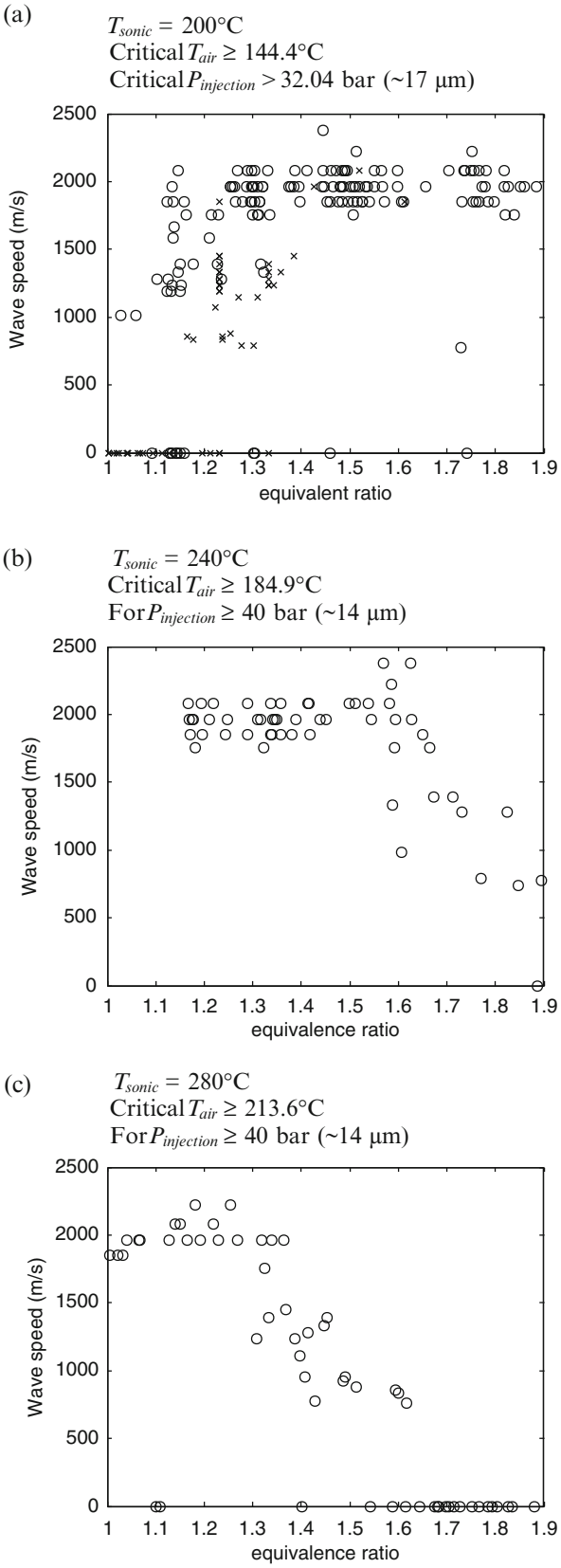

Fig. 4 Heated Jet A-1

of unheated and heated Jet A-1 validates the criterion of t_f/t_e for liquid-fuel PDE.

From experimental results, the DDT run-up distance for Jet A-1/air mixture is around 40 times of the cellular width λ. A semiempirical equation for this criterion can be expressed as follows:

$$\frac{\lambda}{V_{\text{air}}} \geq \text{constant}\frac{d_0^2}{\beta}\left(1-(1-X_v)^{\frac{2}{3}}\right) \tag{2}$$

where $\lambda,\ \beta, X_v = f(T,P)$

This semiempirical equation may be employed for determining the critical parameters corresponding to design operating conditions, and it also serves as a good tool for the design of a flight-weight liquid-fuel PDE.

Conclusions

One of the most crucial parameters for detonation transition of two-phase fuel/air mixtures is the amount of pre-vaporized fuel prior to ignition. Phase equilibrium states and droplet equilibration lifetime to achieve the phase equilibrium are calculated in an attempt to assess whether the fraction of vaporized fuel is sufficient and to establish a criterion for detonation transition of two-phase mixtures on the basis of the ratio between PDE filling time and the droplet equilibration lifetime t_f/t_e. The results show that the most important parameters which determine the critical conditions for liquid-fuel detonation are the mixture temperature and the spray droplet size. Based on the critical conditions found from experiments, a simple criterion for detonation transition of Jet A-1/air mixtures has been established. Because the DDT run-up distance of Jet A-1/air mixture is around 40 times of the cellular width, a semiempirical equation for the criterion function of cellular width, initial droplet diameter, evaporation coefficient, and fraction of vaporized fuel at phase equilibrium state is found (see Eq. (2)).

References

1. Brophy, C.M., Netzer, D.W., Sinibaldi, J., Johnson, R.: High-speed Deflagration and Detonation: Fundamentals and Control Edited by G.D. Roy, S.M. Frolov, D.W. Netzer, amd A.A. Borisov. ELEX-KM Publishers, 2001. Moscow. pp. 207–222 (2001)
2. Tucker, K.C., King, P.I., Schauer, F.R.: J Propul. Power, **24**(4): 788–796 (2008)
3. Frolov, S.M.: J Propul. Power. **22**(6): 1162–1169 (2006)

Numerical Simulation of Reactive Gas Mixes Flows in the Detonation Engines

S.N. Martyushov

Introduction

Conservative mathematical models with accurate energetic balance are needed for correct numerical simulation of detonation wave appearing and propagation. Two mathematical models where used for numerical simulation of flows of reactive gas mixes: the simplified mathematical model of two-phase chemical reaction [1] and model based on the full system of gas dynamics equations accompanied with the system of kinetics equations in the integral form [2]. The state equations of real gas for every component of gas were used. Transition to characteristic variables of full system of the equations for any number of components of gas mixes is carried out. Transition to dimensionless gas dynamics and kinetic unknowns is carried out. Numerical simulation of flows in the combustion chambers of two configurations of detonation engines [3, 4] was carried out. For engine [3], moment of detonation wave appearing and structure of flow were captured. For engine [4], structure of flow was investigated.

Results

Two mathematical models were used: system of the equations of gas dynamics added with full system of the equations of kinetics [2] and the simplified two-phase model [1] including the induction period and the subsequent period of reaction. Gas was assumed nonviscous.

For numerical simulation of flows of reacting mixes, the system of the equations of nonviscous gas and the kinetic equations in the integral form for axial symmetric flows can be presented as follows:

$$d/dt\int_V \vec{Q}dV + \oint_S \vec{n}FdS + \Phi = 0,\ \vec{Q} = (\rho, \vec{m}, \rho e, \rho c_i),\quad i = 1, \ldots n \tag{1}$$

where $F = \left(\vec{m}, \vec{m}\cdot\vec{m}/\rho + PI, \vec{m}(e+p)/\rho, \vec{m}\vec{B}\right)$, $c_i = \rho_i/\rho$—concentration of gas mix component per unit mass $\Phi = (0, 0, 0, 0, \rho f_i)$ - source term and pressure $P = \rho R_B T\sum_i \frac{c_i}{\mu_i}$ equation of state $e = R_B T\sum_i \frac{c_i}{\mu_i}/(\gamma - 1) + \vec{V}^2/2 + \sum_i c_i h_i$—full energy of finite volume $\sum_i c_i h_i$—internal energy of chemical reactions. Equations of chemical reactions can be presented as follows:

$$\sum_{i=1}^{n}\alpha_{ij}A_i = \sum_{i=1}^{n}\beta_{ij}B_i, j = 1, \ldots, m\,.f_i = \frac{dc_i}{dt} = \sum_{j=1}^{m}\left(\beta_{ij} - \alpha_{ij}\right)w_j(\vec{c}, T), \tag{2}$$

$$w_j(\vec{c}, T) = k_f(T)\prod_{i=1}^{n}c_i^{\alpha_{ij}} - k_b(T)\prod_{i=1}^{n}c_i^{\beta_{ij}}$$
$$k_{f,b} = A_{f,b}T^{l_{f,b}}\exp\left(-E_{f,b}/RT\right)$$

where n and m are the number of reactions and components of the gas mix and α_{ij} and β_{ij} are the stoichiometric coefficients of direct and inverse reactions. Scheme with nine hydrogen–air reactions, similar to that used in [2], was used.

Transition to characteristic unknowns was performed by Roe–Pike method. For calculation of flow through the bound of control volume, we have the next relations:

$$F_{i+1/2} = \frac{1}{2}(F_L + F_R) - \frac{1}{2}\sum_{k=1}^{m}\Delta_{i+1/2}W_k\left|\widetilde{\lambda}_k\right|r_k \tag{3}$$

S.N. Martyushov (✉)
The Moscow Aviation Institute, National Research University, Volokolamskoe shosse 4, 125993 Moscow, Russia
e-mail: martyush@mail.ru

G. Ben-Dor et al. (eds.), *30th International Symposium on Shock Waves 1*, DOI 10.1007/978-3-319-46213-4_70

where ΔW_k is the intensity of characteristic wave and $\vec{r}_k$ and $\vec{L}_k$ are the right and left eigenvectors of Jacobian matrix $A\left(\vec{Q}\right) = \partial\vec{F}/\partial\vec{Q}$. For finding $\Delta\vec{W} = \vec{L}\Delta\vec{Q}$, one can use equality:

$$\Delta\vec{W}\vec{R} = \Delta\vec{Q},$$

$$\Delta\vec{Q} = (\Delta\rho,\Delta(\rho U),\Delta(\rho V),\Delta E,\Delta(\rho c_1),\ldots\Delta(\rho c_n))^T, i = 1,n.$$

The system of the right eigenvectors $\vec{r}_k$ can be taken in the form $\vec{r}_1 = (0,0,1,V,0,\ldots,0)^T$ $\vec{r}_2 = (1,U,V,\omega,0,\ldots,0)^T$
$\vec{r}_3 = (1,U+a,V,H+Ua,c_1,\ldots,c_n)^T$
$\vec{r}_4 = (1,U-a,V,H-Ua,c_1,\ldots,c_n)^T$
$\vec{r}_5 = (0,0,0,h_1,1,0,\ldots,0)^T$
$\vec{r}_6 = (0,0,0,h_2,0,1,0,\ldots,0)^T$
$\vec{r}_n = (0,0,0,h_n,0,0,\ldots,1)^T$, where $U = V_n$ and

$V = V_T$—normal and tangential to bound of control volume components of gas velocity. Denoting $\Delta W = (\alpha_1,\alpha_2,\alpha_3,\alpha_4,\alpha_5,\ldots,\alpha_n)$, we can solve system (Eq. (4)) for finding ΔW components. System (Eq. (4)) has the simple decision for arbitrary number of gas mix components:

$$\begin{aligned}&\alpha_1 = \Delta(\rho V) - V\Delta\rho;\\ &\alpha_2 = \left(\Delta\rho\left(H - U^2 - \sum_{i=1}^{n} c_i h_i\right) + \Delta(\rho U)U + \sum_{i=1}^{n} h_i\Delta(\rho c_i) - \bar{E}\right)/\omega\end{aligned} \tag{5}$$

$$\alpha_3 = (-(U-a)\Delta\rho + \Delta(\rho U) - a\alpha_2)/2a$$

$$\alpha_4 = ((U+a)\Delta\rho - \Delta(\rho U) - a\alpha_2)/2a$$

$$\alpha_{i+4} = \Delta(\rho c_i) - c_i(\Delta\rho - \alpha_2), i = 1,n$$

$$\bar{E} = \Delta E - V(\Delta(\rho V) - V\Delta\rho).$$

Analogous formulae can be written for three-dimensional case, but in this paper for three-dimensional calculation, simplified mathematical model of two-phase chemical reaction [1] was used with the same procedure (Eqs. (4) and (5)) for finding left eigenvectors.

In formulae (Eqs. (4) and (5)), we consider $\omega = a^2/(\gamma-1)$ for ideal gas and $\omega = H - \rho u^2/(\partial P/\partial i)$ for the equation of state for real gas in connection with [5]. For real gas, adiabatic quotient was calculated by formula $\gamma = \sum_{i1} 5c_i/7 + \sum_{i2} 5c_i/3 + \sum_{i3} 4c_i/3$, where i_1, i_2, i_3, the number of one atomic, two atomic, and multi-atomic components of gas mix. In numerical algorithm for the equation of state for real gas, pressure and temperature on new time level were calculated by iterative procedure:

$$P = (\gamma-1)\left(\rho e - \rho\vec{V}^2/2 + \sum_i \rho_i h_i(T_n), T_{n+1} = P/\rho R_B \sum_i \frac{c_i}{\mu_i}\right. \tag{6}$$

Due to high speed of chemical reactions for both mathematical models, normalizing similar to the one used in [1] was performed. The next characteristic values were used for normalizing $\rho_0 \cdot q$ for pressure, q/R for temperature, $l/\sqrt{q}$ for time, and $\sqrt{q}$ for sound speed and gas velocity; enthalpies of formation for components were normalized by q; energies of activation and exponential factors in Arrhenius formulae (Eq. (2)) were normalized by q and $\sqrt{q}$, respectively, where q, R, and l are the enthalpy of formation for water, gas constant for dry air, and characteristic length of the problem, respectively.

For fluxes calculation, Harten scheme [6, 9] of second order of accuracy was used. The Runge–Kutta approximation of third order of accuracy was used for temporal approximation. Curvilinear structural grids for two and three dimensions were constructed on the basis of Thompson-type algorithm [10]. Detonation engine is a type of propulsion system that utilizes detonation waves for efficient combustion of the fuel and oxidizer mixture. Different designs of detonation engine have been proposed and investigated during the past decades. Numerical simulation of flows in two types of detonation engines where produced. Construction of those detonation engines based on periodic closing of injection of fuel through the ring Laval nozzles, namely, pulsing detonation engine of Levin–Tarasov [3] and rotating detonation engine [4], which is developing of Voizehovsky construction [7].

For pressure on the exit section of Laval nozzle with relation to between area of exit section and area of critical section, $S/S_* = \lambda$, and values of gas dynamics parameters in receiver ρ_m, P_m and values of pressure P', P'' for supersonic and subsonic regimes will be roots of equation:

$$\begin{aligned}&(P/P_m)^{1/\gamma}\left(1 - (P/P_m)^{(\gamma-1)/\gamma}\right)^{1/2}\\ &= (2/(\gamma+1))^{1/(\gamma-1)}((\gamma-1)/(\gamma+1))^{1/2}/\lambda\end{aligned} \tag{7}$$

The next boundary conditions can be formulated for injection of gas through the Laval nozzle [8]:

$$\begin{aligned}&u = 0 \ for \ P_m < P_p, P = P_p \ for \ P' < P_p < P_m P\\ &= P', for \ P' > P_p\end{aligned}$$

$$u = u_{\max}\sqrt{1 - (P/P_m)^{(\gamma-1)/\gamma}}, \rho = \rho_m(P/P_m)^{1/\gamma},$$
$$for \ P'' < P_p < P_m$$

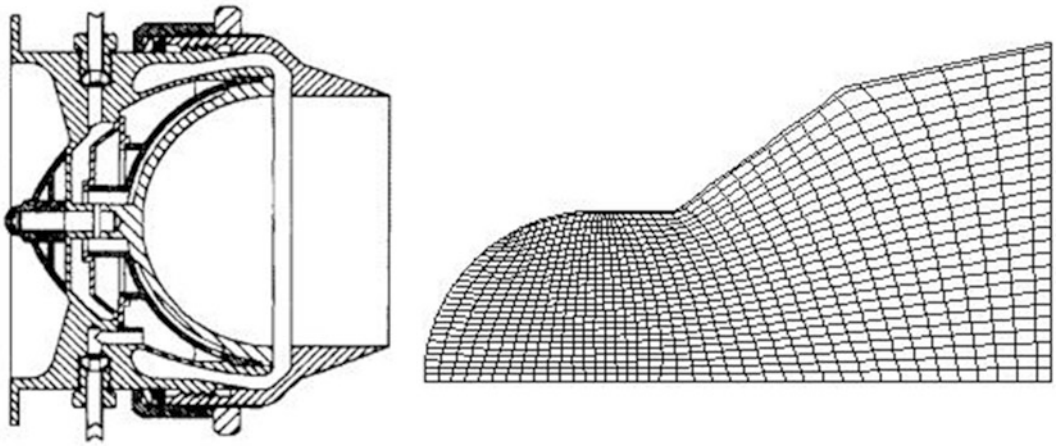

Fig. 1 Scheme of resonator for Levin–Tarasov engine (*left*) and calculation grid for area, including resonator and area of engine jet (*right*)

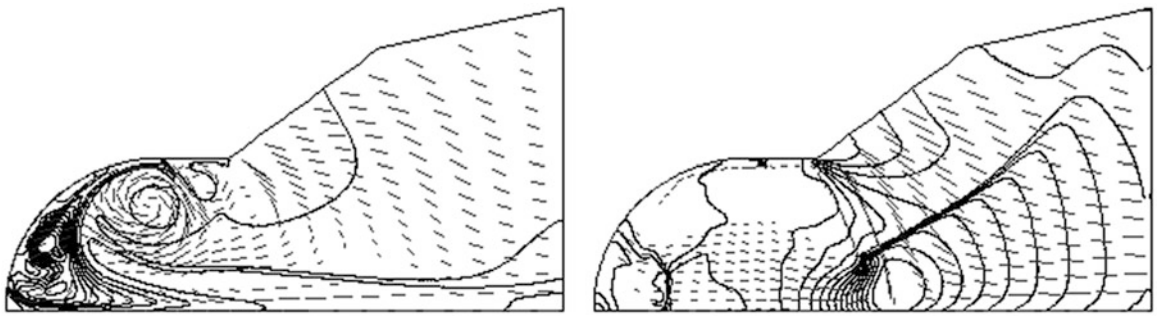

Fig. 2 Isopicts in time moments of closing ring nozzle (*left*) and detonation wave appearing (*right*)

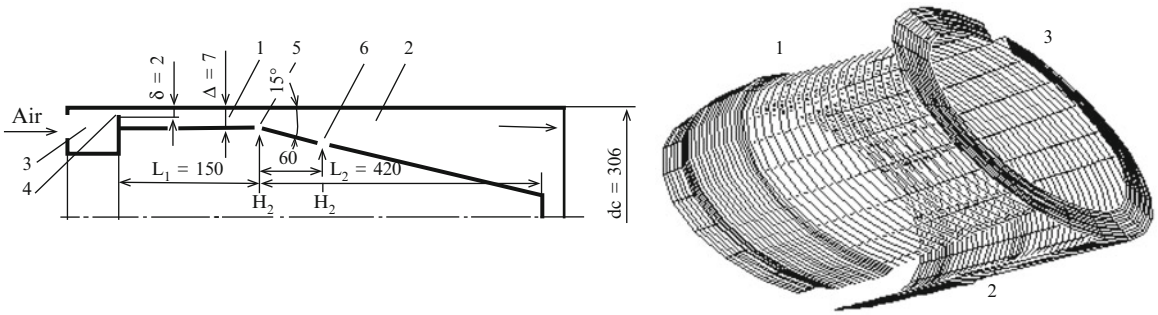

Fig. 3 Engine construction [4] (*left*) and calculation grid (*right*), every fifth coordinate line is drawn; in front, lower border; behind, up border; to the right, exit from engine border

$$\rho u S = \rho_* u_* S_*, \gamma P/(\gamma - 1)\rho + u^2/2 = u_{\max}^2/2$$

On the basis of full system of gas dynamics and kinetics (Eq. (1)), flow in pulsing detonation engine [3] was calculated. This engine comprises a reactor, where fuel–oxidizer mixture is prepared for detonation and resonator chamber of semisphere form (Fig. 1). Gaseous mixture flows from the reactor into the resonator through a ring nozzle. On the exit section of the ring nozzle, the gas dynamics parameters are defined as the decision of Laval's nozzle problem (Eq. (7)). The aim of numerical simulation was defining of flow structure at the moments of detonation wave appearing and closing of ring nozzle. Pictures of isopicts in time moments of closing ring nozzle (left) and detonation wave appearing (right) are drawn in Fig. 2.

In the resulted variants of calculation, the values of parameters, similar to the one used in [3], have been chosen.

In [4] introduced construction of rotating detonation engine with separate injection of air and fuel. The engine consists of two parts: cylindrical channel (Fig. 3, left, 1) and channel with conical internal boundary (Fig. 3, left, 2). At

the initial moment, air begins to move from reactor 3 through the ring nozzle 4. Hydrogen begins to move from second chamber through the injectors 5 or 6. Detonation initiated by explosion of aluminium foil on internal boundary of conical channel 2. Results of numerical simulation show propagation of initial detonation wave in azimutal direction and formation after detonation wave irregular structures similar to detonation cells.

Conclusions

Transition to characteristic variables of full system of the equations for any number of components of gas mixes is carried out. Decomposition on eigenvectors was made for real tabular equations of state. For realization of numerical algorithm on the basis of mathematical model, transition to dimensionless unknowns is carried out, namely, for gas dynamics unknowns, constants of kinetics of chemical reactions, and table constants of the equations of state. The formulation of boundary condition for reactive gas mixes is discussed. Numerical simulation of flows in the combustion chambers of two configurations of detonation engines was carried out.

References

1. Korobeinikov, V.P., Levin, V.A., Markov, V.V., et al.: Propagation of blast wave in a combustible gas. Astronautica Acta. **7**, 529–537 (1972)
2. Liberman, M.A.: Introduction to physics and chemistry of combustion. Springer, Berlin, Heidelberg (2008)
3. Levin, V.A., Nechaev, Y.N., Tarasov, A.I.: Control of detonation processes, pp. 197–201. Elex-KM, Moscow (2000). G. Roy (Ed.)
4. Bykovskii F.A., Zhdan S.A., Vedernikov F.F.: Continuous spin and pulse detonation of hydrogen-air mixtures in supersonic flow generated by a detonation wave. Proceedings of 22 ICDERS, Minsk, Belarus (2009)
5. Glaister, P.: An approximation linearised riemann solver for the three-dimensional euler equations for real gas using operator splitting. J. Comp. Phys. **77**, 361–383 (1988)
6. Harten, A.: A high resolution scheme for the computation of weak solutions of hyperbolic conservation laws. J. Comp. Phys. **49**, 357–393 (1983)
7. Voizehovsky, B.Y.: Stationary detonation. Doclady USSR Acad. Sci. **129**(6), 1251–1256 (1959)
8. Zhdan, S.A., Bykovskii, F.A., Vedernikov, E.F.: Numerical simulation of spin detonation in hydrogen-oxygen-gas mix. In: Frolov, S.M. (ed.) Pulsing detonation engines. Torus, Moscow (2006)
9. Martyushov S.N. Martyushova Y.G. Numerical simulation of nonstationary flows on the block regular grids. Proc. of 5-th Intern. Conf. on numerical analys and applications, In Wasnewski J (Ed.), Lect. Notes in Comp. Sci. Rousse, pp. 16–19. Springer, Bulgaria (2009)
10. Martyushov S.N. Conctruction of calculation grids on the basis of Poisson equation decosion. Proc. of 15-th IMACS World Congress on Sci. Comp., Modelling and Appl. Math., vol 2, pp. 191–195, Berlin, (1997)

Stabilization of Detonation Combustion of a Supersonic Flow due to Using the Special Form Plane Channel

V.A. Levin and T.A. Zhuravskaya

Introduction

The interest in the study of detonation in a gas mixture is closely connected with practical demands. So the intention to use detonation in energy generating plants, for example, in detonation engines requires fundamental knowledge about detonation combustion of high-velocity flows. In particular, the detection of the technique of a control of detonation propagation in a supersonic gas flow and determination of conditions that provide detonation stabilization in a flow are of great interest. So the method of detonation stabilization in a supersonic gas flow in a plane channel with parallel walls by means of weak discharges has been proposed in [1, 2]. However the detonation stabilization without any expenditure of energy is of more interest. So, the formation of stabilized detonation in supersonic flows of hydrogenous mixtures in an axisymmetric nozzle was investigated (see, e.g., [3]). Stabilization of rotating detonation in an axisymmetric combustion chamber was studied in [4]. The formation of stationary detonation in the plane channels with a wedge-shaped part for some combustible gas mixtures was examined in [5, 6]. Using quasi-one-dimensional model detonation stabilization in a supersonic flow in a channel with variable cross section area was studied too [7].

In the present research, the possibility of detonation combustion stabilization in a supersonic flow of a stoichiometrical hydrogen–air mixture due to using the special form plane channels (without any energy input) was investigated.

V.A. Levin
Institute of Mechanics, M.V. Lomonosov Moscow State University, Michurinskiy Avenue, 1, Moscow, Russia

Institute of Automation and Control Processes, Far Eastern Branch of RAS, Radio Street, 5, Vladivostok, Russia

T.A. Zhuravskaya (✉)
Institute of Mechanics, M.V. Lomonosov Moscow State University, Michurinskiy Avenue, 1, Moscow, Russia
e-mail: zhuravskaya@imec.msu.ru

Mathematical Model

Detonation propagation in a premixed stoichiometrical hydrogen–air mixture flowing into a plane channel (inflow cross section and outflow one are perpendicular to the incoming flow direction) is studied. The combustible gas mixture under the normal conditions ($p_0 = 1$ atm, $T_0 = 298$ K) is incoming into the channel at a supersonic velocity that essentially exceeds a velocity of self-sustaining detonation propagation in the quiescent mixture with incoming flow parameters: that is, $M_0 > M_{J0}$ (here, M_0 is the flow Mach number, M_{J0} is the Mach number of self-sustaining detonation).

The set of gas dynamics equations describing a plain two-dimensional nonstationary flow of the inviscid reactive multicomponent gas mixture is as follows:

$$\frac{\partial \rho}{\partial t} + \frac{\partial (u\rho)}{\partial x} + \frac{\partial (v\rho)}{\partial y} = 0$$

$$\frac{\partial (\rho u)}{\partial t} + \frac{\partial (\rho u^2 + p)}{\partial x} + \frac{\partial (\rho uv)}{\partial y} = 0$$

$$\frac{\partial (\rho v)}{\partial t} + \frac{\partial (\rho vu)}{\partial x} + \frac{\partial (\rho v^2 + p)}{\partial y} = 0$$

$$\frac{\partial (\rho(u^2+v^2)/2 + \rho h - p)}{\partial t} + \frac{\partial (u\rho((u^2+v^2)/2 + h))}{\partial x} + \\ + \frac{\partial (v\rho((u^2+v^2)/2 + h))}{\partial y} = 0$$

$$\frac{\partial (\rho n_i)}{\partial t} + \frac{\partial (u\rho n_i)}{\partial x} + \frac{\partial (v\rho n_i)}{\partial y} = \rho \omega_i$$

where x and y are the Cartesian coordinates; u and v are the corresponding velocity components; t is the time; ρ, p, and

G. Ben-Dor et al. (eds.), *30th International Symposium on Shock Waves 1*, DOI 10.1007/978-3-319-46213-4_71

h are the density, the pressure, and the enthalpy, respectively; n_i is the molar concentration of the ith species in the mixture; and ω_i is the rate of formation/depletion of the ith component. The examined mixture consists of ten species: H_2, O_2, H, O, OH, HO_2, H_2O, H_2O_2, N_2, and Ar.

The equations of state for the mixture have the usual form

$$p = \rho R_0 T \sum_i n_i \,, \; h = \sum_i n_i h_i(T)$$

Here, T is the temperature, and R_0 is the universal gas constant. The partial enthalpy $h_i(T)$ of the ith mixture component is determined by the Gibbs reduced energy of this component [8].

The inflow boundary conditions are the incoming flow parameters; the outflow boundary condition is necessary only in boundary points with a subsonic velocity of gas outflow (in this case, flow parameters are determined by the solution of the problem about gas outflow into a region with the pressure p_{out}: $p_{out} = p_0$). Slip condition is imposed at the channel surface.

A set of Euler gas dynamics equations coupled with detailed chemical kinetics equations [9] (in case of symmetrical channels with narrowing) and [10] (for channels of special shape) has been solved using a finite-difference method based on Godunov's scheme. The adaptive computational mesh was used for numerical simulation of studied flows with detonation waves. The size of mesh was selected so that the flow behind the detonation front (in particular, the flow in the induction zone) was represented correctly. Thus the computational mesh with cell size 0.03 mm − 0.01 mm was used in numerical calculations.

Detonation Stabilization in a Channel with Narrowing

The possibility of stabilization of formed detonation without any energy input in the combustible gas mixture flowing at a supersonic velocity into the symmetrical plane channel with narrowing cross section was investigated. The schematic of the upper part of the channel is shown in Fig. 1a: the inflow boundary is $x = x_4$, the outflow boundary is x =0, and the channel width is a continuously differentiable function of a longitudinal coordinate. The initial condition is the steady supersonic plane two-dimensional flow of the gas mixture in this channel obtained by the stabilization method. The initial instantaneous supercritical energy input E_0 in the narrow layer-shaped domain located near the $x = x_1$ section (shaded region in Fig. 1a) was used for detonation initiation. Two detonation waves are formed as a result of the energy input: the first one propagates downstream (this wave is transferred by the flow) and the other propagates upstream. The influence of geometrical parameters of the channel on propagation of the latter detonation wave has been studied. It has been established that for some values of the incoming flow Mach number M_0, the geometrical channel parameters may be selected so that the detonation wave is stabilized in the flow without any energy input.

So, the pressure field and the density contours in case of detonation stabilization in the divergent (in the line of flow) part of the channel for M_0 =5.2 are presented in Fig. 1b and Fig. 1c. In the case under consideration, the detonation wave initiated by energy input near the $x' = 5$ ($x' = x_1/l$) section moves upstream and is stabilized with time at a short

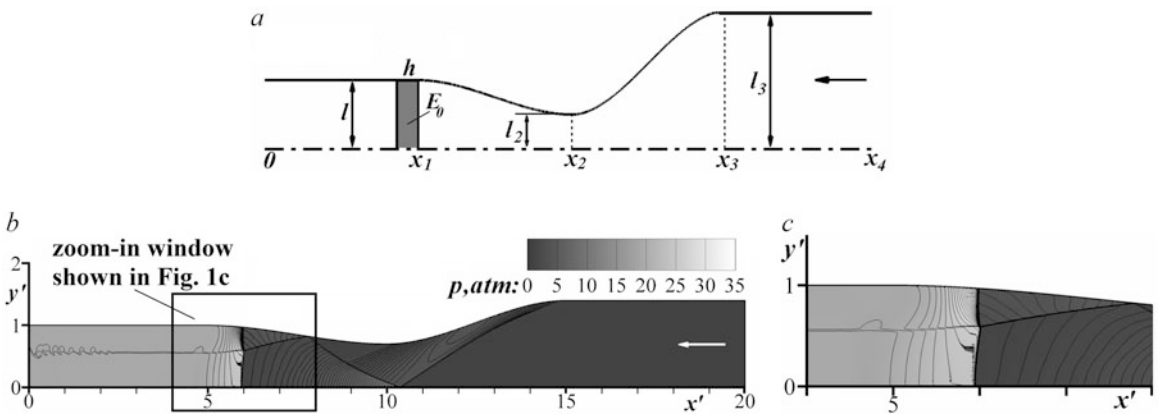

Fig. 1 Detonation stabilization in the channel with narrowing: (**a**) the schematic of the upper part of the channel; (**b**) detonation stabilization in the divergent part of the channel for M_0 = 5.2; (**c**) zoom-in window showing stabilized detonation. Here and further $x' = x/l$, $y' = y/l$, where l is the half of the outflow section width; the *arrow* shows the flow direction

distance from the $x' = 6$ section. Decrease of a wave velocity and subsequent detonation stabilization are determined by the presence of transversely extended flow region with a large value of the longitudinal velocity in front of the wave in the divergent part of the channel. The stabilized detonation wave and the oblique shock wave of the initial steady flow form a Mach configuration; the formed flow with stabilized detonation is unsteady.

In the case of detonation stabilization for $M_0 = 5.2$, the energy input in a narrow layer-shaped domain was used for testing the stability of this flow with the stabilized wave. The energy input E_{test} ($E_{\text{test}} = 100$ J/m) with the exponential dependence of energy input density on transversal coordinate and with uniform density in the domain containing the stabilized detonation front and in a domain placed in front of detonation was considered. It has been established that in spite of a disturbance of stabilized detonation after energy release, the energy input under consideration does not break the wave stabilization and does not change the location of the stabilized detonation wave (Fig. 2a). Moreover, the flow disturbance by the energy input E_{test} with the exponential dependence of energy input density on transversal coordinate in the domain located near the $x' = 7$ section was considered. In this case, energy supply E_{test} leads to formation of a new detonation wave upstream. However, this wave is transferred by the flow and is stabilized with time in that place where the initial stabilized detonation was located (Fig. 2b). These results indicate the stability of the flow under consideration with the stabilized detonation wave to strong disturbances of a certain type.

Formation of Stabilized Detonation in the Plane Channel of Special Shape

In the case of channel with narrowing cross section, the initial energy input was used for detonation initiation. For the determination of a channel shape which gives detonation initiation and its stabilization in the flow without any expenditure of energy, a plane two-dimensional supersonic flow of the combustible gas mixture with Mach number $M_0 = 5.5$ and 6 about the symmetrical semi-infinite plane obstacle placed along the stream was considered. The obstacle configuration was chosen so that the flow with detonation was formed. There is formation of a detonation wave stabilized near the obstacle due to a flow velocity which is more than a detonation one ($M_0 > M_{J0}$). In cases under consideration, the flow with the stabilized detonation is unsteady due to transverse waves propagating along the detonation front (Fig. 3).

In the case of $M_0 = 5.5$, the structure of the stabilized ahead of the obstacle detonation wave was considered. It has been established that the detonation wave is divided into three sections with different structures (Fig. 4). So a part of the wave near the symmetry plane is an overdriven detonation; with the increase of the distance from the plane of symmetry, the left-running transverse waves (facing upstream) propagate along the detonation front (Fig. 4c); with the further distance increase, the transverse waves of both sets (left-running and right-running) are formed (Fig. 4d) and define a cellular structure that is qualitatively similar to a plane detonation wave structure [11]. The detected structure of the detonation wave stabilized ahead

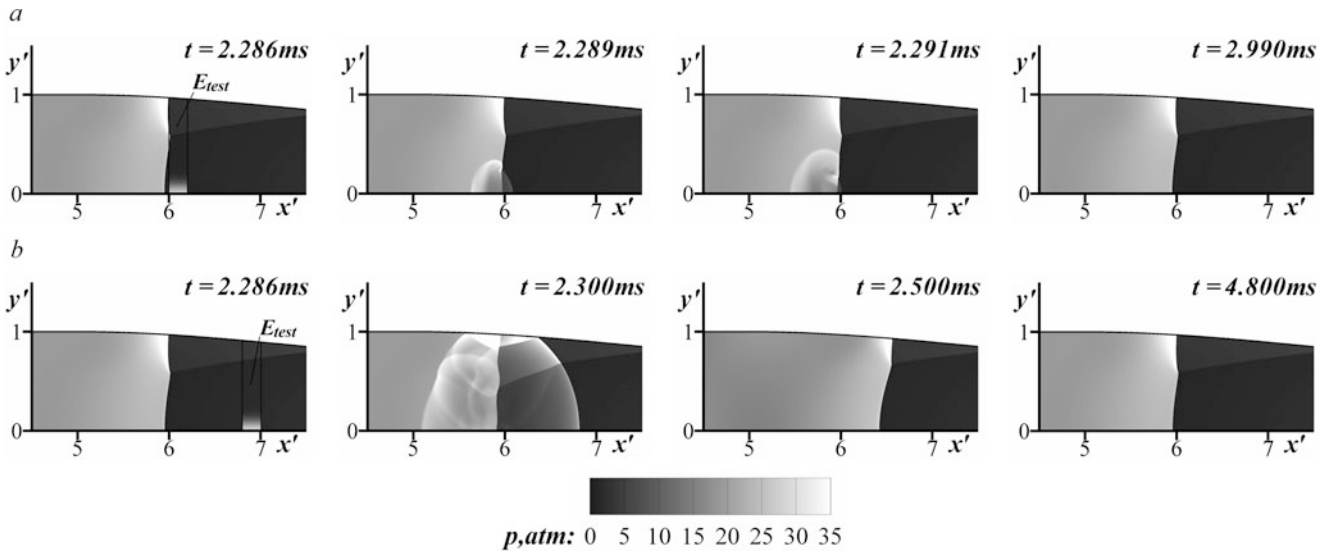

Fig. 2 The conservation of detonation stabilization in case of energy input E_{test} (at the moment of time $t = 2.286$ ms) with the exponential dependence of energy input density on transversal coordinate: (**a**) the energy input domain is located in front of the detonation wave; (**b**) the energy input domain is located near the $x' = 7$ section

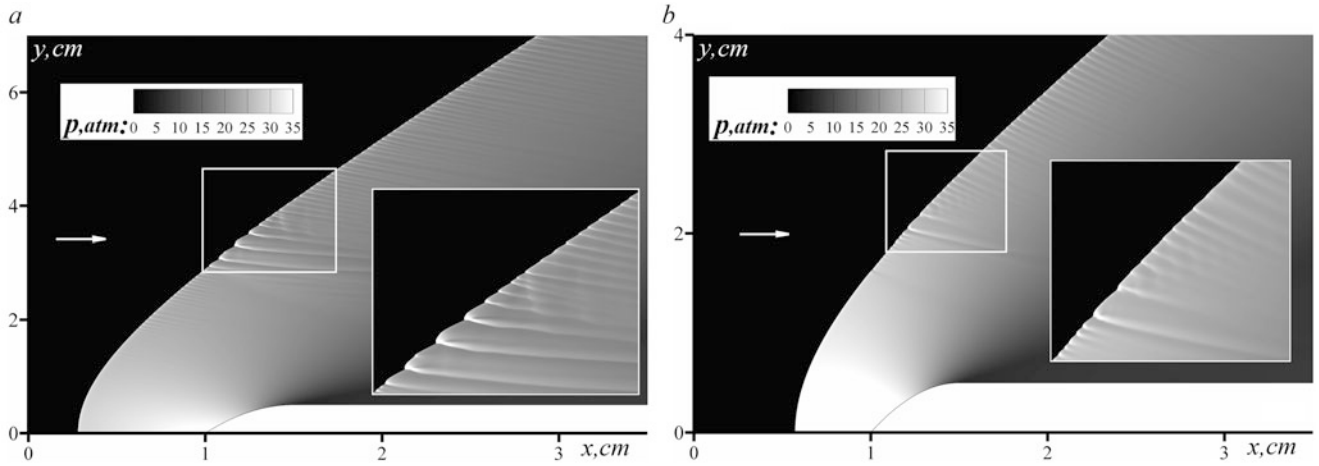

Fig. 3 The detonation wave stabilized ahead of the obstacle: (**a**) $M_0 = 5.5$; (**b**) $M_0 = 6$

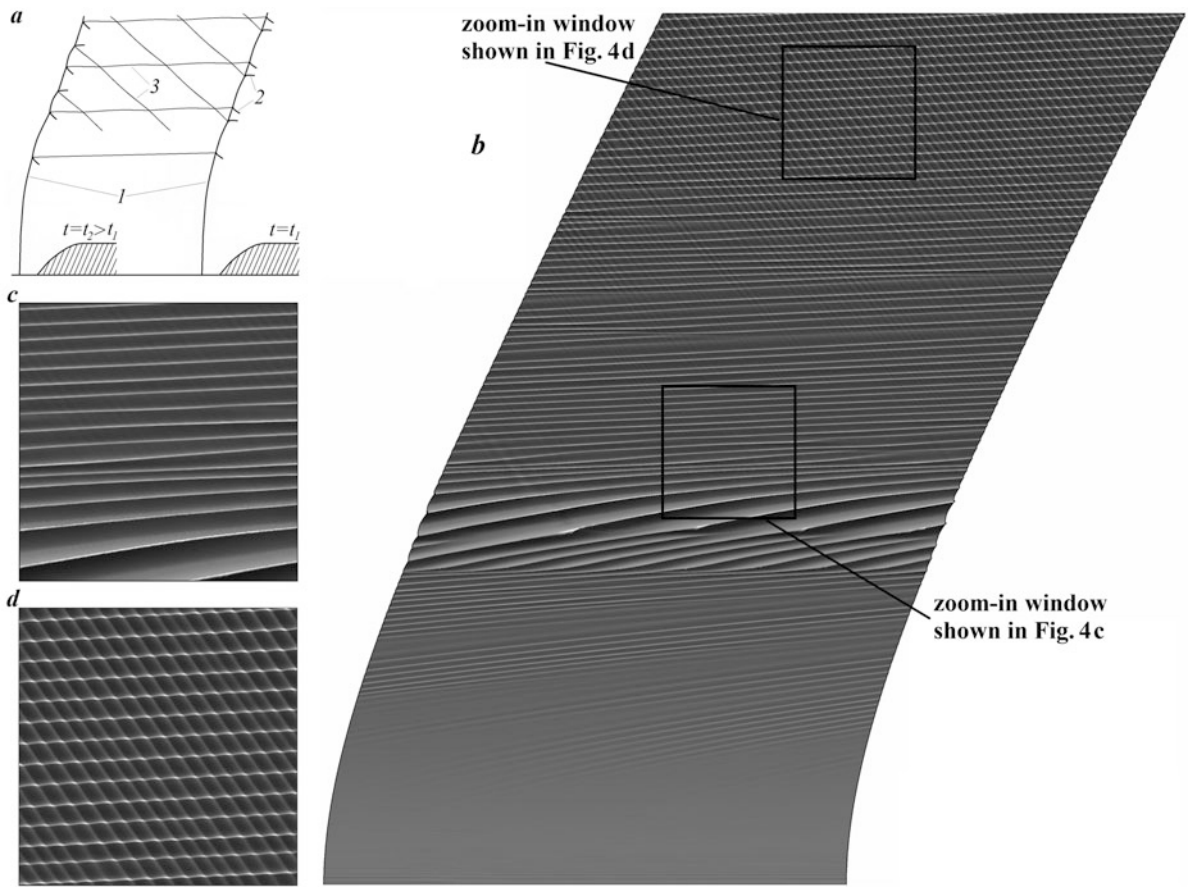

Fig. 4 The structure of a detonation wave stabilized ahead of the obstacle in the coordinate system connected with the flow: (**a**) schematic of the cellular structure of the wave (*1*, the detonation front; *2*, transverse waves; *3*, trajectories of triple points); (**b**) numerical soot foil showing the trajectories of triple points in the stabilized detonation structure in the case of $M_0 = 5.5$ (axes scale is equal); (**c**, **d**) zoom-in windows showing the detonation structure

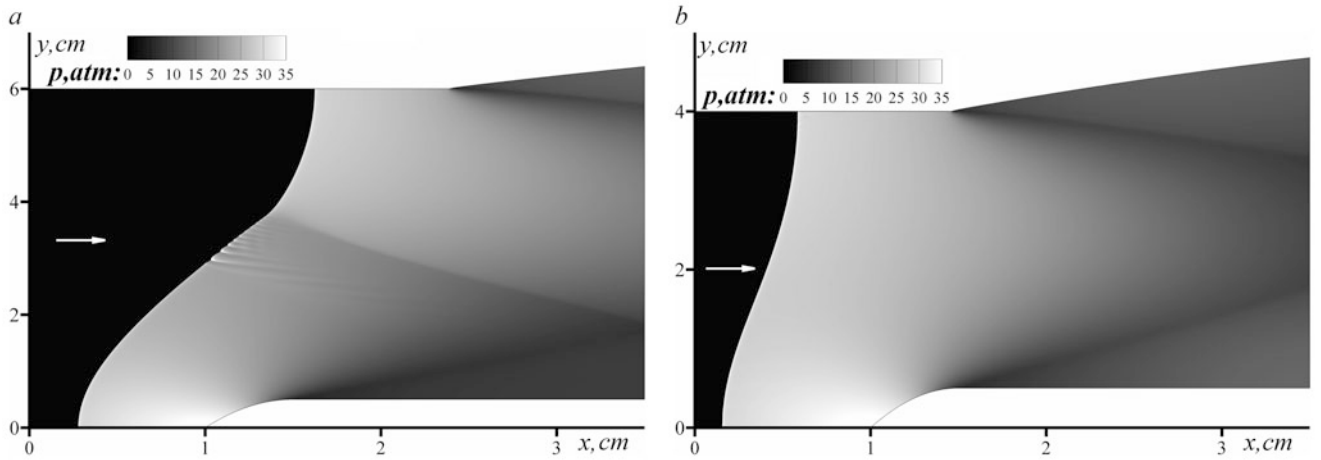

Fig. 5 Flow in the channel of the special shape in the case of $M_0 = 5.5$: (**a**) formation of stabilized detonation in the channel with supercritical width of the inflow cross section; (**b**) the detonation wave moves upstream from the channel in the case of subcritical width of the inflow cross section ($t = 0.985$ ms)

of the obstacle is conformed with a structure of a wedge-induced oblique detonation wave [12, 13].

Then detonation combustion of the gas mixture flowing at the same velocity into plane channels (the top walls of which are determined by streamlines of the flow under consideration, the bottom one is determined by the plane of symmetry and by the obstacle surface) was studied. The initial condition is the incoming gas flow.

It has been established that for fixed incoming flow Mach number M_0, the detonation wave is stabilized in the channel, the shape of which is defined in this way, if the width of the inflow cross section is more than some critical one (Fig. 5a). In the case of subcritical width of the inflow cross section, the detonation wave moves upstream from the channel (Fig. 5b).

Conclusions

The possibility of stabilization of a formed detonation wave without energy input in a stoichiometrical hydrogen–air mixture flowing at a supersonic velocity into the plane channel with narrowing cross section has been determined. The stability of the flow with stabilized detonation in the channel with narrowing has been examined. For some Mach numbers of the incoming flow, the method of determination of the channel shape which gives detonation initiation and its stabilization in the flow without any expenditure of energy is proposed.

In the case of a plane two-dimensional supersonic flow of the gas mixture about the plane obstacle placed along the stream, it has been established that the detonation wave stabilized ahead of the obstacle is divided into three sections with different structures.

Acknowledgments This research has been partly supported by the Russian Foundation for Basic Research (14-01-00742, 16-29-01092), by the President Grant for Support of Leading Science Schools of the Russian Federation (NSh-8425.2016.1), by the Presidium of the RAS (the program No. 24), and by the complex program for basic research of the Far Eastern Branch of the RAS "Far East." The study of the stability of the flow with stabilized detonation in the channel with narrowing cross section and the investigation of the structure of the detonation wave stabilized ahead of the obstacle have been supported by the Russian Science Foundation (14-19-01759 and 14-11-00773, respectively). This research has been supported by the Supercomputing Center of the Lomonosov Moscow State University.

References

1. Zhuravskaya, T.A., Levin, V.A.: Investigation of certain techniques for stabilizing detonation waves in a supersonic flow. J. Fluid Dynam. **47**(6), 793–801 (2012)
2. Levin, V.A., Zhuravskaya, T.A.: The problem of detonation stabilization in a supersonic gas flow in the different plane channels. Proc. 24th Int. Colloquium on the Dynamics of Explosions and Reactive Systems (ICDERS), ICDERS_0125.pdf, (2013)
3. Tunik, Y.V.: Numerical modeling of detonation combustion of hydrogen-air mixtures in a convergent-divergent nozzle. J. Fluid Dynam. **45**(2), 264–270 (2010)
4. Fujiwara, T., Hishida, M., Kindracki, J., Wolanski, P.: Stabilization of detonation for any incoming Mach numbers. Combust. Explos. Shock Waves **45**(5), 603–605 (2009)
5. Trotsyuk, A.V., Kudryavtsev, A.N., Ivanov, M.S.: Numerical investigations of detonation waves in supersonic steady flows. In: Roy, G., et al. (eds.) Pulse and continuous detonation propulsion, pp. 125–138. Moscow, Torus press (2006)
6. Fan, H.Y., Lu, F.K.: Numerical modelling of oblique shock and detonation wave induced in a wedged channel. Proceedings of the Institution of Mechanical Engineers Part G. J. Aerospace Eng. **222**, 687–703 (2008)
7. Levin, V.A., Manuilovich, I.S., Markov, V.V.: Excitation and quenching of detonation in gases. IFZh **83**(6), 1174–1201 (2010)

8. Glushko, V.P. (ed.): Thermodynamic properties of individual substances. Nauka, Moscow (1978)
9. Warnatz, J., Maas, U., Dibble, R.W.: Combustion. Physical and chemical fundamentals, modeling and simulation, experiments, pollutant formation. Springer, Berlin (2001)
10. Starik, A.M., Titova, N.S., Sharipov, A.S., Kozlov, V.E.: Syngas oxidation mechanism. Combust. Explos. Shock Waves **46**(5), 491–506 (2010)
11. Lee, J.H.S.: The detonation phenomenon. Cambridge University Press, New York (2008)
12. Gui, M.Y., Fan, B.C., Dong, G.: Periodic oscillation fine structure of wedge-induced oblique detonation waves. Acta Mach. Sin. **27** (6), 922–928 (2011)
13. Verreault, J., Higgins, A., Stowe, R.: Formation of transverse wave in oblique detonations. Proc. Comb. Inst. **34**, 1913–1920 (2013)

Role of Wall Temperature on Shock Train in a Rectangular Isolator

Lianjie Yue, Hongbo Lu, Yabin Xiao, Lihong Chen, and Xinyu Chang

Aimed at the problem of isolator being seriously heated by aeroheating, effects of wall temperature on flow characteristics of isolator are experimentally and numerically investigated. The results show that shock train is affected by the dual mechanism of isolator wall temperature and airflow total temperature. With an increase of wall temperature and a reduction of total temperature, the length of shock train increases. This tendency can be characterized by the variation of shock train length with ratio of wall temperature to total temperature. Based on numerical data, both the ratio of wall temperature to total temperature and specific heat ratio are introduced to modify the correlation of Waltrup and Billig for predicting shock train length of practical design with the coverage of more physical influencing factors.

Introduction

An isolator module is a constant or nearly constant area duct located between the inlet and combustor of scramjet [1, 2]. Its role is to house shock train induced by heat release in a combustor and extend engine operation conditions such as higher equivalence ratio without incurring spillage or unstart [3]. In engine design, the isolator length has to be optimal to minimize the weight and drag of the overall system and fully hold shock train, and therefore it is vital to well understand shock train behavior and accurately calculate shock train length in the isolator under flight conditions. To resolve these issues, numerous investigations [4–9] have been performed to examine the influence of parameters such as the entrance conditions, the exit back pressure ratio, and the geometric effects. It is found that the occurrence of shock train strongly depends on the upstream Mach number and the boundary layer thickness.

These fruitful achievements promote a deep understanding of shock train structures and isolator design, but most of results are obtained using room-temperature supply air or cold air as flow gas ($T_t = 300$ K), so that the role of air temperature and heat transferred from airflow to the isolator wall cannot be taken into account. At real flight conditions, the air temperature in the isolator is high, and the isolator walls are also subjected to severe aerodynamic heating [10], resulting in the isolator surfaces being heated up. Accordingly, the boundary layer thickness on the wetted surfaces increases, as well as an increase of the gas static temperature in the boundary layer, reducing the fullness of boundary layer profile and the gas density. Thus an increase of wall temperature will lead to a more likely separation of boundary layer. From these results, it can be inferred that the ability of isolator holding shock train will go down with an increase of wall temperature. This tendency coincides with the research results of Cuffel [10], Fisher et al. [11, 12], and Lin et al. [13, 14], but is contrary to the findings of Fischer and Olivier [15]. Fischer and Olivier [15] believed that the opposite effect should be attributed to the wall being heated up beyond the recovery temperature of the airflow. Furthermore, the boundary layer profile in the correlation of Waltrup and Billig [5] is denoted by boundary layer momentum thickness, which indirectly involves the wall temperature influences, but whether it fully covers the wall temperature effects or not still needs be checked. As mentioned above, the effects of surface temperature and gas temperature on shock train have not been well elucidated. This paper describes our recent efforts in confirming the effects of surface temperature on shock train and isolator performance by a combination of experimental and numerical tests.

L. Yue (✉) • Y. Xiao • L. Chen • X. Chang
Institute of Mechanics, Chinese Academy of Sciences, No.15 Beisihuanxi Road, Beijing 100190, China
e-mail: yuelj@imech.ac.cn

H. Lu
Chinese Academy of Aerospace Aerodynamics, Beijing 100074, China

G. Ben-Dor et al. (eds.), *30th International Symposium on Shock Waves 1*, DOI 10.1007/978-3-319-46213-4_72

Experimental and Numerical Description

Experimental Description

Experiments were carried out in a direct-connect test facility, composed of a heater, a 2D nozzle, an isolator, and a throttle valve to simulate back pressure rise induced by heat release. In the heater, compressed dry air was heated to the required total temperature (T_t) and total pressure (P_t) by hydrogen combustion and oxygen replenishment. A two-dimensional nozzle designed for a Mach number of 2.5 was used in conjunction with a nearly constant area isolator with a length of 600 mm and a cross-sectional area of 50 × 70 mm^2. Isolator walls were uniformly heated by a heated ceramic chip, and wall temperatures of vertical and horizontal sides were almost identical. Wall static pressure taps were located on the centerline of the top, bottom, and side walls, respectively, as shown in Fig. 1. On the top wall, there were 24 pressure transducers at intervals of 20 mm, denoted by "T1 ~ T24" in Fig. 1. On the bottom wall, there were 13 pressure transducers at intervals of 40 mm, denoted by "B1 ~ B13" in Fig. 1. On the side wall, there were eight pressure transducers, denoted by "S1 ~ S8" in Fig. 1. Additionally, 12 K-type sheathed thermocouple denoted by "T_w1 ~ T_w12" in Fig. 1 was located on the centerline of the bottom wall to monitor the heating process of isolator walls. Pressure profiles on isolator walls were measured at different isolator wall temperatures for different back pressures.

Numerical Description

In addition to the measurements, numerical simulations were performed on a 2D domain including nozzle and isolator to provide tremendous information to understand the flow phenomenon. The full N–S equations for two-dimensional turbulent flow are solved by the finite volume method. The turbulence model of k-ω SST is employed to close the governing equations. The numerical flux through each cell face is evaluated using a second-order total variation diminishing (TVD) scheme based on an approximate Riemann solver named Harten–Lax–van Leer contact (HLLC). The minmod limiter is used to suppress spurious oscillations near the discontinuities, while high-order accuracy is retained away from the jumps. A second-order fully implicit scheme is employed to discretize the time terms. In addition, methods of multigrid and dual time-step are used to accelerate the convergence.

Results and Discussion

This section presents the effects of wall temperature and back pressure on shock train and isolator performance at two experimental flow conditions and one numerical flow condition. Condition I corresponds to the experimental condition of total temperature T_t = 1500 K, total pressure P_t = 1.0 MPa, and Mach number Ma_1 = 2.5 at the isolator entrance. Condition II corresponds to the experimental condition of total temperature T_t = 1000 K, total pressure P_t = 0.84 MPa, and Mach number Ma_1 = 2.5 at the isolator entrance. In order to enrich flow information, numerical tests with a constant specific heat ratio of 1.33 are also performed on a two-dimensional domain including a nozzle and isolator where the nozzle wall temperature is specified as 300 K, identical to experimental tests. Although two-dimensional numerical results cannot reflect three-dimensional effects in a rectangular isolator, they assist to elucidate experimental phenomenon and qualitatively demonstrate the influencing trend of wall temperature on shock train and isolator performance.

Shock Train Length

Figure 2 shows the experimental wall pressure distributions for different wall temperatures at the condition I and $P_{B13}/P_{T1} \approx 3.9$. From Fig. 2a, b, it can be seen that little difference exists in wall pressure profiles and the starting position of pressure rise for T_w = 300 K, T_w = 700 K, and T_w = 900 K, which is identical to the results of Fischer and Olivier [15] at a

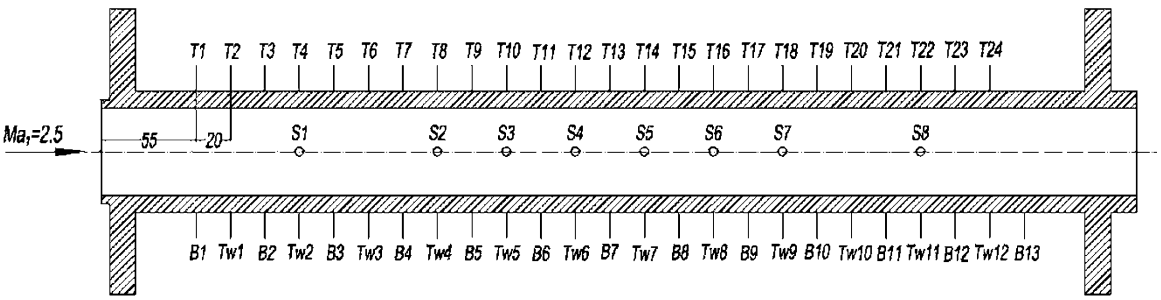

Fig. 1 Schematic of experimental isolator and measuring tap distributions

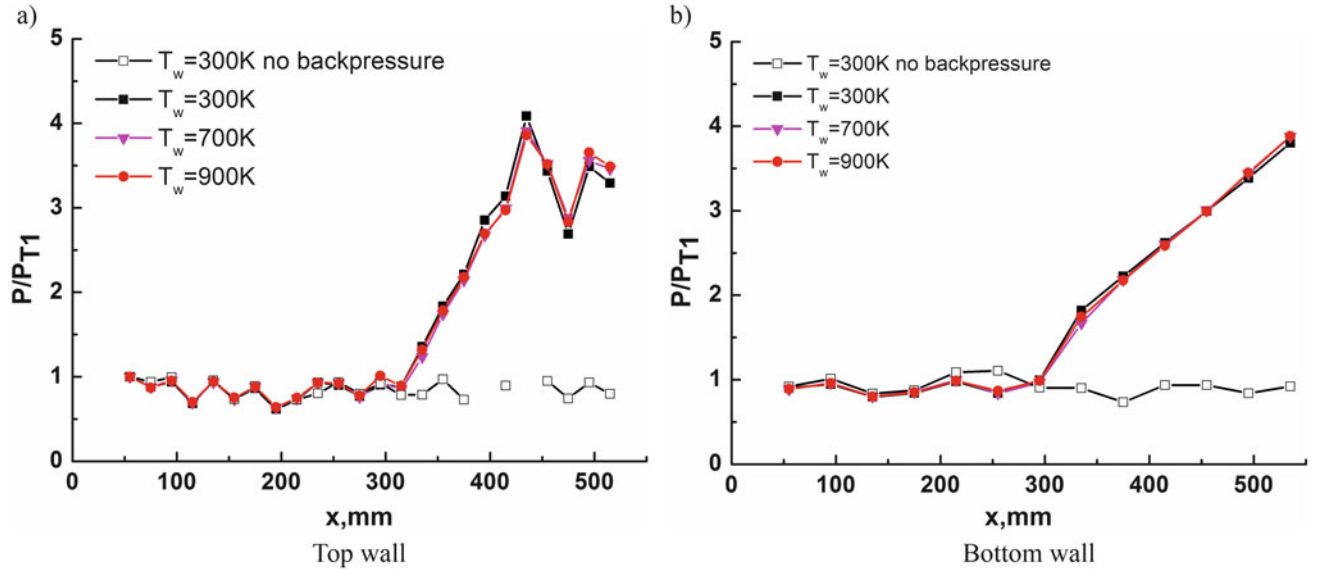

Fig. 2 Wall pressure distributions of the rectangular isolator for different wall temperatures at the condition I and $P_{B13}/P_{T1} \approx 3.9$ (experiment)

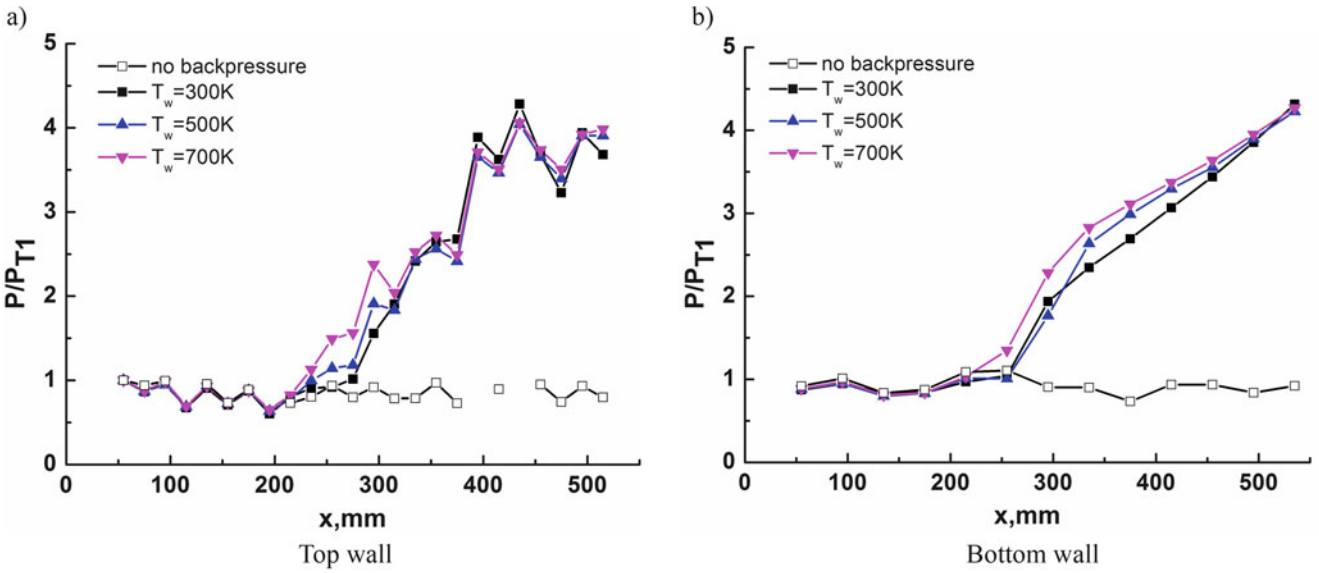

Fig. 3 Wall pressure distributions of the rectangular isolator for different wall temperatures at the condition I and $P_{B13}/P_{T1} \approx 4.3$ (experiment)

low back pressure level. This indicates wall temperature has little influence on shock train length at a low back pressure level. With an increase of back pressure to $P_{B13}/P_{T1} \approx 4.3$, a notable difference is observed from the top and bottom wall pressure distributions for $T_w = 300$ K, $T_w = 500$ K, and $T_w = 700$ K at the condition I, as shown in Fig. 3. With an increase in wall temperature, the starting position of shock train moves upstream, but that close to the exit is approximate to the same pressure level. This suggests that shock train length increases with an increase in wall temperature, leading to a reduction in the ability of isolator holding shock train.

Figure 4 shows a series of experimental data distributions on variation of shock train length s with back pressure ratio P_{B13}/P_{T1} between $T_w = 300$ K and $T_w = 900$ K at the condition I. Here shock train length s for a specific back pressure ratio P_{B13}/P_{T1} is defined as the streamwise distance between the last measure point B13 and the shock train starting position x_{st}. x_{st} is specified as the first measure point whose pressure being greater than or equal to $1.1P_{T1}$. Due to the existence of some scatter in Fig. 8, a fitted curve is plotted to specifically underline the effect of wall temperature on shock train length. For a constant shock train length, back pressure ratio P_{B13}/P_{T1} reduces with an increase of wall

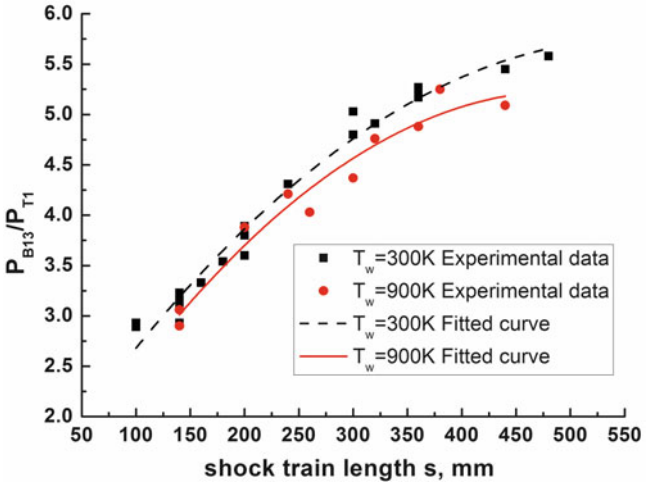

Fig. 4 Statistical analysis on variation of shock

temperature. The difference in shock train length between $T_w = 300$ K and $T_w = 900$ K increases with an increase of P_{B13}/P_{T1}. The extent of wall temperature effect enhances with an increase of back pressure. Thus it can be inferred that wall temperature effect mainly appears in the interaction of waves with boundary layer. It is well known that shock train mainly consists of a series of X-type shock patterns at Mach 2.5 and the number of X-type shock patterns grows with back pressure. Naturally, wall temperature effect is strengthened by an increasing number of X-type shock patterns. At a low back pressure, shock train just contains few X-type shock patterns so that wall temperature effect is extremely weak and cannot be visible in wall pressure distributions due to the lack of an enough dense measure point. At a high back pressure, shock train contains a series of X-type shock patterns, and therefore wall temperature effect is bound to be more apparent.

According to the correlation of Waltrup and Billig [5] expressed as Eq. (1), shock train length varies directly with $\theta^{0.25}$. For a constant Mach number and Reynolds number, shock train length predicted by Eq. (1) should gradually tend to be the same value for different wall temperatures when back pressure increases. This predicted tendency is contrary to our results. Consequently, wall temperature effect cannot be elucidated by the boundary layer momentum thickness θ, the only parameter involving wall temperature effect in Eq. (1), and another dimensionless parameter has to be introduced to elucidate this influence. To figure out this parameter, a further numerical computation is performed at the conditions I and II, as shown in Tables 1 and 2. Shock train length obtained from the condition I is almost identical with that obtained from the condition II as long as the ratio of wall temperature to gas total temperature is approximately the same. For example, when $T_w/T_t \approx 0.3$, shock train length for $T_w = 300$ K and $T_t = 1000$ K is 256 mm at $P_b/P_1 = 4.8$, while that for $T_w = 500$ K and $T_t = 1500$ K is 261 mm:

Table 1 Shock train length distributions at the condition I

Wall condition	T_w (K)	500	700	900	Adiabatic wall
Back pressure	T_w/T_t	0.33	0.47	0.6	≈1
$P_b/P_1 = 4.8$	s (mm)	261	270	279	296

Table 2 Shock train length distributions at the condition II

Wall condition	T_w (K)	300	500	700	Adiabatic wall
Back pressure	T_w/T_t	0.3	0.5	0.7	≈1
$P_b/P_1 = 4.8$	s (mm)	256	277	284	295

$$\frac{s\left(Ma_1^2-1\right)\mathrm{Re}_\theta^{1/4}}{D^{1/2}\theta^{1/2}} = 50\left(\frac{P_b}{P_1}-1\right)+170\left(\frac{P_b}{P_1}-1\right)^2 \quad (1)$$

Correlation of Shock Train Length and Wall Temperature Effects

Although Eq. (1) is derived from the cold airflow experiments with a cylindrical isolator, it still works in principle for rectangular cross sections if the parameter D is replaced by the duct height H [11]. As noted in Sec. III.A, it is concluded that the ratio of wall temperature to gas total temperature should be introduced to characterize wall temperature effect on shock train. Thus we propose the following relationship denoted by Eq. (2) to cover the relevant parameters.

$$f\left(\frac{T_w}{T_t}\right)\frac{s\left(Ma_1^2-1\right)\mathrm{Re}_{\theta_1}^{1/4}}{H^{1/2}\theta_1^{1/2}} = 50\left(\frac{P_b}{P_1}-1\right)+170\left(\frac{P_b}{P_1}-1\right)^2 \quad (2)$$

It is known that the specific heat ratio γ will reduce with an increase of static temperature when static temperature is larger than 400 K. Thus the specific heat ratio effect also need be considered. From the oblique shock relationship, we know that pressure ratio P_2/P_1 across an oblique shock with shock angle of β will reduce with a reduction of γ for a constant approach Mach number, contributing to a longer shock train. In view of shock train consisting of a series of X-type shock pattern, Eq. (3) is adopted to characterize specific heat ratio effect on shock train. To coincide with Eq. (1) for $\gamma = 1.4$ at the absence of wall temperature effect, we obtain $\varphi_0 = 1.7\text{-}\frac{1.4}{Ma_1^2}$. It can be noted that shock train length given by Eq. (3) increases with a reduction of γ for a fixed back pressure, consistent with physical mechanism.

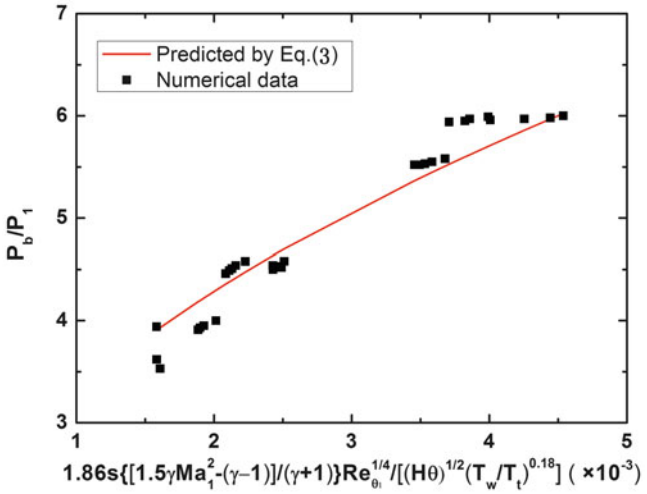

Fig. 5 A comparison of our numerical data train length with back pressure ratio P_{B13}/P_{T1} against those from Eq. (3)

$$f\left(\frac{T_w}{T_t}\right)\frac{s\left(\frac{\varphi_0\gamma}{\gamma+1}Ma_1^2-\frac{\gamma-1}{\gamma+1}\right)\mathrm{Re}_{\theta_1}^{1/4}}{H^{1/2}\theta_1^{1/2}} = 50\left(\frac{P_b}{P_1}-1\right)+170\left(\frac{P_b}{P_1}-1\right)^2 \quad (3)$$

According to Eq. (3), the function $f(T_w/T_t)$ can be calculated using the known parameters of s, Ma1, γ, θ_1, $\mathrm{Re}_{\theta 1}$, P_b/P_1, and H, where the subscript 1 denotes the starting location of shock train. From numerical results, it can be found that the function $f(T_w/T_t)$ reduces nonlinearly with an increase of the ratio T_w/T_t. A power function expressed $f\left(\frac{T_w}{T_t}\right)=\varphi_1\left(\frac{T_w}{T_t}\right)^{\varphi_2}$ is introduced to characterize this tendency, where φ_1 and φ_2 are viewed as the constants. From numerical data, $\varphi_1 = 1.91$ and $\varphi_2 = -0.18$. Figure 5 shows the degree of success obtained in the correlation Eq. (3). Some scatter is present but Eq. (3) adequately represents all of the data. Compared with the correlation Eq. (1) of Waltrup and Billig [5], the modified correlation covers more physical influencing factors, not only considered the wall temperature effect, but counted for the specific heat ratio influence, and can well explain the main factor effects on shock train length. The prediction accuracy of Eq. (3), especially at other flow conditions and geometries, needs to be verified by the further experimental data.

Conclusions

Experiments were carried out to study effects of temperature on shock train structures and isolator performance in a direct-connect test facility using high-temperature vitiated air. A 2D supersonic nozzle with Mach number of 2.5 was used to provide the supersonic flow entering the isolator with a 50 mm × 70 mm rectangular configuration. Wall static pressures and surface temperatures along isolator walls were measured to characterize shock train length s and pressure profiles at two typical experimental conditions. Numerical simulations were performed on a 2D domain including nozzle and isolator to provide more tremendous information. The major conclusions were as follows:

1. Wall temperature plays an important role in the length of shock train. With an increase of wall temperature, shock train length increases and isolator performance degrades. An improved correlation of Waltrup and Billig is urgently needed to accounting for wall temperature effects.
2. Wall temperature effect can be can be characterized by the ratio of wall temperature to gas total temperature. Shock train length increases with ratio of wall temperature to gas total temperature. In view of the difference in specific heat ratio between high-temperature vitiated air and cold airflow, both the ratio of wall temperature to total temperature and specific heat ratio are introduced to improve the correlation of Waltrup and Billig. The modified correlation covers more physical influencing factors and can well explain the variation trend of shock train length with the main factors.

Acknowledgments This work was sponsored by the China National Natural Science Foundation (Grant Nos. 91216115 and 11472279). The authors wish to thank all the members of our work group.

References

1. Heiser, W.H., Pratt, D.T.: Hypersonic airbreathing propulsion. AIAA, Washington DC (1993)
2. Curran, E.T., Murthy, S.N.B.: Scramjet propulsion. AIAA, Washington, DC (2001)
3. Billig, F.S., Dugger, G.L., Waltrup, P.J. Inlet combustor interface problems in scramjet engines. The First International Symposium on Air Breathing Propulsion, Marseille, France, June 1972
4. Mtsuo, K., Miyazato, Y., Kim, H.D.: Shock train and pseudo-shock phenomena in internal gas flows. Prog. Aerospace Sci. **35**, 33–100 (1999)
5. Waltrup, P.J., Billig, F.S.: Structure of shock waves in cylindrical ducts. AIAA J **11**(10), 1404–1408 (1973)
6. Carroll, B.F., Dutton, J.C.: Characteristics of multiple shock-wave/turbulent boundary-layer interactions in rectangular ducts. Jet Propul. **6**(2), 186–193 (1990)
7. Carroll, B.E., Dutton, J.C.: Turbulence phenomena in a multiple normal shock Wave/turbulent boundary layer interaction. AIAA J. **30**(1), 43–48 (1992)
8. Matsuo, K.: Shock train and pseudo-shock phenomena in supersonic internal flows. J. Thermal Sci. **12**(3), 204–208 (2003)

9. Weiss, A., Grzona, A., Olivier, H.: Behavior of shock trains in a diverging duct. Exp. Fluids **49**, 355–365 (2010)
10. Cuffel, R.F., Backf, L.H.: Flow and heat transfer measurements in a pseudo-shock region with surface cooling. AIAA J. **14**(12), 1716–1722 (1976)
11. Fischer, C., Olivier, H. Experimental investigation of the internal flow field of a scramjet engine. AIAA pp. 2009–7369 (2009)
12. Fischer, C., Olivier, H. Experimental investigation of the shock train in an isolator of a scramjet inlet. AIAA pp. 2011–2220 (2011)
13. Lin, K.C., Tam, C.J., Jackson, K.R., et al. Characterization of shock train structures inside constant-area isolators of model scramjet combustors. AIAA pp. 2006–0816 (2006)
14. Lin, K.C., Tam, C.J., Eklund, D.R., et al. Effects of temperature and head transfer on shock train structures inside constant-area isolators. AIAA pp. 2006–0817 (2006)
15. Fischer, C., Olivier, H.: Experimental investigation of wall and total temperature influence on a shock train. AIAA J. **52**(4), 757–766 (2014)

The Correlation Between Detonation Cell Size and Ignition Delay Time

Y.F. Liu, W. Zhang, and Z. Jiang

Introduction

Gaseous detonation is a supersonic self-sustained combustion wave propagating in the premixed combustible gas. The leading shock wave compresses the combustible gas to implement autoignition in a very short distance. With the help of energy release from combustion, detonation maintains self-sustained propagation [1].

The study of the mechanism of detonation propagation is very important because shock wave dynamics and chemical reaction kinetics couple together on the detonation front. The classical Chapman-Jouguet (C-J) theory is the first theory which explains the thermodynamic characteristics of self-sustained detonation. It is essentially a consideration of the possible theoretical solutions of steady one-dimensional detonation. For a given explosive mixture, C-J detonation propagates at a unique velocity, and there is a sonic condition behind the leading shock.

On the basis of C-J theory, the ZND model describes the one-dimensional detonation structure as a leading shock wave followed by a chemical reaction zone. The reaction zone is divided into two parts, i.e., induction zone and heat release zone. In the induction zone, chemical reaction rate is very slow and the temperature and pressure are not very high. In the heat release zone, a strong exothermic process is completed very fast, and the pressure and temperature rise rapidly.

Furthermore, Lee proposed the SWACER (shock wave amplification by coherent energy release) mechanism [1] indicating that most self-sustained detonation is unstable. The instabilities are essentially the coupling of shock dynamics and the chemical energy release. Jiang put forth the INWPCR (interaction of nonlinear wave propagation and chemical reaction) mechanism [2]. This theory further points out that the essence of the detonation propagation lies in the coupling mechanism between shock dynamics and chemical reaction kinetics. These two theories qualitatively point out that detonation propagation process is essentially the coupling process of gas flow and combustion process, but the key parameters controlling the coupling process are not known yet.

Detonation cell size is a very important characteristic of detonation propagation. And the ignition delay time is a very important characteristic of chemical reaction kinetics. In this paper, we study the correlation relationship between detonation cell size and ignition delay time and discuss the key mechanism of self-sustained detonation propagation.

Governing Equations and Models

The analysis is based on the two-dimensional Euler equations implemented with two models. Model-1 is an improved one-step overall Arrhenius-type chemical kinetic model [3, 4]. In this model, the specific heat ratio is a variable, not a constant. Model-2 is a detailed chemical reaction kinetic model [5].

The governing equations are numerically solved using a three-order ENO scheme, the flux vector splitting according to Steger and Warming's method. The time-marching integration is performed using three-order TVD Runge-Kutta integration. The detonation gas is the stoichiometric H_2/air mixture at initial pressure $P_0 = 0.1$ MPa and initial temperature $T_0 = 300$ K.

Y.F. Liu (✉) • W. Zhang
The State Key Laboratory of High Temperature Gasdynamics, Institute of Mechanics, CAS, Beijing 100190, China
e-mail: liuyunfeng@imech.ac.cn

Z. Jiang
LHD, Institute of Mechanics, Chinese Academy of Sciences, No.15 Beisihuanxi Road, Beijing 100190, People's Republic of China

G. Ben-Dor et al. (eds.), *30th International Symposium on Shock Waves 1*, DOI 10.1007/978-3-319-46213-4_73

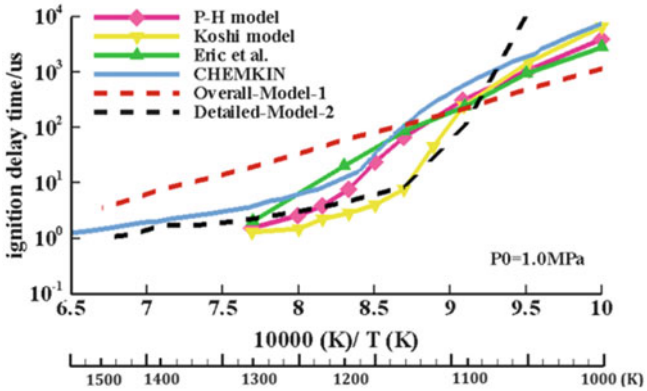

Fig. 1 Comparison of ignition delay times predicted by different chemical reaction models

Results

The ignition delay time is a very important parameter describing the chemical reaction kinetics of a detonation model. Figure 1 gives the comparison of ignition delay times predicted by different chemical reaction models at 1.0 MPa, including three detailed kinetics, CHEMKIN, and a revised one-step overall model. We can see that different model has different ignition delay times under the same pressure and temperature. The shape of the detailed model likes an S-type curve in the logarithmic coordinates, while the shape of one-step model likes a straight line. At high-temperature region, 1200 K < T < 1400 K, the ignition delay time of one-step model is about one order longer than that of detailed model.

In addition, the ignition delay time of one-step model is independent of pressure, while the ignition delay time of detailed models is inversely proportional to the pressure. Therefore, at higher pressure, for example, 2.0 MPa, the ignition delay time of one-step model is about two-order longer than that of detailed models.

In the induction zone, chemical reaction rate is very slow and the temperature and pressure are not very high. In the heat release zone following the induction zone, a strong exothermic process is completed very fast, and the pressure and temperature rise rapidly. We are more interested in the ignition delay time in the induction zone of detonation because the time in the heat release zone is negligible compared with that of induction zone. Also, the length of the heat release zone is negligible to that of induction zone. For the stoichiometric H_2/air mixture at initial pressure $P_0 = 0.1$ MPa and initial temperature $T_0 = 300$ K, the pressure and temperature in the induction zone are about 2.7 MPa and 1500 K. Therefore, the ignition delay time under these pressure and temperature will be very important for self-sustained detonation propagation.

We did two-dimensional numerical simulations of cellular detonation using Model-1 and Model-2. For Model-1, different domain sizes and grid scales are investigated in order to guarantee that the numerical results are independent of numerical algorithm. The uniform mesh sizes are $\Delta x = \Delta y = 10$ μm and $\Delta x = \Delta y = 20$ μm, and the computational domain width w is 3.00, 4.00, 8.00 and 16.30 mm, respectively. Computational domain aspect ratio is greater than 6, so the effects of open boundary conditions can be ignored.

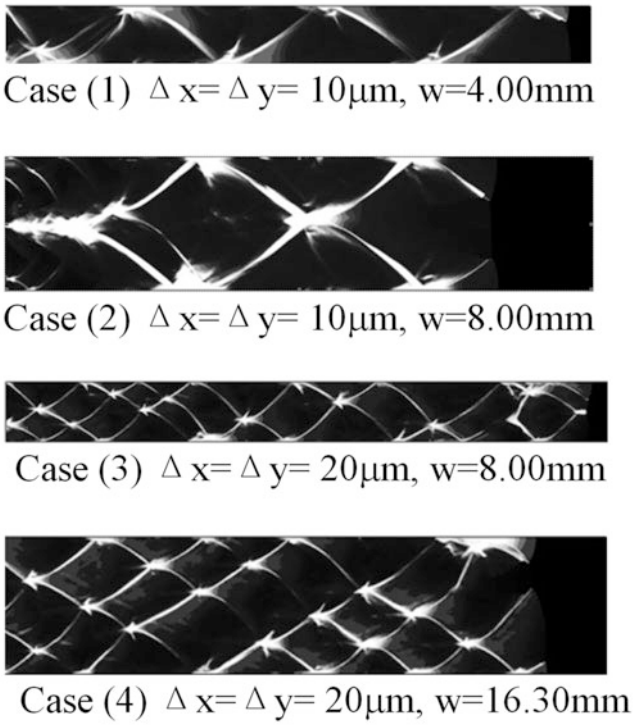

Fig. 2 Cellular structures simulated by Model-1

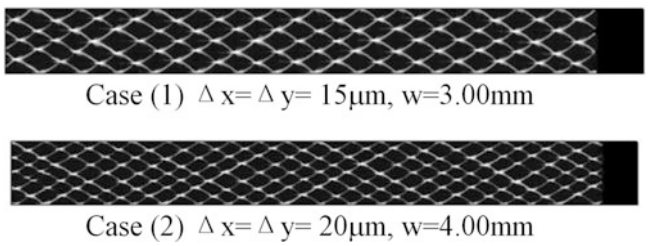

Fig. 3 Cellular structures simulated by Model-2

Figure 2 shows the cellular structures simulated by Model-1. When $w = 4.00$ mm, we get half a cell in the direction perpendicular to the direction of the detonation propagation, and when w = 8.00 mm, a complete cell. When w is increased to 16.30 mm, two cells appear in the computational domain. The numerical results are independent of domain sizes and grid scales. The average cell size is 8.82 mm for all the four cases in this numerical simulation, which is consistent with experimental results [6] quantitatively.

Figure 3 shows the cellular structures simulated by Model-2. When $w = 3.00$ mm, we get three cells in the

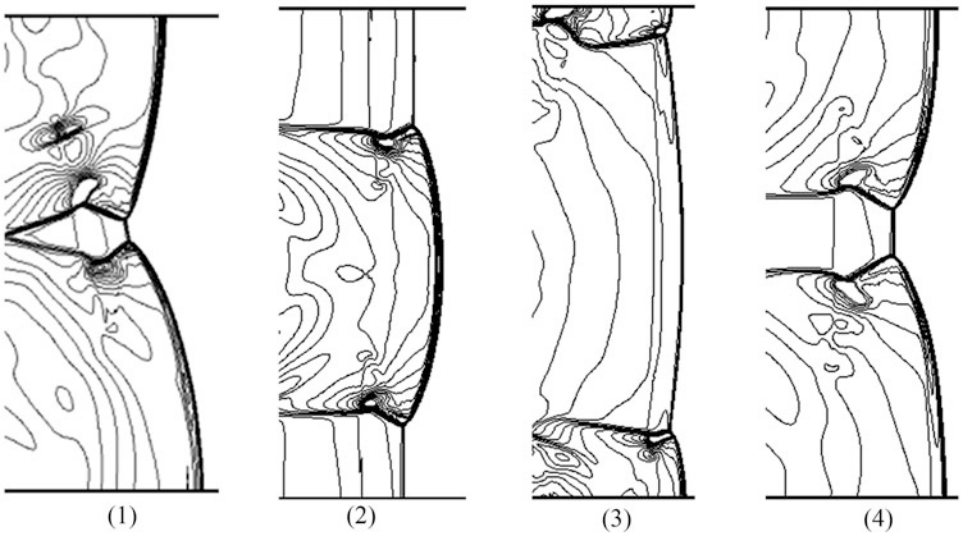

Fig. 4 Movement of triple-wave points showed with the pressure contour in the numerical simulation using Model-1

direction perpendicular to the direction of the detonation propagation. When w is increased to 4.00 mm, four detonation cells appear. The numerical results are independent of domain sizes and grid scales. The average cell size is 1.00 mm for all the two cases in this numerical simulation. The average cell size predicted in the induction zone by Model-1 is bigger than the cell size predicted by Model-2. The ignition delay time predicted by Model-1 is longer than the ignition delay time predicted by Model-2. We first find that the longer the ignition delay time is, the bigger the cell size will be.

Figure 4 shows the movement of a pair of triple-wave points with the pressure contour in the numerical simulation using Model-1. The interval of each frame is 2 μs. In this case, the cycle of this movement is about 3 μs. In the detonation propagation, the unburned gas in the induction zone behind the incident shock wave is crucial, and the ignition delay time of these gases is the chemical time scales characterizing a detonable mixture. For a stoichiometric H_2/air detonation with $P_0 = 0.1$ MPa and $T_0 = 300$ K, the average pressure is about 2.7 MPa, and the average temperature is about 1500 K in the induction zone behind the incident shock of the two-dimensional detonation. The ignition delay time is 3.46 μs at 1500 K. The average movement period of triple-wave points is almost equal to the ignition delay time of gas in the induction zone behind the incident shock wave. The other three cases using Model-1 and detailed model Model-2 also come to the same conclusion.

Figure 5 shows the movement of three pairs of triple-wave points within the cellular structure in the numerical simulation using Model-2. The trajectories showed is the way the three pairs of triple-wave points passed. The interval of each frame is 0.1 μs. In this case, the cycle of this movement is about 0.9 μs. The average ignition delay time is 0.94 μs in the induction zone. The movement period of triple-wave points is equal to the ignition delay time of gas in the induction zone behind the incident shock wave as same as the conclusion obtained by using Model-1.

The numerical results are summarized in Table 1. From Table 1, we find that the shock dynamics and chemical reaction are closely coupled by the characteristic time. The movement period of triple-wave points shows the gas characteristics of detonation. Ignition delay time is considered as chemical reaction kinetic characteristics of detonation. These two characteristic times are essentially coupled together during detonation propagation.

Conclusions

In this paper, two-dimensional numerical simulations were conducted to study the correlation relationship between detonation cell size and ignition delay time of self-sustained stoichiometric H_2/air detonation. Two detonation models were used, one is an improved one-step overall model and the other one is a detailed chemical reaction kinetic model. The numerical results demonstrate that different chemical kinetic models have different ignition delay times and the differences are even more than one order. The ignition delay time in the induction zone is a very important parameter which controls the movement of triple-wave points. The longer the ignition delay time is, the bigger the cell size will be. The average ignition delay time in the induction zone equals to the average period of triple-wave point movement. The shock dynamics and chemical reaction kinetics of gaseous detonation are closely coupled by these two important characteristic time scales, which maintains the self-sustained propagation of detonation.

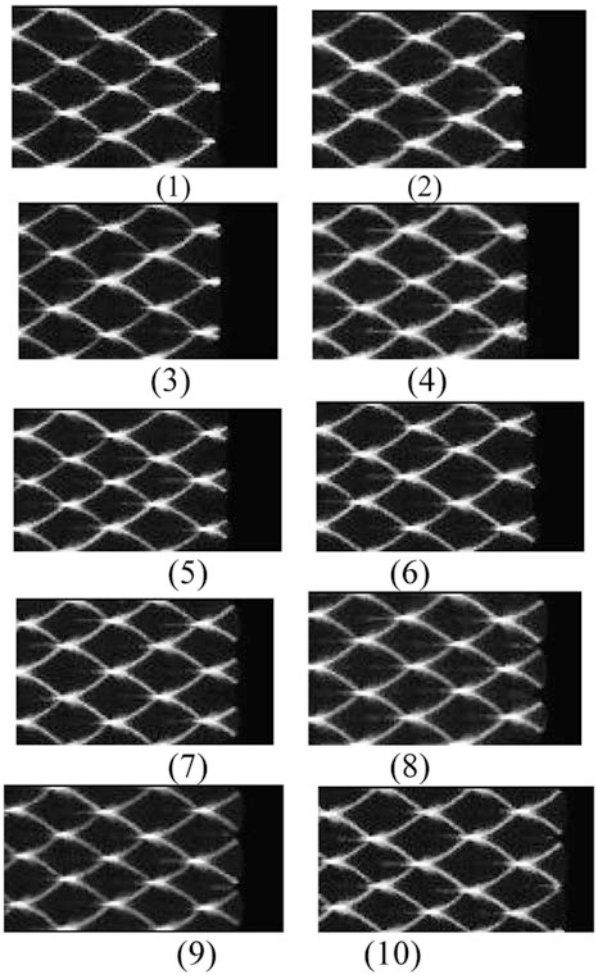

Fig. 5 Movement of triple-wave points showed with the cellular structure in the numerical simulation using Model-2

Table 1 Key parameters of detonations

Model	Average ignition delay time in induction zone (μs)	Period of triple-wave point movement (μs)	Average cell size (mm)	Experimental result [6] (mm)
Improved one-step overall model Model-1	3.46	3	8.82	8 ~ 15
Detailed chemical reaction model Model-2	0.94	0.9	1.0	8 ~ 15

Acknowledgments This paper is supported by the Innovation Grant of Chinese Academy of Sciences and the National Nature Science Foundation of China (11532014, 11672312).

References

1. Lee, J.H.S.: The detonation phenomenon. McGill University, Montréal, Canada (2008)
2. Jiang, Z.L., Teng, H.H. Research on some fundamental problems of the universal framework for regular gaseous detonation initiation and propagation [J]. Sci. Sin-Phys. Mech. Astron. **42**(4), 421–435 (2012)
3. Liu, Y.F., Jiang, Z.L.: Study on the chemical reaction kinetics of detonation models (in Chinese). Sci. Sin-Phy. Mech. **41**, 1–11 (2011)
4. Zhang, W., Liu, Y.F., Jiang, Z.L.: Study on the relationship between ignition delay time and gaseous detonation cell size (in Chinese). Sci. Sin-Phy. Mech. **46**(6), 977–981 (2014)
5. Burke, M.P., Chaos, M., Ju, Y.G., Dryer, F.L., Klippenstein, S.J.: Comprehensive H2/O2 Kinetic Model for High-Pressure Combustion. Int. J. Chem. Kinet. **44**, 444–474 (2012)
6. Shepherd, J.E. Detonation database. Technical Report FM97-8, GALCIT (1997)

An Investigation of the Prompt Oblique Detonation Wave Induced by a Finite-Length Wedge

Yan Liu and Jianping Wang

Introduction

Oblique detonation wave (ODW) is the detonation wave stabilized over an obstacle in the supersonic flow of detonative mixtures. It is regarded as a potential combustion mechanism for supersonic vehicles and received lots of attention in the past decades. Extensive work on the ODW [1–12] has been done by the prior researchers.

According to the experimental results of Verreault and Higgins [1], there are two distinct types of transition to an ODW. The first was the delayed ODW. For the delayed ODW, an initially inert oblique shock wave (OSW) was attached to the cone tip, followed by a kink where the ODW is initiated. The second was the prompt ODW. For the prompt ODW, the detonation wave was attached to the cone tip directly. In the numerical results of Li et al. [2], the structure of the delayed ODW consisted of an OSW, an induction zone, a set of deflagration waves, and an oblique reactive shock wave, namely, the ODW front. By numerical simulation, Figueira da Silva and Deshaies [3] found two kinds of OSW-ODW transitions, the smooth OSW-ODW transition and the abrupt OSW-ODW transition. In the numerical results of Papalexandris [4], the smooth OSW-ODW transition was observed to take place at small wedge angles, and the abrupt OSW-ODW transition was observed to take place at high wedge angles. In the numerical results of Papalexandris [4], Walter et al. [5], and Pimentel et al. [6], the delayed ODW induced by a finite-length wedge was found to be weakened by the expansion waves (EWs) emanated from the corner. The weakened ODW would decouple or decay to a Chapman–Jouguet (CJ) detonation wave.

Kasahara et al. [7–9] found that the prompt ODW initiated by a projectile would decay to a CJ detonation wave or decouple. The decoupled ODW was followed by another ODW, and this wave configuration was named as straw-hat type. In the experiments of Maeda et al. [10], the second ODW of the straw-hat type was observed to slide back relative to the projectile. Lefebvre and Fujiwara [11] found that the ODW at low inflow Mach number would propagate upstream from its initiation location and eventually stabilize at the cone tip (prompt ODW). By numerical simulation and theoretical analysis, Liu et al. [12] found that the upstream propagation of the ODW resulted from the influence of the high-pressure combustion products behind the induction region. For the stabilized prompt ODW, the flow behind the ODW is supersonic. Therefore, theoretically, the length of the wedge used to induce the prompt ODW can be very short. This is a desirable feature for its application. However, according to Kasahara et al. [9], whether the prompt ODW can be sustained downstream is influenced by the dimension of the wedge. In this study, the roles played by the initial condition and the wedge length in the formation and structure of the prompt ODW are studied. It is significant and helpful in the application of the ODW.

Physical Model and Numerical Method

In this study, viscosity, thermal conduction, and mass diffusion of the mixtures are neglected. The two-dimensional Euler equations in generalized coordinates coupled with a two-step chemical reaction model [13] are solved. The parameters in the chemical reaction model are the same with those of Liu [14] for stoichiometric hydrogen–air mixtures. The temperature and pressure of the incoming mixtures are fixed at 300 K and 1 atm.

The Steger–Warming approach [15] is adopted to split the flux vectors, and the fifth-order weighted essentially non-oscillatory (WENO) scheme [16] is used to integrate

Y. Liu (✉) • J. Wang
Department of Mechanics and Engineering Science, Center for Combustion and Propulsion, CAPT and SKLTCS, College of Engineering, Peking University, Beijing 100871, China
e-mail: liuyandeyoux@126.com

G. Ben-Dor et al. (eds.), *30th International Symposium on Shock Waves 1*, DOI 10.1007/978-3-319-46213-4_74

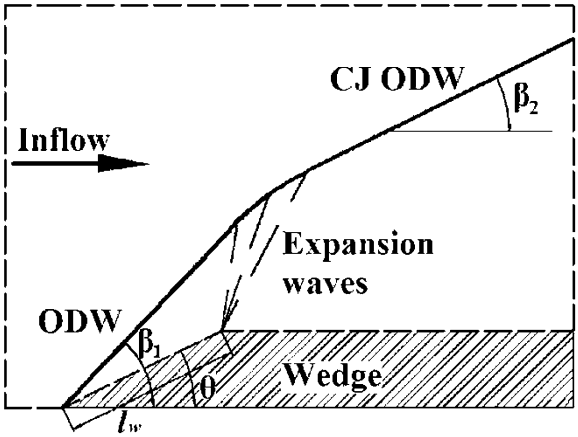

Fig. 1 Schematic of the computational domain

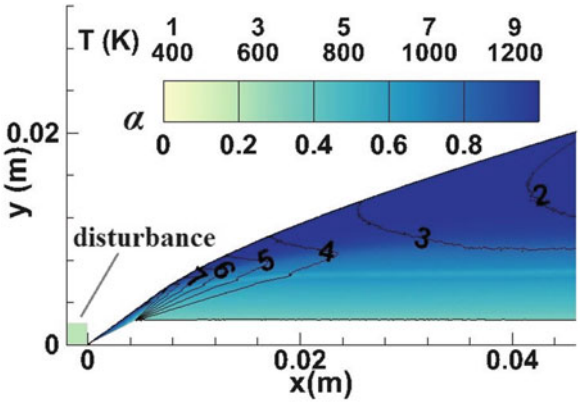

Fig. 2 Temperature contours and the distribution of induction process value α of the OSW at $Ma = 7.0$ and $l_w = 5$ mm

the splitted flux vectors. The third-order Runge–Kutta scheme is adopted to integrate the discretized equations in time. Figure 1 shows the schematic of the computational domain which is surrounded by dashed lines. The height of the computational domain is set to out of the reach of the ODW. The grid sizes used in this study are always smaller than 0.02×0.02 mm^2. The hydrogen–air mixtures flow into the computational domain through the left boundary. Therefore, the boundary conditions at the left boundary are fixed at the initial values. The boundary conditions at the upper boundary are also fixed at the initial values. A slip boundary condition is adopted at the wedge surface and wedge shoulder. A zero-gradient condition is imposed to the right boundary and the first part of the bottom boundary.

Results and Discussion

Initial Conditions

Figure 2 shows the temperature contours behind the shock wave at inflow Mach number $Ma = 7.0$ and wedge length $l_w = 5$ mm. The flow field is obtained by shutting down the exothermic reaction of the mixture. As observed in Fig. 2, the post-shock temperature field above the wedge is constant, and the post-shock temperature $T_{p\text{-}s}$ is about 1263 K. The induction length $l_{p\text{-}s,ind}$ determined by the flow state above the wedge is about 8.17 mm which is longer than $l_w = 5$ mm. Therefore, the induction process cannot be completed in this high-temperature region. As the mixture passes through the expansion waves (EWs) emanated from the corner, the temperature decreases rapidly. As a result, the induction process is dramatically slowed down and cannot be completed in the computational domain. The similar phenomena have also been observed by Papalexandris [4]. The distribution of the induction parameter α behind the shock wave is also shown in Fig. 2. The value of α is above zero in the flow field. The similar phenomenon is also observed in the cases of $Ma = 6.5$ and $l_w = 5$, 7, and 9 mm. The induction processes are all not completed in the computational domain. Therefore, the exothermic reaction of the mixtures cannot start if the shock waves induced by these wedges are taken as the initial conditions, and the ODWs cannot take place spontaneously.

To investigate the influence of the initial condition on the formation of the ODW, a disturbance of partially induced hydrogen–air mixture with $\alpha = 0.2$ is introduced into the flow field, as shown in Fig. 2. The disturbance locates upstream of the OSW with a size of 2×2 mm^2. As will be shown in the following sections, with such a disturbance, the prompt ODWs are successfully initiated and stabilized over the wedge.

Fully Coupled Prompt ODW

Figure 3 shows the formation process of the ODW at $Ma = 7.0$ and $l_w = 5$ mm. Attributing to the abovementioned disturbance, the ignition of combustion takes place above the wedge as shown in Fig. 3a. After the ignition, the ODW featured by the transverse waves is formed in the flow field. The newly formed ODW does not stabilize at its initiation location; instead it propagates upstream. At $t = 70.0$ μs, as shown in Fig. 3b, the ODW stabilizes near the tip of the wedge. The length of the induction region $l_{num,ind}$ in Fig. 3b is apparently smaller than that in Fig. 3a. Moreover, the value of $l_{num,ind}$ in Fig. 3b is only about a fifth of the induction length $l_{p\text{-}s,ind}$, 8.17 mm, determined by the post-shock state of the OSW induced by the wedge. It is a typical characteristic of the prompt ODW. Therefore, the ODW in this case is a prompt ODW. According to our numerical results, for the ODW

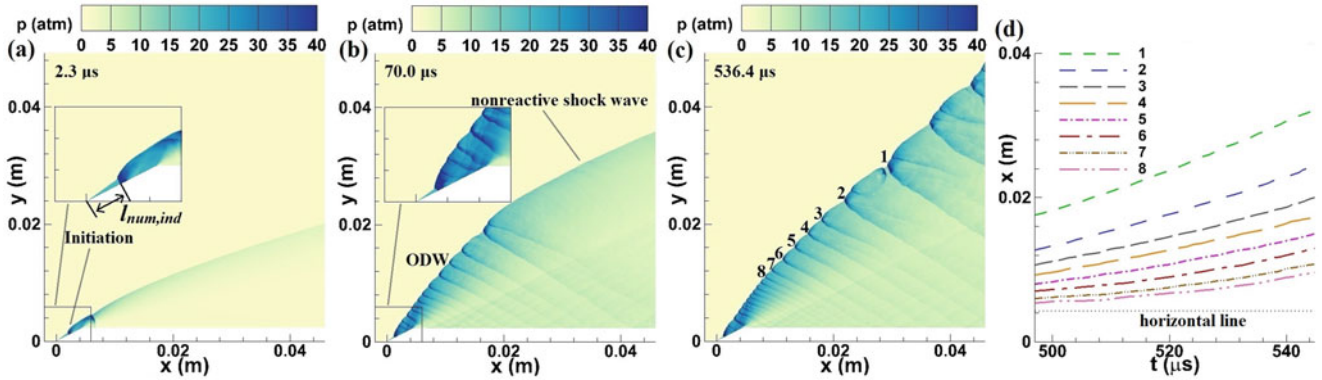

Fig. 3 Formation process of the prompt ODW at $Ma = 7.0$, $l_w = 0.5$ cm, and $\theta = 27°$

sustained by an infinite-length wedge, the ODW at $Ma = 7.0$ is a prompt ODW as well.

As shown in Fig. 3b, the initially initiated ODW is followed by a smooth nonreactive shock wave. This phenomenon is also observed in the experiments of Kasahara et al. [8]. The downstream nonreactive shock wave is triggered eventually, and a fully coupled prompt ODW is formed as shown in Fig. 3c. Because the detonation wave above the wedge is out of the influence of the EWs emanated from the corner, its angle keeps almost constant at about 53.5°. It compares well with the value, 53.1°, obtained by R–H analysis. Resulting from the weakening effect of the EWs, the detonation wave in the vicinity of the corner becomes weak, and its angle decreases [9]. Out of the EWs, the angle of the detonation wave keeps almost constant. The constant wave angle is about 43°, and the corresponding normal Mach number is 4.77. It is in good agreement with the CJ Mach number, 4.84, of hydrogen–air mixture at 1 atm and 300 K.

Eight upstream facing transverse waves (UF TWs) are marked in Fig. 3c with digits 1–8. The x-coordinates of these UF TWs between 497 and 545 μs are shown in Fig. 3d. It is observed that all these UF TWs propagate downstream. In the EWs, because of the decrease of the angle of the detonation wave, the post-shock tangential velocity increases as the detonation wave extends downstream. As a result, the movement of the UF TWs accelerates in the EWs. Therefore, the spacings between the UF TWs increase as they slide downstream as shown in Fig. 3c, d. Furthermore, the formation of the downstream facing transverse waves (DF TWs) is almost failed in this case. It results from the influence of the EWs, and this will be discussed in the following section. Because of the large spacings between the UF TWs, the detonation wave front becomes slightly irregular. According to Lee [17], the detonation velocity depends only on the energetics of the mixture. Therefore, the normal Mach number of the detonation wave is still in good agreement with the CJ Mach number. According to Radulescu and Lee [18], for such an irregular detonation, transverse wave interactions are essential in its propagation mechanism. Therefore, the downstream sliding UF TWs should play an important role in sustaining the fully coupled prompt ODW.

Partially Coupled Prompt ODW

At $Ma = 6.5$ and $l_w = 9$ mm, the straw-hat type ODW presented by Kasahara et al. [7–9] is established in the flow field as shown in Fig. 4a, b. The first ODW begins from the wedge tip. The length of the induction region $l_{num,ind}$ is less than 1 mm which is much shorter than $l_{p\text{-}s,ind}$, 17.4 mm. Therefore, this ODW is a prompt ODW. Under the influence of the EWs, the wave angle of detonation decreases in the interaction region. In contrast to the fully coupled prompt ODW at $Ma = 7.0$ and $l_w = 5$ mm, the prompt ODW at $Ma = 6.5$ and $l_w = 9$ mm is only partially coupled and ended by a nonreactive shock wave. As noted in Fig. 4a, b, the second ODW slides downstream. The similar phenomena have also been observed in the experiments of Kasahara et al. [8] and Maeda et al. [10]. As shown in Fig. 4c, the second ODW slides out of the computational domain eventually. Then the wave configuration consists of a prompt ODW and a nonreactive shock wave. Figure 4d shows the temperature field of the ODW in Fig. 4c. As shown in this figure, the products of the prompt ODW and the shocked mixtures behind the nonreactive shock wave are separated by a combustion wave.

Figure 5 shows the evolution process of the transverse waves of the prompt ODW at $Ma = 6.5$ and $l_w = 9$ mm. Two UF TWs are marked out in Fig. 5. A comparison of these two UF TWs in Fig. 5a, b shows that the UF TWs propagate upward. It is contrast to the phenomena observed at $Ma = 7.0$ and $l_w = 5$ mm. Therefore, the downstream nonreactive shock wave cannot be ignited by the UF TWs. To investigate the evolution process of the DF TWs, three close-up views of Fig. 5b are listed and numbered by digits

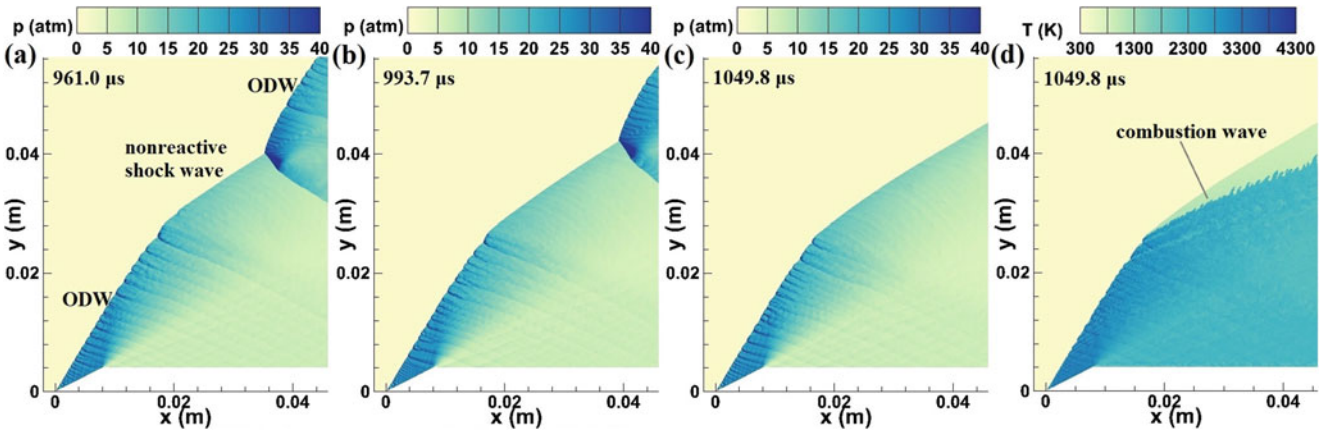

Fig. 4 Evolution process of the straw-hat type ODW at $Ma = 6.5$ and $l_w = 9$ mm

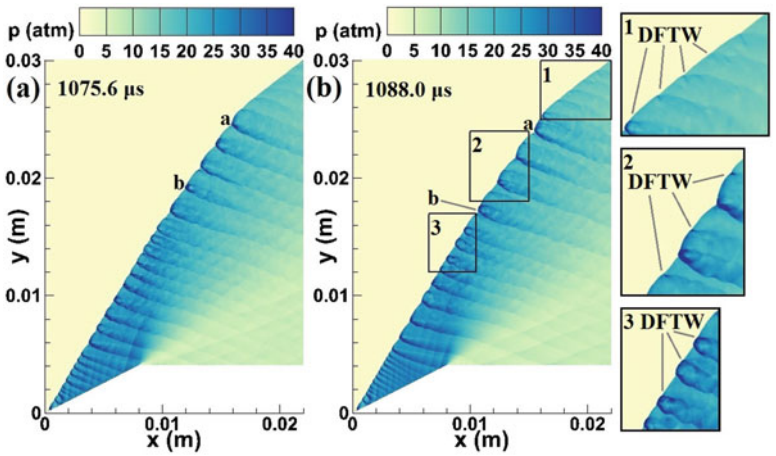

Fig. 5 Evolution process of the transverse waves of the partially coupled prompt ODW at $Ma = 6.5$ and $l_w = 9$ mm

1–3. As mentioned above, the detonation wave is weakened by the EWs. For the DF TWs, their post-shock temperature and pressure are decreased, and consequently their post-shock reaction process is slowed down. As a feedback, the DF TWs become more and more weak as they pass through the EWs as shown in the close-up views of Fig. 5b. Moreover, as observed in the close-up view numbered 1, the DF TWs become so weak that they cannot ignite the nonreactive shock wave. In summary, both the UF TWs and DF TWs cannot ignite the nonreactive shock wave in this case. Therefore, a partially coupled prompt ODW can be formed at $Ma = 6.5$ and $l_w = 9$ mm.

As observed in Fig. 4d, the detonation products and the shocked mixtures are separated by a combustion wave. Furthermore, the geometry of this combustion wave is irregular. It folds and extends into the shocked detonable mixtures. The similar phenomenon is also observed in the experiments of Verreault and Higgins [1], Kasahara et al. [8], and Maeda et al. [10]. According to our numerical results, the irregularity of the combustion wave results the compressing of the weakened DF TWs shown in the close-up view numbered 1.

As shown in Fig. 6a, b, a shock wave is observed to take place in the shocked detonable mixtures resulting from local explosion near the combustion wave. The similar phenomenon has also been observed in the experiments of Maeda et al. [10]. This local explosion should result from the instability of the combustion wave. Resulting from the local explosion, the shocked detonable mixtures are all ignited, and a fully coupled detonation wave is formed as shown in Fig. 6c. The wave angle of the detonation decreases under the weakening effect of the EWs and reaches a constant value eventually. The normal Mach number of the weakened detonation wave is about 4.9 that compares well with the CJ Mach number, 4.84. In contrast

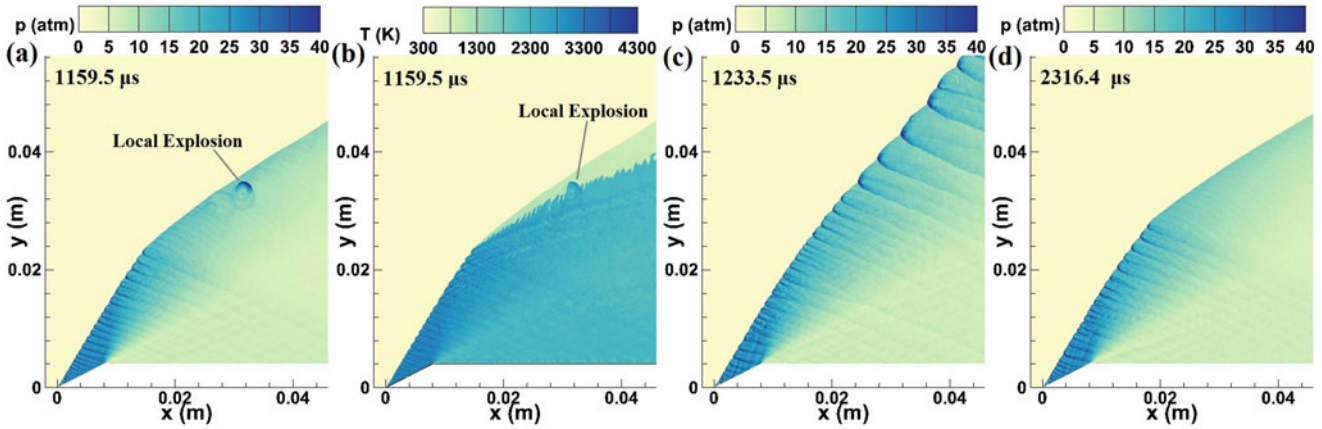

Fig. 6 Destabilization process of the partially couple prompt ODW at $Ma = 6.5$ and $l_w = 9$ mm

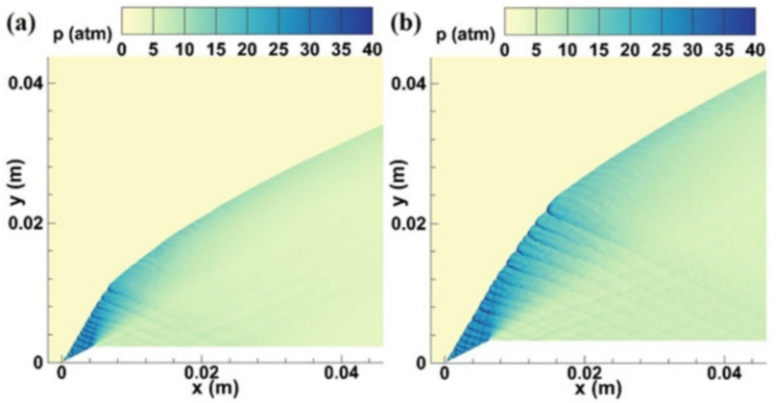

Fig. 7 Pressure fields of the ODWs with $Ma = 6.5$, $l_w =$ (**a**) 5 mm and (**b**) 7 mm

to the detonation wave at $Ma = 7.0$ and $l_w = 5$ mm, this fully coupled detonation wave cannot persist for long. It is observed to decay gradually, and a new partially coupled prompt ODW is eventually formed as shown in Fig. 6d. The destabilization process of the partially coupled prompt ODW shown in Figs. 6a–d occurred twice in our numerical results at $Ma = 6.5$ and $l_w = 9$ mm. The disturbed prompt ODWs both restabilize to the partially coupled prompt ODW as shown in Figs. 4c and 6d.

To investigate the influence of the length of the wedge on the partially coupled prompt ODW. The numerical simulations with $l_w = 5$ and 7 mm are performed. Figure 7 shows the pressure fields of the decoupled prompt ODWs at $l_w = 5$ and 7 mm. The height of the prompt ODW at $l_w = 5$ mm is only 10.8 mm; it is obviously smaller than the height of the prompt ODW at $l_w = 7$ mm, 22.0 mm. Furthermore, the height of the prompt ODW at $l_w = 9$ mm, more than 25.0 mm, is larger than that at $l_w = 7$ mm. Even though the height of the prompt ODW fluctuates resulting from the upstream propagation and formation of the transverse waves, the tendency mentioned above remains for these three cases.

Conclusions

The prompt ODWs induced by finite-length wedges are investigated by numerical simulations. The numerical results show that premature ignition resulting from the initial conditions can result in the formation of the prompt ODWs that cannot take place spontaneously over the wedge. The fully coupled and the partially coupled prompt ODWs are observed in the flow field. The UF TWs of the fully coupled prompt ODW slide downstream, and consequently the detonation can be sustained. For the partially coupled prompt ODW, the UF TWs propagate upstream, and the DF TWs become too weak to ignite the shocked detonable mixtures under the weakening effect of the EWs. Moreover, the height of the detonation wave increases with the wedge length. The partially coupled prompt ODW is unstable and destabilized occasionally by the local explosion resulting from the instability of the combustion wave. The destabilized ODW will restabilize to a partially coupled ODW.

References

1. Verreault, J., Higgins, A.J.: Initiation of detonation by conical projectiles. Proc. Combust. Inst. **33**, 2311–2318 (2011)
2. Li, C., Kailasanath, K., Oran, E.S.: Detonation structures behind oblique shocks. Phys. Fluids. **6**, 1600–1611 (1994)
3. Figueira da Silva, L.F., Deshaies, B.: Stabilization of an oblique detonation wave by a wedge: a parametric numerical study. Combust. Flame. **121**, 152–166 (2000)
4. Papalexandris, M.V.: A numerical study of wedge-induced detonations. Combust. Flame. **120**, 526–538 (2000)
5. Walter, M.A.T., Figueira da Silva, L.F.: Numerical study of detonation stabilization by finite length wedges. AIAA J. **44**(2), 353–361 (2006)
6. Pimentel, C.A.R., Azevedo, J.L.F., Figueira da Silva, L.F.: Numerical study of wedge supported oblique shock wave-oblique detonation wave transitions. J. Braz. Soc. Mech. Sci. **XXIV**, 149–157 (2002)
7. Kasahara, J., Takeishi, A., Kuroda, H., Horiba, M., Matsukawa, K., Leblanc, J.E., Endo, T., Fujiwara, T.: Experimental observation of oblique detonation waves around hypersonic free projectiles. In: Takayama, K., Sasoh, A. (eds.) Ram accelerators, pp. 263–270. Springer, Heidelberg (1998)
8. Kasahara, J., Fujiwara, T., Endo, T., Arai, T.: Chapman–Jouguet oblique detonation structure around hypersonic projectiles. AIAA J. **39**, 1553–1561 (2001)
9. Kasahara, J., Arai, T., Chiba, S., Takazawa, K., Tanahashi, Y., Matsuo, A.: Criticality for stabilized oblique detonation waves around spherical bodies in acetylene/oxygen /krypton mixtures. Proc. Combust. Inst. **29**, 2817–2824 (2002)
10. Maeda, S., Inada, R., Kasahara, J., Matsuo, A.: Visualization of the non-steady state oblique detonation wave phenomena around hypersonic spherical projectile. Proc. Combust. Inst. **33**, 2343–2349 (2011)
11. Lefebvre, M.H., Fujiwara, T.: Numerical modeling of combustion processes induced by a supersonic conical blunt body. Combust. Flame. **100**, 85–93 (1995)
12. Liu, Y., Dan, W., Yao, S.-B., Wang, J.-P.: Analytical and numerical investigations of wedge-induced oblique detonation waves at low inflow mach number. Combust. Sci. Tech. **187**(6), 843–856 (2015)
13. Korobeinikov, V.P., Levin, V.A., Markov, V.V., Chernyi, G.G.: Propagation of blast waves in a combustible gas. Astronaut. Acta **17** (4-5), 529–537 (1972)
14. Liu, Y.-F.: Numerical studies on detonation and pulse detonation engines. Peking University, Beijing (2004)
15. Steger, J.L., Warming, R.F.: Flux vector splitting of the inviscid gasdynamic equations with application to finite-difference methods. J. Comput. Phys. **40**(2), 263–293 (1981)
16. Balsara, D.S., Shu, C.-W.: Monotonicity preserving weighted essentially non-oscillatory schemes with increasingly high order of accuracy. J. Comput. Phys. **160**(2), 405–452 (2000)
17. Lee, J.H.S.: The detonation phenomenon. Cambridge University Press, New York, NY (2008)
18. Radulescu, M.I., Lee, J.H.S.: The failure mechanism of gaseous detonations: experiments in porous wall tubes. Combust. Flame **131**, 29–46 (2002)

Formation of 3D Detonation in Supersonic Flows by Solid Walls of Special Shape

V.A. Levin, I.S. Manuylovich, and V.V. Markov

Introduction

This paper presents the results of research on the fundamental problems of detonation associated with new ways of initiation without volume energy supply, in which the decisive role is played by the interaction of gas mixtures with solid boundaries of the flow, the effects of cumulation, and the formation of complex shock wave structures. Besides, this study was carried out to analyze the possible use of solutions of two-dimensional (2D) nonstationary flows of combustible mixture to evaluate the stationary supersonic flows in three-dimensional (3D) channels of variable cross section. In this regard, the results of numerical simulation of detonation in flat chambers with movable walls and detonation in 3D channels of variable cross-sectional size, as well as in 3D helical channels, blown by supersonic flows of combustible mixture, are presented. The study is carried out in a framework of one-step combustion kinetics by numerical method based on the S.K. Godunov scheme [1].

Mathematical Model and Calculation Method

The ideal perfect gas model is used in the study. It is assumed that the gas is a mixture of chemically reactive components.

V.A. Levin
Institute of Mechanics, M.V. Lomonosov Moscow State University, Michurinskiy Avenue, 1, Moscow, Russia

Institute of Automation and Control Processes, Far Eastern Branch of RAS, Radio Street, 5, Vladivostok, Russia

I.S. Manuylovich
Institute of Mechanics, M.V. Lomonosov Moscow State University, Michurinskiy Avenue, 1, Moscow, Russia

V.V. Markov (✉)
Steklov Mathematical Institute of RAS, 119991, Gubkin str. 8, Moscow, Russia
e-mail: markov@mi.ras.ru

Unsteady 3D flows of the reactive gas mixture are described by the system of differential equations in Cartesian coordinates and in usual notation:

$$
\begin{aligned}
&(\rho)_t + (\rho u)_x + (\rho v)_y + (\rho w)_z = 0,\\
&(\rho_i)_t + (\rho_i u)_x + (\rho_i v)_y + (\rho_i w)_z = \omega_i,\\
&(\rho u)_t + (p + \rho u^2)_x + (\rho uv)_y + (\rho uw)_z = 0,\\
&(\rho v)_t + (\rho uv)_x + (p + \rho v^2)_y + (\rho vw)_z = 0,\\
&(\rho w)_t + (\rho uw)_x + (\rho vw)_y + (p + \rho w^2)_z = 0,\\
&(H - p)_t + (H u)_x + (H v)_y + (Hw)_z = 0,\\
&P = \sum_{i=1}^{N} (\rho_i / \mu_i) R_0 T,\\
&H = \sum_{i=1}^{N} \rho_i h_i + \rho (u^2 + v^2 + w^2)/2
\end{aligned}
$$

A stoichiometric mixture of propane with air is considered using one-step kinetics:

$$C_3H_8 + 5O_2 + 20N_2 \rightarrow 4H_2O + 3CO_2 + 20N_2.$$

The air is considered as a mixture of oxygen and nitrogen in a molar ratio 1:4, and propane–air mixture is defined by ratio 1:5:20. In case of airflows in the absence of fuel, $\omega_i = 0$.

The study is carried out numerically using a modified Godunov method of the first order in space and time [1], which is implemented in an original software package, the "virtual experimental installation" intended for solving a wide range of problems related to multidimensional detonation. This paper presents the results of calculations performed on the MSU supercomputer "Lomonosov."

Flows in a Plane Chamber with Deformable Walls

The flows in a contracting square chambers filled with air were studied for different constant values of square side velocity. Complicated wave patterns of the flows were obtained (Fig. 1).

G. Ben-Dor et al. (eds.), *30th International Symposium on Shock Waves 1*, DOI 10.1007/978-3-319-46213-4_75

The problem of detonation initiation in a square region with sinusoidally varying length of the side was studied. The dependence of the side length on time was defined as $h = H - A[1 - \cos(2\pi t/T)]$, where $H = 0.06$ m is the initial side length, A amplitude, and T period. In order to identify all possible flow regimes, 196 simulations for different pairs (A, H) have been performed (Fig. 2). A variable changed from 2 to 28 mm with 2-mm step. T changed from 10 to 140 μs with 10 μs step.

Several different flow regimes were found. Detonation may occur instantly in the first period along the whole perimeter of the square or in the first period in the corners.

Initiation of detonation can take place after some time at the center in the first period or after several periods. Calculations revealed that in the latter case, detonation may occur also on the sides, in the corners, or at the center. The calculations revealed flow regimes with initiation of detonation only after six periods of square size oscillations. All possible flow regimes are divided in a plane "amplitude-period" by critical curves.

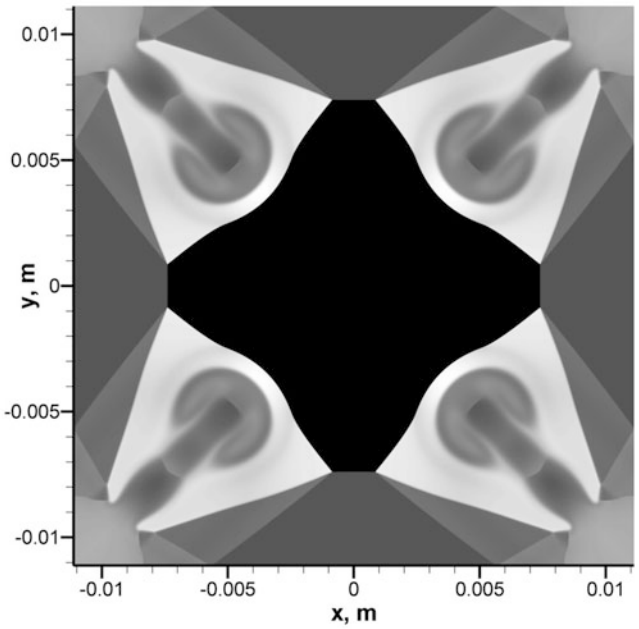

Fig. 1 Temperature field in air inside the contracting square chamber. The velocity of sides is 1500 m/s

Supersonic Flows in 3D Channels of Variable Square Cross Section

In the problem of the formation of detonation in three-dimensional channel with square variable cross section, detailed stationary (Fig. 3) and unsteady flow patterns with and without detonation have been found.

The critical values of gas-dynamic parameters separating different flow regimes were obtained. Hypersonic analogy of flat and three-dimensional flows, allowing the use of two-dimensional solutions to estimate the parameters of three-dimensional supersonic flows, has been confirmed. The limitations of the analogy have been determined. It was shown that the "chocking" of the burning flow (Fig. 4) is the main limitation.

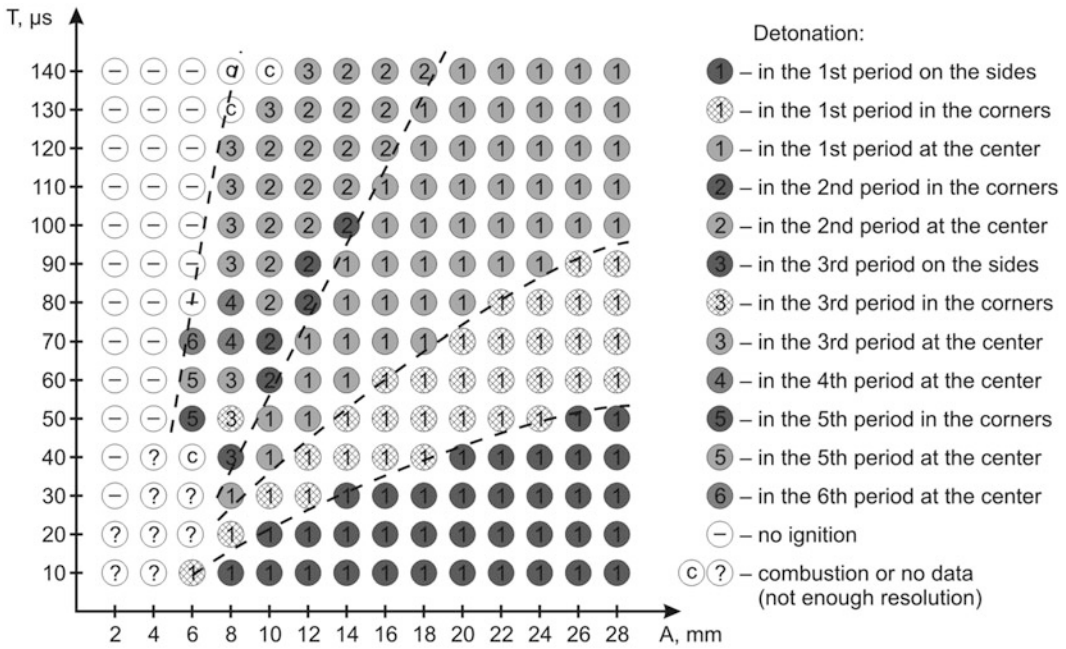

Fig. 2 Diagram of flow regimes in a plane "amplitude-period"

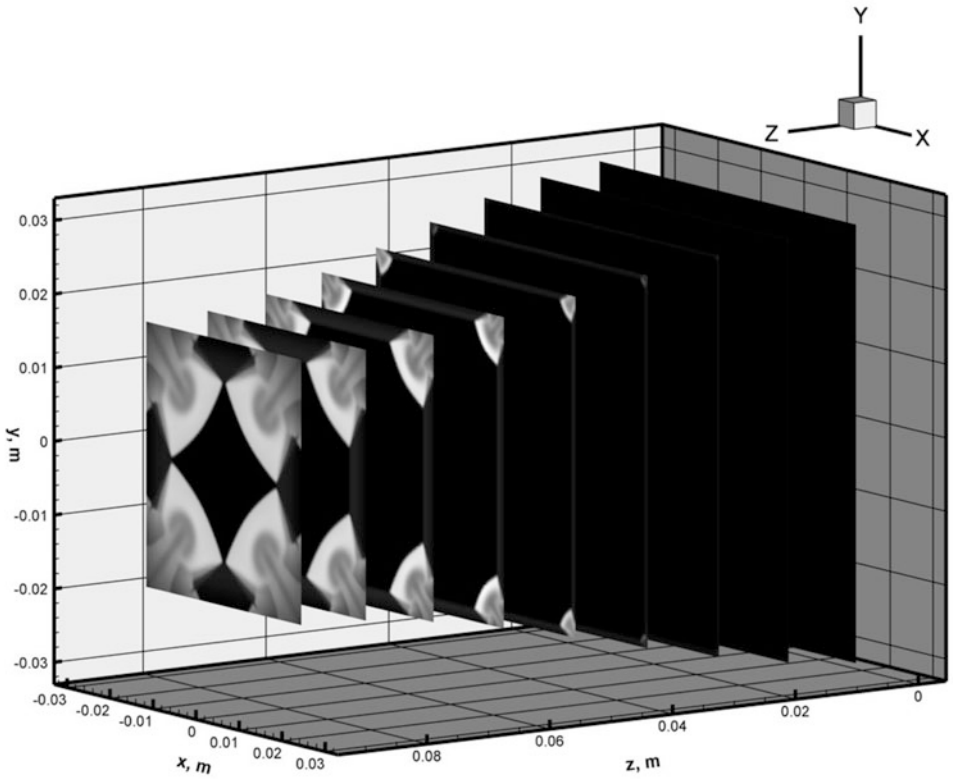

Fig. 3 Temperature field slices in the case of stationary detonation of supersonic combustible mixture flow in 3D channel

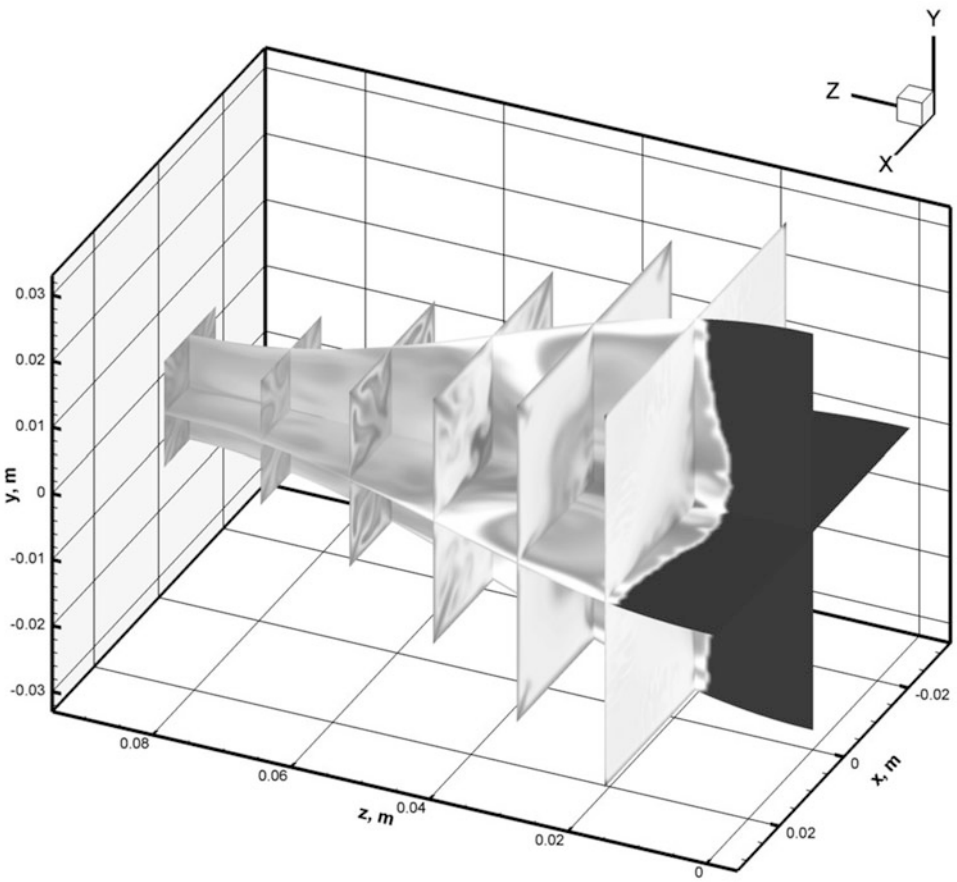

Fig. 4 Temperature field slices for detonation in supersonic combustible mixture flow with choking effect and inapplicability of hypersonic analogy

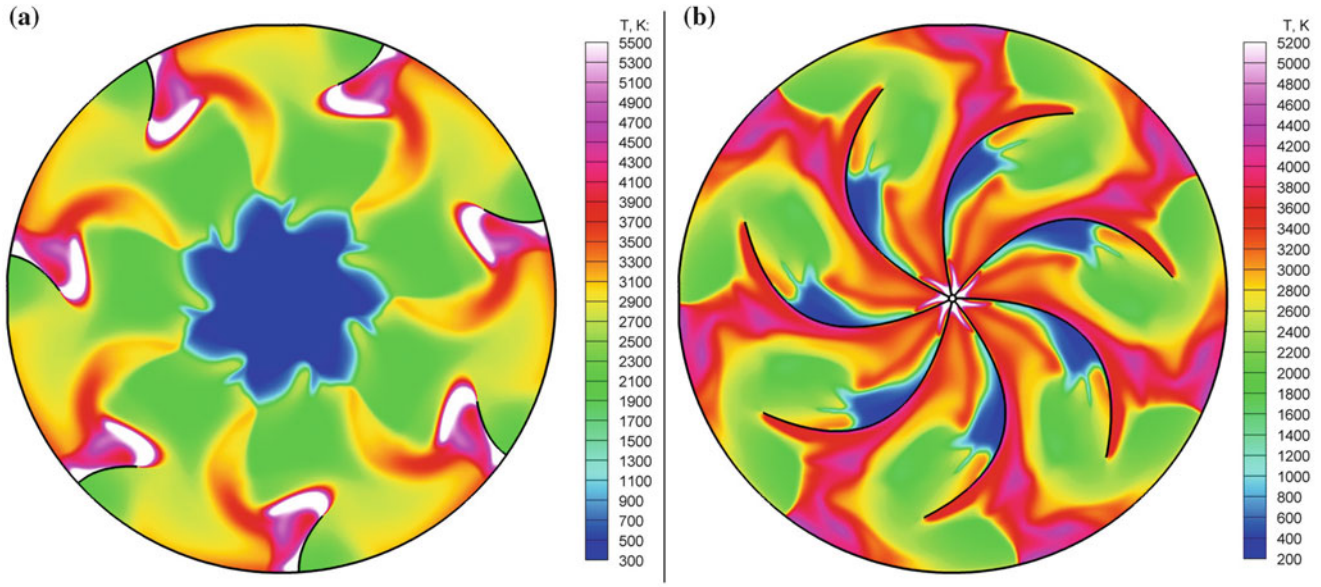

Fig. 5 Formation of detonation inside the rotating cylinder with parabolic blades (**a**) and inside the cylinder with rotating star in the center (**b**)

Flows in 2D Rotating Channels and Supersonic Flows in 3D Helical Channels

Detonation initiation using rotation of the elliptic cylinder enclosed in the circular cylinder, both filled with stoichiometric air–propane mixture, was numerically investigated. The feasibility to form detonation both inside and outside the elliptic cylinder was stated. Two critical angle velocities of cylinder rotation, which govern the quantitative and qualitative flow pattern, were found. The possibility of rapid detonation initiation by rotating parabolic blades was studied in two configurations (Fig. 5a, b).

Calculations revealed the possibility to initiate detonations in supersonic flow of combustible mixture inside 3D helical channel of elliptic cross section (Fig. 6). The results are consistent with 2D calculations of corresponding unsteady flows.

Relying on the results presented by Fig. 5b and on the analogy based on plane section hypothesis, calculations of supersonic combustible mixture flow have been performed for cylindrical channel with 3D helical blades connected to the central axis. In this problem several flow regimes were observed—without detonation, with detonation exiting the channel, and with stationary detonation—shown on Fig. 7 by a transverse slice of stationary temperature field.

Acknowledgments This work was supported by the Russian Science Fund (Grant No. 14-19-01759) and by the Supercomputing Center of Lomonosov Moscow State University [2].

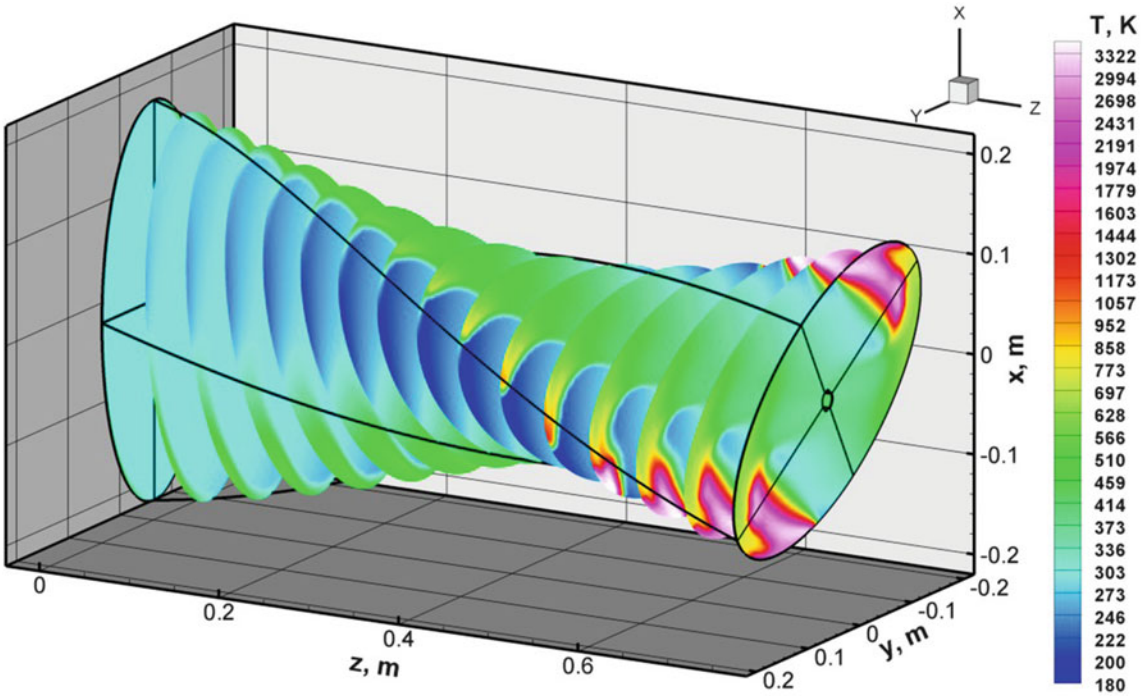

Fig. 6 Slices of stationary temperature field under detonation in helical channel of elliptic cross section

Fig. 7 A slice of stationary temperature field with detonation in channel with blades

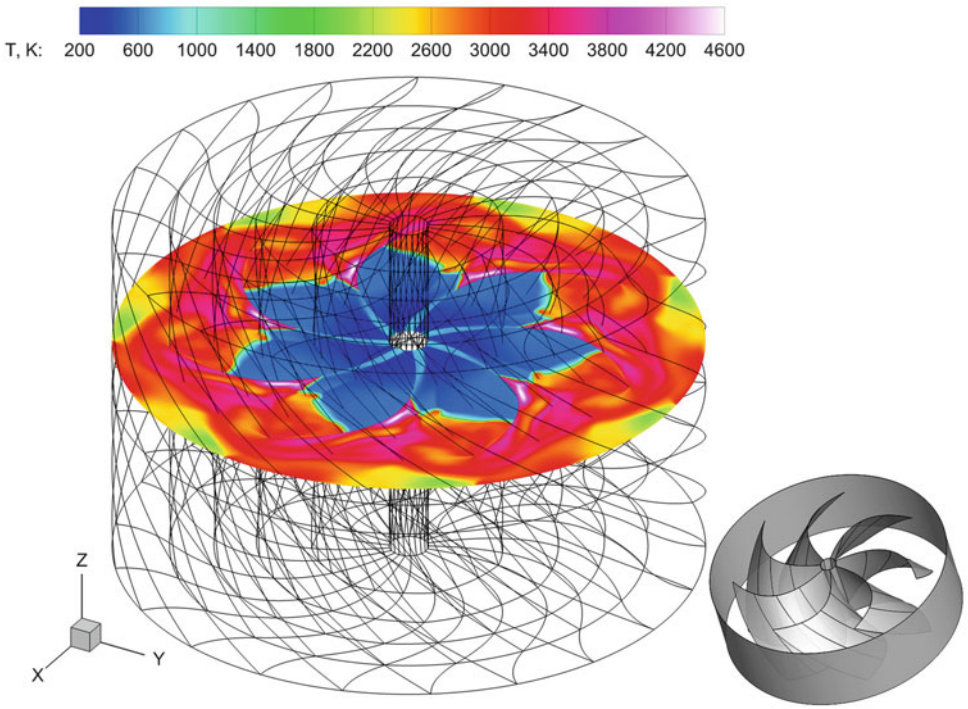

References

1. Godunov, S.K., Zabrodin, A.V., Ivanov M.Ya, et al.: Numerical solution of multidimensional problems in gas dynamics. Moscow: Nauka, 400 p. (1976)

2. Voevodin Vl. V., Zhumatiy S.A., Sobolev S.I., Antonov A.S., Bryzgalov P.A., Nikitenko D.A., Stefanov K.S., Voevodin Vad.V.: Practice of "Lomonosov" Supercomputer // Open Systems J. – Moscow: Open Systems no.7. http://www.osp.ru/os/2012/07/13017641/ (2012) (In Russian)

Cellular and Spin Detonation in 3D Channels

V.A. Levin, I.S. Manuylovich, and V.V. Markov

Introduction

Gas detonation is a complex multidimensional process. In nature, the multidimensionality of detonation manifests itself in the cellular structure and in the spin. The cellular and spin detonations are formed due to instability of the burning zone behind the head shock wave, due to which small perturbations increase, and periodic spatial flows arise with transverse waves in the flow behind the head shock and with breaks of its front [1, 2]. In this work, we simulated in the 3D unsteady formulation the process of spontaneous formation of the 3D detonation structure observed in experiments and its propagation in the channels of square, rectangular, round, and elliptic cross sections. We investigated in detail the process of spontaneous increase in small perturbations and the transformation of the 1D flow into the flow with the substantially 3D detonation structure, which is called cellular by analogy to the 2D case. In case of circular cross section, we simulated the process of spontaneous formation of spin detonation and investigated stability of spin detonation to disturbances caused by changing diameter of the channel. In all cases the initial distribution of parameters was one-dimensional.

V.A. Levin
Institute of Mechanics, M.V. Lomonosov Moscow State University, Michurinskiy Avenue, 1, Moscow, Russia

Institute of Automation and Control Processes, Far Eastern Branch of RAS, Radio Street, 5, Vladivostok, Russia

I.S. Manuylovich
Institute of Mechanics, M.V. Lomonosov Moscow State University, Michurinskiy Avenue, 1, Moscow, Russia

V.V. Markov (✉)
Steklov Mathematical Institute of RAS, 119991, Gubkin str. 8, Moscow, Russia
e-mail: markov@mi.ras.ru

Mathematical Model

The ideal perfect gas model is used in the study. It is assumed that the gas is a mixture of chemically reactive components.

Unsteady flows of the reactive gas mixture are described by the system of differential equations in Cartesian coordinates and in usual notation:

$$
\begin{aligned}
&(\rho)_t + (\rho u)_x + (\rho v)_y + (\rho w)_z = 0,\\
&(\rho_i)_t + (\rho_i u)_x + (\rho_i v)_y + (\rho_i w)_z = \omega_i,\\
&(\rho u)_t + (p + \rho u^2)_x + (\rho uv)_y + (\rho uw)_z = 0,\\
&(\rho v)_t + (\rho uv)_x + (p + \rho v^2)_y + (\rho vw)_z = 0,\\
&(\rho w)_t + (\rho uw)_x + (\rho vw)_y + (p + \rho w^2)_z = 0,\\
&(H - p)_t + (Hu)_x + (Hv)_y + (Hw)_z = 0,\\
&P = \sum_{i=1}^{N} (\rho_i/\mu_i) R_0 T,\ H = \sum_{i=1}^{N} \rho_i h_i + \rho\left(u^2 + v^2 + w^2\right)/2
\end{aligned}
$$

A stoichiometric mixture of propane with air is considered using one-step kinetics [3]:

$$C_3H_8 + 5O_2 + 20N_2 \rightarrow 4H_2O + 3CO_2 + 20N_2.$$

The study is performed using a modified Godunov method of the first order in space and time [4], which is implemented in an original software package, the "virtual experimental installation" intended for solving a wide range of problems related to multidimensional detonation.

Below we present the results of virtual experiments for channels of 1 m in length and of various shapes and sizes of cross section. In order to simulate correctly and study the laws of transformation of detonation, we carried out the calculations in the entire space of the 3D channel instead of only within its part containing the detonation wave. The detonation of a stoichiometric propane-air mixture at rest was considered at the pressure $p_0 = 1$ atm and the temperature $T_0 = 300$ K. It was assumed that the detonation is

G. Ben-Dor et al. (eds.), *30th International Symposium on Shock Waves 1*, DOI 10.1007/978-3-319-46213-4_76

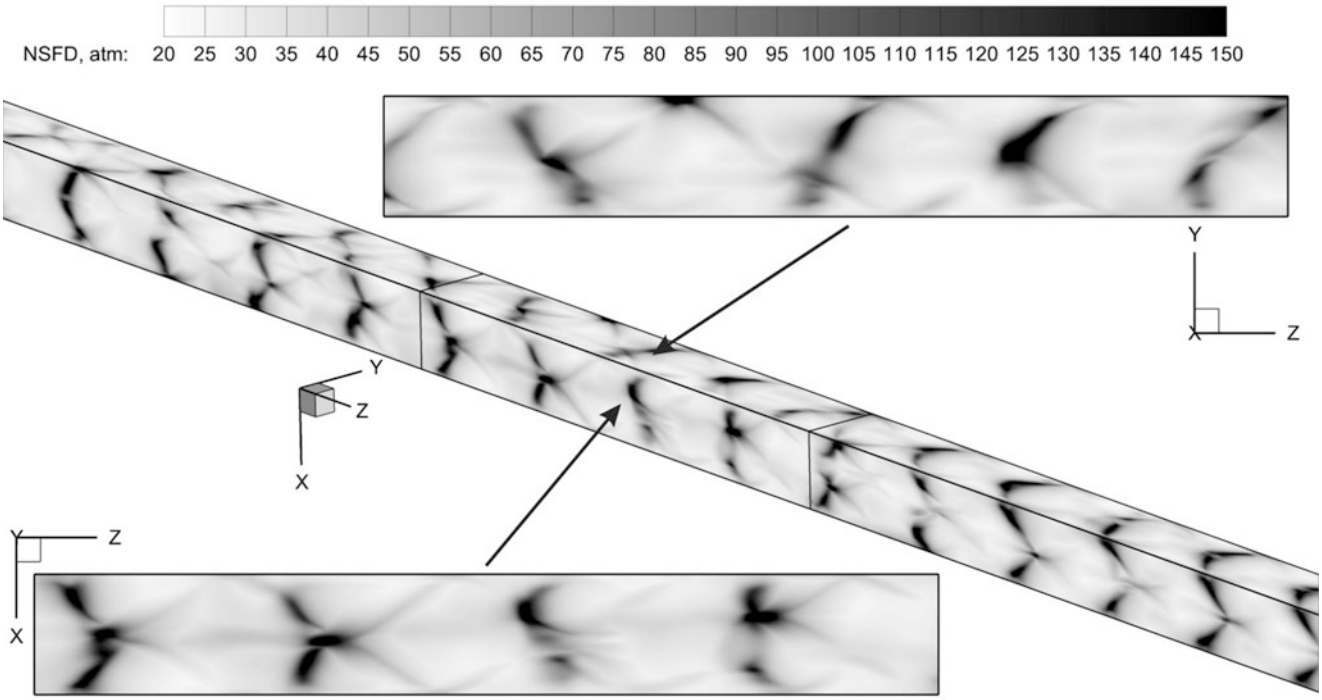

Fig. 1 Numerical soot foil diagram on the surfaces of the square cross-sectional channel and its fragments for $H_x = H_y = 10$ mm

initiated by an instant uniform supply of energy in the 3-cm zone near the closed end of the channel ($0 < z < 3$ cm). The calculations were carried out on the Lomonosov supercomputer at Moscow State University using grids with the number of cells from 0.1 to 10 billion. The flow structure was reflected in the spatial numerical trace patterns and analyzed from these patterns on the cross sections of the channel and on its lateral surface.

Cellular Detonation in Channels of Rectangular Cross Section

According to the calculations, it is first the 1D plane detonation wave that propagates in the mixture along the axis z as a result of the initiation. Under the action of small perturbations present in the numerical calculations, the detonation gradually acquires an irregular 3D cellular structure for a reasonably large cross section of the channel.

One of the series of calculations was carried out for 3D channels with the rectangular cross section $H_x \times H_y$ with the sizes H_x and H_y in the range from 1 to 20 mm on the Cartesian grid with a constant step. The effect of the channel size along the third coordinate on the flow was considered, and the limiting transition $H_x \to 0$ was carried out at $H_y = 20$ mm for this purpose.

The calculations showed that the 2D cellular structure of the detonation is implemented for a certain small H_x. For example, the numerical trace pattern on one of the surfaces of the 3D channel in the plane yz at $H_x = 1$ mm practically did not differ from a similar pattern obtained in the 2D calculation. However, already at $H_x = 1$ mm at a certain distance from the origin of the cellular structure, we observed a weak dependence of the gas-dynamic parameters on the coordinate x. For $H_x = 2$ mm and $H_y = 10$ mm, the trace pattern on the wide sides of the 3D channel proved to be very smeared, and the flow parameters along the axis x were substantially variable.

According to the calculations, it is the principally 3D cellular detonation structure with the transverse waves propagating in the cross-sectional plane that is implemented in the channels with reasonably large sides H_x and H_y. In this case, the shape of traces on the channel surface differs from the rhomboid one, but remains periodic, although "chaotic." In Fig. 1, we show the numerical trace pattern on the surface of the channel with the square cross section with $H_x = H_y = 10$ mm and its fragments on two sides parallel to the planes xz and yz. According to the calculations, the front of the head shock wave has several breaks moving along it during its propagation, while the flow behind it has a very complex structure. In particular, a burning front of a complex shape is observed behind it enveloping individual unburned volumes of the propane-air mixture.

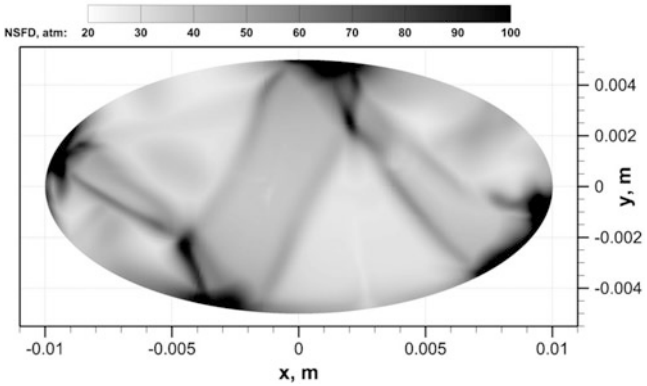

Fig. 2 Cut at $z = 0.5$ m of the 3D numerical soot foil diagram obtained for the elliptic channel with $a = 1$ mm and $b = 0.5$ mm

Cellular Detonation in Channels of Elliptic Cross Section

A large series of calculations was carried out for the channels of elliptic and, in particular, circular cross section. For reasonably large lengths of ellipse semiaxes a and b, we observed an irregular chaotic cellular structure of transverse waves. The strong cumulation of transverse waves near the channel generatrices passing through the ends of the large axis of the elliptic cross section (Fig. 2) is inherent for the 3D detonation in the channels of elliptic cross section. It is related to the larger curvature of the surface near the straight lines indicated.

Spin Detonation in Channels of Circular Cross Section

According to the calculations, the spontaneous transformation of the 1D detonation into the spin one passes through four phases:(1) The propagation of the 1D detonation wave with increasing perturbations introduced because of the limited accuracy of arithmetic operations(2) The detonation with an irregular chaotic 3D structure related to the presence of intense transverse waves(3) The phase of the gradual transformation of transverse waves in one rotating transverse detonation wave(4) The spin detonation at which its front uniformly rotates around the axis of symmetry moving along it.

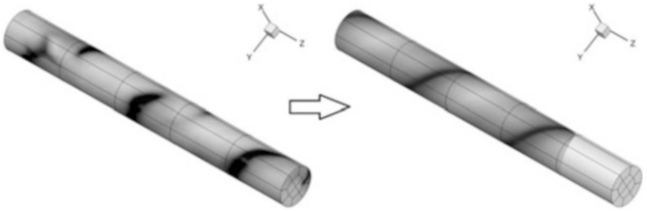

Fig. 3 Formation of spin detonation in the circular channel

Calculations showed that the detonation is transformed into spin one if diameter of the channel lies in some interval of values. Figure 3 shows the fragments of the numerical soot foil diagram at the stage of formation of the spin detonation (the left-hand side) and at the stage of the steady spin detonation (the right-hand side) in the channel of 6 mm in diameter.

Spin detonation transition from 6-mm diameter channel to the channel of larger or smaller diameter through a short section of conical shape was investigated. Calculations have shown that there is a range of values of diameter such that the spin detonation maintains or recovers. Figure 4 is presented to compare 3D views of different channel fragments with numerical soot foil diagrams upon spin detonation exiting the channel of 6-mm diameter and entering channels with diameters 4, 5, 8, and 10 mm. For 10 mm the spin detonation mode is destroyed. For 8 mm the spin detonation recovers, passing a phase with wave pattern close to two-head spin detonation. For 5 mm spin detonation also persists. The case 4 mm is on the border of the mentioned

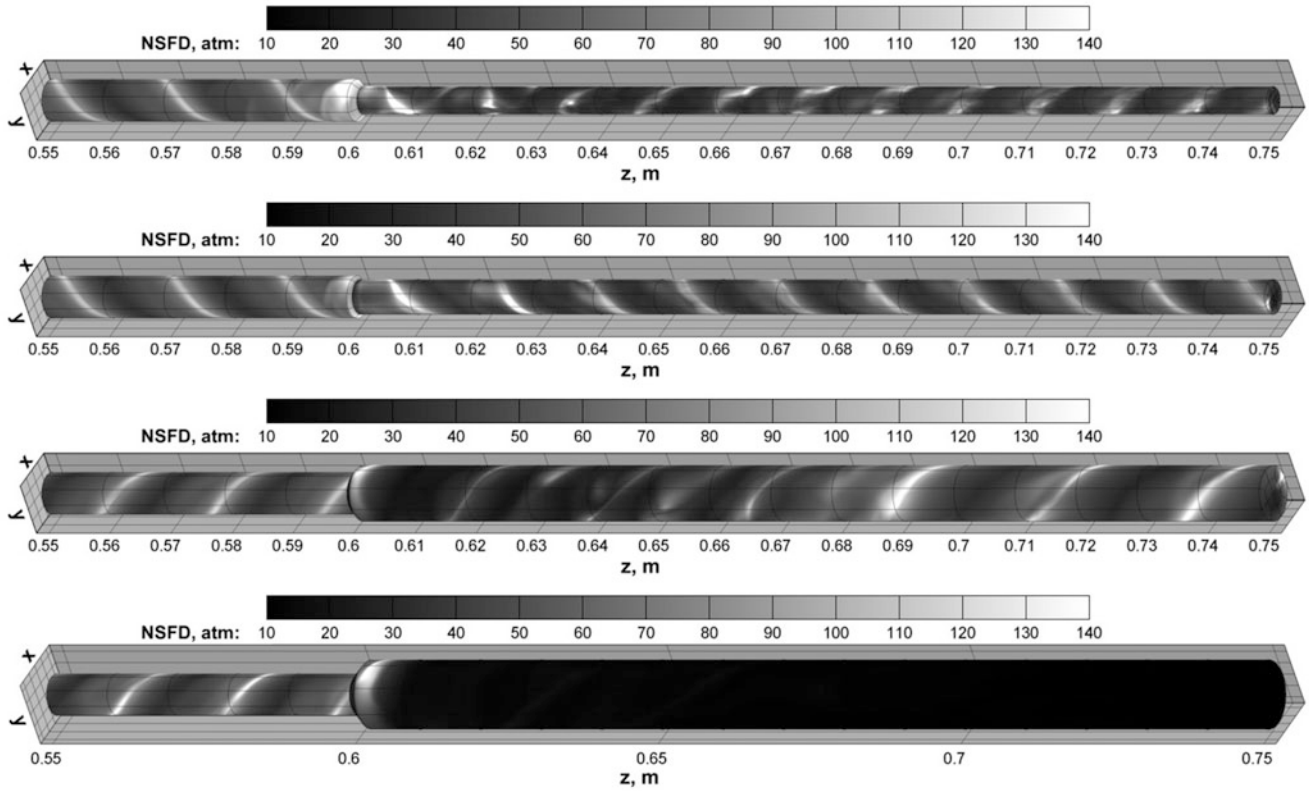

Fig. 4 Channels' fragments with numerical soot foil diagrams upon spin detonation exiting the channel of 6-mm diameter and entering channels with diameters 4, 5, 8, and 10 mm

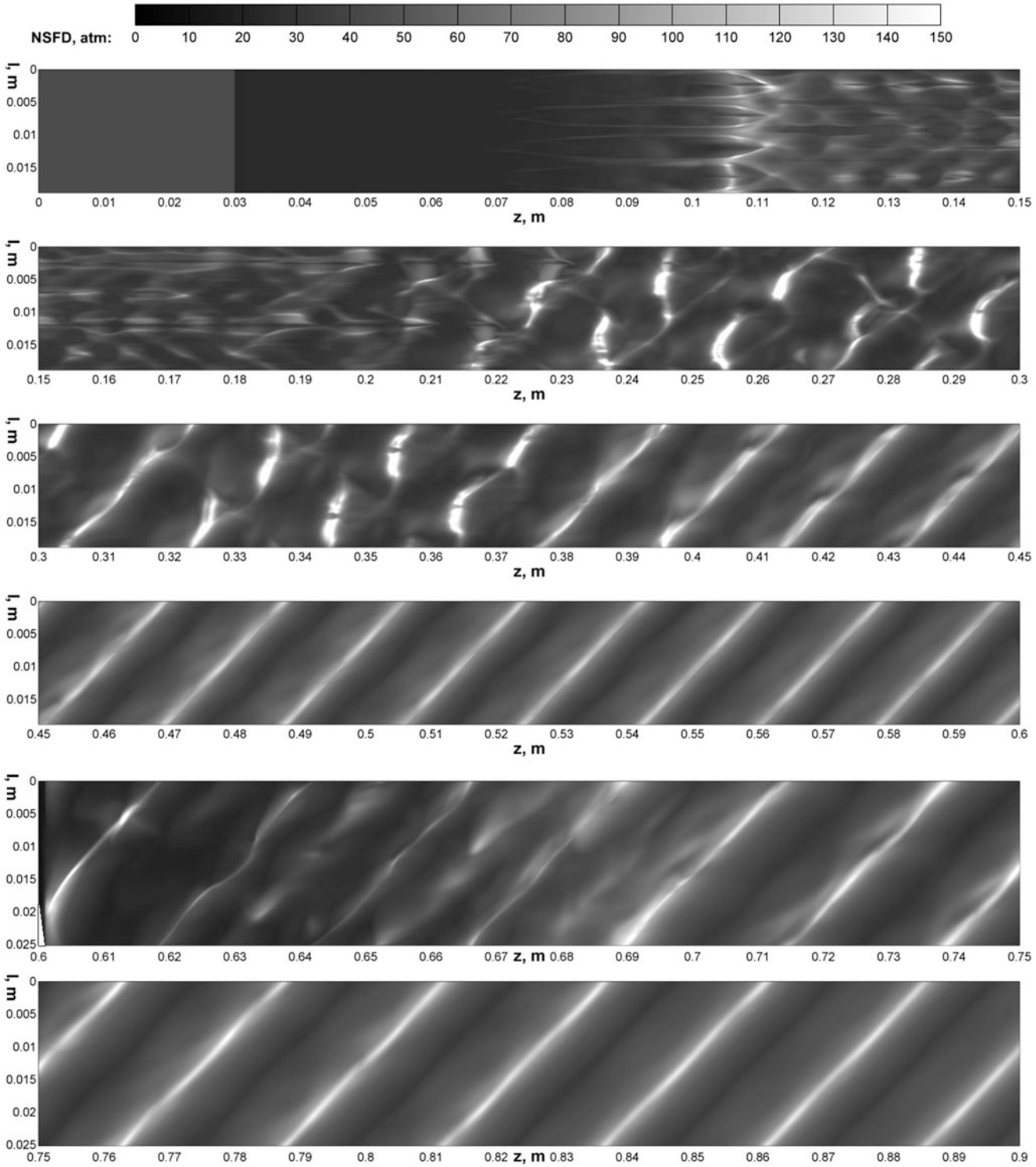

Fig. 5 Sweep of lateral surface with numerical soot foil diagram obtained for the channel widened from 6 to 8 mm

range. It corresponds to uncertain mode, but also with rotation which goes in opposite direction. To analyze the patterns of flow that emerge in calculations, the sweeps of lateral channel surface coated with soot foil diagrams were also visualized (Fig. 5, for 6–8-mm channel, split by 15-cm fragments).

Acknowledgement This work was supported by the Russian Science Fund (Grant No. 14-19-01759) and by the Supercomputing Center of Lomonosov Moscow State University [5].

References

1. Soloukhin, P.M.: Usp. Fiz. Nauk **80**(4), 525 (1963)
2. Levin, V.A., Manuilovich, I.S., Markov, V.V.: Dokl. Phys. **56**(7), 391 (2011)
3. Westbrook, C.K., Dryer, F.L.: Chemical kinetic modeling of hydrocarbon combustion. Progr. Energ. Combust. Sci. **10**, 1–57 (1984)
4. Godunov S. K., Zabrodin A. V., Ivanov M. Ya., Kraiko A. N., and Prokopov G. P.: Numerical solution of multidimensional problems of gas dynamics [in Russian]. Nauka, Moscow. 400 p. (1976)
5. Voevodin Vl. V., Zhumatiy S.A., Sobolev S.I., Antonov A.S., Bryzgalov P.A., Nikitenko D.A., Stefanov K.S., Voevodin Vad.V.: Practice of "Lomonosov" Supercomputer // Open Systems J. – Moscow: Open Systems no.7. http://www.osp.ru/os/2012/07/13017641/ (2012) (In Russian)

Galloping Detonation in a Fuel Mixture Jet

V.A. Levin, I.S. Manuylovich, and V.V. Markov

Introduction

Many problems arise in connection with the use of detonation in engines and other power plants. The most important among them are detonation excitation and stabilization in combustion chambers. The detonation initiation within a layer under conditions of unbounded space and a fluid at rest was experimentally investigated in [1]. In the case of a combustion chamber bounded in the transverse direction, some new effects accompanying the detonation might be expected. The problem of detonation initiation in a supersonic flow of a stoichiometric propane-air mixture occupying partially or completely the cross-section of a channel is considered. The initiation in the flow is produced by a step of cylindrical form or by cylindrical rod with a spherical rounding. 2D and 3D statements of the problem are considered.

V.A. Levin
Institute of Mechanics, M.V. Lomonosov Moscow State University, Michurinskiy Avenue, 1, Moscow, Russia

Institute of Automation and Control Processes, Far Eastern Branch of RAS, Radio Street, 5, Vladivostok, Russia

I.S. Manuylovich (✉)
Institute of Mechanics, M.V. Lomonosov Moscow State University, Michurinskiy Avenue, 1, Moscow, Russia
e-mail: ivan.manuylovich@gmail.com

V.V. Markov
Steklov Mathematical Institute of RAS, 119991, Gubkin str. 8, Moscow, Russia

Mathematical Model and Formulation of the Plane Problem

We will consider a plane finite-length channel consisting of two sections with constant different widths h_1 and h_2 and a connecting section whose lower boundary is a quarter of a circle with radius $r = h_2 - h_1$. The right and left ends of the channel are open. It is assumed that a supersonic flow enters into the channel from the right and flows out of it through the left end into a large-volume reservoir. Let the channel and the reservoir be filled with air at rest at a pressure p_0 , a density ρ_0 , and a temperature T_0, and let at the moment $t = 0$ a uniform supersonic flow of air or a propane-air mixture with the same parameters p_0 and T_0 start to enter into the channel through its right end at a constant velocity U . As a result, an unsteady flow will occur in the channel.

The plane unsteady flows of the reactive gas mixture are described by the system of differential equations in Cartesian coordinates and in usual notation:

$$\begin{gathered}(\rho)_t+(\rho u)_x+(\rho v)_y=0,(\rho_i)_t+(\rho_i u)_x+(\rho_i v)_y=\omega_i,\\(\rho u)_t+(p+\rho u^2)_x+(\rho uv)_y=0,(\rho v)_t+(\rho uv)_x+(p+\rho v^2)_y=0,\\(H-p)_t+(Hu)_x+(Hv)_y=0,\end{gathered} \tag{1}$$

$$P=\sum\nolimits_{i=1}^{N}(\rho_i/\mu_i)R_0T,\ \ H=\sum\nolimits_{i=1}^{N}\rho_i\,h_i+\rho\,(u^2+v^2)/2.$$

A stoichiometric mixture of propane with air is considered using one-step kinetics [2]:

$$C_3H_8+5O_2+20N_2\rightarrow 4H_2O+20N_2.$$

The study is carried out numerically using a modified Godunov method of the first order in space and time [3], which is implemented in an original software package, the "virtual experimental installation," intended for solving a wide range of problems related to

G. Ben-Dor et al. (eds.), *30th International Symposium on Shock Waves 1*, DOI 10.1007/978-3-319-46213-4_77

multidimensional detonation. This paper presents the results of calculations performed on the MSU supercomputer "Lomonosov."

Combustible Mixture Inflow Across the Entire Section

The results obtained for $p_0 = 1$ atm, $T_0 = 20\,^\circ$ C, $h_1 = 0.12$ m, and $r = 0.05$ m are presented below.

According to calculations, the minimal Mach number M_0, starting from which a steady airflow can be formed, is 2.8.

Let $M > M_0$ and at the moment when the airflow becomes stationary a homogeneous stoichiometric propane-air mixture with the parameters U, p_0, and T_0 start to flow into the channel across the entire section.

The calculations show that if M is smaller than the critical value $M_* = 3.7$, the detonation is absent. For $M > M_*$ the shock wave transforms in a detonation wave. If $M_* < M < M_{**} = 9$, the formed detonation wave travels upstream, and the flow is unsteady owing to the "choking" induced by heat supply. For $M > M_{**}$, an overcompressed detonation wave is formed; it stabilizes near the step in a stationary flow, similarly to the detached shock wave.

Inflow of a Combustible Mixture Jet

The results presented below are for the case in which the combustible mixture enters only in the part of the channel adjoining its lower wall and the jet thickness is equal to the step height. Here the critical Mach number M_* coincides with the value determined above. The critical Mach number M_{***}, starting from which the detonation wave stabilizes and the flow becomes stationary throughout the entire channel, equals to 5.3. In this case, the detonation wave in the burning layer is adjoined by the shock wave in the air (Fig. 1). The pressure contours plotted in this figure make it possible to see the complicated wave pattern of the steady-state flow thus formed.

Of particular interest is the case $M_* < M < M_{***}$ in which there is no a steady-state flow. The calculations show that for $M_{**} < M < M_{***}$, where $M_{**} = 4.25$, the detonation wave travels toward the entry section and the configuration consisting of the shock wave in the air and the denotation wave retains its shape in the process of propagation.

For $M_* < M < M_{**}$ a new, previously unknown regime of detonation in a supersonic flow is realized, namely, the galloping detonation in a layer. In this case, the detonation wave has a trend to be swept by the flow or to stabilize at a certain location. However, the shock wave formed due to the choking effect overtakes the detonation wave and penetrates into the fresh combustible mixture. As result, the detonation advances forward jumpwise leaving behind the shock front which has favored its jumpwise advancement. The wave front pattern and the temperature field are presented in Fig. 2 at several moments; it demonstrates the main stages of the galloping detonation. The continuous white curve

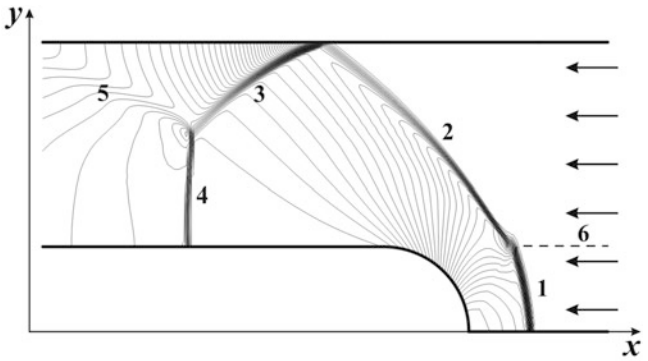

Fig. 1 Pressure contours during stationary detonation at $M = 7.6$, detonation wave, (*2*) shock wave in the air adjoining the detonation wave, (*3*) shock wave reflected from the upper wall, (*4*) Mach stem, (*5*) shock wave reflected from the lower wall, and (*6*) jet boundary

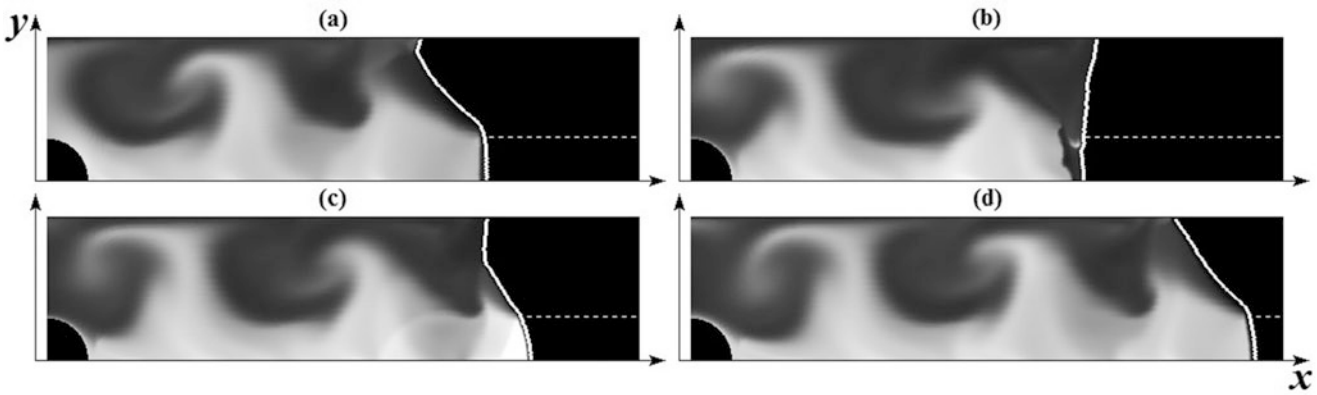

Fig. 2 Wave fronts and temperature fields at several moments of time illustrating the galloping detonation stages in the channel with a step

shows the shock wave separating the disturbed flow region from the oncoming supersonic stream. The broken line is the jet boundary. The lightest region is occupied by high-temperature detonation products. The less light region behind the shock contains the shock-heated air. They are separated by a contact surface. Figure 2a corresponds to the moment at which the air shock wave lagging behind the detonation wave starts to overtake it. In Fig. 2b it leads the detonation wave behind due to the fact that the latter is more intensely swept by the flow. A small-size ignition zone (dark region between the white curve and the light zone) is visible at the air/combustible mixture interface, behind the leading shock front. Figure 2c shows the wave pattern of the flow in which the shock-heated mixture has completely detonated and the detonation front has left the shock wave in the air behind. Figure 2d presents the temperature field at the end of the galloping period. The wave front and the temperature field are in complete agreement with the data of Fig. 2a, but the whole pattern has been displaced toward the entry section of the channel.

As in the case of the combustible mixture inflow across the entire section, the critical values M_*, M_{**}, and M_{***} depend on the channel step and jet width. The presence of the galloping detonation regime is closely related with the channel boundedness in the transverse direction. An increase in the channel width at a fixed jet thickness and the same step height leads to a decrease in M_{***} down to the value of M_* with the result that the galloping detonation regime ceases to exist.

Galloping Detonation in Axisymmetric Channel with a Rod in the Center

The plane problem described above can be transformed to axysimmetrical, leaving the features of geometry unchanged. In this case detonation initiation takes place in cylindrical channel near central rod with spherical rounding. In axysimmetric case the regime of galloping detonation has also been found (Fig. 3). The sufficient condition for this regime is the same (as in plane problem) ratio of inlet and exit cross-sectional areas.

Galloping Detonation in 3D Channel with a Cylindrical Step

3D statement of the problem for the case of cylindrical step was also considered.

3D channels differed by the step sizes, their location and orientation (angle with the incoming flow), and combustible mixture jet cross-sectional form and location. For several configurations the obtained patterns of the flow were similar to patterns of 2D flows. Particularly, the 2D galloping regime of detonation was observed in 3D calculations. In some cases the unsteady wave structure of the flow was much more complicated as compared with 2D galloping detonation due to propagation of strong transverse shock waves. Figure 4 shows the scheme of the 3D channel with

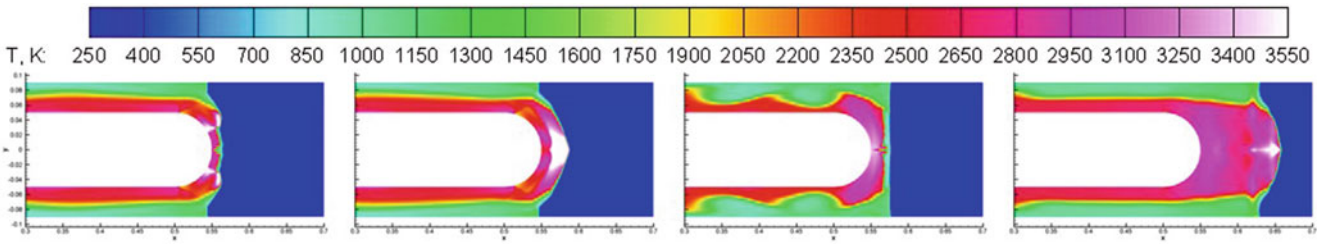

Fig. 3 Galloping layered detonation in a circular channel with a rod in the center

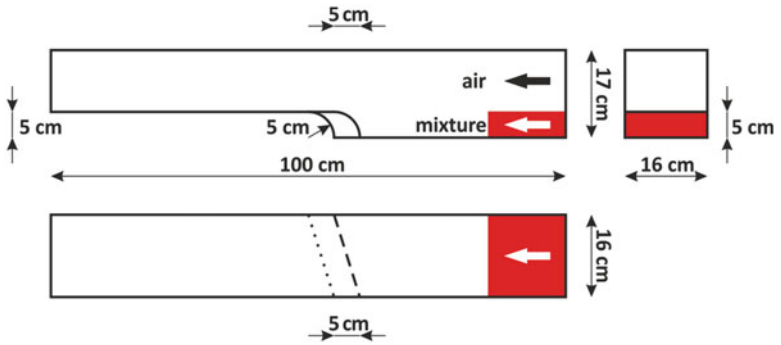

Fig. 4 Three projections of the 3D channel with sizes, air, and mixture jet shown

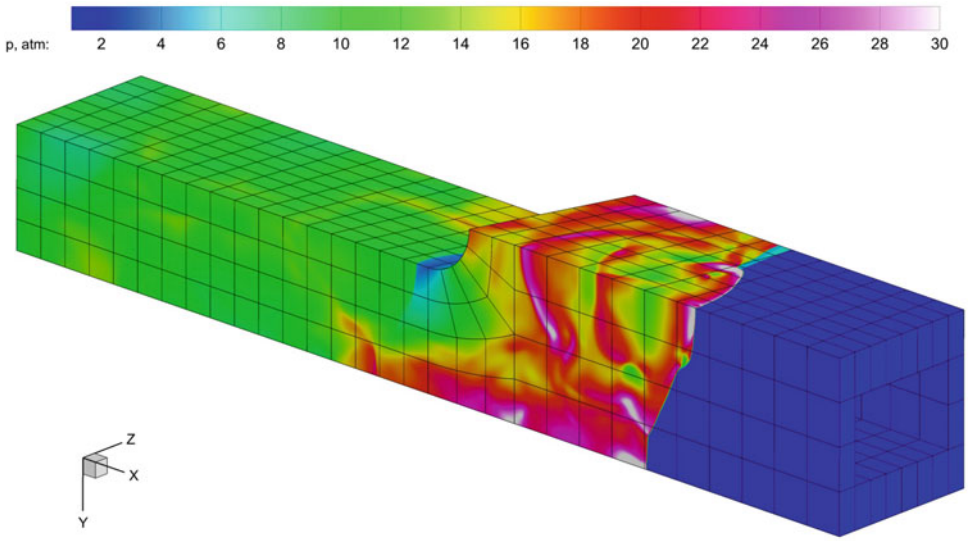

Fig. 5 Pressure field under 3D galloping layered detonation in a channel with inclined step. The layer is located near the *upper wall*

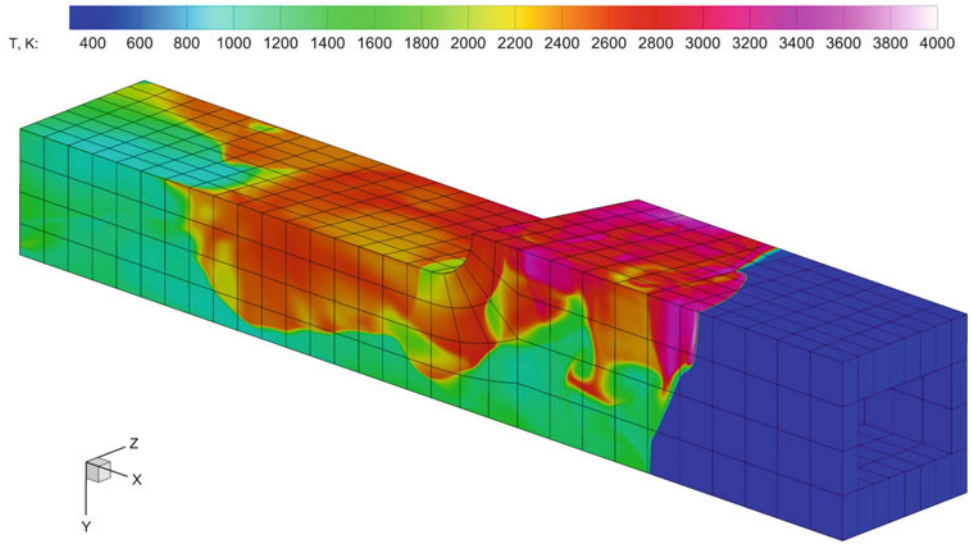

Fig. 6 Temperature field under 3D galloping layered detonation in a channel with inclined step. The layer is located near the upper wall

a step inclined with respect to incoming flow. For this channel a range of incoming flow velocities was found, for which galloping detonation occurs. Figures 5 and 6 illustrate pressure and temperature fields under 3D galloping layered detonation in the channel with incoming flow velocity equal to 1450 m/s.

Acknowledgments This work was supported by the Russian Science Fund (Grant No. 14-19-01759) and by the Supercomputing Center of Lomonosov Moscow State University [4].

References

1. Vasilev A.A., Zak D.V.: Detonation of gas jets. Fiz. Goreniya i Vzryva 22(4), 82 (1986)
2. Westbrook, C.K., Dryer, F.L.: Chemical kinetic modeling of hydrocarbon combustion. Progr. Energ. Combust. Sci. **10**, 1–57 (1984)
3. Godunov S.K., Zabrodin A.V., Ivanov M. Ya., Kraiko A.N., Prokopov G.P. Numerical solution of multidimensional problems of gas dynamics [in Russian]. Nauka, Moscow. 400 p.(1976)
4. Voevodin Vl.V., Zhumatiy S.A., Sobolev S.I., Antonov A.S., Bryzgalov P.A., Nikitenko D.A., Stefanov K.S., Voevodin Vad.V. Practice of "Lomonosov" Supercomputer // Open Systems J. – Moscow: Open Systems Publ., 2012, no.7. http://www.osp.ru/os/2012/07/13017641/ (In Russian)

Propagation of Out Warding Flame for Combustible Gas in Cylindrical Confinement

Wenhu Han and Wenjun Kong

Introduction

Outwardly propagation of flames in cylindrical bomb geometry and measures to laminar flame speeds under the constant-pressure combustion is investigated experimentally and theoretically [1, 2]. Previous studies find that interaction of the wall with the flow causing from thermal expansion across the flame modifies the flame propagation speed due to the cylindrical boundary confinement and results in a significant distortion of the flame surface for large flame radius. Additionally, flame front structure is changed by intrinsic instabilities resulting from the density discontinues across the flame and stemming from the diffusion imbalance between heat and mass [3]. Kelley and Bechtold et al. [4] study the propagation of a premixed flame inside of a confining vessel filled with combustible fluid by using large activation energy asymptotic. Xin and Yoo et al. [2] investigate self-accelerated of cylindrical flame by numerical simulation. However, the acceleration mechanism of flame in cylindrical confinement from laminar to turbulent still is unclear. The formation of the gradient mechanism also needs to be identified and investigated for cylindrical flame.

In the paper a high-resolution parallel code is employed to simulate the process of cylindrical flame in cylindrical bounding condition. The goal is to find the effect of gas compressibility on flame acceleration and identify whether a gradient mechanism can appear and how to form if it can.

Governing Equations and Numerical Method

The compressible reaction Navier-Stokes equations including advection, diffusion, and reaction source are as follows:

$$\frac{\partial(\rho)}{\partial t}+\frac{\partial(\rho u_i)}{\partial x_i}=0 \tag{1}$$

$$\frac{\partial(\rho u_i)}{\partial t}+\frac{\partial}{\partial x_j}\left(\rho u_i u_j+\delta_{ij}p-\zeta_{ij}\right)=0 \tag{2}$$

$$\frac{\partial}{\partial t}\left(\rho e+\frac{1}{2}\rho u_i u_i\right)+\frac{\partial}{\partial x_j}\left(\rho u_j h+\frac{1}{2}\rho u_i u_i u_j+\sigma_j-u_i\zeta_{ij}\right)=0 \tag{3}$$

$$\frac{\partial(\rho Y)}{\partial t}+\frac{\partial}{\partial x}\left(\rho u_i Y-\frac{\mu}{\mathrm{Sc}}\frac{\partial Y}{\partial x_i}\right)=-A\rho Y\exp\left(-E_a/R_pT\right) \tag{4}$$

$$p=\rho R_pT/M \tag{5}$$

where Y is the mass fraction of combustible gas, $e=QY+C_VT=QY+R_pT/(\gamma-1)$ is the internal energy, $h=QY+C_pT=QY+R_pT\gamma/(\gamma-1)$ is enthalpy, Q is the heat of reaction, and C_V and C_p are the specific heat at constant volume and at constant pressure, respectively. R_p is the perfect gas constant, M is the molar mass, and γ is the adiabatic exponent of the combustion gas. The stress tensor ζ_{ij} and the energy diffusion vector σ_j are

$$\zeta_{ij}=\mu\left(\frac{\partial u_i}{\partial x_j}+\frac{\partial u_j}{\partial x_i}-\frac{2}{3}\frac{\partial u_k}{\partial x_k}\delta_{ij}\right) \tag{6}$$

$$\sigma_j=\mu\left(\frac{C_p}{\mathrm{Pr}}\frac{\partial T}{\partial x_j}+\frac{Q}{\mathrm{Sc}}\frac{\partial Y}{\partial x_i}\right) \tag{7}$$

where $\mu\equiv\rho\nu$ is the dynamic viscosity coefficient, ν is the molecular kinetic viscosity, and $\mathrm{Pr}=0.75$ and $\mathrm{Sc}=0.75$ are Prandtl and Schmidt number. δ_{ij} is Kronecker symbol, if $i=j,\delta_{ij}=1$, else $\delta_{ij}=0$. Furthermore, ρ is the density, p the pressure, T the temperature, Y the reactant mass

W. Han (✉) • W. Kong
Key Laboratory of Light-Duty Gas-Turbine, Institute of Engineering Thermophysics, Chinese Academy of Sciences, Beijing 100190, China
e-mail: wenhuhan@126.com

G. Ben-Dor et al. (eds.), *30th International Symposium on Shock Waves 1*, DOI 10.1007/978-3-319-46213-4_78

fraction, Q the heat of reaction, E_a the activation energy, $\gamma = 1.4$ the specific heat ratio, and A the pre-exponential factor. The parameters in the model can be seen in the literature by Bychkov and Valiev [5].

To numerically solve the governing equations, we apply the fifth-order local characteristics based on the WENO conservative finite difference scheme [6] to discretize the advection term and the sixth-order center difference to the diffusion term, with third-order TVD Runge-Kutta time discretization [6].

Numerical Verification

Take a circle computational domain, filled fully with ethylene-oxygen mixture, and the diameter is 10 mm. A circle and weak ignition source is set at the center spot in which the temperature and pressure are 2400 K and 1 atm, and flow velocity is zero. In the premixed mixture gas, initial temperature and pressure are respectively 300 K and 1 atm, and the gas is quiescent. Outside boundary is non-slip wall and there is no the loss of heat. By the theory, $L_f = \nu/\rho S_f$, the flame thickness calculated is approximately 6 μm. At first, mesh resolution is verified by using 10 pts/ L_f, 20pts/L_f, and 30pts/L_f. The evolution of flame front at different mesh resolutions is shown in Fig. 1. For 10pts/L_f, instability of the flame can still be captured in the stage of the laminar flame, while the finer structure of flame front is not clear, and globally the flame surface is relatively smooth, which shows the mesh resolution is not enough, as shown in Fig. 1a. For 20pts/L_f and 30pts/L_f, good grid convergence can be observed and the flame fronts are almost overlapping at the same time. Although the 30pts/ L_f can capture the finer structure, the larger computational resource leads to very low computing efficiency. Hence, 20pts/L_f is selected by compromising the resolution and computing resource. In main simulations, we use 20 pts/L_f to simulate the flame propagation.

Other conditions are stayed, and the diameter and the initial pressure are changed as 796 mm and 0.5 atm. For initial pressure $p_0 = 0.5$ atm, the flame thickness increases and reaches approximately 6 mm, and the mesh step is 0.3 mm. Hence, total mesh number is about 500 million. The number of the CPU processors is 256, and the simulation is done in high-performance cluster. The numerical results are given in Sect. 4.

Numerical Results and Discussions

In this section, we mainly discuss propagating process mechanism of cylindrical flame. Figure 2 shows whole process of flame acceleration from the laminar to the turbulent. Initially, an expanding flame with smooth front is created by weak source energy at the center. Due to intrinsic instability, the flame becomes locally wrinkled, which increases the surface of the flame and further accelerates the flame propagation. At $t = 659.2$ μs, cellular flame forms and fine structure can be observed at flame front, which increases the burning surface area and leads to flame acceleration. As the flame accelerates, compression wave appears in front of flame and preheats the unreacted gas, which leads to the formation of preheated zone shown in Fig. 3b. The formation of the preheated zone is displayed detailedly in

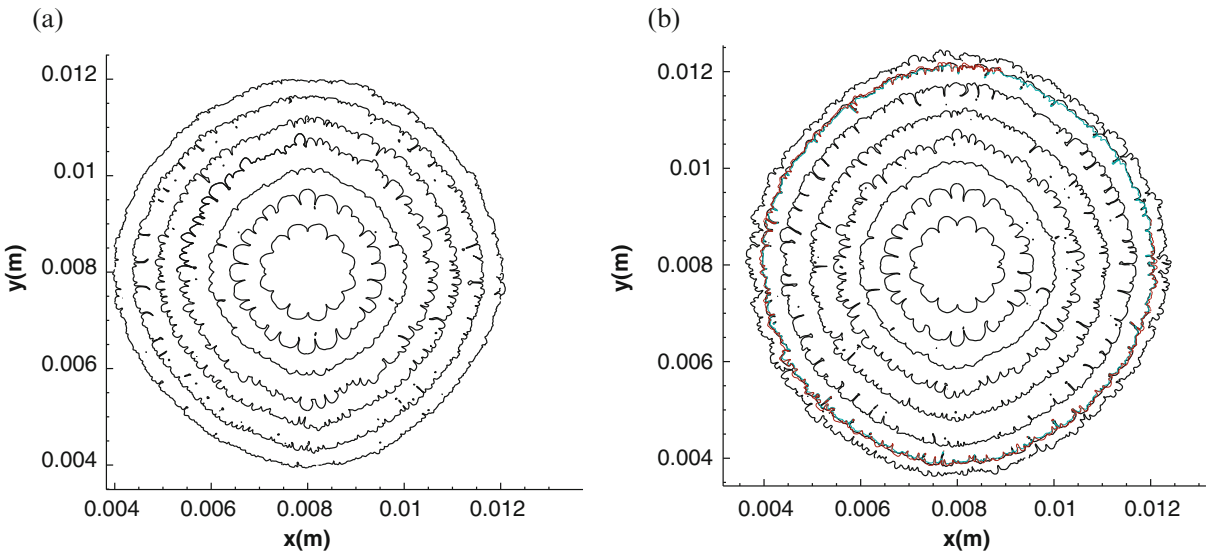

Fig. 1 Verification of relative grid convergence

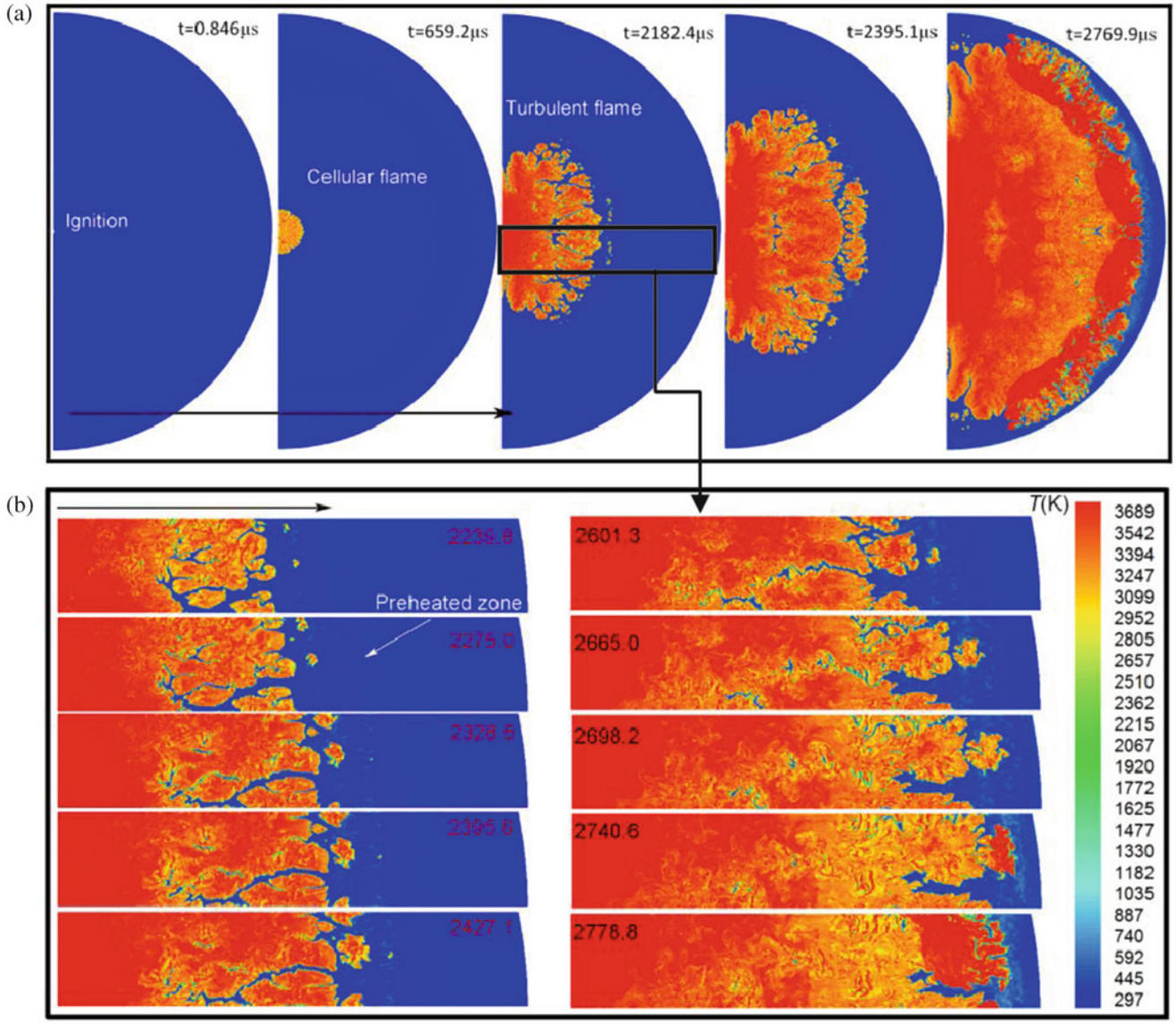

Fig. 2 Propagation of cylindrical flame in the space with cylindrical confinement

Fig. 2b. It is further seen that preignition in the preheated zone appears and in turn makes the flame further accelerate. Eventually, turbulent flame can be formed at $t = 2.1824$–2.7699 μs.

Figure 3 shows the profile of the pressure and flow velocity along radius. Note that as the flame propagates, flow in front of flame appears and increases over time, as shown in Fig. 3a. The profile of flow velocity consists of inverse-flow behind flame front and positive-flow in front of flame. The flow velocity in front of flame decreases along radius and tends to be zero at wall. With flame acceleration, gradient in leading edge of flow velocity profile increases. Corresponding evolution of pressure profile further shows that at $t = 2768.6$, compression wave forms and the leading edge has obvious discontinuity shown in Fig. 3, which can preheat unreacted gas in front of flame.

Averaged velocity of globally cylindrical flame can be calculated by the means of the averaged flame front in Ref. [2] and is shown in Fig. 4. It is observed that flame velocity contains coarsely three stages, namely, power exponent, linear, and turbulent acceleration. Coupling above discussion, we know that in the first stage, exponent acceleration mainly is led by internal instability, which also agrees with that in Ref. [2]. In the second stage, the flame accelerates linearly due to compression effect of gas. After the formation of the positive feedback mechanism, the flame develops into turbulent flame, and rapidly its velocity reaches approximately 400 m/s. Hence, it can be known that cylindrical flame still can propagate self-acceleration and develop into turbulent flame and further create gradient mechanism in cylindrical bounding domain.

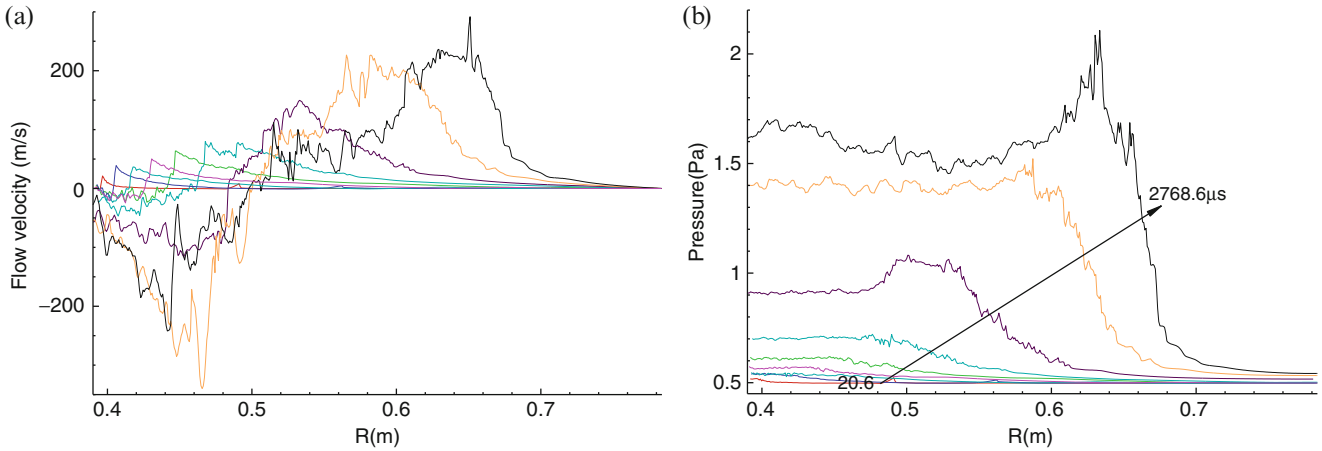

Fig. 3 Evolution of the pressure and flow velocity along radius

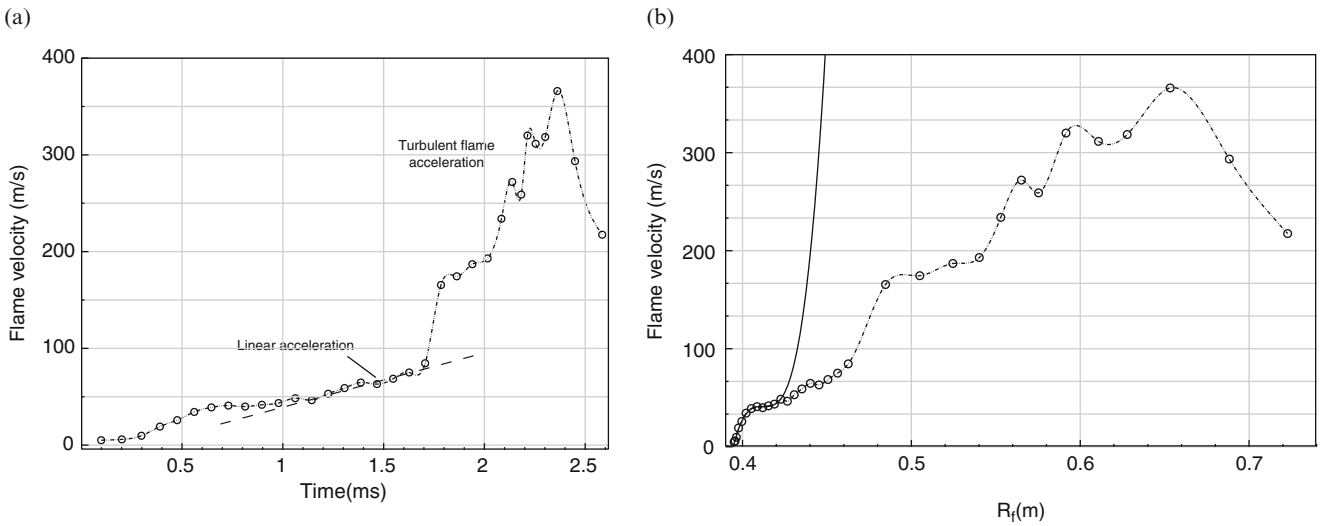

Fig. 4 Curve of the averaged flame velocity with time and radius

Conclusions

In the paper outward propagation of cylindrical flame in confinement geometry is investigated by high-resolution simulations. It is first found that globally cylindrical flame acceleration contains three stages: exponential self-acceleration, linear acceleration, and ultrafast acceleration. The numerical results show that linear acceleration is as result of gas compressibility, coupling positive-feedback mechanism. With formation of turbulent flame, gradient mechanism is observed, while transition to detonation does not occur.

Acknowledgment This work was supported by the National Natural Science Foundation of China (Nos. 11402137 and 91441131) and the National Key Basic Research Program of China (No. 2014CB239603).

References

1. Burke, M.P., Chen, Z., Ju, Y.G., Dryer, F.L.: Effect of cylindrical confinement on the determination of laminar flame speeds using outwardly propagating flames. Combust. Flame **156**, 771–779 (2009)
2. Xin, Y.X., Yoo, C.S., Chen, J.H., Law, C.K.: A DNS study of self-accelerating cylindrical hydrogen-air flames with detailed chemistry. Proc. Combust. Inst. **35**, 753–760 (2015)
3. Barenblatt, G.I., Zeldovich, Y.B., Istratov, A.G.: On diffusional-thermal stability of a laminar flame. J. Appl. Mech. Tech. Phys. **4**, 21–26 (1962)
4. Kelley, A.P., Bechtold, J.K., Law, C.K.: Premixed flame propagation in a confining vessel with weak pressure rise. J. Fluid Mech. **691**, 26–51 (2012)
5. Bychkov, V., Valiev, D., Eriksson, E.: Physical mechanism of ultra-fast flame acceleration. Phys. Rev. Lett. **101**, 164501 (2008)
6. Jiang, G.S., Shu, C.W.: Efficient implementation of weighted ENO schemes. J. Comput. Phys. **126**, 202 (1996)

Investigation on PIV and PLIF Laser Diagnostics in Turbulent Combustion Field

Long Zhang, Furong Yang, Tie Su, Shuang Chen, Jianjun Yang, and Yungang Wu

Introduction

High fuel efficiency and low pollution emissions are important technical specifications for high-performance gas turbine engine. Research institutions around the world always attach great significance to high-performance gas turbine engine and related technology. There is an urgent need to know the specific information of combustion flow in combustion chamber in order to improve the performance of combustion chamber of gas turbine engine; especially complex flow structure information is very important for the research of stability of flame. Conventional contact instruments such as hot-wire anemometer cannot be applied in combustion chamber for the complex combustion flow with high temperature and high pressure. Although laser Doppler velocimeter (LDV) can measure velocity field of combustion flow in a nonintrusive method, the application of single-line scan mode for velocity measurement can only get the average velocity field rather than complex flow structure information for whole field. Particle image velocimetry (PIV) [1] overcomes the limitation. It is widely used in complex measurement of flow. However, it is still a challenge for PIV to be used in measurement of combustion flow.

The difficulty of conventional PIV applying in measurement of combustion chamber flow mainly comes from three parts.

1. There is a complex combustion flow with high temperature and high pressure in combustion chamber, and the temperature of flame is higher than 1500 K. The tracer particles with high vaporization temperature should be used, and the high-pressure particle-seeding device should be specially designed.
2. Particle images cannot be recorded efficiently because high intensity of broadband visible light from flame results in pixel photosensitive saturation on optical pieces of PIV camera.
3. There are still problems, such as laser sheet incident, particles, and fuel droplet pollution around optical windows.

Planar laser-induced fluorescence (PLIF) is an attractive flow measurement technique in combustion aerodynamics research. This laser-based diagnostics is advantageous in some special and severe environments and flow fields, because they are nonintrusive and robust. PLIF can measure two-dimensional (2D) concentrations of molecules, such as OH, CH, NO, and CO [2–5]. Moreover, the two-color PLIF method offers the advantage of 2D temperature measurement that yield information about special structure and temperature distributions with high temporal and spatial resolution [6–8]. OH is an important reactive intermediate in combustion. Thus, using OH radicals as indicator is a perfect choice because of its abundant concentration at high temperature and its spectroscopic characters.

Therefore, a double-pulse PLIF experiment system is set up to study the two-color OH-PLIF thermometry technique.

In this method the temperature distribution of flow has been acquired by laser-induced fluorescence (LIF) imaging and calculation with the data of the two spectrum lines selected. However, the spectrum data used are difficult to confirm and correct in complex combustion environment, thereby influencing the accuracy of the OH-PLIF measurement. Therefore, an effective calibration method is needed.

In order to solve these problems, tests have been carried out to measure flow field of important cross section with PIV and OH-PLIF technique on high-temperature pure air incoming flow combustion chamber equipment (HTPA-IFCCE). The test can provide important valid data for the development of 3-D massive parallel numerical simulation software platform.

L. Zhang (✉) • F. Yang • T. Su • S. Chen • J. Yang • Y. Wu
China Aerodynamics Research & Development Center, Mianyang 621000, China
e-mail: zhanglong404@163.com

G. Ben-Dor et al. (eds.), *30th International Symposium on Shock Waves 1*, DOI 10.1007/978-3-319-46213-4_79

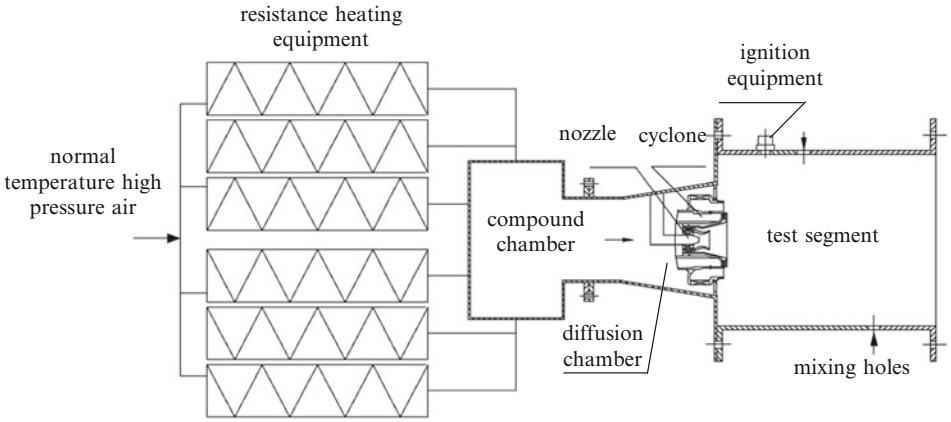

Fig. 1 Scheme of HTPAIFCCE combustion chamber equipment

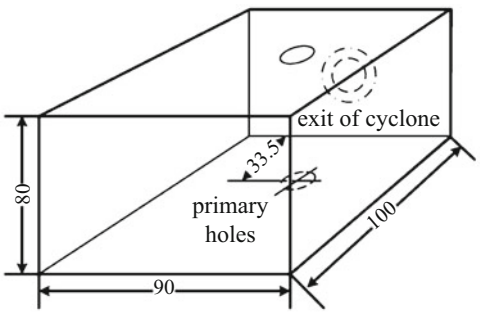

Fig. 2 Diagrammatic sketch and physical map of the model

Equipment and Model

Depressurization simulation is a widely used method around the world developing optical measurement on the flow in combustion chamber and investigating of combustion mechanism for single fuel nozzle of combustion chamber, cut the cost, simplify the method in the experiment, and shorten the research cycle. Combustion efficiency and exit temperature field same as actual combustion chamber can be gained by using depressurization simulation method.

Single fuel nozzle rectangular model test is carried out by depressurization simulation on HTPAIFCCE (Fig. 1). The experiment is heated by using heat-storage electric heater. The incoming flow in the experiment is pure air. The exit temperature of the experiment is in the range of 500–1050 K, the flux is in the range of 0.75–2.0 kg/s, and the stagnation pressure is in the range of 0.6–5.0 MPa. The steady duration is longer than 300 s.

Figure 2 shows diagrammatic sketch. The combustion chamber is 100 mm in length, 90 mm in width, and 80 mm in height, with two pieces of quartz glass in which thickness is 29.5 mm on two sides. The distance between the center of primary hole and exit of cyclone is 33.5 mm. The diameter of primary hole is 8 mm.

Diagnostic Technology

PIV System and Test Scheme

PIV test equipment contains digital camera, image acquisition system, dual-cavity ND:YAG laser system, isochronous controller, stereo optical system, etc.

The digital camera is PowerView Plus 4MP. The resolution is 2 K × 2 K (4 M) and the size of a pixel is 9 μm. The gray level of an image is 12bit. The minimum exposure time interval in PIV model is shorter than 200 ns. The maximum frame rate is 15f/s. The shot of the camera is NIKKOR 85 mm/F1.8 with appropriative narrow-band filter (532 ± 5 nm).

Image acquisition system contains computer, high-speed image acquisition card, Insight PIV analysis software, and Tecplot analysis process software. This system can acquire and process images, display the flow quantitatively, and control external trigger timing of synchronizer via interface RS-232.

The wavelength of dual-cavity ND:YAG laser is 532 nm. The energy of a single pulse is 500 mJ. The pulse width is 6–8 ns, and the repeat frequency rate is 1–15 Hz.

Double-pulse laser and CCD working sequence are controlled by the computer via isochronous controller.

Laser (532 nm) propagates into combustion chamber through a quartz window on after body of the model. Laser light arms and sheet light system are 100 mm away from the quartz window. Sheet light is wide enough to cover the whole area in combustion chamber and the thickness is about 1 mm. The measuring requirements for 2-D PIV are satisfied. The camera is placed on one side of combustion chamber. The optical axis is vertical to the light plane. The distance between the camera and the quartz window is about 450 mm, as shown in Fig. 3.

PLIF System and Test Scheme

According to the LIF-thermometry principle, a double-pulse OH-PLIF experimental setup is shown in Fig. 4. An instantaneous temperature measurement requires two laser pulses with wavelengths according to two special absorption lines of the OH radical and with a temporal delay shorter than the time scale for the fastest process that can freeze the structure of the flame. Tunable UV laser pulses (282.25 and 282.74 nm) are generated by two laser systems (Continuum PR2 8010, named 1# and 2#, respectively), which consisted of the frequency-doubled Nd:YAG lasers (532 nm), dye laser pumped by 532 nm laser, and UVT (creating UV laser near 282 nm by frequency doubling of the dye laser). The two UV laser pulses became planar laser sheet (thickness of 0.5 mm, width of 100 mm) and through the flame by optic combiner and lens system. Both UV laser pulses have a duration of less than 10 ns. Typical pulse energy is about 10 mJ per pulse, at a bandwidth of 0.5 cm − 1. The fluorescence signals of the OH are detected by two intensified-CCD camera systems (Andor DH734,1024 × 1024 pixels) using UV lenses and interference filters (WG305 and UG11), which are used to clean up laser scattering and reflecting.

The two cameras are placed on the same side of the flame and laser sheet at a right angle (Fig. 5). The intensity distribution of the laser sheets is monitored using quartz cells filled with Rhodamine 590 dye solution and equipped with two additional charge-coupled device (CCD) camera systems. Furthermore the energies of the laser pulses are detected by an energy meter and monitored by an oscilloscope (Tektronix DPO7104). Thus, each set of cameras records the fluorescence signal from the excitation of the two rotational levels and the laser intensity distributions; the oscilloscope records the energy of the two laser pulses.

Generating an appropriate trigger for the laser systems and cameras is necessary to measure the simultaneous temperature distribution. The signal processing arrangement consists of one control computer and two pulse delay generators (SRS, DG535). When the first laser sheet pulse reached the flame position, the intensifier of the ICCD 1# is activated to capture the fluorescence induced. The second intensifier is active when the other laser pulse reached with a relative time delay of 200 ns. The method of data calculation and processing has been described in detail in Ref. [9]. An effective calibration method is needed for the accuracy of measurement.

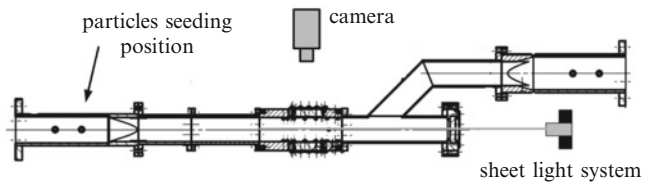

Fig. 3 Placement of equipment in 2-D PIV measurement

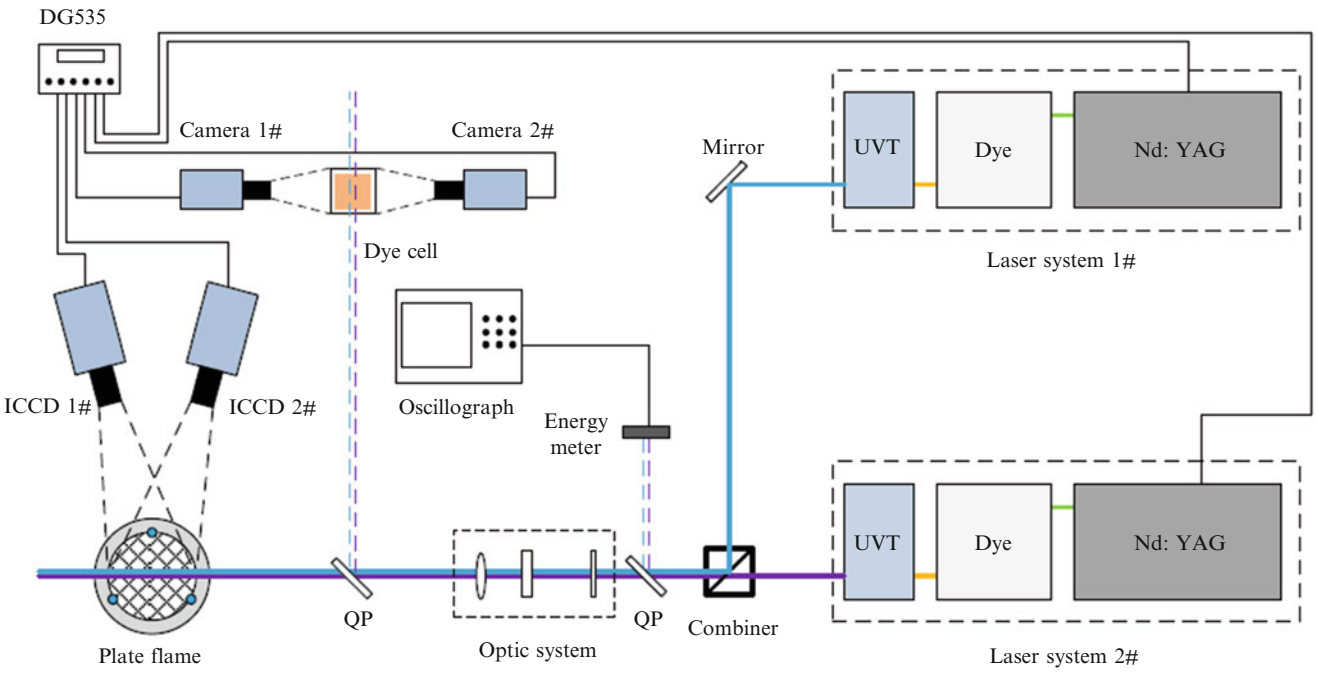

Fig. 4 Scheme of double-pulse OH-PLIF experimental setup

Results of Experiment

The temperature of the incoming flow is 300 K (300 K, 0.55 Mpa, 0.747 kg/s). 2-D velocity field distribution of longitudinal section of centrosymmetric plane is shown in Fig. 6a. At the same environment parameters, numerical simulating result (Fig. 6b) can be obtained using a LES method of combustion developed by CARDC.

The temperature of the incoming flow is 865 K. The pressure is 0.55Mpa. The air flux is 0.451 kg/s and the fuel flux is 9.97 g/s. The OH radical relative concentration distribution of longitudinal section of centrosymmetric plane from OH-PLIF is shown in Fig. 7a. At the same environment parameters, numerical simulating result (Fig. 7b) can be obtained using a LES method of combustion developed by CARDC.

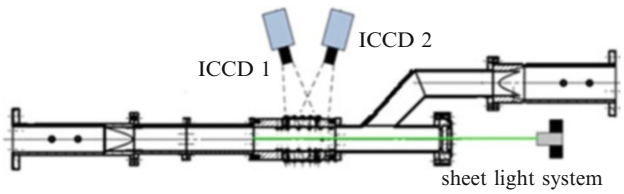

Fig. 5 Placement of equipment in PLIF measurement

Conclusions

The PIV and PLIF technique provides an effective measuring method for the investigation of complex flow in the combustion chamber of turbo engine and may be further applied to the study of combustion jet of turbo engine. Especially the results prove the feasibility of LES method of combustion developed by CARDC to some extent, as shown in Figs.6 and 7. This can provide validation data for the research on 3-D numerical simulation method in combustion flow.

In conclusion, simultaneous PIV and OH-PLIF measurements are studied, and a calibration method based on the recognized premix flame is performed using PLIF technique. The method offers a simple solution to quantitate temperature, avoiding complex calculation and uncertainty of the parameters in functions. The calibration experimental results are used to measure the temperature of the turbulent flame. Consequently, this method is proven to be useful to the combustion laser diagnosis. It would work well in low-pressure flows. However, in an environment with high pressure, the calibration results are not appropriate. Therefore accurate temperature results by OH-PLIF diagnostic method has not obtained in this experiment. Consequently, a more accuracy calibration method with theoretic

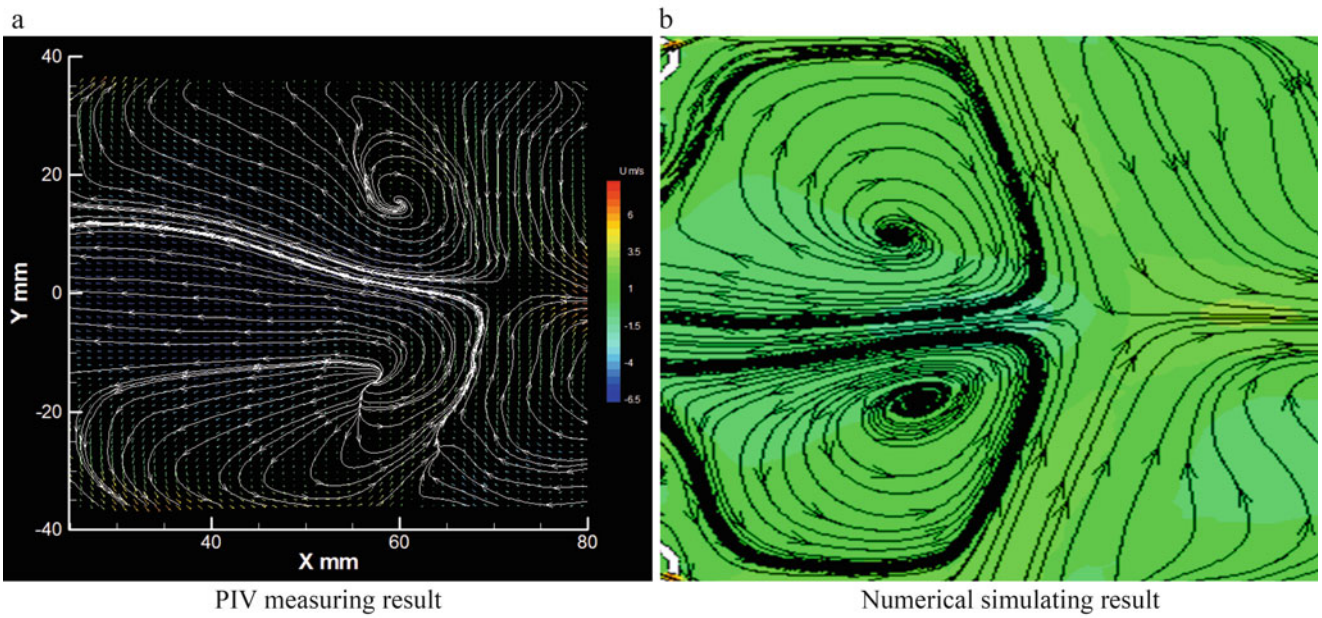

Fig. 6 Contrast of PIV measuring result and numerical simulating result of the flow in combustion. (**a**) PIV measuring result, (**b**) numerical simulating result

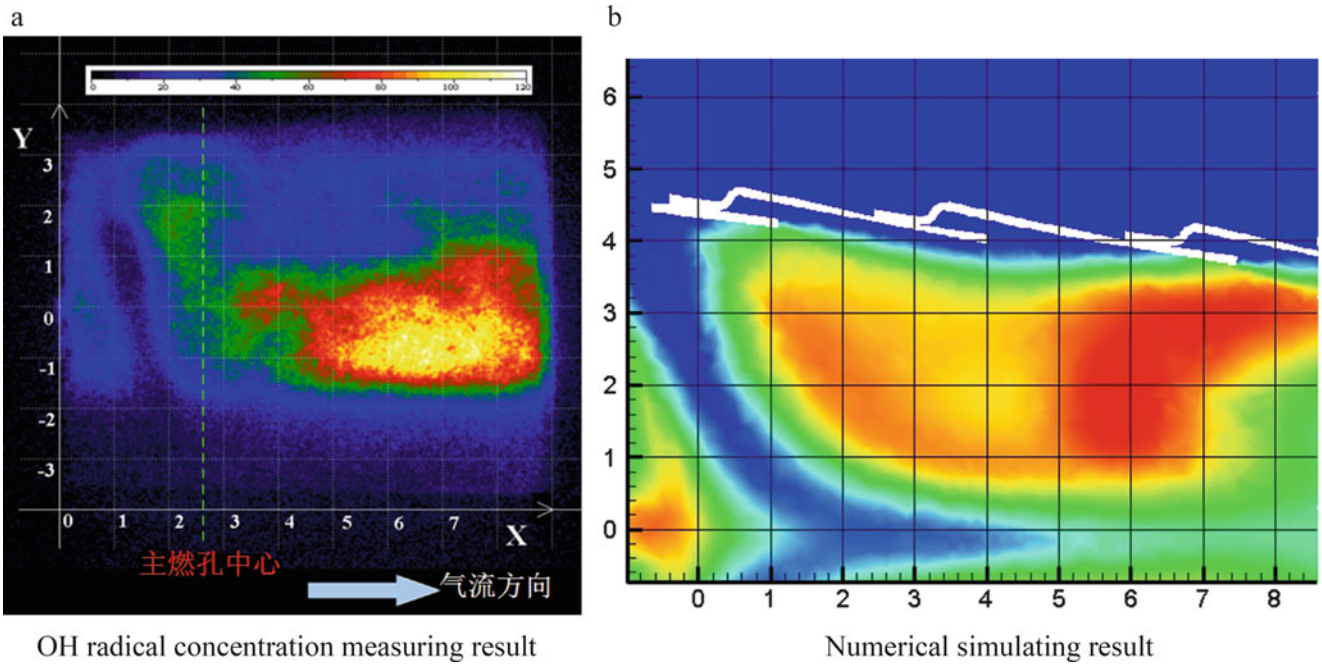

Fig. 7 Contrast of OH-PLIF measuring result and numerical simulating result of the flow in combustion. (**a**) OH radical concentration measuring result, (**b**) numerical simulating result

calculation and a special burner with high-pressure environment should be required.

References

1. Guo, L., Zhang, L., Yang, F.: Non-intrusive measurement technology in wind tunnel [M]. National Defense Industry Press **12** (2013). In Chinese
2. Seitzman, J.M., Hanson, R.K.: Planar fluorescence imaging in gases. Academic, London (1993)
3. Bessler, W.G., Schulz, C., Lee, T., Jeffries, J.B., Hanson, R.K.: Appl. Opt. **24**, 4922 (2003)
4. McMillin, B.K., Palmer, J.L., Hanson, R.K.: Appl. Opt. **32**, 7532 (1993)
5. Lee, M.P., McMillin, B.K., Palmer, J.L., Hanson, R.K.: J. Propulsion Power **8**, 7298 (1992)
6. Seitzman, J.M., Hanson, R.K.: Appl. Phys. B **57**, 384 (1993)
7. Seitzman, J.M., Hanson, R.K., DeBarber, P.A., Hess, C.F.: Appl. Opt. **33**, 4000 (1994)
8. Palmer, J.L., Hanson, R.K.: Appl. Opt. **35**, 485 (1996)
9. Chen, S., Su, T., Yang, T., Zhang, L.: Calibration method for 2D instantaneous OH-PLIF temperature measurements in flame. Chin. Opt. Lett. Col. **11**(5), 053001 (2013)

Modeling of Aerobic Combustion

T. Hartmann, E. Rottenkolber, and A. Boimel

Introduction

It is widely known that the combustion process of the detonation products is a crucial factor for internal detonations [1]. This is true not only for blast-enhanced explosives, which can be characterized as a composition of a high explosive and metal powder, but also for conventional CHNO explosives containing TNT, RDX, HMX, or PETN.

During the last several years, a lot of internal detonation trials have been conducted with metallized and conventional explosives. The experimental results suggested that combustion does not only depend on chemistry but on a lot of additional parameters, like the position of the charge within the detonation chamber and on the confinement of the charge itself.

Despite its importance for internal detonations, most of the commercial hydrocodes do not offer the possibility to simulate the combustion of detonation products in air.

Modeling of Aerobic Combustion

In order to close this gap, a thermodynamic model of combustion was developed and implemented in the hydrocode SPEED [2]. The requirement was to simulate the propagation of the detonation shock and to model the reaction of the expanding detonation products with the surrounding atmosphere.

Referring to the findings in Ref. [1], it can be assumed that most of the (metal) fuel in many blast-enhanced explosives is oxidized already during anaerobic expansion, and it is thus not necessary to model particulate burn. Instead, the situation in the combustion of these blast-enhanced explosives is exactly identical to the combustion of CHNO explosives, where the under-oxidized detonation products are mainly carbon, carbon monoxide, methane, and hydrogen.

Hence, the approach taken to model the combustion process more generally follows the suggestions made by Kuhl et al. [3], who applied their model, e.g., to TNT and PETN charges. Particularly, it is assumed that turbulent mixing controls the combustion and that reaction of detonation products with air takes place instantaneously wherever these materials occupy the same computational cell of the hydrocode.

In order to be applicable to a wide range of engineering problems, the presented model has to incorporate the possibility to describe the propagation of the detonation shock, the anaerobic expansion, and the reaction of the detonation products with air. Thus, there are four species to be modeled by an equation of state (EOS):

- The solid explosive
- The detonation products
- The surrounding atmosphere (air)
- The combustion products (coming from stoichiometric proportions of detonation products and air)

The solid explosive is modeled by a Murnaghan EOS, in which κ and n are material-dependent parameters and ρ denotes the material density:

$$p_{sol} = \frac{1}{\kappa n}\left(\eta^{-n} - 1\right) \tag{1}$$

$$\eta = \frac{\rho_0}{\rho} \tag{2}$$

In mixed cells, the solid explosive is assumed to be in pressure equilibrium with the gases, but is separated from them adiabatically. For the detonation products, the JWL

T. Hartmann (✉) • E. Rottenkolber
NUMERICS GmbH, Mozartring 6, 85238 Petershausen, Germany
e-mail: thomas.hartmann@numerics-gmbh.de

A. Boimel
Boimel Consulting, 60 hertzel Street, Petah-tiqwa 49435, Israel

G. Ben-Dor et al. (eds.), *30th International Symposium on Shock Waves 1*, DOI 10.1007/978-3-319-46213-4_80

equation of state is applied. Pressure p_s and specific internal energy u_s along the CJ expansion isentrope are defined by the following equations:

$$p_s(v) = Ae^{-R_1 V} + Be^{-R_2 V} + CV^{-\omega-1} \tag{3}$$

$$u_s(v) = A\frac{v_0}{R_1}e^{-R_1 V} + B\frac{v_0}{R_2}e^{-R_2 V} + C\frac{v_0}{\omega}V^{-\omega} \tag{4}$$

where v denotes specific volume, $V = v/v_0$ is the scaled volume, and the other symbols stand for material-specific parameters. Air and the combustion products are treated as ideal gases, and pressure and specific internal energy of the mixture of detonation products, air and combustion products are given by:

$$p(v,T) = \left[p_s(v) + \frac{\omega}{v}c_v(T - T_s(v))\right] \cdot x_{\text{Det}} + \frac{R^{\text{Air}}T}{v}x_{\text{Air}} + \frac{R^{\text{Comb}}T}{v}x_{\text{Comb}} \tag{5}$$

$$\begin{aligned} u(v,T) = {} & [u_s(v) + c_v(T - T_s(v))] \cdot x_{Det} \\ & + \left[a_{\text{Air}}T^2 + b_{\text{Air}}T + c_{\text{Air}}\right] \cdot x_{\text{Air}} \\ & + \left[a_{\text{Comb}}T^2 + b_{\text{Comb}}T + c_{\text{Comb}}\right] \cdot x_{\text{Comb}} \end{aligned} \tag{6}$$

Herein, R, a, b, and c are the respective ideal gas constants, the x's stand for the mass fractions, and T is the absolute temperature. As emphasized by Davis [4], the second law of thermodynamics, or more specifically the existence of the thermodynamic potentials like the free energy, $f(T,v)$, imposes some restrictions, i.e., integrability conditions, upon the equation of state. An explicit form of the integrability condition is

$$\frac{\partial u}{\partial v} = T\frac{\partial p}{\partial T} - p \tag{7}$$

For an ideal gas, it follows from this condition that the internal energy must be an arbitrary function of the temperature alone. However, in our case it turns out that the specific heat c_v must be constant and the temperature along the isentrope T_s in terms of the reference state T_{s0} must have the form:

$$T_s(v) = T_{s0}\left(\frac{v}{v_{s0}}\right)^{-\omega}. \tag{8}$$

Compared to the combustion model proposed in Ref. [3], the following enhancements and modifications were introduced:

- Inclusion of the solid un-detonated explosive
- Strict obedience to the second law of thermodynamics, as expressed by T_s and c_v
- Application to a broader class of explosives

Model Application

The described combustion model is applied to the partially confined detonation tests conducted by Edri et al. [5]. For comparison and for pointing out the necessity of considering the combustion process, the tests are simulated both with and without using the proposed combustion model.

Test Setup

TNT charges of different sizes were detonated in a detonation chamber with inner dimensions of 2.9 m by 2.9 m by 2.7 m (L/W/H) and with a circular opening (diameter 1.2 m) in the roof for venting. The edges of all inner walls of the chamber were truncated by 20 cm triangles (see Fig. 1). The masses and dimensions of the investigated charges are summarized in Table 1.

The box-shaped charges were placed at the center of the detonation chamber and initiated from the top. Thereby, the long side of the charge was always directed toward the wall instrumented with the pressure gauges sketched in Fig. 1.

Hydrocode Model

A three-dimensional quarter model of the detonation chamber was set up in the Eulerian hydrocode SPEED [2] (outlined in Fig. 2). The deformations of the confining concrete structure are neglected in the model, and the walls and the roof, respectively, are taken to be rigid. The spatial resolution of the mesh is 10 mm, which must be regarded as rather coarse. However, while the resolution clearly influences the peak pressures and their arrival times, the peak impulse, which was in the focus of the evaluations in Ref. [5], is only slightly influenced.

The parameter set used to model the TNT were determined with the thermochemical code XBKW [6] and are summarized in Table 2, where ξ denotes the oxidizer/fuel mass ratio that is required for the combustion.

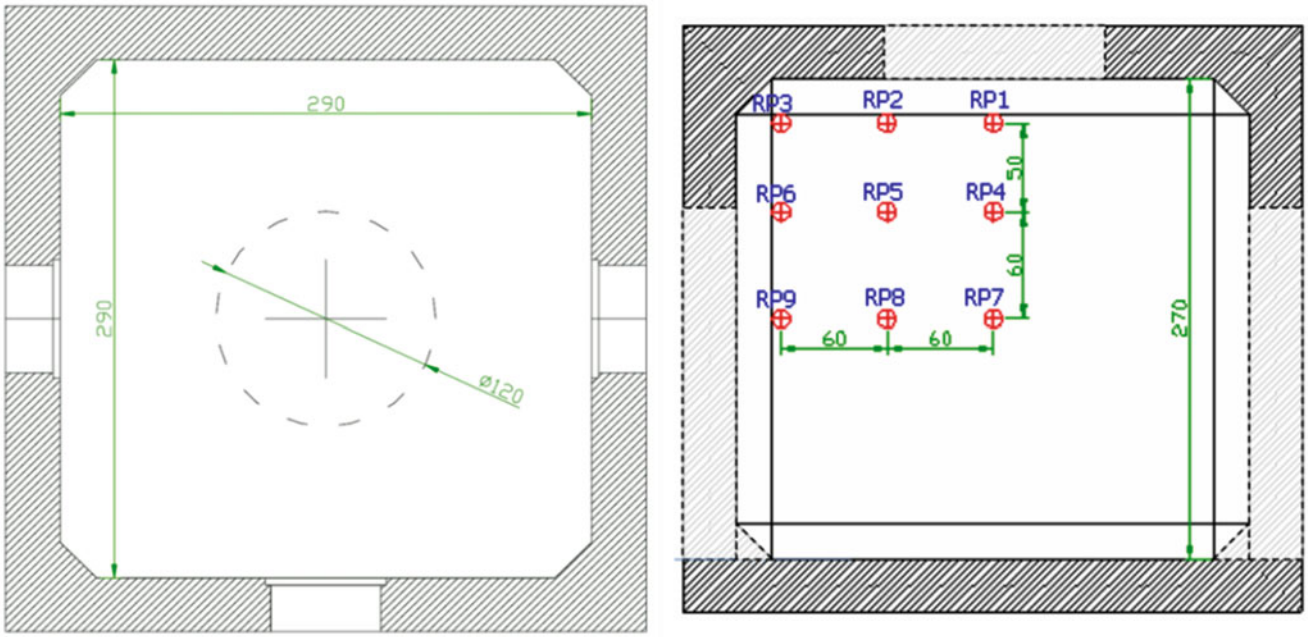

Fig. 1 Sketch of the detonation chamber [5]: plan view (*left*) and cross-sectional view (*right*)

Table 1 Masses and dimensions of investigated TNT charges [5]

	Test 1	Test 2	Test 3	Test 4	Test 5
TNT [kg]	0.5	1.0	1.5	2.0	4.0
Length [mm]	104	134	156	134	208
Width [mm]	67	104	134	104	134
Height [mm]	52	52	52	104	104

Simulation Results

All simulations were stopped after at $t = 100$ ms. Figure 3 exemplarily shows the material and temperature distributions in the cross-sectional plane at $t = 1.5$, 5, and 20 ms.

One and a half millisecond after firing the shock front has just been reflected from the floor and the sidewalls, but the reflections have not yet reached the detonation products again. At the interface between the detonation products and air, a kind of vortex flow has already developed. After 5 ms, violent turbulences have developed at the material interfaces. The required mixing is powered by the reflected shock waves traveling through the chamber. Each time a pressure wave crosses a density gradient, the vorticity of the flow changes, and more and more swirls are created. Combustion is nearly completed at $t = 20$ ms, when most of the (not yet exhausted) detonation products have been mixed with air.

The pressure records in the gauges were evaluated in all simulations and compared to the experimental results presented in Ref. [4]. Figure 4 exemplarily illustrates the evaluation of the pressure signals for gauge #5 with the 2 kg charge. Besides the expected slight deviations in peak pressures and arrival time, the experimental and numerical records show indeed very good agreement. However, while the peak impulse is nearly identical (deviation less than 3 %), the delay in shock arrival times due to the relatively coarse mesh and the consequently delayed mixing and combustion accumulates over time and leads to a slower increase of the numerical impulse curve compared to the integration of the experimental pressure signal. For comparison and to emphasize the importance of combustion, the result of an additional simulation without combustion modeling is presented (blue curve in Fig. 4). While the peak pressure is identical in the two simulations, a significant difference in the overpressure after the first shock reflection can be observed, and the effect of the additional energy supply from the combustion process becomes obvious. This difference in overpressure also substantially affects the delivered impulse, which is about 60 % (!) lower than in the simulation with combustion and in the experiment, respectively.

To avoid the presentation of an excessive amount of data, only the evaluation of the delivered impulse in gauges #3, #5, and #7 (c.f. Fig. 1) is presented here. The respective simulation results are compared to the experiments in Table 3. It can be found that the peak impulse in the simulations mostly stay slightly below the experimental values.

This slight underprediction of the experimental results can also be observed in the comparison of the average impulse over all gauge points, which is illustrated in Fig. 5. However, the mean deviation is less than 4 % and is practically negligible.

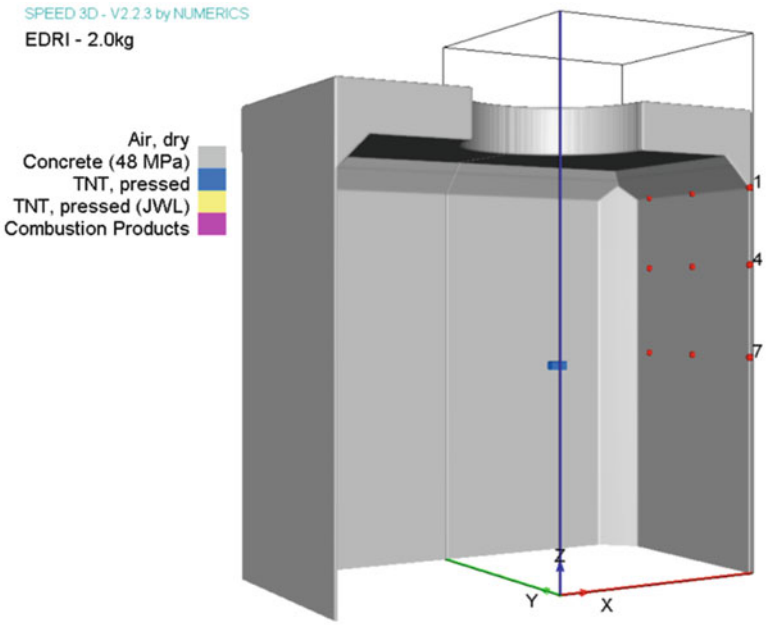

Fig. 2 3D model for the simulation of internal detonation tests

Table 2 Parameter set for TNT used in the simulations

Po [g/cm^3]	κ [1/GPa]	n[−]	A [GPa]	B [GPa]	R_1[−]
1.6	8.274	9.608	575.4	8.55	5.0604
R_2[−]	ω[−]	e [J/kg]	c_v [J/(kgK)]	ξ [−]	
1.1866	0.2614	4905840	972.2	3.203463	

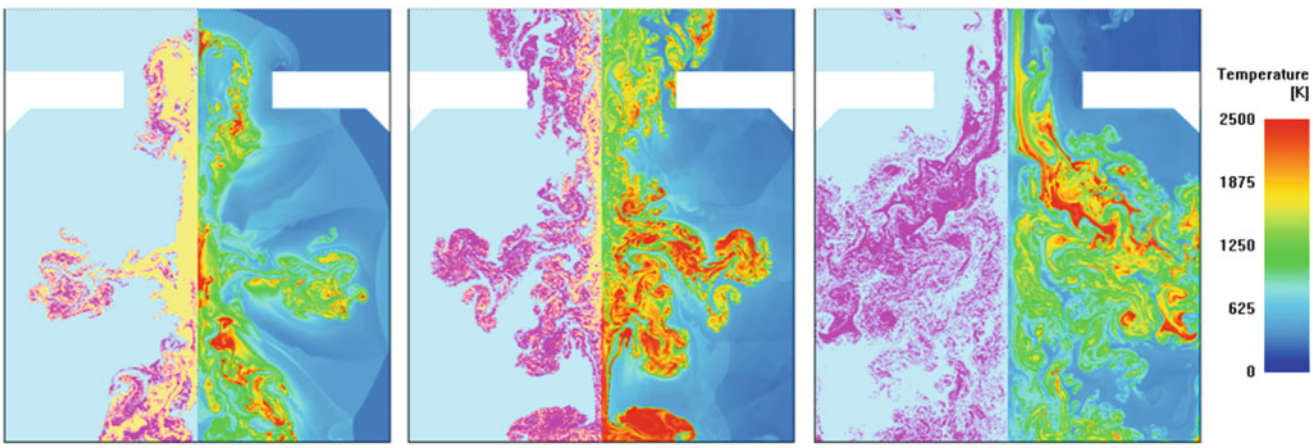

Fig. 3 Material (*left*) and temperature (*right*) distributions inside the chamber at $t = 1.5$ ms, $t = 5$ ms, and $t = 20$ ms

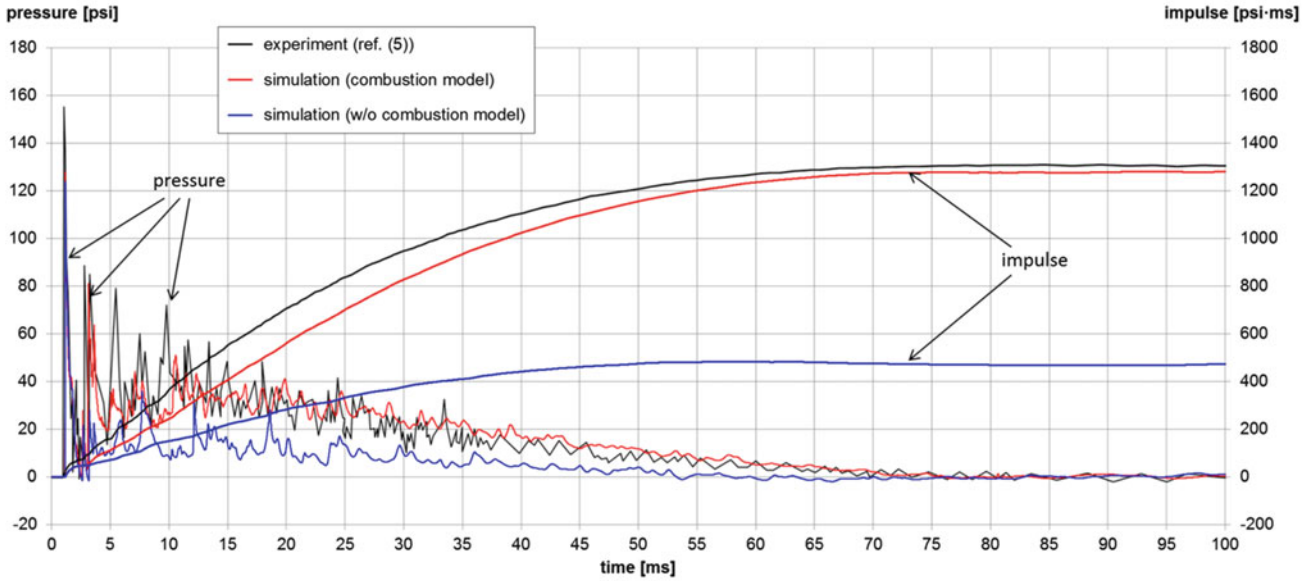

Fig. 4 Comparison of simulation result and experimental data for gauge #5 @ 2 kg TNT

Table 3 Comparison of maximum impulse from simulation and experiment[5]

	Peak impulse [psi · ms]								
	Gauge #3			Gauge #5			Gauge #7		
Test	Sim.	Exp.	Δ	Sim.	Exp.	Δ	Sim.	Exp.	Δ
1(0.5 kg)	291.0	292.9	−1 %	250.4	276.5	−9 %	304.2	334.3	−9 %
2(1.0 kg)	585.3	601.5	−3 %	528.7	578.6	−9 %	591.8	620.3	−5 %
3 (1.5 kg)	909.6	987.9	−8 %	815.5	878.1	−7 %	912.8	971.3	−6 %
4 (2.0 kg)	1428.2	1356.7	+5 %	1270.1	1305.0	−3 %	1448.3	1463.6	−1 %
5 (4.0 kg)	2304.5	2434.6	−5 %	2107.7	2181.2	−3 %	2429.9	–	–

Fig. 5 Comparison of average simulation and test results

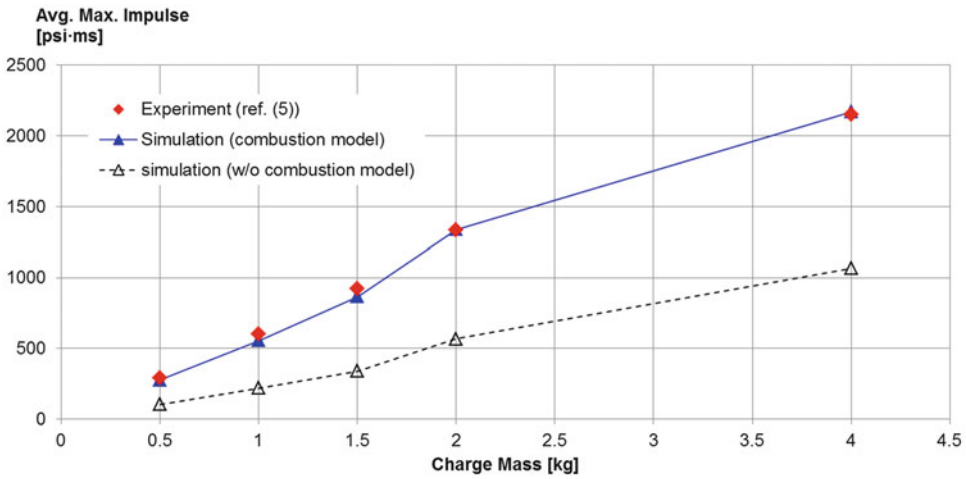

Conclusions

A thermodynamic model of aerobic combustion of detonation products, which extended the original model [3] to include the simulation of the propagation of the detonation wave and which is implemented in the hydrocode SPEED, was presented.

The model was applied to the partially confined detonation tests conducted by Edri et al. [5] yielding throughout good agreement between the experimental and numerical results. All simulations were also conducted without the proposed model showing that the combustion makes the lion's share of the delivered impulse. A detailed evaluation of the simulations further made clear that the required mixing of detonation products and air—and thus the complete combustion process—is strongly enhanced by the reflected shock waves traveling through the chamber.

Summing up, it can be stated that while the described model well represents the combustion of detonation products in air, neglecting aerobic combustion in the investigated internal detonation events leads to a massive underprediction of the impulse delivered to the surrounding structure.

References

1. Rottenkolber E., Greulich S., Arnold W.: Modeling of blast enhanced explosives. Proceedings of the 20th International Symposium on Military Aspects of Blast and Shock, Oslo, Norway, (2008)
2. Numerics GmbH.: SPEED – Theory Manual. Numerics GmbH (2014)
3. Kuhl A.L., Howard M., Fried L.: Thermodynamic model of afterburning in explosions. Proceedings of the 34th International Conference of ICT, Karlsruhe, Germany, (2002)
4. Davis W.C.: Equations of state for detonation products. Proceedings of the 11th International Detonation Symposium, Snowmass, Colorado (1998)
5. Edri I., Savir Z., Feldgun V., Karinski Y., Yankelevsky D. On blast pressure distribution due to a partially confined explosion: I. Experimental studies. Int. J. Protect. Struct. **2**(1): (2011)
6. Rottenkolber E.: XBKW 1.1 – User Manual (in German). NUMERICS/TDW (2005)

Investigations of Equivalence Ratio on Operational Liquid-Fuel Pulse Detonation Engines

J. Li, Teo Chiang Juay, L. Li, K.S. Lim, and Boo-Cheong Khoo

Introduction

Liquid-fuel detonations or spray detonations are always of interest due to their important roles in several practical applications, such as explosion prevention in the presence of leakages occurring in liquid-fuel storage tanks and pipelines or the onset of two-phase detonations in developing detonation engines such as PDE or RDE. A PDE is a combustion system which relies on repetitive detonations that are cyclically initiated in a tube. Within one combustion cycle, the processes of fuel/air filling, detonation initiation, detonation propagation, and blowdown of burned products proceed sequentially. When liquid fuels are employed in PDEs, tremendous difficulties arise during the detonation initiation process due to the inherent insensitivity of droplet-air mixtures. To overcome this problem, high-vapor-pressure fuels (such as *n*-hexane and *n*-heptane) were adopted [1] owing to their rapid vaporization rates. Another strategy is to operate the liquid-fuel PDE mimicking a gaseous-fuel PDE by preheating the air and/or fuels [2]. Tucker et al. demonstrated liquid-fuel PDE operation up to 15 Hz with the inlet air heated to 123 °C or 149 °C, wherein different liquid fuels with varying volatility levels were preheated to 192/279 °C or even unheated. From a practical point of view, the fuel may coexist in both the liquid and vapor phases, especially at relatively low temperatures. It is well known that the choice of an appropriate equivalence ratio plays a vital role in ensuring the successful operation of a gaseous-fuel PDE. However, for the case of liquid-fuel PDE, the definition of the equivalence ratio becomes more ambiguous. It is possible to adopt a global (or overall) equivalence ratio based on the total amount of fuel or a vapor-phase equivalence ratio based only on the amount of fuel present in the vapor phase. It is of interest to experimentally investigate which definition of equivalence ratio is more relevant for the successful operation of liquid-fuel PDE.

In the 1980s, Lin et al. [3] used a predetonator to initiate clouds of decane droplets and air at 50 °C. They found that when the vapor-phase equivalence ratio to the global equivalence ratio $\phi_v/\phi = 0.42$, for which $\phi = 1.72$ and $\phi_v = 0.72$, spray detonation can be achieved, and it was an essentially gaseous detonation based on the measured detonation velocity. Note that ϕ_v/ϕ is identical to the percentage of vaporized fuel. In 2001, Brophy et al. [4] successfully initiated spray detonations in JP-10/air in a PDE in which a JP-10/oxygen predetonator was used. They obtained detonations for conditions where the inlet air temperature was higher than 102 °C, and more than 70 % of the fuel had vaporized, corresponding to $\phi_v/\phi = 0.7$. From these studies, it is fairly acceptable that the amount of fuel present in the vapor phase prior to detonation ignition has an important effect on heterogeneous spray detonations. However, the most pivotal factors for achieving successful spray detonations, e.g., ϕ, ϕ_v, or ϕ_v/ϕ, still remain unresolved. In this paper, a series of experiments performed on a Jet A1/air PDE with varying air temperatures and global equivalence ratios are conducted for this purpose.

Experiments and Results

First, experiments using a global equivalence ratio slightly above unity were carried out at a high inlet air temperature. This is to ensure the capability of the present experimental rig in successfully achieving detonations when the liquid fuels are fully vaporized. As shown in Fig. 1, when the

J. Li (✉) • L. Li • K.S. Lim • B.-C. Khoo
National University of Singapore, Singapore 117576, Republic of Singapore
e-mail: tslljm@nus.edu.sg

T.C. Juay
Department of Mechanical Engineering, National University of Singapore, Block EA, #07-08, 9 Engineering Drive 1, Singapore, Singapore

G. Ben-Dor et al. (eds.), *30th International Symposium on Shock Waves 1*, DOI 10.1007/978-3-319-46213-4_81

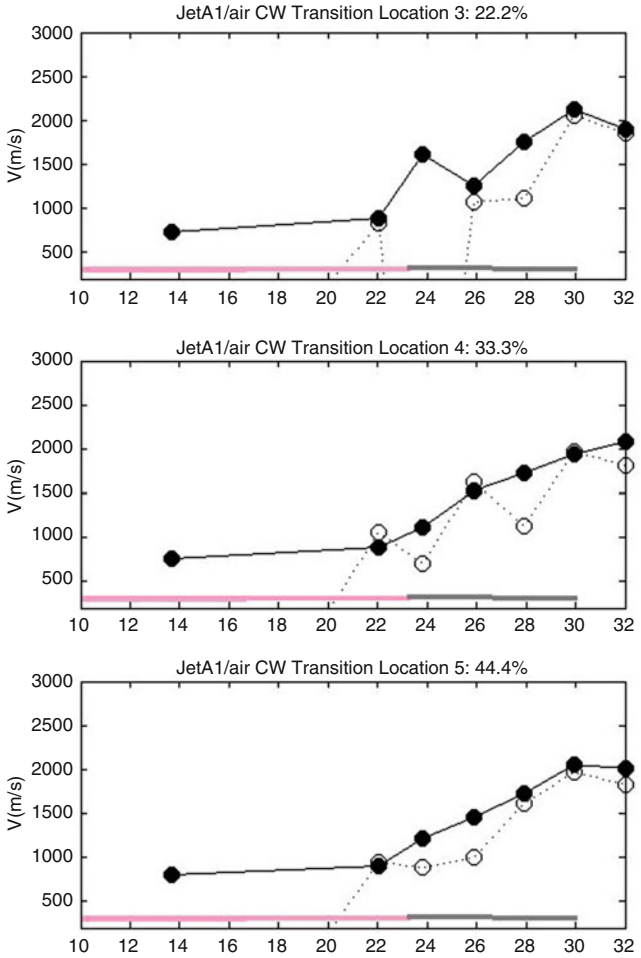

Fig. 1 Wave speed run-up during the DDT process (CW *filled circle* and PW *open circle*)

global equivalence ratio $\phi = 1.17 - 1.21$ and the air temperature is 186 °C, detonation transitions are observed. The PDE was fired in succession at a frequency of 2 Hz for nine times. Detonation transitions were attained in the tube for all nine firings, with 22.2, 33.3, and 44.4 % of the total transitions occurring at three different locations, respectively. The subsequent set of experiments was conducted at a relatively lower air temperature to evaluate the dependence of air temperature on the detonability.

As shown in Fig. 2a, at a relatively lower temperature where the global equivalence ratio was slightly above unity, successful detonations were not achievable. At $T_{air} = 167$ °C, the maximum wave velocity at the last measurement location was only 1500 m/s. However, when the global equivalence ratio was subsequently increased to yield a more fuel-rich mixture, corresponding to $\phi = 1.57–2.0$, detonations were obtained as long as $T_{air} \geq 152$ °C. This implies that an increase in the global equivalence ratio has enabled the onset of detonation to occur at a relatively low temperature.

Finally, experiments were conducted at relatively low temperatures with the global equivalence ratio increased to extremely high values. As shown in Figs. 3 and 4, as the air temperature was gradually reduced, the global equivalence ratio was increased to extremely high values. To our surprise, the Jet A1/air PDE was able to operate successfully for the entire range of air temperatures, even though the air temperature was only 70 °C. The measured wave velocities for all shots were in the range of 1790–1967 m/s. These results indicate that the use of extremely high global equivalence ratios is favorable for attaining spray detonations at relatively low temperatures. Using the NIST phase equilibria code SUPERTRAPP, the vapor-phase equivalence ratio corresponding to the global equivalence ratio at different temperatures can be calculated. The question arises as to

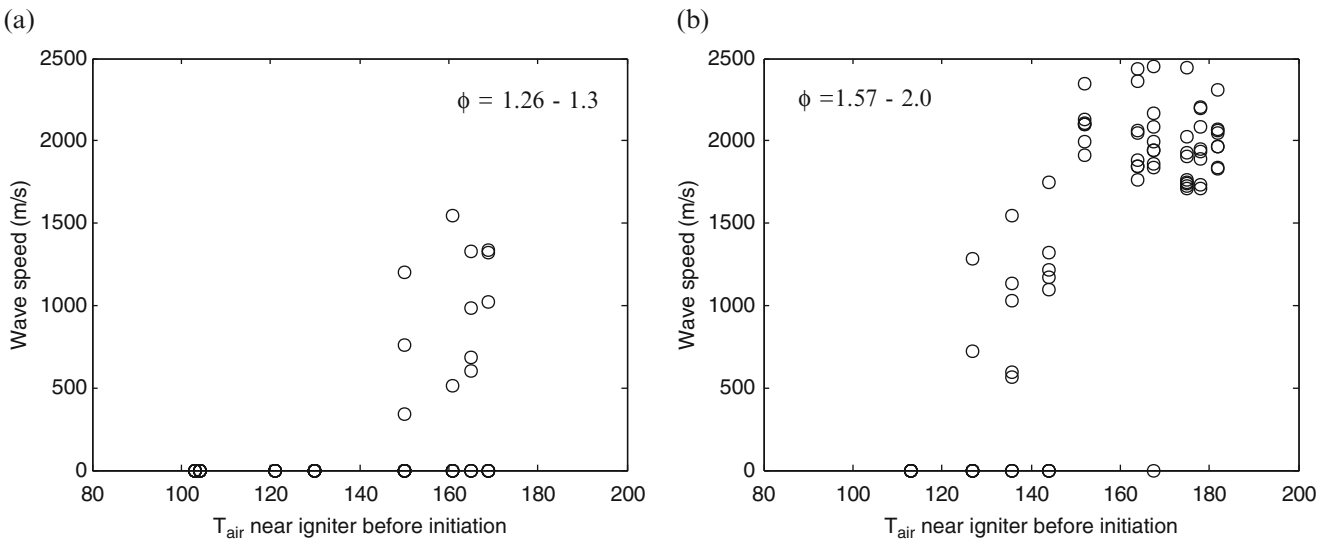

Fig. 2 Wave velocity at the last measurement location for different air temperatures

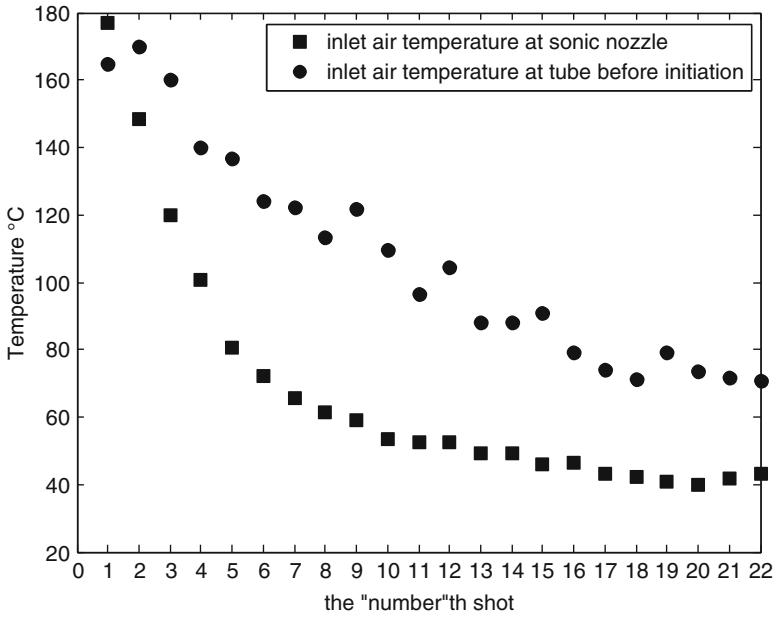

Fig. 3 T_{noz} and T_{air} for the final experiments

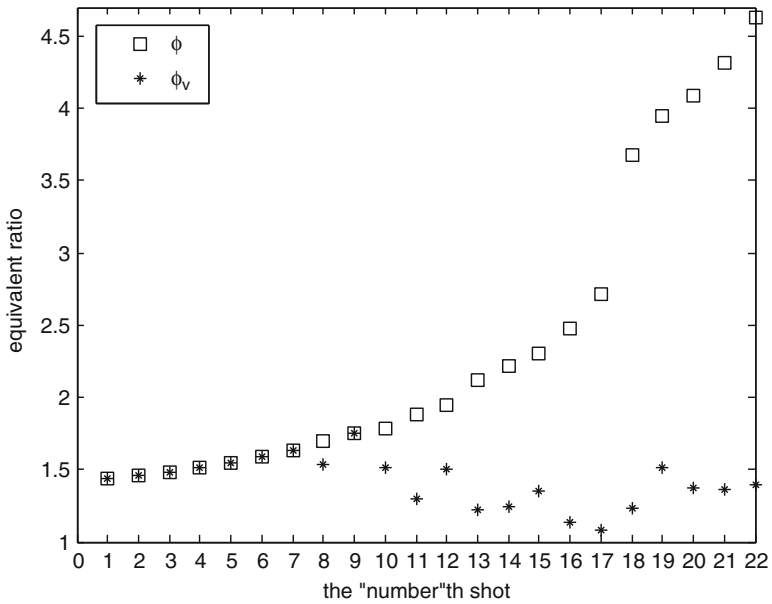

Fig. 4 Global equivalence ratio and vapor-phase equivalence ratio for the final experiments

whether phase equilibrium is established during the fuel filling time. During the testing, the droplet diameter was maintained at a SMD of 10 μm for a total of 22 shots. Applying a simple D^2 law, the equilibration lifetime to reach $\phi_v = 1.35$ is estimated to be approximately 0.00122 s. This value of equilibration lifetime is much less compared to the filling time for the present testing conditions. Therefore, it is likely that phase equilibrium is established during the testing. From Fig. 4, we can find that the use of extremely high global equivalence ratios at relatively low temperatures actually leads to a corresponding vapor-phase equivalence ratio ϕ_v lying in the range of slightly above unity (Fig. 5).

As the previous studies [3, 4] focused on the role of the fraction of vaporized fuel on spray detonations, the fractions of vaporized fuel (or ϕ_v/ϕ) in our final experiments are estimated (see Fig. 6). Corresponding to shots 1–7 and 9, the fuel has fully vaporized and thus $\phi_v/\phi = 1$. When a relatively low air temperature is applied, a cool saturated fuel in the vapor phase ($\phi_v/\phi < 1$) is present. In this experiment, even when the fraction of vaporized fuel is as low as 0.3, successful liquid-fuel PDE operation is still accomplished, which can be attributed to the vapor-phase equivalence ratio attaining a composition that is easier to undergo detonation. From Figs. 4 and 6, it is realized that the amount of vaporized fuel sufficient for spray detonations depends

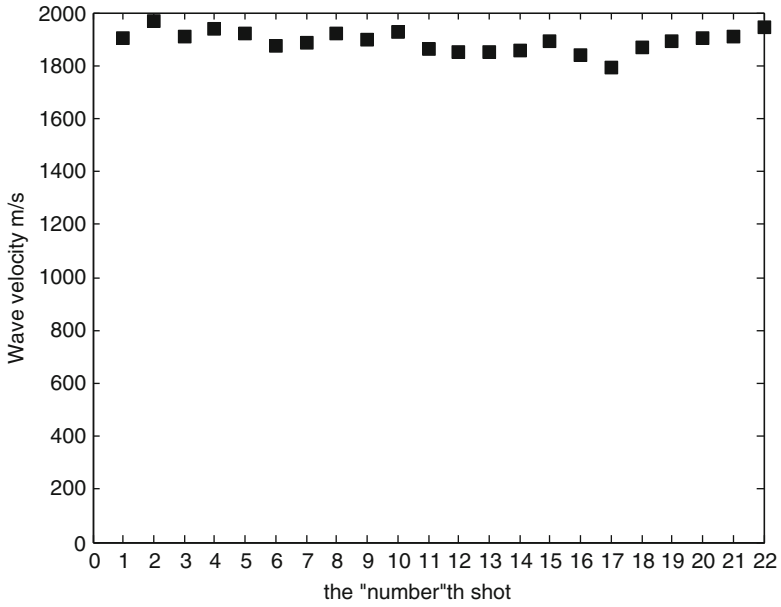

Fig. 5 Wave velocity measurements for the final experiments

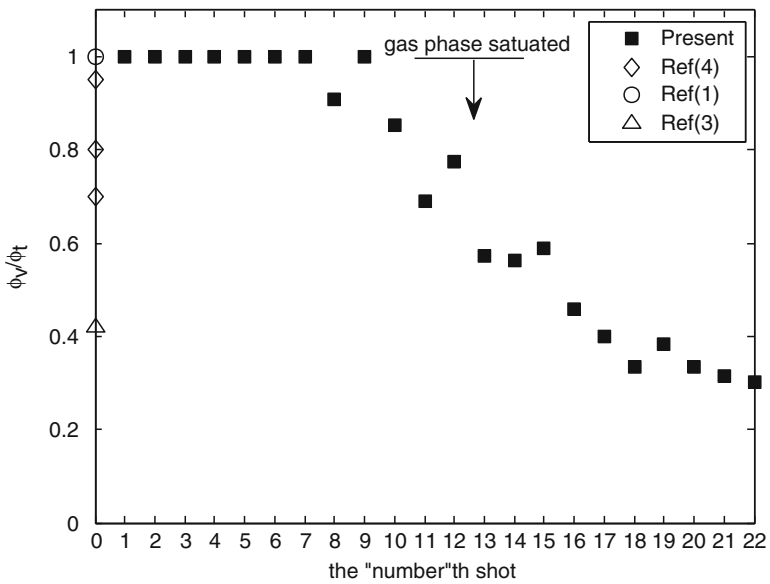

Fig. 6 Fraction of vaporized fuel (or ϕ_v/ϕ) for the final experiments

not only on the mixture/air temperature but also on the global equivalence ratio being applied. Comparing to the existing data from the available literature [1, 3, 4] (see Fig. 7), successful detonations were achieved when ϕ_v of the liquid fuel was near stoichiometric or slightly fuel-rich. This indicates that the vapor-phase equivalence ratio plays a pivotal role in ensuring the successful operation of liquid-fuel PDEs. One could thus elevate the air temperature, increase the global equivalence ratio, or use a highly volatile liquid fuel to attain a suitable vapor-phase equivalence ratio. To quantitatively ascertain the amount of vaporized fuel which is present in the mixture of reactants and thus to obtain an appropriate vapor-phase equivalence ratio, an in situ optical diagnostics technique for quantifying the concentration of vaporized liquid fuel is currently under development.

Conclusions

Based on a series of experiments, it has been shown that the vapor-phase equivalence ratio plays a pivotal role in ensuring the successful operation of liquid-fuel PDEs. Based on the existing data from the literature and the present study, successful detonation experiments using liquid fuels are generally achieved when the vapor-phase equivalence ratio

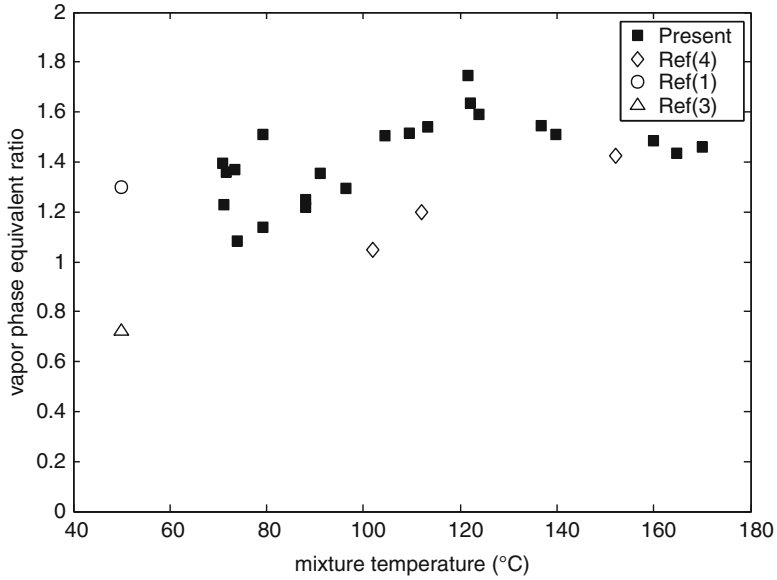

Fig. 7 Vapor-phase equivalence ratio for successful detonations reported in previous studies [1, 3, 4] and for the present study

is near stoichiometric or slightly fuel-rich. At a relatively low temperature, an increased global equivalence ratio would thus be favorable for achieving an appropriate vapor-phase equivalence ratio.

References

1. Frolov, S.M.: Liquid-fueled, air-breathing pulse detonation engine demonstrator: operation principles and performance. J. Propuls. Power **22**(6), 1162–1169 (2006)
2. Tucker, K.C., King, P.I., Schauer, F.R.: Hydrocarbon fuel flash vaporization for pulsed detonation combustion. J. Propuls. Power **24**(4), 788–796 (2008)
3. Lin, Z.C., Nicholls, J.A., Tang, M.J., Kauffman, C.W., Sichel M.: Vapor pressure and sensitization effects in detonation of a decane spray. Twentieth Symposium International on Combustion, pp. 1709–1716 (1984)
4. Brophy, C.M., Netzer, D.W., Sinibaldi, J., Johnson, R.: Detonation of a JP-10 aerosol for pulse detonation applications. Book: High-Speed Deflagration and Detonation, pp. 207–222 (2001)

Detonation of Mechanoactivated Mixture of Ammonium Perchlorate with Aluminum

Alexander Dolgoborodov, Vladimir Kirilenko, Michael Brazhnikov, Arseny Shevchenko, and Victor Teselkin

The production technique of mechanoactivated energetic composition (MAEC) based on ammonium perchlorate (AP) and aluminum has been developed. For preparation of the mixtures, regular powders of AP (20–100 μm) and Al powders—pyrotechnic powder PP-2 (flake particles 50–200 μm by thickness 2–5 μm) and Al(8) (average size of particles ~280 nm)—were used. The components were mixed and activated in an Activator-2SL planetary ball mill (JSC "Activator," Novosibirsk) with steel balls and drums and with water cooling. The optimum conditions of mechanical activation were found so that the maximum homogenization of the mixture was provided in the absence of the reaction between reagents. The structure of MAEC was studied by X-ray diffraction analysis and scanning electron microscopy. The results of research of explosive properties (deflagration to detonation transition (DDT) in Al/AP loose-packed charges, dependence of detonation velocity (DV) on density for the pressed charges, and mechanical sensitivity) have been received.

Mechanical sensitivity was investigated by the method of the collapsing shell. The value of critical pressure P_{cr} corresponding to the transition from mechanical destruction of charges in the shell of PMMA without an explosion to destruction with explosion was measured. For activated Al/AP (20/80) $P_{cr} = 0.61$ GPa and occupies an intermediate position between such sensitive explosives as bis (trinitroethyl)nitramine and lead azide.

The study of DDT was carried out in steel and duralumin tubes with a diameter of 10 mm at a porosity of samples about 80 %. Measurements of DV for Al/AP were carried out at a distance of 80 mm from the point of ignition. Increasing activation time T_{act} from 2 to 10 min, the process speed increases sharply from 100 to 2700 m/s and with a further T_{act} increasing DV gradually decreases to 2300 m/s D (T_{act}) for MAEC Al/AP (20/80) as shown in Fig. 1.

The results of measurements of speed of a detonation depending on density of the pressed charges of MAEC Al/AP (20/80) are shown in Fig. 2. The DV maximum has

A. Dolgoborodov (✉)
JIHT RAS, Moscow, Russia

NRNU MEPhI, Moscow, Russia
e-mail: aldol@ihed.ras.ru

V. Kirilenko • M. Brazhnikov • V. Teselkin
ICP RAS, Moscow, Russia

A. Shevchenko
NRNU MEPhI, Moscow, Russia

G. Ben-Dor et al. (eds.), *30th International Symposium on Shock Waves 1*, DOI 10.1007/978-3-319-46213-4_82

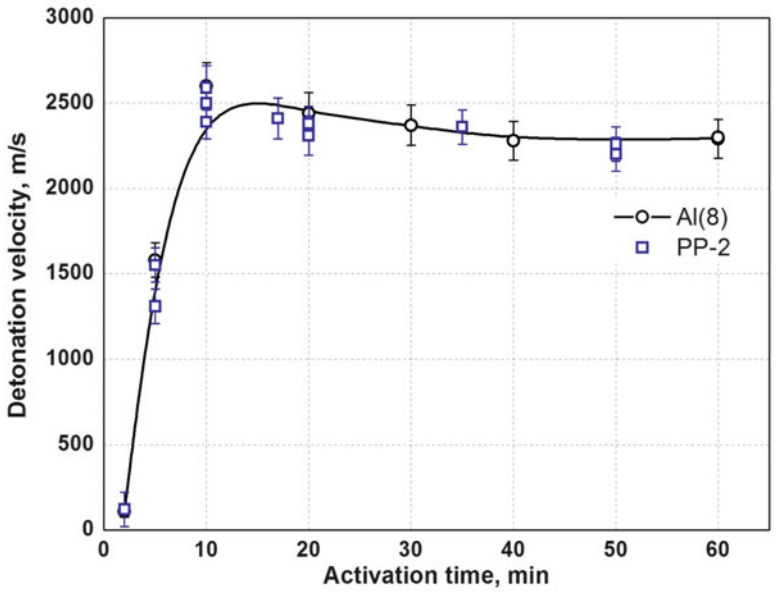

Fig. 1 Dependence of detonation velocity of loose-packed charges Al/AP (20/80) on the activation time

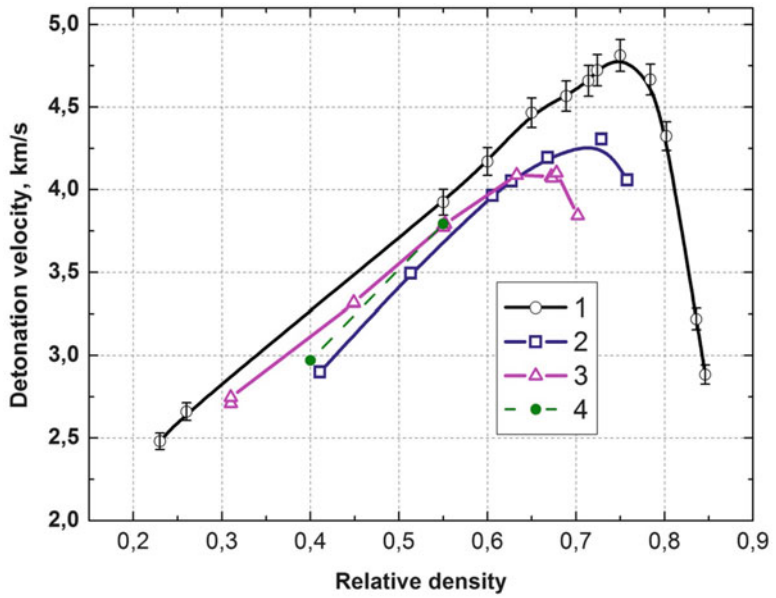

Fig. 2 Dependence of detonation velocity on the relative density. *1* MAEC Al/AP (20/80) $T_{act} = 10$ min, *2* - *4* Donna Price data [1], *2* AP, *3* Al/AP 10/90, *4* Al/AP (20/80)

been received for MAEC with a ratio of components Al/AP (20/80). In comparison with data for usual non-activated mixtures, Al/AP [1]-mechanoactivated composites show essentially higher DV that can be connected with increase in reactionary ability of the activated mixes in the course of a detonation. Mechanoactivation of Al(PP-2)/AP (Tact = 10 min) allowed one to shift the DV-value up to a maximum 4.8 km/s at relative density ~ 0.75 and charge diameter = 25 mm. In general, the results of the work showed that the use of mechanochemical activation allows us to regulate the detonation ability of explosive oxidizer-fuel mixtures.

Acknowledgments This work was supported by the Russian Foundation for Basic Research (Grant No. 16-29-01030) and Grant Program of the Presidium of RAS "Thermophysics of High Energy Density".

Reference

1. Price, D., Clairmont, A.R., Erkman, J.O. Explosive behavior of aluminized ammonium perchlorate. Naval Ordnance Laboratory Report NOLTR 72-15, White Oak, MD, USA, (1972)

Detonation Transition in Relatively Short Tubes

M. Kuznetsov, A. Lelyakin, V. Alekseev, and I. Matsukov

Introduction

A problem of run-up distance for the detonation onset and the effect of tube length on detonation transition is of the great importance from practical and theoretical points of view. Critical conditions for flame acceleration and DDT in obstructed channels were evaluated in papers [1, 2]. The run-up distance from ignition to sonic flame and then to detonation in obstacle-laden tubes was experimentally investigated in paper [3]. Such conditions significantly differ from that in smooth tubes without obstacles. There are some experimental data on the effects of tube diameter on the run-up distance to detonation for tubes without obstacles [4, 5]. The ratio of run-up distance to tube diameter was found to be in the range from 15 to 40. Such an attempt is very conservative and does not take into account the mixture reactivity, geometry, and roughness of the channel.

The influence of tube roughness, boundary layer, and mixture reactivity in terms of chemical reaction length δ and detonation cell size λ was recently investigated in papers [6, 7]. To take into account a factor of mixture reactivity, the run-up distance to DDT x_D was evaluated for hydrogen–oxygen mixtures in terms of a detonation cell width as a ratio x_D/λ which has to be larger than 500. For ethylene–oxygen mixtures, characteristic time for detonation onset t_D normalized by chemical reaction time τ as a measure of chemical reactivity has to be of the order of 25 (t_D/τ ~25). In terms of chemical reaction length, the critical ratio x_D/δ is about 1500–1700. The authors [6] demonstrated that the detonation onset may occur at dimensionless distances expressed in a tube diameter x_D/D in the range from 1 to 50 depending on initial pressure (changes from 8 to 0.2 bar, respectively). Reducing the reactivity by reducing the initial pressure, the run-up distance might be comparable with a tube length.

The authors [6] also analyzed an effect of boundary layer thickness and a mixture reactivity on DDT run-up distance. As they found for highly reactive mixtures with a tube diameter $D > 20 \cdot \lambda$, the run-up distance $x_D/D = 1 \div 100$ and actually does not depend on tube diameter. Only for mixtures with $10 \cdot \lambda < D < 20 \cdot \lambda$, the ratio $x_D/D = 15$–25 depends on tube diameter. And, again, for low reactive mixtures, the run-up distance does not depend on tube diameter. It usually relates to so-called relatively short tubes. The criteria for relatively short tube can be the ratio $t_D/t_s \ll 1$, where $t_s = L/c_s$ is the time of reflected shock passing through the tube length. In this case, the effect of precursor shock reflection on DDT can be dominant, and we may classify the tube as relatively short. Adiabatic compression of the mixture and shock–flame interaction affected the mixture preconditioning prior the DDT. Using a relatively short tube with a tube length almost equal or even less than run-up distance to detonation, the detonation can be earlier initiated after a collision or several collisions of reflected precursor shock wave with a flame front. An abrupt flame acceleration due to Richtmyer–Meshkov instability may also lead to additional reaction rate increase and then to deflagration-to-detonation process.

The objective of this work is to investigate the DDT process for stoichiometric hydrogen–oxygen mixture in relatively short tubes. To change mixture reactivity, the run-up distances for the onset of detonations were studied in a series of tests as a function of initial pressure.

M. Kuznetsov (✉) • A. Lelyakin
Institute for Nuclear and Energy Technologies, Karlsruhe Institute of Technology, Hermann-von-Helmholtz Platz 1, 76344 Eggenstein-Leopoldshafen, Germany
e-mail: kuznetsov@kit.edu

V. Alekseev • I. Matsukov
Kurchatov Institute, Kurchatov sq.1, 123182 Moscow, Russia

G. Ben-Dor et al. (eds.), *30th International Symposium on Shock Waves 1*, DOI 10.1007/978-3-319-46213-4_83

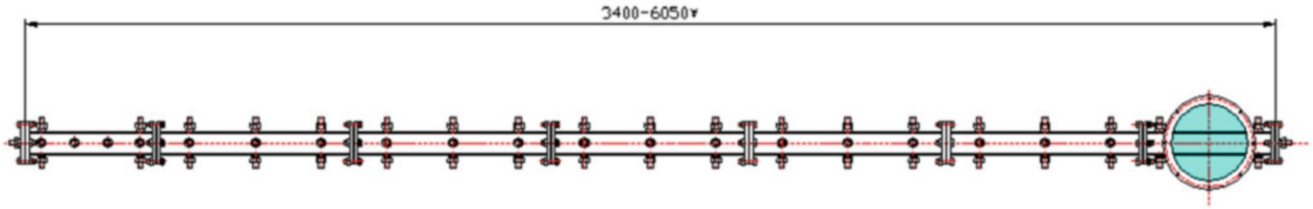

Fig. 1 Scheme of experimental facility

Table 1 Combustion characteristics of test mixtures

Initial pressure	Adiabatic combustion pressure	Expansion ratio	Sonic velocity in products	Laminar burning velocity	Laminar flame thickness	Chapman–Jouguet velocity	Chapman–Jouguet pressure	Detonation cell size
p, bar	P_{aicc}, bar	σ	c_p, m/s	S_L, m/s	δ_T, mm	D_{CJ}, m/s	P_{CJ}, bar	λ, mm
0.1	0.92	7.93	1331	5.8	3.42	2717	1.8	17.8
0.2	1.88	8.10	1347	6.8	1.56	2755	3.7	8.52

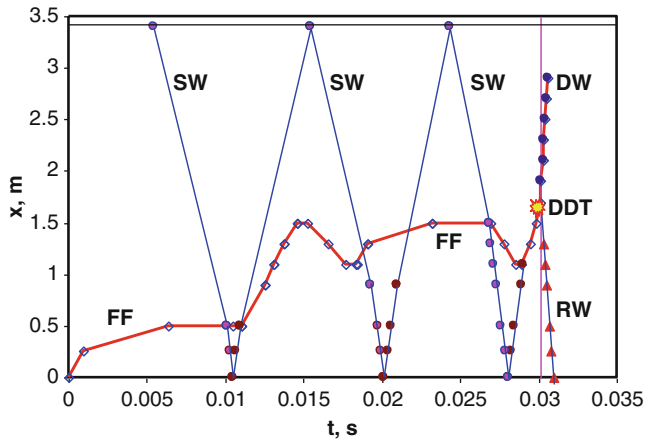

Fig. 2 *X–t* diagram of DDT process in a short tube: FF is the flame front (*red line*); SW is shock wave (*blue lines*); DW is detonation wave (*red line*); RW is retonation wave (*blue line*)

Experimental Results and Discussion

A series of experiments have been carried out in stainless steel detonation tube of 3.5–6 m long with rectangular cross section of 50 × 50 mm. Flame acceleration (FA) mechanism and triggering from subsonic to sonic flame with following detonation onset were investigated using light sensors and a high-speed camera combined with an optical Schlieren system. An optical access (l = 30 cm) to the combustion process was provided by optical section with two transparent quartz windows. The section has a variable position along the tube to capture images of the combustion process at different stages, from an ignition to steady-state detonation propagation (Fig. 1). Detailed description of the experimental facility is given in our previous paper [7].

Stoichiometric hydrogen–oxygen mixtures at pressures 100 and 200 mbar have been used as test mixtures to provide so-called short tube conditions. Table 1 gives main combustion properties of test mixtures.

Figure 2 shows a typical distance–time diagram for flame acceleration and DDT processes in a short tube. Initially, the flame accelerates as a "finger" flame pushing a precursor shock ahead the flame. It accelerates exponentially only due to enhanced side surface of "finger" flame, as written by Liberman et al. [8]. In relatively short tube, the detonation occurs after multiple shock wave reverberations because the pressure and the temperature of unburned material will reach the conditions for the flame to be accelerated fast enough for DDT. For instance, in comparison with an initial state, the pressure grows in six times, the temperature in two times, and the laminar flame speed in six times after five reflections (Fig. 3). The pressure and temperature of unreacted gas were calculated from shock wave velocity obtained by high-speed movie.

This means that shock–flame interaction and adiabatic compression of unreacted material play very important role for detonation preconditioning and DDT process in short tubes. A boundary layer and a turbulence may play not so significant role for DDT in relatively short smooth tubes filled with highly reactive mixtures.

As one can see in Fig. 4, an interaction of flame front initially propagating with a velocity v_0 = 30 m/s with reflected shock at velocity v_s = 550 m/s occurred in Frame #1. Then the flame moves backward after the interaction with shock wave in Frames #2–#3. Such a shock interaction with a density gradient across the flame surface leads to dramatic flame area increase due to the Richtmyer–Meshkov instability. As a result of Richtmyer–Meshkov instability, the combustion velocity suddenly increases in ten times to 300–400 m/s. It significantly reduces the run-up distance to

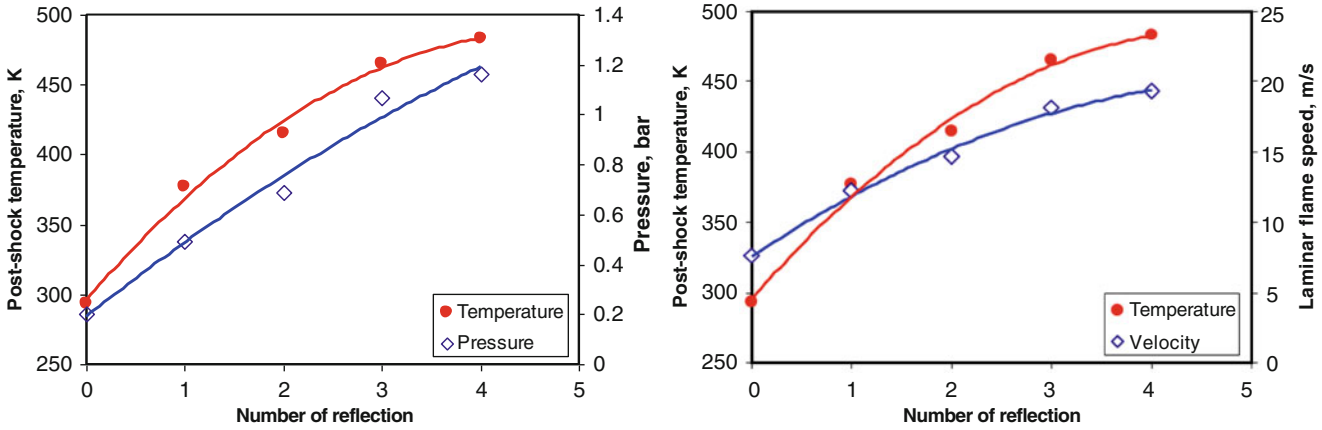

Fig. 3 Actual post-shock pressure, temperature, and combustion velocity of unreacted material due to multiple reflections (initial pressure 200 mbar)

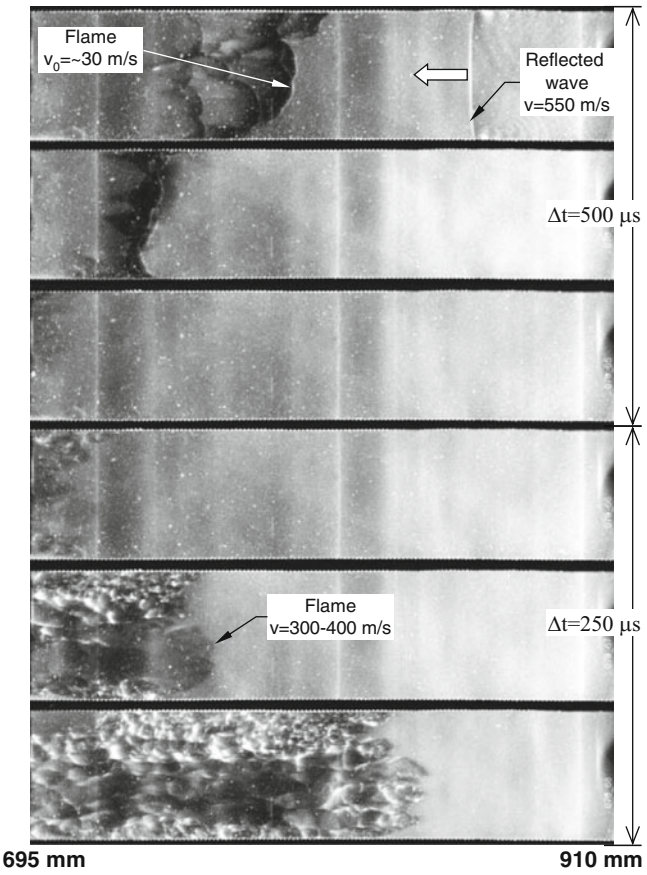

Fig. 4 Shadow photographs of shock–flame interaction process (p_o = 0.2 bar, 680–910 mm)

DDT. For instance, rough evaluation of run-up distance for initial pressure of 100 and 200 mbar based on the effect of boundary layer on DDT [6] gives the values of 4.8 m and 10.7 m, respectively. As it follows from *x*–*t* diagram (Fig. 2), the run-up distance to DDT in a short tube reduces to 1.7–2.5 m (3–4 times shorter).

1D Numerical Simulation

A series of 1D numerical simulations of hydrogen–oxygen mixture at subatmospheric pressures in a tube 12.5 m long was done to model gas dynamic effects in a short tube on DDT. In order to simplify the program and to make it more quick and flexible, the program was based on the following assumptions [9]:

- Solution of the reactive Euler equations, i.e., neglect of molecular transportation processes such as diffusion, thermal conduction, and viscosity
- No turbulence
- 1D geometry, i.e., neglect of real tube geometry (variable cross section) and radial gradients of concentrations, pressure, temperature, and velocity
- Global dominant reaction for the H_2/O_2 combustion
- Prescribed flame acceleration law
- Temperature-dependent thermodynamic data for all components (H_2, O_2, H_2O, N_2)
- First-order solution procedure, numerical cell size is 1–2 mm
- Adiabatic assumption (no heat losses of gas to tube wall)
- Reflecting boundary conditions at the tube ends

In particular the last assumption leads to conservative results during the pressure computation. Simulation of flame propagation was based on flame position tracking taking into account real exponential flame acceleration law in a smooth channel as a "finger flame":

$$u(t) = u_0 \exp(k \cdot t) \tag{1}$$

where $k = \sigma \cdot S_L/R$ is the exponential factor depending on the expansion ratio of unburned and burned components

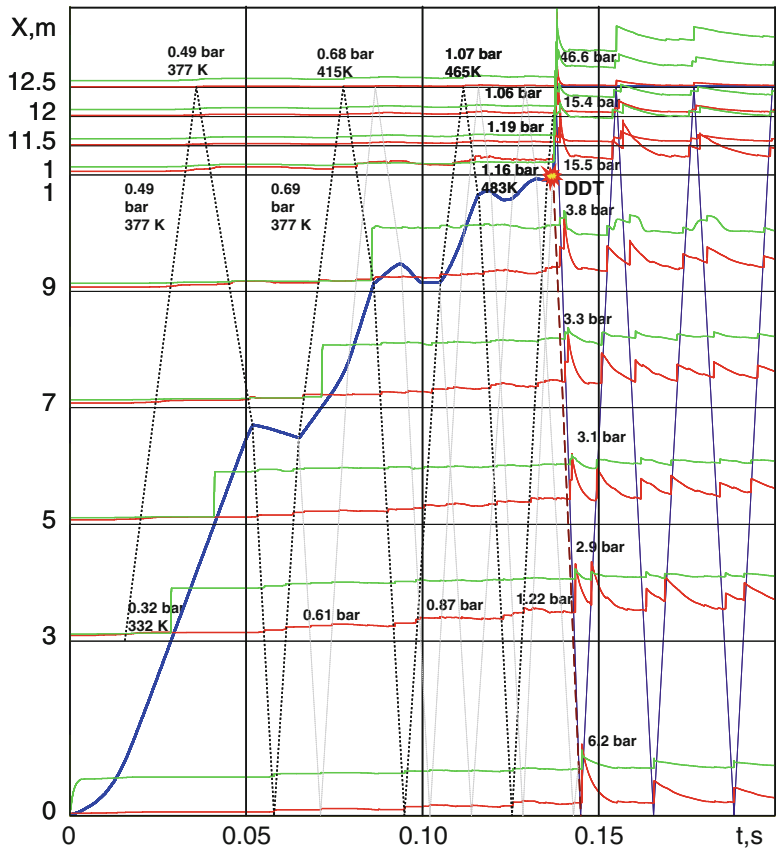

Fig. 5 Distance–time (x–t) diagram for combustion process in 1D simulation ($p_o = 0.2$ bar, $2H_2$:O_2:4.5 N_2, $x_D = 11$ m, marked as *star*): flame front (*blue line*); shock wave (*dotted black lines*); pressure signal (*red line*); light signal (*green line*). Local pressures are labeled

$\sigma = \rho_u/\rho_b$ and a tube radius R; $u_0 = S_L$ is the effective initial flame speed. So that with a smaller tube size R and a higher mixture reactivity defined as $\sigma \cdot S_L$, the flame accelerates faster. To approach the results of numerical simulations to real scenario, the parameters R, σ, and u_0 should be implemented into the code in advance.

For general description of the deflagration, three main parameters are necessary: the initial flame speed u_0, the flame acceleration distance x_a which is a function of Eq. 1, and the maximum flame speed S_{max} which is of the order of speed of sound in reactants. At the given DDT point x_D, the flame speed is increased suddenly to the speed of sound in the burned gas c_p, which can be determined from thermodynamic calculations (Table 1). This value of the flame speed corresponds to the CJ detonation. The run-up distance x_D should be given to satisfy the "short tube" conditions.

The tube was virtually equipped with pressure and light sensors to register pressure signals and a flame position. Temperature profiles were used as light signals assuming that the flame radiation is proportional to the temperature. Stoichiometric hydrogen–oxygen mixture at normal temperature and subatmospheric pressure of 200 mbar was used as a test mixture. To a more efficient approach to the "short tube" conditions, stoichiometric hydrogen–oxygen was additionally diluted with nitrogen to the ratio $2H_2$:O_2:4.5 N_2.

Calculated dynamics of the flame and shock waves during the combustion process is shown in Fig. 5 together with pressure and light signals. The flame initially exponentially accelerates producing a precursor shock wave with a strength of 0.5 bar (377 K). Then it reflects pushing flame backward after the collision. After reflection from ignition end, the shock is getting stronger (0.7 bar, 415 K) and it turns the flame again forward. Such interaction repeats one more time leading to final pre-detonation pressure 1.16 bar and temperature 483 K. Then the detonation occurs with a CJ detonation pressure 15.5 bar which is five times higher than for a long tube. Finally the detonation pressure reaches the value of 47 bar after reflection which is unexpected for initial pressure of 0.2 bar and might be very dangerous from practical point of view. The run-up distance of 11 m in short tube is roughly three times shorter than 30 m evaluated for a long tube according to paper [6].

Figure 6 shows calculated pressure and temperature record at a distance of 11 m from ignition point. It is shown that in case of multiple reflections of precursor shock wave, the post-shock temperature may reach 500 K. The strength of precursor shock in terms of overpressure may increase seven times in comparison with incident precursor shock wave. These simulations demonstrate that even a limited space and a reduced pressure may lead to very strong hydrogen

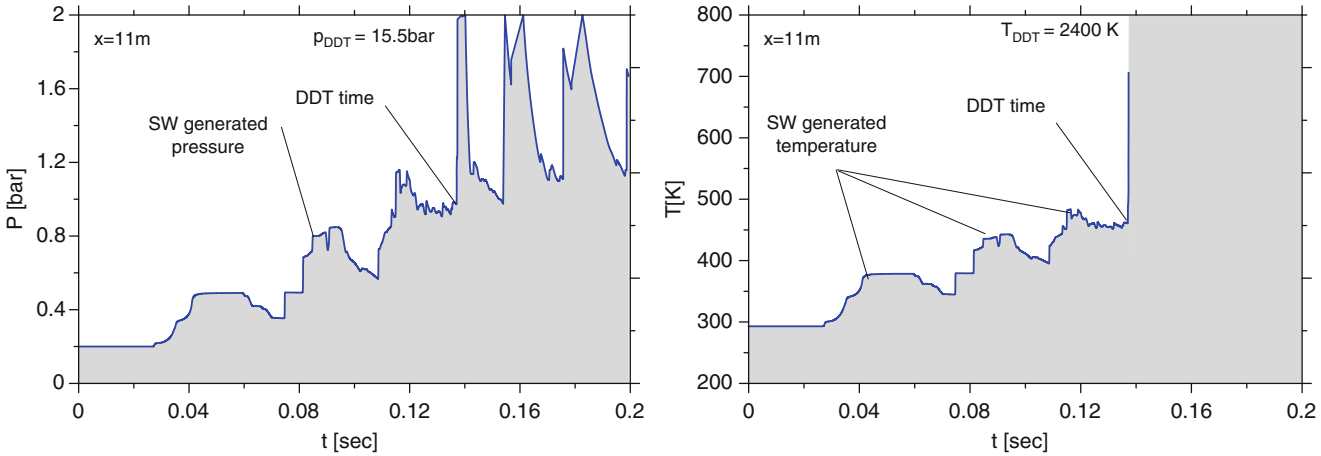

Fig. 6 Pressure and temperature records at 11 m from ignition ($p_0 = 0.2$ bar, $2H_2$:O_2:4.5 N_2)

explosion with a maximum pressure of 100 times higher than initial subatmospheric pressure. The probability of detonation is also increased due to the reduced run-up distance. Of course, the 1D numerical model is not able to simulate the Richtmyer–Meshkov instability and effect of turbulence on flame acceleration and DDT, but even gas dynamics demonstrates strong effect of adiabatic pre-compression on flame behavior and detonation preconditioning.

Conclusions

Experimental data and numerical simulations on flame acceleration, shock–flame interaction, and deflagration-to-detonation transition mechanism for stoichiometric hydrogen–oxygen mixtures in relatively short tubes have been analyzed. It was shown that detonation occurs as a result of multiple reflections of precursor shock wave and its interaction with flame. Adiabatic compression and heating of unreacted gas a front of the flame together with flame surface increase due to Richtmyer–Meshkov instability provide preconditioning of the DDT process. Several times higher pressure, temperature, and reaction rate within a preconditioning zone lead to significant decrease of run-up distance to DDT in relatively short tubes. Results of the work will provide detailed information on mutual shock–flame interactions leading to the DDT process and for numerical code validations.

References

1. Dorofeev, S.B., Sidorov, V.P., Kuznetsov, M.S., Matsukov, I.D., Alekseev, V.I.: Effect of scale on the onset of detonations. Shock Waves **10**, 137–149 (2000)
2. Dorofeev S.B., Kuznetsov M.S., Alekseev V.I., Efimenko A.A., Breitung W.: Evaluation of limits for effective flame acceleration in hydrogen mixtures. J. Loss Prev. Proc. Ind. **14/6**, 583–589 (2001)
3. Veser, A., Breitung, W., Dorofeev, S.B.: Run-up distances to supersonic flames in obstacle-laden tubes. J. Phys. IV France **12**(7), 333–340 (2002)
4. Schelkin, K.I., Sokolik, A.S.: The effect of chemical presentation on the initiation of the detonation wave. Soviet. Zhurn. Phys. Chem. **10**, 479–485 (1937)
5. Bollinger, L.E., Fong, M.C., Edse, R.: Experimental measurements and theoretical analysis of detonation induction distance. Am. Rocket Soc. J. **31**, 588–596 (1961)
6. Kuznetsov, M., Alekseev, V., Matsukov, I., Dorofeev, S.: DDT in a smooth tube filled with hydrogen–oxygen mixtures. Shock Waves **14** (3), 205–215 (2005)
7. Kuznetsov, M., Liberman, M., Matsukov, I.: Experimental study of the preheat zone formation and deflagration to detonation transition. Comb. Sci. Tech. **182**(11), 1628–1644 (2010)
8. Liberman, M.A., Kuznetsov, M., Ivanov, A., Matsukov, I.: Formation of the preheated zone ahead of a propagating flame and the mechanism underlying the deflagration-to-detonation transition. Phys. Lett. A **373**, 501–510 (2009)
9. Kuznetsov, M., Lelyakin, A., Breitung, W.: Numerical simulation of radiolysis gas detonations in a BWR exhaust pipe and mechanical response of the piping to the detonation pressure loads. In: Angermann, L. (ed.) Numerical Simulations - Examples and Applications in Computational Fluid Dynamics, p. 440. InTech, Rijeka, Croatia (2010)

Propagation of a Pressure-Dependent Detonation with Different Acoustic Impedance Confinements

Jianling Li, Xiaocheng Mi, and Andrew J. Higgins

Introduction

The study of how detonation waves respond to losses is the primary experimental and theoretical means of understanding detonation dynamics. Specifically, for condensed explosives, quantifying the relationship between the diameter of a cylindrical charge with yielding confinement, propagation velocity, and front curvature is the principal technique used to develop models for detonation propagation for a given explosive. The previous studies [1, 2] have showed that the confining material can also influence the velocity deficit. Campbell et al. [1] pointed out experiments in which fully developed detonations in one confining material can quench when subjected to a different confining material. However, the current popular theoretical analysis methods for nonideal detonation in condensed explosives [3, 4] only consider detonation dynamics under no confinement or weak confinement conditions.

Hence, this chapter focuses on the effect of the acoustic impedance of confinements on the propagation of a pressure-dependent detonation with losses in charges. A series of numerical simulations was performed with different values of impedance confinement (greater than, less than, and equal to that of the explosive) both for two-dimensional slabs and axisymmetric geometries, and different values of the reaction rate pressure exponent ($n = 2$ and 3) was also tested.

J. Li (✉)
School of Power and Energy, Northwestern Polytechnical University, Xi'an 710072, Shaanxi, China
e-mail: lijianling@mail.nwpu.edu.cn

X. Mi • A.J. Higgins
Department of Mechanical Engineering, McGill University, Montréal, H3A 2K6 Quebec, Canada

Problem Descriptions and Numerical Technique

The problem examined is detonation propagation in a charge of explosive bounded by inert, yielding confinement, as shown schematically in Fig. 1.

The detonation was initialized as a one-dimensional ZND-type wave propagating at the ideal CJ detonation velocity and was then allowed to propagate into a layer of finite thickness (in two-dimensional simulations) or a cylinder of finite diameter (in axisymmetric simulations) bounded by an inert medium. The yielding confinement of the inert layer resulted in the detonation wave decaying to a sub-CJ steady-state velocity or failing entirely. For simplicity, an ideal gas equation of state was used with a pressure-dependent reaction rate that resulted in a stable detonation wave structure.

Simulations were performed with different values of the reaction rate pressure exponent ($n = 2$ and 3) and different values of impedance confinement (greater than, less than, and equal to that of the explosive). The impedance of the confinement was varied by inversely changing the temperature and density of the confinement while maintaining the pressure as constant. Currently, the density of the confinement was varied from 0.5 to 10 times of the initial density of explosive.

The governing unsteady, two-dimensional in-viscid Euler equations with the pressure-dependent reaction rate source term described above in Cartesian coordinates and cylindrical coordinates were solved on a uniform computational grid for two-dimensional and axisymmetric geometries, respectively. The computations were performed in the lab-fixed reference frame, with the computational domain reinitialized at finite intervals to always contain the leading shock front and downstream limiting characteristic within the domain. Generally, the chemical reactions have much shorter time scales than those associated with the flow, resulting in stiffness due to coupling the fluid dynamics and the chemical

G. Ben-Dor et al. (eds.), *30th International Symposium on Shock Waves 1*, DOI 10.1007/978-3-319-46213-4_84

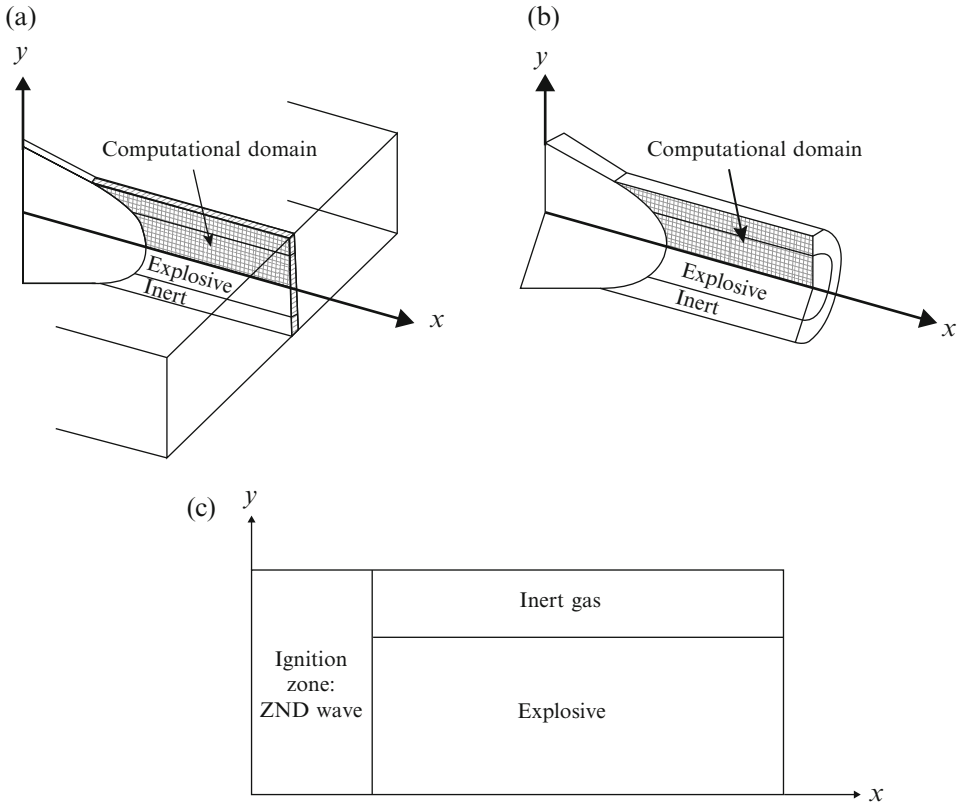

Fig. 1 Schematic representation of the problem to be studied showing the computational grid for (**a**) two-dimensional slab and (**b**) axisymmetric geometries and (**c**) the initial conditions

kinetics. In order to isolate this stiff source term, a second-order accurate Strang operator splitting method [5] is employed. The Euler equations with a reactive source term is thus split into a homogeneous partial differential equation for the fluid dynamics and an ordinary differential equation for the chemical reaction. The AUSM+ Scheme [6] is used to deal with the inviscid flux as a sum of the convective and pressure terms due to recognizing the convection and acoustic waves as two physically distinct processes. A third-order TVD Runge–Kutta method [7] is used for the temporal discretization. The boundary condition along the x-axis was a mirror boundary condition (axis of symmetry), so that only the upper half of the layer is simulated in the case of a two-dimensional slab an axisymmetric cylinder. The upper boundary of the computational domain (above the inert layer) was a supersonic outflow condition to ensure that no reflected waves return into the computational domain.

Results and Discussions

For the case of the confinement with acoustic impedance equal to the explosive, the structure of steady detonation wave obtained in two-dimensional (planar) numerical simulations with pressure exponent $n = 2$ is shown in Fig. 2a. The reaction is only about only half complete at the location of the sonic plane, which is a significant contribution to the large velocity deficit. The velocity deficit is not predominately attributed to momentum losses. It is due to incomplete reaction at the sonic plane. The result differs from that of detonation governed by Arrhenius reaction rates with divergence flow. The reaction zone is very smooth. It also means that ideal, stable detonation was realized by using a pressure-dependent reaction rate. This structure obtained is in good qualitative agreement with the reaction zone proposed by Bdzil [8], and similar to simulation results by Sharpe and Braithwaite [9]. For the case of the confinement with acoustic impedance smaller than the explosive, a similar structure of steady detonation wave was obtained with a larger shock front curvature, as shown in shown in Fig. 2d. Figures 2b, c plots the structure of steady detonation waves obtained in two-dimensional (planar) numerical simulations with pressure exponent $n = 2$ for the cases of confinement with density 5 times and 10 times the explosive. The structures of steady detonation waves obtained in two-dimensional (planar) numerical simulations demonstrated that for the case of high impedance confinement, the sonic surface is no longer attached to the shock front at the point where the shock impinges upon the confinement, and the outward expansion of the products in the reaction zone is significantly reduced.

The variation of the detonation velocity with the shock front curvature k ($k = 1/Rc$, where Rc is the radius of

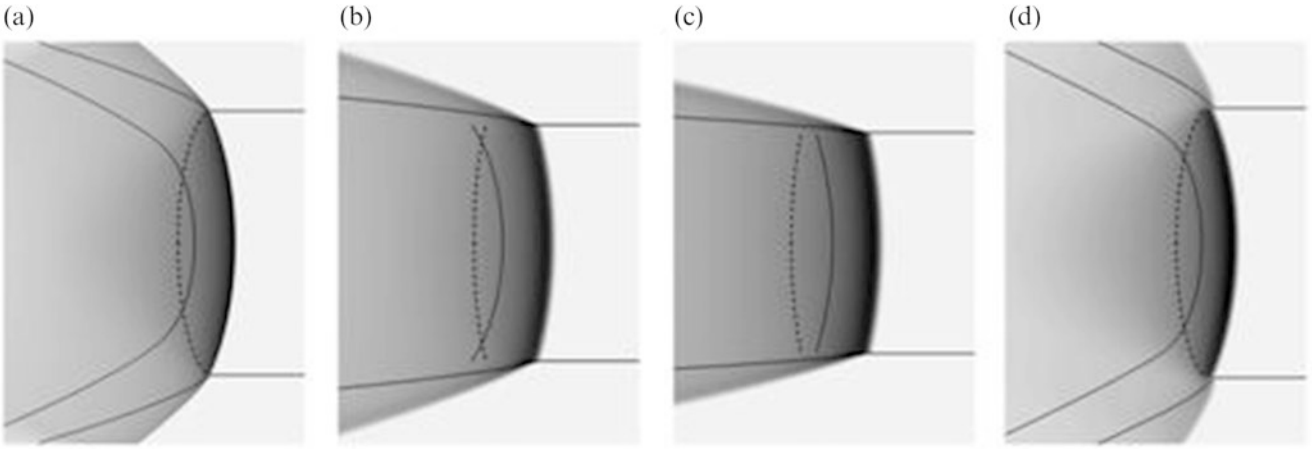

Fig. 2 The structure of steady detonation waves obtained in two-dimensional (planar) numerical simulations with pressure exponent $n = 2$ for the cases of (**a**) confinement with density equal to explosive, (**b**) confinement with density five times the explosive, (**c**) confinement with density ten times the explosive, and (**d**) confinement with density half that of the explosive

curvature) for the cases of different acoustic impedance confinements with pressure exponent $n = 2$ is plotted in Fig. 3. The a-axis is non-dimensionalized by the half-reaction thickness of the ideal CJ detonation ($L_{1/2}$), and the y-axis is normalized by the ideal CJ velocity. The results showed that the detonation velocity is decreased with the increase of the curvature. With different values of impedance confinement, all the measured shock front curvature and detonation velocity relation agrees with the classic model of Wood and Kirkwood [10].

In Fig. 4, the propagation velocity of the detonation with the density of inert bounding gas equal to (a) ρ_0, (b) $5\rho_0$, (c) $10\rho_0$, and (d) $0.5\rho_0$ is plotted for pressure exponent $n = 2$, respectively, as obtained after the wave had propagated a distance sufficient to result in a steady wave velocity. The velocity is plotted as a function of the inverse of the diameter ($L_{1/2}/d$) or twice the thickness of the explosive layer ($L_{1/2}/2\ t$). The a-axis is nondimensionalized by the half-reaction thickness of the ideal CJ detonation, and the y-axis is normalized by the ideal CJ velocity. The wave velocity is plotted in this fashion, following the convention of the condensed phase detonation literature, so that extrapolation to the y-axis should yield the ideal CJ velocity. By quantitative comparison, the results showed the ability of higher impedance confinement to enable the detonation wave to propagate at greater velocity for the same charge thickness.

Additionally, the computational simulations were compared to a simple, analytic model that treated the interaction of the confinement with the detonation products via Newtonian theory [4] and a model that assumed a continuous variation in shock front curvature with the shock angle at the interface with the confinement matching the angle determined by shock polar analysis [11]. As shown in Fig. 4, the Newtonian model works well for the case of high impedance confinement, while the shock front curvature model agrees with the simulations for the case of low impedance.

Conclusions

For the propagation of a pressure-dependent detonation in homogeneous explosive media, the following conclusions can be drawn:

1. The confinement has a strong influence on the structures of steady detonation waves. With the confinement of equal impedance of explosive and low impedance confinement, the sonic surface has a lens-like shape attaching to the shock/confinement point; while for the case of high impedance confinement, the sonic surface is no longer attached to the shock front at the point where the shock impinges upon the confinement, and the outward expansion of the products in the reaction zone is significantly reduced. Higher impedance confinement enhances the propagation of detonation wave at greater velocity for the same charge thickness.
2. With different values of impedance confinement and pressure exponent, all the measured shock front curvature and detonation velocity relation agrees with the classic model of Wood and Kirkwood.
3. For different values of acoustic impedance confinement, the feasibility of different theoretical models should be carefully validated. The Newtonian model works well for the case of high impedance confinement, while the shock front curvature model agrees with the simulations for the case of low impedance.

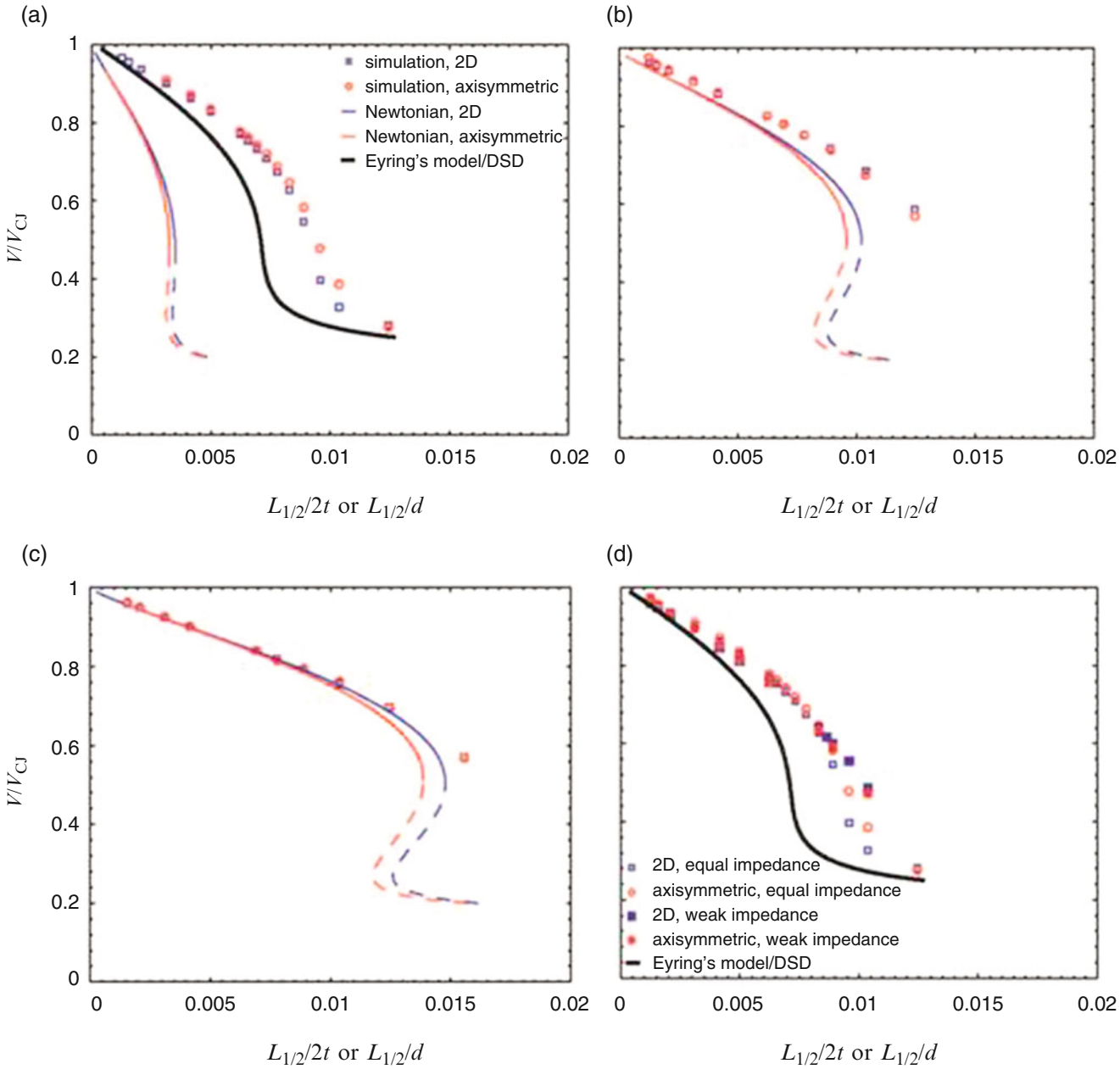

Fig. 3 Detonation velocity as a function of the inverse charge diameter or thickness

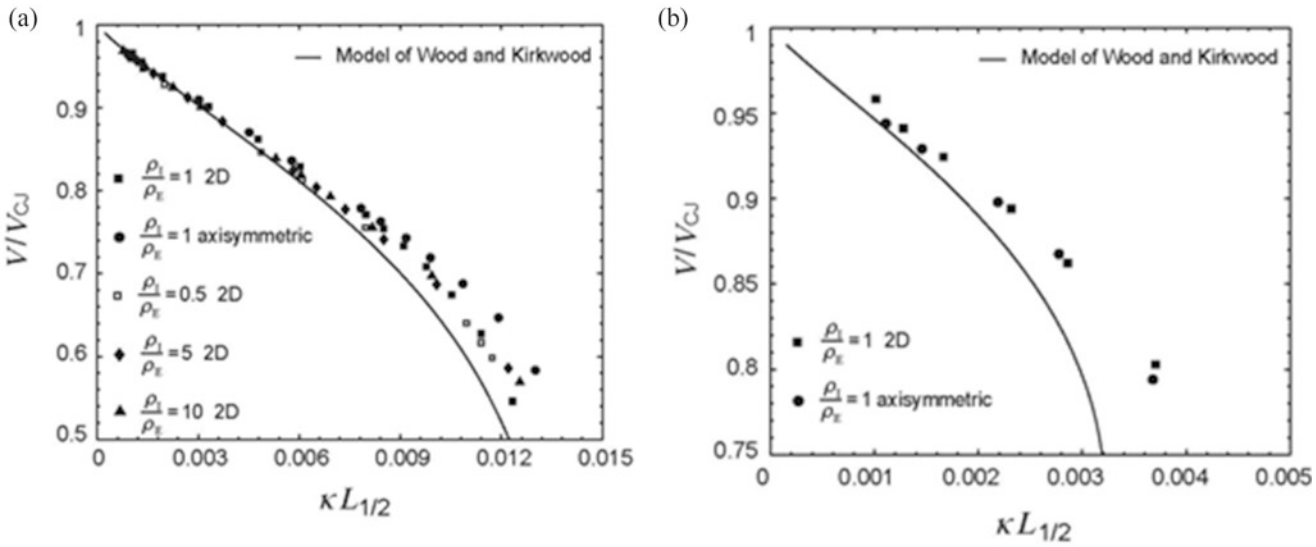

Fig. 4 The variation of the detonation velocity with the shock front curvature for $n = 2$

Acknowledgments This work was supported by the National Natural Science Foundation of China (No. 11572258, No. 91441201) and Science Challenging Program (No. JCKY2016212A501).

References

1. Campell, A., Malin, M., Holland, T.: Detonation in homogeneous explosives. In: 2nd ONR Symposium on Detonation (1955).
2. Higgins, A.: Discrete effects in energetic materials. J. Phys.: Conf. Ser. **500**(5), 052016 (2014)
3. Bdzil, J., Stewart, D.: Modeling two-dimensional detonations with detonation shock dynamics. J. Fluid Mech. **108**, 195–226 (1981)
4. Tsuge, S., Furukawa, H., Matsukawa, M., Nakagawa, T.: On the dual property and the limit of hydrogen-oxygen free detonation waves. Astronaut. Acta. **15**(5), 377–386 (1970)
5. Strang, G.: On the construction and comparison of difference schemes. SIAM J. Numer. Anal. **5**(3), 506–517 (1968)
6. Liou, M., Steffen, C.: A new flux splitting scheme. J. Comput. Phys. **107**(1), 23–39 (1993)
7. Shu, C., Osher, S.: Efficient implementation of essentially non-oscillatory shock-capturing schemes. J. Comput. Phys. **77**(2), 439–471 (1988)
8. Bdzil, J., Aslam, T., Catanach, R., Hill, L., Short, M.: DSD front models: nonideal explosive detonation in ANFO. In: 11th International Symposium on Detonation (2002).
9. Sharpe, G., Braithwaite, M.: Steady non-ideal detonations in cylindrical sticks of explosives. J. Eng. Math. **53**, 39–58 (2005)
10. Wood, W., Kirkwood, J.: Diameter effect in condensed explosives. The relation between velocity and radius of curvature of the detonation wave. J. Chem. Phys. **22**(11), 1920–1924 (1954)
11. Eyring, H., Powell, R., Duffy, G., Parlin, R.: The stability of detonation. Chem. Rev. **45**(1), 69–181 (1949)

Kerosene Ignition and Combustion: An Experimental Study

Alexander Burcat, Erna Olchansky, Ulla Steil, and Marina Braun-Unkhoff

Introduction

Kerosene, the main fuel for all aircrafts, civil and military, is a complex fuel containing hundreds of individual chemicals. Furthermore, their concentrations and identity change, not only according to the source of the fuel but also according to the refinery where the fuel was distilled. However, in order to cope with the demands of international civil and military aviation, kerosene is the only fuel produced under very strict physical standards defined as Jet-A, Jet-A1, JP-4, JP-5, etc. (American military). The chemical composition is not a part of these standards. The physical standards take care of the transport and flow of the jet fuel in the jet aircraft, but the combustion is a function of the fuel's chemical components.

During four decades, small hydrocarbons and small aromatics were investigated and modeled [1–7]; by comparing the model prediction to the experimental evidence, much was learned about the kinetics of combustion of these fuels.

In the last decade, long-chained fuels such as *n*-decane [8–14] and even hexadecane [15] were investigated. An excellent review of the combustion of the ingredients of kerosene was written by Battin-Leclerc [16].

The lessons learned were that normal hydrocarbons as well as the branched ones behave almost the same for ignition delay times τ regardless of the number of carbon atoms in the molecule if analyzed according to an empiric formula such as Lifshitz formula [17]:

$$\tau/\,\mathrm{s} \;=\; \beta\exp(+\mathrm{E}/\mathrm{RT})\;[\mathrm{C_{12}H_{23}}]^{a}[\mathrm{O_2}]^{b}[\mathrm{Ar}]^{c} \qquad (1)$$

The values of a are ~ 0.5, the values of b are -1.05 to -1.35, and the value of c, the diluent, is practically zero. Beta is a pre-exponent equivalent to 1/A in the Arrhenius formula. The species concentrations are given in mol percent, T in K, R in calories $\mathrm{mol}^{-1}\,\mathrm{K}^{-1}$, and E in calories mol^{-1}.

The detailed modeling of the combustion of kerosene is a challenging task, as it may contribute in solving problems of combustion control, reducing emission of pollutants such as NOx, PAH, soot, and fuel consumption. A validated reaction mechanism is also needed in order to elaborate a reduced reaction mechanism to enable 3D-CFD calculations [13, 14, 26].

The idea of *surrogate fuel* was introduced where a limited and restricted number of compounds were supposed to represent kerosene with its numerous different species [18]; however, there are up to date nearly as many proposals of surrogate fuels as there are groups dealing with combustion modeling [19–22].

The goal of the present work was to provide a database for autoignition of kerosene mixtures, over a wide range of parameters. The experiments reported on in the present paper result from a cooperation between the two institutes involved (Technion Haifa and DLR Stuttgart). Within this collaboration, a few hundred experiments were performed in Stuttgart and in Haifa using in both places two different kerosene: one from Haifa and the second from Stuttgart airport. The experimental results, together with regression analysis, are shown in the present paper, allowing prediction of ignition delay times at other conditions. In addition, ignition delay times were simulated by the use of detailed reaction models, for *n*-decane [8] and the surrogate mixture (70 % *n*-decane, 30 % propylbenzene) [20, 23].

A. Burcat (✉) • E. Olchansky
Faculty of Aerospace Engineering, Technion - Israel Institute of Technology, Haifa 32000, Israel
e-mail: aer0201@technion.ac.il

U. Steil • M. Braun-Unkhoff
German Aerospace Center (DLR), Institut für Verbrennungstechnik, 70569 Stuttgart, Germany

G. Ben-Dor et al. (eds.), *30th International Symposium on Shock Waves 1*, DOI 10.1007/978-3-319-46213-4_85

Experimental

Two different shock tube devices were used for measuring the ignition delay time data, behind reflected shock waves. The experiments covered a temperature range of 1200–1800 K at pressures between 2.4 and 6 bar. The reflected shock temperature T_5 in both shock tubes was calculated from the measured incident shock wave speed using standard conservation equations and the ideal gas equation of state assuming frozen chemistry. Thermodynamic data for all the species were taken from [24]. The temperature uncertainty error was about ±20 K.

The Jet-A1 aviation fuels investigated were provided from the Haifa refineries and nicknamed Haifa kerosene (H) and the other from the Stuttgart airport local stock and nicknamed Stuttgart kerosene (St). In total, 32 mixtures were used and 377 individual experiments were carried out.

Single-Pulse Shock Tube at Haifa

Ignition delay time experiments were performed behind reflected shock waves in a heated single-pulse shock tube. This instrument was described in another paper [8].

Oxygen and argon of pure quality 98 % were purchased from Oxygen Store, Haifa, for the Technion experiments. The gases were used without further purification. A 10 L heated glass bulb was used to store the mixtures. The liquid fuel was injected with a calibrated syringe into the evacuated container, and the amounts were calculated to evaporate on injection and not to exceed the expected dew point. On top of the kerosene, oxygen and then argon were added. The mixtures, left for about 24 h to mix, served as stock for the individual experiments. No adsorption of kerosene on the shock tube walls was detected, and no soot was detected in rich mixture experiments.

The Stuttgart Shock Tube

The experiments were performed in a thick-walled, stainless steel shock tube behind reflected shock waves. Driver and driven sections have a length of 2.5 m and 4.85 m, respectively. The internal diameter of the shock tube which had no dump tank is 46 mm. Aluminum sheets of different gauges served as diaphragms. For details, see [25, 31].

The shock tube was heated to a temperature level of 130 °C, for taking into account the high boiling points of kerosene. All mixtures were prepared in a stainless steel tank of about 64 l volume which was maintained at a temperature of 200 °C. The fuels were mixed in the tank with respective amounts of oxygen (99.995 % purity, Linde) and diluted with highly purified argon (99.999 purity, Linde).

All mixtures exhibited a relatively strong propensity for wall adsorption. Therefore, in most experiments, the initial concentrations of the kerosene mixtures were examined by the use of gas chromatographic analysis of samples taken from the shock tube immediately before the experiment. The deviation between (GC) analyzed and filled initial kerosene concentration is found to be about ±5 %.

Results

The two kerosene types used were analyzed by GC mass spectrometer at DLR Stuttgart, and their chromatograms compared to a kerosene chromatogram [20]. The analysis shows that the Stuttgart kerosene contains about 50 % more *n*-decane than the Haifa kerosene, as well as considerably more *n*-nonane and undecane, but less longer non-branched hydrocarbons.

The oxidation of kerosene was investigated by measuring the ignition delay of the kerosene–oxygen–argon mixtures in the shock tubes described above. The end plate pressure traces were used to measure the ignition delay time in the Haifa experiments, and CH emission at $\lambda = 431$ nm taken 5 mm away from the end plate was used in the Stuttgart experiments.

Experimental Data Sets

Twenty individual mixtures of kerosene–oxygen compositions diluted with argon (ten of Haifa kerosene and ten of Stuttgart kerosene) were prepared in Haifa. In summary, 248 shocks were performed. Additional 12 mixtures of experiments, 9 with Stuttgart kerosene and 3 with Haifa kerosene, were performed at DLR Stuttgart resulting in 129 shocks. Hence, a total of 377 experiments were done in both locations. The Stuttgart experiments have a 5–10 higher dilution factor compared to the ones performed in Haifa.

All Stuttgart and Haifa kerosene experiments carried out at the shock tube device at Haifa are presented in Fig. 1 after a 5-parameter regression analysis of the 121 experiments with Haifa kerosene and 127 experiments with Stuttgart kerosene, performed separately for each kerosene. The least square was tested for 2σ (i.e., 95 % confidence limit) and had to satisfy the Lifshitz equation [17].

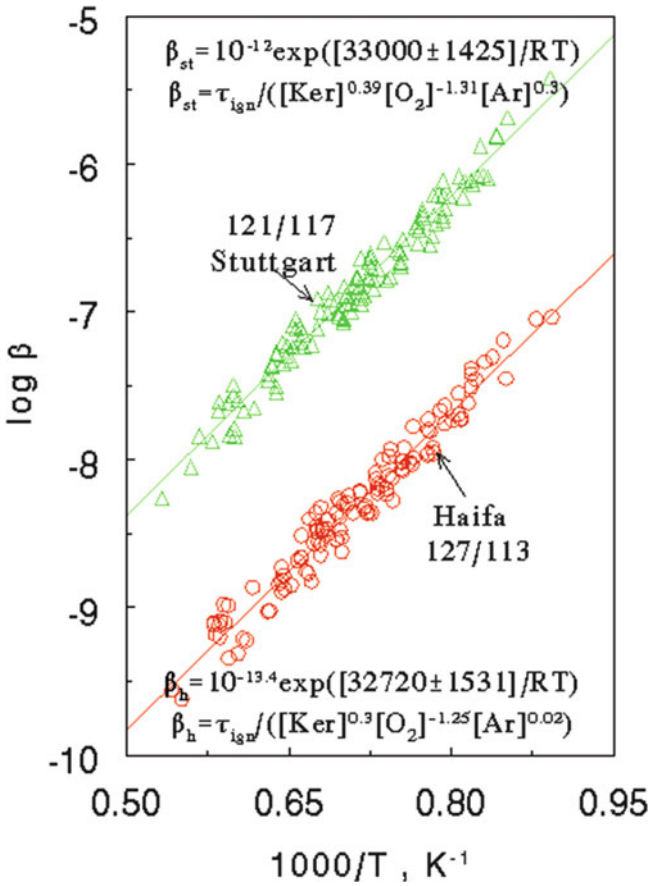

Fig. 1 Measured ignition delay times: five-term regression analysis with a 95 % confidence limit (2σ) of (i) all experiments of Stuttgart kerosene (*green triangle*; 117 out of total 121) and (ii) all experiments of Haifa kerosene (*red circles*; 113 out of total 127). Experiments performed in Haifa

From Fig. 1 it is obvious that the two kerosene from different places must have different chemical composition because they give different values showing that these are separate mixtures. The two equations found for the kerosene are:

$$\tau / s = 10^{-12}\exp[(+33000 \pm 1500)/\mathrm{RT}] \times [C_{12}H_{23}]^{0.39}[O_2]^{-1.31}[Ar]^{0.3} \text{for Stuttgart kerosene and}$$

$$\tau/s = 10^{-15.4}\exp[(+32720 \pm 1500/\mathrm{RT}) \times [C_{12}H_{23}]^{0.3}[O_2]^{-1.25} \times [Ar]^{0.02} \text{for Haifa kerosene.}$$

Comparison of Experimental Kerosene Data Sets with *n*-Decane Data Set

Since the two kerosene contained large quantities of *n*-decane, we have tried to include in the regression analysis the 181 experiments of *n*-decane ignition [8].

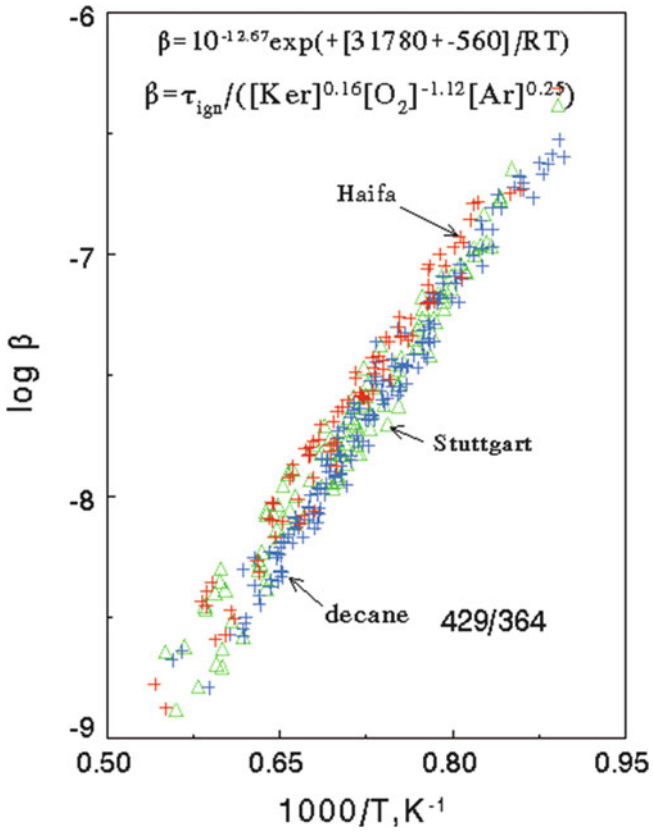

Fig. 2 Measured ignition delay times: five-term regression analysis with a 95 % confidence limit (2σ) of (i) Haifa kerosene (*red crosses*), (ii) Stuttgart kerosene (*green triangles*), and (iii) *n*-decane (*blue crosses*) taken from Olchanski and Burcat [8]. Experiments performed in Haifa

When the three groups of experiments—two kinds of kerosene and *n*-decane, all done in Haifa—are regressed together, as shown in Fig. 2, for 364 out of 429 experiments, the regression least square reads:

$$\tau/s = 10^{-12.67}\exp[(+31780 \pm 560)/\mathrm{RT}]\,[\mathrm{Fuel}]^{0.16}[O_2]^{-1.12}[Ar]^{0.25}.$$

This kerosene regression did not fit to the one obtained with pure *n*-decane which regressed alone to a value of:

$$\tau/\mathrm{s} = 10^{-12.1}\exp[(+32240 \pm 560)/\mathrm{RT}]\,[C_{10}H_{22}]^{0.60}[O_2]^{-1.30}[Ar]^{0.08}$$

and almost fit to the kerosene regression.

If the two kerosene run in Haifa are regressed together (without *n*-decane), i.e., 248 experiments, the regression equation reads:

$$\tau/s = 10^{-11.31}\exp[(+30780 \pm 1000)/\mathrm{RT}]\,[C_{12}H_{23}]^{0.49}[\mathrm{O2}]^{-1.28}[Ar]^{0.19}.$$

The same process shown above for the experiments performed in Haifa with the kerosene was repeated in Stuttgart when the concentrations in the Stuttgart shock tube were much lower.

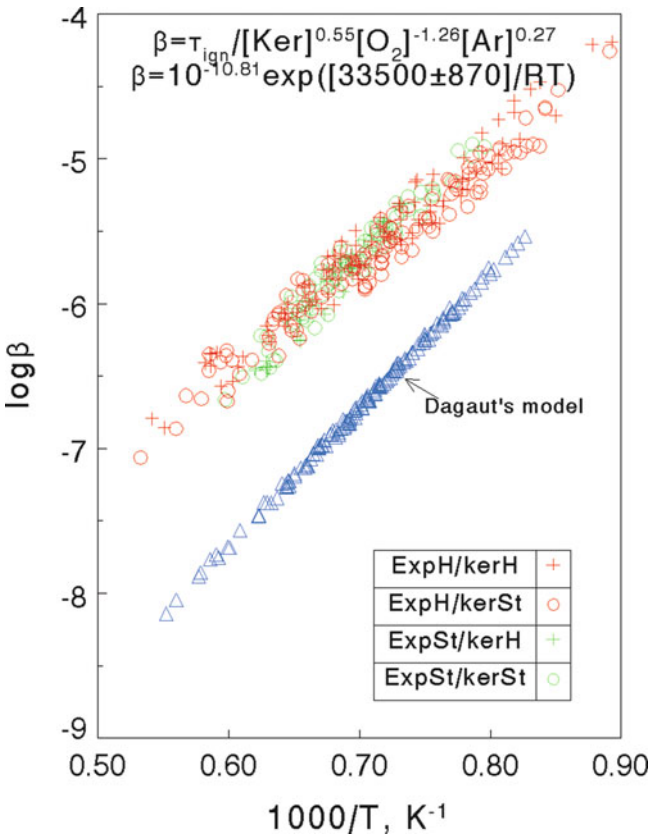

Fig. 3 Ignition delay times: five-term regression analysis with a 95 % confidence limit (2σ) of experiments performed in Haifa (*red*) and Stuttgart (*green*), with Haifa kerosene (+) *and* Stuttgart kerosene (o). Shown also is the surrogate fuel calculation (*blue*) assuming a mixture of 70 % *n*-decane and 30 % propylbenzene using the detailed reaction model from Dagaut [20, 23]

In Fig. 3, we show the five-term statistical regression of all the experiments performed in Haifa (red) and Stuttgart (green). Fifty experiments had to be discarded out of a total of 377 in order to get a 95 % confidence limit. Although the activation energy of the Stuttgart experiments is a little bit higher, the regression formula for the four sets of experiments shows excellent correlation as it reads:

$$\tau/\,s \;=\; 10^{-10.81}\exp[(+33500)/\mathrm{RT}]\;[\mathrm{C_{12}H_{23}}]^{0.55}[\mathrm{O_2}]^{-1.26}[\mathrm{Ar}]^{0.27}.$$

This finding is interpreted as a final proof that the two different kerosene from different countries investigated experimentally in two different shock tube devices with two different detection methods produce ignition delay times that are in agreement with each other as they can be represented by a single statistical correlation.

Simulation of Kerosene Combustion

Modeling Ignition Delay Time of Kerosene by Using a Surrogate Fuel

The way to simulate practical fuels such as kerosene is disputed for many years among the researchers. This dispute has introduced a new concept called *surrogate fuels*. Surrogate fuels are supposed to be a group of two or more known pure chemicals which—in a certain concentration combination—can simulate the real fuel combustion experiments, such as species profiles or autoignition or heat release.

The simulation of kerosene was traditionally done by comparing surrogate fuel calculation with experimental results of kerosene combustion. A very comprehensive review on different kerosene compositions and surrogate fuels was published by eleven groups of investigators representing leading world universities and research institutes [19].

If the experimental kerosene concentration should be represented by a surrogate fuel in order to enable a detailed modeling, the number of carbon atoms has to be matched and must be kept constant. The formula used in the present study for kerosene, namely $C_{12}H_{23}$, was the one proposed by NASA [27], checked and corrected at DLR [28]. The formula was used by other researchers, too [29]; however, different formulas are also existing, e.g., $C_{11}H_{23}$, used by Dagaut [30]. Other researchers [32] report inaccurate H/C ratios. It is clear that any formula used for kerosene is only a kind of indication and may have no strict meaning since the actual analysis may change from one kerosene batch to another.

However, the picture shown in the review [19] is very different from the evidence found in our research. From the measured GCs, we found that the randomly picked kerosene in Haifa and Stuttgart contains more than 90 % by volume of *n*-alkanes and *iso*-alkanes of C_9–C_{16}. The aromatic and cycloalkanes content is less than 10 %. A similar picture appears from the chromatogram published by Dagaut [20]. There, the concentrations show about 80 % aliphatic compounds and ~20 % aromatics and cycloalkanes.

Peters et al. [32] report that most surrogates proposed are based on decane as the main hydrocarbon while the minority uses dodecane as the main fuel. Among the surrogates that use decane, the minor aromatic component is either propylbenzene (mainly in Europe) or 1,2,4-trimethylbenzene.

Models Using Surrogate Fuel Mixtures Containing One and Two Components

It has been shown in Fig. 2 that the experiments of *n*-decane and of kerosene run in Haifa fit together very well, as all measured ignition delay time data can be represented by a single expression according to the Lifshitz equation [17]. Therefore, we started our modeling simulations concerning the autoignition of kerosene mixtures, with two reaction mechanisms, representing the two different surrogate fuels as (i) pure *n*-decane and (ii) a mixture of 70 % *n*-decane and 30 % propylbenzene.

Comparing the very dilute experiments performed at Stuttgart with a model that assumes the kerosene can be represented by 100 % *n*-decane, we get excellent agreement as shown in Fig. 4. However, the same is not obtained with kerosene ignition experiments performed in Haifa; these are less diluted and, consequently, have 5–10 times higher concentrations of reactants. In this case, the modeling of the individual ignition experiments applying the detailed reaction model for *n*-decane according to Olchanski and Burcat [8] (as opposed to the experiments of decane themselves shown in Fig. 2 where a perfect agreement of modeling results and experimental results at other conditions is given) results in ignition delay time data predicted lower than measured in the kerosene experiments. Therefore, it is concluded that at high dilution—such as those used in Stuttgart—the concentrations of the cycloparaffins and benzene-like compounds in each experiment obviously may be too low to exhibit any significant influence on the combustion kinetics, i.e., leading to ignition delay times of the modeling that do not differ substantially, for *n*-decane or kerosene as fuel.

This is also a reminder that modeling experimental data with a detailed reaction mechanism by assuming a surrogate is not the same thing as the experiments themselves.

Then, a mixture of 70 % *n*-decane and 30 % propylbenzene was used as a surrogate fuel (ii) for kerosene according the suggestion by Dagaut [20]. Using his detailed reaction model, which has been elaborated for describing the combustion of *n*-decane–propylbenzene mixtures by 1700 elementary reactions and 300 species [20, 23] for predicting kerosene ignition delay time for each of the individual experimental data, leads to a statistical fit that does not exhibit a good agreement with the statistical fit calculated for the experimental data (Fig. 3). The predicted values of the ignition delay time fall below the experimental determined kerosene data, and their activation energy is ~10 kcal mol^{-1} higher than was found experimentally.

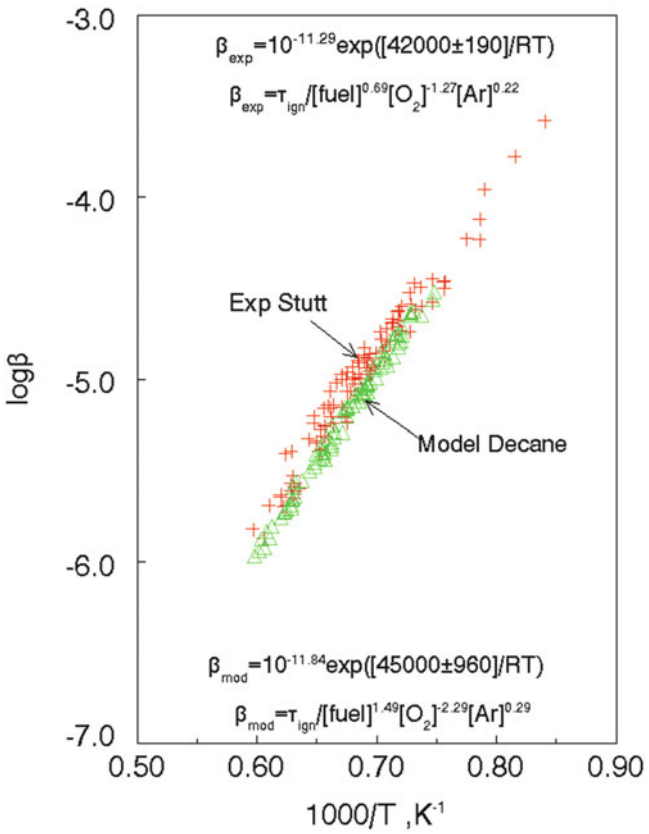

Fig. 4 Ignition delay times: five-term regression analysis with a 95 % confidence limit (2σ) of experiments performed in Stuttgart (*green*), with Haifa kerosene (+) and Stuttgart kerosene (o). Shown also is the simulation assuming pure *n*-decane as surrogate fuel using the detailed reaction model of Olchanski and Burcat [8]

Thus, the surrogate fuel (ii) suggested previously does not fit the experimental evidence of the present work. It should be mentioned that further experiments using mixtures of 70 % *n*-decane and 30 % propylbenzene as fuel were carried out in Stuttgart [31]. However, when fitting these experimental data together with those obtained for kerosene, the statistical program discards all the surrogate experiments from the combined kerosene and surrogate data.

For these reasons, it can be concluded that (i) the proposed 70 % *n*-decane—30 % propylbenzene mixture—is not a good choice for representing autoignition of kerosene, according to the findings of the present investigation, and, furthermore, that (ii) the concentration of benzene-like and cycloparaffins in the kerosene investigated is by far lower than 30 % and thus not so influential.

Finally, Vasu, Davidson, and Hanson (2008) have thoroughly investigated this problem [21] and found that this surrogate among many others is not a good choice. Peters et al. [32] concluded the same.

Conclusions

It is clear that the conditions performed in the present research, which are used for kinetic combustion calculations, are not exactly the same compared to the combustion in a real jet combustor. In the real combustor, the fuel droplets evaporate gradually, thus probably differentiating between the compounds with lower boiling point and those with a boiling point which will evaporate "later." In the shock tubes, it is assumed that the fuel is already evaporated and thus the components are homogeneously mixed. These problems started being taken into account only recently [16, 33, 34].

In the present work, measurements of ignition delay time τ of two different kerosene samples were reported. These experiments were carried out by two different groups, in two different shock tube devices, with two different detection methods (pressure rise, CH* emission). The data were gathered over a wide range of parameters for temperatures between 1100 to 1900 K, pressures between about 2.4 and 6 bar, and different initial concentrations of the mixtures, diluted with argon.

By applying statistical fits to these experimental data, it was found that the two kerosene samples differ, in accordance to their chemical composition determined by GC/MS. However, when applying the statistical procedure to *all* experimental data, a single statistical fit was found to represent the whole set of measured ignition delay time data τ (see Fig. 3). Hence, it can be concluded that all experimental data agree to each other, although gathered under different experimental conditions (place, device, detection method).

Modeling calculations were also performed assuming two different surrogate mixtures as fuel for representing kerosene: (i) pure *n*-decane and (ii) a mixture of 70 % *n*-decane and 30 % propylbenzene. It was found that the experimental data are in better agreement with the ones predicted by assuming *n*-decane as the surrogate. It was also found that the diluted Stuttgart experiments were in very good agreement with *n*-decane as a surrogate in contradiction with the experiments run in Haifa. Obviously, when measuring ignition delay times of kerosene under high dilution, the non-paraffin content of the kerosene has no effect, and we see only the influence of the paraffin components all very similar to *n*-decane [33]. A surrogate consisting of 30 % propylbenzene besides *n*-decane fails in predicting autoignition of kerosene probably because propylbenzene is found in very minute quantities only in both types of kerosene investigated and, thus, irrelevant to the combustion mechanism.

Acknowledgments A.B. thanks the DFG—SFB 606: Unsteady Combustion: Transport Phenomena, Chemical Reactions, Technical Systems—for supporting his visit to DLR Stuttgart during two consecutive summers making this cooperative research possible. U.S. and M.B.U. would like to thank M. Kapernaum and C. Wahl for analyzing the kerosene samples. They also appreciate N. Ackermann's assistance in the sampling technique. The help of C. Naumann in the experimental setup and his assistance in the experiments is gratefully acknowledged.

References

1. Seery, D.J., Bowman, C.T.: Combust. Flame **14**, 37 (1970)
2. Lifshitz, A., Scheller, K., Burcat, A., Skinner, G.B.: Combust. Flame **16**, 311 (1971)
3. Burcat, A., Crossley, A., Scheller, K., Skinner, G.B.: Combust. Flame **18**, 115 (1972)
4. Burcat, A., Lifshitz, A., Scheller, K., Skinner, G.B.: Proc. Comb. Inst. **13**, 745 (1970)
5. Skinner, G.B., Lifshitz, A., Scheller, K., Burcat, A.: J. Chem. Phys. **56**, 3853–3861 (1972)
6. Burcat, A., Radhakrishnan, K.: Combust. Flame **60**, 157–169 (1985)
7. Radhakrishnan, K., Burcat, A.: Comb. Sci Technol. **54**, 85–101 (1987)
8. Olchanski, E., Burcat, A.: Int. J. Chem. Kinet. **38**, 703 (2006)
9. Skjøth-Rasmussen, M.S., Braun-Unkhoff, M., Frank, P., Naumann, C.: Modeling study of n-decane using new measurements of ignition delay time and flame speed. WIP, Proc. Comb. Symp. **28** (2002).
10. Skjøth-Rasmussen, M.S., Braun-Unkhoff, M., Naumann, C., Frank, P.: Paper # 012, European Combustion Meeting, Orleans, France (2003)
11. Dagaut, P., Reuillon, M., Cathonnet, M., Voisin, D.: Jour. de Chim. Phys. et de Phys.-Chim. Bio. **92 I**. 1, 47–76 (1995)
12. Bikas, G., Peters, N.: Combust. Flame **126**, 1456–1475 (2001)
13. Zeppieri, S.P., Klotz, S.D., Dryer, F.L.: Proc. Comb. Inst. **28**, 1587–1595 (2000)
14. Zhukov, V.P., Sechenov, V.A., Starikovskii, A.Y.: Combust. Flame. 130–136 (2008)
15. Fournet, R., Battin-Leclerc, F., Glaude, PA., Judenherc, B. Warth, V., Côme, GM., Scacchi, G., Ristori, A., Pengloan, G., Dagaut, P., Cathonnet, M.: Int. J. Chem. Kin. **33,** 574 (2008)
16. Battin-Leclerc, F.: Prog. Energy Combust. Sci. **34**(4), 440–498 (2008)
17. Lifshitz, A.: Ignition delay times. In: Handbook of Shock-Waves, vol 3, pp. 211–256. Academic, Cambridge, MA (2001)
18. Edwards, T., Maurice, L.Q.: J. Prop. Power **17**, 461 (2001)
19. Colket, M., T. Edwards, T., Williams, S., Chernansky, N.P., Miller, D.L., Egolfopoulos, F., Lindstedt, P., Seshadri, K., Dryer, F.L., Law, C.K., Friend, D., Lenhert, D.B., Pietsch, H., Sarofim, A, Smooke, M., Tsang, W.: Development of an experimental database and kinetic models for surrogate jet fuels. 45th AIAA Aerospace Sciences Meeting and Exhibit 2007. Reno, Nevada, p. 770 (2007)
20. Dagaut, P.: Phys. Chem. Chem. Phys. **4**, 2079 (2002)
21. Vasu, S.S., Davidson, D.F., Hanson, R.K.: Combust. Flame **152**, 125–143 (2008)
22. Gauthier, B.M., Davidson, D.F., Hanson, R.K.: Combust. Flame **139**, 300–311 (2004)
23. ElBakali, A., Braun-Unkhoff, M., Dagaut, P., Frank, P., Cathonnet, M.: Proc. Comb. Inst. **28**, 1631–1638 (2000)

24. Goos, E., Burcat, A., Ruscic, B.: Extended third millennium ideal gas and condensed phase thermochemical database for combustion with updates from active thermochemical tables, ANL-05/20 TAE 960 (2005). burcat.technion.ac.il/dir, or garfield.chem.elte.hu/burcat/Burcat.html
25. Steil, U., Braun-Unkhoff, M., Naumann, C., Frank, P.: Paper #002, European Combustion Meeting, Louvain-la-Neuve, Belgium (2005)
26. Slavinskaya, N.: Paper no. 0992, 46th AIAA Aerospace Sciences Meeting and Exhibit. Reno, Nevada (2008)
27. Gracia-Salcedo, C.M., Brabs, T.S., McBride, B.J.: NASA TM 101475. (1988)
28. M. Rachner, report ISBN DLR Mitt-98-01 1 (1998) (in German)
29. Neguyen, H.L., Ying, S.J.: AIAA 26th Joint Propulsion conference. Orlando, Florida, AIAA-90-2439 (1990)
30. Dagaut, P.: Trans. ASME. **129**, 394 (2007)
31. Steil, U., Braun-Unkhoff, M.,Frank, P., Aigner, M.: Paper no. 973, 46th AIAA Aerospace Sciences Meeting and Exhibit. Reno, Nevada (2008)
32. Honnet, A., Seshadri, K., Niemann, U., Peters, N.: Proc. Comb. Inst. **32**(1), 485–492 (2009)
33. Dagaut, P., Karsenty, F., Dayma, G., Dievart, P., Hadj-Ali, K., Mze-Ahmed, A., Braun-Unkhoff, M., Herzler, J., Kathrotia, T., Kick, T., Naumann, C., Riedel, U., Thomas, L.: Combust Flame **161**, 835–847 (2014)
34. Mzé-Ahmed, A., Dagaut, P., Hadj-Ali, K., Dayma, G., Kick, T., Herbst, J., Kathrotia, T., Braun-Unkhoff, M., Herzler, J., Naumann, C., Riedel, U.: Energy Fuels **26**(10), 6070–6079 (2012)

On Influence of Carbon Tetrachloride on Combustible Mixtures Ignition at Various Temperature Ranges

A. Drakon and A. Eremin

Introduction

Various halogenated hydrocarbons are widely used for fire extinguishing. Particularly, carbon tetrachloride, known as Halon-104, in spite of its noticeable toxicity and ozone-depleting properties still could be considered to be a perspective flame and detonation suppressant for unmanned facilities due to its quite high pyrolysis endothermicity and effective inhibiting of the chain reactions of combustion.

The basic of chemical inhibition mechanism which is considered to be an important feature of haloalkanes providing their fire extinguishing efficiency was presented by Hastie several decades ago [1]. A counter-promoting influence of chlorinated species on ignition at particular conditions, though, was already mentioned in that classic work and was also reported later [2]. In a number of recent works, it was shown that haloalkanes considered as flame inhibitors may as well accelerate methane ignition [3, 4] and even be combustible themselves [5]. Thus, the experimental studies of ignition of haloalkane-containing mixtures in a wide range of parameters which can support the development of a comprehensive model of pyrolysis and oxidation of haloalkanes and their influence of combustion development are still an actual scientific task of a great importance for the development of modern fire extinguishing systems and an analysis of industrial risks.

In present work an investigation of influence of CCl_4 admixture on ignition of various combustible mixtures behind shock waves was performed in a wide range of temperatures.

A. Drakon (✉) • A. Eremin
Joint Institute for High Temperatures RAS, Izhorskaya 13 b. 2, Moscow, Russia
e-mail: drakon.a.v@gmail.com

Experimental Methods

Experiments were carried out behind the reflected shock waves in a shock tube of a standard design with inner diameter of 50 mm. Lengths of high- and low-pressure sections were 1.5 and 3.0 m correspondingly. Tube was equipped with several piezoelectric gauges which allow measuring incident shock wave velocity with an accuracy ~0.5 % and calculating parameters of shock-heated mixtures behind the reflected wave using common iteration method based on one dimension theory of shock tube.

Acetylene- and hydrogen-oxygen mixtures were investigated at low temperatures (900–1100 K), where CCl_4 molecule can be considered as stable one. Methane ignition was observed at much higher temperatures (1400–1900 K), where CCl_4 decomposes rapidly.

During the pilot experiments, spectral properties of a reaction zone in various combustible mixtures were investigated using high-speed ICCD camera (*LaVision GMbH)*. Being coupled with external spectrograph and operating in so-called StreakStar mode, it allowed to register a time-resolved spectrum of radiation with a time resolution about 10 μs and spectral resolution ~5 nm. The sample of raw camera frame obtained in experiment in methane-oxygen mixture and the spectrum extracted during the analysis of these data are presented in Fig. 1.

Temperature during the induction time was too low for noticeable emission intensity, so camera had registered just black background there. During the initial phase of combustion, strong lines of CH radical (431.5 nm) and Swan bands (473, 516 nm) were registered. OH radical emission (306–310 nm) and strong line of sodium (589 nm) were observed during the whole after-ignition time.

Comparison of the spectra obtained in pure methane-oxygen mixtures and the mixtures containing carbon tetrachloride admixture has shown that the presence of CCl_4 causes disappearance of Swan bands and dramatically reduces CH peak intensity. Possible explanation of this

G. Ben-Dor et al. (eds.), *30th International Symposium on Shock Waves 1*, DOI 10.1007/978-3-319-46213-4_86

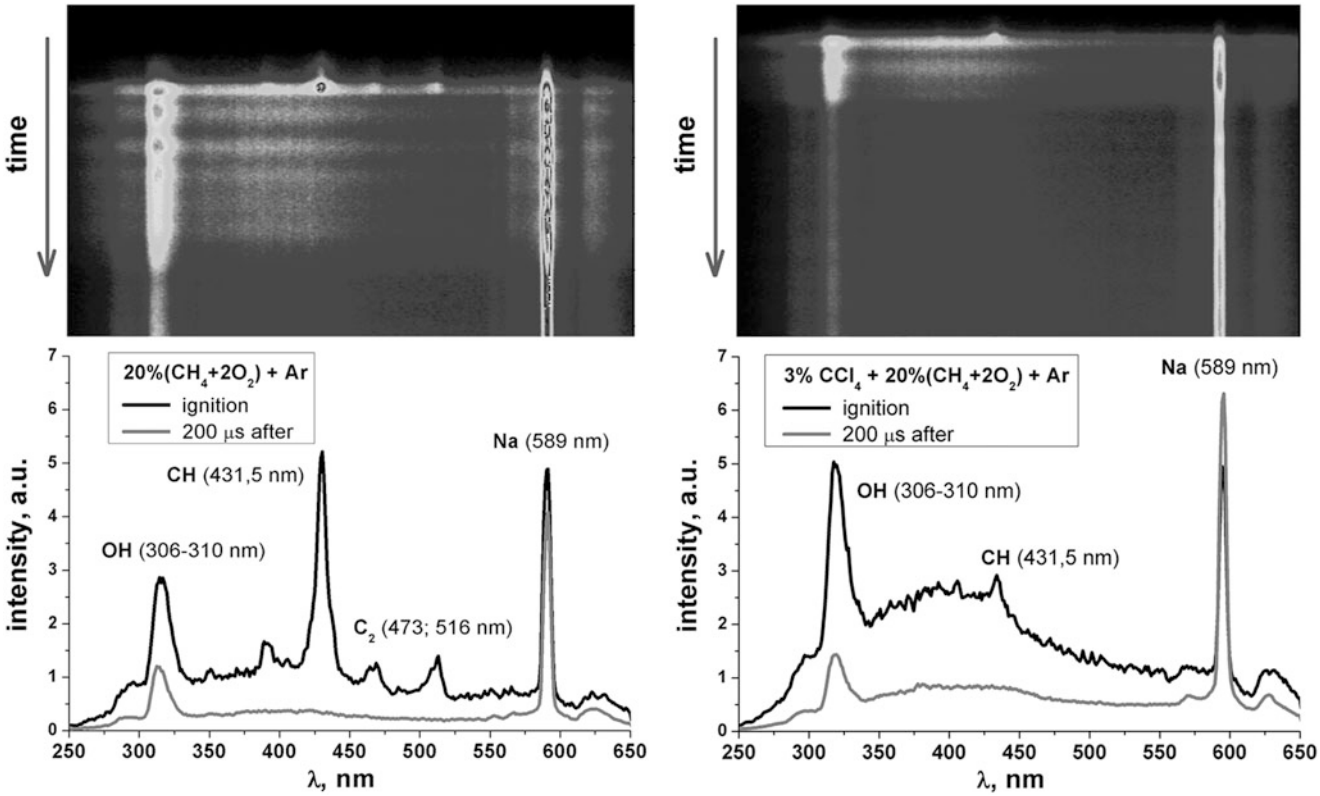

Fig. 1 Raw frame and extracted spectra of combustion zone in mixtures 20 % ($CH_4 + 2O_2$) + Ar and 3 % CCl_4 + 20 % ($CH_4 + 2O_2$) + Ar

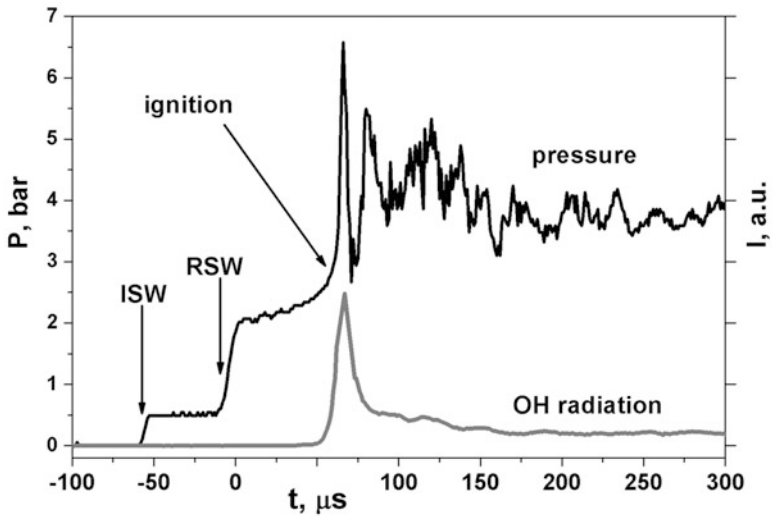

Fig. 2 Typical experimental signals obtained in mixture 15 % ($C_2H_2 + 2.5O_2$) + Ar

effect assumes that haloalkanes due to high pyrolysis endothermicity decelerate temperature increasing and, thus, reduce the amount of methane undergoing full decomposition up to atomic carbon subsequently forming C_2 dimers.

Radical OH is the characteristic species for hydrogen and hydrocarbons combustion. During the following experiments, an OH signal registered by the photomultiplier equipped with interference filter 310 ± 5 nm was used for the determination of delay times in all investigated mixtures. A moment of the rapid rise of OH emission was considered as ignition. Simultaneously an increase of pressure was registered by pressure gauge in the investigated section of shock tube. Typical experimental signals of pressure and OH emission are presented in Fig. 2.

Kinetic modeling was performed using ChemKin software package in an approximation of constant pressure

reactor which should fit shock tube conditions well enough during the induction time. The results of calculations were the time profiles of considered species. Similarly to experimental approach, the modeled induction time was determined as the moment of rapid increase of OH radical concentration.

Results and Analysis

Hydrogen Ignition

Mixtures 2 % CCl_4 + 10 %$(2H_2 + O_2)$ + Ar and 3 % CCl_4 + 20 %$(2H_2 + O_2)$ + Ar, as well as the reference mixtures 10/20 %$(2H_2 + O_2)$ + Ar, were investigated. The measured values of ignition time delays are presented in Fig. 3 as dots. It was observed that CCl_4 presence significantly increases ignition delay times and shifts the temperature dependence to higher temperature region.

For the modeling a modern kinetic scheme of hydrogen combustion presented in recent work [6], consisting of 20 reactions, was used. As one can see in Fig. 3, where calculated ignition delay times are shown as lines, this mechanism provides much better fit for obtained data than common GRI-Mech 3.0 scheme [7].

Obviously, the observed inhibition effects are the case of general combustion suppression mechanism [1] suggesting that generalized halogenated species X participates in the following reactions:

$$O + X + M \rightarrow OX + M \quad (1)$$

$$O + X_2 \rightarrow OX + M \quad (2)$$

$$RX + H \rightarrow HX + R \quad (3)$$

where R is a radical, less active than H and/or O. These reactions are in concurrence with the chain reactions that determine combustion progress:

$$H + O_2 \rightarrow OH + O \quad (4)$$

$$O + H_2 \rightarrow OH + H \quad (5)$$

$$OH + H_2 \rightarrow H_2O + H \quad (6)$$

Detailed description of the inhibition kinetic, though, is quite difficult due to high complexity of carbon tetrachloride pyrolysis and oxidation mechanisms involving numerous active species. Thus, the kinetics of radicals consumption barely can be reduced to several key reactions, and the thorough design of corresponding mechanism has to be the subject of particular study.

Acetylene Ignition

An influence of carbon tetrachloride on acetylene ignition was studied in mixtures 0.5%CCl_4 + 3.5 %$(C_2H_2 + 2.5O_2)$ + Ar, 2 % CCl_4 + 10 %$(C_2H_2 + 2.5O_2)$ + Ar, and 3%CCl_4 + + 20 %$(C_2H_2 + 2.5O_2)$ + Ar. For the reference, mixtures 3.5/10/15/20/35 %$(C_2H_2 + 2.5O_2)$ + Ar were investigated. Obtained values of ignition delay times are presented in Fig. 4 as dots.

One can see that similar to hydrogen-oxygen mixtures, the ignition delay times in acetylene in the presence of CCl_4 considerably increased, i.e., this admixture had considerable

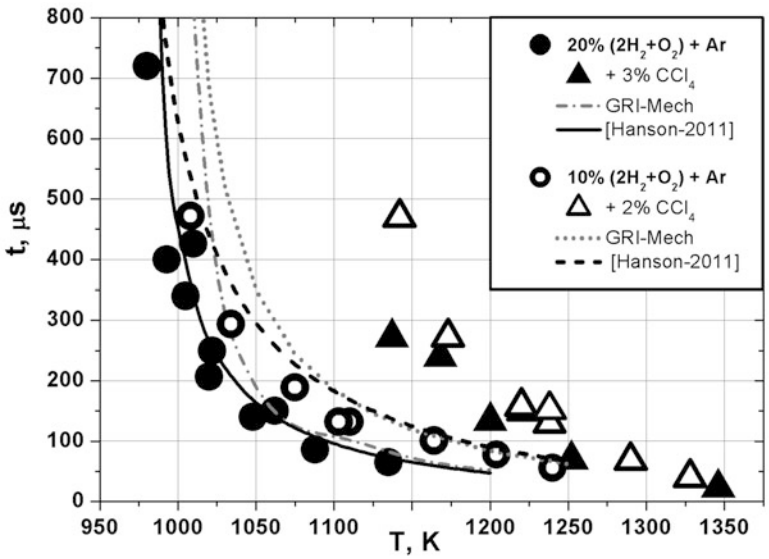

Fig. 3 Experimental (*dots*) and modeled (*lines*) temperature dependencies of ignition delay times in hydrogen-oxygen mixtures doped with haloalkanes at pressures 2.0–2.6 bar

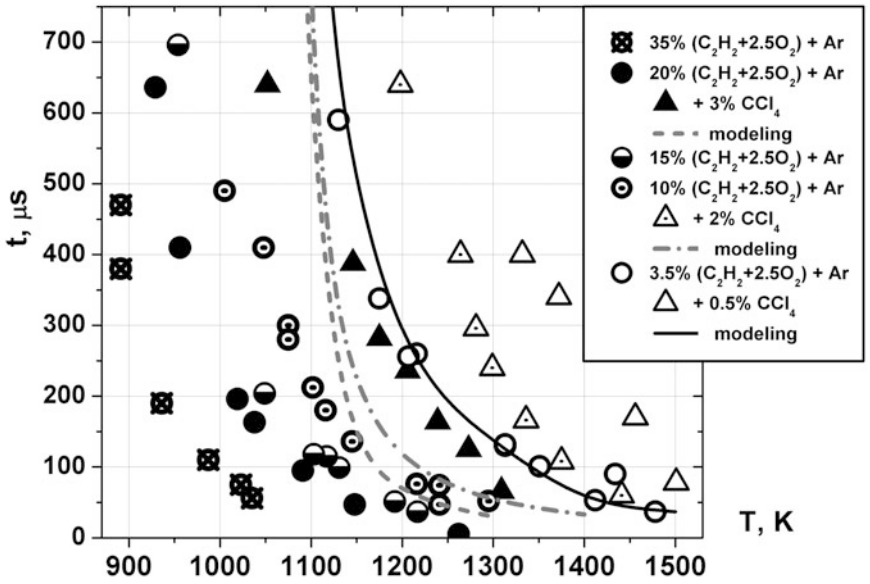

Fig. 4 Experimental (*dots*) and modeled (*lines*) temperature dependencies of ignition delay times in acetylene-oxygen mixtures doped with CCl_4 at pressures 2.0–2.6 bar

inhibiting effect. As GRI-Mech mechanism included acetylene-related reactions is nevertheless declared to be unsuitable for modeling of pure acetylene combustion [7], a comprehensive kinetic scheme of acetylene oxidation [8] was used during analysis of obtained data. Calculated values of ignition delay times are shown in Fig. 4 as lines. One can see that there is good agreement between experimental and modeling results for 3.5 %(C_2H_2 + 2.5O_2) + Ar mixture, but for less diluted mixtures, the measured induction times occur to be much shorter than numerical simulations.

It is notable that among the data reviewed, there is a work [9] where authors reported ignition delay times in C_2H_2/O_2 mixtures which also are not satisfactorily described by suggested kinetic mechanism and are much shorter than ones predicted by general heuristic dependence of ignition delay time (measured in microseconds) on temperature and mixture components concentration. Authors [8] suggest that such results were caused by impurity, but one should note that work [9] is the only one of 9 sources and 20 datasets providing data in 950–1200 K region, and the study was performed behind the reflected shock waves in moderately diluted 10.8%C_2H_2 + 8.5%O_2 + Ar mixture, while in all other works, C_2H_2 concentration does not exceed 3.0 %. For the other hand, 20 % diluted hydrogen-oxygen and methane-oxygen stoichiometric mixtures studied in present work at the same conditions seem not strongly affected by such flaws in spite of comparable energy release. Thus, we can conclude that obtained results indicate actual kinetic features of C_2H_2 oxidation, decomposition, and polymerization leading to ignition accelerating. An indirect evidence of such kinetic processes is the considerable pressure rise during the induction time (see Fig. 2) registered in acetylene-oxygen mixtures only, while inert gases and hydrogen- and methane-oxygen mixtures of the same dilution demonstrate just the very minor pressure rise behind the reflected wave which is the common feature of shock tube.

One should also note that, contrary to common acetylene ignition, previously investigated acetylene self-decomposition and non-oxygen detonation, occurring at temperatures 1100–1400 K, are also dramatically accelerated in the presence of CCl_4 due to atomic chlorine release and C_2H radical formation in reaction $C_2H_2 + Cl \rightarrow C_2H + HCl$, which subsequently initiates the chain decomposition of acetylene [10].

Methane Ignition

In contrast to hydrogen- and acetylene-oxygen mixtures, methane ignition was significantly accelerated in the presence of carbon tetrachloride. Experimentally measured ignition delay times in mixtures 0.5/3.0 % CCl_4 + 20 % (CH_4 + O_2) + Ar are shown in Fig. 5 as dots.

Preliminary analysis has shown that the key reaction involving products of CCl_4 decomposition is $Cl + CH_4 \rightarrow CH_3 + HCl$ where the formation of active CH_3 radicals subsequently initiating chain combustion reactions takes place. Thus, since there are currently no thoroughly tested conventional models of CCl_4 pyrolysis, our task was specified as a design (working out) of simplified kinetic mechanisms allowing rather accurate modeling of Cl formation.

It was assumed that main channel of CCl_4 decomposition and atomic chlorine release is

$$CCl_4 \rightarrow CCl_3 \rightarrow CCl_2 \rightarrow C_2Cl_4 \rightarrow C_2Cl_2 \rightarrow C_2 + 2Cl \quad (7)$$

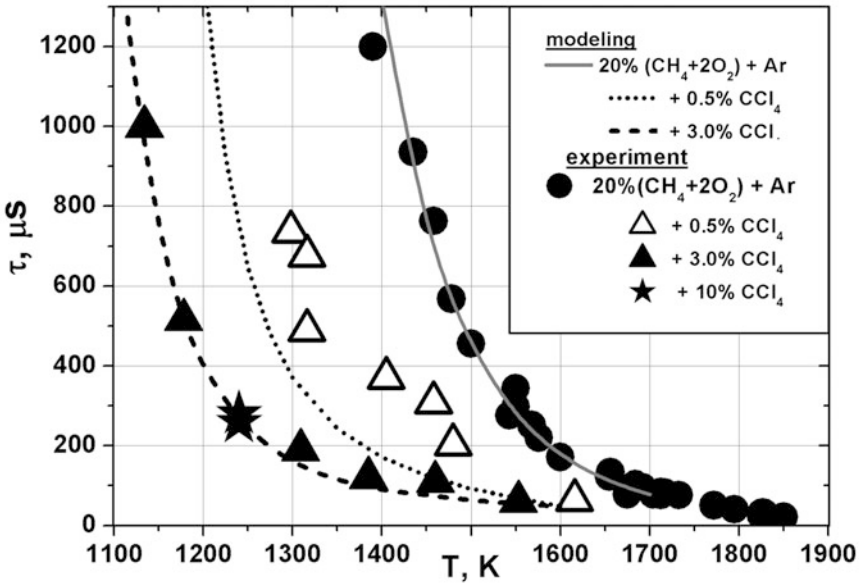

Fig. 5 Experimental (*dots*) and modeled (*lines*) temperature dependencies of ignition delay times in methane-oxygen mixtures doped with CCl_4 at pressures 4.2–5.6 bar

Reaction $CCl_4 \xrightarrow{k_1} CCl_3 + Cl$ was well studied [11], but due to obvious experimental hardship of CCl_3 radical decomposition study, there are quite a few reliable data about $CCl_3 \xrightarrow{k_2} CCl_2 + Cl$ reaction, which is no less important for determination of atomic chlorine release. A cautious estimation $k_2 = 0.1\ k_1$ was applied [12]. The value of rate constant of the key reaction $Cl + CH_4 \rightarrow CH_3 + HCl$ measured experimentally [13] was used. Most important secondary reactions as well as limited number of reactions of interaction of chlorine species with active radicals H, O, OH, and HO_2 were collected from several literature sources [14–16].

The values of ignitions delay times obtained during kinetic modeling are shown in Fig. 5 as lines. One can see that suggested kinetic mechanism including 51 reactions provides remarkably well agreement between experimental and modeling results.

Conclusions

The results of performed study prove that chemical stability of CCl_4 molecule is quite essential for successive ignition chemical suppression under given conditions. At low temperatures it only participates in some chain braking reactions, inhibiting the ignition. Toward higher temperatures, one can expect reversal effect of shock wave-induced combustion development promotion by released atomic chlorine. Therefore, the thorough analysis and necessary precautions should be made during designing of fire extinguishing system using carbon tetrachloride as active specie.

Acknowledgments This work was supported by the Russian Science Foundation project №14-19-00025.

References

1. Hastie, J.W.: Molecular basis of flame inhibition. J. Res. Nat. Bur. Stand. **77A**, 733–754 (1973)
2. Shin, K.S., Park, K., Kim, K.: The addition effect of CH_3Cl on methane ignition behind reflected shock waves. Bull. Korean Chem. Soc. **22**, 330–332 (2001)
3. Babushok, V., Noto, T., Burgess, D.R.F., Hamins, A., Tsang, W.: Influence of CF_3I, CF_3Br, and CF_3H on the high-temperature combustion of methane. Combust. Flame **107**, 351–367 (1996)
4. Azatyan, V.V., Shebeko, Y.N., Shebeko, A.Y., Navtsenya, V.Y.: Promotion and inhibition of the combustion of methane in oxidative gases with various oxygen concentrations by fluorinated hydrocarbons. Rus. J. Phys. Chem. B **4**, 760–768 (2010)
5. Babushok, V.I., Linteris, G.T., Meier, O.C.: Combustion properties of halogenated fire suppressants. Combust. Flame **159**, 3569–3575 (2012)
6. Hong, Z., Davidson, D.F., Hanson, R.K.: An improved H_2/O_2 mechanism based on recent shock tube/laser absorption measurements. Combust. Flame **158**, 633–644 (2011)
7. Smith G.P., Golden D.M., Frenklach M., Hanson R.K. et.al.: GRI-Mech 3.0. http://www.me.berkeley.edu/gri_mech/
8. Wang H., Laskin A.: Comprehensive kinetic model of ethylene and acetylene oxidation at high temperatures. http://ignis.usc.edu/Mechanisms/C2-C4/c2.pdf
9. Bradley, J.N., Kistiakowsky, G.B.: Shock wave studies by mass spectrometry. II. Polymerization and oxidation of acetylene. J. Chem. Phys. **35**, 264–270 (1961)
10. Drakon, A.V., Emelianov, A.V., Eremin, A.V.: Influence of CF_3H and CCl_4 additives on acetylene detonation. Shock Waves **24**, 231–237 (2014)
11. Kumaran, S.S., Su, M.-C., Lim, K.P., Michael, J.V., Wagner, A.F., Harding, L.B.: Ab initio calculations and three different applications of unimolecular rate theory for the dissociations of CCl_4, $CFCl_3$, CF_2Cl_2, and CF_3Cl. J. Phys. Chem. **100**, 7541–7549 (1996)

12. Michael, J.V., Lim, I.P., Kumaran, S.S., Kiefer, J.H.: Thermal decomposition of carbon tetrachloride. J. Phys. Chem. **97**, 1914–1919 (1993)
13. Michelsen, H.A., Simpson, W.R.: Relating state-dependent cross sections to non-Arrhenius behavior for the $Cl + CH_4$ reaction. J. Phys. Chem. A **105**, 1476–1488 (2001)
14. Kumaran, S.S., Su, M.-C., et al.: Experiments and theory on the thermal decomposition of $CHCl_3$ and the reactions of CCl_2. J. Phys. Chem. A **101**, 8653–8661 (1997)
15. Baulch, D.L., Duxbury, J., Grant, S.J., Montague, D.C.: Evaluated kinetic data for high temperature reactions: Volume 4. Homogeneous gas phase reactions of halogen and cyanide containing species. J. Phys. Chem. Ref. Data **10**, 1–721 (1981)
16. Leylegian J.C., Law C.K., Wang H.: Laminar flame speeds and oxidation kinetics of tetrachloromethane. In Proc. of 27th Symp. Combust, 529–536 (1998)

Temperature Measurements in the Combustion Zone Behind the Reflected Shock Waves

A. Drakon, A. Eremin, E. Gurentsov, and E. Mikheyeva

Introduction

Investigation of combustion of various mixtures is still a hot topic concerning the increase of application of various fuels as well as searching for replacement of fire suppressants [1] which produce environment pollutions and have a hazard of the climate change. Experimental study of ignition and combustion processes of simple substances such as CH_4, C_2H_2, as well as more complex blends of hydrocarbons mixed with air or oxygen is generally including only the measurements of temperature dependences of ignition delays and time histories of reactants, transient radicals (OH, CH_3), stable intermediates, and combustion products (CO_2, H_2O). The temperature-time profile during ignition and combustion is important as additional significant integral characteristic for validation and elaboration of detailed reaction mechanisms.

The goal of this study was the development of emission-absorption spectroscopy technique for the time-resolved temperature measurements in the zone of combustion of different fuels in standard shock tube experiments.

Method of Temperature Measurements

The experiments were performed behind the reflected shock waves (RSW) in a conventional diaphragm-type shock tube with an inner diameter of 50 mm. The initial temperature T_5 and the pressure P_5 behind the front of the RSW were determined based on measured incident shock wave (ISW) velocity by applying one-dimensional gas-dynamic theory with the assumption of "frozen" reaction conditions. An inaccuracy of the temperature T_5 calculation was about 1–1.5 % for all range of experiments and was caused by an uncertainty of ISW velocity measured by three pressure transducers.

The temperature measurements during the reaction time were performed by line reversal spectroscopy technique. This method is based on simultaneous detection of emission and absorption of reactive mixture at the same wavelength. The measurements were carried out by two identical optical channels that focus the light from the probe region via the pair of the calcium fluoride windows installed in a horizontal plane of the shock tube and further via lenses onto two photomultipliers (Fig. 1).

The first channel registered an emission only. The second channel was exposed to radiation from reference source of known brightness temperature that passed through the investigation cross section of shock tube. Thus the second channel detected the combination of absorption and emission of reaction mixture. Taking into account Lambert-Beer's and Kirchhoff's laws, one can get the expression for the temperature determination [2]:

$$T(t) = \frac{h\nu}{k}\left\{\ln\left[1 + \left(e^{\frac{h\nu}{kT_0}} - 1\right)\left(1 - \frac{I_a(t) - I_o}{I_e(t)}\right)\right]\right\}^{-1} \quad (1)$$

where $\nu = hc/\lambda$; h is the Planck constant, c is the speed of light, λ is the diagnostic wavelength, k is the Boltzmann constant, T_0 is the brightness temperature of reference source, I_0 is the initial intensity of radiation of the reference source, $I_e(t)$ is the measured emission signal via first optical channel, and $I_a(t)$ is the measured emission + absorption signal via second optical channel. The main advantage of this temperature measurement technique is that it requires only a calibrated light source, without knowledge of either

A. Drakon • A. Eremin • E. Gurentsov
Joint Institute for High Temperatures of Russian Academy of Sciences, Izhorskaya St. 13 Bd. 2, Moscow, Russia

E. Mikheyeva (✉)
Joint Institute for High Temperatures of Russian Academy of Sciences, Izhorskaya St. 13 Bd. 2, Moscow, Russia

Bauman Moscow State Technical University, ul. Baumanskaya 2-ya, 5, Moscow, Russia
e-mail: mikheyeva@ihed.ras.ru

G. Ben-Dor et al. (eds.), *30th International Symposium on Shock Waves 1*, DOI 10.1007/978-3-319-46213-4_87

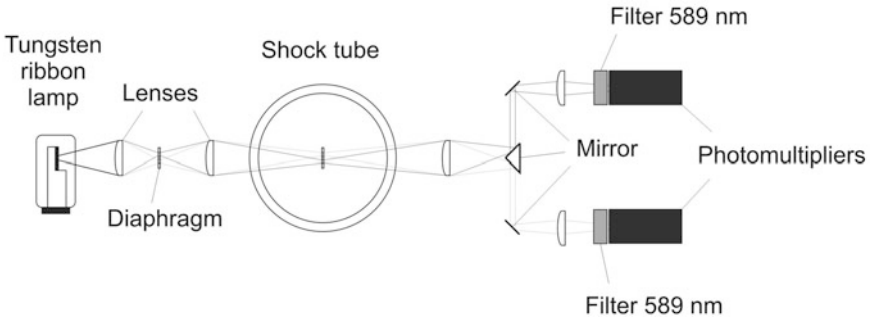

Fig. 1 The scheme of emission-absorption spectroscopy diagnostic for temperature measurements

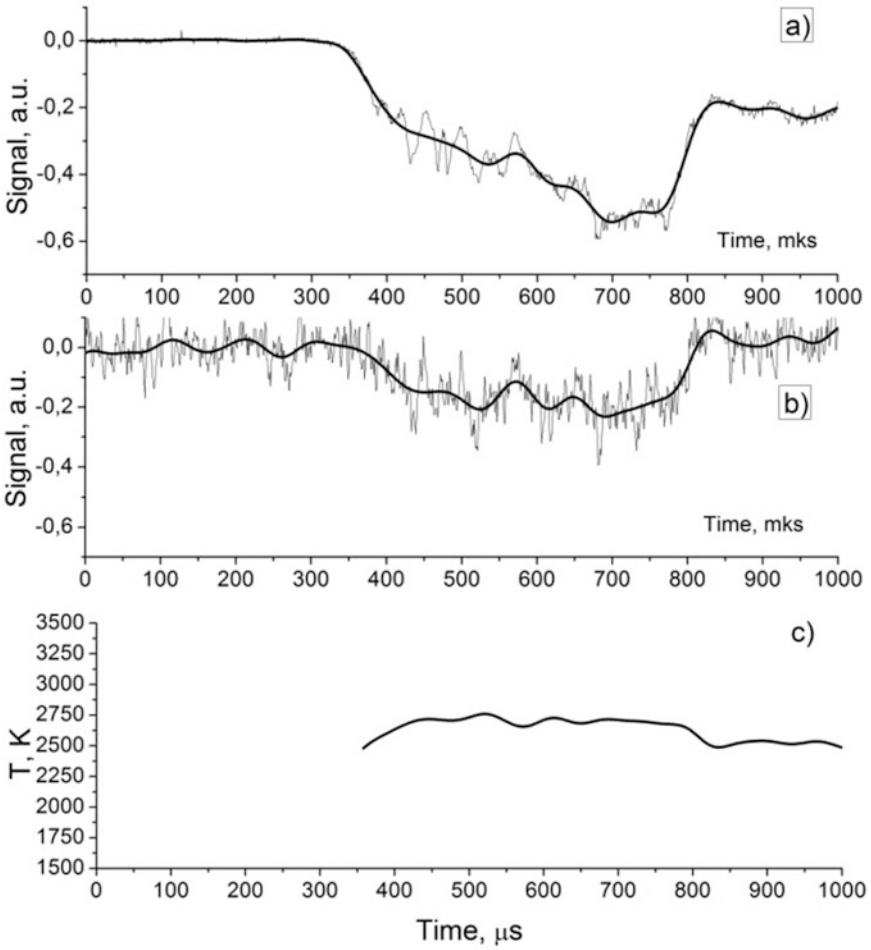

Fig. 2 Temperature measurements performed in mixture of 10 % (CH_4 + 2 O_2) + Ar. Calculated "frozen" conditions after ISW: $T_2 = 895$ K, $P_2 = 1.2$ bar; after RSW: $T_5 = 1618$ K, $P_5 = 5.1$ bar. Emission signal (**a**), emission + absorption (**b**), evaluated temperature-time profile (**c**). *Noisy curves* observed signals, *smooth curves* signals treated with FFT filters

optical properties of observable reaction mixture or the spectral sensitivity of the detection system. The tungsten ribbon lamp was used as the reference source for absorption channel. In reaction zone of combustion, the nonequilibrium excitation of different radicals and products of exothermic reactions could take place [3]. To avoid the possible influence of overequilibrium radiation, the wavelength of 589 nm (centered using a band pass filter with FWHM 20 nm) corresponding to sodium D-line was chosen. The sodium atoms are the inherent natural impurity in argon. The nonequilibrium excitation of the sodium atoms was not observed in the system CH_4-O_2 [4]. In present study the thermal equilibrium between electronically excited sodium atoms and the local mixture temperature is also assumed. The reaction zone is optically thin at 589 nm; thus the influence of the cold boundary layers on the walls of shock tube could be neglected.

The examples of measured signals of emission and absorption are presented at Fig. 2a, b by noisy curves. The initial observed signals treated with smoothing accomplished by removing Fourier components with frequencies higher than a cutoff frequency (FFT filter) are presented via

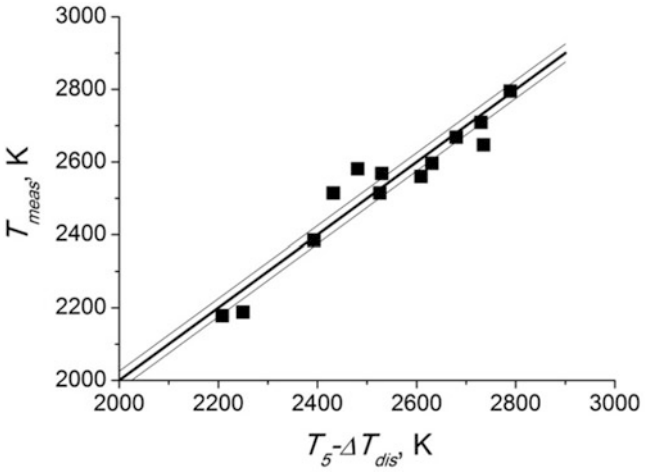

Fig. 3 Results of temperature measurements in mixture of (1–10) % CO_2 + Ar. *Bold line* the calculated "frozen" temperature behind RSW, T_5, *thin lines* the uncertainty of determination of T_5, *points* measurements by emission-absorption technique

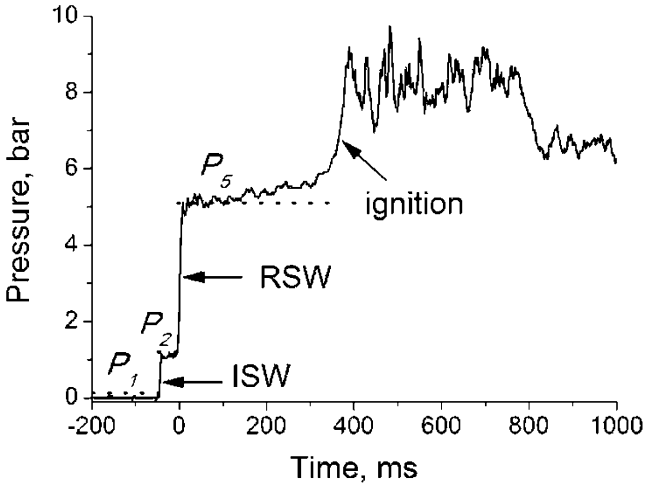

Fig. 4 Pressure-time profile measured in mixture of 10 % (CH_4 + 2 O_2) + Ar. Calculated "frozen" conditions after ISW: T_2 = 895 K, P_2 = 1.2 bar; after RSW: T_5 = 1618 K, P_5 = 5.1 bar

smooth curves. The time scale started with arrival of RSW. The nonzero signals were observed after time delay that corresponded to ignition delay time. The time profile of temperature evaluated with equation [1] is presented in Fig. 2c.

For verification of adjusted technique, the test experiments with the nonreactive mixtures of 1–10 % CO_2 + Ar in the initial temperature range of T_5 = 2200–2800 K (see Fig. 3) were carried out. At these temperatures the dissociation of carbon dioxide does not exceed 5 % and corresponding temperature decrease is within ΔT_{dis} = 100 K. The uncertainty of measurements depended on the signal-to-noise ratio and the difference between the temperature of reactive mixture and the brightness temperature of reference source T_0. When the value of T_0 was varied in the range of 2400–2600 K, the total error of temperature measurements was amounted to ± 5 %.

Results and Discussion

The main series of experiments were performed in the mixtures of methane with oxygen and additions of fire suppressants: carbon tetrachloride CCl_4 (Halon-104) and fluoroform CF_3H (Freon-23). Methane is the most studied fuel due to its simplicity and widespread occurrence. The measurements of temperature in preignition and combustion zone in the mixtures with additions of CCl_4 and CF_3H are of interest because of investigation of inhibition/promotion effect of these admixtures [5]. The typical measured pressure profile is presented at Fig. 4. The first plateau is the initial pressure (P_1), the second plateau is the pressure behind the incident shock wave (ISW) (P_2), and the third plateau is the pressure behind the RSW (P_5). The pressure transducer in these experiments was located at 13 mm from the end plate of the shock tube. The gradual increase in pressure after RSW is regarded to the effect of boundary layer after ISW. The next rapid rise of pressure afterwards indicates the ignition. After some period of ragged behavior of pressure caused by flow turbulization, the decrease of pressure due to rarefaction wave arrival is observed.

The range of temperature after the RSW (T_5) in these experiments was 1300–1800 K that is not enough for noticeable radiation of sodium atoms. Therefore the meaningful temperature measurements have started after ignition where the temperature in combustion zone in our mixtures is much higher than 2000 K resulting in reliable emission and absorption of sodium atoms.

The time-resolved temperature profile in the region after ignition shows approximately the constant value. The temperature measurements performed in combustible mixture of 10 % (CH_4 + 2O_2) + Ar in the conditions of T_5 = 1600–1800 and P_5 = 4.7–5.3 bar where ignition delay times were in the range of 50–500 μs are presented at Fig. 5a. The uniform temperature of T = 2700 ± 50 K was observed. The temperature is resulted by the integral heat release of combustion which is determined as the difference between thermal effect of combustion reactions and energy consumption on heating of combustion products. These processes are weakly dependent on small initial pressure and temperature variation.

The addition of 2 % CF_3H to the mixture of 10 % (CH_4 + 2O_2) + Ar did not cause any temperature change, while ignition delay times have slightly decreased that is in agreement with [5]. The addition of 2 % CCl_4 to the mixture

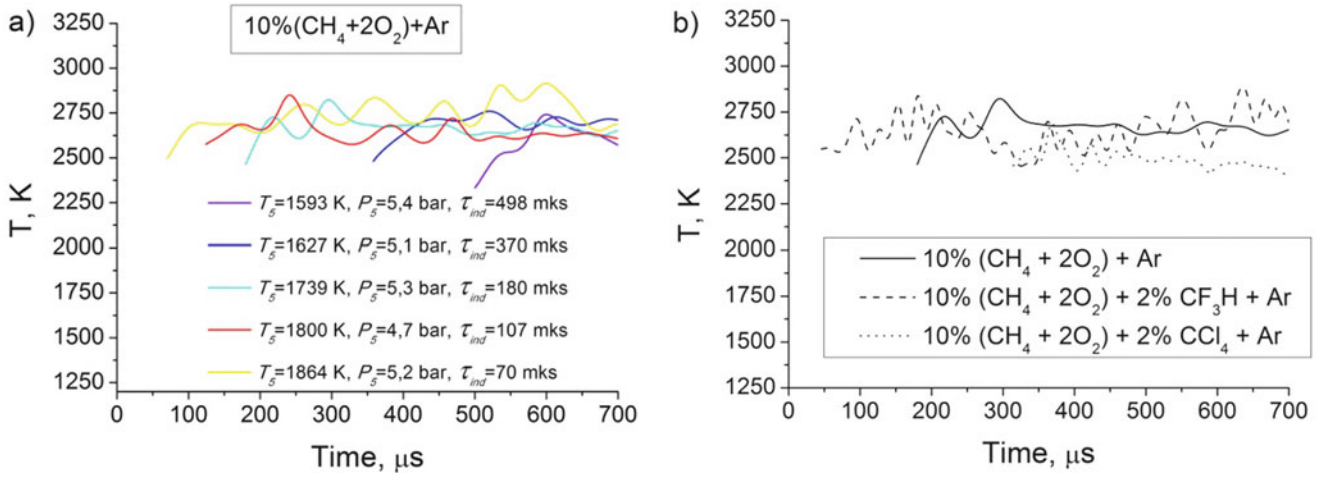

Fig. 5 Temperature measurements performed in: mixture 10 % ($CH_4 + 2\ O_2$) + Ar at different initial conditions—(**a**); mixtures of methane with additions—(**b**). T_5, P_5—temperature and pressure after RSW, τ_{ind}—ignition delay time. Conditions for (**b**): 10 % ($CH_4 + 2\ O_2$) + Ar, $T_5 = 1739$ K, $P_5 = 5{,}3$ bar, $t_{ind} = 180$ μs; 10 % ($CH_4 + 2\ O_2$) + 2 % CF_3H + Ar, $T_5 = 1736$ K, $P_5 = 5{,}0$ bar, $t_{ind} = 40$ μs; 10 % ($CH_4 + 2O_2$) + 2 % CCl_4 + Ar, $T_5 = 1410$ K, $P_5 = 6{,}6$ bar, $t_{ind} = 310$ μs

of 10 % ($CH_4 + 2O_2$) + Ar resulted in the temperature decrease in 200 K and significant decrease of ignition delay times. The main pathway of CCl_4 decomposition under the given conditions is $CCl_4 \rightarrow CCl_3 \rightarrow CCl_2 \rightarrow C_2Cl_2 \rightarrow C_2 + 2Cl$[5]. The combustion-promoting influence of CCl_4 resulting in the shortening of ignition delay could be attributed to atomic chlorine participating in the reaction $Cl + CH_4 \rightarrow CH_3 + HCl$, accelerating the formation of CH_3 radicals [5]. For the other hand, the observed temperature decrease is possibly caused by heat consumption during carbon tetrachloride decomposition.

The work is in progress. In addition to the measurements of combustion temperature, the measurements of temperature-time profile in the region of preignition are planned. This data will be useful for validation of chemical influence of additions of CCl_4 and CF_3H on methane-oxygen combustion process. For this purpose the optical scheme will be complimented by measurements in IR region of spectra.

Conclusions

The emission-absorption technique at D-line of sodium appeared to be a good nonintrusive tool for measurements of combustion temperature in the range of 2200–3000 K under shock tube conditions. The experimental data of temperature behavior is important in case of lack of reliable kinetic mechanisms for prediction of ignition and estimation of combustion and detonation parameters.

Acknowledgements This work was supported by the Russian Science Foundation project №14-19-00025.

References

1. Takahashi, F., Katta, V., Linteris, G., Babushok, V.: Combustion inhibition and enhancement of cup-burner flames by CF_3Br, C_2HF_5, $C_2HF_3Cl_2$, and $C_3H_2F_3Br$. Proc. Combust. Inst. **35**(3), 2741–2748 (2014)
2. Gaydon, A., Hurle, I.: Shock Tube in the Chemical Physics of High Temperatures. Chapman and Hall Ltd., London (1963)
3. Greig, J.: The sodium D-line reversal method of temperature measurement in ionized flame gases. Brit. J. Appl. Phys. **16**, 957–964 (1965)
4. Zaslonko, I., Kogarko, S., Mozzhukhin, E.: Excitation of sodium in certain reactions behind shock waves. Combust Explos Shock Waves **6**(2), 175–182 (1970)
5. Drakon A., Eremin A.: Promotion of methane ignition by the fire suppressants CCl_4 and CF_3H. Combust. Flame. **162**(5), 2746–2747 (2015)

On the Initiation of Combustion by Means of Supersonic High-Enthalpy Jet

S.S. Katsnelson, G.A. Pozdnyakov, and D.A. Aleksandrovsky

Introduction

The issues of plasma initiation of combustion were intensively studied by many researchers (see, e.g., the review [1]). However, there are only few results on combustion initiation in a flow by means of a plasma jet and practically absent results on combustion initiation by means of a high-enthalpy supersonic jet. The interaction of a supersonic plasma jet with a flow is extremely complicated and was not studied in sufficient detail [2]. The jet boundary in a submerged space (tangential discontinuity) is a streamline along which the pressure remains constant and equal to the ambient pressure in the case of exhaustion into a quiescent medium. In the region of the first "barrel," a comparatively small part of the total mass flow of the gas in the jet (less than 20 %) passes through the Mach disk, even if the central shock (Mach disk) has a rather large size. The main part of the gas moves over the periphery. A thin gas layer with a comparatively high density is formed near the jet boundary.

Additional investigations of injection of a supersonic plasma jet generated by a rail gun into a submerged space were performed to understand the result obtained and to develop an adequate mathematical model.

S.S. Katsnelson • G.A. Pozdnyakov (✉)
Khristianovich Institute of Theoretical and Applied Mechanics SB RAS, Institutskaya st. 4/1, Novosibirsk, Russia

Novosibirsk State University, Pyrogova st. 2, Novosibirsk, Russia
e-mail: georg@itam.nsc.ru

D.A. Aleksandrovsky
Novosibirsk State University, Pyrogova st. 2, Novosibirsk, Russia

Results

A scheme of the experimental setup [3] is shown in Fig. 1. The processes occurring in 350-mm-diameter 400-mm-high sealed cylindrical reactor chamber *1* were monitored through optical window *3* with a clear aperture of 100 mm.

The plasma was accelerated by coaxial electrodynamics accelerator (Marshall gun) *2*, which generated plasma bunches with velocities from several km/s to a few tens of km/s, the initial gas pressure being up to a few kilopascals. The inner diameter of the 300-mm-long channel of the plasma accelerator was 20 mm. Capacitor bank *4* with a capacitance of 6.6 μF and charge voltage of 30 kV was connected to the Marshall gun via controlled switch gap *5*. The device operated as follows. The working volume was evacuated via pipe *7* to pressure lower than 1 Pa and was then filled with natural gas to pressure 500 Pa (a methane-ethane mixture also containing other hydrocarbons). The capacitor bank was charged, and the measurement equipment was prepared for a shot. The discharge of the capacitor bank generated plasma *6*, which was accelerated to a high speed by the electrodynamic force. Then, the accelerated plasma bunch entered the working volume filled with natural gas. In our experiments, we recorded the emission spectrum from the reaction zone, performed streak imaging of the interaction process, and measured the accelerator voltage and current. Streak images were taken with slits oriented across and along the accelerator axis.

Typical streak images taken with two mutually perpendicular orientations of the slits are shown in Fig. 2a, b. Figure 2a shows a longitudinal streak image taken along the axis of the plasma flow, while Fig. 2b shows a transverse streak image taken in one of the transverse cross sections located consecutively along the axis. Description of results and analysis is to be presented with graphs, figures, and tables included in the text, at the appropriate place.

In the experiment described above, an equilibrium methane plasma flow with a velocity of ~10 km/s, temperature of

G. Ben-Dor et al. (eds.), *30th International Symposium on Shock Waves 1*, DOI 10.1007/978-3-319-46213-4_88

~10,000 K, and pressure of several tens of megapascals is formed at the exit of the rail gun channel. The exhausting jet is strongly underexpanded; as it follows from the processing of the photographic records of the process, the jet rapidly expands with a mean velocity u equal to 4.51, 8.05, and 10.0 km/s at a distance of 15, 30, and 45 mm from the channel exit, respectively. Owing to radiation and rapid expansion, the temperature at the jet boundary decreases to $T \sim 4000$ K (the gas is still luminous). Let us estimate the parameters of the mixing region on the interface between the jet and the ambient medium (methane), where the temperature is $T_0 = 300$ K. The estimates of the mixing region based on temperature and diffusion equation are $\lambda/\ell = 3\ln(T/T_0)\, u/\bar{v} \gg 1$ and $\lambda/l = 3\ln(n/n_0)u/\bar{v} \gg 1$, where λ is the mean free path, ℓ is the characteristic size of the mixing region, and $\bar{v} = \sqrt{8kT/(\pi\mu)}$. Thus, $\ell/\lambda \ll 1$ in the mixing region and the nonequilibrium state in terms of the translational temperature of particles should be taken into account.

The study was performed within the framework of the model described in [4], which implies the nonequilibrium state in terms of the temperature of groups of particles.

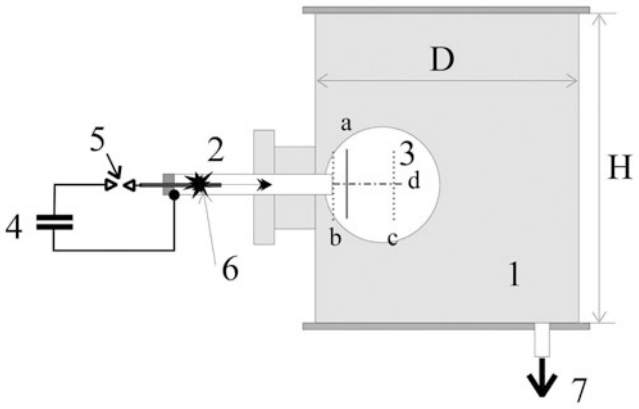

Fig. 1 Scheme of the experimental setup: (*1*) chamber, (*2*) Marshall gun, (*3*) optical window, (*4*) capacitor bank, (*5*) controlled switch gap, (*6*) plasma, and (*7*) pumping out

Such models are often used in studying kinetic schemes and finding details of individual mechanisms and a possibility of kinetic scheme reduction. The reacting system in this model is considered in the two-temperature approximation with the following temperature groups: "cold" particles including the species of the initial methane-air mixture and the products of its decomposition and "hot" particles including hydrogen and carbon atoms of the recombining methane plasma. At the above-said level of temperatures in the mixing region, the concentrations of charged particles are negligibly low, and their contribution to the kinetic scheme can be neglected.

The kinetic scheme proposed in [5] was taken as a basis for investigating combustion of the methane-air mixture. The upper boundary of the confidence interval of temperatures does not exceed 3000–4000 K for the majority of rate constants of elementary reactions of hydrocarbon combustion [6]. This fact determines the level of admissible temperatures of the initial reagents.

Below are the results of calculations for CH_4:O_2 = 1:1, $T_{h0} = 3000$ K, and $P_{h0} = 0.3$ MPa (Figs. 3, 4, 5, 6, 7, 8, and 9).

Based on calculations, it can be concluded that combustion initiation by a supersonic high-enthalpy jet requires intense mixing of the plasma jet and reagents. Experimental results obtained in two facilities for this purpose are reported below.

Results of Experiments Performed in Facility 1

The natural gas was injected into a supersonic air flow with the Mach number M = 3 at the exit from a conical nozzle, which entered a constant-section channel. A system for combustion initiation (coaxial electrodynamic accelerator of the plasma) was located slightly downstream from the injectors. The accelerator injected a plasmoid, which had a velocity of 10 km/s, a temperature higher than 10000 K, and a pressure of several tens of megapascals. The plasmoid was injected normal to the flow. The facility where the

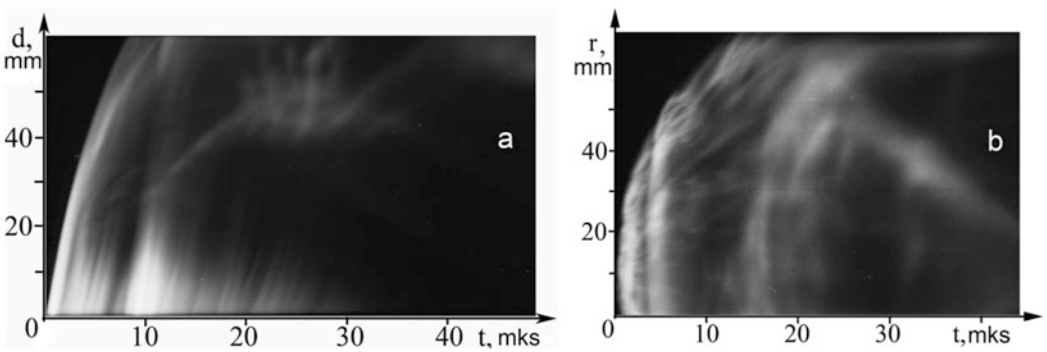

Fig. 2 Streak images (**a**) longitudinal, (**b**) transverse

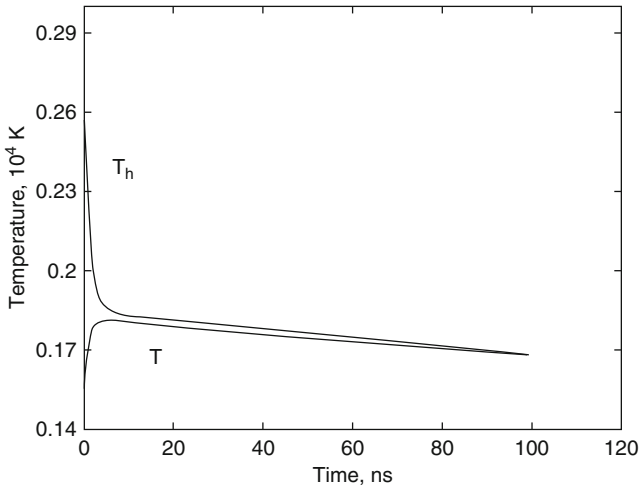

Fig. 3 Temperature change over time

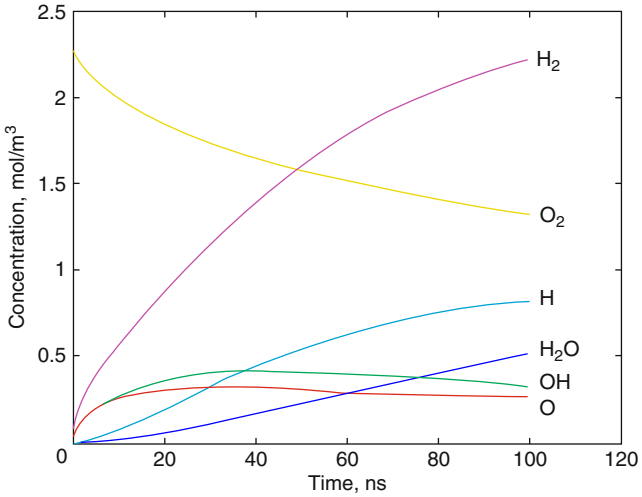

Fig. 4 Substances involved in the burning of hydrogen

experiments were performed is schematically shown in Fig. 9. The experimental setup after a series of tests is shown in Fig. 10. The overall pattern of plasmoid interaction with a supersonic flow is illustrated in Fig. 11.

Figure 12 shows the maximum values of pressure measured at different points for two regimes: with (2) and without (1) injection of the natural gas.

The results were obtained for the initial pressure of air $P_{0air} = 1$ MPa at the temperature $T_0 = 300$ K. The curves in the graphs reveal a significant decrease in pressure in the compression wave during its propagation in the flow without natural gas injection and an almost constant value of this variable in the second case. This behavior confirms that combustion of the natural gas is initiated owing to propagation of the compression wave over the flow of a non-premixed mixture of air and natural gas in the second case.

Results of Experiments Performed in Facility 2

The experiments were performed in the IT-302 M hotshot wind tunnel based at ITAM SB RAS with the use of a model of a combustion chamber with a cavity in the attached pipeline regime. A rail gun was attached to the sidewall of the model in the vicinity of the cavity. This rail gun was used for injection of a plasmoid, which had a velocity of 10 km/s, a temperature higher than 10000 K, and a pressure of several tens of megapascals. The plasmoid was injected normal to the flow. Figure 13 shows the photograph of one fragment of the combustion chamber model. Through the windows, one can see the combustion chamber configuration and the orifice of the plasma injector. The gas-dynamic contour of the model is marked by the white line. The invisible parts of the contour are shown by the dotted lines.

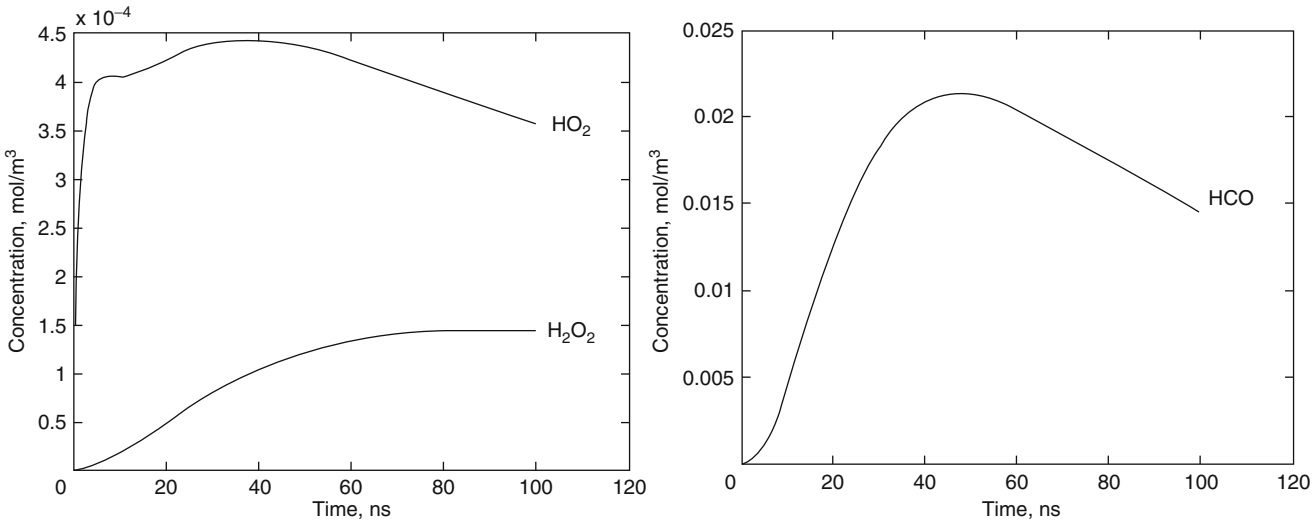

Fig. 5 Concentrations of radicals

Figure 14 shows the frames of the movie taken after initiation. Luminescence was observed in 15 consecutive frames, i.e., during 15 ms. The first frame shows a bright flash from the rail gun. After that, gas glowing in the cavity is observed. The brightness is unstable, which is clearly seen in the frames. Frames from 7 to 12 are similar to frames from 3 to 6, therefore they are not shown here. Luminescence of the gas in the cavity is not accompanied by any noticeable increase in pressure (the mean level of the pressure increase is 6 %).

Conclusions

The following conclusions can be drawn from the experiments:

1. Despite of a short-duration process of combustion and a low level of heat release, the possibility of ignition of hydrocarbon fuels has been confirmed at high speeds of flows in channels.

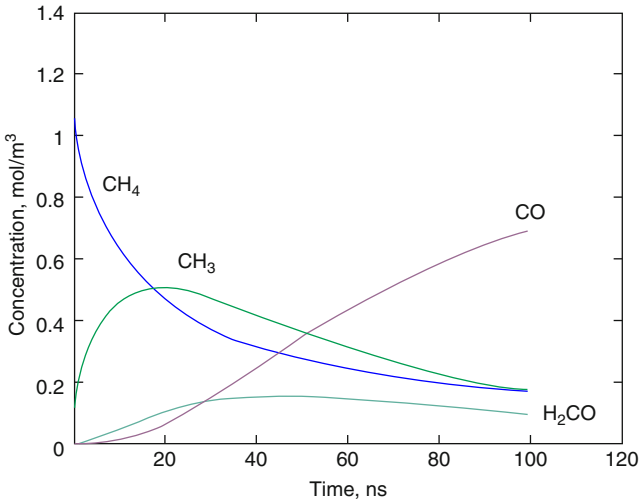

Fig. 6 Substances involved in the combustion of methane

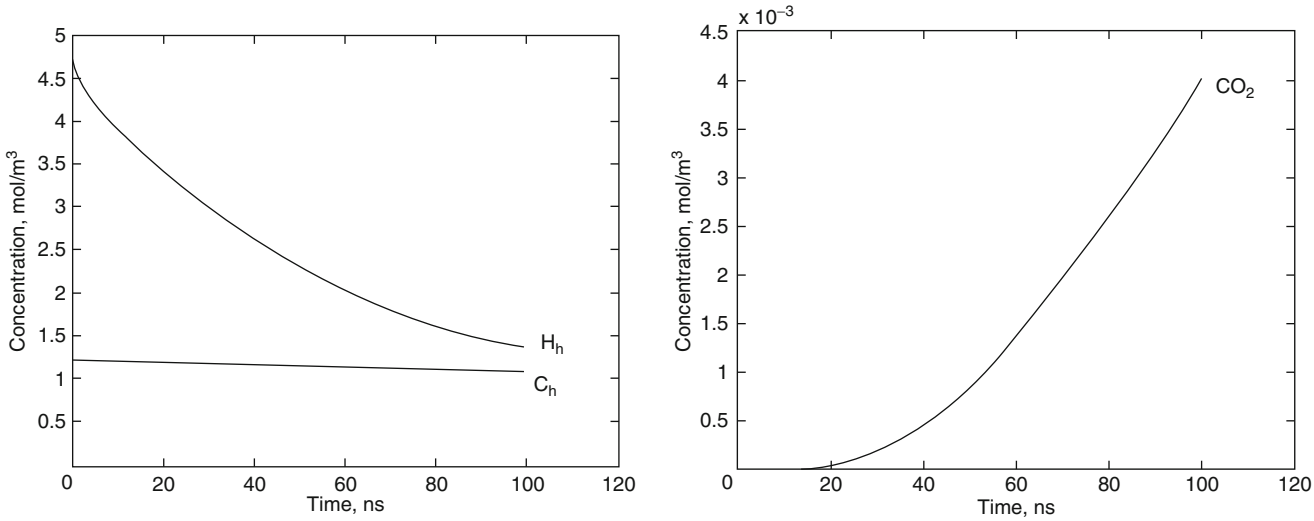

Fig. 7 Concentration of "hot" hydrogen and carbon atoms, carbon dioxide

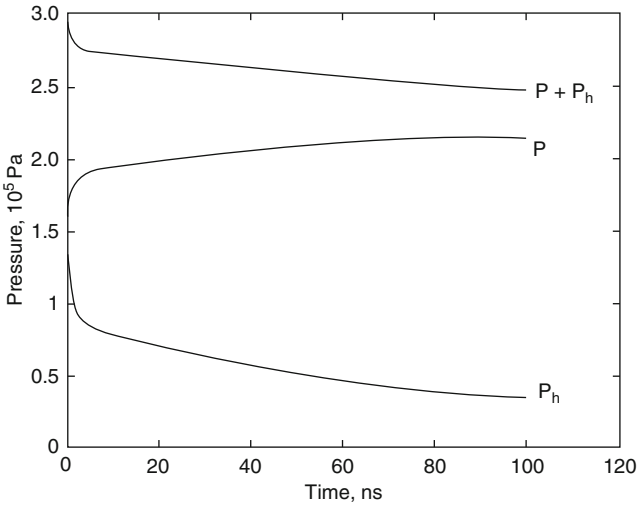

Fig. 8 The pressure change over time. P_h pressure "hot" components, P is pressure for "cold" components

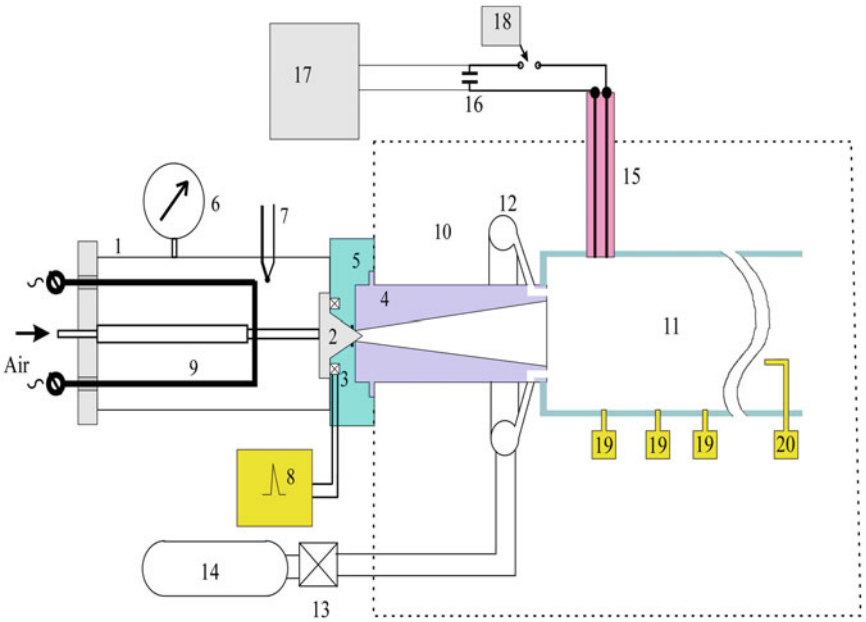

Fig. 9 Experimental facility: *1* settling chamber, *2* pulsed valve, *3* coil, *4* supersonic conical nozzle, *5* dielectric plate, *6* pressure gauge, *7* thermocouple, *8* pulsed current source, *9* ohmic heater of the test gas, *10* test section, *11* test channel, *12* collector, *13* electromagnetic valve, *14* gas holder with the natural gas, *15* rail gun, *16* capacitor battery, C = 6.6 μF, *17* high-voltage source, *18* system for rail gun actuation, *19* static pressure strain gauges, and *20* Pitot pressure gauge

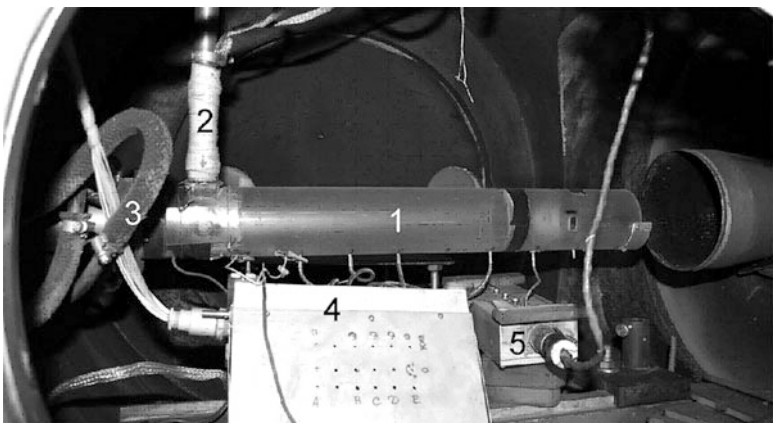

Fig. 10 Test section. *1* cylindrical channel, *2* rail gun, *3* system for natural gas injection, *4* static pressure gauges with amplifiers, and *5* Pitot pressure gauge with an amplifier

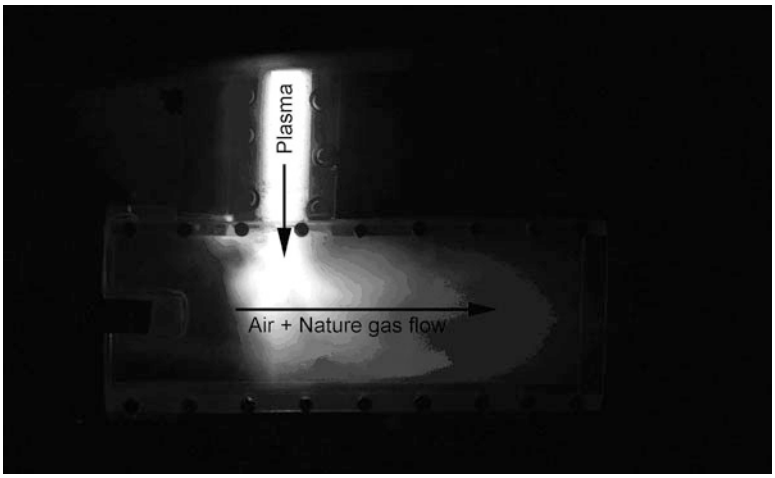

Fig. 11 Effect of the plasmoid on the flow

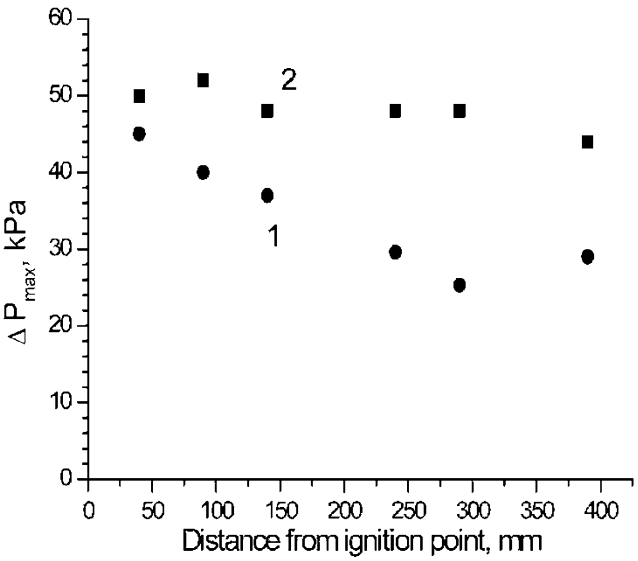

Fig. 12 Maximum values of the pressure amplitude in the compression wave in the flow. *1* without combustion initiation, *2* with combustion initiation

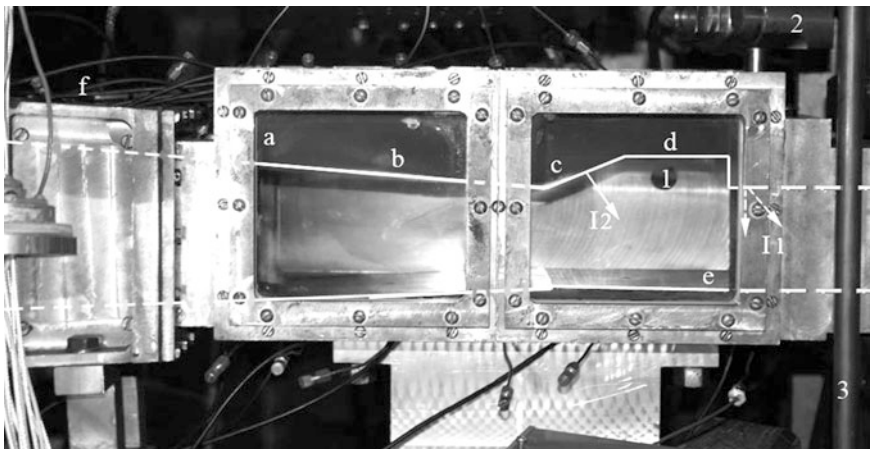

Fig. 13 Photograph of the combustion chamber. *1* orifice for plasma injection, *2* valve for injection of the natural gas through injectors I1, *3* tube for natural gas supply, *I2* second place of natural gas injection, and a–f stations of static pressure measurements

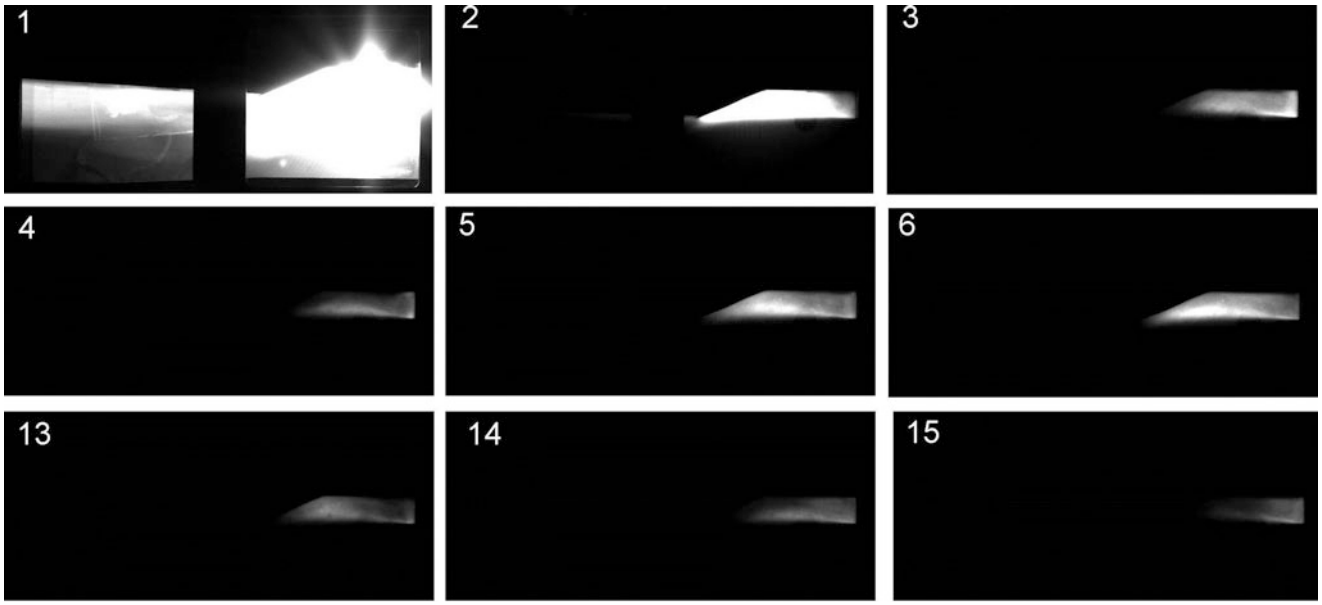

Fig. 14 Fragment of a high-velocity movie from the instant of initiation to luminescence quenching. The frame frequency is 1 kHz

2. The suggested kinetic scheme of initiating combustion allows one to determine the nature and conditions of ignition and to understand the reasons for the fast termination of the combustion process at artificial initiation.
3. The railgun can be one of the most promising sources of initiating combustion in supersonic flows.

This work was supported by the Russian Foundation for Basic Research (Grant No. 13-08-00786).

References

1. Starikovskaia, S.M.: Plasma assisted ignition and combustion. J. Phys. D Appl. Phys. **39**, 265–299 (2006)
2. Lukyanov, G.A.: Supersonic plasma jet. Mashinostroenie, Moskow (1985) (in Russian)
3. Golubov A.I., Katsnelson S.S., Pozdnyakov G.A Interaction of a high-enthalpy plasma jet with surfaces chemically active media. IEEE Trans. Plasma Sci. **38**(8): 1840-1849 (2010).
4. Katsnelson S.S., Pozdnyakov G.A Initiation of combustion in a hydrogen-oxygen mixture under the action of a low-energy strong-current electron beam. Combust. Explosion Shock Waves **43**(2): 132–138 (2007)
5. Dautov, N.G., Starik, A.M.: On the problem of choosing a kinetic scheme for the homogeneous reaction of methane with air. Kinet. Catalysis **38**(2), 185–208 (1997)
6. Gardiner, W.C., Jr. (ed.) Combustion Chemistry. Springer, New York (1984)

A Test of Ignition Behaviors Induced by a Smoothly Convergent Cylindrical Shock

Yang Jianting, Yujian Zhu, and Jiming Yang

Introduction

Shock wave can be used to ignite combustible gas mixtures. Because the flow information across a shock wave is fundamentally accessible and the heating process is almost instantaneous, the shock-induced ignition (SII) technique becomes an effective experimental method for studies of gas ignition, flame propagation, combustion characteristics of fuels, and so on. The application of SII technique must follow a certain rule. That is, the initially produced incident shock should be weak enough so as to avoid undesirable disturbances caused by the diaphragm rupture process, especially the ignition in the vicinity. After the incident shock wave reaches its ideal state, a secondary enhancement of the shock wave is then required to further promote the post-shock temperature to the cliff of chain reactions. There are two general types of shock enhancement methods in literature—a head-on reflection on a planar wall and shock focusing. Ignition with the former method is referred to as the reflected-shock-induced ignition (RSII). The RSII method is widely applied in studies of induction length of combustible mixture and fuel characteristics [1]. It has flaws, nevertheless. Firstly, the interaction of the reflected shock and the boundary layers induced by the incident shock is unavoidable, and will greatly affect the ignition process, which makes the RSII an impure shock-induced ignition and the measured induction length underestimated. Secondly, the RSII allows only discrete tests of specific conditions, which forbids the examination of the impact of the continuous variation of certain critical gas parameters (e.g., temperature). On the other hand, the shock focusing method can be divided into reflected focusing or direct focusing. In general, the reflected focusing utilizes a designed concave wall or cavity on the end of shock tube to concentrate the reflected shock wave toward a spot or a limited region and thereby to create a localized high-temperature environment for ignition. Varied ignition phenomena can be observed depending on the shape of the wall or cavity and the incident shock strength [2]. The ignition is complicated though, because of the highly irregular shock reflection process, leaving the ignition development as well as the underlying mechanisms in ambiguity. By comparison, the direct focusing of a cylindrical or spherical shock wave leads to a much simpler configuration in respect of the wave patterns and the flow. Creating a cylindrical/spherical shock wave presents the main challenge in this category. Multiple techniques have been developed including the fully cylindrical focusing realized by annular shock tube [4] and the partially cylindrical focusing realized by gas lens [3] or design channel wall based on the shock dynamic theory [5]. Moreover, the direct focusing shock wave propagates in a complete undisturbed gas and sweeps a continuous range of temperature and pressure conditions, which makes it a good method to detect some of the combustion limits. Exact application of it on the study of ignition process with combustible mixtures, however, is still rare. On the basis of previous study [5], in this paper we design a specific experiment section with the shock dynamics theory to carry out the SII experiment and to study the ignition of premixed combustible gas and the flame propagation process in it.

Method

The experiment is conducted on a rectangular shock tube platform. The overall arrangement of the shock tube platform as well as the flow visualization system is shown in Fig. 1. The test section (Fig. 2) is installed downstream of the driven section of the shock tube. Downstream of the test section connects a pressure relief tube. The driving and driven sections of the shock tube are 2.5and 1.5 m in length,

Y. Jianting • Y. Zhu • J. Yang (✉)
Department of modern mnechanics, University of science and Technology of China, Hefei 230027, China
e-mail: jmyang@ustc.edu.cn

G. Ben-Dor et al. (eds.), *30th International Symposium on Shock Waves 1*, DOI 10.1007/978-3-319-46213-4_89

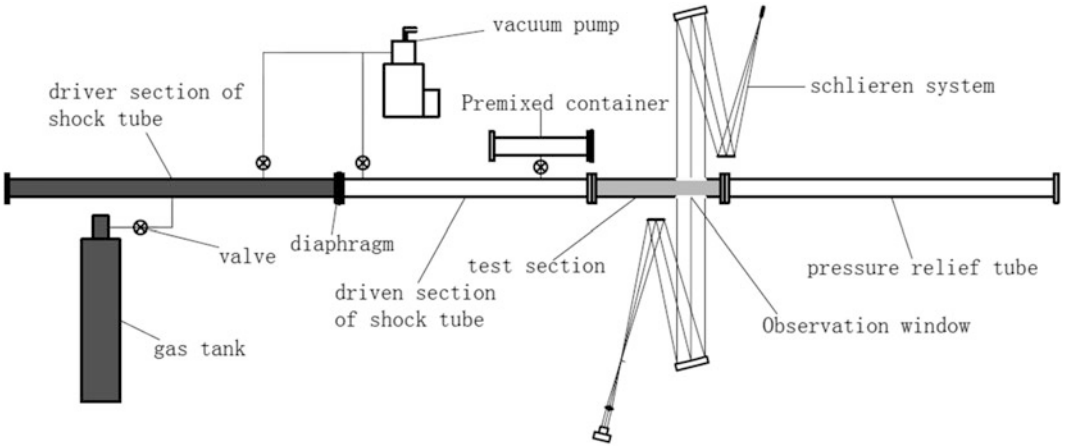

Fig. 1 Schematic of the experimental platform

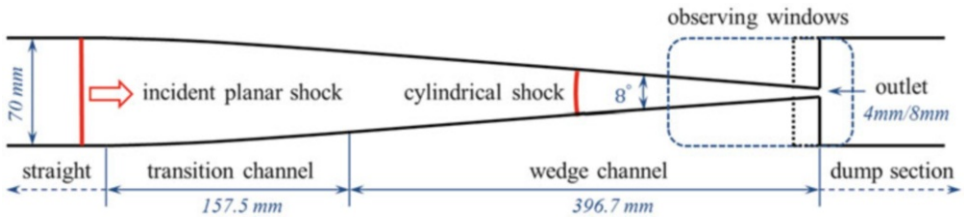

Fig. 2 Schematic of the test section

respectively. The cross sections of the shock tube, the pressure relief tube, and openings of the test section are all of 40 mm × 70 mm.

As shown in Fig. 2, the test section of the present study consists of four connected parts—a short straight leading section, a transition section, a constantly convergent wedge channel, and dump section serves as a port to the pressure relief tube. The transition section is carefully designed with the shock dynamics theory. Interacting with the walls of the transition section, the incident planar shock can be transformed continuously and smoothly into a segment of cylindrical shock [6]. The cylindrical shock continues to converge in the succeeding wedge channel. By this process, the intensity of the cylindrical shock is enhanced continuously. Providing that the wedge channel is filled with premixed combustible gas in advance and the intensity of the convergent shock is strong enough, ignition will occur in the shock converging process. In this study, the convergent wedge channel has an angle of 8 degrees and is cut open before it reaches a dead end. This forms an outlet opening directly to the dump section. By cutting the wedge channel at different positions, two different sizes of the outlet are tested. One is 4 mm in height and the other is 8 mm. The outlet is designed to avoid quick reflection of the cylindrical shock and leave enough time for the development and observation of SII in the convergent channel.

The main diagnostic technique of the study is flow visualization. As shown in Figs. 1 and 2, a pair of observing windows is placed on the test section to cover the final part of the convergent channel where ignition is likely to occur. High-speed schlieren system with a frame rate up to 40,000 fps and an exposure time of 1 μs is employed to visualize the flow field through the windows.

Tests are performed with the following procedure. After the diaphragm is installed, the driven section (hereafter stands for all tube sections downstream of diaphragm) is evacuated with a vacuum pump. Combustible gas premixed in the premixing container is then filled into the driven section to a certain test pressure. Helium is used as the driving gas. A shock wave is generated instantaneously as the diaphragm ruptures. At the same time, the high-speed camera is triggered and starts to record the flow field via the schlieren optics. In this study, the burst pressure of the diaphragm is around 0.65 MPa, and the produced shock Mach number changes from 2.6 to 3.2 depending on the initial pressure in driven section.

Preliminary numerical simulation and experimental verification indicate that the transition section designed with the shock dynamics theory may effectively suppress irregular disturbances when converting the planar shock wave into a segment of cylindrical shock wave. This ensures the clearance of flow field and is beneficial to the observation and study of the details of SII occurring in the shock converging process. The resulted cylindrical shock is found to be rather neat, which ensures a relatively even variation of the flow parameters (e.g., temperature) behind the shock.

The continuous and uniform increase of the shock strength in the process of shock convergence is expected to provide a good examination of the temperature characteristic of the fuel and the critical ignition process.

Results and Discussion

In this paper, H_2-Air mixture with a proportion near stoichiometry, 30%H_2 + 70%Air, is used to investigate the convergent shock-induced ignition (CSII) process. For comparison and to understand the pure gas dynamics, H_2–N_2 mixture with the same volume fraction of H_2 is also tested. For there is no chemical reaction, the flow of H_2-N_2 mixture is referred as the cold flow. Relative properties of the two mixtures are close to each other, which makes the basis for comparison (Table 1).

Figure 3 shows the cold flow field in the convergent channel with an outlet of 4 mm. The incident shock Mach number is 3.0. We can see that in the process of shock convergence (0–40 μs), the flow field is clean without obvious disturbance, indicating the designed geometry of the convergent channel accomplishes its mission quite well. However, from 80 μs, after the incident shock goes far beyond the outlet, there come trains of Mach waves in the supersonic channel flow. The Mach waves might be the result of the fluctuations of the turbulent boundary layers over imperfect walls. Thickening and upsetting of the boundary layers are evidently visualized in the schlieren images from 40 to 80 μs, which is in correspondence with the emergence of the Mach waves. The scenario is as well supported by the fact that the inception points of the Mach waves keep migrating or shifting instead of stationed.

The intensifying incident shock wave induces an unstable supersonic channel flow whose Mach number rises in the converging direction. It evolves gradually toward a stable distribution in which the Mach number of the supersonic flow decreases till it resumes one at the outlet. In this process, the flow Mach number at the end of the channel drops, which causes the Mach waves to raise steeper (80–120 μs). Along with the building up of pressure in the dump section, the channel flow goes choked then and a normal shock wave emerges and propagates upstream. The shock wave eventually runs head-on into the contact region at about 280 μs.

Figure 4 shows the CSII process with the combustible mixture in the convergent channel. The cylindrical shock converges neatly at first. When it is enhanced to a certain strength, ignition occurs, and a combustion wave is generated and propagating upstream. Velocity analysis indicates that the combustion wave develops into a detonation wave in the later stage. Comparing with the cold flow in Fig. 4, we can see that the occurrence of ignition is far earlier than the formation of the reflected shock wave. Mach waves are also observed upstream of the outlet in a limited region before 100 μs which suggest that the flow of the combustion products in this region is supersonic. Followed by a reflected shock wave (120–220 μs) similar to that in the cold flow, the supersonic region is finally erased.

Details of the ignition are demonstrated in the time-resolving sequential images of Fig. 5. Although in the shock converging process the maximum temperature of the flow field appears right after the cylindrical shock front, the ignition lags behind the shock front for a certain distance. At 8 μs, an x-shaped density abnormal reflecting chemical reaction of the flow comes forth at about 20 mm behind the shock wave. By analyzing the induction time of mixture, an explanation for this effect is illustrated in Fig. 6. The red dash line represents the time of SII for gas elements distributing along the channel. With the increase of the shock Mach number, the induction time of the gas element

Table 1 Relative properties of the test gases

Mixture	Molecular weight (g/cm^3)	Sound speed (298 K) (m/s)	Specific heat ratio
30 % H_2 + 70 % Air	20.9	407.6	1.4
30 % H_2 + 70 % N_2	20.2	414.6	1.4

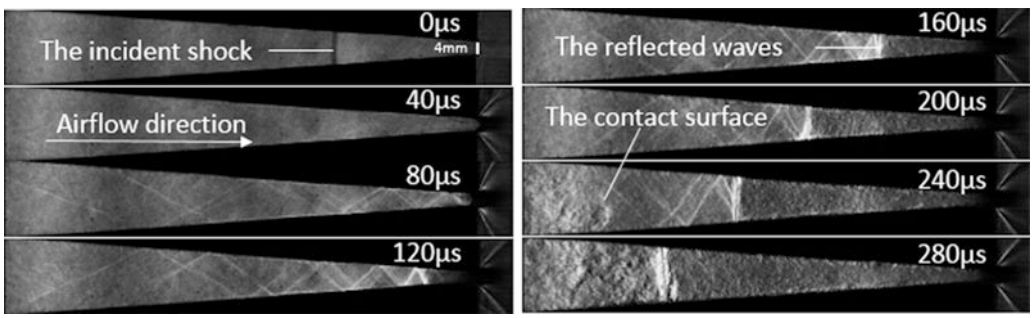

Fig. 3 Schlieren pictures of the cold flow of the shock convergence process. Experimental gas: 30%H_2 + 70%N_2. Initial pressure: 5.99 kPa. incident shock Mach number:3.0

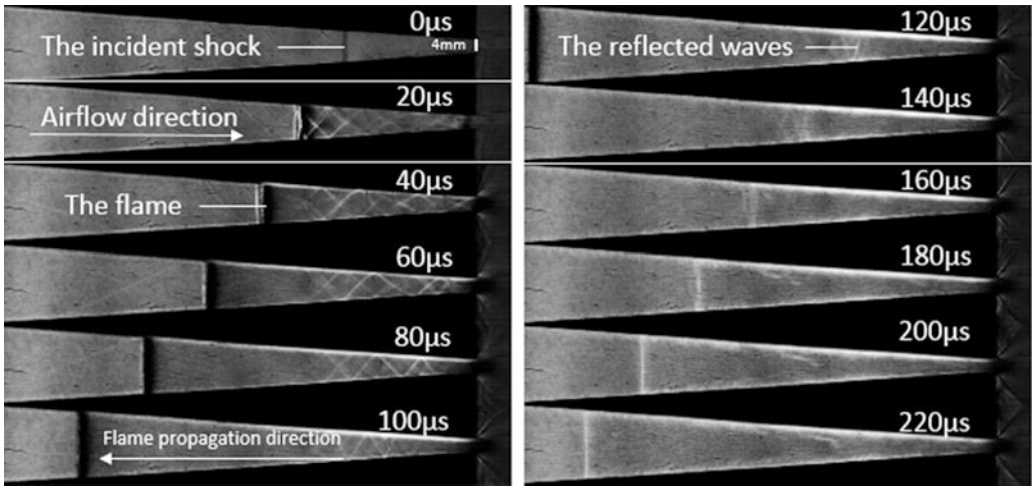

Fig. 4 Schlieren pictures of the ignition process induced by convergent shock experimental gas: 30%H_2 + 70%air. Initial pressure: 6.05 kPa. Incident shock Mach number: 3.0

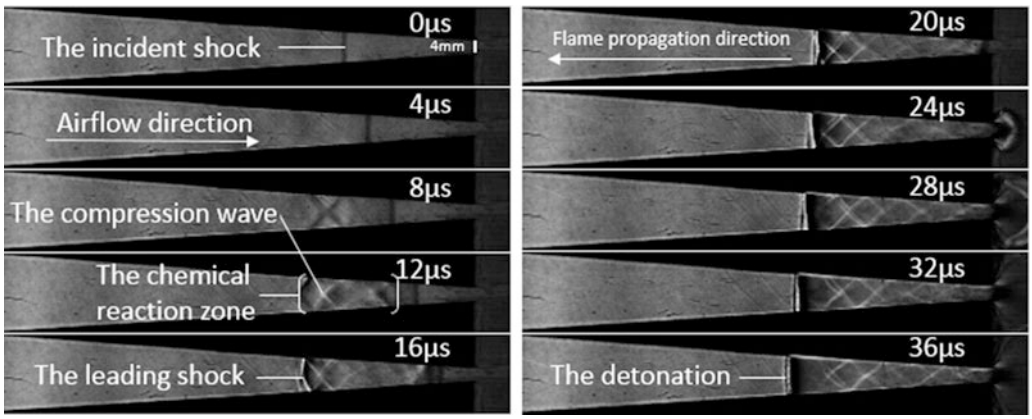

Fig. 5 Details of the ignition and flame propagation process

heated by the shock drops dramatically. The stacking of the induction time and the arrival time of the shock wave creates a pioneering point of ignition locates a bit distant behind the shock front. The chemical reaction zone grows rapidly and sends out compression waves propagating in both directions. The accumulation of the compression waves builds up pressure and temperature, which in turn enhances the chemical reaction in the flame. For the backward traveling wave, at about 16 μs, a coupled structure of a leading shock and a flame is established. The instable shock-flame structure accelerates gradually, which transforms into a detonation wave eventually (60 μs).

When the incident shock Mach number decreases, the location of ignition moves downstream. Before the occurrence of a completely dummy shot, the ignition may occur somewhere downstream of the outlet for a proper incident shock Mach number. The case may happen as well when the wedge channel is cut open earlier (therefore with a larger outlet) to expel the supposed ignition location.

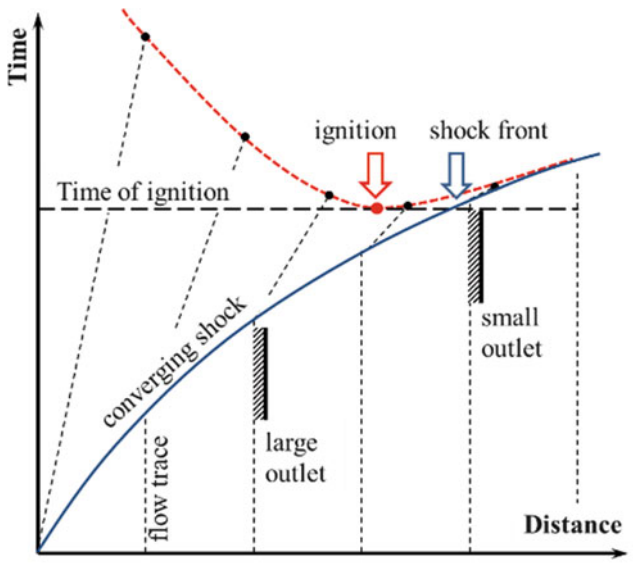

Fig. 6 X-t map illustrating the shock-induced ignition process

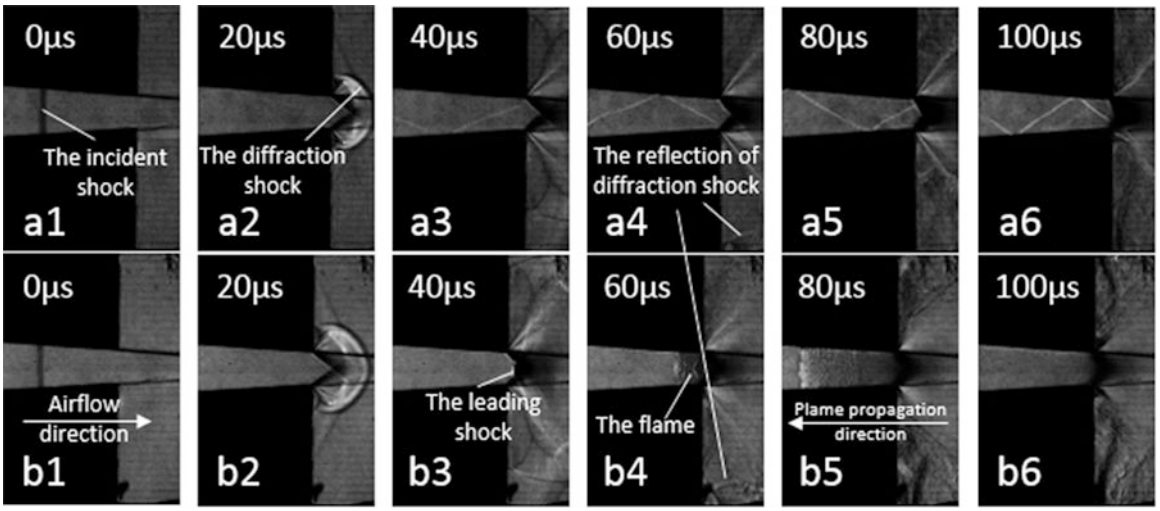

Fig. 7 Schlieren pictures of ignition occur downstream of the convergent channel. (**a**) Experimental gas: 30%H_2 + 70%N_2. Initial pressure: 7.21 kPa. Incident shock Mach number: 2.7. (**b**) Experimental gas: 30%H_2 + 70%air. Initial pressure: 7.25 kPa. Incident shock Mach number: 2.7

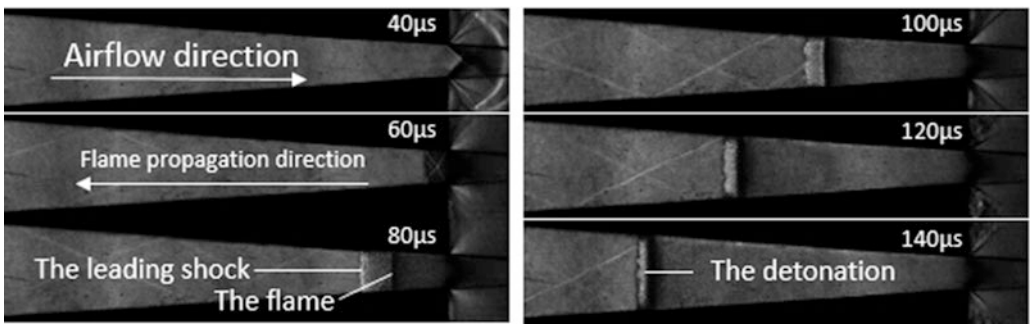

Fig. 8 Schlieren pictures of the flame propagation process in the channel

Figure 7 shows the flows around an 8 mm outlet with a relatively lower shock Mach number of 2.7. The upper images are for cold flow and the bottom are for reactive flow.

The early stage dynamic processes of the cold flow and the reactive flow are essentially identical. The incident shock wave runs into the open chamber of the dump section, which first diffracts at the frontal end of the chamber and then reflects on the upper and lower walls. Rarefaction fans develop from the corners of the outlet and intersect at the center. For the flow is supersonic, the head of the expansion fan leans toward the flow direction. Because the flow Mach number at the outlet keeps dropping, the rarefaction fans gradually go straight up. Upstream of the rarefaction fans is a zone that is not yet affected by the sudden expansion. For the reactive flow (Fig. 7b), an ignition occurs on the tip of undisturbed zone (40 μs). This can also be explained with Fig. 6. The large outlet locates upstream of the earliest possible ignition point marked with red dot. Therefore if there will be an ignition, the ignition will always happen at the frontier of the undisturbed zone. From Fig. 7b, one may find that the ignition seems to drive immediately a precursor shock wave which makes the flame possible to counterstrike the supersonic flow and propagate upstream into the channel. The further development of the shock-flame structure is demonstrated in Fig. 8. Velocity measurement suggests that the shock-flame structure is a detonation wave. Distorted wave front resulting from uneven ignition might be responsible for the thickened wave front structure.

Further decreasing the intensity of the incident shock, the pure cooking of the incident shock wave may not be able to cause an ignition. The flow can still be ignited nevertheless. The two sets of reflected shock waves from the upper and bottom walls of dump section may help to the ignition through a collision at the center of the jet flow.

Conclusions

1. In this paper, a new experimental method to realize a cylindrically focusing shock wave with little nonideal disturbances is presented and is utilized for the experimental study of shock-induced ignition in combustible gas. The experimental results confirm the feasibility and the superiority of the method.
2. It is found that the ignition process behaves differently for different compression degrees, and two kinds of ignition modes are observed. When the intensity of the incident shock is strong enough, the convergent shock induces directly a strong ignition of the combustible gas in the convergent channel. With the weakening of the incident shock wave, the ignition is delayed. When the incident shock Mach number goes below a certain value, the ignition occurs outside of the convergent channel. The corresponding ignition position is found to be the frontier of the supersonic zone unaffected by the expansion. For both modes, the flame finally develops to a detonation wave, and the heating and compression of the incident shock wave plays a dominant role for the ignition.

References

1. Vermeer, D.J., Meyer, J.W., Oppenheim, A.K.: Auto-ignition of hydrocarbons behind reflected shock waves. Combust. Flame **18**, 327–336 (1972)
2. Gelfand, B.E., Khomik, S.V., Bartenev, A.M., Medvedev, S.P., Gronig, H., Olivier, H.: Detonation and deflagration initiation at the focusing of shock waves in combustible gaseous mixture. Shock Waves **10**, 197–204 (2000)
3. Dimotakis, P.E., Samtaney, R.: Planar shock cylindrical focusing by a perfect-gas lens. Phys. Fluids **18**, 031705 (2006)
4. Hosseini, S.H.R., Takayama, K.: Experimental study of toroidal shock wave focusing in a compact vertical annular diaphragmless shock tube. Shock Waves **20**, 1–7 (2010)
5. Zhai, Z., Liu, C., Qin, F., Yang, J., Luo, X.: Generation of cylindrical converging shock waves based on shock dynamics theory. Phys. Fluids **22**, 041701 (2010)
6. Han, Z., Yin, X.: Shock Dynamics. Science Press, Beijing (1993)

Part VIII

Propulsion

Nonstationary Interaction of Incoming Flow with Ablative Jet in Supersonic Laser Propulsion

A.A. Schmidt and Yu. A. Rezunkov

Introduction

Laser propulsion is considered as a promising low-cost technology for many branches of space activity: satellite launches and orbit maneuvers, space cleaning, etc. Considerable efforts have been directed on investigations of laser propulsion engines (LPE) for space applications. Supersonic laser thrust producing in interaction of a laser-ablated jet with incoming supersonic gas flow in a nozzle can be perspective also for atmospheric flights. In this case laser thrust is formed due to transformation and additional acceleration of the flow behind the ablation region. The processes accompanying supersonic laser propulsion have been less investigated. A quasi-stationary regime of thrust generation at high-repetition rate of laser irradiation of supersonic jet was considered, for example, in [1], and was manifested as one of the perspective operation modes. In particular, in paper [2] for stationary regime, it was shown that possible efficient of laser thrust formation can reach level of 3×10^{-3} N/W.

However, results of numerical simulation presented in [2] demonstrate also that depending on parameters of the laser beam and of the incoming flow, stationary or quasi-stationary modes of laser propulsion can transit into significantly nonstationary regime even at stationary laser irradiation. This can dramatically affect the laser thrust.

The paper is devoted to analysis of nonstationary processes characteristic to supersonic laser propulsion. Numerical simulation has been carrying out of flows in a nozzle formed by ring nozzle wall, central body which is conical forebody and off-axial parabolic afterbody. The afterbody serves as laser beam concentrator (see Fig. 1). Interaction of the incoming flow with ring ablative jet due to irradiation of the nozzle wall by laser beam produces laser thrust.

Acceleration of the flow behind the ablative jet propagating from the focus of the off-axial paraboloid on the outer lip is seen. Domain in the vicinity of the off-axial paraboloid is characterized by low gas velocity and by pressure which is significantly higher than that in case without ablative jet.

Figure 2 demonstrates pressure distribution in the supersonic nozzle with the off-axis paraboloid, without ablative jet, (a), and with ablative jet, (b). It is seen that the ablative jet changes the flow structure significantly. As characteristic rarefaction zone downstream of the critical cross section disappears, the shock wave, appearing in the vicinity of critical cross section due to interaction of the incoming flow with the ablative jet, results in rise of the pressure in divergent part of the nozzle, near the afterbody, and, therefore, in rise of the thrust.

The paper is devoted to analysis of nonstationary processes characteristic to supersonic laser propulsion. Numerical simulation has been carrying out of flows in a nozzle formed by ring nozzle wall, central body which is conical forebody and off-axial parabolic afterbody. The afterbody serves as laser beam concentrator (see Fig. 1). Interaction of the incoming flow with ring ablative jet due to irradiation of the nozzle wall by laser beam produces laser thrust. Acceleration of the flow behind the ablative jet propagating from the focus of the off-axial paraboloid on the outer lip is seen. Domain in the vicinity of the off-axial paraboloid is characterized by low gas velocity and by pressure which is significantly higher than that in case without ablative jet.

A.A. Schmidt (✉)
Computational Physics Laboratory, Ioffe Institute, 194021 Saint Petersburg, Russia
e-mail: alexander.schmidt@mail.ioffe.ru

Yu.A. Rezunkov
Laboratory of Laser-Physical Investigations, Institute of Optoelectronic Instrument Engineering, Sosnovyi Bor, Russia

G. Ben-Dor et al. (eds.), *30th International Symposium on Shock Waves 1*, DOI 10.1007/978-3-319-46213-4_90

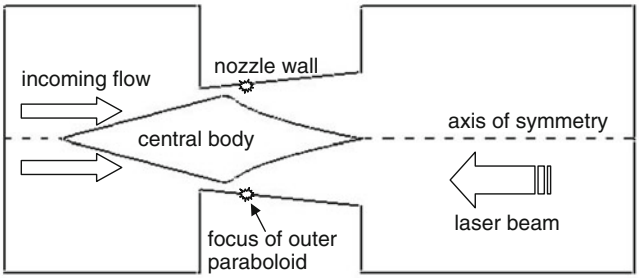

Fig. 1 Schematic diagram of the LPE nozzle

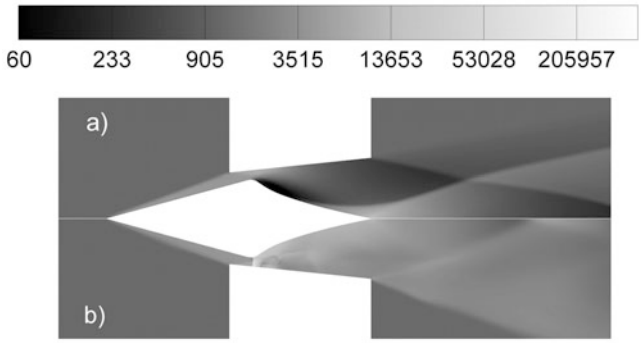

Fig. 2 Pressure distribution in the supersonic nozzle of LPE: without ablative jet (**a**) and with ablative jet (**b**)

Mathematical Model and Computational Method

A mathematical model is based on the Navier–Stokes equations. In this case, the model equations can be written in vector form as

$$\frac{\partial}{\partial t}\int_V \mathbf{W}dV + \int_S (\mathbf{F}-\mathbf{G})d\mathbf{S} = 0.$$

In these equations vectors **W**, **F**, and **G** can be written in conventional notation as

$$\mathbf{W} = \begin{bmatrix} \rho \\ \rho u \\ \rho v \\ \rho w \\ \rho E \end{bmatrix}, \quad \mathbf{F} = \begin{bmatrix} \rho\mathbf{V} \\ \rho\mathbf{V}u + p\mathbf{i} \\ \rho\mathbf{V}v + p\mathbf{j} \\ \rho\mathbf{V}w + p\mathbf{k} \\ \rho\mathbf{V}E + p\mathbf{V} \end{bmatrix}, \quad \mathbf{G} = \begin{bmatrix} 0 \\ \tau_{xi} \\ \tau_{yi} \\ \tau_{zi} \\ \tau_{ij}v_j + \mathbf{q} \end{bmatrix}.$$

These equations were used for solving the model problem in which the interaction of a 2D or axisymmetric supersonic flow at the surface of a plate or a cylinder with a transverse supersonic jet imitating an ablation torch was analyzed. We also considered the solution of the problem of a supersonic flow of a gas through the standard axisymmetric parabolic nozzle as well as the nozzle with an external paraboloid of revolution taking into account the interaction of the flow with transverse jets.

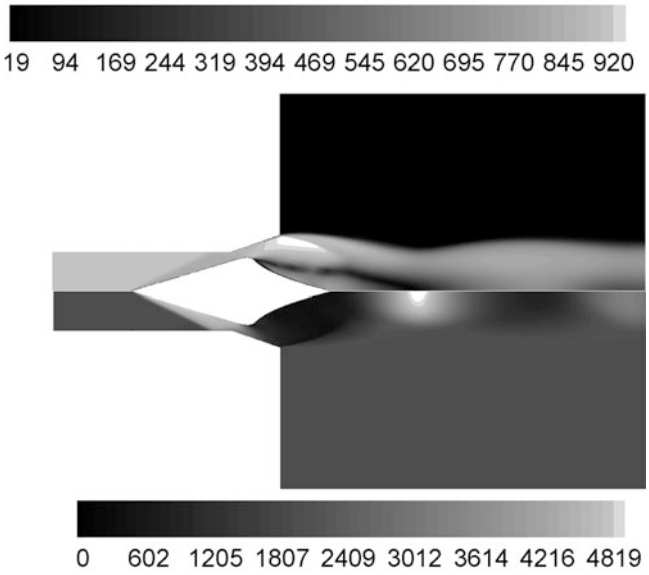

Fig. 3 Velocity (*upper*) and pressure (*below*) distributions in the LPE nozzle without ablative jet

In the numerical solution of the initial equations, their discretization and explicit linearization in the computational mesh are carried out. To improve the stability of the computational algorithm, a transition from the conservative to main variables was performed in the term containing the time derivative.

The main difficulty of numerical solution of the problem associates with the computation of convective fluxes at the faces of the control volume. For this purpose, the upwind scheme [3] is used. The scheme provides explicit expressions for convective fluxes at the faces of computational meshes without solving the Riemann problem.

Results

Two schemes of the LPE nozzle were considered. The first scheme is shown in Fig. 1; the second one differs from the first by the shape of the nozzle wall. Parabolic wall is chosen to focus the laser beam on the afterbody. Thus, the laser beam is focused on the nozzle wall by the off-axial parabolic afterbody and on the afterbody surface by the parabolic nozzle wall. The idea is to provide more efficient deposition of the laser energy and more intensive counter ablative jets.

Some results of LPE flow simulations for the first scheme are presented below. Interaction of the supersonic flow with the laser ablative jet in a parabolic nozzle (nozzle exit section diameter is 10 cm) is shown in Figs. 2, 3 and 4.

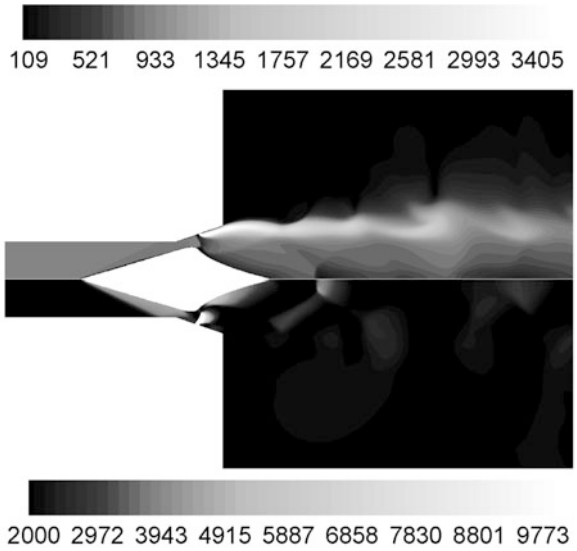

Fig. 4 Velocity (*upper*) and pressure (*below*) distributions with ablative jet

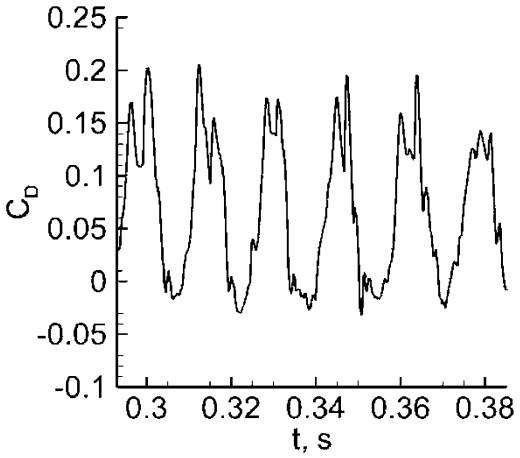

Fig. 5 Dependence of the pressure coefficient on time for high mass flow rate in ablative jet

Effect of the ablative jet at the mass flow rate equal to 0.07 kg/s is seen in Fig. 1. Comparison velocity and pressure distributions for the regimes with and without the ablative jet is presented in Figs. 3 and 4. The mass flow rate of the ablative jet is equal to 0.032 kg/s. The presence of the ablative jet results in redistribution of the velocity and pressure. The pressure in the flow is transformed in such a way that its peak is shifted to the nozzle wall. This, in turn, leads to producing thrust.

Analysis shows that laser propulsion production depends on the ablation mass flow rate. Comparison of Figs. 2 and 4 demonstrates rise of the pressure and, therefore, thrust, but the mass flow rate exceeds a certain value, the flow becomes unstable as well as the thrust production. Figure 5 presents typical variation in time of the pressure coefficient for the nozzle walls at $Q = 0.225$ kg/s.

Oscillating behavior of the pressure coefficient is a result of nonstationary processes accompanying interaction of the incoming flow and the ablative jet.

The second scheme which could be considered as more efficient in fact demonstrates poor thrust production which is probably due to losses in multiple shocks in the LPE nozzle flow. These shocks are results of interaction of counter ablative jets with each other and with incoming flow.

Conclusions

The above results demonstrate the possibility of effective formation of laser thrust as a result of the interaction of the ablative jet with the supersonic flow in the LPE nozzles. It appeared the increasing the deposited energy of the laser beam (or ablative jet mass flow rate) the structure of flow in the LPE becomes very complicated and unstable.

To increase the efficiency of supersonic laser propulsion, optimization of gasdynamic characteristics of initial flow, geometrical parameters of the LPE nozzle, and laser beam energy is necessary.

References

1. Shi, L., Chen, H., Ma, L., Chen, Y., Xu, Z., Hong, H. The influence of the in flow speed on air-breathing supersonic laser propulsion. Proc. of SPIE. **8904**: 8904ON (2013)
2. Rezunkov, Y., Schmidt, A.: Supersonic laser propulsion. Appl. Optics **53**, 31 (2014)
3. Roe, P.L.: Characteristic-based schemes for the Euler equations. Annu Rev Fluid Mech. **18**, 337–365 (1986)

Axisymmetric Compressible Flow for the Resistojet Thruster Module

S.M. Chang

Introduction

NEXTSat-1 is the next-generation small-size artificial satellite system planed by the Satellite Technology Research Center (SatTReC) in Korea Advanced Institute of Science and Technology (KAIST). For the control of attitude and transition of the orbit, the system has adopted a RHM (Resistojet Head Module), which has a very simple geometry with a reasonable efficiency.

The basic concept of resistojet thruster combines the simplicity of heating inert gas and economic feasibility for the propulsion of small space vehicles [1]. In addition to these design qualities, gas thrusters reduce spacecraft contamination and pollution in low-altitude orbit near the earth. However, the performance of a resistojet is substantially less than other propulsive methods, for example, the specific impulse is 48 s using a driver gas of Xe in a commercial thruster [2]. To improve this, the operating temperature must be increased, but the limitations of thermal management in space make this challenging.

In preliminary research [3], the microscale shock wave structure of a resistojet is studied in the region of underexpanded jet. A model of the axisymmetric flow is proposed to study the effect of geometry. Several key parameters were investigated using numerical simulation for the optimization of output performance. A simplified nozzle shape is designed to maximize the specific impulse (ratio between the thrust force and the mass flow rate), considering the viscous and thermal conduction effects in the gas and structure.

Experiment and Computation

The experimental apparatus is motivated from the PCV (Positive Crankcase Ventilation) valve that is installed at the intake channel of internal combustion engines to recirculate the blow-by gas leaked from the piston ring. This valve contains a very small gap that controls the gas mass flow. Figure 1a, b is the experimental setup to measure the mass flow rate for given vacuum pressure, which is linked to the dump tank of an expansion tunnel.

In Fig. 1b, the domain of interest is located between two pressure transducers. The circular rod, inserted along the center line, is adjusted with micrometer. The inlet is exposed to the ambient air, and the flow passes through a MFM (mass flow meter) at the vacuum side.

For the corresponding computation, the axisymmetric, compressible Navier–Stokes equations [4] are simulated:

$$\begin{aligned}
&\frac{\partial}{\partial t}\begin{pmatrix}\rho\\ \rho u_r\\ \rho u_z\\ \rho e\end{pmatrix}+\frac{\partial}{\partial r}\begin{pmatrix}\rho u_r\\ \rho u_r^2+p\\ \rho u_r u_z\\ \rho u_r\left(e+\frac{p}{\rho}\right)\end{pmatrix}\\
&+\frac{\partial}{\partial z}\begin{pmatrix}\rho u_z\\ \rho u_r u_z\\ \rho u_z^2+p\\ \rho u_z\left(e+\frac{p}{\rho}\right)\end{pmatrix}+\frac{1}{r}\begin{pmatrix}\rho u_r\\ \rho u_r^2\\ \rho u_r u_z\\ \rho u_r\left(e+\frac{p}{\rho}\right)\end{pmatrix}\\
&=\begin{pmatrix}0\\ \frac{\partial\tau_{rr}}{\partial r}+\frac{\partial\tau_{rz}}{\partial z}\\ \frac{\partial\tau_{rz}}{\partial r}+\frac{\partial\tau_{zz}}{\partial z}\\ \frac{\partial q_r}{\partial r}+\frac{\partial q_z}{\partial z}+\Phi\end{pmatrix}+\frac{1}{r}\begin{pmatrix}0\\ \tau_{rr}-\tau_{\theta\theta}\\ \tau_{rz}\\ u_r\tau_{rr}+u_z\tau_{rz}\end{pmatrix}
\end{aligned}\tag{1}$$

S.M. Chang (✉)
School of Mechanical and Automotive Engineering, Kunsan National University, 558 Daehak-ro, Gunsan-shi, Jeonbuk 54150, Korea
e-mail: smchang@kunsan.ac.kr

G. Ben-Dor et al. (eds.), *30th International Symposium on Shock Waves 1*, DOI 10.1007/978-3-319-46213-4_91

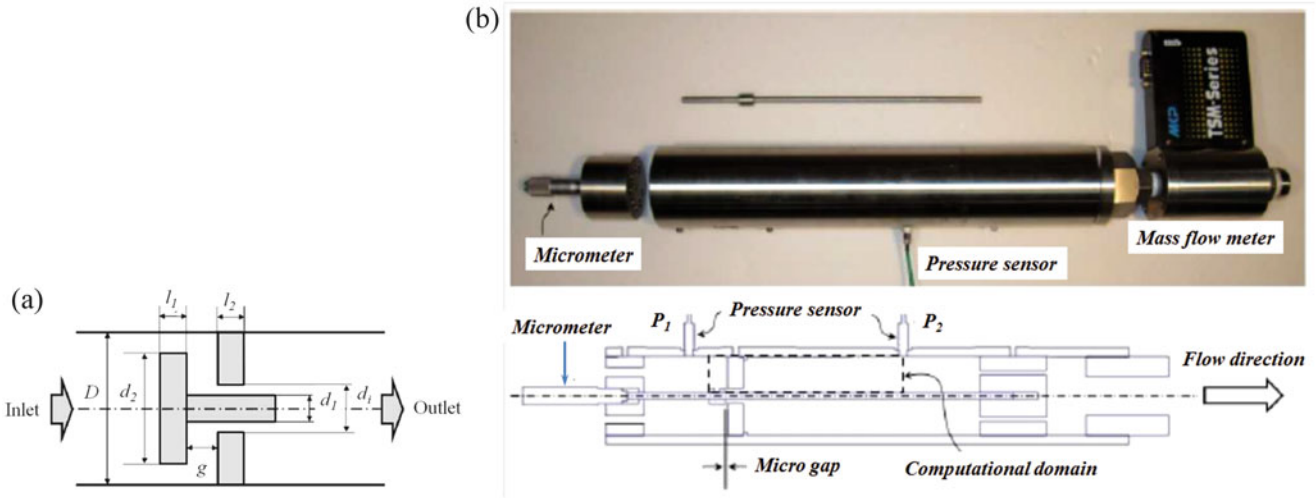

Fig. 1 Experimental apparatus: (**a**) schematic, (**b**) photograph, and drawing

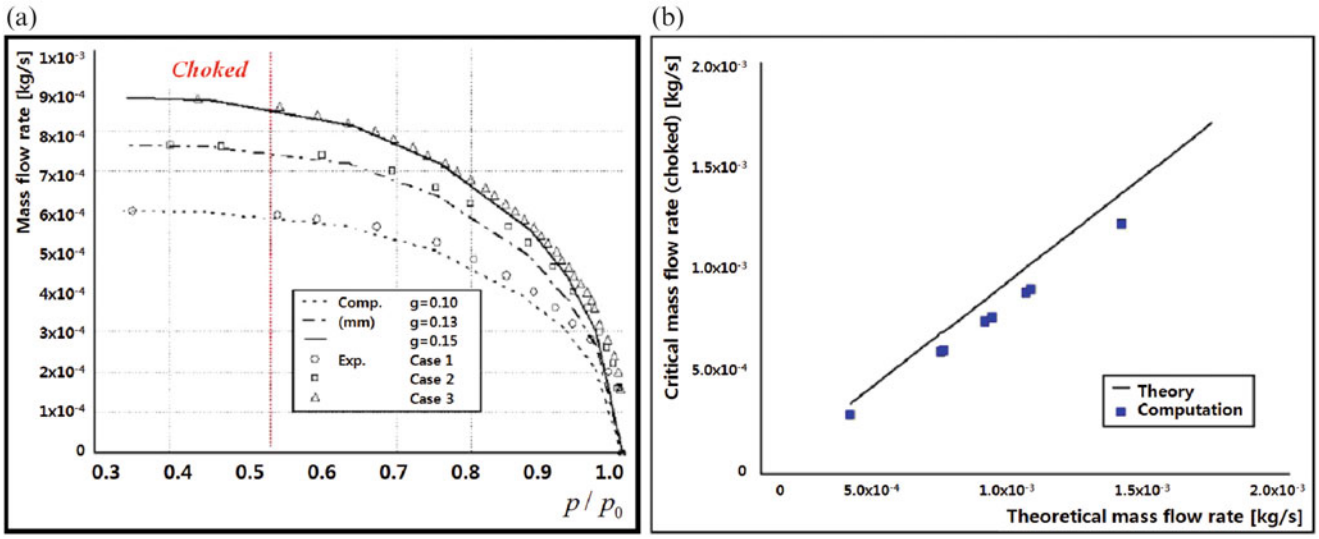

Fig. 2 Mass flow rate comparison with (**a**) experiment and (**b**) computation

where

$$q_r = k\frac{\partial T}{\partial r},\ q_z = k\frac{\partial T}{\partial z},\ T = \frac{(\gamma-1)}{R}\left[e - \frac{1}{2}\left(u_r^2 + u_z^2\right)\right];$$

$$\tau_{rr} = \mu\left(2\frac{\partial u_r}{\partial r} - I\right),\ \tau_{rz} = \mu\left(\frac{\partial u_z}{\partial r} + \frac{\partial u_r}{\partial z}\right),$$
$$\tau_{zz} = \mu\left(2\frac{\partial u_z}{\partial z} - I\right),\ \tau_{\theta\theta} = \mu\left(2\frac{u_r}{r} - I\right)$$

$$I = \frac{2}{3}\left(\frac{\partial u_r}{\partial r} + \frac{u_r}{r} + \frac{\partial u_z}{\partial z}\right);\ \Phi = \frac{\partial}{\partial r}\left(u_r\tau_{rr} + u_z\tau_{rz}\right) + \frac{\partial}{\partial z}\left(u_r\tau_{rz} + u_z\tau_{zz}\right)$$

and ρ is density, (u_r, u_z) are radial and axial component of velocity, p is static pressure, T is absolute temperature, k is the thermal conductivity, γ is the specific heat ratio, μ is the dynamic viscosity, and $R \equiv \Re/M$ is the gas constant where $\Re$ and M are the universal gas constant and molecular mass per unit mole, respectively.

The computational domain is also marked in Fig. 1b. A special treatment for the jet boundary condition is used at the outlet. The no-slip condition is used for the wall boundaries. The subsonic flow from the inlet is accelerated to supersonic flow after passing through the throat formed by the gap. The flow downstream of the gap is under-expanded.

Figure 2a, b is the comparison of computed and measured mass flow rate. The mass flows in the experiment are slightly higher than those of computation near $p/p_0 \approx 1$ in

Fig. 2a since the effect of viscosity is dominant in the slow flow regime, while the computational value of choked mass flow rates is less than those of theoretical ones in Fig. 2b, which is affected by the thickness of boundary layer and heat loss at the wall.

The full structure of waves inside the under-expanded flow region is shown in the zoomed view, Fig. 3a–d. The pressure is expanded from the gap to low pressure in Fig. 3a, and the complex wave structure at the jet boundary is sketched in Fig. 3b. Inside the jet boundary, shocks and expansion waves are observed to reflect from the jet slip layer. The reflected waves change from compression to expansion or vice versa. In Fig. 3c, the Mach number indicates that the flow is accelerated to supersonic where the maximum is over $M > 3$ in a region of 8 mm from the gap. Figure 3d visualizes acceleration and deceleration by compressive and expansive waves inside the jet, respectively.

Application to Thruster

One of the proposed thruster designs is the electrical gas thruster shown in Fig. 4. A multiphysics simulation for the axisymmetric body has been developed for the conceptual design of the RHM for NEXTSat-1 project, and the objective specific impulse is targeted more than 60 s [5]. The computational domain and boundary conditions are also shown in Fig. 4. The heat conduction equation is solved in the solid body with radiation boundary condition at the outer surface.

$$c_p \frac{\partial T}{\partial t} = \frac{1}{r}\frac{\partial}{\partial r}\left(kr\frac{\partial T}{\partial r}\right) + \frac{\partial}{\partial z}\left(k\frac{\partial T}{\partial z}\right) + q_s \qquad (2)$$

where c_p is the heat capacity and q_s is the heat source per unit time and mass.

A FEM (finite element method)-based commercial code, COMSOL Multiphysics ver. 4.4, is used for the solution of Eqs. (1) and (2). At the exit of nozzle, the flow is highly under-expanded to the pressure corresponding to an altitude of 800 km, and we expect to obtain a jet structure similar to Fig. 3, and the Knudsen number should be considered in assessing the validity of the Navier–Stokes equations. The calculated value is $\mathrm{Kn} = 0.005$ within the main part of the nozzle.

Figure 5a–d is the sample of field properties plotted for the RHM model: (a) pressure from the stagnation from the gas tank is $p_0 = 3$ bars; (b) Mach number at the nozzle exit is up to 7.57 but affected by the viscous boundary layer at the nozzle wall; (c) the maximum local gas temperature is 2,099 K to overcome the heat loss from the body; and (d) the maximum local temperature at the solid is 5 K more than that of the gas. The material properties of body must be carefully considered to ensure long thruster life at these temperatures.

The optimized design parameter is the specific impulse (I_s) with the unit of time, defined as the ratio between net thrust force (F_z) and mass flow rate ($\dot{m}$), which is divided by the gravitational acceleration (g_0) at the surface of the earth:

$$I_s = \frac{F_z}{\dot{m}\, g_0} \qquad (3)$$

The integrated values in Eq. (3) are obtained as:

$$\dot{m} = 2\pi \int_0^{R_e} \rho u_z r dr \qquad (4)$$

$$F_z = 2\pi \int_0^{R_e} \left(\rho u_z^2 + p\right) r dr \qquad (5)$$

where u_z is the velocity component in the axial direction and R_e is the inner radius at the nozzle exit.

The result of the parametric study is given in Table 1. The optimum nozzle was smaller and slenderer than the baseline device. To maximize specific impulse, the diameter of nozzle throat and the slant length of nozzle are decreased, and the angle from the axis of symmetry is also decreased from the baseline. The increase of specific impulse is 5.8 %

Conclusions

The conceptual design of RHM model for the operation of a small artificial satellite system is analyzed using a numerical simulation technique for an axisymmetric compressible flow. The highly under-expanded jet flow through an annular gap is studied with both experiments and computations. The conceptual design of RHM of NEXTSat-1 was optimized to obtain a 5.8 % improvement of specific impulse using a simplified choice of parameters.

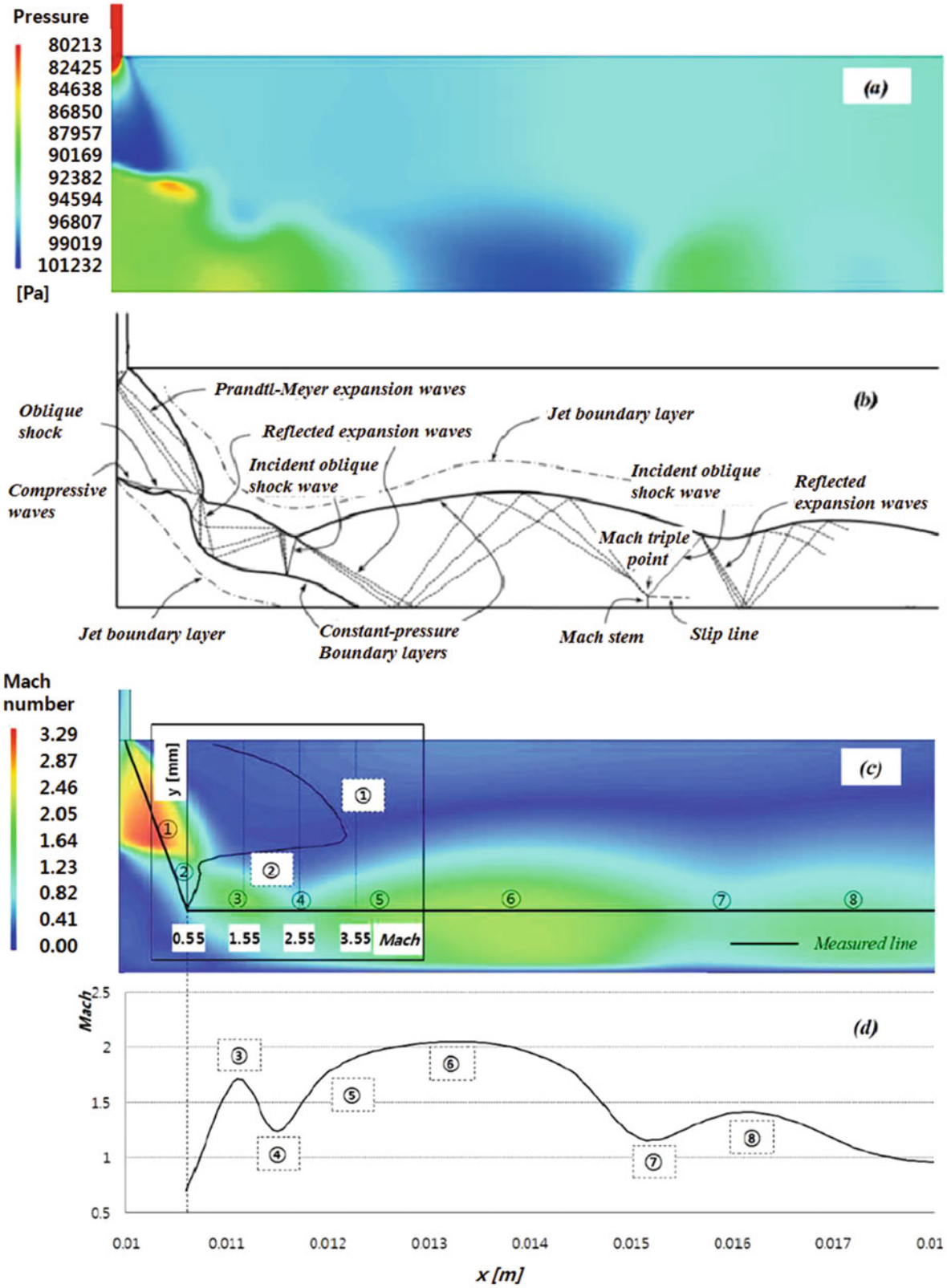

Fig. 3 Zoomed view of computational results: (**a**) pressure, (**b**) schematic of waves, (**c**) Mach number, and (**d**) Mach number along jet axis

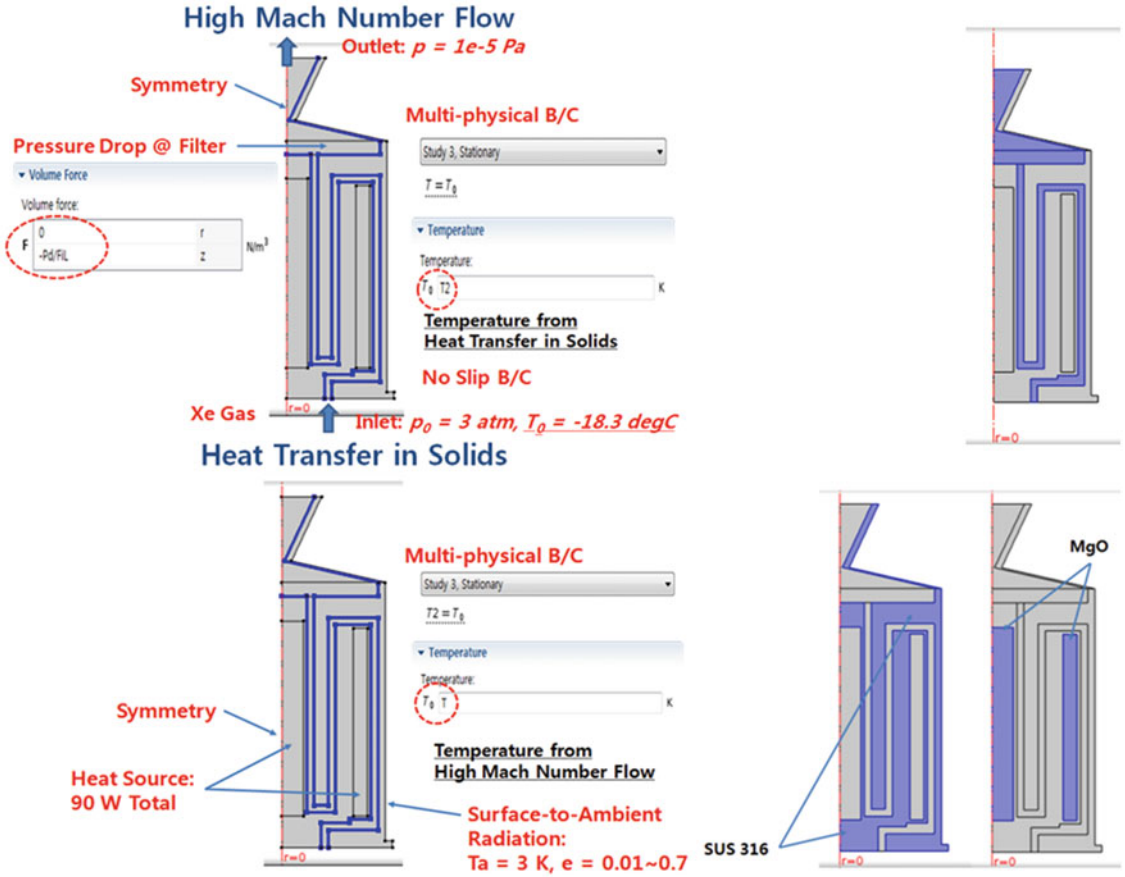

Fig. 4 Computational domain and boundary condition for the simulation of RHM

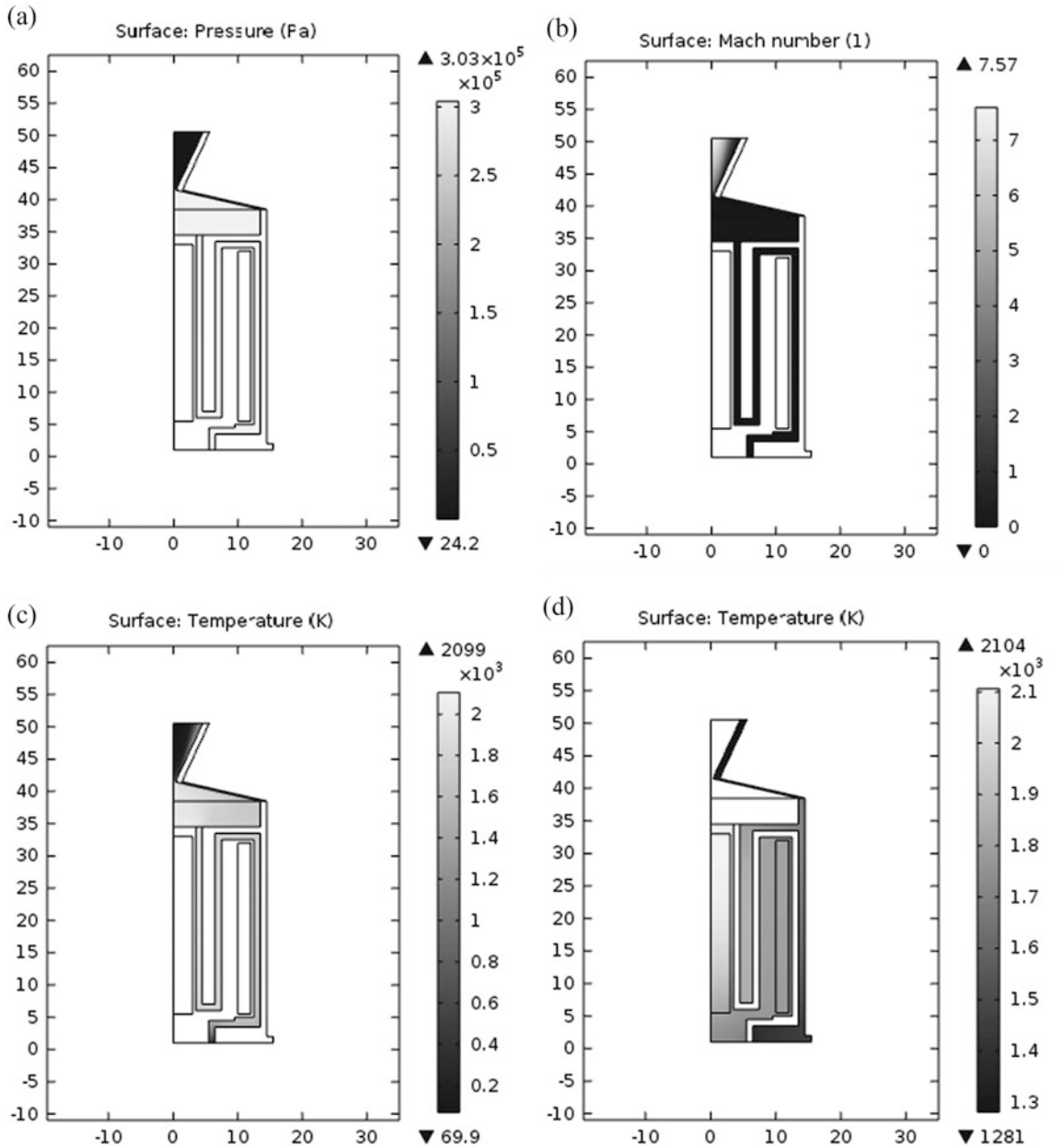

Fig. 5 Computation of the baseline case: (**a**) pressure, (**b**) Mach number, (**c**) temperature of gas, and (**d**) temperature of solid

Table 1 Parameters of baseline and final design

Design	Parameter *(Symbol)*	Value	Unit
Baseline	Power ratio, pre-/main	40/50	*W/W*
	Throat diameter (d)	0.7	*mm*
	Slant length of nozzle (L_s)	10	*mm*
	Angle of nozzle (θ)	30	*deg.*
	Depth of reservoir(Δz)	4	*mm*
	Mass flow rate ($\dot{m}$)	0.217	*g/s*
	Thrust force (F_z)	131	*mN*
	Specific impulse (I_s)	61.6	*s*
Final	Power ratio, pre-/main	0/90	*W/W*
	Throat diameter (d)	0.6	*mm*
	Slant length of nozzle (L_s)	7.5	*mm*
	Angle of nozzle (θ)	27.5	*deg.*
	Depth of reservoir(Δz)	2	*mm*
	Mass flow rate ($\dot{m}$)	0.149	*g/s*
	Thrust force (F_z)	95.1	*mN*
	Specific impulse (I_s)	65.1	*s*

References

1. Jahn, R.G., Choueiri, E.Y.: Electric Propulsion article in Encyclopedia of Physical Science and Technology, vol. 5, 3rd edn, pp. 125–141. Academic, San Diego (2002)
2. Surrey Satellite Technology US LLC. Surrey Micro Gas Propulsion System. http://www.sst-us.com/downloads/datasheets/gas-propulsion-system
3. Kim, S.S., Chang, S.M.: Compressibility effect in the axisymmetric internal flow past a microgap. Trans. KSME B. **34**(12), 1061–1069 (2010)
4. Sandberg, R.D., Fasel, H.F.: Numerical investigation of transitional supersonic axisymmetric wakes. J. Fluid Mech. **563**(1), 1–41 (2006)
5. Chang, S.M., Choi, J.C., Han, C.Y., Shin, G.H.: Multi-physical simulation for the design of an electric resistojet gas thruster in the NEXTSat-1. J. Comput. Fluids Eng., 21(2), 112–119 (2016)

Secondary Injectant Gas Thermodynamic Properties Effects on Fluidic Thrust Vectoring Performances of a Supersonic Nozzle

A. Chpoun, M. Sellam, V. Zmijanovic, and L. Leger

Introduction

The transverse injection in a supersonic cross-flow is problematic which can be encountered in several aerodynamic applications such as fuel injection in scramjet combustor, missile control, drag reduction, and thrust vector control. In recent years, an extended analytical, numerical, and experimental work has been carried out by the authors [1, 2] to investigate the vectoring performances of a supersonic axisymmetric nozzle using secondary fluid injection. Secondary gas injection thrust vector control (SITVC) or shock vector control (SVC) is considered as an alternative way to control the thrust direction of a rocket nozzle beside the classical use of mechanical device such as fluidic actuators. In the context of SITVC operation, the nature and source of injectant gas may raise efficiency-related issues. In previous studies [3–6], it is well established that injection of gas with low molar mass promotes better jet penetration and therefore will be a better choice for SITVC operation. To assess this point, an experimental test campaign has been conducted in the hypersonic test facility EDITH of the CNRS institute ICARE in Orléans, France. The focus of the study is to analyze the secondary injectant gas thermodynamic properties influence on the global vectoring performance of a supersonic nozzle. For this purpose, performance aspects of fluidic thrust vectoring concept have been experimentally investigated on a truncated ideal contour (TIC) nozzle model using a variety of gas species (with low to moderate molar mass) as injectant. Qualitative and quantitative diagnostics consisted of Z-Schlieren visualization, 3-axis force balance, and static and dynamic parietal pressure measurements. The experimental results are compared to the numerical and analytical findings.

A. Chpoun (✉) • M. Sellam
Laboratoire de Mécanique et d'Energétique d'Evry LMEE, Université d'Evry Val d'Essonne, 40 rue du Pelvoux, 91020 Evry Cedex, France
e-mail: a.chpoun@iut.univ-evry.fr

V. Zmijanovic • L. Leger
Institut ICARE/CNRS, 1C avenue de la recherche scientifique, Orléans, France

Analytical and Numerical Approaches

The cross injection of a secondary sonic jet into a main supersonic flow due to its practical relevance was extensively investigated by many authors. In some works, the phenomenon was analytically modeled [7]. The main purpose of the analytical model was to draw a relation between the injectant fluid properties, the main and secondary flows stagnation conditions, and the secondary jet penetration height as a main relevant parameter. In short, the analytical model was based on the concept of the secondary flow acting as a blunt body vis-à-vis the main flow (Fig. 1). The 1D momentum and mass conservation laws are applied to the flow surrounding the obstacle. Depending on the geometry of the injection orifice, circular or slot, the fluidic obstacle is assumed as being a quarter sphere or a quarter cylinder, respectively. The model necessitates additional correlations for the magnitude of the plateau pressure and the flow separation region beginning and extension. Later, the analytical approach was successfully applied by Mangin [7] to the shock-induced thrust vector control of a planar (2D) nozzle. The present analytical model proposed by the authors is an extension to axisymmetrical nozzle of the latest mentioned work. It fully takes into account the axisymmetrical nature of the flow for the pressure gradient and the boundary layer calculations. A detailed description of the model can be found in Ref. [2].

For the numerical part of the work, a finite-volume 3D code CPS developed by Bertin and CNES (Centre National d'Etudes Spatiales) for propulsive nozzle flows has been employed. The code solves Favre Averaged Navier–Stokes (FANS) equations for compressible multispecies reacting flows with fully accounted viscous effects on an unstructured 3D computational grid. Time splitting is used for the

G. Ben-Dor et al. (eds.), *30th International Symposium on Shock Waves 1*, DOI 10.1007/978-3-319-46213-4_92

explicit scheme of order up to four in time and up to three in space. The fluxes are computed on the cell interfaces with HLLC (by Toro) scheme or Roe's upwind difference splitting scheme for ideal gases. In the present study, flux vectors are evaluated at each time step using a second-order scheme. The turbulence is modeled using the classical k − ε closure. Main airflow and secondary gas injectant are modeled as perfect gases with power-law expressions for $\gamma(T)$ and $C_p(T)$ as seventh degree polynomials. Integration is achieved with a fully explicit solver, setting the time step control range from unsteady for highest time accuracy to the steady optimized time step with the Courant–Friedrichs–Lewy (CFL) condition parameter up to 0.3.

Figure 2 shows a typical mesh used in the computations. It contains 5.15 million mapped hexagonal elements in the nozzle domain and 1.05 million in the exterior domain. Preliminary studies of grid convergence have been carried out. The final computations were done and are presented here according to the conclusions drawn from the preliminary studies.

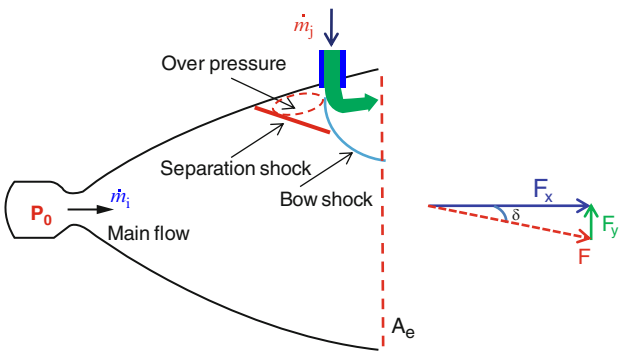

Fig. 1 Schematic view of fluidic thrust vectoring

Experimental Work

The experiments were conducted in the EDITH hypersonic/supersonic test facility of ICARE/CNRS institute at Orléans, France. Initially, it was a continuous running Mach 5 wind tunnel supplied with 9 bars total pressure by a volumetric compressor. At downstream side, the pressure in the test chamber is lowered by two powerful volumetric vacuum pumps of a total 345 KW power. The authors modified the installation in order to perform tests on small-scale nozzle. Small test nozzles were placed inside the test chamber to take advantage of high vacuum environment supplied by pumps. It permits to simulate high-altitude operation conditions. In the modified version of the installation, clean, oil-free air is first dried, compressed till 300 bars, and stored in several 320 L tanks. The air is supplied via 8 mm pipeline system to a pressure regulator and after to a radial flow splitter. Through six uniformly distributed 8 mm tubes, air is supplied to the settling chamber of 160 mm diameter and 200 mm length and exhausted through the nozzle into the depressurized tunnel test section.

The secondary flow gas is furnished to a second settling chamber and then smoothly injected via a convergent duct into the tested nozzle. For the secondary flow, pressurized 80 L bottles are used as the source for helium, argon, carbon dioxide, and nitrogen tests. A schematic view of the test bench is given in Fig. 3.

Results

The investigation was conducted to examine four injectant gas species of different molar mass (air, He, CO_2, Ar) (Table 1) on two major injection condition sets: setting the

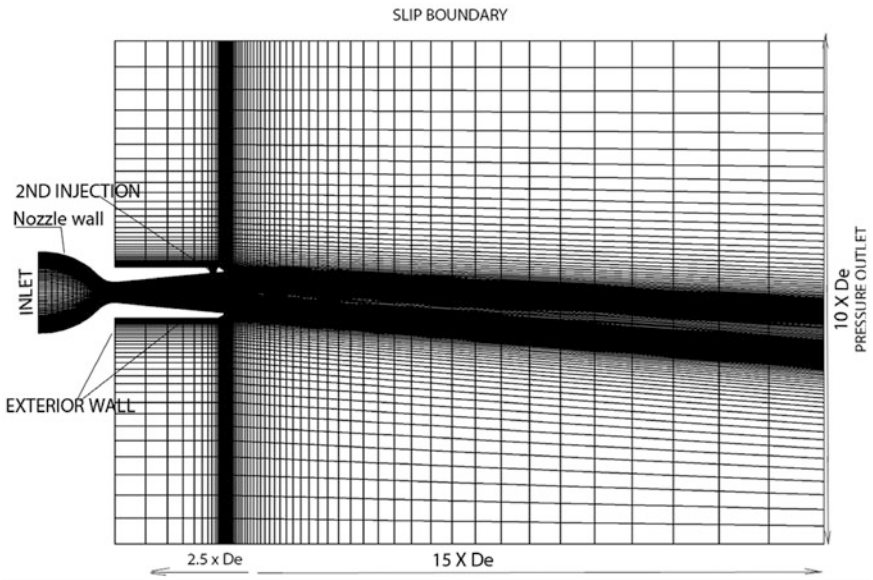

Fig. 2 A typical mesh used in computations

Fig. 3 Experimental installation

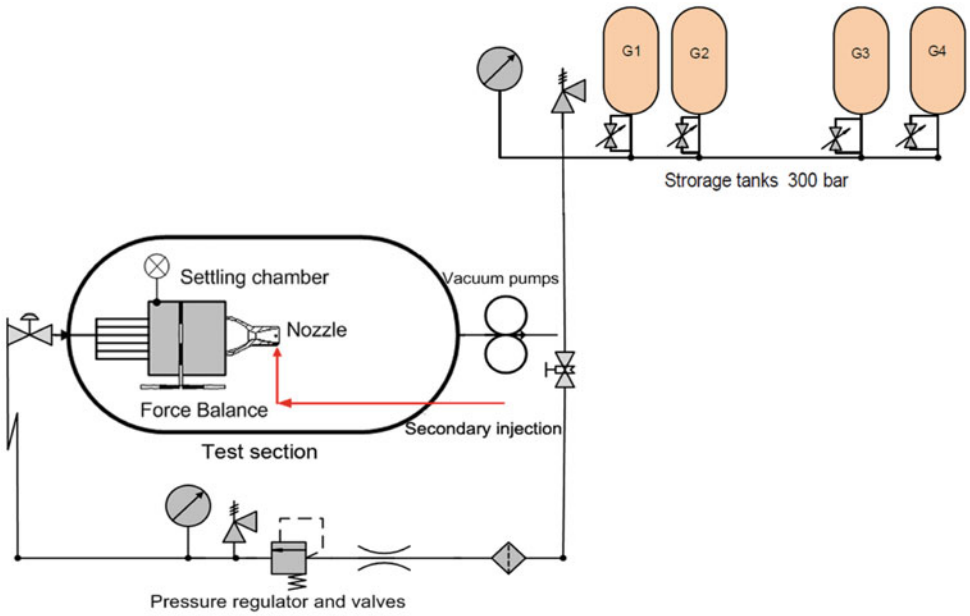

Table 1 Thermodynamic gas properties and corresponding injection conditions

	M_{gj}	γ_{gj}	$M_{gj}\gamma_{gj}$	f_m (SPR = 1)	SPR (P_{0j}/P_0) ($f_m = 0.076$)
Air	28.960	1.4	40.544	0.076	1.
He	4.0026	1.66	6.6698	0.03	2.534
Ar	39.948	1.66	66.460	0.095	0.803
CO_2	44.009	1.29	57.080	0.091	0.833

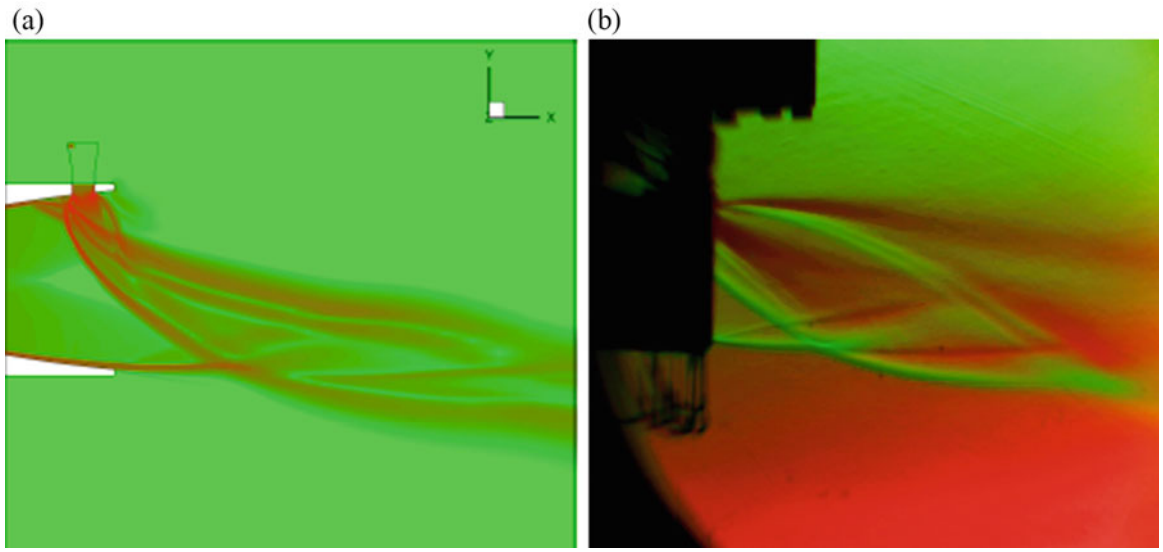

Fig. 4 Numerical (**a**) and experimental (**b**) Schlieren for SPR = 1 (CO_2 into Air)

constant secondary injection pressure ratio (SPR) for all species and by setting constant the secondary to the main flow mass flow rates f_m.

Figure 4 shows the flow topology extracted from numerical results (left) by plotting density gradients and that obtained by bicolor Schlieren technique. The case corresponds to the injection of a secondary flow of carbon dioxide into the main airflow for SPR = 1. The two visualizations show a global di-symmetry in flow topology resulting in side forces. The flow structures are similar from

both approaches. The difference between the two pictures can be explained by the difference between the two visualization techniques; the numerical Schlieren represents the extracted density gradient on the plane of symmetry, whereas the experimental Schlieren technique integrates these density gradients over the full depth of the nozzle jet flow. It is worth to mention that the flow details inside the nozzle can only be shown from numerical results. However, both pictures show the fluidic obstacle bow shock leaving the nozzle and interacting with the expanding jet boundary.

Iso-Mach contours in the symmetry plane of the nozzle from numerical simulations are presented in Figure 5. The left (a) and middle (b) plots correspond, respectively, to the injection of argon and carbon dioxide which have close molar mass, whereas the right (c) plot corresponds to the injection of helium with a lower molar mass. In all cases, the secondary mass flow rates were the same corresponding to a secondary to the main flow mass flow rates of $f_m = 0.076$. Numerical results show that in the case of helium injection, the secondary jet penetrates deeper inside the nozzle resulting in a more extended flow separation zone. Therefore, the performance of helium-based SITVC operation is better than those employing argon and carbon dioxide.

Tables 2 and 3 show, respectively, the vectoring performances in term of thrust deviation angle δ for different injectant/main flow gas couples and for different secondary injection conditions. From these results, it is evident that it is possible to achieve better vectoring performance for the same pressure ratio with smaller mass flow rate as is the case of a lighter gas as helium comparing to the more inert gas species. In other words, one can achieve a far better deviation angle with the same mass flow rate using helium as injectant.

As a consequence, the mass of injectant gas required for a launcher controlling task can be divided by a factor of two or more depending on the molar mass of the gas.

This trend is also depicted in Fig. 6 which shows comparison between numerical, analytical, and experimental approaches for the thrust vectoring angle evolution versus the ratio of injectant to the main flow gas product of gas molar mass and specific heats ratio. It is well known that this parameter plays a dominant role in the jet penetration phenomenon. The comparison between numerical, analytical,

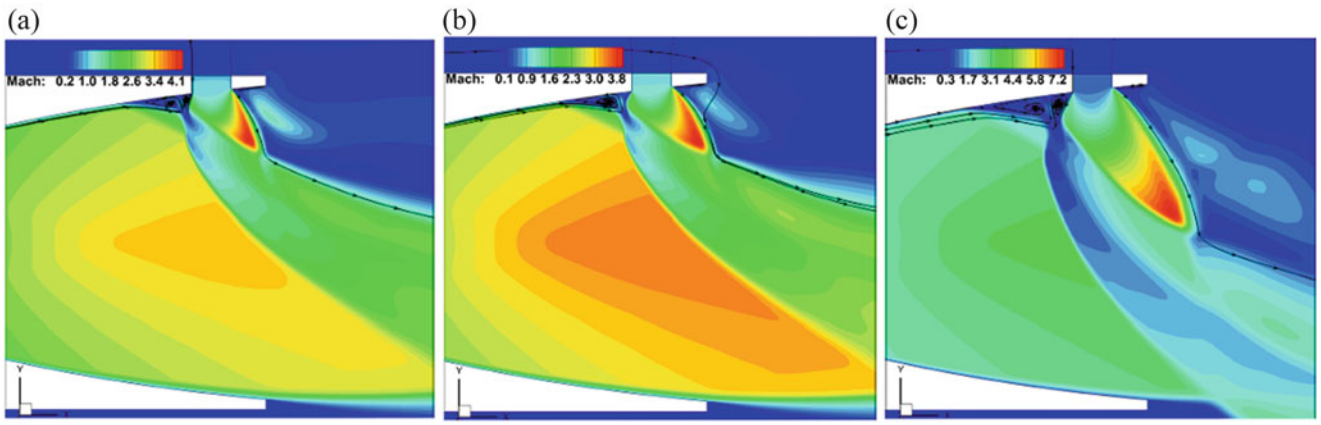

Fig. 5 Mach contours plots, (**a**) Ar-Air, (**b**) CO_2-Air, (**c**) He-Air, in symmetry plane of the TIC nozzle at $f_m = 0.076$

Table 2 Force components and thrust vector pitch angle at SPR = 1

	f_m	$\Sigma F_{ynum}[N]$	$\Sigma F_{yexp}[N]$	$\Sigma F_{y\ mod}[N]$	$\Sigma F_{xnum}\ [N]$	$\Sigma F_{x\ exp}[N]$	$\Sigma F_{x\ mod}[N]$	$\delta\ [^\circ]_{num}$	$\delta\ [^\circ]_{exp}$	$\delta\ [^\circ]_{mod}$
Air–air	0.076	16.473	16.37	16.03	136.21	131.1	134,23	6.89	7.1 ± 0.5	6.81
He–air	0.0303	16.958	18.6	16.27	136.13	133.1	134,23	7.10	8.0 ± 0.5	6.91
Ar–air	0.096	16.615	17.13	17,27	136.22	130.8	134,23	6.95	7.4 ± 0.5	6.91
CO_2–air	0.092	16.135	16.55	15.93	136.97	130.2	134,23	6.76	7.2 ± 0.5	6.76

Table 3 Force components and thrust vector pitch angle at $f_m = 0.076$

	SPR	$\Sigma F_{y\ num}\ [N]$	$\Sigma F_{y\ exp}\ [N]$	$\Sigma F_{y\ mod}\ [N]$	$\Sigma F_{x\ num}\ [N]$	$\Sigma F_{x\ exp}\ [N]$	$\Sigma F_{x\ mod}\ [N]$	$\delta\ [^\circ]_{num}$	$\delta\ [^\circ]_{exp}$	$\delta\ [^\circ]_{mod}$
Air–air	1.0	16.473	16.37	16.03	136.21	131.1	134,23	6.89	7.1	6.81
He–air	2.534	39.251	/	34.18	135.11	/	134,53	16.20	/	14.25
Ar–air	0.803	13.967	12.7	14.06	135.94	129.6	134.16	5.87	5.6	5.98
CO_2–air	0.833	13.062	10.42	13.46	135.68	139.8	134.16	5.49	4.6	5.73

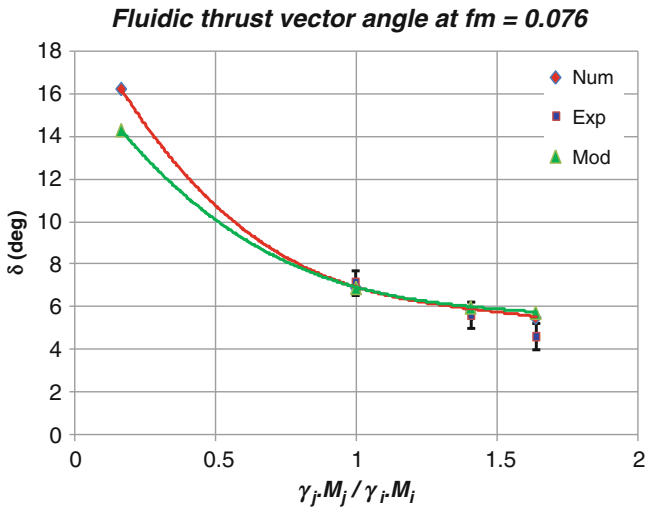

Fig. 6 Fluidic thrust vectoring angles

and experimental methods shows the same trend and gives close results considering error margin in all these triple approaches.

Summary and Conclusion

Supersonic nozzle thrust vector control by mean of secondary fluid injection has been investigated experimentally, numerically, and analytically. The main focus of the study was to investigate the injectant gas thermodynamic properties on vectoring efficiency. The study showed that significant vectoring angle (up to 15°) can be achieved with secondary to primary mass flow rates ratio of 7.5 %. Employing lower molar mass gas such as helium can lead to a vectoring efficiency of approximately 2°/% (degree per percent of secondary to primary flow mass flow rates). Whereas this efficiency is close to 1°/% for usual gas (air into air) injection. For fixed injection conditions, it was found that vectoring angle is higher when the injected gas $M_j\gamma_j$ product is less than $M_i\gamma_i$ of the primary gas. Moreover, the experimental results, confirmed by the numerical calculations and by those from the analytical model, showed that the injection of a gas such as helium can produce the same deflection with a much lower injection mass flow rate.

Finally, as it is found that the secondary total pressure and the sonic velocity of the species are dominant over the injected mass flow rate, a scaling law relation can be given between the reciprocal specific heat ratio and molecular mass product and the performance coefficients. Smaller $M_j\gamma_j$ largely ameliorates the performance curves, while the heavy and small specific heat ratio gases are on the lower performance end.

Acknowledgment This work was supported by French space agency CNES, acknowledgments and gratitude to the S. Palerm and J. Oswald for supporting and helping us on this project. Our thanks also go to N. Gouillon and E. Depussay for their technical assistance during the experiments.

References

1. Zmijanovic, V., Lago, V., Sellam, M., Chpoun, A.: Thrust shock vector control of an axisymmetric conical nozzle via transverse gas injection. Shock Waves J. **24**, 97–111 (2014)
2. Sellam, M., Chpoun, A., Zmijanovic, V., Lago, V.: Fluidic thrust vectoring of an axisymmetrical nozzle: An analytical model. Int J Aerodyn. **2**, 193–209 (2012)
3. Wing D.J., Giuliano V.J.: Fluidic thrust vectoring of an axisymmetric exhaust nozzle at static conditions. ASME FEDSM. 97–3228 (1997).
4. Waithe K.A., Deere K.A.: Experimental and computational investigation of multiple injection ports in a Convergent-Divergent nozzle for Fluidic Thrust Vectoring. AIAA paper 2003–380. 21st AIAA Applied Aerodynamics Conference, Orlando, Florida, (2003)
5. Spaid, F.W., Zukoski, E.E.: Study of the interaction of gaseous jets from transverse slots with supersonic external flows. AIAA. J. **6**(2), 205–212 (1968)
6. Zukoski, E.E.: Turbulent boundary-layer separation in front of a forward-facing step. AIAA. J. **5**(10), 1746–1753 (1967)
7. Mangin B., Chpoun A., Jacquin L.: Experimental and numerical study of the fluidic thrust vectoring of a two-dimensional supersonic nozzle. AIAA paper 2006–366. 24th AIAA Applied Aerodynamics Conference San Francisco, California, (2006)

Part IX

Shock Wave Reflection and Interaction

Three-Dimensional Bow-Shock Interactions Between High-Speed Slender Bodies at Incidence

S.J. Hooseria and B.W. Skews

Introduction

The study of interfering bodies in supersonic airflow is important to the development of a number of flight vehicles, since the aerodynamic loads experienced by the body of interest (the receiver) can be influenced significantly by the interference created when in close proximity to a disturbance generator. Of particular significance is the three-dimensional bow shock emanating from the disturbance generator, striking the cylindrical surface of the slender, disturbance receiver. The impinging forebody bow shock not only causes local elevations in the receiver's surface pressure but modifies the flow angularity over the body as well. In addition, altering the attitude of the receiver to the free stream flow introduces additional complexity to the interaction, since the impinging disturbance shock wave undergoes a mutual interaction with the separated flow on the leeside of the inclined receiver. Many researchers have reported integrated force and moment characteristics of bodies in interference flow fields, but in most cases, limited explanation of the underlying flow physics and wave dynamics of the interaction is given.

Euler predictions conducted by Volkov and Durenov [1] investigated the interference effect of the separation distance between a pair of axially aligned cone-cylinder bodies at $M_\infty = 4.03$, due to its relevance in a vast number of practical aerodynamic applications. The application of computational fluid dynamics (CFD) allowed the flow field structure to be assessed in detail, where multiple reflected and diffracted shock waves were observed in the inter-model region, due to the close proximity of the bodies. However, their observations were limited to inviscid phenomena. A similar dual slender body arrangement was studied by Mowatt and Skews [2], with the aim to investigate the shock wave boundary-layer interaction (SWBLI) on the cylindrical surface of the receiver. The disturbance field strength was varied by varying the forebody profile of the bodies at a fixed separation distance. They observed that the leeside boundary-layer thickened as a result of the swept flow from the windward side to the leeside, induced by the shock impingement on the cylindrical surface. As a result, the diffracted shock was observed to reform on the leeside at a distance away from the body's surface.

Chaplin et al.[3] conducted an extensive study into the aerodynamic effects of varying geometric parameters such as axial stagger, in-plane receiver body incidence and disturbance field strength, where changes in the aerodynamic coefficients were quantified for two slender bodies in close proximity. The investigation indicated that the interference aerodynamics is highly dependent on specific arrangements of the bodies and that the likelihood of collision of the bodies is increased as the impinging conical shock wave moves closer to the trailing edge of the receiver. Hooseria and Skews [4] aimed to uncover some of the underlying flow physics and gas dynamics that emerge when the pressure wave systems generated by slender bodies of revolution interact, with the body of interest at relatively high in-plane incidence. A complex far field flow structure was predicted in their studies, where the recirculating leeside flow of the inclined receiver was observed to significantly influence the approaching disturbance-shock. Aft of disturbance impingement, the complex, three-dimensional shock/vortex interaction generated a complex wave structure towards the base of the body. This was attributed to the inherent low pressure generated in the leeward region of the receiver, as well as the local rotational velocity field induced by the body vortices.

The current investigation focuses on gaining insight into the flow physics, vortical structures and pressure wave phenomena generated when the receiver body is at large angles of sideslip relative to the generator, at a fixed separation

S.J. Hooseria (✉) • B.W. Skews
Flow Research Unit, University of the Witwatersrand, PO WITS 2050, Johannesburg, South Africa
e-mail: ShalanHooseria@gmail.com

G. Ben-Dor et al. (eds.), *30th International Symposium on Shock Waves 1*, DOI 10.1007/978-3-319-46213-4_93

distance. Although researchers have reported that the interference problem is highly configuration specific [2–4], no studies to date have been conducted with the receiver body at out-of-plane angles of incidence relative to the generator body, where complete three-dimensional flow asymmetry exists. An experimentally validated computational modelling technique [5] was employed to conduct these investigations, which allowed a detailed analysis of the gas dynamics of the interaction to be conducted. The methods employed are discussed, and the results and conclusions derived from these studies are presented in contrast to those of an undisturbed or isolated body configuration.

Methodology

The computational predictions were carried out using the commercial flow solver, STAR-CCM+ V8.04. A time-averaged coupled flow solver was employed, and the Reynolds-Averaged Navier–Stokes (RANS) equations were computed to second-order spatial accuracy. Turbulence in these viscous simulations was modelled using Mentor's $k - \omega$ Shear Stress Transport (SST) model, with the bodies and stings prescribed as non-slip solid walls. Inlet boundary conditions were set to mimic the free stream conditions in the supersonic wind tunnel used for the experimental work ($P_0 = 410\ kPa$, $T_0 = 298\ K$ and $M_\infty = 3.0$), and the final outlet boundary face pressure and temperature were extrapolated using reconstruction gradients from adjacent cell values. The domain was discretised using the meshing continuum contained within STAR-CCM+, where a uniform polyhedral cell grid was initially generated with wall $y+ \leq 1.0$. Subsequently, a custom solution-based adaptive mesh refinement scheme, using first-order derivative operators, was employed to obtain fine resolution of key phenomena in the flow domain. Refinement levels were determined through grid sensitivity studies, and all results presented in this paper were established to be adequately iteratively converged and mesh independent. The computational method employed was both qualitatively and quantitatively validated for numerous receiver incidence settings using experimental techniques, as documented by Hooseria and Skews [5]. This provides additional confidence that the flow physics predicted by the numerical simulations conducted in the current investigation are representative of those in the experimental flow field.

Results

For purposes of this paper, only a single sideslip interference configuration will be discussed in detail, i.e. a pair of slender bodies with hemispherical leading profiles that are spaced laterally by $\Delta z/D = 2.92$ with the receiver body at $\beta_R = 15°$ relative to a free stream at $M_\infty = 3.0$. A comparison of the surface pressure distribution and near-surface flow topologies developed over the disturbed receiver (left) and isolated body (right) is presented in Fig. 1 for various roll orientations of the bodies. Upstream of shock impingement, the surface pressure distribution and surface flow topology of the disturbed receiver are identical to that of the isolated body. However, at approximately 3.6 calibres downstream of the receiver's nose apex, the impinging shock wave's pressure footprint on the disturbed body's nearside and windward surfaces is distinct and causes substantial distortions to the nearside primary crossflow separation region, as well as a local change in flow angularity over the receiver's windward surface. As the impinging wave diffracts to the body's farside, it also modifies the farside primary separation region in comparison to that developed over the isolated body. However, the severity of these distortions occurs to a lesser extent on the farside than that observed on the body's nearside, due to the inherent attenuation associated with shock wave diffraction.

On the receiver's leeward surface, the skin-friction streamlines indicate that there is a substantial reorganisation of the crossflow separation and reattachment regions, in comparison to that developed over the isolated body. This has particular relevance, since the vortical structures in the leeward region evolve from shear layers that spring up from these separation regions. As a result, any modifications to the separation and reattachment regions on the body would cause modifications to the receiver's body vortices. To demonstrate this effect, a comparison of the body vortices disposed by the isolated slender body is compared to that disposed by the disturbed body in Fig. 2. The effect of disturbance shock impingement on the disturbed receiver's nearside vortices is immediately identifiable and varies substantially in form to those disposed by the isolated body. In fact, it appears that between $4.0 < x/D < 5.0$, a portion of the primary vortex is shed into the leeward region.

The shedding of the primary nearside vortex correlates to the local disbandment of the primary separation region, as demonstrated in Fig. 1, and once the primary separation region is re-established due to the sustained incidence-induced crossflow, an attached primary vortex is regenerated. As the attached portion of the primary nearside vortex evolves along the body, it starts to entrain the shed portion of the vortex, due to its rotational velocity field. The mechanism that facilitates the vortex shedding is local vorticity cancellation through the transport of counterrotating fluid from the windside towards the leeside. This is induced by the favourable circumferential pressure gradient towards the leeside due to shock impingement, as well as the displaced fluid departing the shock-induced separation region, as demonstrated in Fig. 3.

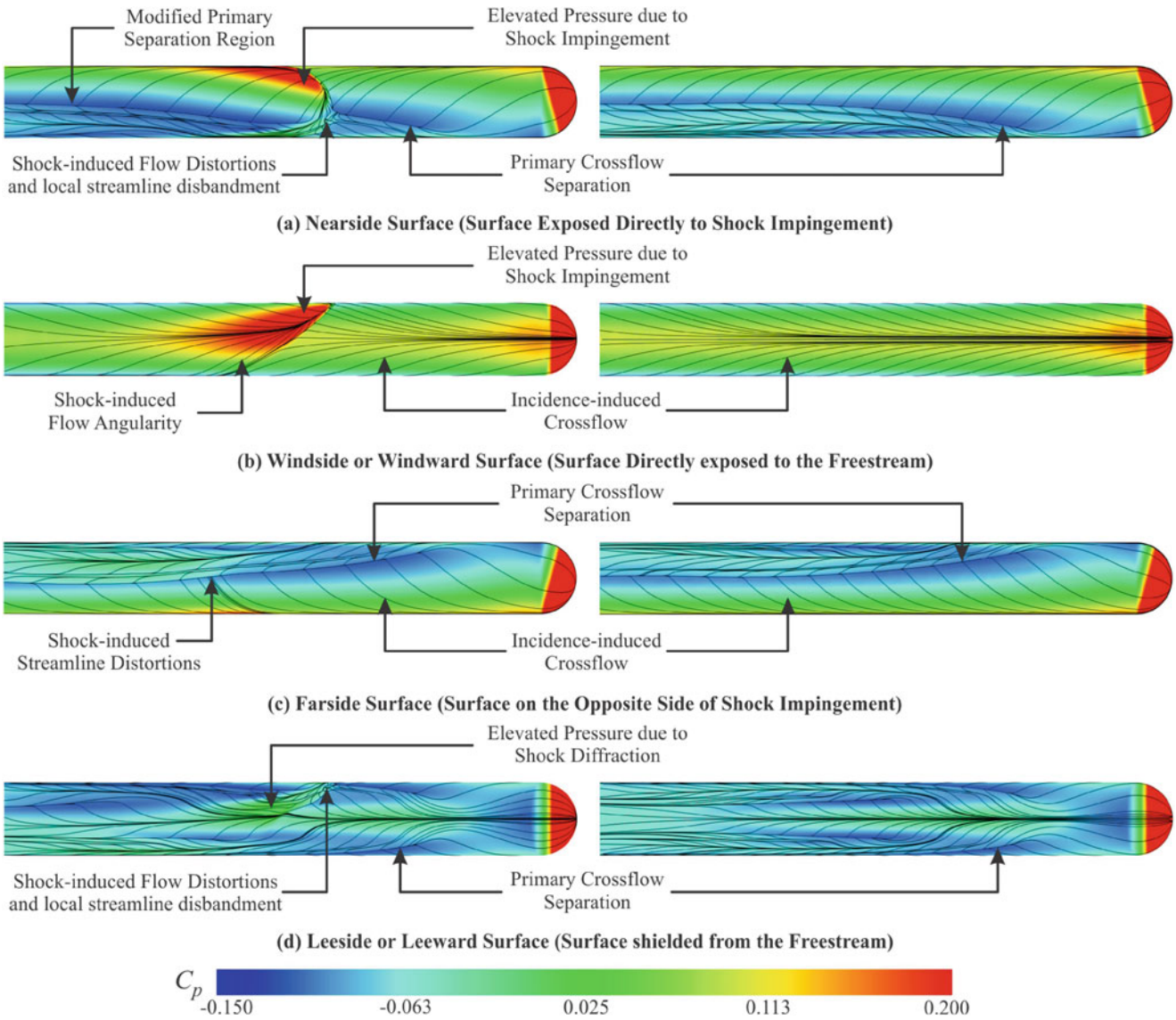

Fig. 1 Skin-friction streamlines and surface pressure distribution of the isolated and disturbed bodies ($M_\infty = 3.0$ with the disturbed body on *left* and undisturbed body on *right*)

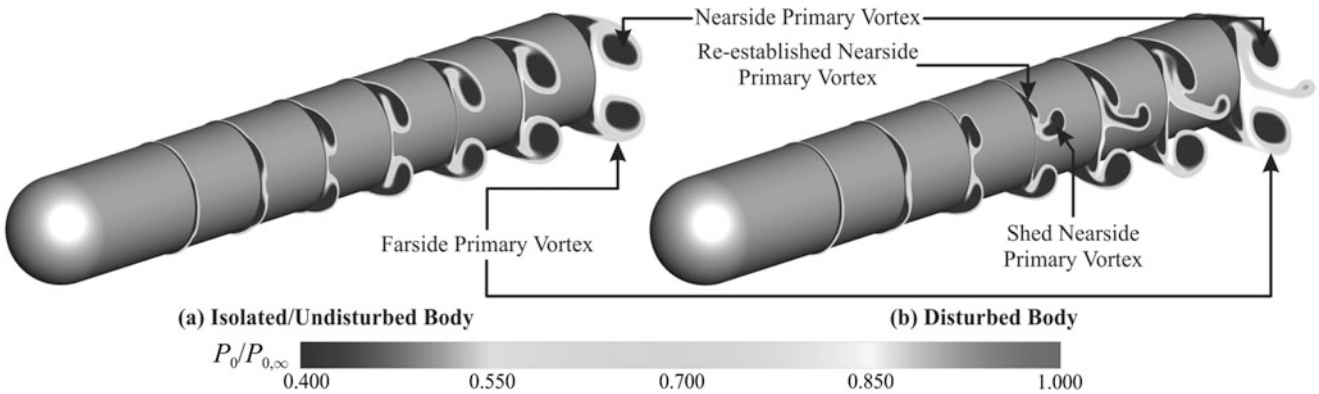

Fig. 2 Crossflow slices of total pressure, truncated between $0.4 < P_0/P_{0,\infty} < 1.0$, in one calibre increments from $x/D = 2.0$ up to the base of the bodies ($x/D = 8.0$) with the isolated body on the *left* and disturbed body on the *right*

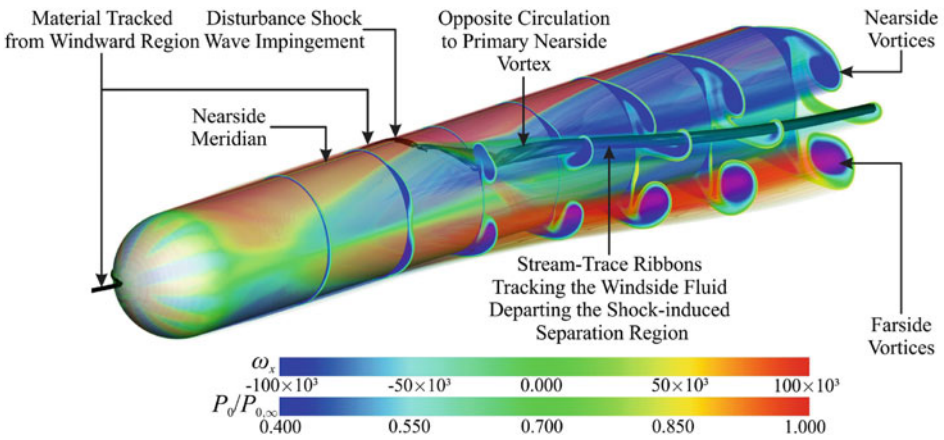

Fig. 3 Crossflow slices of total pressure, truncated between $0.4 < P_0/P_{0,\infty} < 1.0$, in one calibre increments from $x/D = 2.0$ up to $x/D = 8.0$ enclosed by translucent iso-surface contours of ωx

The streamtrace ribbons indicate that the boundary-layer fluid leaving the shock-induced separation region originates from the body's windside and has opposite circulation to that of the primary nearside vortex. As a result, when this fluid interacts with the primary nearside vortex, a vorticity cancellation effect occurs, causing the initial shedding of the vortex and subsequent degenerate evolution of the shed portion of the primary nearside vortex along the body. The receiver's farside vortices are not influenced substantially in comparison, but the primary farside vortex core is located slightly further away from the body, in comparison to that of the isolated body case. Overall, the vortex dynamics generated by the interaction is driven by complex mechanisms and produces complex vortical structures in the receiver's leeward region. However, not only does the disturbance shock wave modify the receiver body's vortex structure, but the vortices also substantially influence the disturbance wave's diffraction process over the body, towards the farside region. To demonstrate this mutual interaction, the wave system developed in the leeward region of the receiver is shown at several stations along the body in Fig. 4.

At $x/D = 4.5$, the diffracted portion of the disturbance shock has passed through the nearside vortex system, which has locally altered the curvature of the wave in the direction of circulation of the primary nearside vortex. The reflected shock wave structure also appears to be influenced by the nearside vortex system. Although the vortex shock is a standard feature of slender bodies at high incidence, it adds complexity to the wave geometry in the leeward region in the current configuration, forming a Mach shock at its intersection with the reflected wave at $x/D = 5.0$. Moreover, since the local rotational velocity field of the primary nearside vortex favours the direction of transit of the diffracted wave over the body, it does not oppose the wave's progression towards the body's farside. However, the converse occurs when the wave meets the primary farside vortex, which has opposite circulation to that of the nearside primary vortex and opposes the passage of the diffracting wave. In fact, the primary farside vortex is strong enough to cause a segmentation of the attenuated diffracted wave, i.e. the portion of the wave closest to the receiver's surface is swept into the vortex, and because its density is greater than that of the surrounding fluid, it is pushed through the vortex by centrifugal action, re-emerging in the leeward region with opposite curvature to that of the residual portion of the diffracted wave, as shown at $x/D = 5.0 - 6.0$. At this stage, the residual segment is no longer in contact with the body and anchors to the primary farside vortex, which prevents its further progression over the body.

Overall, the global wave structure (Fig. 5) is highly complex, with shock/vortex interactions and multiple three-shock intersections, requiring a more detailed analysis for full characterisation.

Conclusions

The current investigation aimed to uncover some of the underlying flow physics and gas dynamics that emerge when two high-speed slender bodies are in close proximity, with the body of interest at a high angle of sideslip relative to the generator. An experimentally validated computational modelling technique was used to resolve the flow field and predicted that complex flow mechanisms are generated by the interaction. The impinging shock wave induced substantial alterations to the receiver's vortex structure, in comparison to that disposed by an equivalent isolated body, including shedding of the primary nearside vortex. However, the shock/vortex interaction was observed to be mutual, with the local rotational velocity fields of the primary vortices influencing the wave topology in the receiver's leeward region significantly.

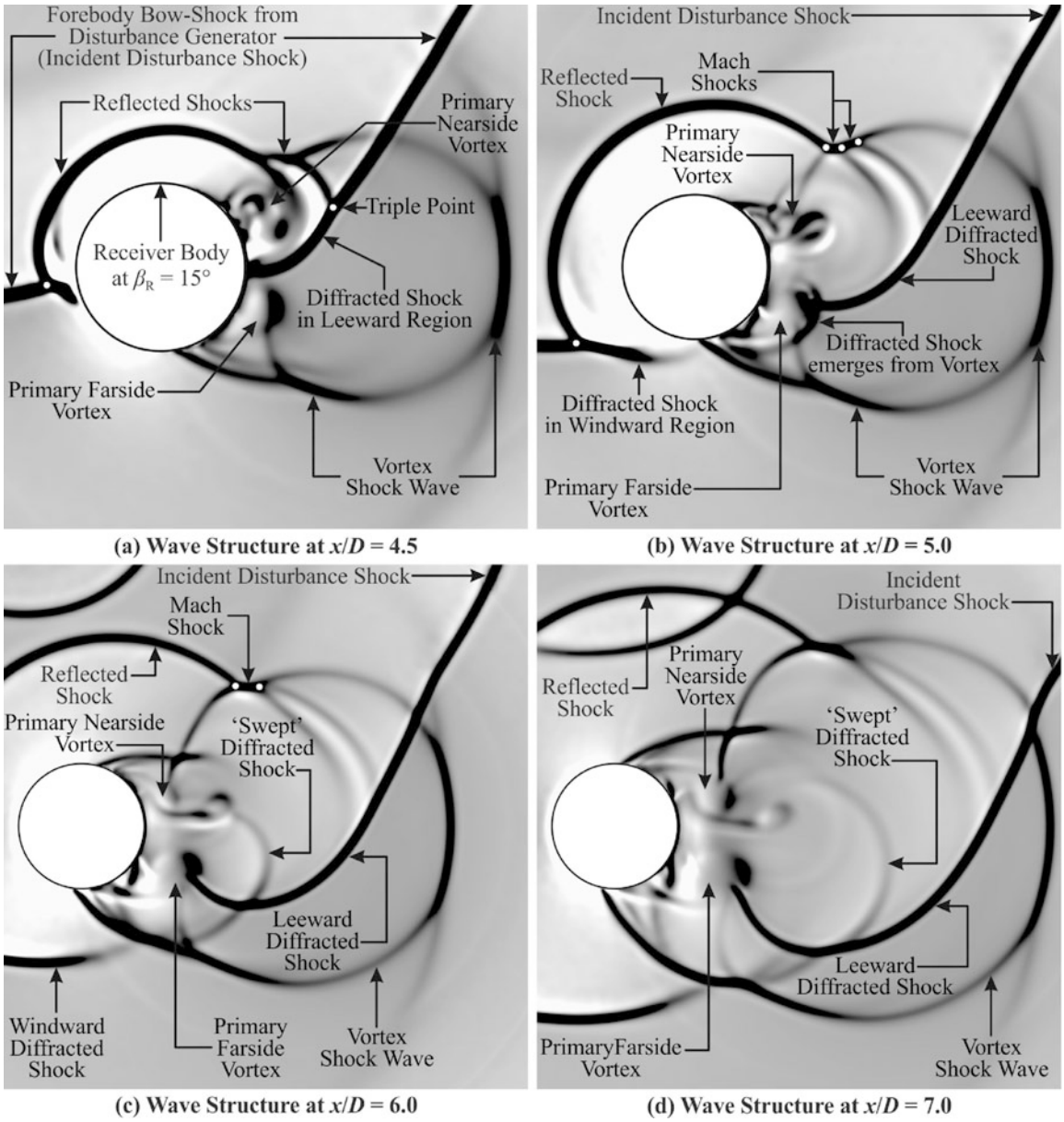

Fig. 4 Detailed view of the wave system surrounding the inclined receiver at various stations ($x/D = 4.5$–7.0) along the body using grayscale renditions of numerical colour schlieren

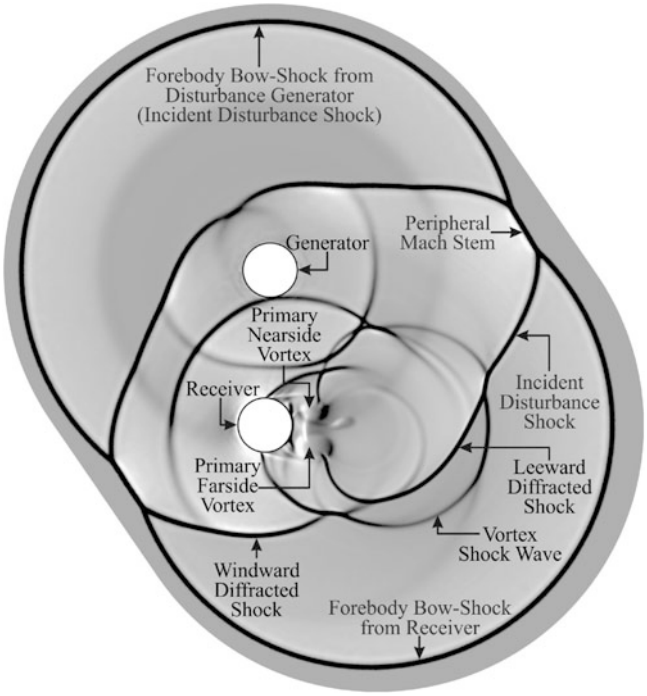

Fig. 5 Global view of the wave system surrounding the generator and the receiver towards the base of the bodies ($x/D = 8.0$) using a gray-scale rendition of numerical colour schlieren

References

1. Volkov, V., Derunov, E.: Interaction of a combination of bodies in supersonic flow. Interference and diffraction of shock waves in flow over two bodies of revolution. J. Eng. Phys. Thermophys. **79**(4), 712–721 (2006)
2. Mowatt, S., Skews, B.W.: Three-dimensional shock wave/boundary layer interactions. Shock Waves **21**, 467–482 (2011)
3. Chaplin, R., MacManus, D., Leopold, F., Martinez, B., Gauthier, T., Birch, T.: Computational and experimental investigation into aerodynamic interference between slender bodies in supersonic flow. Comput. Fluids **50**, 155–174 (2011)
4. Hooseria, S.J., Skews, B.W.: Three-dimensional, curved shock wave interactions with slender bodies at incidence. 29th International Symposium on Shock Waves (ISSW 29), Madison, USA (2013)
5. Hooseria, S.J., Skews, B.W.: Colour surface flow visualisation of interfering slender bodies at Mach 3. J. Vis. **18**(3), 413–423 (2015). doi: 10.1007/s12650-014-0242-1

Flow Behind Mach Reflection and the Neumann Paradox

A. Sakurai

Introduction

After so many years with numerous contributions, it has gradually been recognized that the cause of the Neumann paradox [1, 2] is its origin in the flow field behind reflected and Mach stem shock waves, and especially the singular nature near its triple point [3, 4]. Neumann's three-shock theory [5, 6] based on nonviscous gas dynamics assumes there are two parallel uniform flows separated by a slip stream line, and it provides shock angles in excellent agreement with experiment data for strong Mach reflection cases. Paradoxically, there is no agreement at all for weaker cases.

In these experiments and numerical simulations, we can indeed observe uniform flows with a slip line for the stronger cases, but this becomes blurred for weaker cases, in which we can see a disturbance from the edge to the triple point [7, 8]. The entire flow field is nonuniform, and this should provide a modification of the condition given by the solution of three-shock theory. The problem is thus to find the details of the flow field, especially the singular nature near the triple point. To do this, we must use an analytical approach because of the singularity, for which the conventional numerical approach is not effective.

The three-shock configuration appears both in steady and unsteady flows, representatively in supersonic inlet flow for the former and advancing plane shock wave over a sharp wedge surface for the latter. The "Neumann Paradox phenomenon" occurs in both flows for their weak cases. We use the Navier–Stokes system for both the steady and unsteady flows, simply because the nonviscous Euler system provides the same result as that given by the three-shock theory.

Flow Field Behind Weak Mach Reflection: Steady-Flow Case

We consider the flow field in the angular region between the reflected and the Mach stem behind a steady Mach reflection. It is convenient to use the polar coordinate system (r, θ) with the basic line $\theta = 0$ at the x-axis for the direction of incoming flow with its origin at the triple point. The Mach stem m is thus at $\theta = -\lambda$, and the reflected wave R is at $\theta = \omega'$ (Fig. 1). Let $\boldsymbol{v} = (V_r, V_\theta)$, be the flow velocity, its r, θ components and p, ρ be the pressure and density of the flow field; and they are all functions of the variables r, θ. We use the Navier–Stokes system of equations given as

A. Sakurai (✉)
Tokyo Denki University, Senju, Tokyo 120-8551, Japan
e-mail: sakurai@cck.dendai.ac.jp

G. Ben-Dor et al. (eds.), *30th International Symposium on Shock Waves 1*, DOI 10.1007/978-3-319-46213-4_94

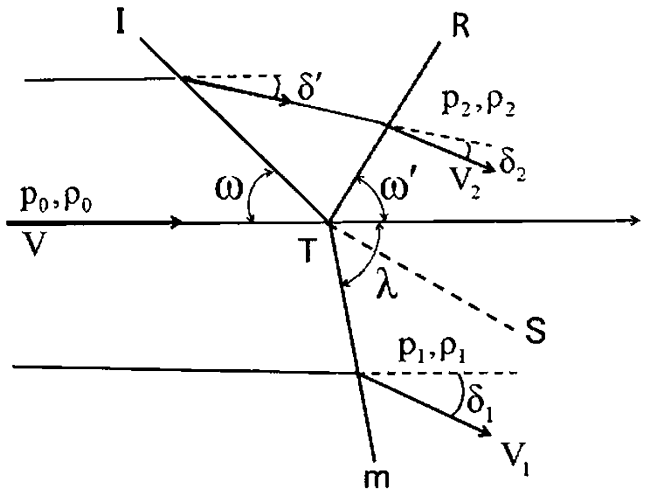

Fig. 1 Three-shock configuration

$$
\begin{aligned}
&r\frac{\partial}{\partial r}\rho V_r+\rho V_r+\frac{\partial}{\partial\theta}\rho V_\theta=0,\\
&\left[\rho\left(V_r r\frac{\partial V_r}{\partial r}+V_\theta\frac{\partial V_r}{\partial\theta}-V_\theta^2\right)=r\frac{\partial p}{\partial r}\right]r=\mu\left[\Delta V_r-V_r-2\frac{\partial V_\theta}{\partial\theta}+\frac{r^2}{3}\frac{\partial}{\partial r}\frac{1}{r}\left(\frac{\partial rV_r}{\partial r}+\frac{\partial V_\theta}{\partial\theta}\right)\right]\\
&\left[\rho\left(V_r r\frac{\partial V_\theta}{\partial r}+V_\theta\frac{\partial V_\theta}{\partial\theta}+V_rV_\theta\right)+\frac{\partial p}{\partial\theta}\right]r=\mu\left[\Delta V_\theta-V_\theta+2\frac{\partial V_r}{\partial\theta}+\frac{r}{3}\frac{\partial}{\partial\theta}\frac{1}{r}\left(\frac{\partial rV_r}{\partial r}+\frac{\partial V_\theta}{\partial\theta}\right)\right]
\end{aligned}
\tag{1}
$$

$$
\begin{aligned}
&\left[\rho\left(V_r r\frac{\partial}{\partial r}+V_\theta\frac{\partial}{\partial\theta}\right)E+p\left(V_r r\frac{\partial}{\partial r}+V_\theta\frac{\partial}{\partial\theta}\right)\frac{1}{\rho}\right]r=\kappa\Delta T+\mu\Phi\\
&\Phi\equiv\left[2\left(r\tfrac{\partial V_r}{\partial r}\right)^2+2\left(\frac{\partial V_\theta}{\partial\theta}+V_r\right)^2+\left(\tfrac{\partial V_r}{\partial\theta}+r\tfrac{\partial V_\theta}{\partial r}-V_\theta\right)^2-\frac{2}{3}\left(r\frac{\partial V_r}{\partial r}+\frac{\partial V_\theta}{\partial\theta}+V_r\right)^2\right]\\
&\Delta\equiv r^2\frac{\partial^2}{\partial r^2}+r\frac{\partial}{\partial r}+\frac{\partial^2}{\partial\theta^2},
\end{aligned}
$$

these are supplemented by the equations of a perfect gas, $E=c_vT$, $p=\rho RT$. where E, T, R, c_v are respectively the internal energy, temperature, gas constant and the specific heat of constant volume;μ is the coefficient of the viscosity, and κ is the heat conductivity, which are assumed to be constant.

We seek here a solution suitable for the angular region between the two axes at the reflected and Mach stem shocks and utilize this solution along a circle $r=$ const. of the variable θ only, for which the equations in Eq. (1) are simplified. Using ’ for $d/d\theta$ we have

$$
\begin{aligned}
&(\rho V_\theta)'+\rho V_r=0\\
&3V_r''-3V_r-7V_\theta'=3r/\mu\cdot\rho V_\theta\left(V_r'-V_\theta\right)\\
&4V_\theta''-4V_\theta+7V_r'=3r/\mu\cdot\left[\rho V_\theta\left(V_\theta'-V_r\right)\right]\\
&\kappa T''+\mu(\phi)_{r=0}=r\rho V_\theta\left[E'+p(1/\rho)'\right]
\end{aligned}
\tag{2}
$$

The solution of this system of equations is expected to have something like a spiral stairs surface. Its basic property is given by the nature at $r=0$ for which we can utilize the solution of the system above with $r=0$. This reduced

system is the same as the one given in the first order term of the power series expansion in r of the original system of Eq. (1) [7]. Its smooth solution is given in there as

$$
\begin{aligned}
V_\theta &= (A/\cos\theta_\theta)(1+k\theta)\sin(\theta-\theta_0)\\
V_r &= -(A/\cos\theta_\theta.)[(1+k\theta)\cos(\theta-\theta_0)+(k/7)\sin(\theta-\theta_0)]\\
\rho &= Ek^{6/7}(1+k\theta)^{-6/7}\\
p &= \rho\left\{-\frac{\gamma-1}{\gamma}\sigma\frac{4}{49}kC/\cos\theta_0\left[7\theta^2+\cos 2(\theta-\theta_0)\right]F\theta+G\right\},
\end{aligned}
\tag{3}
$$

where γ is the specific heats ratio and σ is Prandtl's number; A, C, E, F, k, and θ_0 are integration constants to be determined together with angles λ and ω′ values by eight shock wave values: (ρ_1, p_1, $V_{\theta1}$, V_{r1}) and (ρ_2, p_2, $V_{\theta2}$, V_{r2}) respectively at $\theta = -\lambda, \omega'$.These provide two equations to determine angles λ and ω′ for the given incident shock angle ω and strength ζ which is the inverse of the pressure ratio of at the incident shock. ζ is larger for weaker cases approaching to one. λ and ω′ so determined are shown in Ref. [9] in the form of λ versus ω and ω′ versus ω graphs for various ζ values. Figure 2 below reproduces one of the graphs given there and depicts ω′ versus ω graph for $\varsigma = 0.9$ representing a weaker case, in comparison with corresponding experiment data and the result from the three-shock theory. We can see that these angles from the present theory are reasonably consistent with experiment data, indicating the effect of the nonuniformity of the flow field due to the singularity at the triple point.

This solution is illustrated in Fig. 3 (a) for velocity $\boldsymbol{V}$ and (b) for density ρ. The flow spreads from the origin T as it widens the slip stream line, providing a correction to the three-shock theory condition of parallel flows. Although this solution is valid only along the boundary of two shock fronts with a fan-like singularity at their intersecting point $r = 0$, we can expect that it approximates the flow for $r > 0$. In fact, numerical simulation [10] provides density distribution along a circle of $r > 0$ similar to that of $r = 0$ above. For details of the flow for $r > 0$, we can construct a Prandtl-Meyer type solution [6] that is valid along a circle of $r =$ constant > 0 depending on the angle variable θ only.

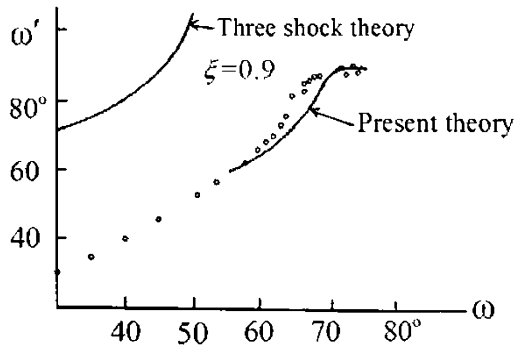

Fig. 2 ω′ versus ω graph for $\varsigma = 0.9$ from the present theory compared with Harrison and Bleakney's data and three-shock theory results [9]

Flow Field Behind Weak Mach Reflection: Unsteady Flow Case

We consider a single Mach reflection as illustrated in Fig. 4, where I, R, and m represent its incident, reflected, and Mach stem shock fronts that intersect each other at the triple point T. The incident wave I is assumed to be propagating in a uniform atmosphere of pressure p_0 and density ρ_0 with velocity U over a wedge of angle δ. Assume a coordinate system in x, y with the origin O as the apex of the wedge (Fig. 4), and let $V = (u, v)$ be the velocity, p the pressure, and ρ the density. The system of the time t-dependent Navier–Stokes equations system is

Fig. 3 (**a**) Velocity (**b**) Density

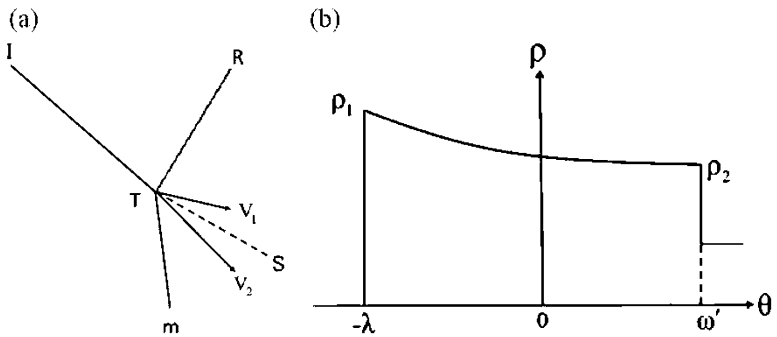

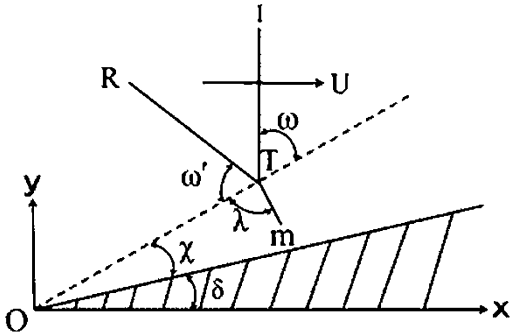

Fig. 4 Configuration of single Mach reflection over a straight wedge

$$\frac{D\rho}{Dt}+\rho\, div\mathbf{V}=0, \rho\frac{D\mathbf{V}}{Dt}+grad\, p=\mu[(1/3)grad.div\mathbf{V}+\Delta\mathbf{V}],\ \frac{p}{\gamma-1}\frac{D}{Dt}(\log p\rho^{-\gamma})=\mu\Phi+\kappa\Delta T$$
$$\text{where } \frac{D}{Dt}\equiv\frac{\partial}{\partial t}+\mathrm{u}\frac{\partial}{\partial \mathrm{x}}+\mathrm{v}\frac{\partial}{\partial y},\ \Phi\equiv 2\left[\left(\frac{\partial u}{\partial x}\right)^2+\left(\frac{\partial v}{\partial y}\right)^2\right]+\left(\frac{\partial u}{\partial y}+\frac{\partial v}{\partial x}\right)^2-\frac{2}{3}(div\mathbf{V})^2 \tag{4}$$

Here we utilize the self-similar nature of the flow under the given boundary of the straight wedge and set

$$X=\frac{x}{ct},\ Y=\frac{y}{ct},\ U=\frac{u}{c}-X,\ V=\frac{v}{c}-Y, P=\frac{p}{\bar{p}},\ R=\frac{\rho}{\overline{\rho}}\ \text{and}\ s=\frac{\mu}{\bar{p}t}. \tag{5}$$

Introduce the dimensionless variables X, Y and s defined by where $\bar{p}, \overline{\rho}$ are the pressure and the density values of a certain uniform state, and $c^2=\gamma\bar{p},\overline{\rho}$.

The above system of Eq. (4) is then transformed into

$$\begin{aligned}
&DR+R(divV+2)=s\partial R/\partial s\\
&R(D+1)V+(1/\gamma)grad\, P=s[\mathbf{V}_s+(1/3)grad.div\mathbf{V}+\Delta\mathbf{V}]\\
&DP+\gamma P(divV+2)=s\Big\{P_s+(\gamma-1)\Big[2(U_X+1)^2+2(V_Y+1)^2\Big]\\
&+(U_Y+V_X)^2-(2/3)(div\mathbf{V}+2)^2,+(\gamma/\sigma)\Delta(P/R)\Big\}\\
&\text{where } D\equiv U\partial/\partial X+V\partial/\partial Y,\ \mathbf{V}=(U,V)
\end{aligned} \tag{6}$$

We seek a solution depending on X, Y only at a certain fixed s or time t, shift the origin of the coordinate system from 0 to the triple point T, and introduce the polar coordinate system (r, θ), yielding

$$
\begin{aligned}
&r\frac{\partial RV_r}{\partial r}+RV_r+\frac{\partial RV_\theta}{\partial \theta}+2rR=s\frac{\partial R}{\partial s}\\
&\left[R\left(V_r r\frac{\partial V_r}{\partial r}+V_\theta\frac{\partial V_r}{\partial \theta}-V_\theta^2+rV_r\right)+\frac{r}{\gamma}\frac{\partial P}{\partial r}\right]r=s\left[\frac{\partial V_r}{\partial s}+\Delta V_r-V_r-2\frac{\partial V_\theta}{\partial \theta}+\frac{r^2}{3}\frac{\partial}{\partial r}\frac{1}{r}\left(\frac{\partial rV_r}{\partial r}+\frac{\partial V_\theta}{\partial \theta}\right)\right]\\
&\left[R\left(V_r r\frac{\partial V_\theta}{\partial r}+V_\theta\frac{\partial V_\theta}{\partial \theta}+V_rV_\theta+rV_\theta\right)+\frac{1}{\gamma}\frac{\partial P}{\partial \theta}\right]r=s\left[\frac{\partial V_\theta}{\partial s}+\Delta V_\theta-V_\theta+2\frac{\partial V_r}{\partial \theta}+\frac{r}{3}\frac{\partial}{\partial rr}\left(\frac{\partial rV_r}{\partial r}+\frac{\partial V_\theta}{\partial \theta}\right)\right]\\
&\left[V_r r\frac{\partial P}{\partial r}+V_\theta\frac{\partial P}{\partial \theta}+\gamma P\left(V_r+\frac{\partial V_\theta}{\partial \theta}+r\frac{\partial V_r}{\partial r}\right)\right]r=s\left[R\frac{\partial P}{\partial s}+\frac{\gamma}{\sigma}\Delta\left(\frac{P}{R}\right)+\overline{\Phi}\right],\\
&\overline{\Phi}\cong(\gamma-1)\left[2\left(r\frac{\partial V_r}{\partial r}\right)^2+2\left(\frac{\partial V_\theta}{\partial \theta}+V_r\right)^2+\left(\frac{\partial V_r}{\partial \theta}+r\frac{\partial V_\theta}{\partial r}-V_\theta\right)^2-\frac{2}{3}\left(r\frac{\partial V_r}{\partial r}+\frac{\partial V_\theta}{\partial \theta}+V_r\right)^2\right]
\end{aligned}
\tag{7}
$$

We need a solution suitable for the fan-like region between the two axes at the reflected and Mach stem shocks and utilize for this, as in the previous case of steady flow, a solution at a fixed time t along a circle $r = \text{const.}$ of the variable θ only, from which the above equations are simplified. Using$'$ for $d/d\theta$ again we have

$$
\begin{aligned}
&(RV_\theta)'+RV_r=-2rR\\
&3V_r''-4V_r-7V_\theta'=3(r/s).RV_\theta(V_r'-V_\theta)\\
&4V_\theta''-3V_\theta+7V_r'=3(r/s)RV_r(V_\theta'-V_r)]\\
&\frac{\gamma}{\sigma}\left(\frac{P}{R}\right)''+(\gamma-1)(\phi)_{r=0}=(r/s)[V_\theta P'+\gamma P(V_r+V_\theta')]
\end{aligned}
\tag{8}
$$

This solution somehow corresponds to the situation of observing density distribution along a circle in a photograph at a certain moment in the Mach–Zehnder measurement to the shock tube experiment.

The basic property of the solution is again from its singular nature at $r = 0$ as is the case for a steady flow in the previous section, and we can utilize this for the solution of the system above of $r = 0$. Furthermore, the shock boundary values at shocks R and m are also the same as given in the previous section. We can thus have the same system as given in the steady flow case for the same angle ω' and λ values as above in the steady flow case.

The flow for $r > 0$ should be sought in the same way as suggested in the previous section for the steady case. This is not expected to differ significantly from the $r = 0$ case for small r, although the solution is not the same as the one given in the steady case because additional terms for $r > 0$ are different from each other as seen in Eq. (2) (steady case) and Eq. (9) (nonsteady case).

Conclusions

The singular nature of the flow near the triple point is investigated analytically based on a solution of the Navier–Stokes equations system with special attention on the cause of the Neumann paradox in relation to the nonuniformity of the flow field behind the Mach reflection. It gives a centered fan-like flow from the triple point in widening the slip flow region, resulting in modification of the three-shock theory conditions for determining the reflected and Mach stem shock angles. The angles determined from the modified conditions are consistent with experiment data, supporting the above view.

References

1. Birkoff, G.: Hydrodynamics, A Study in Logic, Fact, and Similitude, 1st edn. Princeton University Press, Princeton, NJ (1950)
2. Bleakney, W., Taub, A.H.: Interaction of shock waves. Rev. Modern Phys. **21**, 584–605 (1949)
3. Sternberg, J.: Triple-shock-wave interactions. Phys. Fluids **2**(2), 172–206 (1959)
4. Tesdall, M., Sanders, R., Keyfitz, L.: Self- similar solutions for the triple point paradox in gasdynamics. SIAM. J. Appl. Math. **68**, 1360–137 (2008)
5. von Neumann, J.: Collected Works, vol. 6. Pergamon, New York (1963)
6. Courant, R., Friedrichs, K.O.: Supersonic flow and shock waves, Ith edn, pp. 332–333. Wiley-Interscience, New York (1963)
7. Lighthill, M.J.: Diffraction of blast 1. Proc. Roy. Soc. London A **198**, 454 (1949)
8. Sakurai, A., Takahashi, S.: An analytical solution for weak Mach reflection and its application to the problem of the von Neumann paradox. J. Phys. Soc. Jpn. **74**, 1490–1495 (2005)
9. Sakurai, A.: On the problem of weak Mach reflection. J. Phys. Soc. Jpn. **19**, 1440–1450 (1964)
10. Sakurai, A., Tsukamoto, M., Khotyanovsky, D., Ivanov, M.: The flow field near the triple point in steady shock reflection. Shock Waves **21**, 267–272 (2011)

The Mach Reflection of a Converging Cylindrical Shock Wave Segment Encountering a Straight Wedge

B.J. Gray and B.W. Skews

Introduction

When a planar shock wave moving into stationary fluid encounters a straight wedge inclined at some angle, the resulting reflection configuration will be either a regular reflection (RR) or a Mach reflection (MR) [1]. Hornung et al. [2] note that in order for an MR to form, information regarding the length scale of the system needs to be transmitted to the reflection point. For pseudosteady reflections, this can only happen if the flow behind the reflected shock is subsonic relative to the reflection point. The reflection configuration resulting from a planar shock encountering an inclined wedge can therefore be predicted from the Mach number and angle between the incident shock and the reflecting surface.

However, if the incident shock wave is curved, the angle of incidence and Mach number will vary along the surface of the wedge. For a converging cylindrical shock, the Mach number of the shock wave varies according to a power law [3]. This can lead to the conditions at the reflection point moving from the MR domain into the RR domain, or vice versa. When an MR transitions to an RR, the Mach stem and shear layer are still present and interact with the reflected shock, resulting in a transitioned regular reflection (TRR).

A number of studies have investigated the transition from MR to TRR for a plane shock encountering a concave wedge, notably the experimental and analytical work by Ben-dor and Takayama et al. [4–6]. One method for predicting MR → TRR transition for a very weak shock wave reflecting off a concave cylindrical wedge is to predict the triple point trajectory using three-shock theory [6]. The intersection of the triple point trajectory with the wedge surface is the expected MR → TRR transition point.

Itoh et al. [7] describe a numerical method for predicting the triple point trajectory by using geometry to derive an expression for the Mach stem height as a function of the ratio of Mach numbers of the incident shock and Mach stem. This ratio is estimated by applying Whitham's theory [8]. The triple point trajectory is then obtained by numerically integrating the resulting expression. The current paper applies a similar approach to predict the triple point trajectory of a converging cylindrical shock wave segment encountering a straight wedge.

Analysis

Figure 1 shows a schematic diagram of a shock wave encountering a straight wedge. The curve *AD* represents the position of the incident shock wave when it first encounters the wedge, with radius r_0 and Mach number M_0. The curve *TE* represents the incident shock wave at some later time, with a radius r and Mach number M_i. The line segment *TR* represents the Mach stem of the MR, which has a height y.

This analysis has two objectives. The first is to determine how the Mach number M_i and angle of incidence β vary as the shock propagates along the wedge, while the second is to predict the Mach stem height and triple point trajectory.

Mach Number and Incidence Angle Variation

The radius of a converging cylindrical shock segment varies in time according to a power law, as proposed by Guderley [3]. By taking the time derivative and dividing by the speed of sound, the following expression is obtained for the Mach number as a function of radius.

B.J. Gray (✉) • B.W. Skews
Flow Research Unit, University of the Witwatersrand, PO WITS 2050, Johannesburg, South Africa
e-mail: Brendan.Gray@wits.ac.za

G. Ben-Dor et al. (eds.), *30th International Symposium on Shock Waves 1*, DOI 10.1007/978-3-319-46213-4_95

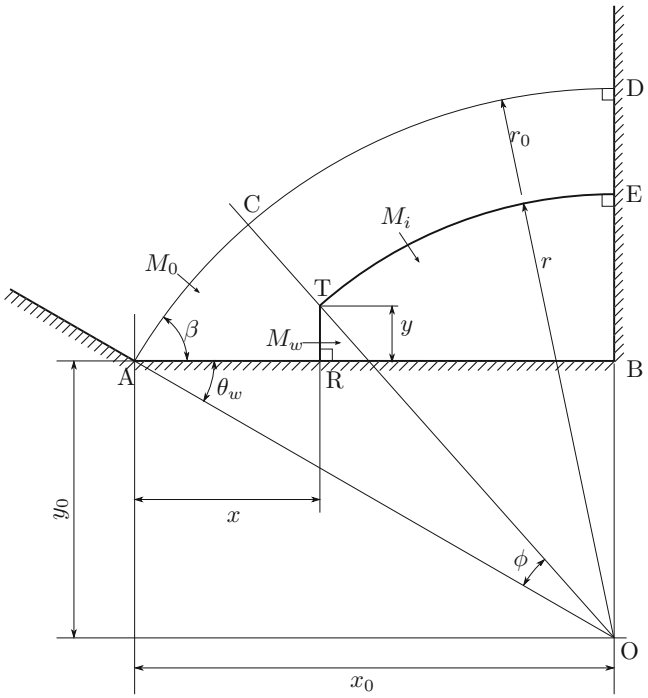

Fig. 1 Schematic diagram of a converging cylindrical shock encountering a straight wedge. The wedge apex (A), the end of the wedge (B), and the geometric centre of the shock wave (O) are labelled

$$\frac{M_i}{M_0} = \left(\frac{r}{r_0}\right)^{\frac{n}{n-1}} \tag{1}$$

where $n = 0.835$ for cylindrical shocks.

The complementary wedge angle may be defined as the angle between the shock wave and a normal to the wedge surface, $\theta_c = \frac{\pi}{2} - \beta$. Note that $\theta_c = \theta_w$ at the wedge apex, but tends toward 90° as the shock approaches the end of the wedge. The following expression for the complementary wedge angle as a function of the shock radius may be derived.

$$\theta_c(t) = \arcsin\left(\frac{r_0}{r(t)}\sin\theta_w + \frac{y(t)}{r(t)}\right) \tag{2}$$

The Mach stem height may be calculated numerically, as in the following section, but no simple analytical expression may be derived. In the interest of obtaining a general purely analytical expression for the variation of complementary wedge angle with Mach number, it will be assumed for now that the height of the Mach stem is small relative to the wedge radius, so that $\frac{y(t)}{r(t)}$ may be neglected. This is exactly true for RR, and experimental results suggest that it is reasonable for MRs for $\theta_w > 30°$. However, it is certainly not true for wedge angles below this, and this must be considered when interpreting the results of this derivation.

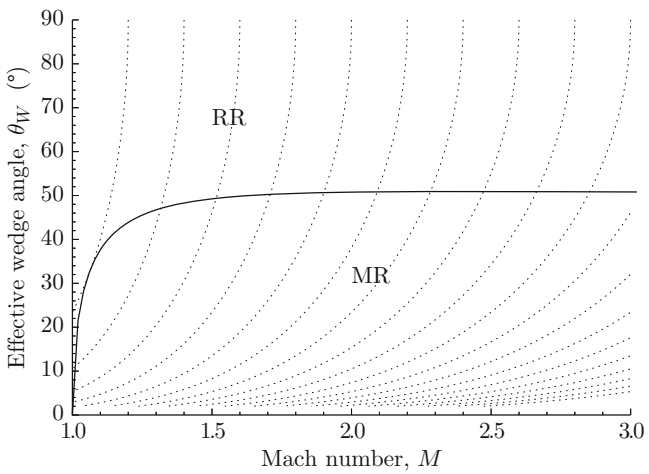

Fig. 2 Theoretical loci of Mach number and complementary wedge angle for converging cylindrical shock wave segments (*dotted curves*), compared to the transition line for pseudosteady reflection of planar shock waves using the information condition (*solid curve*)

Combining Eqs. (1) and (2) gives the following expression

$$\theta_c(M_i) = \arcsin\left[\left(\frac{M_{\max}}{M_i}\right)^{\frac{n}{n-1}}\right] \tag{3}$$

where $M_{\max}$ is the maximum Mach number reached by the shock, which will occur when the shock reaches the end of the wedge, point B. This Mach number is given by

$$M_{\max} = M_0(\sin\theta_w)^{\frac{n-1}{n}} \tag{4}$$

The loci of Mach number and complementary wedge angle calculated from Eq. (3) are shown in Fig. 2. It is interesting to note that this analysis suggests that for a limited range of wedge angles for very weak shocks ($M < 1.05$), it is possible for a reflection to start as regular, transition to irregular, and then transition back to regular. This has not yet been verified experimentally.

Predicting the Mach Stem Height

It is not possible to predict the height of the Mach stem analytically. However, using a simple iterative procedure similar to that of Itoh et al. [7], the height of the Mach stem, and therefore the triple point trajectory of a converging cylindrical shock wave segment reflecting off a straight wedge may be predicted.

Assume that the Mach stem is straight and perpendicular to the wedge surface. The validity of this assumption will be discussed later. If this is the case, the Mach number may be assumed to be constant along the length of the Mach stem.

In a coordinate system measured relative to the wedge apex, as in Fig. 1, the geometric centre of the shock wave is located at the point $(x_0, -y_0) = (r_0\cos\theta_w, -r_0\sin\theta_w)$. If the triple point is located at the point (x, y), then the Mach stem height will be given by

$$y = \sqrt{r^2 - (x_0 - x)^2} - y_0 \tag{5}$$

The derivative of this expression is then

$$\left(\frac{dy}{dx}\right) = \frac{r\left(\frac{dr}{dx}\right) + (x_0 - x)}{(y_0 + y)} \tag{6}$$

Integration of the above expression requires the radius derivative $\frac{dr}{dx}$ to be known. This may be calculated as follows.

$$\left(\frac{dr}{dx}\right) = \frac{\left(\frac{dr}{dt}\right)}{\left(\frac{dx}{dt}\right)} = \frac{-M_i a_0}{M_w a_0} = -\frac{M_i}{M_w} \tag{7}$$

where a_0 is the speed of sound in the undisturbed gas ahead of the shock, and M_i and M_w are the Mach numbers of the incident shock and Mach stem, respectively. Not that $\frac{dr}{dt}$ is negative as the radius of the shock is decreasing.

This Mach number of the Mach stem may be calculated from Whitham's theory [8] with Milton's modification [9].

$$\frac{A_w}{A_0} = \frac{f(M_w)}{f(M_0)} \tag{8}$$

where A_w is the area per unit width of the Mach stem, and A_0 and M_0 are the area and Mach number of a reference shock.

The line segment CT is a ray, and since rays cannot intersect, the incident shock TE originated from the portion CD of the original shock, while the Mach stem RT originated from the portion AC of the original shock. Therefore, all rays intersecting on the line segment RT, with an area per unit width of $A_w = y$, must originate on the arc AC with total area per unit width of $A_0 = r_0\arctan\left(\frac{y_0+y}{x_0-x}\right) - \theta_w$. This expression is undefined when $x_0 - x = 0$, which occurs at the beginning of the wedge. In order to avoid this, the initial triple point trajectory angle was set to that of a planar shock wave with Mach number M_0 and wedge angle θ_w.

This gives enough information to integrate Eq. (6) numerically. This was done using a simple forward marching scheme to obtain triple point trajectories for several Mach numbers and wedge angles.

Experiments

Experiments from a previous study [10] together with additional experiments using the facility designed by Skews et al. [11] were carried out for wedges 72 mm in length and angles between 15° and 50°, and cylindrical shock segments with Mach numbers varying between 1.52 and 2.08 at the wedge apex, with radii between 110 and 125 mm. The resulting reflection patterns were captured using a high speed camera. Schlieren photographs obtained from some of these experiments are shown in Fig. 3.

Discussion

Figure 4 compares the triple point trajectories predicted by the model to those obtained in the experiments. The model is most accurate for the 30° wedge, giving a reasonable approximation of the Mach stem height, and predicting the MR → TRR transition point to within 5 % of the wedge length for all Mach numbers tested. For wedges inclined at 40° or more, the transition point was overestimated by between 10 and 20 %, and the predicted Mach stem height is significantly overestimated. For the 15° wedge, there was reasonable agreement between the predicted triple point trajectory and that obtained in the experiments, and there is close agreement for the maximum height of the Mach stem. However, the shock wave reached the end of the wedge before transition to TRR took place, so no comparison of the transition point could be made for this angle.

The overestimation of the trajectory for steeper wedge angles is likely caused by the fact that the model does predict a triple point trajectory for all wedge angles, even those for which the initial reflection falls within the RR domain. Another limitation of the model is that it assumes that the Mach stem is straight and perpendicular to the wedge, but the Mach stems observed were slightly curved, and began to tilt significantly as they approached the transition point.

However, the model does provide reasonable approximations of the triple point trajectories and MR → TRR transition points for shock waves of moderate strength for wedge angles below 40°.

Conclusion

A simple theoretical model has been developed for estimating the Mach stem height and transition point for a converging cylindrical shock segment encountering a straight wedge. The model gives reasonable predictions for shocks of moderate strength and wedge angles below 40°, but deviates from experimental results for wedges at 40° and above.

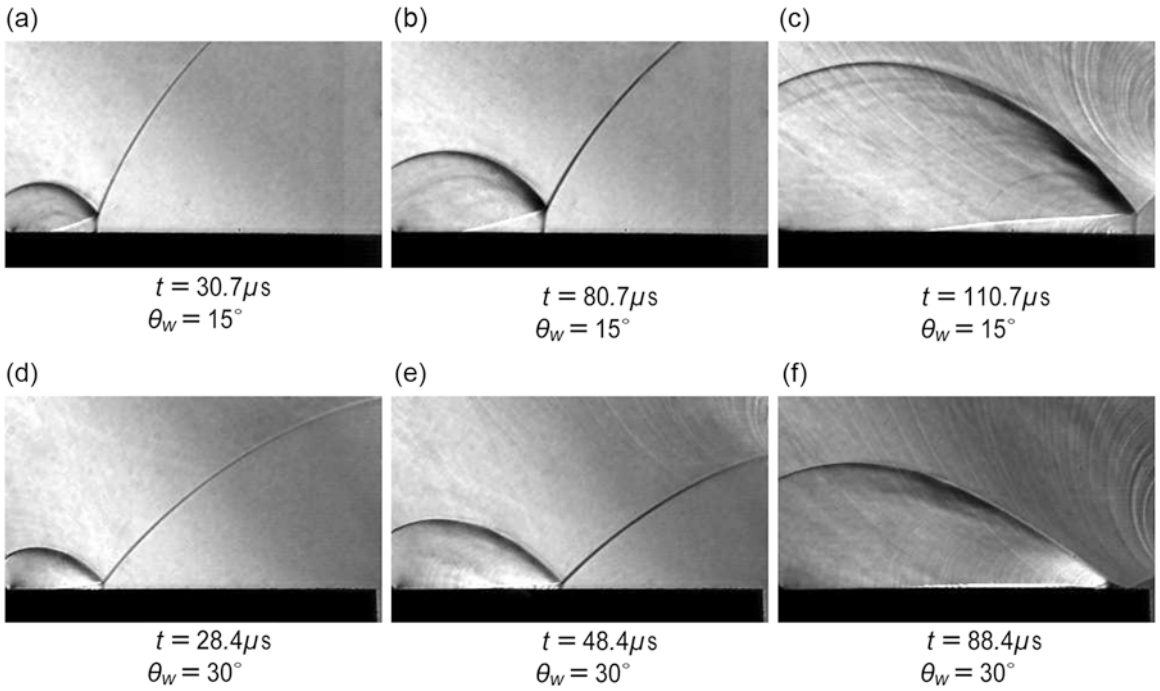

Fig. 3 Schlieren photographs from two experiments of (**a** –**c**) a shock with an apex Mach number of 1.52 reflecting off a 15° wedge, and (**d** –**f**) a shock with an apex Mach number of 1.55 reflecting off a 30° wedge

Fig. 4 Comparison between predicted triple point trajectories and those obtained in experiments

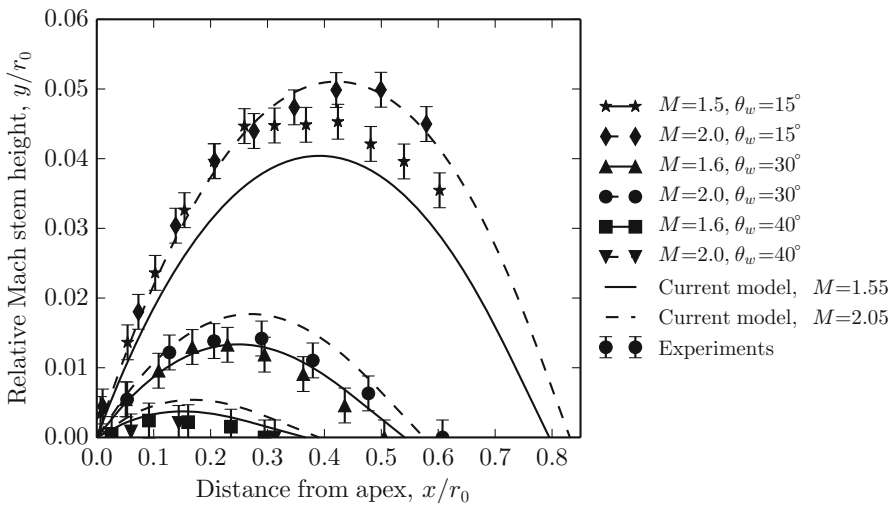

References

1. Ben-dor, G.: Shock Wave Reflection Phenomena. 2nd edn. Springer, Berlin (2007)
2. Hornung, H.G., Oertel, H., Sandeman, R.J.: Transition to Mach reflection of shock waves in steady and pseudosteady flow with and without relaxation. J. Fluid Mech. **90**, 541–560 (1979)
3. Guderley, G.: Stärke Kugelige und Zilindrische Verdichtungsstösse in der Nähe des Kugelmittelpunktes bzw. der Zilinderachse. Luftfahrtforschung **199**, 302–312 (1942)
4. Ben-dor, G., Takayama, K., Kawauchi, T.: The transition from regular to Mach reflection and from Mach to regular reflection in truly nonstationary flows. J. Fluid Mech. **100**, 147–160 (1980)
5. Ben-dor, G., Takayama, K.: Analytical prediction of the transition from Mach to regular reflection over cylindrical concave wedges. J. Fluid Mech. **158**, 365–380 (1985)
6. Ben-dor, G., Takayama, K., Dewey, J.: Further analytical considerations of weak planar shock wave reflections over a concave wedge. Fluid Dyn. Res. **2** (2), 77–85 (1987)
7. Itoh, S., Okazaki, N., Itaya, M.: On the transition between regular and Mach reflection in truly non-stationary flows. J. Fluid Mech. **108**, 383–400 (1981)
8. Whitham, G.B.: A new approach to problems of shock dynamics, Part I: two-dimensional problems. J. Fluid Mech. **2**, 145–171 (1957)
9. Milton, B.E.: Mach reflection using ray-shock theory. AIAA J. **13** (11), 1531–1533 (1975)
10. Gray, B.J., Skews, B.W.: Experimental investigation into converging cylindrical shock wave reflection. In: Proceedings of 29th International Symposium Shock Waves, Madison WI, USA (2013)
11. Skews, B.W., Gray, B.J., Paton, R.T.: Experimental production of two-dimensional shock waves of arbitrary profile. Shock Waves **25** (1), 1–10 (2015)

Reflection of Cylindrical Converging Shock Wave Over Wedge

Zhigang Zhai, Fu Zhang, and Xisheng Luo

Introduction

When a planar shock wave collides with an inclined wedge, the shock reflection phenomenon will be found over the wedge. This shock reflection phenomenon was first reported by Mach [1] who found two different reflection configurations: regular reflection (RR) and Mach reflection (MR). Seventy years later, this shock reflection phenomenon was reconsidered by von Neumann [2] and a simplified two-shock theory (2ST) and a three-shock theory (3ST) were proposed to describe the flows of the RR and the MR, respectively. Based on the 2ST and 3ST, much attention has been paid to the transition between RR and MR (RR↔MR), and several criteria have been proposed to predict the RR↔MR transition. von Neumann deduced the detachment criterion that the transition from RR to MR (RR → MR) occurs when the flow deflected angle through the incident shock exceeds the maximum flow deflected angle through the reflected shock (this critical angle is called detachment angle hereinafter). Another common criterion is mechanical equilibrium criterion, suggested originally by von Neumann. However, the agreement between the various proposed criteria and the experimental results was never satisfactory enough.

It is accepted that there are two extreme conditions for the RR↔MR transition, namely, the detachment condition beyond which the RR is theoretically impossible and the mechanical equilibrium condition beyond which the MR is theoretically impossible. Besides, a dual-solution domain exists, in which both RR and MR are theoretically possible. The existences of two extreme conditions for RR↔MR transition and the existence of the dual-solution domain led Hornung et al. [3] to hypothesize that a hysteresis could exist in the RR↔MR transition process. However, one should recall that the transition criteria were proposed based on the 2ST and 3ST which were developed under the assumption that all the discontinuities are straight in the vicinity of their intersection points. As a consequence, the application of these criteria in unsteady flows is restricted.

The reflection of a shock at a wall in steady flow is simple no matter for a planar or a curved shock reflection at a planar or a curved wall. However, the shock reflection in unsteady flows becomes more complicated. Several experiments have been performed to investigate the reflection of a planar moving shock on a circular wedge [4]. The interaction of a nonconstant velocity shock wave over straight surfaces is another example of a truly unsteady reflection process [5]. Even though, investigation on a curved incident shock reflection over a wedge is seldom performed because of the difficulty in generating manageable curved shock wave in experiment, which motivates this study.

In our previous work, a simple but effective technique was proposed to generate a cylindrical converging shock wave in a horizontal shock tube based on the shock dynamics theory [6]. In this work, the reflection of a converging shock wave over a wedge is experimentally and numerically investigated in this cylindrical shock tube.

Experimental and Numerical Methods

In our previous work, a special converging tube is designed and manufactured based on the shock dynamics theory to convert a planar incident shock into a cylindrical converging one [6]. In the designed shock tube, the controlling parameters of the initial shock Mach number $M_0 = 1.2$, the shock tube height $H_0 = 95$ mm, and the converging angle $\theta_0 = 15°$ are adopted, as shown in Fig. 1a. Under these conditions, the length of the converging section is calculated to be 143.9 mm, and the shock Mach number when the shock enters the converging section is 1.29. In order to investigate

Z. Zhai (✉) • F. Zhang • X. Luo
Advanced Propulsion Laboratory, Department of Modern Mechanics, University of Science and Technology of China, Hefei 230027, China
e-mail: sanjing@ustc.edu.cn

G. Ben-Dor et al. (eds.), *30th International Symposium on Shock Waves 1*, DOI 10.1007/978-3-319-46213-4_96

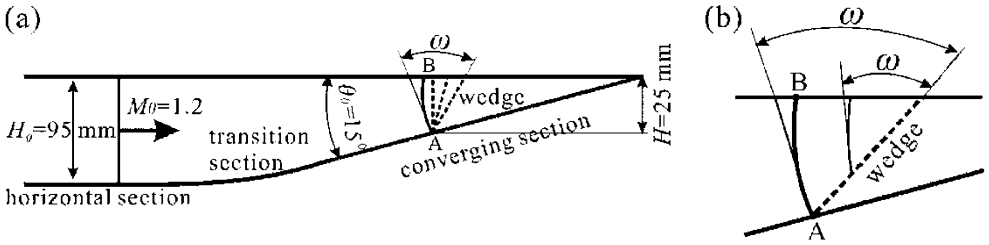

Fig. 1 The sketch of the shock tube (**a**) and the amplification of the test section (**b**)

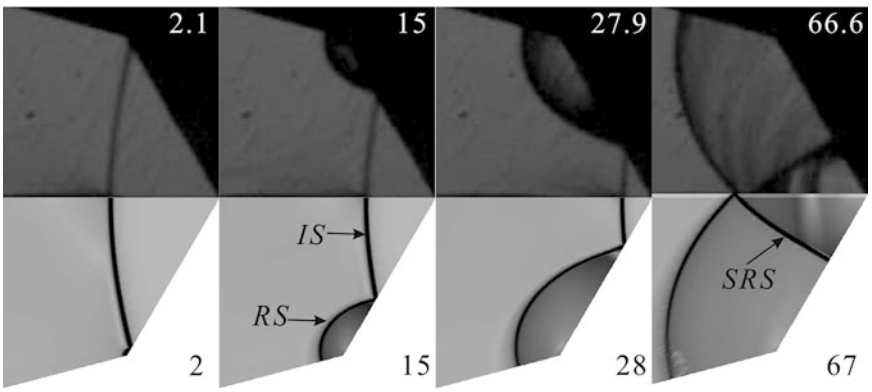

Fig. 2 Comparison of the experimental (*upper*) and numerical (*lower*) results of a cylindrical shock reflection over a wedge with $\omega = 45°$. The numbers indicate the time of the shock impact and the unit is μs (similarly hereinafter). *IS*, incident converging shock; *RS*, reflected shock of the *IS* reflected from the wedge; *SRS*, second reflected shock of the *RS* reflected from the horizontal wall

the reflection of the cylindrical shock wave over a wedge, wedges with different inclined angles are separately embedded into the converging section. In this study, the distance from the start of the converging section to the leading edge, which is fixed, is 47.3 mm. When the shock meets the leading edge, the shock Mach number increases to 1.383. The incident angle ω is defined as the angle between the wedge and the tangent of intersection of the cylindrical shock with the wedge, as indicated in Fig. 1.

The experiments are conducted in a horizontal square shock tube which consists of a 2 m driver section, a 4 m driven section, and a 1 m converging test section. The cross section is 95 mm × 95 mm. A Z-fold schlieren system is adopted to visualize the flow field. Illuminated by a DC regulated light source, the flow field is captured by a high-speed video camera. In the present study, two different incident angles of 45° and 75° are adopted, and the frame rates are 235,000 fps and 175,000 fps, respectively.

The numerical method VAS2D [7], which has been well validated in simulating compressible flows such as the shock–body interaction [7] and shock–bubble interaction [8], is used. In the numerical algorithm, the two-dimensional Euler equations are adopted as the governing equations. The finite volume method is used to discretize the conservation laws by applying them directly to each nonoverlapping control volume. The MUSCL-Hancock scheme is adopted to compute the flux through the cell interface. The unstructured quadrilateral adaptive mesh is employed to refine local complex areas and could effectively capture the wave patterns. The initial temperature and pressure are 293 K and 101 325 Pa, respectively. The initial mesh size of 0.5 mm and the finest mesh size of about 31 μm in the positions where greater density gradient exists are applied.

Results and Discussion

In this section, the experimental and numerical results of a cylindrical shock wave reflection over wedges with different inclined angles are presented and discussed. The moment when the cylindrical shock wave collides with the leading edge of the reflecting wedge is defined as the initial time (i.e., $t = 0$ μs).

It is known that an RR will happen when the incident angle is small enough. Figure 2 illustrates the cylindrical converging shock reflection over a wedge with $\omega = 45°$. Both the experiment and the computation show the occurrence of the RR ($t = 15$, 28 μs). After the converging shock is reflected from the cuspidal point, the reflection of the reflected shock from the horizontal wall is also regular ($t = 67$ μs), forming a second reflected shock (*SRS*). When

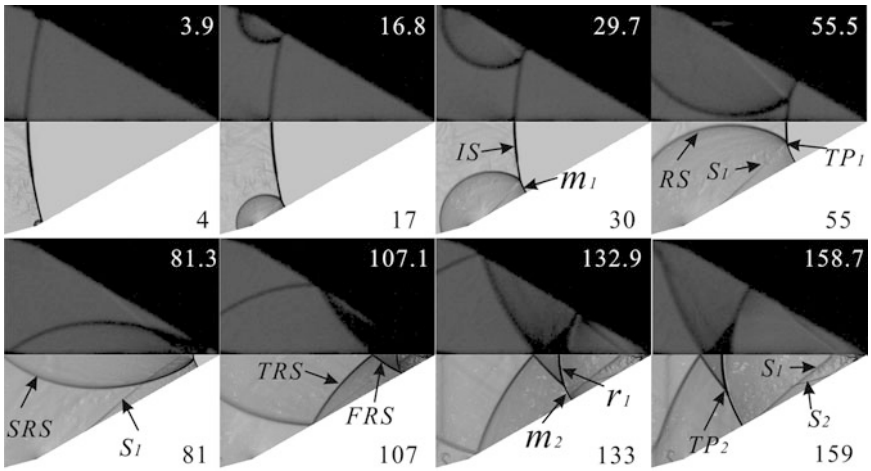

Fig. 3 Comparison of the experimental (*upper*) and numerical (*lower*) results of a cylindrical shock reflection over a wedge with $\omega = 75°$. *m*, Mach stem; *S*, slip line; *TP*, triple point; r_1, the reflected shock from the cuspidal point; *TRS*, the third reflected shock from the SRS reflection over the wedge. *FRS*, the fourth reflected shock from the *TRS* reflection at the horizontal wall. The other symbols are the same as those in Fig. 2

the incident angle exceeds a certain value, the RR is impossible and an MR occurs instead. The experimental and numerical results of the converging shock reflection over a wedge with $\omega = 75°$ are given in Fig. 3. It is found that when the cylindrical shock encounters the wedge, an MR happens with the formation of a Mach stem (m_1) and a triple point (TP_1) ($t = 17$ μs). As time proceeds, the length of the Mach stem increases, and a slip line (S_1) becomes evident ($t = 30$–55 μs). As the converging shock moving towards the cuspidal point, the incident converging shock is completely occupied by the Mach stem and the triple point terminates at the horizontal wall. The reflection of the reflected shock from the horizontal wall generates a second reflected shock ($t = 81$ μs). After the m_1 is reflected from the cuspidal point, this reflected shock, called r_1, propagates back in the converging part. Once again the third reflected shock (*TRS*) from the reflection of the second reflected shock at the wedge is formed and the reflection of the third reflected shock at the horizontal wall forms a fourth reflected shock (*FRS*) ($t = 107$ μs). The fourth reflected shock interacts with the shock r_1, resulting in the generation of a second Mach stem (m_2) and a second triple point (TP_2), together with a second slip line (S_2) ($t = 133$–159 μs). From the comparison, it is found that the experimental results coincide well with the numerical results, allowing us to further explore the cylindrical shock reflection phenomena using numerical method.

The formation of a Mach stem indicates the occurrence of an MR. Therefore, the height of the Mach stem is an important quantity during the MR process. Figure 4 gives the time-variation of the height of the first Mach stem for $\omega = 75°$. It can be observed that the height variation of the first Mach stem can be divided into three stages. Firstly, the height

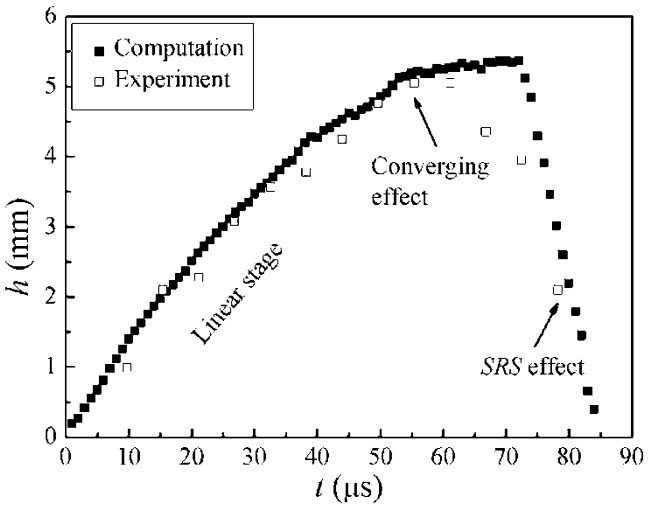

Fig. 4 Variation of the Mach stem height for $\omega = 75°$

increases quickly with nearly a linear velocity. Subsequently, the height still increases and the growth rate slows down. As the shock moving forwards, the shock strength is increasing and the incident angle is decreasing. As we know, the larger the shock strength, the smaller the critical angle. In other words, the critical angle is decreasing as the shock moving forwards.

The MR, however, is always maintained, which means that the incident angle is always larger than the critical angle. In this work, during the converging shock moving along the wedge, the variation range of the incident angle is about 15° if the perfectly cylindrical shape of the shock is assumed (cylindrical assumption hereinafter). However, the variation of the critical angle caused by the shock strength increase is

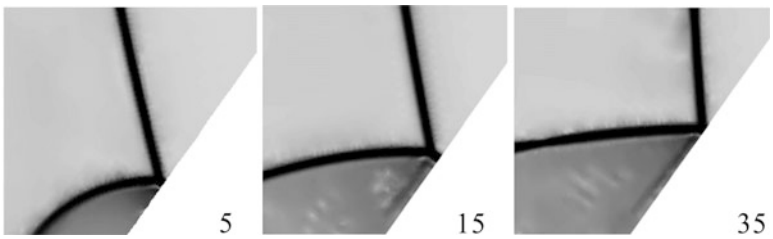

Fig. 5 Numerical results of the converging shock reflection over the wedge with $\omega = 50.5°$ at three instants. The numbers indicate the time and the unit is μs

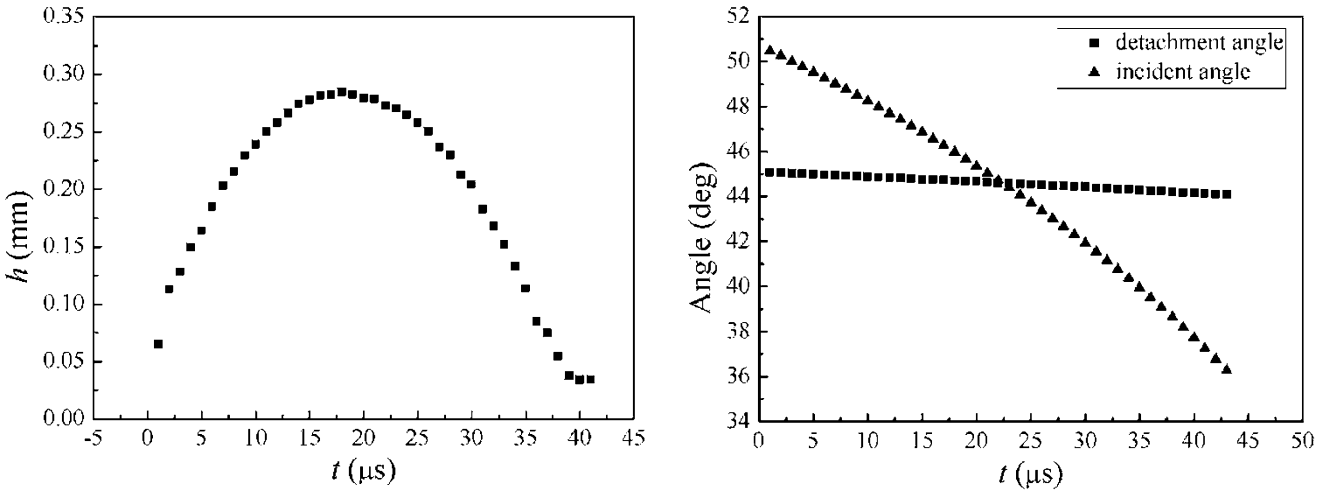

Fig. 6 Variation of the Mach stem height (*left*) and time-variations of the incident angle and the detachment angle (*right*) for $\omega = 50.5°$

no more than 2° before the first Mach stem absolutely occupies the incident shock wave. Consequently, the reduction rate of the incident angle is greater than the critical angle. The reduction of the incident angle suppresses the growth of the Mach stem. When the first triple point terminates at the horizontal wall, the incident shock is absolutely occupied by the first Mach stem. Afterwards, with the disturbance of the second reflection shock and the shock converging effect, the height of the first Mach stem drops dramatically until disappears.

As mentioned before, during the shock propagating along the wedge, the reduction rate of the incident angle is greater than the critical angle. If an RR occurs when the shock encounters the leading edge, it is hardly converted into MR in following evolution. However, once an MR occurs first, on one hand, if the incident angle is always larger than the critical angle before the Mach stem occupies the incident shock, the MR will be persisted; otherwise, the case that the incident angle smaller than the critical angle may take place, which indicates the occurrence of the MR → RR transition. From the results, one can find that the RR is persisted for $\omega = 45°$ while the MR is persisted for $\omega = 75°$, indicating that in former case, the incident angle is always smaller than the critical angle, while in latter case, the incident angle is always larger than the critical angle. Due to the shock converging effect, the flow after the cylindrical shock passage is unsteady. According to point of Ben-Dor [9], detachment criterion is adopted for the shock reflection in unsteady flows. For a planar shock with the Mach number of 1.383 in air, the detachment angle is 45.09°. As stated before, the RR is impossible beyond the detachment angle. As a consequence, it is possible to find the RR when $\omega = 45°$ and reasonable to observe the MR when $\omega = 75°$.

In order to investigate the MR → RR transition during the shock moving along the wedge, an initial incident angle of $\omega = 50.5°$ is given to numerically explore the cylindrical shock reflection phenomena over the wedge, as shown in Fig. 5. A small Mach stem can be observed after about 5 μs of the shock impact. Subsequently, the Mach stem gradually disappears after about 35 μs, which means that the MR is transited into RR. The variation of the Mach stem height is shown in Fig. 6 (left) from which one can find the height of the Mach stem increases first and then decreases. The MR → RR transition occurs at about 40 μs after the shock arriving at the wedge. The variations of the incident angle and the detachment angle are presented in Fig. 6 (right). Note that the incident angle and the detachment angle are calculated based on the cylindrical assumption. As the shock moving, both the incident angle and the detachment angle are gradually decreasing with different rates. After about 23 μs, the incident angle is smaller than the detachment angle, possibly illustrating the MR → RR transition. At

this time, the detachment angle is calculated to be 44.59°. However, we note that the time of the MR → RR transition predicted by the detachment criterion is earlier than the time observed from the numerical images, and the incident angle when the Mach stem disappears is measured to be 37.25°, which is much smaller than the detachment angle. The assumption that the strength and the shape of the cylindrical shock is unaffected with the presence of the wedge results in, on one hand, a larger detachment angle and, on the other hand, a smaller incident angle. Nevertheless, further examination indicates that the cylindrical assumption results in about 1° difference for the incident angle measurement, and about 2.3 % difference of the shock Mach number and the resulted about 1° difference for the detachment angle calculation. Therefore, one could conclude that the hysteresis process is presented during the MR → RR transition.

Conclusions

The unsteady reflection of a cylindrical converging shock wave over a plane wedge is experimentally and numerically investigated. The results show that for a small incident angle, an RR happens on the wedge, and for a large incident angle, an MR happens and is persisted on the wedge. As the cylindrical shock moving forwards, the shock strength increases, and both the incident angle and the critical angle decrease. The results show that the incident angle varies greatly compared with the critical angle. The RR, MR, and the MR → RR transition may occur along the wedge, depending on the initial incident angle. The critical angle of the RR → MR transition when the shock encounters the wedge is predicted by the detachment criterion, and the prediction agrees well with the numerical results. Nevertheless, the detachment criterion fails to provide a good prediction for the MR → RR transition because of the existence of the hysteresis process.

Acknowledgments This work was supported by National Natural Science Foundation of China (11302219).

References

1. Mach, E.: Uber den verlauf von funkenwellen in der ebene und imraume. SitzungsbrAkadWiss Wien. **78**, 819–838 (1878)
2. Neumann J von. Oblique reflection of shock. Explos. Res. Rep. 12, Navy Dept., Bureau of Ordinance, Washington, DC (1943)
3. Hornung, H.G., Oertel, H.J., Sandeman, R.J.: Transition to Mach reflection of shock waves in steady and pseudo-steady flow with and without relaxation. J. Fluid Mech. **90**, 541–560 (1979)
4. Skews, B., Blitteswijk, A.: Shock wave reflection off coupled surfaces. Exp. Fluids **21**, 491–498 (2011)
5. Glass II, H.T.C.: Blast wave reflection trajectories from a height of burst. AIAA J. **24**, 607–610 (1986)
6. Zhai, Z., Liu, C., Qin, F., Yang, J., Luo, X.: Generation of cylindrical converging shock waves based on shock dynamics theory. Phys. Fluids **22**, 041701 (2010)
7. Sun, M., Takayama, K.: Conservative smoothing on an adaptive quadrilateral grid. J. Comput. Phys. **150**, 143–180 (1999)
8. Zhai, Z., Si, T., Luo, X., Yang, J.: On the evolution of spherical gas interfaces accelerated by a planar shock wave. Phys. Fluids **23**, 084104 (2011)
9. Ben-Dor, G.: Shock Wave Reflection Phenomena. Springer, Berlin (2007)

Numerical Study of the Interaction Process Between a Planar Shock Wave and a Square Cavity Filled with Different Gases

Dan Igra and Ozer Igra

Introduction

Flows in which shock wave interact with a rigid boundary are found in many engineering applications and therefore draw a lot of attention during the past seven decades. The rigid boundary may have different geometry, a building where an explosive air blast took place, a mine tunnel in which an accidental blast propagates, an internal combustion engine where inflow and outflow valves are periodically opened and closed, etc. In order to correctly predict loads acting on rigid boundary and to reduce them one has to understand the complex flow evolved during such interactions. A relatively simple example is the flow resulted from the diffraction of a planar shock over a square cavity installed in a duct; this was studied experimentally and numerically in [1]. Later, a similar geometry was studied numerically in [2]; in that case the square cavity was filled with small dust particles in order to reduce the pressure acting on the square cavity walls. The present chapter is a further step in this topic; it investigates numerically the case when an incident shock wave propagates in a duct, shown in Fig. 1; black square indicates the location where pressure was computed. In the present case, the square cavity was filled with either Helium, Argon, Air, or SF_6 while the rest of the duct contained only Air.

D. Igra (✉)
RAFAEL, Aerodynamics Group, P.O.B. 2250, Haifa 31021, Israel
e-mail: danigra@gmail.com

O. Igra
Professor Emeritus, Department of Mechanical Engineering,
Ben Gurion University of the Negev, P. O. Box 653,
Beer Sheva 84105, Israel

Numerical Scheme

The computational domain is two dimensional. Computations were performed using a compressible inviscid flow model, solving the Euler equations listed below.

$$\frac{\partial U}{\partial t}+\frac{\partial F}{\partial x}+\frac{\partial G}{\partial y}=0 \tag{1}$$

$$U=\begin{Bmatrix}\rho\\ \rho u\\ \rho v\\ \rho E\end{Bmatrix};F=\begin{Bmatrix}\rho u\\ \rho u^2+p\\ \rho uv\\ u(\rho E+p)\end{Bmatrix};$$

$$G=\begin{Bmatrix}\rho v\\ \rho uv\\ \rho v^2+p\\ v(\rho E+p)\end{Bmatrix}$$

$$e=E-\frac{1}{2}\left(u^2+v^2\right) \tag{3}$$

$$p=(\gamma-1)\rho e \tag{4}$$

where ρ and p are density and pressure, respectively. E and e are total and internal specific energies and u, v are velocity components in the x, y directions, respectively. γ is the specific heats ratio (for each gas the appropriate γ was used). The ideal gas equation of state (4) was employed in the numerical simulations.

Simulations were conducted using the commercial FLUENT code, with the coupled (density based) solver based on a second order AUSM upwind scheme. The solver is second order in both space and time. The AUSM (Advection Upstream Splitting Method) is a flux vector splitting scheme. This scheme separates the flux to convective and pressure parts. First an interface Mach number is computed based on velocities from the neighboring cells. This interface Mach

G. Ben-Dor et al. (eds.), *30th International Symposium on Shock Waves 1*, DOI 10.1007/978-3-319-46213-4_97

number is then employed to compute the convective and pressure fluxes.

The grid is composed of quadrilateral cells. In these cells the flow was solved using a finite volume scheme. The conservation equations of mass, momentum, and energy were solved in each cell for unsteady flow. The grid contained 620,560 cells.

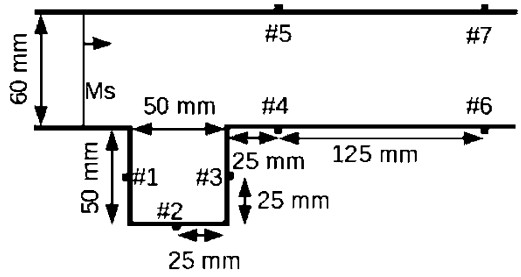

Fig. 1 Schematic description of the investigated square cavity. The incident shock wave is shown prior to its diffraction into it

Results and Discussions

Computations were conducted for compressible flows inside the two-dimensional duct as shown in Fig. 1. In all computations the duct is filled with air; different gases (air, argon, helium, or SF_6) filled the cavity. The same initial pressure prevails in the duct and in the cavity.

In Fig. 2, pressure histories computed at locations #1, #2, and #3 marked in Fig. 1 are shown for the four different gases placed inside the square cavity. It is apparent from Fig. 2 that the acoustic impedance and density of the gas

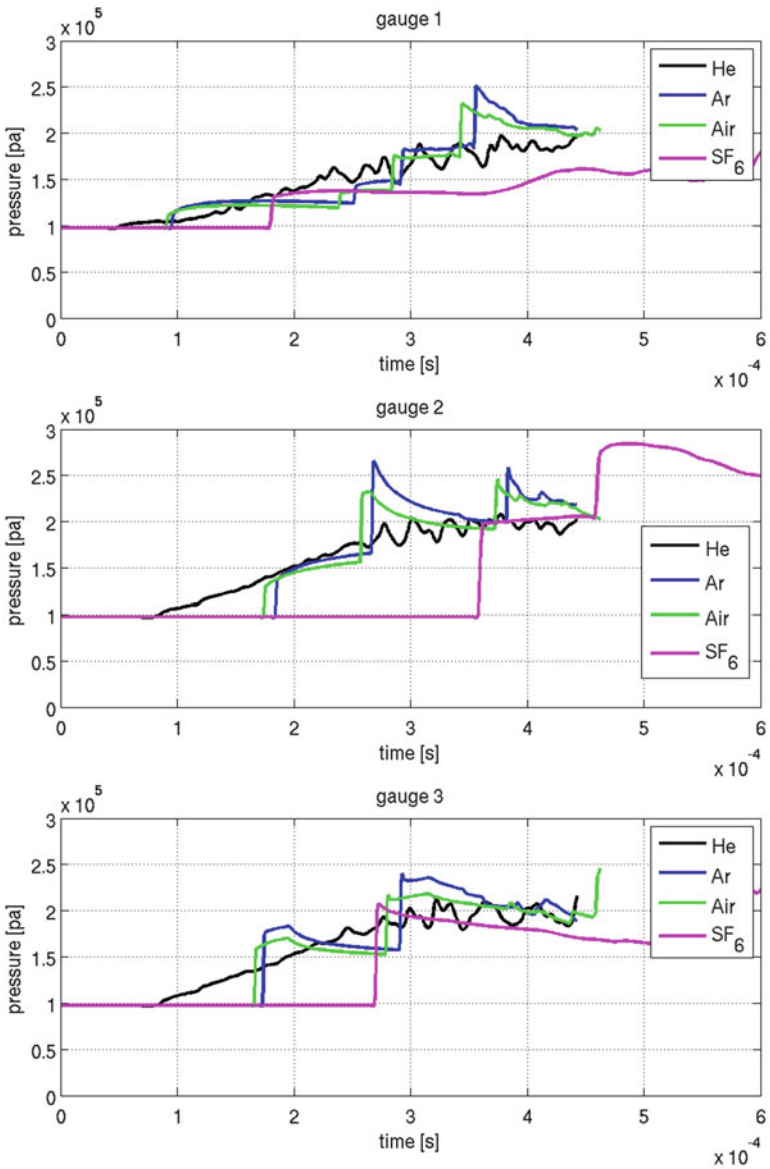

Fig. 2 Computed pressure variations inside the cavity. Initial conditions are: $M = 1.3$, $T_0 = 23.3\ ^\circ\mathrm{C}$, and $P_0 = 0.97$ bar

filled inside the square cavity have pronounced effect on the shape and strength of the diffracting shock wave. In the case of a light gas (helium), the diffracting shock wave is reduced to almost a compression wave. Also, the lowest pressure is experienced inside the cavity when helium gas is used. Argon and air have similar acoustic impedance and therefore similar shock diffraction patterns are evident in these cases. SF_6 is significantly heavier than the other three gases and it has the lowest specific heat ratio, $\gamma = 1.096$, resulting in the strongest pressure jump across the diffracting shock wave. All cases were solved for the same initial conditions, i.e., $M = 1.3$, $T_0 = 23.3$ °C, and $P_0 = 0.97$ bar.

In the pressure histories computed at locations #1 and #2, three shock waves are present. The first is the pressure jump across the diffracting shock over the first (left) wall of the cavity while the second jump is across the reflected shock from the cavity bottom; the third pressure jump seen at these locations is the pressure jump across the shock wave reflected from the cavity exit (right) wall. As expected, the pressure jump across reflected shock wave is larger than the one prevailing across the incident/diffracting shock wave. In the computed pressure history at location #3, for the SF_6 case, one sees only the pressure jump when the diffracted shock over the first (left) wall of the cavity reached the cavity right wall. In the cases when the cavity is filled with air or argon, one observes (at #3) the pressure jump across the diffracted shock and across the reflected shock wave from the cavity left wall. When the cavity contains SF_6, the shock propagation velocity inside the cavity is significantly lower and as a result the reflected shock waves from the cavity left (entrance) wall have not reached station #3 during the computation time.

Pressure variations inside the cavity for the case when the incident shock wave Mach number is $M = 2.03$, $T_0 = 22.6$ °C, and $P_0 = 0.9$ bar are shown in Fig. 3. As expected, larger pressure jumps are witnessed in this case. Now a clear,

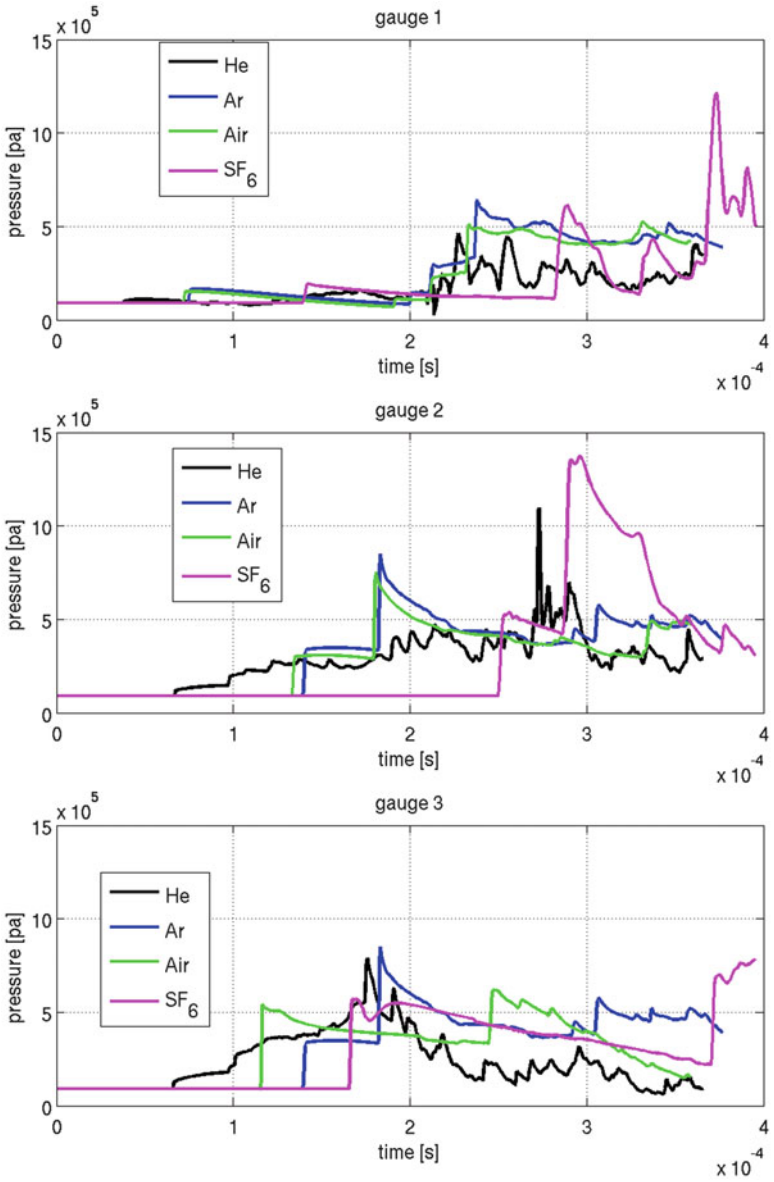

Fig. 3 Computed pressure variations inside the cavity. Initial conditions are: $M = 2.03$, $T_0 = 22.6$ °C, and $P_0 = 0.9$ bar

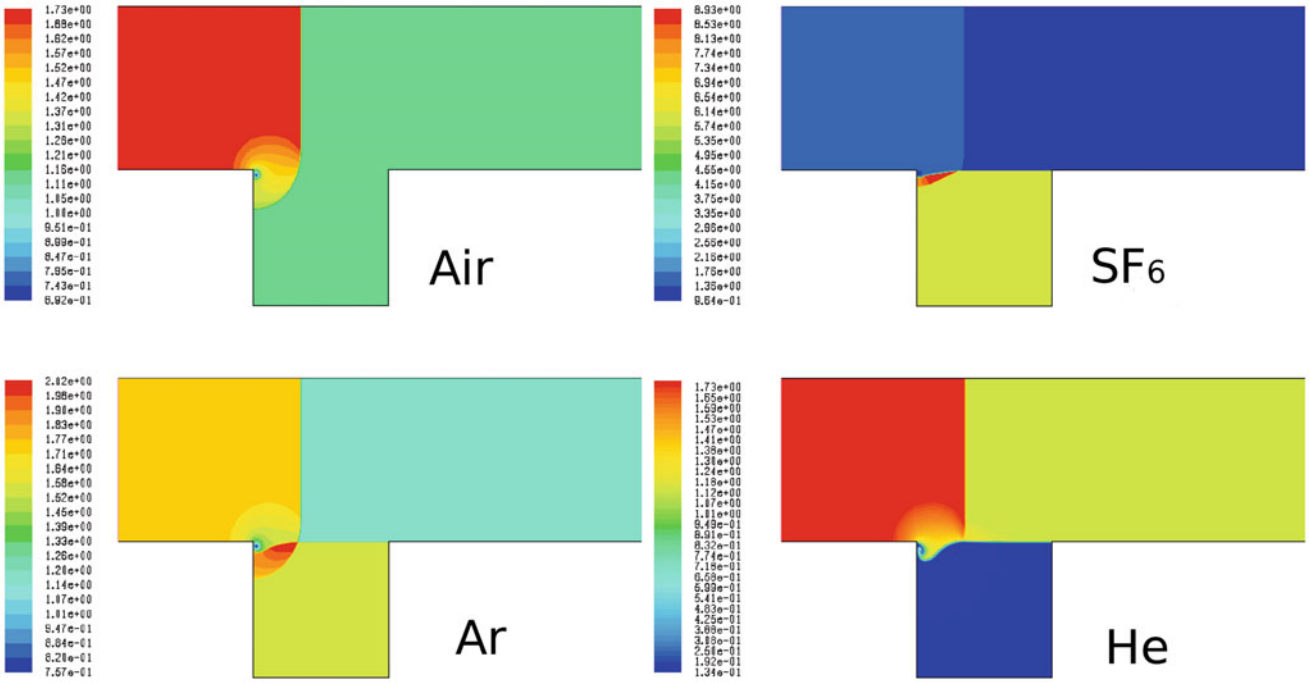

Fig. 4 Computed density variations inside the cavity at early time, 40 μs after the incident shock wave reached the cavity entrance. Initial conditions are: $M = 1.3$, $T_0 = 23.3$ °C, and $P_0 = 0.97$ bar

weak shock, not a compression wave is observed in the case when the incident shock wave diffracted into a cavity filled with helium gas. Again, lower pressure values are witnessed in the helium case. In both cases (Figs. 2 and 3), when the cavity contains helium, the computed pressure histories indicate highly nonstationary flow inside the cavity. This is most probably a result of the high speed of sound in helium resulting in multiple Mach wave reflections between the cavity walls.

It is of interest to see the density variations during the incident shock wave diffraction into the cavity. Results presented in Fig. 4 highlight the early part of the diffraction process, at 40 μs after the incident shock wave reached the cavity entrance. It is evident from this figure that in the case of SF_6 we have the slowest shock; it hardly started its diffracting into the cavity. The fastest (and the weakest) shock is seen in the case when the cavity is filled with helium, where the head of the diffracting shock wave made more than half of its way toward the cavity bottom. As already seen in Fig. 2, similar diffraction is witnessed in the air and in the argon cases due to similarity in their acoustic impedances. Density variations at a later time (at 160 μs after the incident shock wave reached the cavity entrance) are shown in Fig. 5.

It is clear from this figure that similar behavior is observed in the argon and air cases. In both one notices the reflection of the diffracted shock from the cavity bottom and from the cavity right wall; also seen is part of the diffracting shock wave front propagating toward the cavity right bottom corner, where the pre-shock gas is still at ambient conditions (green color). A completely different situation is observed in the cases where helium or SF_6 are present inside the cavity. While in the SF_6 case the diffracted shock wave is still propagating down the cavity toward its bottom, in the helium case the situation is completely different. As the propagation velocity of the shock wave in the helium gas is higher than in the other cases, now we see that the reflected shock from the cavity bottom has exited the cavity and it propagates up toward the duct upper wall, (see in Fig. 5).

From results shown so far it is clear that due to the difference in the acoustic impedance, and γ of the gases contained inside the cavity different flows developed inside the cavity. For checking the influence of these gases on the flow developed downstream of the cavity, pressure histories were computed at locations #4, #5, #6, and #7 shown in Fig. 1. Obtained results are shown in Fig. 6. It is apparent from this figure that effects associated with the usage of different gases inside the cavity on the post-cavity flow are marginal. This is not surprising since the amount of these gases in the cavity is very small in comparison with the amount of air contained inside the investigated duct.

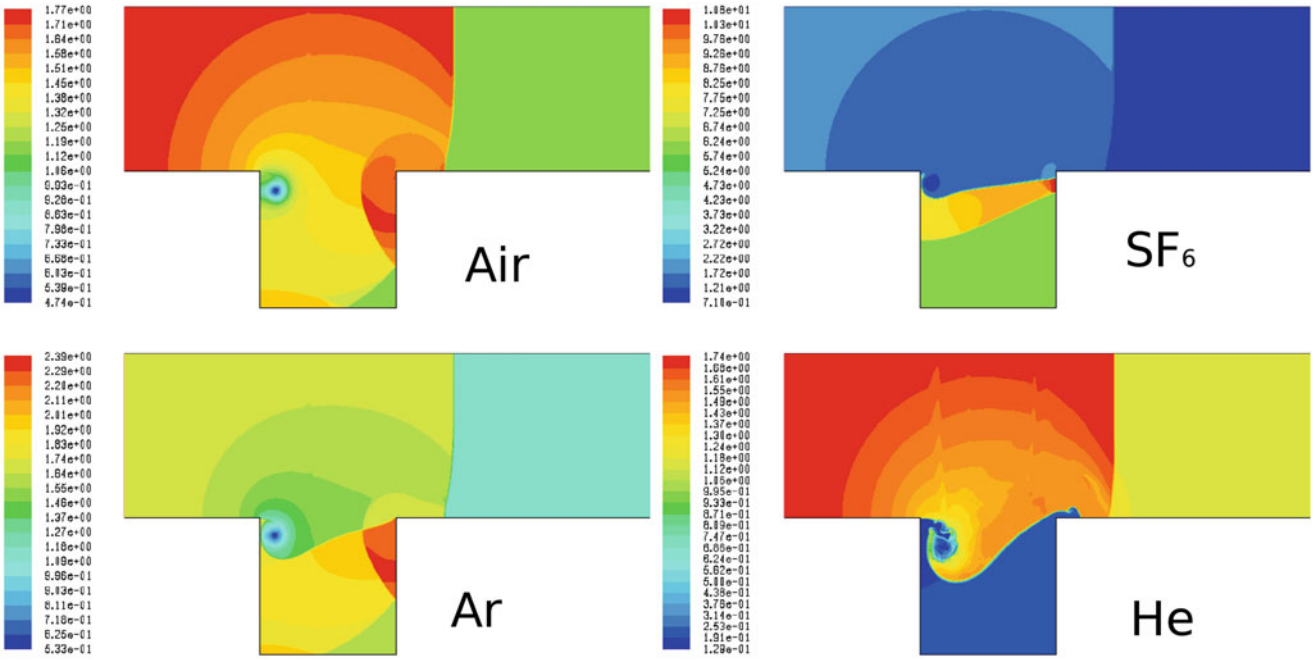

Fig. 5 Computed density variations inside the cavity at a later time, 160 μs after the incident shock wave reached the cavity entrance. Initial conditions are: $M = 1.3$, $T_0 = 23.3$ °C, and $P_0 = 0.97$ bar

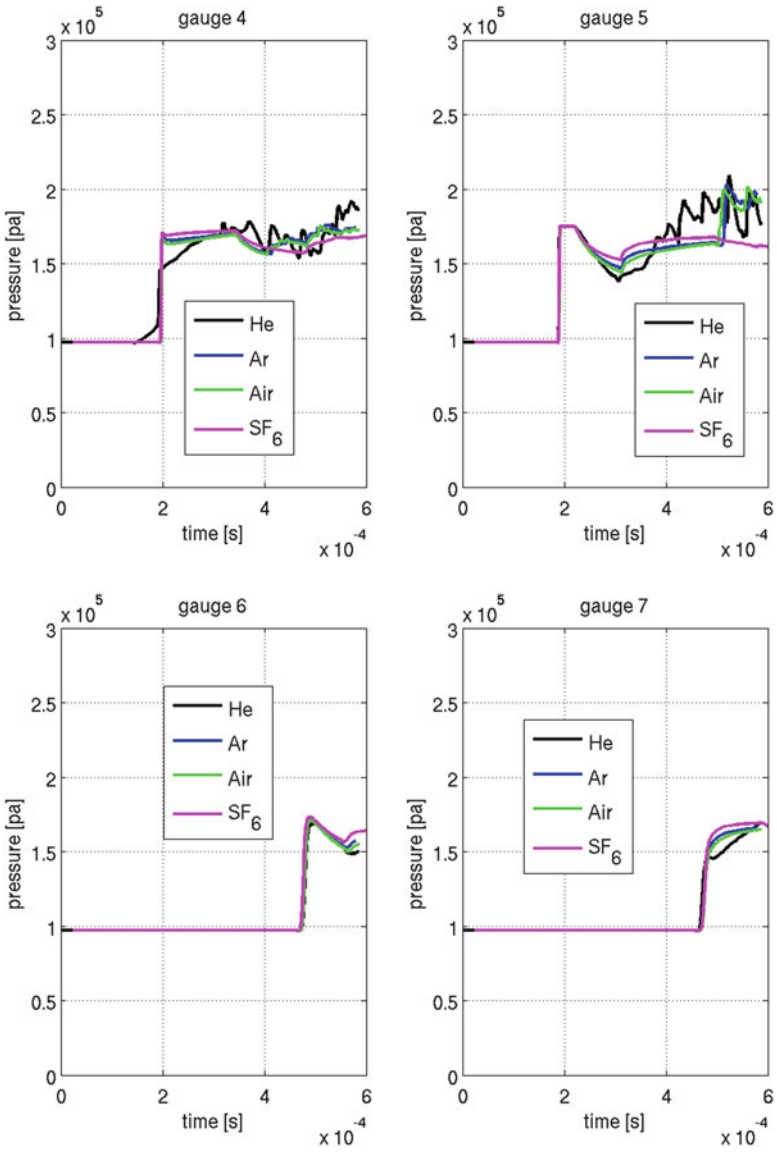

Fig. 6 Computed pressure histories at various locations downstream of the cavity exit. Initial conditions are: $M = 1.3$, $T_0 = 23.3$ °C, and $P_0 = 0.97$ bar

Conclusions

While the presence of different gases inside the cavity have significant effect on the flow field evolved inside the cavity, it has negligible effect on the prevailing pressure downstream of the cavity. Therefore, if one wants to avoid a sudden pressure jump and to reduce the acting pressure inside the cavity, helium gas should be used inside the cavity.

References

1. Igra, O., Falcovitz, J., Reichenbach, H., Heilig, W.: Experimental and numerical study of the interaction process between a planar shock wave and a square cavity. J. Fluid Mech. **313**, 105–130 (1996)
2. Wang, B.Y., Wu, Q.S., Wang, C., Igra, O., Falcovitz, J.: Shock wave diffraction by a square cavity filled with dusty gas. Shock Waves J. **11**, 7–14 (2001)

Flow Phenomena of An Expansion Wave Entering a Cylindrical Cavity

M.S. Whalley, B.W. Skews, and R.T. Paton

Introduction

Previous research on wave focusing has concentrated on shock wave cavity flows [1]. Expansion wave cavity flows have not been investigated before. This paper looks at the flow resulting from an expansion wave entering a cylindrical cavity. Initially numerical simulations were run with the assumption of a plane diaphragm, however after experimental testing it was found that an investigation of the effect of a curved diaphragm also needed to be done. An expansion wave is a pressure wave which causes the fluid it travels through to decrease in pressure. As expansions cause a decrease in pressure they tend to flatten out (decrease in gradient) as they travel through a fluid. This makes them difficult to visualise as generally they are associated with weak gradients [2]. The interaction between shock and expansion waves has been investigated, as has the diffraction of an expansion wave around a corner [3].

Experimental Apparatus

The apparatus used was a unique shock tube with split windows which allowed the diaphragm to be clamped within the window area allowing the flow immediately around it to be visualised. The shock tube is shown in Fig. 1. In this image the shock tube is open and ready for a new diaphragm to be inserted. The test piece can be seen in the left hand section, this is the part which is pressurised for a test. The shock tube allows the test piece to be positioned at different distances from the diaphragm, as well as the use of different shape test pieces. A maximum gauge pressure of 6 bar can be used with this shock tube. The test section has a 100 × 100 mm square cross-section and the test piece a 50 mm radius.

A schlieren optical set-up was used with a high speed camera to capture images from tests. Initially a simple schlieren set-up with a knife-edge was used, but a colour schlieren set-up was later adopted due to the weak density gradients associated with expansion waves. The filters used are shown in Fig. 2. The central filter was found to give the best results, however further development is being done to improve the filters.

Diaphragm Investigation

One of the issues when conducting experimental tests was the large curvature on the diaphragm when loaded. Initially a plastic diaphragm was used and as can be seen in the first row of images in Fig. 3 the diaphragm deflects up to half the width of the test section before bursting. This leads to significantly different flow compared to the ideal case of a plane diaphragm burst. In order to try and reduce the curvature an investigation into the use of different materials for the diaphragm was done. The best material was found to be 0.1mm thick aluminium foil, shown in the second row of images in Fig. 3. This material was found to give a consistent and symmetrical burst when the material was previously scored diagonally with very little diaphragm deflection before bursting. A very limited supply of aluminium was available and additional tests will be performed with aluminium diaphragms once more material is acquired.

Numerical Simulations

The computational software used for numerical simulations were Ansys Fluent 15 and STAR CCM+ 9. The Fluent simulations were run on a standard quad-core computer.

M.S. Whalley (✉) • B.W. Skews • R.T. Paton
Flow Research Unit, University of the Witwatersrand, PO WITS 2050, Johannesburg, South Africa
e-mail: matthew_wh@mweb.co.za

G. Ben-Dor et al. (eds.), *30th International Symposium on Shock Waves 1*, DOI 10.1007/978-3-319-46213-4_98

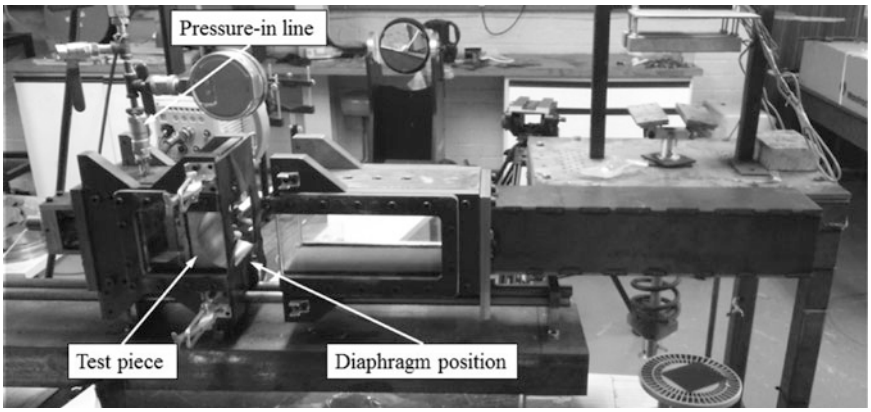

Fig. 1 Shock tube

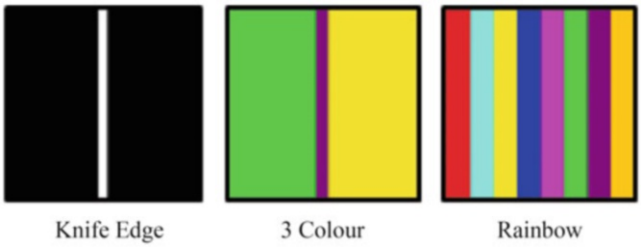

Fig. 2 Schlieren filters

The STAR CCM+ simulations were run using Crunchyard.com, a high powered computing facility at the University of the Witwatersrand.

Results

Numerical simulations for both plane and curved diaphragms were done to determine how significant an effect this had on the flow features. The results are shown in Fig. 4. There are significantly different features for the two cases and thus the features for both geometries need to be considered. The main feature of interest is the focusing phenomenon.

A comparison of the numerical results for a curved diaphragm and experimental colour schlieren results using a plastic diaphragm is given in Fig. 5. The experimental results don't show well-defined features as the density gradients present are weak, however there is visible correlation for the expansion entering the cavity in images 2 to 4. The 5th image appears to show similar features to the numerical result with the leading edge of the expansion waves having crossed over the symmetry line, but the contrast in the experimental image is not high enough to say this definitively. A low pressure region is definitely formed in the cavity, as is predicted by the numerical results, as at a later time the diaphragm is drawn into the cavity. This unfortunately results in the flow features being obstructed from view. The appearance of a shock wave in the experimental result at a much later time is also predicted by the numerical data. These correlations were deemed sufficient to consider the numerical results accurate while the experimental procedure is improved to obtain more definitive validation.

A comparison of the numerical results for different CFD packages was done as an additional validation. Figure 6 shows the results for a STAR CCM+ (first row) and a Fluent (second row) simulation. The results correlated very well, both in the shape of the flow features and the flow property values.

The focus region for both the plane and curved diaphragm case will now be considered in more detail. The focusing process is shown briefly in Fig. 4. When a curved diaphragm bursts the initial shock and expansion are already two dimensional waves. The transverse part of the expansion moves toward the centreline causing the flow to move both down the tube and towards the walls. The shock waves reflect off the wall and move towards the centreline of the tube, following the expansion wave. This results in the transverse expansion waves being trapped between two shock waves. The area enclosed by the contact surface and the transverse shock waves contains a concentrated expansion. It is formed almost immediately after diaphragm burst (as soon as the compression/shock waves have reflected off the wall). As the shock waves move towards the centreline and the focus region gets smaller the pressure, temperature and density of the fluid decreases until they reach a minimum just before the shock waves cross on the centreline. Once the shock waves have completely crossed the focus is completed.

For the plane diaphragm the expansion wave enters the cavity and causes the flow to accelerate out of the cavity. The curvature causes a reflected expansion wave to accelerate the fluid in the transverse direction as well as in the longitudinal direction (from the initial expansion wave). As a result, for continuity, the flow near the walls needs to be slowed once it leaves the cavity, causing compression waves to form at the walls at the start of the cavity. As the

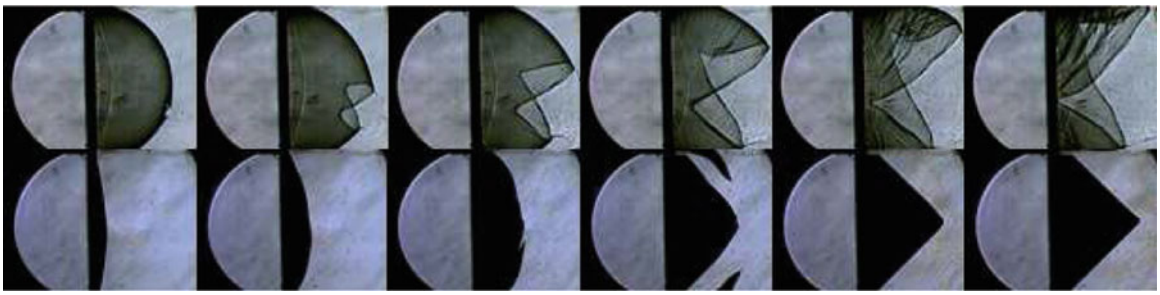

Fig. 3 Comparison of diaphragm bursts for plastic (*top*) and aluminium foil (*bottom*)

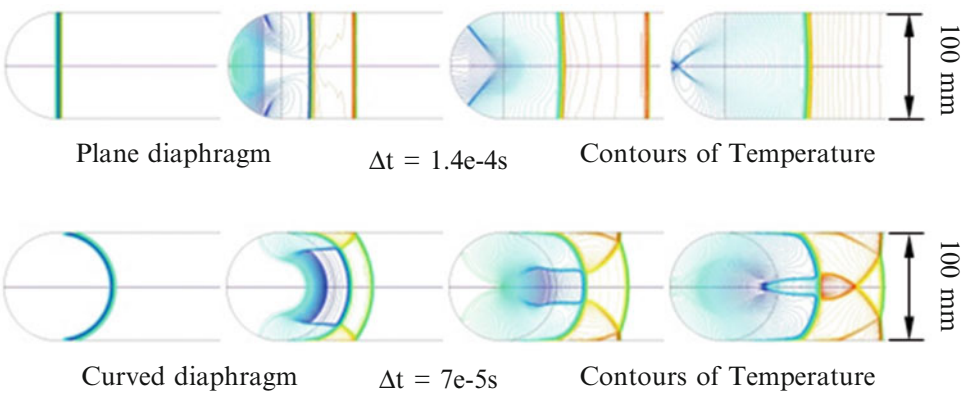

Fig. 4 Comparison of plane and curved diaphragm simulations (PR = 5)

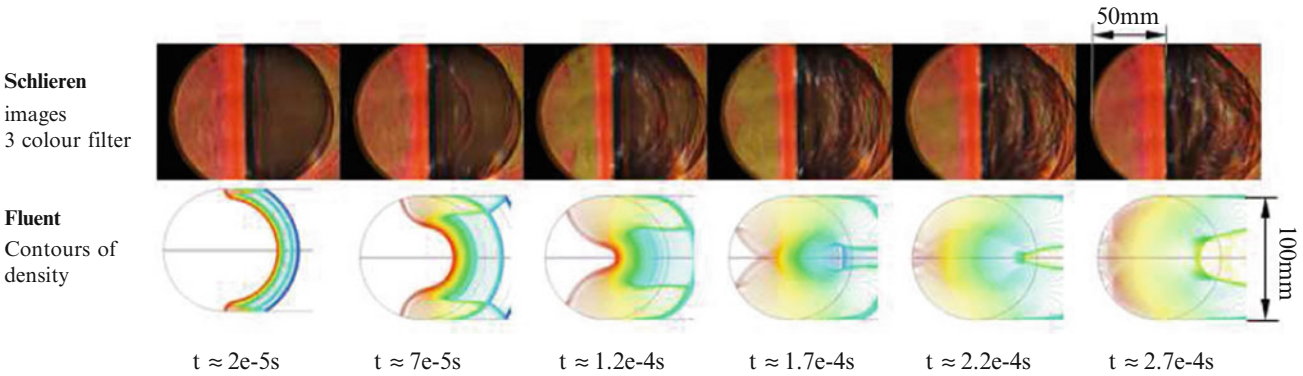

Fig. 5 Expansion wave entering a cylindrical cavity from a curved diaphragm (PR = 5)

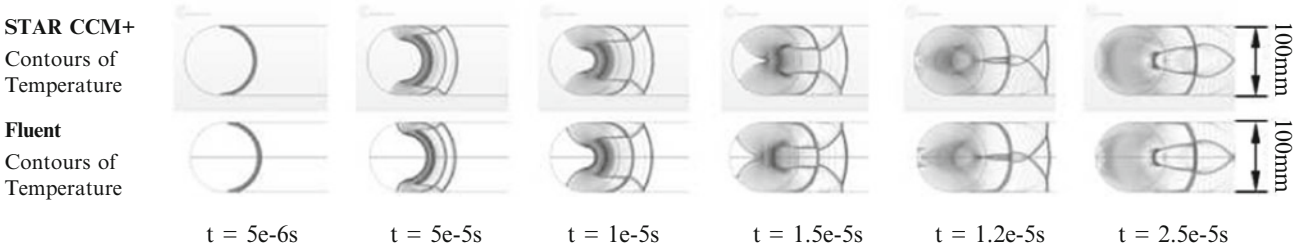

Fig. 6 Comparison of numerical results (PR = 5)

expansion wave moves further into the cavity the transverse waves get stronger and thus the flow speed increases. This causes the compression waves to get stronger until they form shock waves. The shock waves grow towards the centreline as flow further from the wall needs to be slowed. Once the shock waves meet at the centreline an enclosed region of

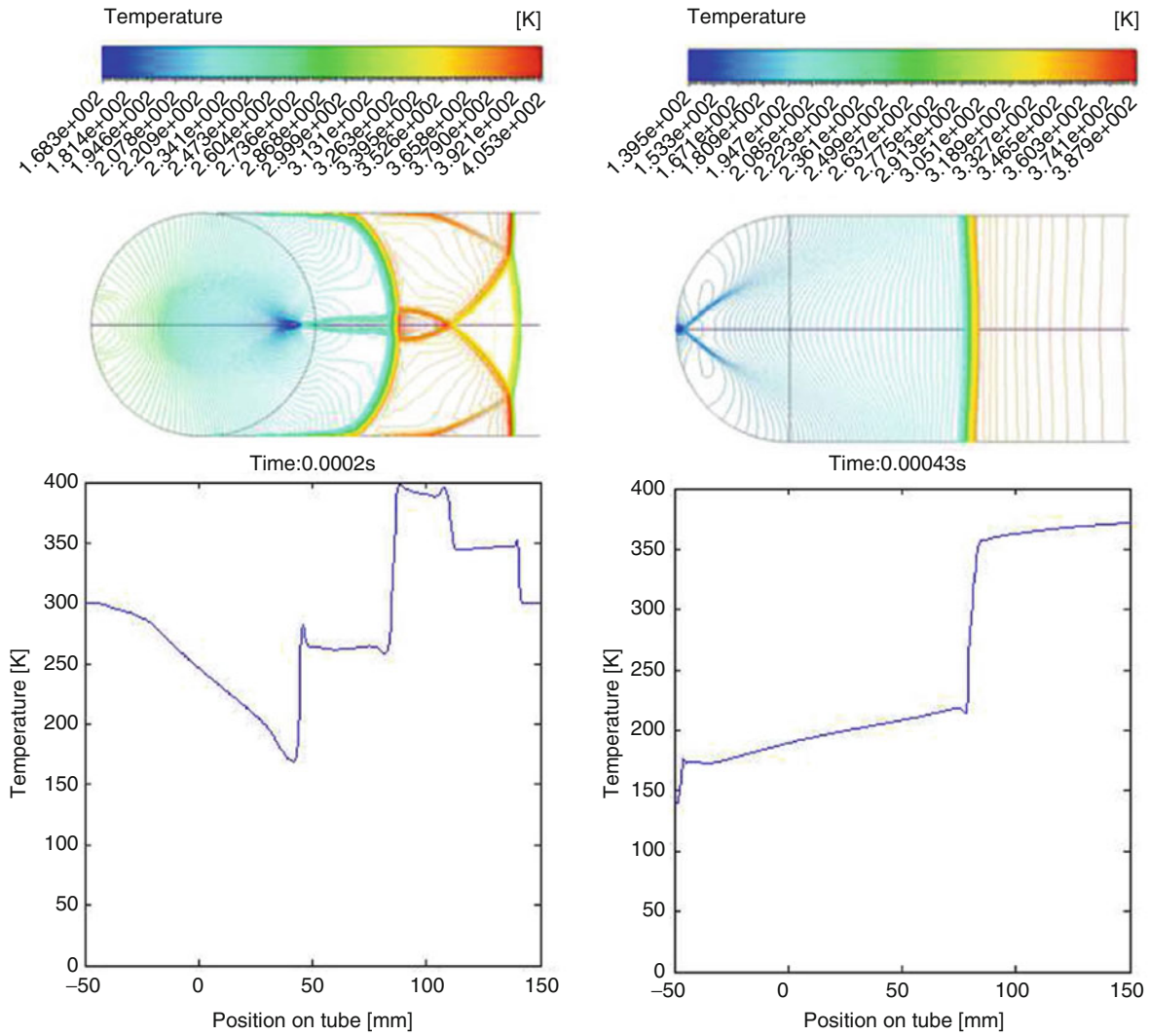

Fig. 7 End of focus for curved (*left*) and plane (*right*) diaphragms (PR = 5)

flow is formed. This can be considered the start of focus. The fluid in this area continues to be expanded by the transverse expansion waves, resulting in an area of low pressure, density and temperature, with high velocities just before the shock waves. The shock waves are then drawn into the cavity in order to maintain continuity. The fluid properties reach their lowest value just before the root of the shock waves cross at the centreline. When the shock waves crosses at the wall the focus is completed.

Figure 7 compares the end of focus for the curved and plane diaphragm simulations. The graphs show the temperature distribution along the centreline. Temperature is used as it most clearly shows the focus. The focus for the curved diaphragm (on the left) is less sharp than the plane diaphragm as the region is not completely enclosed by the transverse shocks. The graph on the right, for a plane diaphragm, clearly shows the small enclosed region just ahead of the shocks where the temperature is well below that of the rest of the fluid.

Figure 8 shows surface plots of temperature against position along the centreline of the tube and flow time. These plots help explain the movement of the waves in the fluid. For the curved diaphragm the presence of transverse waves is visible from the additional shock lines behind the main shock, representing transverse shock waves moving across the centreline. The focus region in this case continues to decrease in temperature up until the point where the shocks cross, resulting in a sharp point on the surface along both the position and time axes. For the plane diaphragm the transverse waves are only formed later, seen from the plane surface representing the initial shock wave travelling down the tube. The focus region is also quite different to that of the curved diaphragm. In this case the temperature reaches a minimum and is almost constant for a small period of time

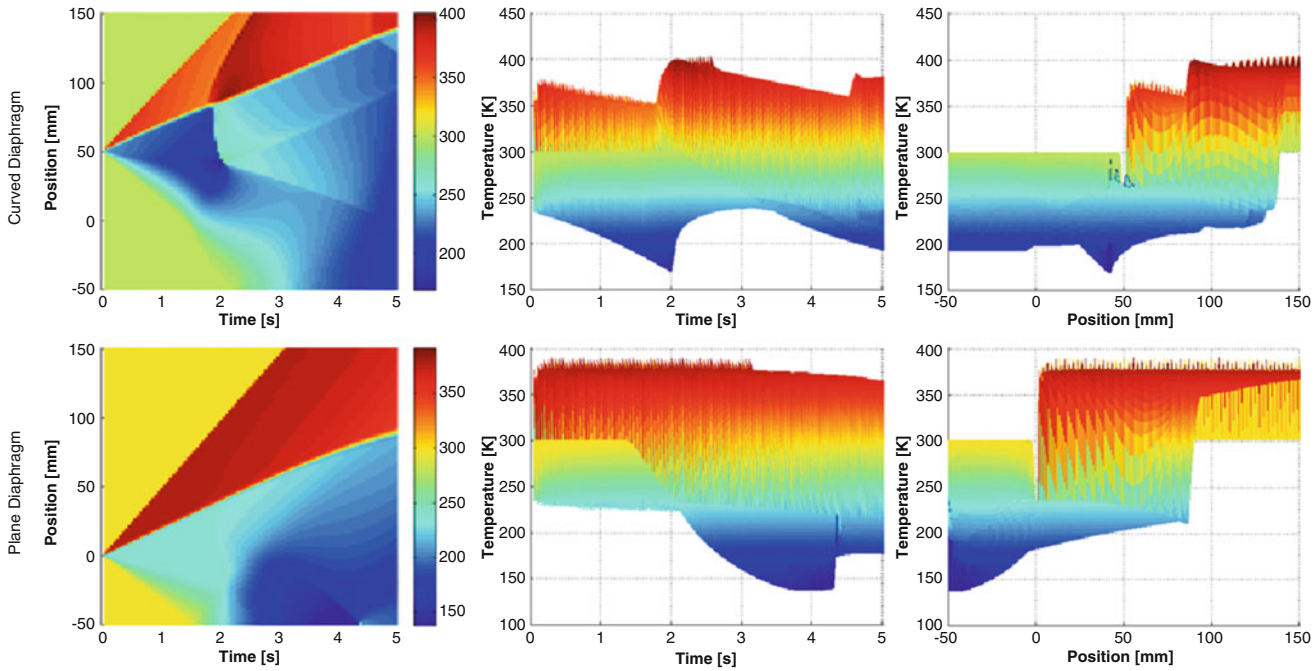

Fig. 8 Temperature distance time plots for curved diaphragm (*top*) and plane diaphragm (*bottom*) (PR = 5)

before the shock waves cross. This results in a region of almost constant low temperature of decreasing size which becomes a point just before the focus is completed.

Conclusions

The flow resulting from an expansion wave entering a cylindrical cavity is highly dependent on the shape of the initial expansion wave. For a plane expansion wave shock waves are formed at the entrance of the cavity which then move into the cavity. The area ahead of the shock waves decreases to a very low temperature, pressure and density. This is considered a focus region in the same way that the region of high pressure, density and temperature in shock wave cavity flows is considered a focus region. An initially curved expansion results in a focus at the diaphragm rather than in the cavity. For experimental work with expansion cavity flows, the deflection of the diaphragm is as important as the burst pressure and should be one of the primary criteria when selecting a diaphragm material.

References

1. MacLucas, D.A.: Shock wave-induced flow features in concave profiles. PhD Thesis, University of the Witwatersrand (2012)
2. Glass, I., Gordon Hall, J.: Shock Tubes. Handbook of Supersonic Aerodynamics, Section 18. University of Toronto, Toronto (1959)
3. Mahomed, I.: Two-dimensional expansion wave diffraction around a 90 degree convex corner. Masters Dissertation, University of the Witwatersrand (2013)

Investigation of an Expansion Fan/Shock Wave Interaction Between Low Aspect Ratio Wedges

L. Nel and B.W. Skews

Introduction

Considering a body in supersonic flow, shock waves and expansion fans develop as a mechanism for the fluid to traverse the contours of the body. In instances where bodies are in close proximity—such as store carriage and release from aircraft, supersonic engine inlets, and formation flying—these shock waves and expansion fans interact, resulting in an interesting flow field with complex wave patterns. Consequently, a fundamental understanding of such a flow field is of importance and an investigation of an expansion fan/shock wave interaction between bodies in close proximity is merited.

The basic physics of an expansion fan/shock wave interaction was suggested by Li and Ben-Dor [1], following a two-dimensional analytical study of such an interaction. An oblique shock wave, upon interacting with an expansion fan, is curved towards the origin of the expansion fan while passing through it and emerges from the fan as a straight shock once again. The expansion fan, subsequent to intersecting the shock wave, is deflected away from the shock's origin. Considering the expansion fan as a series of discrete Mach waves, there is a variation in entropy and flow properties above and below each Mach wave after intersection with the shock—due to the differing shock angle through which the fluid flows above and below the point of intersection—and consequently a slipline is formed. Each of the sliplines is curved in the same direction as the shock wave while traversing the expansion fan, just as each Mach wave of the expansion fan is curved when passing through the sliplines. (In reality, an expansion fan comprises of an infinite number of Mach waves and is therefore an expansive region, resulting in the formation of a slip region rather than discrete sliplines following the interaction with the shock wave.) Downstream of the expansion fan/shock wave interaction, the shock undergoes either a regular or Mach reflection off the surface generating the expansion fan, and the expansion fan is reflected from the surface generating the shock wave. Figure 1 shows a schematic (as adapted from Li and Ben-Dor [1]) and 2D CFD results (the authors' own) illustrating the flow phenomena occurring in an expansion fan/shock wave interaction.

The objective of the present research is to extend this understanding to include the three- dimensional flow phenomena present in an expansion fan/shock wave interaction. This forms part of a larger study to investigate the effect of varying the horizontal relative position of the bodies on the two- and three-dimensional nature of the interaction, as would pertain to one body moving past another.

Methodology

The methodology was to model an expansion fan/shock wave interaction between two wedges both experimentally, in a supersonic wind tunnel, and numerically, using Computational Fluid Dynamics (CFD). The experimental results provided insight into the flow field, as well as being utilized to validate the CFD results. Once validated, the CFD results were used to extract information about the three-dimensional nature of the flow field.

L. Nel (✉)
Aeronautic Systems Competency, Defence Peace Safety and Security, Council for Scientific and Industrial Research, 627 Meiring Naudé Road, Pretoria, South Africa

Flow Research Unit, University of the Witwatersrand, PO WITS 2050, Johannesburg, South Africa
e-mail: lnel@csir.co.za

B.W. Skews
Flow Research Unit, University of the Witwatersrand, PO WITS 2050, Johannesburg, South Africa

G. Ben-Dor et al. (eds.), *30th International Symposium on Shock Waves 1*, DOI 10.1007/978-3-319-46213-4_99

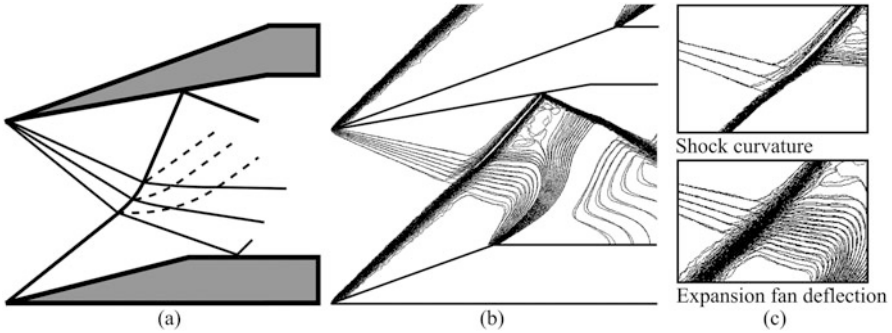

Fig. 1 Flow phenomena occurring in an expansion fan/shock wave interaction, (**a**) schematic, (**b**) density contours plotted from CFD results and (**c**) magnified view of the CFD results illustrating the shock curvature and expansion fan deflection

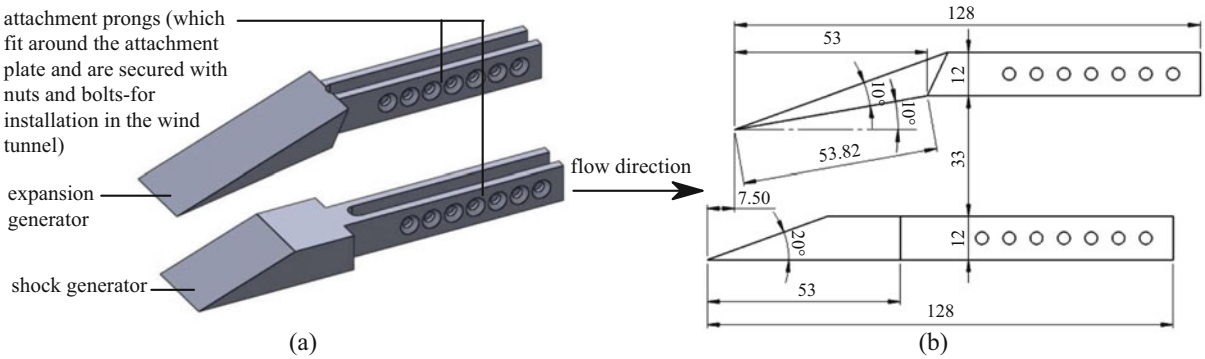

Fig. 2 Schematic of the wind tunnel model, (**a**) labelled trimetric view and (**b**) dimensioned side view (all dimensions in mm)

Experimentation

The expansion fan/shock wave interaction was modelled experimentally between two wedges, one generating the expansion fan (referred to as the expansion generator) and one generating the incident oblique shock wave (referred to as the shock generator). The expansion generator had a chord length of 53.82 mm (defined as the length of the lower surface of the wedge), a width of 25 mm, a wedge angle of 10° and afforded a flow deflection angle of 10°. The shock generator had a 53 mm chord length, a width of 25 mm and a 20° wedge angle (equal to the flow deflection angle). The wedges were mounted from the upper wall of the supersonic tunnel, with the expansion generator 33 mm above and 7.5 mm behind the shock generator. A dimensioned schematic of the wedges is shown in Fig. 2.

The experimentation was conducted in the supersonic wind tunnel test facility at the University of the Witwatersrand. The wind tunnel is an air pressure driven blow down tunnel with a square cross section, of dimension 101.6 mm × 101.6 mm, at the test section. The expansion fan/shock wave interaction was modelled in a Mach 2.5 freestream, with a settling chamber stagnation pressure of 250 kPa and an ambient temperature of 25 °C.

A classical colour schlieren system was used to visualize the interaction. The system was illuminated with a continuous 900 lumen LED light source and the light beam was parallelized between two off-axis parabolic mirrors, of diameter 152.4 mm and focal length 1.2 m, at a schlieren angle of 3°. The light source was cut-off at the focal point of the first parabolic mirror using a rectangular slit; at the focal point of the second mirror a band lattice mask, as proposed by Schardin [2], was used as the cut-off. The images were captured using a Nikon D90 DSLR camera with a shutter speed of 1/1250s. A two-dimensional image of the three-dimensional flow field is produced, as a consequence of the summation of the light deflections along the light's path, which should be considered when analysing the results.

Numerical Simulations

The expansion fan/shock wave interaction was modelled numerically using the Star CCM+ CFD package. The geometry was generated according to the specifications given in the Experimentation section, with a far-field bounding box extending 0.6 m forward, 2 m behind and 1 m above, below and on either side of the origin (placed in line with the back of the expansion generator, at the intersection of the two longitudinal centre planes). The fluid region was meshed using unstructured polyhedral cells, with prism cells on the wedge surfaces to model the boundary layer. A Reynolds-averaged Navier-Stokes simulation was performed, using a density-based, coupled solver with a second order accurate

AUSM flux-splitting scheme, to resolve the flow field. The air flow was considered steady and to behave as an ideal gas and turbulence was modelled using a k-ω SST model with low y+ wall treatment. The far-field boundary conditions were set to equal the wind tunnel freestream conditions, i.e. a Mach 2.5 flow with a 14.632 kPa static pressure and a static temperature of 132.51 K. Mesh convergence was confirmed by completing four simulations of varying mesh density. The CFD results were validated using experimental data, as discussed in the following section.

Results and Discussion

Validation of CFD Results with Experimental Data

For the validation of the CFD results, the flow features as resolved by the simulation are compared with the flow features as imaged from the experiment. The experimental image, CFD results and a schematic with an explanation of the flow features are given in Fig. 3.

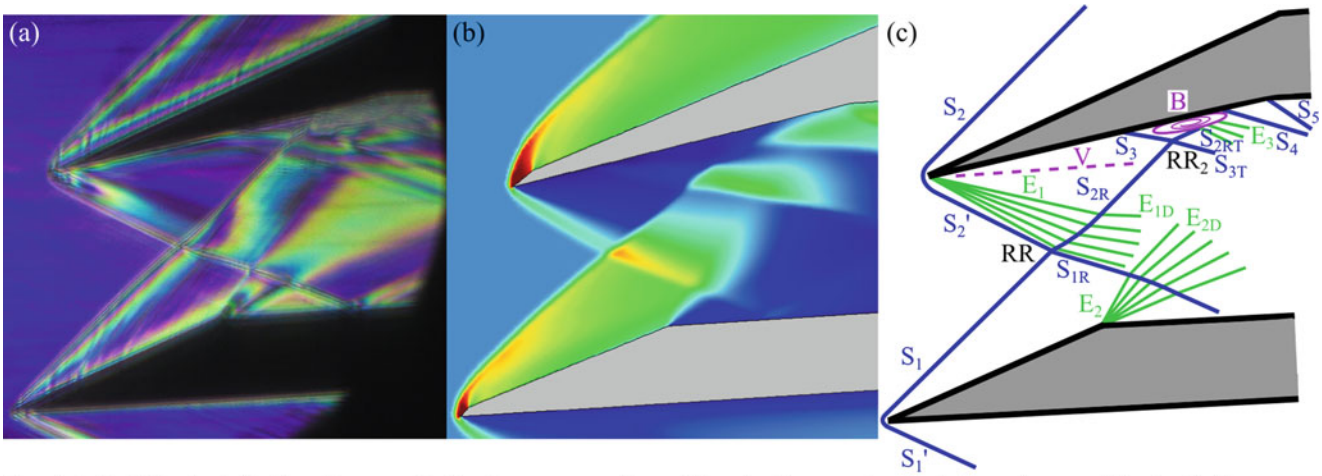

S_1: detached shock deflecting flow parallel to the upper surface of the shock generator (detachment, caused by the finite leading edge of the wedge, results in a shock S_1' on the underside of the wedge)
S_2: detached shock deflecting flow parallel to the upper surface of the expansion generator (detachment, caused by the finite leading edge of the wedge, results in a shock S_2' on the underside of the wedge)
E_1: expansion fan deflecting flow parallel to the lower surface of the expansion generator
E_2: expansion fan deflecting flow around the shoulder of the shock generator
RR: regular reflection at point of intersection of S_1 and S_2'
S_{1R}: reflected shock of S_1, undergoes curvature upon interaction with E_2 and is transmitted as a straight oblique shock following this interaction
S_{2R}: reflected shock of S_2', undergoes curvature upon interaction with E_1 and is transmitted as a straight oblique shock following this interaction
E_{1D}: deflected expansion fan, following the interaction of E_1 with S_{2R}
E_{2D}: deflected expansion fan, following the interaction of E_2 with S_{1R}
V: vortex shed from the tip of the wedge (not seen in the CFD image since it is a plot of the flow field on the centre plane of the geometry, rather than an integration of light deflections through the whole flow field as with the schlieren image)
B: boundary layer separation bubble, resulting from the shock wave/boundary layer interaction of shock S_{2R} with the boundary layer on the lower surface of the expansion generator
S_3: separation shock, deflecting flow around the boundary layer separation bubble
RR_2: intersection of S_{2R} with S_3 (regular reflection)
S_{2RT}: transmitted shock of S_{2R}
S_{3T}: transmitted shock of S_3
E_3: reflection of S_{2RT} as an expansion fan, deflecting flow over the boundary layer separation bubble
S_4: reattachment shock, deflecting flow parallel to the lower surface of the expansion generator once again
S_5: shock deflecting flow around the shoulder of the expansion generator

Fig. 3 Flow features in an expansion fan/shock wave interaction, (**a**) schlieren image from experiment, (**b**) density contour plot from CFD and (**c**) explanatory schematic

Considering the experimental modelling of the expansion fan/shock wave interaction, two deviations from the ideal case occur. Firstly, the shocks deflecting flow over the upper surfaces of the wedges (S_1 and S_2 in Fig. 3c) are detached due to the finite leading edge of the manufactured wedges. This results in a shock S_2' followed by the expansion fan E_1 under the expansion generator and both S_2' and E_1 interact with the shock emanating from the shock generator (S_1). Secondly, the wind tunnel model experienced a nose-down pitching moment on tunnel start-up, slightly altering the incidence angles of the wedges.

Both of these deviations were modelled in the CFD simulation to produce comparative results for validation. From a comparison of the CFD results with the schlieren image, it can be observed that the CFD adequately resolves all the flow features present in the experiment and can therefore be considered valid.

A numerical simulation of the ideal case of an expansion fan/shock wave interaction (where the shocks remain attached and the variation of the wedge incidence angles from the nose-down pitching was excluded) was performed to provide fundamental insight into the three-dimensional flow phenomena. The CFD results of the ideal case are also considered to be valid, given the validity of the results of the non-ideal case with the more complex flow field and since the flow features resolved in the ideal case are similar to those in the non-ideal case (excepting the features arising from the shock detachment from the wedges). The results from the ideal case are used in the discussion of the three-dimensional aspects of an expansion fan/shock wave interaction.

Discussion of a Three-Dimensional Expansion Fan/Shock Wave Interaction

Two phenomena occur as a consequence of the three-dimensional flow—wave diffraction and tip vortices shed from the edges of the wedges. The presence of these phenomena, intensified by the low aspect ratio of the wedges, affects the expansion fan/shock wave interaction and resultant flow field; this is of particular interest.

In the ideal case of an expansion fan/shock wave interaction, the shock deflecting flow over the upper surface of the expansion generator remains attached and the expansion fan, which develops under the expansion generator, interacts with the shock generated by the shock generator. A three-dimensional view of this interaction is shown in Fig. 4—density contour plots of a series of chord-wise slices is presented, coupled with a span-wise slice at the edge of the wedges (to give the three-dimensional perspective) and streamtraces from the centre plane to the edges (to indicate the flow direction). From Fig. 4a it can be observed that both the shock generated by the shock generator and the shock above the expansion generator diffract on either side around the edges of the respective wedge. As the shocks diffract their strength is decreased, resulting in a conical shock wave with a decreasing density ratio across the shock boundary as the cone is traced around the corner. The Mach waves comprising the expansion fan also diffract around the edge of the wedge, but to a lesser extent than the shocks due to their being weaker. Thus, the three-dimensional flow field around the expansion generator consists of a high pressure region above transitioning, via diffraction of both the shock

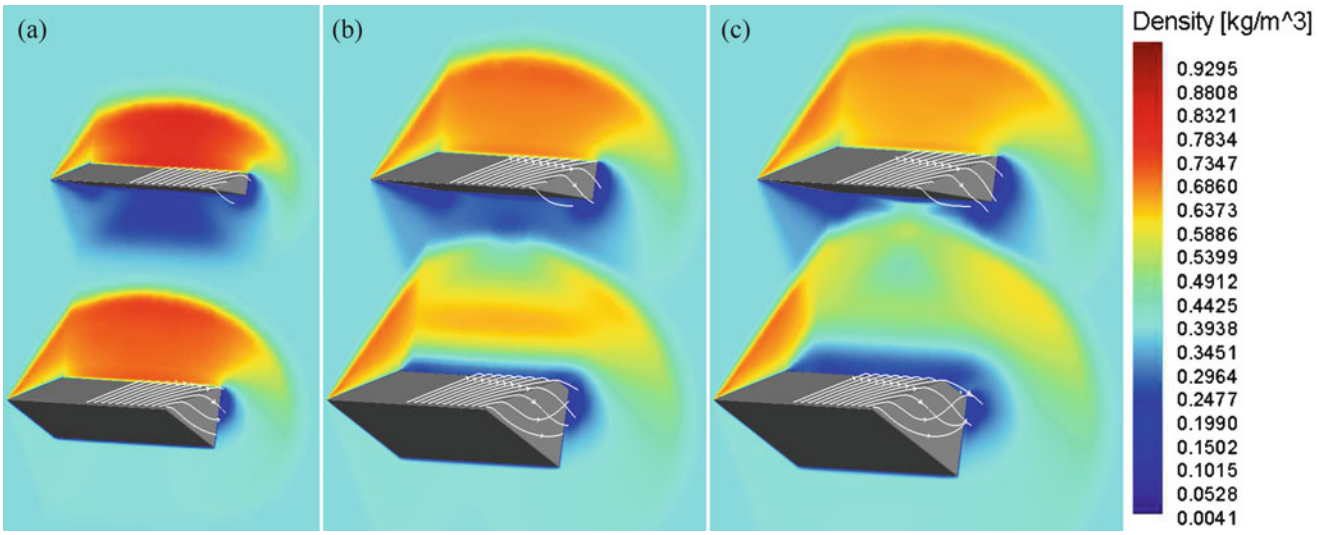

Fig. 4 3D view of the wedges with density contour plots along the chord, (**a**) 18 mm, (**b**) 31 mm and (**c**) 37 mm from leading edge of expansion generator

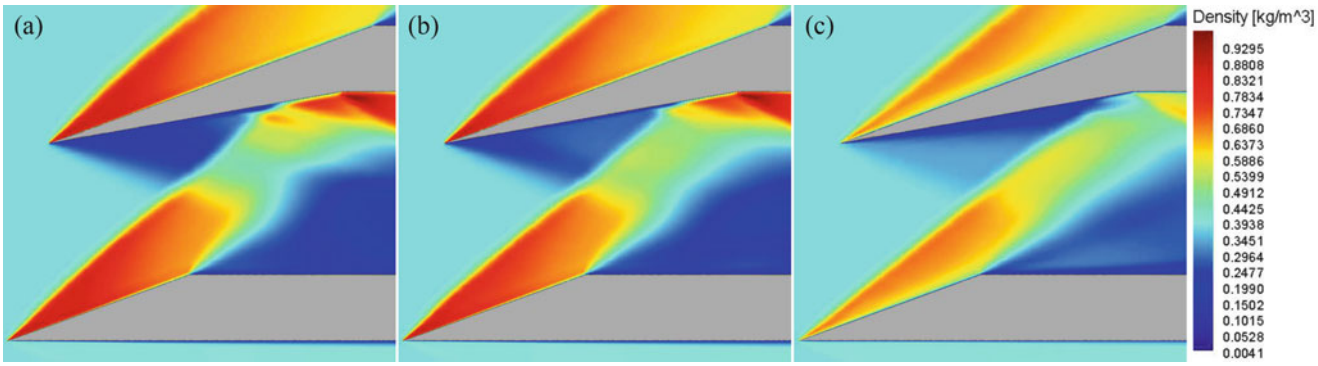

Fig. 5 Density contour plots along the span of the wedges, (**a**) centre plane, (**b**) 6.25 mm from centre and (**c**) 12.5 mm from centre (edge of wedge)

and the expansion fan, into a low pressure region below the wedge.

The pressure differential between the upper and lower surface of both the expansion generator and the shock generator cause a vortex to be shed from the tips of each wedge, as seen from the streamtraces in Fig. 4. The pressure differential is exacerbated in the case of the expansion generator, with the result that the vortex flow is shifted to below the wedge and interferes with the expansion fan/shock wave interaction (as opposed to the case of the shock generator where the vortex travels alongside the wedge). The presence of the vortices below the expansion generator, and the subsequent flow of air from the upper to the lower surface, causes an increase in pressure and density below the wedge—thereby weakening the expansion fan towards the wedge edges. Both the expansion fan and the tip vortices interact with the shock generated by the shock generator. Upon interacting with the expansion fan, the shock is curved (seen in Fig. 5) and the strength of the shock is decreased (as evidenced by the region of decreased density and the lower density ratio across the shock boundary in Fig. 4b, c). As a consequence of interaction with the weakened expansion fan and arising from the shock/vortex interaction, there is less curvature of the shock (seen in Fig. 5) and the density behind the shock is decreased to a lesser extent (seen in Fig. 4b, c) near the wedge edges. During the interaction with the tip vortices, the conical shape of the shock is altered—on initial intersection with the vortices the shock forms two bulges (Fig. 4b); as the interaction progresses these bulges increase in size and shift towards the centre plane until they coalesce and form a cusp in the centre, giving the shock a teardrop shaped cross section (Fig. 4c). This shock goes on to reflect off the lower surface of the expansion generator.

Conclusions

An expansion fan/shock wave interaction between low aspect ratio wedges gives rise to a complex flow field, in which wave diffraction and vortices shed from the wedge tips influence the interaction. Diffraction of the shocks and the expansion fan is present, resulting in an interesting transition from a high pressure region to a low pressure region around the wedge generating the expansion fan. The tip vortices shed from this wedge both weaken the expansion fan and interact with the shock generated by the other wedge—altering the shape of the shock cross section from an ellipse to a teardrop. Further investigation of this interaction would include the effect of altering the flow deflection angles, the influence of varying the horizontal relative position of the wedges and characterizing a dynamic expansion fan/shock wave interaction (where one of the wedges is rapidly accelerated).

References

1. Li, H., Ben-Dor G.: Oblique-shock/expansion-fan interaction—analytical solution. AIAA J. **34**(2) Technical Notes, 418–421 (1996)
2. Schardin, H.: Die Schlierenverfahren und ihre Anwendungen. Ergebnisse der Exakten Naturwissenschaften, **20**, 303–439, (1942). English translation available as NASA TT F12731, April 1970 (N70-25586)

Studying Shock Wave Reflections over Double Cylindrical Concave Wedge Reflectors

Vineet Soni, Meital Geva, O. Ram, Abdellah Hadjadj, Arnab Chaudhuri, Oren Sadot, and Gabi Ben-Dor

Introduction

The inherent properties of the complex flow features resulting from the shock wave reflections are essential to solve real-world problems, such as the aviation safety and the human safety near detonations, since these phenomena involve drastic changes in pressure and temperature. Thus, it has intrigued the researchers to carry out thorough investigations of these flow features from past several decades.

Extensive studies have been carried out to understand different shock wave reflection structures, such as regular reflection (RR) and Mach reflection (MR), and their transitions. A comprehensive study on these features in steady, pseudo-steady, and unsteady flows is detailed by Ben-Dor in [1]. The shock reflections off concave cylindrical surfaces, in particular, are the area of interest in this chapter. Several examinations were carried out using cylindrical concave reflectors by Izumi et al. [2], Skews and Kleine [3], and Shadloo et al. [4]. However, these studies concentrated on the shock focusing and post shock focusing characteristics. Additionally, Skews et al. in [5, 6] performed experiments using different circular shapes in combination with various slopes. But, the circular reflectors were convex. In [7], Gruber studied the shock reflection features over cylindrical concave cavities and suggested the transition angle of MR to RR stage for low incident Mach numbers. Very recently, Geva et al. [8] conducted a study about shock wave reflections over double circular reflectors of a combination of concave and convex surfaces. However, it was restricted to only one geometrical configuration. In contrast, shock reflections over double concave/convex wedge reflectors were analyzed experimentally by Ben-Dor [9] with different configurations of the wedge angles and incident Mach numbers. However, these studies involved straight reflecting surfaces. Hence, the desire to expand the knowledge of the shock reflection phenomenon for the case of concave double wedges reflectors becomes the motivation of the current study.

In this study, an attempt is made to explore the shock reflection patterns for concave double wedges reflectors. The shock reflection structures over simple concave reflector are well known for long. However, it involves a significant curiosity to know the reflection patterns, if the shock encounters a sudden change of the angle of the reflecting surface. Thus, for this understanding, a series of numerical simulations have been performed with various incident Mach numbers and initial wedge angles.

Computational Set-Up

The computations are carried out using an in-house massively parallel compressible code, named CHOC-WAVES. It uses immersed boundary method (IBM) for the fluid–solid interactions [10–13]. The complex solids are generated using the Ray-tracing technique. The Euler equations' solver is chosen for the compressible and inviscid computations of

V. Soni
Normandie Université, CNRS-University & INSA of Rouen (CORIA-UMR 6614), Rouen, France

M. Geva • O. Sadot
Mechanical Engineering Department, Faculty of Engineering Sciences, Ben Gurion University of the Negev, Beer Sheva 8410501, ISRAEL

O. Ram
Department of Mechanical Engineering, Protective Technologies Research and Development Center, Faculty of Engineering Sciences, Pearlstone Center for Aeronautical Engineering Studies, Ben-Gurion University of the Negev, Beer Sheva, Israel

A. Hadjadj (✉)
CORIA – UMR 6614 CNRS – INSA Rouen and Normandie Université, Avenue de l'Université, 76801 Saint-Étienne-du-Rouvray, France
e-mail: hadjadj@coria.fr

A. Chaudhuri
Department of Aerospace Engineering and Engineering Mechanics, San Diego State University, San Diego, CA 92182, USA

G. Ben-Dor
Pearlstone Center for Aeronautical Engineering Studies, Department of Mechanical Engineering, Faculty of Engineering Sciences, Ben-Gurion University of Negev, Beer Sheva, Israel

G. Ben-Dor et al. (eds.), *30th International Symposium on Shock Waves 1*, DOI 10.1007/978-3-319-46213-4_100

the present work. The space and time discretization are performed using WENO5 [14, 15] and Runge–Kutta 3 schemes, respectively. The boundary conditions are set to inlet and outlet at the left and right of the domain, and a slip condition is applied at both top and bottom boundaries. The computations are performed using a regular Cartesian grid with equally spaced mesh, $\Delta x = \Delta y = 80$ μ m throughout the domain, for all considered cases.

The solid reflector used for the simulations is shown in Fig. 1. The present study focuses only on the effect of the wedge angles of the concave reflectors, φ_{w1} and φ_{w2} on the shock reflection. Hence, the rest of the parameters, such as $r_1 = r_2 = 50$ mm and $\omega_1 = \omega_2 = 75^\circ$, are kept constant. The simulations are performed using different incident shock wave Mach numbers, $M_s = 1.2$, $M_s = 1.6$, $M_s = 1.9$, and $M_s = 2.5$. Different wedge angles of the concave reflectors are considered, $\varphi_{w1} = \varphi_{w2} = 0^\circ$, $\varphi_{w1} = \varphi_{w2} = 10^\circ$, $\varphi_{w1} = \varphi_{w2} = 20^\circ$, and $\varphi_{w1} = \varphi_{w2} = 30^\circ$ for each M_s. The initial flow is specified using the Rankine-Hugoniot jump conditions for different M_s. The obtained results are discussed in the following section.

Results and Discussion

Different unsteady shock wave reflection configurations are analyzed with the help of numerical flow visualizations through schlieren pictures [16]. In the case of $\varphi_{w1} = \varphi_{w2} = 0^\circ$, the shock reflection patterns are similar to those reported in [1, 3] on the first concave reflector, where the compression waves generating from the steepening of the concave wall angle form a kink in the incident shock. As the shock progresses, an inverse Mach reflection (InMR) is formed with a structure of three shock waves and a contact discontinuity (slipstream) meeting at a triple point (TP). A transition from InMR to TRR takes place as TP collides with the surface of the wall. This leads to a reflection structure, in which a new reflected shock is formed emanating from the junction of the incident shock and the wall. The new reflected shock has a new triple point supported by an additional shock (see [17]). Until this point, the shock reflection phenomenon is fairly similar in all undertaken configurations with a slight variation in the computed transitioned regular reflection angle (θ_w^{tr}). However, as the incident shock wave propagates further and reaches the second concave reflector, the shock reflection pattern varies notably with the incident shock wave Mach number, as well as with the initial wedge angle. The following points describe the distinctive features reported with the different geometrical aspects on the second concave reflector:

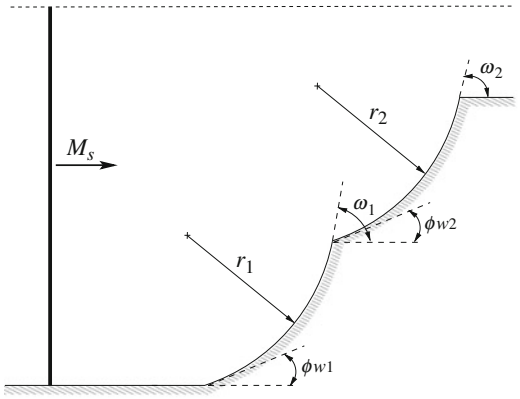

Fig. 1 Schematic diagram of the concave double wedges reflector

$$M_s = 1.2, \varphi_w = 0^\circ$$

Once the incident shock wave reaches the second concave reflector, it brings the additional shock wave that appeared on the first concave reflector (TRR) along with it. However, the additional shock never catches up with the incident one and always lags behind it. The shock reflection patterns are shown in Fig. 2, which resembles the one observed on the first reflector, i.e., InMR → TRR transition.

$$M_s = 1.6, \varphi_w = 0^\circ$$

In this case, the additional shock wave that is generated during TRR on the first concave reflector, initially, falls behind the incident shock on the second reflector. But, it eventually catches up and meets the incident shock to form an MR with a triple point and a slipstream. However, as the triple point moves closer to the wall, the additional shock wave starts falling behind, which leads to the appearance of another MR with a reflected wave and a new clearly defined

Fig. 2 Numerical schlieren pictures for $M_s = 1.2$ and $\varphi_{w1} = \varphi_{w2} = 0^\circ$ showing the time evolution of the shock reflection over the second concave surface. The origin of time is chosen such as the incident shock hits the inlet lip of the first reflector

Fig. 3 Numerical schlieren pictures for $M_s = 1.6$ and $\varphi_{w1} = \varphi_{w2} = 0°$ showing the time evolution of the shock reflection over the second concave surface

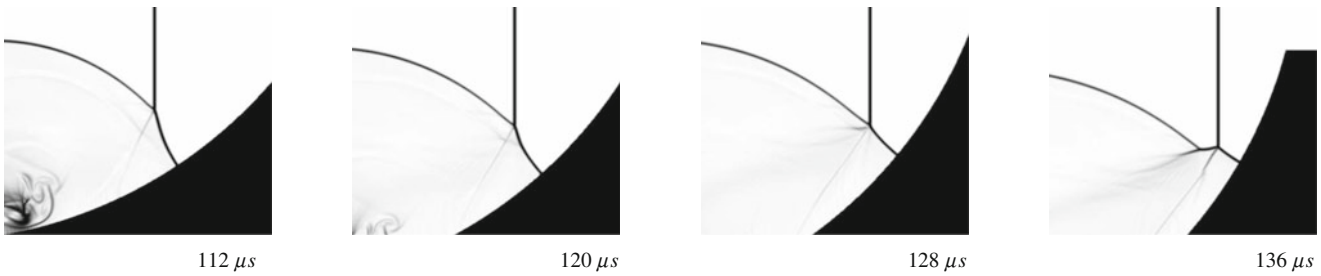

Fig. 4 Numerical schlieren pictures for $M_s = 1.9$ and $\varphi_{w1} = \varphi_{w2} = 0°$ showing the time evolution of the shock reflection over the second concave surface

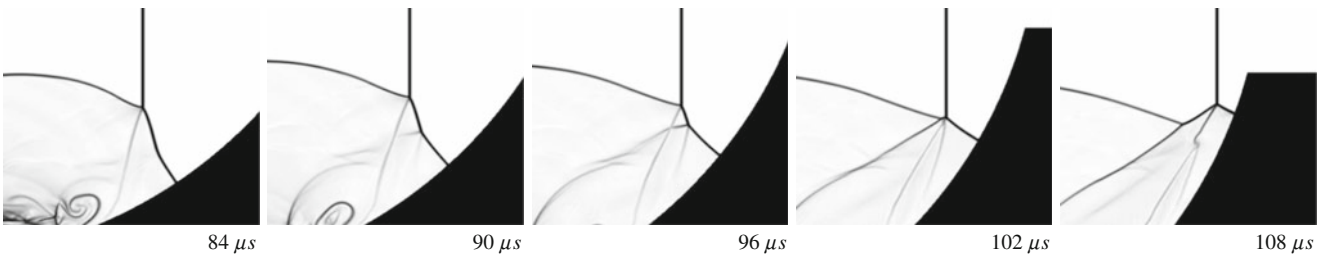

Fig. 5 Numerical schlieren pictures for $M_s = 2.5$ and $\varphi_{w1} = \varphi_{w2} = 0°$ showing the time evolution of the shock reflection over the second concave surface

slipstream from the triple point, as depicted in Fig. 3. This reflection structure continues until a transition from InMR → TRR occurs.

$$M_s = 1.9, \varphi_w = 0°$$

The shock reflection phenomenon is similar to what has been observed in $M_s = 1.6$ case. However, the length of the Mach stem formed in the initial MR is quite substantial. Furthermore, it starts to bend inward, as the incident shock moves forward, until a new MR is formed, as shown in Fig. 4.

$$M_s = 2.5, \varphi_w = 0°$$

Very complex shock reflection structures occur in this case. The additional shock wave catches up with the incident one right from the beginning on the second concave reflector. The initial MR has a large Mach stem, and as observed in the case of $M_s = 1.9$, it bends inward with time. However, the Mach stem curvature becomes significantly sharp that it breaks down in two, with two new slipstreams emanating from the broken point. The upper part of the Mach stem continues to decrease in size, while the additional shock retracts back allowing another MR to take place. As displayed in Fig. 5, three slipstreams merge together at one point in time, when the second MR is about to appear.

$$M_s = 1.6, \varphi_w = 20°$$

With the initial wedge angle of 20°, the shock reflection structure now becomes a single-Mach reflection (SMR) over the first concave reflector. A transitional-Mach reflection (TMR) appears with a slight kink visible in the middle-left of Fig. 6. Upon the triple point collision with the reflector surface, the wave configuration becomes a TRR, before the

incident shock reaches the second concave reflector. As soon as the incident shock reaches the second reflector, a Mach reflection (MR) appears. This configuration resembles slightly to a double-Mach reflection (DMR) without a visible slipstream emanating from the second triple point. The additional shock wave that was formed during the TRR state penetrates the reflected wave of the MR, as shown in the middle-right of Fig. 6. The triple point associated with this wave structure moves towards the wall, which leads later to a TRR transition. It is worth noting a considerable kink in the TRR configuration (right of Fig. 6).

$$M_s = 2.5, \varphi_w = 20^\circ$$

The shock reflection configurations are similar to that reported in $M_s = 1.6$ case on the first concave reflector, as shown in the left and middle-left sides of Fig. 7. However, the kink in TMR stands out distinctly in the current case. Also, as in the previous case, the additional shock wave of TRR penetrates to the reflected wave of MR resembling to DMR (without a visible slipstream emanating from the second triple point) on the second concave reflector (middle-right Fig. 7). As the incident shock further progresses, interestingly the DMR transitions back to a TMR (right Fig. 7) followed by a TRR at the end.

The left and right parts of Fig. 8 show the transitioned regular reflection angle θ^{tr} over the first and the second concave reflectors, respectively. As it can be seen, θ^{tr} increases for higher M_s. However, θ^{tr} decreases with the increase in the initial wedge angle φ_w over both reflectors. It is also interesting to note that θ^{tr} is higher on the second concave reflector compared to the first one for the same configurations. These shock patterns behavior can be perceived as its property to retain the flow memory.

Summary

In this study, we tried to investigate the shock reflection phenomenon over the complex geometry of the concave cylindrical double wedge reflectors. Numerous simulations were carried out in order to investigate the changes in the reflected wave structure with regard to the parametric changes in the geometry of the concave reflectors as well as the changes in the incident shock wave Mach number. The numerical solver uses the Euler equations in conjunction with the WENO5 and Runge–Kutta TVD schemes for space and time integrations, respectively. The results reveal several interesting shock reflection behaviors. As reported in previous works on the shock reflection over cylindrical concave reflector with no initial wedge angle, it begins with a Mach reflection (MR), followed by the transitional regular reflection (TRR) on the first reflector. With the lower Mach number, this additional shock always lags behind the incident shock, while an MR takes place which transitions to a TRR. In contrast, with the high Mach numbers, the additional shock meets the incident

Fig. 6 Numerical schlieren pictures for $M_s = 1.6$ and $\varphi_{w1} = \varphi_{w2} = 20^\circ$ showing the time evolution of the shock reflection over the first (*left*, *middle-left*) and the second (*middle-right*, *right*) concave surface

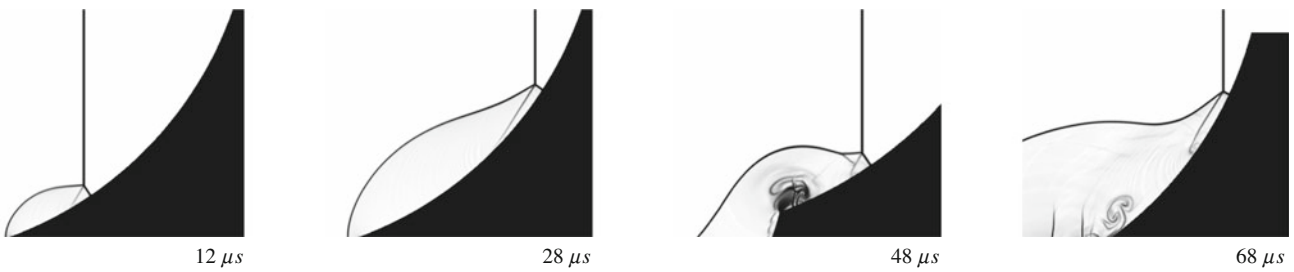

Fig. 7 Numerical schlieren pictures for $M_s = 2.5$ and $\varphi_{w1} = \varphi_{w2} = 20^\circ$ showing the time evolution of the shock reflection over the first (*left*, *middle-left*) and the second (*middle-right*, *right*) concave surface

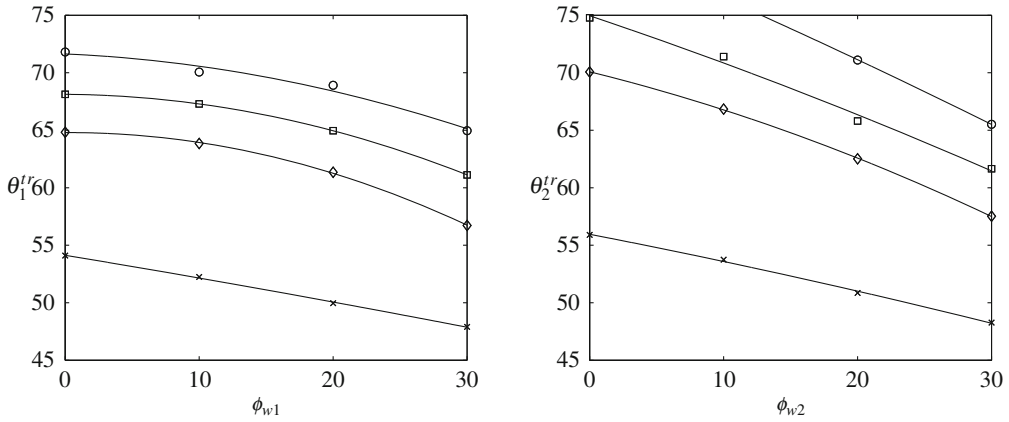

Fig. 8 Transitioned regular reflection angle over the first concave reflector (*left*) and the second concave reflector (*right*) by varying initial wedge angles φ_{w1} and φ_{w2} for different initial Mach numbers, ○—$M_s = 2.5$, ■—$M_s = 1.9$, ◇—$M_s = 1.6$, ×—$M_s = 1.2$

shock forming an MR with a fading slipstream. However, the additional shock later falls behind creating another MR with a distinct slipstream. The shock reflection with an initial wedge angle of 20° exhibits a very different behavior compared to the zero wedge angle case. It starts with the single-Mach reflection (SMR) which then transitions to a transitional-Mach reflection (TMR) followed by a TRR on the first concave reflector. The kink in the TMR is more prominent with the increase in the incident Mach number. The additional shock formed during a TRR on the first reflector penetrates the reflected wave of MR on the second reflector. It looks very similar to a double-Mach reflection (DMR) with no visible slipstream from the second triple point, which further transitions to a TRR for low Mach numbers and a TMR for high Mach numbers. From this behavior, it can be deduced that the shock wave bears a characteristic of holding its memory. The present work needs an experimental investigation for further comparison and validation.

Acknowledgments The authors gratefully acknowledge the support of ANR "Agence Nationale de la Recherche" under grant ANR-13-MONU-0002 (MAPIE project). The work is performed using high-performance computing (HPC) resources from Centre de Resource Informatique de Haute Normandie (CRIHAN), Rouen, France.

References

1. Ben-Dor, G.: Shock wave reflection phenomena, 2nd edn. Springer, New York (2007)
2. Izumi, K., Aso, S., Nishida, M.: Experimental and computational studies focusing processes of shock waves reflected from parabolic reflectors. Shock Waves **3**(3), 213–222 (1994)
3. Skews, B.W., Kleine, H.: Flow features resulting from shock wave impact on a cylindrical cavity. J. Fluid Mech. **580**, 481 (2007)
4. Shadloo, M.S., Hadjadj, A., Chaudhuri, A.: On the onset of postshock flow instabilities over concave surfaces. Phys. Fluids **26**(7), 076101 (2014)
5. Skews, B.W., Blitterswijk, A.: Shock wave reflection off coupled surfaces. Shock Waves **21**(6), 491–498 (2011)
6. Skews, B.W., Kleine, H.: Shock wave interaction with convex circular cylindrical surfaces. J. Fluid Mech. **654**, 195–205 (2010)
7. Gruber, S.: Weak shock wave reflections from concave curved surfaces. M.sc. thesis, University of Witwatersrand, South Africa (2012)
8. Geva, M., Ram, O., Sadot, O.: The non-stationary hysteresis phenomenon in shock wave reflections. J. Fluid Mech. **732**, R1 (2013)
9. Ben-Dor, G., Dewey, J.M., Takayama, K.: The reflection of a plane shock wave over a double wedge. J. Fluid Mech. **176**, 483–520 (1987)
10. Chaudhuri, A., Hadjadj, A., Chinnayya, A.: On the use of immersed boundary methods for shock/obstacle interactions. J. Comput. Phys. **230**(5), 1731–1748 (2011)
11. Chaudhuri, A., Hadjadj, A., Sadot, O., Ben-Dor, G.: Numerical study of shock-wave mitigation through matrices of solid obstacles. Shock Waves **1**(23), 91–101 (2013)
12. Chaudhuri, A., Hadjadj, A., Sadot, O., Glazer, E.: Computational study of shock-wave interaction with solid obstacles using immersed boundary methods. Int. J. Numer. Methods Eng. **8**(88), 975–990 (2012)
13. Glazer, E., Sadot, O., Hadjadj, A., Chaudhuri, A.: Velocity scaling of a reflected shock wave off a circular cylinder. Phys. Rev. E Stat. Nonlin. Soft Matter Phys. **83**(6 Pt 2), 066317 (2011)
14. Jiang, G.S., Shu, C.W.: Efficient implementation of weighted ENO schemes. J. Comput. Phys. **12**, 202–228 (1996)
15. Liu, X.D., Osher, S., Chan, T.: Weighted essentially non-oscillatory schemes. J. Comput. Phys. **115**(1), 200–212 (1994)
16. Hadjadj, A., Kudryavtsev, A.: Computation and flow visualization in high-speed aerodynamics. J. Turbul. **6**, N16 (2005)
17. Ben-Dor, G., Elperin, T.: Analysis of the wave configuration resulting from the termination of an inverse mach reflection. Shock Waves **1**(3), 237–241 (1991)

High Resolution Experimental Investigation of the Reflection Over a Convex-Concave Cylindrical Model

Meital Geva, O. Ram, S. Sadot, and Gabi Ben-Dor

Introduction

Predicting pressure profiles at high-speed flows is crucial for accurate calculation of forces and loadings in aircraft design and in the field of explosions protection. Since shock wave configurations dictate these complicated profiles, the investigation of transient reflections was the focus of many studies over the past four decades [1]. The most common scenario studied was the propagation of a constant velocity moving shock towards a cylindrical surface. In this case, the shock wave interacts and adapts constantly to a changing surface angle. When the shock interacted with a concave cylindrical surface, the transition began as a Mach reflection (MR) that later transitioned to a regular reflection (RR). The angle in which the transition was obtained was larger than the known steady and pseudo-steady-state criteria. Whereas, the reverse transition, i.e., RR → MR over convex surfaces, was obtained at smaller angles than those reported by the steady and pseudo-steady criteria [2]. In most studies, the transition angle was determined by identifying the point of disappearance or appearance of the triple point or the Mach stem of the MR. Then, the transition point was obtained by extrapolating the length of the Mach stem to zero. Kleine et al. [3] stated that previous studies were incapable of resolving the early stages of the Mach stem formation since a detectable characteristic length below approximately 0.05 mm was not achieved. Attempts to study a more complicated scenario of the successive transitions began in the investigation of "double-wedge" models. These models consist of two consecutive planar surfaces with different inclinations ([4, 5] and more). A detailed description of the multiple shock configurations obtained using these kind of models is found in Ben-Dor [1]. Skews and Blitterswijk [6] examined the reflection over a circular surface followed by a plane section and a plane wall having a circular arc section at either ends. They demonstrated how the wave is influenced and informed about the surface. Babinsky et al. [7] presented a detailed description of the reflection evolution of concave reflectors when a blunt entry lip is used. Apparently, enhancement of shock focusing can be achieved by introducing elaborated configurations.

Methodology

Analyzing the transient nature of the shock wave reflection phenomenon requires both the use of high-resolution imaging together with high spatial resolution. While the former enables the examination of the evolution, the later guarantees the ability to detect fine features in the flow. The transient evolution has caught the interest of many studies that have utilized high speed imaging systems. Despite the obvious advantages, these systems suffer from relatively low spatial resolutions when increasing the frame rate. In several studies, shock wave diffraction is captured by a single-lens reflex (SLR) camera. This method, which enables capturing only one image per experiment, generates high-resolution images. Unfortunately, it does not enable following the transient shock propagation along the reflecting surface. However, one can combine the images of an SLR camera into one set of experiments if the initial conditions of the experiment are sufficiently repeatable. This was done by Skews and Blitterswijk [6] and Gruber and Skews [8]. To achieve the highest resolution possible, a "single shot-single experiment" method was chosen in the present study. The experimental facility is located at the

M. Geva (✉) • O. Ram • S. Sadot
Department of Mechanical Engineering, Faculty of Engineering Sciences, Pearlstone Center for Aeronautical Engineering Studies, Ben-Gurion University of the Negev, Beer Sheva, Israel
e-mail: schaim@post.bgu.ac.il

G. Ben-Dor
Pearlstone Center for Aeronautical Engineering Studies, Department of Mechanical Engineering, Faculty of Engineering Sciences, Ben-Gurion University of Negev, Beer Sheva, Israel

G. Ben-Dor et al. (eds.), *30th International Symposium on Shock Waves 1*, DOI 10.1007/978-3-319-46213-4_101

shock tube laboratory in the Protective Technologies R&D Center of the Faculty of Engineering Sciences of the Ben-Gurion University of the Negev. An automated shock tube in which the driver and the driven sections are separated by a fast opening valve (FOV) was used. The entire operation was computer controlled and automated.

Each experiment produced a single high-resolution image (16.2 M pixel). A detailed description of the facility and its operation can be found in Ram et al. [9]. Due to high repeatability in terms of the incident shock wave Mach number, images were grouped into a single reflection process having 1–2 μs temporal resolution. The repeatability is demonstrated in Fig. 1 where the actual derived Mach numbers of approximately 1200 individual experiments are presented. These distributions collect all the measurement errors and any parameter that can affect the measurement of the incident shock wave Mach number. The standard deviation was less than 0.0033 for each one of the incident wave Mach numbers. Due to the high repeatability, the method enabled capturing a large amount of high-resolution images, which were then used to track the fine features in the transient evolution of the shock wave reflection. The size of each pixel was 0.03 mm and thus the smallest discernable feature in the flow field would have a characteristic length of 0.06 mm. Each image was analyzed using our in-house automated image processing procedure described in Geva et al. [10].

Results

A planner moderate shock wave was reflected over a convex cylindrical model followed by a concave cylindrical model. The dimensions of the model which was machined out of Al are shown in Fig. 2a. The reflection process is schematically described in Fig. 2b. The reflection begins as an RR (t_1) that later transforms to an MR (t_2). When the Mach stem of the MR reaches the concave surface, the reflecting angle increases. The MR does not transition back to an RR as was expected. Instead, the wave begins to curve forward and a secondary MR is formed at its foot (t_3). At t_4, the triple point of the inverse-MR approaches the surface as the surface angle increases. The MR configuration later transitions to an RR (not seen in the figure). The distance of the triple point from the reflecting surface as a function of the reflecting surface angle was extracted from each image. Results for the entire process are shown in Fig. 3.

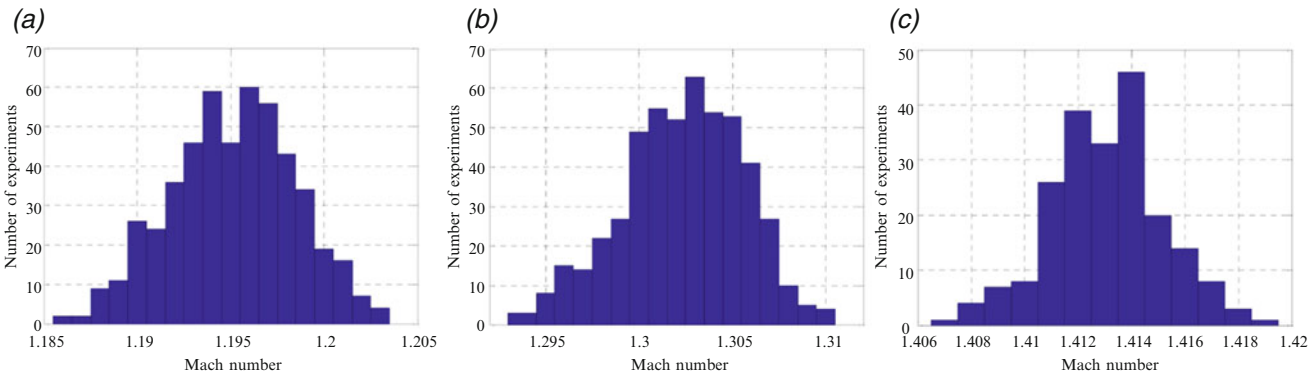

Fig. 1 Shock wave Mach number distribution of three moderate shock strength

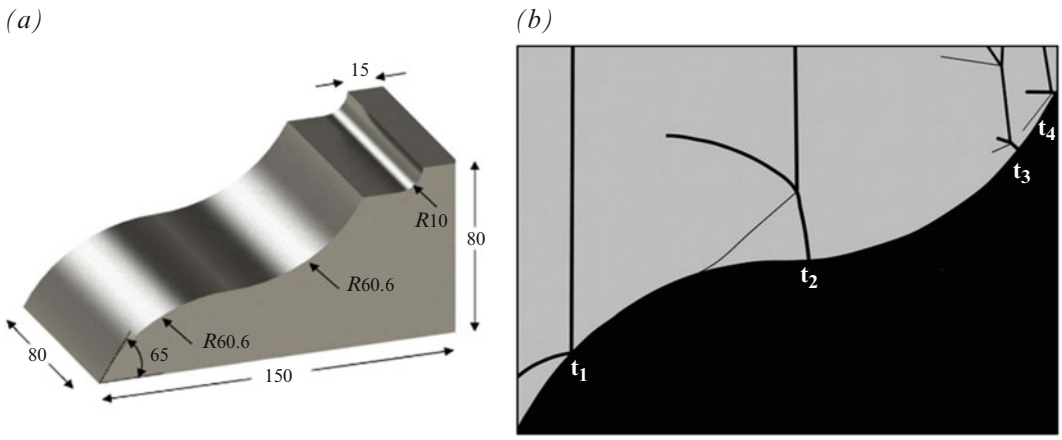

Fig. 2 The convex-concave model. (**a**) The model dimensions and (**b**) schematic description of the reflection process

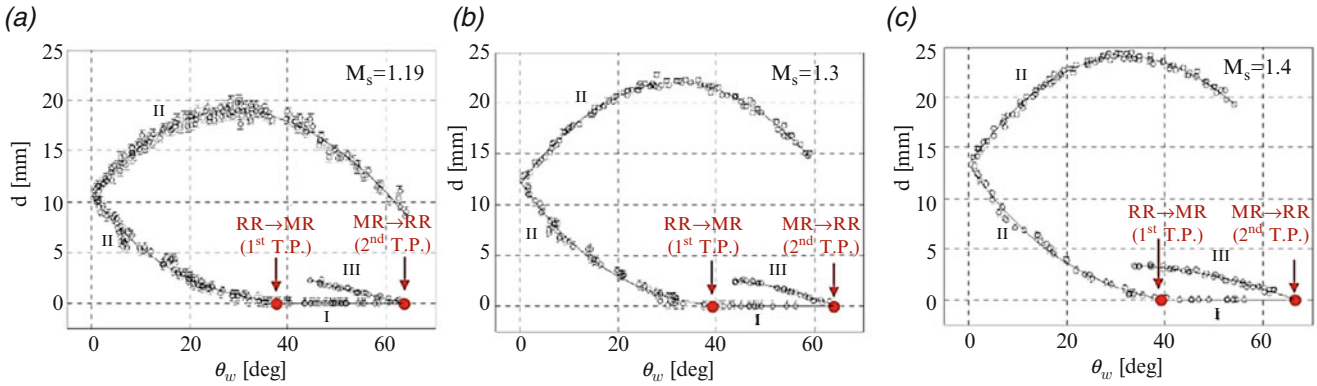

Fig. 3 The triple point distance from the reflecting surfaces vs. the surface angle at three incident shock wave Mach numbers: (**a**) 1.19, (**b**) 1.3 and (**c**) 1.4

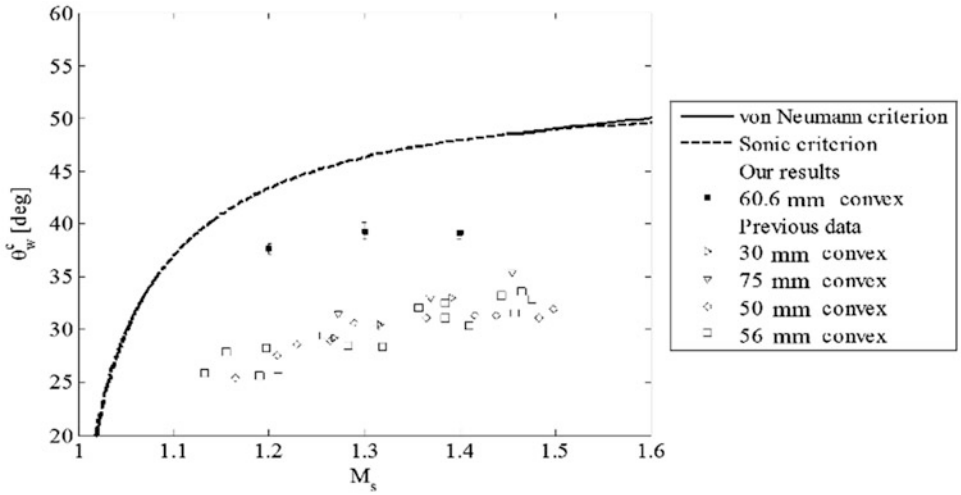

Fig. 4 The RR → MR transition angles. Black squares current results [9]. Previous data are from Ben-Dor [1] and Skews and Kleine [11]

RR → MR Transition Over the Convex Segment

The RR → MR transition angles were obtained by extrapolating branch II (Fig. 3) to zero. It should be noted that the extrapolation was made over an angle span that was about the same order as the angle difference between adjacent measurements. In contrast to previous experiments, in which the transition angle was determined by identifying the formation of a triple point and therefore was subjected to human interpretation; in the present study, the triple point location was obtained automatically and was based on a very large amount of measurements. Therefore, high statistical certainty of the identification of the transition angles was obtained. The RR → MR nonstationary transition angles are shown if Fig. 4 together with previous experimental results. It can be seen that the transition occurs earlier at larger angles than those previously reported.

In Fig. 5, one can see both the reflection process at a 37.18° surface angle and its magnification. A 0.088-mm-long Mach stem was detected by the automatic image processing procedure (Fig. 5b).

The three-shock configuration must have evolved before reaching a 30° surface angle. This reinforces the claim that transition occurs earlier in the process. Although the present method provided closer results to the pseudo-steady state reflection case, it still predicted a difference of about 5° and more. Kleine et al. [3] stated that the transition angle is expected to be only 1° delayed from that predicted by the pseudo-steady criterion. Figure 6 shows a comparison of the Mach stem height normalized by the surface radius obtained in the current study and results presented in Kleine et al. [3]. The ±10 pixels limiters are of the size of the width of the incident shock wave. They were taken to represent a measuring error of 10 pixels in each direction (see Fig. 6b). Examining the results presented in Fig. 6a implies that even by considering the extreme error limiters, a fit that approaches the transition angle that is derived from the detachment criterion to within 1° cannot be found. It is the authors' belief that it is unlikely that new transition angles will be found outside the angles domain bounded by the two extra conservative proposed limiters.

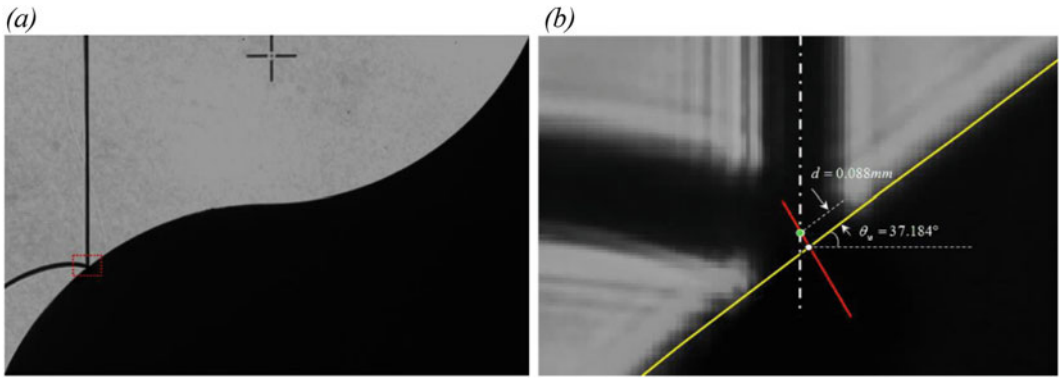

Fig. 5 Images taken after the RR → MR transition for a shock wave having a Mach number of 1.302 37.18°: (**a**) original image and (**b**) magnification

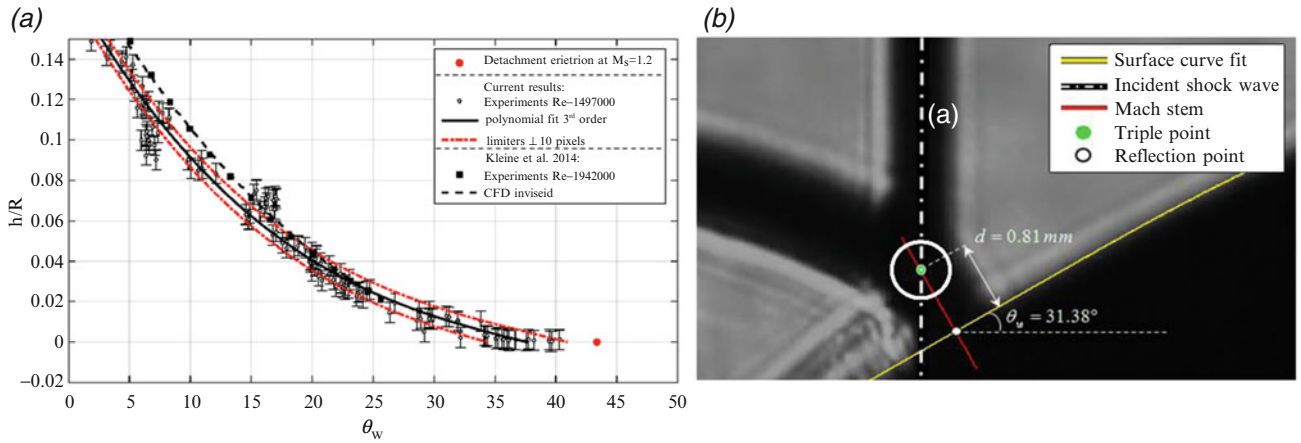

Fig. 6 (**a**) Comparison of the measured results and the inviscid numerical simulations of Kleine et al. [3]. (**b**) A 10-pixel error radius chosen to represent the error in determination of triple point

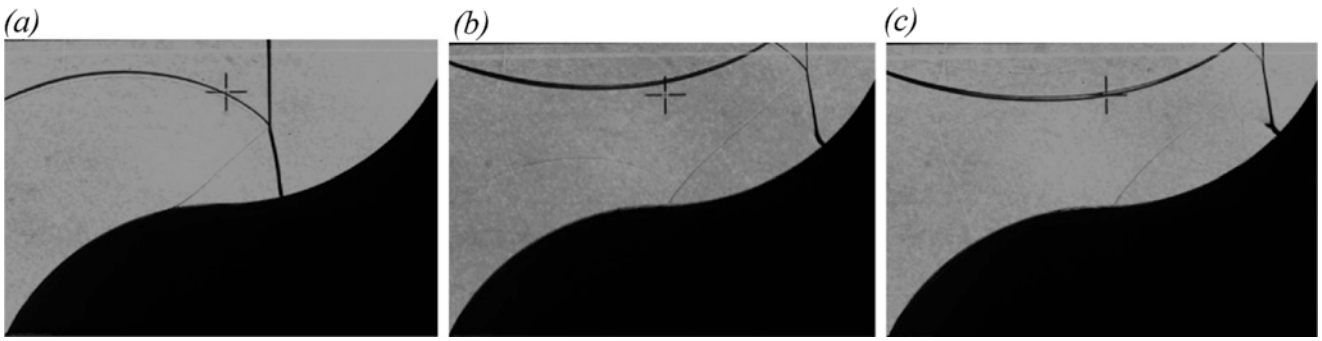

Fig. 7 The evolution of the MRMR over the concave segment. (**a**) A backward curved Mach stem, (**b**) forward leaning arch at the foot of the Mach stem and (**c**) new Mach stem is formed at the original Mach stem (MRMR)

Reflection Over the Concave Segment

Figure 7 illustrates the formation process of the secondary MR at the foot of the primary Mach stem. The Mach stem had arched backwards as it leaves the plateau region (Fig. 7a). As the surface angle increased, the velocity of the foot of the primary Mach stem increased as well and started to move faster than the remaining part of the primary Mach stem. By this time, a new forward leaning arch was formed at the foot of the foot of the Mach stem (Fig. 7b). The

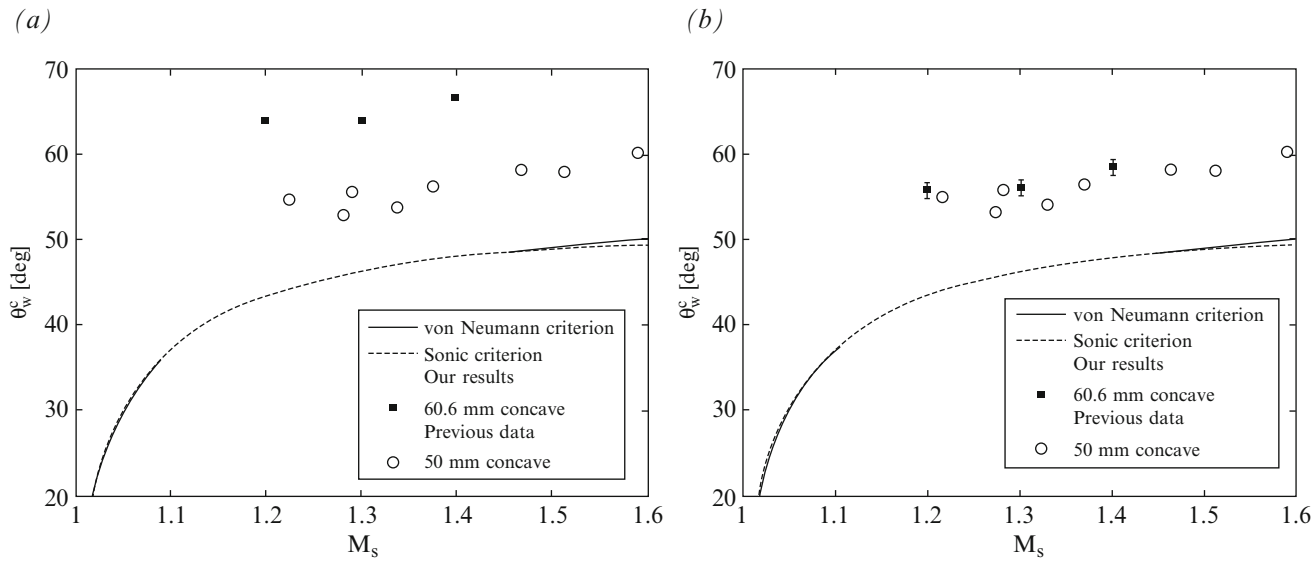

Fig. 8 The MRMR → RRMR transition angles in comparison to MR → RR transition angles [1]: (**a**) original data and (**b**) adjusted angles

backward curving is still apparent at the remaining part of the Mach stem. This fact might suggest that the change in the boundary conditions near the foot of the primary Mach stem was too fast to affect the remaining part of the Mach stem. At a certain surface angle, the forward curved foot of the primary Mach stem leaned so far ahead that a secondary triple point was formed. The new three wave configuration can be seen in Fig. 7c. From here on it will be referred to as MRMR. The formation of a triple point by a curve shock was described in Skews and Kleine [12]. Yet, while Skews and Kleine [12] described the formation of a triple point out of the original incident-shock wave, here the secondary triple point evolved at the foot of the Mach stem of the primary Mach reflection. A similar shock configuration (Fig. 7c) was reported by Ben-Dor et al. [4] when the reflection occurred over double-wedge surfaces. As the Mach number increases, the information about the changing surface travels faster causing the early formation of the secondary triple point. As the MRMR configuration continues to travel along the concave angle, the lower triple point travels towards the surface until it impinges the surface and an RR configuration is formed at the original Mach stem. This configuration will be referred to as MRRR.

The MRMR → MRRR transition angles, as were obtained from Fig. 3, are plotted in Fig. 8. The reflection process over the concave segment depends on the first reflection process. Since the later dictates a specific relative angle between the incident shock wave and the original Mach stem.

This angle can be used to adjust the MRMR → MRRR transition angles. Even though this three-shock configuration originated from the Mach stem, it was found that the adjusted transition angles were close to the MR → RR transition angles reported in the literature. The corrected values are plotted in Fig. 8b. A $\pm 1^o$ error bars were added to account for the uncertainty in the evaluation of the relative angle. Since the original Mach stem is curved, the assessment of the angle is problematic.

Conclusion

The use of a fully automated computer controlled system enabled the refined investigation of the evolution process of a shock wave reflecting over convex segment followed by a concave segment. The transition angles of the RR → MR reflection that were determined with high accuracies were closer to the detachment criterion than in past studies. Based on the error estimation that was conducted, it is reasonable to conclude that even if higher experimental resolutions will become available, the actual transition angles for the range $1.2 \leq M \leq = 1.4$ will remain about 3^o–8^o smaller than those predicted by the transition criterion in pseudo steady flows. The formation of the MRMR wave configuration and the conditions of the MRMR → MRRR transition over the concave segment were described. This new transition process was found to be more closely related to the previously reported MR → RR transition of incident shock waves over cylindrical surfaces.

References

1. Ben-Dor, G.: Shock Wave Reflection Phenomena. Springer, Berlin (2007)
2. Takayama, K., Sasaki, M.: Effects of radius of curvature and initial angle on the shock transition over concave and convex walls. Rep. Inst. High Speed Mech. **46**, 1–30 (1983)

3. Kleine, H., Timofeev, E., Hakkaki-fard, A., Skews, B.: The influence of Reynolds number on the triple point trajectories at shock reflection off cylindrical surfaces. J. Fluid Mech. **740**, 47–60 (2014)
4. Ben-Dor, G., Dewey, J.M., Takayama, K.: The reflection of a plane shock wave over a double wedge. J. Fluid Mech. **176**, 483–520 (1987)
5. Ben-Dor, G., Dewey, J.M., Mcmillian, D.J., Takayama, K.: Experimental Investigation of the asymptotically approached Mach reflection over the second surface in a double wedge reflection. Exp. Fluids **6**, 429–434 (1998)
6. Skews, B.W., Blitterswijk, A.: Shock wave reflection off coupled surfaces. Shock Waves **21**, 491–498 (2011)
7. Babinsky, H., Onodera, O., Takayama, K., Saito, T., Voinovich, P., Timofeev, E.: The influence of entrance geometry of circular reflectors on the shock wave focusing. Comput. Fluids **27**(5–6), 611–618 (1998)
8. Gruber, S., Skews, B.: Weak shock wave reflection from concave surfaces. Exp. Fluids **54**, 1–14 (2013)
9. Ram, O., Geva, M., Sadot, O.: High spatial and temporal resolution study of shock wave reflection over a coupled convex–concave cylindrical surface. J. Fluid Mech. **768**(2015), 219–239 (2015)
10. Geva, M., Ram, O., Sadot, O.: The non-stationary hysteresis phenomenon in shock wave reflections. J. Fluid Mech. **732**, 1–11 (2013)
11. Skews, B.W., Kleine, H.: Shock wave interaction with convex circular cylindrical surfaces. J. Fluid Mech. **654**, 195–205 (2010)
12. Skews, B. W., Kleine, H.: Flow features resulting from shock wave impact on a cylindrical cavity. J. Fluid Mech. **580**, 481–493 (2007)

Characteristic Properties of the Formation of Shock-Wave Reflection Configurations in Unsteady Flows

I.V. Krassovskaya and M.K. Berezkina

Introduction

Unsteady shock wave reflection can be obtained when a planar shock wave propagating with a constant velocity encounters a non-straight surface. Most attention has been paid to the shock wave reflection off convex and concave cylindrical surfaces. For a concave reflecting surface, the reflection pattern changes from irregular to regular. In the case of convex reflecting surface, the reflection pattern changes from regular to irregular. To this day the question of determination of transition parameters has been one of the unanswered questions. Until recently the unsteady reflection was generally described as a series of consequential changes of reflection configurations depending on an incident shock Mach number and a local slope angle associated with reflection of shock waves off convex/concave cylindrical surfaces [1–4]. The experimental and numerical data show that for cylindrical reflecting walls the regular-to-Mach reflection transition (RR ↔ MR) parameters do not agree with the sonic/detachment criteria provided by the von Neumann theory for the straight wedges. The question arises of whether it would be correct to use the criteria obtained for pseudo-steady flows (shock reflection from the straight wall) for the analysis of the transition in unsteady flows (shock reflection from curved reflecting surfaces).

Now it is well known that the reflection configurations arising in the course of the unsteady process look like ideal ones observed in pseudo-steady flows but are not determined by the incident shock Mach number and the local wedge angle, and thus cannot be described with the use of the von Neumann theory. So it is not quite understood, why it should be expected that the RR ↔ MR transition occurs at the transition parameters predicted by the von Neumann theory. Moreover, it is necessary to clarify the term *transition* in the case of pseudo-steady flows.

The critical parameters provided by the von Neumann theory determine the boundary between the domains of two different reflection types. Each pseudo-steady reflection process has to start at the leading edge of the reflecting wedge. The term *transition* does *not* mean that the change of the reflection patterns will occur continuously during the process of propagation of a shock wave along the plane surface.

In the course of propagation of a shock wave along a non-straight surface, the continuous changing of the shock wave configurations occurs. That is, the whole reflection process can be interpreted as sequence of transitions from one configuration to another. In this chapter we continue to develop the idea that not a single incident shock but shock wave configuration is involved in the process of unsteady interaction with the reflecting surface. The main objective of this chapter is to elucidate the mechanism of formation of various configurations that arise while a planar shock wave propagates along smooth convex surfaces. For better understanding of the process, numerical simulation of a shock reflection off a polyhedron circumscribed around a cylinder have been carried out.

Results

To elucidate the physical mechanism of formation of reflections configurations we performed numerical calculation for incident Mach number $M = 2.5$, specific heat ratio $\gamma = 1.29$ and for 1/4 of tetraicosagon (24 facets) as the reflecting surface. Figure 1 shows the numerical density contours for different instances.

The regular reflection configuration arises at the time $t = 0$. Figure 1a corresponds to the moment $t = 0.1$, at which the RR configuration formed on the first facet changes to other RR configuration on the second surface. The

I.V. Krassovskaya (✉) • M.K. Berezkina
Ioffe Institute, 26 Politechnicheskaya, St. Petersburg 194021, Russia
e-mail: i.kras@mail.ioffe.ru

G. Ben-Dor et al. (eds.), *30th International Symposium on Shock Waves 1*, DOI 10.1007/978-3-319-46213-4_102

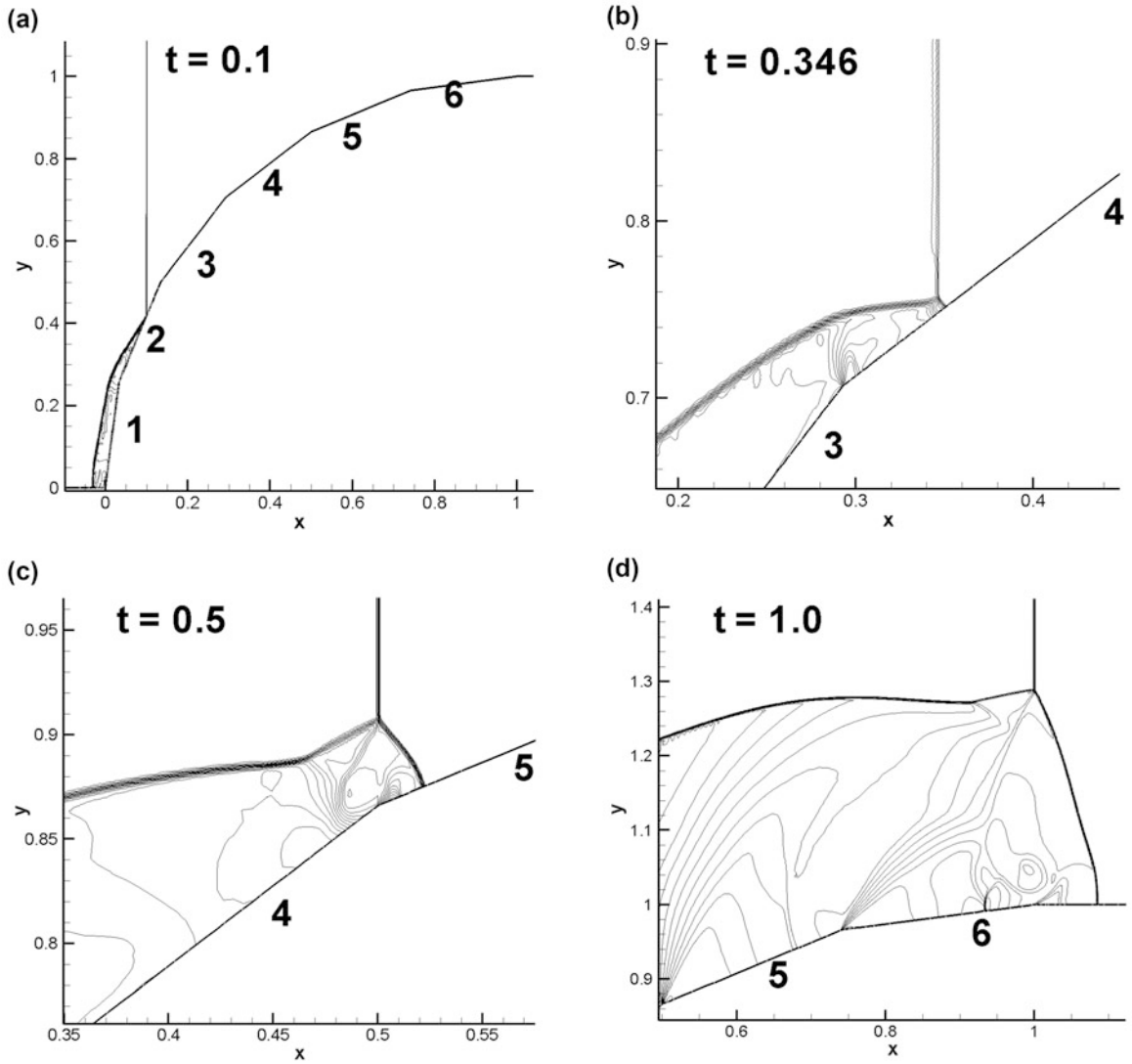

Fig. 1 Shock reflection off a polyhedron, $M = 2.5$, density contours

transition RR → RR occurs on the third facet also. On the 4th facet the RR pattern transits to MR configuration (Fig. 1b). In the instant $t = 0.5$ (Fig. 1c) the three-shock reflection configuration with the curved Mach stem is formed. This shape of the Mach stem is a result of the diffraction of the Mach stem of the previous MR pattern over the fifth facet. The diffraction point on the Mach stem is clearly seen. A kink on the reflected wave is apparently a result of influence of flow deflection process on the shock reflection. The diffraction point moves along the Mach stem and can reach the main triple point on the incident shock wave and interacts with it. New three shock configuration with the Mach stem not perpendicular to the fifth surface forms. The shock wave configuration on the sixth facet for $t = 1.0$ is presented in Fig. 1d. The formation of the configuration results from the similar processes. The given numerical results clearly demonstrate the mechanism of formation of the reflection configurations and the role of the diffraction process in it.

The most important point is the transition from RR to MR, which takes place on the leading edge of the 4^{th} surface. We found that when the RR configuration has to interact with the new wedge and the angle between the reflected wave and the new wedge is greater than 180°, the RR configuration arises. If this angle is less than 180°, the three shock configuration arises. It might be considered as the condition of transition from RR to MR.

Figure 2 shows the comparison between two processes: a shock reflection off the convex polyhedron (Fig. 2a–c) and a shock reflection off the concave polyhedron (Fig. 2d–f). In both cases not a single incident shock but a shock wave configuration interacts with the surfaces. In the case of

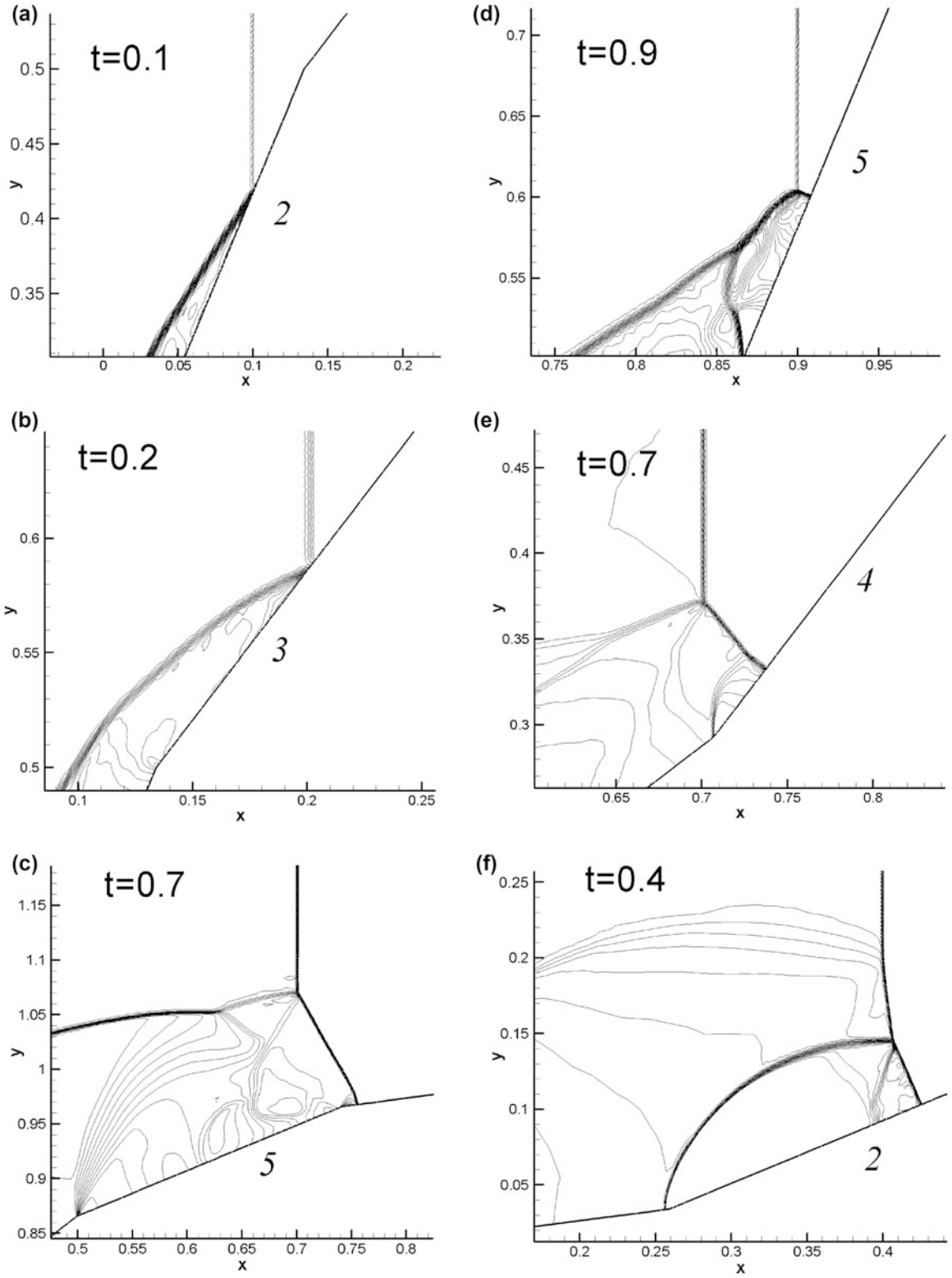

Fig. 2 Shock reflection off a convex/concave polyhedron, $M = 2.5$, density contours

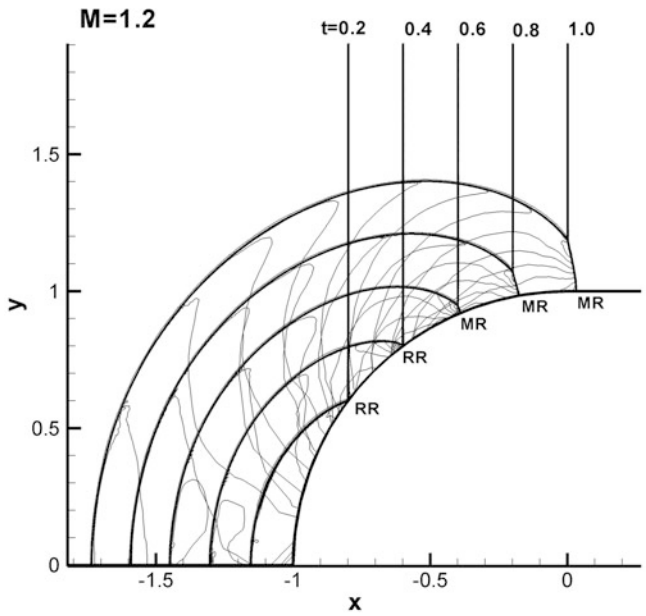

Fig. 3 Shock reflection off a convex cylindrical wall, density contours

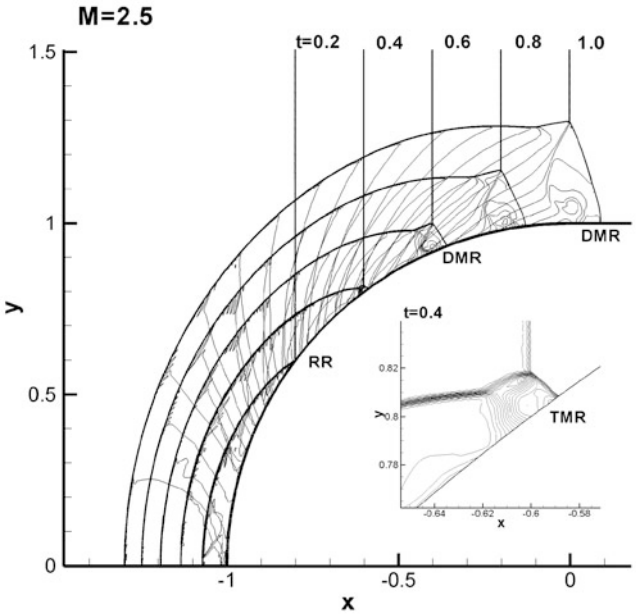

Fig. 4 Shock reflection off a convex cylindrical wall, density contours

convex wall, the diffraction processes make a contribution to the formation of the reflection configurations. In the case of a concave reflecting surface, the reflections of the foot of the shock have influence on the formation of the reflection configurations.

Numerical calculations of shock wave reflections off a convex cylindrical wall were conducted for various incident shock Mach numbers ($M = 1.2$, 1.3, 1.4, 1.5, 2.5, 5.0). Figures 3, 4 and 5 show the histories of the reflection processes for $M = 1.2$, $M = 2.5$ and $M = 5.0$, respectively. For weak shock wave (Fig. 3), the consecution of reflection configurations is: RR → RR → MR → MR → MR. For $M = 2.5$ the consecution of reflection configurations is: RR → TMR → DMR → DMR (here TMR means transitional Mach reflection and DMR is for double Mach reflection). For strong incident shock wave (Fig. 5) with supersonic flow behind it, the process of incident shock flow deflection markedly affects the process of shock reflection. As a result of interference of these processes, the configurations of double Mach reflection with the additional triple point on the Mach stem are formed.

Numerical simulation of shock wave reflections off a concave cylindrical wall were also done for various incident shock Mach numbers ($M = 1.2$, 1.3, 1.4, 1.5, 2.5, 5.0). Figures 6, 7 and 8 show the histories of the reflection processes for $M = 1.2$, $M = 2.5$ and $M = 5.0$, respectively. For weak shock wave (Fig. 6), the consecution of reflection configuration is: von-Neumann reflection (vNR) → MR → RR followed by the formation of the RR structure with an additional triple point on the reflected wave.

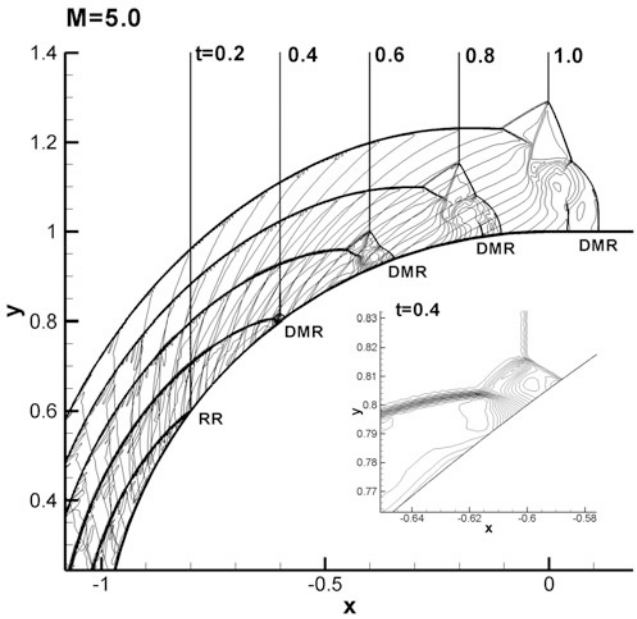

Fig. 5 Shock reflection off a convex cylindrical wall, density contours

This pattern is known as transitioned regular reflection (TRR). It should be emphasized that in this case the TRR configuration follows the RR. For $M = 2.5$ (Fig. 7) this wave configuration arises immediately after the termination of the MR, i.e. in the instant of transition from MR to RR. The numerical results show that MR → RR transition does not necessarily imply the formation of a TRR. For strong incident shock wave (Fig. 8) with supersonic flow

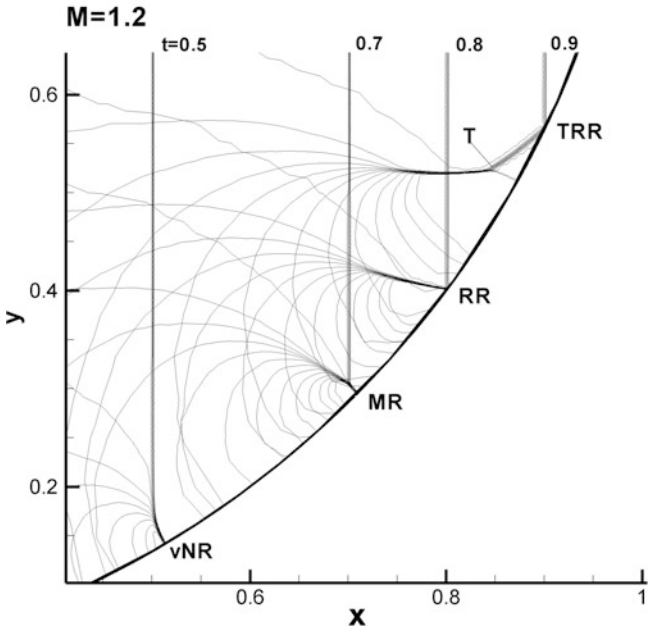

Fig. 6 Shock reflection off a concave cylindrical wall, density contours

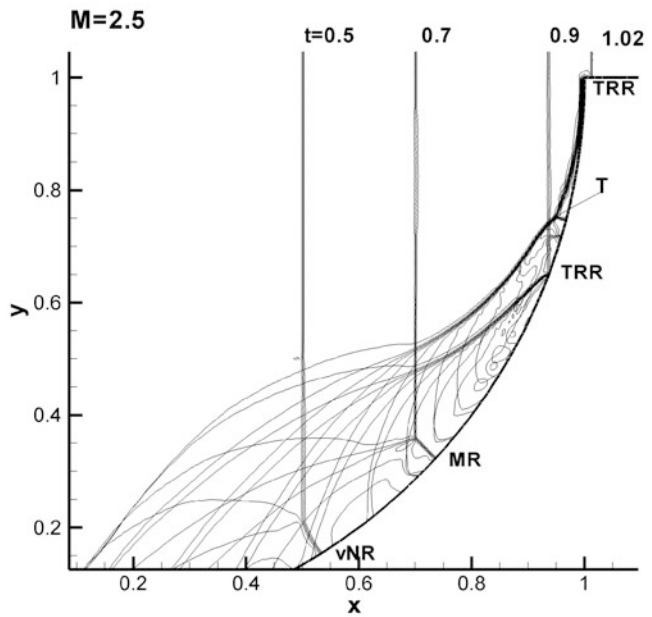

Fig. 7 Shock reflection off a concave cylindrical wall, density contours

behind it, the process of incident shock flow deflection markedly affects the process of shock reflection. As a result of interference of these processes, the configuration of transitional Mach reflection and double Mach reflection are formed at early stages of reflection. Subsequently, the RR configuration with two additional triple points on the reflected wave is formed.

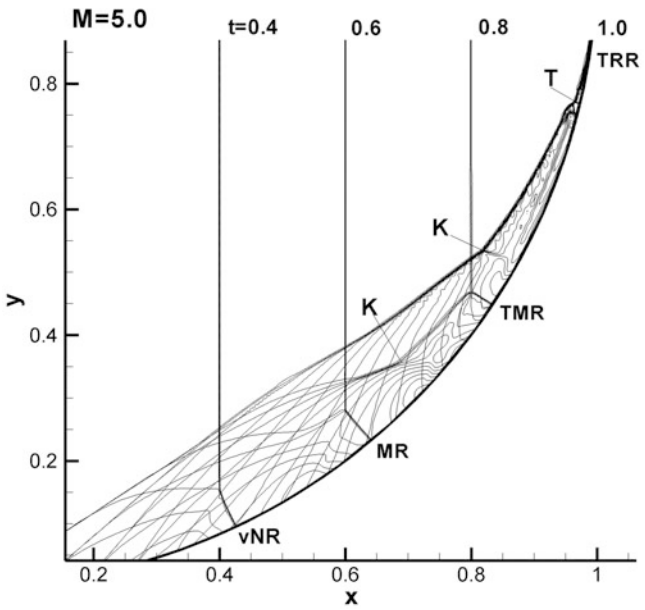

Fig. 8 Shock reflection off a concave cylindrical wall, density contours

Conclusions

Numerical simulation of unsteady reflection of a planar shock wave off convex/concave cylindrical walls is performed. The model of a polyhedron circumscribed around a cylinder as the reflecting surface provided understanding of the mechanism of the formation of shock wave configurations in unsteady flows. It is shown that the configurations being formed during the unsteady reflection process are not determined by the incident shock Mach number M and angle of the wedge, but result from complex sub-processes and cannot be described with the use of von-Neumann theory.

References

1. Ben-Dor, G.: Shock wave reflection phenomena, 2nd edn. Springer, Berlin (2007)
2. Skews, B.W., Kleine, H.: Shock wave interaction with convex circular cylindrical surfaces. J. Fluid Mech. **654**, 195–205 (2010)
3. Geva, M., Ram, O., Sadot, O.: The non-stationary hysteresis phenomenon in shock wave reflections. J. Fluid Mech. **732**, 1–11 (2013)
4. Timofeev, E., Hakkaki-Fard, A.: On unsteady shock reflections from convex circular surfaces. 21st International Shock Interaction Symposium, pp. 237–238. Riga, Latvia (2014)

Analytical Approach to the Problem of Three-Dimensional Steady Shock Wave Interactions

Chun Wang, Gaoxiang Xiang, Z. Jiang, and Yang Yang

Introduction

Shock wave is a fundamental issue related to supersonic and hypersonic aviation in the atmosphere. The interaction of shock waves has important effects on the gasdynamic performance of supersonic and hypersonic aircraft. Shock/shock interactions cause the main wave drag of such aircrafts, the complex flow features induced by the interactions of shock waves and boundary layers near the surfaces of aircraft. The gasdynamic heating by interactions of shock/shock and shock/boundary layer is also an important topic for the design of a hypersonic aircraft or reentry aviation.

Up to now, the theory to two-dimensional shock reflection has been studied thoroughly, which gives us a deep knowledge of complex supersonic and hypersonic flow. Ben-Dor G. systematically summarized the progress in 2D shock wave reflection phenomena study and its analytical theory in the past in his book, including both steady shock reflection and pseudo-steady shock reflection [1]. According to his new state-of-the-knowledge of shock reflections, the possible shock reflection configurations in 2D pseudo-steady flows are presented, and various types of shock-wave reflection configurations were schematically illustrated [1].

Interactions of three-dimensional steady shock waves are concerned widely in the field of supersonic and hypersonic aerodynamics, such as those existing in the three-dimensional hypersonic inlet. The most often observed three-dimensional shock wave interactions are those induced by two wedges intersecting each other with a certain angle. Three-dimensional planar shock wave interaction results in a bridge shock and a corner flow, which causes serious total pressure loss. Due to the complexity of shock interaction pattern and its interaction boundary layer near the surface of the wedges, there is no widely accepted analytical theory to solve it in mathematics. It is obvious that the analytical solution to the three-dimensional shock wave interaction is useful to understand the fundamental mechanisms of three-dimensional supersonic and hypersonic aerodynamics.

Results

As shown in Fig. 1, there are two intersecting wedges in a supersonic or hypersonic flow. Due to the compression of surface of wedges, shock waves form over the wedges and 3D shock interaction is induced. Planar shock S1 is induced by the bottom wedge and planar shock S2 is induced by the lateral wedge. Shock S1 and shock S2 will intersect with each other. Two basic shock interaction configurations may exist according the results of numerical simulation, that is, regular interaction and Mach interaction.

An approach of "spatial dimension reduction" was proposed to solve such problems [2]. The basic idea is, by transforming one spatial dimension to a temporal dimension, the problem of 3D steady shock interaction can be transformed to that of 2D moving shock interaction, either for regular interaction or for Mach interaction. By defining the direction of the intersecting line OB of shock plane S_1 and S_2 as the characteristic direction, the planes perpendicular to OB can be taken as the characteristic planes of the flow structure of three-dimensional steady shock/shock interaction. In the whole flowfield, the velocity component in the direction of characteristic direction is unique and maintains

C. Wang (✉) • G. Xiang
State Key Laboratory of High Temperature Gas Dynamics, Institute of Mechanics, Chinese Academy of Sciences, Beijing 100190, China
e-mail: wangchun@imech.ac.cn

Z. Jiang
LHD, Institute of Mechanics, Chinese Academy of Sciences, No.15 Beisihuanxi Road, Beijing 100190, People's Republic of China

Y. Yang
Research & Development Center, China Academy of Launch Vehicle Technology, Beijing 100190, China

G. Ben-Dor et al. (eds.), *30th International Symposium on Shock Waves 1*, DOI 10.1007/978-3-319-46213-4_103

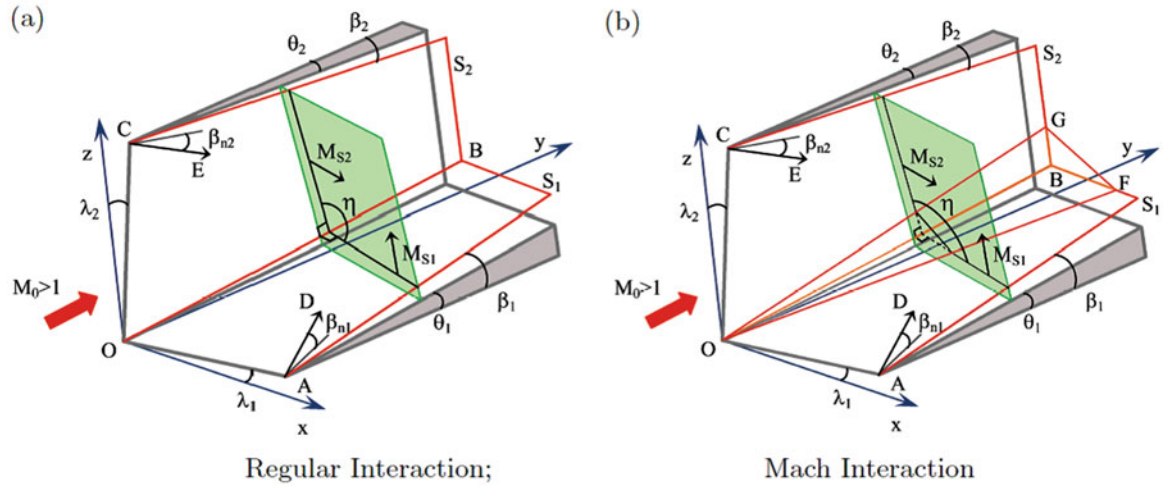

Fig. 1 Two basic shock patterns for three-dimensional steady shock/shock interaction. (**a**) Regular interaction, (**b**) Mach interaction

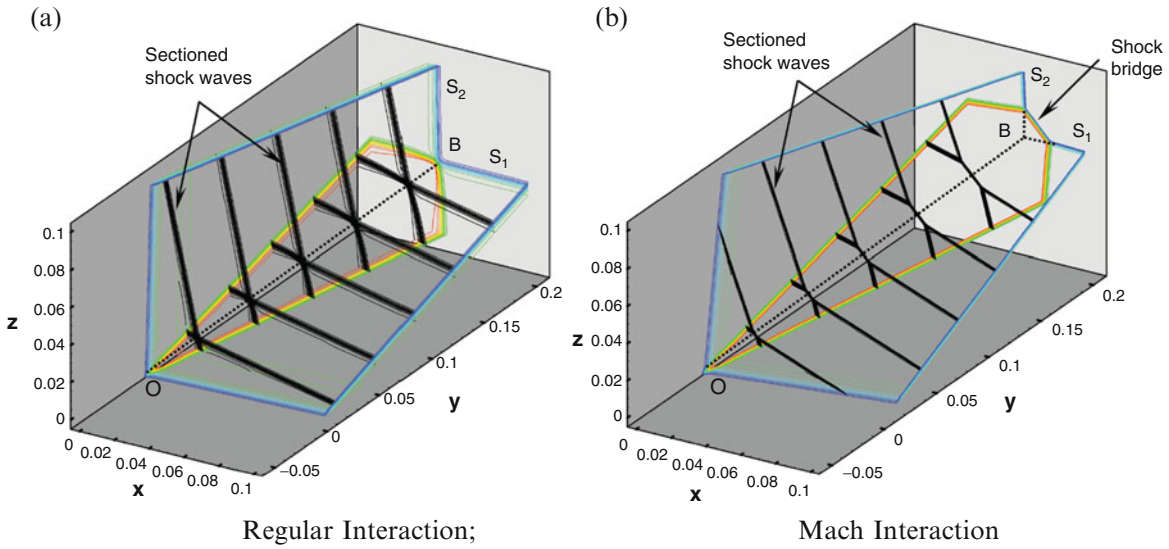

Fig. 2 Numerical examples for the idea of "dimension reduction." (**a**) Regular interaction, (**b**) Mach interaction

a constant value, due to the properties of oblique shock planes S_1 and S_2. It implies that the velocity component in the characteristic direction OB can be handled individually, in other words, the spatial distance in the characteristic direction which relates to the unique velocity component can be handled individually, such as a variable varying with the time evolution. On the characteristic planes perpendicular to the characteristic direction OB, three-dimensional steady shock wave interaction is reduced to two-dimensional moving shock wave with the time evolution, if all the characteristic planes are suppressed and projected to one characteristic plane, which is the basic idea of "spatial dimension reduction." By the approach of "spatial dimension reduction," the problem of 3D steady shock wave interaction is transformed to that of 2D moving shock wave interaction fully, if regular interaction or Mach interaction of 3D steady shock waves takes places.

Figure 2 shows the examples of regular interaction and Mach interaction of numerical simulations. In the characteristic direction, the flowfield is self-similar, which is the basis of "spatial dimension reduction" approach, either for regular interaction or for Mach interaction. If the sectioned shock waves were projected to one of the characteristic planes, the 3D steady shock wave interactions can be transformed to the 2D moving shock wave interactions. The numerical results gave a validation to the theoretic approach of "spatial dimension reduction" for 3D steady shock wave interactions.

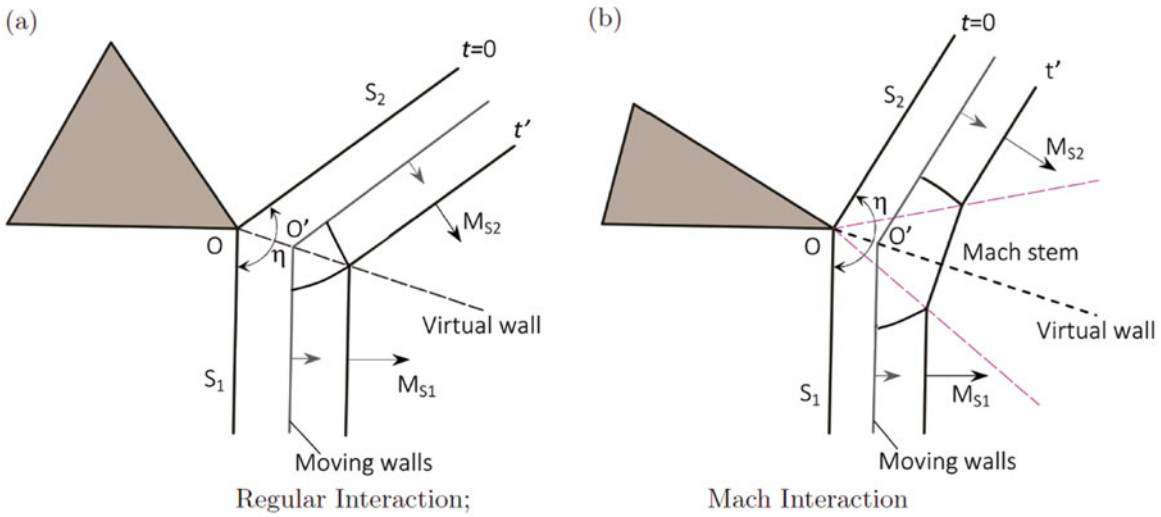

Fig. 3 Problem transformation to the interaction of two-dimensional moving shock/shock interaction. (**a**) Regular interaction, (**b**) Mach interaction

With the approach of "spatial dimension reduction," the problem of 3D steady shock wave interaction is converted to that of 2D moving shock/shock interaction, as shown in Fig. 3. In a two-dimensional plane corresponding to the characteristic planes, two moving shock waves meet at the origin point O and begin interacting with each other from $t = 0$. The Mach numbers of the two shock waves are M_{S1} and M_{S2}, which are correspondent to the components of inflow Mach number normal to shock planes S_1 and S_2. The interacting angle between them is h, which is correspondent to the interacting angle between shock planes S_1 and S_2.

The problem of two-dimensional shock/shock interaction can be solved with the theory of shock-polars and shock dynamics. The detailed analytical approach was presented in [3]. With such analytical theory, the interaction configuration of two-dimensional moving shock/shock interaction can be analyzed. Also, the interaction configuration of three-dimensional steady shock/shock interaction can be analyzed. There are various interaction configurations in three-dimensional steady shock/shock interactions, which have correspondent interaction configurations in two-dimensional moving shock/shock interactions.

Conclusions

With the approach of "spatial dimension reduction," the problem of 3D steady shock wave interaction is converted to that of 2D moving shock/shock interaction. Also, the interaction configuration of three-dimensional steady shock/shock interaction can be analyzed by use of the current two-dimensional moving shock/shock interaction. There are various interaction configurations in three-dimensional steady shock/shock interactions, which have correspondent interaction configurations in two-dimensional moving shock/shock interactions.

References

1. Ben-Dor, G.: Shock Wave Reflection Phenomena, 2nd edn. Springer-Verlag Press, Berlin (2007)
2. Yang, Y.: The investigations on complex flow of three dimensional shock/shock interaction (in Chinese), Ph.D. thesis, University of Chinese Academy of Sciences (2012)
3. Yang, Y., Wang, C., Jiang, Z.L.: Analytical and numerical investigations of the reflection of asymmetric nonstationary shock waves. Shock Waves **22**(5), 435–449 (2012)

The Effect of Acoustic Impedance of Reflecting Surface on Oblique Shock Reflection

S. Kobayashi and T. Adachi

Introduction

Oblique shock reflection has been well investigated when the reflecting wedge is solid. In that case, the acoustic impedance is extremely high and no transmitted wave is considered. However, the acoustic impedance of elastic materials is not so high compared with metal that some inherent reflection characteristics can be expected.

It is reported that spreading water over the floor of a gunpowder magazine greatly mitigates the pressure rise due to explosion [1]. The cooling effect of water evaporation cannot affect the whole gas phase instantaneously, so the cause of pressure mitigation should be sought in the acoustic impedance of the reflecting surface.

In the present investigation, we investigated the effect of acoustic impedance by using soft materials such as rubber and silicone as the reflecting surface.

Experiment

Method

We conducted experiments in our institute using a conventional shock tube. The working gas was air, and the driven section was set to room temperature and atmospheric pressure for each experiment run. The models are ordinary smooth wedges, on which a smooth plate of soft material with some thickness d is attached (Fig. 1). Three kinds of material are used: sponge, silicone, and rubber. When sponge is used, a sheet of paper is pasted over the surface to avoid the effect of surface roughness. The incident shock Mach number M_i is 1.30 ± 0.005, and the reflecting wedge angle θ_w is 30°. Rigorously, the angle ranged from 30.63° to 30.73°.

The leading edge O is taken as the origin. The abscissa ξ is taken along the reflecting surface and the ordinate η is defined perpendicular to the abscissa. The locations of the reflection point and the triple point (ξ, η) can be converted to (x, y), where x is the abscissa taken in the shock-propagation direction and y extends upward normal to the x-axis.

A shadowgraphy method was employed to visualize the reflection configuration. The light source was a xenon flash lamp with a 180-ns pulse width. The flash lamp was triggered by the output of the pressure gauge nearest the test section via a digital delay circuit. The reflection configuration at any desired instant could be photographed by regulating the delay time.

The angle between the incident and reflected waves ω_{ir} and the coordinates (ξ, η) of the triple point or the reflection point are measured directly from photographic negatives enlarged by a factor of 50 using a profile projector. We compare these results with those for hard reflecting surfaces, to investigate the effect of acoustic impedance on oblique shock reflection.

Physical Properties

The data given in *Rika Nenpyo* [2] are used for the Young's modulus of rubber and brass. Specifically, the value for rubber ranges from 1.5×10^6 to 5.0×10^6 Pa, so an approximate median value is used. Other data for the Young's modulus and density of all materials were measured. The sound speed and acoustic impedance were calculated from the following formulae.

S. Kobayashi (✉) • T. Adachi
Saitama Institute of Technology, 1690 Fusaiji, Fukaya-shi, Saitama, Japan
e-mail: kobayasi@sit.ac.jp

G. Ben-Dor et al. (eds.), *30th International Symposium on Shock Waves 1*, DOI 10.1007/978-3-319-46213-4_104

$$c = \sqrt{K/\rho}$$

$$I = \rho c = \sqrt{\rho K}$$

The physical properties of the materials used in the present experiment are tabulated in Table 1.

Results

Trajectory of Triple Point and/or Reflection Point

The visualized wavefront has a finite thickness, so we defined the location of the triple point T as illustrated in Fig. 2, in which i, r, m, and s denote the incident shock, reflected shock, Mach stem, and slipstream. The reflection point P was similarly defined. In consequences, even when the reflection is regular, η may not be zero.

The measured location of the reflection point of RR and the triple point of MR is plotted in Fig. 3. These data almost overlap each other. The data for sponge seem generally below the others.

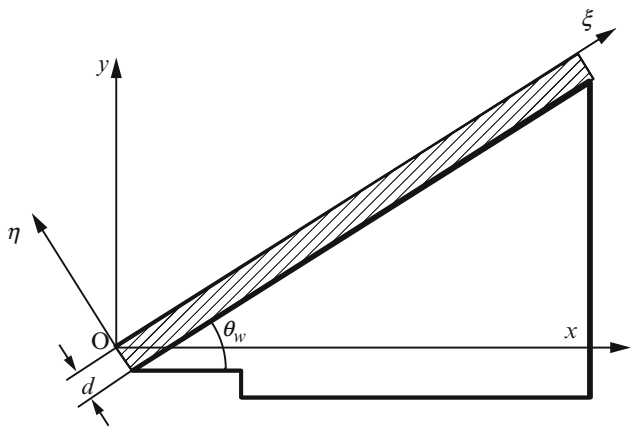

Fig. 1 Model wedge and its coordinate system

Development of Wave Configuration

To illustrate the wave development at an early stage, visualized reflection configurations are presented in Fig. 4 for sponge and Fig. 5 for brass.

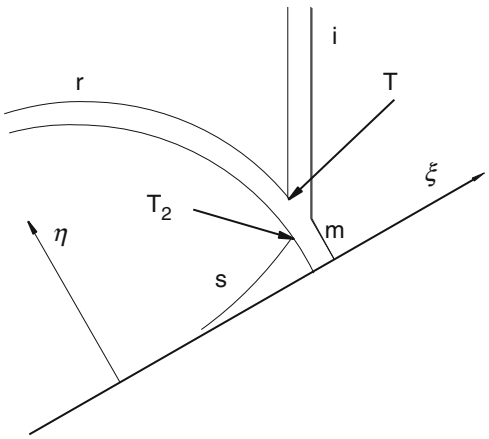

Fig. 2 Location of measured point

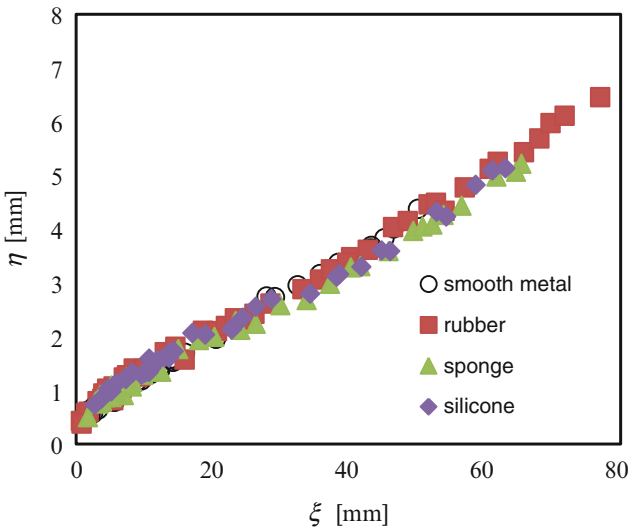

Fig. 3 Location of reflection point and triple point

Table 1 Physical properties of reflecting-surface material

	Sponge	Silicone	Rubber	Brass
Density ρ [kg/m^3]	156.8	998.8	1220	8411
Young's modulus K [Pa]	1.44×10^5	3.10×10^5	3.00×10^6	1.01×10^{11}
Sound speed c [m/s]	30.3	17.6	49.6	3460
Acoustic impedance I [kg/(m^2 s)]	4.75×10^3	1.76×10^4	6.05×10^4	2.91×10^7

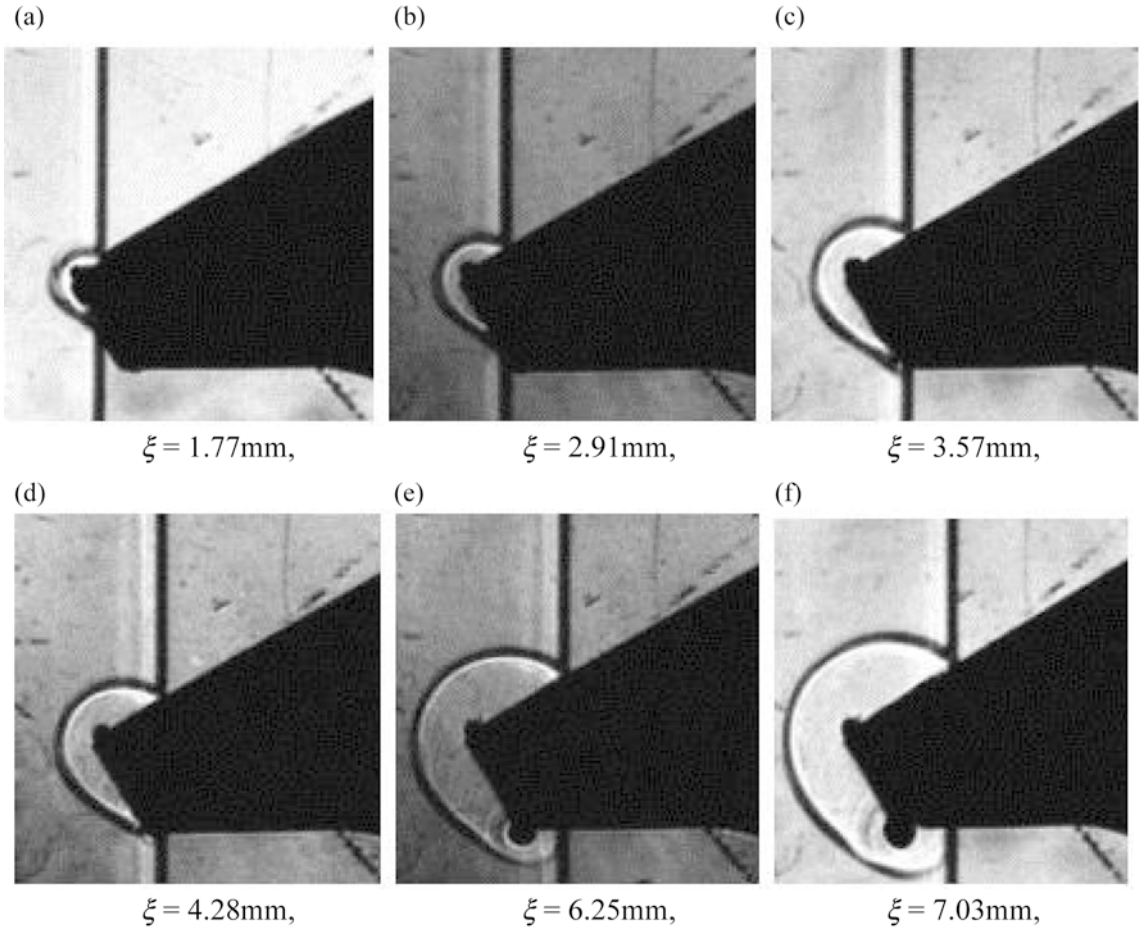

Fig. 4 Development of wave configuration (sponge). (**a**) $\xi = 1.77$ mm; (**b**) $\xi = 2.91$ mm; (**c**) $\xi = 3.57$ mm; (**d**) $\xi = 4.28$ mm; (**e**) $\xi = 6.25$ mm; (**f**) $\xi = 7.03$ mm

For sponge (Fig. 4a–c), the reflection remains regular. In Fig. 4a–f, the small black spot attached at the corner is a vortex. In Fig. 4d, the sprout of a slipstream can be observed along the reflecting surface. The slipstream is distinctly observed in Fig. 4e, while no Mach stem is observed yet. In Fig. 4f, both the slipstream and the Mach stem are observed.

Without soft material pasted onto the model wedge (bare brass), the development of the reflection configuration is similar. In Fig. 5a, the reflection is regular, but a slipstream is observed as early as Fig. 5b, c. Mach reflection (MR) is established in Fig. 5d, and thereafter MR develops.

Introduction of Take-Off Distance and Its Relation with Acoustic Impedance

A comparison between the reflections over sponge and brass indicates that the dynamic transition from RR to MR occurs earlier for brass than for sponge. In a dynamic transition, it is convenient to define take-off distance d_{to} as the distance from the wedge tip to the location where the transition occurs (Fig. 6).

We estimated the take-off distance for each reflecting surface from approximate line based on the least-squares method. We only used several data just after the transition. In this estimation, we used the location of the root of slipstream T_2 (ξ_2, η_2) instead of T (see Fig. 2) to decrease the effect of wave thickness.

Figure 8 plots the dependency of the take-off distance on the acoustic impedance. The take-off distance decreases as the acoustic impedance increases.

Variation of the Angle Between Incident and Reflected Waves

The variation of the angle ω_{ir} between the incident and reflected shocks is compared in Fig. 9. The error in angle measurement is as large as $\pm 3^\circ$ near the wedge tip and it

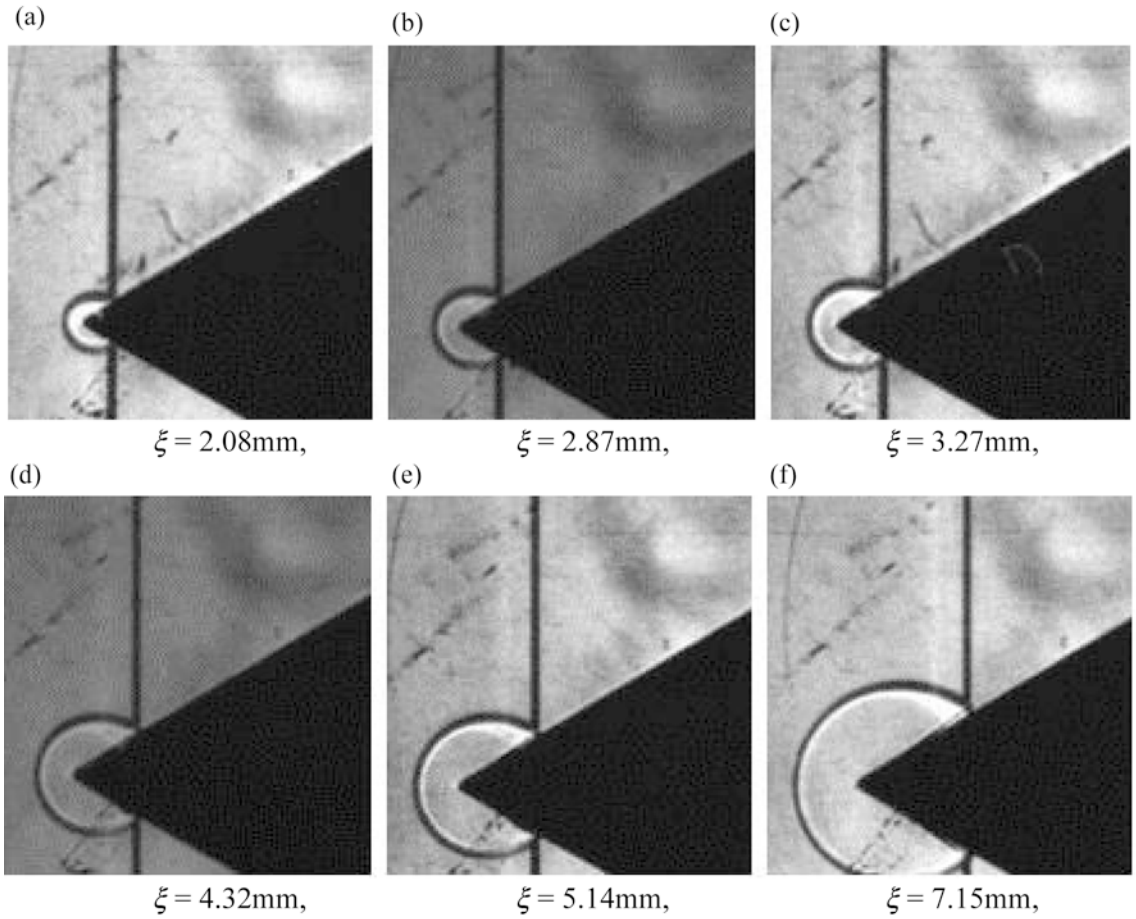

Fig. 5 Development of wave configuration (brass). (**a**) $\xi = 2.08$ mm; (**b**) $\xi = 2.87$ mm; (**c**) $\xi = 3.27$ mm; (**d**) $\xi = 4.32$ mm; (**e**) $\xi = 5.14$ mm; (**f**) $\xi = 7.15$ mm

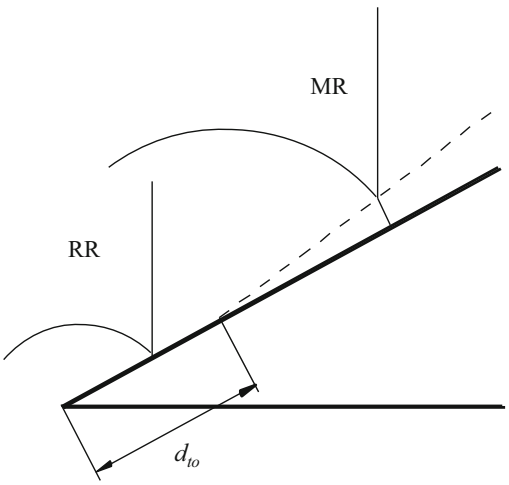

Fig. 6 Definition of take-off distance

decreases towards the rear of the model as the radius of curvature of the reflected shock increases. Considering the error, the difference in wave angle is not remarkable.

Hypothesis on the Reason for the Take-Off Distance Increase

We now consider the physical reason why the take-off distance increases when the reflecting surface is soft. For a hard solid surface, the flow direction must be parallel to the surface, i.e., in the same direction as the incoming flow (see Fig. 10a). When this is no longer possible, MR occurs (Fig. 10b). However, for a soft surface, the higher pressure behind the reflected shock might deform the surface, thus allowing the flow to shift towards the original surface. This would explain the delay in the dynamic transition.

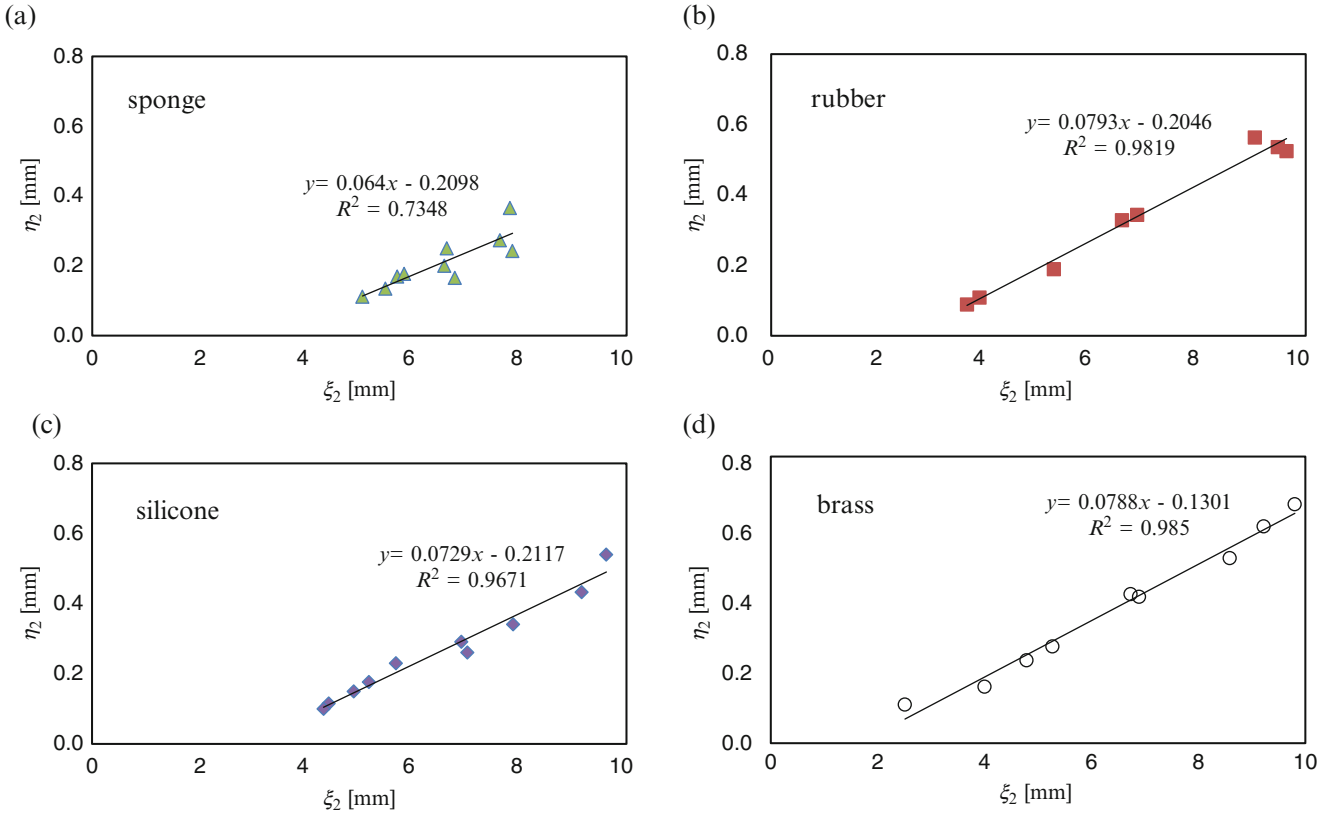

Fig. 7 Trajectory of T_2 after transition. (**a**) Sponge; (**b**) rubber; (**c**) silicone; (**d**) brass

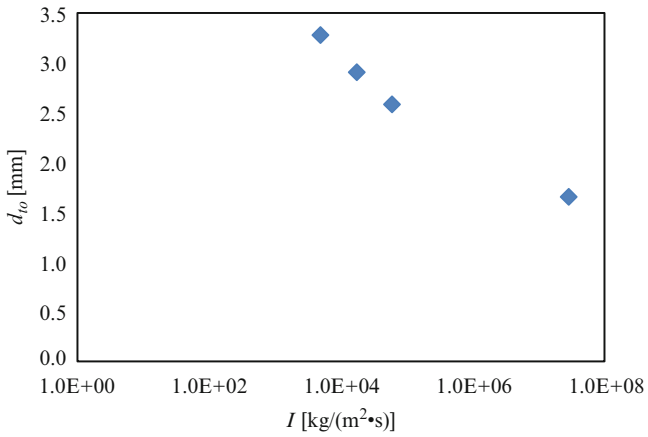

Fig. 8 Relation between take-off distance and acoustic impedance

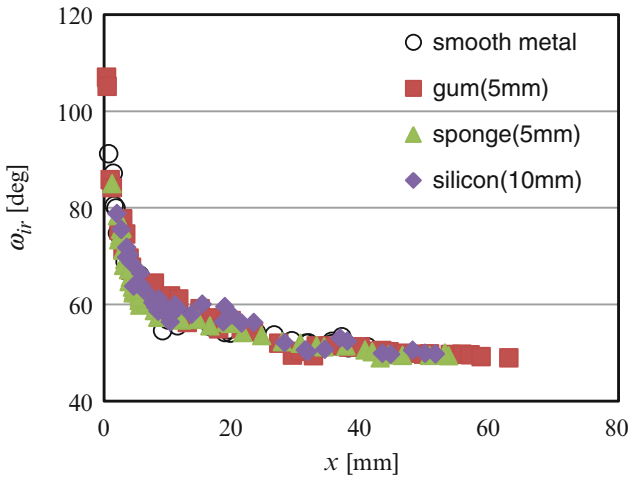

Fig. 9 Variation of the angle between incident and reflected shocks

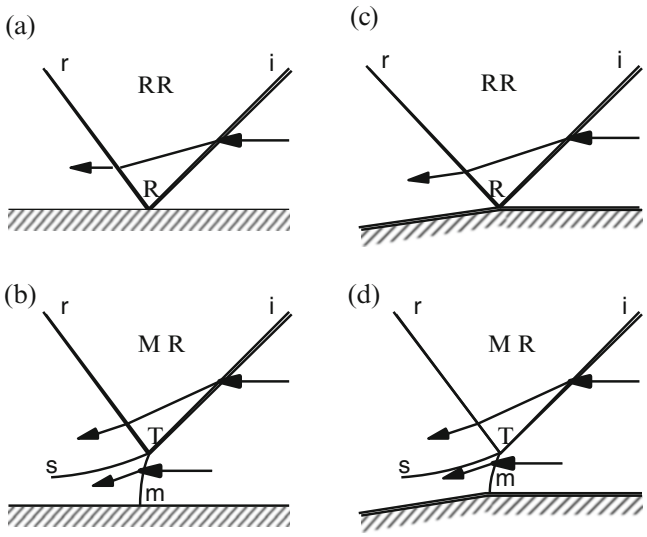

Fig. 10 Flow-field of RR and MR

Conclusions

When using certain kinds of soft material as a reflecting surface, the most remarkable result was that the dynamic transition from RR to MR was delayed.

References

1. Homae, T. et al.: High-speed photography of explosion in subsurface magazine (in Japanese). 2A1-4, Symposium on Shock Waves in Japan, (2014).
2. National Astronomical Observatory of Japan (ed.): Chronological Scientific Tables (Rika Nenpyo) (in Japanese). Maruzen (1997)

Experimental Investigation of Normal Shock Wave-Counter Flow Interactions

T. Tamba, N.M. Tuan, A. Iwakawa, and A. Sasoh

Introduction

The interactions between a shock wave and various flows are important research subjects in various fields. Investigations of shock wave interaction with hot bubbles and that with turbulence lead to important applications in aerospace engineering. Energy deposition in supersonic flow has been investigated in recent years as the method to moderate a shock wave and reduce the wave drag. Previous results showed the drag was reduced by up to 21 % with laser-induced bubbles at Mach number of 1.92 flow [1]. Yet, if hot bubbles are connected with each other to form a long column, the drag reduction is expected to be much enhanced [2]. The shock wave-hot bubble column interaction was investigated using a single shock tube and a repetitive pulse laser; however the deformation of the shock wave was not observed because of the limitation of the facility performance [3]. Also, the interaction between a weak shock wave and turbulence has been investigated in order to understand basic processes of sonic boom propagating through the atmospheric turbulence. Some reports indicated that a weak shock wave is greatly modulated by the turbulence [4]; however the mechanisms of the modulation have not been well understood.

Many shock wave interaction experiments have been conducted in a shock tube. In a previous study, the interaction between a reflected shock wave and turbulent flow induced in the post-shock flow behind an incident shock wave was investigated using a single-driver shock tube [5]. However, in a single-driver shock tube, the conditions of the reflected shock wave and the post-shock flow are coupled with each other, cannot be controlled independently.

T. Tamba (✉) • N.M. Tuan • A. Iwakawa • A. Sasoh
Department of Aerospace Engineering, Nagoya University, Furo-Cho, Chikusa-ku, Nagoya 464-8603, Japan
e-mail: tamba@fuji.nuae.nagoya-u.ac.jp

In this study, a Counter-Driver Shock Tube (CD-ST) has been developed, which has two driver section to generate two shock waves and post-shock flows, respectively, and control each condition independently. Therefore the interaction of the shock wave and the post-shock flow can be investigated in various conditions. Using the CD-ST, the interactions between the shock wave and a column of bubbles generated by laser energy depositions was experimentally studied.

Counter-Driver Shock Tube (CD-ST)

Figure 1 shows the schematic of the CD-ST. The CD-ST has two Driver section (L-Driver and R-Driver) at the each end of the driven section (Fig. 1a). This configuration allows to generate Left- and Right-incident shock wave (L-iSW and R-iSW) independently, and Left- and Right-post-shock flow (L-PSF and R-PSF) are induced behind each shock wave. R-Driver is activated with proper delay so that the interaction occurs in test section (Fig. 1b). After the head-on collision of the two incident shock waves (Fig. 1c), Left- and Right-transmitted shock wave (L-tSW and R-tSW) are formed as new shock waves. R-tSW is used as an interacted shock wave and is propagating to left while interacting with L-PSF in the test section (Fig. 1d). The conditions of R-tSW and L-PSF are determined by the initial conditions of each driver. Therefore the investigation of shock wave-counter flow interactions can be conducted on the CD-ST while the condition of the interacted shock wave and the flow field are controlled independently. However the generation of each incident shock wave must be controlled temporally so that the interaction occurs in the test section. Therefore, in this study, the active rupture system using pneumatic cylinders is developed and the characteristics of the system are evaluated.

Figure 2 shows the whole system of the CD-ST. The shock tube is composed of a circular tube ($\phi = 70$ mm)

G. Ben-Dor et al. (eds.), *30th International Symposium on Shock Waves 1*, DOI 10.1007/978-3-319-46213-4_105

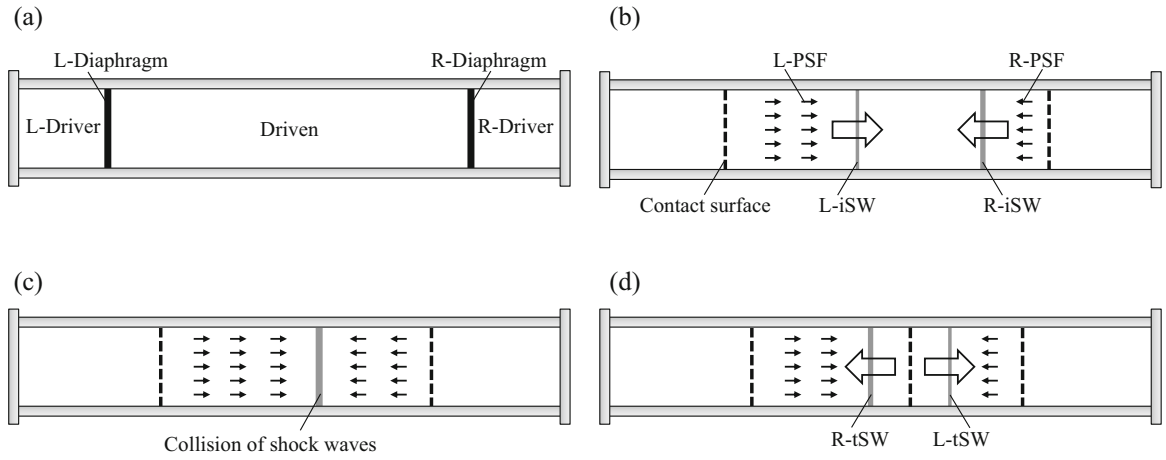

Fig. 1 Schematic of CD-ST. (**a**) Initial condition; (**b**) generation of shock waves and flows; (**c**) collision of shock waves; (**d**) interactions between shock waves and flows

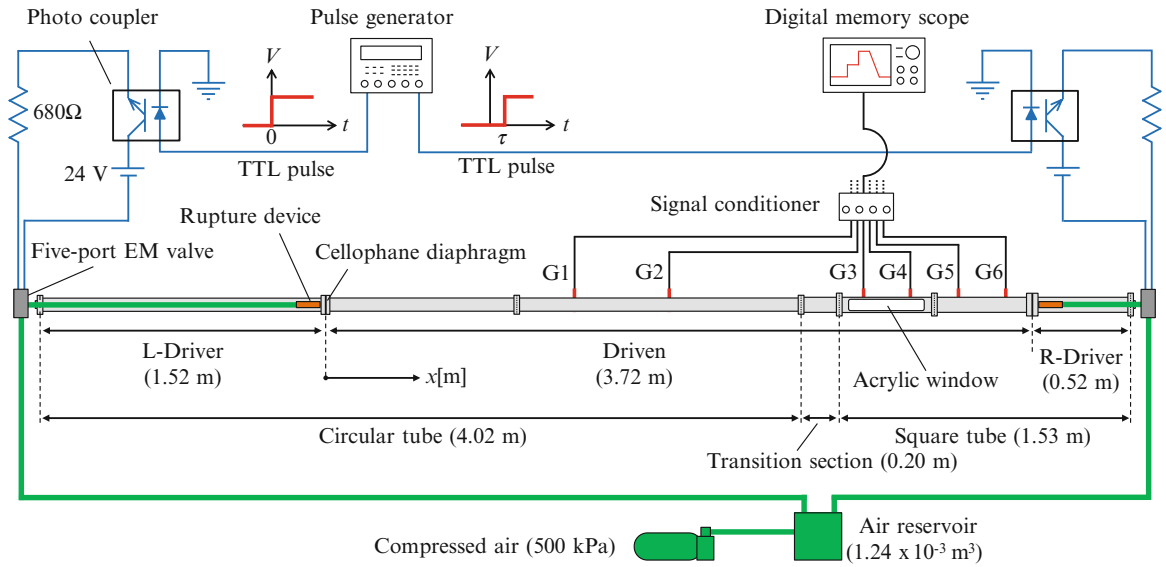

Fig. 2 System of CD-ST

and square tube (62 × 62 mm). Each section is connected by transition section as the cross section is not changed. The test section is located in the square tube and the interactions can be visualized through acrylic windows. To obtain pressure histories, six pressure transducers are installed on the inner wall of the driven section. The pneumatic cylinders are driven by compressed air (0.5 MPa) provided by the electromagnetic valves. Therefore the ruptures in each drivers is controlled by the time difference of the TTL signals from a pulse generator to the electric circuit of the electromagnetic valves. The delay time of the generation of each shock wave is calibrated in advance since the active rupture system using a pneumatic cylinder drives in finite time.

Results

Figure 3 shows the x-t diagram of the operation test of the CD-ST. Based on the delay time obtained by the calibrations, the rupture TTL signal to R-driver was sent 24 ms after the signal to L-driver. Each incident shock waves (L- and R-iSW) collided at $x = 3.3$ m, then formed transmitted shock waves (L- and R-tSW) propagating in the shock tube. In the test section, the interaction between R-tSW and L-PSF induced by L-iSW was realized. The Mach numbers of L-iSW and R-tSW obtained from the pressure histories were $M_s = 1.04$ and $M_s = 1.30$, therefore

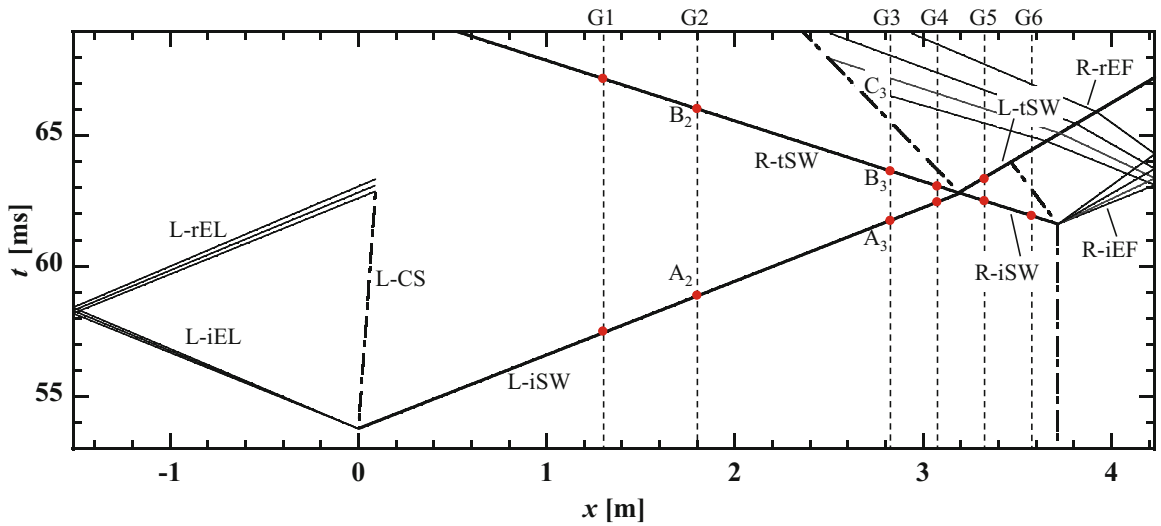

Fig. 3 *x-t* diagram

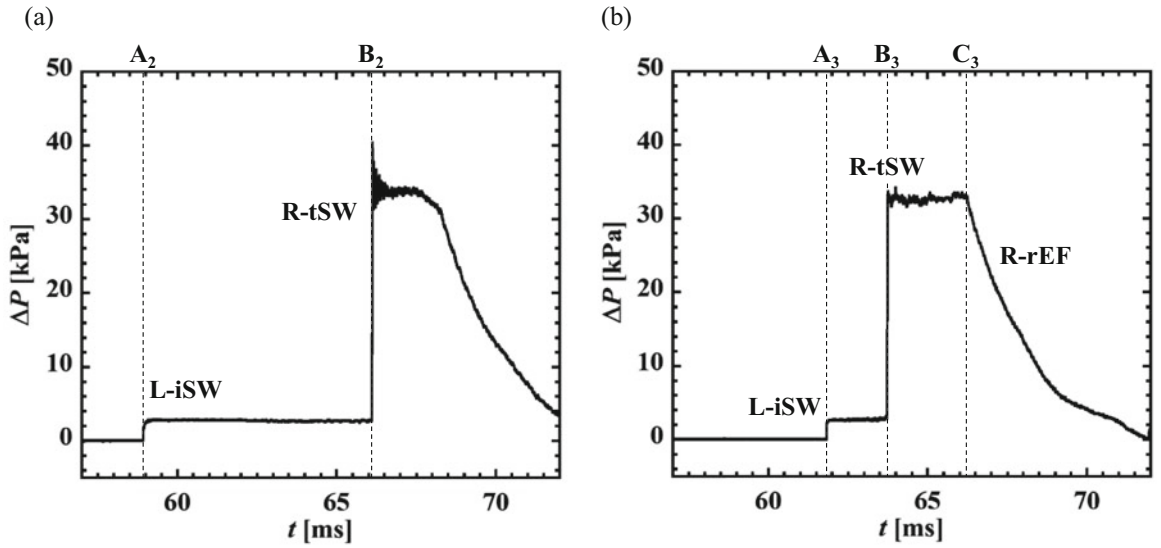

Fig. 4 Pressure histories correspond to Fig. 3. (**a**) G2 ($x = 1.8$ m); (**b**) G3 ($x = 2.8$ m)

the interacted shock Mach number (of R-tSW) and counter flow speed decided by L-iSW were controlled independently by the CD-ST. Also, since the collision point of the shock waves was less than 34 mm in 5 shots in the demonstration, the CD-ST has an enough accuracy for the interaction experiments.

Figure 4 shows the pressure history obtained by the pressure transducers G2 and G3 correspond to Fig. 3. On these sensors, two step pressure jumps were observed. The first jump was caused by L-iSW and L-PSF induced by the shock wave. The second jump corresponds to R-tSW propagating through the counter flow L-PSF. After that, the pressure decreased since the expansion fan from the R-driver reached the gauges.

As one of the example using the CD-ST, Fig. 5 shows the experimental schematic of the shock wave-a laser induced bubble column interaction. A repetitive pulse laser (Nd:YLF laser, Edgewave, $\lambda = 1064$ nm, repetitive frequency $f = 4$ kHz, pulse energy $E = 7.0$ mJ) was focused at $x = 3.1$ m. The Mach number of L-iSW was set in 1.02 so that L-PSF induced by L-iSW was low enough to generate a hot bubble column by a repetitive pulse laser. In L-PSF, a hot bubble was generated at a focal point after the previous bubble has been drifted by the flow, therefore a hot bubble

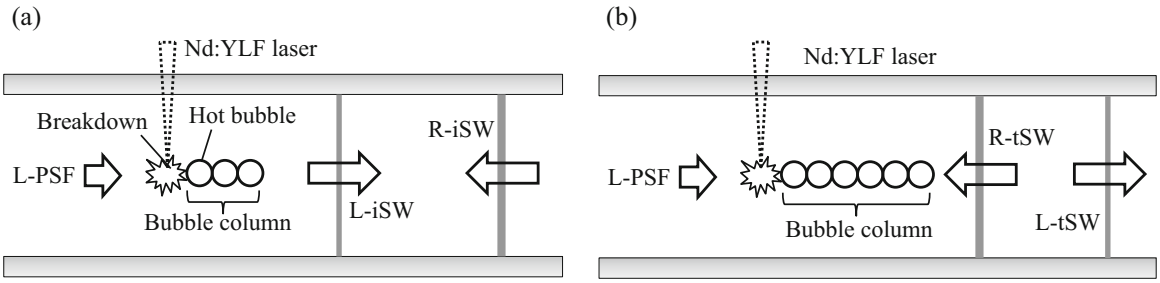

Fig. 5 The interaction with a laser-induced bubble column. (**a**) Generation of a bubble column; (**b**) Interaction between R-tSW and the bubble column

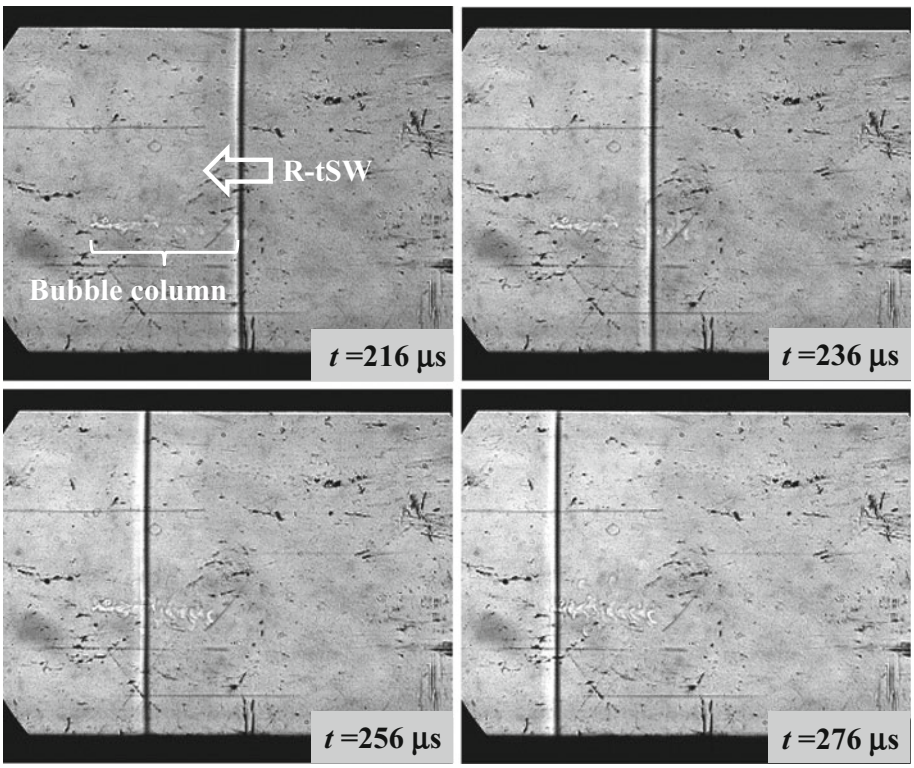

Fig. 6 Schlieren images of the interaction with a laser-induced bubble column

column was formed in L-PSF (Fig. 5a). After the collision of the shock waves, R-tSW propagated to left and interacts with the bubble column (Fig. 5b). In the experiment, the Mach number of R-tSW was 1.27 and the velocity of L-PSF was 11.9 m/s.

Figure 6 shows the Schlieren images of the experiment. The distance between bubbles is calculated as 3.0 mm by the velocity of L-PSF and the repetition frequency of laser pulses. Since the distance is calculated shorter than the diameter which is 1.8 mm from Schlieren images, the bubbles connected each other and formed a dense bubble column. Then, R-tSW propagated through the bubble column. Using the CD-ST, the strong shock wave R-tSW could be adopted for the interaction while the counter flow speed was kept in slow speed to form a dense bubble column. Although more experiments need to be done in the CD-ST, the usefulness of CD-ST on the shock wave-counter flow interactions has been demonstrated.

Conclusions

The Counter-Driver Shock Tube (CD-ST) has been developed, in which the interaction of the shock wave and the post-shock flow can be investigated in various conditions has been developed. Using the CD-ST, the interactions between a shock wave and a laser induced bubble column was experimentally studied and the availability of the CD-ST was demonstrated.

Acknowledgments The authors acknowledge the technical supports provided by the Technical Division of Nagoya University. This study was supported by Japan Society for the Promotion of Science (JSPS) "KAKENHI" through a Grant-in-Aid for Scientific Research, (S) 22226014, and that for Challenging Exploratory Research No. 25630390.

References

1. Kim, J.H., Matsuda, A., Sakai, T., Sasoh, A.: Wave drag reduction with acting spike induced by laser-pulse energy depositions. AIAA J. **49**, 2076–2078 (2011)
2. Kremeyer, K., Sebastian, K., Shu, C.W.: Computational study of shock mitigation and drag reduction by pulsed energy lines. AIAA J. **44**, 1720–1731 (2006)
3. Takeya, K., Yokota, S., Sasoh, A.: In: Proceedings of 44th Fluid Dynamics Conference, 1A12 (JSASS–2012–2015–F/A)
4. Kane, E.J.: Some effects on the atmosphere on sonic boom. Proceedings of a conference on sonic boom research, pp. 49–64, (1967)
5. Agui, J.H., Briassulis, G., Andreopolos, Y.: Studies of interactions of a propagating shock wave with decaying grid turbulence: velocity and vorticity fields. J. Fluid Mech. **524**, 143–195 (2005)

Shock Wave Reflection Over Roughened Wedges

Dan Igra, Kazuyoshi Takayama, and Ozer Igra

Introduction

The transition of reflected shock waves from wedges is one of the fundamental topics in shock wave research. We have experimentally studied the effect of surface roughness on the transition of reflected shock waves and found that the critical transition angles were drastically decreased with increase in the sawtooth roughness [1]. Previously we assumed that the pressure loss behind the reflected shock wave is a result of the local interaction between the oncoming flow and the saw roughness produced by the tooth-like surface of the considered wedge. Hence, based on empirically measured pressure losses (for tooth depth of 0.1 mm, 0.2 mm, 0.8 mm, and 2.0 mm) an appropriate term corresponding to the saw-teeth depth was introduced into the conservation equations [1]. In Fig. 1, variations in the critical transition angle based on the detachment criterion [2] versus the inverse shock pressure ratio for individual sawtooth roughness is shown [1]. The roughness effect on the critical transition angle is clearly visible in this figure.

Experimental Results

0.1 mm Sawtooth Roughness

Experiments were performed in a 40 mm × 100 mm conventional shock tube, the incident shock wave Mach number was 1.46 and experiments were conducted in air at 50 kPa and 292 K. The scatter in the incident shock Mach numbers was about ±1.0 %. A right angle sawtooth roughness of 0.1 mm in depth was machined onto a 40 mm × 100 mm and about 7 mm thick brass plate. The sawtooth roughened plate was attached to a movable wedge that was installed inside the test section and its inclination angle was readily adjustable to a desired angle, from outside the test section. A direct shadowgraph showing a Mach reflected shock wave from a 43° wedge and a regular reflection from a 53° wedge are shown in Fig. 2a, b, respectively. In Fig. 2b, between the reflected shock from the wedge surface and the indecent shock wave a kink is formed. From the kink point a slip line emerges. Such a kink was not observed during shock reflection from smooth wedges.

0.2 mm Sawtooth Roughness

Figure 3a, b shows shock reflections from wedges having 0.2 mm sawtooth roughness at $M_s = 1.86$ in air at 40 kPa and 290.5 K: In Fig. 3a (Run#84012325) a transitional Mach reflection from a 43° wedge is shown, and in Fig. 3b (Run#84012322) a regular reflection from a 46° wedge is presented. We can see a kink in the reflected shock in Fig. 3b. A slip line emanating from this kink is visible.

0.8 mm Sawtooth Roughness

Figure 4 shows direct shadowgraphs of shock wave ($M_s = 1.47$) reflection from wedges having a 0.8 mm deep sawtooth rough surface placed in air at 50 kPa and 292.1 K. In Fig. 4a (Run#80050916) a Mach reflection from a 33° wedge is shown while in Fig. 4b (Run#80050906) a regular reflection from a 40° wedge is visible. In Fig. 4a, b vortices were created at the backward facing sawtooth corners following passage of the incident shock wave. The vortices enlarged their diameter reaching a maximum at about the

D. Igra (✉)
RAFAEL, Aerodynamics Group, P.O.B. 2250, Haifa 31021, Israel
e-mail: danigra@gmail.com

K. Takayama
Emeritus Tohoku University, Sendai, Japan

O. Igra
Professor Emeritus, Department of Mechanical Engineering,
Ben Gurion University of the Negev, P. O. Box 653,
Beer Sheva 84105, Israel

G. Ben-Dor et al. (eds.), *30th International Symposium on Shock Waves 1*, DOI 10.1007/978-3-319-46213-4_106

fifth corner and thereafter gradually diminished with increasing distance. In Fig. 4b, the incident shock just collides with the frontal surface of the sawtooth and shows a regular reflection. This reflected shock intersected with the reflected shock wave from the wedge and thereby forming a noticeable kink.

2.0 mm Sawtooth Roughness

Figure 5 shows direct shadowgraphs of shock wave ($M_s = 1.47$) reflection from wedges having 2.0 mm deep sawtooth rough surface placed in air at 50 kPa and 292.7 K. In Fig. 5a (Run#80051206) a Mach reflection from a 27° wedge is shown while in Fig. 5b (Run#80050803) a regular reflection from a 48° wedge is visible. In Fig. 5a a Mach reflection is evident; behind its Mach stem vortices were detached from the sawtooth corners and the cylindrical shocks driven by these vortices merged with the reflected shock. In Fig. 5b, the Mach reflection was terminated and transferred to a regular reflection. The individual cylindrical shocks generated at sawtooth corners merged and formed a regular reflection. At the foot of the Mach stem, a formation of very small vortex at the sawtooth corner can be seen. The multiple interactions between these cylindrical shocks and with the main reflected shock from the wedge surface formed the kink seen in Fig. 5b.

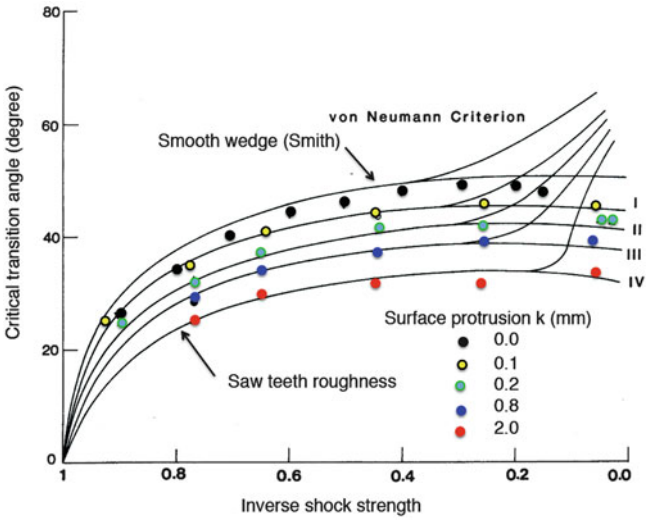

Fig. 1 The critical transition angle vs. inverse shock strength [1]

Discussion

In Figs. 2, 3, 4, and 5, shadowgraphs of shock wave reflection from 0.1 mm, 0.2 mm, 0.8 mm, and 2.0 mm sawtooth roughened wedge surface are shown, respectively. In all these cases, soon after the passage of the colliding shock wave a kink was observed in the reflected shock. In Fig. 5a, a Mach reflection is evident from the 27° wedge having a 2.0 mm surface roughness. This type of reflection terminated when the wedge inclination increased to 35°. In Fig. 5b, showing a wedge at 48° inclination, the previously observed Mach reflection transited already to a regular reflection with the addition of a kink on the reflected shock.

The process of incident shock reflections from a smooth wedge is defined as self-similar. However, in the case of shock reflection from wedges having sawtooth surface, the self-similarity no longer exist. The vortices generated at the sawtooth corner significantly attenuated the reflected shock wave. The sawtooth corners successively drove cylindrical shocks, which locally carried the expansion and thereby attenuating the reflected shock. The degree of reflected shock attenuation was directly linked with the sawtooth geometry. Hence the larger is the sawtooth depth; the stronger is the reflected shock attenuation. The incident shock

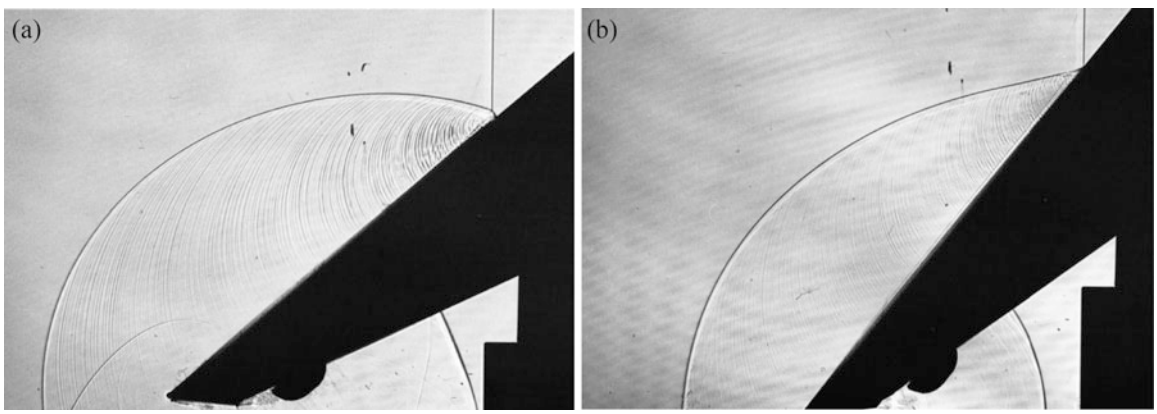

Fig. 2 Sawtooth model of 0.1 mm roughness at $M_s = 1.46$ in air at 50 kPa, 292 K: (**a**) Run #80050919 Mach reflection; and (**b**) Run#80050924 regular reflection

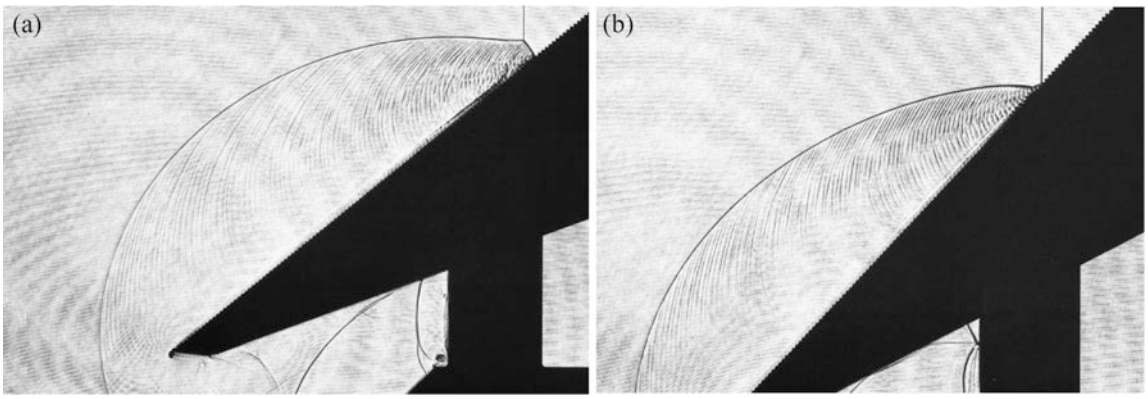

Fig. 3 Sawtooth model of 0.2 mm roughness at $M_s = 1.86$ in air at 40 kPa, 290.5 K: (**a**) Run #84012325 transitional Mach reflection; and (**b**) Run#84012325 regular reflection

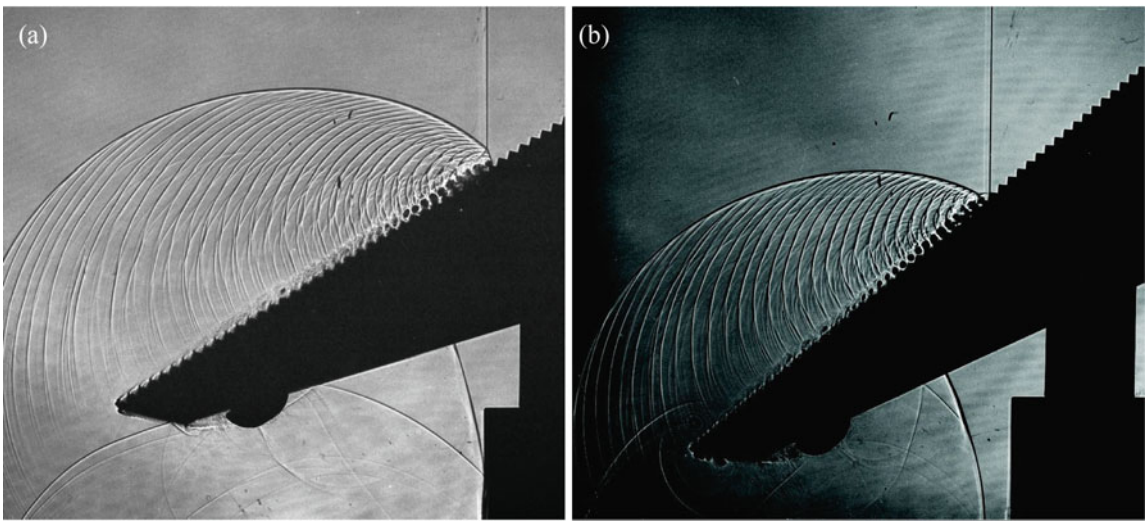

Fig. 4 Sawtooth model of 0.8 mm roughness at $M_s = 1.47$ in air at 50 kPa, 292.1 K: (**a**) Run #80050916 a Mach reflection; and (**b**) Run#80050906 a regular reflection

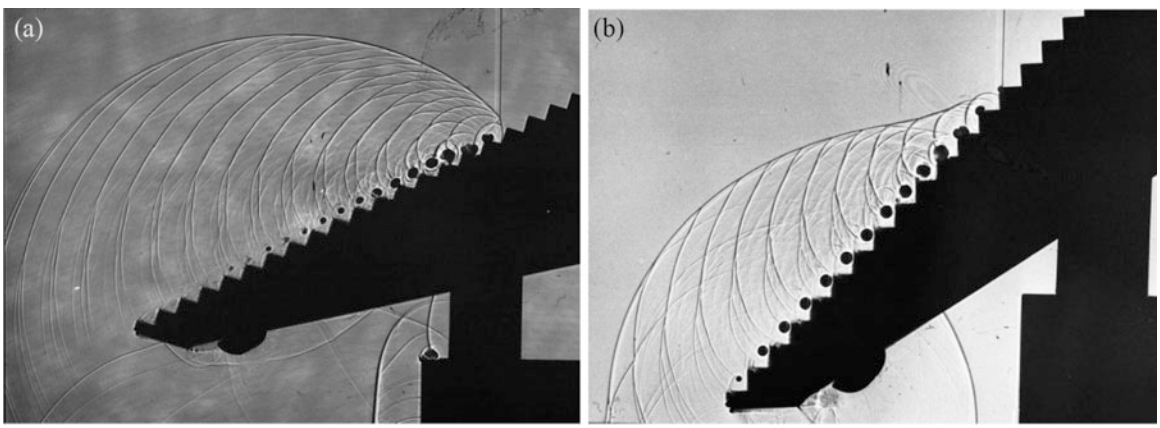

Fig. 5 Sawtooth model of 2.0 mm roughness at $M_s = 1.47$ in air at 50 kPa, 292.7 K: (**a**) Run#80051206 a Mach reflection; and (**b**) Run#80050803 a regular reflection

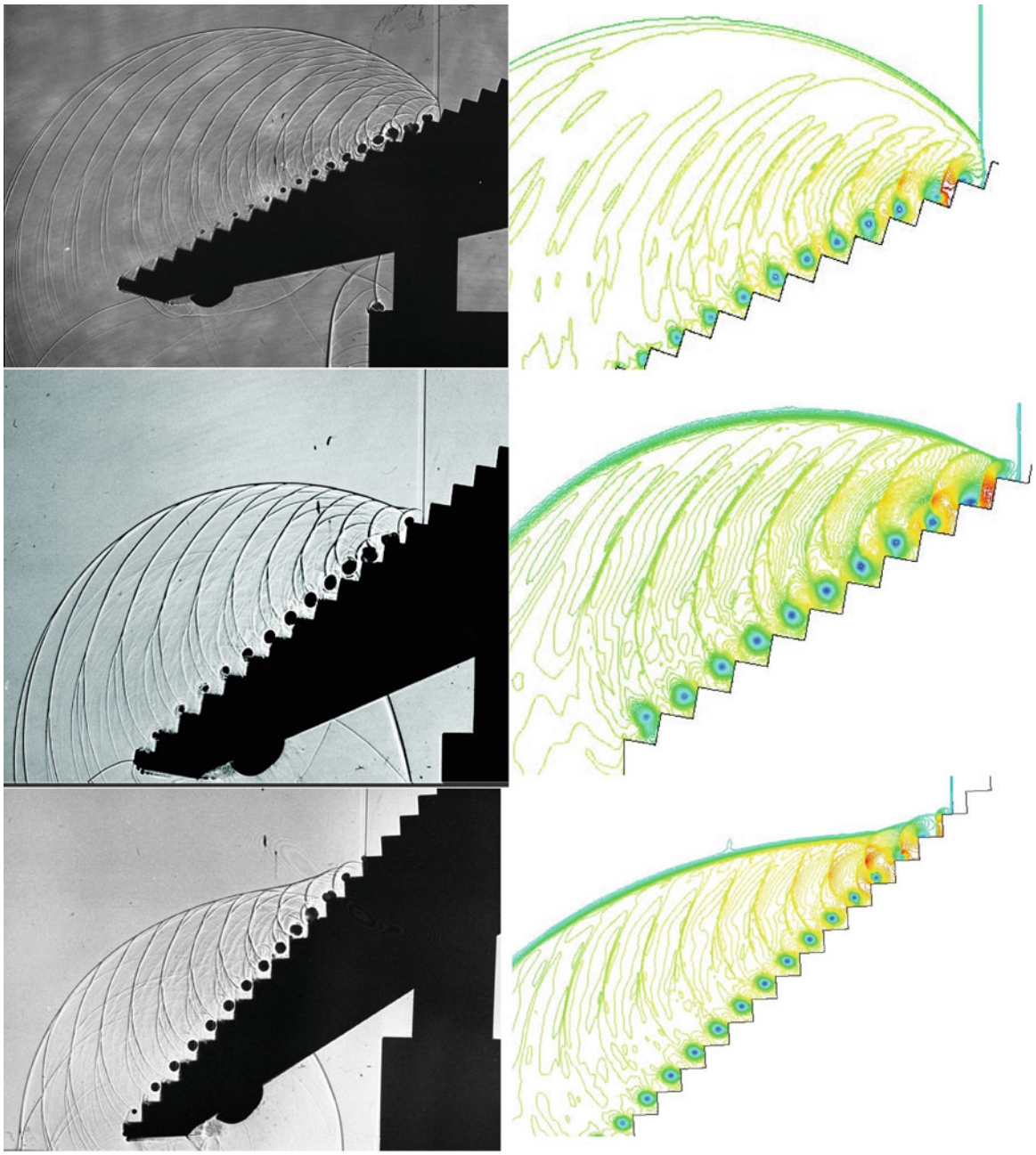

Fig. 6 2.0 mm sawtooth roughness at $M_s = 1.47$ in air at angles of 27°, 35° and 48°. Comparison between experiments and CFD results

propagated independently of the depth of the sawtooth roughness whereas, when the wedge angle increases, particularly in the case of 2.0 mm sawtooth, the main reflected shock from the wedge attenuated significantly.

The incident shock interacted with local sawtooth geometry independently of the main reflected shock. The waves resulted from the local interaction between the incident shock wave and local sawtooth corners intersected with the reflected shock and formed a kink.

In 1980 when these images were produced advanced computational capabilities were not available and hence it was not possible to explain this interpretation. We hope that reproducing the presented experimental findings numerically will enlighten the physical aspect of these reflections. The trend we observed in the 2.0 mm sawtooth case was observed also in the 0.8 mm and in the 0.2 mm sawtooth roughness cases. This peculiar reflection pattern is observable in reflections from wedges having sawtooth roughness.

Numerical Results

The computational domain is two dimensional. Computations were performed using a compressible inviscid flow model, and then solving the Euler equations. Simulations were conducted using the commercial FLUENT code, with the coupled (density based) solver based on a second order AUSM upwind scheme. The solver is second order in both space and time. The AUSM (Advection Upstream Splitting Method) is a flux vector splitting scheme. This scheme separates the flux to convective and pressure parts. First an interface Mach number is computed based on velocities from the neighboring cells. This interface Mach number is then employed to computes the convective and pressure fluxes.

The grid is composed of quadrilateral cells. In these cells the flow was solved using a finite volume scheme. The conservation equations of mass, momentum and energy were solved in each cell for unsteady flow. The grid contained 422,800 cells. Computations were conducted only for the case of a 2 mm rough surface wedge at three different inclination angles 27°, 35° and 48°. Obtained numerical results along with appropriate shadowgraph photos are shown in Fig. 6. It is apparent from this figure that the present numerical results simulate well the recorded wave structure and could therefore be implemented for predicting wave reflections from wedges having different form/size of surface roughness.

Summary

Shock wave reflection from rough wedges was investigated experimentally and numerically. It was shown that for wedges whose inclination angle was close to the critical transition angle, the foot of the incident shock interacted locally with the sawtooth steps and merged with part of shock waves reflected from the sawtooth walls. This trend was observed for all the sawtooth wedges. Good agreement exists between recorded shadowgraph photographs and their simulations indicating the reliability of the used physical model and its numerical solution.

References

1. Takayama, K., Gotoh, J., Ben-Dor, G.: Influence of surface roughness on shock wave transition in quasi-stationary and truly non-stationary flows. In: Proceedings of 13th ISST&W, Buffalo, pp. 326–334 (1981)
2. Ben-Dor, G.: Shock Wave Reflection Phenomena. Springer Verlag, Heidelberg (2007)

Surface Oxidation Study of ZrB_2–SiC Composite for Re-entry Applications Using Free Piston-Driven Shock Tube

Jayaram Vishakantaiah, T. Venketeswaran, C. Venkateswaran, M.R. Ajith, Suraj Natarajan, and K.P.J. Reddy

Introduction

During re-entry, the aerothermodynamic heating due to the shock layer is very high, and to protect the vehicle from this heat, thermal protection system (TPS) is used. The aerodynamic performance of future hypersonic vehicles could be greatly improved with sharp leading edges and sharp fuselage tips [1] with new high temperature materials. This requires the leading edge TPS material to withstand high temperatures for extended times. Ultra-high temperature ceramics (UHTC) exhibit desirable thermal conductivities and emissivities and are well suited for use as leading edges for re-entry applications. Zirconium and Hafnium diboride-based ceramic composites belong to the UHTC category because these materials can be used for applications with temperatures beyond 2300 K [2]. Silicon carbide is also added to the transition metal diboride to increase its thermal and mechanical properties [3]. In general, behaviour of TPS materials is studied under atmospheric conditions [4]. Studies of oxidation reactions are essential to understand the catalytic activity of high temperature ceramic materials. Oxidation resistance properties of silicon carbide in presence of shock-heated oxygen are reported [5]. The novel method of investigating the oxygen interaction with the ZrB_2–SiC–$MoSi_2$ (ZSM) composite for short duration using shock tubes is not reported in the literature. In the present study, free piston-driven shock tube (FPST) has been used to investigate the interaction of strong shock-heated oxygen on ZSM pellet and the material characterization of the same is discussed in the chapter.

J. Vishakantaiah (✉)
Shock Induced Materials Chemistry Laboratory, Solid State and Structural Chemistry Unit, Indian Institute of Science, Bangalore, India
e-mail: jayaram@sscu.iisc.ernet.in

T. Venketeswaran
HWMD, MMG, Vikram Sarabhai Space Centre, Thiruvananthapuram 695022, India

C. Venkateswaran • M.R. Ajith
AMCD, MMG, Vikram Sarabhai Space Centre, Thiruvananthapuram 695022, India

S. Natarajan • K.P.J. Reddy
Department of Aerospace Engineering, Laboratory for Hypersonic and Shock Wave Research, Indian Institute of Science, Bangalore 560012, India

Experimental

For this oxidation study, ZrB_2-based composite is prepared using SiC and $MoSi_2$ as sintering additives. The average particle sizes of ZrB_2, SiC and $MoSi_2$ are 2.8 μm, 0.8 μm and 2.6 μm, respectively. ZSM composite being processed in this work consists of 10 wt% SiC and 10 wt% $MoSi_2$. Ball milled composite powders are poured into the graphite die and initial load of 20 t is applied to obtain green compact. The whole system is charged inside the vacuum hot press and evacuated to vacuum level of ~10^{-3} Pa before starting the heating cycle. Vacuum hot pressing of the composite powder is carried out at 1800 °C for a holding period of 30 min at applied pressure of 30 MPa.

Free piston-driven shock tube (FPST), which is a part of hypersonic shock tunnel 3 (HST3), consists of a gas reservoir, compression tube and a shock tube. A 20 kg piston is mounted at the interface of the gas reservoir and the compression tube. Aluminium diaphragm of 3 mm thickness with one-fourth depth grooved is placed between the compression tube and the shock tube. Provisions are made to mount the ZSM composite on the end flange of the shock tube. The compression tube is filled with 100 kPa pressure of helium gas. The shock tube is purged many times with ultra-high pure (UHP) Argon. A mixture of UHP Argon (99.999 %) and UHP Oxygen (99.999 %) of 5 kPa pressure each, totaling to 10 kPa pressure is filled into the shock tube. Sudden supply of the high pressure gas by opening valves behind the piston sets the piston into instantaneous motion in the compression tube. Motion of the piston in compression

G. Ben-Dor et al. (eds.), *30th International Symposium on Shock Waves 1*, DOI 10.1007/978-3-319-46213-4_107

tube adiabatically compresses the helium gas and thereby increasing its pressure and temperature. This adiabatically compressed helium gas bursts the diaphragm producing a strong primary shock wave. Shock wave travels into the shock tube filled with test gas, which is reflected finally at the end of the shock tube to generate higher stagnation temperature and pressure. This high pressure and temperature test gas interacts with the ZSM composite pellet. The working principle and detailed experimental procedure of FPST is described elsewhere [6, 7]. The shock speed and reflected shock pressure P_5 is measured by dynamic pressure sensors mounted in the shock tube portion. The reflected shock temperature T_5 is estimated using 1D normal shock relations [8]. In the present case, the obtained shock Mach number is 7.25 which corresponds to a reflected shock temperature of ~9900 K and reflected shock pressure of ~7 MPa for a short duration of 1.5 ms. The ZSM composite pellet mounted on the end flange of the shock tube is exposed to multiple shocks (6 times) in presence of Ar + O_2 gas mixture to study its surface oxidation.

Characterization

The characterization techniques such as X-ray diffraction (XRD), scanning electron microscopy (SEM), energy dispersive spectroscopy (EDS) and X-ray photoelectron spectroscopy (XPS) are used to analyse the ZSM composite before and after exposure to shock waves. Powder XRD study is carried out in X-ray diffractometer (PANalytical Empyrean) with an X-ray source of CuKα ($\lambda = 1.5418$ Å), recorded from 20° to 90°, to investigate the crystal structure. SEM and EDS study is carried out to observe the changes in surface morphology and elemental composition (FEI Quanta 250 FEG). XPS study is carried out using AlKα (1486.6 eV) radiation source (AXIS Ultra DLD, Kratos Analytical), which provides an accuracy of ±0.1 eV in binding energy (BE) to understand the changes in chemical composition of ZSM composite.

Results and Discussion

The XRD of ZSM composite before exposure to shock shows peaks corresponding to the mixture of ZrB_2 (JCPDS number 075-0964), SiC (JCPDS number 074-1302) and $MoSi_2$ (JCPDS number 041-0612) crystal structures as shown in Fig. 1a. After subjecting the ZSM composite to six shock treatments in presence of Ar + O_2 gas mixture, presence of ZrO_2 (JCPDS number 078-1807) and SiO_2 in cristobalite form (JCPDS number 003-0272) can also be seen in addition to the earlier peaks, as shown in Fig. 1b.

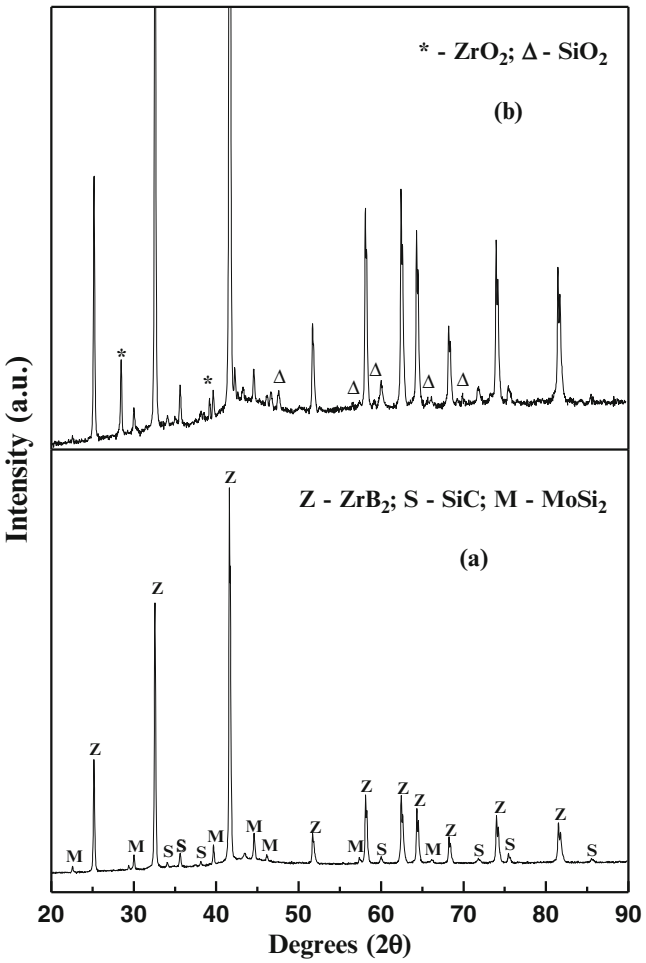

Fig. 1 XRD pattern of ZrB_2–SiC–$MoSi_2$ (ZSM) ceramic composite pellet: (**a**) before shock, (**b**) after six shock treatments in presence of Ar + O_2 gas mixture

SEM is used to study the microstructure of ZSM composite before and after shock treatments and micrographs at 500× and 50,000× magnifications are shown in Figs. 2 and 3, respectively. Figure 2a, b shows the SEM micrograph of ZSM composite before exposure to shock treatment. The EDS spectra of the surface and the weight% of elements present in the ZSM composite are shown in Fig. 2c and inset of Fig. 2c, respectively. Black spots indicated on the SEM micrograph as shown in Fig. 2a are identified as SiC by EDS spectra and elemental analysis (figure not shown).

ZSM composite after shock treatment undergoes changes in surface morphology due to the reaction with shock-heated Ar + O_2 gas mixture as shown in Fig. 3a, b. The surface morphology of the ZSM pellets show spherical particles formed due to oxidation as shown in Fig. 3b and it is identified as SiO_2 from EDS spectra and elemental analysis (figure not shown). The ZSM surface after shock treatment is observed to have more oxygen content, which is confirmed by the EDS spectra in Fig. 3c. The elemental analysis of the

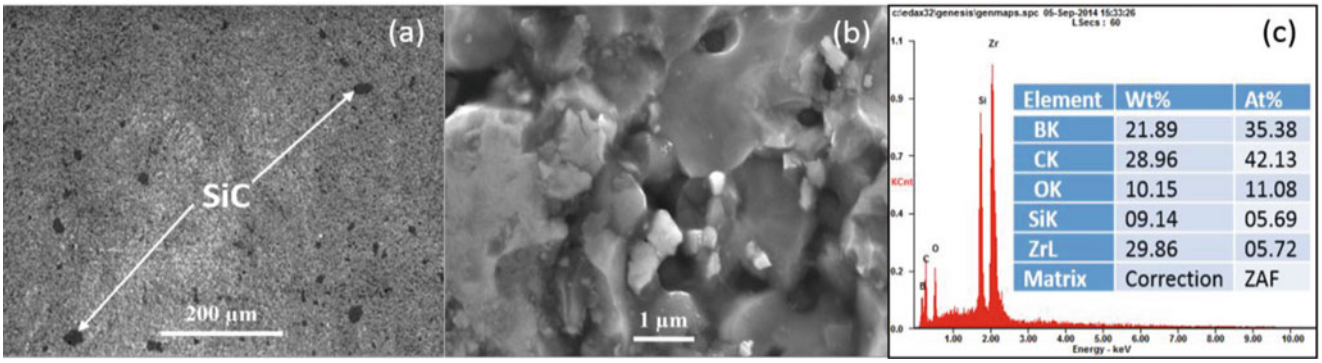

Fig. 2 SEM micrographs of ZSM pellet before exposure to shock: (**a**) at 500×, (**b**) at 50,000×, (**c**) EDS spectra of ZSM pellet

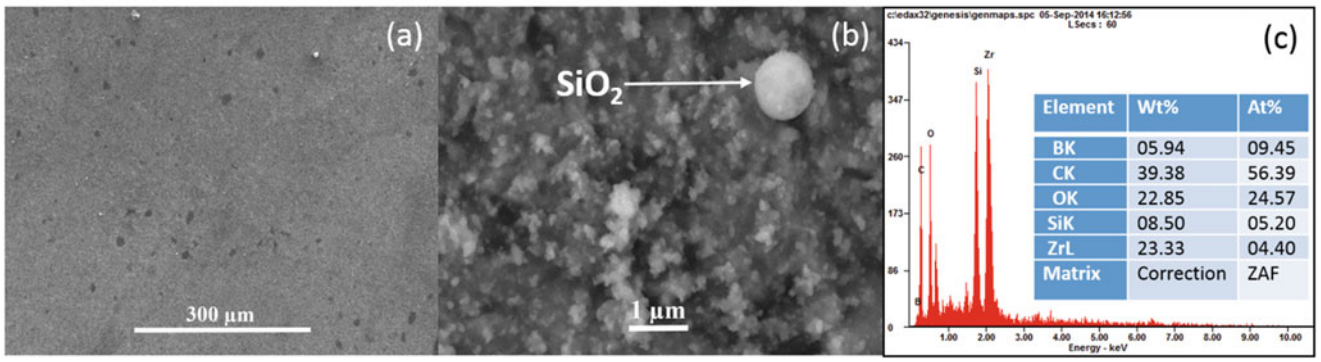

Fig. 3 SEM micrographs of ZSM pellet after six shock treatments in presence of Ar + O_2 gas mixture: (**a**) at 500×, (**b**) at 50,000×, (**c**) EDS spectra of ZSM pellet

surface shows increase in weight% of oxygen and decrease in weight% of boron as shown in the inset of Fig. 3c.

XPS study is a surface analysis technique and it is significant in understanding the changes in chemical composition of ZSM composite surface due to interaction with shock-heated Ar + O_2 gas mixture. XPS spectra of Zr3d, B1s and Si2p of ZSM composite, before and after shock treatment, are shown in Fig. 4. All core level spectra are deconvoluted and the peak positions have been attributed to the compounds formed due to surface oxidation in comparison with the reported literature [9, 10].

XPS spectra of Zr3d and B1s of ZSM composite before exposure to shock is deconvoluted into five distinct peaks as shown in Fig. 4a (left). The peaks of Zr3d at 178.1 eV ($Zr3d_{5/2}$) and 180.6 eV ($Zr3d_{3/2}$) are attributed to Zr–B bonds in ZrB_2 compound [9]. The peaks of Zr3d at 182.5 eV ($Zr3d_{5/2}$) and 184.7 eV ($Zr3d_{3/2}$) are due to Zr–O bonds in ZrO_2 [9], which might be due to some impurity on the surface. The peak at 187.1 eV is attributed to B1s peak in ZrB_2 compound [9]. After shock treatments in presence of Ar + O_2 gas mixture, the deconvoluted XPS spectra for Zr3d is found to have two distinct peaks at 182.4 eV and 184.7 eV due to the formation of ZrO_2 as shown in Fig. 4b (left), which confirms the surface oxidation of ZrB_2.

Deconvoluted XPS spectra of Si2p of ZSM composite before exposure to shock shows three distinct peaks occurring at 99.1 eV, 100.2 eV and 102.75 eV, as shown in Fig. 4a (right). These peaks can be respectively attributed to Si–Mo [10], Si–C and Si–O [9] bondings. After shock treatments in presence of Ar + O_2 gas mixture, the Si2p XPS spectra of ZSM pellet is found to have only one peak at 102.75 eV as shown in Fig. 4b (right), corresponding to the Si–O bond indicating the formation of SiO_2 on the surface.

Conclusions

Oxidation study is carried out on ZrB_2–SiC–$MoSi_2$ (ZSM) ceramic composite by exposing it multiple times to shock-heated Ar + O_2 gas mixture at a reflected shock temperature of 9900 K and pressure of 7 MPa for 1.5 ms using the FPST facility. The deconvoluted XPS core level spectra of Zr3d indicate peaks at 182.5 eV and 184.7 eV, due to formation of ZrO_2. The peak at 102.75 eV is observed in the deconvoluted

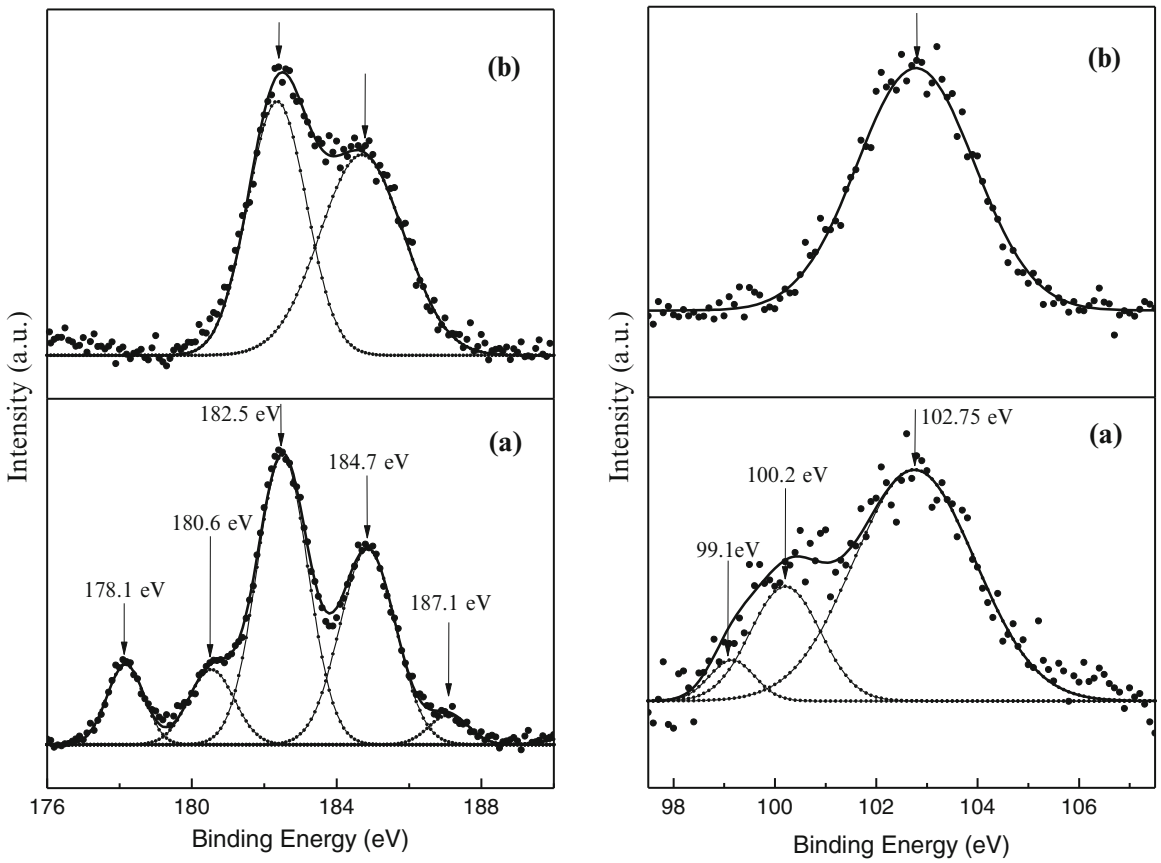

Fig. 4 *Left*: XPS spectra of Zr3d and B1s in ZSM pellet: (**a**) before shock, (**b**) after six shock treatments in presence of Ar + O_2 gas mixture. *Right*: XPS spectra of Si2p in ZSM pellet: (**a**) before shock, (**b**) after six shock treatments in presence of Ar + O_2 gas mixture

XPS core level spectra of Si2p due to formation of SiO_2, confirming the surface oxidation of ZSM composite. After shock treatment, SEM micrographs show the formation of spherical particles of SiO_2 and EDS analysis indicates increase in oxygen content on the surface of ZSM pellet. XRD spectra show the presence of diffractions lines corresponding to ZrO_2 and SiO_2 crystal structure, indicating the effect of oxidation of ZSM composite. Further studies are required to understand the oxidation of ZSM composite in presence of shock waves.

Acknowledgments Financial support for this research work from ISRO-IISc Space Technology Cell, JATP and DRDO, Government of India is gratefully acknowledged.

References

1. Savino, R., Fumo, M.S., Paterna, D., Serpico, M.: Aerothermodynamic study of UHTC-based thermal protection systems. Aerosp. Sci. Technol. **9**, 151–160 (2005)
2. Monteverde, F., Savino, R., Fumo, M.S., Di Maso, A.: Plasma wind tunnel testing of ultra-high temperature ZrB2–SiC composites under hypersonic re-entry conditions. J. Eur. Ceram. Soc. **30**, 2313–2321 (2010)
3. Patel, M., Prasad, V.V.B., Jayaram, V.: Heat conduction mechanisms in hot pressed ZrB2 and ZrB2–SiC composites. J. Eur. Ceram. Soc. **33**, 1615–1624 (2013)
4. Zhang, X., Hu, P., Han, J., Meng, S.: Ablation behavior of ZrB_2-SiC ultra-high temperature ceramics under simulated atmospheric re-entry conditions. Compos. Sci. Technol. **68**, 1718–1726 (2008)
5. Thanganayaki, N., Reddy, K.P.J., Jayaram, V.: Oxidation resistance studies of silicon carbide thin film in a free piston-driven shock tube. In: 29th International Symposium on Shock Waves, Madison, July 14–19 (2013)
6. Stalker, R.J.: A study of the free piston shock tunnel. J. AIAA **5**(12), 2160–2165 (1967)
7. Reddy, K.P.J., Hedge, M.S., Jayaram, V.: Material processing and surface reaction studies in free piston driven shock tube. In: 26th International symposium on Shock Waves, Gottingen, July 15–20, pp. 35–42 (2007)
8. Gaydon, A.G., Hurle, I.R.: The Shock Tube in High Temperature Chemical Physics, pp. 23–28. The Reinhold Publishing Corporation, New York (1963)
9. Scatteia, L., Borrelli, R., Cosentino, G., Beche, E., Sans, J.-L., Balat-Pichelin, M.: Catalytic and radiative behaviors of ZrB_2-SiC ultrahigh temperature ceramic composites. J. Spacecr. Rocket. **43** (5), 1004–1012 (2006)
10. Lee, J.H., Lee, Y.S., Jeon, M.S., Song, J.K., Jeong, C.W., Han, D. B., Rha, S.K.: Study of the post-annealing effect for the $MoSi_2$ compound. J. Ceram Proc Res. **10**(3), 335–339 (2009)

Shock Wave Reflections Over Newtonian and Non-Newtonian Wedges: Experimental Investigation

H. Jeon, N. Amen, and V. Eliasson

Introduction

Many researchers have studied shock wave dynamics to protect humans and building structures from bombings and high explosives. Explosive materials rapidly generate high pressures, creating a blast wave. The resulting overpressure is able to directly damage not only the surrounding people, but also building structures, causing collapse [1]. Therefore, blast-hardening technologies are recommended, especially to protect buildings from vehicle bomb attacks [2].

Since understanding shock wave reflections are a fundamental study of shock wave dynamics, many studies have attempted to solve reflection problems following the pioneering work of von Neumann [3]. Numerous researchers have tried to verify von Neumann's mathematical theory using analytic, numerical, and experimental methods. However, these results have never agreed and have caused the so-called von Neumann's paradox. Ben-Dor et al. [4] summarized benefits and disadvantages of previously suggested theories and compared to experimental results. Takayama et al. [5] studied shock wave reflections in pseudo-steady flows, including non-solid surfaces (water wedges), and showed that transition angles between regular shock wave reflections (RR) and irregular shock wave reflections (IR) are different from those of solids.

Recently, Waitukaitis and Jaeger [6] studied dense suspension solidification of cornstarch suspensions (non-Newtonian shear thickening liquids) by means of aluminum-rod impact. They developed a model for the dynamic solidification of a cornstarch suspension. They successfully verified the physical reactions of cornstarch suspensions and compared with numerical results.

The present research focuses on shock wave reflections over different types of liquids, both Newtonian and non-Newtonian.

Theoretical Background

Figure 1 shows a schematic illustration of the regular and irregular reflection. When a planar incident shock wave encounters a compressive wedge, it is reflected by the surface. Depending on the incident shock Mach number (M_s), gas specific heat ratio (γ), and deflection angle (θ_w), different types of reflections happen for IR reflections, generally, a Mach stem and slipstream are generated since the shock Mach numbers are different in each region. Therefore, in the RR case, two shock waves (incident and reflected shock waves) meet at the deflecting surface. In the IR case, three shock waves (incident, reflected, and Mach stem) are observed and those meet at one point. This point, called triple point, is located above the deflecting surface. There are four different theories to explain different reflection configurations (detachment, length scale, mechanical equilibrium, and sonic criterion), of which, the length scale concept suggested by Hornung et al. [7] most likely explains transition angles in steady, pseudo-steady, and unsteady flows. However, little work has been done to understand shock reflection off liquid surfaces due to analytical and experimental difficulties.

Experimental Setup

Figure 2 shows the shock tube that consists of three parts (driver, driven, and test section). The shock tube design is motivated by the inclined shock tube used by Takayama et al. [5]. The internal cross section of the driver section is 2.9

H. Jeon • N. Amen
University of Southern California, Los Angeles, CA, USA

V. Eliasson (✉)
University of Southern California, Los Angeles, CA, USA

University of California, San Diego, La Jolla, CA, USA
e-mail: eliasson@ucsd.edu

G. Ben-Dor et al. (eds.), *30th International Symposium on Shock Waves 1*, DOI 10.1007/978-3-319-46213-4_108

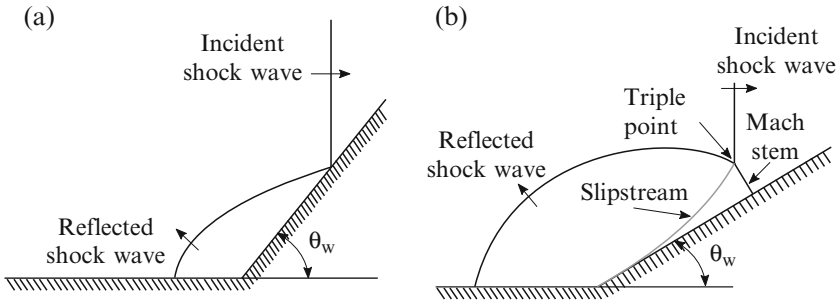

Fig. 1 Schematic illustration of shock wave reflections. (**a**) Regular shock wave reflection; (**b**) irregular shock wave reflection

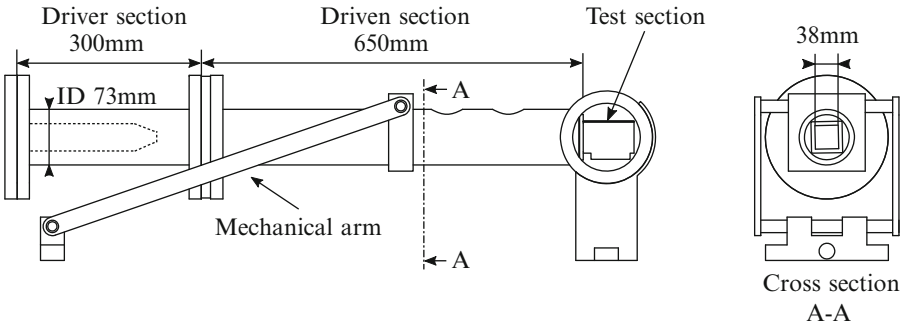

Fig. 2 Schematic description of inclined shock tube

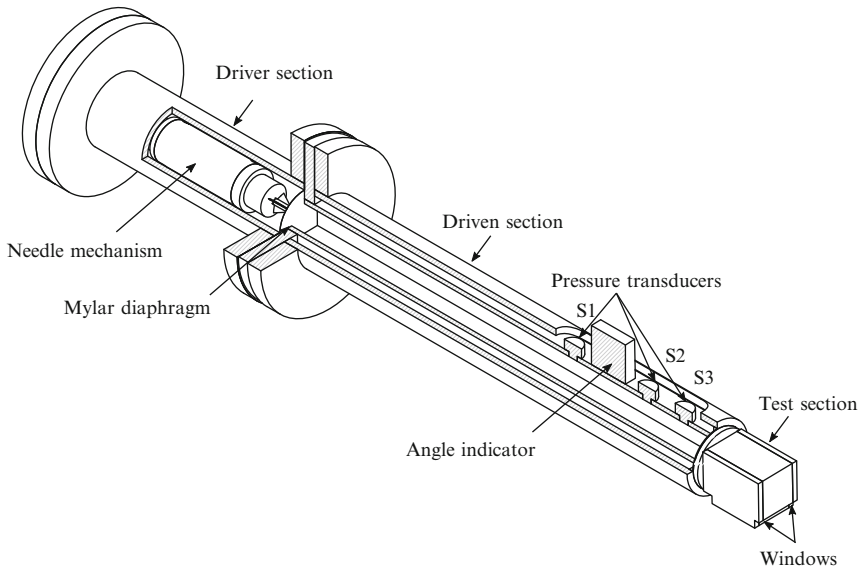

Fig. 3 Detailed schematic description of inclined shock tube

times larger than the internal area of the driven section because the area reduction can help to create stronger shock waves [8]. The length of the driven section is 17 times longer than its width in order to allow shock wave formation before the shock enters the test section [9]. At the same time, the cross section is kept constant up to the test section to generate a 2-D planar shock wave. These three sections are supported by two mechanical arms that allow the shock tube to be inclined at a specific angle.

As depicted in Fig. 3, a needle mechanism is located inside the driver section to rupture a Mylar diaphragm (moisture-resistant polyester film) placed between the driver and driven sections. The thickness of the Mylar diaphragm is varied between 25.4 and 76.2 μm depending on the required pressure of the driver section. To control the inclination angle of the shock tube, a digital angle indicator (Wixey, WR365, $\pm 0.1^\circ$ accuracy) is used. Pressure is measured by using piezoelectric pressure transducers (PCB 113B21 and 113B31, flush mounted) placed 400 mm, 510 mm, and 565 mm downstream of the location of the Mylar diaphragm. Typical pressure histories of incident shock waves measured by three pressure transducers (S1, S2, and S3) are shown in

Fig. 4. Note that the pressure signals are filtered using a fast Fourier transform (FFT) since the natural frequency of the transducers is 400 kHz. Pressure signals are recorded by an oscilloscope (LeCroy Wave Surfer 24 Xs-A). The high-speed camera (Phantom V711) is triggered by the pressure signal from S1. The high-speed camera collects high-speed images by using a continuous white light source (Cree XLamp, XP G-2 LEDs, Cool White) and a z-folded schlieren setup [10].

In this experiment, two different liquids, deionized (DI) water and a cornstarch–water mixture (55 wt% of cornstarch, Clabber girl), are investigated. The concentration of the mixture is known to display strong shear-thickening suspensions [6, 11] and density is approximately

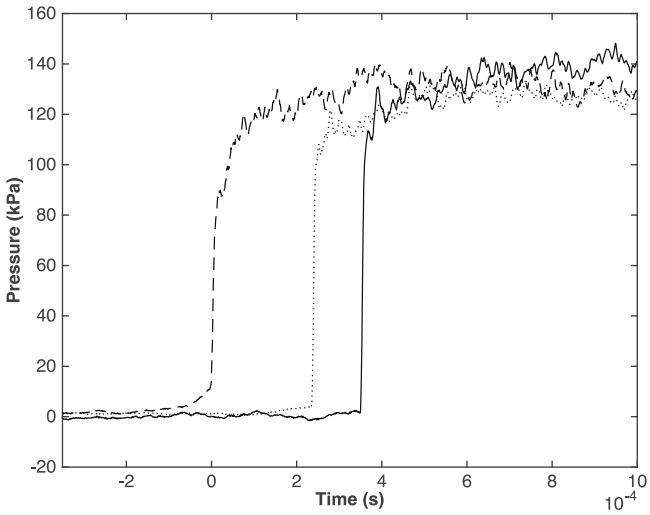

Fig. 4 Pressure histories of incident shock waves measured by S1, S2, and S3 obtained during a single experiment

1550 kg/m^3 [12].

Results

In Fig. 5, an irregular shock wave reflection (single-Mach reflection, SMR) over cornstarch suspensions is shown at $Ms = 1.48 \pm 0.14$ and $\theta_w = 30 \pm 0.5°$. The relatively high uncertainty of Mach number and the transition angle is calculated from the high-speed images and the angle indicator. The procedure of the experiments is following: (1) The wedge angle is initially chosen to produce an IR reflection; (2) The wedge angle (or the reflecting angle) is then incremented while keeping the Mach number constant; (3) The location of the triple point is measured by the trajectory angle (χ). Following these steps, various experiments are performed at different angles and transition to RR reflection is found at 42°. Using the same procedure, the transition angle of the water wedges is found at $\theta_w = 44°$ and this result is comparable to the previous work by Takayama et al. [5] who reported a value of $\theta_w = 37°$ at $M_s = 1.36$.

Conclusions

The reflection of shock waves over water and cornstarch–water mixture is studied experimentally. The transition angles of those two different wedges are different and the viscous effects generated by boundary layers above the two wedges are assumed to be the primary cause. Future studies will be performed to understand why the IR-RR transition angle is different for the two cases.

Acknowledgments This work is supported by NSF grant #CBET-143741.

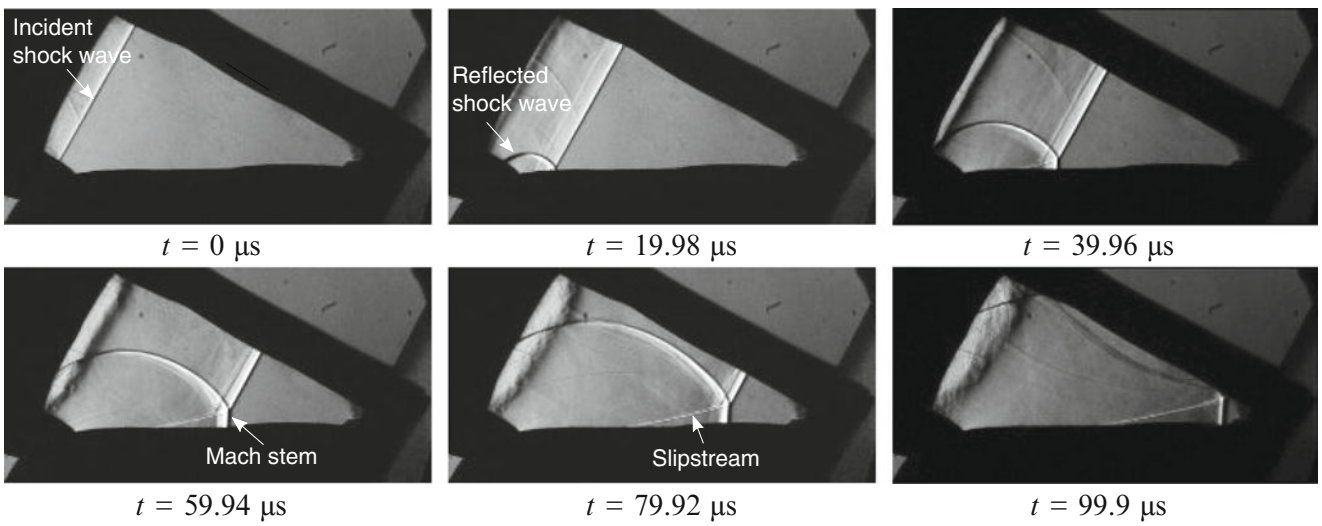

Fig. 5 Irregular shock wave reflections of cornstarch suspensions ($M_s = 1.48$, $\theta_w = 30°$)

References

1. Mallonee, S., Shariat, S., Stennies, G., Waxweiler, R., Hogan, D., Jordan, F.: Physical injuries and fatalities resulting from the Oklahoma City bombing. JAMA **276**(5), 382–387 (1996)
2. Longinow, A., Mniszewski, K.R.: Protecting buildings against vehicle bomb attacks. Pract. Period. Struct. Des. Constr. **1**(1), 51–54 (1996)
3. Von Neumann, J.: Oblique Reflection of Shocks. Navy Department, Washington, DC (1943)
4. Ben-Dor, G.: Shock Wave Reflection Phenomena, p. 42. Springer, Berlin (2007)
5. Takayama, K., Ben-Dor, G.: Pseudo-steady oblique shock wave reflections over water wedges. Exp. Fluids **8**(3–4), 129–136 (1989)
6. Waitukaitis, S.R., Jaeger, H.M.: Impact-activated solidification of dense suspensions via dynamic jamming fronts. Nature **487**(7406), 205–209 (2012)
7. Hornung, H.G., Pertel Jr., H., Sandeman, R.J.: Transition to Mach reflexion of shock waves in steady and pseudosteady flow with and without relaxation. J. Fluid Mech. **90**, 541–560 (1979)
8. Alpher, R.A., White, D.R.: Flow in shock tubes with area change at the diaphragm section. J. Fluid Mech. **3**, 457–470 (1958)
9. Bleakney, W., Weimer, D.K., Fletcher, C.H.: The shock tube: a facility for investigation in fluid dynamics. Rev. Sci. Instrum. **20** (11), 807–815 (1949)
10. Eliasson, V., Mello, M., Rosakis, A.J., Dimotakis, P.E.: Experimental investigation of converging shocks in water with various confinement materials. Shock Waves **20**(5), 395–408 (2010)
11. White, E.E.B., Chellamuthu, M., Rothstein, J.P.: Extensional rheology of a shear-thickening cornstarch and water suspension. Rheologica acta **49**(2), 119–129 (2010)
12. Yang, J., Sliva, A., Banerjee, A., Dave, R.N., Pfeffer, R.: Dry particle coating for improving the flowability of cohesive powders. Powder Technol. **158**(1), 21–33 (2005)

Ground Effect of Transonic and Supersonic Projectiles: Influence of Mach Number and Ground Clearance

C. Sheridan, J. Young, Harald Kleine, Koju Hiraki, and Satoshi Nonaka

Introduction

The ground effect experienced by transonic/supersonic projectiles with a diameter d flying at a distance h above a solid surface has been the subject of several studies in recent years [1–3]. A projectile was chosen for these studies to simplify the analysis of the influence the ground has because a projectile at zero angle of attack would not be subjected to any force (or moment) other than drag, hence the occurrence of other forces and moments could directly be attributed to the presence of the ground. All investigations showed that the presence of the ground, indeed, altered the drag force and introduced a lift force and a pitching moment that did not exist when the bullet was in free flight far away from any solid surface.

One of the main observations in the aforementioned studies was that for high supersonic Mach numbers such as $M_\infty = 2.4$, the ground-induced lift force was always directed away from the ground for all distances h of the projectile at which a ground effect was observed [1]. For transonic Mach numbers ($M_\infty = 1.1$ [2, 3]), however, this force could change sign depending on the ground clearance. One aim of the present study is to examine under which conditions this change will occur, i.e., to find at which Mach number a ground plane-induced suction force on the projectile can no longer be established. Preliminary tests had indicated that this change would already be seen for mildly supersonic flows, and therefore the current study concentrates on the Mach number range $M_\infty = 1.1$–1.5. The investigation is conducted primarily by means of a numerical analysis and a number of wind tunnel tests for both qualitative and quantitative validation.

The projectile investigated here is the Nosler 50 gn S.H.O.T. commercial transonic projectile that was already used in previous studies [2, 3]. The wind tunnel model is a 7.5 times larger replica of the actual projectile.

Numerical Method

A 64-bit commercial, finite-volume RANS solver (Fluent 14.5) was used for all simulations. A density-based, implicit coupled solver was combined with second-order upwinding to provide adequate steady-state solution accuracy. Spin of the projectile was neglected in this study as previous work had shown that the effect of spin on the aerodynamic forces is negligible [1]. Similarly, the rifling striations were also excluded as previous work had identified that they only marginally affect the yawing and the pitching moment coefficients [4]. Excluding small disturbances assists the mesh generation as edge sizing around the model would require considerable attention and cells would need to be clustered in these areas to account for such minor flow disturbances. The turbulent intensities and viscosity ratios were selected to have arbitrarily low values of 1 % and 0.1 %, respectively, for both the inlet flow and outlet. These values were deemed suitable for the model, given that in real-life the projectile is in most cases encountering quiescent air. All cases were run until changes in residuals, forces, moments, and inlet/outlet mass flow rates became negligible over a period of time (less than 0.1 % over 500–1000 successive iterations).

A half-model geometry is used for ground effect analysis with no spin, where the ground plane can be set either as a moving wall or a symmetry plane. The boundary conditions

C. Sheridan • J. Young
University of New South Wales, Canberra, ACT, Australia

H. Kleine (✉)
SEIT, University of New South Wales, Canberra, ACT, Australia
e-mail: h.kleine@adfa.edu.au

K. Hiraki
Kyushu Institute of Technology, Kitakyushu, Fukuoka, Japan

S. Nonaka
Japan Aerospace Exploration Agency (JAXA), ISAS, Sagamihara, Kanagawa, Japan

G. Ben-Dor et al. (eds.), *30th International Symposium on Shock Waves 1*, DOI 10.1007/978-3-319-46213-4_109

used in the calculations are chosen to match those of the wind tunnel experiments that are described in the next section. As the model in the experiments used symmetry to model the ground effect, the ground plane in the CFD simulations was enforced as a symmetry boundary condition. The outer domains of the volume were set as far-field boundaries to represent the walls at an infinite distance away from the model. This is not a true representation of the wind tunnel as there were minor blockage effects present irrespective of how small the model is relative to the test section, however, the chosen domain size was compatible to that used in earlier studies [1] and did also not lead to excessively high computational cost. The chosen domain extends one projectile length upstream and between 10 and 12 projectile lengths both downstream and radially, depending on the flow regime investigated. The domain size underneath the projectile changes for varying ground separation clearances. A structured hexahedral mesh was used, with cells clustered in regions where complex flow features and high viscosity exist, i.e., immediately surrounding the projectile surface, near-base wake, and the ground plane, and in the shock and expansion structures via solution-adaptive meshing.

Military projectiles are typically used at very low altitudes under extreme dynamic loads. They are usually designed with a surface finish that encourages the immediate transitioning of the flow into turbulence. A number of different turbulence models were tested and after qualitative flow field comparisons with experimental tests and comparisons of predicted surface pressure distributions, aerodynamic forces, shock impingement locations, and convergence times, it was decided that the SST variant of the k-ω model [5] was the most suitable for this study.

Mesh independence was evaluated both quantitatively and qualitatively. A standard mesh with no pressure gradient cell adaptation was compared with two meshes that had different levels of cell adaptation across a pressure gradient. The cell adaptation changed aerodynamic forces and moments by only 0.5 % and 0.05 % for the first and second refinement, respectively, which indicates that the standard mesh is already adequate for obtaining forces and moments. The refinement improves, however, the shock resolution in the key regions of the flow field, which is critical, particularly for differentiating between Mach and regular shock reflection patterns for low Mach-stem heights. A mesh with cell adaptation across a pressure gradient of 1000 Pa was therefore selected over the standard model. For a Mach number of $M_\infty = 1.2$ and $h/d = 1.25$, the used mesh had 4.3×10^6 cells. Details of the used meshes and their performance are given in [6].

Experimental Details

The experiments were conducted in the transonic blowdown wind tunnel of the Institute of Space and Astronautical Science (ISAS) of the Japan Aerospace Exploration Agency (JAXA). The wind tunnel has a cross section of 600 mm × 600 mm and a typical test run time is 20 s. The reservoir pressure in all conducted tests was $p_0 = 150$ kPa. As seen in Fig. 1, a symmetry (mirror image) setup was chosen to replicate the ground effect [7]. One of the two identical

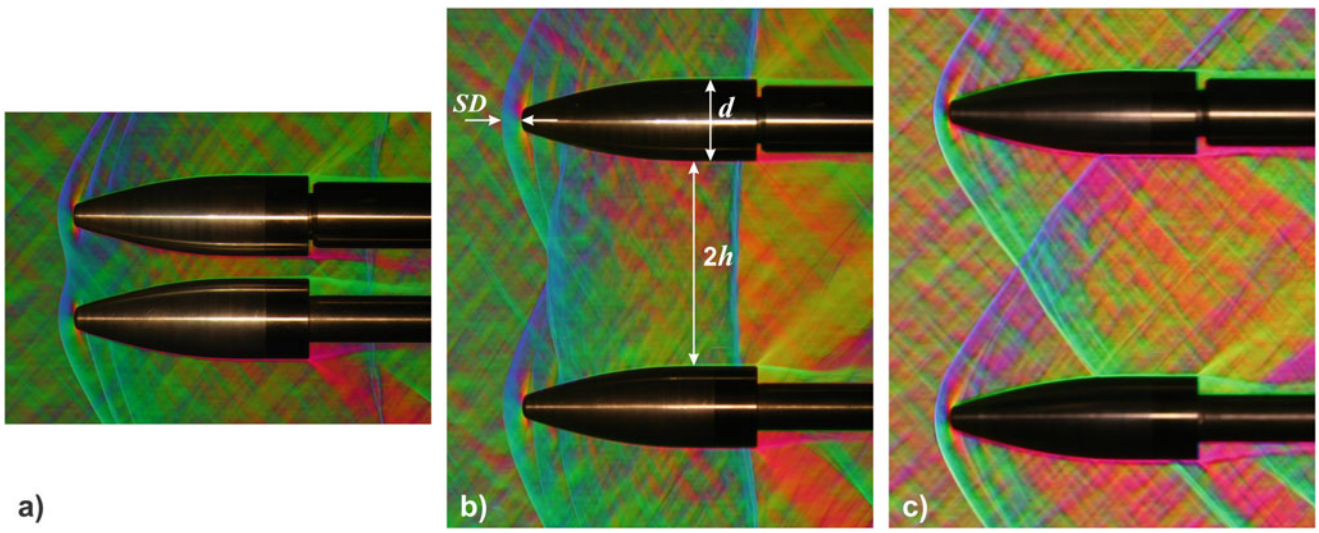

Fig. 1 Direction-indicating color schlieren images of the different reflection patterns observed for transonic projectiles in ground effect: (**a**) no reflection, but smooth forward bending of the bow shock so that it meets the symmetry plane at a right angle ($h/d = 0.125$, $M_\infty = 1.3$); (**b**) Mach reflection ($h/d = 1.25$, $M_\infty = 1.2$); (**c**) regular reflection ($h/d = 1.25$, $M_\infty = 1.3$). The upper model is mounted on a strain gauge balance. (**b**) also indicates the definitions of ground clearance h, diameter d, and stand-off distance SD.

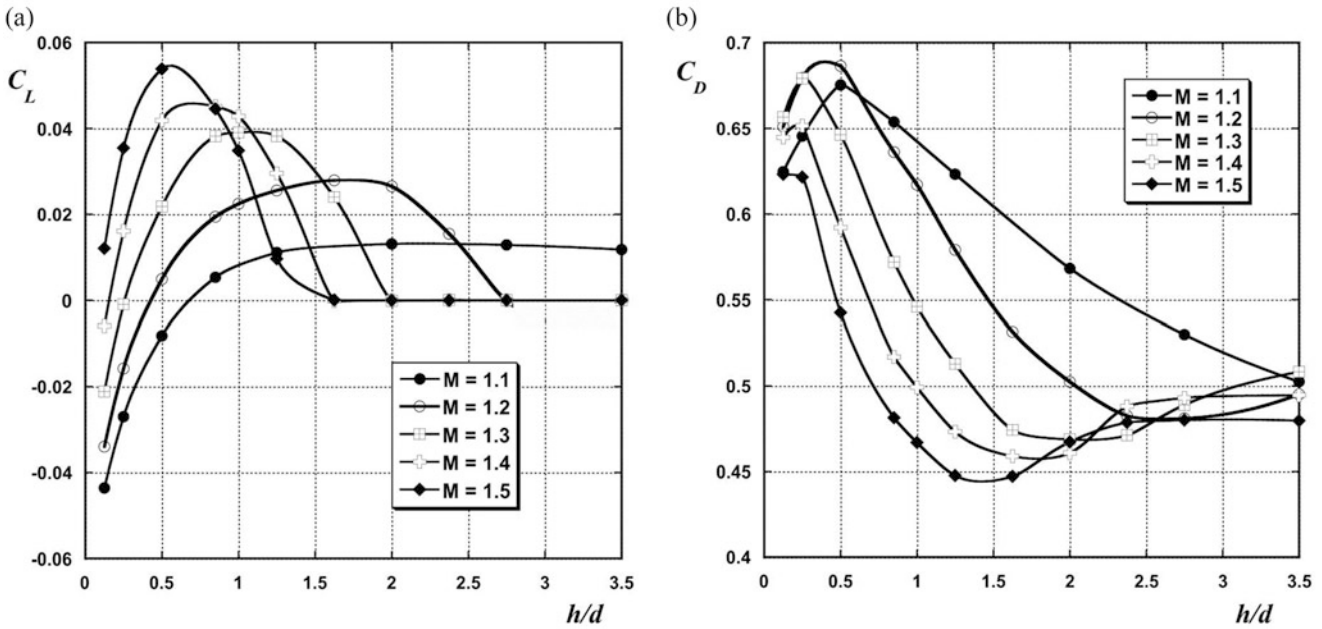

Fig. 2 Coefficients of (**a**) lift and (**b**) drag vs. ground clearance h/d for the Mach number range $1.1 \leq M_\infty \leq 1.5$; numerical results

projectile models was equipped with a strain gauge balance, which allowed one to measure lift and drag as well as pitching moment. The presence of the sting mounting strongly affects the drag measurement, which is why only the lift and moment data were further evaluated. Forces were measured for the ground clearances $h/d = 0.125$, 0.5, 0.85, and 1.25. In addition to the force measurement, single-image flow visualization by means of direction-indicating color schlieren was used in each test to obtain data on the geometry of the flow field. The images were recorded with a standard SLR camera (CANON EOS 10D).

Results

Forces and Moments

Once the projectile is in close proximity to the surface, the resulting asymmetry of the pressure distribution leads to the establishment of a previously non-existent lift force and a modification of the drag force. The associated lift and drag coefficients C_L and C_D are shown in Fig. 2 as a function of ground clearance and Mach number. Several trends become evident from the lift coefficient curve (Fig. 2a): with increasing Mach number, the region of influence of the ground effect is reduced; at the same time, the peak C_L both increases and translates left to a closer ground clearance. For all Mach numbers considered here, the slope of the lift coefficient curve, that is, the sensitivity to changes in h/d, is greatest immediately beyond the minimum tested ground clearance of $h/d = 0.125$. Furthermore, once $M_\infty = 1.5$, a suction force no longer exists for $h/d \geq 0.125$. The experimental data available at the time of writing this manuscript consistently confirm the trends predicted by CFD.

The overall drag is highly sensitive to the complex physical flow-field features, which is reflected in the shape of the drag coefficient curve (Fig. 2b). Immediately beyond the lowest ground clearance there is a drag peak with a magnitude and width that decreases with an increase in Mach number. Following the peak, all curves exhibit a significant drop in drag with the steepness becoming larger for higher Mach numbers, resulting in the local minimum occurring at lower h/d locations. This is largely due to where the reflected shock impinges on either the projectile or wake. Viscous forces were found to change negligibly when the reflected shock strikes the projectile; therefore the primary driver for the changes in total drag is the effect that the shock reflections have on the pressure and wake drag, i.e., any distortion, deflection, or combination of both, of the wake. For low ground clearances, the wake, which is bounded by a shear layer that encapsulates the flow, thickens immediately downstream of the base and is pulled towards the ground due to the large concentration of low pressure constrained between the wake and the solid plane. This results in a non-linearly behaving interaction of two low pressure recirculation regions within the wake, which are no longer symmetric about the projectile lengthwise axis as one tends to compress the other, depending on the direction of wake deflection. The described drag peak occurs for all cases in which the reflected shock strikes the projectile wake between the projectile body and the stagnation point that encapsulates the two low speed recirculation regions.

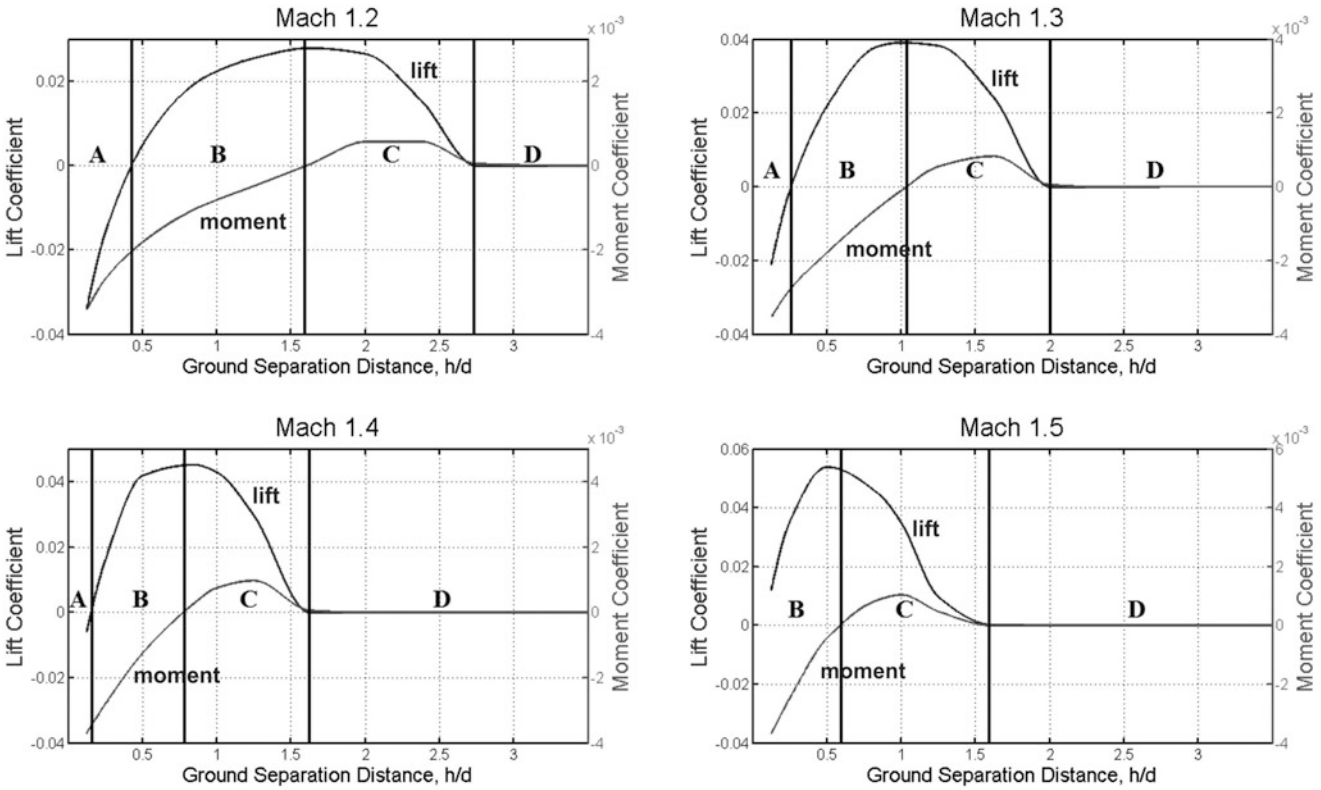

Fig. 3 Lift and moment coefficient curves and associated flight regimes A–D (see text for definition)

Ground Effect Flight Configurations

The moment coefficient (taken about the nose of the projectile) has generally the same shape for all investigated Mach numbers as shown in Fig. 3: a nose-down moment exists at low values for h/d, followed by a range of ground clearances where the moment is positive (nose-up) until the moment coefficient approaches the free-flight value of zero. Combining the moment and lift data as seen in Fig. 3, one can identify four possible lift/moment configurations that may be experienced by a projectile in ground effect: negative lift and nose-down moment (labelled as region A), positive lift and nose-down moment (region B), and positive lift and nose-up moment (region C), followed eventually by the free-flight regime where lift and moment coefficient return to zero. The results indicate that the range of ground clearances associate with configurations A and B shrink with increasing Mach number, until eventually, for $M_\infty = 1.5$, configuration A is not observed any more.

Bow-Shock and Stand-Off Distance

The curves presented in Fig. 4 depict the strong dependency between shock stand-off ratio, SD/d, and the ground clearance, h/d, particularly for lower Mach numbers. The values for $M_\infty = 1.2$–1.4 are presented with the same scale to highlight both the magnitude of increase of SD/d and the size of the region that is affected by the ground plane. It is obvious that already at $M_\infty = 1.3$, the stand-off distance is only marginally affected by the ground—at $h/d \leq 1.5$, SD/h is only 4 % larger than the free-flight value. For $M_\infty = 1.1$ and 1.2, on the other hand, the maximum differences amount to 68 % and 26 %, respectively. Experimental values (obtained from the schlieren records) are higher than the numerical ones, which is attributed to a blockage effect not fully accounted for in the simulation. The value of SD/d is mainly influenced by the vertical extent of the volume occupied by the subsonic zone.

Summary and Conclusions

A range of ground clearances and Mach numbers was investigated to determine the qualitative and quantitative influence of the ground effect once a projectile travels within close proximity of a solid plane. Experimental data were in good agreement with numerical predictions. The following main results were obtained:

- For each investigated Mach number there always exists a certain range of ground clearances h/d at which the

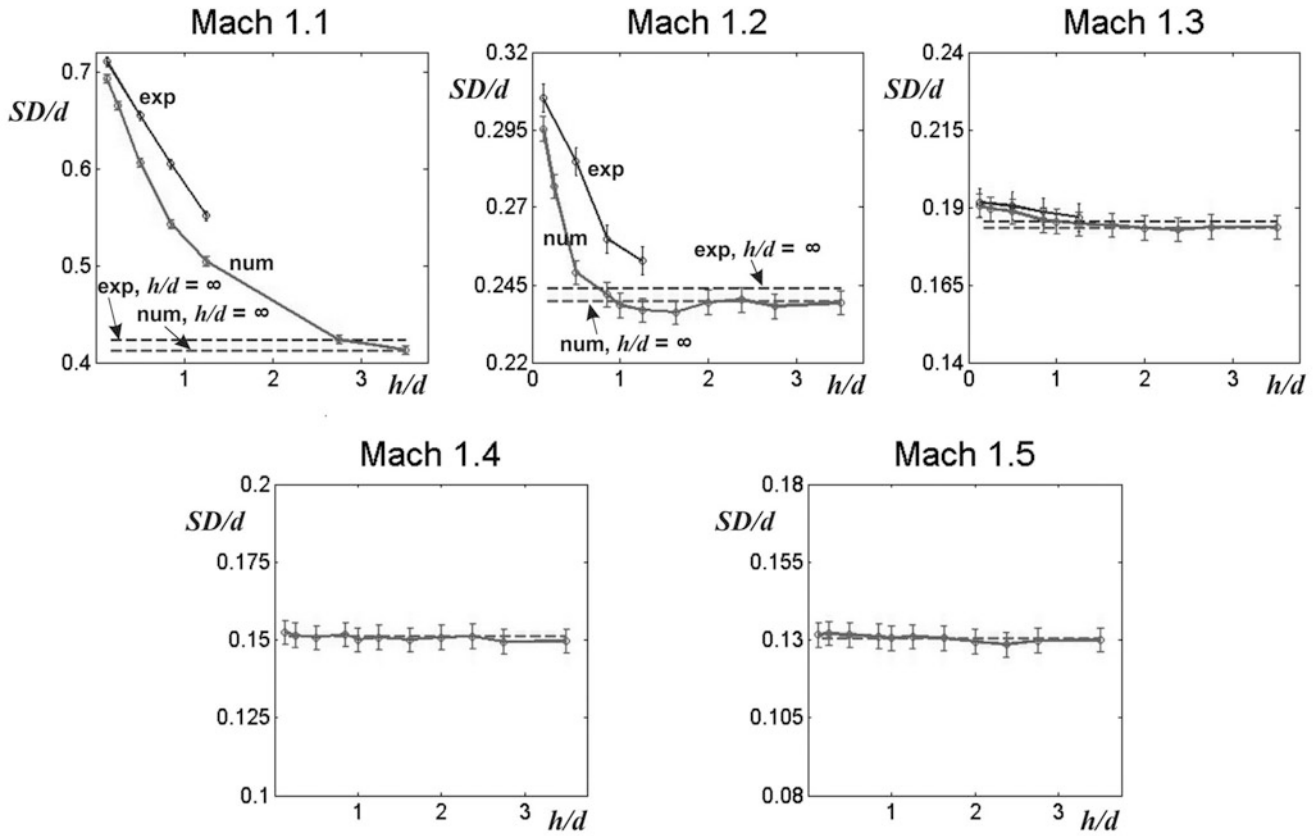

Fig. 4 Stand-off distance *SD* as function of Mach number and ground clearance. No experimental data currently exist for $M_\infty = 1.4$ and 1.5.

ground plane induces a positive lift force on the projectile.

- Suction forces are only observed for small ground clearances, and the larger the Mach number becomes, the smaller the ground clearance must be to generate a force directed towards the ground.
- For the chosen projectile, suction no longer exists once $M_\infty = 1.5$.
- The magnitude of the ground effect-generated positive lift increases with Mach number, but the range of ground clearances over which such lift is experienced decreases if M_∞ is increased.
- Variations in drag also occur, and a drag peak is observed at low clearances, but it becomes less appreciable as the Mach number is increased.
- The non-linear behavior of the wake being pulled towards and deflected away from the ground is seen to be a significant contributor to the drag as the recirculation zones in the near-base region deflect and distort the wake.
- One can distinguish three different lift/moment configurations while the projectile is in ground effect: Configuration A (suction, pitch nose up), typically seen at low ground clearances, B (lift, pitch nose up) at intermediate ground clearances, and C (lift, pitch nose down) at large ground clearances.
- The values of h/d at which the configurations change from one to another decrease as the Mach number increases, to the extent that for $M_\infty = 1.5$, configuration A is no longer seen, with B similarly reducing in size when M_∞ is increased.
- The non-dimensional bow shock stand-off distance SD/d increases as much as 68 % (compared to the stand-off distance of the single free-flight projectile with $h/d = \infty$) for $M_\infty = 1.1$, but this increase reduces to 4 % for $M_\infty = 1.3$ and essentially disappears for higher Mach numbers. This process is largely driven by the subsonic zone that occupies the volume surrounding the blunt nose and ogive forebody. The vertical extent of this zone reduces with increasing Mach number such that it can no longer interact with the ground plane. While such an interaction occurs the subsonic zone pushes the bow shock forward.
- The subsonic zone strongly influences the shock reflection pattern. A shock bending that avoids the formation of a reflected wave can occur for $M_\infty < 1.4$. A Mach reflection pattern is observed for a relatively narrow region of

Mach number/ground clearance combinations, while at high distances and high Mach numbers, a regular reflection pattern can be seen.

References

1. Doig, G., Barber, T.J., Leonardi, E., Neely, A.J., Kleine, H.: Aerodynamics of a supersonic projectile in proximity to a solid surface. AIAA J. **48**(12), 2916–2930 (2010)
2. Kleine, H., Young J., Oakes B., Hiraki K., Kusano H., Inatani Y.: Aerodynamic ground effect for transonic projectiles. In: Proceedings of the 28th International Symposium on Shock Waves, vol. 2, pp. 519–524. Springer, Manchester (2012). ISBN 978-3-642-25684-4
3. Carriage, K., Young, J., Kleine, H., Hiraki, K.: Reynolds-Averaged Navier-Stokes Computation of Transonic Projectiles in Ground Effect. In: Proceedings of 18th Australasian Fluid Mechanics Conference, Launceston, Australia, 3–7 Dec 2012. ISBN 978-0-646-58373-0
4. Weinacht, P.: Validation and prediction of the effect of rifling grooves on small-caliber ammunition performance. AIAA paper AIAA 2006-6010 (2006)
5. Shih, T., Liou, W.W., Shabbir, A., Yang, Z., Zhu, J.: A new k-ε eddy viscosity model for high Reynolds number turbulent flows—model development and validation. Comput. Fluids **24**(3), 227–238 (1995)
6. Sheridan, C.: A computational analysis of ground effect influence on a transonic/supersonic projectile. Bachelor of Engineering Thesis, School of Engineering and IT, UNSW Canberra (2014)
7. Doig, G., Barber, T., Leonardi, E., Neely, A., Kleine, H.: Methods for investigating supersonic ground effect in a blowdown wind tunnel. Shock Waves **18**(2), 155–159 (2008)

The Influence of Concave Wedge Tips on Shock Reflection Patterns

Harald Kleine, Federico Alzamori Previtali, and Evgeny Timofeev

Introduction

The subject of this chapter is a combined, numerical and experimental, inquiry on a recently discovered shock reflection phenomenon, namely the dependence of the eventually established reflection pattern on the geometry of the initial portion of the reflecting surface, even if this initial portion comprises only a small part of the reflector. More specifically, it was demonstrated recently [1] in numerical simulations of shock wave reflection from wedges that the resulting reflection pattern may be of regular or irregular type for the same wedge angle, incident shock Mach number, and ratio of specific heats, depending on whether the tip of the reflecting wedge is straight or initially curved. Subsequent numerical studies [2] pointed to an interesting possibility that even a minuscule tip could possibly be the cause of differing reflection patterns, see Fig. 1. In this chapter, parametric numerical studies of the phenomenon are carried out with the goal of explaining it and establishing the range of flow and geometrical parameters in which the effect takes place. Furthermore, it is attempted to obtain the first experimental demonstration of the influence of the wedge tip on the resulting reflection pattern.

Research Tools

The simulations are performed with the Euler (inviscid, non-heat-conducting) model by an adaptive unstructured second-order finite-volume flow solver [3]. The gas is assumed to be ideal with constant specific heats. The computational domain ABCDEF and the initial position of the incident shock are shown in Fig. 2. The concave tip formed by a cylindrical surface with the radius R is introduced for a given wedge angle θ_w so that the line corresponding to the straight portion of the wedge comes to the point of origin. In the *inviscid* flow model, all results are scalable with the radius of curvature R, and therefore all angular values are independent of R. In case a Mach reflection is present in the flowfield, the location of its triple point is characterized by the so-called triple point angle χ as shown in Fig. 2.

The domain is discretized with an unstructured background mesh composed of triangular elements and having an average grid spacing of $\Delta L = 0.33R$. Transient grid refinement/coarsening is applied in the course of computations, with the grid spacing being locally reduced by two times when one grid refinement level is added.

This amounts, for example, to the minimum grid spacing of $\approx 0.00125R$ with 8 levels of refinement (the total number of nodes exceeds 500,000 at the end of a computational run in this case).

The numerical results presented in the next section are obtained with the number of grid refinement levels ranging from 5 to 8, as it is dictated by preliminary grid convergence studies (the smaller the angle χ is, the finer meshes are required). For both straight and curved tip wedges it is found that, with the shock propagation along the wedge, the triple point angle converges to a constant value. This very important observation serves as the evidence that the triple point trajectory asymptotically approaches the straight line originating from the origin (0, 0). This fact is not self-evident for wedges with a rounded tip.

The experimental arrangement and diagnostics are largely similar to the ones described in [4]. All experiments are conducted with air as test gas (at ambient temperature in the range from 290 to 293 K) in a conventional shock tube with rectangular cross section (150 mm high, 75 mm wide). The length of the wedge (along its surface) is 170 mm. In the

H. Kleine (✉)
SEIT, University of New South Wales, Canberra, ACT, Australia
e-mail: h.kleine@adfa.edu.au

F.A. Previtali • E. Timofeev
Mechanical Engineering, McGill University, Montreal, QC, Canada
e-mail: evgeny.timofeev@mcgill.ca

G. Ben-Dor et al. (eds.), *30th International Symposium on Shock Waves 1*, DOI 10.1007/978-3-319-46213-4_110

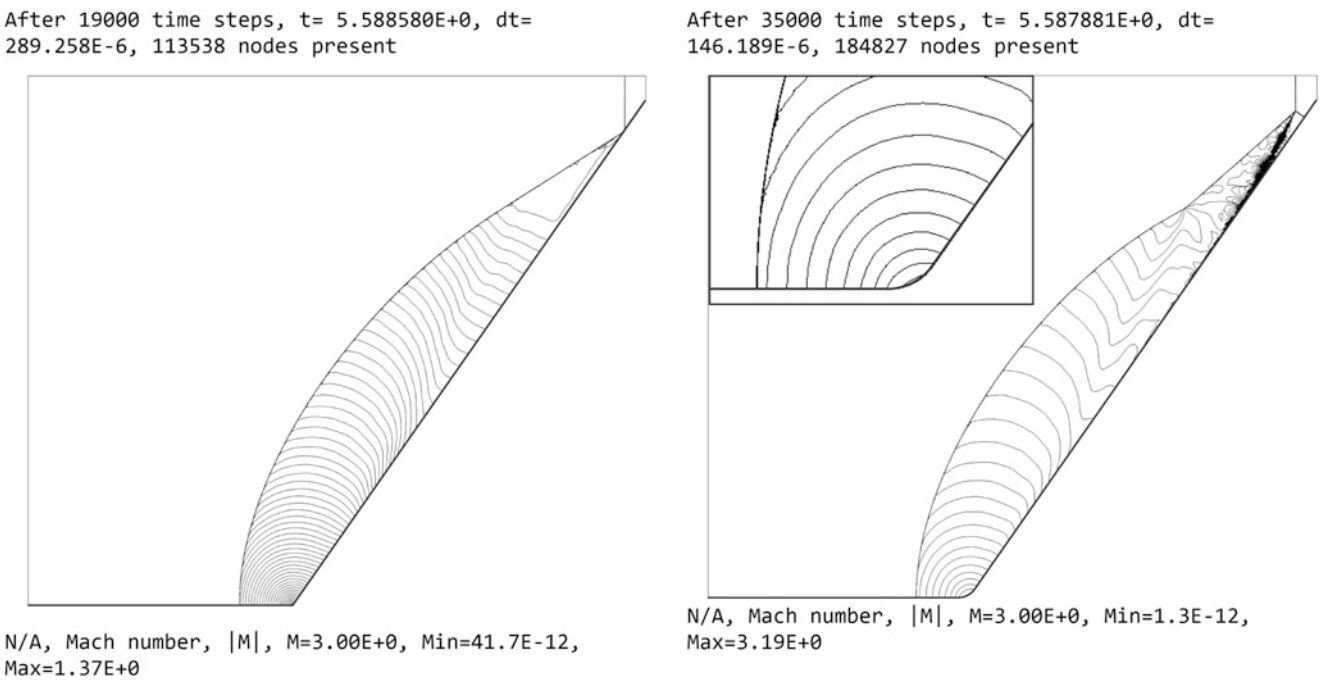

Fig. 1 The reflection of a $M_s = 3$ incident shock from a 55° wedge ($\gamma = 1.4$). *Left*: straight wedge; *right*: straight wedge with a concave circular tip (insert shows magnified view of curved inlet)

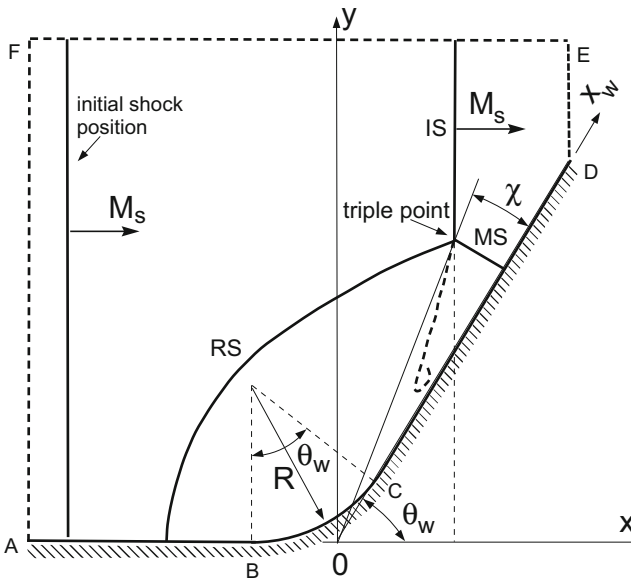

Fig. 2 Schematics of the computational domain ABCDEF and relevant angles. The initial shock position and a developed Mach reflection pattern for a concave-tip wedge are shown: *IS* incident shock, *RS* reflected shock, *MS* mach stem

experiments presented in this chapter the radius R of the concave tip is equal to 12 mm. Different initial pressures in the test section, ranging from 3.7 to 16 kPa, are used to obtain desirable shock Mach numbers M_s, which are determined from time-of-arrival data obtained by means of three KISTLER pressure transducers. The driver gas is helium. A high-speed video camera (Shimadzu HPV-1; 10^6 frames per second; exposure time of 250 ns; resolution 312 × 260 pixels) provides time-resolved shadowgraph or schlieren visualization.

Results and Discussion

We consider a range of moderate shock Mach numbers, namely $M = 1.5$, 2.0, 2.5, and 3.0, for the specific heat ratio of 1.4. For each Mach number a range of wedge angles is considered, and for each selected angle computations for the straight and concave-tip geometries are conducted. Typical results of such parametric studies are shown in Fig. 3 for $M_s = 1.5$ and 2.5. If for the straight tip case the angle χ is shown to be zero, it means that only regular reflection is observed with these parameters. If the angle χ is shown to be zero for the concave tip case, it means that for these parameters the Mach reflection induced by the concave part of the reflecting surface eventually undergoes transition to the transitioned regular reflection (TRR) [5].

The following conclusions can be drawn from the numerical results: (1) For the straight tip wedges, the transition from Mach to regular reflection occurs very close to the detachment/sonic point for all Mach numbers considered; (2) For the concave tip wedges and $M_s = 2.0$, 2.5, and 3.0, Mach reflection is observed well beyond the sonic point (Fig. 3b). The triple point angle decreases with the increase of the wedge angles and eventually transition to TRR takes

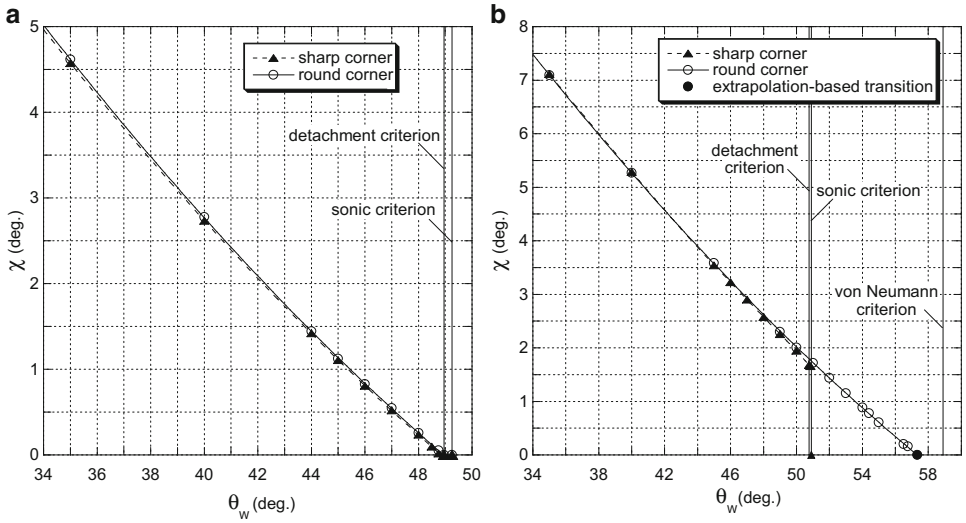

Fig. 3 Results of numerical experiments for (**a**) $M_s = 1.5$ and (**b**) $M_s = 2.5$. The triple point angle X (see Fig. 2) is shown vs. the wedge angle θ_w for wedges with straight and round (concave) tips. For the sake of clarity and the ease of application of the extrapolation technique, the results with zero triple point angles are not shown in Fig. 3b for concave tip wedges

place at the wedge angles rather close but not identical to the von Neumann angle. To obtain the transition angle, a quadratic fit is applied to the concave tip points, and it is *assumed* that the transition point can be obtained by extrapolation to zero triple point angle (see the solid circle in Fig. 3b). It appears from the results that gradual disappearance of the Mach stem takes place at the MR → TRR transition, as opposed to the abrupt change of the Mach stem height from a finite value to zero in the MRMR → RR transition for straight tip wedges (see Fig. 3b); (3) In view of all the above it becomes clear that for $M = 2.0$, 2.5, and 3.0 there is a relatively wide range of wedge angles for which the resulting reflection pattern differs depending on the wedge tip geometry; sharp wedges produce regular reflection while rounded ones result in Mach reflection. However, for $M_s = 1.5$ (see Fig. 3a) the results are the same for both wedge tip geometries: the transition occurs near the detachment/sonic point; (4) For wedge angles below the detachment/sonic point, both wedge tip geometries produce a Mach reflection and the triple point angle appears to be very close for straight and concave wedge tips.

Further insight into the phenomenon can be obtained by plotting the transition points described above on the shock Mach number/wall angle diagram together with the sonic, detachment, and von Neumann lines, see Fig. 4. It becomes clear that the effect of having differing reflection patterns for straight and concave wedge tips is confined to the dual solution domain where both regular and Mach reflection are physically admissible. For straight tip wedges, as soon as the wedge angle exceeds the sonic angle, the comer signal cannot catch up with the reflection point anymore, and regular reflection takes place. In the process of shock reflection from a concave wedge tip, Mach reflection is *always* induced at the initial stages of the process. If the wedge angle is within the dual solution domain, the initially induced Mach reflection does not have to revert to regular reflection and it may remain in place. It would be logical to assume that, similarly to the straight tip case, the transition (MR → TRR) should happen when the comer signal is no longer able to catch up with the reflection configuration and gets separated from it, see also [5]. As it is clear from Fig. 4, this occurs rather close to the von Neumann point.

The above numerical results are obtained for the *inviscid* flow model, i.e., for high Reynolds numbers. However, the Reynolds number based on the abovementioned pressure value and radius of curvature is as low as ∼30, 000. The boundary layer growth may have a significant influence, and the effect of interest should be observed, as argued in [6], at lower wedge angles. Furthermore, as it was found in our numerical simulations, the size of Mach stem decreases with the increase of the wedge angle, which may lead to difficulties with its detection via optical imaging since the length of the wedge is limited by the size of the test section. In view of the above circumstances, it is decided to conduct experimental tests for the wedge angle of $\theta_w = 52°$, which is still within the dual solution domain provided by the inviscid two/three shock theory but closer to the lower boundary of the angle range in which the effect of interest takes place.

For $\theta_w = 52°$ many experimental trials were performed for shock Mach numbers from 2.25 to 3.30. All results are found to be consistent: for the wedge with a straight tip, regular reflection was always observed while the addition of the concave tip with $R = 12$ mm invariably led to the resulting Mach reflection. A typical example is shown in Fig. 5 where the only difference between the respective experiments is the presence of a concave tip in the experiment shown in Fig. 5a. The inspection of the preceding movie frames of this experiment confirms that the Mach stem is clearly growing in this field of view and there is no

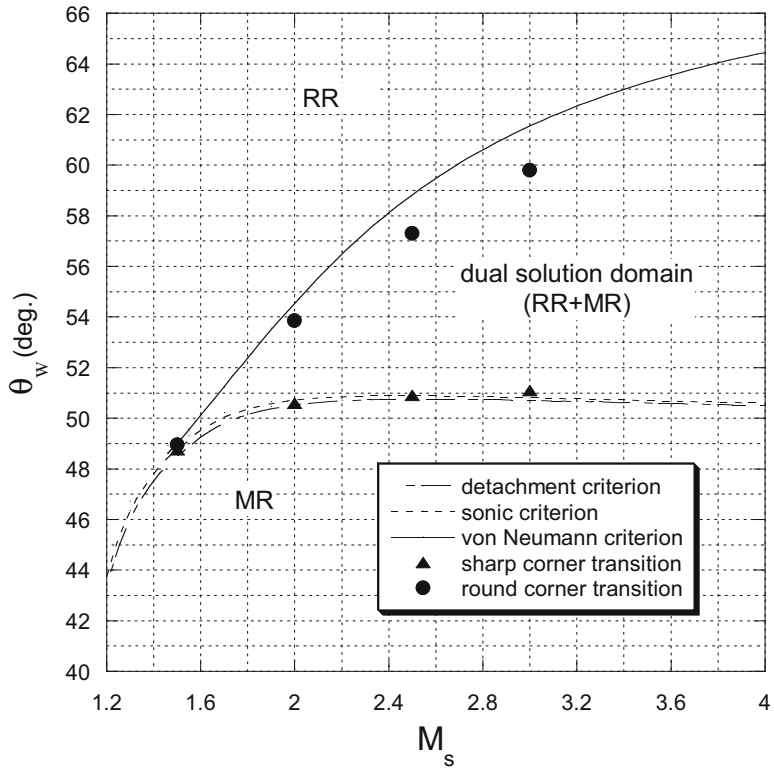

Fig. 4 Incident shock Mach number—wedge angle diagram. The *lines* correspond to the three major transition criteria: sonic, detachment, and von Neumann (for $\gamma = 1.4$) while the symbols designate transition points obtained from numerical simulations. For the MR → TRR transition on the concave tip wedges extrapolation-based values are shown as *solid circles* similarly to Fig. 3b

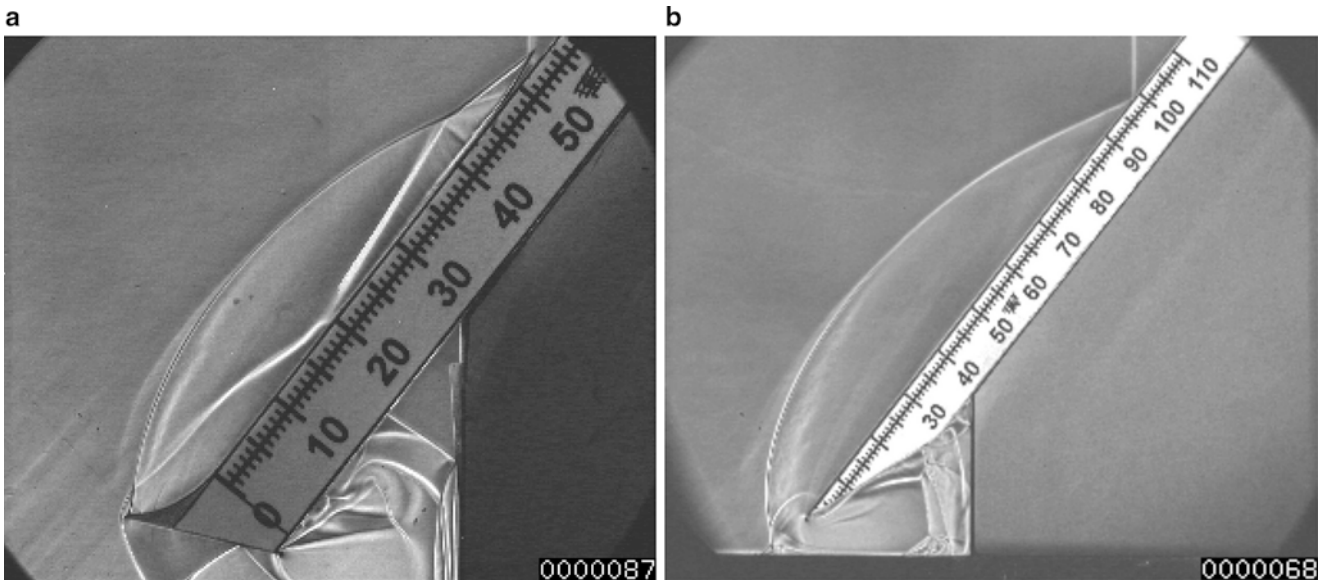

Fig. 5 Experimental schlieren images *for* $M_s = 2.88$ and $B_w = 52°$: (**a**) concave tip; (**b**) straight tip. The scale on the wedges indicates length in millimeters

reason to believe that this behavior changes for larger distances. This is also supported by another experiment with a very close shock Mach number of 2.93 (see [6]) in which the field of view is much wider. It was demonstrated clearly, for a Mach number of 2.87 nearly identical to that in Fig. 5b and using a narrower field of view with higher magnification, that in the case of the straight tip regular reflection is maintained for the entire length of the wedge in the test section, see the image in [6]. Analogous results exist for Mach numbers as low as $M_s = 2.25$ (see [6]). At the time of writing, there is also limited evidence that the same effect is observed for smaller values of R (4 mm).

Conclusions

In this chapter, unsteady shock wave reflections from wedges having straight and concave tips are studied numerically and experimentally. The two most important results of the study are as follows. It is shown that the presence of a curved, concave tip influences the reflection outcome only if the wedge angle is within a certain range, which is, for a given shock Mach number, almost as wide as the dual solution domain where both regular and irregular (Mach) reflections are physically admissible. The second major outcome is the first confirmation that the influence of the wedge tip type described above can, indeed, be observed experimentally.

Acknowledgments The study is supported by the NSERC Discovery grant 2014-05427 and the FQRNT Team grant 172458. One of the authors (F.A.P.) is the recipient of SURE (Summer Under graduate Research in Engineering) award funded in part by the McGill's Faculty of Engineering. Dr. R. Tahir's advise and support regarding Masterix is greatly appreciated.

References

1. Lau-Chapdelaine, S.S., Radulescu, M.I.: Non-uniqueness of solutions in asymptotically self-similar shock reflections. Shock Waves **23**(6), 595–602 (2013)
2. Alzamora Previtali, F., Timofeev, E.: On shock reflection from the straight wedges with circular concave tips. In: Podlaskin A., Krasovskaya I. (eds.) Book of Proceedings of 21st International Shock Interaction Symposium, August 3–8, 2014, University of Latvia, Riga, p. 236.
3. Masterix-2D, multiblock, multi-gas, adaptive, unstructured mesh, unsteady and steadystate, CFD software. Ver. 3.40.0.3018, RBT Consultants, Toronto, 2010–2013
4. Kleine, H., Timofeev, E., Hakkaki-Fard, A., Skews, B.: The influence of Reynolds number on the triple point trajectories at shock reflection off cylindrical surfaces. J. Fluid Mech. **740**, 47–60 (2014)
5. Ben-Dor, G.: Shock wave reflection phenomena, 2nd edn. Springer, New York (2007)
6. Alzamora Previtali, F., Timofeev, E., Kleine, H.: On unsteady shock wave reflections from wedges with straight and concave tips. AIAA Paper 2015-2642

Shock Tunnel Studies on Shock–Shock Interaction

Abhishek Khatta and Gopalan Jagadeesh

Introduction and Motivation

The interaction of a Shockwave with another Shockwave is an unavoidable phenomenon in high speed flows. These interactions may lead to high pressure and thermal loads on the surface in the vicinity, deteriorates the aerodynamic performance of the system if present internally, and may also lead to the un-start of Scramjet engine due to presence of the subsonic flow downstream of the interaction point. Edney [1] identified and classified these interactions into six different types using a blunt body in a Hypersonic Wind Tunnel. This phenomenon has motivated many research groups to study them and try to figure out the critical conditions for the pressure and thermal loads. Wieting and Holden [2] experimentally studied the shockwave interference heating on a cylinder at Mach 6 and Mach 8. Sanderson, Hornung, and Sturtevant [3] studied the interacting shockwaves in dissociating gas.

Most important feature of these interactions is the increase in the pressure and heat flux on the nearby surface, where the waves after the interaction meet the surface. Though much effort has been put both experimentally and computationally into the understanding of these interactions, only few groups lead the study in short duration facilities, where high enthalpy flows can be generated.

For the present work, the Hypersonic Shock Tunnel–2 (HST-2), at Laboratory of Hypersonic and Shock wave Research (LHSR), Indian Institute of Science, is used to generate a flow of Mach 5.64, obtained by the straight-through mode operation of the tunnel. Here, a wedge is used to generate a planar shock wave, which is allowed to interact with a bow shock formed in front of a hemispherical body. The model assembly is designed in such a way that keeping the hemispherical body fixed, the wedge can be moved, thereby changing the distance between the wedge tip and nose of hemispherical body. Different location of the wedge relative to the hemispherical body leads to the change in location on bow shock where the planar shock interacts with it. Thus, by changing the relative location of the wedge with respect to the hemispherical body makes the interaction point to move along the trajectory of the bow shock from a low subsonic region of the bow shock to the near normal region of the bow shock near the nose region. This leads to the formation of different interaction patterns which were classified by B. Edney [1] as Type I, Type-II, Type-III, Type-IV, Type-V, and Type VI. Present investigation aims at mapping the heat transfer rates and pressure distribution on the surface of hemispherical body in the presence of a planar oblique shock wave.

For all the experiments reported here, air is used as the test gas at 1.06 MJ/kg of total enthalpy at the following test conditions using HST-2.

Models are fabricated to allow the housing of Platinum thin film heat transfer gauges, along the centerline of the hemispherical body. The photographs of the model and the heat transfer gauges are shown in Figs. 1 and 2, respectively. Along with the Platinum Thin Film gauges, Kulite pressure transducers were mounted at discrete locations to map the time history of surface pressure on the hemispherical body. A schematic of the model assembly showing the dimensions of the model is shown in Fig. 3.

Simultaneous flow visualization, using schlieren technique, was done to understand and characterize different interaction patterns and the corresponding relation to the measured heat transfer rates and pressure distribution along the surface of the hemispherical body.

A. Khatta (✉) • G. Jagadeesh
Department of Aerospace Engineering, Indian Institute of Science, Bangalore 560012, India
e-mail: aabhi.ak@gmail.com

G. Ben-Dor et al. (eds.), *30th International Symposium on Shock Waves 1*, DOI 10.1007/978-3-319-46213-4_111

Table 1 Typical freestream conditions in HST2

Flow Mach no.	Pressure (kPa)	Temperature (K)	Density (kg/m^3)	Unit Reynold's No. (/m)
5.64	1.86	143.59	0.0508	6.98×10^6

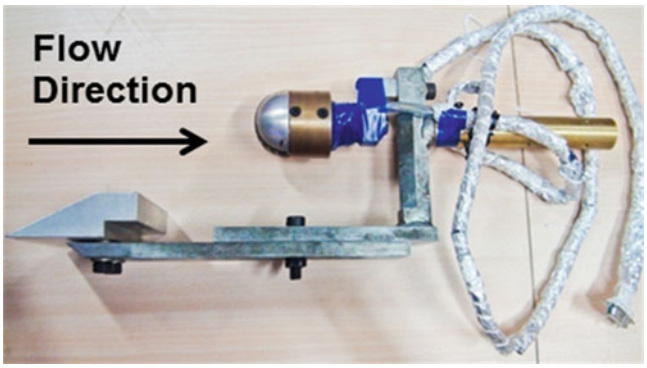

Fig. 1 Complete model assembly

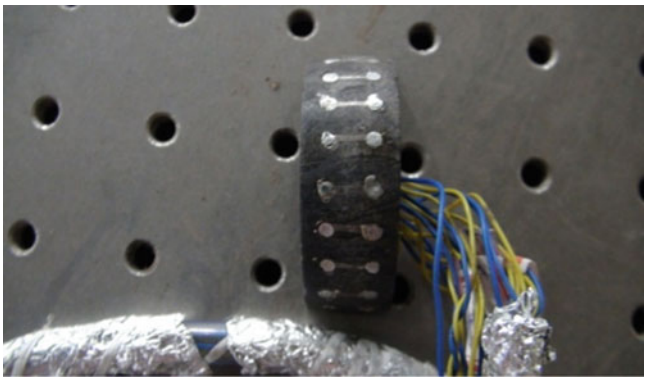

Fig. 2 Macor substrate with platinum thin film gauges on the surface

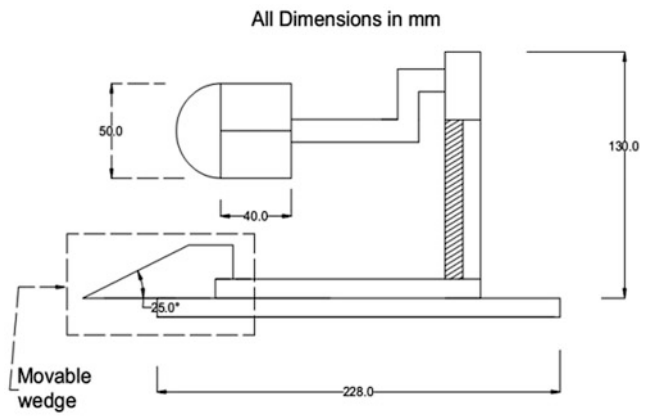

Fig. 3 Schematic drawing of model assembly

Results and Discussions

As the wedge is moved to provide different interaction point of the planar shock on the bow shock wave trajectory, the resulting interaction patterns are accompanied by different pressure distribution and heat transfer distribution on the surface. The different interaction patterns which were so obtained were identified through schlieren visualization and corresponding convective heat transfer distribution and pressure distribution on the surface were analyzed to throw light on the reasons for difference in measurements for different interactions.

One PCB Piezoelectronics pressure transducer was mounted at the nose point of the hemispherical body. Two Kulite pressure transducers were mounted, at 75° off from the nose with center of hemisphere as the reference. Sensor located close to the wedge is given the location −75°, while sensor located farther away from the wedge is given the location +75°.

TYPE-I Interaction

This type of interaction is obtained when the oblique shock interacts with the bow shock far away from the nose, such that the two shock waves are of different families and intensities of the impinging shock waves are almost same, the simplest type of interaction appears. Since the interaction happens outside the sonic region, the shock stand-off distance is unaltered when compared to the undisturbed case.

Pressure data obtained in TYPE-I interaction is taken as reference and all pressure values are normalized using the nose point surface pressure obtained in TYPE-I interaction. Figure 4a shows the normalized surface pressure distribution for TYPE-I interaction, where at vertical axis P_SI stands for measured pressure in presence of shock interaction and P__UD stands for measured pressure at nose point for TYPE-I interaction.

It can be seen from Fig. 1 that both pressure distribution and heat transfer distribution on the surface are having symmetrical distribution owing to the fact that bow shock around the hemispherical body is symmetrical as seen in the corresponding schlieren image.

TYPE-II Interaction

When the intensity of the bow shock wave increases as we go close to nose point, TYPE-II interaction appears, characterized by a normal shock, separating the oblique

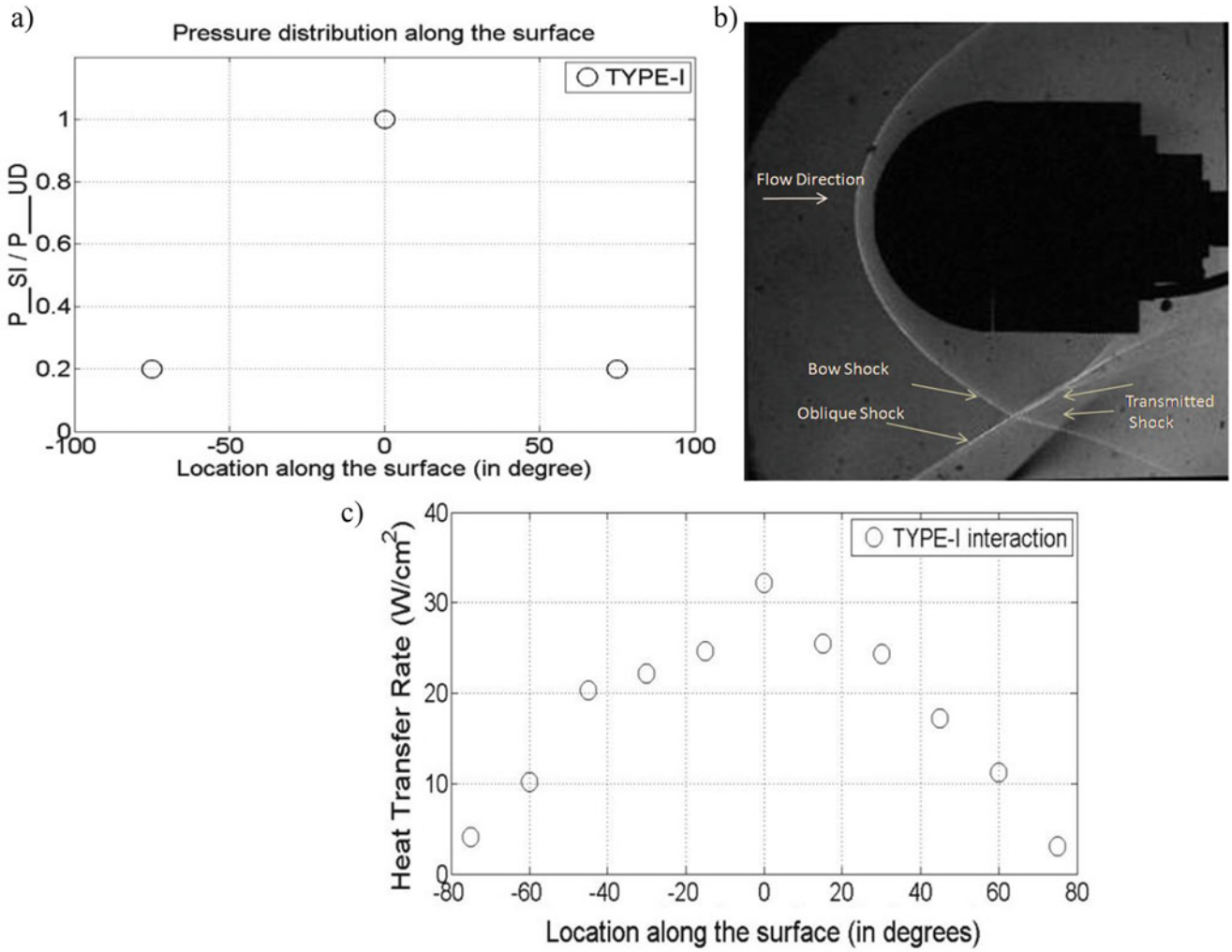

Fig. 4 (**a**) Pressure distribution along the surface of hemispherical body; (**b**) schlieren image showing TYPE-I interaction; (**c**) heat transfer distribution along the surface of hemispherical body

shock wave and bow shock wave. The shape of the shock elsewhere and the shock stand-off distance remains unchanged as the interaction is still far away from sonic line. Two triple points appear in the vicinity of the surface. The transmitted shock from one of the triple points is seen to hit the surface. Figure 5b shows the schlieren image of TYPE-II interaction. The normal shock is clearly seen and enlarged in the inset, where the transmitted shock is also seen to hit the surface of the hemispherical body. From the pressure distribution plot it can be seen that the presence of an additional wave near the bottom half of the hemispherical body tends to rise the surface pressure and destroys the symmetrical distribution. On the other hand, the surface heat transfer distribution is not much changed, and follows the trend of TYPE-I interaction.

TYPE-III Interaction

As the oblique shock impinges on the lower region of sonic circle, a slip line is formed separating the subsonic region behind the bow shock and supersonic region behind the transmitted shock. The slip line hits the body surface, and the presence of supersonic flow below the slip line causes the presence of shock wave off the surface. The shock pattern above the point of interaction is changed, and the bow shock is no more normal to the body surface at the nose point of the body. This is reflected in the surface pressure distribution plot as the normalized pressure at 0° is less when compared with that of TYPE-I interaction. The surface heat transfer distribution is greatly modified and lower half of the model experiences comparatively higher heat transfer rates. The

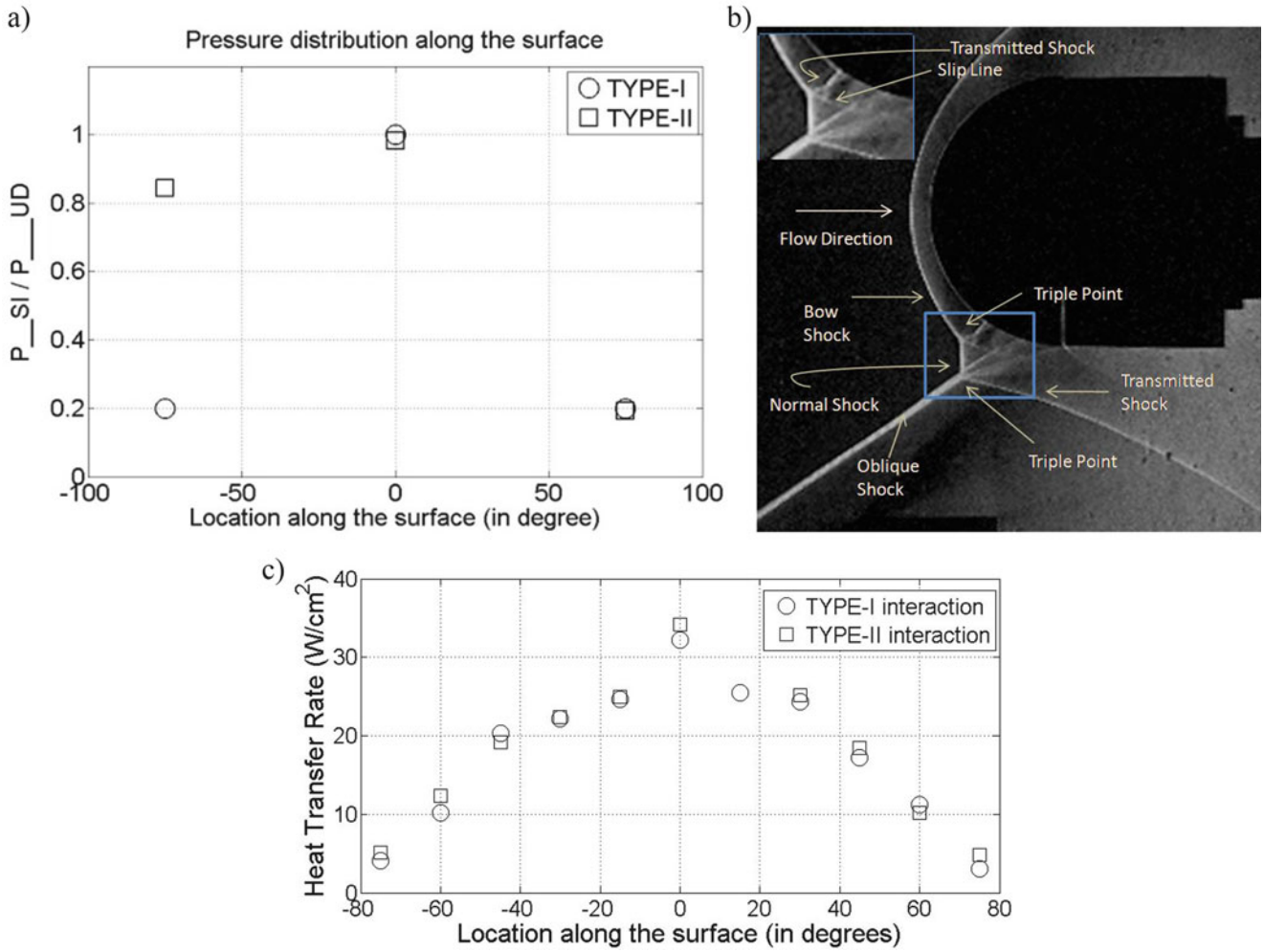

Fig. 5 (**a**) Pressure distribution along the surface of hemispherical body; (**b**) schlieren image showing TYPE-II interaction; (**c**) heat transfer distribution along the surface of hemispherical body

heat transfer rates on the upper half of the body follows the trends of TYPE-I interaction.

Conclusions

Shock–shock interaction studies were carried out in HST-2, at 5.64 Mach and total enthalpy of 1.06 Mj/kg. A hemispherical body of 50 mm diameter, made of aluminum, produced a bow shock when immersed in a hypersonic flow, and a wedge of 25° angle was used to generate planar oblique shock wave, which hits this bow shock. The wedge mounting assembly is made in such a way that the relative distance between the hemispherical body nose and the wedge tip can be changed from run to run. Depending upon the location on bow shock where the oblique shock hits, different interaction patterns are observed. Schlieren visualization was performed to analyze the flow structures generated during different interactions and simultaneously, pressure measurement and convective heat transfer measurement on the surface along the centerline of the hemispherical body was made to correlate with the schlieren images.

It was seen that TYPE-I interaction gives symmetrical distribution of both pressure distribution on the surface and heat transfer distribution on the surface. Since in TYPE-I interaction, the oblique shock wave and the bow shock wave meet far downstream and do not disturb the flow in the vicinity of the hemisphere, the measured values of surface pressure and measure heat transfer rates for all interactions were compared with those of TYPE-I interaction. The presence of additional waves in TYPE-II interaction causes the surface pressure distribution to deviate from symmetrical distribution, but the heat transfer distribution is not much disturbed and follows the trends of TYPE-I interaction. Type-III interaction leads to the change of shock shape above the point of interaction between the oblique shock wave and the bow shock wave, and this leads to the reduction of the surface pressure at the nose point of

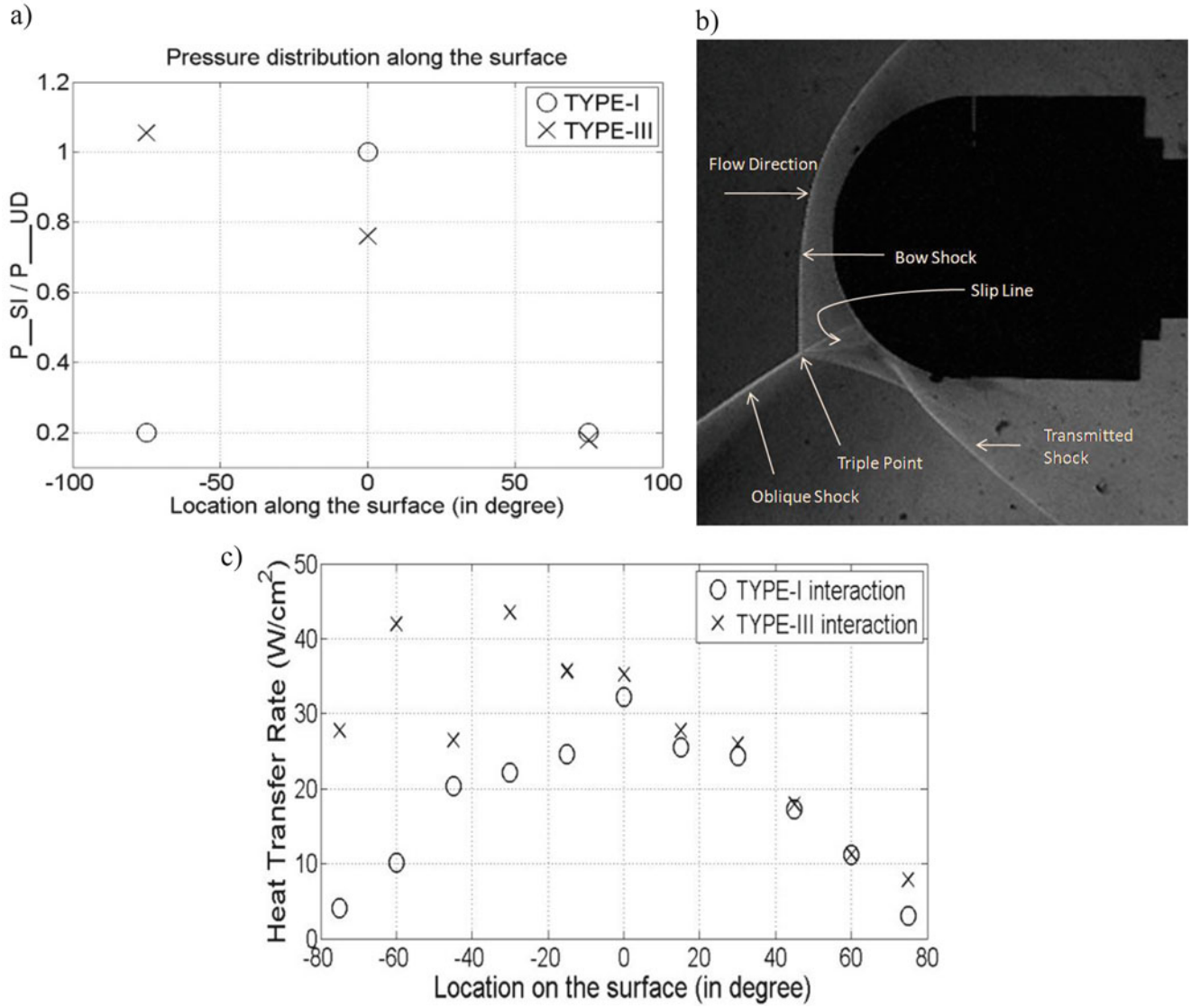

Fig. 6 (**a**) Pressure distribution along the surface of hemispherical body; (**b**) schlieren image showing TYPE-III interaction; (**c**) heat transfer distribution along the surface of hemispherical body

hemispherical body. The measured heat transfer rate on the surface also shows deviation and increase in the values as compared to TYPE-I interaction, at the bottom half of the hemispherical body.

The study and analyses of TYPE-IV, TYPE-V, and TYPE-VI interaction patterns will be presented during the conference.

References

1. Edney, B.: Effects of shock impingement on heat transfer around blunt bodies. AIAA J. **6**(1), 15–21 (1968)
2. Wieting, A.R., Holden, M.S.: Experimental shock-wave interference heating on a cylinder at Mach 6 and Mach 8. AIAA J. **27**, 1557–1565 (1989)
3. Sanderson, S.R., Hornung, H.G., Sturtevant, B.: Aspects of planar, oblique and interacting shock waves in an ideal dissociating gas. Phys. Fluids **15**, 1638–1649 (2003)

A Study on Unsteady Shear Layer–Shock Interaction in a Vacuum Ejector-Diffuser System

R. Arun Kumar and G. Rajesh

Introduction

Ejectors are devices that are used to transport fluids or mix one stream of fluid with another by pure shearing action of the two streams. A conventional ejector system consists of a primary duct which supplies fluid with high momentum to a mixing chamber and the shearing action of the primary jet causes entrainment of secondary fluid into the mixing chamber. These systems find wide applications in engine thrust augmentation, mixing applications, refrigeration facilities, etc. Recently, ejector principle has been used to generate vacuum conditions and such facilities are generally termed as vacuum ejectors. Unlike the conventional ejector system, where a constant supply of secondary fluid is maintained, a vacuum ejector system draws secondary stream from a closed chamber, thereby creating a vacuum condition at secondary chamber. These systems are primarily used to create controlled vacuum exit conditions in high altitude testing (HAT) of rocket engines.

Most of the previous researches on vacuum ejectors were focused on the level of vacuum attained inside the secondary chamber and the flow field after the establishment of steady state with vacuum secondary conditions [1–3]. Kim et al. [4] performed an experimental investigation on the transient effects in ejector and found out that the initial secondary chamber pressure drops and settles to a lower steady value in due time. Later, Lijo et al. [5] reported that the establishment of a steady state as observed by Lee is owing to the formation of a dynamic pressure equilibrium condition in the mixing chamber. A recent numerical study by Ankit et al. [6] on vacuum ejectors reported that the initial process of induction of air from the vacuum or secondary chamber using the primary jet is extremely transient owing to the formation of a highly dynamic separation bubble in the mixing section. They also observed that during this transient regime of the ejector flows, repeated flow reversals are also observed and corresponding oscillations in the flow properties are attributed to the extension and retraction of the separation bubble produced by the primary jet shock wave, into the secondary chamber. Numerical study by Manikanda et al. [7] reported that the secondary chamber vacuum level increases with increase in primary jet mass flow rate till the ejector is in un-started mode [8]. As the ejector turns into started mode, the secondary chamber vacuum level decreases with increase in primary jet mass flow rate.

Even though a fair understanding on the steady state vacuum ejector operation has been achieved through many previous researches, the flow evolution during the transient starting state is not well understood. The present experimental know how to substantiate some of the past numerical investigations on the starting transients in vacuum ejectors are also in sufficient. The current work aims at an experimental investigation on the transient flow field in the vacuum ejector-diffusers system with a focus on many interesting and unexplored phenomena such as shock wave unsteadiness due to the secondary flow transients, unsteady shock–shear layer interactions and shock structure transformation.

The experimental setup for the current study consists of a primary duct (sonic nozzle), a secondary chamber and a mixing chamber/straight exhaust diffuser as shown in Fig. 1. Initially, a symmetric model for all the components was used. Later, full model experiments were also carried out. The starting of vacuum ejectors was carried out by suddenly opening the primary nozzle inlet valve until the primary jet total pressure reaches 5 bar absolute with secondary inlet closed. For the primary jet, a total pressure of 5 bar was chosen since a series of initial schlieren experiments revealed that the ejector will operate at started condition for this pressure.

R.A. Kumar • G. Rajesh (✉)
Indian Institute of Technology Madras (IITM), Chennai, Tamil Nadu, India
e-mail: rajesh@ae.iitm.ac.in

G. Ben-Dor et al. (eds.), *30th International Symposium on Shock Waves 1*, DOI 10.1007/978-3-319-46213-4_112

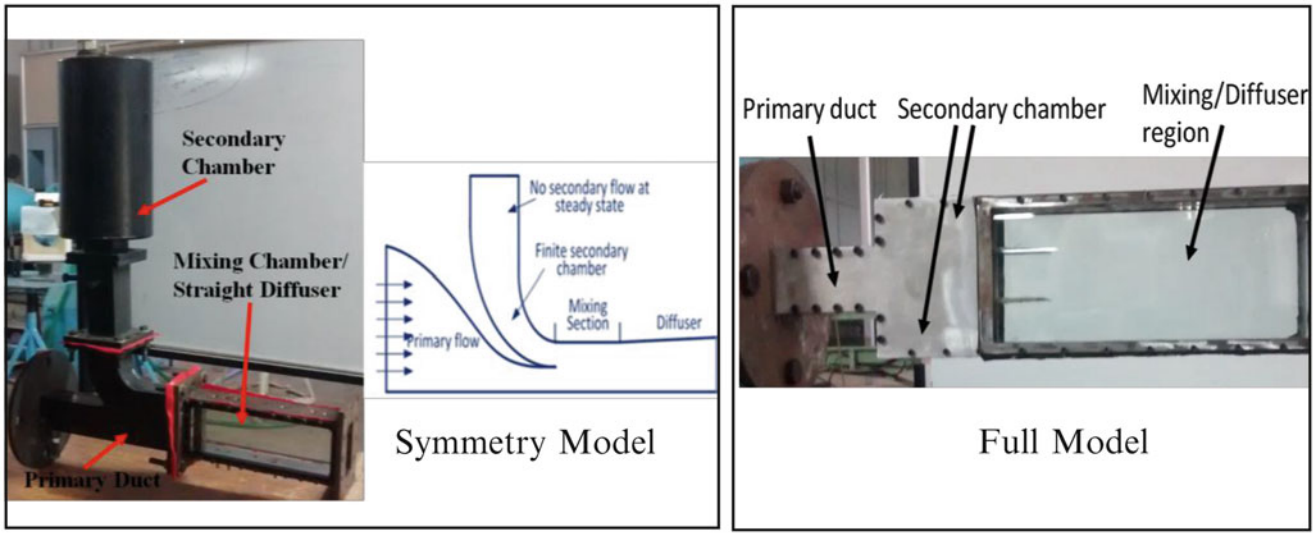

Fig. 1 Vacuum ejector experimental models

The current experimental investigation consists of flow visualization of mixing chamber and static pressure measurement in the secondary/vacuum chamber. Flow visualization was carried out by capturing the density gradients in the transient flow field using high-speed schlieren imaging. A z-type schlieren system was used with image captured using Photron Fastcam SA4 high-speed camera. Piezo resistive transmitters (Keller) were used to measure the pressure fluctuations in the secondary chamber.

Results

Flow characteristics and shock structure evolution in a symmetric vacuum ejector system is shown in Fig. 2. From Fig. 2b it can be observed that as the primary jet valve opening progresses an oblique shock wave is formed at downstream of the under expanded primary jet. The primary reason for the existence of this shock wave is to match the jet exit pressure with the ambient. It is interesting to note that this oblique shock wave neither penetrates nor reflects as expansion waves from the shear layer rather it reflects as shock wave itself from the shear layer. The nonexistence of shock wave penetration into the secondary region suggests that the secondary region is still subsonic. As the primary valve opening process continues, the primary jet expands further increasing the vacuum level at secondary chamber. This process eventually leads to hitting of shear layer on the diffuser wall causing the diffuser to operate at started condition [8]. The shear layer after hitting the wall forms a mixed region where the secondary stream and primary stream are indistinguishable. Further expansion of primary jet due to the continuous reduction in mixing chamber pressure (due to the secondary mass entrainment into the primary) makes the mixed region supersonic and as this process continues, the regular reflection of the shock wave transforms into a Mach reflection with Mach stem penetrating into the mixed region. This Mach reflection can be visualized from the schlieren picture shown in Fig. 2d. The existence of Mach disc in the mixed region shows that a supersonic regime is established in the mixed region and the flow is chocked at some upstream location.

Schlieren pictures showed in Fig. 2b–e reveal that as the shear layer interacts with the wall, the shock structure in the mixing chamber starts oscillating. During the shock oscillation period, the upstream movement of shock structure shows a reduction in Mach disc strength while the downstream movement increases the Mach disc strength, which can be qualitatively observed from Schlieren pictures in Fig. 2c, d, respectively. This phenomenon may be due to the fact that the mixed region behaves similar to the divergent portion of a supersonic nozzle with upstream side pressure (towards the throat) higher compared to downstream and when the shock is located at downstream position a more stronger shock wave is required for pressure matching compared to the upstream position of the shock.

The cause for the shock oscillations were further investigated by comparing the schlieren pictures and the static pressure variations in the secondary chamber at different times. For the current experiment, the schlieren imaging was started at the instant when the primary jet valve was opened (starting of vacuum ejector) while pressure data acquisition was started much earlier than the starting of vacuum ejector. As soon as the primary jet emanates into the mixing chamber, shearing action causes entrainment of secondary jet and the secondary chamber pressure reduces

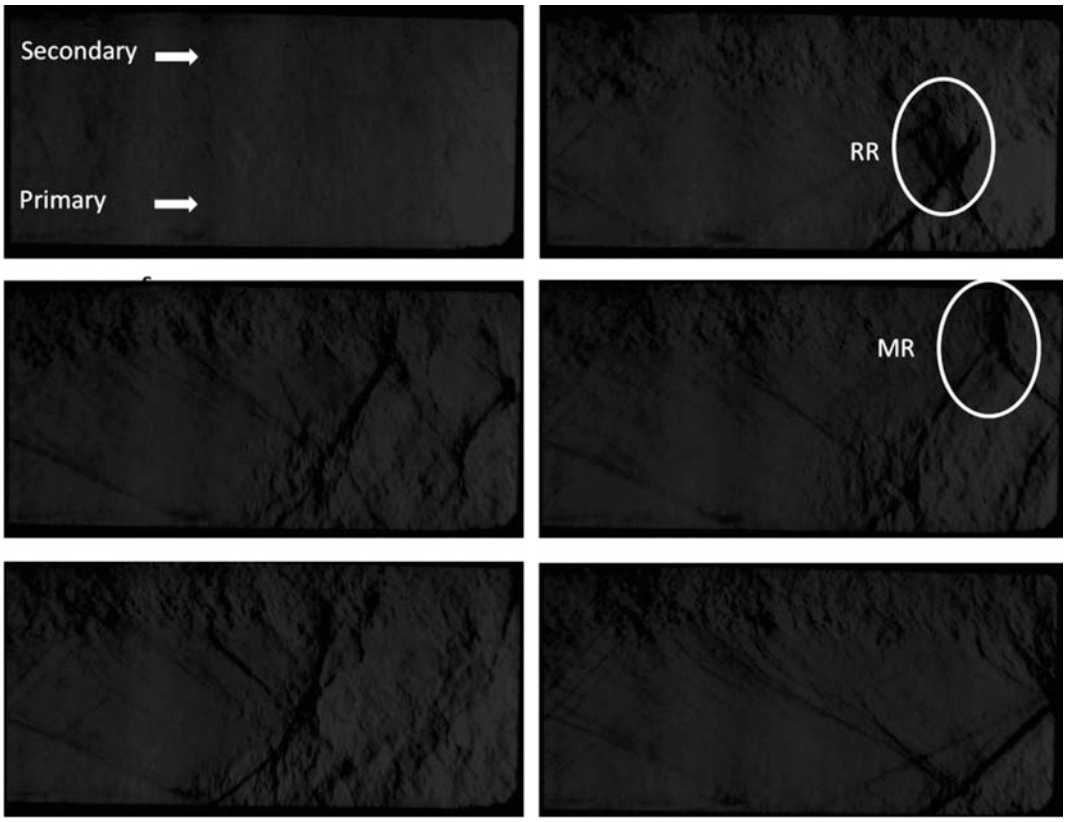

Fig. 2 Flow evolution for a symmetric vacuum ejector during start-up. (**a**) $t = 0$; (**b**) $t = 0.206$ s; (**c**) $t = 0.2613$ s; (**d**) $t = 0.2627$ s; (**e**) $t = 0.2652$ s; (**f**) 0.4112 s

which corresponds to the starting of vacuum ejector. In the secondary chamber pressure plot, Fig. 3, point 'A' corresponds to the vacuum ejector starting point where the secondary chamber pressure starts to dip. This was taken as the reference point $t = 0$ in the pressure plot, so that flow visualization (schlieren) and pressure measurement can be compared from same reference time (instant at which vacuum ejector was started). The schlieren picture corresponding to the vacuum ejector starting state is shown in Fig. 2a, which indicates that the primary jet just began to flow. Point 'B' in Fig. 3 corresponds to the initiation of secondary chamber pressure oscillation (which happens at $t = 0.18$ s approximately from the reference point A) and continues till point 'C' ($t = 0.42$ s). Schlieren pictures shown in Fig. 2c–e (which is a random selection of one shock oscillation cycle) show that the time period at which shock oscillates is within the time period limit at which pressure oscillates in the secondary chamber (point B to point C). This establishes that the shock oscillations are primarily due to the pressure fluctuations in the secondary chamber. The pressure fluctuations in the secondary

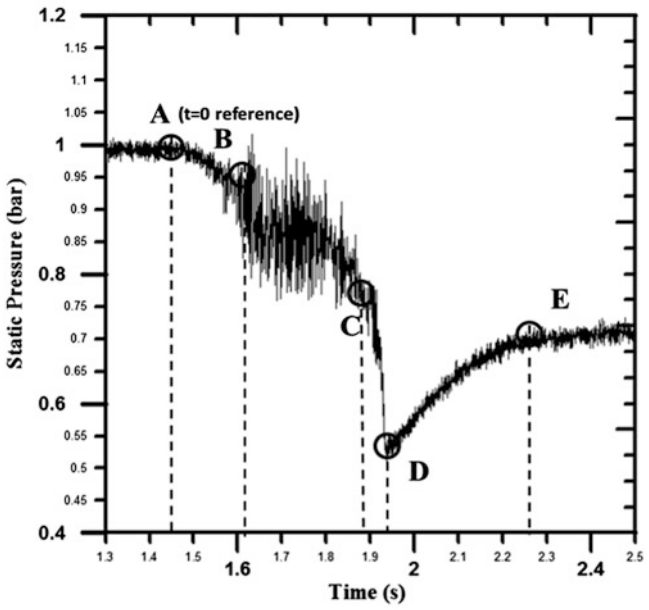

Fig. 3 Secondary chamber pressure data for symmetry model

chamber indicate that during the starting period the secondary chamber mass flux oscillates to and fro. The fluctuations in the secondary chamber total pressure make the shock structure in the mixed region to oscillate.

The pressure perturbations in the secondary chamber may be due to the elastic collision of the shear layer with the mixing region wall and this in turn produces damped shear layer oscillations. These pressure fluctuations are instantly communicated to the upstream secondary chamber through the subsonic part of the shear layer. As time progresses these elastic collisions settles down (point C) and after which the pressure suddenly drops to reach a minimum value, point 'D', without much fluctuations. After point 'D' the secondary chamber pressure again raises to a higher pressure (point 'E') and settles at that level. This may be due to the fact that the hitting of supersonic shear layer with mixing section wall and its sudden turning produces compression waves which may penetrate into the subsonic shear layer region and communicates the increased pressure levels to the secondary chamber. During this period the Mach reflection pattern transforms back into regular reflection as shown in Fig. 2f. The reason for this transformation is not clear and needs further investigation.

Figure 4 shows the secondary chamber static pressure data for the full model experiment. The pressure data for the full model qualitatively resembles as that of symmetry model with large scale oscillations during the initiation of vacuum ejector operation. Schlieren pictures for the full model experiment, Fig. 5, reveal that shock wave undergoes a transformation from regular reflection to Mach reflection as the secondary chamber evacuation process progresses. At this point it is not clear why this transformation is happening and further experiments are being carried out to investigate this.

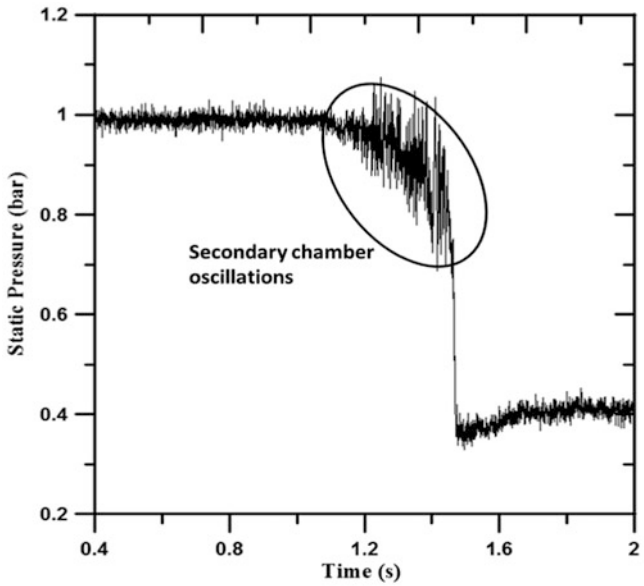

Fig. 4 Secondary chamber pressure data for full model

Conclusions

Experimental study on vacuum ejectors revealed that the initial starting process was subjected to flow oscillations in the secondary chamber. This can be observed from the pressure measurements in the secondary chamber which show oscillations during the initial period of evacuation. The pressure oscillations can be attributed to the elastic collision of the shear layer with the mixing region wall which subsequently leads to a damped oscillation of the shear layer. The schlieren flow visualization for a symmetry vacuum ejector shows that the initial shock structures formed in the downstream side of the mixing chamber/diffuser also oscillates in concurrence with the secondary chamber pressure fluctuations. During these oscillations, the Mach disc structure in mixing region traverse upstream and downstream with Mach disc strength reducing and increasing, respectively. With the fluctuations dying out, a sudden evacuation of the second chamber takes place with

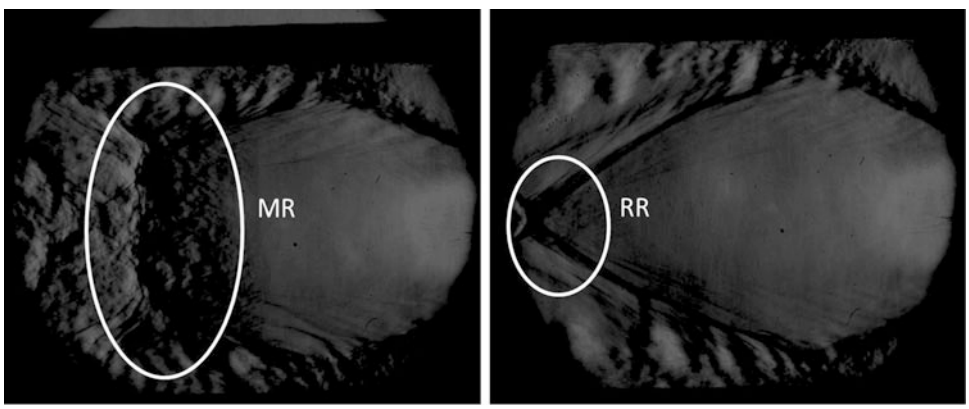

Fig. 5 Shock transformation in the full model during the secondary evacuation process. (**a**) 2.175 s; (**b**) 2.5244 s

the pressure reaching a minimum value. After reaching this minimum value, the secondary chamber pressure rises again and settles to a steady state value. This rise in pressure can be attributed to the generation of compression wave due to the sudden turning of shear layer after hitting the mixing region wall. The pressure rise across the compression waves is communicated to the upstream secondary chamber through the subsonic shear layer. Schlieren pictures for the full model experiments show that a shock transformation from a Mach reflection (MR) to regular reflection (RR) happens during the evacuation process. Further investigations are being carried out to understand this transformation.

References

1. Chen, F.C., Hsu, C.T.: Performance of ejector heat pumps. Energy Res. **11**(2), 289–300 (1987)
2. Dutton, J.C., Carroll, B.F.: Optimized ejector-diffuser design procedure for natural gas vapor recovery. J. Energy Res. Technol. **105**(3), 388–393 (1983)
3. Munday, J.T., Bagster, D.F.: A new ejector theory applied to steam jet refrigeration. Ind. Eng. Chem. Process. Des. Dev. **16**(4), 442–449 (1977)
4. Kim, H.D., Lee, J.S. an experimental study of supersonic ejector for a vacuum pump. In: Proceedings of the Korean Society of Mechanical Engineers, Annual Fall Meeting, vol. B, Korean Society of Mechanical Engineering, Seoul, Republic of Korea (1994)
5. Lijo, V., Kim, H.D., Rajesh, G., Setoguchi, T.: Numerical simulation of transient flows in a vacuum ejector-diffuser system. J. Aerosp. Eng. **224**(7), 777–786 (2010)
6. Mittal, A., Rajesh, G., Lijo, V., Kim, H.D.: Starting transients in vacuum ejector-diffuser system. J. Propuls. Power **30**(5), 1213–1223 (2014)
7. Manikanda, R.K., Vivekanand, P.K., Sundararajan, T., Kumaresan, K., Raja, D.M.: Optimization of second throat ejectors for high-altitude test facility. J. Propuls. Power **25**(3), 697–706 (2009)
8. German, R.C., Panescl, J.H., Clark, H.J.: Zero secondary flow ejector-diffuser performance using annular nozzles. Technical documentary report, AFSC program. AEDC-TDR-62-196, January (1963)

The Compressible Shear Layer of a Mach Reflection

R.E. Hall, B.W. Skews, and R.T. Paton

Introduction

Background to Shear Layers

A shear layer exists between two flows of different properties such as velocity or density. A finite thickness exists across a shear layer due to a velocity gradient forming on each side. The associated shear creates a region of mixing that increases in thickness from the point where the fluids first meet. Previous studies on shear layers [1, 2] revealed that the growth rate decreases as the shear velocity increases. Brown and Roshko [3] studied incompressible shear layers of different velocity and density ratios. Papamoschou [1] compared the visual growth rate of compressible shear layers to their incompressible values at the same velocity and density ratios. These values were plotted against M_c, a parameter derived by Bogdanoff [4] in an attempt to investigate and correlate the effect of compressibility on the growth rate of the turbulent shear layer. Rikanati et al. [2] measured the spread angle of shear layers in a Mach reflection for a Mach number range of 1.55 to 2.78 and proposed a theoretical model similar to that found in Dimotakis [5]. The spread angle of the shear layer increased to a maximum of 8° before decreasing with the effect of compressibility. For Reynolds numbers (Re/mm) below 2×10^3 the theoretical model proposed by Rikanati failed to match the experimental spread angles. Previous work by Rubidge and Skews [6] revealed the Kelvin-Helmholtz Instability (KHI) occurring along the shear layer for Mach numbers of 1.34, 1.46 and 1.61. The spread angle of the shear layer was found to be approximately half of Rikanati's measured angle, for the same Reynolds number.

R.E. Hall (✉) • B.W. Skews • R.T. Paton
Flow Research Unit, University of the Witwatersrand, PO WITS 2050, Johannesburg, South Africa
e-mail: russellhall14@hotmail.com; beric.skews@wits.ac.za; randall.paton@wits.ac.za

Mach Reflection and Three Shock Theory

The Mach Reflection (MR) configuration was first described by von Neumann [7] and consists of an incident shock (i), reflected shock (r), Mach stem (m), and shear layer (s). In order to obtain the velocity and density ratios across the shear layer of a Mach reflection, Three Shock Theory (3ST) is used. Consider a moving shock wave of strength M_s approaching a wedge of angle θ_w resulting in an MR (shown in Fig. 1a. The (i), (r), and (m) shocks meet at a singularity known as the triple point (t) from which the shear layer grows. The triple point follows a linear trajectory from the wedge surface denoted by angle χ. By fixing a reference frame on the triple point, normal oblique shock relations can be used to obtain the flow variables in the different regions (shown in Fig. 1b). The boundary conditions imposed on the flow in regions (2) and (3) are that the shear layer is isobaric ($p_2 = p_3$) and the net deflection for both streamlines is equal ($\theta_1 - \theta_2 = \theta_3$).

Experimental Facilities

Shock Tube

A large scale shock tube was used for experimental testing. The test sections dimensions are: Length = 2000 mm, Height = 450 mm, and Width = 100 mm. The viewing windows are 315 mm in diameter and are mounted in a 1.1 m diameter frame that can rotate, this allows visualisation of different regions of interest in the test section. The Mach numbers used for testing were $M_s = 1.26$, 1.37 and 1.44 with an uncertainty of ± 0.01. The larger scale of the experiment was hoped to visualise greater detail of the KHI structures and the frequency of their occurrence along the Mach reflection shear layer.

G. Ben-Dor et al. (eds.), *30th International Symposium on Shock Waves 1*, DOI 10.1007/978-3-319-46213-4_113

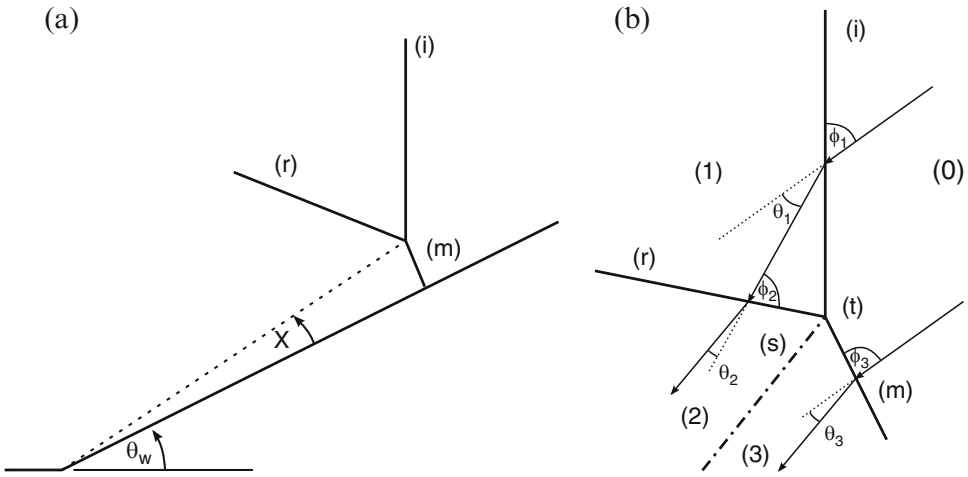

Fig. 1 Three Shock Theory of a Mach reflection. (**a**) Definition of parameters from wedge apex. (**b**) Definition of parameters in a fixed triple point reference frame

Table 1 Test piece dimensions

Wedge angle	Surface length	Height	Length	Width
[°]	[mm]	[mm]	[mm]	[mm]
30	778.4	386.3	674.1	98.5
40	600.4	385.9	459.9	98.5

Test Pieces

Two plane wedges were manufactured out of steel channel. The wedge surfaces were polished and painted black to prevent any reflections interfering with the flow visualisation. The specifications of each wedge are shown in Table 1:

The wedge angles were selected to compare with previous studies by Rubidge and Skews[6]. A steeper wedge angle (40°) was manufactured in order to investigate the effect of boundary layer proximity on the shear layer behaviour. Unfortunately an incident occurred where a test section window was damaged and only a single test was conducted using the 40° wedge.

Optical Visualisation

A shadowgraph optical system was used for flow visualisation. A xenon light source was used with an exposure of 1.5 μs, this was triggered by an adjustable delay connected to an oscilloscope. A 12 megapixel camera was used to obtain a single high resolution image of each test.

Results and Discussion

The following angles were measured at the triple point: incident shock to reflected shock (ω_{ir}), incident shock to Mach stem (ω_{im}) and reflected shock to shear layer (ω_{rs}). The triple point trajectory (χ) could not be measured from the wedge apex as it was not visible during testing. Successive test images were used to measure the triple point trajectory.

Using the experimental data, a computer program was written that required user input of the testing conditions (P_0 and T_0), wedge angle (θ_w), incident Mach number M_s, and measured shock angles (ω_{ir}, ω_{im}, ω_{rs}). As expected for the weak shock domain, the boundary conditions across the shear layer were not met when Three Shock Theory was used. Using an oblique shock analysis resulted in solutions that were within the boundary condition limits calculated in Olim and Dewey [8].

The velocity ratio ($r = U_3/U_2$), density ratio ($s = \rho_3/\rho_2$), shear velocity (ΔU), convective velocity (U_c) and convective Mach number (M_c) were calculated for the shear layer. U_c and M_c were calculated using equations in Papamoschou [1]. A summary of the measured experimental data is shown in Table 2.

The increase in Mach number results in a decrease in velocity ratio across the shear layer and associated increase in shear velocity (ΔU). The denser fluid is on the low speed side (as $s > 1$) of the layer: this inhibits the growth rate of the shear layer [2].

The progression of the Mach reflection for two different Mach numbers is shown in Figs. 2 and 3. A clear thickening of the shear layer is visible from the triple point and a braided pattern resembling the KHI is visible near the wedge surface. The KHI pattern extends midway along the shear layer to the wedge surface. The shear layer growth rate was measured by importing the experimental images into a CAD package and fitting a constant radius curve through the centre of the shear layer. The visual thickness δ_{vis} was measured at discrete points from the triple point. Shown in Fig. 4 is the measured thickness for two different shock strengths. For the Mach 1.26 case, no visible change in thickness was observed. The error in measuring the

Table 2 Measured angles and calculated shear layer data

θ_w	M_s	χ	ω_{ir}	ω_{rs}	ω_{im}	r	s	ΔU	U_c	M_c
[°]	[-]	[°]	[°]	[°]	[°]	[-]	[-]	[m/s]	[m/s]	[-]
30	1.26	4.1	48.6	84.7	158.0	0.864	1.049	46.47	318.89	0.0602
30	1.37	4.3	58.5	80.8	156.7	0.794	1.070	74.58	325.11	0.0938
30	1.44	5.4	61.4	78.4	155.6	0.787	1.035	77.97	328.38	0.0945

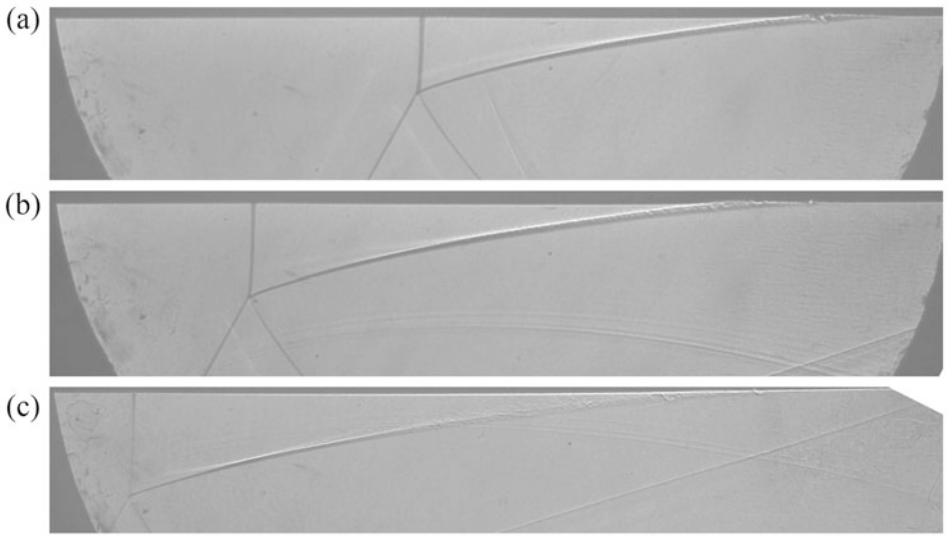

Fig. 2 Shear layer development for 30° Wedge. $M_s = 1.37$. (**a**) 3200 μs, (**b**) 3300 μs, (**c**) 3400 μs

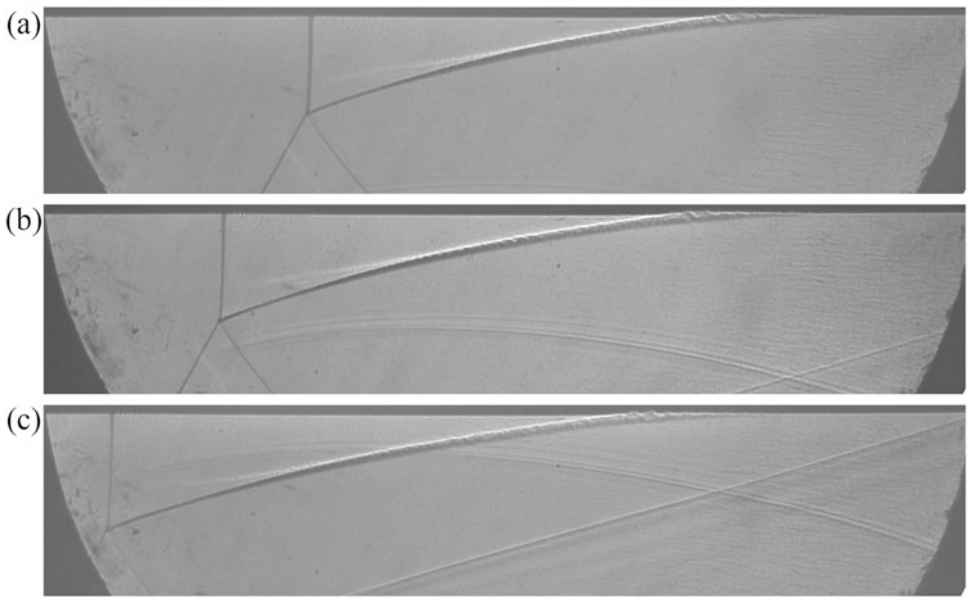

Fig. 3 Shear layer development for 30° Wedge. $M_s = 1.44$. (**a**) 3100 μs, (**b**) 3150 μs, (**c**) 3200 μs

thickness is estimated at ±0.25 mm and distance from the triple point ±2 mm. The visual growth rate δ'_{vis} was obtained by fitting a line of best fit through the data points.

Although a velocity shear is present across the shear layer of a Mach reflection, it is clear from Table 2 that compressibility does not play a large role in the growth of the mixing layer. The convective Mach numbers are small and when the growth rates obtained from Fig. 4 are plotted against Papamoschou's data (δ'_{vis} vs $\Delta U/U_c$), the linear trend is still maintained. When comparing the visual growth rates to the model proposed by Rikanati et al. [2], their theoretical growth rates were approximately double. This coincides with the conclusion reached by Rubidge and Skews [6] regarding the spread angle.

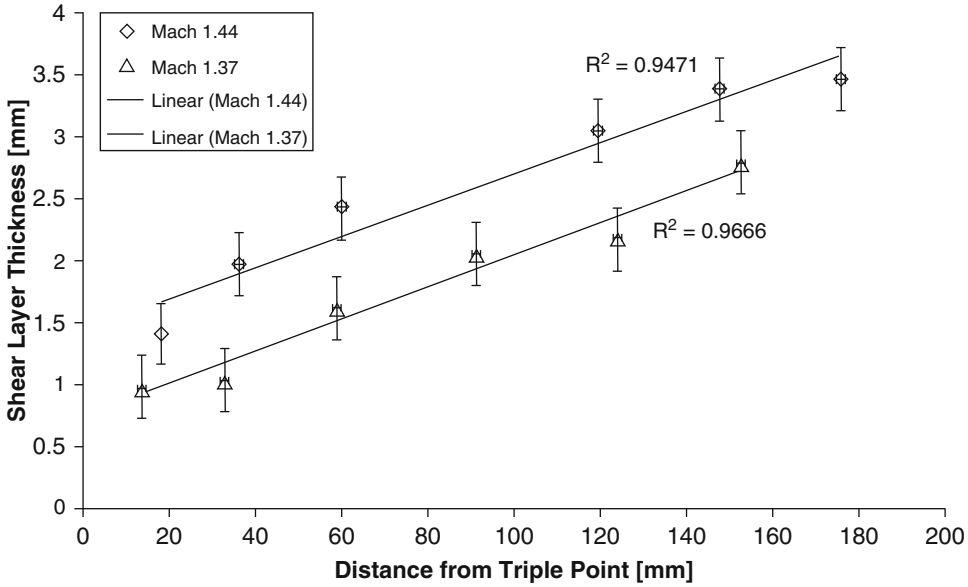

Fig. 4 Shear layer thickness from the triple point. $\delta'_{vis} = 0.013$ and is approximately the same for both Mach numbers

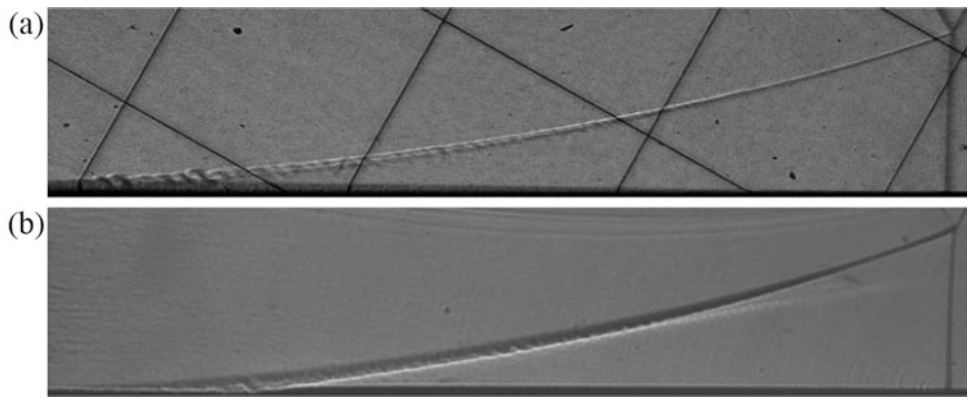

Fig. 5 Shear layer development for 30° Wedge. (**a**) $M_s = 1.46$ with Mach stem height of 17 mm[6], (**b**) $M_s = 1.44$ with Mach stem height of 34 mm

Effect of Scale

The self-similarity of the shear layer was assessed by utilising previous experimental images from Rubidge and Skews [6] obtained in a much smaller shock tube. The shear layer development was compared by scaling the images by Mach stem height (shown in Fig. 5). The larger scale experiment reveals a thicker shear layer when compared to an image obtained at half the scale and similar Mach number. The KHI structures are less discernible in the shear layer, indicating a breakdown into turbulence due to the increase in Reynolds number associated with the larger scale.

Conclusion

A large scale study of Mach reflection revealed the breakdown into turbulence of the shear layer. With increasing Mach number the shear layer thickness increases from the triple point and grows linearly at a similar growth rate. Theoretical velocity and density ratios were calculated using a three shock calculator for the experimental conditions. This revealed for a Mach reflection (in the range $1.26 < M_s < 1.44$) that the convective Mach numbers are low, resulting in small growth rates of the shear layer. This was verified by measurements of the shear layer from experimental images. Due to the larger scale of the experiment, the shear layer becomes turbulent and obscures any KHI structures present. The application of Three Shock Theory to the weak shock domain failed to find a solution when experimental shock angles were used.

References

1. Papamoschou, D., Roshko, A.: The compressible turbulent shear layer: an experimental study. J. Fluid Mech. **197**, 453–477 (1988)
2. Rikanati, A., Sadot, O., Ben-Dor, G., Schvarts, D., Kuribayashi, T., Takayama, K.: Shock-wave Mach-reflection slip-stream instability: a secondary small-scale turbulent mixing phenomenon. Phys. Rev. Lett. **96–17**, 1–4 (2006)
3. Brown, G.L., Roshko, A.: On density effects and large structure in turbulent mixing layers. J. Fluid Mech. **64**, 775–816 (1974)

4. Bogdanoff, D.W.: Compressibility effects in turbulent shear layers. AIAA **21–6**, 926–927 (1983)
5. Dimotakis, P.E.: Two-dimensional shear-layer entrainment. AIAA **24–11**, 1791–1796 (1986)
6. Rubidge, S.R., Skews, B.W.: Shear-layer instability in the Mach reflection of shock waves. Shock Waves **24–5**, 479–488 (2014)
7. von Neumann, J.: Explosives Research Report No. 12: Oblique Reflection of Shocks. Bureau of Ordinance, Navy Department, Washington DC (1943)
8. Olim, M., Dewey, J.M.: A revised three-shock solution for the Mach reflection of weak shocks ($1.1 < M_i < 1.5$). Shock Waves **2**, 167–176 (1992)

Experimental Study of Mach Reflection in Cellular Detonation of C_2H_2–O_2–8.17Ar

Jie Liu and DU Zhong-hua

Introduction

Mach reflection of detonation waves is an important and complex phenomenon in gaseous detonation field, which usually happens when a detonation wave propagates in a convergent channel. The Mach reflection also has been extensively studied by previous researchers. Meltzer [1] used smoked foils to record cellular structure of the Mach reflection in $2H_2$–O_2–XAr. Akbar [2] used Schlieren to obtain photographs of the Mach reflection in C_2H_2–$2.5O_2$–14Ar and $2H_2$–O_2–XAr, and also measured χ between trajectory formed by Mach triple point and wedge surface. Actually, the trajectory of Mach triple point in detonation wave is not a straight line but a curve, which has been noticed by Trotsyuk [3]. Therefore, A discrepancy of the Mach reflection between shock wave and detonation wave is that the Mach reflection of shock wave is self-similar, but not with detonation wave. According to analysis of Shepherd [4], due to a finite thickness of detonation front and movement of transverse waves, the presence of characteristic length of induction and reaction zones and instability of transverse waves renders the self-similarity is invalid for the Mach reflection of detonation wave. A more detailed discussion [5] of the failure of the self-similarity for Mach reflection of detonation wave is that the trajectory of Mach triple point is no longer a straight line starting from instead of a fluctuant curve. Therefore, curvature of the trajectory cannot be overlooked and χ angle between the trajectory and the apex of wedge always changes in whole process of the Mach reflection in detonation wave. Therefore, one purpose in this study is to find tendency of the trajectory of the Mach reflection against the three-shock theory established by von-Neumann [6]. Another characteristic of the trajectory is fluctuation because of the movement of transverse waves in Mach stem and incident detonation front. So it is necessary to study the effect of track angle formed by transverse wave movement in the end.

J. Liu (✉) • D. Zhong-hua
Nanjing University of Science and Technology, Xiaolingwei No. 200, Nanjing, China
e-mail: liujie8812@gmail.com

Experimental Setup Details

In the experiments, the Mach reflection of stable mixture C_2H_2–$2.5O_2$–8.17Ar was investigated. Detonation waves propagate in a narrow rectangular channel, which geometric sizes of cross section are 100 × 25 mm. The range of initial pressure is from 3 to 10 kPa. Wedge angles are 20°, 30°, 35°, and 40°. Three igniters in series connection charged by a high voltage capacitor at a voltage of 18 kV are used to initiate the mixture. A Z-type Schlieren apparatus is applied to visualize density perturbations, for this reason two sides of the channel are tempered glass plates. Smoked foils are used to record the cellular structures of detonation waves. Figure 1 shows three positions surrounding the wedge where the smoked foils are placed, which is used to obtain the 3-D cellular structure of detonation wave traveling the wedge because the true structure of an actual detonation wave is transient and three-dimensional, even though the transverse wave in thickness direction is suppressed and weakened in narrow channel. The smoked foils are located in front of the position of the wedge, on the side (on the wall) and on the surface of the wedge, respectively. Therefore, three smoked foils can be obtained ideally in an experiment.

Experimental Results and Discussions

Experimental Results of Mach Reflection

Figure 2 shows smoked foils which recorded cellular pattern of the Mach reflection over different wedges at 5 kPa initial pressure. After detonation waves propagating over wedges, cell sizes behind incident detonation wave and Mach stem

G. Ben-Dor et al. (eds.), *30th International Symposium on Shock Waves 1*, DOI 10.1007/978-3-319-46213-4_114

are clearly observed and inconsistent for wedge angles of 20° and 30°, also the cell size in overdriven zone is smaller than the behind incident detonation wave. But for larger wedge angle of 35° or 40°, the cells are so small that to distinguish cellular structure instead of uniform part. The foils on the wall show that cellular structures behind Mach stem are different with the incident wave due to the overdriven detonation. The cells behind the Mach stem change from large to small suddenly and then grow along the surface of wedges. The above, transition process of cellular structure, also occurs at foils on the surface of wedges and it is clearer than on the wall because the width of the channel is about 1/4 of the height of the channel.

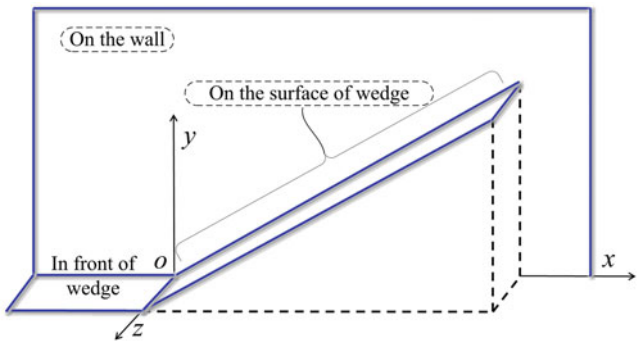

Fig. 1 Sketch of positions of smoked foils

One trend of the trajectory of Mach triple point is approaching wedge surface with the increasing of wedge angle, also seen in Fig. 2. Therefore, for wedge angle 40°, the trajectory is almost reaching a critical angle for the transition from Mach reflection to regular reflection. The region of cellular structure behind Mach stem also becomes smaller due to the overdriven degree with wedge angle increasing. For foils on the surface of wedge, some larger cells exist in the beginning of wedge. The existing of larger cells demonstrates that detonation wave does not adjust immediately when it travels up wedge instead of propagating some distance and then the overdriven behavior appears. It is hard to determine the correlation between wedge angle and the distance of larger cell propagating at the beginning of wedge. Nearly all of larger cells propagating distance obtained from different wedges fluctuate up and down around one L and below $2L$ definitely and the L is cell length. At the starting of the overdriven zone, transition region is definitely found from larger cells to smaller cells. Also note that the same situation exists in the foils located on the wall. Hence, it can be confirmed that whether foils are located on

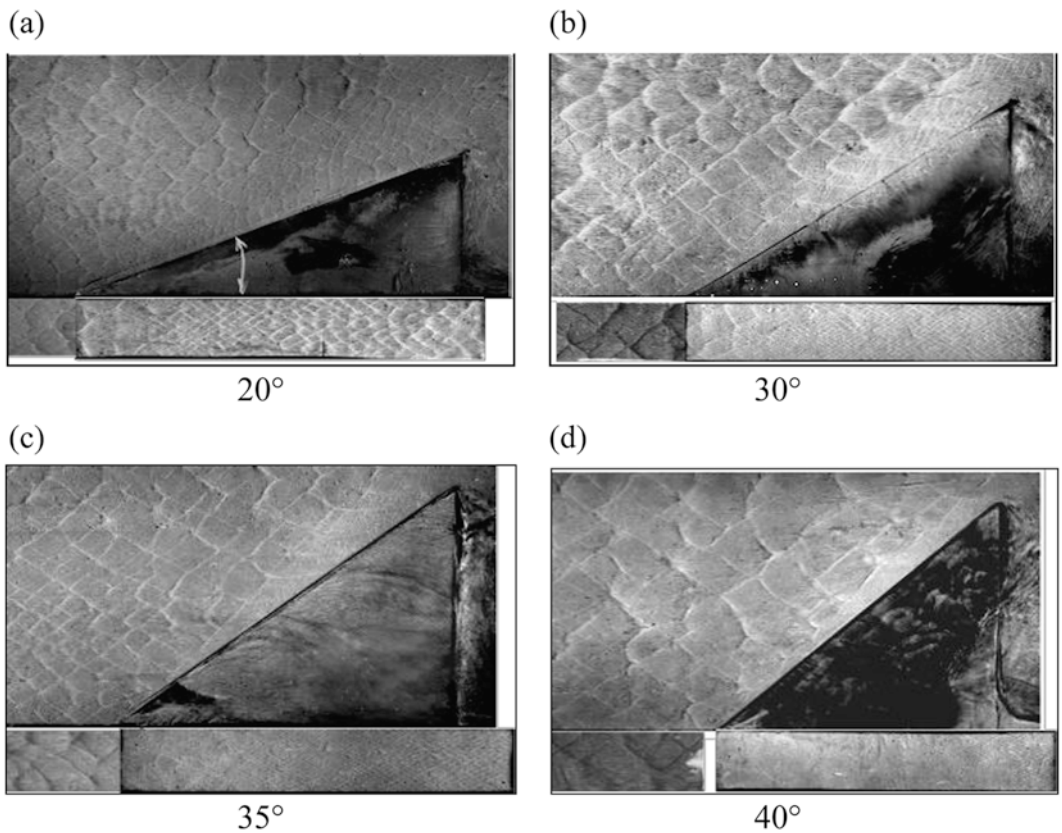

Fig. 2 Smoked foil over wedges at initial pressure 5 kPa. (**a**) 20°; (**b**) 30°; (**c**) 35°; (**d**) 40°

the wall or the surface, both have similar phenomenon about cellular transition.

Figure 3 shows smoked foils for C_2H_2–$2.5O_2$–8.17Ar at 10 kPa initial pressure over wedge angles of 20° and 35°. Small cells along the surface of wedge exist due to overdriven behavior. To compare smoked foils at initial pressure 5 kPa, the fluctuation of the trajectory of Mach triple point becomes gentler due to cell size λ decreasing.

Figure 4 shows Schlieren photographs of Mach reflection happened at different positions along wedge surface. It is clear to observe the position of Mach triple point and Mach stem. At the beginning of wedge, Mach stem is small and short. At the end of wedge, Mach stem grows gradually.

As seen in Fig. 5, experimental evidence for Mach reflection of detonation wave has shown that the slipstream is curled toward the Mach stem. This is due to a wall pressure gradient which is formed from difference in stagnation pressures for flows on either side of the slipstream striking wedge. A bundle of compression waves is generated which is strong and consequently visible.

Non-self-similarity of Mach Reflection

Figure 6a shows height of Mach triple point of detonation wave propagating over different wedges from 20° to 40° at

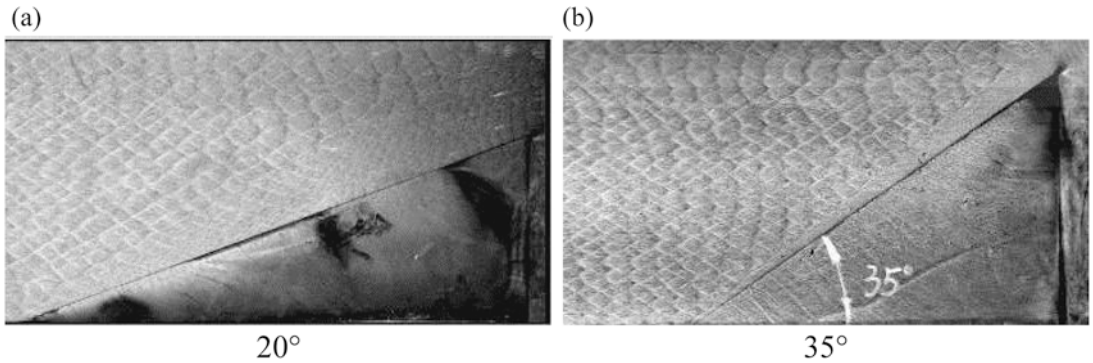

Fig. 3 Smoked foil over wedges at initial pressure 10 kPa. (**a**) 20°; (**b**) 35°

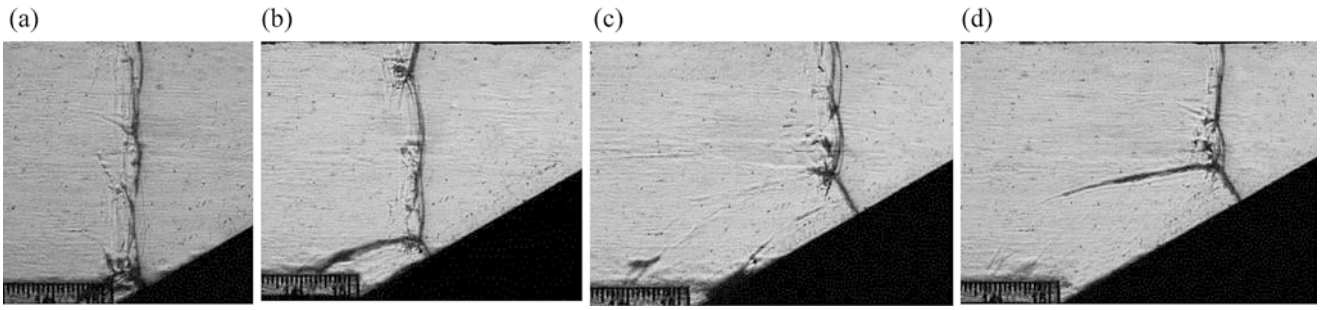

Fig. 4 Schlieren photographs over 30° wedge at initial pressure 5 kPa

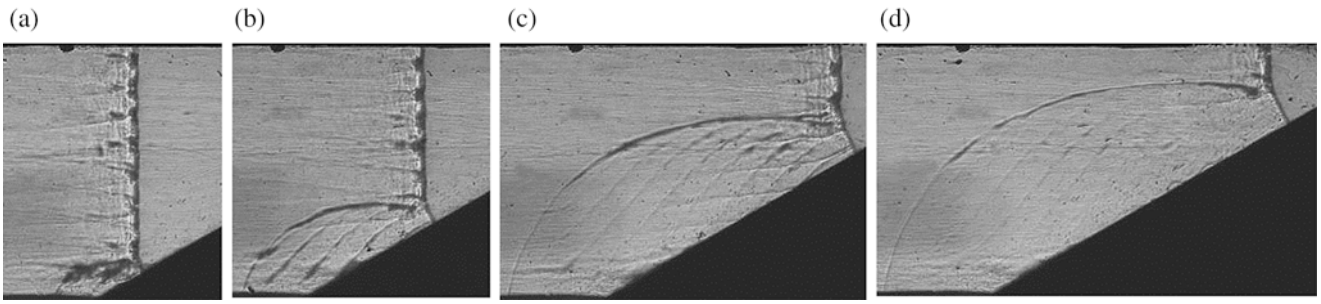

Fig. 5 Schlieren photographs over 30° wedge at initial pressure 10 kPa

initial pressure 10 kPa. Every trajectory of Mach triple point has a large or little fluctuation and approaches surface of wedge with wedge angle increasing. Height of Mach triple point shown in Fig. 6b, as apparent evidence, indicates that the trajectory of Mach triple point is a curved line and has a little fluctuation, and also shows a comparison between height of Mach triple point and the three-shock theory. The trajectory of Mach reflection follows triple point trajectory of nonreactive shock theory at beginning of wedge, and then falls on a line parallel to triple point trajectory of reactive shock theory when transition of Mach reflection happens. Because of the thickness of detonation front, behavior of Mach reflection is similar with shock wave before transform happened. After the overdriven happened, the thickness of reaction zone is decreasing and leads to characteristics of Mach reflection to approach the detonation wave.

According to the height of Mach triple point measured from Schlieren photographs and smoked foils, it is clear that the trajectory of Mach triple point is a curve to increase gradually for detonation wave. So we suppose a curve to fit experimental data is monotonically increasing and can be defined as a function $y = f(x)$. Hence, first derivative value of $y = f(x)$ is greater than zero, namely $f'(x) > 0$. And a limited condition is $\varphi > \Phi/2$ or $\alpha/2$ which is also known from the experimental results, where the φ is an instant angle for Mach triple point.

First for shock wave, in Fig. 7a

$$\Delta l = \mathrm{OP2} - \mathrm{OP1} \tag{1}$$

$$\mathrm{OP2} = \frac{(t + \Delta t) \cdot D_{\mathrm{CJ}}}{\cos(\theta + \chi)} \tag{2}$$

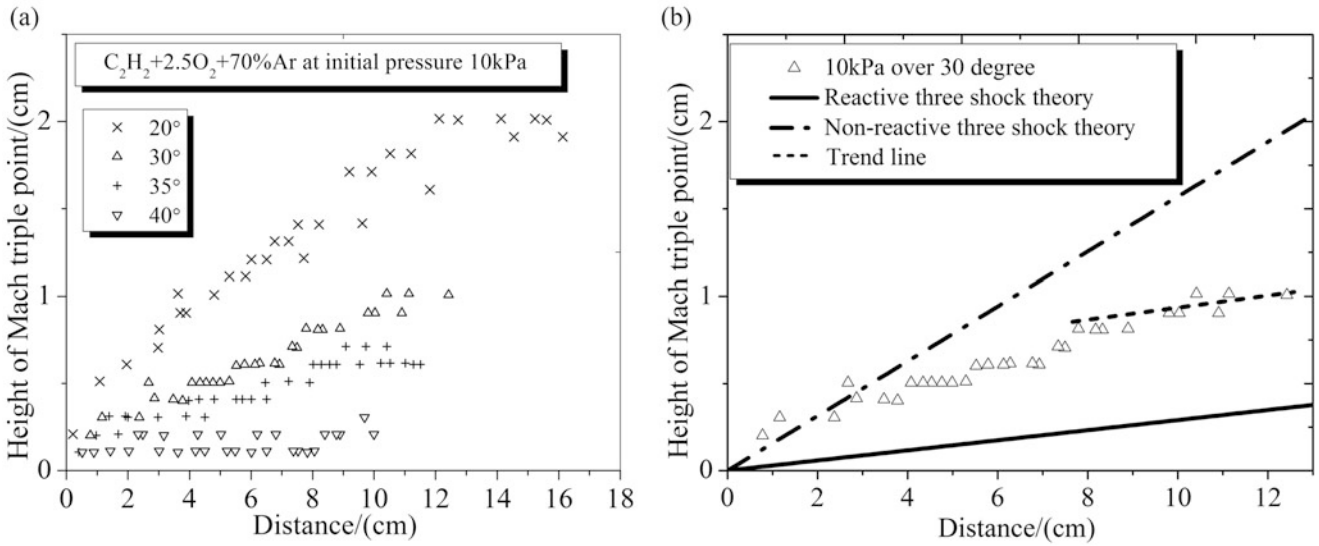

Fig. 6 Height of Mach triple point

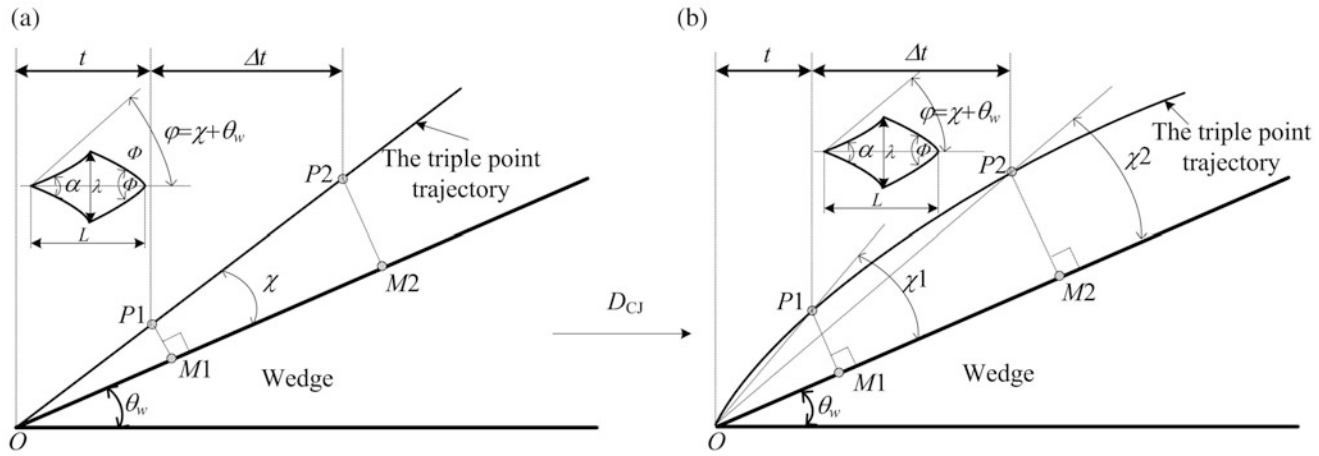

Fig. 7 Schematic of Mach reflection

$$\begin{cases} \mathrm{OM1} = t \cdot D_{\mathrm{CJ}} \cdot \dfrac{\cos(\chi)}{\cos(\theta+\chi)} \\ \mathrm{OM2} = \mathrm{OP2} \cdot \cos(\chi) = \dfrac{(t+\Delta t) \cdot D_{\mathrm{CJ}} \cdot \cos(\chi)}{\cos(\theta+\chi)} \end{cases} \tag{3}$$

$$M2M1 = \Delta t \cdot D_{\mathrm{CJ}} \cdot \frac{\cos(\chi)}{\cos(\theta+\chi)} \tag{4}$$

And for detonation wave, in Fig. 7b,

$$M2M1 = t \cdot D_{\mathrm{CJ}} \cdot \left[\frac{\cos(\chi 2)}{\cos(\theta+\chi 2)} - \frac{\cos(\chi 1)}{\cos(\theta+\chi 1)}\right] + \Delta t \cdot D_{\mathrm{CJ}} \cdot \frac{\cos(\chi)}{\cos(\theta+\chi)} \tag{5}$$

where $\frac{\cos(\chi 2)}{\cos(\theta+\chi 2)} - \frac{\cos(\chi 1)}{\cos(\theta+\chi 1)}$ is a negative but near zero.

At same condition of time interval Δt and Mach number, the propagating distance of detonation wave along surface of wedge is shorter than shock wave. Therefore, the height of Mach triple point in detonation wave is lower than the shock wave.

Effects of Track Angle on Trajectory of Mach Reflection

Considering this complex phenomenon of the Mach reflection, a simplified model confined in a cellular structure is used to analyze the effects of track angle on triple point trajectory, which is illustrated in Fig. 8. The track angle α or Φ, an instant angle φ of Mach triple point are also shown in Fig. 8.

The entrance angle Φ and exit angle α are collectively called as track angle in detonation wave. In general, both of the two angles should be approximately equal to each other for stable mixture, namely $\Phi \approx \alpha$. Based on previous experimental results [7], the range of both angles is from 56° to 70°, and the φ is from 35° to 50°. A simplifying function is established about length of the trajectory T, track angle α, and instant angle φ.

$$h = \lambda \cos(\alpha/2) \tag{6}$$

$$l_{T1} = h/\sin\left(\frac{\alpha}{2}+\varphi_1\right) = \lambda\cos\left(\frac{\alpha}{2}\right)/\sin\left(\frac{\alpha}{2}+\varphi_1\right) \tag{7}$$

$$l_{T2} = h/\sin\left(\frac{\alpha}{2}+\varphi_2\right) = \lambda\cos\left(\frac{\alpha}{2}\right)/\sin\left(\frac{\alpha}{2}+\varphi_2\right) \tag{8}$$

Because the range of α is from 56° to 70°, $(\pi-\alpha)/2$ should belong to 55°–62°. Whereas the range of φ from 35° to 55°, the former is large than the latter.

$$\begin{aligned} T &= l_{T1} + l_{T2} + l_{T3} + \cdots \\ &= h \cdot \sum_{i=1}^{n}\left(1/\sin\left(\frac{\alpha}{2}+\varphi_i\right)\right) \\ &= \lambda\cos\left(\frac{\alpha}{2}\right) \cdot \sum_{i=1}^{n}\left(1/\sin\left(\frac{\alpha}{2}+\varphi_i\right)\right) \end{aligned} \tag{9}$$

The above simplifying model is based on the supposition that there is no relationship between three parameters which are cell size λ, track angle α, and instant angle φ. According to (8), the effect of track angle α and angle φ of Mach triple point on the ratio of l_{T1}/λ is obtained and shown in Fig. 9, respectively.

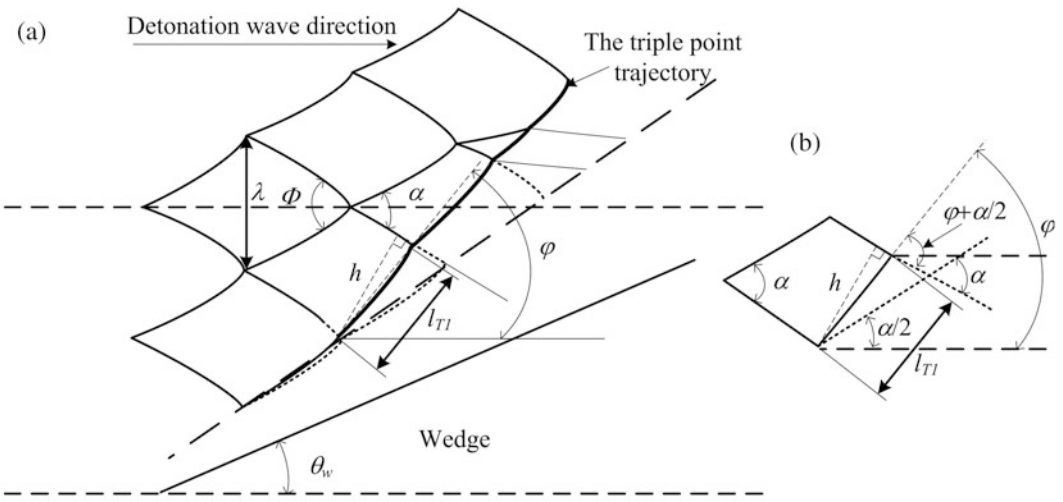

Fig. 8 Schematic of Mach triple point trajectory

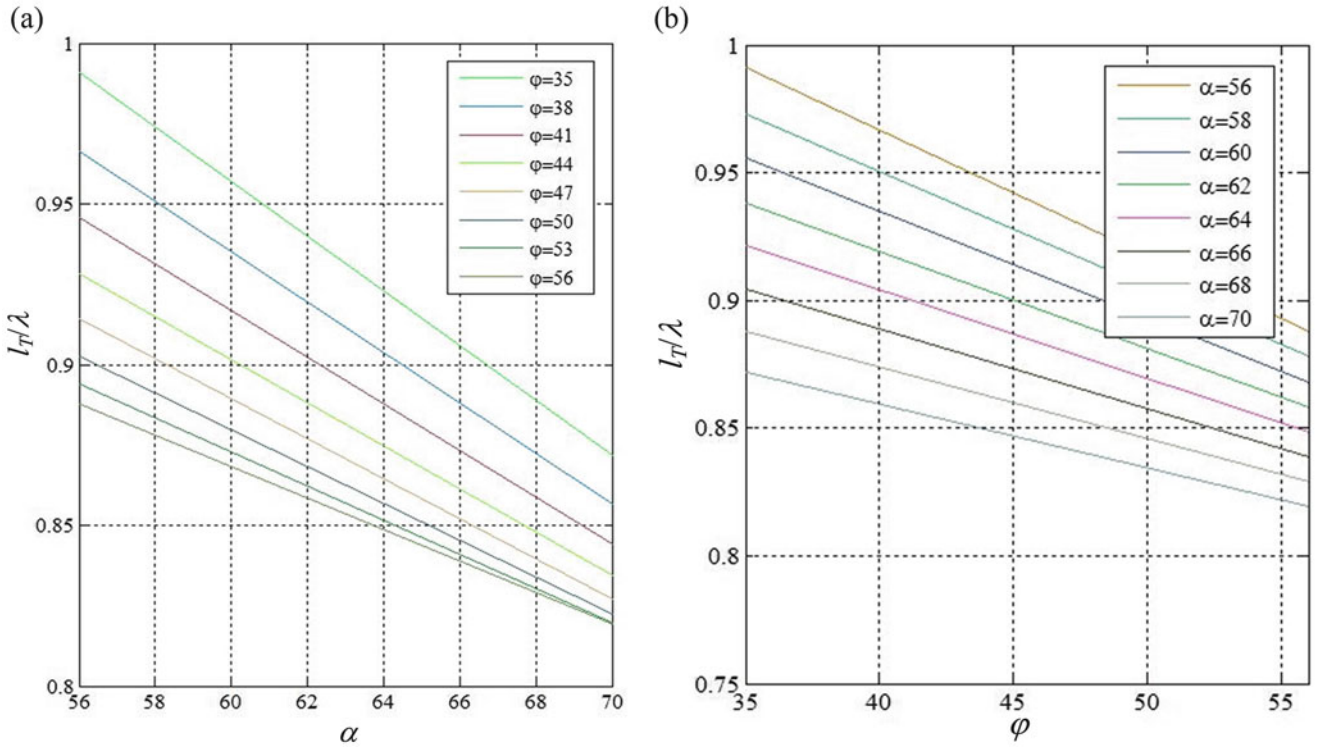

Fig. 9 Effect of α and φ on ratio of l_{T1}/λ

Figure 9 shows the effect of track angle α and angle φ of Mach triple point on the trajectory of Mach triple point, respectively. In Fig. 9a, the ratio of the trajectory over cell size λ is almost linear decreasing with the increasing of track angle at different angle φ. But for angle φ, there is a similar tendency of the effect on the ratio shown in Fig. 9b.

Conclusions

Two main understandings about Mach reflection of cellular detonation wave have been identified in this study. One is that the trajectory of Mach triple point does seem to follow the three-shock theory except for initial propagation of Mach stem near the beginning of wedge. Another is the effect of track angle and the angle of Mach triple point on the trajectory of Mach triple point. With increasing of the track angle or the angle of Mach triple point, the ratio of the trajectory of Mac triple point over cell size λ decreases.

References

1. Meltzer, J., Shepherd, J.E., Akbar, R., Sabet, A.: Mach reflection of detonation waves. Prog. Astronaut. Aeronaut. **153**, 78–94 (1993)
2. Akbar, R.: Mach reflection of gaseous detonations. Ph.D. Dissertation, Rensselaer Polytechnic Institute, Troy (1997)
3. Trosyuk, A.V.: Numerical study of the reflection of detonation waves from a wedge. Combust. Explos. Shock Waves **35**(6), 690–697 (1999)
4. Shepherd, J.E., Schultz, E., Akbar, R.: Detonation diffraction. In: Proceedings of 22nd International Symposium on Shock Waves, pp. 41–48 (2000)
5. Fortin, Y., Liu, J., Lee, J.H.S.: Mach reflection of cellular detonations. Combust. Flame **162**, 819–824 (2015)
6. Neumann, J. von.: Reflection, intersection and reflection of shock waves. USA (1943)
7. Austin, J.M.: The role of instability in gaseous detonation. Ph.D. California, California Institute of Technology Pasadena (2003)

The Existence of a Consistent Stationary Mach Reflection in Shock Tube Flows

Kazuyoshi Takayama and Gabi Ben-Dor

Introduction

A shock wave reflected from a solid wall takes either a regular reflection (RR) or a Mach reflection (MR). In general, the patterns of Mach reflections (MR) are locally divided into a direct MR, a stationary MR, and an inverted MR [1]. In a direct MR, its triple point moves away from the wall surface and hence its pattern is locally self-similar. If the shock wave reflects from a straight wedge, the reflection of shock waves is called pseudo-steady. In a stationary MR, its triple point moves exactly parallel to the wall surface, which should exist only in a steady supersonic flow. In an inverted MR, its triple point moves toward the wall surface and after its impingement on the wall it eventually terminates to RR. Hence, the inverted MR belongs to a truly unsteady reflection. Figure 1 shows shock polar diagrams that define the patterns of these reflection patterns [2].

The shock reflection from a straight wedge is defined as self-similar and takes the pattern of either the direct MR or RR, whereas the shock reflection over a concave wall would take successively the three shock reflection patterns and eventually would become RR [2]. By putting a short wedge on a longer wedge, we can form a double wedge. Then the shock reflection over it would eventually create one of the abovementioned reflection patterns. We found that this reflection pattern is maintained on the second wedge surface. A similar pattern as a stationary MR appears depending on the combination of the wedge angles. However, the stationary MR is maintained only temporally. This chapter discusses experimentally the appearance of the stationary MR on a double wedge and whether or not it violates the existence of the pseudo-steady flows.

K. Takayama (✉)
Emeritus Tohoku University, Sendai, Japan
e-mail: k.takayama@mac.com

G. Ben-Dor
Pearlstone Center for Aeronautical Engineering Studies, Department of Mechanical Engineering, Faculty of Engineering Sciences, Ben-Gurion University of Negev, Beer Sheva, Israel

Experiments

The shock tube experiment was carried out, by using a direct shadowgraph, in a 40 mm × 80 mm shock tube of the Institute of High Speed Mechanics Tohoku University. The Institute was renamed as the Institute of Fluid Science in 1989. We then modified the experimental setup to a 60 mm × 150 mm one, which was combined with diaphragm-less operation and achieved a higher degree of reproducibility. It was equipped with double exposure holographic interferometry [3].

In the series of double wedge experiments, we placed double wedges on a movable stage, with which we could adjust the inclination angle of the first wedge arbitrarily.

Results and Discussion

Figure 2 shows a direct shadowgraph of a stationary MR pattern at the incident shock Mach number of $M_s = 1.26$ in air at 650 hPa and 295 K. The first and second wedge angles are 25° and 45°, respectively. We can see a short Mach stem and a slip line parallel to the second wedge surface. Although the detailed wave interaction that was created at the leading edge of the second wedges was not clearly observable, the slip line is parallel to the second wedge surface so that we then defined, according to the definition [1], that this shock reflection pattern was very similar to a typical stationary MR. The slip line is, in principle, an interfacial discontinuity that is readily subjected to interfacial instability. However, in observing in Fig. 2, we found that the slip line is parallel to the second wedge surface, which supports a consistent presence of a stationary MR in a shock tube flow!

G. Ben-Dor et al. (eds.), *30th International Symposium on Shock Waves 1*, DOI 10.1007/978-3-319-46213-4_115

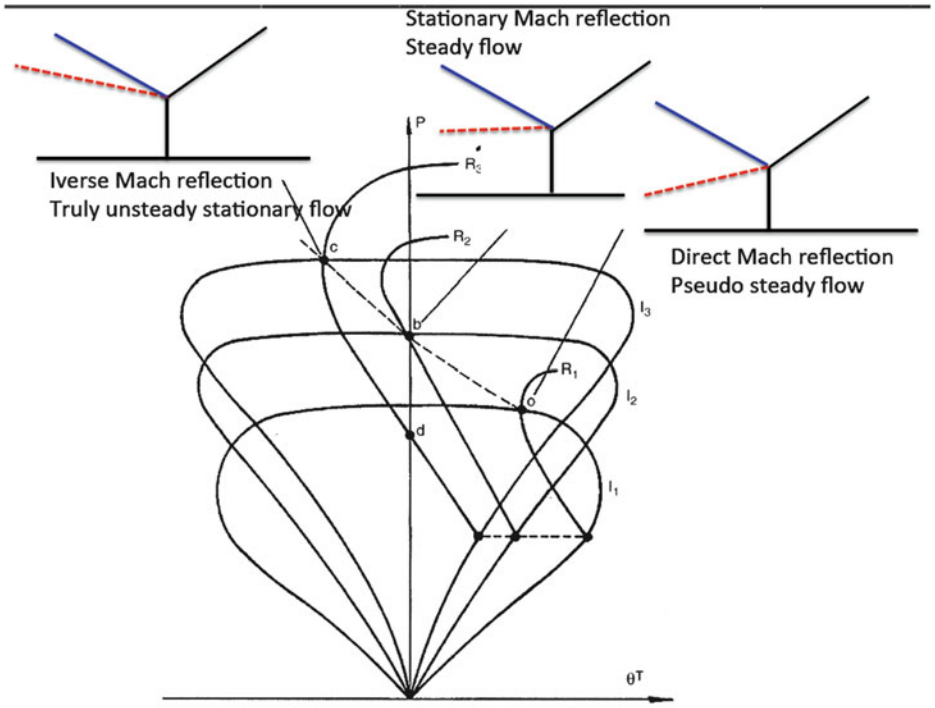

Fig. 1 Shock polar diagrams and three reflection patterns

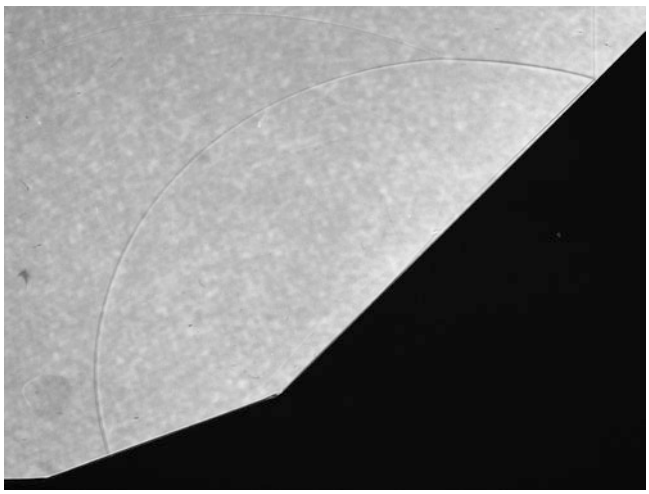

Fig. 2 Stationary MR, direct shadowgraph, over a 25°–45° wedge at $M_s = 1.26$ in air at 650 hPa and 295 K, #8008208, delay time of 150 μs

However, we were skeptic whether or not with the direct shadowgraph we could truly observe the stationary MR. Figure 3a shows a holographic interferometric image, which was collected in a 60 mm × 150 mm shock tube with the first and second wedge angles of 32.5° and 57.5°, respectively. The test condition was at $M_s = 1.754$ in air at 500 hPa and 288 K. Figure 3b shows the enlargement of Fig. 3a. The interferogram is much more informative than direct shadowgraphs.

In Fig. 3b, we can see that the slip line is parallel to the wedge surface but is gradually broadened with the distance from the triple point. Nevertheless the wave pattern clearly agrees with the stationary MR pattern. In the stationary MR appeared even a pseudo-steady shock tube flows, the particle velocity behind the Mach stem is constant across the slip line and then the slip line is maintained to be exactly parallel to the wall surface. This condition is, however, held at least in the vicinity of the triple point in Fig. 3a, b.

However, the slip line can't necessarily be maintained to be straight in real shock tube flows, because the diffusion across the density discontinuity acts to broaden the slip line structure with the distance from the triple point. At far distance, the slip line is far deviated from simple broadening. In Fig. 3b, we readily see that the interfacial instability rolls up the slip line and forms vortices.

The slip line is broadened due to the viscous effect, which would promote the termination of the stationary MR. The upper boundary of the broadened slip line would fulfill the condition for an inverted MR to exist so that the stationary MR will eventually convert to the inverted MR.

It is known that the transition from RR to MR over a straight wedge is delayed when the inclination angle is close to the critical transition [4]. The Reynolds number, Re, affects not only the wall boundary layer but also the development of slip lines. The lower the Re became, which means the lower the initial pressure, the slip line would be more significantly broadened. When the condition under which the stationary MR is not satisfied, the stationary MR would eventually transit to the inverted MR.

Conducting an experiment in a larger shock tube, hence with a longer wedge, we will be able to achieve a stationary

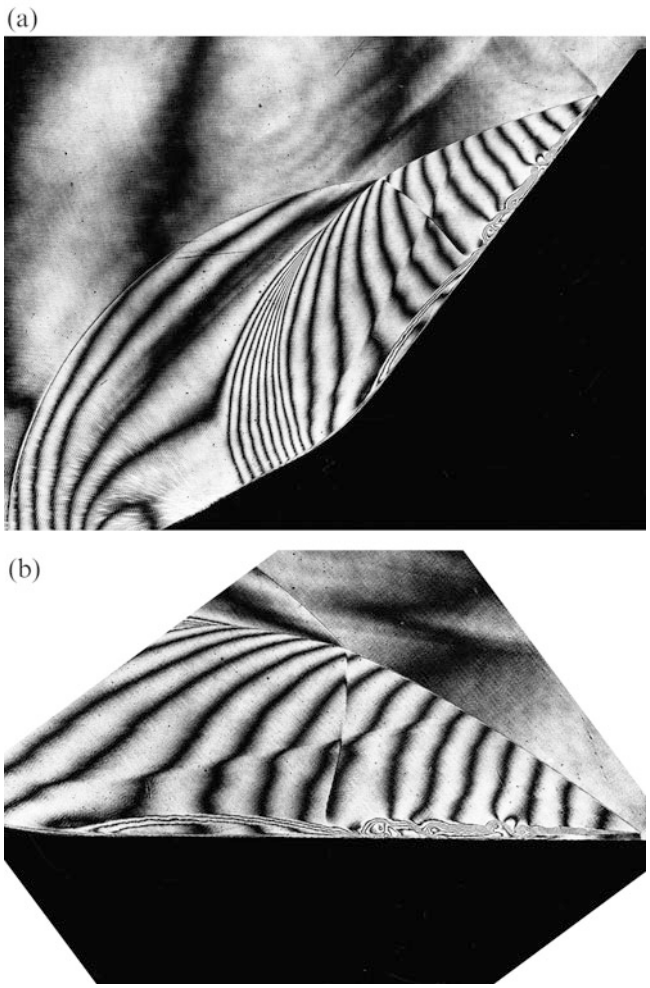

Fig. 3 Stationary MR, holographic interferometry, over a 32.5°–57.5° wedge at $M_s = 1.754$ in air at 500 hPa and 288 K, #88022501, delay time of 70 μs: (**a**) the whole view (*top*); and (**b**) enlarged image of (**a**) (*bottom*)

MR, which would be maintained relatively for longer period of time than in smaller shock tubes. However, nevertheless such a stationary MR would terminate sooner or later to an inverted MR. Hence we will speculate that the experimental results would be different depending on the shock tube geometry.

Sometime in the mid-1990, we tried to numerically reproduce stationary MR by solving an Euler solver. All the results so far achieved failed to reproduce the stationary MR but eventually the inverted MR appeared. With the advent of highly developed super-computations, in inherited Euler solvers, numerical simulation unconsciously introduced an imaginary viscosity and hence the slip line was broadened. Then the stationary MR terminated as inverted MR. Recently a fine Euler simulation revealed that the stationary MR eventually terminated and transited to the inverted MR [5].

Figure 4 shows a resulting transition of a stationary MR to an inverted MR over 80 mm radius concave wall at

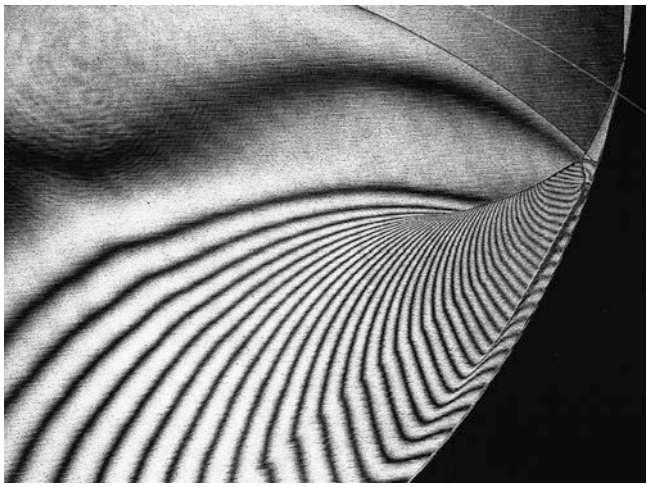

Fig. 4 Resulting transition of the stationary MR to inverted MR, #84040917 $M_s = 1.490$ in air at 800 hPa and 284 K in delay time of 590 μs

$M_s = 1.490$. The inverted MR eventually transits to RR. The reflection on the right shows a final RR. A secondary triple point appears behind the RR, which was the triple point of the stationary MR and later became that of the inverted MR. When the inverted MR terminated, the triple point reflected from the wall. As the slip line once created is unable to disappear, then the triple point was maintained to form the secondary triple point.

Conclusions

The temporal existence of a stationary MR on a double wedge was experimentally presented but this reflected shock patter would transit to an inverted MR. In conclusion, the truly stationary reflection never exists in shock tube flows.

Acknowledgments The authors wish to acknowledge Professor I. Krasovskaya for her discussion. The authors would like to express their sincere gratitude to Dr. Dan Igra for his kind helps in organizing this chapter.

References

1. Courant, R., Friedrichs, K.O.: Supersonic Flow and Shock Waves. Wiley Inter science, New York (1948)
2. Ben-Dor, G.: Reflection of Shock Waves. Springer, Heidelberg (2008)
3. Takayama, K.: Application of double exposure holographic interferometry to shock wave research. Proc SPIE **398**, 174–180 (1983)
4. Henderson, L.F., Takayama, K., Crutchfield, W.Y., Itabashi, S.: The persistence of regular reflection during strong shock diffraction over rigid ramps. J. Fluid Mech. **431**, 273–296 (2001)
5. Krasovskaya, I.: Private communication (2015)

Analysis of Wide-Driver Shock Tube Flow with Sharp Area Transition

J. Falcovitz, Dan Igra, and Ozer Igra

Introduction

Shock wave propagation in conduits having varying cross-section is frequently encountered in fluid-dynamics engineering practice. An abrupt area transition is also utilized in the design of shock tubes or tunnels. For example, in the high-enthalpy shock tunnel at Göttingen a sharp transition from the main tube of 150 mm to a nozzle of 22 mm takes place [1]. Another example is a detonation driven shock tunnel at the Institute of Mechanics in Beijing [2], where the transition between the driver and driven sections is through an abrupt area reduction.

The analytic modeling proposed here is analogous to that developed for studying the interaction of an incident shock wave with a long narrow segment of sharp area contraction [3]. It is based on the key assumptions that *a steady quasi-one-dimensional flow evolves in the entry segment*, and that all downstream waves are *simple waves*.

In the absence of a smooth connecting duct, how can an alternate characteristic length be associated with the flow through the sharp entrance to the narrow duct? Having inspected 2-D (axisymmetric) simulations of this flow process (obtained by the GRP method [4]), we observed that at large times the flow immediately downstream the entrance was approximately steady. Thus, in the absence of a smooth converging duct segment, the sharp corner produces streamtubes that form a virtual vena-contracta flow segment of length L_v proportional to the narrow tube diameter D. The ratio L_v/D depends on the driver-to-driven pressure ratio, and it is generally of $O(1)$.

The existence of such "virtual duct flow" implies that the present model can be formulated, in analogy with the previously mentioned study [3], as a flow field comprising an entry segment of steady flow, followed by a set of self-similar transmitted waves leading to the transmitted shock wave. Referring to the schematic diagrams in Fig. 1, the wide driver is regarded as a virtual plenum chamber consisting of quiescent fluid ("stagnation state"), feeding a steady converging flow into the narrow conduit. However, unlike the shock-interaction model in [3], the narrowest ("throat") streamtube in that flow is not taken as the narrow conduit itself, but rather assumed to be a virtual ("hydrodynamic") vena-contracta of an unknown area ratio, due to the flow separation immediately downstream of the sharp entry. The actual area ratio is determined by (approximately) matching the analytic model to numerical solutions.

Outline of the Flow Model

The flow evolving at the entry to the narrow duct and downstream is depicted schematically in Fig. 1. There are three cases: in case (a) the flow at the interface between the steady and self-similar flow regimes is subsonic; in case (b) the flow through the steady/self-similar interface is sonic; in case (c) the flow through the steady/self-similar interface is supersonic. Referring to the index marking flow states on the model diagram, the flow process is described as follows.

- The driver is taken as a large plenum chamber with a high-pressure quiescent state $(\cdot)_2$, which serves as an effective stagnation state for the flow expansion into the narrow duct. For the total duration of the flow considered here, the driver volume is so large that the stagnation pressure $(\cdot)_2$ may well be taken as constant.

J. Falcovitz
Institute of Mathematics, The Hebrew University of Jerusalem, Jerusalem, Israel

D. Igra (✉)
RAFAEL, Aerodynamics Group, P.O.B. 2250, Haifa 31021, Israel
e-mail: danigra@gmail.com

O. Igra
Professor Emeritus, Department of Mechanical Engineering, Ben Gurion University of the Negev, P. O. Box 653, Beer Sheva 84105, Israel

G. Ben-Dor et al. (eds.), *30th International Symposium on Shock Waves 1*, DOI 10.1007/978-3-319-46213-4_116

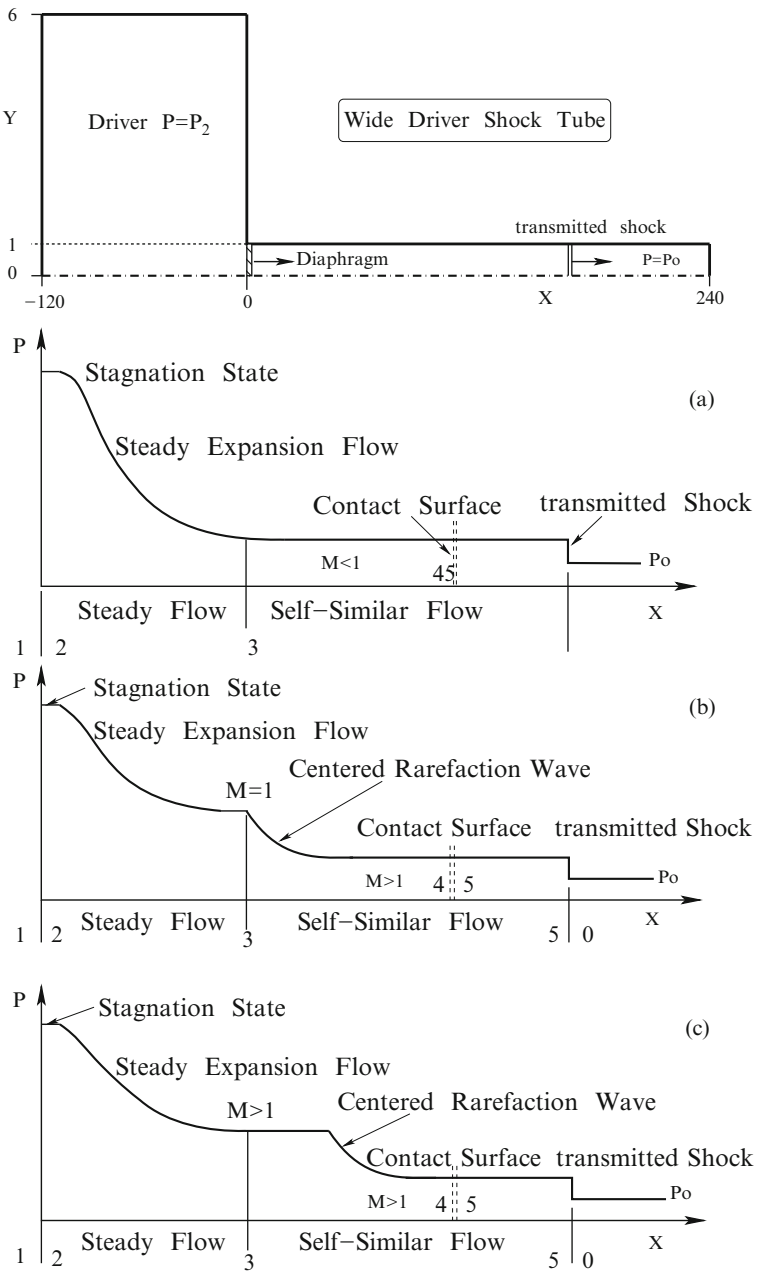

Fig. 1 Flow model downstream of duct entrance: (**a**) Subsonic case; (**b**) Sonic case; (**c**) Supersonic cases

- A steady subsonic expansion flow evolves between the virtual stagnation state $(\cdot)_2$ ($M_2 = 0$) and the interface state $(\cdot)_3$ ($M_3 < 1$).
- In the subsonic case ($M_3 < 1$) there is no pressure gap ($P_3 = P_4$) and no CRW arises. Note that a CRW cannot be matched to a steady subsonic flow, since the leading edge of a CRW propagates at *sonic* speed into the upstream flow.
- In the sonic case ($M_3 = 1$) a centered-rarefaction-wave (CRW) evolves to bridge the pressure gap ($P_3 > P_4$) between the interface and the contact surface states.
- In the supersonic case ($M_3 > 1$) the pressure gap ($P_3 > P_4$) is likewise matched by a CRW. However,the CRW propagates upstream into a *supersonic* flow, so that the joint cross-section appears to move in the positive direction at speed $(U_3 - C_3) > 0$, giving rise to an additional (self-similar) constant flow segment.
- A contact discontinuity separating states $(\cdot)_4$ and $(\cdot)_5$ is always formed. Note that the gas on the left $(\cdot)_4$ is that of the driver, while the gas $(\cdot)_5$ is the (air) gas compressed by the transmitted shock wave.
- State $(\cdot)_5$ is produced by the transmitted shock propagating into ambient state $(\cdot)_0$.

Some remarks concerning this flow model are due. As in [5], where a CRW propagating through a smooth converging

segment into a narrow conduit was studied, a stationary interface separating a (quasi-1D) steady flow segment from an expanding self-similar flow segment arises (here it is point 3). The significance of the contact discontinuity, not required in the case of an isentropic CRW [5], is that the state $(\cdot)_4$ fluid is produced by isentropic expansion flow from the "plenum chamber" $(\cdot)_2$, while state $(\cdot)_5$ is produced by the transmitted shock propagating into the ambient state $(\cdot)_0$. The entropy difference between these two states (separated by the contact discontinuity) is thus analogous to the entropy difference across the contact surface in a shock tube (Riemann) problem.

The analytic model is presented in some detail below. From the model equations it was found out that for a perfect gas having $\gamma = 1.40$, and for some fixed driver state *temperature*, the sonic case requires a driver pressure P_s that depends on the temperature. For example, in the case considered below the driver gas is air at constant temperature $T_2 = 1744\ K$, so the sonic pressure value (ambient pressure is $P_0 = 0.1\ [MPa]$) is $P_s = 1.077\ [MPa]$. Thus, the subsonic case is for the range $P_2 < P_s$, the sonic case is for $P_2 = P_s$, and the supersonic case is for $P_2 > P_s$.

Flow Model Equations

The steady isentropic expansion flow between stagnation state $(\cdot)_2$ and interface state $(\cdot)_3$ is given by

$$P_3 = P_2\left[1+\tfrac{\gamma-1}{2}M_3^2\right]^{-\frac{\gamma}{\gamma-1}}, \qquad \rho_3 = \rho_2\,(P_3/P_2)^{\frac{1}{\gamma}}, \tag{116.1}$$

$$C_3 = \sqrt{\gamma P_3/\rho_3}\,, \qquad U_3 = M_3 C_3\,,$$

where in the subsonic case $M_3 < 1$, in the sonic case the value of $M_3 = 1$, and in the supersonic case $M_3 > 1$. Assuming the latter two cases, a CRW separating states $(\cdot)_3$ and $(\cdot)_4$ is governed by the Riemann-Invariants relations

$$U_4 + \frac{2}{\gamma-1}C_4 = U_3 + \frac{2}{\gamma-1}C_3\,, \qquad C_4 = \sqrt{\gamma P_4/\rho_4}\,, \qquad P_4/\rho_4^{\gamma} = P_3/\rho_3^{\gamma}\,. \tag{116.2}$$

Across the contact we have continuity of pressure and velocity

$$U_5 = U_4\,, \qquad P_5 = P_4\,, \tag{116.3}$$

(1)–(3) and the relations across the transmitted shock are

$$M_{s,t} = \left(\frac{\gamma+1}{4}\right)\left(\frac{U_5}{C_0}\right) + \left[1+\left(\frac{\gamma+1}{4}\right)^2\left(\frac{U_5}{C_0}\right)^2\right]^{\frac{1}{2}},$$
$$P_5 = P_0\left[1+\frac{2\gamma}{\gamma+1}\left(M_{s,t}^2-1\right)\right], \quad \rho_5 = \rho_0\frac{\mu^2 P_0 + P_5}{P_0+\mu^2 P_5}, \quad \mu^2 = \frac{\gamma-1}{\gamma+1}\,, \tag{116.4}$$

where by ρ, P, C, γ, U, M, $M_{s,t}$ we denote, respectively, the fluid density, pressure, speed of sound, polytropic index, flow velocity and Mach number, and transmitted shock wave Mach number.

In the **sonic case** $(M_3 = 1)$ the system (1)–(4) is interpreted as follows. The expansion (steady) flow is evaluated from Eq. (1), where in the supersonic case the value of $M_3 > 1$ is determined by matching to numerical solution, as will be shown in the sequel. The remaining equations constitute a *Riemann problem* resolved by a right-facing shock, a left-facing CRW, the two waves being separated by a contact discontinuity. Having evaluated state $(\cdot)_3$, the sub-system (2)–(4) is solved by calculating the intersection of the left and right U, P interaction curves, thus producing the contact velocity and pressure.

In the **subsonic case** the CRW vanishes and states $(\cdot)_3$,$(\cdot)_4$ are identical. However, the *contact discontinuity* $(\cdot)_4 - (\cdot)_5$ remains, subject to the pressure and velocity continuity relations Eq. (3). The system Eqs. (1)–(4) reduces to a kind of Riemann problem, where the right wave is the transmitted shock and the left wave is replaced by the steady expansion flow $(\cdot)_2 - (\cdot)_3$. The state $(\cdot)_4 = (\cdot)_3$ is evaluated as function of M_3 using Eqs. (1)–(3). The post-shock state $(\cdot)_5$ is evaluated, as before, by Eq. (4). Here again, the solution is determined by solving the velocity and pressure continuity at the contact surface $(\cdot)_4$–$(\cdot)_5$.

In the **sonic case** $M_3 = 1$, a CRW evolves and states $(\cdot)_3$, $(\cdot)_4$ are related by Eq. (2).

In the **supersonic case** $M_3 > 1$, a CRW evolves and states $(\cdot)_3$,$(\cdot)_4$ are related by Eq. (2), and an additional supersonic state $(\cdot)_3$ evolves upstream to the CRW. The value of $M_3 > 1$ is approximately determined by inspecting numerical solutions where the flow through the entrance to the driven segment shows a vena-contracta pattern of steady, isentropic expansion flow to supersonic speed.

Numerical Solution

In our sharp area contraction model we envision the flow driven into the narrow tube through a "vena contracta" formed by an imaginary converging streamtube. This pattern is observed in the flow maps produced by the (GRP-2D [4]) numerical integration, using the configuration shown schematically in Fig. 1. The driver segment is 120 m long and its radial dimension is 6 m. The driven tube is 240 m long and of radius 1 m. A uniform grid of 0. 05 $\times$ 0. 05 m^2 square zones is used, corresponding 20 zones over the radial dimension of the tube—a rather fine resolution for an inviscid flow computation.

The simulation flow maps shown in Fig. 2 are taken at the early time $t = 40$ ms, and are nearly identical to later time maps, indicating a steady expansion flow through the sharp entrance. Note that these maps are on a sub-domain of the full computation domain, centered about the entrance to the long tube ($-2 < X < 2$ in X direction, and $0 < Y < 2$ in the radial direction). It seems the vena-contracta pattern corresponds to a minimal cross-section radius of 0.95 m, i.e. roughly 19 zones out of the 20 zones spanning the tube width. For choked flow and expansion to supersonic speed, this area ratio corresponds to a Mach number of about $M_3 = 1.38$.

At points further downstream the flow becomes almost one-dimensional. We have recorded X-wise flow profiles of cross-section averaged values, and we show the Mach number profiles at three times in Fig. 3 below. The profiles show a steady flow segment with $M \approx 1.38$ that increases with time to $X \approx 30$ at the latest time. The profile from that point on clearly shows a self-similar pattern, comprising of all elements depicted schematically in Fig. 1.

Furthermore, a comparison with the calculated self-similar profile at the latest time $t = 160$ is shown in Fig. 4. There is an approximate agreement here between the two Mach number profiles. Considering that the computational flow is not strictly one-dimensional and not exactly steady and isentropic at the entrance to the tube, the agreement is quite good. It clearly validates the approximate self-similar model.

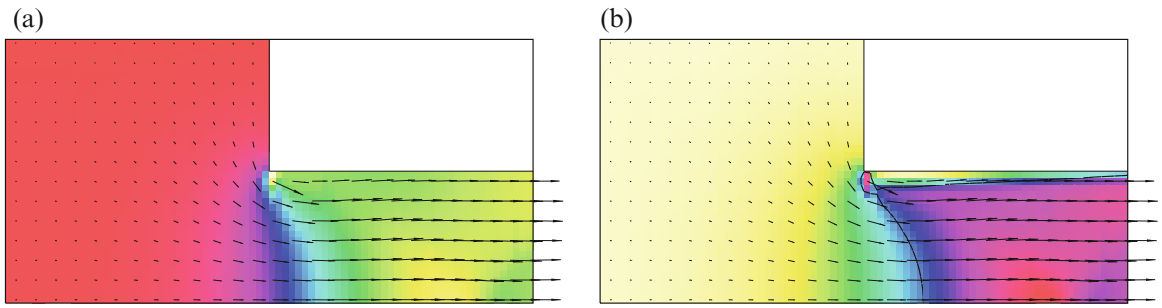

Fig. 2 Pressure and Mach number flow maps. $P_2 = 10$ $[MPa]$. Mach plot isoline corresponds to $M = 1$. (**a**) Isobar map. (**b**) Mach number map

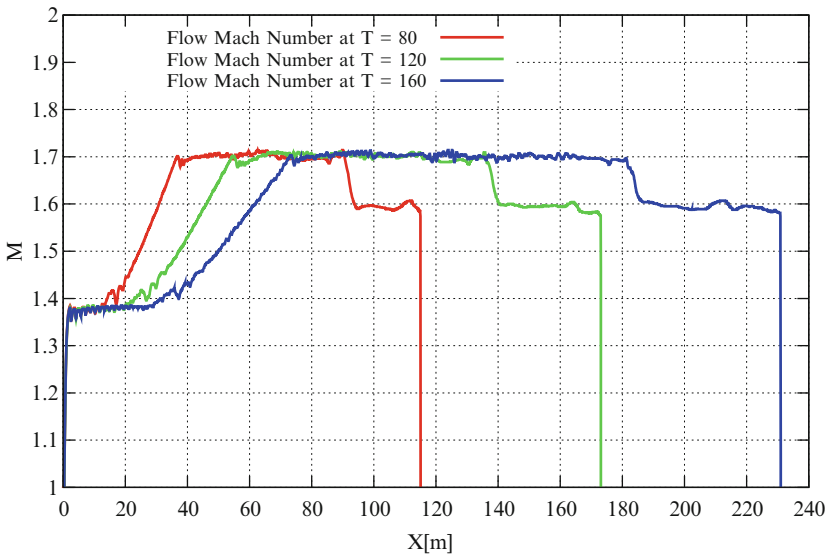

Fig. 3 Mach number flow profiles at times $t = 50, 120, 160$

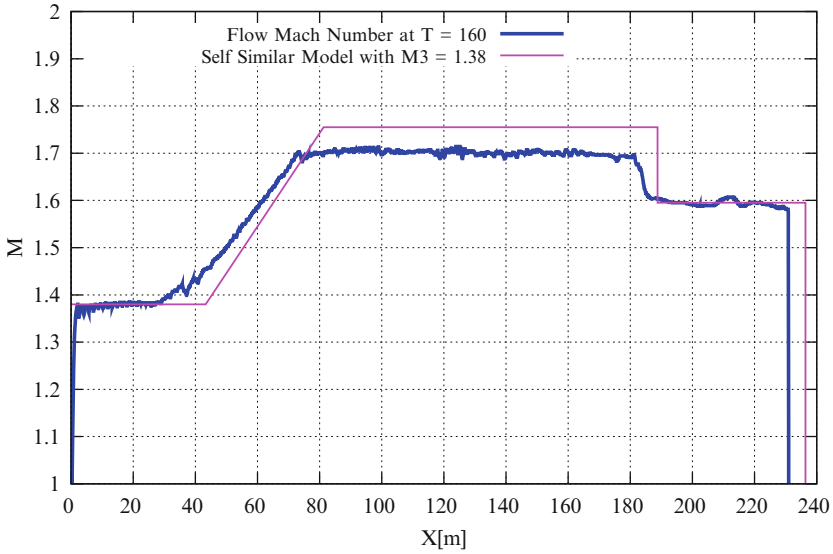

Fig. 4 Mach number flow profiles at time $t = 160$, compared to the self-similar model at $t = 160$

Concluding Remarks

The present model assumes that a nearly steady isentropic expansion flow evolves at the abrupt large area contraction from a very wide driver and a narrow long driven segment. By our model, at a point further downstream, where the flow becomes nearly one-dimensional, a self-similar pattern of simple waves evolves between the end of the steady flow and the front of the transmitted shock wave. The agreement between the self-similar model and an accurately computed profile (Fig. 4) is a validation of the model, while providing an explanation to the overall flow pattern in terms of basic fluid-dynamical theory (isentropic flow, simple waves, self-similar time-dependent flow).

References

1. Beck, W.H., Eitelberg, G., McIntyre, T.J., Baird, J.P., Lacey, J., Simon, H.: The high enthalpy shock tunnel in Göttingen. Proceedings of the 18th International Symposium on Shock Waves, July 21–26, 1991, Sendai, Japan
2. Yu, H.R.: Recent developments with gaseous detonation drivers for shock tunnel. In: Proceedings of the 24th International Symposium on Shock Waves, July 11–16, 2004, Beijing, China
3. Falcovitz, J., Igra, O.: Model for shock interaction with sharp area reduction. Proc. IMechE: Vol. 222 Part G: J. Aerospace Eng. **222**,789–800 (2008)
4. Ben-Artzi, M., Falcovitz, J.: Generalized Riemann Problems in Computational Fluid Dynamics. Cambridge University Press, London (2003)
5. Igra, O., Wang, L., Falcovitz, J.: Non-stationary compressible flow in ducts with varying cross-section. Proc. Instn. Mech. Eng. Part G **212**, 225–243 (1998)

Shock Waves Initiated by Optical Pulsing Discharge in the Supersonic Air Flow

Tatiana Bobarykina, Vladimir Chirkashenko, and Vladimir Yakovlev

The paper presents the method of the active action of the flow pattern near the flowed body. Input of the laser radiation energy is the promising technique of the action on the flow [1–2]. This is the convenient non-contact method of action. The area of energy input is dictated by the optical breakdown of the air in the needed point and conditions created for the effective absorption of the laser radiation energy in the formed plasma [3].

The purpose of this work is to obtain experimental data about shock waves and gas-dynamic parameters near the extended breakdown plasma in the supersonic air flow; to study interaction between the thermal wake and the shock-wave from the flowed body.

The supersonic stationary air flow corresponding to the Mach number Maxa $M = 1.36$ was organized in the wind tunnel; the profiled nozzle with the cut diameter $d_c = 50$ mm was applied. The experiments were carried out without Eifel chamber, the pressure in the settling chamber was $P_o = 0.3$ MPa (design flow mode, flow density 1.8 kg/m^3) and 0.5 MPa (off-design flow mode, flow density in the focusing area 2.8 kg/m^3). For the flow structure visualization, a system of shadow and Schlieren measurements was utilized.

The optical breakdown was formed at the focusing ($f = 63$ mm) of the impulse-periodical radiation of a CO_2 laser with the mechanical Q-switching. The average generation power was up to 3.5 kW, pulse repetition rate from 54 to 150 kHz, peak power—up to 200 kW. The laser radiation was input perpendicularly to the supersonic flow velocity vector. The diameter of the radiation spot in the lens focus was about 100–150 mm, which provided the specific power in the optimum operation mode of the laser of about $(7–15) \times 10^8$ W/cm^2.

Figure 1 shows the flow pattern obtained by the Schlieren method. The photos show the shock waves from the laser sparkle and low-density areas which result from the absorption of the CO_2 laser energy by the breakdown plasma. Ahead of the energy-outflow area, the head shock wave forms.

With the shot exposition time (150 ns), it is possible to see the dynamics of propagation of individual low-density areas in the supersonic flow. The wake structure consists of localized almost-spherical low-density disturbance areas; their size slightly varies downstream. The distance between the cavities decreases as the pulse repetition frequency rises.

Figure 2a shows the flow with the laser plasma moving around the model (the flow pattern averaged by 30 pulses), Fig. 2b presents a shot of the same, the pulse repetition frequency is 150 kHz. In the supersonic flow, along with the shock waves generated by the model, there is a head shock wave forming ahead of the energy-release area; it is an envelope for the shock waves generated by periodical optical discharges as the explosion center is shifted downstream with the flow speed.

Both shock waves from the model registered as the energy release is missing in the studied area, are not observed below the thermal wake if the laser radiation energy is supplied into the flow. It means that high density gradients really undergo changes (reduce) and probably quite dramatic weakening of the shock waves takes place as they are interacting with the thermal wake.

T.Bobarykina (✉)
Physics Department, Novosibirsk State University, Novosibirsk, Russia

Lab 5, Hypersonic Technologies, Khristianovich Institute of Theoretical and Applied Mechanics SB RAS, Novosibirsk, Russia
e-mail: bobarykina@ngs.ru

V. Chirkashenko • V. Yakovlev
Lab 5, Hypersonic Technologies, Khristianovich Institute of Theoretical and Applied Mechanics SB RAS, Novosibirsk, Russia

G. Ben-Dor et al. (eds.), *30th International Symposium on Shock Waves 1*, DOI 10.1007/978-3-319-46213-4_117

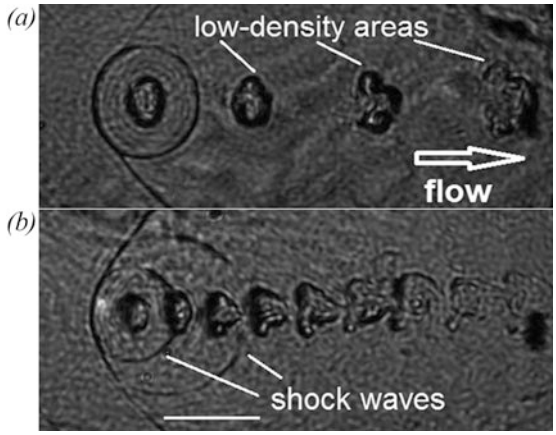

Fig. 1 Schlieren images of the flow. The pulse-periodical radiation frequency: (**a**) −60 kHz, (**b**) −150 kHz

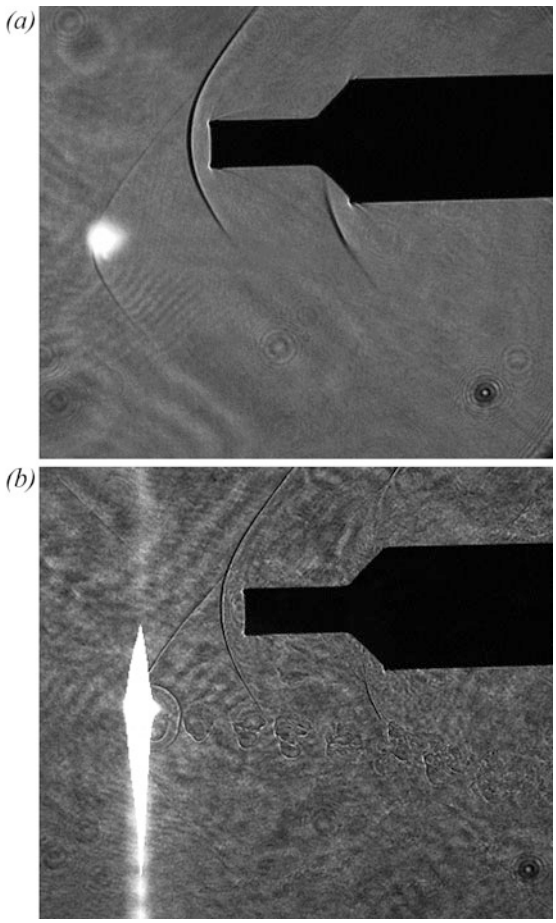

Fig. 2 Schlieren images of the flow. (**a**) Shot exposure time 200 microseconds, (**b**) shot exposure time 150 ns

References

1. Georgievskij, P.Y., Levin, V.A.: Supersonic flow around the bodies at the presence of external sources of heat release. Lett. J. Appl. Phys. **14**(8), 684–687 (1988)
2. Tret'jakov, P.K., Garanin, A.F., Grachevв, N., Krajnev, V.L., Ponomarenko, A.G., Ivanchenko, A.I., Yakovlev, V.I.: Control of the supersonic flow around bodies with the powerful optical discharge. DAN **351**(3), 339–340 (1996)
3. Malov, A.N., Orishich, A.M., Bobarykina, T.A., Chirkashenko, V.F.: Absorption of CO_2-laser radiation in the optical discharge plasma in a supersonic air flow. In: XV International Conf. on Methods of Aerodynamical Research, Novosibirsk, 2010r. Part 2. p. 157

Part X

Shock Wave Interaction with Obstacles and Porous Media

Stationary Regular Reflection: Viscous and Rarefaction Effects

Georgy Shoev, A.A. Kokhanchik, M. Yu. Timokhin, and Yevgeny A. Bondar

Introduction

After shock waves were discovered, many investigations were performed to study their interaction and internal structure. It is well known that the classical Rankine–Hugoniot relations predict only the flow parameters behind the shock wave, but provide no information about the shock wave structure. The problem of the internal structure of the shock wave, which became the classical problem of the kinetic theory of gases, was analytically solved by Becker [1] on the basis of the Navier–Stokes equations. This solution describes the internal structure of the shock wave; in particular, it predicts a local peak of entropy. However, theoretical investigations of shock wave interaction and reflection were usually performed in the inviscid approach, i.e., the internal structure of shock waves was ignored. Half a century after Mach's discovery of two types of shock wave reflection, von Neumann proposed two-shock and three-shock theories [2] based on the Rankine–Hugoniot relations for the description of flow parameters in the vicinity of shock wave branching points. Configurations predicted by these theories do not describe the internal structure of the domain of shock wave interaction either.

An inviscid solution in the vicinity of the reflection point at regular reflection can be obtained analytically and consists of three zones with constant parameters, which are separated by two infinitely thin discontinuity lines: incident and reflected shock waves. In the case of a viscous gas, these shock waves have a finite thickness, and a viscous flow region with a size of approximately ten mean free paths is observed near the reflection point; moreover, there is a wake with a length of about 100 mean free paths downstream of this region [3]. It should be noted that this problem in a certain sense is an extension of the classical problem of the kinetic theory of gases about the structure of a plane shock wave. However, the present problem is more complicated due to two-dimensional effects. As in the problem of the shock wave structure, viscosity plays a key role in the present problem. At high Mach numbers, effects of rarefaction and thermal nonequilibrium may also be important. The goal of this work is a numerical analysis of the influence of the abovementioned effects on the flow near the reflection point by means of comparisons of results simulated with the use of different mathematical models: Navier–Stokes equations, regularized 13-moment Grad equations (R13), and Boltzmann equation (Direct Simulation Monte Carlo (DSMC) computations). The use of these models allows evaluation of the effects of viscosity, heat transfer, and thermal nonequilibrium on the flow in the vicinity of the reflection point.

Problem Formulation and Numerical Technique

Interaction of oblique shock waves arising in a supersonic steady two-dimensional monatomic gas flow between two symmetrically located wedges is considered. Two different (regular and Mach) shock wave configurations can be

G. Shoev • A.A. Kokhanchik
Novosibirsk State University, 2 Pirogova Street, 630090 Novosibirsk, Russia

Khristianovich Institute of Theoretical and Applied Mechanics SB RAS, 4/1 Institutskaya Street, 630090 Novosibirsk, Russia

M. Yu.Y. Timokhin
Novosibirsk State University, 2 Pirogova Street, 630090 Novosibirsk, Russia

Moscow State University, 119992 Moscow, Russia

Y.A. Bondar (✉)
Khristianovich Institute of Theoretical and Applied Mechanics SB RAS, 4/1 Institutskaya Street, 630090 Novosibirsk, Russia

Novosibirsk State University, 2 Pirogova Street, 630090 Novosibirsk, Russia
e-mail: bond@itam.nsc.ru

G. Ben-Dor et al. (eds.), *30th International Symposium on Shock Waves 1*, DOI 10.1007/978-3-319-46213-4_118

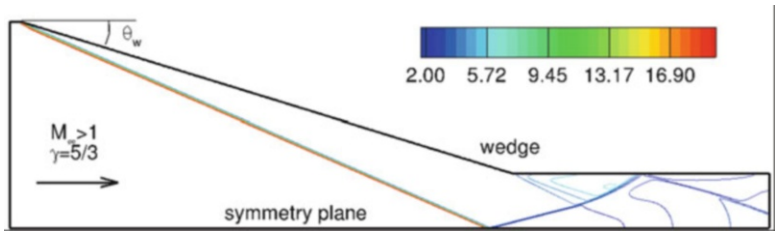

Fig. 1 Regular reflection in the plane of symmetry. $M_\infty = 20$, $\gamma = 5/3$, $\theta_w = 17.0619°$

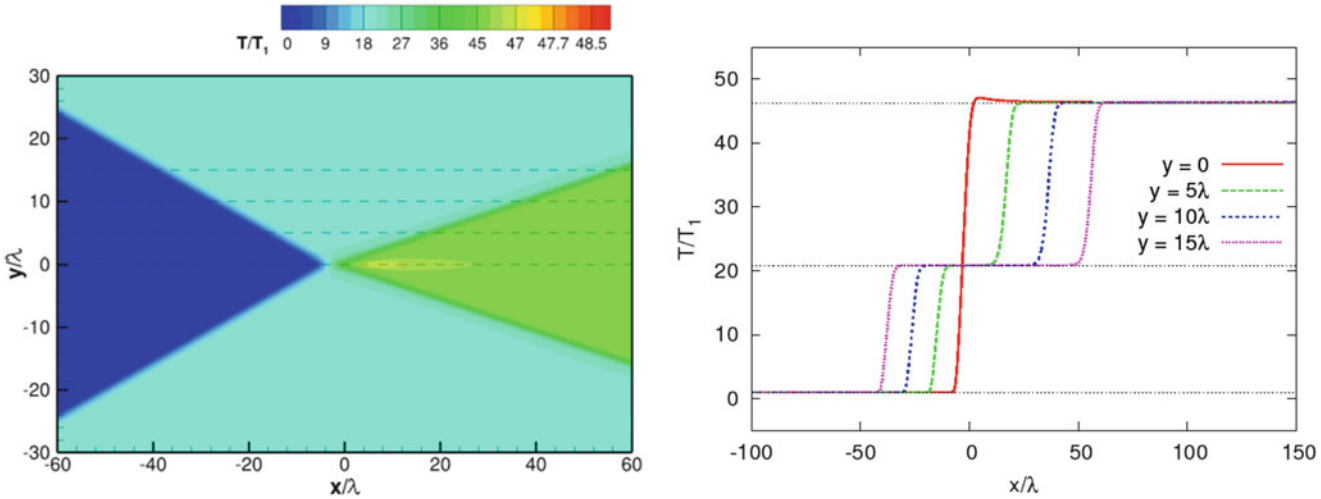

Fig. 2 Temperature flowfield and profiles in the NS solution. $M_\infty = 20$, $\gamma = 5/3$, $\theta_w = 17.0619°$

formed in such flows [4, 5]. The case of regular reflection is analyzed in the present work (Fig. 1).

The DSMC computations were performed by a SMILE software system [6] developed at ITAM and based on the majorant frequency scheme [7].

The Navier–Stokes (NS) computations were performed by a CFS3D [8] flow solver (developed at ITAM). CFS3D uses a time-explicit shock-capturing code based on fifth-order WENO reconstruction [9] of convective fluxes and central fourth-order approximation of dissipation terms.

The R13 system was solved numerically by an in-house code developed at the Moscow State University. Godunov's method having an elevated order of accuracy [10] and involving linear reconstruction of flow parameters was chosen as a numerical method for the main flow domain. The fluxes of conservative variables through the faces of the control volume were calculated by means of the approximate solution of the Riemann problem by the HLL method [11, 12].

All numerical simulations were performed on a very fine mesh that allowed full spatial resolution of the internal structure of the shock waves. The left boundary of the computational domain (Fig. 1) was a supersonic inflow with the freestream flow parameters imposed. The right boundary of the domain was placed far enough downstream to ensure supersonic outflow conditions there, which can be seen in Fig. 1. At the lower boundary of the domain, boundary conditions of symmetry were used. A boundary layer was ignored in order to provide the same incident shock wave angle in all simulations (non-permeability boundary conditions for NS and R13 and specular reflection for DSMC were used). The computations were started with a uniform supersonic flow filling the entire computational domain. The computation was then continued until a steady state was achieved.

Computations were performed in a monatomic gas (argon, $\gamma = 5/3$) at the freestream Mach number $M_\infty = 20$ and the wedge angle $\theta_w = 17.0619°$. The conditions were chosen specially to provide the configuration of regular reflection and the Mach number normal to the incident shock wave M_n equal to 8 (the value of 8 is a common case in calculations of the shock wave structure).

Results

Figures 2, 3, and 4 (left) show the temperature flowfields predicted by the NS, DSMC, and R13 solutions, respectively. The spatial coordinates are normalized to the mean free path in the free stream, and the temperature is normalized to the freestream temperature. It is seen that the DSMC method and R13 equations predict an appreciably greater thicknesses of the incident and reflected waves than the NS equations owing to the thermal nonequilibrium

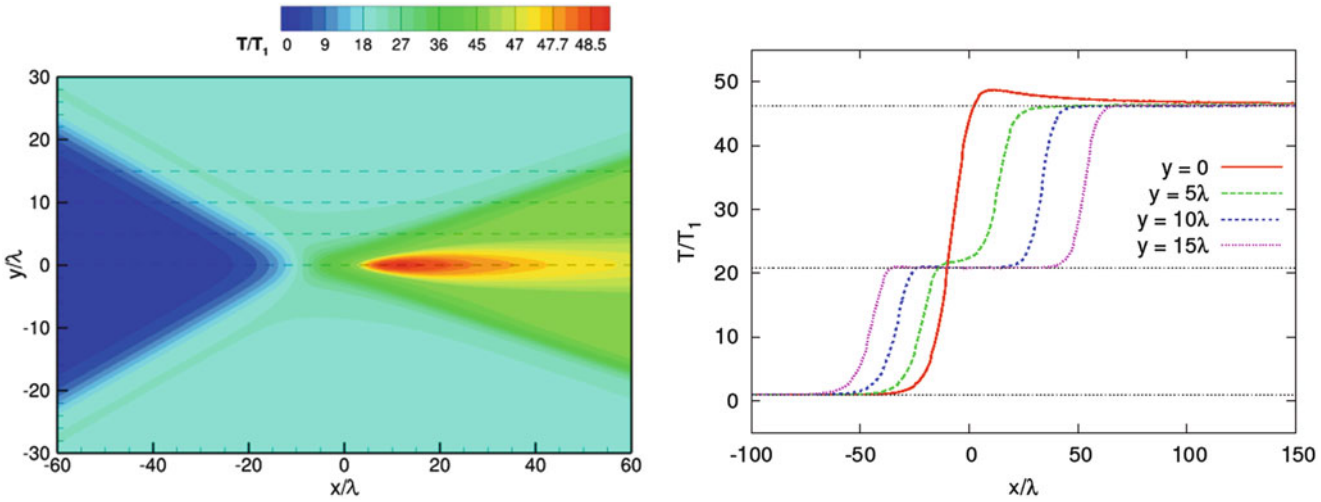

Fig. 3 Temperature flowfield and profiles in the DSMC solution. $M_\infty = 20$, $\gamma = 5/3$, $\theta_w = 17.0619°$

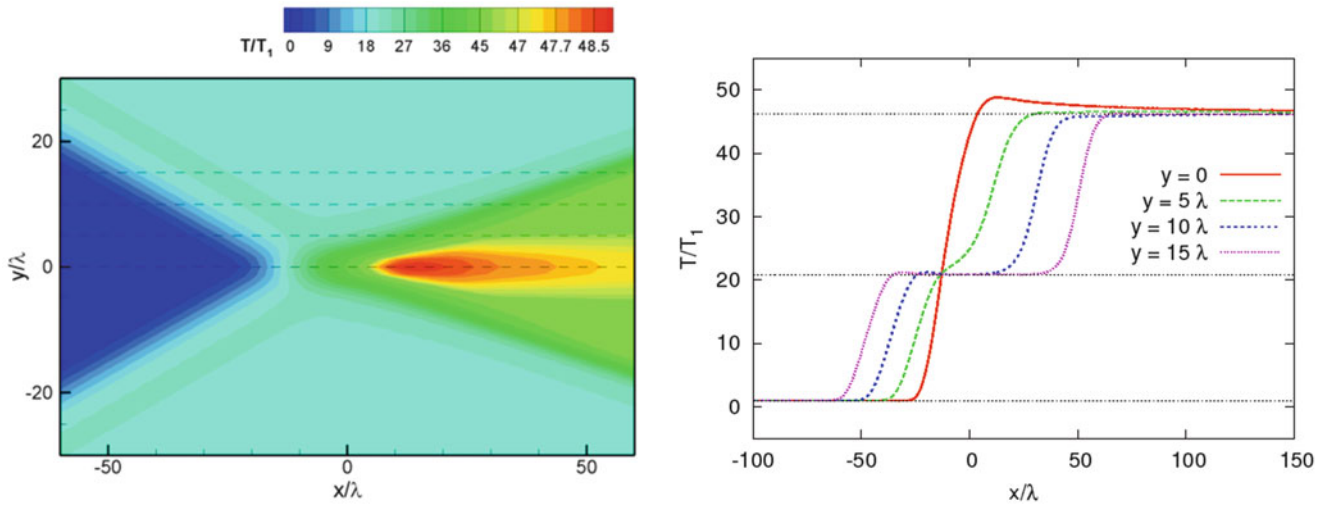

Fig. 4 Temperature flowfield and profiles in the R13 solution. $M_\infty = 20$, $\gamma = 5/3$, $\theta_w = 17.0619°$

effects taken into account. The temperature fields in the DSMC and R13 solutions have a clearly expressed temperature peak in the wake behind the reflection point.

Figures 2, 3, and 4 (right) show the temperature profiles along the horizontal lines $y = \{0\lambda, 5\lambda, 10\lambda, 15\lambda\}$ (shown by the dashed lines in Figs. 2, 3, and 4, left). The horizontal dotted lines show the theoretical values of macroparameters derived from the Rankine–Hugoniot relations. It is seen that the temperature in the DSMC and R13 results reaches a constant value (behind the reflected wave front) along the plane of symmetry at a distance of about 150λ from the origin of the coordinate system, while the constant temperature in the NS simulations is reached much faster (about 25λ). In the plane of symmetry, the temperature profiles predicted by the DSMC and R13 solutions have considerable peaks whose magnitude (relative to the value behind the reflected wave front) is severalfold higher than the corresponding value in the NS computations. At a certain distance from the plane of symmetry, long-time equalization and temperature peaks are not observed. In this case, there is an intermediate plateau on the profiles (corresponding to the zone behind the incident wave front). A significant difference between the shock thicknesses in the DSMC and NS simulations should also be noted.

As the flow structure along the plane of symmetry resembles the structure of a one-dimensional shock wave, these configurations are compared further in the chapter. The density profiles for the one-dimensional shock wave with the Mach number equal to 8 (left) and the flow along the plane of symmetry in a two-dimensional problem of regular

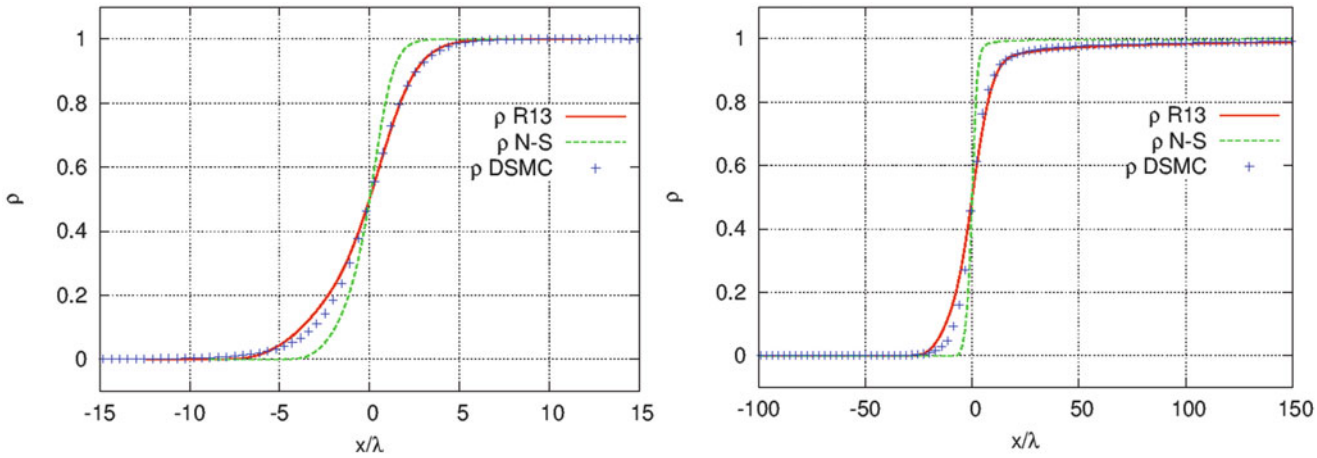

Fig. 5 Density profiles in the one-dimensional shock wave (*left*) and in the flow along the plane of symmetry (*right*)

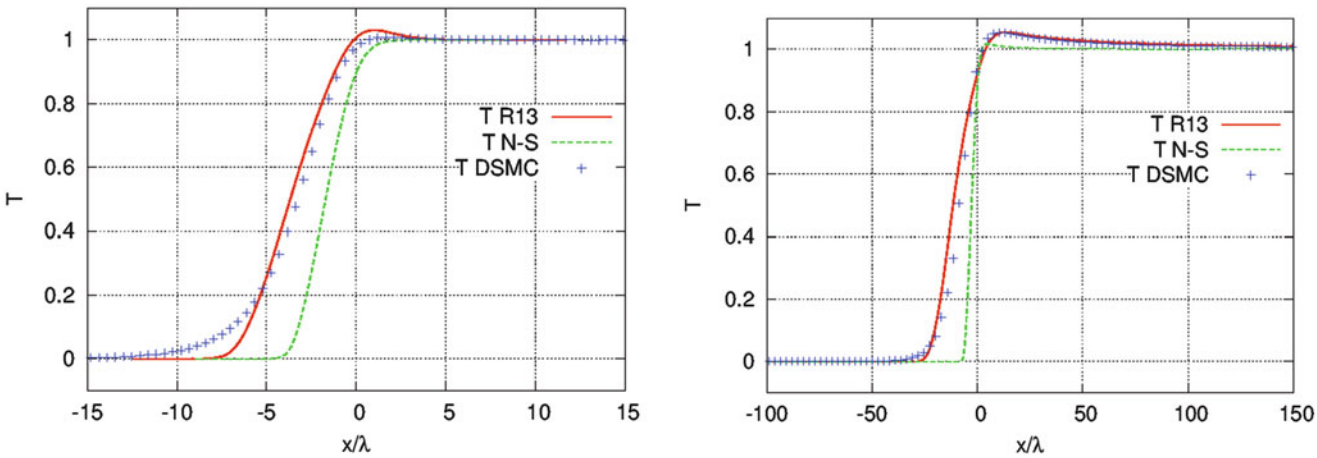

Fig. 6 Temperature profiles in the one-dimensional shock wave (*left*) and in the flow along the plane of symmetry (*right*)

reflection (right) are compared in Fig. 5. Figure 6 shows a similar comparison for the temperature profiles. The density and temperature are normalized by the formulas

$$\overline{\rho} = \frac{\rho - \rho_1}{\rho_2 - \rho_1}, \quad \bar{T} = \frac{T - T_1}{T_2 - T_1}$$

(the subscripts 1 and 2 are used to indicate the values in the free stream and behind the front of the one-dimensional wave or behind the front of the reflected wave in the case of regular reflection, respectively). For convenience, we use the term "front" to indicate the region where the macroparameter values differ appreciably from 0 and 1 both for the plane wave and for regular reflection. It is seen from the figures that the thickness of the one-dimensional shock wave in the DSMC and R13 solutions is smaller than ten mean free paths, while the thickness of the "front" in the flow along the plane of symmetry is significantly greater (as was previously noted, the density and temperature reach constant values at a distance of about 150λ from the origin of the coordinate system). The NS equations predict a much smaller thickness of the "front." In the case of a one-dimensional shock wave, there is a small temperature peak in the front (about 1 % with respect to the value behind the wave front) in the temperature profiles obtained by the DSMC method. The temperature in the R13 solution exceeds this peak (about 2–3 %), and the NS solution does not contain this peak at all. For the flow along the plane of symmetry, all methods predict a temperature peak, and its value in the DSMC and R13 solutions is about 5 %, which is substantially greater than the peak predicted by the NS solution (about 2 %).

A similar comparison for the temperature components T_x, T_y, and T_z in the DSMC and R13 solutions is shown in Fig. 7.

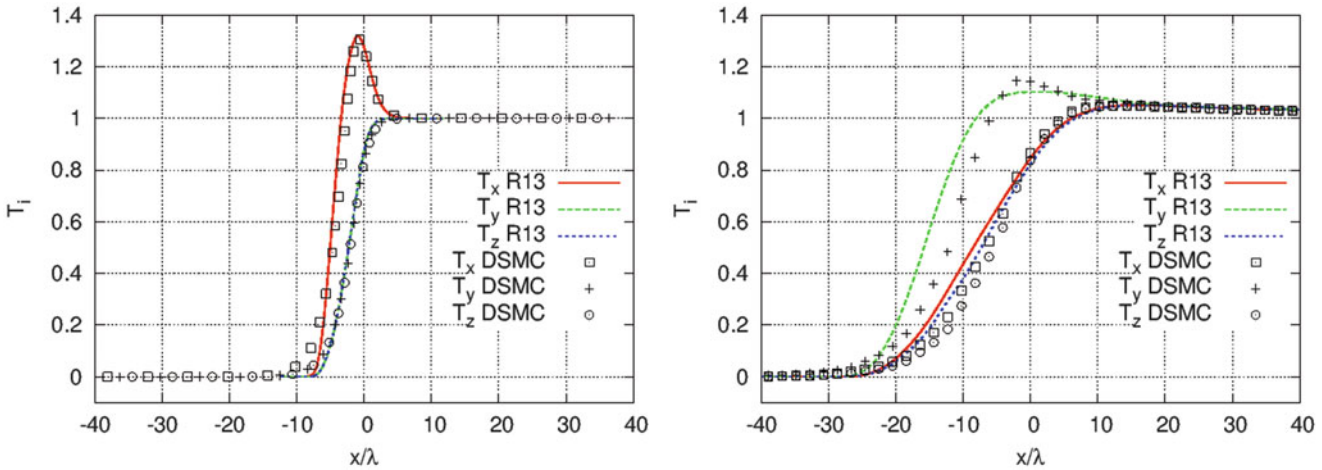

Fig. 7 Profiles of the temperature components in the one-dimensional shock wave (*left*) and in the flow along the plane of symmetry (*right*)

In the case of the one-dimensional shock wave, there is a considerable peak in the temperature profile T_x, while the temperature components T_y and T_z are identical owing to symmetry. A principal difference of the flow along the plane of symmetry in the two-dimensional problem from the one-dimensional shock wave is the fact that the temperature component T_x is monotonic and coincides with T_z except for a small region in the upper part of the wave front; T_y has a significant peak in the wave front, which is caused by the presence of a tangential component of velocity with respect to the wave.

Conclusions

The internal structure of the region of shock wave interaction is numerically studied. A significant effect of viscosity and heat transfer on the internal structure of this region is demonstrated. The numerical results show that the vicinity of the reflection point is a zone of a strongly nonequilibrium flow, which is not described by the continuum approach. The DSMC method and R13 equations predict appreciably greater thicknesses of the reflection zone than the NS equations owing to the thermal nonequilibrium effects. The flow along the symmetry plane is qualitatively different from the 1D plane shock profile, as is shown by the distinction in the "front" thicknesses and temperature components.

References

1. Becker, R.: Stosswelle und detonation. Z. Phys. **8**(1), 321–362 (1922)
2. von Neumann, J.: Oblique reflection of shocks. Explosive Research Report No. 12. Navy Dept. Bureau of ordinance, Washington (1943)
3. Khotyanovsky, D., Bondar, Y., Kudryavtsev, A., Shoev, G., Ivanov, M.: Viscous effects in steady reflection of strong shock waves. AIAA J. **47**, 1263–1269 (2009)
4. Ben-Dor, G.: Oblique shock wave reflections. In: Ben-Dor, G., Igra, O., Elperin, E. (eds.) Handbook of shock waves, vol. 2. Academic, New York (2001). Chap. 8
5. Hornung, H.: Regular and Mach reflection of shock waves. Annu. Rev. Fluid Mech. **18**(1), 33–58 (1986)
6. Ivanov, M.S., Markelov, G.N., Gimelshein, S.F.: Statistical simulation of reactive rarefied flows: numerical approach and applications. AIAA Paper **98** (1998)
7. Ivanov, M., Rogasinsky, S.: Analysis of the numerical techniques of the direct simulation monte carlo method in the rarefied gas dynamics. Sov. J. Numer. Anal. Math. Modell. **3**, 453–465 (1988)
8. Kudryavtsev, A., Khotyanovsky, D.: Numerical investigation of high speed free shear flow instability and mach wave radiation. Int. J. Aeroacoust. **4**(3–4), 325–344 (2005)
9. Jiang, G.S., Shu, C.-W.: Efficient implementation of weighted ENO schemes. J. Comput. Phys. **126**, 202–228 (1996)
10. Ivanov, I.E., Kryukov, I.A.: Quasi-monotonous higher order accuracy method for numerical simulations of internal and jet flows of inviscid gas. Mat. Modelir. **8**(6), 47–55 (1996) (in Russian)
11. Gu, X.J., Emerson, D.R.: A computational strategy for the regularized 13 moment equations with enhanced wall boundary conditions. J. Comput. Phys. **225**, 263–283 (2007)
12. Harten, A., Lax, P.D., van Leer, B.: On upstream differencing and Godunov-type schemes for hyperbolic conservation laws. SIAM Rev. **25**, 35–45 (1983)

Simplified Models of Shock Waves Interaction with Rigid and Flexible Obstacles

V.R. Feldgun, Y.S. Karinski, and D.Z. Yankelevsky

Introduction

It is well known that explosions and primarily resulting shock waves can threaten people's lives as well as the security of communications, transport and services infrastructure, etc. The models and the corresponding equations, which describe the above phenomena, are complex and are difficult to be worked out and modified to analytical solutions and therefore various numerical methods should be used. In the general case, these methods produce results that are in excellent agreement with experimental data, but because of the high level of complexity and the time-consuming computation, such simulations are often not suitable for daily usage, especially during the early stages of a given problem investigation. Alternative simplified analysis methods are most attractive and may well suit this purpose. This chapter deals with some simplified models of shock waves interaction with rigid and flexible obstacles that have been developed at the National Building Research Institute during a long-term research. This chapter focuses on shock wave interaction with obstacles and their response due to confined or partially confined internal explosions.

Results

Consider an interior explosion within a room with an opening (Fig. 1a) that may be initially closed with a heavy cover (Fig. 1b, c). From the foregoing experimental and theoretical analysis, it is known that the process of a partially confined explosion is composed of two stages: the very short nonstationary phase and the relatively long-duration process of the quasi-stationary pressure relief. The initial internal gas pressure induced by a nonstationary phase may be predicted, for example, by an analytical approach developed in [1, 2].

The approach derives the initial pressure p_b and density ρ_b for the current pressure $p(t)$ and density $\rho(t)$ at the quasi-stationary pressure relief phase. An effective simplified model with lumped parameters based on the Bernoulli equation has been developed for the quasi-stationary phase of detonation products outflow. It is assumed that after the end of the nonstationary explosion phase the detonation products can be treated as a perfect gas with constant specific heat capacities; the flow is barotropic, isentropic (reversible and no heat transfer). It is also assumed that the gas within the room can be treated as spatially lumped (i.e., that gas properties within the room vary only with time). The differential equation of the gas mass $M(t)$ filling the room can be written as:

$$dM(t)/dt = \rho_\infty V(t) S_\Omega \qquad M(t)\big|_{t=t_0} = \rho_b \Theta, \qquad (1)$$

where $p_\infty = 1$ bar, $\rho_\infty = 0.001225$ g/cm^3 are pressure and density of the undisturbed air (at atmospheric pressure); Θ is the room volume, and $V(t)$ is the outflow velocity through the surface Ω. The area S_Ω of the surface Ω is constant and equals to the vent cross section area in the case of an opening without a cover or depends on the cover displacement $w(t)$ otherwise. The time t_0 is the time at which the nonstationary phase of the process ends and when the phase of quasi-stationary gas outflow and pressure relief from the room with initial pressure starts. According to the Bernoulli equation, the outflow velocity $V(t)$ is calculated as follows:

V.R. Feldgun (✉) • Y.S. Karinski
National Building Research Institute, Technion, Haifa 32000, Israel
e-mail: aefeldgo@technion.ac.il

D.Z. Yankelevsky
Faculty of Civil and Environmental Engineering, Technion, Haifa 32000, Israel

G. Ben-Dor et al. (eds.), *30th International Symposium on Shock Waves 1*, DOI 10.1007/978-3-319-46213-4_119

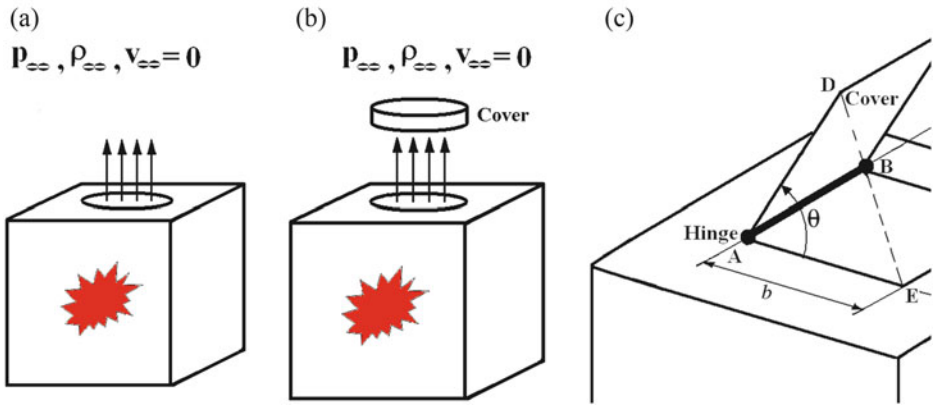

Fig. 1 Vented interior explosions—without cover (**a**); circular cover (**b**); hinged cover (**c**)

$$V(t) = \begin{cases} \sqrt{2\gamma p_\infty/((\gamma-1)\rho_\infty)\left[(p(t)/p_\infty)^{(\gamma-1)/\gamma}-1\right]}, & p(t) \geq p_\infty(2/(\gamma+1))^{-\gamma/(\gamma-1)} \\ \sqrt{\gamma p_\infty/\rho_\infty (p(t)/p_\infty)^{(\gamma+1)/\gamma}}(2/(\gamma+1))^{(\gamma+1)/(2(\gamma-1))}, & p(t) < p_\infty(2/(\gamma+1))^{-\gamma/(\gamma-1)} \end{cases}, \quad (2)$$

where $\gamma = C_P/C_V$ is the ratio of the specific heat capacities at constant pressure and volume.

The integration of Eq. (1) in view of Eq. (2) yields the mass time history $M(t)$. The corresponding pressure time history is calculated according to the Poisson's adiabate as:

$$p(t) = p_\infty(\rho(t)/\rho_\infty)^\gamma = p_\infty(M(t)/(\Theta\rho_\infty))^\gamma. \quad (3)$$

When $t > t_0$ the cover with mass m separates from the vessel and moves along the z-axis direction under the action of the pressures $p(t)$ and $p_e(t)$:

$$md^2w(t)/dt^2 = (p(t) - p_e(t))S, \quad w(t)|_{t=t_0} = 0, \quad dw(t)/dt|_{t=t_0} = 0, \quad (4)$$

where $p(t)$ and $p_e(t)$ are the pressures on the inner and outer cover surfaces, respectively, and S is the cover area:

$$p_e(t) = p_\infty + \rho_\infty \dot{w}(t)c_\infty, \quad c_\infty = \sqrt{\gamma p_\infty/\rho_\infty}. \quad (5)$$

Application of the Simplified Model to Simulation of Partially Confined Explosions

The following example [3] demonstrates the effective application of the developed simplified model to simulate cases of partially confined explosions. Figure 2a shows the explosion simulation result of 1.1 kg PETN in a container that is composed of a cylindrical chamber to which a circular duct is attached. Figure 2b shows the pressure-time history obtained with AUTODYN numerical simulations for different vent areas.

The horizontal line corresponds to the gas pressure in the case of fully confined explosion. The smooth plotted curves are the pressure decay calculation results according to the above presented simplified method. Figure 2b shows that all the curves that correspond to different values of the venting area intersect at a common point. This point corresponds to the gas pressure level. It is the same pressure in the cases of fully confined explosion and any partially confined explosion. Hence, the gas pressure does not depend on the venting area.

Translation Motion of the Cover Due to a Confined Explosion: Comparison with AUTODYN Solution

Consider the case of a cylindrical TNT charge that explodes at the center of a cylindrical rigid-walled chamber with an opening. The vent is blocked by a circular cover with the mass m. The parameters of the problem are shown in Fig. 3a. The calculations were performed both with the developed simplified approach (Eqs. (1)–(5)) and with a 2D axi-symmetrical numerical model using AUTODYN. Figure 3a demonstrates the time history of the rigid cover

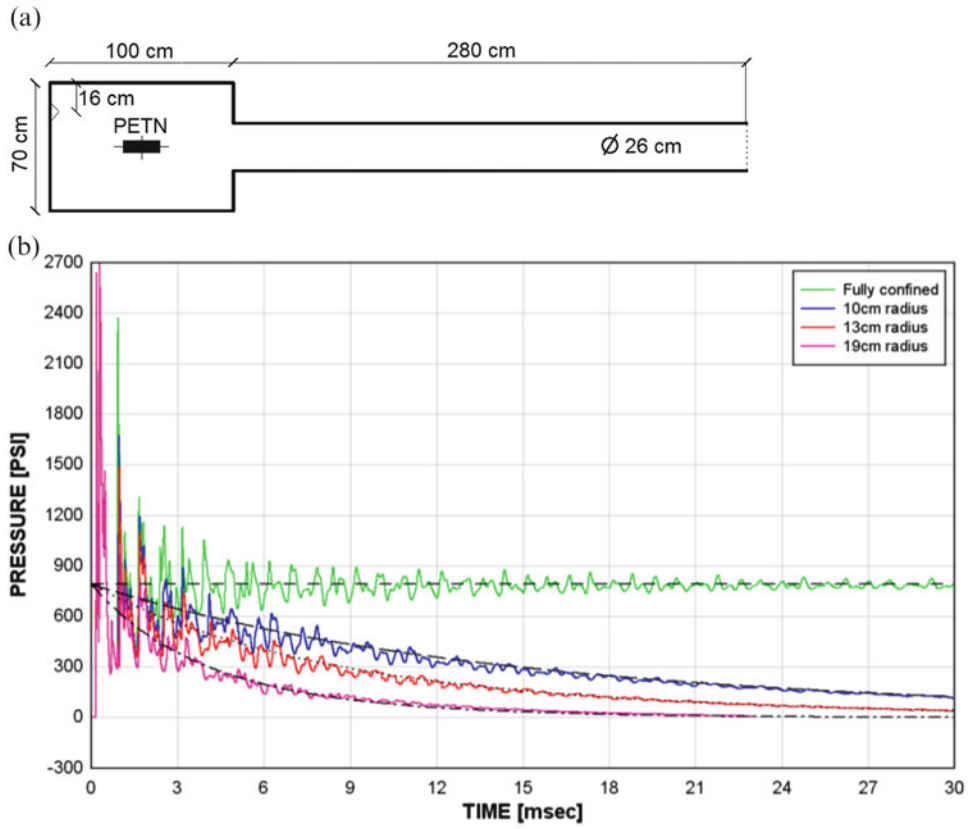

Fig. 2 Simulation of partially confined explosion

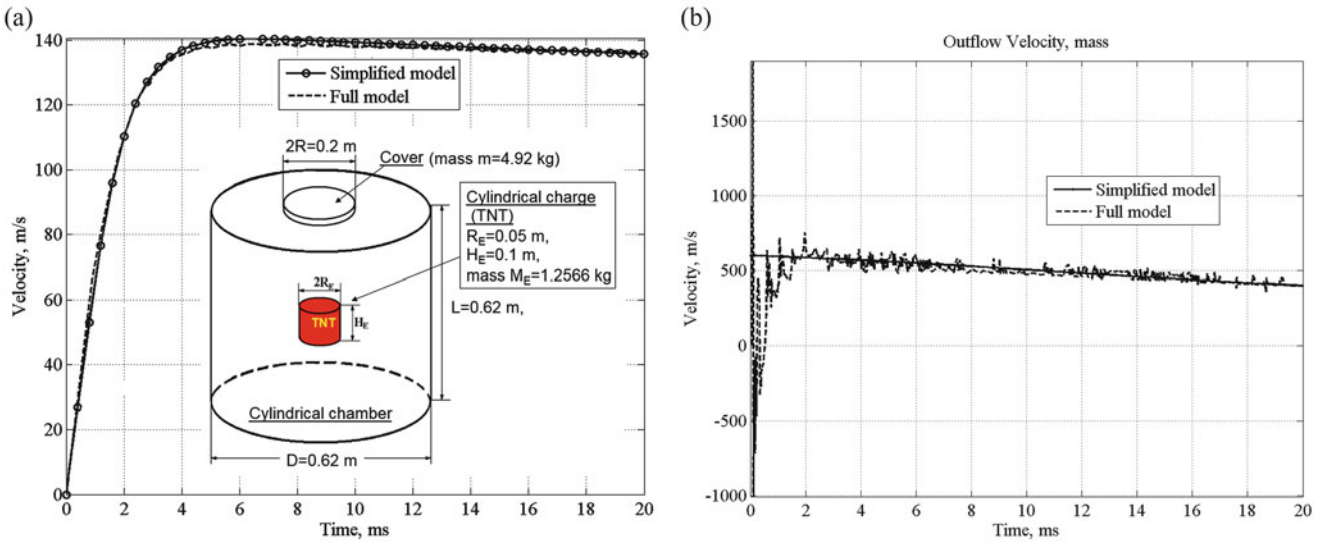

Fig. 3 Time histories—cover velocity (**a**); outflow velocity (**b**)

motion velocity. The gas dynamics of the detonation products outflow from the chamber is shown in Fig. 3b which demonstrates the time history of the gas outflow velocity at the center of the vent area. A good agreement is obtained between the numerical full simulation of the model and the simplified approach calculations.

Translation Motion of the Cover: Comparison with Experiment

The experimental results [4] of a cover separation from a gas-filled high pressure vessel (Fig. 4a) were compared with full 2-D simulations and with the present model calculations

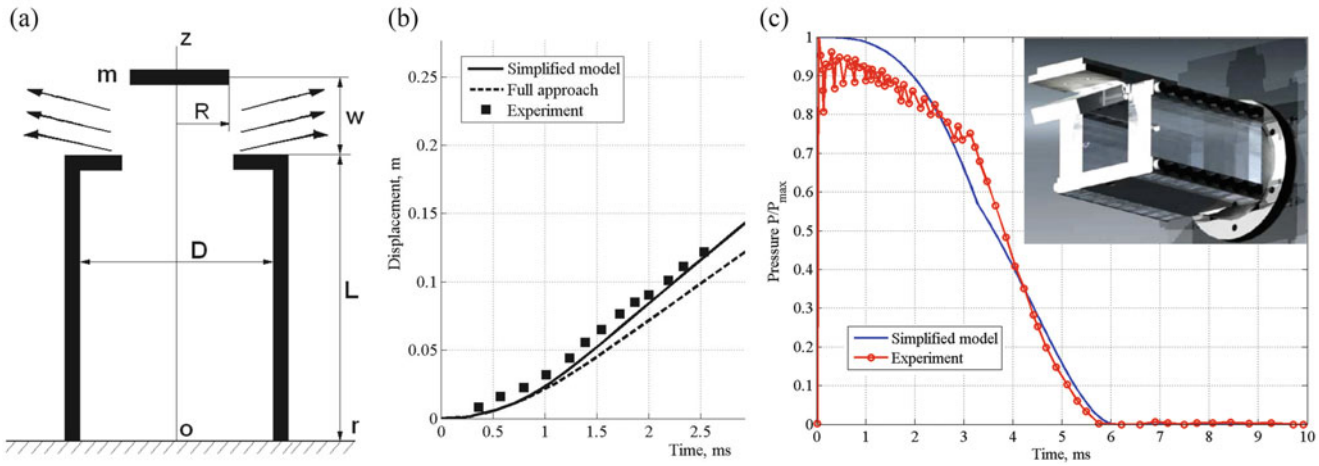

Fig. 4 Translation motion (**a**, **b**) and rotational motion of the hinged cover (**c**)

in order to evaluate the proposed simplified model. The problem parameters correspond to the experimental conditions [4], (Fig. 4a): $L = 20$ cm, $L/D = 2.86$, $m = 100$ g, $p = 17$ bar, $\rho = 9.76 \times 10^{-3}$g/cm^3, $\gamma = 1.4$. Comparison of the calculated and experimental results is given in Fig. 4b which demonstrates the time history of the cover displacement.

A good agreement is shown between the calculation that was performed by the full model (2D-simulation) and the prediction results of the simplified approach as well as with the experimental results.

Rotational Motion of the Hinged Door: Comparison with the Shock Tube Experiment

Consider a movable hinged door mounted at the end (exit) of a conventional shock tube, subjected to an impact of a planar incident shock wave according to experimental studies [5]. In the case of a hinged vent cover (Fig. 1c), the cover can only rotate about the axis and the following equation of motion is used instead of Eq. (4).

$$Jd^2\theta/dt^2 = N(t), \quad \theta|_{t=t_0} = 0, \quad d\theta/dt|_{t=t_0} = 0, \qquad (6)$$

where θ is the instantaneous angle of rotation (the angle between the vent opening and the hinged cover); J is the moment of inertia about the axis of rotation AB; N is the resultant moment exerted by all external forces acting on the cover about the fixed axis AB. It is assumed that the current venting area S_Ω is the gap area between the edges of the cover and the vent opening. The gap, as shown in Fig. 1c, is formed from one rectangular region, based on the cover edge EF opposite to the hinge AB and two triangular regions, based on the pivoting edges of the cover. In the case of a square-shaped cover (Fig. 1c) the area S_Ω of the surface Ω depends on the angle θ as follows:

$$S_\Omega = \begin{cases} 2S_{\mathrm{ADE}} + S_{\mathrm{CDEF}} = b^2\sin\theta + 2b^2\sin(\theta/2), & \text{if } \theta < \pi/2 \\ \pi D^2/4, & \text{if } \theta \geq \pi/2 \end{cases}. \qquad (7)$$

The resultant moment N is calculated as follows:

$$N(t) = (p(t) - p_{\mathrm{e}}(t))\, b^2(b/2) = (p(t) - p_{\mathrm{e}}(t))\, b^3/2. \qquad (8)$$

Figure 4c shows the time history of the normalized pressure $P/P_{\max}$ acting on the back of the rotating aluminum door ($m = 0.376$ kg) in the case of the incident shock wave Mach number $M_{\mathrm{is}} = 1.1$ where $P_{\max}$ is the overpressure behind the reflected shock wave from the closed door. Based on calculations using the idealized 1-D shock tube theory, $P_{\max} - p_\infty = 0.54$ bar.

Application of the Gas Pressure to Simulation of Response of Flexible Structures due to a Confined Explosion

Consider a one-dimensional problem of the dynamic response of a spherical elastic-plastic shell to the internal blast pressure $P(t)$. The calculations were performed for $h_{\mathrm{S}} = 1.3486$ cm (thickness), $R_{\mathrm{S}} = 17.324$ cm (median surface radius), $E_{\mathrm{S}} = 2.1 \times 10^6$ bar (Young's modulus), $\mu_{\mathrm{S}} = 0.3$ (Poisson's ratio),

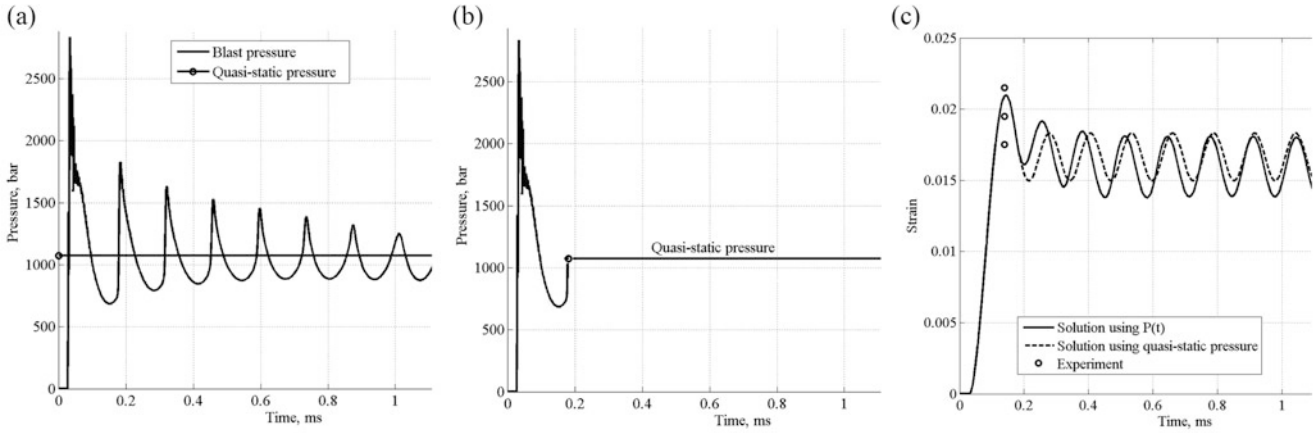

Fig. 5 Time histories—real blast pressure (**a**); simplified pressure (**b**); strain (**c**)

$\rho_S = 7.88$ g/cm^3 (density), $\sigma_Y = 5000$ bar (yield stress), $g_S = 28333$ bar (linear kinematic hardening modulus) for a 700 g spherical "Composition B" charge explosion. The charge density and radius are $\rho_E = 1.717$ g/cm^3 and $R_E = 4.6$ cm, respectively. The problem parameters correspond to the experimental conditions [6]. The internal contact blast pressure time history $P(t)$ is shown in Fig. 5a. The horizontal line corresponds to the residual gas pressure. The shell's blast response was calculated for the full pulse load action (Fig. 5a) and the simplified pulse load action using the quasi-static pressure as shown in Fig. 5b. Figure 5c describes the hoop strain time history. One can see that the shell behavior is elastic-plastic. From Fig. 5 it can be seen that the simplified approach based on the quasi-static pressure properly describes the elastic-plastic shell behavior. It shows a good agreement with test data and with a solution using pressure time history obtained by AUTODYN simulation.

In case of an elastic behavior of the shell the following analytical solution is obtained.

Consider that the internal blast pressure $P(t)$ is a piecewise function of time as follows

$$P_i(t) = \left[(p_{i+1} - p_i)(t - t_i)/(t_{i+1} - t_i) + p_i\right]/\rho_S h_S = a_i t + b_i,$$
$$t_i \le t \le t_{i+1}, \quad i = 1, 2, \ldots \tag{9}$$

where

$$a_i = (p_{i+1} - p_i)/(t_{i+1} - t_i)/\rho_S h_S;$$
$$b_i = \left(p_i - (p_{i+1} - p_i)t_i/(t_{i+1} - t_i)\right)/\rho_S h_S, \tag{10}$$
$$i = 1, 2, \ldots$$

The solution is written as

$$u_1(t) = -b_1 \cos(kt)/k^2 - a_1 \sin(kt)/k^3 + (a_1 t + b_1)/k^2,$$
$$t_1 \le t \le t_2 \tag{11}$$

$$\dot{u}_1(t) = b_1 \sin(kt)/k - a_1 \cos(kt)/k^2 + a_1/k^2,$$
$$t_1 \le t \le t_2 \tag{12}$$

$$u_i(t) = \left[C_{1i-1} + \varphi \cos(kt_i)/k^2\right] \cos(kt) +$$
$$+ \left[C_{2i-1} + \varphi \sin(kt_i)/k^2\right] \sin(kt) + (a_i t + b_i)/k^2 \tag{13}$$
$$t_i \le t \le t_{i+1}, \quad i = 2, 3, \ldots$$

$$\dot{u}_i(t) = -k\left[C_{1i-1} + \varphi \cos(kt_i)/k^2\right] \sin(kt) +$$
$$+ k\left[C_{2i-1} + \varphi \sin(kt_i)/k^2\right] \cos(kt) + a_i/k^2, \tag{14}$$
$$t_i \le t \le t_{i+1}, \quad i = 2, 3, \ldots$$

$$C_{11} = -b_1/k^2; \quad C_{21} = -a_1/k^3 \tag{15}$$

$$C_{1i} = C_{1i-1} + \varphi \cos(kt_i)/k^2, \quad t_i \le t \le t_{i+1}, \quad i = 2, 3, \ldots \tag{16}$$

$$C_{2i} = C_{2i-1} + \varphi \sin(kt_i)/k^2, \quad t_i \le t \le t_{i+1}, \quad i = 2, 3, \ldots \tag{17}$$

$$\varphi = a_{i-1} t_{i-1} + b_{i-1} - a_i t_i - b_i$$

$$k = \sqrt{\frac{2E_S}{\rho_S (1 - \mu_S) R_S^2}}. \tag{18}$$

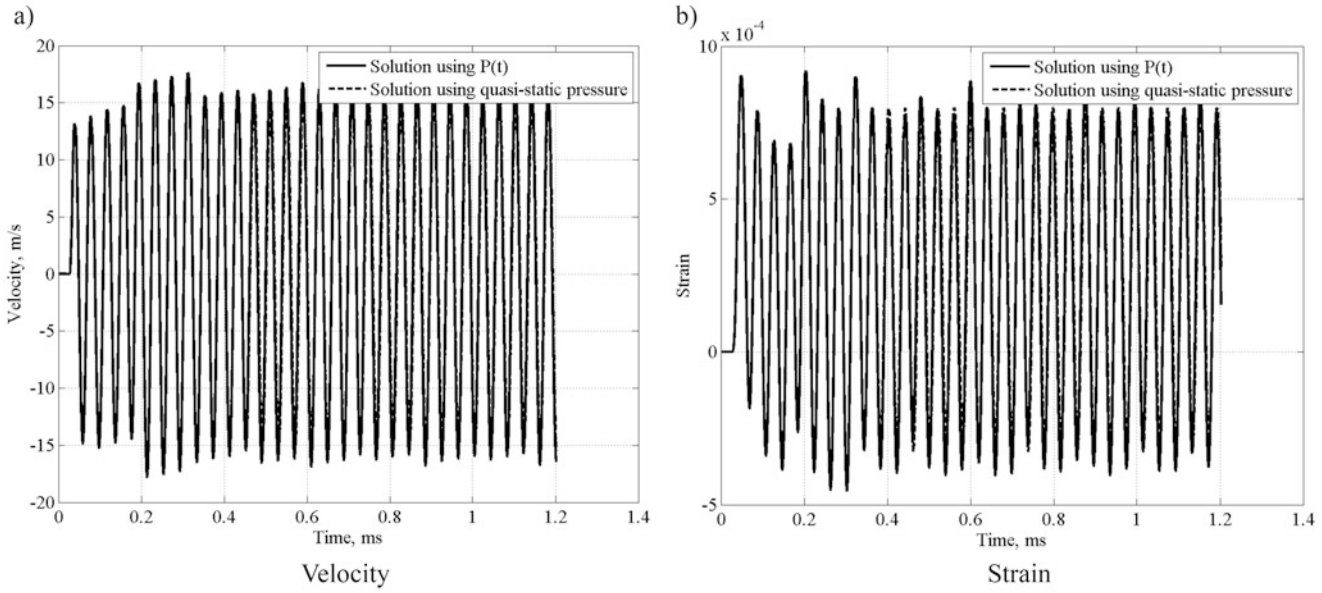

Fig. 6 Time histories (elastic solution) (**a**) velocity, (**b**) strain

Figure 6 shows the solution in the case of elastic shell (obtained with $E_S = E_S \cdot 10$).

Conclusions

An effective simplified model with lumped parameters based on the Bernoulli equation has been developed for the quasi-stationary phase of the detonation products outflow from the room through the venting openings. The model has been successfully applied to the explosion venting due to the separation of an opening protective cover. The developed gas pressure is successfully applied to simulate the confined blast response of flexible structures. It was shown that the simplified approach based on the quasi-static gas pressure properly describes the elastic-plastic shell behavior.

References

1. Edri, I., Feldgun, V.R., Karinski, Y.S., Yankelevsky, D.Z.: Afterburning aspects in an internal TNT explosion. Int. J. Protect. Struct. **4**(1), 97–116 (2013)
2. Feldgun, V.R., Karinski, Y.S., Edri, I., Yankelevsky, D.Z.: Prediction of the quasi-static pressure in confined and partially confined explosions and its application to blast response simulation of flexible structures. Submitted to IJIE.
3. Forsen, R., Bryntse, A., Absil, L., Verbeek, R.: Water mitigation of explosion effects. Part 1: the dynamic pressure from partially confined spaces. In: Blast Mitigation by Water, pp. 44–67. FOI Report N FOI-R-2049-SE (2006)
4. Borisovskaya, V.P., Ivanov, A.N.: A study of the sudden unilateral rupture of a cylindrical gas-filled vessel. Trudy TsAGI **2067**, 10 (1980)
5. Biamino, L., Jourdan, G., Mariani, C., Igra, O., Massol, A., Houas, L.: Experimental investigation of door dynamic opening caused by impinging shock wave. Shock Waves **21**, 19–28 (2011)
6. Tsypkin, V.I., Cheverikin, A.M., Ivanov, A.G., Novikov, S.A., Mineev, V.N., Shitov, A.T.: Study of the behavior of closed steel spherical shells with single-stage internal explosive loading. Strength Mater. **14**(10), 1353–1359 (1982)

Blast Wave Impact on a Parallelepiped Headed with a Semicylindrical Model Drilled with a Rectangular Cavity

R. Tosello, L. Biamino, D. Leriche, C. Mariani, G. Jourdan, J.-C. Loraud, and L. Houas

Introduction

As part of a research program for the protection of people and buildings after an explosion, a series of experiments is carried out. After an explosion in free air, the created blast wave can penetrate into buildings, boats, or underground shelters.

Both experimental and analytical works have been realized on similar investigations, considering shock or blast waves, and principally focused on the transition from Mach to regular reflection of shock waves, Ben-Dor and Takayama [1], or the complex flow features, Igra et al. [2] and Skews and Kleine [3]. More recently the propagation of a shock wave in a branched duct has been conducted by Biamino et al. [4].

When a shock wave interacts with a structure, one can observe several types of interactions which are the most common reflection on the wall, and diffraction when interacting with a cavity or a variation of section. The nature of the diffraction may vary depending on the type of cavities, and complex phenomena of reflection may also occur in the different cavities. Thus, it is of great interest to study phenomena that appear when a shock wave sweeps, cylindrical or various structures breakthrough complex cavities.

The aim of the present work is to try quantifying the part of a blast wave which penetrates in a given cavity after impacting it. In this chapter, the cavity is shaped as a parallelepiped headed with a semicylindrical part drilled by a rectangular cavity. It has been positioned 150 mm from the free exit of a shock tube. Thus, after the coming out of the shock wave from the shock tube end, the model interacts with a blast wave.

R. Tosello (✉) • D. Leriche
DGA Techniques navales, Avenue de la Tour Royale, 83050 Toulon, France
e-mail: lazhar.houas@univ-amu.fr

L. Biamino • C. Mariani • G. Jourdan • J.-C. Loraud • L. Houas
Aix Marseille Université, CNRS-IUSTI UMR 7343, Marseille, France

Experimental Setup

The present experimental investigation was carried out in the T80 IUSTI shock tube in its horizontal position and open at its end. It has an 8 cm by 8 cm square cross section, and a total length of 3.75 m. A detailed description of T80 facility is given in the paper of Biamino et al. [4]. The cavity tested is positioned at the open end of the shock tube as seen in Figs. 1 and 2. The model is located 150 mm from the shock tube exit. S_6 and S_4 pressure transducers, mounted alongside the shock tube, allow the measure of the shock wave velocity before exiting from the shock tube. Note that inside the shock tube a shock wave moves. After coming out from its exit it progressively becomes a blast wave. S_{out} records the blast wave overpressure just before entering the cavity and S_{in} that at the bottom within the cavity.

Coupled with the pressure measurements, a high speed Schlieren visualization device is used to observe the evolved wave pattern outside and inside the model. The images are recorded with a Photron Fastcam SA1 high speed camera with an acquisition frequency of 20,000 frames per second for a spatial resolution of 512 × 512 pixels. Two types of pressure transducers were used. We used PCB (piezoelectric) for S_4 and S_6 positions, and Endevco (piezoresistive) for S_{in} and S_{out} positions.

Results

Table 1 resumes the experimental conditions of the present investigation.

Figure 3 presents an example of the pressure histories recorded during an experiment with an incident shock wave Mach number, M_{is}, measured within the shock tube of 1.11.

G. Ben-Dor et al. (eds.), *30th International Symposium on Shock Waves 1*, DOI 10.1007/978-3-319-46213-4_120

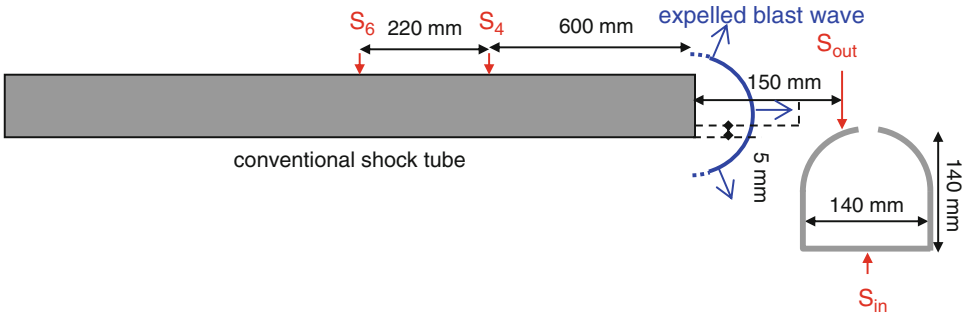

Fig. 1 Scheme of the experimental setup with the model made by a parallelepiped headed with a semicylinder and drilled by a 35 × 20 mm^2 rectangular opening

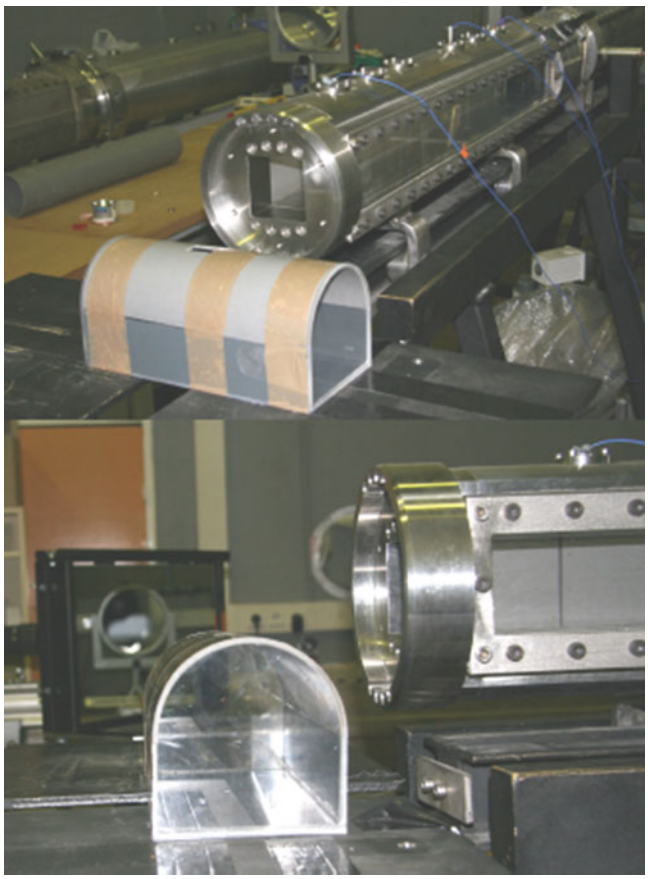

Fig. 2 Views of the experimental setup with the model made by a parallelepiped headed with a semicylinder and drilled by a 35 × 20 mm^2 rectangular opening

A sequence of Schlieren photographs showing the emerging $M_{is} = 1.11$ shock wave from the shock tube exit and its interaction with the model, during the same run, is shown in Fig. 4. The model positioned 150 mm from the shock tube exit is a parallelepiped 300 mm long, 140 mm large, and 140 mm height, headed by a semicircle 140 mm in diameter. We observe that the overpressure generated behind the incident shock wave is about 270 mbar while before entering in the model it reaches about 230 mbar.

Note that, a series of experiments was made before placing the pressure gauges, for Schlieren visualization, then a second series for the same experimental conditions was made including the pressure transducers for pressure measurements. That is why the gauges are not visible on the Schlieren frames.

A sequence of Schlieren photographs showing the emerging $M_{is} = 1.2$ shock wave from the shock tube exit and its interaction with the model is shown in Fig. 5, with more details. The physical behavior of the blast wave is commented for that figure in the following.

After the expelled shock wave becomes a blast wave, it impinges the model, and we observe a regular reflection on the top of the semicylinder. The blast wave is moving from left to right. When it hits the upper part of the semicylindrical part, we observe a regular reflection on frames at $t = 200$ µs and $t = 250$ µs. At about $t = 300$ µs, the blast wave reaches the rectangular aperture. A part of it diffracts inside the model, and the other keeps moving staying in contact with the inner profile. At about $t = 300$ µs, a wave reflected on the opposite edge appears. A part propagates downward inside the cavity, the other upward outside the cavity. The part of the diffracted wave inside, which follows the circular contour, will develop a reflection at about $t = 500$ µs, the consequence of which is the observed configuration seen from $t = 600$ µs and $t = 650$ µs as it propagates on a concave surface. The whole phenomenon described here is well illustrated in the book of Gabi Ben-Dor [5]. Furthermore, we observe that the diffracted wave inside the cavity is accelerated while the incident blast wave follows its moving along the outer profile. Indeed,

Table 1 Experimental conditions for two incident shock wave Mach numbers inside the shock tube of about 1.11 and 1.2

Conditions	M_{is}	U (m/s)	C (m/s)	P (bar)	T (K)	ρ (kg)m^3	W (m/s)
Air	–	–	343	1	293	1.19	–
Air[a]	1.11	60	355	1.27	314	1.41	381
Air[a]	1.2	105	364	1.51	331	1.60	412

M_{is} is the incident shock wave Mach number in the shock tube, U the flow velocity, C the speed of sound, P, T, and ρ are the pressure, temperature, and density of air in the shock tube, respectively, and W is the shock wave velocity
[a]Indicates shocked air values

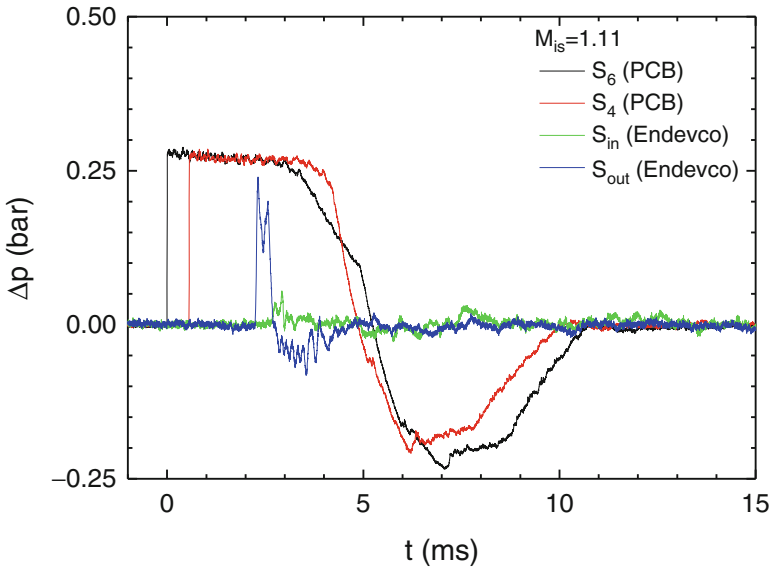

Fig. 3 Pressure histories recorded during the interaction of a blast wave generated from the expelling of a 1.11 plane shock wave from T80 conventional shock tube with the model. Pressure gauges S_6 and S_4 record the shock wave overpressure in the shock tube, S_{out} records the blast wave just before entering the cavity, and S_{in} that at the bottom within the cavity. The incident shock wave is moving from *left* to *right*. Remember that the cavity is a 35 × 20 mm^2 rectangular opening

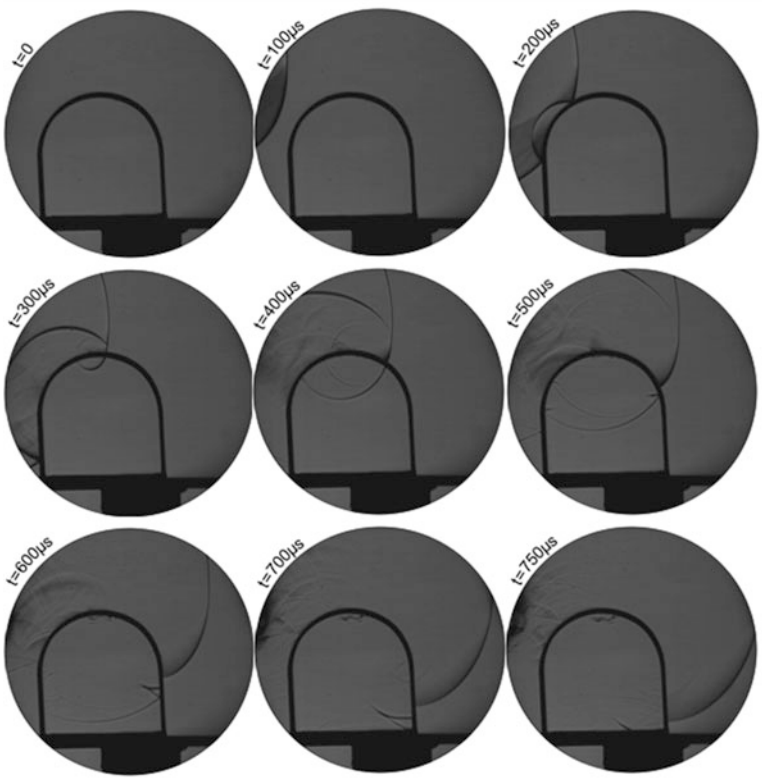

Fig. 4 Sequence of Schlieren photographs (20,000 frames per second) showing the interaction of a blast wave generated from the expelling of a 1.11 plane shock wave from T80 conventional shock tube with the model presented in Fig. 1, and drilled with a 35 × 20 mm^2 rectangular opening. The incident shock wave is moving from *left* to *right*

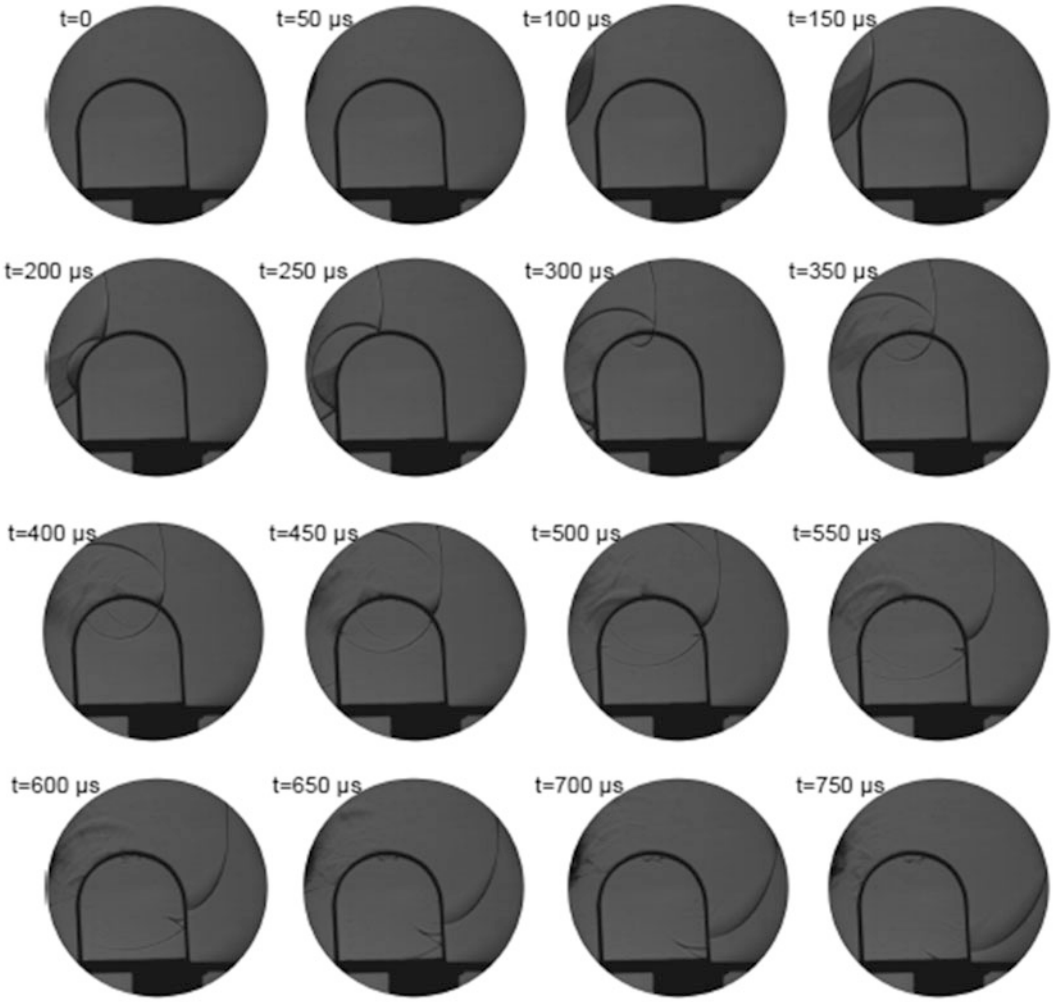

Fig. 5 Sequence of Schlieren photographs (20,000 frames per second) showing the interaction of a blast wave generated from the expelling of a 1.2 plane shock wave from T80 conventional shock tube with the model presented in Fig. 1, and drilled with a 35 × 20 mm^2 rectangular opening. The incident shock wave is moving from *left* to *right*

since $t = 500$ µs, we clearly see that the inside wave exceeds the external one and develops a nonregular reflection.

Conclusions

In the present experiments, a model has been submitted to a blast wave resulting from a 1.11 and 1.2 incident shock wave Mach numbers, after their coming out from a shock tube exit.

The presented model is a parallelepiped headed with a semicylindrical part drilled by a rectangular cavity.

The sizes of the model positioned 150 mm from the shock tube exit is a parallelepiped 300 mm long, 140 mm large, and 140 mm height, headed by a semicircle 140 mm in diameter.

We found that for an overpressure of about 230 mbar outside of the cavity, the maximum overpressure recorded inside and at the bottom of the model is of about 50 mbar, which corresponds in terms of intensity to a blast wave penetration of about 20 %.

References

1. Ben-Dor, G., Takayama, K.: Analytical prediction of the transition from Mach to regular reflection over cylindrical concave wedges. J. Fluid Mech. **158**, 365–380 (1985)

2. Igra, O., Falcovitz, J., Reichenbach, H., Heilg, W.: Experimental and numerical study of the interaction between a planar shock wave and a square cavity. J. Fluid Mech. **313**, 105–130 (1996)
3. Skews, B.W., Kleine, H.: Flow features resulting from shock wave impact on a cylindrical cavity. J. Fluid Mech. **580**, 481–493 (2007)
4. Biamino, L., Jourdan, G., Igra, O., Mariani, C., Tosello, R., Leriche, D., Houas, L.: Experimental investigation of shock wave propagation in a 90° branched duct. Shock Waves **24**, 307–315 (2014)
5. Ben-Dor, G.: Shock wave reflection phenomena, 2nd edn. Springer, New York (2007)

A Comparison of Numerical and Experimental Results of Passive Shock Wave Mitigation Using Obstacles in Two-Dimensional Channels

Q. Wan, M. Nguyen, and V. Eliasson

Introduction

The study of shock wave attenuation has drawn much attention in shock wave community. One of the common ways to attenuate shock waves is to arrange multiple obstacles to block the propagation path of the shock wave [1]. We propose an arrangement of the obstacles by placing square- or cylinder-shaped obstacles along the outline of a logarithmic spiral curve [2, 3] (Fig. 1); by doing this, it is possible to benefit of the ability of the logarithmic spiral to collect the energy of the incident shock wave in its focal region [4–6]. We simulated the process of the shock wave passing through these arrangements using the Euler equations of gas dynamics. Then, to validate the numerical results, we performed corresponding experiments under the same initial conditions. Results show that the numerical and experimental methods agree well, and that placing obstacles along a logarithmic spiral curve can effectively attenuate the transmitted shock waves.

To perform the simulations, Overture, a framework to solve partial differential equations using finite differences on overlapping grids, was used. Information regarding the solver and its packages can be found at http://www.overtureframework.org/. In this study, we used the Composite Grid Compressible Navier–Stokes solver that can be applied for solving either the compressible Navier–Stokes or the inviscid Euler equations. All the work presented here was governed by the two-dimensional inviscid Euler equations for which a second-order Godunov scheme was used. Adaptive mesh refinement is used to accelerate the simulation process.

Q. Wan • M. Nguyen
University of Southern California, Los Angeles, CA 90089-1453, USA

V. Eliasson (✉)
University of Southern California, Los Angeles, CA 90089-1453, USA

University of California, San Diego, La Jolla, CA 92093-0085, USA
e-mail: eliasson@ucsd.edu

The experiments were conducted using a horizontal shock tube, see Fig. 2a. The length of the shock tube is 4.7 m with a 0.65 m long driver section followed by a 3.30 m long driven section. The inner diameters of the driver and driven sections are 91.4 mm and 72.8 mm, respectively. A 95 mm long transition section is put at the end of the driven section and transforms the cross section area from circular to square. The test section is placed downstream of the transition section. Two pressure transducers (PCB Piezotronics 113B21), S1 and S2 in Fig. 2a, are used to measure the pressure change through time. In the experiment, a high-speed V711 Phantom Camera is used to capture the shock wave propagation. Figure 2b shows a side view of the cylindrical obstacle arrangement sample, which is made of aluminum, in the test section.

The simulation setup is shown in Fig. 3. The size of the test section is 711.2×50.8 mm. The distance between the left end of the shock tube and the leading edge of the obstacles is 283.2 mm and the leading edge of the obstacles is set at $x = 0$ mm. Two probes are located in the test section to record the pressure change through time. One is set at $x = -105.4$ mm, which is 177.6 mm away from the left boundary. The other probe is put at $x = 326.1$ mm, which is 102.1 mm away from the right boundary. A two-dimensional duct flow scenario is considered, where obstacles are placed in varying geometric configurations to attenuate a normal shock wave impacting the obstacle configuration from the left. The Mach number of the incident shock is $M_s = 1.2$. The top and bottom walls of the duct are parallel to each other, simulating part of the test section.

Results

For the cylindrical case, the diameter of the cylinders used is 10 mm. Thirteen cylinders are placed along the logarithmic spiral curve. A direct comparison of the schlieren images captured in simulation and experiment is shown in Fig. 4.

G. Ben-Dor et al. (eds.), *30th International Symposium on Shock Waves 1*, DOI 10.1007/978-3-319-46213-4_121

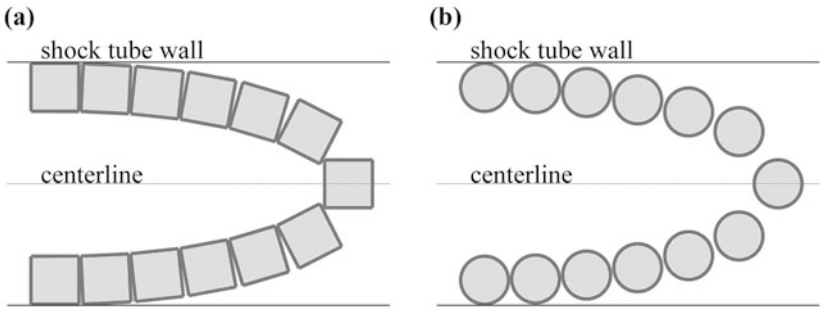

Fig. 1 Positioning of square and cylindrical obstacles along the outline of logarithmic spiral curve. (**a**) Square obstacle arrangement; (**b**) cylindrical obstacle arrangement

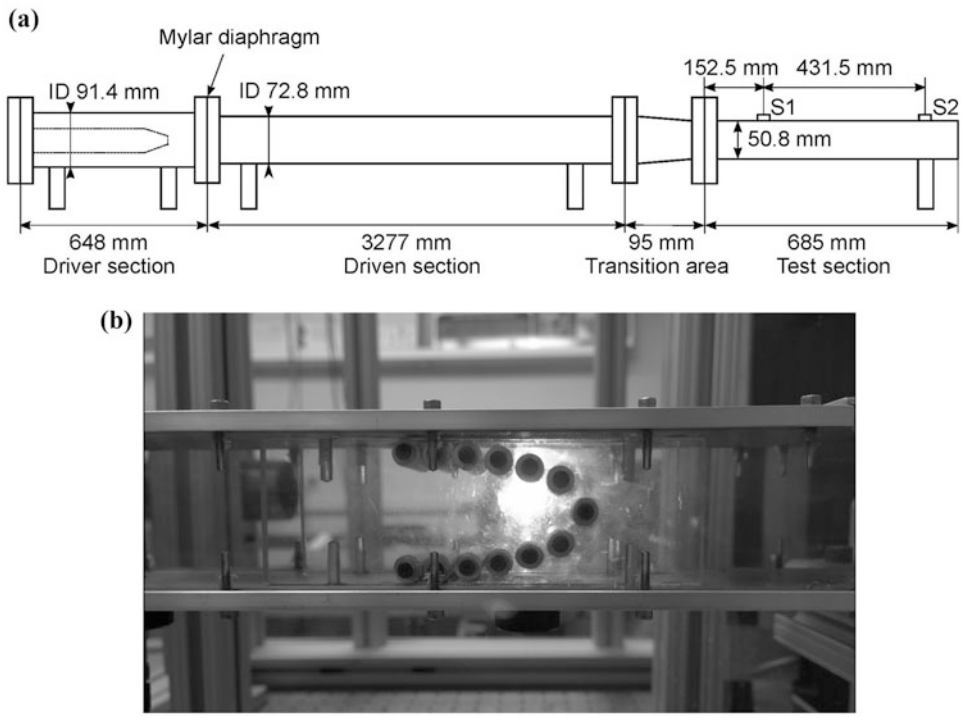

Fig. 2 (**a**) Experimental setup; (**b**) cylindrical case sample in test section

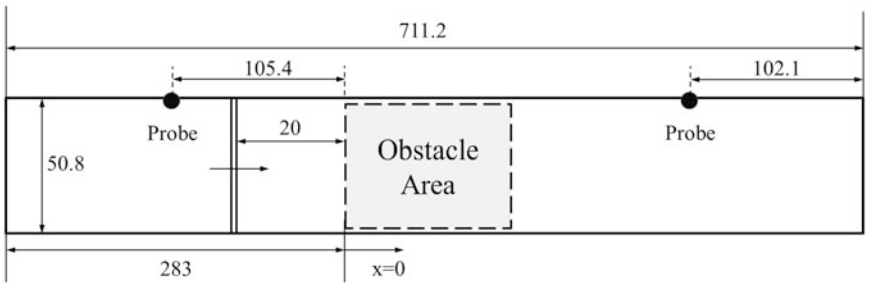

Fig. 3 Simulation and experimental setup. A two-dimensional test section where planar shock wave impacts on the obstacles from *left* to *right*. Distances in mm. Not to scale

The left column shows the experimental results and right column shows the simulation results. It can be seen that the incident shock remains planar but each cylinder produces a reflected cylindrical shock. The cylindrical shock waves interact with each other and a very complex wave pattern behind the incident shock is formed. On the upper and lower sides of the obstacles, a main shock front is transmitted and it is slightly delayed compared to the incident shock wave.

For the reflected shocks, there are two main visible wave fronts that are reflected from the arrangement. The first one is reflected by the leading edge of the arrangement and the second one is due to the deep end of the arrangement. Comparing the simulation and the experiment agree well, it can be seen that the complex wave patterns behind the incident shock agree well.

Moreover, the velocity of the incident shock is measured to compare with that in the simulation. Using the high-speed V711 Phantom camera, the time interval between two consecutive frames is 10 μs. As shown in Fig. 5, the distance that the incident shock wave travels rightward is (4.04 ± 0.29)

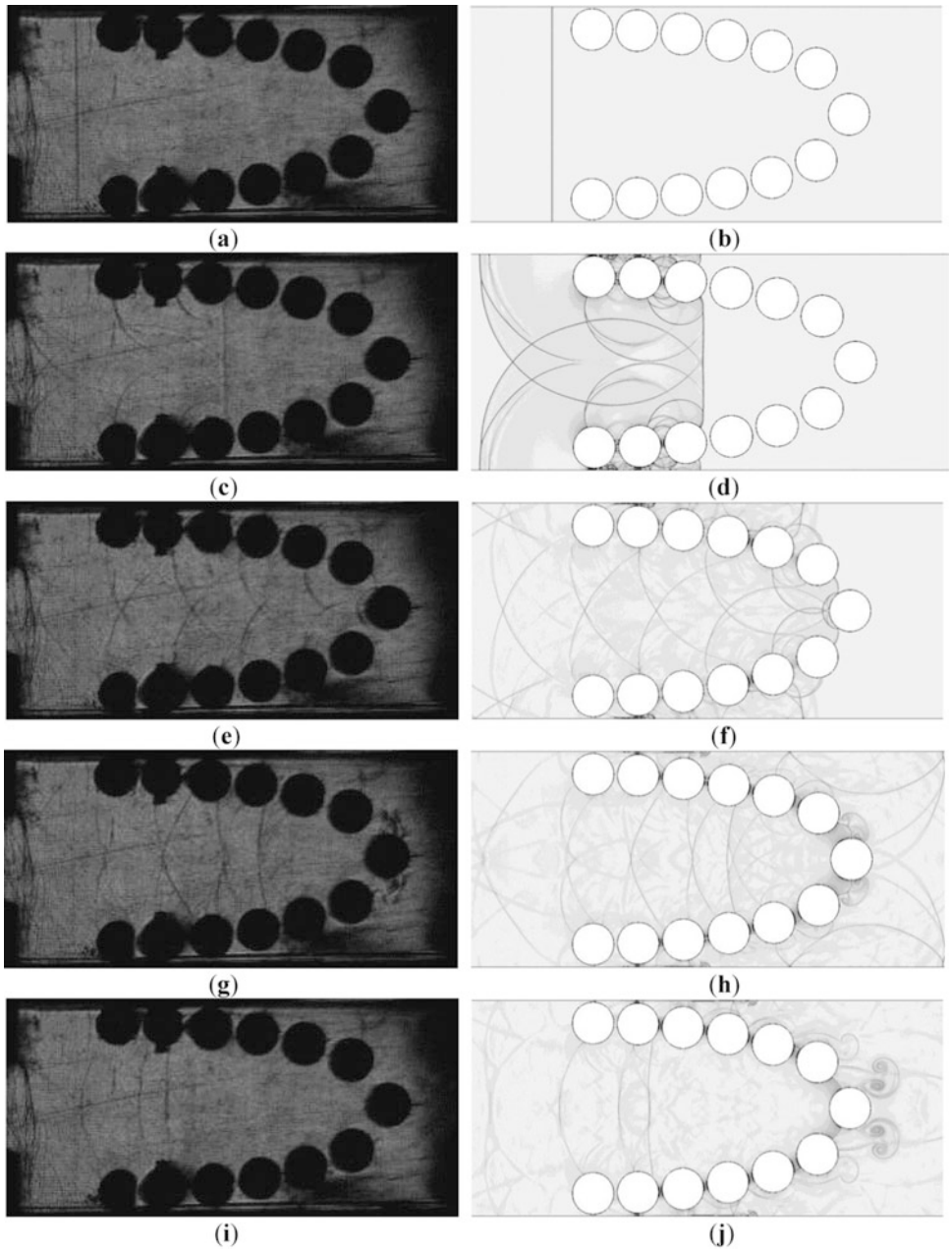

Fig. 4 Comparison between the schlieren images of numerical and experimental result for shock wave propagating through the cylindrical obstacles arrangement. (**a**), (**c**), (**e**), (**g**), and (**i**) are experimental results; (**b**), (**d**), (**f**), (**h**), and (**j**) are numerical results

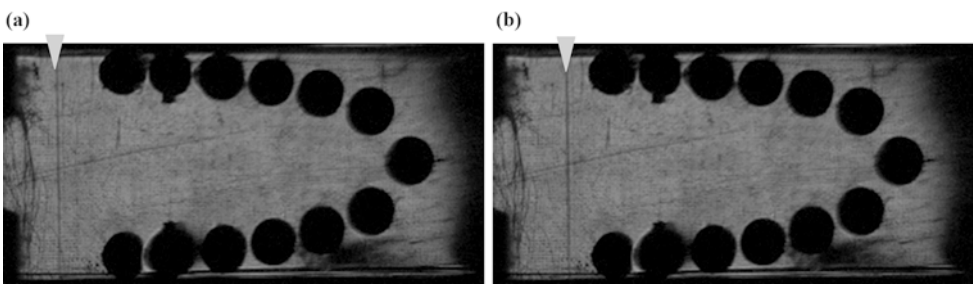

Fig. 5 Calculation of the velocity of the incident shock wave

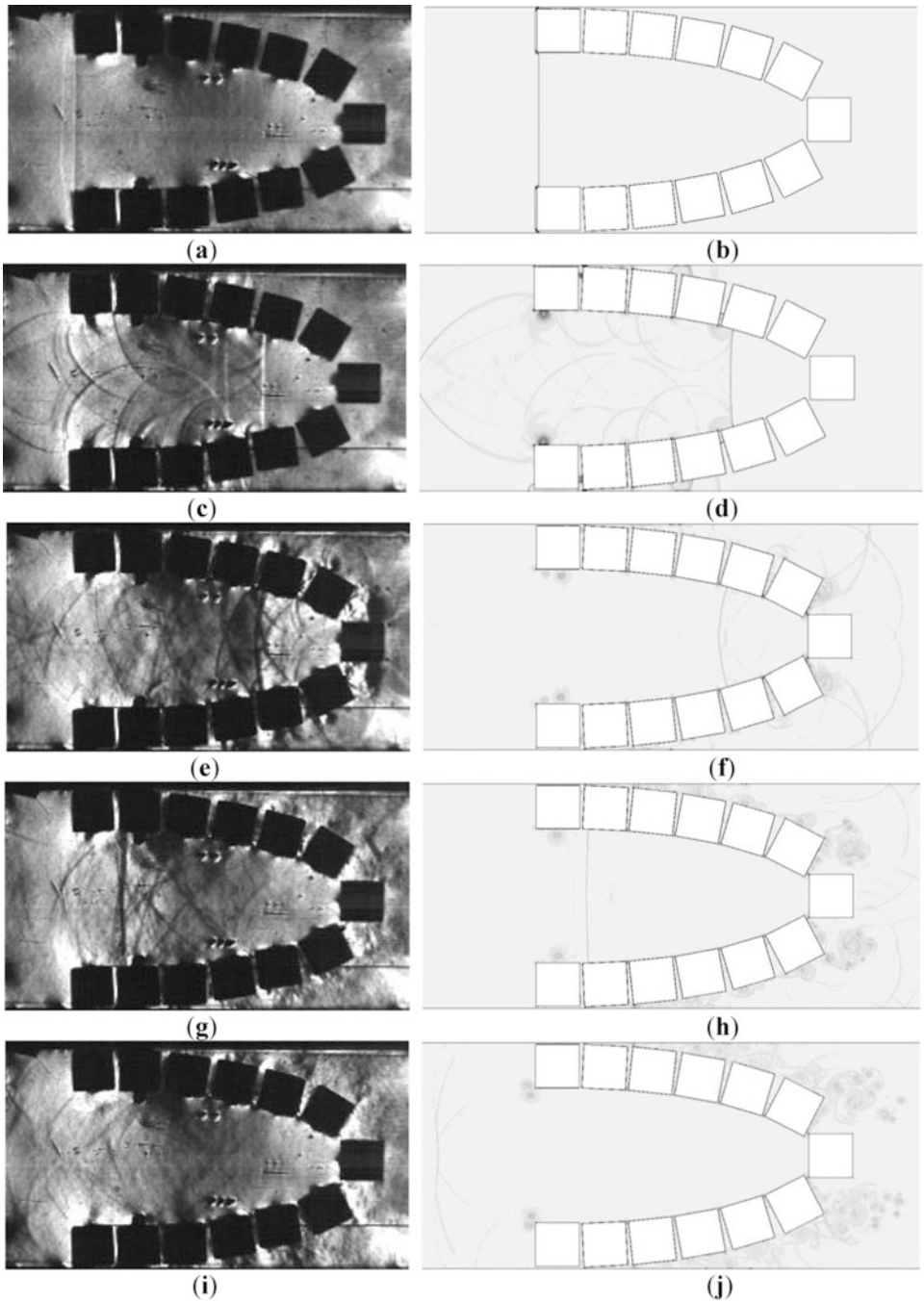

Fig. 6 Comparison between the schlieren images of numerical and experimental result for shock wave propagating through the square obstacles arrangement. (**a**), (**c**), (**e**), (**g**), and (**i**) are experimental results; (**b**), (**d**), (**f**), (**h**), and (**j**) are numerical results

$\times 10^{-3}$ m. Therefore, the velocity of the shock can be easily estimated using the distance divided by the time interval, which is (404 ± 29) m/s. On the other hand, in the simulation, the initial speed of the shock is 412.59 m/s.

For the square case, the methods of obstacle placement are similar to the cylindrical case. At the center of each cylinder, we place a square instead of the cylinder. Furthermore, each square is placed at an angle such that one of the sides of the square shape is tangential to the edge of the logarithmic spiral curve attached.

Figure 6 shows the comparison of the schlieren images between numerical and experimental results for square case. For both simulation and experiment, some vortices are generated near the slits between adjacent square obstacles and it is very clear that the main shock front travelled from left to right and most of it was reflected

back. The reflected shock wave was a little curved near the focal point of the logarithmic spiral curve, but gradually became planar when further reflected. Comparing with results of the cylindrical case, the deviation of the numerical and experimental results in square case looks larger. This could be attributed to the fact that the manufacturing process of the square case arrangement sample is more complex, and thus, the locations and angles of each square obstacle are not exactly the same as in the simulation setup.

Conclusions

Based on the direct comparison of the schlieren images, the wave patterns in both numerical and experimental results for cylindrical case are very similar. Furthermore, in cylindrical case, the velocity of the incident shock measured in the experiment agrees with the initial condition in simulation setup. Regarding square case, the experimental results also look similar to the simulation, but there are more differences with regard to the wave patterns than the cylindrical case. One possible reason could be the difference of the sample shape due to the manufacturing process. In the future, more experiments will be repeated to confirm the reliability of the results.

References

1. Chaudhuri, A., Hadjadj, A., Sadot, O., Ben-Dor, G.: Numerical study of shock-wave mitigation through matrices of solid obstacles. Shock Waves **23**, 91–101 (2013)
2. Whitham, G.: Linear and nonlinear waves. Wiley-Interscience, New York (1974)
3. Wan, Q., Eilasson, V.: Numerical study of shock wave attenuation in two-dimensional ducts using solid obstacles: how to utilize shock focusing techniques to attenuate shock waves. Aerospace **2**(2), 203–221 (2015)
4. Inoue, O., Imuta, S., Milton, B., Takayama, K.: Computational study of shock wave focusing in a log-spiral duct. Shock Waves **5**, 183–188 (1995)
5. Inoue, O., Takahashi, N., Takayama, K.: Shock wave focusing in a log-spiral duct. AIAA J. **31**(6), 1150–1152 (1993)
6. Milton, B., Archer, R.: Generation of implosions by area change in a shock tube. AIAA J. **7**(4), 779–780 (1969)

Mitigation of Weak Shock Waves: Its Applications to Design of Automobile Engine Silencers and Mufflers

Noriaki Sekine and Kazuyoshi Takayama

Introduction

This is a summary of our fundamental shock wave research that was aimed to establish a reliable design of automobile engine silencers and mufflers. The image data we collected during the basic experiments were not properly presented, except few images, in papers and hence the authors believe that their presentation contains still useful information. Traditionally, the design of silencers and mufflers was based on acoustic theory by assuming that waves in exhaust gas pipes were linear waves. Hence the analyses poorly agreed with measured data. Sekine et al. [1] connected an exhaust gas pipe of a prototype automobile engine cylinder to a shock tube test section and visualized the presence of weak shock waves. Hence, to reproduce weak shock waves, we intensively used shock tubes and visualized resulting weak shock waves with double exposure holographic interferometry. In parametric experiments, we distributed baffle plates and obstacles in the shock tube test section and arranged, on the shock tube walls, surface roughness and various shaped perforation at shock Mach number ranging from 1.05 to 1.80 in air.

Then interferometric images so far collected were compared with numerical simulations, then the results were used to design the silencer and muffler of Subaru Legacy 1993 version.

N. Sekine (✉)
Fuji Techno Service Co. Ltd., Ohta, Japan
e-mail: noriaki.sekine@fts.subaru-fhi.co.jp

K. Takayama (✉)
Emeritus Tohoku University, Sendai, Japan
e-mail: k.takayama@mac.com

Shock Waves Generated from Engine Cylinders

We connected an exhaust gas pipeline to a transparent test section and observed the event through a slit by using schlieren arrangement. In Fig. 1, see a streak photo and its sketch. Dark parts are compression waves emanating from the engine cylinder. A distinct thin line shows a weak shock wave.

An exhaust gas pipe of 28 mm in diameter was connected to a 30 mm × 40 mm shock tube. Then the shock tube was connected to a 30 mm × 300 mm diameter test section, in which we installed a rectangular observation section. Figure 2 shows sequential interferograms: (a) shot, Subaru engine was operated at 6800 rpm. A weak shock wave, presumably lower than Ms = 1.1, was transmitting into the test section. Small vortices were observable at the exit corners; (b) shot at 5900 rpm, the transmitting shock wave was reflected from the upper and bottom walls. As exhaust gases contained water droplets and soot, the test windows showed dirt on their surface; (c) shot at 6500 rpm, the reflected shock intersected at the center. We confirmed the presence of weak shock waves generated in exhaust gases.

Mitigation of Weak Shock Waves in a Confined Chamber

In order to reproduce the images shown in Fig. 2, we performed a 60 mm × 150 mm shock tube experiments. In Fig. 3, see sequential interferograms of shock propagation at Ms = 1.16 in air: (a) shot at 370 μs, the shock entered the test section; (b) shot at 550 μs, the transmitting was reflected from the upper and bottom walls; (c) shot at 650 μs, the reflected shocks intersected in the center of the shock tube; and (d) shot at 800 μs, the transmitting shock was reflected from the exit wall. Individual wave interactions created a family of Mach reflection pattern: a reflected wave, a Mach stem, and a slip line which soon transits to vortex line. With

G. Ben-Dor et al. (eds.), *30th International Symposium on Shock Waves 1*, DOI 10.1007/978-3-319-46213-4_122

the elapse of time, we can see that the successive wave interactions promote the attenuation of the transmitting shock wave.

In inserting a baffle plate in the center of the test section, we formed two confined chambers. At the individual entrances we connected a sharp edge. In Fig. 4, see sequential observations of the propagation and interaction of shock waves: (a) shot at 500 μs, a shock wave at Ms = 1.129 entered the chamber; (b) shot at 600 μs, the shock reflected from the front wall, the upper and side walls. The shock front is attenuated and is going to move to the second chamber; (c) shot at 750 μs; and (d) shot at 900 μs, a well-attenuated transmitting shock wave moved into the second chamber.

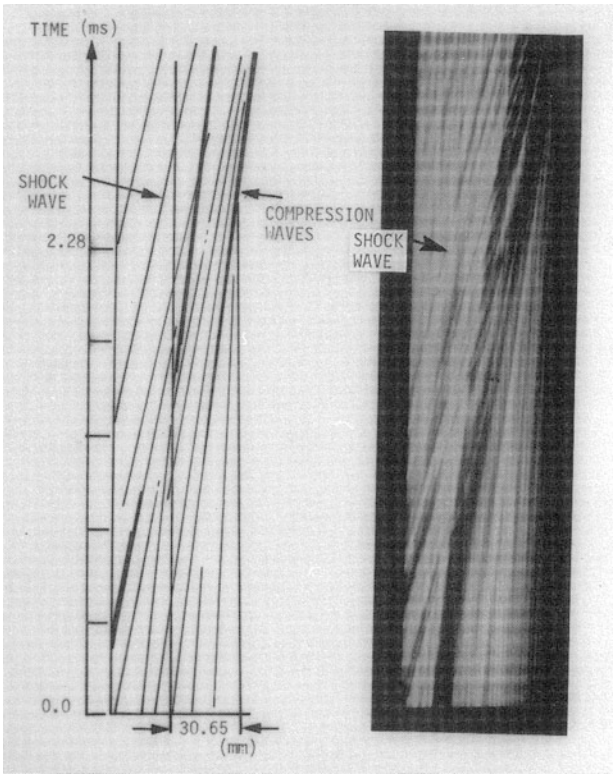

Fig. 1 Streak photo, showing the presence of shock waves in exhaust gases. Time scale and length scale are attached on the figure

Shock Propagation Along Roughened Walls

As seen in Figs. 3 and 4, the incident shock was diffracted at the entrance corner and formed the transmitting shock wave and vortices as well. The transmitting shock waves were reflected from the upper and bottom walls and created complex wave interaction patterns. These wave interactions promoted the attenuation of the transmitting shock wave and the same time generated trains of vortices. Then we observed the mitigation of shock waves over a roughened wall surface.

Experiments were performed in a 60 mm × 150 mm conventional shock tube at shock Mach number Ms = 1.41 in atmospheric air. Surface roughness on the upper and bottom walls consists of distributed grooves of 1 mm width, 1.5 mm interval, and 7 mm in depth. In Fig. 5, see sequential interferograms: (a) shot#90092811 at 600 μs, the incident shock wave entered from a 22 mm wide opening into the test section and formed a twin vortex at the entrance corner; (b) shot#90092810 at 740 μs, the transmitting shock wave was reflected from the upper and bottom walls. The reflected shocks interacted with the incoming flows. It is noticed that individual grooves created coherent disturbances on the reflected shocks and the flow behind them; (c) shot#90092809 at 880 μs, due to temporal absorption of the mass into grooves effectively attenuated the transmitting shock. This information was transferred into the transmitting shock wave via the condition at the foot of the reflection point; and (d) shot#90092807 at 950 μs. In short, the shock interaction with individual grooves created expansion waves which successively transferred into the transmitting shock wave to mitigate.

Effects of Shock Waves on Vehicles Silencer Characteristics

Attenuation Characteristics of Overpressure

A shock tube was applied to study the characteristic of typical vehicles silencers. The pressure variation at the entrance is shown in Fig. 6a–e. Two confined chamber type silencer is shown in Fig. 6c, shock waves are attenuated

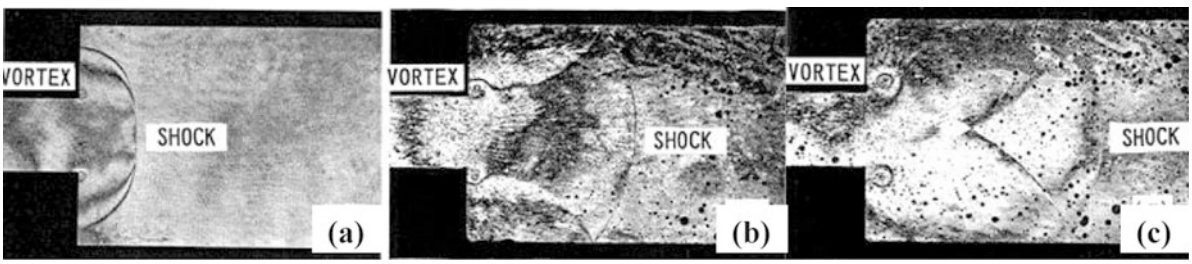

Fig. 2 Sequential interferograms. Weak shock generation from engine cylinders

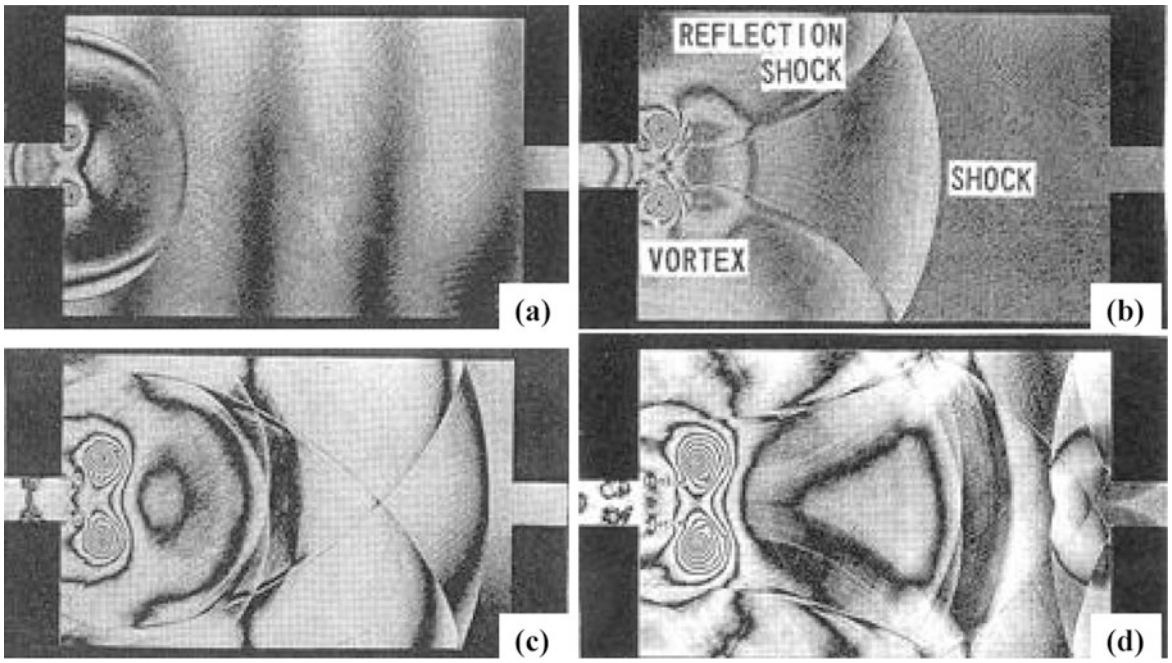

Fig. 3 Sequential analogue experiments of weak shock waves propagation in a shock tube test section, Ms = 1.16 in air

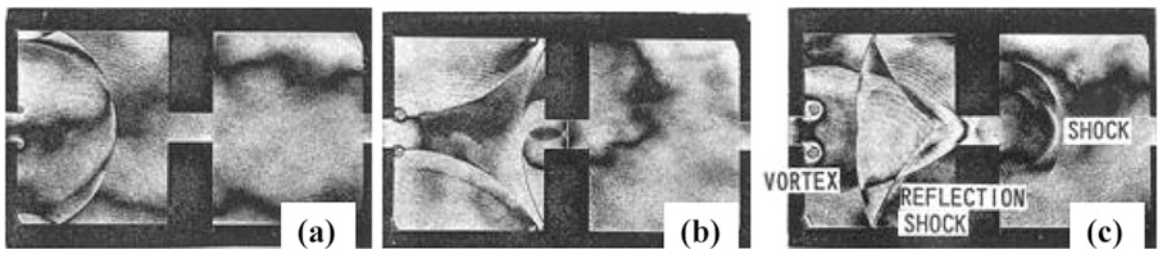

Fig. 4 Attenuation of weak shock waves in a confined chamber at Ms = 1.13 in air

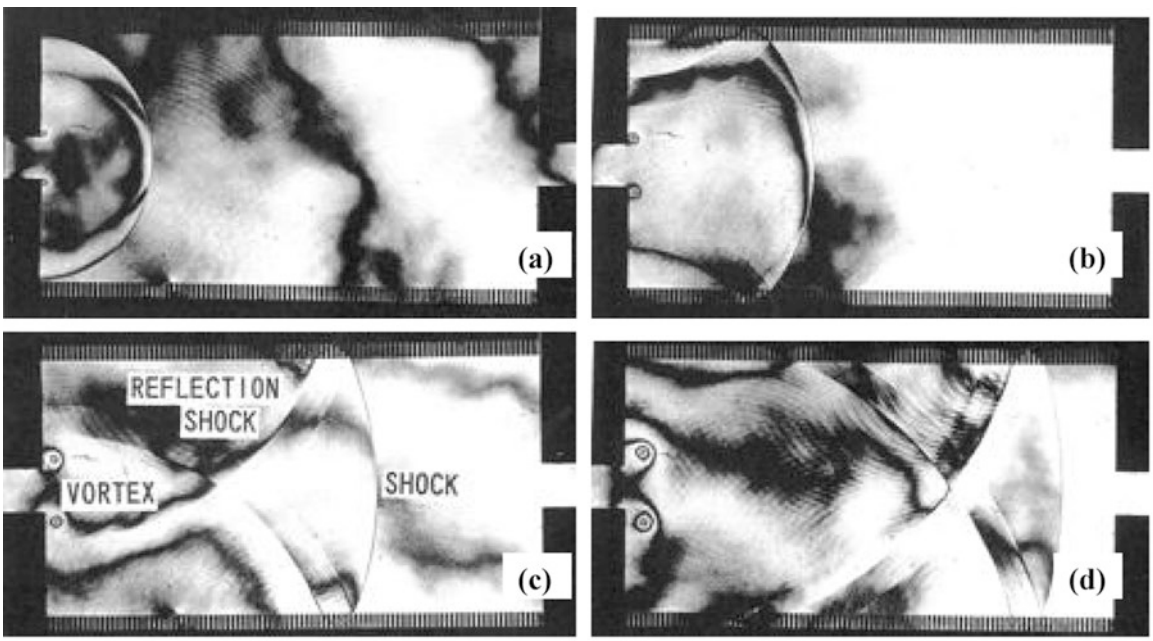

Fig. 5 Shock wave mitigation along a wall with distributed grooves at Ms = 1.41 in air

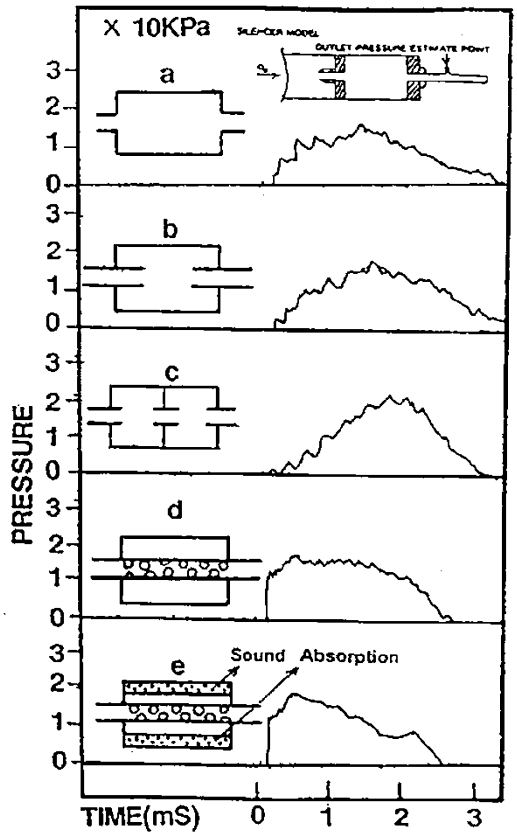

Fig. 6 Pressure variations at the exit of silencers

more effectively than single chamber silencer shown in Fig. 6a, b. However, the pressure variations measured at the exit still contain pronouncing high frequency components. Figure 6d shows the pressure variation in a silencer which has a resonator with many holes. The overpressure, however, was not well attenuated and, as seen in Fig. 6d, sharp peak pressures which are generated due to multiple reflection of shock waves are smoothened. The resonator has a porous wall lining which made from open-cell aluminum sponge is shown in Fig. 6e. In using this resonator, sharp peak pressures were more effectively suppressed than with multi-hole type silencer.

Frequency Characteristics of Overpressure (Insertion Loss)

Frequency characteristics of overpressure were analyzed from results of pressure measurements along a shock tube. This value represents INSERTION LOSS derived by using the acoustic theory. In Fig. 7a–e the insertion loss of various configurations of the silencers. Whereas Fig. 7c can more effectively attenuate the high frequency components in the ranges from approximately 1 to 3 KHz than the other type of silencers. Figure 7e could suppress overpressures of the frequency range over 3 KHz. The frequency of unpleasant exhaust noises caused by shock waves ranges from approximately 1 to 4 KHz.

Based on these results, two confined chamber silencer and having a resonator with holes and sound absorption lining at the rear end of the two confined chamber were examined.

Measurement of Sound Pressure (Conditions and Results)

In order to confirm these results, measurement of sound pressure was carried out on a water cooled 2.0 litter horizontal four-cylinder, four-cycle petrol having multi-point-fuel-injection. The gas temperature measured at the exit of silencer was 500 K and noise was also measured there.

Figure 8 shows spectra of sound pressure levels measured at the outlet of silencer. The frequency band of the noise ranges from approximately 1/3octave band 1–4 KHz.

Two confined chamber combined with a sound absorption lining can reduce both shock-induced noise and flow-generated noises. This type is found to be more effective than any other types of silencers. The shock tube experimental findings agreed well with the experiments.

These results have been successfully adopted in the design of practical exhaust gas pipe systems. **SUBARU vehicles Model IMPRESSA produced in 1992, LEGACY produced in 1993** have already equipped with exhaust gas pipe systems and these silencer systems.

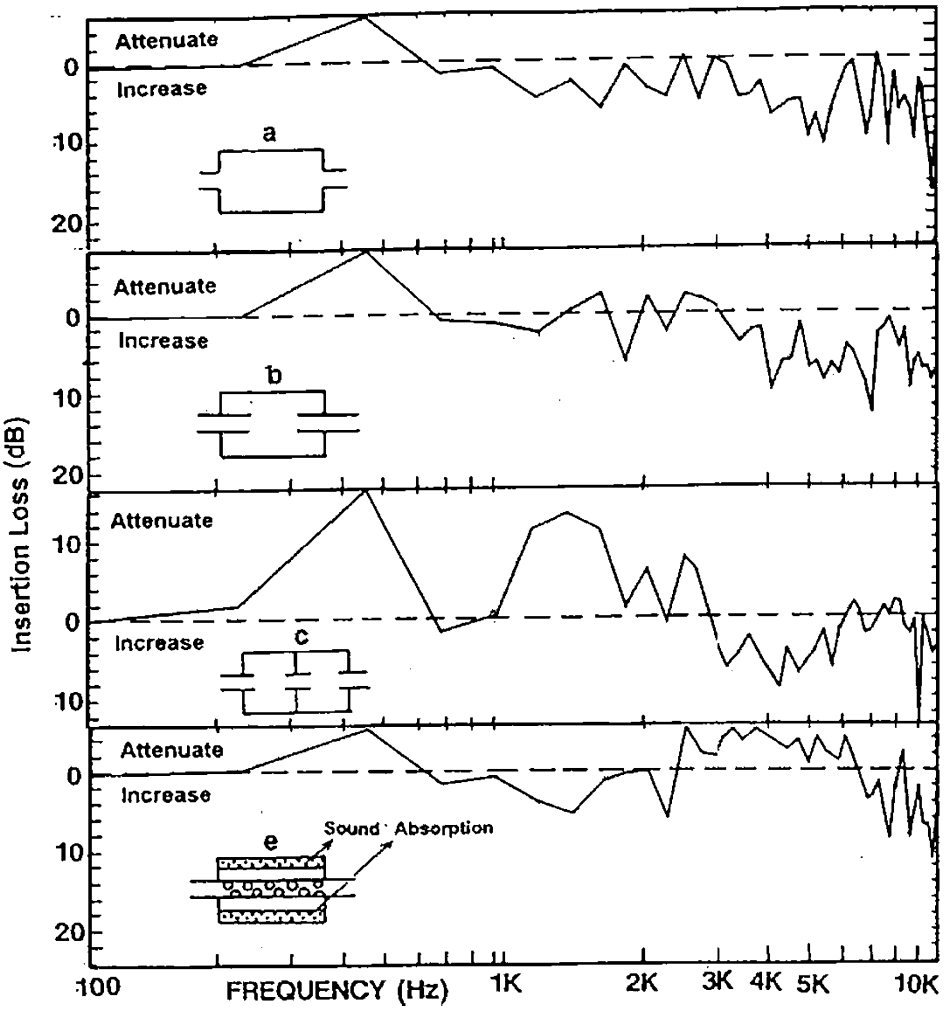

Fig. 7 Insertion loss of various silencers

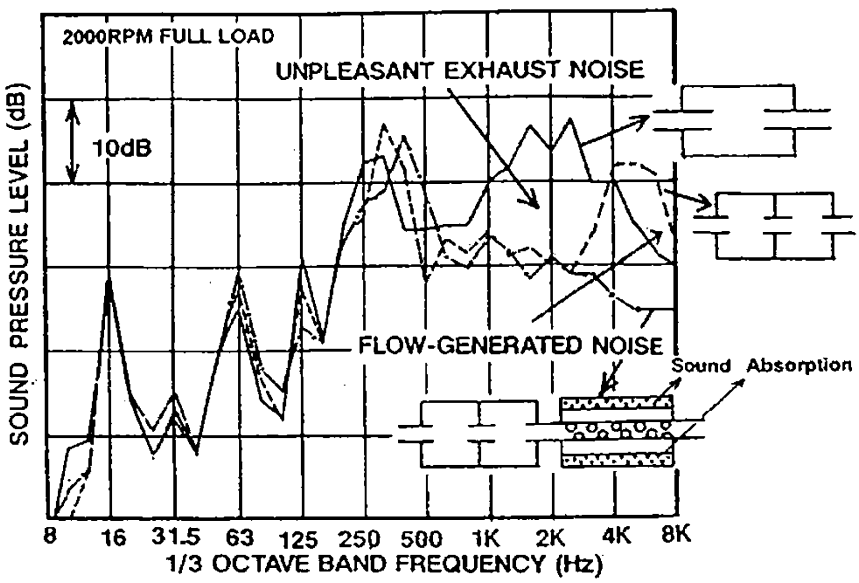

Fig. 8 Spectra of sound pressure levels

Conclusions

1. By using double exposure holographic interferometry, verified the presence of weak shock waves in exhaust gas pipe lines.
2. The parametric shock tube experiment clarified of the mitigation of weak shock waves.
3. These results applied to the design of production automobile engine silencer systems.

Reference

1. Sekine, N., et al.: Generation and propagation of shock waves in the exhaust pipe of a 4 cycle automobile engine. AIP Conf. Proc. **208**, 671–676 (1988)

A New Method to Assess Mitigation Efficiency of a Protective Barrier Against the Effects of a Vapor Cloud Explosion

S. Trélat, E. Vyazmina, A. Beccantini, S. Jallais, and J. Daubech

Introduction

Accidental gas explosions represent an ever-present hazard for process industries handling flammable gases and liquids. There is also an increasing danger of vandals and terrorists using improvised explosive devices in industrial areas neighboring highly populated residential areas. The consecutive pressure wave generation and propagation can result in unacceptable risk exposition of citizens and infrastructures. Therefore, it is necessary to define design rules of protective barriers mitigating the effect of blast wave.

For detonations, there are already published engineering rules for barricades [1] and also CFD (Computational Fluids Dynamics)-based methods [2, 3]. However, for deflagrations (the most likely industrial scenario), no robust and accurate method has been yet published to design protective walls and assess in details their efficiencies.

Consequently, and due to the complexity of the phenomena associated with blast wave interactions with the wall, a CFD-based method has been developed in the framework of a research project, to calculate the blast wave decay before, on, and after the barrier in a far field, in the case of a fast deflagration.

In this chapter, first, the simplified method is presented. Next, the results of this simplified modeling approach using CFD softwares FLACS [4] are compared in free field to one-dimensional precise solution, and then to EUROPLEXUS [5] 2D-results with the presence of a wall. Afterwards, the approach is validated against middle scale experimental data. Experimental results are issued from a recent experimental campaign [6] on blast waves interacting with a wall. The blast was generated by an explosion of stoichiometric hydrogen–oxygen mixtures diluted by nitrogen. Finally, conclusions are drawn on the applications of the proposed approach to industrial cases.

S. Trélat (✉)
IRSN, Fontenay-aux-Roses, France
e-mail: sophie.trelat@irsn.fr

E. Vyazmina • S. Jallais
Air Liquide CRPS, Les Loges en Josas, France

A. Beccantini
CEA, Saclay, France

J. Daubech
INERIS, Verneuil-en-Halatte, France

Build the "Equivalent" Reservoir Burst Problem: A Simplified Approach to Model Blast Wave Propagation

The aim of this paragraph is to present a rapid, precise, and efficient method that will permit to investigate numerically the efficiency of protection barriers to mitigate the pressure wave propagation consecutive to a fast deflagration.

For this purpose, the propagation of a blast wave will be modeled in this chapter with this approach in a free field as a first step, and then, it will be simulated in the environment with a protective barrier (a wall here).

To this end, the problem of pressure waves generated by a constant speed flame propagating in one-dimension geometries in an initially homogeneous medium has been revisited here [6]. Combustion of a gaseous hemisphere is considered. Moreover, it is assumed that, before the flame reaches the interface between the gaseous fresh mixture and the surrounding air, problem deals with a one-dimensional point-symmetrical flow generated by a constant speed flame [7]. Assuming this, if the medium would be considered as homogeneous, the flame width as negligible and the flame velocity as constant, the solution would be self-similar, as pointed out in the works of Sedov [8] and Kuhl [9]. And as showed in [8] and [9], this allows producing a solution extremely accurate and representative of the first stage (i.e., combustion stage) of a hemispheric Vapor Cloud Explosion (VCE). It follows that the computation of the second stage of a VCE can be assimilated to the

G. Ben-Dor et al. (eds.), *30th International Symposium on Shock Waves 1*, DOI 10.1007/978-3-319-46213-4_123

time-decay of this Sedov solution once the combustion is over. Thus the time-decay of this solution is a very good candidate to validate the nonreactive Euler solver of CFD codes used to compute VCE (by the way, this is true in the case of both slow and fast deflagrations).

Incidentally, since the Sedov solution is space dependent and then complex to take into account as initial solution of a CFD computation, it has been decided to proceed in a different way. The simplified approach which is proposed in this chapter consists in building a reservoir burst problem that is equivalent to the Sedov solution. Indeed, if on one hand the time-decay of a slow flame Sedov solution and its equivalent reservoir burst problem present quite different flows (even in the far field), on the other hand they are quite similar in the case of fast flames flows [6]. In other words, for fast deflagrations, in the far field, pressure waves generated after the flame extinction are equivalent to the ones generated by the spherical reservoir burst problem, provided: the "stored internal energy" inside the reservoir is the same as the total energy involved in the Sedov solution; and the initial temperature inside the reservoir is the same as the one in the burnt region of the Sedov solution.

Application of the Approach: A Numerical Verification Exercise for FLACS, in Dealing with Fast Deflagration

It has been shown previously that, in a far field, the energy release from a fast deflagration can be represented by a corresponding high-pressure and high-temperature spherical region equivalent in energy. For current investigation, the following high-pressure and temperature reservoir (see Fig. 1) is considered: this corresponds to the flame velocity of 270 m/s (0.8 of speed of sound), which is approximately equivalent to the strength index of seven of the TNO multi-energy method (fast deflagration). Initial conditions for the equivalent reservoir burst problem are presented in Table 1 where r is the radius of the reservoir.

The objective is to study blast wave propagation in the far field area and with the presence of a protection wall, using CFD codes with the simplified approach. 3D simulations need to be validated first. For this purpose 3D solution obtained with FLACS code is compared to a precise 1D solution called "reference solution" obtained by solving the 1D point-symmetric Euler equations [7] for the vessel burst case in free field. Overpressure results are compared in Fig. 2 at four distances from the center of explosion (5, 10, 20, and 30 m) and fit perfectly; even results with a rough mesh (20 cm) are acceptable. Results of impulses and times of arrival are also satisfying.

Then, 3D-FLACS simulations are compared to a better resolved 2D axisymmetric solution from the EUROPLEXUS code with a wall. For this purpose, a parallelepipedic wall is located 9.2 m downstream of the center of the vessel. This position corresponds to a free field overpressure of about 150 mbarg. The wall is considered to be of infinite length (actually, the same size as the computational domain). This enables comparison between 3D-FLACS results and 2D-axisymmetric EUROPLEXUS results, but pressure effects along the wall sides cannot be taken into account in this way. The height of the wall is set to 2.5 m, its thickness to 0.5 m.

In EUROPLEXUS simulations, the 2D axisymmetric Euler equations are solved using a Finite Volume approach [5]. Initial conditions for 2D simulations have been imposed by projecting on the 2D axial-symmetric mesh the 1D point-symmetric results of the reservoir burst problem just before the interaction with the barrier occurs. In this case, Cartesian meshes similar to the one shown in Fig. 3 (left side) are used. The center of the reservoir is located at the left bottom corner of the mesh.

The computational domain presents a right bottom corner which is 9.2 m far from the right extremity of the barrier. The height of the computational domain is 10 m. The mesh is not uniformly refined. Indeed, close to the barrier the mesh size is ten times smaller than far from the barrier (left and right top corners). In order to investigate the sensitivity of the results with respect to the mesh size, three different meshes are used; the results from the finest mesh (cell size of about 2 cm) are used in the further analysis because they permit to obtain the maximum overpressure (obtained with reference solution) as function of the space with an accuracy of about 10 %. Following boundary conditions are imposed: slip boundary conditions on the soil and on the barrier, absorbing boundary conditions on the top and right boundaries, axisymmetry condition on the right boundary. CFL is equal to 0.5.

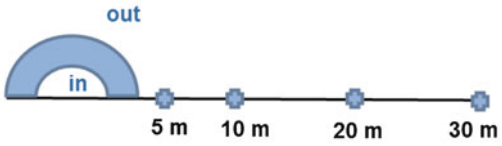

Fig. 1 Hemispheric vessel and pressure monitors in the far field: free field case

Table 1 Initial conditions for a vessel burst problem

	Vessel burst ($r < 2.66$ m)	Outside region ($r > 2.66$ m)
Overpressure (barg)	0.86	0
Temperature (K)	3677	293
Density (kg/m^3)	0.18	1.19
Speed of sound (m/s)	1215	343.10

In 3D-FLACS simulations, the RANS equations are solved on a 3-D Cartesian grid, using a staggered finite volume method. FLACS uses a *k*-epsilon model. A special FLACS setup is used for the hemisphere reservoir representation. More details about vessel burst can be found in the User Guide [4]. The open boundary conditions "PLANE_WAVE" are imposed in the horizontal directions (X and Y) and at the upper boundary in the Z direction. The lower Z boundary corresponds to the ground; hence the wall boundary (no-slip) condition is imposed there. Both CFL numbers are kept low: CFLC = 0.1, CFLV = 0.1 in order to ensure numerical stability and good representation of the blast wave. The option of time step "=KEEP_LOW" is also recommended for calculations of far-field blast propagation [4]. Different simulation domain sizes have been tested to check the influence of domain size on results: 5, 10, and

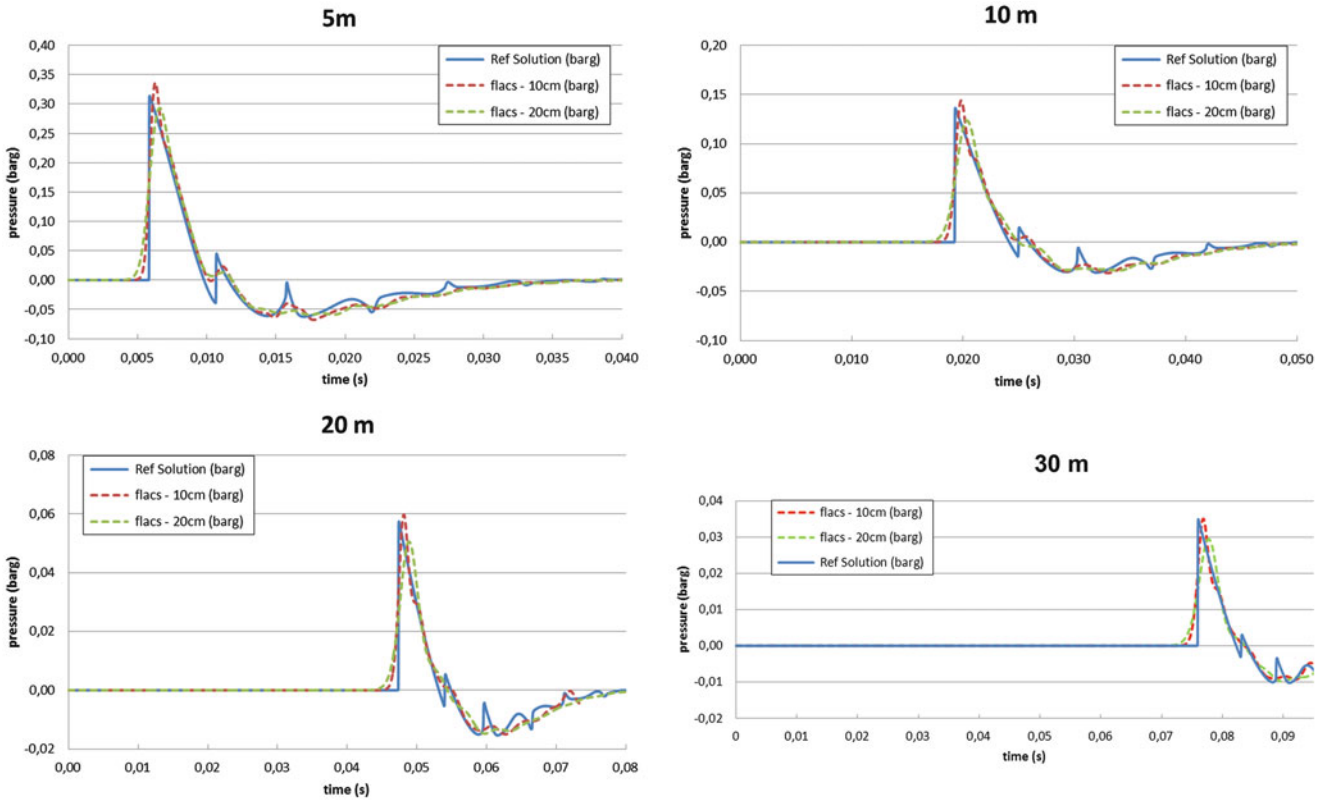

Fig. 2 Overpressure results in free field. 3D-FLACS results versus 1D-reference solution

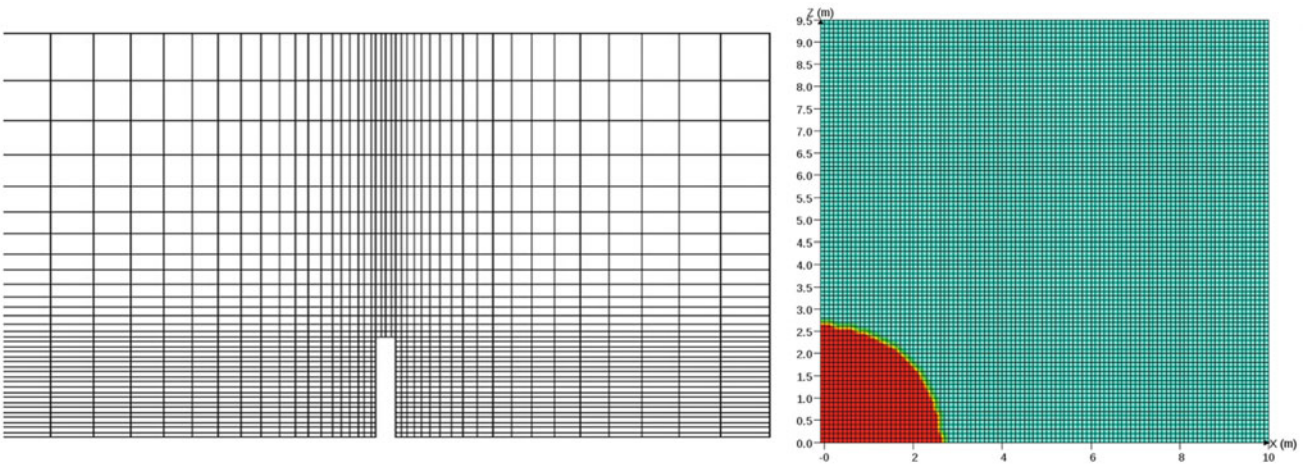

Fig. 3 An example of mesh used by EUROPLEXUS (*left*); by FLACS in free field (*right*)

20 cm cell sizes. Spatial resolution with a cell of 10 cm gives good results.

Figure 4 shows the comparison of the FLACS simulation results obtained with 5 cm (in pink dotted line) and 10 cm (in blue dotted line) resolutions, and results from EUROPLEXUS (in black line) for vessel burst problem with a wall, for monitoring points located upstream of the wall (left side in Fig. 4), and behind the wall (right side in Fig. 4). This comparison shows that FLACS results are in very close agreement with EUROPLEXUS results (even for 10 cm cell size) for the maximum overpressure (corresponding impulse and the time of overpressure arrival are also in good agreement) with an error globally comprised between 2 and 15 %. Figure 5 shows the propagation of blast wave in free field, and around the wall. Reflection phenomena are well represented, even Mach stem formation is observed at time = 0.031 s.

Experimental Validation

The objective of this paragraph is to present deflagration experiments realized at middle scale [6], and to validate with these experimental data FLACS simulation results

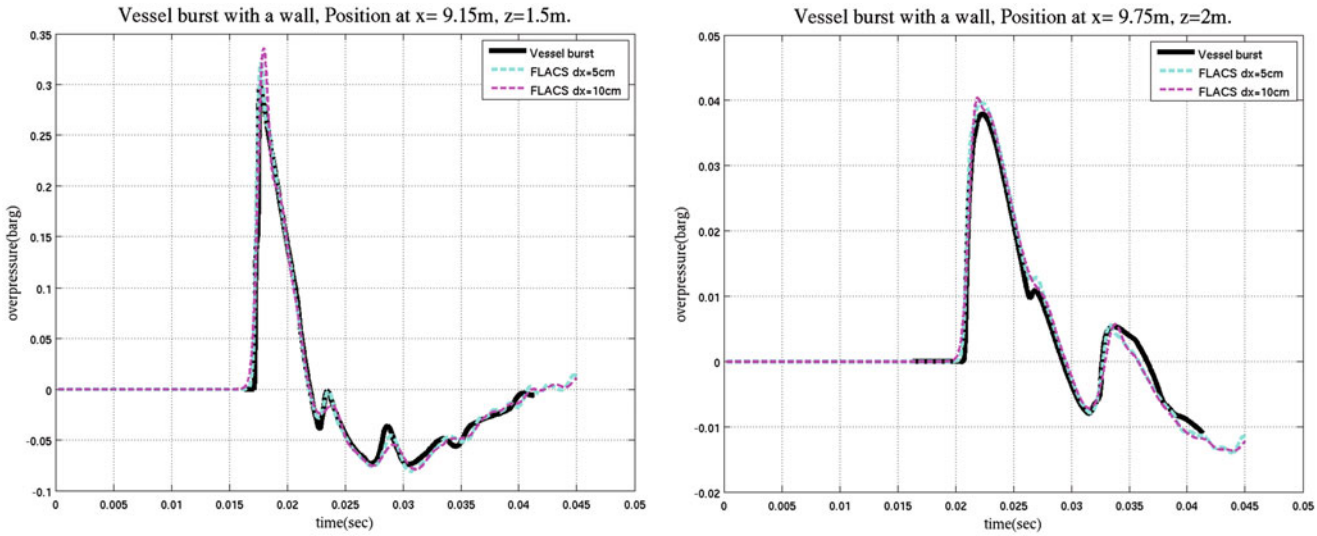

Fig. 4 Cross comparison of FLACS overpressures results with EUROPLEXUS (before the wall $x = 9.15$ m; and after the wall $x = 9.75$ m)

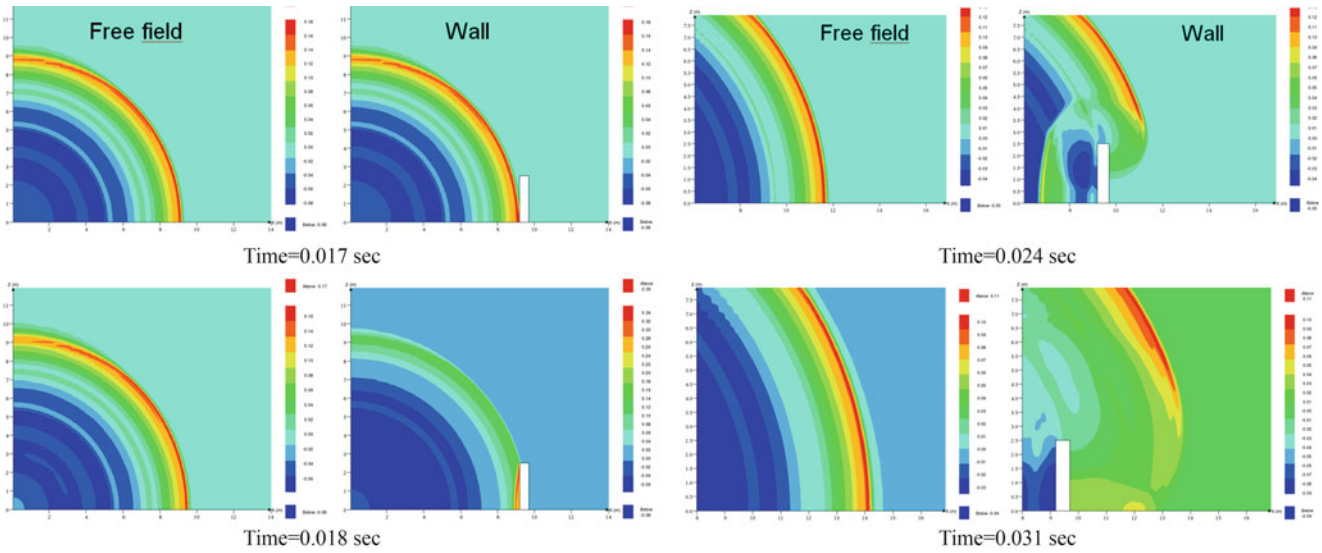

Fig. 5 Wall effect on the overpressure propagation. Snapshots of the overpressure at various times: free field geometry, and geometry with a wall at 9.2 m. (Note that the color bar for free field and geometry with a wall are different)

obtained with the simplified approach. The aim of the experiences was to quantify overpressures and flame velocities. Challenge was to set up an experimental facility that would enable the acceleration of a hydrogen-air flame up to ~130 m/s, so that it is possible to quantify overpressures big enough on the wall located in the vicinity of the explosion. Experiments were conducted at INERIS, France. Pictures of the setup are given in Fig. 6. A hemispheric gaseous cloud of 1.5 m in radius is used. The protection wall is located 10 m from the hemisphere center. The length of the wall is $L = 6.17$ m, its height H is 2 m (corresponding to the aspect ratio of $L/H = \sim 3$) and its width W is 0.15 m. Gas ignition is performed at the center of the hemisphere 5 cm up from the platform. Pressure history is recorded by piezo-resistive transducers. In order to have a sufficient flame speed without obstacles, the following hydrogen oxygen enriched air mixture is used: 40 % H_2–20 % O_2–40 % N_2. On the basis of the measured pressure decay with distance on the free field and measured apparent flame velocity (i.e., 125 m/s), Dorofeev [10] correlations are used to assess overpressure inside the hemisphere, with a laminar flame velocity S_L of 3.90 m/s and an expansion ratio σ of 7.59 according to Sabard [11]. Since concentrations of hydrogen, oxygen, and nitrogen are known, the adiabatic flame temperature equal to 2719 K is calculated using the thermochemistry GASEQ software. The combustion energy of hydrogen contained in the hemisphere is $E = 2.82 \times 10^7$ J.

The equivalent high-pressure and temperature reservoir has the same energy as the experimental hemisphere, hence one can easily find the equivalent vessel radius $R_{eqv} = 7.48$ m. The center of the vessel is located at the point with coordinates (0, 0, 0). A FLACS setup file is used for the hemisphere reservoir representation, using a temperature equal to 2719 K. This is not detailed here but the independence of the numerical solution on the grid has been checked: and solution with a cell size of 10 cm is in a close agreement with the solution obtained on the mesh with a cell of 8 cm. Since the simulations do not represent the combustion process, it is interesting to notice that there is a delay in time between simulations and experimental results. This time shift has been easily estimated from experimental data, corresponding to flame propagation duration inside the experimental hemisphere (i.e., corresponding to the end of the combustion, when the whole amount of mixture is burned out). The comparison of simulation results with experimental data (corrected by the time shift of 0.047 s) in terms of the measured overpressure, in the free field, but also, on the wall and after the wall is very satisfying.

Conclusions

A simple approach to model blast propagation in presence of a wall in the far field has been proposed and validated in this chapter. Indeed, a verification exercise to estimate the capability of numerical codes to reproduce blast waves consecutive to a fast deflagration in a completely unconfined environment and their interaction with a protection wall was carried out. The experiment [6] that was reproduced by the simulations is the explosion of a stoichiometric hydrogen–oxygen mixture diluted by nitrogen in a 3 m diameter hemisphere in an unconfined configuration first, and then with a wall located in the vicinity of the explosion. By comparison of experimental data and different simulations results between themselves, it was shown that most of the calculations reproduced quite well the maximum overpressures that are generated during the explosion. Also the maximum impulse is well captured in most of the simulations. The advantage and innovation of this simplified approach is to enable to assess quite rapidly and efficiently the mitigation effect of a protective wall against the Effects of a Vapor Cloud Explosion. In risks assessments studies, well-known TNO multi-energy curves are commonly used to characterize pressure effects consecutive to a deflagration in the free field (strength indexes from 1 to 9 are considered for slow to fast deflagration, and index ten is used for detonation). Now, a new step would be to build new curves in presence of a wall so as to assess its mitigation efficiency against the effects of the blast; further work is also required about this.

Acknowledgments This work was supported by the BARPPRO research project of the Global Security 2010 Programme of the National Research Agency (project ANR-10-SECU-0008).

Fig. 6 Hemisphere cloud used in the experiments and protection wall

References

1. NOTA recommandations 2009—Guide SFEPA n°9. Guide des Bonnes Pratiques en Pyrotechnie. Version française (2009)
2. Borgers, J.: Blast walls reviewed. In: 21st military aspects of blast and shock, Jerusalem, Israël, 4–8 Oct 2010
3. Eveillard, S., Lardjane, N., Vinçont, J.Y., Sochet, I.: Towards a fast-running method for blast-wave mitigation by a prismatic blast wall. C. R. Mécaniques **341**, 625–635 (2013)
4. FLACS v10.0 User's Manual, GexCon (2013)
5. EUROPLEXUS User's Manual, on-line version: http://europlexus.jrc.ec.europa.eu
6. Rapport final ANR-10-SECU—BARPPRO—Dimensionnement des BARrières Physiques de PROtection contre la propagation d'ondes de souffles consécutives à une explosion. Déflagration: Etude expérimentale à moyenne échelle. Rapport N° ANR-FORM-090601-01-01 (2014)
7. Beccantini, A., Malczynski, A., Studer, E.: Comparison of TNT-equivalence approach, TNO multi-energy approach and a CFD approach in investigating hemispheric hydrogen-air vapor cloud explosions. In Proceedings of the 5th International Seminar on Fire and Explosion Hazards, Edinburgh, UK, 23–27 Apr 2007
8. Sedov, L.I.: Similarity and dimensional methods in mechanics. Academic, New York (1959)
9. Kuhl, A.L., Kamel, M.M., Oppenheim, A.K.: Pressure waves generated by steady flames. In: 14th Symposium (International) on Combustion, The Combustion Institute (1973)
10. Dorofeev, S.B.: Evaluation of safety distances related to unconfined hydrogen explosions. Int. J. Hydrog. Energy **32**, 2118–2124 (2007)
11. Sabard, J.: Etude de l'explosion de mélanges disphasiques: hydrogène et poussières. PhD Thesis, Orléans University, France (2013)

Numerical and Experimental Analysis of the Effect of Different Shapes of Rigid Barriers on Blast Wave Propagation

R. Hajek and M. Foglar

Introduction

Many terrorist attacks have been carried out in the last few years, for example, in Oslo, Norway (2011), and more recently in Boston, USA, and in Volgograd, Russia (both 2013). Terrorist attacks are targeted mainly at public facilities, such as railway stations, government buildings, embassies, and the transport infrastructure. Due to the rise in this kind of threat, research on the effect of blast loading on structures and interiors has gained considerable attention.

The authors' research on blast effects on structures and their surroundings in recent years was presented in multiple articles [1, 2]. This chapter presents reduced-scale experiments on the effect of different shaped rigid barriers on blast wave propagation. The experimental data set was used for calibrating numerical FEM models for use in predicting pressure wave propagation.

The first run of experiments was conducted in November 2013. Interaction between air shock wave and rigid barriers was examined for multiple arrangements of barriers. Results of the experiment were used to develop and calibrate the computer model of propagation of the air shock wave in LS-DYNA. Results of computer modeling exhibited good agreement with experimental measurements for all evaluated barrier layouts. Findings were published in [3].

The second run of experiments was conducted in November 2014. It wasn't focused on arrangement of barriers, but rather on the effects of barrier surface to shock wave mitigation. A single arrangement of barriers was used with varying surface material of the barrier. An additional setup included barriers equipped with steel extension member with varying angle of inclination towards the explosive device.

Experimental Setup

The arrangement of the experiment is shown in Fig. 1. To increase the effectiveness a geometrically complex surface of the barrier was proposed. The results of computer modeling in LS-DYNA suggested a shape of barrier surface similar to acoustic sheeting used in studios to eliminate the echoes caused by sound wave reflections. Based on the analogy between sound and shock wave (both having mechanical nature) the barriers were equipped with acoustic foam facing and the facing of similar shape made of concrete (Fig. 2). Due to the geometric complexity of the proposed concrete wall facing, a special concrete mixture and casting method had to be developed to allow manufacturing of blast effects reduction sheeting of desired shape. The manufacturing process is described in the following chapter.

The concrete walls were equipped with multiple variants of facing:

- Foam pyramid shape acoustic sheeting (Fig. 2)
- Concrete truncated pyramid shape sheeting (Fig. 3)
- Smooth steel angled extension panel (Fig. 4)

Four pressure gauges were placed in the area behind the barrier as shown in Fig. 1. The peak overpressure at the shock front of passing shock wave was measured for each experimental arrangement with each sensor. Detailed discussion of results is presented below.

R. Hajek • M. Foglar (✉)
Department of Concrete and Masonry Structures, Faculty of Civil Engineering, Czech Technical University in Prague, Thakurova 7/2077, Prague, Czech Republic
e-mail: marek.foglar@fsv.cvut.cz

G. Ben-Dor et al. (eds.), *30th International Symposium on Shock Waves 1*, DOI 10.1007/978-3-319-46213-4_124

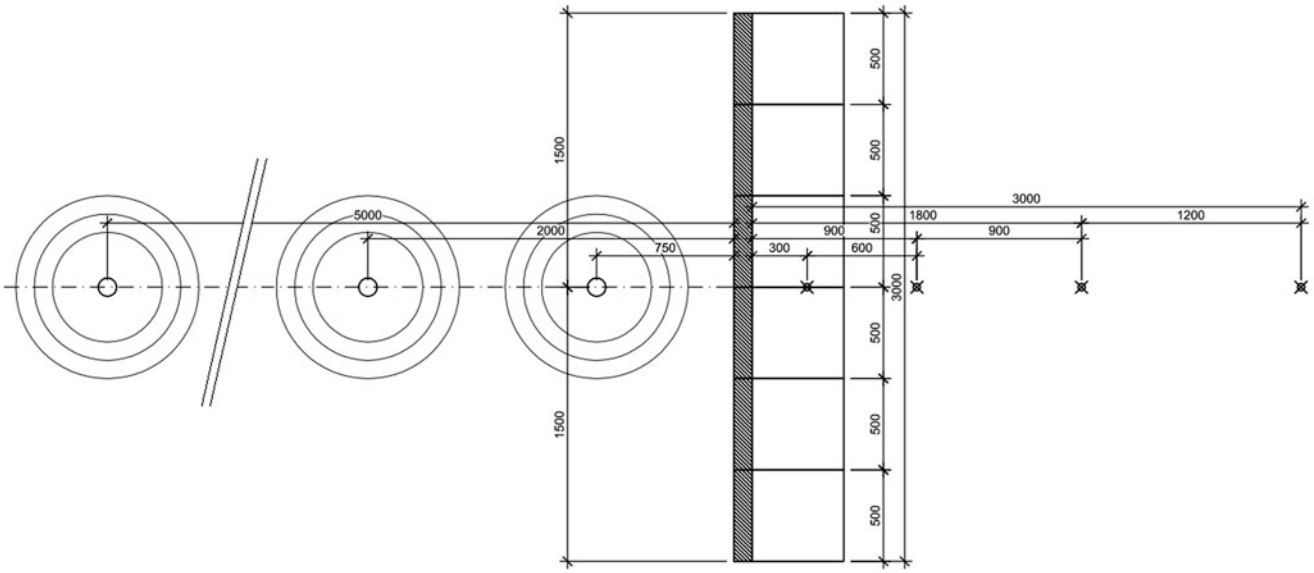

Fig. 1 Arrangement of the experiment

Fig. 2 Barriers equipped with foam acoustic sheeting

Manufacturing the Concrete Facing

The shape of concrete sheeting was developed from the shape of acoustic sheeting used in studios. A truncated pyramid shape was chosen as more suitable for the purpose of concrete casting. To get the concrete sheeting undamaged out of the formwork it was decided to manufacture the formwork with the use of silicone rubber (Fig. 5).

The elastic rubber form effectively prohibited any means of compacting. Also the complex shape and the need for high durability had to be considered. A novelty concrete mixture had to be developed to satisfy all the requirements. The resulting material can be specified as high-strength self-compacting concrete (HSSCC).

The finished sheeting were connected to the concrete precast walls on the site of the experiment using cement-based adhesive. Due to considerable self-weight of the sheeting a high-strength adhesive had to be used. Sufficient bond was achieved just few hours after application.

Results of the Experiment

Measured overpressure behind the barrier was compared to overpressure caused by an open field blast at corresponding scaled distance. First set of blasts was measured without any barrier and served as a basis for comparison. A theoretical curve was proposed to offer a solid basis for evaluation of barrier effectiveness (Fig. 6). The curve is defined by equation (1) below:

$$\Delta p^{+} = \frac{95}{Z} + \frac{450}{Z^2} + \frac{350}{Z^3} \tag{1}$$

where $Z = R/\sqrt[3]{W}$ is the scaled distance, R is the standoff distance of place of measurement from the center of the explosion, and W is the weight of the explosive in kilograms.

Figures 7 and 8 present a summary of measured data. The results show that barriers seem to have noticeable effect on shock wave propagation as the overpressure measured was reduced significantly compared to an open field blast. Also the effectiveness of uneven facing is promising, because barriers equipped with pyramid shape facing had roughly the same overpressure reducing effect as much bigger barriers with steel extensions.

Fig. 3 Barriers equipped with concrete sheeting

Fig. 4 Barriers equipped with steel extensions

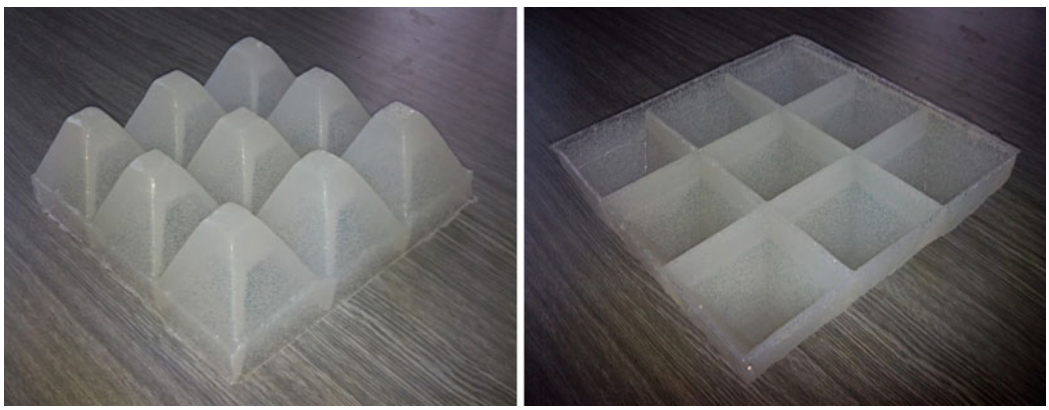

Fig. 5 Silicone rubber form

The effect of the barriers is significant in the area directly behind the barrier. With the increase in standoff distance the overpressure reduction effect disappears rapidly.

According to these results, effectiveness of a blast barrier could be improved with uneven surface facing while keeping the same size. That would allow the barriers to be installed more easily, reduce their space requirements, material consumption, and ultimately their cost as well.

Results of the 2014 experiment were used for necessary recalibration of already developed FEM model. The recalibration of FEM models developed for 2013 experiments was needed because of the variation in ambient temperature,

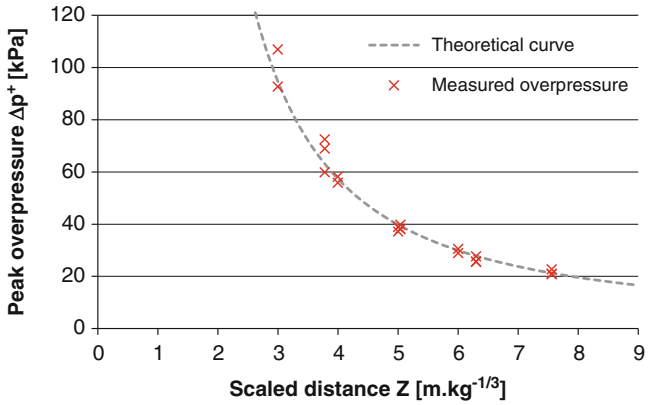

Fig. 6 Barriers equipped with steel extensions

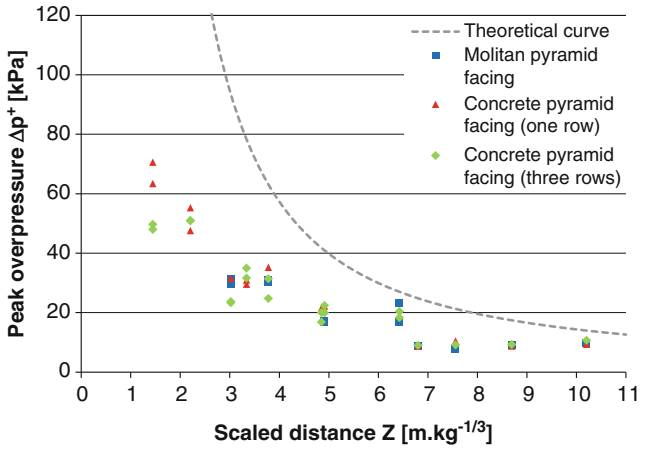

Fig. 7 The peak overpressure behind barrier with pyramid facing

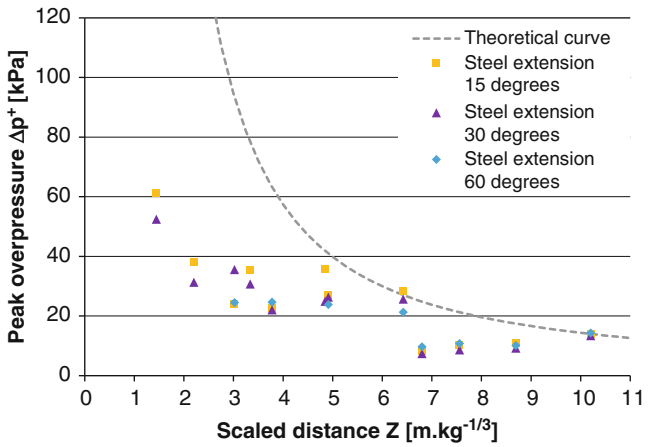

Fig. 8 The peak overpressure behind barrier with steel extensions

humidity, and pressure, as well as possibly partially different performance of TNT explosive charges compared to the charges used in 2013.

The greatest challenge that remains to be solved is the development of effective FEM model for more complex geometry of barriers (e.g., barriers equipped with the truncated pyramid facing), which would allow obtaining adequate results in limited computing time, so to keep the number of elements as small as possible.

At this stage the concrete barriers and pyramids are still modeled as rigid material. A suiting material for molitan foam still has to be developed. Small dimensions together with pointed and faceted shape of pyramids also cause some meshing problems which result in excessive computational time and compromise stability of the explicit solution.

Conclusions

In front of the barriers, the overpressure is increased, because the shock wave is reflected by the rigid barrier surface.

Very good agreement has been achieved between the experimental results and the numerical model results.

The results of the 2013 experiments presented in [3, 4] failed to prove the desired high effectiveness of rigid barriers with smooth surfaces. Barriers had some effect on lowering the peak overpressure, but only in the area directly behind barrier. At a greater distance, the effect diminishes rapidly and the pressure wave reverts to almost its original strength. The main benefit of such barriers would be their ability to absorb potentially harmful flying debris carried by the blast winds.

Experiments in 2014 evaluated barriers with rough surfaces. The results show that the effectiveness of barrier equipped with shock wave reduction sheeting was improved.

Barriers with rough surface seem to have comparable effectiveness as much larger smooth barriers. The increased effectiveness while maintaining compact size is important, because one of the greatest difficulties in using a blast barrier in the design of interior of a building is the disruption in functionality of the interior with a massive obstacle. It would be easier to include smaller and more effective barriers in the design and thus provide additional security.

References

1. Foglar, M., Kovar, M.: Conclusions from experimental testing of blast resistance of FRC and RC bridge deck. Int. J. Impact Eng. **59**, 18–28 (2013). doi:10.1016/j.ijimpeng.2013.03.008
2. Foglar, M., et al.: Blast performance of RC panels with waste steel fibers. Const. Build. Mat. 94, 536–546 (2015). doi: 10.1016/j.conbuildmat.2015.07.082
3. Hajek, R., Foglar, M.: Numerical and experimental analysis of the effect of rigid barriers on blast wave propagation. J. Struct. Eng. **141** (12), 04015061 (2015). doi:10.1061/(ASCE)ST.1943-541X.0001308
4. Hajek, R., Foglar, M.: The reduction of peak overpressure using concrete blast barriers. WIT Trans. Built Environ. **141**, 265–275 (2014). doi:10.2495/SUSI140231

Study on the Effects of Granular Particles on High Speed Gas Flow using DSMC Method

Arun Kumar Chinnappan, G. Malaikannan, and Rakesh Kumar

Introduction

A granular material consists of macroscopic solid particles characterized by the loss of energy whenever the particles collide. One of the fascinating behaviors of granular particle is dissipation of energy due to inelastic collisions. The effect of granular particles on the gas flow at high speeds is not well studied so far. Although not well understood, it is very important to understand the effect of granular particles on gas flow properties in order to simulate a realistic situation. In contrast to the gas molecules, granular particles behave in a very different way, e.g., unlike gas molecules, granular particles don't have thermal motion superimposed on the directed motion. Moreover, granular particles undergo inelastic collisions with each other losing a part of relative translational energy on every collision, whereas the total relative collision energy is assumed to remain constant for gas–gas collisions in non-reacting flows. At the same time, the gas-granular interaction is also dissipative in nature, and involves drag force and skin friction heating due to the relative motion of gas molecules over granular particles. This behavior of granular particles lead to significant energy loss, particularly when granular number density is high. Gradenigo et al. [1] used energy injection mechanism in the form of a thermal bath such that the external energy balances the energy lost in granular–granular collision. If this loss in energy is converted into heat, it can increase the thermal velocity of the gas molecules.

To study the granular flows, researchers used molecular dynamics simulation, event driven method, and Direct Simulation Monte-Carlo (DSMC) Method. The shock instability in granular gases was studied by Srimas et al. [2]. In recent years, DSMC framework is also used to study granular flows [3–5]. In Brey's study, DSMC is used to study the properties of a freely evolving dilute gas of smooth, inelastic hard spheres [3]. The DSMC method provides a useful tool to study low-density inelastic fluids. The results were found to be in good agreement with the analytical solution of the Boltzmann equation using the Enskog approximation, especially for small values of the coefficient of restitution [4]. Francis studied the segregation of an impurity in a granular fluid. In this study, the granular fluid was sheared in such a way that inelastic cooling is balanced by viscous heating [5].

In this work, we consider a gas-granular flow at a Mach number of 10 over a 2D cylinder. The gas considered is argon, a monoatomic gas, so as to clearly understand the effect of granular particles on gas dynamics without considering the internal modes of energy. Ar–Ar collisions are modeled in a probabilistic manner within the DSMC framework. Granular particle is modeled as a hard, inelastic sphere of fixed diameter (d), 1 mm, and a mass (m) of 2.7183×10^{-11} kg. The granular number density is set in such a manner so that the mass fraction of granular particles is 0.1, although a variation in the number density is performed so as to study its effect on the gas-granular flow dynamics. Granular particles are considered to undergo inelastic collisions with each other with a finite coefficient of restitution (α), which is the ratio of relative speed after collision to before collision, and is kept constant for all granular–granular interactions in a simulation. However, in order to study the effect of the coefficient of restitution on gas-granular flow dynamics, different values of α are considered varying from 1 to 0.85. When it comes to gas-granular interactions, every granular particle is considered to experience drag due to the gas and causes skin friction heating to the gas. The heat release due to granular–granular collisions and skin friction heating is accommodated to the gas. To the best of our understanding, such a work involving accommodation of heat release in a gas-granular flow is not attempted before. Furthermore, the

A.K. Chinnappan (✉) • G. Malaikannan • R. Kumar
Department of Aerospace Engineering, Indian Institute of Technology Kanpur, Kanpur, Uttar Pradesh, India
e-mail: arun@iitk.ac.in; mkannan@iitk.ac.in; rkm@iitk.ac.in

G. Ben-Dor et al. (eds.), *30th International Symposium on Shock Waves 1*, DOI 10.1007/978-3-319-46213-4_125

effect of granular particles on a Mach 10 argon gas flow is studied for different number of densities of granular particles and at different values of coefficient of restitution.

Computation Model

A two-dimensional, multispecies parallel in-house DSMC solver is used for the simulation of gas-granular flow with modifications for modeling of granular particle dynamics. The gas-granular model consists of gas–gas collision, gas-granular collision, and granular–granular collision, each of which is discussed below.

Gas–Gas Collision: DSMC Method

The regular DSMC method is used for gas–gas collision. DSMC was first proposed by G. A. Bird for rarefied flows [6]. This method deals with simulated molecules, each of which represents a large number of real molecules. The primary assumption in DSMC is the decoupling of molecular movement and inter-molecular collisions (considered instantaneous), and due to this decoupling, the time step used in DSMC is typically kept less than the mean collision time and the cell size should be less than the mean free path of the gas. The DSMC method involves discretization of the computational domain into cells and sorting of the molecules by their position coordinates. Molecules are moved in a deterministic way followed by the their collisions in a probabilistic manner using the acceptance-rejection method. Post collision velocities are determined using the Variable Hard Sphere (VHS) model. Maxwell [6] and Cercignani Lampis and Lord (CLL) Model [7] are used for the gas-surface interactions. The macroscopic parameters are calculated by time averaging the sampled data.

Granular–Granular Collision

The granular particles are modeled as hard, inelastic spheres. The inelastic collisions between granular particles is governed by the following equation [1]:

$$v_1^t = v_1 - \frac{(1+\alpha)}{2}[(v_1 - v_2).\widehat{\sigma}]\widehat{\sigma} \tag{1}$$

$$v_2^t = v_2 + \frac{(1+\alpha)}{2}[(v_1 - v_2).\widehat{\sigma}]\widehat{\sigma} \tag{2}$$

where v_1, v_2 are pre-collisional velocities, $v^t{}_1$, $v^t{}_2$ are post-collisional velocities, $\alpha \in [0, 1]$ is the coefficient of restitution, and $\widehat{\sigma}$ is the unit vector joining the center of colliding particle "1" to the colliding particle "2". Noteworthy is the fact that for a unity value of the coefficient of restitution α, the elastic collision dynamics is obtained, with relative speed remaining unchanged during collision. The value of α is varied from 1 to 0.85 in this work to take care of the uncertainties, and also to assess the sensitivity of gas-granular flow dynamics to the coefficient of restitution. The loss in the total translational energy of granular particles in a collision cell due to granular–granular collision is added to the random translational energy of gas particles, as given in detail in section "Heat Accommodation".

Gas-Granular Collision

The gas-granular collision is numerically complex because of the huge difference between the masses of a gas and granular particle. Therefore in this work, like other works [1], we have considered only the effect of gas-granular collision without actually modeling it. A granular particle is assumed to undergo drag as it moves, due to the presence of gas. In the first step, flow over a sphere of diameter 1 mm is simulated at different Mach numbers (corresponding to different relative velocities) and different Reynolds numbers, gives drag acting on granular particle. The coefficient of drag C_d thus obtained is used in the modeling of gas-granular collision. The velocity of a granular particle is updated in the following manner:

$$V_g = V_g - \frac{\frac{1}{2}\rho_c v_r^2 A_g C_d \Delta t}{m_g} \tag{3}$$

where V_g is the velocity of a granular particle, ρ_c is the local number density of gas in a collision cell, v_r is the relative velocity between a granular particle and local bulk velocity, A_g is the cross-sectional area of a granular particle, Δt is the time step associated with the DSMC method, and m_g is the mass of a granular particle.

The gas–granular particle interaction also results in viscous dissipation of heat, called as skin friction heating henceforth, and is given by the following equation:

$$Q_{sf} = D_g v_r \Delta t \tag{4}$$

where Q_{sf} is the heat due to skin friction, $D_g = C_d \frac{1}{2}\rho_c v_r^2 \quad A_g$ is the drag of the granular particle, and v_r is the relative velocity between the granular particle and local bulk

velocity of the cell. In the next section, we describe the way with which we accommodate heat to the gas.

Heat Accommodation

The losses in energy during the granular particles motion as mentioned in sections "Granular–Granular Collision" and "Gas-Granular Collision", is converted into heat. The heat thus generated is considered to increase the thermal motion of the gas molecules by a factor that depends on the relative magnitude of heat generation to the total random translational energy in a cell [8]. Thus if Q is the amount of heat produced due to loss in energy and E_t is the random translational energy of molecules, then the velocity components of a gas molecule as modified due to heat generation are given as:

$$u_i^t = \varphi(u_i - U_i) + U_i \tag{5}$$

where i refers to the x, y, and z components of velocity. The heat accommodation factor φ is defined as

$$\varphi = \sqrt{\frac{E_t + Q}{E_t}} \tag{6}$$

The total random translational energy E_t in a cell is given by

$$E_t = \sum_{i=1}^{3}\sum_{n=1}^{N}\frac{1}{2}m(u_{i,n} - U_i)^2 \tag{7}$$

where $u_{i,n}$ represents nth particle in the i direction. U_i represents bulk velocity of the cell in the i direction.

Numerical Parameters

The problem involves flow of argon over a circular cylinder of diameter 0.3048 m at a freestream Mach number 10. The freestream pressure and temperature are 1.377 Pa and 200 K, respectively. The freestream number density of Ar gas and granular particles are 4.986×10^{20} and 2.452×10^{5}. The mass of a granular particle is assumed to be 2.7183×10^{-11} kg, chosen such as to give a granular mass fraction of 0.1. Time step is taken as 5×10^{-7} s, which is less than mean collision time (3×10^{-6} s), and similarly the cell size is kept smaller than the global mean free path based on the free stream number density. Granular particles are assigned the bulk velocity corresponding to Mach 10 at the domain inlet. The effect of granular particles on gas flow properties and surface properties is studied in this work.

Results and Discussions

The results obtained by the in-house solver for gas-granular dynamics are presented as follows. We present the effect of granular particles on bulk gas flow properties and surface properties in the following two sections. In what follows, results obtained for gas-granular flow are compared with those for pure argon case.

Bulk Flow Properties

The comparison of flow properties and x component of velocity along the stagnation streamline for pure argon and gas-granular flow with and without skin friction heating is shown in Fig. 1. The coefficient of restitution chosen is 0.85.

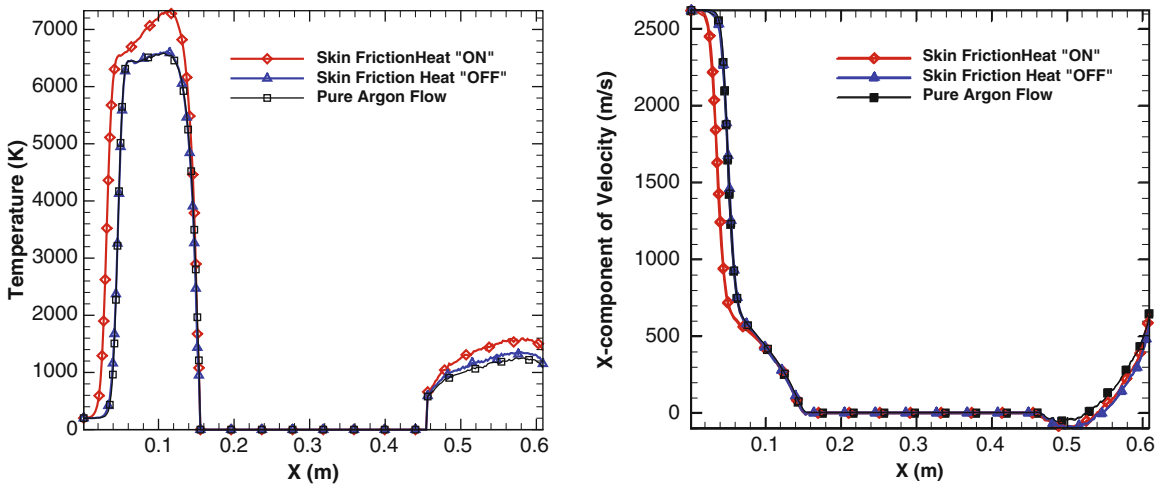

Fig. 1 Comparison of pure argon flow with granular-gas flow

The temperature profile of granular flow without skin friction heating agrees with pure argon flow except in the wake region that shows the effect of heating due to granular–granular collisions. Granular particles enter with same velocity as gas but decays very slowly with time, so the velocity of granular particles is always found to be higher. Since the granular–granular collision is based on relative velocities, the loss in energy due to granular–granular collision is also low. This is the reason why skin friction heat "OFF" case is closely matching with pure argon case. There is a minor difference in temperature in the wake region because the granular particles experience more drag due to the presence of reverse flow in the wake region. Noteworthy is the fact the effect of coefficient of restitution is found to be insignificant, when it is varied from 0.85 to 1.

The difference in temperature is significant for granular flow with the consideration of skin friction heat addition. Since it is a Mach 10 flow, granular particles generate more heat, which is given by Eq. (4) and depends strongly on the relative velocity between the fluid and granular particle section "Gas-Granular Collision". In shock region, the bulk velocity of gas is low, which results in a larger relative velocity between granular particle and the gas. This results in a high energy dissipation due to skin friction, giving rise to a significant change in the temperature along the forebody stagnation streamline is observed. From Fig. 1, it is also evident that shock stand-off distance also increases due to the skin friction heat release. This happens because skin friction heat accommodation to the gas increases the thermal velocity of gas molecules, thus displacing the shock-wave upstream.

To study the effect of granular number density, the same case is simulated by reducing the granular number density to half of its previous value. Figure 2 shows the temperature and x-component of velocity at two different values of granular particle number density. As expected, the temperature profile for reduced number density falls in between the pure Argon case and the higher number density case. The reason is that the number of granular particles is low, resulting in a smaller release of heat to the gas. Thus it can be found that number density of granular particles plays a big role in changing the gas flow dynamics. As observed before, there is no significant change observed in flow properties for different values of the coefficient of restitution, α.

Surface Properties

The normalized pressure distribution, C_p, around the cylinder and normalized heat flux, given as the Stanton number, are plotted in Fig. 3. The heat flux is normalized by free stream gas kinetic energy per unit volume. The pressure distribution for all the cases is same except at the stagnation point. On the other hand, there is a significant change in the Stanton number or surface heat flux due to the addition of skin friction heat to gas. It is found that the Stanton number increases by more than 30 %. The reason for higher surface heat flux can be explained from the consideration that after heat accommodation, the gas particles have higher velocities, and thus they can impart higher energy upon hitting a surface. This result could be very important in high speed flow situations.

Conclusion

A gas-granular flow at a Mach number of 10 over a 2D circular cylinder was studied, wherein the total mass fraction of granular particles was kept at 0.1. At very high speed

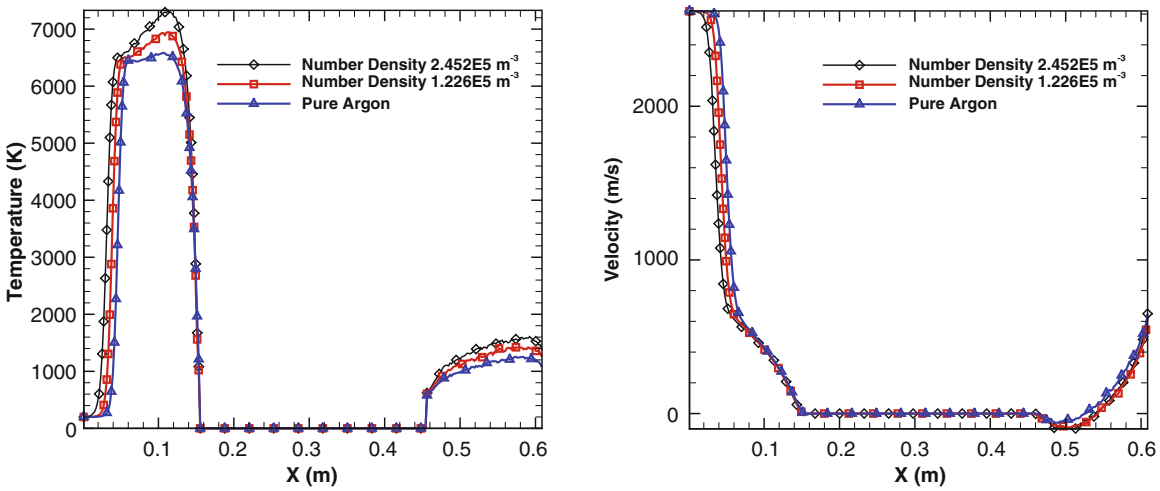

Fig. 2 Gas granular flow with different number densities

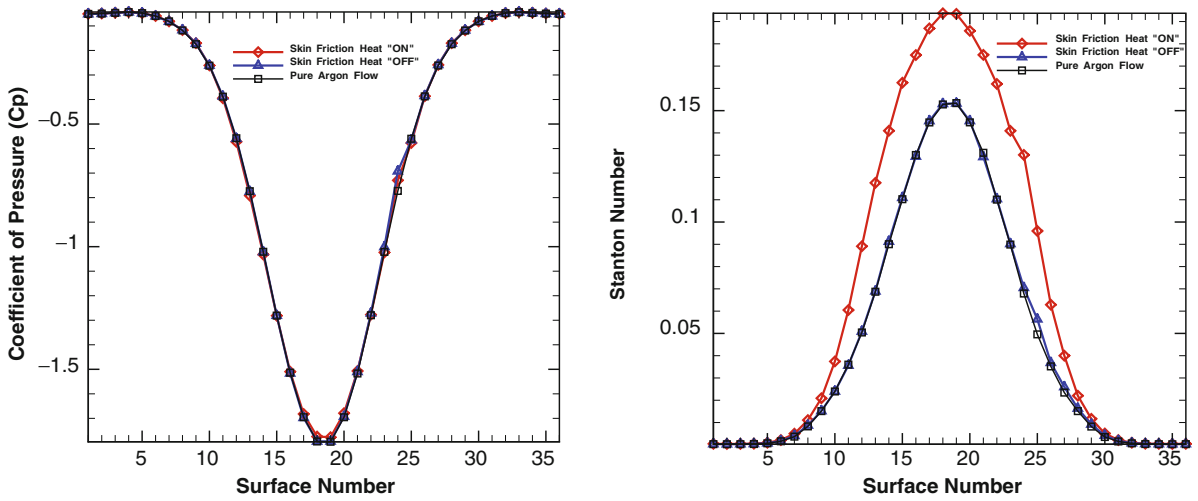

Fig. 3 Cp distribution and Stanton number for Skin friction "ON" and "OFF" case

($M = 10$), the energy loss due to granular–granular interaction is small when compared to the loss due to skin friction. Also, due to the skin friction heat release, there was found a significant increase in the shock stand-off distance. Another significant impact of granular particles was found on the surface heat flux. Number density of granular particles was found to be important in governing gas-granular flow physics. On the other hand, interestingly, the effect of coefficient of restitution was found to be rather small on gas-granular flow dynamics. Further studies need to be done for different flow situations in order to understand the gas-granular flow dynamics in its entirety.

References

1. Gradenigo, G., et al.: Fluctuating hydrodynamics and correlation lengths in a driven granular fluid. J. Stat. Mech. Theory Exp. **2011** (08), P08017 (2011)
2. Sirmas, N., Radulescu, M.: Evolution of shock instability in granular gases with viscoelastic collisions. arXiv preprint arXiv:1407.4202 (2014)
3. Brey, J.J., Ruiz-Montero, M.J.: Direct Monte Carlo simulation of dilute granular flow. Comput. Phys. Commun. **121**, 278–283 (1999)
4. Brey, J.J., Ruiz-Montero, M.J., Cubero, D.: Homogeneous cooling state of a low-density granular flow. Phys. Rev. E **54** (4), 3664 (1996)
5. Francisco, V.R., Garz, V.: Thermal diffusion segregation of an impurity in a driven granular fluid. arXiv preprint arXiv:1407.6308 (2014)
6. Bird, G.A.: Molecular Gas Dynamics and the Direct Simulation of gas Flows. Clarendon Press, Oxford (1994)
7. Padilla, J.F., Boyd, I.D.: Assessment of gas-surface interaction models for computation of rarefied hypersonic flow. J. Thermophys. Heat Transf. **23** (1), 96–105 (2009)
8. Kumar, R., Li, Z., vanDuin, A., Levin, D.: Molecular dynamics studies to understand the mechanism of heat accommodation in homogeneous condensing flow of carbon dioxide. J. Chem. Phys. **135**, 064503 (2011)

Model of Shock Wave Action on Porous Materials and Mixtures

S.A. Kinelovskii and K.K. Maevskii

Introduction

Methods based on shock wave impact on the substance are widely used to create innovative materials throughout the world. The production of composite materials, in particular, materials that based on multicomponent mixtures of metallic and nonmetallic powders are of great interest. Shock wave loading (SWL) of such mixtures can activate the chemical and phase transformations of the substances and contribute to the creation of entirely new materials with unique properties.

Results

Efficiency of SWL studies of the multicomponent mixtures with the aim of creating new materials mostly depends on the possibility of predicting the behavior of the components based on the properties of each component in the mixture and its contribution to the process with different intensities of dynamic effects. Today it seems impossible to construct a model, which will describe all the factors associated with the given process. Therefore the question of creating models that allows you to calculate at least the thermodynamic parameters (pressure, density, mass velocity, and temperature) for each component of the mixture. There are a lot of models, but they all are adapted to the occasion of maximum two condensed components in the mixture and work in limited ranges of possible pressures. The calculation methods based on the use of wide-range equations of state (EOS) of substances should be mentioned separately. They may be used to calculate SWL parameters of multicomponent mixtures, but these EOS for each component of the mixture contain dozens of free parameters and experimentally determined constants. In this regard, the calculations become very cumbersome and time consuming.

The thermodynamic equilibrium components (TEC) model developed to describe the behavior of porous mixtures is based on the assumption that all of the components of the mixture, including gas in pores, are in thermal equilibrium under the shock wave loading. EOS of the Mie–Grüneisen type are used to describe the behavior of the condensed phases. The initial internal energy and pressure of the substances are zero under normal conditions, taking into account the field of use of this model for pressures over 5 GPa. Hence, the equation of state for condensed component with the current and initial densities ρ and ρ_0, pressure P, specific heat c_v and Grüneisen coefficient Γ has the form

$$P = A\left[\left(\frac{\rho}{\rho_0}\right)^n - 1\right] + \Gamma c_V (T - T_0)\rho, \qquad (1)$$

where T and T_0 are the current and initial temperatures. For gas, we use the equation of the state of ideal gas. We write the conditions of dynamic compatibility on the shock wave front, which are laws of conservation of the mass flux for each component of the mixture and laws of conservation of momentum and energy fluxes for the mixture as a whole [1, 2]. The resultant equations combined with the equation of state for each component are sufficient to find dependences of the type of $P(U)$ or $D(U)$ (U and D are the mass and wave velocity, respectively), which can be treated as the shock adiabats (SA) of the multicomponent mixture. We suppose that the Grüneisen coefficient depends explicitly only on the temperature [1, 2]. For the mixture of two condensed components with the initial volume percentage μ_{10} and μ_{20} we can obtain the expressions

S.A. Kinelovskii • K.K. Maevskii (✉)
Lavrentyev Institute of Hydrodynamics, Siberian Branch RAS, Lavrent'eva Pr. 15, Novosibirsk 630090, Russia

Novosibirsk State University, Pirogova Str. 2, Novosibirsk 630090, Russia
e-mail: konstantinm@hydro.nsc.ru

G. Ben-Dor et al. (eds.), *30th International Symposium on Shock Waves 1*, DOI 10.1007/978-3-319-46213-4_126

$$P = \left(Z_1 + Z_2 \frac{\mu_{20}\sigma_1}{\mu_{10}\sigma_2}\right)\left(h_1 + \frac{\mu_{20}\sigma_1}{\mu_{10}\sigma_2} h_2 + \frac{(1-\mu_{10}-\mu_{20})\sigma_1}{\mu_{10}\sigma_g} h_g - \frac{\sigma_1}{\mu_{10}}\right)^{-1}, \tag{2}$$

$$Z_i = A_i\left[\left(h_i - \frac{n_i+1}{n_i-1}\right)\sigma_i^{n_i} + \frac{2n_i\sigma_i}{n_i-1} - h_i - 1\right],$$

$$h_i = \frac{2}{\Gamma_i} + 1, \quad h_g = \frac{2}{\gamma-1} + 1,$$

where A_i and n_i are the constants, $\sigma_i = \rho_i/\rho_{i0}$ are the degrees of compression of the corresponding components, $i = 1$, 2, g. Here ρ_g is the gas density and γ is the ratio of specific heats. We obtain three equations for four unknown variables P, σ_1, σ_2, and σ_g, which allow us to construct the shock adiabat of the mixture on the supposition of the equality of the temperatures of the components. If we assume that $\mu_{20} = 0$ in Eq. (2), which means the absence of the second component, we obtain the equations for a porous medium. If we additionally assume that $\mu_{10} = 1$, then we obtain the system of equations for a solid material. We can easily construct SA for the greater number of components of the mixture generalizing the corresponding equations. Some of the results of the comparison calculations [1, 2] for the TEC method with known experimental and calculated results of the different authors are listed below (SA, dual compression shock waves, evaluation of the temperature).

The calculations for TEC method are shown in Fig. 1 for aluminum when the porosity values m from 1.4 to 8, where m is the ratio of the densities of the solid and porous substances. The calculated data correspond well to the data obtained on the basis of experiment.

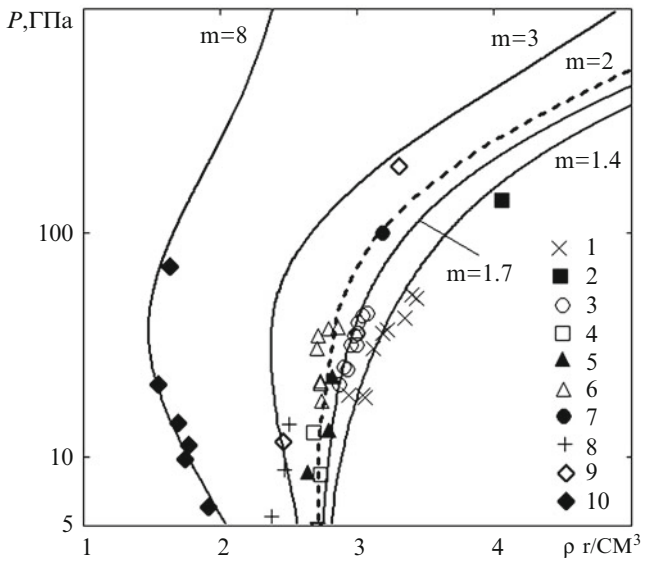

Fig. 1 Pressure-density diagram of porous aluminum. All calculations lines of this work are performed for TEC Method. Data [3] from different sources: *1*, *2*—$m = 1.4$; *3*—$m = 1.7$; *4–7*—$m = 2$; *8*, *9*—$m = 3$; *10*—$m = 8$

In order to obtain information about the thermodynamic properties of substances within the range of densities that exceed the density of a single compression, the states under repeated shock compression are recorded. As is seen from the results shown in Fig. 2, the model under consideration enables the experimental data on the double compression of aluminum to be described with an accuracy of the experiment within the available range of data.

The calculation-experimental estimation [5] of temperature is shown in Fig. 3 along the shock adiabat of solid

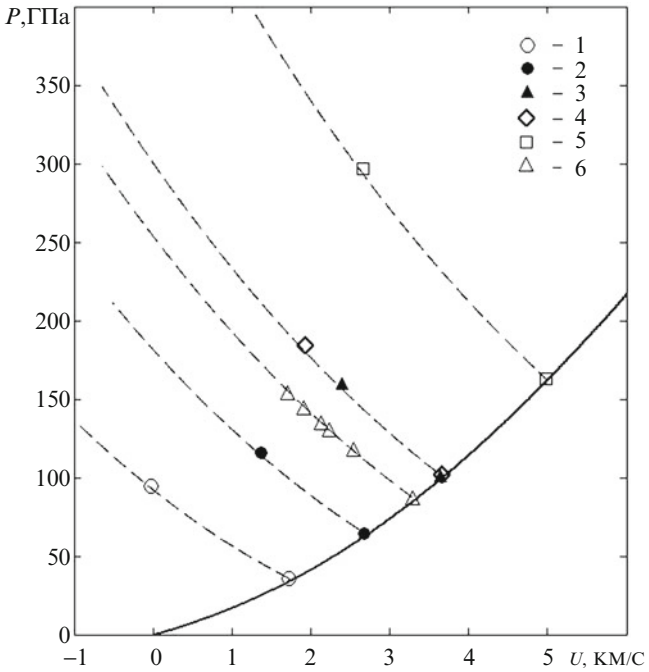

Fig. 2 Shock adiabat and adiabats of double compression of aluminum. TEC model calculations: solid line denotes the shock adiabat, and dashed line denotes the double compression. Experiment: *1*, *6*—[3], *2–5*—[4]

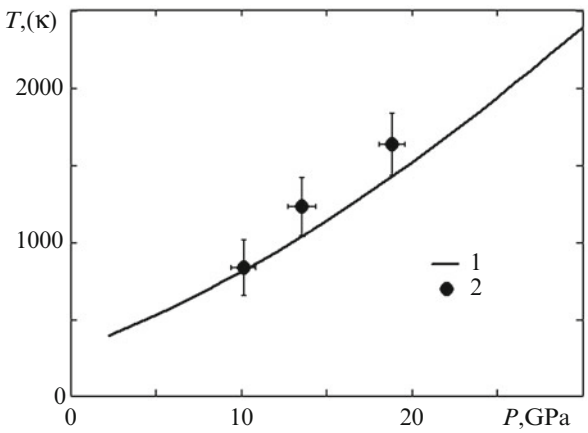

Fig. 3 Comparison of temperatures along the shock adiabat of bismuth. The ten model calculations: *1*. Experiment: *2* [7]

bismuth, as well as the TEC model calculations. The estimation of temperature for bismuth is within the region of the scatter of experimental data. It indicates on the reasonable estimates of temperature by the TEC model.

The TEC model allows us to calculate adequately isentropic unloading of the shock-compressed material. The results of the calculations, shown in Fig. 4 describe well the data obtained on the basis of the experiment when unloading for solid ($m = 1$) and porous bismuth ($m = 2.459$). Note that temperature values 24,500 K and 43,300 K obtained in the calculation for the points began unloading of porous bismuth at pressures 43 GPa and 73 GPa, respectively.

The calculations of the mixtures with two solid phases on the TEC method shows that the model describes well the data of SWL of the mixtures with the components having similar parameters, and for the mixtures with significantly different parameters of the components. The calculations for the mixture of tungsten and paraffin that have the large difference values of density were given in [6] for the three models, with varying degrees of accuracy describing the data obtained on the basis of the experiment. The calculations are shown for the SC-Criterion (single component), the KEA method (kinetic energy averaging). These two methods operate on the principle of additivity, which is widely used, giving a satisfactory description of the experiments at relatively low pressures for alloys. The third model is the Turbulent Entropy Method; the attempt is made to consider the interaction of the components. Adding to the figure from [6] the curve calculated on the TEC method, it can be seen that only the model made it possible to adequately describe all the available data of SWL of the tungsten-paraffin mixture, Fig. 5.

TEC method allows us to describe, in particular, the region of the polymorphic phase transition, considering the material in the region of phase transition as a mixture of phase of low-pressure and phase of high-pressure in SWL. The calculation of SA mixture of quartz SiO_2 and aluminum Al is shown in Fig. 6, when SWL, taking into account the phase transition in quartz. TEC method makes it possible to describe the behavior of the mixture with two components undergoing phase transition at SWL [7]. This calculation is shown in Fig. 7 for nonporous mixture of aluminum nitride AlN and silicon nitride Si_3N_4 with an equal volume fraction, taking into account the phase transition in the nitrides.

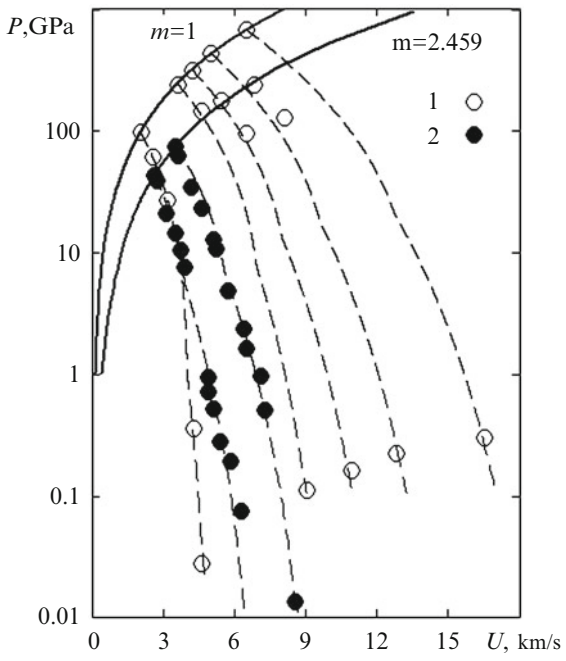

Fig. 4 Shock adiabat (*solid curve*) and unloading isentropes (*dotted curves*) for solid bismuth: *1*—unloading from the SA point with pressure of 96, 240, 314, 430, 670 GPa ($m = 1$); unloading from the SA points with pressures of 43 and 73 ГПа ($m = 2.459$). Experiment: [3]

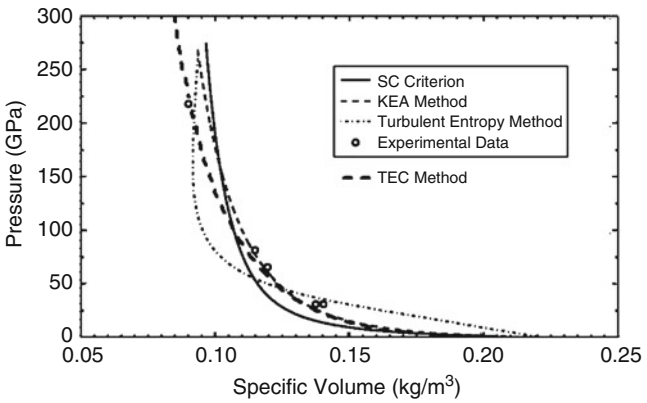

Fig. 5 Pressure-density diagram of mixture tungsten-paraffin

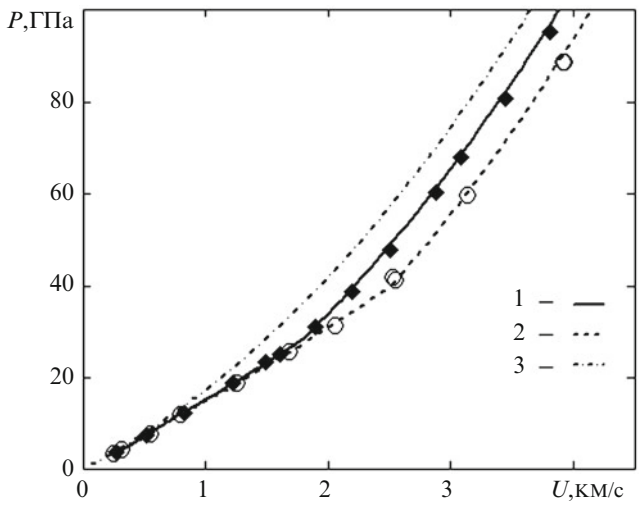

Fig. 6 Shock adiabat of Al, SiO_2, and their mixtures. The calculations lines: *1*—mixture, *2*—SiO_2, *3*—Al. Experiment: [3]

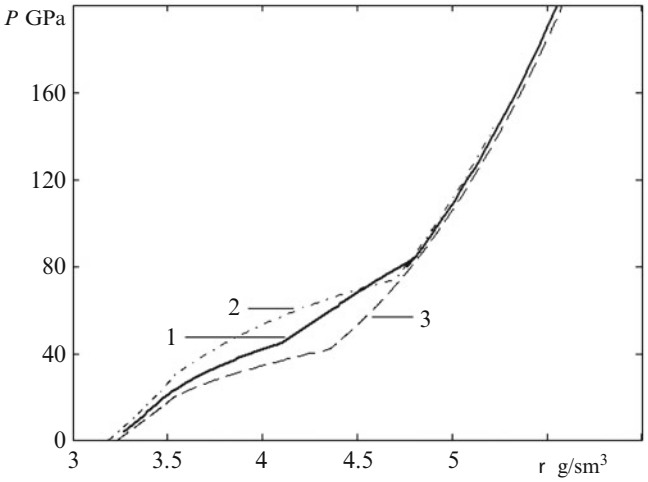

Fig. 7 Shock adiabat of mixtures Si3N4–AlN and nitrides. The calculations lines: *1*—mixture, *2*—AlN, *3*—Si_3N_4

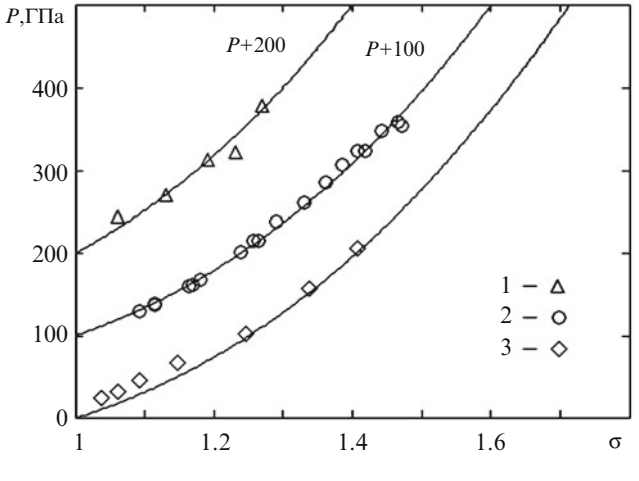

Fig. 9 Pressure–compression diagram for the porous carbides: *1*—WC $m = 1.201$; *2*—TaC $m = 1.125$; *3*—NbC $m = 1.07$. Experiment: [3]

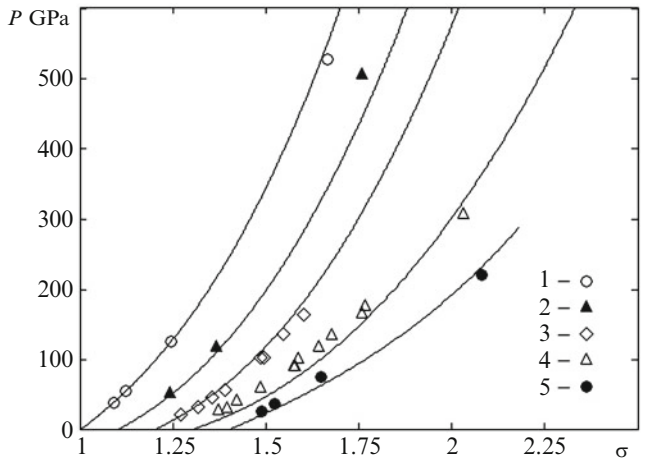

Fig. 8 Pressure–compression diagram for the carbides ($m = 1$). The calculations lines: *1*—WC, *2*—TaC, *3*—NbC, *4*—TiC, *5*—B_4C. Experiment: [3]

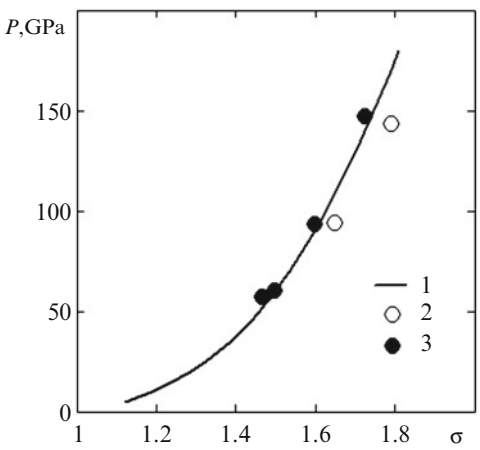

Fig. 10 Pressure–compression diagram for the alloy Bi, Cd, Sn и Pb. Shock adiabat (*solid curve*) for the alloy Experiment: *2*—[8], *3*—[9]

The SWL of carbides with different porosity is described by the TEC method, treating them as the mixture of the corresponding chemical composition. The significant description is obtained for the carbides with equal volume fractions and for boron carbide B_4C having, respectively, a ratio of 1:4 (Fig. 8). Such calculations have not been previously held for boron carbide. Similar results are shown in Fig. 9 for porous carbides.

Adding the appropriate equations, you can write a function similar to Eq. (2) and build SA to materials with lots of components. As an example, the experimental data and the model calculation of the TEC are shown in Fig. 10 for Wood's alloy (density of $\rho_0 = 10.14$ g/cm^3) consisting of four components: bismuth, cadmium, selenium, and lead. The data obtained on the basis of experiments on shock wave loading of this alloy is given in [8, 9], weight composition wt% at % Bi(40), Cd(9.5), Sn(9.5), and Pb(41).

Conclusions

Thus, the presented TEC method allows to describe adequately the known results (shock adiabat, double compression shock waves, adiabatic expansion of shocked substance, and temperature evaluation) in the whole range of possible pressures for virtually all solid and porous materials and mixtures for which experimental data are available. It should be noted that the proposed method of constructing the SA of

the mixture allows you to monitor the compression not only of the mixture as a whole, but also the compression of each component separately.

Acknowledgments This work was supported by the Russian Foundation for Basic Research (project nos. 13-03-00663).

References

1. Kinelovskii, S.A., Maevskii, K.K.: Model of the behavior of the mixture with different properties of the species under high dynamic loads. J. Appl. Mech. Tech. Phys. **54**, 524–530 (2013)
2. Kinelovskii, S.A., Maevskii, K.K.: Model of the behavior of aluminum and aluminum based mixtures under Shock-wave loading. High Temp. **52**, 821–829 (2014)
3. Levashov, P.R., Khishchenko, K.V., Lomonosov, I.V., Fortov, V.E.: Database on Shock-wave experiments and equations of state available via internet. In: Furnish, M.D., Gupta, Y.M., Melville, F.J.W. (eds.) Shock compression of condensed matter—2003, p. 87. AIP, New York (2004) (http://www.ihed.ras.ru/rusbank/, http://www.ficp.ac.ru/rusbank/)
4. Nellis, W.J., Mitchell, A.C., Young, D.A.: Equation-of-state measurements for aluminum, copper, and tantalum in the pressure range 80–440 GPa (0.8–4.4 Mbar). J. Appl. Phys. **93**(1), 304–310 (2003)
5. Partouche-Sebban, D., Pélissier, J.L.: Emissivity and temperature measurements under shock loading, along the melting curve of bismuth. Shock Waves **13**, 69–81 (2003)
6. Oren, E.P., Francois, X.J.: Comparison of methods for calculating the shock hugoniot of mixtures. Shock Waves **20**, 73–83 (2010)
7. Maevskii, K.K., Kinelovskii, S.A.: Model of behavior of nitrides and their mixtures under high dynamic loads. AIP Conf. Proc. **1623**, 391–394 (2014)
8. Trunin, R.F., Gudarenko, L.F., Zhernokletov, M.V., Simakov, G.V.: Experimental data on shock compression and adiabatic expansion of condensed matter. In: Russian Federal Nuclear Center—All Russian Research Institute of Experimental Physics, Sarov (2006) [in Russian]
9. van Thiel, M. (ed.): Compendium of shock wave data. Lawrence Livermore Laboratory, Report UCRL-50108, Livermore (1977), pp. 97–108

The Collapsing Mechanism of Aluminum Foams

Oren Sadot, I. Anteby, S. Gruntman, O. Ram, and Gabi Ben-Dor

Introduction

The response of metallic foams to a high strain or high stress rate loading has received increased attention in recent years due to their potential to absorb large amounts of energy during plastic deformation and crushing (see, e.g., Thornton and Magee [1]). Research of the mitigation of blast effects indicates that the high-energy absorption characteristic of metallic foams makes them very useful as protective layers of critical structural elements. Consequently, understanding the material dynamic properties of metallic foams will enable engineers to better utilize their energy absorption characteristics. Aluminum foam (Al-foam) is a lightweight material with excellent plastic energy absorbing characteristics [2]. The implementation of bare Al-foam as a protective layer is not practical. The material needs to be a part of a multilayer structure (see, e.g., Seitzberger et al. [3]). The foam layer can be exploited as a protective layer in military vehicles where both lightweight and good energy absorption are needed. The ability of aluminum foams to reduce the explosion-generated blast-induced damage from concrete slabs has been demonstrated in the course of high-explosive (HE) field experiments (see, e.g., Hanssen et al. [4, 5] and Sadot et al. [6]). Several studies have been conducted in order to investigate the constitutive model parameters of Al-foams during the past three decades. The effect of the strain rate was one of the important issues needed to be resolved [7]. A constitutive numerical model was validated in the work of Hanssen et al. [4, 5]. The validation procedure was based on three levels: (a) material calibration; (b) non-uniformed compression test at the material level; and (c) numerical validation at the structural interaction level. Several material models from the LS-DYNA library were calibrated. However, discrepancies between the models were found even for relatively simple load configurations. The most important conclusion noted by the authors was the need for further development of more robust fracture models for the Al-foam. This conclusion is crucial especially since there are increasing numbers of Al-foam manufacturers. Various experimental facilities were used to dynamically load the Al-foam at large ranges of strain and stress rates. In the work of Dannemann and Lankford Jr. [8], closed-cell Al-foams were assessed under static and dynamic loads in the strain rate range of 400–2500 s^{-1}. This range was achieved by using split Hopkinson bar apparatuses. It was found that the strain rate effect is significant in high density Al-foams. Deshpande and Fleck [9] suggested that the initial elastic modulus was lower than that of fully dense alloys. Deformation in the cell walls led to stress concentration around the deformation zones, which resulted in a decrease of the modulus. Some inconclusive results regarding the dependence of the stress–strain curve on the strain rate were presented. Deshpande and Fleck [9] and Paul and Ramamurty [10] did not notice any strain rate dependency, in contrast to the findings of Dannemann and Lankford [8] and Paul and Ramamurty [10]. In a later work by Wang et al. [11], experiments were done using an Instron compression

O. Sadot (✉)
Mechanical Engineering Department, Faculty of Engineering Sciences, Ben Gurion University of the Negev, Beer Sheva 8410501, ISRAEL
e-mail: sorens@bgu.ac.il

I. Anteby
Nuclear Research Center—Negev, P.O.B. 2001, Beer-Sheva, Israel

S. Gruntman
Protective Technologies Research and Development Center, Faculty of Engineering Sciences, Ben-Gurion University of the Negev, P.O.B 653, Beer-Sheva 84105, Israel

O. Ram
Department of Mechanical Engineering, Protective Technologies Research and Development Center, Faculty of Engineering Sciences, Pearlstone Center for Aeronautical Engineering Studies, Ben-Gurion University of the Negev, Beer Sheva, Israel

G. Ben-Dor
Pearlstone Center for Aeronautical Engineering Studies, Department of Mechanical Engineering, Faculty of Engineering Sciences, Ben-Gurion University of Negev, Beer Sheva, Israel

G. Ben-Dor et al. (eds.), *30th International Symposium on Shock Waves 1*, DOI 10.1007/978-3-319-46213-4_127

machine at strain rates ranging from 10^{-3} s^{-1} up to 450 s^{-1}. Strain–stress curves constructed and distinct strain rate dependency was noted. In the work of Bastawros et al. [12] efforts were made to understand the morphology of the Al-foam during its collapse. Explanation was given to the cell deformation. However, some observations have been ignored and not fully explained even though some key elements of the deformation were identified. The dynamic behavior of Hydro/Cymat Al-foam material was investigated by Tan et al. [13] under different load conditions. The plastic collapse, the plateau range, and the strain at which the deformation occurred were found. It was demonstrated that the dynamic response depends on the direction of the load with respect to the plate manufacturing orientation. Some load enhancement was observed and was explained by micro-inertial effects. Postimpact observation of partly crushed specimens revealed that the deformation is through crush bends. Feng et al. [14] conducted experiments to investigate the rate dependence of Al-foams having different relative densities. They found that the effect of strain rate increases while increasing the Al-foam density as was found by others. For Al-foams with a relative density of 15 % there was little effect of the strain rate while for heaver foams significant strain rate effect was noted.

In all of these experimental studies the load was generated by laboratory means. In the work of Hanssen et al. [4, 5] the energy absorbed by the Al-foam in a field test with a blast wave was estimated by a pendulum device. In that work the front panel placed on the exposed side of the Al-foam increased the energy absorbed by the foam, especially for close proximity to the charges. Hanssen et al. [4, 5] claimed that the absorbing Al-foam layer controlled the load locally. However, due to the fact that the overall load was not affected by the impulse shape, the global response of the target was not affected by the presence of the Al-foam. Hanssen et al. [4, 5] also added that the shape of the front panel can affect the energy transfer from the blast to the pendulum weight.

In the present study, we have investigated the dynamic behavior of Al-foams using two experimental approaches in which the strain rate was controlled. An impact pendulum was used for the moderate strain rate and a shock tube apparatus was used for high strain rate. In the following, each experimental approach will be briefly presented together with the obtained results.

The Research Methodology and Experimental Systems

The stress–strain curves of Cymat SmartMetal™ Al-foams were developed using a variety of experimental facilities at strain rates relevant to high explosives rates. The aim of the present study was to better resolve the strain rate dependency of the mechanical behavior of Al-foams. A variety of experimental facilities at the various laboratories of the Protective Technologies R&D Center of the Faculty of Engineering Sciences of the Ben-Gurion University of the Negev were used. The mechanical behavior of two types of Al-foams was investigated at room temperature using two different experimental facilities. Each facility produced a different load profile and a different strain rate on the Al-foams. Table 1 details the relevant characteristics of each one of these two experimental facilities that are briefly described in the followings:

Table 1 Characteristics of the experimental facilities

Instrument parameter	Impact pendulum	Shock tube
Max. impact velocity [m/s]	4	25
Specimen strain rate [s^{-1}]	40	500
Specimen dimensions [mm × mm]	150 × 150	80 × 80

Impact Pendulum

The impact pendulum can be raised to a height of about 0.5 m in order to impact specimens placed on a rigid structure. The pendulum weight can be adjusted between 100 and 1000 kg, in order to get different loads. A load cell, placed on the impactor of the pendulum, records the impact produced by the pendulum. The Al-foam specimens are placed on a thick and stiff plate. The experiments are documented using high-speed photography. The Impact pendulum is presented in Fig. 1a.

Shock Tube

80 mm × 80 mm Al-foam specimens, placed and supported by the end-wall of a shock tube, were loaded by shock waves. The shock wave load can be changed by varying the shock wave strength. This is the main advantage of this system. The shock wave strength and velocity were measured by means of piezoelectric pressure transducers. The load on the Al-foam is measured by a load cell located on the supporting end-wall. The experiments are documented using high-speed photography. The shock tube is presented in Fig. 1b.

Experimental Results

In order to investigate the strain rate dependency of the mechanical behavior of the Al-foams, 4 % foams were used (the percent represents the ratio of the sample density to a solid aluminum density). The specimens were 42-mm

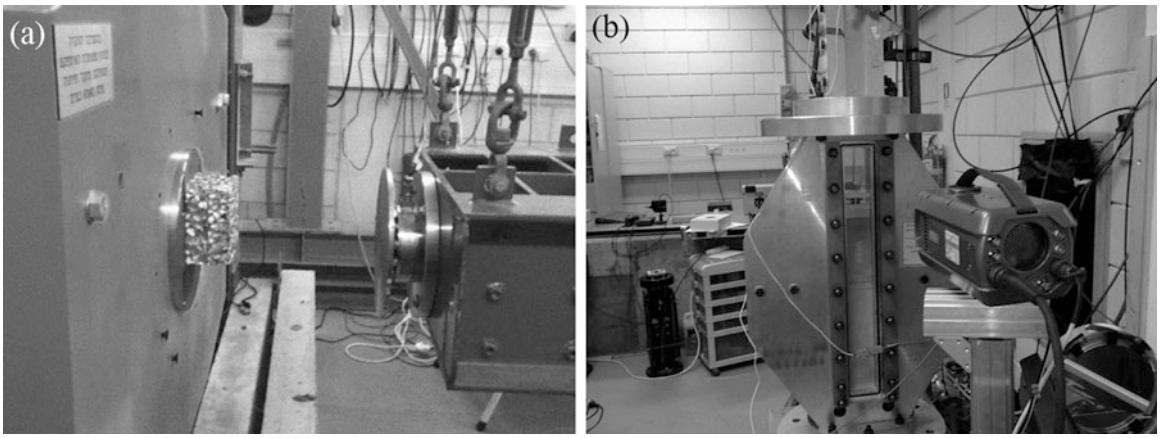

Fig. 1 (**a**) The impact pendulum; (**b**) the shock tube. The mounted Al-foam specimen is shown in the two facilities

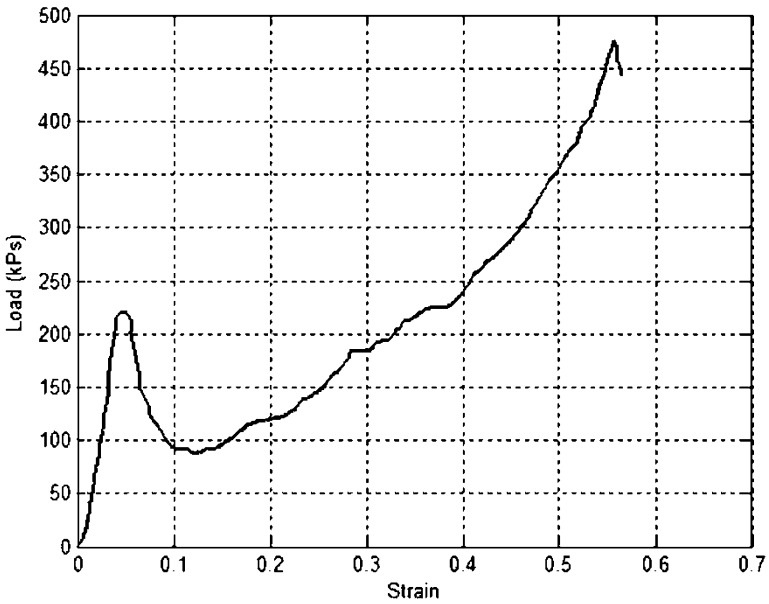

Fig. 2 Experimental results obtained from the impact pendulum for 4 % Cymat SmartMetal™ Al-foam

thick. The next sections present the experimental procedures and the results for each one of the above described experimental facilities.

Impact Pendulum

The impact pendulum was used for low impact velocities. The system is based on a four wires swing weight. The pendulum impactor was equipped with a load cell and accelerometers, and its weight was 500 kg. The Al-foam samples were placed on a heavy steel plate in front of the pendulum impactor. The displacements of the sample were monitored by high-speed photography. The displacements were extracted from the obtained movie using TEMA software. More details about the experimental system can be found in Sadot et al. [6]. The experiments were conducted with 4 % Cymat SmartMetal™ Al-foam samples. The impact velocity was controlled by varying the initial height of the pendulum and was about 2 m/s, which provided a strain rate of about 20 s^{-1}.

The (σ–ε) curve constructed from the measured strains and stresses is shown in Fig. 2.

Shock Tube

Higher strain rate experiments were conducted with 4 % Cymat SmartMetal™ Al-foam using the shock tube (Fig. 3a). In order to prevent Al-foam bubbles from

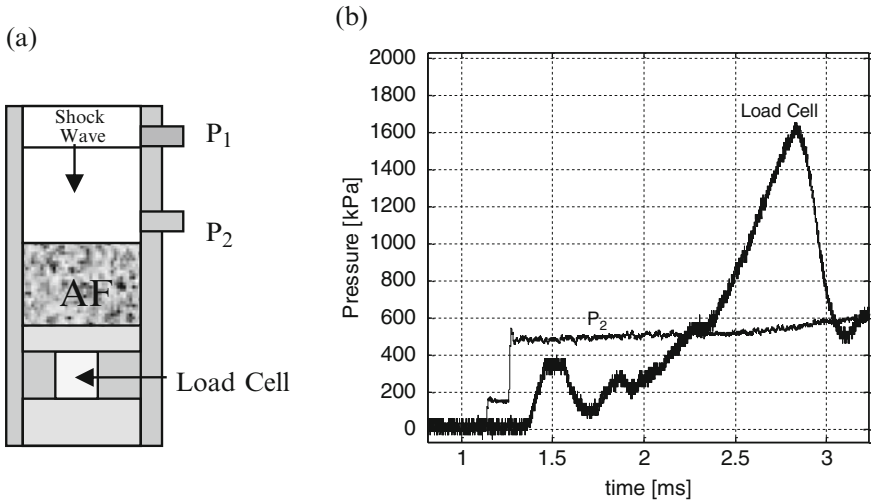

Fig. 3 (**a**) The shock tube test section with the Al-foam sample (AF), two pressure transducers (P_1 and P_2) and the load cell. (**b**) Pressure and load history as measured in the shock tube experiment

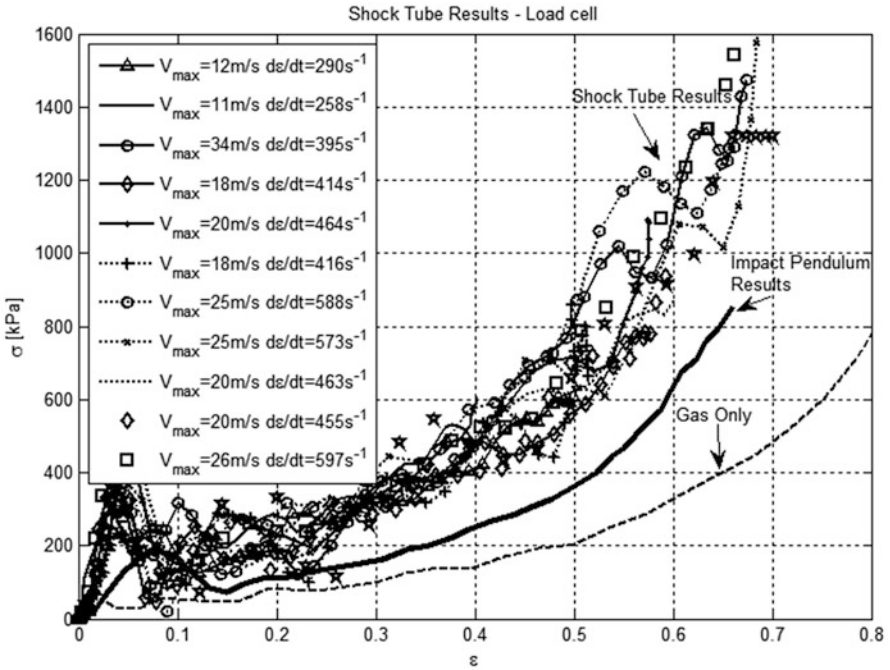

Fig. 4 Experimental results obtained from the shock tube. Each symbol presents a different shock strength. The blue line presents the isentropic compression of the gaseous phase

collapsing by the shock wave, a thin Teflon plate was placed on top of the Al-foam sample. The (σ–ε) curves were constructed using high-speed photography and the load cell. Figure 3b presents typical signals obtained from the pressure transducers and the load cell. At $t = 0$ the shock passed the upper pressure transducer, P_1, and at $t = 1.12$ ms the shock passed the lower pressure transducer, P_2, and a pressure jump was observed (see Fig. 4b). Shortly after, the reflected shock from the Teflon plate passed the lower pressure transducer once again. The load developed at the end-wall did not increase sharply due to the compression and the energy absorption of the Al-foam. The overpressure was observed as the Al-foam decelerated by crashing into the end-wall. After the full compression of the foam (about 3.2 ms) the measured load at the end-wall and the measured pressure reached exactly the same value.

The variation in the strain rate was achieved by varying the incident shock wave strength, i.e., Mach number. The (σ–ε) curves were constructed from the measured stresses and strains.

A summary of the post-processed results is shown in Fig. 4 together with the impact pendulum results. The measured maximum peak velocity and the calculated maximum strain rate are presented for each group of experiments

in the figure's insert. The scattering in the obtained (σ–ε) curves in each group has about the same order of magnitude as the scattering between the different groups. From these results one can conclude that there is no distinct strain rate dependency in these shock-tube experiments. However, a distinct discrepancy is observed between the shock tube and the impact pendulum results.

Further investigations into the different experimental configuration suggest that the sample confinement can be the cause to these discrepancies. The confinement of the Al-foam sample in the shock tube experiments prevents the gaseous phase that is trapped inside the pores of the Al-foam from flowing out to the atmosphere. In the shock tube experiments, a Teflon plate is placed at the front edge of the sample to prevent the shock from penetrating into the Al-foam. This causes the foam to collapse rather than to perforate. To test the assumption that the gaseous phase has a strengthening effect, the same Teflon plate was placed at the same height as if the Al-foam sample was present. It was supported by a thin paper holder, which had no resistance to the compression by the shock wave (zero strength). The gas trapped under the Teflon plate was the only candidate for resisting the plate motion. The acceleration of the plate and therefore the load on it were extracted from the high-speed photography data. In Fig. 4 the extracted load of the Teflon plate is presented and marked with a thin solid line. One can conclude from these results that owing to the gaseous phase there is a significant strengthening in the high strain rate experiments.

In our opinion, this effect can be dominant either in the case where the foam is confined or where the foam plate is large so that a longer time is needed to exhaust the trapped gas inside the pores that are far from the foam edge. The results from the impact pendulum and the shock tube after subtracting from them the effect of the trapped gas were replotted in Fig. 5. Under these conditions it was found that there was no significant strain rate dependency of the investigated type of Al-foams in the investigated range of loadings.

Summary

In the present study, Cymat SmartMetal™ Al-foams were studied under different strain rate loadings utilizing two different experimental facilities. Each experimental facility was aimed at loading the Al-foam at a different strain rate. The impact pendulum and the shock tube were used to generate moderate and high strain rate loadings, respectively. Under these conditions it was found that there is no significant strain rate dependency of this type of Al-foams.

In the shock tube experiments, the overpressure that was measured by the load cell at the end-wall included the inertia of the Al-foam sample that was first compressed and then stagnated on the end-wall. For this reason the overpressure measured with an Al-foam sample exceeded the overpressure that was measured in the case without an Al-foam sample, which was due to the gaseous phase only. This effect was related to the momentum transferred from the shock wave to the Al-foam and from the Al-foam to the end-wall. Furthermore, due to the confined configuration that was used in the shock tube experiments it was noted that there is some contribution from the trapped gas that effectively strengthened the Al-foam layer and contributed to the rate strengthening.

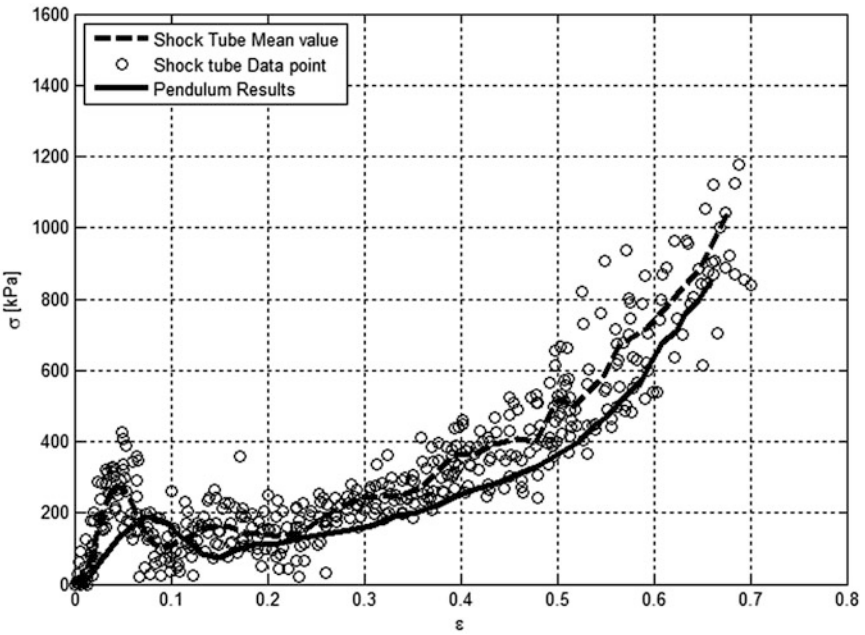

Fig. 5 Combined experimental results (impact pendulum and shock tube) for the 4 % Cymat SmartMetal™ Al-foam

This confined configuration prevented from the gas that was trapped inside the Al-foam to exhaust to the atmosphere and therefore the trapped gas acted against the compression process. It can be assumed that the compression process of the gas was isentropic. This effect is dominant when the Al-foam is confined, at high strain rates and in large foam plates.

Acknowledgments The research was supported by PLASAN Ltd. and CYMAT Ltd. (Contract no. 7272310003).

References

1. Thornton, P.H., Magee, C.L.: Deformation characteristics of zinc foam. Metall. Trans. A **6A**, 1801–1807 (1975)
2. Ashby, M.F., Evans, A., Fleck, N.A., Gibson, L.J., Hutchinson, J. W., Wadley, H.N.G.: MetAl-foams: a design guide. Butterworth-Heineman, Stoneham, MA (2000). ISBN 0-7506-7219-6
3. Seitzbergera, M., Rammerstorfera, F.G., Gradingerb, R., Degischerc, H.P., Blaimscheind, M., Walch, C.: Experimental studies on the quasi-static axial crushing of steel columns with aluminum foam. Int. J. Solids Struct. **37**, 4125–4147 (2000)
4. Hanssen, A.G., Enstock, L., Langseth, M.: Close-range blast loading of aluminum foam panels. Int. J. Impact Eng. **27**, 593–618 (2002)
5. Hanssen, A.G., Hopperstad, O.S., Langseth, M., Ilstad, H.: Validation of constitutive models applicable to aluminium foams. Int. J. Mech. Sci. **44**, 359–406 (2002)
6. Sadot, O., Anteby, I., Harush, S., Levintant, O., Nizri, E., Ostraich, B., Schenker, A., Gal, E., Kivity, Y., Ben-Dor, G.: Experimental investigation of dynamic properties of aluminum foams. J. Struct. Eng. **131**(8), 1226–1232 (2005). doi:10.1061/(ASCE)0733-9445(2005)131:8(1226)
7. Mukai, T., Kanahashi, H., Miyoshi, T., Mabuchi, M., Nieh, T.G., Higashi, K.: Experimental study of energy absorption in a close-celled aluminum foam under dynamic loading. Scr. Mater. **40**(8), 921–927 (1999)
8. Dannemann, K.A., Lankford Jr., J.: High strain rate compression of closed-cell aluminum foams. Mater. Sci. Eng. **A293**, 157–164 (2000)
9. Deshpande, V.S., Fleck, N.A.: High strain rate compressive behavior of aluminum alloy foams. Int. J. Impact Eng. **24**, 277–298 (2000)
10. Paul, A., Ramamurty, U.: Strain rate sensitivity of a closed cell aluminum foam. Mater. Sci. Eng. **A281**, 1–7 (2000)
11. Wang, Z., Shenb, J., Lub, G., Zhaoa, L.: Compressive behavior of closed-cell aluminum alloy foams at medium strain rates. Mater. Sci. Eng. **A528**, 2326–2330 (2011)
12. Bastawros, A.-F., Bart-Smith, H., Evans, A.G.: Experimental analysis of deformation mechanisms in a closed-cell aluminum alloy foam. J. Mech. Phys. Solids **48**, 301–322 (2000)
13. Tan, P.J., Reid, S.R., Harrigan, J.J., Zou, Z., Li, S.: Dynamic compressive strength properties of aluminum foams. Part I-experimental data and observations. J. Mech. Phys. Solids **53**, 2174–2205 (2005)
14. Feng, Y., Zhengang, Z., Fangqiou, Z., Shisheng, H., Pan, Y.: Strain rate effects on the compressive property and the energy-absorbing capacity of aluminum alloy foams. Mater. Charact. **47**, 417–422 (2001)

Part XI

Shock Wave Interaction with Granular and Dusty Media

Study on the Jet Formation During Dispersal of Solid Particles by Shock and Blast Waves

V. Rodriguez, R. Saurel, G. Jourdan, and L. Houas

Introduction

During the last decade, investigations have been achieved to determine the physical mechanism which governs particle jet formation induced by the dispersion of a granular medium exposed to an impulsive pressure load, i.e., by a shock or a blast wave. This kind of such physical mechanism is observed during explosions or in nature as volcanic eruptions [1]. The formation of particle jets is also observed when a solid projectile impacts a particle layer [2]. Previous experiments have been conducted so far in three-dimensional spherical configurations using explosives surrounded by a granular layer [3–7]. In these experiments, the particle jet formation was obtained and clearly observed. The attempt was to correlate the particle jet distribution to the initial parameters like the particle diameter and density, the particle layer thickness and the strength of the incident shock wave in order to understand the breaking mode of a solid particle cluster. Even if it has been shown that the formation of particle jets depends both on the particle material properties and the ratio between the particle layer and the explosive mass [3], it was quite difficult to accurately relate the jet distribution with the initial conditions. More recently, cylindrical experiments were performed by Frost et al. [8] where it was easier to observe the particle jet formation. In spite of these studies, the selection mechanism is still not understood. The present experimental study was conducted in quasi two-dimensional geometry in order to ensure accurate characterization of the phenomenon. We present the concept of the two-dimensional experiments carried out. Parameters such as material density, strength of the incident shock wave, and the initial geometry of particle rings can be changed in order to find out what parameters can control the breaking mode of the particle clusters [9].

V. Rodriguez (✉) • R. Saurel • G. Jourdan • L. Houas
Aix-Marseille Université, CNRS–IUSTI UMR 7343, Marseille, France
e-mail: vincent.rodriguez@ensma.fr

Experimental Setup

Experiments were performed in the laboratory without the use of explosives but using a small conventional shock tube which produce moderate overpressure. The small conventional shock tube (T32) has a 32 mm diameter. It was vertically fitted beneath a Hele-Shaw cell inside which a ring of particles is located. The incident shock wave is directed onto the center of the ring. This one creates a blast wave at its exit, i.e., an impulsive pressure jump followed by a rapid pressure decrease. This blast wave propagates radially into the Hele-Shaw cell and sets in motion the ring of particles. The experimental apparatus is presented in Fig. 1. Thereby, the particle jet formation was visualized with a Photron SA1 high-speed video camera operating typically at 4000 fr/s. Moreover, pressure gauges located along the shock tube (C_1 and C_2) allow the determination of the incident shock wave Mach number. The C_{exit} pressure gauge records the pressure history at the center of the particle ring.

Experimental Conditions

We conducted several experiments for different initial conditions summarized in Table 1.

Results

Recorded frames covering the different steps of jet formation during dispersal of flour particles by a shock wave are presented in Figs. 2 and 3. This solid particle ring was subjected to an incident shock wave Mach number of 1.23. The two-dimensional configuration, through the transparent Hele-Shaw cell, allows the observation inside the ring during the radial dispersion. It highlights the presence of various perturbations in the particle layer exposed

G. Ben-Dor et al. (eds.), *30th International Symposium on Shock Waves 1*, DOI 10.1007/978-3-319-46213-4_128

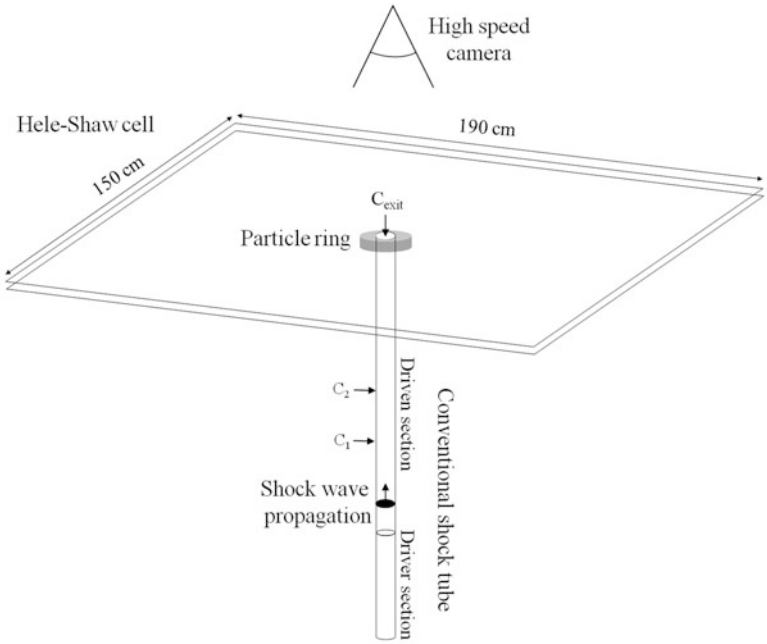

Fig. 1 Sketch of the experimental setup. The driver section of the shock tube is 210 mm long and its driven section is 945 mm long. The space between the plates is 4 mm

Table 1 Experimental conditions

Material	Density (kg/m^3)	Diameter (μm)	Ring diameter D_{ext} (mm)	Thickness of the particle layer (mm)	Incident shock wave Mach number	Overpressure (bars)
Flour	1500	10	40–90	20	1.1–1.45	0.7–4.5
Polystyrene	1050	10				
PMMA	1250	10				
Talc	2500	10				

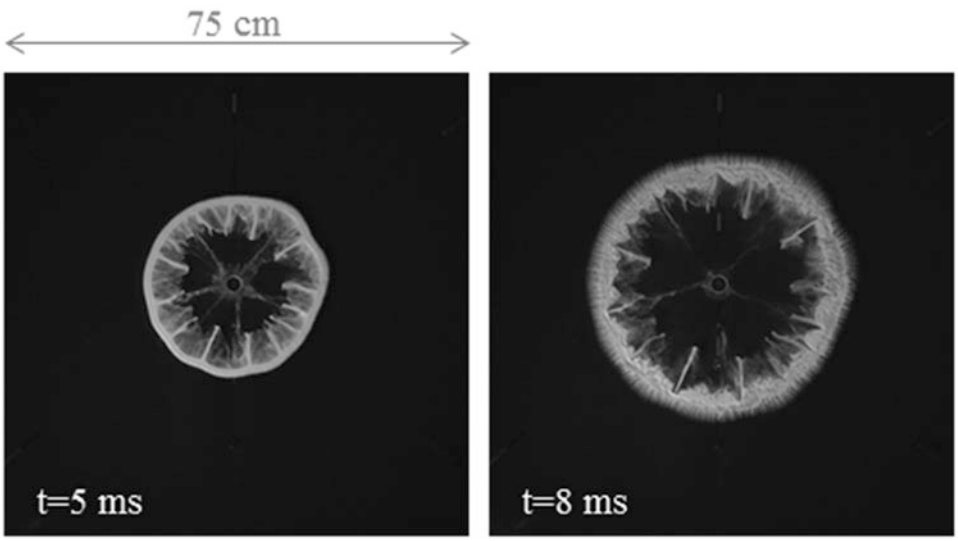

Fig. 2 Sequence of recorded frames covering the beginning of jet formation during dispersal of flour particles by a shock wave. The incident shock wave Mach number is 1.23

to a shock wave. At $t = 0$, the incident shock wave interacts with the particle ring and the dispersion of particles starts. After a very short time (between 0 and 5 ms), particle concentrations appear inside the ring resulting in regular particle jet distribution around the inner surface of the ring, as shown in Fig. 2. During the first moments of the particle propagation, the external front of the particle ring propagates with a smooth interface. After a few milliseconds, very thin perturbations appear around it, as shown in the second frame of Fig. 2. The dispersion of solid particles continues to grow radially inside the Hele-Shaw cell. Then, internal jets go on with the same direction as the particle front propagation which slows down. Thus, internal jets cross the front and are expelled outside as shown in Fig. 3 at $t = 14$ ms. Finally, these external jets continue to grow outside the particle front from $t = 18$ ms to $t = 36$ ms as shown in Fig. 3.

Figure 4 shows the number of particle jets, N_j, normalized by both the ratio of density R and the initial perimeter of the ring, $\pi D_{ext,}$ versus the initial ring acceleration γ averaged on the first 3 ms. R represents the ratio between the density of the used particles and the density of the polystyrene particles taken as reference in this study. All these points are issued from several experiments conducted with different shock wave Mach numbers, particle materials (change in the particle density), and initial ring sizes (change in the external diameter, but keeping constant the thickness of the particle layer). As we can see in Fig. 4, all the experimental points plotted merge into a single curve following a power law of the form $N_j R/\pi D_{ext} = 128.5 + 0.14\gamma^{2.6}$. We can observe that this relation is valid for initial particle layer acceleration until 13 ms^{-2}. Beyond this limit, the number of jets does not increase significantly and logically tends to a maximum number of jets. This point has to be checked.

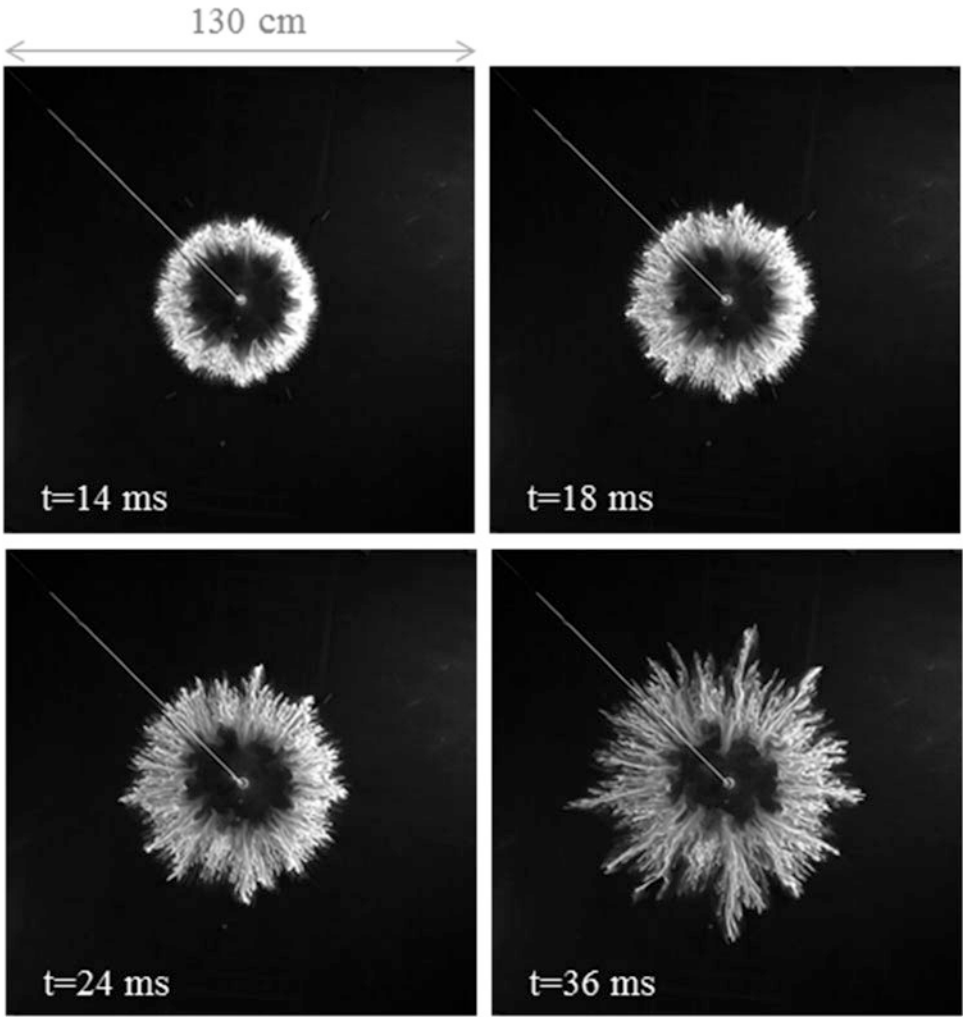

Fig. 3 Sequence of recorded frames covering the subsequent steps of jet formation during dispersal of flour particles by a shock wave. The incident shock wave Mach number is 1.23

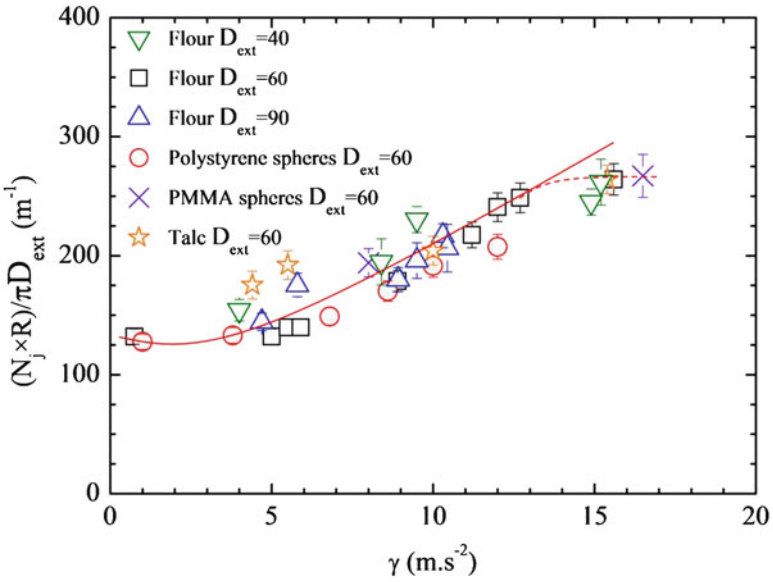

Fig. 4 Number of particle jets, N_j, normalized by both the ratio of density R and the initial perimeter of the ring, $\pi D_{ext,}$ versus the initial ring acceleration γ averaged on the first 3 ms for different initial ring accelerations, material densities, and sizes of the particle ring

Conclusions

This chapter summarizes an experimental investigation and the aim is to consider in two dimensions the jet formation issued from impulsively dispersed solid particles. Several initial parameters such as the particle density, the strength of the initial pressure pulse, and the initial geometry of the ring have been studied. From fast flow visualizations, we notice, in all instances, that the jets are initially generated inside the particle ring and thereafter expelled outward. The number of jets that were generated during the dispersal of solid particles could be extracted. We showed that the normalized number of jets as a function of the initial ring acceleration shows a power law valid for all studied configurations involving various initial conditions but presents a saturation for great accelerations.

References

1. Kedrinsky, V.: Hydrodynamic aspects of explosive eruptions of volcanoes: simulation problems. Shock Waves **18**, 451–464 (2009)
2. Lohse, D., Bergmann, R., Mikkelsen, R., Zeilstra, C., van der Meer, D., Versluis, M., van der Weel, K., van der Hoef, M., Kuipers, H.: Impact on soft sand: void collapse and jet formation. Phys. Rev. Lett. **93**, 198003 (2004)
3. Frost, D.L., Goroshin, S., Zhang, F.: MABS 21, Israel (2010)
4. Zhang, F., Frost, D.L., Thibault, P.A., Murray, S.B.: Explosive dispersal of solid particles. Shock Waves **10**, 431–443 (2001)
5. Frost, D.L., Ornthanalai, C., Zarei, Z., Tanguay, V., Zhang, F.: Particle momentum effects from the detonation of heterogeneous explosives. J. Appl. Phys. **101**, 113529 (2007)
6. Milne, A.M., Parrish, C., Worland, I.: Dynamic fragmentation of blast mitigants. Shock Waves **20**, 41–51 (2010)
7. Parrish, C., Worland, I.: ISSW 28, Manchester (UK) (2011)
8. Frost, D.L., Grégoire, Y., Oren, P., Goroshin, S., Zhang, F.: Particle jet formation during explosive dispersal of solid particles. Phys. Fluids **24**, 091109 (2012)
9. Rodriguez, V., Saurel, R., Jourdan, G., Houas, L.: Solid-particle jet formation under shock-wave acceleration. Phys. Rev. E **88**, 063011 (2013)

Response of Embedded Pipeline to Surface Blast Loading

P. Vivek, T.G. Sitharam, Gopalan Jagadeesh, and K.P.J. Reddy

Introduction

Due to various catastrophic accidents and increasing terrorist activities in recent years, there has been a considerable interest in studying structures exposed to explosive loads. The stability of underground structures like bunkers, tunnels, and pipeline networks are crucial under blast loading. Among the various buried structures, underground pipelines which are used to transport oil and gas are considered here in the study. The work presented here aims at investigating the behavior of an embedded pipe subjected to surface blast loading.

Understanding the explosion in soil and the subsequent response of buried structures like pipeline is extremely difficult because of its dynamic interaction with the soil and structure. Most of the transmission pipelines which are buried in the ground are made of carbon steel. Extensive work has been performed on blast induced effects on buried pipelines and most of the studies are focused on developing analytical expression [1] and numerical studies [2]. However, very few experimental studies have succeeded in the past, due to the limitation of using explosives.

The use of explosives in laboratory is a complex phenomenon, considering the lack of repeatability conditions and safety concerns. Hence, shock tube is used here to generate repeatable blast wave under controlled conditions. The shape of blast wave generated from the shock tube matches the Friedlander wave equation. The reflection and propagation of compression waves induced by the shock wave in a granular medium are studied by various researchers. Kitagawa et al. [3] investigated effect of pressure attenuation of shock wave by porous materials, while Britan et al. [4] investigated the phenomenon of shock wave attenuation by granular filters. The initial set of shock tube experiments were carried out to determine the parametric effect of soil on propagation of pressure wave upon a blast wave impact. This chapter also presents a fully coupled numerical analysis approach, in which the Coupled Eulerian Lagrangian (CEL) method is adopted to model the blast loading on the embedded pipe in the soil deposit. The finite element results were compared with the experiments to show the authority of numerical simulation of shock/blast impact on granular materials like soil.

Experimental Arrangement and Materials

Shock Tube

The vertical shock tube used in the following study consists of a long tube having an inner diameter of 135 mm, separated into driver section and driven section by a metal diaphragm. The driver section is 0.5 m in length, while the driven section is 4.5 m. The diaphragm is ruptured by a compressed high pressure driver gas. The pressure of the driver gas is increased until the diaphragm ruptures and thereby generating shock wave [5], which travels into the driven section. Piezoelectric pressure transducers are mounted on to the end of the driven section to measure the P_5 pressure signal. The vertical shock tube assembly is shown in Fig. 1a. In the present case, Helium was used as the driver gas, while the driven conditions were at atmospheric conditions. The test chamber is mounted at the open end of the driven section as shown in Fig. 1b.

P. Vivek (✉) • T.G. Sitharam
Department of Civil Engineering, Indian Institute of Science, Bangalore, India
e-mail: vivek2387@gmail.com

G. Jagadeesh • K.P.J. Reddy
Department of Aerospace Engineering, Indian Institute of Science, Bangalore 560012, India

G. Ben-Dor et al. (eds.), *30th International Symposium on Shock Waves 1*, DOI 10.1007/978-3-319-46213-4_129

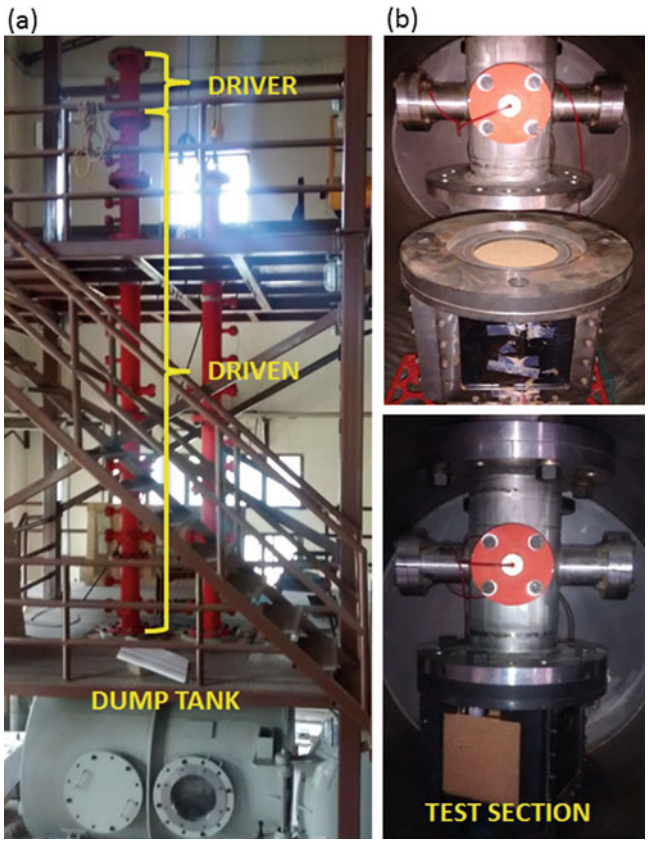

Fig. 1 (**a**) Complete assembly of vertical shock tube and (**b**) test section at the open end of the driven section

Table 1 Gradation property of sand

e_{min}	e_{max}	D_{10} (mm)	D_{30} (mm)	D_{60} (mm)	C_u
0.53	0.88	0.25	0.53	0.84	0.54

Material Properties

The sand used in this investigation was dry river sand, where the particle size distribution of the sand was determined by dry sieve analysis as per IS 2720 (part-4)-1985. The gradation properties of the sand are listed in Table 1, where e_{min} and e_{max} are the minimum and maximum void ratio. D_{10} represents grain size corresponding to 10 % passing, i.e., only 10 % of grains are smaller than 0.25 mm. Coefficient of uniformity C_u is calculated by taking the ratio of D_{60} and D_{10}. The aluminum pipe having outer diameter of 25 mm, with a wall thickness of 1.2 mm is used in the present study.

Test Chamber

The test chamber is made of square section box having the internal dimension of 150 mm. One face of the test chamber is fitted with high grade toughened glass for visualization purpose. Test chamber is where the sand deposit is prepared and is attached to the open end of the driven section of the shock tube. While preparing the sand deposit, it is important to maintain constant relative density such that the deposit can be reproducible for each test. For this purpose, the sand pluviation technique is used, where the sand was poured through a device which has a hopper fitted with a varying height pipe and welded with a 60° inverted cone at the bottom (Fig. 2). The height of fall determines the desired relative density of the sand deposit [6]. In the present study, two set of sand deposits were prepared with an approximate relative density of 63 % and 72 %. The piezoelectric type pressure transducers are placed inside the sand deposit at three different locations to capture the compressive wave propagation and the attenuation of the pressure pulse. The schematic diagram of the test chamber along with the actual sand deposit bed is shown in Fig. 3.

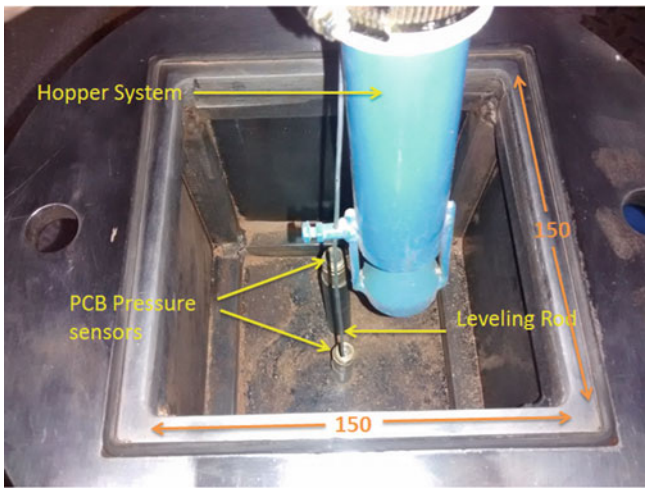

Fig. 2 Sand pluviation technique

Initial set of experiments were carried out only with sand deposit to determine the response of the sand to a blast loading. Later, experiments were performed by embedding an aluminum pipe at a depth of 75 mm from the bottom of the bed (Fig. 4a). The shock tube experiments were carried out with the pipe embedded in the soil. Soil-structure interaction response is captured by mounting a couple of strain gauges along circumferential and longitudinal direction of the pipe as shown in Fig. 4b.

Numerical Simulations

A CEL analysis was performed using Finite Element Package, ABAQUS/Explicit 6.12 [7]. A coupled analysis is performed to determine the soil-structure interaction response.

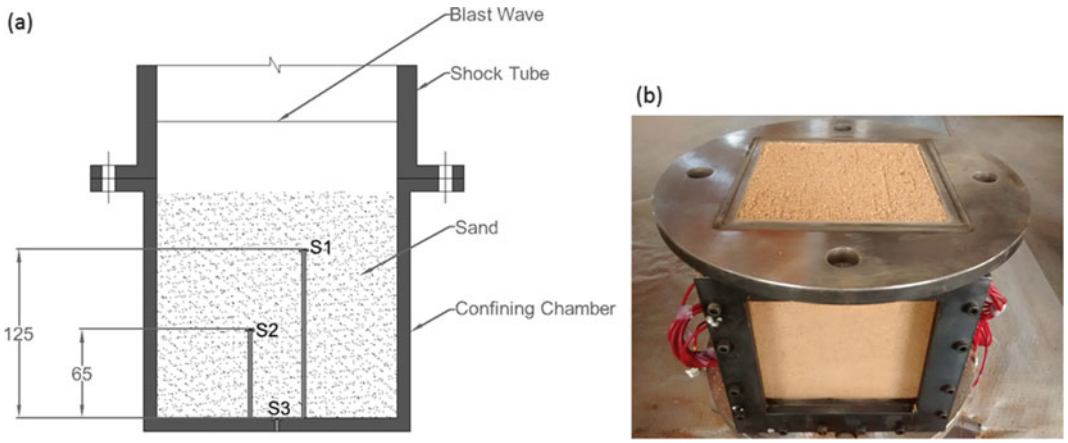

Fig. 3 (**a**) The schematic diagram of test chamber, (**b**) the sand filled test chamber

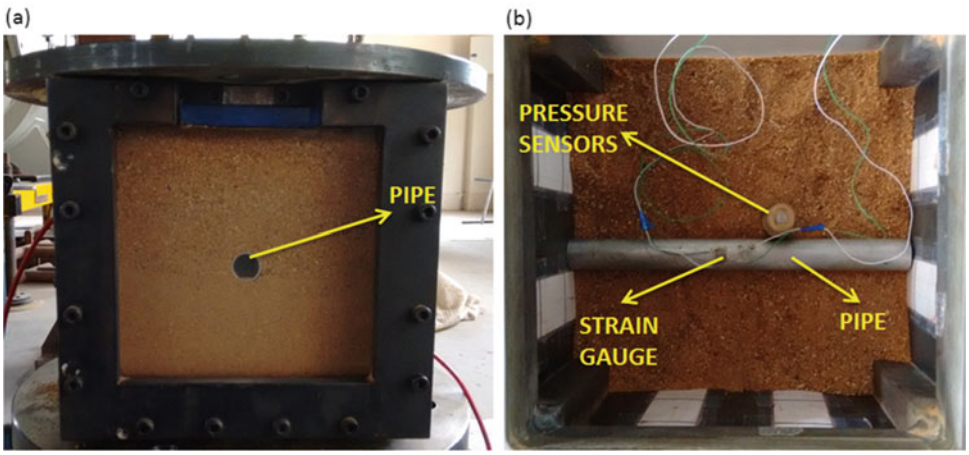

Fig. 4 Embedment of aluminum pipe in the sand deposit

Modeling and Constitutive Relation

The shock tube is modeled into driver and driven sections using Eulerian elements, considering ideal gas equation-of-state. Further, the sand is modeled as continuum medium using Drucker-Prager linear model and pipe is modeled using linear elastic model. For the shock tube geometry, a CEL model was developed using eight-node linear Eulerian brick element with reduced integration and hourglass control. While, the sand and pipe sample is modeled eight-node linear brick element with reduced integration and hourglass control. The desired initial pressure (P_4) is specified indirectly by using a predefined field for the initial temperature and the diaphragm rupture/burst condition is initiated at the start of the analysis, where the two gases interact with each other [8].

Table 2 Validation of Abaqus with analytical solutions

Shock parameters	Abaqus	Analytical	Error (%)
Incident shock pressure (kPa)	442.62	442.08	0.12
Reflected shock pressure (kPa)	1443.6	1445.1	0.11
Particle velocity (m/s)	420.14	414.54	1.33
Shock velocity (m/s)	712.71	684.51	3.96

Shock Tube Validation and Assembly

The shock tube condition is validated with the analytical solutions, popularly known as Rankine-Hugoniot relations. The constant pressure region behind the shock wave (P_2) and the constant pressure region behind the reflect shock wave (P_5) are matching perfectly with the analytical solutions. While the shock velocity and particle velocity has an error up to 4 %, the details are tabulated in Table 2.

The complete shock tube made of Eulerian element is assembled upon Lagrangian model of soil deposit, the contact between the two parts in considered frictionless. The assembly of the complete setup is shown in Fig. 5.

Results

The peak overpressure P_5 generated from the vertical shock tube as shown in Fig. 6 match very closely with the ideal Friedlander wave. Fig. 7 shows the overpressure measured by the embedded sensors when subjected to a blast wave having a peak overpressure of 14 bar. Upon the blast wave impact on the top of the sand deposit, the blast wave transfers the momentum to a two phase granular medium forming compression waves in the sand. The peak overpressure generated in the sand deposit gradually decay with the depth. In the case of sand with relative density of 72 %, the peak overpressure attenuate about 38 %, and 30 % attenuation is seen in sand with relative density of 63 %.

The experiment with the embedded pipe was partially unsuccessful due to damage in strain gauge connectors upon the impact of the blast waves. However, the P_5 signal from the shock tube was captured and the condition was simulated in Abaqus explicit. Fig. 8a shows the pressure contours developed in the shock tube and strain contours in sand deposit. A blast wave of peak overpressure of 40 bar is applied to the sand deposit and subsequently to the embedded pipe. A visual comparison of the deformation of the pipe with the numerical simulation is shown in Fig. 8b. The maximum deformation of pipe physically measured is found to be 2 mm while the numerical simulation predicts it to be 1.2 mm.

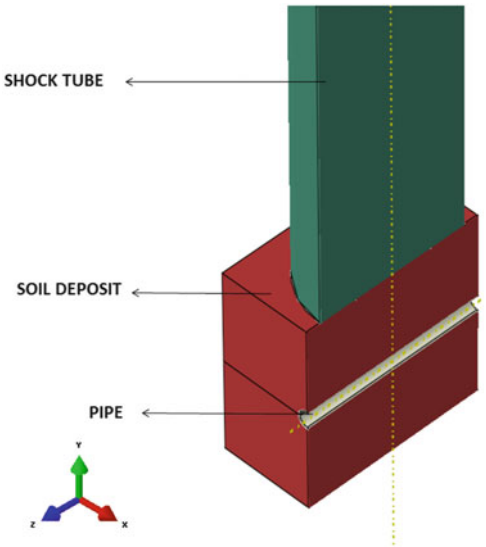

Fig. 5 Complete shock tube made of Eulerian element assembled upon Lagrangian model of soil deposit

Conclusion

The two phase granular medium can dominantly attenuate the compressive waves generated from surface blast wave to about 30–40 %. As the relative density increases, the voids present in the sand decrease. Hence, making it easier to interact with three-dimensional sand particles and thereby decreasing the peak overpressure substantially.

The numerical simulation overestimates the deformation compared to the physical measurement made in the experiment. Few more experiments need to be performed to predict

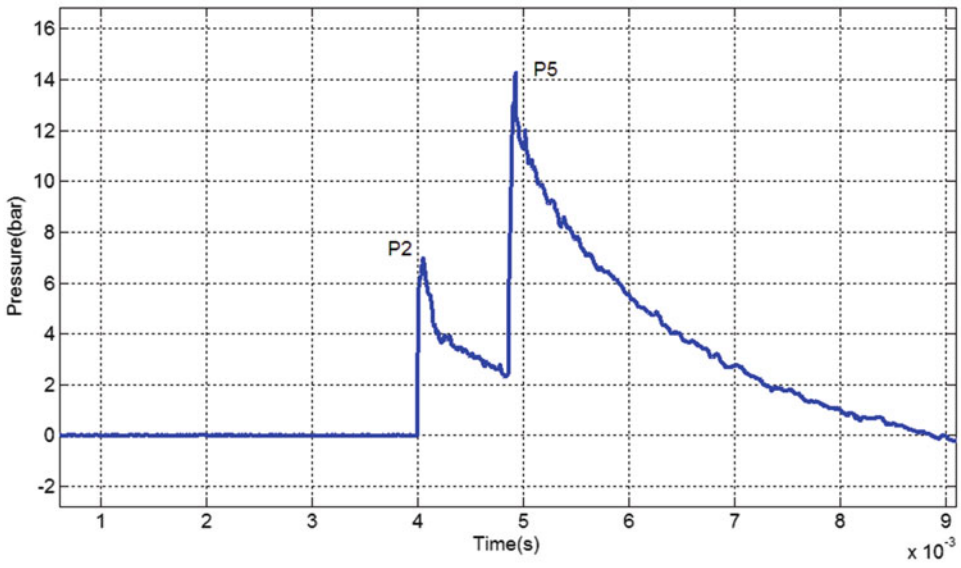

Fig. 6 Blast wave generated using vertical shock tube

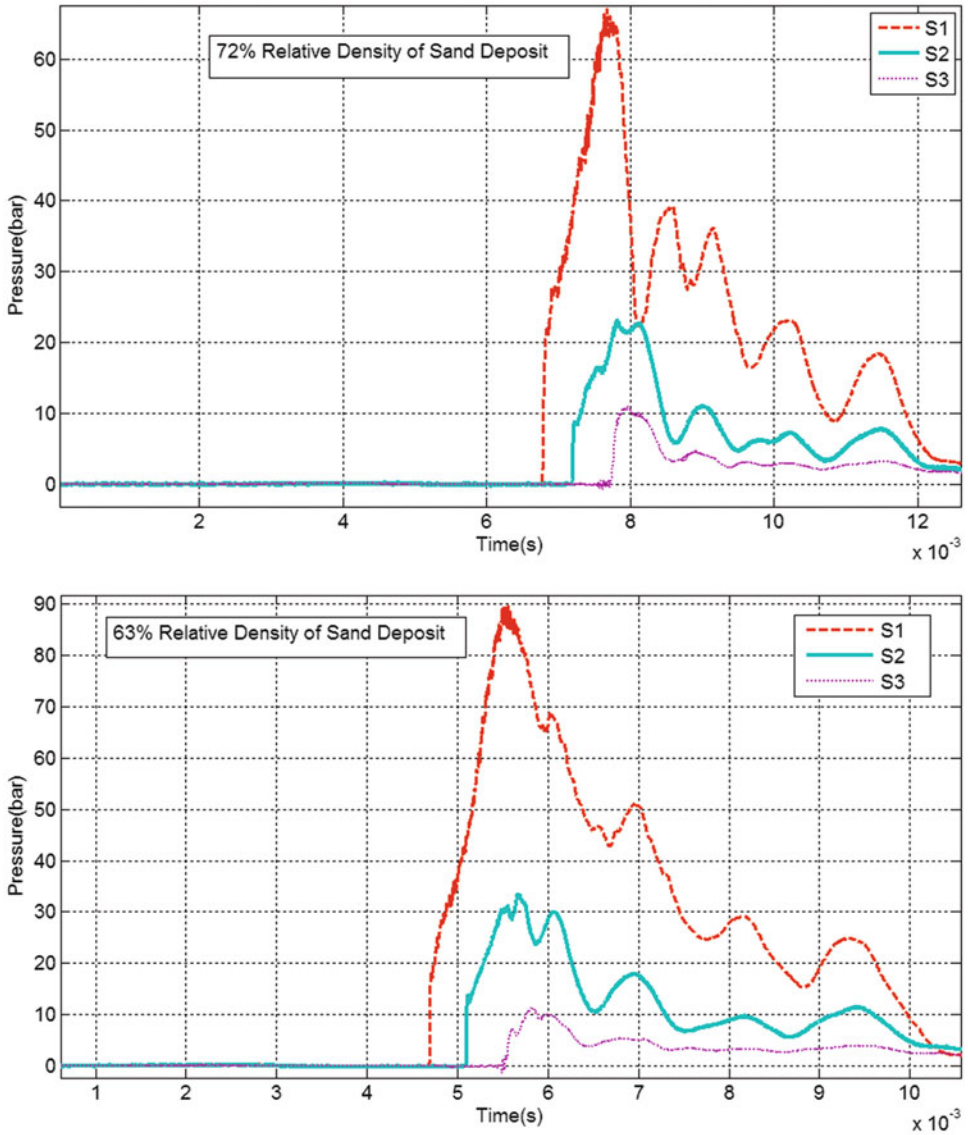

Fig. 7 Measured pressure signals in the sand at *S*1, *S*2, and *S*3 measuring 125, 65, and 0 mm from the bottom of the test chamber

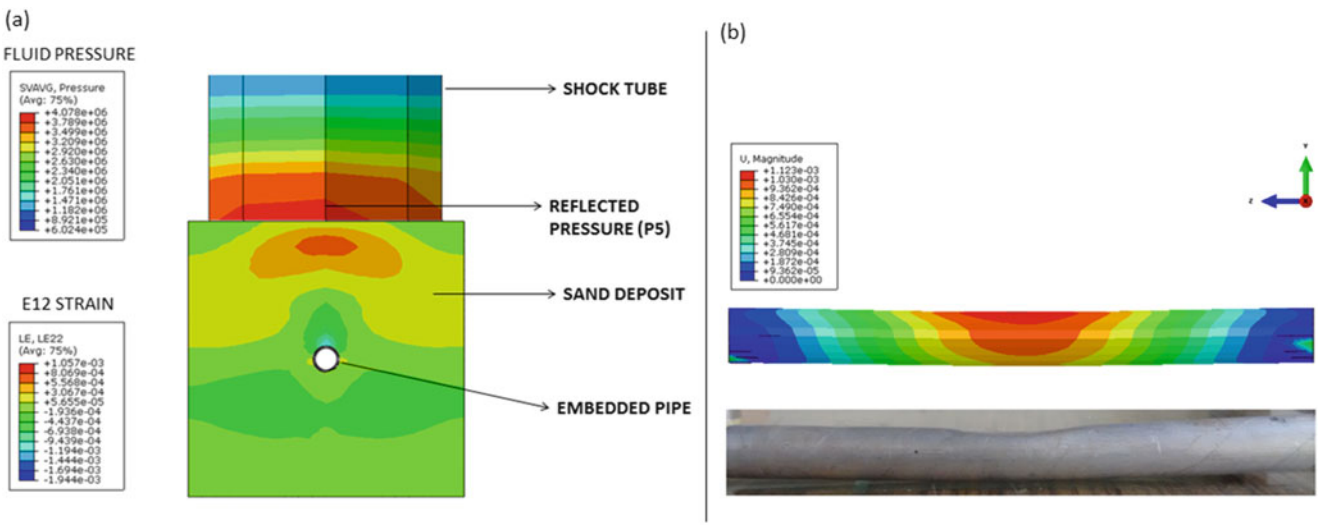

Fig. 8 (**a**) Strain distribution on the soil deposit, (**b**) comparison of the deformation with the experiment

the actual behavior of the embedded pipe along with the scaling law. Results of these experiments along with the important observations will be presented in the conference.

Acknowledgments Financial support from DRDO and IISc are gratefully acknowledged. We express sincere thanks to all the inmates of LHSR with special appreciation to Mr. Obed Samuelraj.

References

1. Kouretzis, G.P., Bouckovalas, G.D., Gantes, C.J.: Analytical calculation of blast-induced strains to buried pipelines. Int. J. Impact Eng. **34**(10), 1683–1704 (2007)
2. Lu, Y., Wang, Z., Chong, K.: A comparative study of buried structure in soil subjected to blast load using 2D and 3D numerical simulations. Soil Dyn. Earthq. Eng. **25**, 275–288 (2005)
3. Kitagawa, K., Yamashita, S., Takayama, K., Yasuhara, M.: Attenuation properties of blast wave through porous layer. Shock Waves **1**, 73–78 (2009)
4. Britan, A., Ben-Dor, G., Igra, O., Shapiro, H.: Shock waves attenuation by granular filters. Int. J. Multiphase Flow **27**, 617–634 (2001)
5. Gaydon, A.G., Hurle, I.R.: The shock tube in high temperature chemical physics. Reinhold Publishing Corporation, New York (1963)
6. Vaid, Y.P., Negussey, D.: Relative density of pluviated sand samples. Soils Found. **24**, 101–105 (1984)
7. Abaqus. Finite Element Package (Explicit). Dassault Systemes Simulia Corp., Providence, RI. v6, 12–2, 6.7.1 ed. (2012)
8. Carlucci, P., Mougeotte, C., Ji, H.: Validation of Abaqus Explicit—CEL for classes of problems of interest to the U.S. Army. SIMULIAN Customer Conference (2010)

Dense Particle Cloud Deflection During Shock Interaction

R.C. Ripley, S.D. Ryan, and C.M. Jenkins

Introduction

Historical studies of particle interaction with air shocks have been largely focused on dusty-gas shock tubes with dilute powder mixtures contained in the driven section, in which the attenuation of the shock wave and displacement of the dust are key metrics. Dense particle concentrations are fundamentally different and are the subject of modern application in explosive dispersal of powders [1, 2] where the dense flow of particles dominates the post-detonation dispersal. Experimental studies of high volume fraction particle layers and slugs have been conducted with initially stationary particles and a moving shock. Examples include shock interaction with layers of loose powders in a vertical shock tube [3], and shock interaction with a curtain of powder falling under gravity [4]. Denser slugs of powders lightly compressed into wafers have also been employed [5]. In shock tube tests, the edge conditions in the vicinity of the particle volume and boundary layer interaction can become problematic. The foregoing examples ideally all involve a planar shock interacting with a planar volume of particles with confining side boundaries. Real-world applications, including explosive dispersal of powders, often involve a high-speed moving particle cloud. Packets of larger dispersed particles may feature an attached bow shock when traveling supersonically, which may subsequently interact with an oncoming shock wave, as illustrated in Fig. 1.

The resulting encounter includes shock-shock interaction and shock-particle interaction in the dense flow regime. This chapter presents work towards quantifying the deflected trajectory and mitigating effects on cloud velocity. Numerical modeling provides a framework for studying the essentially free-field interaction of a particle cloud during a shock encounter. This chapter considers particle collision and analyzes the effects of particle size, cloud concentration, and shock angle. *Approved for public release under case number RW PA-5058*.

R.C. Ripley (✉) • S.D. Ryan
Martec Limited, 1888 Brunswick Street, Suite 400, Halifax, NS, Canada
e-mail: robert.ripley@lr.org

C.M. Jenkins
Air Force Research Laboratory, Eglin AFB, FL, USA

Numerical Methods

The Chinook code (Martec Limited) was used for the numerical investigation presented in this chapter. Particles are represented using a group Lagrange method, in which each solution point represents a collection of physical particles of the same size.

Multiphase Model

The two-phase governing equations for compressible gas dynamics and particle dynamics are solved in an Eulerian-Lagrangian formulation, with source terms for the interacting phases. Drag correlations for clouds of particles are available in the literature, e.g., in the work of Smirnov [6]. Below a volume fraction of 0.08, a dilute drag law is used. For solid fractions between 0.08 and 0.45, a dense drag coefficient is used, followed by a simple correlation for drag in the granular regime. Particles are assumed spherical, rigid, and inert.

To demonstrate the basic multiphase model before application to the configuration depicted in Fig. 1, the data of Rogue et al. [3] for air shock interaction with a bed of particles was used. The results of two cases are shown in Fig. 2. In both examples, the incident shock Mach number is 1.3, the particle density is 2.5 g/cm^3, and the void fraction is 0.35. Comparisons of the pressure history upstream and downstream of the particle bed were used to assess the suitability of the numerical scheme. The present numerical

G. Ben-Dor et al. (eds.), *30th International Symposium on Shock Waves 1*, DOI 10.1007/978-3-319-46213-4_130

method is in reasonable agreement with the experimental results of Rogue et al. [3].

Collision Model

The high volume fraction of particles is likely to lead to particle-particle interaction. Since the number of physical particles represented by the group Lagrange method is large, a probabilistic collision model was selected. The Direct Simulation Monte Carlo (DSMC) method employs stochastic detection of collisions between pairs of particles. In this chapter, the modified DSMC of Pawar et al. [7] was used since the model has been shown to achieve full quantitative agreement with deterministic discrete particle models. The hard-sphere particle collision model conserves momentum and assumes collisions are binary and impulsive, and particles are spherical, rigid, and without rotation. The addition of the collision model did not change the results in Fig. 2 significantly due to the 1D flow assumption.

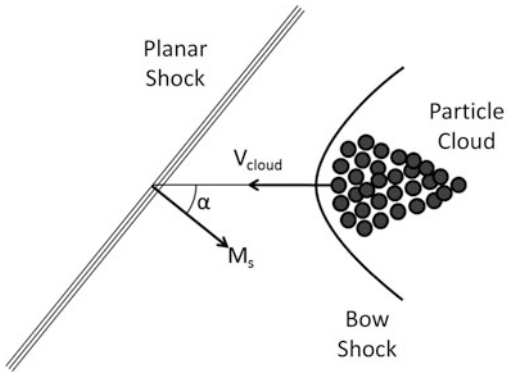

Fig. 1 Schematic of high-speed particle cloud encountering a planar shock wave

Results

A tear-drop shaped particle cloud was used (see Fig. 1) in the simulations, and a steady-state flow field including attached bow shock was reached prior to shock interaction. It was assumed that the cloud remained intact prior to shock encounter. The calculations were performed in a moving frame of reference using the particle cloud velocity. The model was 2D planar with an Eulerian mesh resolution of 2.5 mm. The incoming planar shock was initialized using Hugoniot jump conditions for air. Particles are monodisperse with a solid density of 8 g/cm^3, a coefficient of friction of 0.65, and a restitution coefficient of 0.9.

Particle Size and Collision Effect

Figure 3 shows results from application of the above-described multiphase and collision models to the baseline test case with a 2000 m/s particle cloud in a head-on collision ($\alpha = 0°$) with an oncoming Mach 2 air shock. The initial solid volume fraction (ϕ) is 0.05, corresponding to a one-particle-diameter spacing between particles. During the interaction, the local solid fraction increases up to 0.07, 0.13, and 0.39 for 2 mm, 0.4 mm, and 0.115 mm particles,

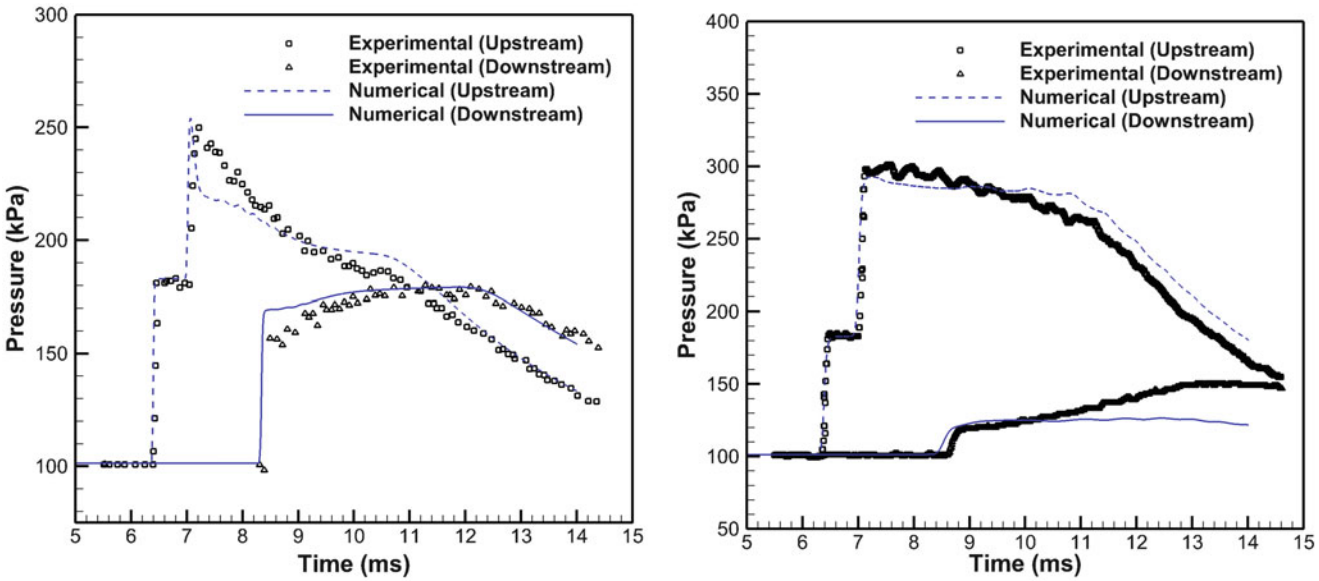

Fig. 2 One-dimensional shock/particle layer interaction. Comparison with experimental data of Rogue et al. [3] for (*left*) 2-mm-thick bed of 2-mm-diameter particles and (*right*) 20-mm-thick bed of 1.5-mm-diameter particles

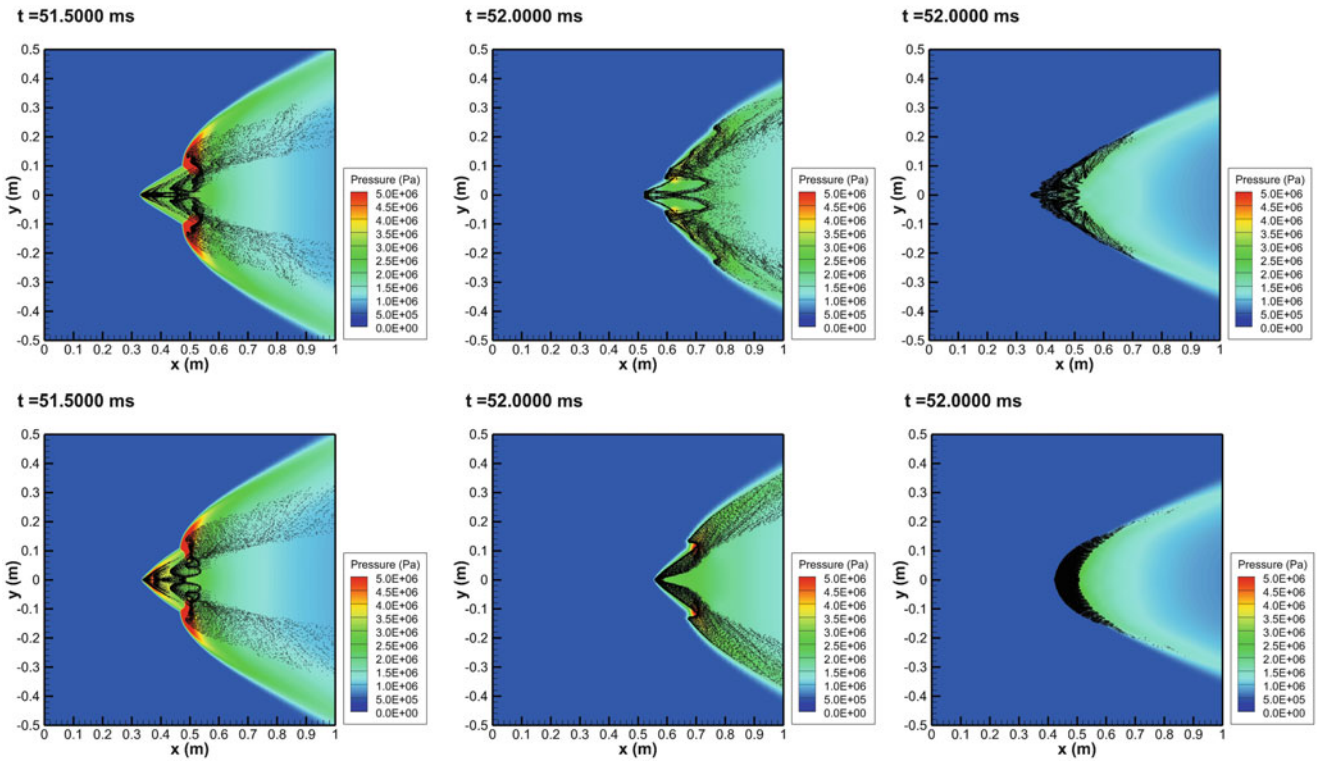

Fig. 3 Effect of particle collision for various particle sizes: (*upper*) noninteracting particles; and (*lower*) inelastic collision model. Results in a moving frame of reference. *Left*: 0.115 mm, *Centre*: 0.4 mm, and *Right*: 2.0 mm particles. Points are particle groups

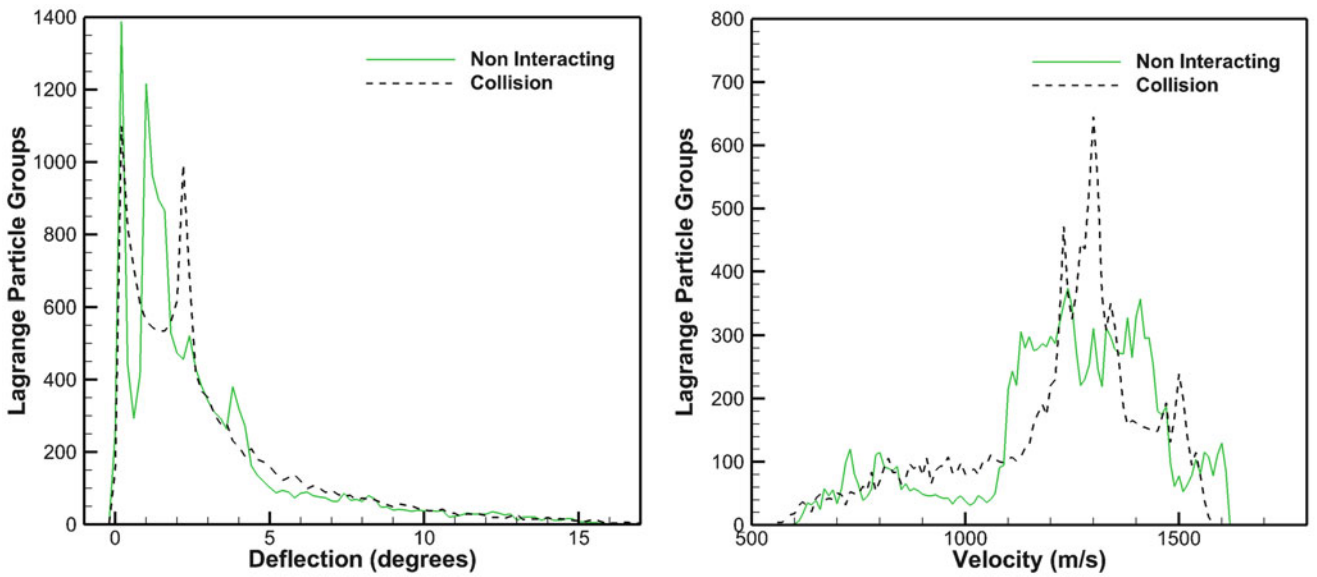

Fig. 4 Effect of particle collision for 0.4-mm-diameter particles. Statistical group results measured at 2 ms following shock interaction

respectively. Figure 4 shows the effect of using the collision model for 0.4-mm-diameter particles on the cloud deflection and velocity 2 ms after shock interaction. The collision model produces a narrower velocity distribution around the peak value.

The number of collisions is dependent on the particle diameter, with the greatest number of interactions occurring between 0.9 and 1.5 ms after shock arrival. The probabilistic collision model affects the dispersion in the direction of motion and deflection from the axis of travel. The general

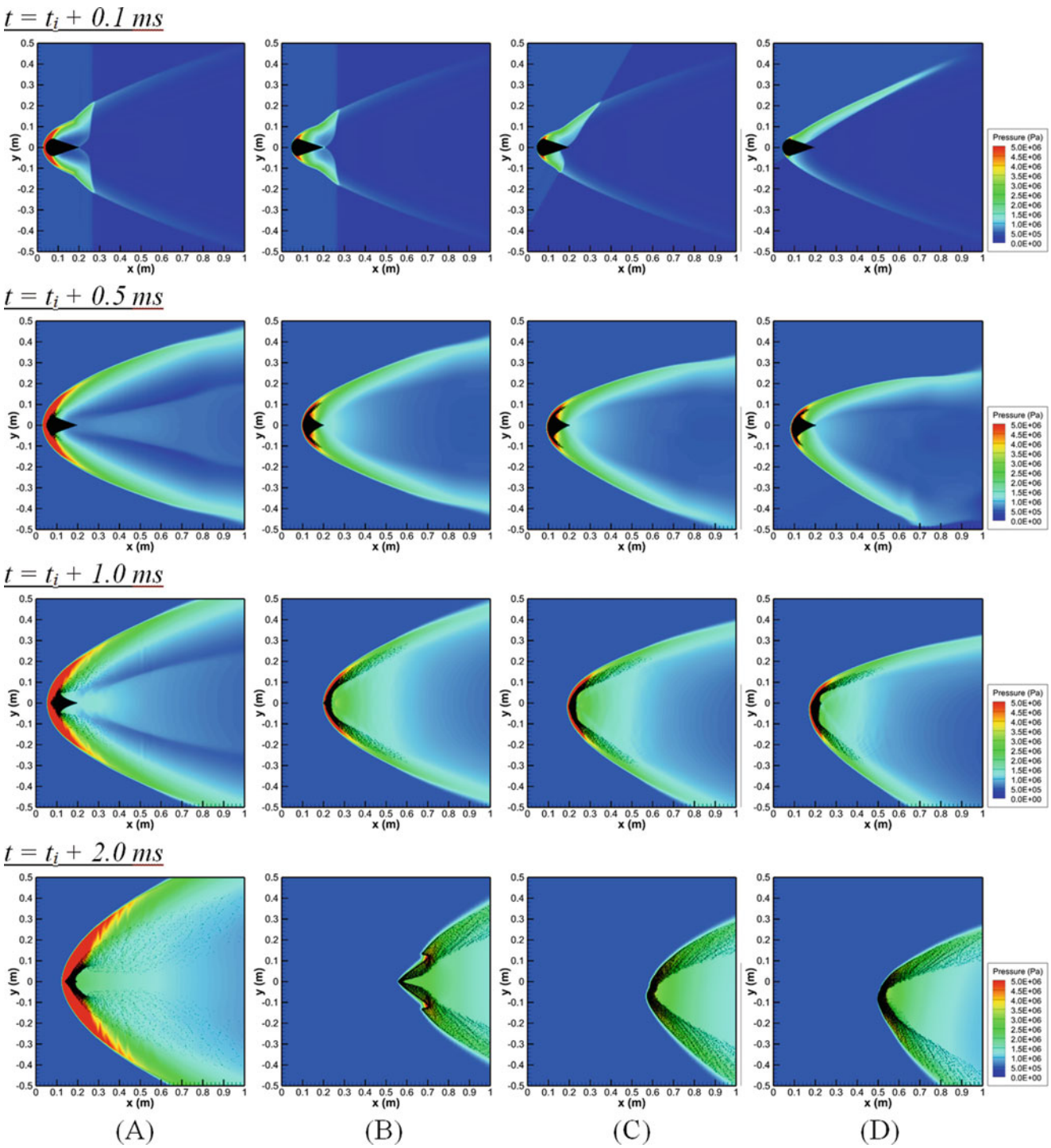

Fig. 5 Progression of particle cloud dispersion and deflection for cloud velocity of 2000 m/s encountering a Mach 2 shock wave: (**a**) $\phi = 0.30$ and $\alpha = 0°$; (**b**) $\phi = 0.05$ and $\alpha = 0°$; (**c**) $\phi = 0.05$ and $\alpha = 30°$; and (**d**) $\phi = 0.05$ and $\alpha = 60°$. Color contours from 0 to 5 MPa

cloud disintegration appears more orderly with the collision model, due to the momentum exchange between particles at the leading edge of the cloud and those on the interior of the cloud. While Fig. 4 shows the distribution of particle velocity changes with the collision model, the average velocity is within 1 % of the noninteracting particle result.

The remainder of the numerical results employs the inelastic collision model. The unsteady flow field development and the particle deflection following the shock arrival are plotted in Fig. 5 for different cloud volume fractions and various shock wave angles.

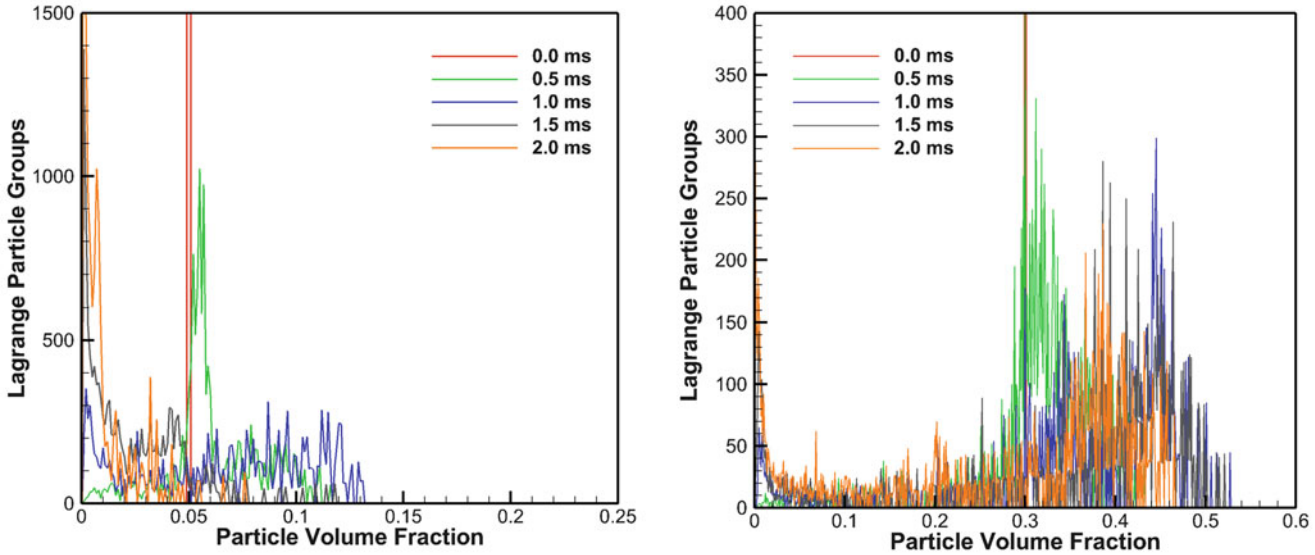

Fig. 6 Evolution of the distribution of particle volume fraction during shock wave encounter: (*left*) initial volume fraction of 0.05; and (*right*) initial volume fraction of 0.3

Cloud Concentration

The initial solid fraction of the cloud was varied from 0.05 to 0.3 to determine the effect of particle concentration. For the same particle size (0.4 mm), the higher solid fraction cloud has six times the number and mass of particles, and the drag coefficient [6] is greater on a per-particle basis. Figure 5 (left two columns) shows the sequence as the particle clouds interact with a head-on shock. The $\phi = 0.3$ cloud remains more dense and in a coherent chevron shape, while the $\phi = 0.05$ cloud accelerates quickly with significant shedding of particles during the interaction. Figure 6 provides the time evolution of the distribution of cloud volume fraction, indicating local densification for the first 1 ms, followed by a wide-ranging dispersion.

Cloud Deflection

Shock interaction angles of 0, 30, and 60° (see Fig. 1) were simulated. The timescale of the shock crossing the particle cloud is 0.1 ms, during which the interaction is mainly shock transmission and diffraction while the particles do not respond significantly. Afterwards, the particle cloud adjusts to the post-shock conditions and begins to break up. Figure 7 quantifies the mitigating effect of the shock encounter. Increasing the shock angle relative to the axis of particle travel resulted in a marginal shift in the vertical deflection distance. However, the reduction in particle velocity in the direction of the initial cloud travel was considerably less for increasing shock angles. The average horizontal particle velocity was 1180, 1229, and 1348 m/s for shock angles of 0°, 30°, and 60°, respectively.

Conclusions

The results of particle cloud interaction with a shock wave were interpreted to assess the cloud deflection and momentum loss as a mitigation mechanism. Results show complex disintegration of the dense cloud, although the range of deflection and influence on the particle trajectory following interaction were not large in the timescale studied. These effects are expected to be more significant for lower cloud velocities.

The normal shock encountered by the cloud mostly provides a new flow condition for the particles, but may be viewed as the initiating event for the breakup of the particle packet. The incoming shock angle mostly influenced the particle velocity in the direction of the cloud travel. Additional parametric evaluation of the effects of particle material, cloud velocity, and shock Mach number is possible using the numerical framework. This work could be extended to the case of a blast wave interacting with a cloud of particles.

A DSMC collision model was applied to the problem of a high-speed particle cloud interacting with a planar shock. The highest collision frequency occurred between 0.9 and 1.5 ms following shock interaction, which corresponded to time of the maximum particle concentration in the cloud. Although the collision model greatly improved the coherency of the cloud following shock interaction, the collision

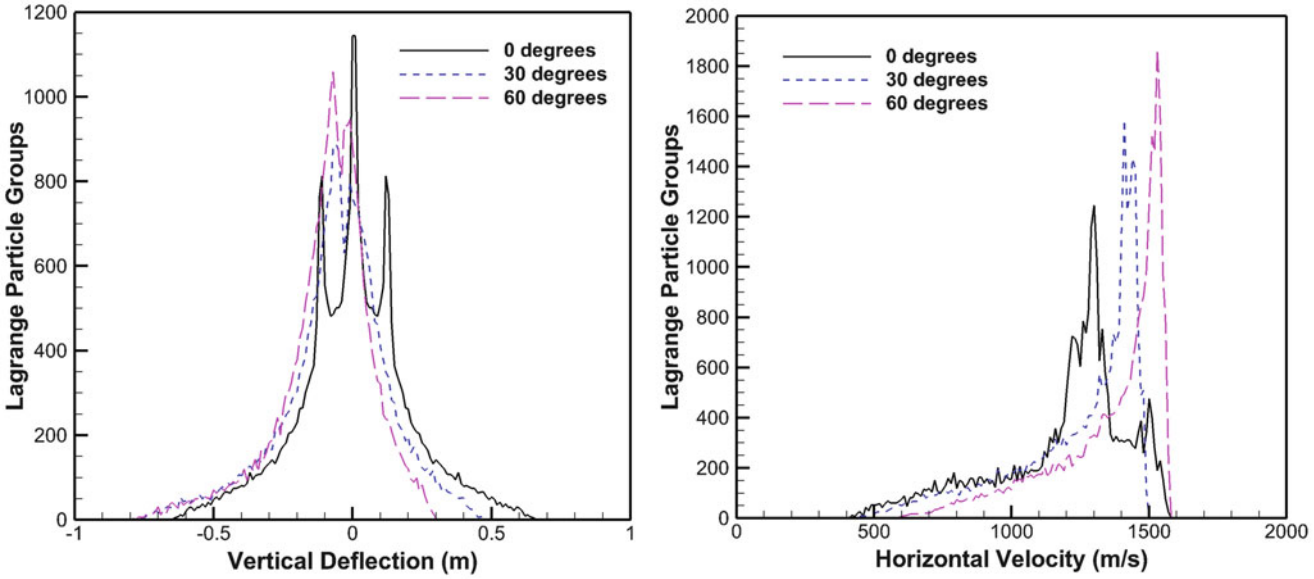

Fig. 7 Statistical distribution of results 2 ms following shock interaction of various angles: (*left*) vertical deflection distance of particles; and (*right*) horizontal velocity component

model should be improved for higher volume fractions, particularly for conditions when the average distance between particles is less than the diameter. In this dense particle-particle collision regime, multi-body collision and a soft-sphere interaction model should be explored.

References

1. Zhang, F., Frost, D.L., Thibault, P.A., Murray, S.B.: Explosive dispersal of solid particles. Shock Waves **10**, 431–443 (2001)
2. Jenkins, C.M., Ripley, R.C., Wu, C.-Y., Horie, Y., Powers, K., Wilson, W.H.: Explosively driven particle fields imaged using a high speed framing camera and particle image velocimetry. Int. J. Multiphase Flow **51**, 73–86 (2013)
3. Rogue, X., Rodriguez, G., Haas, J.F., Saurel, R.: Experimental and numerical investigation of the shock-induced fluidization of a particle bed. Shock Waves **8**(1), 29–45 (1998)
4. Wagner, J., Baresh, S., Kearney, S., Trott, W., Castaneda, J., Pruett, B., Baer, M.: Interaction of a planar shock with a dense field of particles. In: 28th Int. Symp. Shock Waves, Manchester (2011)
5. Kellenberger, M., Johansen, C., Ciccarelli, G., Zhang, F.: Dense particle cloud dispersion by a shock wave. In: 28th Int. Symp. Shock Waves, Manchester (2011)
6. Smirnov, N.: Combustion and detonation in multi-phase media: Initiation of detonation in dispersed-film systems behind a shock wave. Int. J. Heat Mass Transfer **31**(4), 779–793 (1988)
7. Pawar, S.K., Padding, J.T., Deen, N.G., Jongsma, A., Innings, F., Kuipers, J.A.M.: Lagrangian modelling of dilute granular flow—modified stochastic DSMC versus deterministic DPM. Chem. Eng. Sci. **105**, 132–142 (2014)

Shock Mitigation by Dust Lofting: Theoretical Perspective

A. Lipshtat and S. Pistinner

Introduction

Roughly 50–60 % of the total energy released by a nuclear explosion in lower atmosphere air is converted into blast wave [1] mechanical energy. When the burst point is moderately high above the ground such that a crater is not formed (roughly about 7 m scaled height), a significant mass of dust and sand is lofted and entrained into the blast wave flow fields. Detailed computation of the lofting effect is important since this dust may carry adsorbed fission products over large distances. In circumstances where dust is being lofted, the shock wave propagates in a diluted air-particles suspension rather than in a pure air environment. Constitutive characteristics of the suspension may affect the wave propagation dynamics [2]. Thus, in computational modeling of the blast wave several phases have to be accounted for (air, dust, sand etc.), including interphase coupling effects. The lofting phenomenon is a turbulent phenomenon. Due to computer limitation it is impractical to model the turbulent lofting process in a full nuclear blast wave simulation. The dust lofting process is thus modeled analytically and the result is embedded as a boundary condition based on an extended boundary layer theory for blowing boundary layers that takes into account lofting of sand particles into the air flow [3, 4].

Such an approximated blowing analytical sweep-up model [5, 6] was incorporated in a two-phase GRP scheme, aimed at calculating the flow field due to high speed wind flowing over a flat sandy surface (the so-called dust laden). It has been observed that particle saltation takes place at wind velocities higher than some threshold turbulent energy. The sweep-up regime starts at a velocity about an order of magnitude higher than the saltation threshold value, where the turbulent drag force can overcome the gravitational free fall. Gaj and Small [5] provide an approximate expression for the vertical dust mass flux lofted by the wind, as a function of wind velocity and air density.

The GRP hydrodynamic method [7] has been extended to treat a gas-particles suspension using two phases modeling (for details cf. [8]). The resulting scheme, further simplified by assuming dynamic (velocity) and thermodynamic (temperature) equilibrium, was applied to calculate flows with dust lofting from the ground. The boundary conditions for such flows are formulated in terms of a sweep-up model (using blowing turbulent boundary layer theory). This equilibrium approximation is based on the assumption that the gas-particle relaxation time is much smaller than all other time scales of the flow field. The equilibrium suspension is then treated as a (single-phase) compressible fluid. Taking an ideal gas EOS for air, the suspension EOS is also an ideal gas with a load-dependent adiabatic index given by $\gamma = 1 + \frac{\gamma_{\text{air}} - 1}{1 + \gamma_{\text{air}} \frac{\alpha}{1-\alpha} \delta}$, where $\alpha \equiv \frac{\rho_{\text{dust}}}{\rho_{\text{total}}}$ is the dust mass fraction and $\delta \equiv C_{\text{dust}} / C_{\text{P,air}}$ is the heat capacities ratio [9].

The modified GRP code was used to calculate spatial and temporal distribution of lofted dust either by a nuclear burst or by a steady high speed wind. We present and discuss several cases of blast waves with lofted dust distributions obtained by our calculations for a variety of yield and HOB values.

Computational Scheme

Inclusion of lofted dust in blast wave propagation consists of two mutually coupled computational models: (a) a sweep-up model which estimates the mass flux of dust particles and (b) fluid dynamics model which incorporates the thermodynamics of the air-particle suspensions.

Our lofting scheme is based on Mirels' analysis and assumptions [3]. In the following lines we briefly outline this derivation. Above some threshold friction velocity, vertical momentum dissipation of the horizontal momentum is

A. Lipshtat (✉) • S. Pistinner
Soreq Nuclear Research Center, Yavne 81800, Israel
e-mail: Eliezerli@soreq.gov.il

G. Ben-Dor et al. (eds.), *30th International Symposium on Shock Waves 1*, DOI 10.1007/978-3-319-46213-4_131

converted into a vertical mass flow of dust. If the turbulent mass flux is stronger than the gravitational force, the lofted dust particles are coupled to the flow field and get carried by it. When the dust lofted turbulent flow is fully developed, equilibrium conditions must be maintained. Thus, it is assumed that surface momentum dissipation by shear equals the threshold value required to sustain the particles mass flux. Weaker shear does not suffice for dust lofting whereas higher shear value causes excess lofting which mitigates the flow. Thus, the local boundary layer skin friction coefficient $C_f \approx C_{f,t} = 2\left(\frac{u_{*,t}}{U_x}\right)^2$, where $u_{*,t} = \sqrt{\tau/\rho}$ is the threshold shear velocity, and U_x is the horizontal component of fluid velocity out of the boundary layer. Another assumption made by Mirels is that within boundary layer of width δ, both particle density and velocity profile exhibit power-law dependence on height, namely $\frac{U(z)}{U_e} = 1 - \frac{\rho(z)_{\text{dust}}}{\rho_{\text{dust},z=0}} = \left(\frac{z}{\delta}\right)^{1/n}$. This assumption can be justified based on Brighton's work about evaporation from a plane liquid surface [10]. In that context, which is analogous to our problem of particle sweep-up, Brighton showed that even though the power law velocity profile is not an exact solution to the diffusion-advection equation, by taking $n = \ln\left(\frac{\delta}{z_0}\right)$ where z_0 is the roughness length, the power law does provide a good approximation to the law of the wall $U_x(z) = \frac{u_*}{\kappa}\ln\left(\frac{z}{z_0}\right)$, which is consistently used in any turbulent boundary layer theory and the blowing boundary layer theory in particular. Note that roughness length z_0 depends on dust density at ground level and thus is not necessarily a constant. As a result the problem is highly nonlinear and should be solved in a self-consistent manner. In this view the power law and its exponent are not arbitrarily chosen but rather are related to the physical characteristics of the problem.

Based on Mirels' foundations and using experimentally measured parameters, Gaj and Small derived a closed expression for the lofted mass flux [5]. The lofted mass is assumed to equilibrate instantaneously with the flowing suspension and increase its total mass as well as its mass fraction α. The added mass is inserted with no initial velocity, and thus during equilibration it absorbs momentum from the suspension, leading to decrease in its velocity. However, as we show later, this is a minor change which has no significant effect on global dynamics. The initial temperature of the lofted mass contributes to the internal energy of the suspension. In cases of large difference between dust and suspension temperatures, this energy transfer may be of high importance.

Assuming an ideal-gas equation of state for the dust-air suspension, change of mass fraction leads to respective change of adiabatic index, molar weight, and heat capacity. The equilibrium temperature is determined by the new heat capacity and conservation of energy (including the internal energy of the lofted mass). Then, the pressure is deduced based on the equation of state with the updated adiabatic index, energy, and density. As expected, in cases where there is no change in energy per mass (namely, under conditions in which $T_{\text{dust}} = T_{\text{suspension}}$), the pressure is not affected by the dust particles and thus is independent on the mass fraction. However, if the dust ahead of the blast wave is cooler (like in a shock tube) or hotter (as might be the case in different flow regions of a nuclear blast wave flowing over a heated surface), the situation might change drastically.

Results

In order to examine possible effects of dust sweep-up, we have run the simulation code with and without the sweep-up module. Although quantitative comparison of the results shows differences between the two scenarios, the overall dynamics is similar and dust injection does not have a significant effect on the blast wave propagation. The slow-down of suspension flow takes place behind the shock front where the dust mass fraction is noticeable. Since in our scheme the dust particles are forced to move with the suspension flow, no precursor due to particle acceleration is observed. However, there is another mechanism which may cause a similar phenomenon. Radiation can heat the ground and increase its temperature.

If the particles are lofted with higher temperature than ambient temperature, a layer of hot suspension is formed, in which density is lower and sound velocity is higher than those of the "cold" suspension. As a result, the blast wave propagates faster next to the ground than in other levels. This effect is demonstrated in the right column of Fig. 1 which presents an example of an explosion 91 m (300 ft) above ground with a yield of 43 kt. Note that not only the horizontal velocity is higher, but also vertical velocity is affected, resulting in dust carried up to much higher heights (Fig. 2).

We have used the computational scheme mentioned above in order to estimate the total lofting rate and final amount of dust lofted by a nuclear explosion. Yields and heights were taken from real experiments performed by the USA [11]. As expected, lofting rate depends on the explosion yield and the height of burst above ground (Fig. 3). However, in all of the cases we've simulated, there are two distinct stages of sweep-up. In first 3–5 s we observe rapid lofting of large amount of dust particle. Then the rate of sweep-up decreases and the total amount of lofted mass increases slowly. The reason is that after several seconds the speed of the shock front, where most of initial lofting

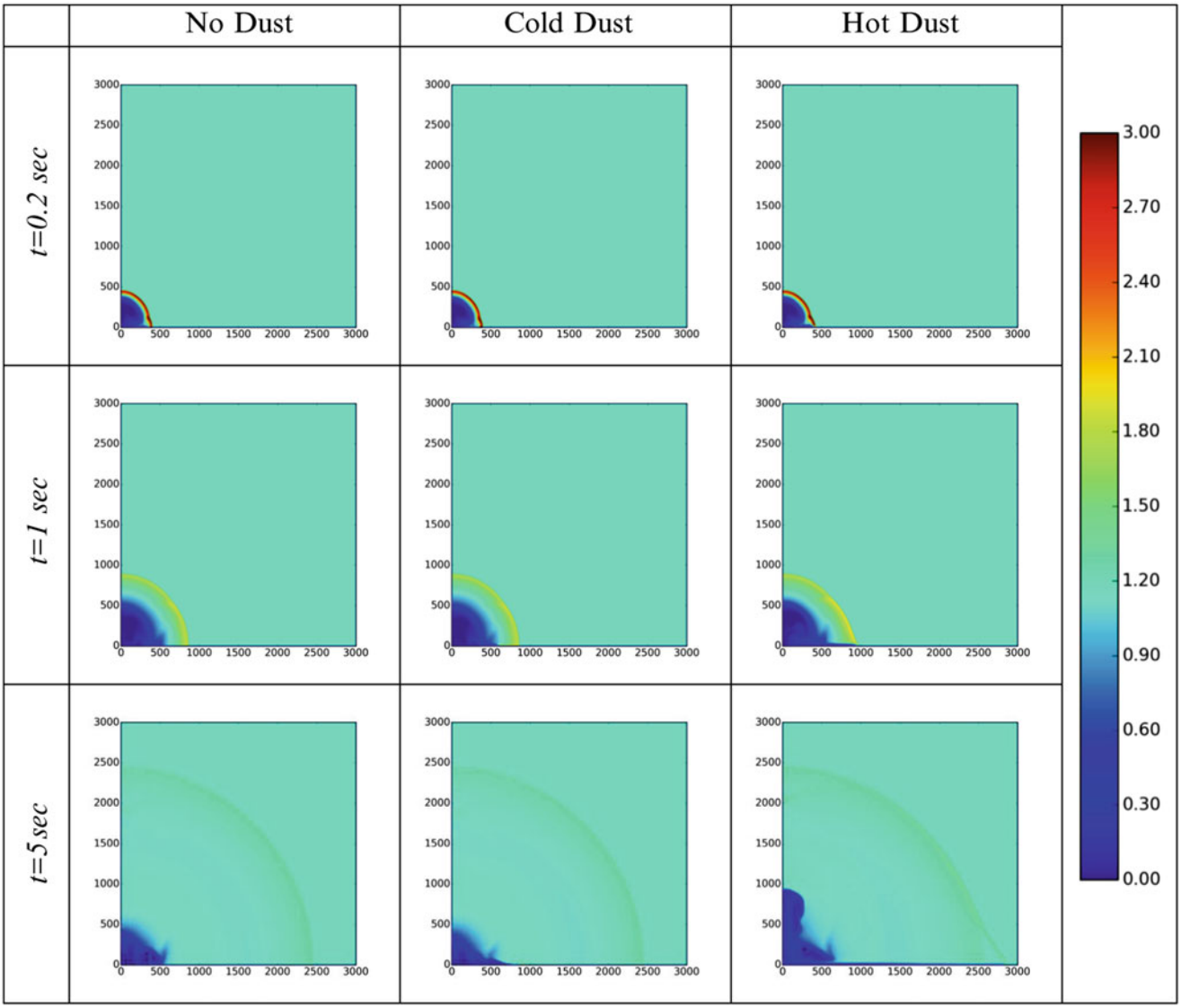

Fig. 1 Total suspension density at three different times for case of pure air without sweep-up (*left column*); sweep-up of dust in room temperature (*middle*); and sweep-up of hot dust (25, 000°, *right column*). Color indicates density in kg/m^3. All values higher than 3 kg/m^3 appear in the same color

takes place, has arrived the threshold value, and subsequent lofting happens due to local instances of high velocity such as in vortices, but not at the front.

Conclusions

The turbulent blowing boundary layer theory is essentially an extension of turbulent boundary layer theory of mass transfer (e.g., evaporation or condensation from a surface). The standard theory is extended for cases in which the turbulent mass flux affects heat or momentum flux. However, the dust lofting boundary layer theory is not fully complete and can be completed if we turn back to the analogous problem of evaporation. Here we demonstrate how the power law dependence of density and velocity on height may relate to physical characteristics of the rough dust laden surface.

The computational scheme has been embedded in a second-order GRP simulation code. Effect of dust lofting on blast wave propagation has been examined for several scenarios of nuclear explosions. It was found that as long as the underlying surface is treated as a rigid ground (underlying surface loading and unloading is ignored), changes of

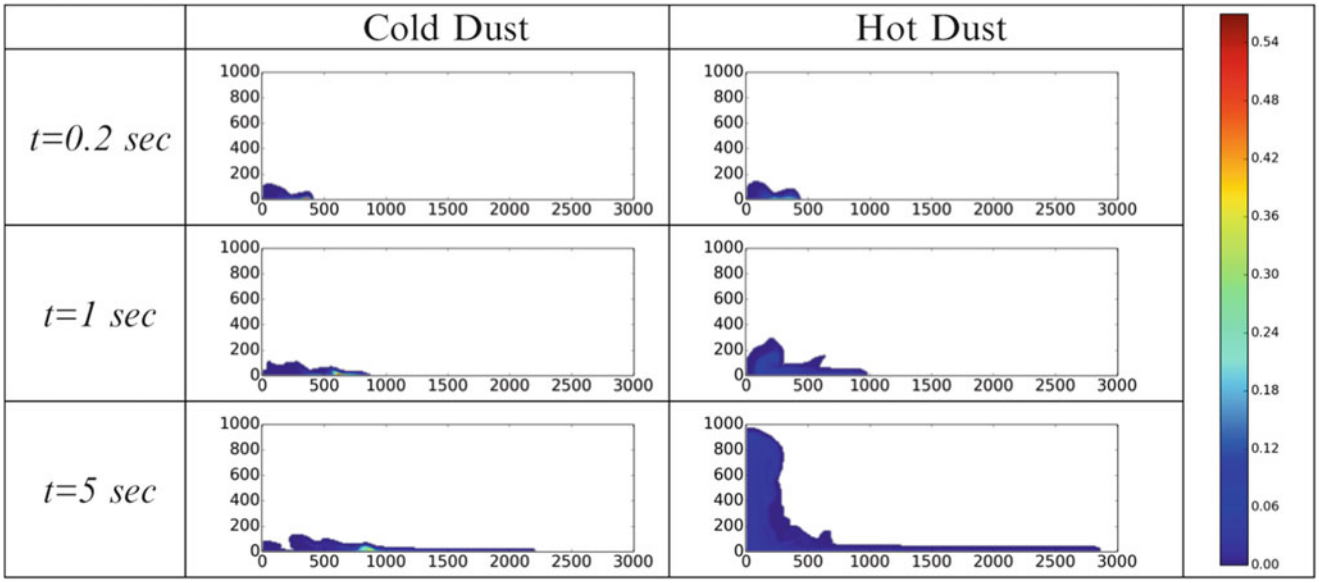

Fig. 2 Dust density at three different times for cases of "cold" (*left*) and "hot" (*right*) dust lofting

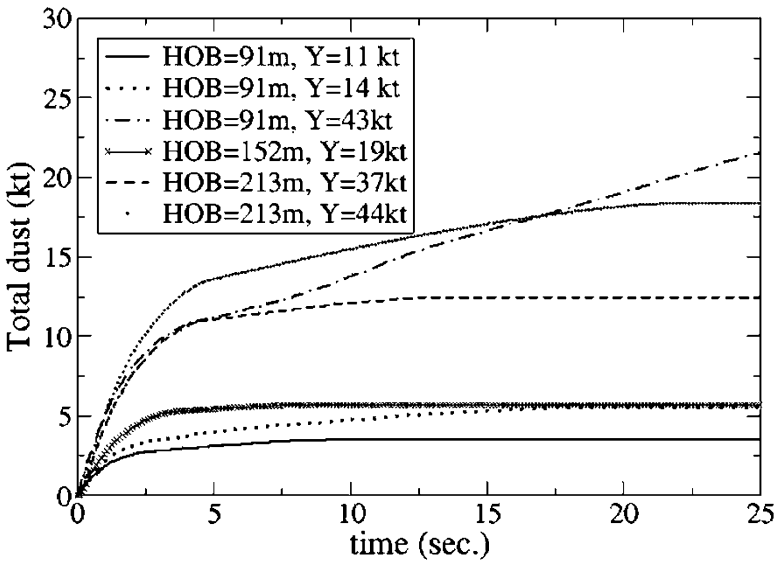

Fig. 3 Total amount of lofted dust (kt) as function of time for various values of yield (Y) and height of burst (HOB)

mass fraction do not make a major difference in blast wave behavior and mitigation due to dust lofting is negligible. However, the initial temperature of the lofted dust has a significant effect on shaping dust distribution and possibly precursor formation.

References

1. Glasstone, S., Dolan, P.J.: The effects of nuclear weapons, 3rd edition. Published by the USUOD & DOE (1977)
2. Needham, C.E.: Blast waves. Springer, Berlin (2010)
3. Mirels, H.: Blowing model for turbulent boundary layer dust ingestion. AIAA J. **22**, 1582–1589 (1984)
4. Hartenbaum, B.: Lofting of particulates by a high speed wind. Technical report No. DNA2737, Prepared by Applied Theory, Inc. for the DNA, Alexandria, VA (1971)
5. Gaj, R.A., Small, R.D.: Target area operating conditions—dust lofting from natural surfaces. Technical Report DNA-TR-90-71, Prepared by Pacific-Syerra Research Corporation for the DNA, Alexandria, VA (1991)
6. Kuhl, A.L., Chien, K.-Y., Ferguson, R.E., Collins, J.P., Glaz, H.M., Colella, P.: Simulation of a turbulent, dusty layer behind a shock. In: Kim, Y.W. (ed.) Proc 17th Intl Symp on Shock Waves and Shock Tubes AIP Conference Proceedings, vol. 208. American Institute of Physics, New York (1990)

7. Ben-Artzi, M., Falcovitz, J.: Generalized Riemann problems in computational fluid dynamics. Cambridge University Press, Cambridge (2003)
8. Lefler, Y., Pistinner, S., Sadot, O., Yaffe, A.: Dust lofting behind shock wave, these proceedings Chapter 132.
9. Rudinger, G.: Fundamentals of gas-particle flow. Elsevier, New York (1980)
10. Brighton, P.W.M.: Evaporation from a plane liquid surface into a turbulent boundary layer. J. Fluid Mech. **159**, 323–345 (1985)
11. Hawthorne, H.A. (Ed.): Compilation of local fallout data from test detonations 1945–1962. DNA, Alexandria, VA (1979)

Dust Lofting Behind a Shock Wave

Y. Lefler, S. Pistinner, Oren Sadot, and A. Yaffe

Introduction

Dust lofting behind shock waves is an intriguing physical phenomenon with significant implications on different applicable processes. The most well-known applications are coal dust explosions and nuclear blast waves [1]. Explosions that take place in air above ground surface generate a blast wave that eventually hits the ground surface. The initial blast wave front is reflected off surface creating a shear flow behind the reflected shock. The reflected shock might merge with the first shock generating a Mach stem.

When the surface is covered with or composed of granular material such as sand or dust, the shock wave sliding on the granular surface might induce particle lifting. However, prior to shear lifting the ground, unloading process might result in lifting as well. Following this initial impact lifting, the reflected shock front moves over the terrain surface and generates a turbulent boundary layer, in which significant amounts of dust might be lofted into the air.

Dust lofting from eroding surfaces is not unique to the phenomena of flows behind shock or blast waves. In fact it is quite ubiquitous in daily life and windblown dust is a fairly well-known and studied phenomenon. In this study, we aim to identify dust lofting features that are unique to shock wave, as opposed to subsonic flows generated in wind tunnels [2]. The present study, which is carried in conjunction with shock tube experiments, corresponds to the dilute suspension regime of dust lofting. The shock tube physics adds to the wind tunnel physics ingredients of high-pressure and temperature region created behind the shock wave, and the transient time dependent phenomena associated with the pressure loading and unloading from the underlying surfaces.

The shock tube capabilities are adequate to study the pressure range induced at the late times of blast wave propagation. Whereas, in simulations of blast waves [3], due to computer limitation, one needs to take the dust lofting effect into account via analytical boundary conditions. The smaller dimension of a shock tube, the limitations associated with full scale blast simulations are somewhat less strict, and allow one a higher resolution modeling of the dust lofting process.

In all cases of dust lofting, or ablating/eroding surfaces, in air, the gas flow is the main flow, and it is injected and mixes with small solid particles, i.e., dust. These particles possess different thermodynamic properties, and are denser compared to the main gas flow. In order to demonstrate dust injection from the dust laden into the gas flow, a model must allow for dynamic boundary conditions that are affected by the shear flux above the dust laden.

The shock tube experiments modeled here are as follows: a shock wave propagates through a shock tube filled with air. As it moves into an experimental chamber it flows over a dusty surface (100 μ NaCl) which is resting on the bottom of the shock tube. The burst of air trailing the shock wave generates a turbulent boundary layer over the dusty surface, and lofts dust either from this process or due to the release of the pressure wave which is reflected from the bottom of the sock tube after it has traversed the dust layer.

Governing Equations

As a first step, we describe the dust and air mixture, assuming the volume fraction of the levitating dust is low enough, such that at every point of flow the dusty phase volume is negligible as compared to the air volume. Under this approximation, the dust particles don't collide, hence the dusty phase does not generate its own stress field. The dust density

Y. Lefler (✉) • S. Pistinner
Soreq Nuclear Research Center, Yavne, Israel
e-mail: yaeleff@gmail.com

O. Sadot
Mechanical Engineering Department, Faculty of Engineering Sciences, Ben Gurion University of the Negev, Beer Sheva 8410501, ISRAEL

A. Yaffe
Ben-Gurion University of the Negev, Beer Sheva, Israel

G. Ben-Dor et al. (eds.), *30th International Symposium on Shock Waves 1*, DOI 10.1007/978-3-319-46213-4_132

(as a solid) is greater than that of the air (the particles have a density of the order 1–3 g/cm^3, while the gasses have a density of 1–2 $\times$ 10^{-3} g/cm^3), so it is not possible to assume that the air-dust mixture is without significant effect on the flow characteristics.

Given below are the governing equations for dilute suspension flow containing gas and dust, when the dust volume is negligible to the volume of gas (but the mass fraction is comparable). These are expressed in vector differential form in full three dimensions:

$$\frac{\partial}{\partial t}\rho + \nabla \cdot (\rho \bar{V}) = 0. \tag{1}$$

Equation (1) is the *continuity* equation of the mixture; ρ denotes the mixture density and V the velocity field of the mixture.

The momentum and energy equations of particles with a given radius r are solved assuming they move with main flow in the direction perpendicular to the gravitational field, and reach terminal velocities in the direction parallel to the gravitational field. Thus, it implicitly implies local mechanical equilibrium. Another assumption is that the dust and air are in thermal equilibrium. According to the above assumptions, it is required to formulate and solve numerically only the mass conservation equation for particles within a radius of r. The corresponding equation is:

$$\begin{aligned}\frac{\partial(\rho\alpha_{\mathrm{m}})}{\partial t} + \nabla \cdot (\rho\alpha_{\mathrm{m}}\bar{V}) + \nabla \cdot (\rho\alpha_{\mathrm{m}} V_{\mathrm{T}}\hat{z}\,) \\ = \nabla \cdot [\kappa_{\mathrm{M}} \nabla(\rho\alpha_{\mathrm{m}})],\end{aligned} \tag{2}$$

where α_{m} denotes the mass fraction, V_{T} represents the terminal velocity for a falling particle within radius r, and κ_{M} is the turbulent diffusion coefficient. The implicit assumption is that there is instantaneous momentum equilibration and thus, a negligible velocity difference between the gas and the solid particles in the horizontal direction and that the particle falls at its terminal velocity. For simplicity in these simulations using Prandtl's mixing length theory we set:

$$\kappa_{\mathrm{M}} \approx \kappa_{\mathrm{vk}} U_* z \quad V_{\mathrm{T}} \approx 0\,, \tag{3}$$

where $\kappa_{\mathrm{vk}} \approx 0.4$ is the von Karmann coefficient, U_* is the turbulent friction velocity and its value is roughly 5 % of the free upstream value (U_0), which in this case is velocity behind the shock. The momentum equation of the mixture is:

$$\frac{\partial(\rho\bar{V})}{\partial t} + \nabla \cdot (\rho\bar{V}\bar{V}) = -\nabla p + \rho g + \nabla \cdot (\mu_{\mathrm{MOM}} \nabla \bar{V}), \tag{4}$$

where μ_{MOM} is the turbulence viscosity, g the gravity of earth, and p is the mixture pressure (particulates do not have a pressure of their own).

The energy equation of the mixture is:

$$\frac{\partial(\rho E)}{\partial t} + \nabla \cdot (\rho\bar{V}h) = \nabla \cdot (\kappa_{\mathrm{E}} \nabla \bar{T}), \tag{5}$$

where h is the enthalpy of the mixture, E is its internal energy, and κ_{E} its heat transfer coefficient. All transport coefficients are given by:

$$\kappa_{\mathrm{E}} \approx P_{r,t}\,\mu_{\mathrm{MOM}} \quad ; \kappa_{\mathrm{M}} \approx D_{a,t}\,\mu_{\mathrm{MOM}} \tag{6}$$

where $P_{r,t}$ and $D_{a,t}$ are the turbulent Prandtl and Dalton number, respectively, and their values range between 0.85 and 1.

To complete this set of equation, we can make use of the ideal gas equation of state. We deal with a diluted suspension. Thus, the energy of the suspension is given by [4]:

$$E = C_{\mathrm{v\,air}} T[1 - \alpha_{\mathrm{m}} + \gamma_{\mathrm{air}}\alpha_{\mathrm{m}}\delta_{\mathrm{eff}}(t)],$$

$$\delta_{\mathrm{eff}}(t) \equiv \delta\left[1 - \mathrm{e}^{-\left(\frac{t}{\tau_{\mathrm{eq}}}\right)} + \frac{\Delta T}{T}\mathrm{e}^{-\left(\frac{t}{\tau_{\mathrm{eq}}}\right)}\right], \tag{7}$$

where δ is the heat capacity ratio of the gas and the solid phase, ΔT is the initial temperature difference between the initial gas and solid particles temperature, lastly τ_{eq} is the equilibration time between the solid particles temperature and the air temperature. For a wind tunnel $\Delta T = 0$, or $t \gg \tau_{\mathrm{eq}}$, for a shock tube or a heated surface $\Delta T = T_{\mathrm{surf}} - T$ and the ratio t/τ_{eq} depends on the time scale of shock propagation vs. the time scale for heat equilibration (which depends on a typical particle radius). If the surface is heated [3], the temperature difference is positive and the mass addition heats the gas. In a shock tube it is negative and cooling of the gas might occur. Having used $\delta_{\mathrm{eff}}(t)$, the pressure is related to the density and internal energy by the ideal gas equation of state via:

$$p = \{\gamma[\alpha_{\mathrm{m}}(t)] - 1\}\rho E, \tag{8}$$

where the suspension adiabatic index is given by:

$$\gamma[\alpha_{\mathrm{m}}(t)] = \gamma_{\mathrm{air}} \frac{1 - \alpha_{\mathrm{m}}[1 - \delta(t)]}{1 - \alpha_{\mathrm{m}}[1 - \gamma_{\mathrm{air}}\delta_{\mathrm{eff}}(t)]}, \tag{9}$$

$\gamma_{\mathrm{air}} \approx 1.4$ is the adiabatic index of air. Assuming instantaneous thermodynamic equilibrium between the gas and the dust implies setting $t \gg \tau_{\mathrm{eq}}$, an assumption that is physically valid for wind tunnel experiments but might be physically invalid for shock tube experiments. In the case of shock tubes, the valid assumption is $t \leq \tau_{\mathrm{eq}}$, and $\Delta T < 0$. The case of blast waves might be even more complicated [3]. Thus, the variant composition influences the internal energy since the dust has its own heat capacity that differs

from air. The pressure depends on the dust fraction mass only if the dust had a different temperature. In other words—the suspension pressure and the air pressure are exactly the same as long as the initial temperature of the lofted dust is ignored and instantaneous temperature equilibration is assumed ($t \gg \tau_{eq}$).

If temperature equilibration occurs within the boundary layer, the problem is analogous to a problem of thermally ablated surface, which was utilized [5] to calculate momentum dissipation under the so-called blowing boundary layer theory. Ignoring gravity it is possible [5, 6] to get an expression for the sweep-up masses. The expression for dust lofting appropriate for the high flow (wind) speeds associated with shock tubes and blast waves or tornado flow for that matter. This model depends explicitly on the threshold shear velocity-$U_{*\,\mathrm{th}}$ (and hence on surface type) required to initiate dust lofting:

$$F \approx \frac{1.80\rho_0}{U_{*\mathrm{th}}^{0.24}[2.87 + 1.58\log(x/K_\mathrm{s})]^{2.80}} {U_0}^{1.24} \approx 6 \times 10^{-4}\rho_0 U_0 \left(\frac{U_0}{U_{*\mathrm{th}}}\right)^{0.24}, \quad (10)$$

where x is the distance behind the shock wave and $K_\mathrm{s} \approx 0.001$ m is the roughness height in shock tubes (containing 100 μ NaCl particles) for $x = 0.02$ m. The assumption is that the threshold friction velocity remains constant throughout the period sweep process and is characteristic for different granular material types. The latter is converted in terms of material parameters to:

$$F \approx \frac{1.80\rho_0}{U_{*\mathrm{th}}^{0.24}[2.87 + 1.58\log(x/K_\mathrm{s})]^{2.80}} {U_0}^{1.24} \approx 6 \times 10^{-2}\rho_0 U_0 \left(\frac{U_0}{U_{*\mathrm{th}}}\right)^{0.24}. \quad (11)$$

Utilizing this in terms of boundary conditions in the OpenFOAM platform, assuming $\alpha_\mathrm{m} = 0.6$ at the surface, we get as influx speed to the total mass at the bottom:

$$v_\mathrm{z} \approx 4 \times 10^{-2}\rho_0 U_0 \left(\frac{U_0}{U_{*\mathrm{th}}}\right)^{0.24}. \quad (12)$$

Numerical simulations were carried out using this modified version of OpenFOAM. In these simulations the supply of surface particles is unlimited and the particles reach velocity and temperature equilibration with the ambient fluid soon after their injection into the boundary layer.

Results

In Fig. 1, we show part of the test chamber of the shock tube (30 cm length, 8 cm height). In Fig. 1a, one can clearly see the shock and the fact that no dust is lofted yet. In Fig. 1b, the shock has left the frame and dust lofting is observed.

In Fig. 2, we show preliminary numerical simulations. In Fig. 2a, the shock propagates in the shock tube but has not yet reached the test chamber. In Fig. 2b, the shock has flown above the test chamber and dust lofting (the colored layer) right behind the shock front can be observed.

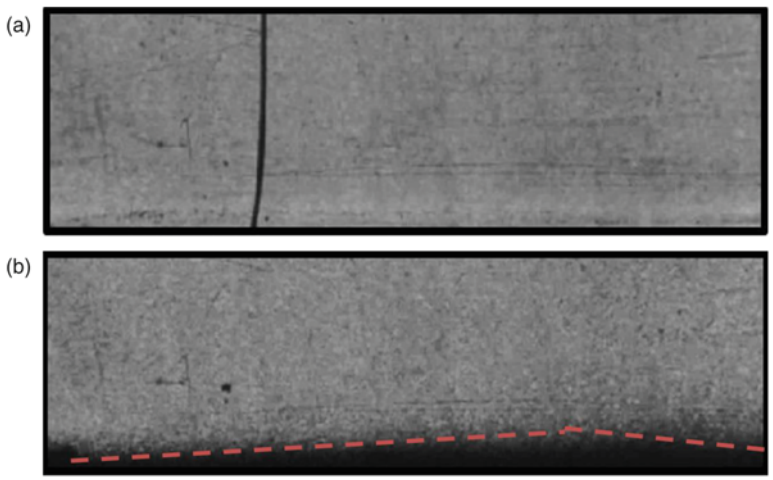

Fig. 1 Test chamber of the shock tube

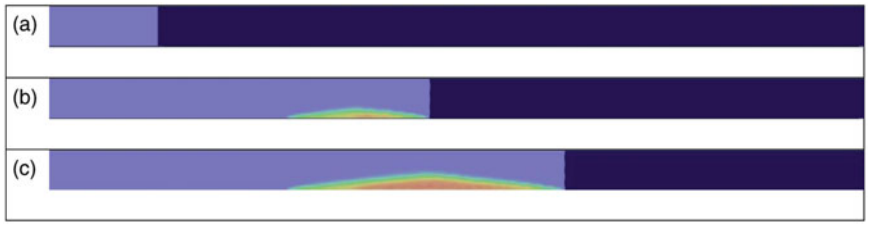

Fig. 2 Dust fraction ( ) overlaid with the shock front as a function of time

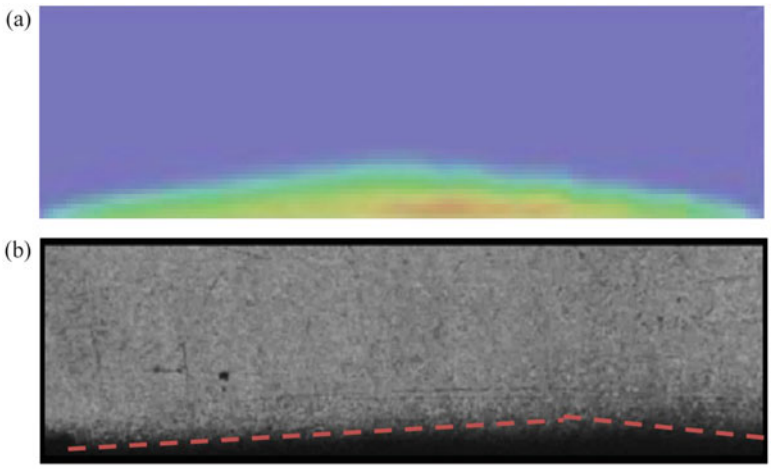

Fig. 3 A qualitative comparison of the numerical model (**a**) and experimental results (**b**)

Figure 2c shows the dust layer continuous to evolve and grow. Figure 3 shows a qualitative visual comparison of the experiment and the numerical model.

Conclusions

In this chapter, we present preliminary results of dust lofting in shock tubes and their numerical modeling. The role of the dust initial temperature [3] and its affect on utilizing experimentally calibrated expression for dust lofting are discussed. It is shown that the initial dust temperature might play an essential role on the proper parameterization of dust lofting under shock or blast conditions. Future numerical simulations will include a consistent modeling of the turbulent boundary layer via equations that model turbulence. Despite the raw state of the numerical model it manages to describe qualitatively all the essential ingredients of the dust lofting phenomenon.

References

1. Needham, C.E.: Blast waves. Springer, Berlin (2010)
2. Gillette, D.A.: Tests with a portable wind tunnel for determining wind erosion threshold velocities. Atmos. Environ. **12**, 2309–2313 (1978)
3. Lipshtat, A., Pistinner, S.: These proceedings
4. Rudinger, G.: Fundamentals of gas-particle flow. Elsevier, New York (1980)
5. Mirels, H.: Blowing model for turbulent boundary layer dust ingestion. AIAA J. **22**, 1582–1589 (1984)
6. Gaj, R.A., Small, R.D.: Target area operating conditions-dust lofting from natural surfaces. Technical report, Pacific-Sierra Research Corporation (1991)

Shock Ignition of Reactive Particles

M.G. Omang and J.K. Trulsen

Introduction

In this paper we study shock ignition of reactive particles in a shock tube environment. When shock propagates through a dust cloud consisting of reactive particles, the cloud is shifted, compressed, and the internal cloud temperature increased. In most experimental studies a closed-end shock tube is used to allow the shock to reflect and propagate through the cloud a second time, further increasing the dust particle temperature. We use a multi-phase version of the numerical Regularized Smoothed Particle Hydrodynamics (RSPH) method [1], to study shock ignition, and discuss important parameters that affect the particle ignition process.

Combustion Model

SPH is a Lagrangian simulation method [2]. In single-phase SPH the fluid, for instance a gas, is modelled by a population of interacting simulation (or interpolation) particles, each with properties like position, velocity, mass, density, pressure, and internal energy. The evolution of each particle is determined by a suitable set of equations of motion. In RSPH the accuracy of the simulation method is improved by subjecting the particle populations to a periodic spatial regularization process [3]. In two-phase SPH, for instance a gas and a dust particle cloud, each phase is described by separate populations of simulation particles and corresponding separate sets of equations of motion. The two sets of equations of motion are coupled through source terms [1]. In the case of non-reactive particles, the two phases are coupled mainly through heat exchange and drag terms. In the present work we use Ingebo drag coefficient [4], the heat exchange Nusselt number [5], and dynamic viscosity [6].

In the case of reactive particles subject to ignition and combustion processes, radiation and mass exchange between the phases must also be taken into account. The ignition and combustion process is described in terms of a mass burning rate given as a function of particle temperature. As a result of the burning process, particle mass is transformed into the gas phase, with a corresponding transfer of internal energy. In the present work reactive aluminum particles with a typical size of 10 μm are studied. The aluminum particle cloud is assumed to be dilute, with an aluminum void fraction $\theta_{\mathrm{d}} \ll 1$, allowing effects of particle–particle collisions to be neglected.

Two different burning rate models are studied in closer detail. The simplest mass burning rate model is given in [7]

$$J_{\mathrm{diff}} = \frac{3\theta_d \widehat{\rho_d}}{\tau}(1 + 0.276\sqrt{Re}) \tag{1}$$

where

$$\tau = \frac{K d_d^2}{\phi^{0.9}}. \tag{2}$$

Here ϕ is the sum of the molar fraction of oxidant in the gaseous phase, $\widehat{\rho}_d$ is the particle mass density per unit volume, d_{d} is the particle diameter, K is a constant, and the particle Reynolds number Re is given as

$$Re = \frac{\rho_g \theta_g d_d |v_g - v_d|}{\mu}, \tag{3}$$

M.G. Omang (✉)
Institute of Theoretical Astrophysics, University of Oslo, Postbox 1029 Blindern, Oslo, Norway

Norwegian Defence Estates Agency, Postbox 405 Sentrum, Oslo N-0103, Norway
e-mail: momang@astro.uio.no

J.K. Trulsen
Institute of Theoretical Astrophysics, University of Oslo, Postbox 1029 Blindern, Oslo, Norway

G. Ben-Dor et al. (eds.), *30th International Symposium on Shock Waves 1*, DOI 10.1007/978-3-319-46213-4_133

where v is the velocity and μ is the dynamic viscosity. The burning is assumed to set in as soon as the particle temperature $T_{\rm d}$ exceeds a given threshold temperature $T_{\rm ign}$. Different values of $T_{\rm ign}$ for Al particles have been suggested in the literature. In the present study an ignition threshold value of $T_{\rm ign} = 1350$ K is used [8].

In the second burning rate model [9] a more gradual transition to the burning stage is assumed

$$J_{\rm tot} = \left(\frac{1}{J_{\rm kin}} + \frac{1}{J_{\rm diff}}\right)^{-1}, \tag{4}$$

with $J_{\rm kin}$ given as

$$J_{\rm kin} = Z_{hyb}\frac{6\theta_d}{d}\exp -\frac{E_a}{RT_d}. \tag{5}$$

In this model the specification of a particle ignition temperature $T_{\rm ign}$ is replaced by a specification of the constant E_a. Five different values for E_a are studied. Different E_a values give rise to different "effective" ignition temperatures, with smaller E_a-values corresponding to lower ignition temperature. The values of the constants $Z_{\rm hyb}$, E_a, K used in this study are given in Table 1. The difference between the two burning rate models is illustrated in Fig. 1a for a chosen value of E_a. The ignition temperature for the simple burning rate model is indicated by the vertical red line. The two models give rise to significantly different simulation results.

When shock propagates through a cloud of aluminum particles, the shock is locally retarded, and the aluminum cloud is displaced, compressed, and heated. In a closed-end shock tube the shock is reflected and propagates through the cloud a second time, further increasing the aluminum particle temperature.

Table 1 Test parameters for the hybrid combustion model

Figure	K	$Z_{\rm hyb}$	E_a	ϕ	d [μm]	ρ [kg/m^3]
1b, 4a–c	$1.5 \cdot 10^6$	3500	$1.6 \cdot 10^8$	1.0	10	2702
1b, 4c	$1.5 \cdot 10^6$	3500	$1.8 \cdot 10^8$	1.0	10	2702
1a, b, 4c	$1.5 \cdot 10^6$	3500	$2.0 \cdot 10^8$	1.0	10	2702
1b, 4c	$1.5 \cdot 10^6$	3500	$2.2 \cdot 10^8$	1.0	10	2702

Problem Description and Results

The number of experimental studies on shock ignition of aluminum particles published is rather sparse and often not fully documented. Here we have designed a representative test experiment, as illustrated in Fig. 2, where a sketch of the shock tube is presented. The shock tube is a closed-end tube $L_{\rm ST} = 5$ m long, with a narrow driver section of $L_{\rm Dr} = 0.5$ m (Table 2), filled with high pressure and high density gas, generating a Mach $M_{\rm s} = 3.69$ shock wave propagating from left to right. In our 2D simulation the propagating shock hits an initially homogeneous, stationary circular-shaped aluminum dust cloud of radius 0.4 m located at $L_{\rm Al} = 1.5$ m. The aluminum has an initial temperature of 293.15 K and a void fraction of 0.0005. In Fig. 3 the two upper panels show the gas and aluminum particle temperatures prior to ignition, whereas the lower panels show gas and aluminum particle temperatures after ignition, when the particle burning process has started. The temperature scales reflect the maximum temperature for the each panel.

When the shock propagates through the aluminum dust cloud, the shock is locally retarded, and the original plane shock front is curved. The aluminum cloud is shifted, heated, and strongly deformed [10, 11]. Due to the curving of the shock front, a Mach reflection will form on the rear side of the cloud. Since the tube is closed-end, the shock is reflected and interacts with the deformed dust cloud a second time. As illustrated in the figure for time $t = 4.2$ ms, a significant, inhomogeneous aluminum temperature increase is observed at the rear end of the cloud. At time $t = 4.4$ ms the reflected shock has propagated further into the rear part of the aluminum cloud, leading to an additional increase in the

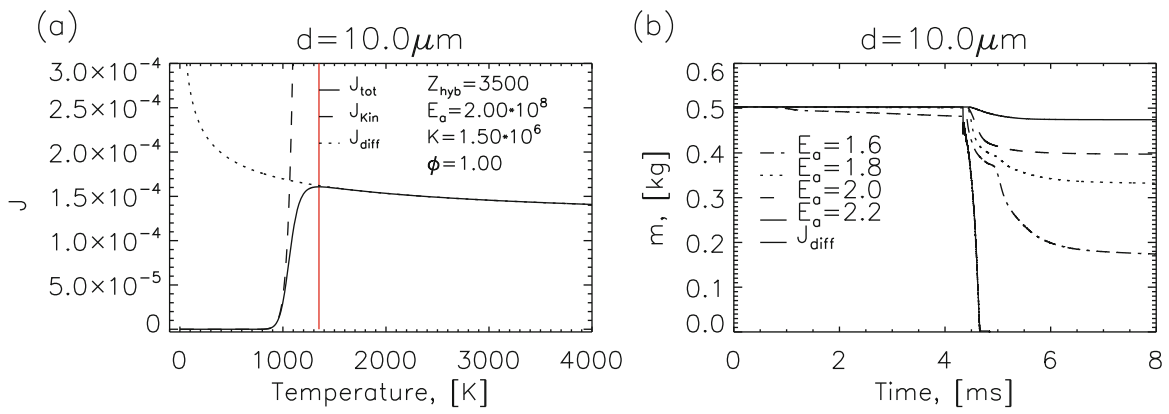

Fig. 1 (**a**) The total aluminum burning rate, $J_{\rm tot}$, (**b**) aluminum mass reduction for different mass-burning ratios

temperature and an ongoing aluminum dust burning. For the simulation results presented in Fig. 3, the mass-burning description J_{diff} is used, with a threshold ignition temperature of 1350 K. The burning aluminum dust is transformed into gas phase, the burning process leading to a significant local increase in gas temperature. As the aluminum particles burn, the total aluminum mass decreases, and the particles eventually disappear.

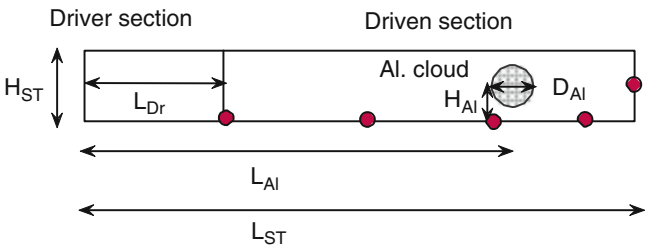

Fig. 2 Sketch of the closed-end shock tube, with a short driver section. An aluminium cloud is positioned in the test section

Figure 1b illustrates the total mass loss due to aluminum particle burning, for different burning rate models and different choices of parameters. As the figure illustrates, the choice of the simplified mass-burning rate J_{diff} clearly is the most efficient for aluminum particle burning. The other four curves illustrate the effect of changing the E_a parameter in the J_{tot} model. The lower the choice of the E_a value is, the lower is the temperature level for which significant burning is observed.

In the case of $E_a = 1.6 \cdot 10^8$ an extra kink in the total mass curve is observed in Fig. 1b at time $t \approx 5.0$ ms. This is probably due to the geometry of the burning aluminum cloud, as illustrated in Fig. 4a at time $t = 4.7$ ms. The temperature is higher and the burning is present both in the smaller separate parts of the strongly deformed dust cloud

Table 2 Shock tube parameters

Test	L_{ST} [m]	H_{ST} [m]	L_{Dr} [m]	L_{Al} [m]	H_{Al} [m]	D_{Al} [m]
1	5	3	0.5	1.5	1.5	0.4

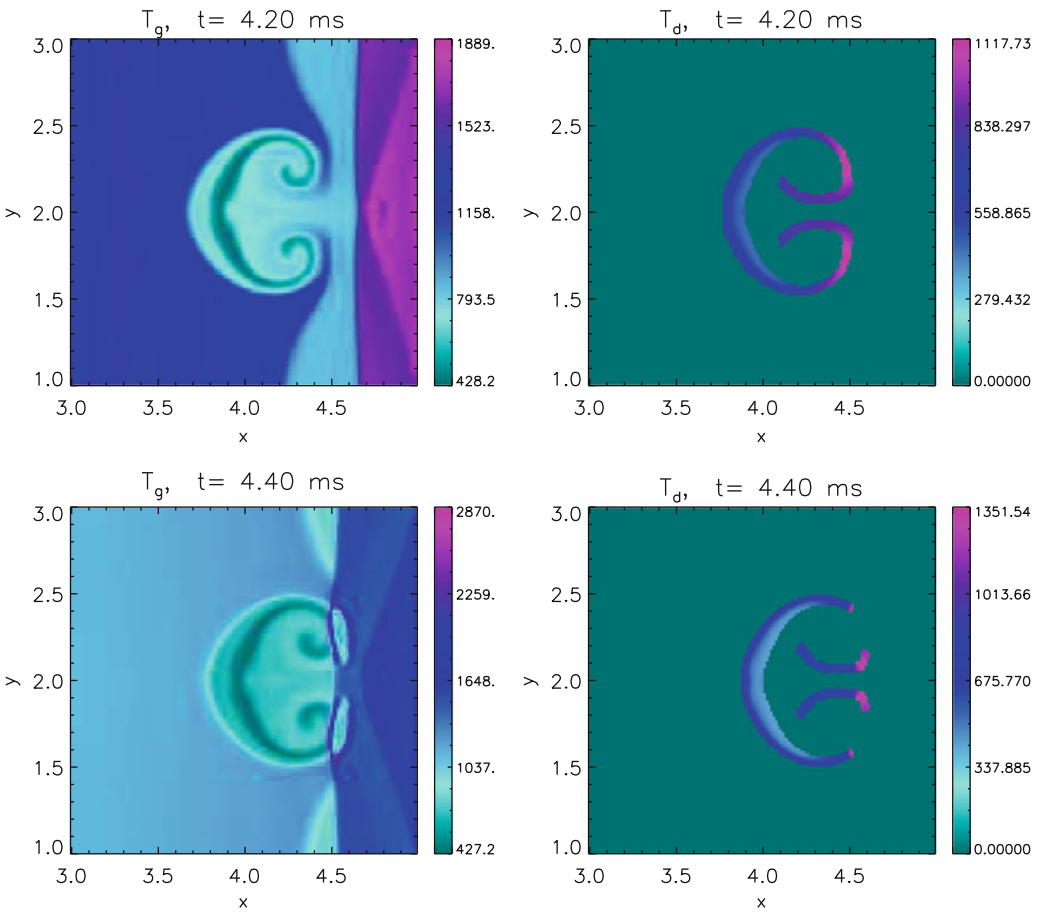

Fig. 3 *Left two panels*: gas temperature and aluminium particle temperature prior to ignition. *Right two panels*: gas and ignited aluminum particles temperature after shock reflection and particle ignition

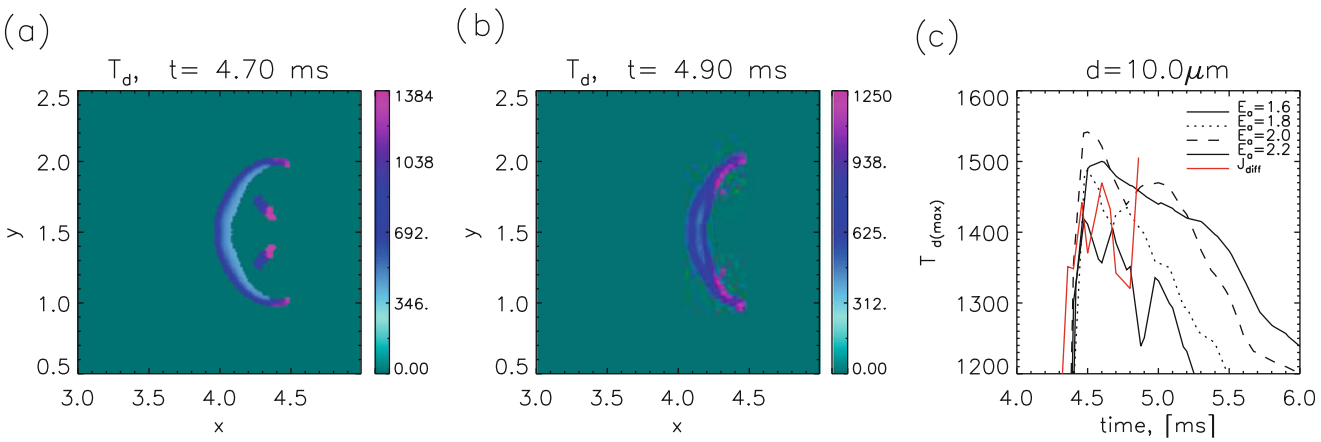

Fig. 4 Temperature of burning aluminum dust at (**a**) $t = 4.70$ ms, and (**b**) $t = 4.9$ ms. (**c**) maximum overall aluminum dust temperature at selected time-steps

close to the centerline, as well as on the side wings of the half circle. Due to the limited amount of aluminum mass presently available for the burning process, the mass transfer rate is decreasing. At the later time $t = 4.9$ ms depicted in Fig. 4b the central parts of the cloud have burned out, but the reflected shock is now approaching the remaining central front part of the cloud. With the now increasing aluminum mass available for the burning process, the mass transfer rate is about to pick up.

Figure 4c is a plot of the maximum dust temperature for a selection of regularly distributed time-steps. The solid line represents the $E_a = 1.6 \cdot 10^8$ choice, whereas the red solid line shows the J_{diff} model. In the case of the latter model, the aluminum particles burn out at $t = 4.87$ ms, which is why the curve ends here. The dip in the maximum temperature for $E_a = 1.6 \cdot 10^8$ seen at time $t \approx 4.9$ ms shows good correlation with the behavior of the total aluminum mass curve in Fig. 1b. With the reduced aluminum mass transfer rate due to particle burnout, the particle temperature cannot be maintained. It is only as the burning process reaches the remaining central part at the front of the original dust cloud that the particle temperature is again temporarily increased.

Conclusions and Further Work

In the present study we investigated some important parameters in the process of shock ignition of aluminum dust clouds. Due to lack of available detailed and complete experimental data we have been led to design a number of numerical tests for different burning rate models and model parameters. For the validation of numerical codes detailed quantitative experiments are highly desired.

The burning of aluminum particles is described with a mass-exchange formulation, and two different models are studied in closer detail. The results presented clearly illustrate the importance of the choice of model, and choices of parameters. Seemingly small changes in the models may lead to significant changes in the final results. The mass-exchange model J_{diff} with its sudden onset of burning at the ignition temperature T_{ign} is demonstrated to be much more efficient in the burning of aluminum particles, even if the J_{tot} burning model is designed to start at a slightly lower temperature. We have restricted the present study to look at shock wave interactions with dust clouds of a single particle size, using between 200,000 and 600,000 simulation gas particles, and 14,000 simulation dust particles. In future work the effect of changing the particle size or considering clouds with particles of different sizes will be of interest. The results demonstrate that the RSPH method is promising one for more complex two-phase shock and combustion studies.

References

1. Omang, M.G., Trulsen, J.K.: Multi-phase shock simulations with smoothed particle hydrodynamics (sph). Shock Waves **24** (5), 521–536 (2014)
2. Monaghan, J.J.: Smoothed particle hydrodynamics. Rep. Prog. Phys. **68** (8), 1703–1759 (2005)
3. Børve, S., Omang, M., Trulsen, J.: Regularized smoothed particle hydrodynamics: a new approach to simulating magnetohydrodynamic shocks. Astrophys. J. **561**, 82–93 (2001)
4. Ingebo, R.D.: Drag coefficients for droplets and solid spheres in clouds accelerating in air streams. Technical Report TN 3762, NACA Technical Note TN (1956)
5. Knudsen, J.G., Katz, D.L.: Fluid Mechanics and Heat Transfer. McGraw-Hill, New York (1958)
6. Chapman, S., Cowling, T.G.: The Mathematical Theory of Non-Uniform Gases. Cambridge University Press, Cambridge (1961)

7. Khasainov, B.A., Veyssiere, B.: Analysis of the steady double-front detonation structure for detonable gas laden with aluminium particles. Arch. Combust. **7** (3/4), 333–352 (1987)
8. Veyssiere, B., Khasainov, B.A.: A model for steady, plane, double-front detonations (DFD) in gaseous explosive mixtures with aluminum particles in suspension. Combust. Flame **85**, 241–253 (1991)
9. Briand, A., Veyssiere, B., Khasainov, B.A.: Modelling of detonation cellular structure in aluminium suspensions. Shock Waves **20** (6), 521–529 (2010)
10. Omang, M., Trulsen, J.: Shock propagation through bounded dust clouds. In: Book of Proceedings, 20th International Shock Interaction Symposium. Department of Mechanics, pp. 125–128. KTH, Stockholm (2012)
11. Omang, M., Trulsen, J.: Shock interactions with reacting and non-reacting particles. In: Krassovskaya, I., Podlaskin, A. (eds.) Book of Proceedings, 21th International Shock Interaction Symposium, Riga, Latvia, pp. 34–37 (2014)

Author Index

G. Ben-Dor et al. (eds.), *30th International Symposium on Shock Waves 1*, DOI 10.1007/978-3-319-46213-4

Subject Index

G. Ben-Dor et al. (eds.), *30th International Symposium on Shock Waves 1*, DOI 10.1007/978-3-319-46213-4

T